Progress in Landslide Research and Technology

Biljana Abolmasov
Irasema Alcántara-Ayala
Željko Arbanas
David Huntley
Kazuo Konagai
Snježana Mihalić Arbanas
Matjaž Mikoš
Maneesha V Ramesh
Kyoji Sassa
Shinji Sassa
Huiming Tang
Binod Tiwari
Editors

Progress in Landslide Research and Technology, Volume 3 Issue 1, 2024

OPEN ACCESS

Springer

Progress in Landslide Research and Technology

The Open Access book series of the International Consortium on Landslides (ICL) aims to be the common platform for the publication of recent progress in landslide research and technology for practical applications and the benefit of society contributing to the Kyoto Landslide Commitment 2020, which is expected to continue up to 2030 and even beyond for the global promotion of understanding and reducing landslide disaster risk as well as the 2030 Agenda Sustainable Development Goals. The contributions include original and review articles, case studies, activity reports and teaching tools for the promotion of understanding and reducing landslide disaster risks.

Biljana Abolmasov • Irasema Alcántara-Ayala •
Željko Arbanas • David Huntley •
Kazuo Konagai • Snježana Mihalić Arbanas •
Matjaž Mikoš • Maneesha V. Ramesh •
Kyoji Sassa • Shinji Sassa • Huiming Tang •
Binod Tiwari
Editors

Progress in Landslide Research and Technology, Volume 3 Issue 1, 2024

Springer

ISSN 2731-3794 ISSN 2731-3808 (electronic)
Progress in Landslide Research and Technology
ISBN 978-3-031-55119-2 ISBN 978-3-031-55120-8 (eBook)
https://doi.org/10.1007/978-3-031-55120-8

Cover illustration: Aratozawa landslide induced by the Iwate-Miyagi Inland Earthquake in Miyagi Prefecture, Japan. The total volume of this landslide is estimated to be 67 million m3. The frontal part of this landslide entered into the Aratozawa dam reservoir and caused a tsunami of up to 9 m. (Photograph taken by Kazuo Konagai)

This Springer imprint is published by the registered company Springer Nature Switzerland AG
The registered company address is: Gewerbestrasse 11, 6330 Cham, Switzerland

If disposing of this product, please recycle the paper.

Foreword by Motoko Kotani

In March 2011, the Great East Japan Earthquake attacked the Tohoku Region of Japan. The earthquake triggered a big Tsunami wave. Both the earthquake and the Tsunami gave serious damages on city and town along the coast of the Tohoku area. The third World Congress on Disaster Risk Reduction (WCDRR) was organized in March 2015, the World Bosai Forum every 2 years since then in Sendai, Japan. Tohoku University, where I work as a professor and a vice president for research, locates at Sendai and established the International Research Institute of Disaster Science. The event influenced me a lot to reconsider the relationship between science and society. University has been creating knowledge but to engage more with society, it requires more engagement to transform existing scientific evidence into actionable knowledge and insights, inform policymaking, and steer action toward desired outcomes.

On 16 March 2015 during the 3rd WCDRR, a working session No.4 "Underlying Risk Factors" was co-organized by the International Consortium on Landslides (ICL) and ICL supporting organizations (UNESCO, UNDRR, ISC, IUGS, IUGG, and others). As an output of this session, the Sendai Landslide Partnerships 2015–2025 for Global Promotion of Understanding and Reducing Disaster Risk was adopted. A joint signing ceremony was organized in Sendai city. The Sendai Landslide Partnerships was established with signature by 16 organizations including ISC on the day.

Toward the end of term 2025, to continue this initiative, the ICL and ICL supporting organizations organized the launching session of the Kyoto Landslide Commitment 2020 on 5 November 2020 in Kyoto Japan. In this session, 90 global organizations and David Malone (Under-Secretary-General of the United Nations, UNU Rector) as the chair of the General Conference of KLC2020 signed it. The opening greetings were from Mami Mizutori (UN Special representative for DRR), Daya Reddy President of ISC at that time, and others. KLC2020 was formally launched by the adoption of 2020 Kyoto Declaration "Launching of KLC2020" at the end of session.

I learned the ICL and ICL supporting organizations have launched a new open access book series "Progress in Landslide Research and Technology" to implement for the Kyoto Landslide Commitment 2020. I am honored to write a foreword at the third-year publication (Volume 3) of this new book series. I wish the ICL with ICL supporting organization to succeed to develop the book series as a platform of the Kyoto Landslide Commitment 2020: A Commitment to the Sendai Landslide Partnerships 2015–2025, the Sendai Framework for Disaster Risk Reduction 2015–2030, the 2030 Agenda Sustainable Development Goals, the New Urban Agenda, and the Paris Climate Agreement.

Motoko Kotani
Tohoku University, Sendai, Japan
The International Science Council
for Science and Society, Paris, France

Editorial Board of the Book Series

Qunli Han, Co-chair of the Global Promotion Committee of the International Programme on Landslides and Kyoto Landslide Commitment 2020
Nicola Casagli, Immediate past President of the International Consortium on Landslides
Peter Bobrowsky, Past President of the International Consortium on Landslides

Advisory Members for KLC2020
Abou Amani, Director, Division of Water Sciences, Secretary, Intergovernmental Hydrological Programme (IHP), UNESCO
Soichiro Yasukawa, Chief of Disaster Risk Reduction Unit, UNESCO
Daniel Lebel, Director General, Geological Survey of Canada, Natural Resources Canada, Canada
John Ludden, President of the International Union of Geological Sciences (IUGS)
John LaBrecque, Chair of IUGG GeoRisk Commission, Center for Space Research, University of Texas at Austin, USA
Vassilis Marinos, President of the International Association for the Engineering Geology and the Environment (IAEG)
Paolo Canuti, past President of the International Consortium on Landslides (ICL), Italy
Sàlvano Briceño, First chair of the Global Promotion Committee of the International Programme on Landslides
Badaoui Rouhban, Chair of the KLC2020 Launching Session and Moderator of ISDR-ICL Sendai Landslide Partnerships 2015–2025 Session of 3rd WCDRR in 2015

KLC2020 Official Promoters
Host Organization
International Consortium on Landslides (ICL)/Željko Arbanas

Public Sectors: KLC2020 Official Promoters-Public
International Unions/Associations, Governmental Organizations, Universities and Research Institutes
- The International Union of Geological Sciences (IUGS)/John Ludden
- The International Union of Geodesy and Geophysics (IUGG)/Chris Rizos
- The International Association for the Engineering Geology and the Environment
- Vassilis Marinos International Geosynthetics Society (IGS)/John Kraus
- Geological Survey of Canada, Natural Resources Canada, Canada/Daniel Lebel
- Faculty of Civil and Geodetic Engineering, University of Ljubljana, Slovenia/Matjaž Mikoš
- China University of Geosciences, Wuhan, China/Huiming Tang
- Department of Civil Engineering, National Taiwan University, Chinese Taipei/Louis Ge
- Institute of Rock Structure and Mechanics, the Czech Academy of Sciences/Josef Stemberk
- Institute of Cold Regions Science and Engineering, Northeast Forestry University, China/Wei Shan

Private Sectors: KLC2020 Official Promoters-Private
Companies and Corporation
- Marui & Co. Ltd, Japan
- Nippon Koei Co., Ltd, Japan
- Ellegi srl, Italy
- Chuo Kaihatsu Corporation, Japan
- Godai Kaihatsu Corporation, Japan
- Kiso-Jiban Consultants Co., Ltd, Japan
- Kokusai Kogyo Co., Ltd., Japan
- OSASI Technos, Inc., Japan

Global Promotion Committee of the International Programme on Landslides and Kyoto Landslide Commitment 2020

A Commitment to the Sendai Framework and the Sustainable Development Goals

Chair
Matjaž Mikoš (Faculty of Civil and Geodetic Engineering, University of Ljubljana)

Co-chairs
Qunli Han (Integrated Research on Disaster Risk, IRDR)
Soichiro Yasukawa (Chief of Disaster Risk Reduction Unit, UNESCO, Paris)
Hiroshi Kitazato (Treasurer of IUGS)
John LaBrecque (Chair of IUGG GeoRisk Commission)

Secretary
Kyoji Sassa (IPL World Centre, Director)

Members of the IPL-KLC Global Promotion Committee

ICL Full Members
Geotechnical Engineering Office, Hong Kong, China; The State Key Laboratory of Geohazard Prevention and Geoenvironment Protection (SKLGP), Chengdu University of Technology; UNESCO Chair for the Prevention and the Sustainable Management of Geo-hydrological Hazards—University of Florence, Italy; Faculty of Civil and Geodetic Engineering, University of Ljubljana (ULFGG), Slovenia; and other members (total 57 members from 27 countries/regions).

ICL Supporting Organizations
UNESCO, UNDRR, WMO, FAO, UNU, ISC, WFEO, IUGS, IUGG

KLC2020 Official Promoters
Host Organization
International Consortium on Landslides (ICL)/Željko Arbanas

Public Sectors: KLC2020 Official Promoters—Public
- The International Union of Geological Sciences (IUGS)/John Ludden
- The International Union of Geodesy and Geophysics (IUGG)/Chris Rizos
- The International Association for the Engineering Geology and the Environment (IAEG)/Vassilis Marinos
- International Geosynthetics Society (IGS)/John Kraus
- Geological Survey of Canada, Natural Resources Canada, Canada/Daniel Lebel
- Faculty of Civil and Geodetic Engineering, University of Ljubljana, Slovenia/Matjaž Mikoš
- China University of Geosciences, Wuhan, China/Huiming Tang

- Department of Civil Engineering, National Taiwan University, Chinese Taipei/Louis Ge
- Institute of Rock Structure and Mechanics, the Czech Academy of Sciences/Josef Stemberk
- Institute of Cold Regions Science and Engineering, Northeast Forestry University, China/Wei Shan

Private Sectors: KLC2020 Official Promoters—Private

- Marui & Co. Ltd, Japan
- Nippon Koei Co., Ltd, Japan
- Ellegi srl, Italy
- Chuo Kaihatsu Corporation, Japan
- Godai Kaihatsu Corporation, Japan
- Kiso-Jiban Consultants Co., Ltd, Japan
- Kokusai Kogyo Co., Ltd., Japan
- OSASI Technos, Inc., Japan

IPL World Centre

IPL World Centre (IWC) was established in 2006 by the Tokyo Action Plan to serve, as it does, as the secretariat of IPL, GPC/IPL as well as of UNITWIN UNESCO-KU-ICL Programme. IWC also serves as the secretariat of KLC2020. IWC is a part of the legal body (NPO-ICL registered in Kyoto, Japan) of ICL. The Council of the IWC consists of advisors from Ministry of Education, Sports, Science and Technology, Ministry of Agriculture, Forestry and Fisheries, Ministry of Land, Infrastructure and Tourism of the Government of Japan, UNESCO, and of members from ICL Headquarters, chairs of GPC/IPL-KLC, presidents and officers of ICL.

Secretariat of GPC/IPL-KLC

Secretary

Kyoji Sassa
International Consortium on Landslides
138-1 Tanaka-Asukai cho, Sakyo-ku, Kyoto 606-8226, Japan Tel: +81 (75) 723 0640
Fax: +81 (75) 950 0910
E-mail: secretariat@landslides.org
URL: https://www.landslides.org/; https://www.landslides.org/ipl-info/

Contents

The Third-Year Publication of the Open Access Book Series "Progress in Landslide Research and Technology"

Kyoji Sassa

Abstract

The Kyoto 2020 Commitment for Global Promotion of Understanding and Reducing Landslide Disaster Risk (Kyoto Landslide Commitment 2020: KLC2020) was launched on 5 November 2020 by the adoption of 2020 Kyoto Declaration at the end of the launching session of the Kyoto Landslide Commitment 2020. The KLC2020 was signed by 90 worldwide partners. On 3 November 2021, during the fifth World Landslide Forum (WLF5) held in a hybrid mode (onsite, online-virtual, and pre-recorded modes) in Kyoto, Japan, the ICL and the KLC2020 partners launched the new open-access book series "Progress in Landslide Research and Technology" to promote the Kyoto Landslide Commitment 2020 for global promotion of understanding and reducing landslide disaster risk in 2022.

The KLC 2020 Secretariat called for the KLC2020 official promoters which promote the Kyoto Landslide Commitment 2020 and provide the financial support for the implementation of the KLC2020 activities including the Open Access Book Series "Progress in Landslide Research and Technology (P-LRT)." At the same time, the Secretariat called for contribution of articles and voluntary editors. Thanks to strong support and contribution, the P-LRT could publish and edit 4 issues and now we have entered in the third-year publication. This article is the report of founding two issues Volume 1, Issue 1 and Issue 2, and the progress report of Volume 2, Issue 1 and Issue 2 published in 2023, and introduce the collected articles for Vol. 3, Issue 1 published in 2024.

Keywords

Open access book series · Kyoto landslide commitment 2020 · ICL book article award · IPL-KLC award for success

1 Introduction

1.1 Background

The International Consortium on Landslides (ICL) and the ICL supporting organizations (each of five United Nations Organizations (UNESCO, WMO, FAO, UNDRR, UNU) and two global organizations in Science and Engineering (ISC and WFEO) exchanged the Memorandum of Understanding to promote the 2006 Tokyo Action Plan and established an International Programme on Landslides (IPL) in 2006 (Sassa 2006).

The Global Promotion Committee of the IPL (GPC/IPL) consists of the ICL and above seven global stakeholders. ICL and GPC/IPL organized triennial World Landslide Forum and established the ISDR-ICL Sendai Landslide Partnerships (Landslide Sendai Partnerships) 2015-2025 for global promotion of understanding and reducing landslide disaster risk. This partnership is a voluntary commitment to the Sendai Framework for Disaster Reduction 2015-2030 (Sassa 2015).

Partners has established the Kyoto Landslide Commitment 2020 (KLC2020) to continue and expand the Sendai Landslide Partnerships even after 2025 (the end of the Sendai Landslide Partnerships). The Kyoto Landslide Commitment is a Commitment to the ISDR-ICL Sendai Partnerships 2015–2025, the Sendai Framework for Disaster Risk Reduction 2015–2030, the 2030 Agenda Sustainable Development Goals, the New Urban Agenda and the Paris Climate Agreement (Sassa 2021).

KLC2020 was signed by 90 United Nations, International and National organizations by 2020. At the opportunity of

K. Sassa (✉)
International Consortium on Landslides, Kyoto, Japan
e-mail: secretariat@landslides.org

B. Abolmasov et al. (eds.), *Progress in Landslide Research and Technology, Volume 3 Issue 1, 2024*, Progress in Landslide Research and Technology, https://doi.org/10.1007/978-3-031-55120-8_1

the sixth World Landslide Forum in Florence, Italy, 16 new organizations have signed it and joined the partnerships in the Plenary session of WLF6 on 14 November 2023.

All organizations including the ICL member organizations which have some aspects of activities related to understanding and reducing landslide disaster risk as their intrinsic missions are invited to KLC2020 members. Intrinsic missions of the whole KLC2020 members promote understanding and reducing landslide disaster risk, namely contribute to the Sendai Framework 2015-2030, the Sendai Landslide Partnerships 2015-2025 and SDGs-No.11 Make cities and human settlements inclusive, safe, resilient and sustainable.

1.2 Open Access Book Series

The worldwide information dissemination of the progress in landslide research and technology and strengthening of the network for landslide risk reduction is a key component of the success and sustainability of the Kyoto Landslide Commitment. The ICL in cooperation with ICL supporting organizations has published International full color journal "Landslides: Journal of International Consortium on Landslides" since 2004.

2022 impact factor of the journal is 6.7, the 2022 published page total is 3060 pages. It is free contribution. The journal has contributed to the publication of Landslide Science. University professors and students can read the article though the subscription fee is very expensive. Practitioners and community people in landslide prone areas can neither access Landslides, nor purchase single chapter (it is very expensive). Furthermore, the article is not always understandable for practitioners and community people, because articles are written for the same field of scientists.

Science and Practice, namely understanding and reducing landslide disaster risk need different approach.

Then, ICL and GPC/IPL and the panelists of the high-level panel discussion in the Fifth World Landslide Forum held in November 2021, Kyoto, Japan proposed and adopted the Launching Declaration of the ICL Open Access Book Series "Progress in Landslide Research and Technology" for the Kyoto Landslide Commitment 2020 on 3 November 2021, Sassa (2022).

The new open access book series "Progress in Landslide Research and Technology" was launched in 2022. The outline of two publications of the ICL new book series and the ICL journal since 2004 is summarized in Table 1.

- ICL book series aims to promote reducing landslide disaster risk, and publishes original article for practice and society, while ICL journals aims to promote understanding landslide disaster risk through the publication of original research for landslide science.
- The whole book or any article of ICL book series are free to download to read, while any article published in the ICL journal is charged for downloading. It is very expensive for practitioners and community leaders.
- Publication of an article in the ICL book series is charged, while publication of an article in ICL journal is free if accepted.

Some categories of the open access book series are unique for the purpose to promote practical application of landslide science and technology for landslide risk reduction. The categories of the book series, and planned page number and explanation of each category is compiled in Table 2.

In order to write an article understandable for practitioners without investigating many references and visual in figures/illustration/photo, the maximum page length is not decided, but the minimum page length is decided as 4 pages, 8 pages or 20 pages.

Category names of Original articles, Review articles, and Technical notes are the same with the Journal "Landslides."

However, the content of each category the book is characterized for its aim of the book series for Practice and Society.

- Original articles are such as practical applications of new models, new equipment, and other advanced research and technology

Table 1 The aim and scope of ICL book series "P-LRT" and ICL Journal "Landslides"

ICL Journal/Book	ICL Book Series "P-LRT" since 2022	ICL Journal "Landslides" since 2004
Aim	Promotion of reducing landslide disaster risk	Promotion of understanding landslide disaster risk
Scope	Original articles for practice and society	Original research for landslide science
Online access	Open access (free)	Charged access
Publication fee	Book processing charge: 50 USD/page (0–25 USD/page until 10 pages/year for ICL members and KLC official promoters)	Free
Pages/issue	400–500 pages	250–350 pages
No of issue	2 books/year	12 issues/year
Publication style	Electronic and print	Electronic and print
Publication size	210 mm × 280 mm	210 mm × 280 mm

Table 2 Categories of articles in the Book Series "P-LRT"

No	Category	Page number	Contents
1	Original articles	Min. 8 pages	Original articles for practice and society, such as practical applications of new models, new equipment, and other advanced research and technology
2	Review articles	Min. 8 pages	Review of landslide research and technology in a thematic area of landslides. A review article integrating a series of research and technology of the author or its group is also applicable
3	ICL landslide lessons	Min. 20 pages	Lessons by global and emerging experts with distinguished achievements in one of specific aspects in understanding and reducing landslide disaster risk
4	IPL/WCoE/Kyoto commitment	Min. 8 pages	Progress or achievements of the projects of the International Programme on Landslides (IPL) and the World Centres of Excellence on Landslide Risk Reduction (WCoEs), and Kyoto Landslide Commitment
5	Teaching tools with online extras (video)	Min. 8 pages	User-friendly teaching tools with extras (i.e., photos, illustration, videos, guidelines and manuals) online to fill the gap between the available level of science and technologies and the practical use in the society
6	Technical note and case studies	Min. 4 pages	Technical note and case studies on landslides and landslide disaster risk reduction practice
7	World Landslide Reports	Total page of this category is Max. 40 pages /issue	Landslide reports from landslide-prone developing countries and urbanizing areas of the developed countries from around the world

- Review articles are for a thematic area of landslides, such as a review integrating a series of research and technology of the author or its group is also applicable.
- Technical notes are technical note including case studies on landslides and landslide disaster risk reduction practice.

Category names of ICL landslide lessons,

IPL/WCoE/Kyoto Commitment, Teaching tools with online extras (video) and World Landslide Reports are different from Journal Landslides.

- ICL landslide lessons are long articles by global and emerging experts with distinguished achievements in one of specific aspects in understanding and reducing landslide disaster risk. The minimum length is 20 pages, such as 40 pages, or 80 pages.
- IPL/WCoE/Kyoto Commitment: This category was included in ICL Journal "Landslides" before the start of this book series. Aim of this category is for reducing landslide disaster. It is suitable for ICL book series. So, this category in the Landslides was terminated from 2022.
- Teaching tools with online extras (video): This category is to promote practical application by providing how to use advanced equipment, software and technologies with video tutorials.
- World Landslide Reports: This is information in and from developing countries. Article publication for this category is free. However, the total pages of articles in this category are around 40 pages such as four 10-pages article from various countries and regions per issue.

2 Front Covers of the Published and Publishing Issues

Figures 1, 2 and 3 show the front cover of Volume 1, Issue 1 and Issue 2, Volume 2, Issue 1 and Issue 2, Volume 3, Issue 1. Two issues of Volume 1 were published in January 2023 and two issues of Volume 2 were published in December 2023. Volume 3, Issue 1 has just been published.

The cover photo and cover editors of Volume 3, Issue 1 was decided in October 2023, though he cover design will be made by Springer Nature.

Each cover photo is selected from the published articles in each issue and decided by the all editors' zoom meeting over the world (very early morning to midnight from Europe, Asia and America continents).

Cover photos used from Volume 1, Issue 1 to Volume 3, Issue 1 are explained as below.

- Volume 1, Issue 1: Aranayake landslide in Kegalle District, Sri Lanka. It occurred in May 2016, after a long rainfall. It killed 127 persons and destroyed 75 houses.
- Volume 1, Issue 2: A large-scale rapid landslide was induced by the mainshock of the 2016 Kumamoto Earthquake. The landslide hit the Aso-Ohashi Bridge on the national road and it disappeared.
- Volume 2, Issue 1: Buzulgan landslide occurred in August 2020 and blocked the Gerkhozhan-Su River valley in Northern Caucasus of Russia.
- Volume 2, Issue 2: In the Thompson River valley, south-central British Columbia, Canada, thick (>100 m) accumulations of glacial lake sediments, tills, and outwash

Fig. 1 Published cover of Volume 1, Issue 1 and Volume 1, Issue 2

Fig. 2 Published cover of Volume 2, Issue 1 and Volume 2, Issue 2 in 2023

have a complex history of sudden rapid translational failure and liquefaction in the past, and slower rotational slumping along toe slopes, head scarps, and tributary channels at present.

- Volume 3, Issue 1: Aratozawa landslide induced the Iwate-Miyagi Inland Earthquake in Miyagi Prefecture, Japan. The total volume of this landslide is estimated to be 67 million m3. The frontal part of this landslide entered into the Aratozawa dam reservoir and caused a tsunami of up to 9 m.

Fig. 3 Book cover for Volume 3, Issue 1

3 Management of P-LRT

Important matters on the management of P-LRT are examined and decided by the periodical all editors zoom meeting crossing the world (America, Europe and Asia from very early morning to midnight).

3.1 Basic Components for P-RLT

Publication of this open access book series is only possible under the following basic three components of voluntary contribution.

1. Authors to contribute to this book series
2. Voluntary editors/reviewers to review articles of this book series
3. Financial and other supports to publish this book series.

3.2 Editors on the Front Cover

The front cover of each issue is shown in Figs. 1, 2 and 3. The editors on the front cover are listed in Table 3.

The cover editors on the initial volume are core editors for publication: Editor-in-Chief, three Assistant Editor-in-Chief, and the publication director of the Editorial office. Those five persons are working as EIC role in the Editorial Manager of P-LRT (EquinOCS).

The number of cover editors has been increased from 5 to 12 as shown in Table 3. Since Vol. 1, Issue 2, the editors on the front cover are alphabetical order as seen in Figs. 1, 2 and 3.

Within three basic components, authors are the most important component. Authors as well as editors writing more than two articles in the past issues (up to 3) were invited to be cover editors on the issue.

Book Processing Charge (BPC) as well as the financial supports from KLC2020 official promoters are the financial

Table 3 Editors on the front cover

	Vol. 1, Issue 1 2022	Vol. 1, Issue.2 2022	Vol. 2, Issue.1 2023	Vol. 2, Issue.2 2023	Vol. 3, Issue 1 2024
1	Kyoji Sassa	Irasema Alcántara-Ayala	Irasema Alcántara-Ayala	Irasema Alcántara-Ayala	Biljana Abolmasov
2	Kazuo Konagai	Željko Arbanas	Željko Arbanas	Željko Arbanas	Irasema Alcántara-Ayala
3	Binod Tiwari	David Huntley	Sabatino Cuomo	David Huntley	Željko Arbanas
4	Željko Arbanas	Kazuo Konagai	David Huntley	Kazuo Konagai	David Huntley
5	Shinji Sassa	Matjaž Mikoš	Kazuo Konagai	Snježana Mihalić Arbanas	Kazuo Konagai
6		Kyoji Sassa	Snježana Mihalić Arbanas	Matjaž Mikoš	Snježana Mihalić Arbanas
7		Shinji Sassa	Matjaž Mikoš	Maneesha V Ramesh	Matjaž Mikoš
8		Huiming tang	Kyoji Sassa	Kyoji Sassa	Maneesha V Ramesh
9		Binod Tiwari	Shinji Sassa	Shinji Sassa	Kyoji Sassa
10			Huiming Tang	Huiming Tang	Shinji Sassa
11			Binod Tiwari	Binod Tiwari	Huiming Tang
12					Binod Tiwari

Table 4 Book processing charge

Types of Authors	BPC: up to 20 pages	BPC: additional pages
Regular	50 USD/page	40 USD/page
[a] ICL associates, supporters, editors	25 USD/page	40 USD/page
[a] ICL full members, KLC official promoters	0 USD/page	40 USD/page

[a] The reduced BPC (25 USD/page and 0 USD/page up to 20 pages) is applicable for one article from each member organization for each year (each volume). (Editors are working editors each year)

Table 5 Awardees of the ICL Book Article Award

Category	Authors	Title	Vol./Issue/page
Original article	Damiano Vacha, Giuseppe Mandrone, Donato Morresi, and Matteo Garbarino	Mapping post-fire monthly erosion rates at the catchment scale using empirical models implemented in GIS. A case study in northern Italy	Volume 1/ Issue 1/99-112
IPL/WCoE/Kyoto Landslide Commitment	Steven Moncayo and Guillermo Ávila	Landslide travel distances in Colombia from National Landslide Database Analysis	Volume 1/ Issue 1/315-325
Technical notes & case studies	Stefano Luigi Gariano, Massimo Melillo, Maria Teresa Brunetti, Sumit Kumar, Rajkumar Mathiyalagan, Silvia Peruccacci	Challenges in defining frequentist rainfall thresholds to be implemented in a landslide early warning system in India	Volume 1/ Issue 1/409-416

source. The International Consortium on Landslides (ICL) is the leading host organization of the KLC2020 official promoters. The amount of BPC is different in regular members, KLC official promoters, ICL full members, associates, supporters. BPC for each type of authors is listed in Table 4.

3.3 New Awards

The ICL launched the new open access book series in 2022. To promote the authors contributing to landslide risk reduction for society through writing articles, the ICL created one new award and revised one existing award.

I. ***ICL Book Article Award***

- Award is free BPC for 20 pages.
- The effective period is one year after the decision of the award.
- The number of annual awards is 1-3 in different categories.

(1) Candidate nomination (around 10) is from EIC members (5) of OCS-web and a few editors (1-3) who read almost all articles.
(2) Nomination of Award (2-3) is voting by editors of P-LRT who attend the periodical (around 2-4 times for one issue) editorial meeting of the Book.

The first awardees of this award for Volume 1 was decided by the all editors meeting in October 2023 as shown in Table 5.

II. ***IPL-KLC Award for Success***

- Award is 3000 USD by cash.
- The number of awards for each Forum is 1-3 in different categories (similar to the previous IPL Award for Success).

(1) Candidates are authors of ICL open access book series (prerequisite condition) and Journal "Landslides" to report IPL-KLC activities.
(2) The first nomination is around 10 from EIC members (5) of P-LRT and the screening editors of Landslides who monthly read submitted articles.
(3) The approval is by IPL-KLC Global Promotion Committee.
(4) This award for success will be approved at the 2023 IPL-KLC Global Promotion Committee on 13 November 2023 in Florence, Italy.

4 Countries /Regions of the Authors

- Figure 4 presents the number of authors from each country, United Nations organization, and international organization in the six categories of articles published in Vol.1, Issue 1. The first issue was contributed by authors from 24 countries and an United Nations organization (UNESCO), and an international Society. Twenty authors from Italy and Japan are largest.

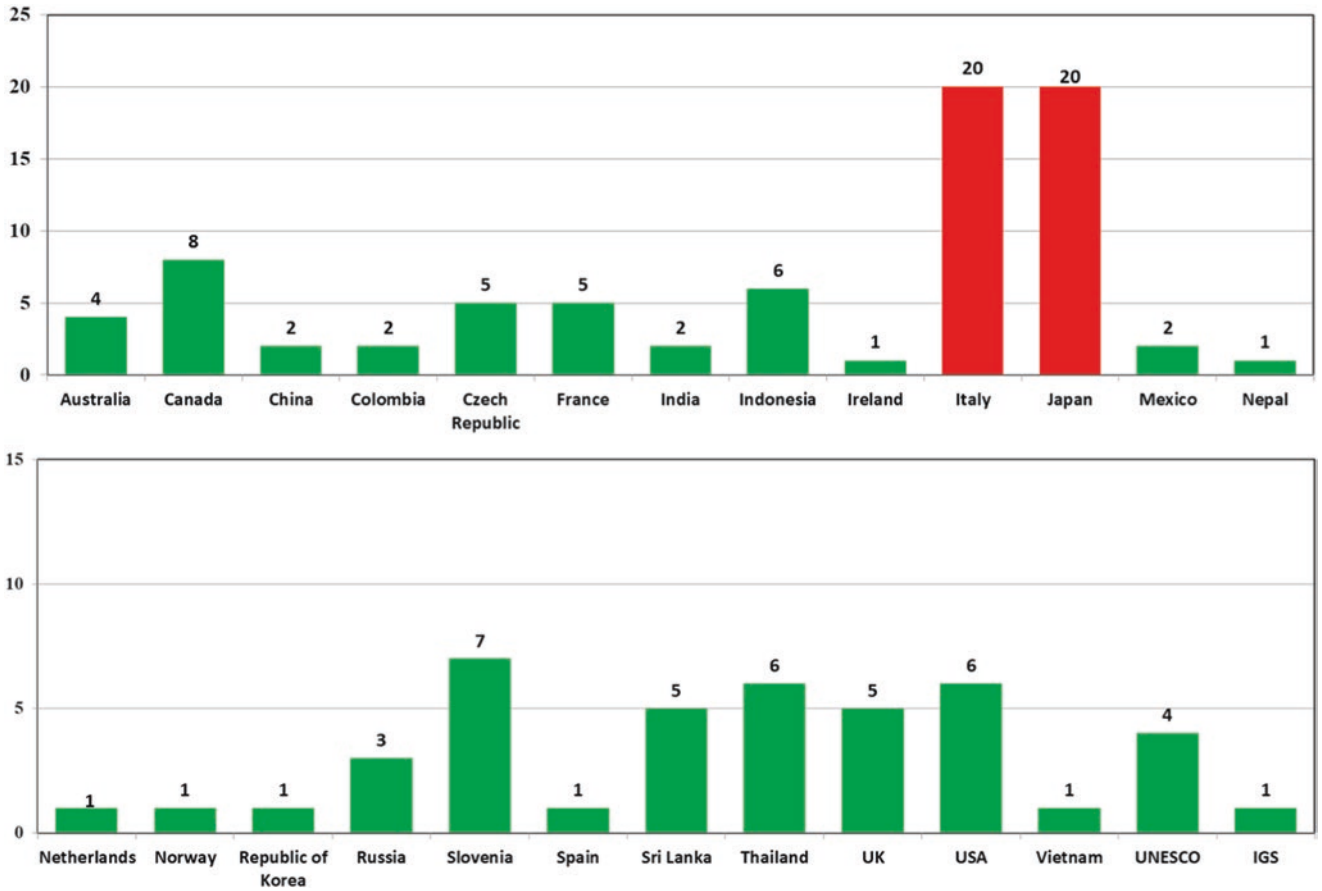

Fig. 4 The number of authors from each country/region in the six categories of articles published in Vol. 1, Issue 1

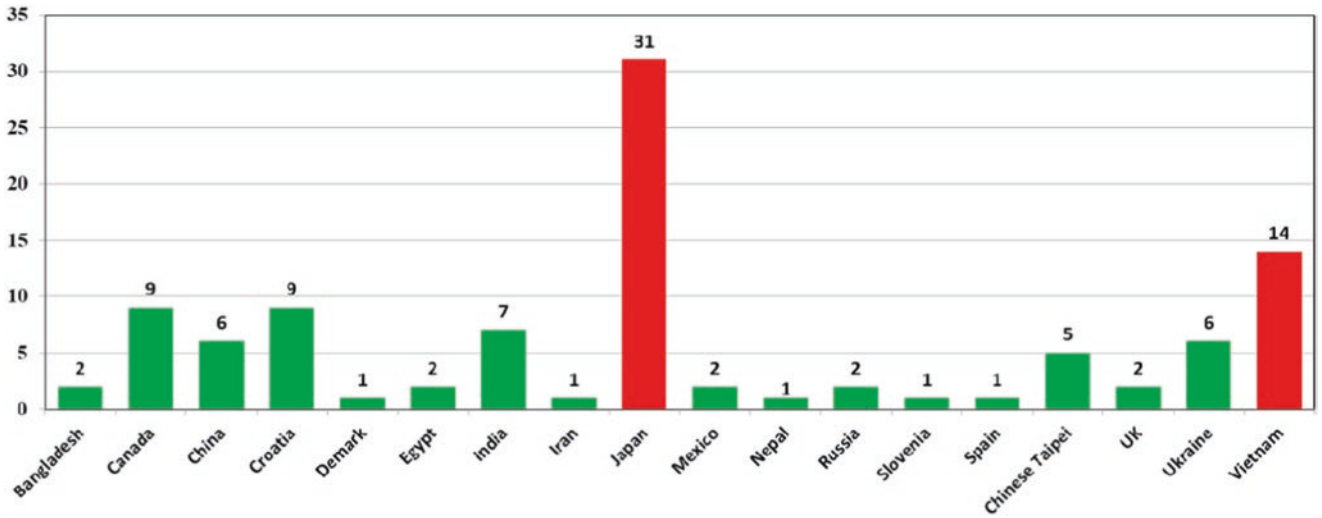

Fig. 5 The number of authors from each country/region in the seven categories of articles published in Vol. 1, Issue 2

- Figure 5 presents the number of authors from 18 countries in Volume 1, Issue 2. Thirty-one authors from Japan is the largest, followed by 14 authors from Vietnam.
- Figure 6 presents the number of authors from 13 countries in Volume 2, Issue 1. Twenty-one authors from Vietnam and 10-15 authors from Italy, Croatia, Japan and Russia.
- Figure 7 presents the number of authors from 21 countries in Volume 2, Issue 2. Twenty-three authors from Italy is the largest, 12-17 authors from China and Croatia.

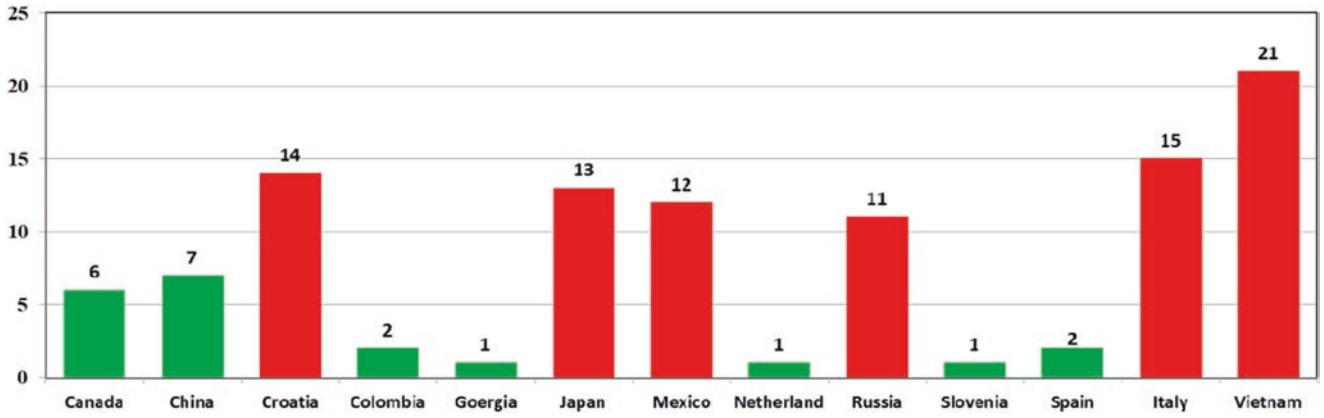

Fig. 6 The number of authors from each country/region in the seven categories of articles published in Vol. 2, Issue 1

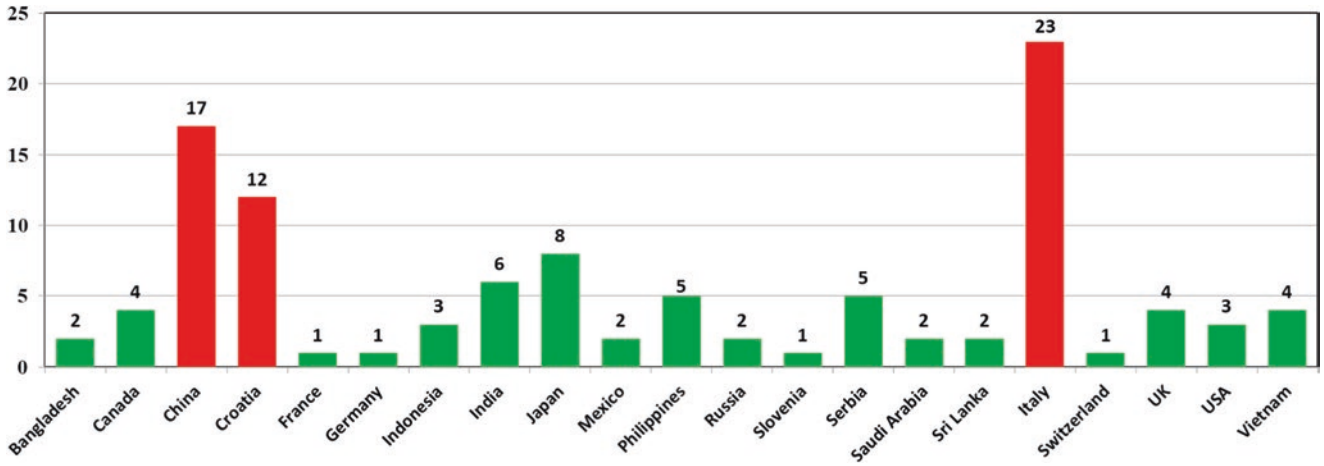

Fig. 7 The number of authors from each country/region in the seven categories of articles published in Vol. 2, Issue 2

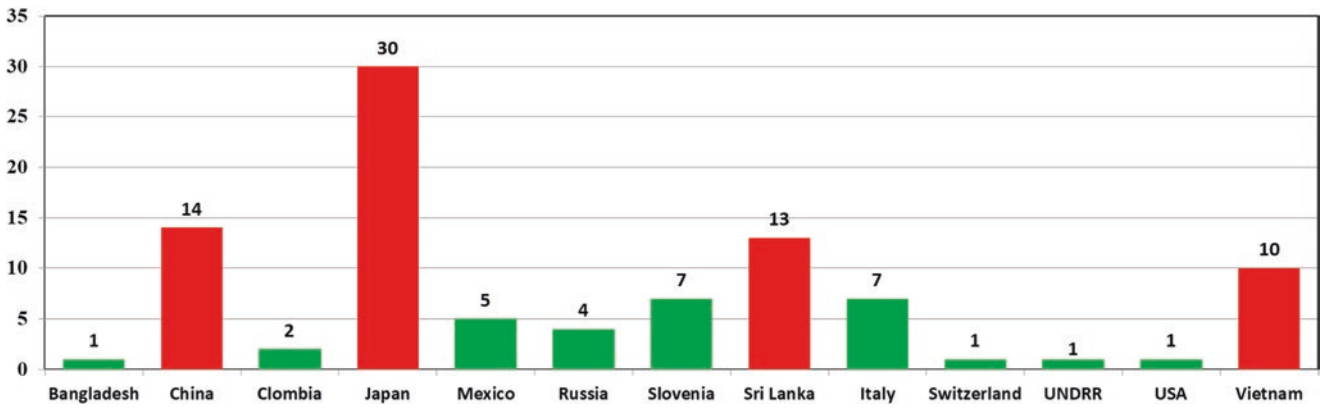

Fig. 8 The number of authors from each country/region in the seven categories of articles published in Vol. 3, Issue 1

- Figure 8 presents the number of authors from 12 countries and the United Nations Office for Disaster Risk Reduction (UNDRR) in Volume 3, Issue 1. Thirty authors from Japan is the largest and 10-14 authors from Sri Lanka, China and Vietnam.

5 Composition of Categories of each Issue

Table 6 presents the total pages of each issue, and its breakdown including number of articles and page num-

Table 6 Total page and Breakdown of Vol. 1, Issue 1 and Issue 2, Vol. 2, Issue 1 and Issue 2, Vol. 3, Issue 1

	Vol.1, No.1		Vol.1, No.2		Vol.2, No.1		Vol.2, No.2		Vol.3, No.1	
Breakdown	No. of articles	No. of pages	No. of articles	No. of pages	No. of articles	No. of pages	No. of articles	No. of pages	No. of articles	No. of pages
Front matters	3	9	3	8	3	7	3	9	3	8
Forewords	6	12	0	0	0	0	0	0	1	2
Table of contents	1	4	1	4	1	4	1	4	1	4
Editorial/Preface	3	60	1	8	1	7	0	0	1	13
ICL Landslide Lesson	0	0	0	0	2	124	2	107	1	45
Original articles	11	135	13	161	9	113	13	164	15	161
Review articles	1	5	6	76	0	0	3	37	4	62
IPL/WCOE/KLC activities	10	118	4	61	5	79	3	27	3	28
Teaching tools	1	64	2	44	2	26	1	25	0	0
Technical notes and case studies	1	8	1	9	3	32	1	6	4	32
World landslide reports	0	0	3	37	0	0	2	27	2	21
Official promoters	16	46	16	46	16	46	14	38	14	38
Back matters	1	3	1	3	1	2	1	3	1	3
Total	54	464	51	457	43	440	44	447	50	417

ber of each category, front matters, back matters. and others from Volume 1, Issue 1 to Volume 3, Issue 1.

Figure 9 is a graphical review of article number and article page numbers in each category since Volume 1, Issue 1 to Volume 3, Issue 1. The portions of original articles are the largest through all issues both in number and pages.

The category of IPL/WCoE/KLC (purple color) is core of this book series. This category of articles is published in all issues. Technical Notes & Case studies were published in all issues, though the page number is not large.

- Articles of the ICL landslide lessons (Green color: Minimum 20 pages is necessary) started from Volume 2, Issue 1. This article is important for capacity development and contribution for practical application of advanced research and technology.
- Teaching tools (dark green color) including video tutorial is the important article for technical transfer. This category of articles was published except Volume 3, Issue 1.
- Editorial/Preface was polished other than Volume 2, Issue 2. The initial volume published the ICL history and IPL review in this category.
- Articles for the category of World Landslide Report are free BPC to promote contribution from developing countries. Articles on landslides in developing countries are also included in this category to promote articles reporting landslide disaster and risk reduction in the countries/regions where reports are seldomly published. The total page of the category of this article is limited to be around 40 pages/issue

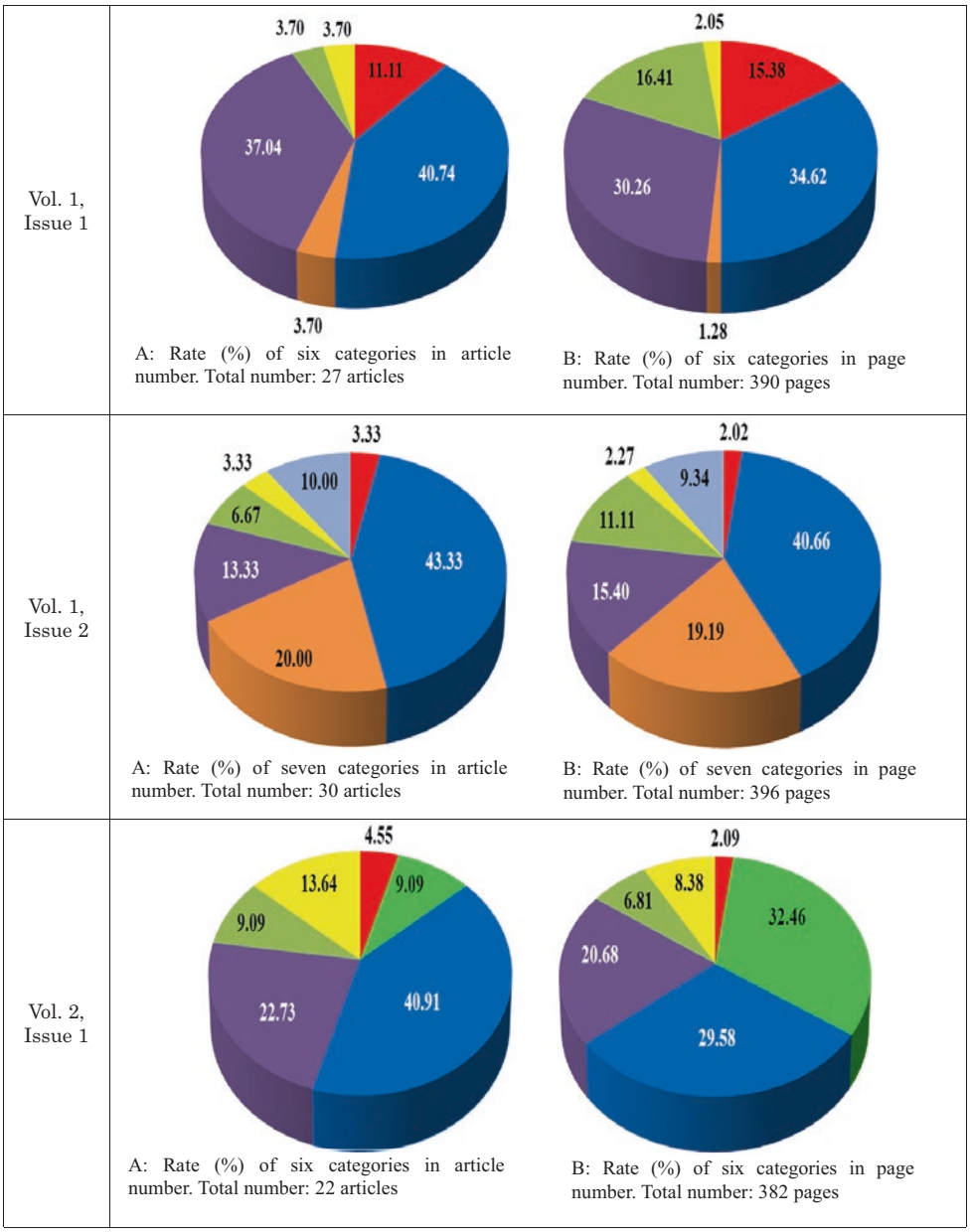

Fig. 9 Share (%) of categories in Vol.1-1, Vol.1-2, Vol.2-1, Vol.2-2, Vol.3-1

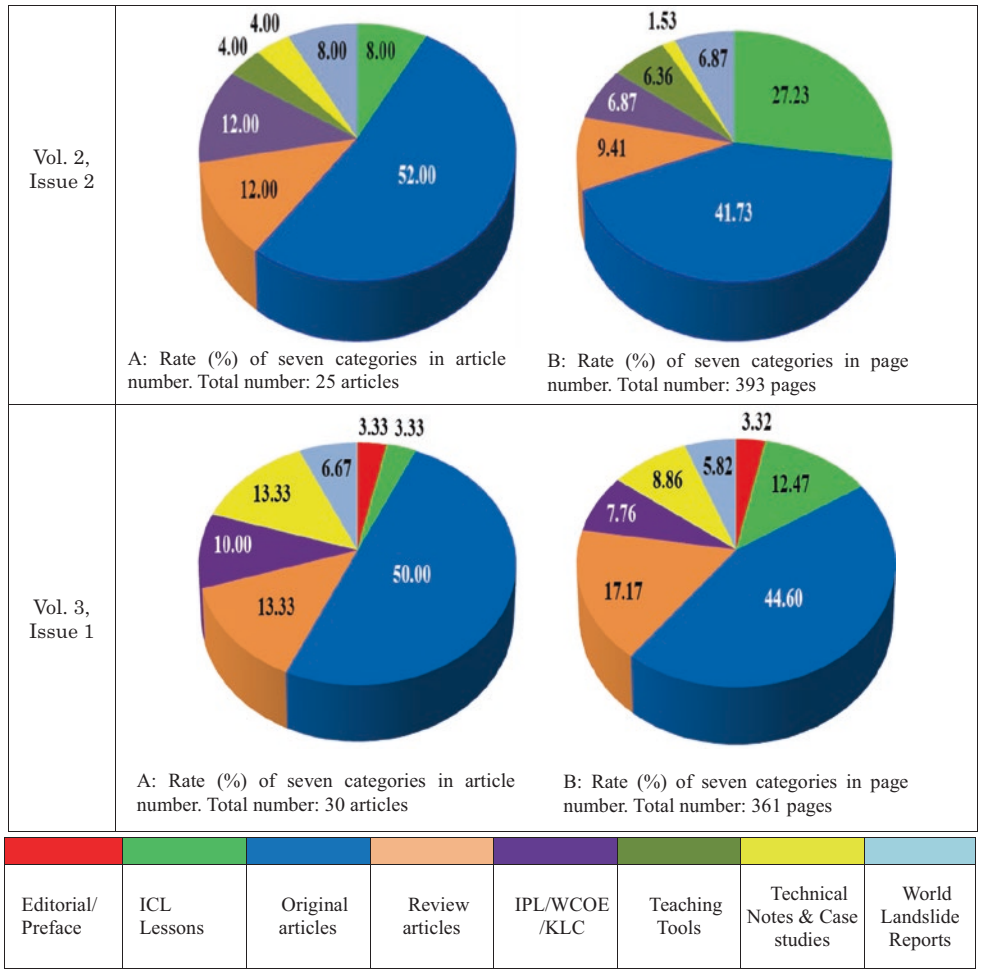

Fig. 9 continued

6 Call for Articles to Volume 3, Issue 2

The Kyoto Landslide Commitment 2020 was launched in 2020. The Sixth World Landslide Forum and ICL Board meeting and the Global Promotion Committee of the IPL and KLC2020 was organized in Florence, Italy on 13-17 November 2023.

The Plenary session programme is uploaded in WLF6 web https://wlf6.org/opening-plenary-session/.

KLC2020 General Conference 2023 and High-level panel discussion were organized on 14 November 2023.

16 new signatories of KLC2020 after 90 signatories in 2020 were invited to attend this general conference and sign the KLC2020. A joint signing ceremony and a joint photo together with all panelists of the high-level panel discussion to adopt the Florence Declaration on Landslide Risk Reduction for further development of KLC2020 were organized.

This new open access book series "Progress in Landslide Research and Technology" is a core activity and platform for the KLC2020 for Practice and Society. Landslide researchers, engineers and practitioners were invited to contribute to Volume 3, Issue 2 published in 2024.

Contribution of an article for understanding and reducing landslide disaster risk is an activity of the Kyoto Landslide Commitment 2020, which is a commitment to the ISDR-ICL Sendai Partnerships 2015–2025, the Sendai Framework for Disaster Risk Reduction 2015–2030, the 2030 Agenda Sustainable Development Goals, the New Urban Agenda and the Paris Climate Agreement.

Contact: Kyoji Sassa, KLC2020 Secretariat klc2020@landslides.org.

References

Sassa K (2006) "2006 Tokyo action plan"—strengthening research and learning on landslides and related earth system disasters for global risk preparedness. Landslides 3(4):361–369

Sassa K (2015) ISDR-ICL Sendai partnerships 2015-2025 for global promotion of understanding and reducing landslide disaster risk. Landslides 12(4):631–640

Sassa K (2021) The Kyoto landslide commitment 2020: launched. Landslides 18(1):5–20

Sassa K (2022) The fifth world landslide forum and progress of the open access book series for Kyoto landslide commitment 2020. Landslides 19(1):1–5

Part I

ICL Landslide Lesson

Interpretation and Mapping for the Prediction of Sites at Risk of Landslide Disasters: From Aerial Photography to Detection by DTMs

Toyohiko Miyagi, Koji Ikeda, Haruna Ishikawa, Loi Doan, Nguyen Kim Thanh, Pham Van Tien, Yuxin Li, and Feng Zhang

Abstract

By grasping the slope topography three-dimensionally and typifying and mapping the landform features, it is possible to visualize the areas at risk of landslide-induced disasters. This effort began with the interpretation of aerial photographs, and, in recent years, has shown great development with the advancement of remote sensing technology. In this chapter, we introduce the characteristics that can be extracted from remote sensing data that can be used to identify potential areas exposed to mass movement processes and landslide-induced disasters. In addition, we created a manual for landslide recognition by aerial photographs, AW3D-based wide-area maps, and specific landslide microtopography maps, which can be freely used to identify landslide landforms.

Keywords

Landslide mapping · Site prediction · Digital 3D map · Sri Lanka · Vietnam

T. Miyagi (✉)
International Consortium on Landslides (ICL), Kyoto, Japan
e-mail: miyagi@iclhq.org

K. Ikeda
Tohoku Development Consultant Co., Ltd., Sendai, Japan
e-mail: ko-ikeda@mail.tkca.co.jp

H. Ishikawa
Advantechnology Co. Ltd., Sendai, Japan
e-mail: ishikawa@advantechnology.co.jp

L. Doan
International Consortium on Landslides (ICL), Kyoto, Japan

Institute of Transport Science and Technology, Hanoi, Vietnam

N. K. Thanh
Institute of Transport Science and Technology, Hanoi, Vietnam

P. Van Tien
Institute of Geological Sciences, Vietnam Academic of Science and Technology, Hanoi, Vietnam

Y. Li
Beijing Normal University, Beijing, China
e-mail: lyx2019@mail.bnu.edu.cn

F. Zhang
Dalian University of Technology, Dalian, China
e-mail: zf1176758006@mail.dlut.edu.cn

1 Introduction (Basic Focus, Pointing Out Issues, etc.)

Assessing and mapping the potential of slope disasters is essential for disaster prevention. In geomorphology, we have promoted the understanding of the geomorphological characteristics of slopes and have made efforts to mitigate slope-induced disasters with this knowledge. Part of this effort was greatly expanded by the acquisition of technology to grasp the terrain in three dimensions. For example, the topographic classification of slopes by substantive visual interpretation of aerial photographs, which began half a century ago, can be shown. On the other hand, remote sensing technology has advanced rapidly in recent years. This progress is not just cutting-edge. Both sensing tools and analysis software are revolutionizing the ease of using them. In the past, cutting-edge technology was the domain of some experts. It was common for highly trained technicians to obtain results with large budgets. However, in recent years, high-precision sensing equipment can be purchased at an extremely affordable price, and free analysis software can be used to achieve this goal by general engineers and anyone interested quickly. Aerial photo interpretation techniques obtained by accumulating long-term study of thumb *are sometimes evaluated as "a masterly performance."* The recent "generalization of advanced technology" *related to sensing may be able* to "obtain results for the time being" *without a sufficient understanding of the nat-*

B. Abolmasov et al. (eds.), *Progress in Landslide Research and Technology, Volume 3 Issue 1, 2024*, Progress in Landslide Research and Technology, https://doi.org/10.1007/978-3-031-55120-8_2

ural phenomenon itself. As a result, there are some examples where it is difficult to say that disaster prevention maps represent reality. Perhaps there is some difference between mapping by visual interpretation of aerial photographs and mapping by utilizing digital sensing technology alone.

This report summarizes the current geomorphological understanding that contributes to slope disaster prevention. In addition, the manual covers from the interpretation of aerial photographs to creating slope disaster prevention materials using UAVs. We will not only visualize the topographical understanding by visual interpretation of aerial photographs, but also try to achieve a common understanding among the parties concerned. A three-dimensional (Hereafter abbreviated as 3D) understanding of topography will pave the way for the extraction of landslide topography by detection from the contour lines. If these experiential abilities are fostered, it will be an opportunity to realize various effects in the 3D display of DEM-based terrain.

2 Mass-Movement on Slopes and Typology of Slope Disasters

2.1 Geomorphological Understanding of Slope Mass-Movement

Typifying and understanding the slope mass-movement phenomenon is a basic procedure for natural science and landslide disaster prevention. There are two directions to this. One is for the mechanistic understanding of phenomena, and the other is for understanding their spatial distribution. Mapping is, of course, the latter. Contributing to disaster science is similar to predicting potentially unstable areas. Here, there are some points to remember when implementing slope variation and mapping from a geomorphological point of view. Starting with grasping the actual distribution of phenomena, grasping the actual distribution of slope fluctuations based on a morphological understanding of slope variation characteristics, developing it into a place-based assessment of disaster potential, summarizing them and visualizing them as a map. In doing so, it should be noted that (1) the categorization is sufficiently discussed and valid. (2) It will be possible to grasp and confirm the typified phenomenon in various situations where the actual slope area and topography are grasped. In order to grasp and map topography geomorphologically, it is necessary to understand from the following four perspectives. It is the viewpoint of shape, material composition, formation action, and formation time (Miyagi et al. 2004). Here, the shape and material composition can be grasped by observation. On the other hand, the formation process and formation time are understood as a result of consideration. Shape is an introduction to topographical understanding, and if it is considered and mapped, it will be an achievement (Figs. 1 and 2).

The erosion effect is conspicuous by the effect of water currents that create water systems and valleys. However, slope-altering failures and landslides are also linked to valley development (Miyagi 2014).

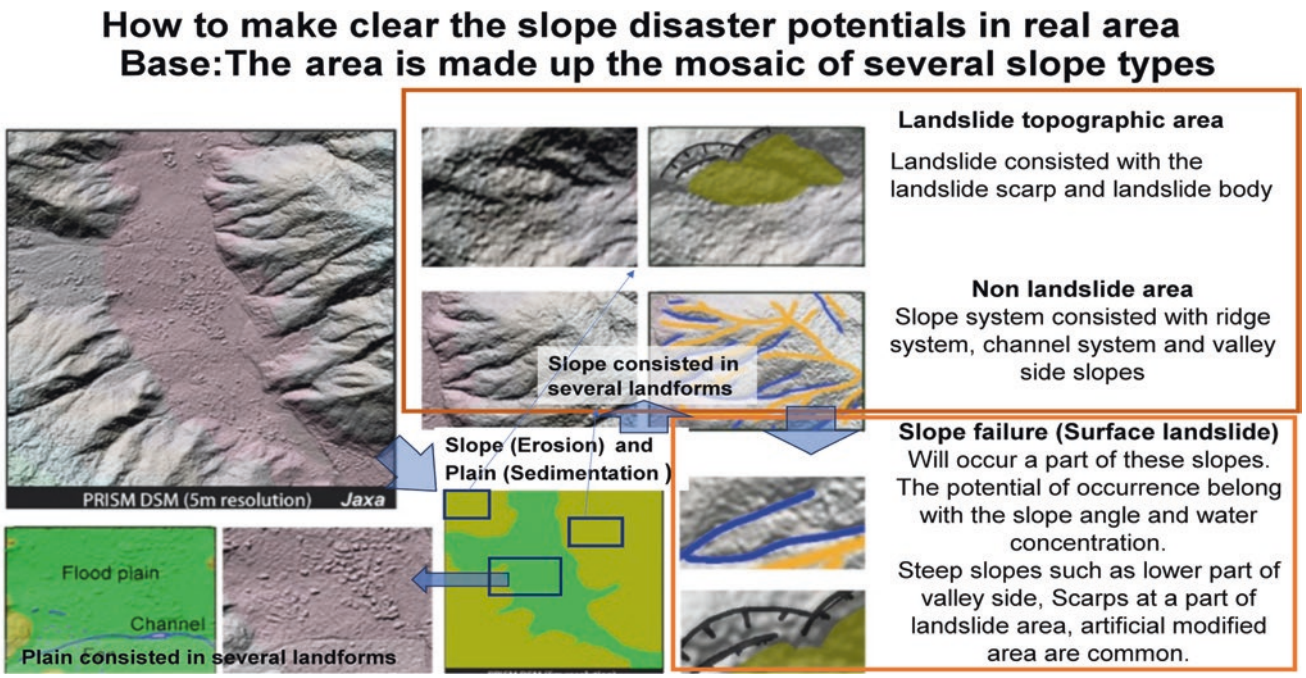

Fig. 1 What elements does the terrain consist of? Shadow maps using 5 m DEM can grasp the distribution of the terrain that constitutes the ground surface with an accuracy of about 1/10,000. Of course, the accuracy of the data itself must be good

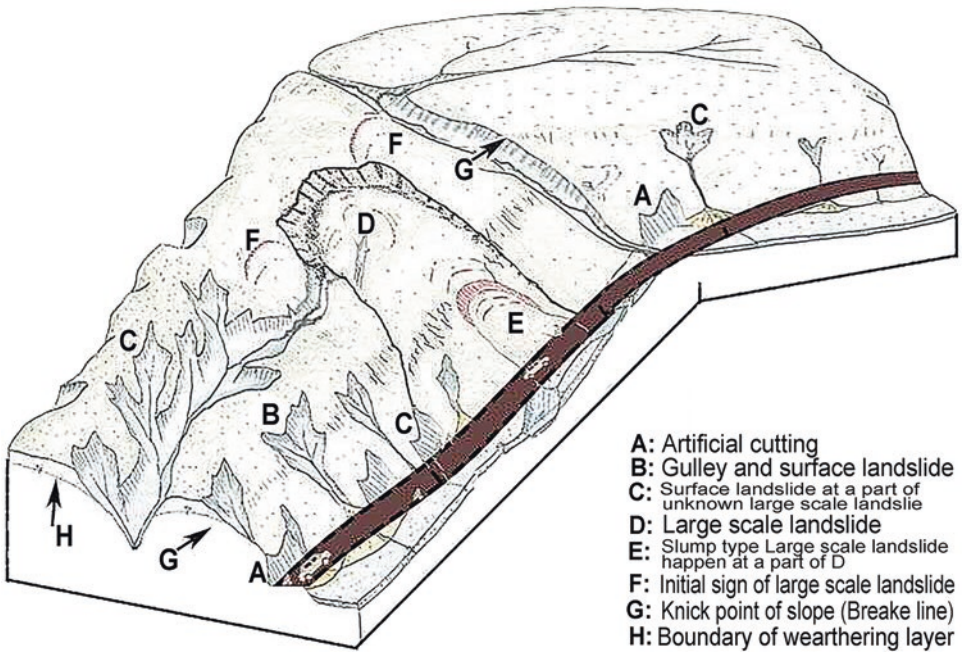

Fig. 2 Let's consider what characteristics the slope consists of terrain

2.2 The First Step in Understanding Slope Topography, Such As Landslides

Landslides, typical of slope fluctuations, are greatly feared by local residents because of the tremendous movement and enormous damage caused by the fluctuations. Therefore, much effort was put into elucidating the mechanism of its occurrence and formulating countermeasures. UNDRR (2015) termed the word Disaster: "A serious disruption of the function of community or society at any scale due to hazardous events interaction with the condition of exposure, vulnerability and capacity, leading to one or more of the following: human, material, economic and environmental losses and impacts". If we apply disruption here in the context of this report, it will correspond to the slope change caused at hand. From a geomorphological point of view, it can be positioned as the latest scene of various topographic change phenomena on slopes. If we can accurately grasp the changes in the shape of the slope in this single frame, we can find "traces of similar changes" that have been carried out in the surrounding slope areas using this as a document. In this way, if we can separate and map areas where similar effects are dominant and where they are not, we can provide basic data on slope disaster risk. At least in humid areas, the current topographic change phenomenon seems to have continued during the Holocene (Ex. Nakayama and Miyagi 1984; Miyagi et al. 1995).

As the scope of human activity expands and becomes more complex, the areas with the potential for new disasters to occur will expand, and the content of the vulnerability of disasters will also change. It can be said that the present age is an era in which the technology for observing topography (land) is almost complete. If so, based on understanding geomorphological characteristics, we should systematically predict where and how the slopes caused by landslides exist, when they move, and how many disasters their fluctuations are likely to occur, and realize rational and safe land use.

In Japan, as an institutional project of the National Research Institute for Earth Science and Disaster Resilience, from 1982 to 2014, we completed the deciphering work of landslide topography throughout Japan. We made it into a GIS database and made it public. Since "landslides" are also a phenomenon of topographic deformation on the ground surface, the authors had the prospect that by carefully observing the terrain, it would be possible to grasp the actual situation of "where" and "how". A typical example of this can be found in a sketch of the shape and structure of a landslide. For example, from Vernes (1978) to Highland and Bobrowsky (2008) through Oyagi (2007), many cases have illustrated the relationship between the shape of landslides and their mode of motion and material composition. The following three points are common to many of these figs. (1) Landslides and land have clear topographic boundaries between the surrounding non-landslide lands. (2) In the land caused by landslides, there are three topographic areas: sliding cliffs, moving bodies, and, in some cases, slippery surfaces. (3) Even if a landslide causes the terrain, the micro-topographical characteristics of (1) and (2) are obscured by vegetation recovery, obedience in geomorphology, erosion due to gully extension, etc.

2.3 Synthesize and Categorize the Slope Mass-Movement Phenomena

Mass movements, which are erosion effects on slopes, are extremely diverse in shape, scale, speed, continuity of fluc-

tuations, predispositions and incentives. Here, mass movements are summarized into three major categories from a geomorphological perspective: surface failure (shallow landslide), debris flow, and landslide. Surface failure (shallow landslide) is a mass movement that occurs under the control of the characteristics of the profile (slope longitudinal profile) from the existing ridge to the valley floor, and lumps together what is called debris flow in some regions.

The slope between the ridge and the valley floor is called the valley wall slope. Due to the shape, material composition, and supply of precipitation on the slope of this valley wall, the water table rises in a part of the slope, and an increase in pore water pressure and saturated surface currents occur, causing part of the soil mass to move. The movement of this type of slope material is called surface failure or surface landslide. Unstable materials will accumulate on the slopes of the valley walls due to various weathering and creep, and these materials will be temporarily deposited at the slope legs and valley floors. This sediment is carried and removed by occasional runoff and running water, so the slope legs are always unstable as a mass movement.

Debris flow is a phenomenon in which moving substances caused by mass movements generated in a part of a slope and sediment stored in mountain streams flow down with a large amount of outflow. Debris flows are transported and deposited differently from collapses and landslides. Surface failure and debris flow are destructive slope mass transfers on valley wall slopes. These mass transfers create distinct microtopography through destruction. However, unlike the following landslides, it does not leave moving objects on the mass transfer path of the slope.

The third type of landslide is a mass movement that is also influenced by the geological structure and occurs to deform the slope shape itself. Landslides are notable for their microtopographic composition and scale. At the same time, it is characterized by the accumulation of fluctuating unstable soil masses called mobile bodies on the slopes, forming landslide landforms. This topographic type is also diverse in shape, scale, and movement mode. Still, the unity is clearer than the previous two. This mass movement is a topographic unit separated from the surrounding slope by a clear inclination turning line. This mosaic consists of three topographic units: the main scarp, the moving body, and the sliding surface. The main scarp forms the boundary between the landslide area and the surrounding slopes. The slippery surface is exposed depending on the exercise, such as a slump. The mobile body is a fluctuation area caused by a landslide, and part remains on the slope. A slippery surface bounds the immovable area. As shown in Figs. 4 and 5, the moving body results from landslide fluctuations and is a micro landform composed of preliminary materials for the next fluctuation. From the viewpoint of slope disaster prevention, Japan adopts three types of slope fluctuations: steep slope landslides, debris flows, and landslides (Fig. 3).

2.4 Autonomous Destruction Process by Landslides

In landslides, elementary fracture occurs on the slope, causing deformation and alteration of the internal structure of the moving body, making it vulnerable. The moving body in the landslide terrain will undergo an autonomous fracture process (Fig. 4), giving rise to new microtopographic features. Here, we focus on (2) the basic topographic characteristics of landslides mentioned above. The occurrence of primary landslides on a part of a slope is synonymous with creating new landforms on the slopes.

Depending on the scale of the landslide and the movement style, it is common for a part or all of the moving body to not move completely on the slip surface and stop on the slope. If a part of the slope fluctuates as a large mass, the

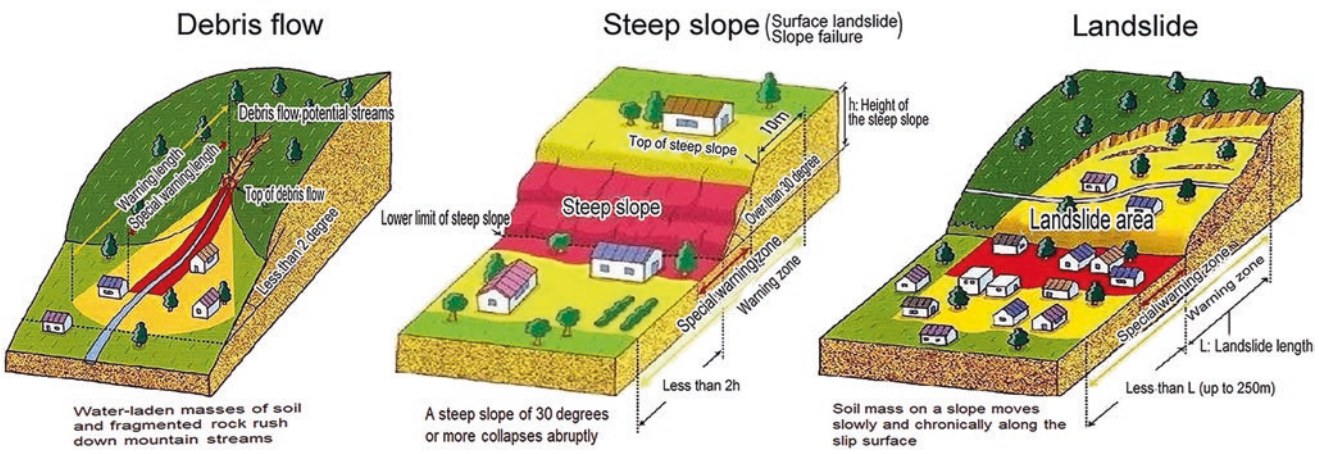

Fig. 3 Classification of slope disasters in Japan (Ministry of LITT, Japan 2020)

Initial situation (Stress field, solid-state of rock, Geology) Geomorphic setting (Stages of geomorphic development) Slope gradient

Autonomous destruction process		Solid-state of rock	Destruction			Landform features			Triggar of action	
			Type	Scale	Frequency	Plan	Scarp	Micro landform	Outer	Inner
Stage I	Release from residual stress	Elastic	Destruction dominant	Large	Seldom	Round	Crack Sugging Linear graben	Original shape Warp	Deepening Shape of mountain	
Stage II	Glide at bedding plain Slump as describe an arc						Large Separation scarp Slide scarp	Block	Type and magnitude of rainfall	Inner stress field distribution
Stage III	Fracturral slip Folding slide Debris slide						Minor scarp	Pressure ridge		relocation of water by micro landform
Stage IV	Flow type slide	Fluidic	Viscosty flow dominant	Small	Frequent	Long obal	Small scarp	Slghtly hammocky wavey smooth		Trap

Fig. 4 The autonomous destruction process: Initial landslide causes secondary deformation and alteration of moving bodies and surrounding topography (Miyagi et al. 2004)

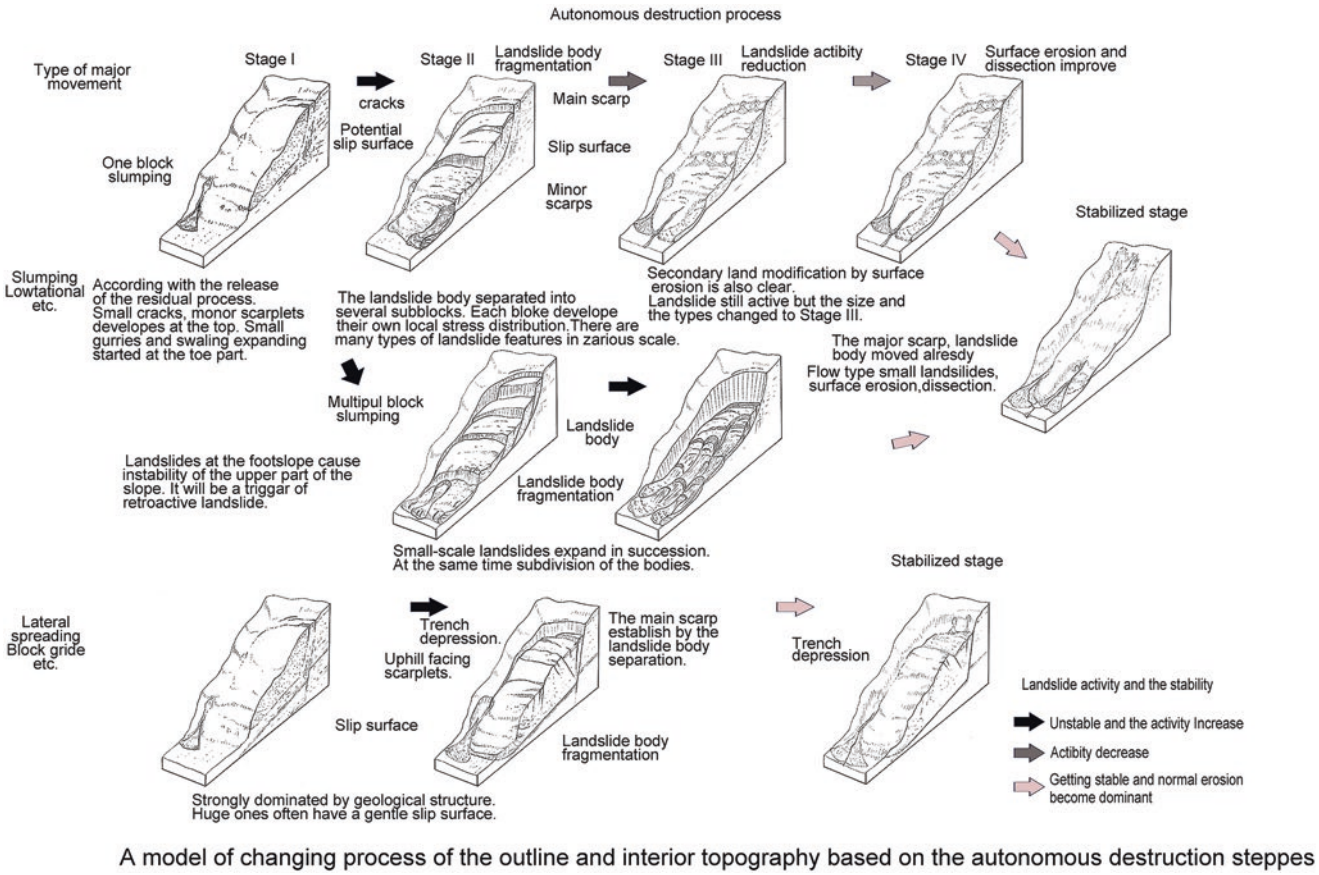

Fig. 5 Landslide deformation is caused by surface weathering, soil erosion, and development of water systems. As the landslide deformation process ends, the landslide microtopography gradually becomes obscured. (Modified from Miyagi et al. 2004)

fluctuated mobile body will be more or less crushed. This fracturing alters the mobile body's mechanical, hydrological, and chemical properties, and some of these changes are likely to be reflected in topographic deformation. At this time, depending on the scale of the landslide deformation, the shape of the slope that occurs, the material to be deformed, the amount of moisture, etc., most of the moving body is transported, deposited on the slope leg, or washed away. In the case of landslides, the autonomous destruction process of moving soil masses generated by landslides (Miyagi et al. 2004; 2021) can be interpreted asmicrotopography (Fig. 5). Needless to say, the various deformations due to landslides described here are phenomena that should be observed three-dimensionally.

3 Actual Interpretation of Landslide Topography and Utilization of Digital 3D Information

3.1 Development of Real Visual Interpretation of Landslide Topography

Since the landform is three-dimensional, observing it as a three-dimensional object is desirable. If you can observe the terrain from a bird's eye view and in three dimensions, you can grasp the whole picture and details, and above all, it is directly linked to mapping. From this point of view, the actual vision of aerial photography was an extremely important goal. It is also understandable that visible aerial photographs remain military secrets in many countries. The use of aerial photography in Japan became common after the 1960s. Technological progress in grasping and expressing topography in three dimensions has been remarkable in recent years. In recent years, advances in digital 3D technology seem to have changed drastically. This change began with the emergence of highly accurate digital 3D topographic maps by acquiring LiDAR data. Globally, SRTM data from the 90-m grid by NASA in the United States has long been made available free of charge. AW3D data is being prepared by Japan's JAXA/ RESTEC/ NTT data, and DEM data for the 30 m grid can also be used free of charge here. In addition, the Geographic Agency of Japan has made GIS information public, the development of national land numerical information has progressed, and the free use of aerial photographs and topographic maps managed by the Geospatial Information Authority of Japan has been achieved, and 5 m DEM can be used in most of the national land. Approaches such as SAR, which use various types of satellite sensor data and utilize data with various accuracy as needed, are also common. In addition to LiDAR data, the accuracy of land information by applying multi-view photogrammetry technology is also progressing. One of the features of recent technological progress is the simplification of processing technology and the reduction of the price of measuring instruments in data acquisition and subsequent visualization processing.

3.2 Considering the Significance of the Shift from Physical Vision to 3D Data Processing

We are a group of researchers and engineers related to slope disasters. We are considering how to visualize slope disaster potential by capturing topography three-dimensionally and using our respective technologies. Furthermore, we take seriously the need to realize the visualized image as a common understanding among as many people as possible. The acquisition and retention of technology will not be completed simply by creating a manual. It is naturally necessary to visualize it in three dimensions.

Reading the actual vision of aerial photographs is a great deal of difficulty. Needless to say, the image by real vision is obtained by synthesizing the data obtained by both eyes with the brain. This image can only be visualized by the reader himself. Therefore, even if a distribution map of the landslide terrain was created by transcribing the reading results on a topographic map, "such an image could be created from these aerial photographs, and the topographic characteristics of this area would be such a thing. Therefore, we have certified this area as a landslide landform." Suppose the distribution map of the completed landslide terrain is examined in situ. The diagram accurately grasps the distribution entity. In that case, it will never lead to the acquisition of deciphering skills, even if it suggests that the reading technician is excellent.

On the other hand, the high accuracy, lower cost, and simplicity of digital 3D information brought about by various sensing tools can facilitate the 3D imaging (visualization) realized in the brain in aerial photo interpretation. Progress in this area has been extremely rapid. In 2023, like the iPhone 14 Pro, Su-Mart phones will be equipped with this function, allowing them to create three-dimensional stereoscopic images of the terrain in front of them in a crowded field of vision, and share and observe them (Fig. 6).

Fig. 6 Using the functions of iPhone 14 Pro, digital 3D information can be acquired and processed to explain the landslide deformation of familiar places in an easy-to-understand manner. It can be easily applied to various applications such as disaster prevention patrols with local residents, basic materials for regional disaster prevention charts, and on-site medical records for disaster management. (Personal data taken by Koike 2023)

4 Mapping Slope Changes Using AW3D

4.1 Mapping AW3D Data to Slope Variation

The 3D informatization described in Chap. 3 summarizes the progress of that tool. Figure 9 shows an example of slope disaster prevention mapping in northern Vietnam's mountainous province. Topographic analyses were performed using 5 m and 10 m contour maps generated from AW3D's 2.5 m grid DSM and DEM. The step was to (1) extract ridge and valley lines by reading contour lines' flexion patterns to grasp spatial distribution characteristics such as slope scale and slope. This is because, as already mentioned, collapse-type topographic changes occur on the slopes of the valley walls, so the longitudinal section from the ridge to the valley floor is characterized as a basic unit. Since debris flows have a collapse source at the top and often flow down the water system, it is meaningful to obtain an aqueous system. Next, the landslide terrain area was extracted. (2) Since the landslide topography consists of a steep slope that forms a horseshoe-shaped plan called the main sliding cliff and a gentle slope that extends in front of the slope called a landslide-moving body, the location of the bending characteristics of such contour lines was extracted. (3) Using contour lines, the slope of each grid was calculated and stratified. The steep slope of Japan is designated as a dangerous slope at about 30 degrees. (4) Using Google Earth images, slopes where vegetation was destroyed by surface failure and debris flow were extracted as places where slope disasters occurred in the near past.

There were two major difficulties with aerial photography. One is that three-dimensional topography recognition through physical vision is realized in the brain, and sharing the details with others is difficult. Therefore, to educate and acquire this technology, it is necessary to realize a common understanding by verbalizing images by conducting topographic surveys and training in visual interpretation. The second difficulty is that some countries still treat aerial photographs as military secrets, and civilians, engineers, and researchers are not allowed to handle them freely.

On the other hand, digital 3D information obtained using various sensing technologies can be said to have realized the visualization of the work performed in the brain called physical vision. It is also necessary to note that the characteristics of the sensing tool itself vary, and its mechanical accuracy and difficulty in acquiring data depend on the land cover situation and cloud cover to be surveyed. However, it is now possible to easily expose the state and shape of the earth's surface as digital 3D visible information with various accuracy technically, economically, and operationally.

Interpretation of landslide topography from contour maps: Since contour lines are data as shown in Figs. 7, 8, and 9, the flexion, density, and spatial distribution pattern of these contour lines are considered to reflect the state of the terrain itself. Therefore, we will understand what shape the actual landslide terrain is, and assume how the landform is drawn as contour lines. Based on this assumption, by carefully observing the contour map, we judge that "such flexion, density, and their spatial distribution pattern are topography that can only be formed by landslides." This is called deciphering landslide terrain.

Based on this assumption, by carefully observing the contour map, we judge that "such flexion, density, and their spatial distribution pattern are topography that can only be formed by landslides." This is called deciphering landslide topography.

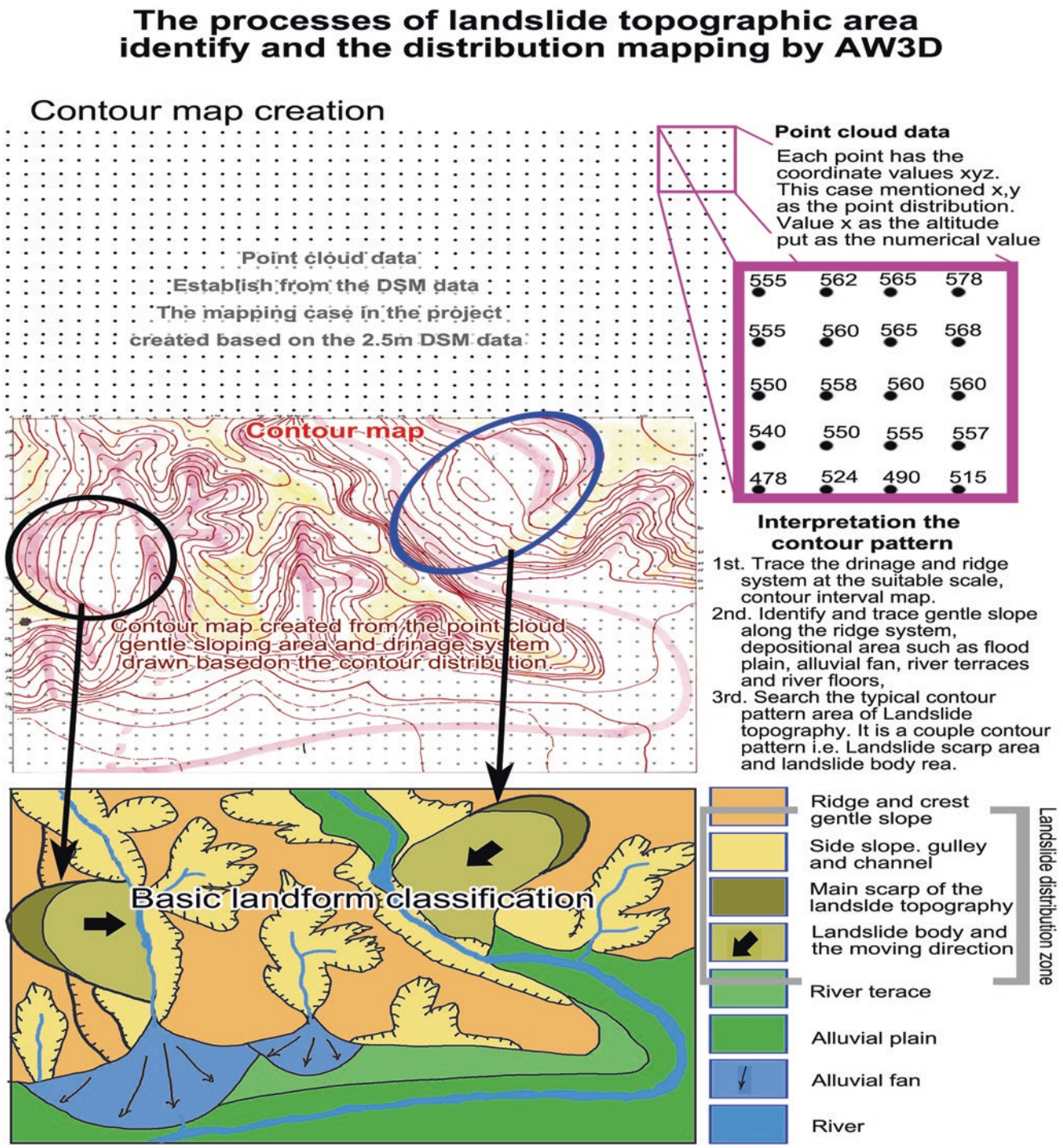

Fig. 7 Generate contour lines from point cloud data, judge topographic areas such as water systems, ridges, landslide landforms, and rapid lines by focusing on the bending patterns, and create a topographic classification map

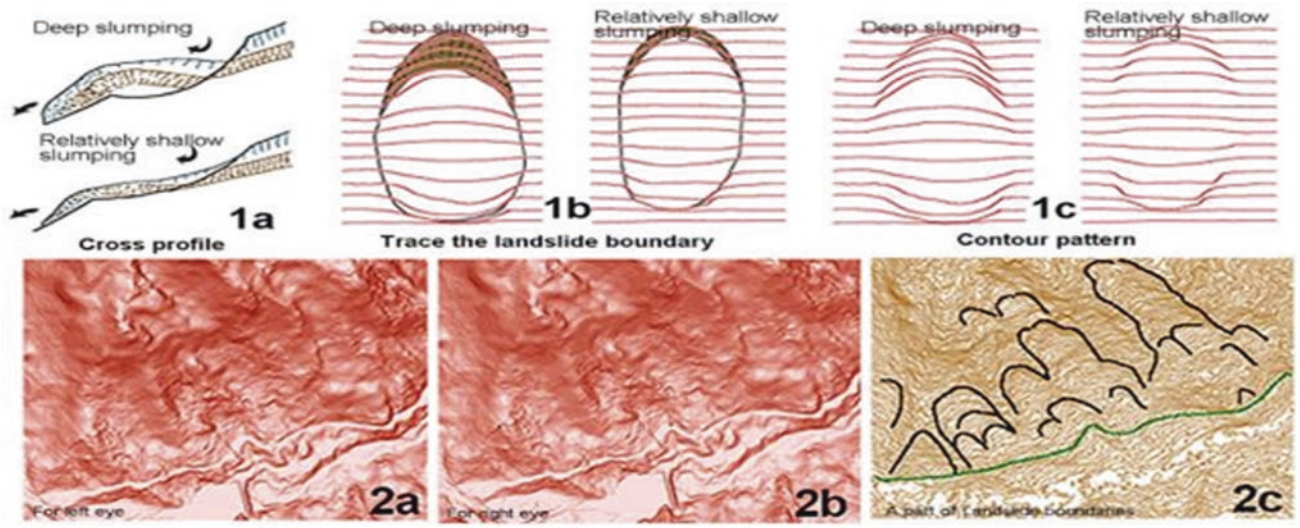

Fig. 8 Various characteristics of landslide topography are summarized and illustrated1a: Cross-section of a typical Slump type landslide. Upper step: When the slippery surface depth is deep, the main sliding cliff slopes steeply. Lower level: If the slippery surface depth is shallow, the main slide cliff becomes gently inclined. 1b: Decipher the topographic boundary from the contour line, draw the boundary, and make it a landslide terrain. 1c: The distribution pattern of contours corresponding to each of 1a. 2 a,b: Images for real-world vision obtained from a shadow diagram by AW3Dde-ta. 2c: A and b are read by real vision and draw the boundary of the terrain that appears to be a landslide terrain

4.2 Example of Landslide Topography Distribution Map

4.2.1 AW3D-Based Landslide Topography Mapping in Vietnam and Sri Lanka

From 2011 to now, it has implemented three projects in the mountainous regions of Vietnam and Sri Lanka. Those are SATREPS (Development of Landslide Risk Assessment Technology along Transport Arteries in Viet Nam, 2011–2017, Representative, Kyoji SASSA) and SATREPS (The Project on Development of Early Warning Technology of Rain-induced Rapid and Long-travelling Landslides in Sri Lanka, 2020–2025, Representative, Kazuo KONAGAI). During this period, JICA Grassroots Technical Cooperation Project in Northern Vietnam's Mountain Province (Capacity Building of Local Community for Slope Disaster Risk Reduction, 2020–2023, Project manager, Toyohiko MIYAGI). In these projects, AW3D data constructed by JAXA/RESTEC/NTT data are used to generate contour lines, decipher them, extract landslide topography, and map them.

As described in the ICL Landslide Teaching Tools (2014) above, this series of tasks uses topographic decoding and mapping techniques to identify the locations inherent in the risk of landslides. In Vietnam, aerial photography could not be purchased freely, and a huge budget was required to conduct new aerial photography of the survey area. However, around that time, the AW3D data (5mDEM) of the title was released and sold, and the price was less than 10% of the cost of aerial photography. This was purchased, and the topographic representation of its contours was evaluated (Dung et al. 2016). After that, the necessary parts are purchased sequentially and diagrammed. Before purchasing, you need to verify the quality of your data. Data quality varies. For example, in places strongly affected by clouds, it is difficult to acquire images repeatedly, which is directly linked to the accuracy of topographic expression.

4.2.2 Mapping Results

Vietnam and Sri Lanka are far apart and have different national conditions. However, the geological characteristics of the mapped areas were generally similar. Both were granite gneiss areas from the Precambrian to the Ordovician period. There was another decisive fact. The distribution of landslide terrain is also "wider and *more numerous than expected!*" In Japan's granitic areas, landslide fractures are not very frequent. In the early days of mapping, we expected landslides to occur on granitic land to be exceptional. However, the more I compared the site with the map, the more I deepened my understanding, thinking, "I see; that's why I say that!" *Even in granite areas, landslide topography existed widely and densely* (Fig. 10).

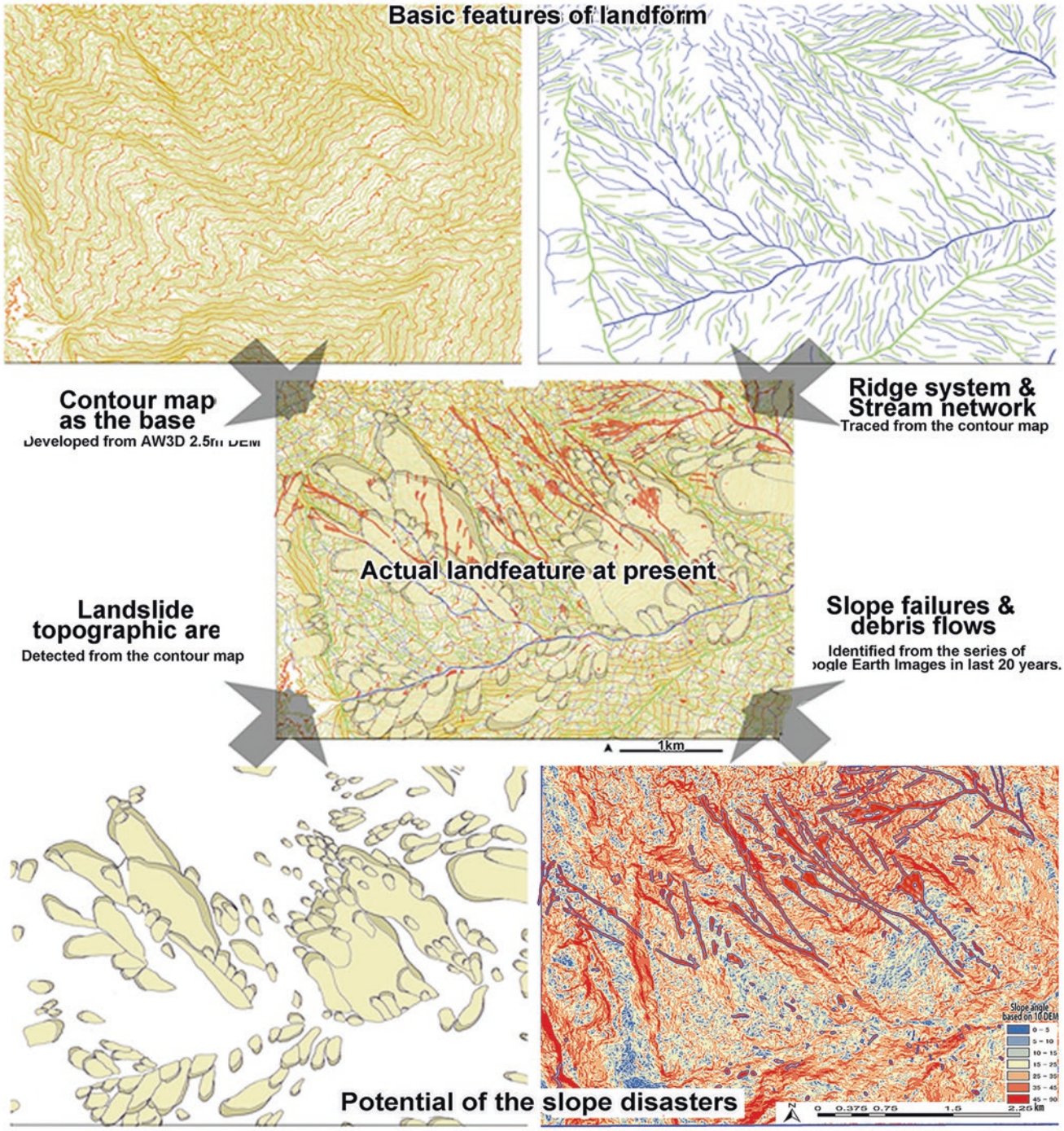

Fig. 9 Contour lines are generated from the AW3D data 2.5 m DSM (note that it is not 2.5 m DEM), and (1) the water system and ridge line, which are skeletal topographic indicators, are deciphered and drawn. (2) Observe the spatial distribution of contour lines, estimate the landslide topographic area, and map its outline. The landslide terrain consists of a main sliding cliff and a moving body, each decipherable from the spatial pattern of contour bending

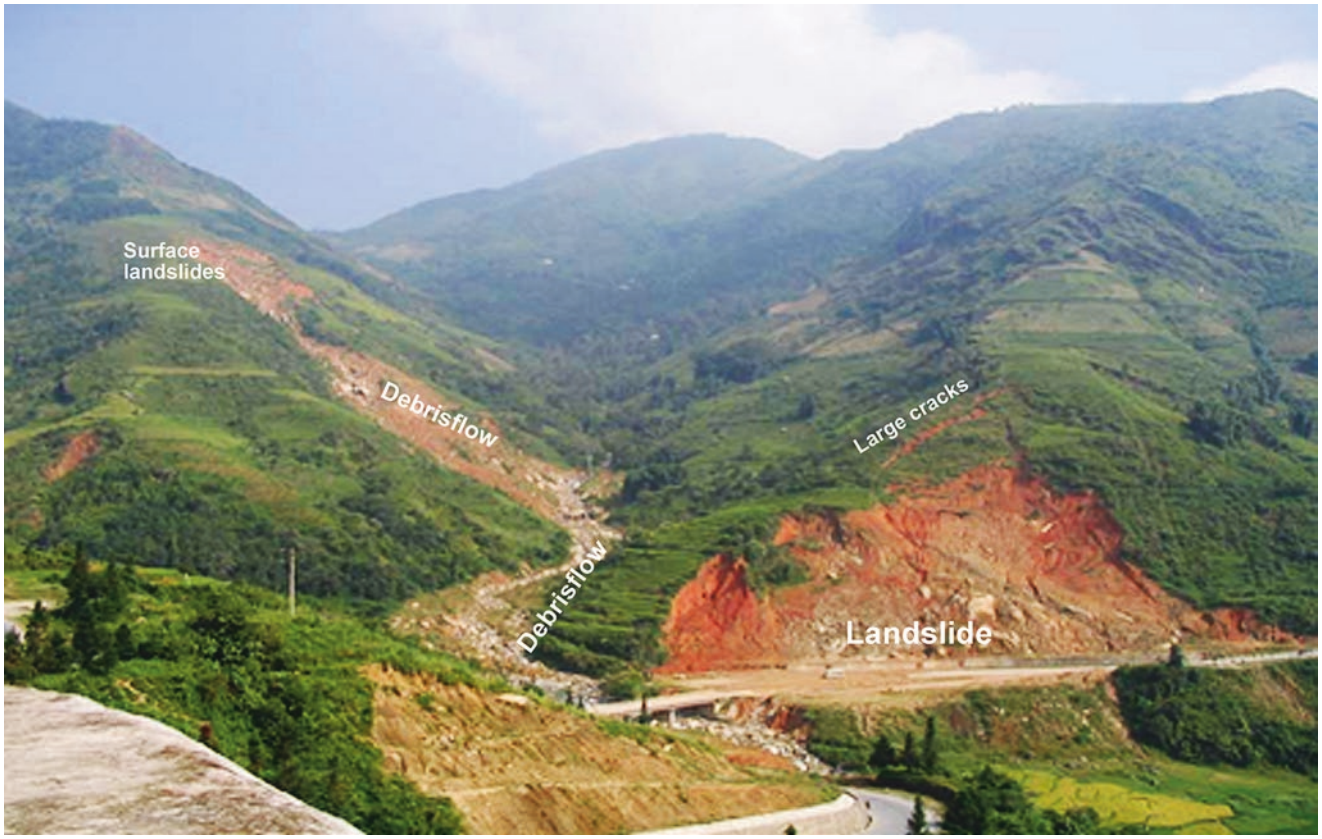

Fig. 10 A slope disaster in Lao Cai Province in northwestern Vietnam in Sept. 2004. All large-scale landslides, shallow landslides, and debris flows (Put some wards to Yem 2006)

4.2.3 Wide-Area Landslide Topographic Distribution Map 1/25000

Figure 11 shows an example of a distribution map of a part of the project's target area. Contour maps of 5 m and 25 m were created for about 60% of the data acquisition area, and this topographic map was deciphered.

As shown in the Index, the data acquisition range was divided into a grid of north-south and east-west 10 km and deciphered sequentially. Interpretation was carried out in the form of repeated prototypes according to the progress of the project, so there were differences in the legend and display for each figure width. In that sense, it is a draft version.

In the upper right (northeast) and part of the northwest of Fig. 12, there are places where a huge landslide topography with an area of several square kilometers is located. On the other hand, in the lower half of the area, small and medium-sized landslide topography develops at a high density. Broadly speaking, the granitic great relief mountain slopes correspond to the former, and the middle relief mountain slopes composed of Paleozoic metamorphic rocks and sedimentary rocks correspond to the latter. Two new findings can be obtained here. (1) In general, in Japan, there is not much distribution of landslide topography on mountainous slopes composed of granites, but here it is extremely dense and widely distributed. (2) There was no recognition that the landslide topography was distributed this way. Depending on the type of analysis data and analysis method, the existence of such a natural phenomenon will be revealed as a completely new fact. By grasping these facts, we can think about what kind of understanding and management of slopes will develop in the future.

As a division of the SATREPS project in Sri Lanka (Landslide Assessment Group), it conducts multiple mapping and surveys in four districts: Aranayake, Kandy, Athweltota and Kotamare. A part of it is introduced in Figs. 13 and 14.

Figure 13 shows the generation of contour lines with contour spacing of 5 m from AW3D 2.5 m DSM data for the Kandy area of the central highlands of Sri Lanka, and deciphering the water system, ridgeline, and landslide topography (main slip cliff and moving body) from this contour line. The western part of Fig. 13, a-b is distinguished by a steep ridge extending in the south-north direction. Only a few small landslides can be seen on the northeast side of this steep ridge. On the other hand, at the foot of this ridge, there is a gentle slope that seems like a cliff cone. Large-scale landslide topography with a width of about 0.4 ~ 1 km is concentrated at the upper end of the water system in c, d,

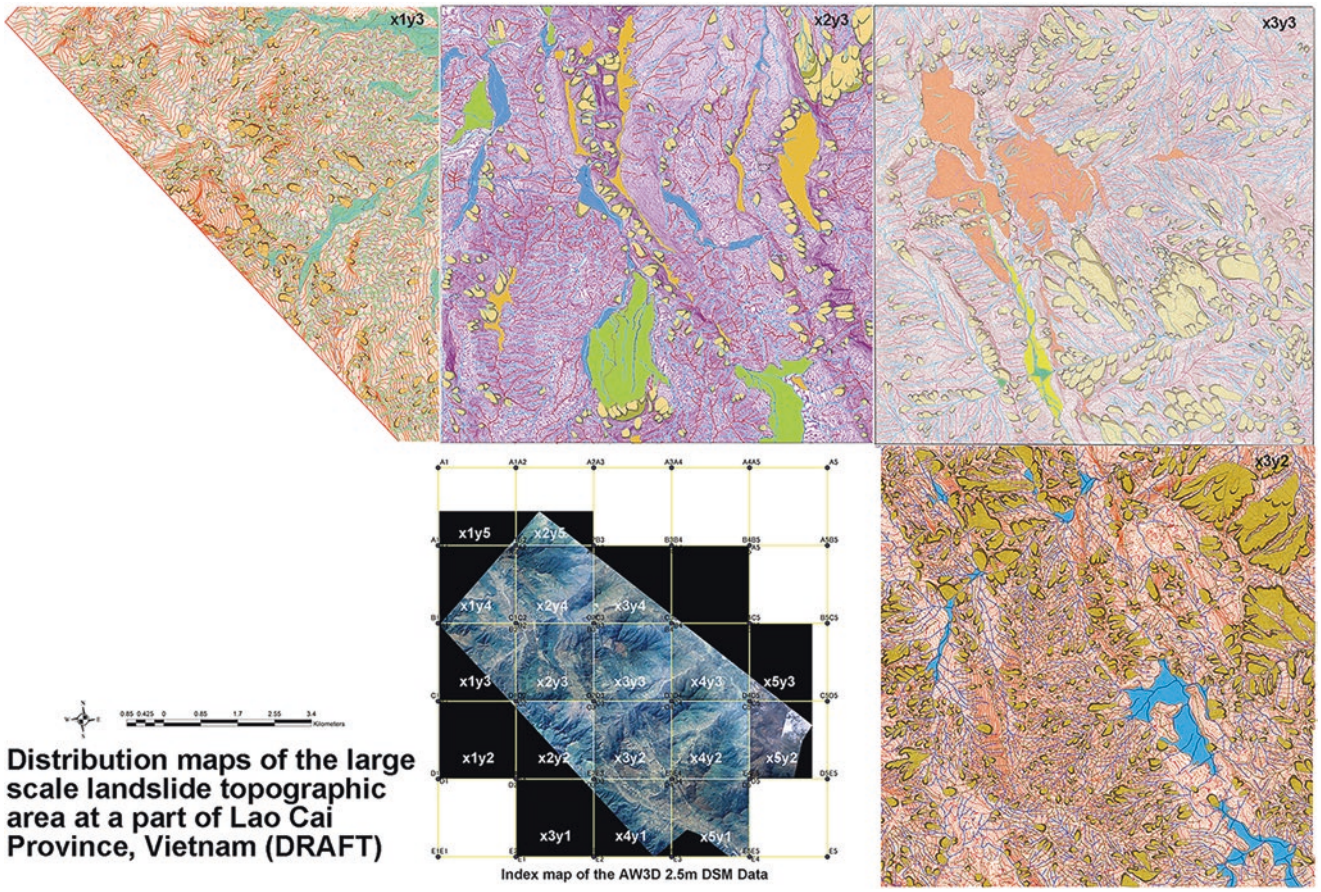

Fig. 11 Landslide topographic distribution map in some areas of Lao Cai Province in northwestern Vietnam

e, f, etc. The lower end of f is further subdivided, and debris-flowing topography g can be confirmed. Low mountains and hills spread around the river at the northern end of the figure, but landslide topography collects some areas such as h and i.

5 Toward an Era in which Everyone Can Grasp the Terrain in Three Dimensions

Substantive reading of aerial photographs has long been used as an expert competence. However, it was difficult to share the contents of the reading with others. This is because substantive vision is an image in the brain. This led to the availability of digital 3D information, such as AW3D data, and three-dimensional information could be shared. UAVs can even acquire, process, and visualize data on their own. It is possible to visualize things on the earth's surface in three dimensions and share their reality with multiple people. In modern times, it may be said that the meaning of aerial photography reading has already been lost. In the first place, to grasp the characteristics of landslide topography and slopes, it is essential to have the ability to create an opinion such as "Observing an unspecified number of slopes, is this a slope with such characteristics?" Even if it is possible to convert wide-area 3D digital information into 3D data at once, it is also true that the empirical knowledge of both sides is necessary to grasp the distribution of instability with different characteristics from that vast area.

If this is the case, the significance of the visual interpretation of aerial photographs will continue to be considered material for inferring the actual state of topographic change.

In the next chapter, starting with the visual interpretation of aerial photographs, we will briefly explain the technology for mapping slope changes, such as landslide topography using precise contour lines, the technology for visualizing topography, especially the microtopography of landslide terrain using DEM, and the technology for sharing microtopographic information that is familiar and problematic using UAVs.

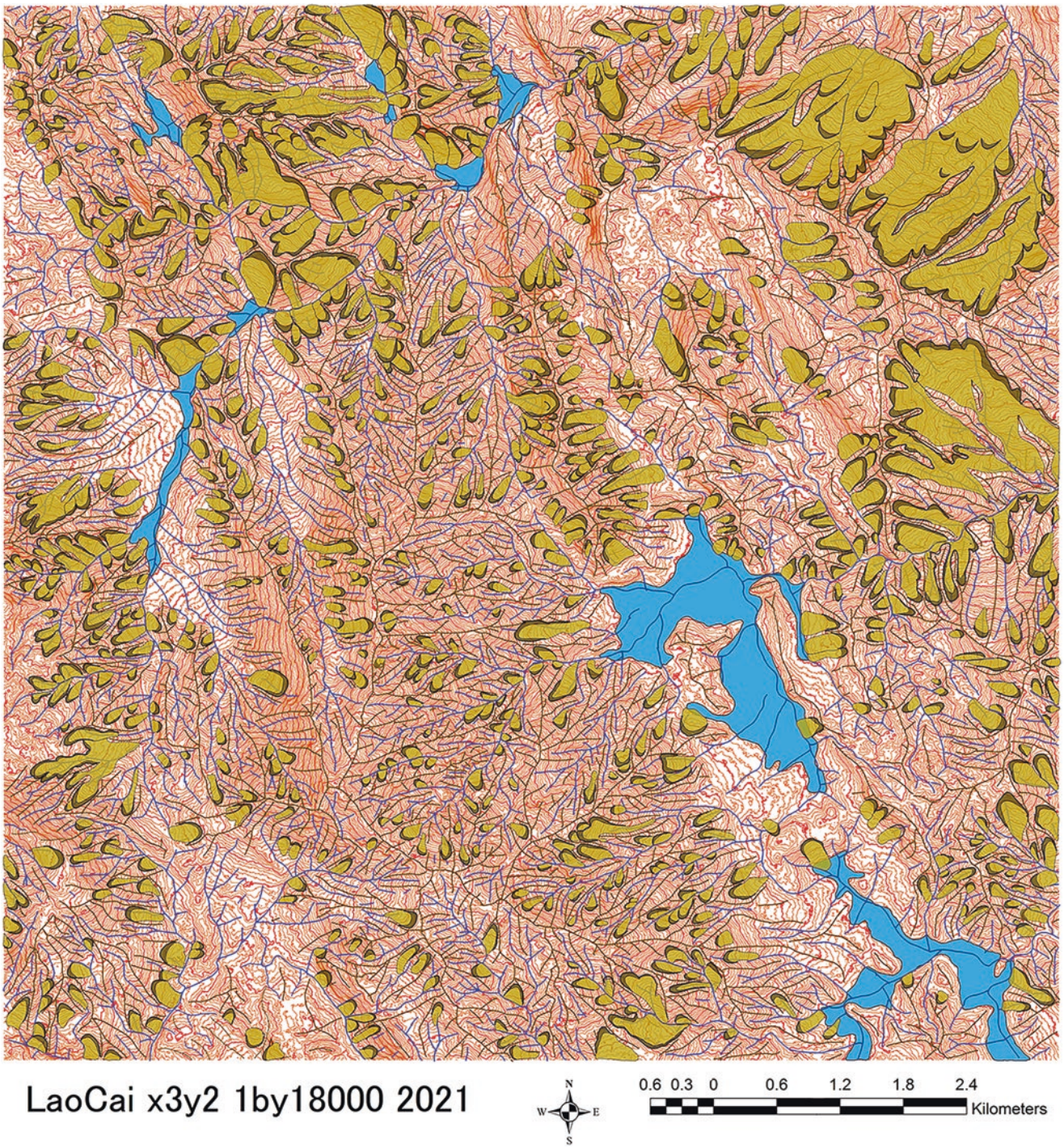

Fig. 12 Landslide topography distribution in some areas of Lao Cai Province, Vietnam

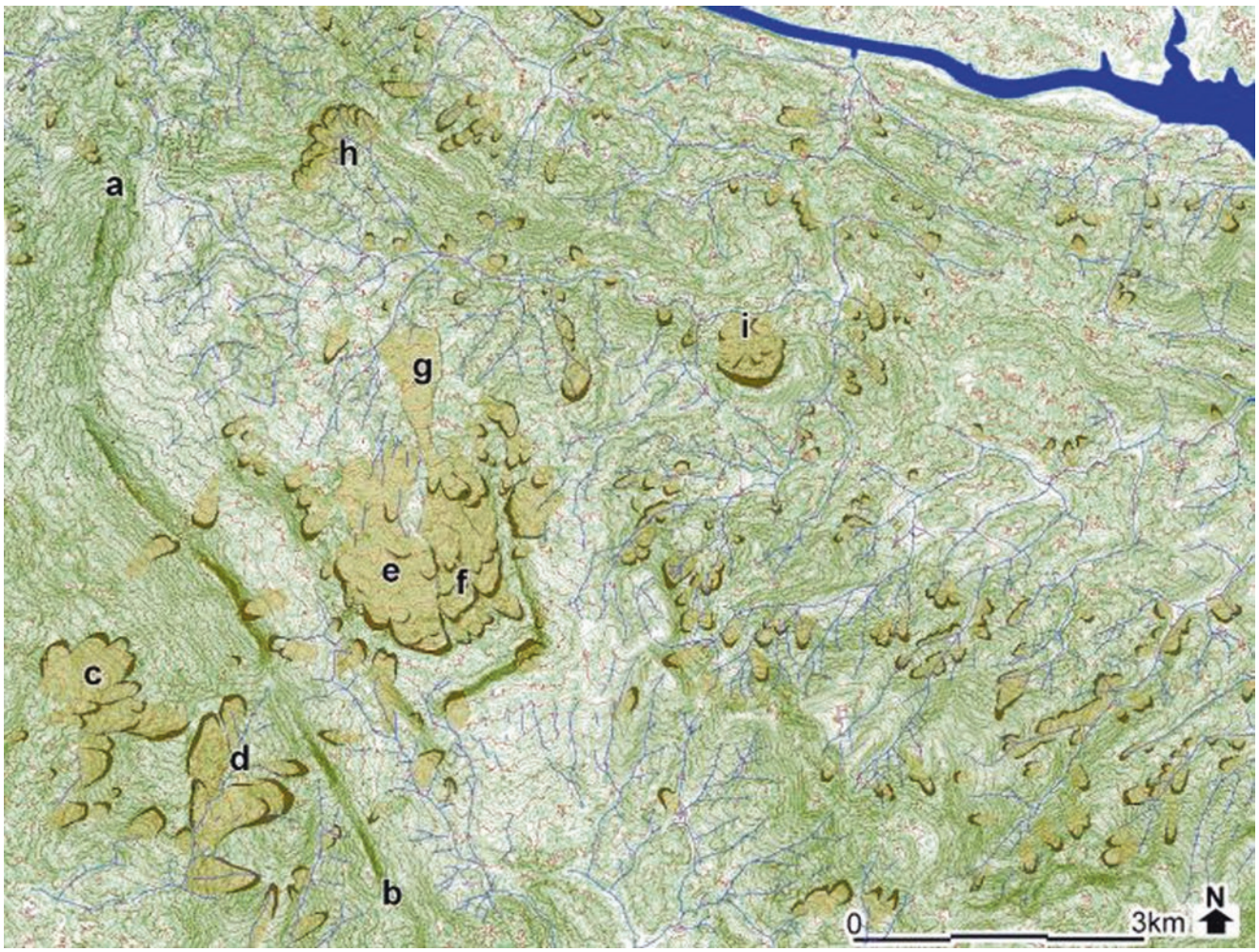

Fig. 13 Landslide topographic distribution map near Kandy in the central highlands of Sri Lanka

6 Aerial Photo Interpretation and Slope Disaster Risk Mapping Training for Beginners

6.1 Focus and Aim

The method of 3D interpretation of aerial photographs has been practiced for about 50 years. This method is to see two overlapping photos as entities, so there is no need to create the data itself. Taking aerial photographs is often a national undertaking. As end users, we purchase, download, and use it. On the other hand, it requires a unique technique of "using two photographs to see the material". Each sees a different image with both eyes, and the two images materialize and are observed in the brain. A third party can't see the observer's brain. Herein lies the difficulty of reading aerial photographs. Third parties will have no choice but to accept or reject the distribution map of the landslide topographic map prepared by skilled observers as if it were a priori fact. This is the background to deciphering landslide topography, where a masterly performance is born. This suggests there is a limit to the establishment and deployment of technology. Here, we will devise ways to gain a common understanding of the entrance to topographic interpretation by aerial photographs. To understand the reality of topographic interpretation assembled by the brain with a third party, I would like to explain the process from interpretation to diagramming in five steps. Some people may find it troublesome, but you can skip reading.

6.2 Aerial Photo Interpretation "Steps for the Technicalization"

6.2.1 Stage 1: Seeing Aerial Photography As a Reality

Observing the terrain three-dimensionally: The terrain is three-dimensional. Therefore, it is better to look at it three-

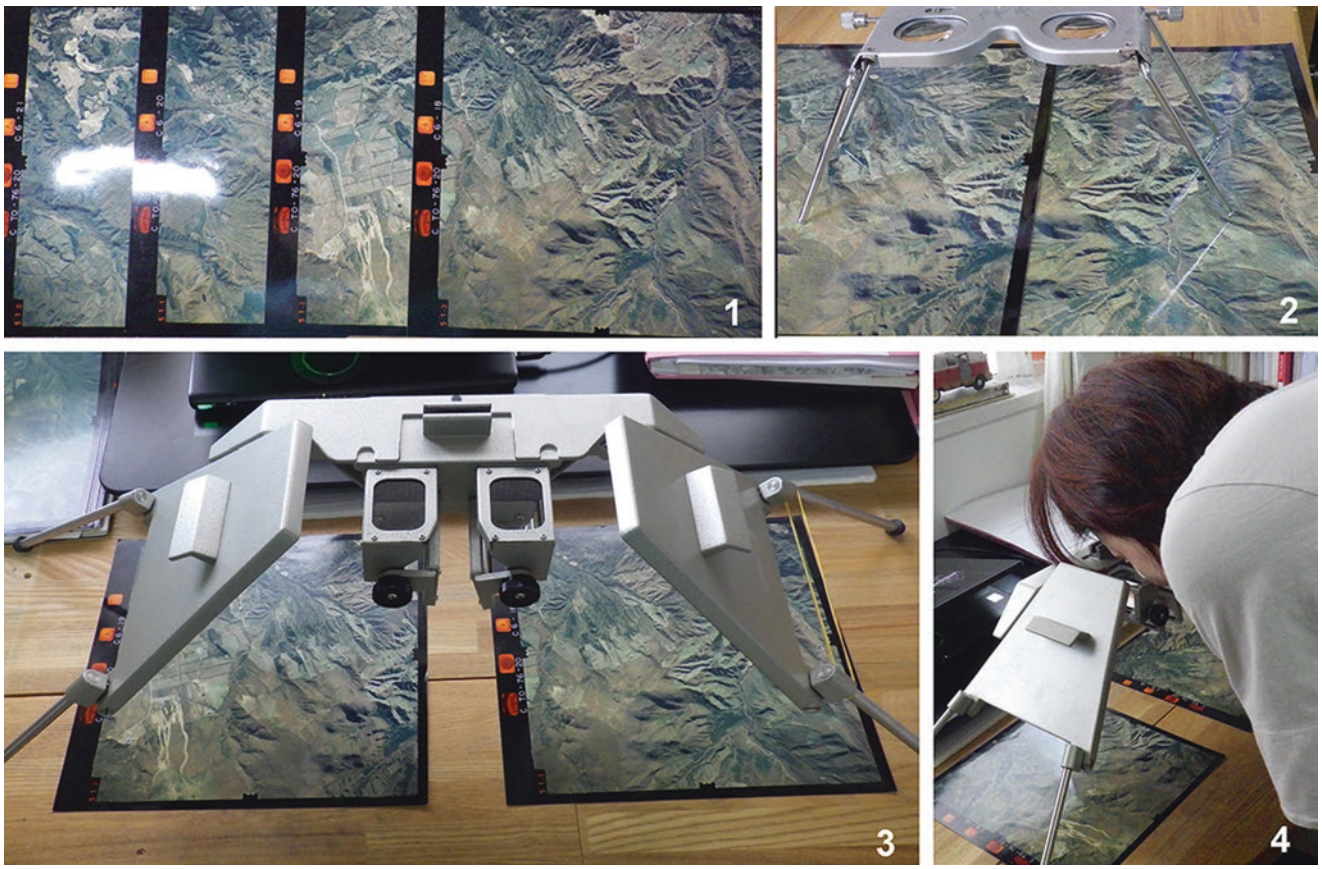

Fig. 14 Three-dimensional observation of aerial photographs of stereo pairs. 1. The close-contact print version of the aerial photograph describes the flight course, scale, shooting time, etc. 2, A photo of a simple stereo mirror and a stereo pair that can emphasize the undulations by about 2 times. 3, Reflective stereo mirror and photo. Pay attention to the distance between the two photos. 4, To facilitate real vision with this stereoscope, the eye is placed on the eyepiece prism from vertically above. The spacing between the two photographs should be fine-tuned to make it easier for the observer to see

dimensionally to get closer to the actual situation. Then, how much range do you think humans see as three-dimensional? In technology, to see an object three-dimensionally, it is necessary to use (1) "parallax" to look at the object from different angles with both eyes. (2) The difference in parallax obtained by these two eyes is synthesized in the brain and transformed into a three-dimension. Humans can perceive objects three-dimensionally within 10 m at most. In aerial photo decipherment, you look at two pictures with two eyes. A camera with a central projection took each photo from the sky. Adjacent images are taken so that they overlap about 60%, so even if they look similar, there will be a misalignment. It artificially creates parallax. There is a tool called an aerial stereoscope (Fig. 14). It puts two photos side by side, making it easier to see each separately with both eyes. With this tool, you can easily experience stereoscopic images of aerial photographs.

*Let's take a look first***:** Prepare a stereo mirror and two or more sequential aerial photographs. Aerial photographs are marked with the time taken and the code number. First, let's arrange the photos (Fig. 14-1). This photo was taken closely on a roll film with a scale of 1.15000 and a width of about 24 cm. When magnified about 2–3 times, it has a resolution of about 1 m. Adjacent sequential-numbered photographs can be viewed three-dimensionally with the naked eye (also called the naked eye), a simple stereoscope (Fig. 14-2), or a reflective stereoscope (Fig. 14-3). The overlapping photos are shifted, each viewed with the right and left eyes. Still, the distance between the pupils of both eyes is about 6.5 cm, so shifting the same subject by about 4–6 cm makes it easier to see three dimensions. Since the observation range is very narrow, it will be easier to see the photograph three-dimensionally if you observe it at a distance like a reflective stereo mirror (Fig. 14-4).

If you are a complete beginner, let's observe it. What do you think? Those who see aerial photography for the first time are almost always surprised. It's amazing, it looks three-dimensional, it looks like it looks more detailed, it's like a bird!

6.2.2 Stage 2: Talk About Impressions of "Things" That You See As a Reality

Verbalization of visible things and things: If you look at an aerial photo three-dimensionally using a simple tool, everyone has some image. So, the question is. What did the terrain look like? *Tell me in your own words what you see and what you see. If I'm not there, talk to yourself*. Then, I can share the image, too. Since I observed the same photos beforehand, I imagine that what you are looking at is "maybe something like this." This will never be known to a third party.

Of course, what you see will vary from person to person. However, most people recognize unevenness, ridges, valleys, mountain tops, and plains.

You may even notice cliffs and steep slopes. Here, the observer observes the actual terrain three-dimensionally. I notice that.

6.2.3 Stage 3: Focus on the Terrain (this Is the Core)

For example, in the plains, Fig. 15 shows two monochrome aerial photographs of Japan taken around 1980. Within this range, I think it can be easily observed three-dimensionally.

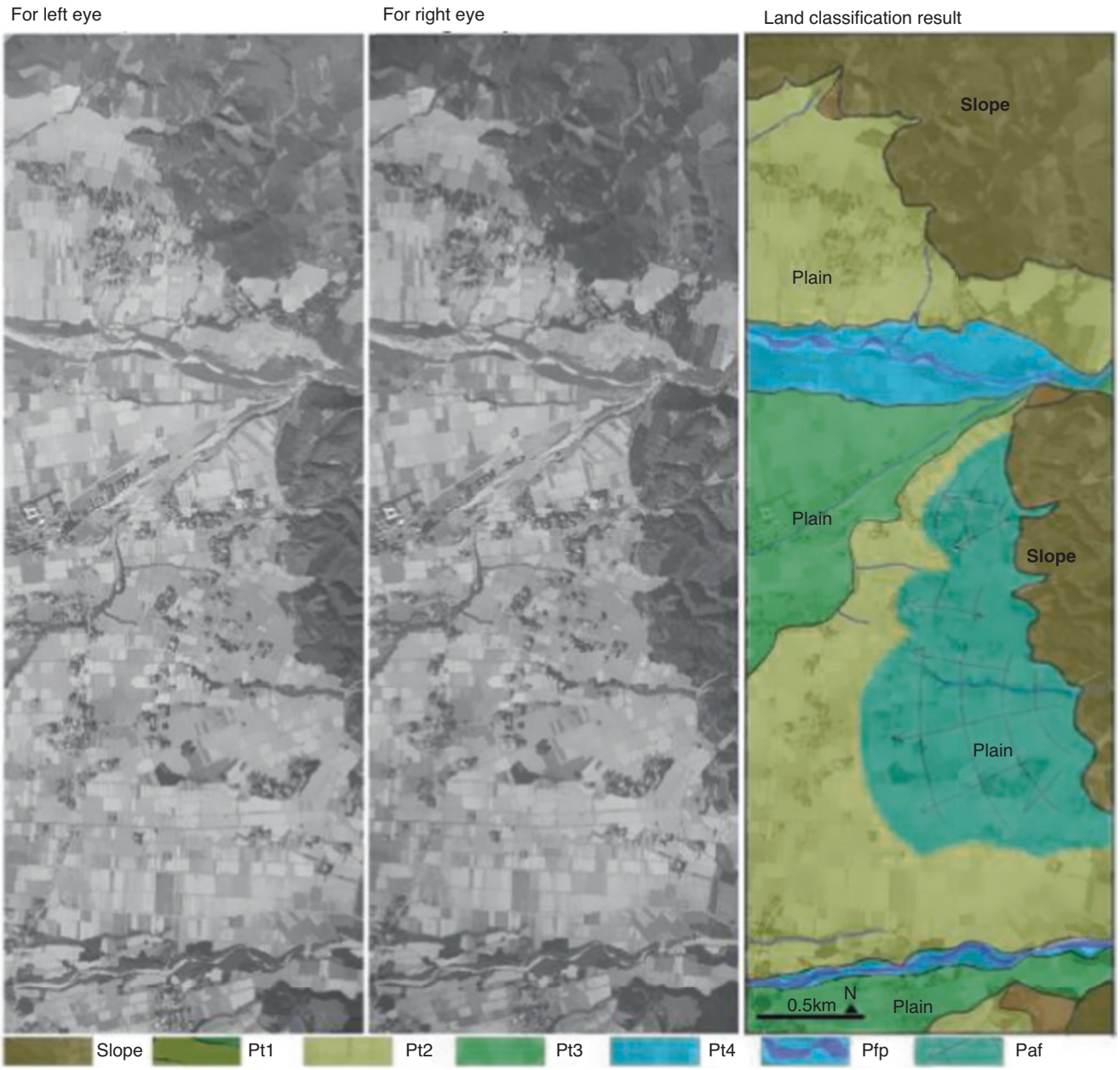

Fig. 15 Interpreting the plain

In general, the pupil distance between both eyes is about 6.5 cm. Here, the distance between the same points in the left and right images was adjusted to about 4.5 cm to make it easier to observe. You will see three when you look at two photos and realize they are three-dimensional images. The left and right are not three-dimensional, while the center image is three-dimensional and clearer. Your brain observes this situation, so the third party does not know. Observing the terrain in this way is called "substantive visual interpretation".

The landforms seen and deciphered as real are arranged on the right as a topographic classification map. At first glance, you can see that there is a plain (smooth land) in this range and a slope (ridge, valley, etc.) on the right (eastern). Roughly speaking, in which direction does the river flow? If you observe the plains carefully, you can also observe river channels, lowlands on both sides of the river that seem like floodplains, and small steps (cliffs). The plain also seems to have some steps. Here, the lowlands along the river are divided into Pt 1, 2, 3, and 4, focusing on the step difference in the lowlands along the river. You may also notice that near the mountains, there are fan-shaped slopes (Paf) that slope gently towards the plains and small plateaus (Pt1) that are even higher.

If you make a diagram of what you read above, you will have made a topographic classification map. The slopes are jumbled compared to the plains, and the terrain looks detailed and complex. On the other hand, even in plains, it is not simply flat and quite complicated. The photographs show more than just the terrain so that you can imagine the correspondence between the topography of the plains and land use. There are no settlements in PT1, which is small and attached to the slope, and Pt4, which seems to be greatly affected by rivers. It seems to indicate the possibility that land use is being carried out in response to the risk and convenience of flood damage. PAF is a terrain called an alluvial fan, a land formed by repeated flooding and debris flows flowing out of the mountains during heavy rains. Settlements are also scattered here. Observing these situations lets you consider the relationship between disasters, people, and topography.

Seeing the slope substantially: What terrain will the slope area be made of? The slopes are *complex and messy*, but they are places that suffer erosion. The terrain is mainly eroded by rainwater, and its sediment is carried by rivers and deposited in plains and seas. If this is the case, it can be seen that the seemingly complex slope area is in a situation where rainwater and rivers erode the terrain, making it complicated. The water from rainfall becomes surface water and groundwater, which gather and exert an erosion effect. Due to erosion, the valley muscle develops, a water system is formed, and the not-eroded part becomes an elongated ridge. If you take a bird's-eye view of the slope area, you will notice that the valleys and ridges form a water system. Figure 16 shows a part of the slope area extending to the east of Fig. 15 and shows an image for real vision and its interpretation results. Let's take a 3D look. Complex slope areas are building a system that drains water like tree branches. The slope area, consisting of small ridges and valleys, is like a treetop, so to speak. In the water drainage system, countless treetops gather, forming large valleys and growing into rivers. The set of small valleys and surrounding ridges is called the valley head. On the ridges, rainwater moves divergently, so the erosion power is not exerted. On the other hand, in the valley, water gathers and exerts great erosion and transportation power. This large difference in action in the system creates a complex and undulating terrain.

6.2.4 Stage 4: Observing the Longitudinal Profile from the Ridge to the Valley Floor and Considering the Formation Process

What is the slope condition between the ridge line (ridge) and the mountain stream (valley floor)? The slope between the ridge and valley lines is wide and is named the side slope. I enlarged a part of Fig. 16 in Fig. 17. The ridge is difficult to erode, and the valley floor is where erosion and transportation are extremely intense, including running water. What kind of action works on the valley wall slopes separated by these two landforms? The most important feature of the valley wall slope is the steep slope.

Figure 17 schematically shows the characteristics of the longitudinal section from the ridge to the valley. Figure 17 divides the valley wall slope into three parts. The red color looks like a collapsed mark on a slope with no vegetation. This is the site where a shallow landslide (surface failure) has recently occurred. The areas shown in yellow-green are noisy with vegetation compared to the surrounding area. Perhaps herbs and shrubs are sticking to it. Other valley wall slopes seem to be covered with forests. In addition, in the lower quarter of the figure, there is a place where you can observe several elongated streaks that lack vegetation. Looking at these planar distributions, it can be said that the valley wall slope is a place where sediment moves toward the valley floor. Sediment movements range from recent occurrences (bare ground) to past occurrences and vegetation recovery, and in some places, debris flow seems to have occurred. In summary, valley wall slopes can be considered as slopes formed by shallow landslides (surface failures) and debris flows that occur repeatedly over a long period of time at various times, scales, and intensities.

Figure 18 shows an aerial view of a debris flow in Hiroshima City in 2014. The disaster brought total rainfall to 2000 mm and resulted in 74 casualties caused by numerous debris. The debris flow is seen as long, narrow streaks

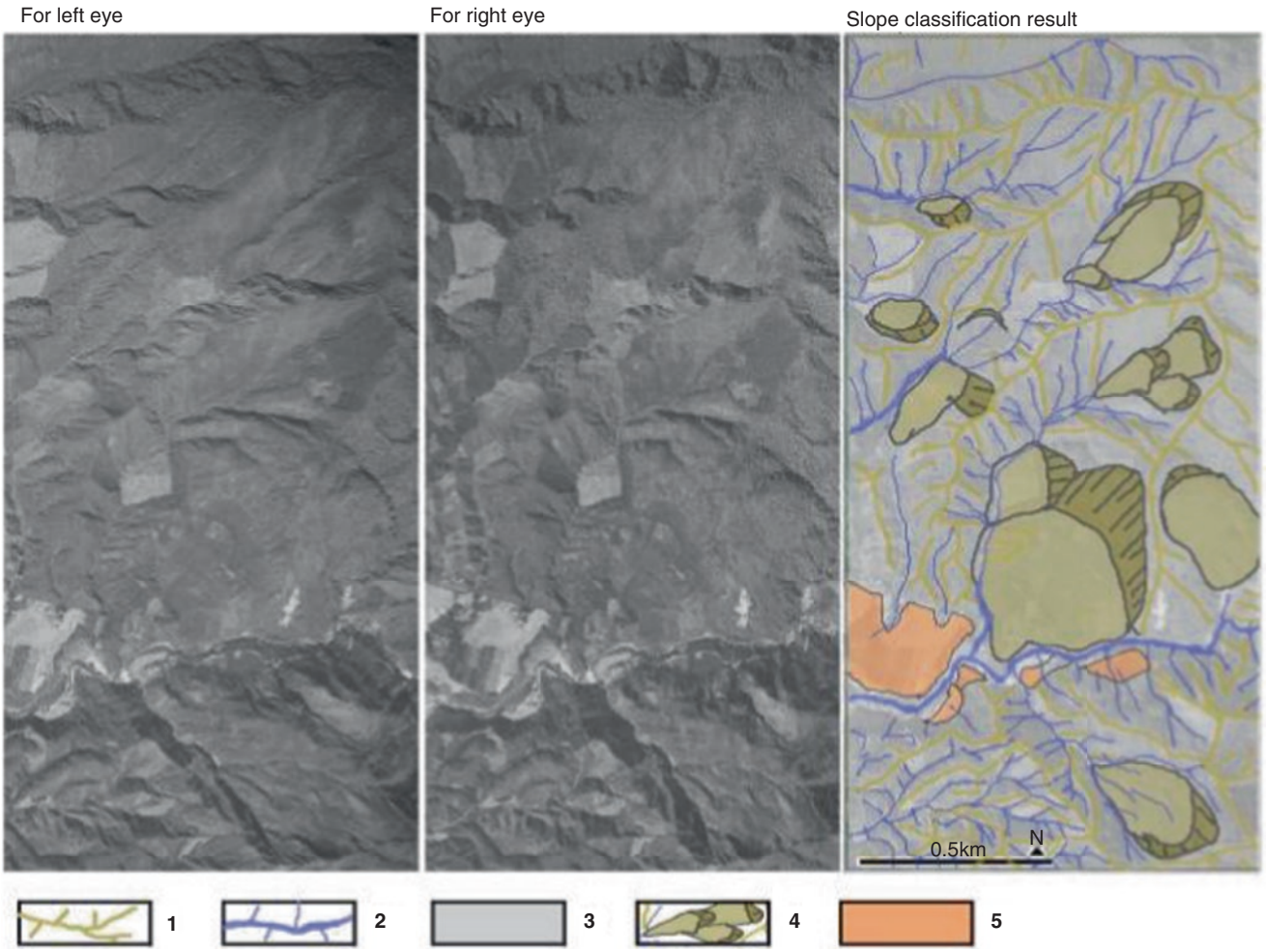

Fig. 16 Topographic composition of the place where the slope spreads 1; Crest/ridge system, 2; Stream network 3; Valley side slope, 4; Landslide scarp and the body, 5; River terrace

carving the slope. Looking at individual streaks, we can observe places where vegetation is lacking, which is considered to be the origin of debris flows, mountain streams where bedrock has been exposed by erosion downstream, and gentle slopes due to the accumulation of moving sediment. The affected residential area is located on a gentle slope. The place where the debris flow began to accumulate and diffuse seems to be at the upper end of this gentle slope. It can be judged that the damaged residential area was created on a debris flow fan formed by the accumulation of repeated debris flows in the past. It can be judged that a phenomenon similar to the debris flow that caused the 2014 disaster has occurred repeatedly. The streak-like microtopography in part of Fig. 17 seems to be the lower part of a small debris flow. Rivers quickly transport sediment brought in by debris flows. However, some parts of the river have sediment accumulations, and there was a large-scale sediment supply in the past.

6.2.5 Stage 5: Deciphering Landslide-Induced Terrain

In Fig. 16, many sites that are thought to have been created by landslides have also been identified. This kind of thing is called landslide topography. Landslide terrain is a landform formed by a part of a slope causing landslide deformation. This terrain has topographical features that are very different from the phenomenon on the slopes we deciphered in Stage 4. Typical examples are illustrated by Vernes (1978) and others. Landslide topography created by landslide action is a terrain composed of topographic elements such as main sliding cliffs, moving objects, and slippery surfaces. Among them, the slip surface is the boundary between the moving body and the immovable body, and in many cases, it does not appear on the ground surface. Landslide topography varies in size from (1) deforming part of the slope to a huge landslide that changes the distribution of ridges and water systems. (2) Geological conditions are often involved in forming the slip surface. (3) Once destruction occurs, an autonomous destruc-

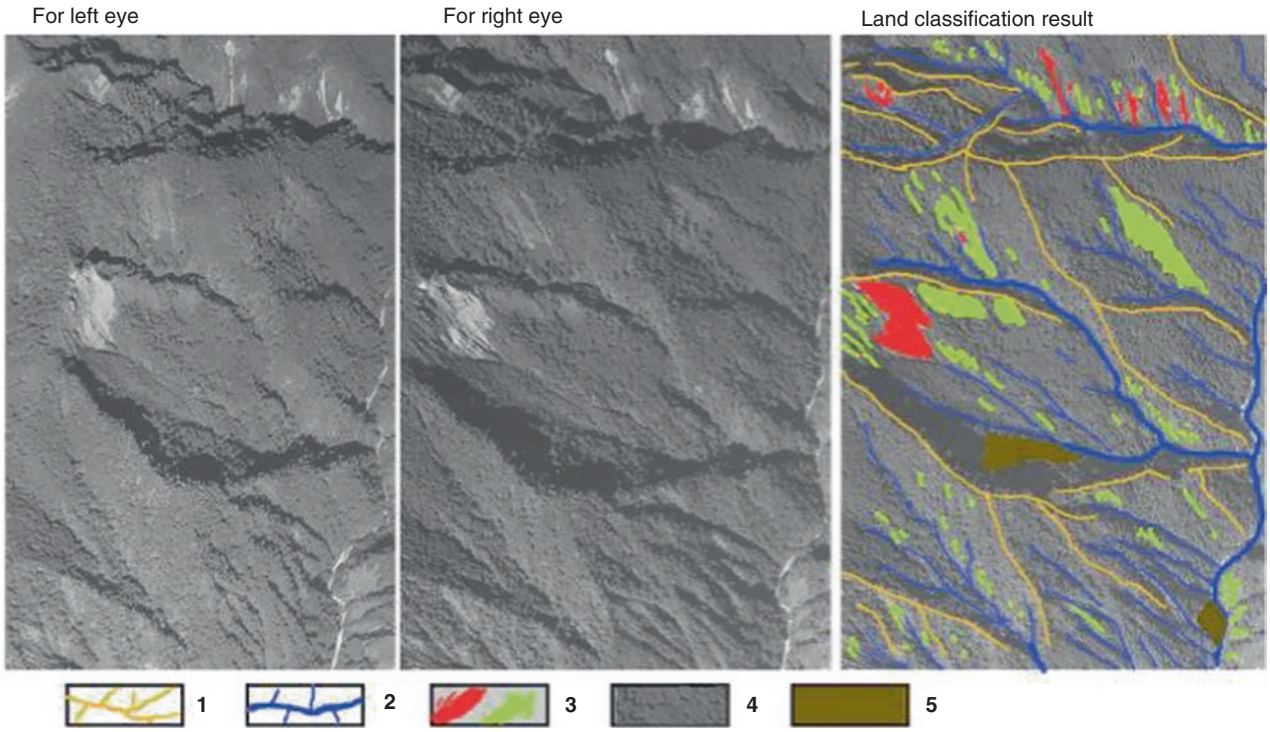

Fig. 17 Close up the valley side slope 1; Crest/ridge system, 2; Stream network, 3; Surface landslide / Slope failure (Red: non-vegetation, Light green: poor vegetation), 4; Vegetation covered side slope, 5; Scree/Talus slope

tion process is followed as described later. (4) The time from the first destruction to the end of the landslide itself is about 103 ~ 5 years. It is quite different from the destruction of the ground surface, which fluctuates depending on the topographic conditions of the slope.

Why should landslide landforms, which result from landslide movements, attract attention in slope disaster prevention? There are two main reasons. (1) Since the factors that cause fluctuations in landslide topography are maintained as they are, even if they are the result of landslide fluctuations, there is a possibility that the slope surface liquefaction will become destabilized again if pore water pressure near the slip surface due to a large amount of precipitation, elevation, earthquake motion, etc. occurs. (2) Land that has suffered landslide fluctuations has suffered many changes in physical properties, shape, water, weathering, and other chemical composition. These changes seem to have increased their vulnerability compared to before the landslide movement. In other words, it will be more vulnerable than immutable land. It can be considered that this vulnerability will predispose to future fluctuations, and further weakening due to fluctuations will create a predisposition to the next fluctuation. Considering this, it can be evaluated that the landslide terrain itself is a sloped area with a risk of landslide fluctuations. The idea that chains trigger primary landslide fluctuations to the next is described as "Autonomous Destruction Process of Landslide Landforms" (Figs. 3 and 4 in this paper, Miyagi et al. 2004, Miyagi 2021)". Figure 19 shows a seismically pumped giant landslide, which is thought to have occurred by expanding upward from a large-scale landslide that had occurred in the past. Figure 20 seems to be an active landslide, but as shown in the image on the right at a time interval of about 25 years, vegetation seems to have recovered if the movement is slow.

Aerial view for real vision (1/1.5000 taken in 1976) Google Earth image taken in 2021.

Repeated large-scale landslide fluctuations can cause major changes in the distribution of the water systems and ridgelines that make up the slope area. Figure 8 shows an example. Landslide topographic changes seem to proceed differently from surface failure (shallow slippage).

6.2.6 Stage 6: Find and Map Landslide Terrain Using Aerial Photography

So far, we have observed various features of the terrain (undulations, steps, slopes, longitudinal sections, etc.), starting with the experience of seeing aerial photographs as reality. In Stage 4, we focused on the slope and shape from the ridge to the valley floor. On the slopes of the valley walls, sediment movements such as surface failures and debris flows frequently occurred. I could imagine the possibility that the slopes of the valley walls, which are now covered with vegetation, have been repeatedly subjected to similar sediment movements. Stage 5 focused on

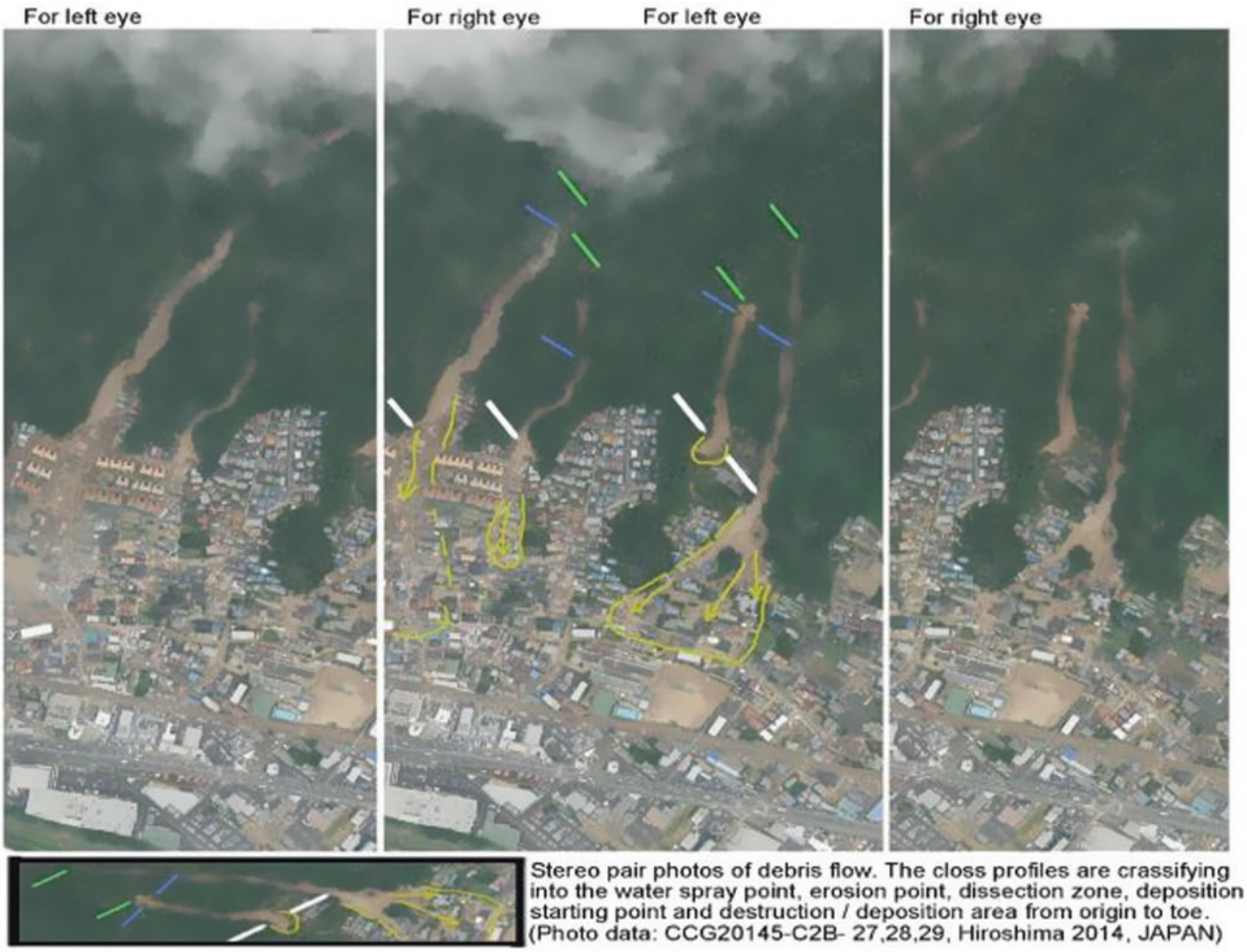

Fig. 18 Detail of Debris flow that occurred in 2014 in Hiroshima City, Japan

large-scale landslide terrain. I realized that large-scale landslides are phenomena that boldly deform microtopography, such as ridges, valleys, and valley wall slopes. As shown in Stage 3 (Fig. 15), the land formed by such a landslide was scattered like a mosaic in the slope area, as shown in Stage 4. By the way, Fig. 15 is a landslide topographic distribution map.

The slope area is probably a mixture of the slope area that can be grasped in the longitudinal section of the ridge-valley wall slope-valley floor and the area of large-scale landslide terrain. For example, suppose this condition is illustrated on a 1:25,000 topographic map. In that case, there will be a limit to the ability to express the evidence of surface failure and debris flow that occurred in the area that can be grasped in the longitudinal section. Moreover, even slopes currently covered with vegetation themselves are slopes where soil and vegetation have been regenerated after slope failures or debris flows have occurred. It will be difficult to read this minute situation in detail from the contour lines of the topographic map.

On the other hand, terrain created by large-scale landslides has features that stand out from the surrounding slopes due to microtopography, such as sliding cliffs, moving objects, and slippery surfaces, as exemplified in Stage 5. In this case, in some cases, microtopography may also be expressed on the contour lines of the topographic map. Figure 21 shows such an example. Think about the landslide terrain, why you can say so, what the evidence is, what kind of drawing you can draw on the topographic map, etc., and draw it on the topographic map on the far right. If the distribution of landslide terrain is shown extensively, it will be a landslide topographic distribution map, and it will be data that suggests slope instability.

The terrain formed by a large-scale landslide is a set of steep cliffs (steep slopes that border the surrounding immovable area and the landslide's moving body, such as main sliding cliffs, side cliffs, and secondary cliffs that occur partially in the moving body), and mobile bodies (A part of moving materials of earth that slide separated by cliffs and stop on the slope).

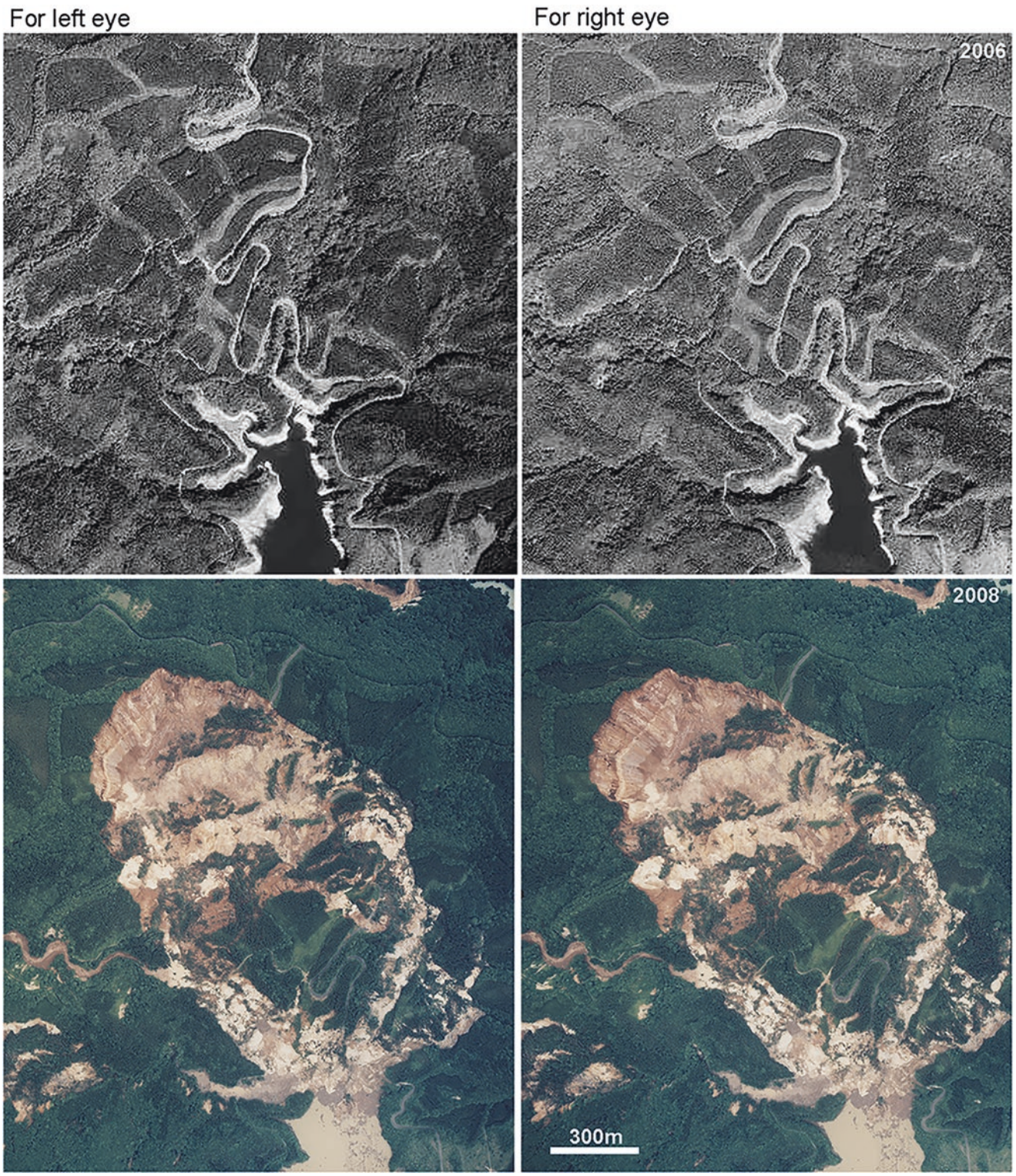

Fig. 19 Seismically pumped giant landslides (bottom: Aratosawa landslides caused by the 2008 Iwate Miyagi Inland Earthquake). Above: State before the 2008 earthquake (multiple landslide topography that fluctuated greatly can be confirmed) The C-14 age of the buried trees in this mobile body was measured to be older than 46,000 years

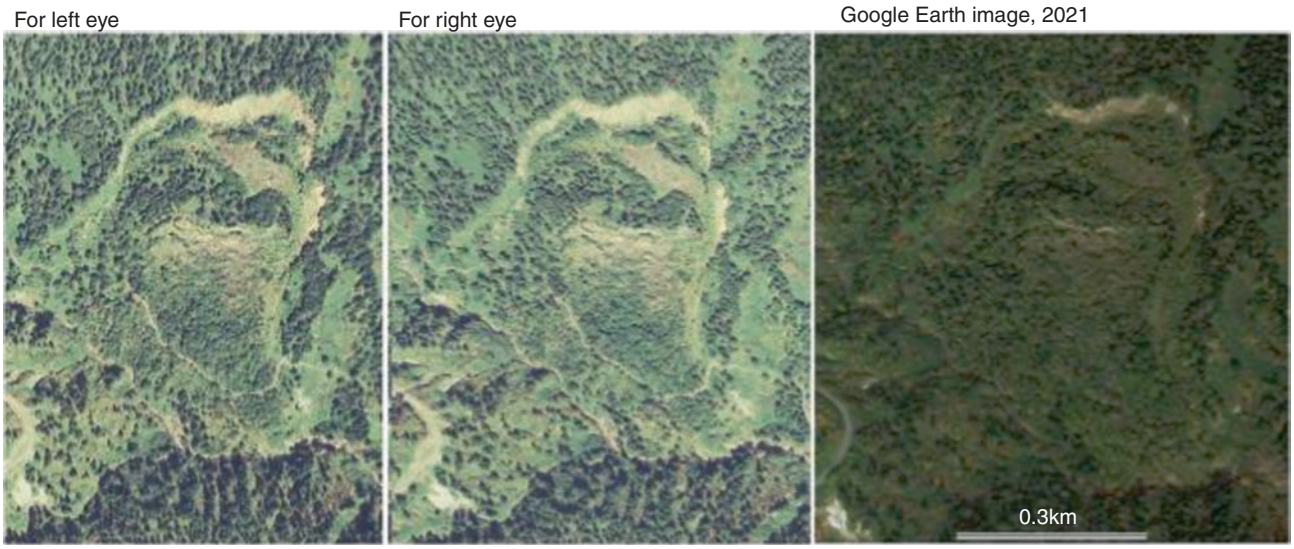

Fig. 20 The Toshichi hot spring large-scale landslide continues to fluctuate vigorously

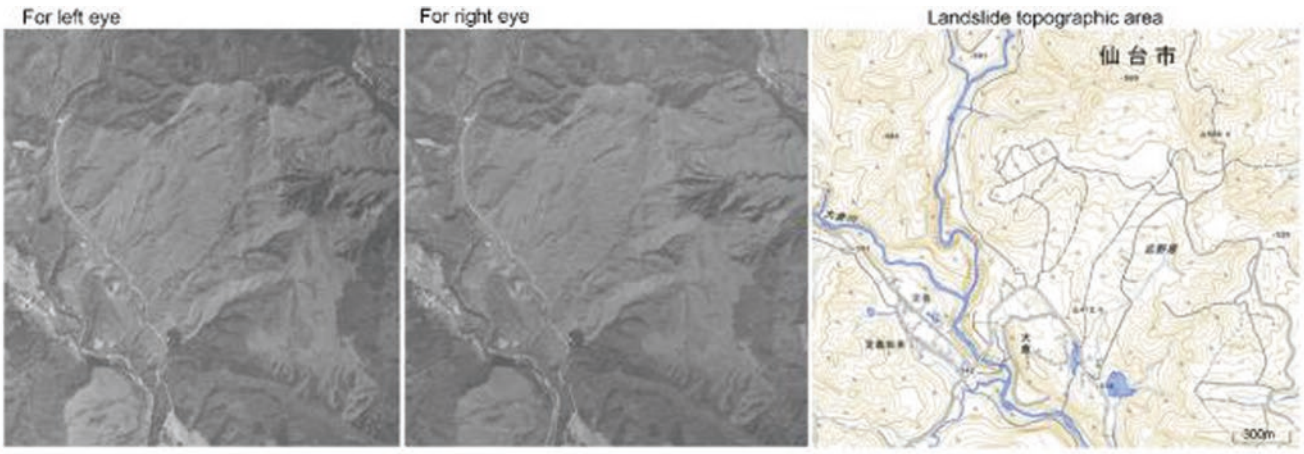

Fig. 21 Photograph of landslide topography for real vision and base map for creating landslide topographic distribution map

7 Understanding Landslide Topography Using Contour Lines and Training for Evaluating Slope Instability

7.1 Perspectives and Approaches

By reading aerial photographs, we could visually grasp large-scale landslide topography, shallow landslides (surface failure), debris flows, etc., and map them. However, it was necessary to transcribe it on a topographic map to map it. For this purpose, accurately reading the contour lines is also necessary. In modern times, if you create a GIS-based reading result with position coordinates, it can be converted semi-automatically to contour maps and statistical data. However, it is difficult to automate this part of deciphering aerial photographs in the first place because the judgment *proceeds in a three-dimensional form in the brain***.** On the other hand, contour lines should faithfully reproduce the terrain. It can be said that the image of the brain is visualized with information called contour lines. In recent years, numerical information on the ground surface has progressed, and it has become easy to create contour maps, shadow maps, stereo images, etc., using this information. Such numerical digital information can be point-cloud data or multi-view photogrammetry-based data. Here, we train to identify landslide topography by reading contour maps, and to evaluate slope stability from the distribution of contour lines.

7.2 Reading Data

The data used in this process uses LiDAR data to decipher precise topography (contour lines of about 1 m) to grasp the precise topography. In addition, the data is somewhat coarse (data accuracy of about 2.5-5 m grid). AW3D data captured and maintained by JAXA, RESTEC, and NTT data is used to judge terrain. The digital data used here is DSM (numerical surface model: data on the top surface that covers the earth's surface such as land, buildings, vegetation, etc.) and DTM (digital terrain model, but it is used in the same way as the DEM digital elevation model). DSM reproduces the ground surface's altitude by decreasing vegetation and man-made objects). The method of acquiring data can be broadly divided into point cloud data when using laser pulses. Also, when using images (such as SfM), it will be photogrammetric data.

7.3 Stages Using Airborne LiDAR Data

A huge amount of 3D point cloud data obtained using an aircraft-mounted laser measuring device is processed by filtering and other processing and acquired as high-precision 3D digital point cloud data, which is further processed to create contour maps. Extremely high-precision digital data can be obtained, but depending on demand, performing data acquisition work and post-processing, such as filtering, is necessary. Therefore, it is made to order and extremely expensive. Here, using a helicopter-mounted high-precision laser data measurement system (Naka Nihon Air survey SAKURA-1), we verified the extent to which laser pulses pass through the forest cover layer to reproduce microtopography in mangrove forests where cross-sectional surveys of topographic vegetation have been conducted (Fig. 22). The SAKURA-1 is a waveform recording type, laser pulse firing frequency of 100,000 rounds per second, measurement density more than 4/m2. The upper row of Fig. 22 shows the laser point cloud two-dimensional distributed contour line and altitude stage size in a range of 1 m in width, including the survey line. The lower part is a topographic vegetation measurement cross-section. They correspond well with each other, and high-precision laser surveying proved that the microtopography of the forest floor can be accurately grasped even in mangrove forests with a canopy cover density of about 85% (Makabe et al. 2015, Unome 2020).

In the case of general measurement accuracy ($1/m^2$), when the tree canopy cover exceeds 80% and forest floor vegetation exists, it is difficult to acquire topographic information with an accuracy of several tens of centimeters even if LiDAR measurement is performed. However, it has great applicability by acquiring data with various accuracy depending on the ground surface characteristics to be measured and the measurement purpose.

During the 2008 Iwate-Miyagi Nairiku Earthquake, 3500 landslides and landslides occurred, including the Arato Landslide (Miyagi et al. 2011). Aerial laser measurements were conducted over a wide area to grasp the details of this slope disaster. Figure 23 is a cut out of a part thereof. The created point cloud density was about $1/m^2$ and used here as a contour map with 2 m intervals.

With this level of accuracy, landslide topography can be easily grasped, and bare ground formed by shallow landslides that destroy valley wall slopes/surface failures can be grasped as subtle bends of contour lines.

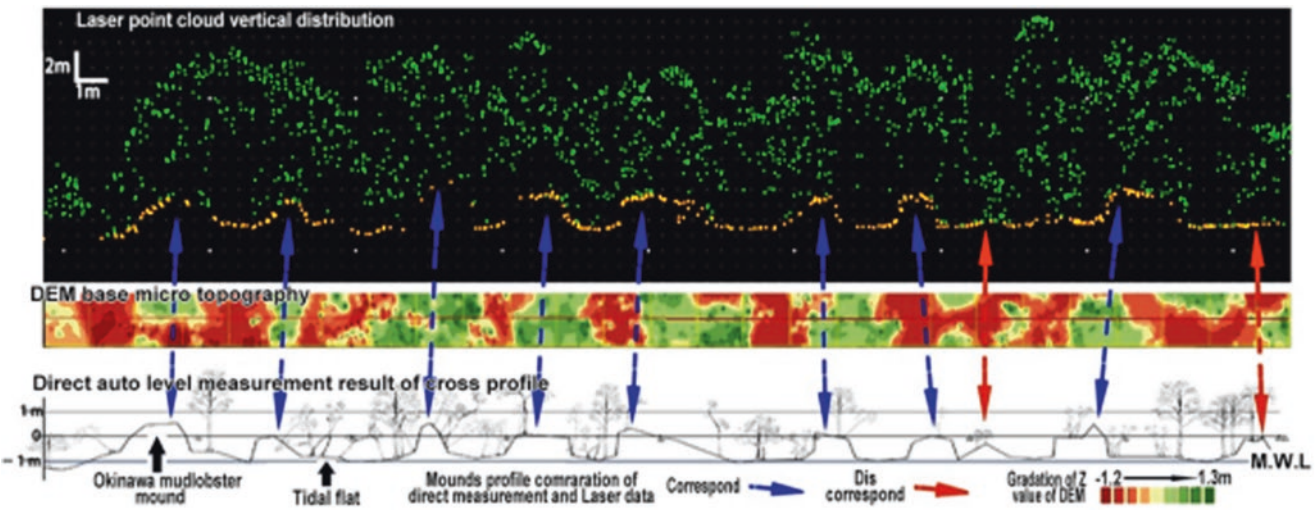

Fig. 22 Comparison of aerial laser measurement data (acquired in 2006) and microtopography, vegetation measurement cross-section of mangrove forests including Okinawa Mudlobster mounds (Makabe et al. 2015; Unome 2020)

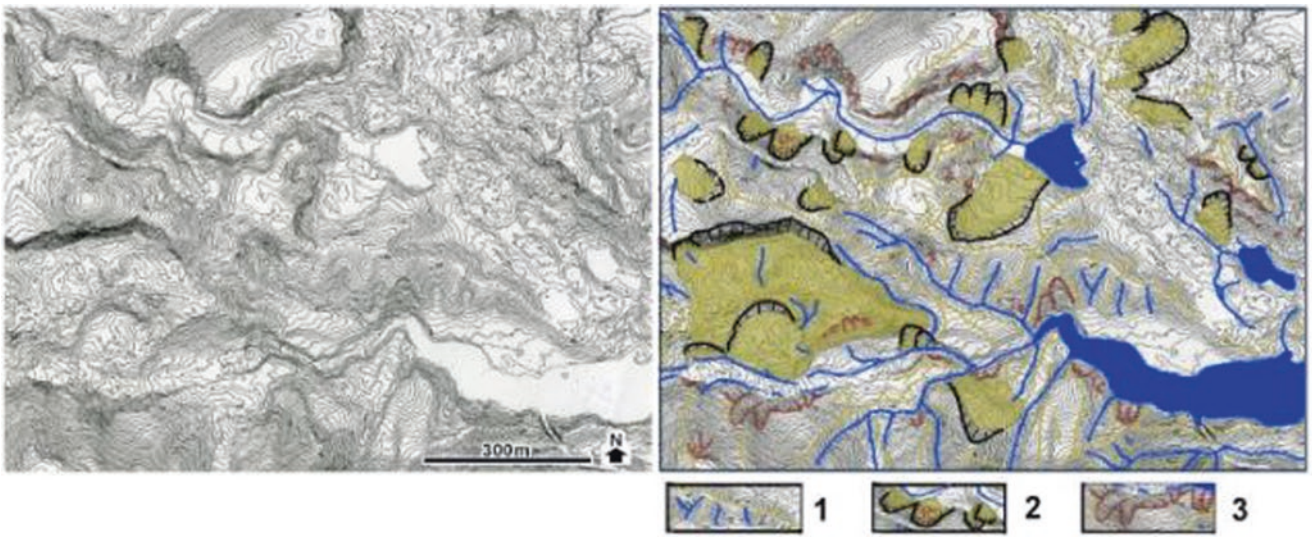

Fig. 23 LiDAR data of terrain destruction during the 2008 Iwate Miyagi Inland Earthquake. A 2-m contour map created from LiDAR data (left) and a distribution map of landslide topography and slope fluctuations extracted from LiDAR data (right). 1; ridge and valley lines and water bodies, 2; Landslide main sliding cliffs and moving bodies, 3; Newly generated slope failures and debris flows

7.4 Extracting Landslide Topography with AW3D Data

AW3D is the name of a data group created from Advanced World 3D Map. This public-private partnership project between JAXA, RESTEC, and NTT Data. Using four million global images taken by the Advanced Land Observing Satellite "ALOS" launched by JAXA in January 2006, and supplementing Maxer's images as appropriate, 3D digital data with 0.5 ~ 5 m accuracy worldwide was constructed, and it has been put into service sequentially since 2014. This is a countermeasure to the fact that conventional aircraft and manual measurements are extremely expensive and impossible to cover the entire world. AW3D is high-precision digital image information. This is converted into DSM data, and land cover information is processed appropriately to convert it into DEM data. Therefore, if it is widely covered with dense vegetation, the terrain implemented by the DEM may not be able to reproduce roughly. When purchasing data, it's important to understand how accurate the data in that location is. Other satellite images are the same, but each data has different characteristics. Figure 24 shows the distribution of the accuracy of the data acquired in a region. Clouds usually cover humid tropics, and mountainous areas with extremely dense vegetation. Therefore, it is difficult to obtain good-quality data in such areas. You should also understand the process of generating a DEM from DSM.

On the other hand, in areas with poor vegetation (e.g., deserts, high mountains, cold regions), the DSM and DEM are almost identical, and extremely reproducible topographic information can be obtained. Figure 25 shows an example of observing landslide topography on cold and dry mountain slopes. As you can see from the Google Earth image of C and the sketch of D, there is a steep slope in the upper right corner of the slope, a slope with a slight slope directly below it, a steep slope with a slight step in front of it, and a gentle slope below it where you can see the invasion of gullies. There is also a small but distinct cliff in the lower left of the figure. Figure 25(a) shows a topographic map depicting 10 m contour lines from AW3D 2.5 m DEM data. (b) shows contour lines deciphering ridges and valley lines, from which the characteristics of contour lines that are thought to be landslides are deciphered. I tried to decipher the microtopography that constitutes the landslide terrain while comparing it with (c and d). Parts of the main and side cliffs can be identified as steep slopes, and landslide movers can be identified as gentle slopes half-wrapped by steep slopes that make up these cliffs. The end of the moving body cannot be grasped like c.

7.5 Samples of the Landslide Topographic Area Mapping

We are working on the SATREPS project "Development of Landslide Risk Assessment Technology along Transport Arteries in Viet Nam, 2011-2017, Principal Investigator: Kyoji Sasa "We were the first in the world to map the distribution of landslide topography along Action Route 7 in Vietnam (Dung et al. 2016). Figure 26 shows the generation of contour lines from 5 m DEM to 10 m. As a result of examining the Grand Trusse, it was found that the outline of the landslide terrain can be well grasped even on a 5 m DEM basis. Figure 26 shows the landslide topography and local

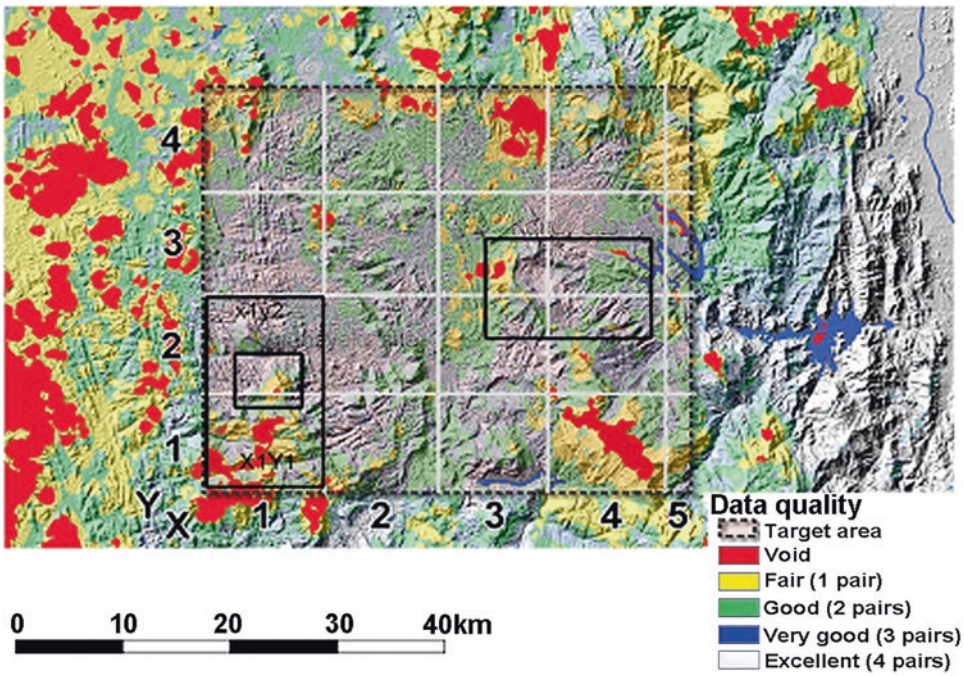

Fig. 24 Since it is based on the principle of constructing digital 3D data from the parallax of satellite image data, the higher the number of images obtained repeatedly, the higher the accuracy of the data. Depending on the region, a lot of cloud cover, and valid data may not be available

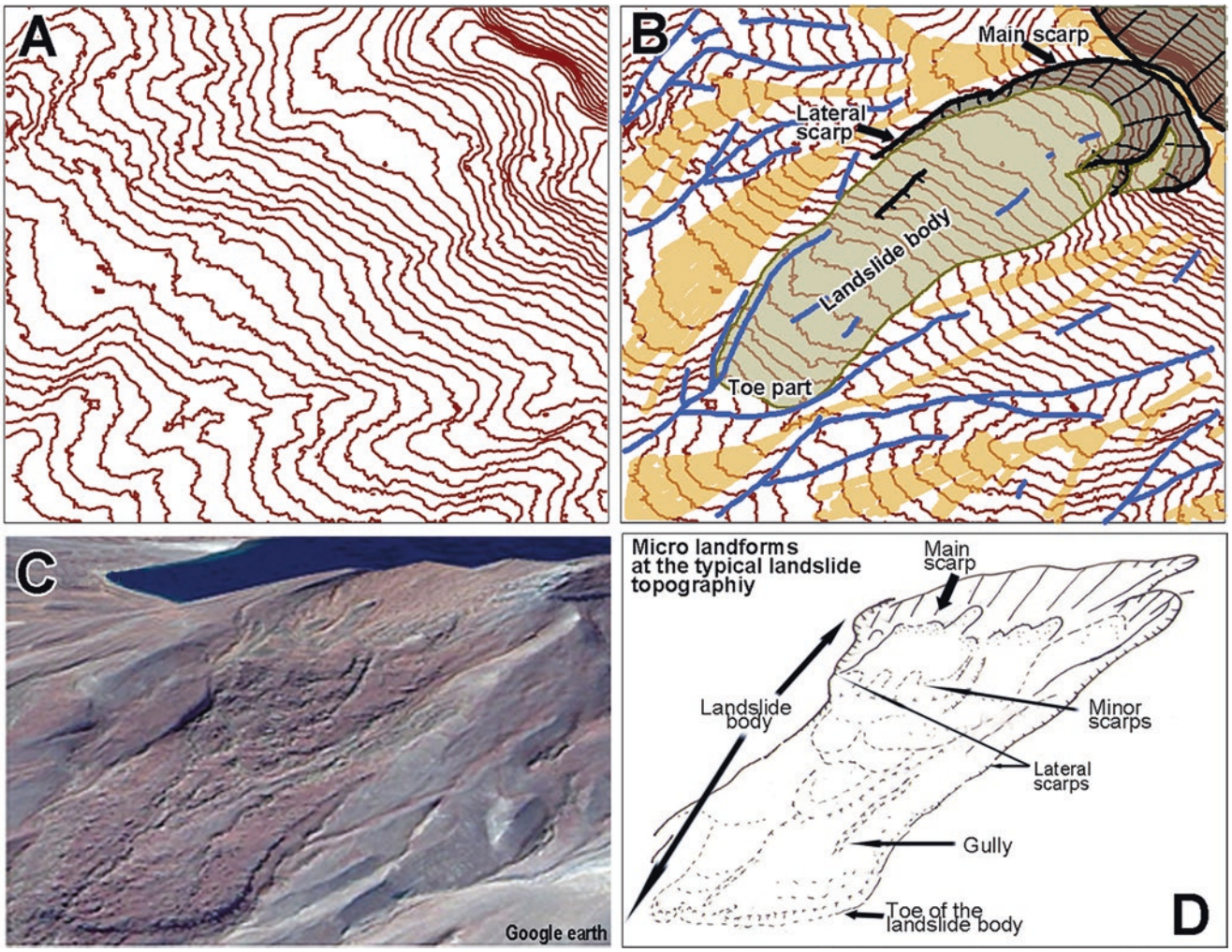

Fig. 25 Contour map generated from AW3D 2.5mDEM data, topographic readability status, etc. (**a**): 10 m contour map, (**b**): Landslide topography deciphered from contour lines, ridge lines, valley lines, (**c**): Google Earth image of almost the same location, D: C topographic situation sketch

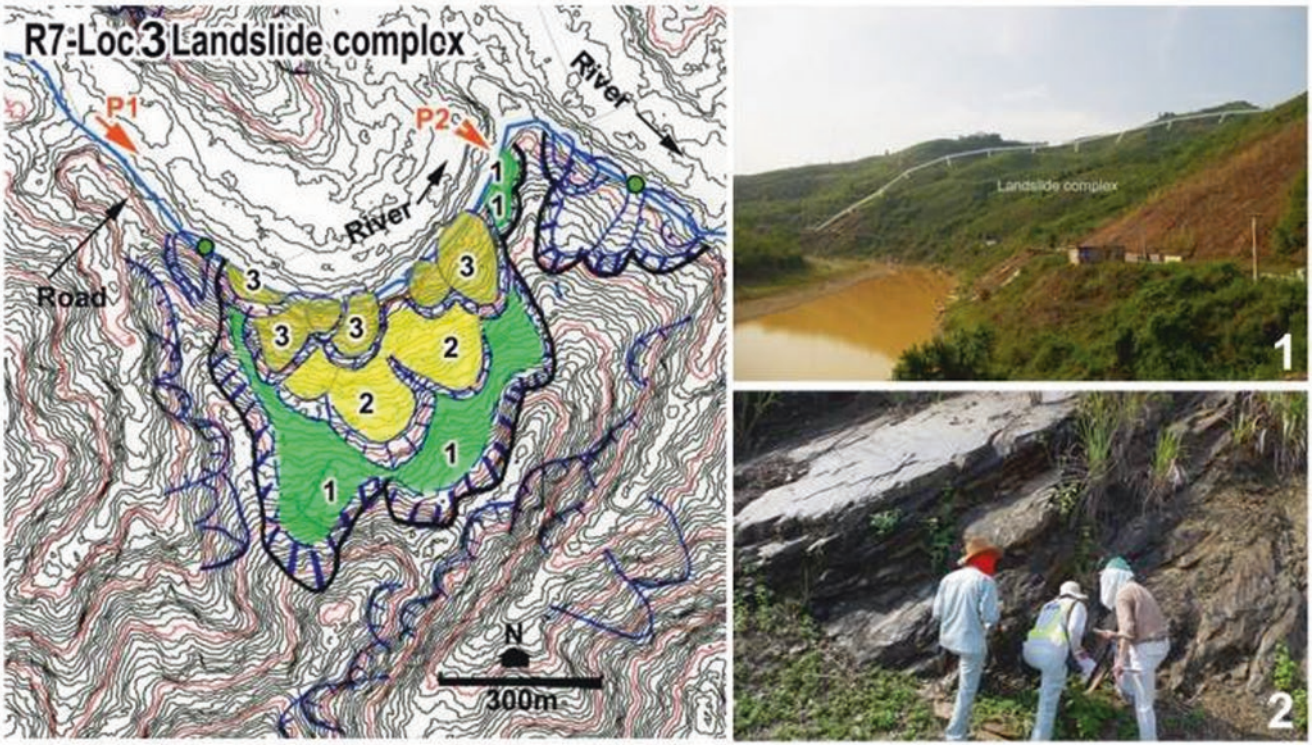

Fig. 26 Landslide topographic distribution map along National Highway seven in central Vietnam and site conditions. Landslide topography is widely distributed throughout the region. The landslide topography facing the river is large, but the inside of the moving body is subdivided like a number. From the landscape and landslide edge of the entire region, it can be assumed that the flow bed-like landslide fluctuation is repeated (Dung et al. 2016)

conditions. From the two photographs in Fig. 26, the vegetation in the actual area was never dense forest.

We also use AW3D 2.5 m data in Sri Lanka to create a wide-area landslide topographic distribution map. Figure 27 shows that even with AW3D2.5 m data, there is a subtle difference in the contour flexion pattern between DSM and DEM.

Fig. 27a shows a 20 m contour line generated from DEM data, and (b) shows a 5 m contour line generated from DSM data. (a and b) are enlargements of parts of A and B. The red areas in these figures are where surface collapse has recently occurred. Fig. a shows the rough topography of the area. B does not remove vegetation information, so it seems difficult to understand because there is a lot of noise. However, the reality is that the rough contour lines of A do not accurately represent the terrain. When exploring microtopography, how to handle vegetation information is considered. Here, I decided to read the DSM data of b carefully. The result is the upper right figure.

Today, digital 3D data from all over the world and free visible images such as Google Earth are freely available. However, each has its characteristics, limitations, and points to remember. It can be said that we have entered an era where it is important to understand and master each individuality.

8 Procedure for Preparing a 3D Map to Detect the Landslide Topography

8.1 3D Topographic Map for Landslide Topography Detection

Topographic information calculated from the elevation value of the DTM is called topographic quantity. It is mainly divided into those that represent the inclination of the slope and those that represent the unevenness of the slope, such as curvature and opening.

Combining these multiple topographic quantities makes it possible to express the topography in 3D using a plan view. This is called a 3D topographic map. 3D topographic maps created from high-precision DTMs can accurately reproduce the topography without the vegetation's influence.

Ikeda (2020) devised a "3D microtopographic map (MT3DM)" to detect landslide topography using 5mDTM. Here, we will introduce the creation procedure.

8.1.1 The 3D Microtopography Map (MT3DM)

Several topographic maps using DTM have already been devised (Toda 2014). Ikeda (2020) followed the basic concept of CS stereographic drawings and devised parameters

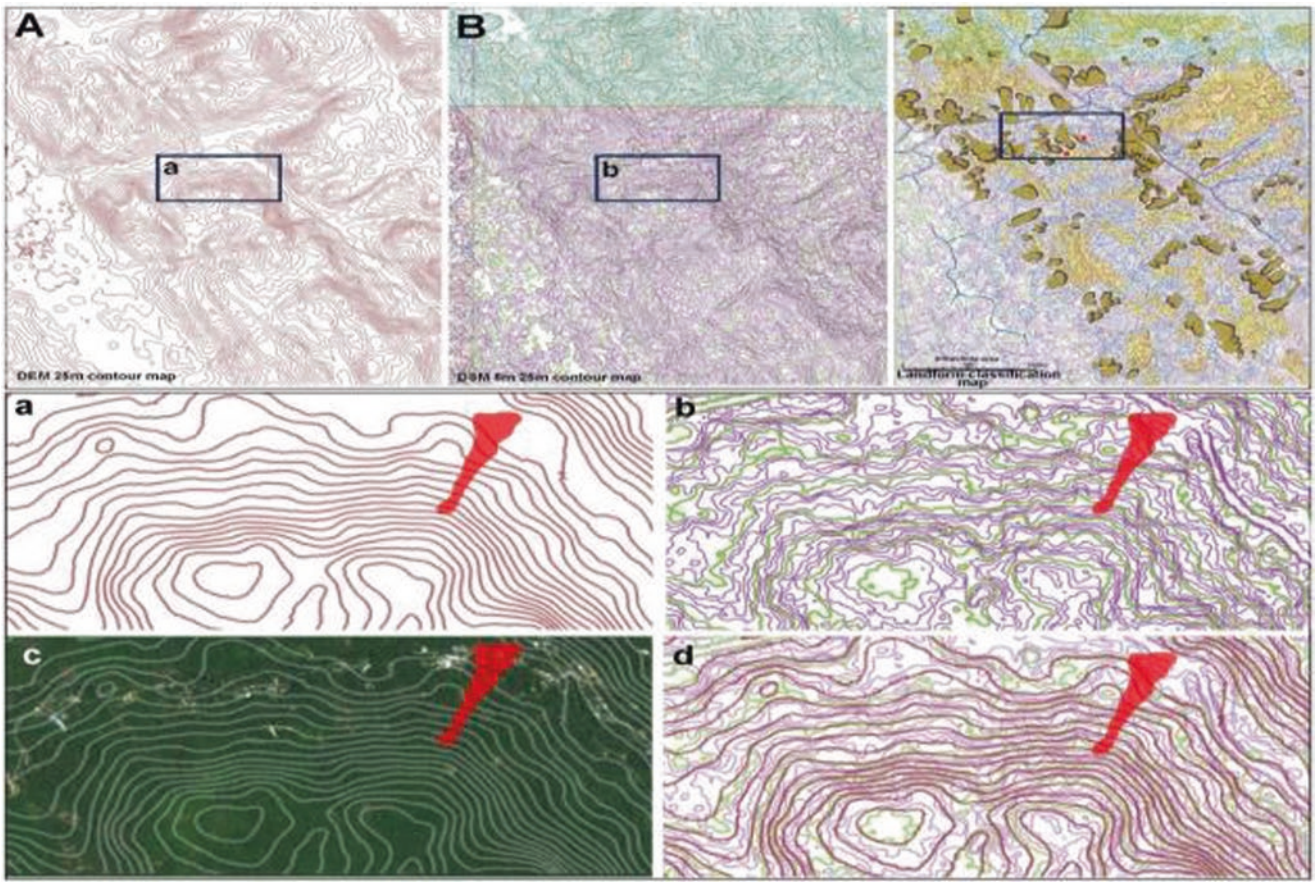

Fig. 27 Landslide topographic distribution map in Sri Lanka and contour characteristics of AW3D 2.5 m data

with better reproducibility of landslide topography. The main advantages are:

In interpretation of the landslide topography, it is important to extract microtopography such as cracks peculiar to landslides. In order to emphasize these microtopographic boundaries, a curvature map is also created from the high-definition DTM, colored in a warm red color, and superimposed on the topographic map with transparency processing.

In order to grasp the specific height difference between the main scarps and the undulations of the landslide-moving body, it is important to express the stage color according to the altitude. Here, an elevation map with colors set according to elevation is superimposed to make it easier to recognize the terrain elevation visually.

In addition, the color tone of each terrain quantity and the threshold value when considering the color tone is also set to emphasise the representation of the landslide microfeature.

8.2 Creating a Three-Dimensional Microtopographic Map (MT3DM)

8.2.1 Software for Processing the MT3DM

MT3DM is created using open-source GIS. QGIS (http://qgis.org/ja/site/) is used.

8.2.2 (1) Setting and Transforming the Coordinate System

As a general rule, the coordinate system of QGIS uses a projected coordinate system, such as a planar rectangular coordinate system or UTM. It does not use a geographic coordinate system. In topographic analysis, unit inconsistencies occur between Z: elevation data (unit: m) and X, Y: plane distance (unit: degrees), and correct results cannot be obtained.

The coordinate system of the project is set in "Project>", "Properties", > "Coordinate Reference Systems (CRS)" (Figs. 28, 29, 30 and 31). Search with Filter and set the coordinate system.

If you need to convert vector and raster data, right-click on each layer of data, click Export >Save Features As, enter

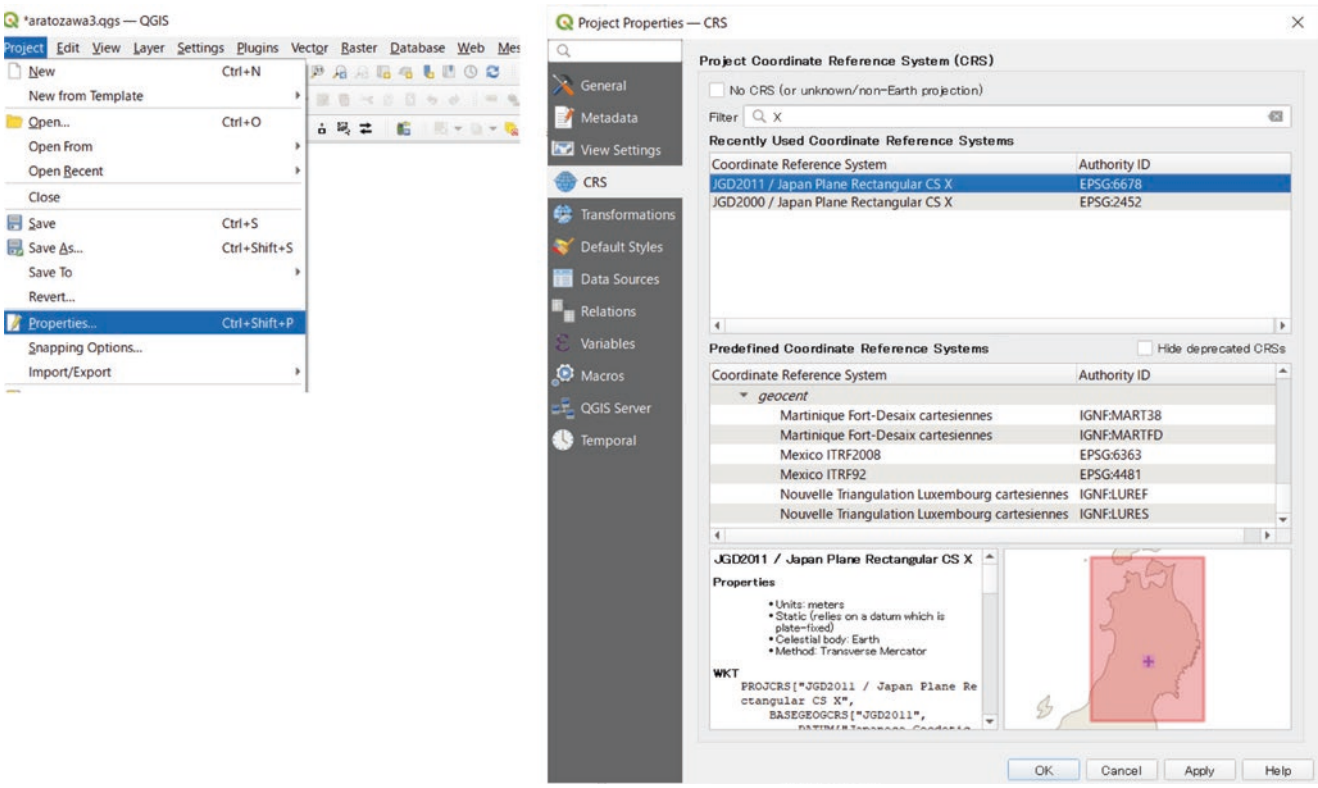

Fig. 28 Project coordinates

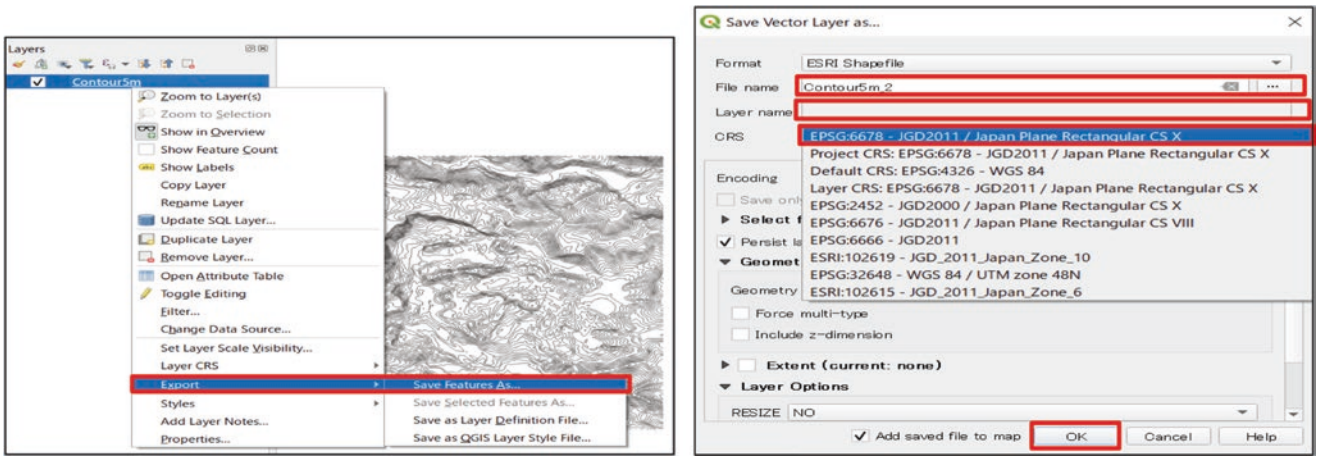

Fig. 29 Coordinate variation of geographic information data (shp, raster)

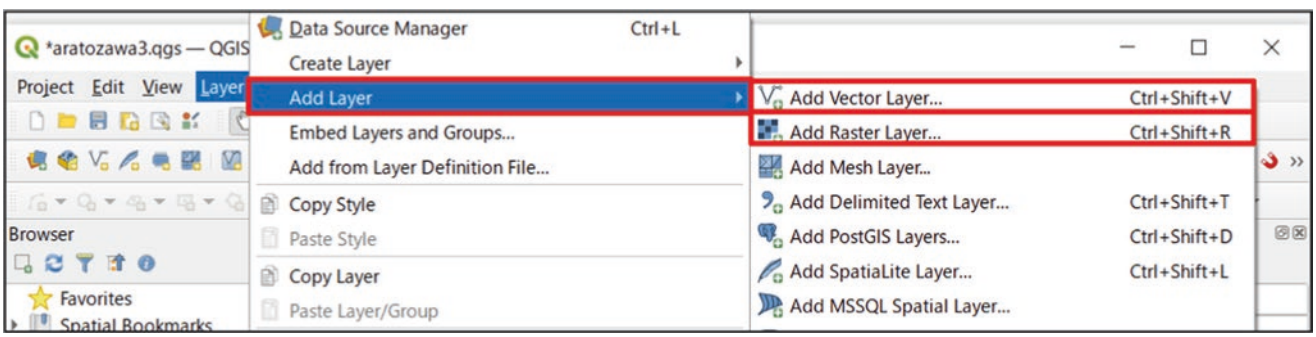

Fig. 30 How to add a layer

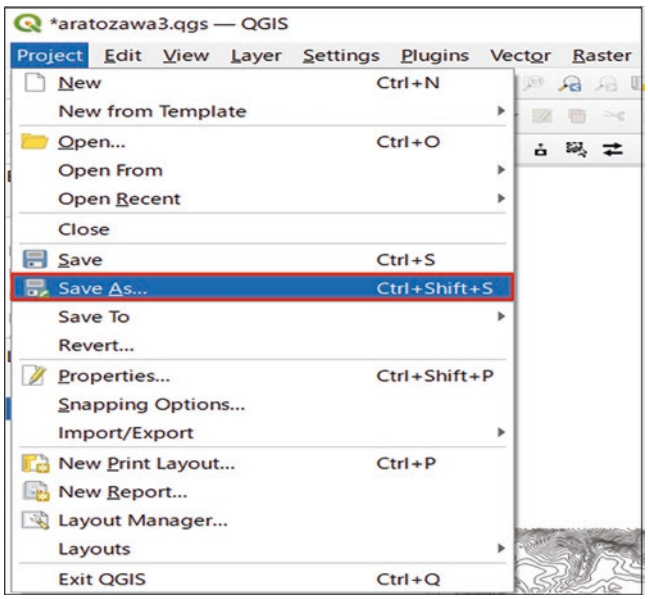

Fig. 31 Data storage method

a File name, select Coordinate Reference System (CRS), and click "OK" to output the data after coordinate conversion.

8.2.3 (2) How to Add Layers

To add layers> from "Layer" to "Add Vector Layer" and "Add Raster Layer" to deploy on QGIS.

8.2.4 (3) How to Save Project Data

Click Save As > Project, enter a File name, and click Save S to save the project data.

8.3 Preparation for 3D Microtopographic Map

1. **Preparing DTM Data**

Prepare DTM (GeoTIFF, etc., hereinafter referred to as DTM raster) in raster data format obtained by aerial laser surveying, etc. In the case of ground data only, it is converted to raster data with GIS software, etc.

2. **Deploy DTM rasters on QGIS**

Deploy the prepared DTM raster on QGIS. Adding layers is described above.

3. **Extraction of the scope of coverage**

Preparation for topographic mapping: carving out the area of interest (landslide terrain). To crop, click "Raster", > "Extraction" > "Clip Raster by Extent" (Fig. 32). Select the DEM raster of the

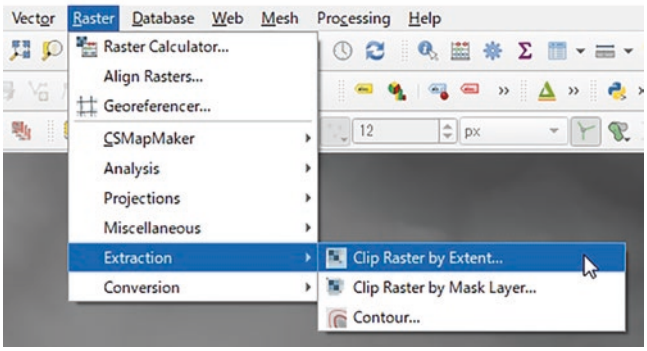

Fig. 32 Crop target area command

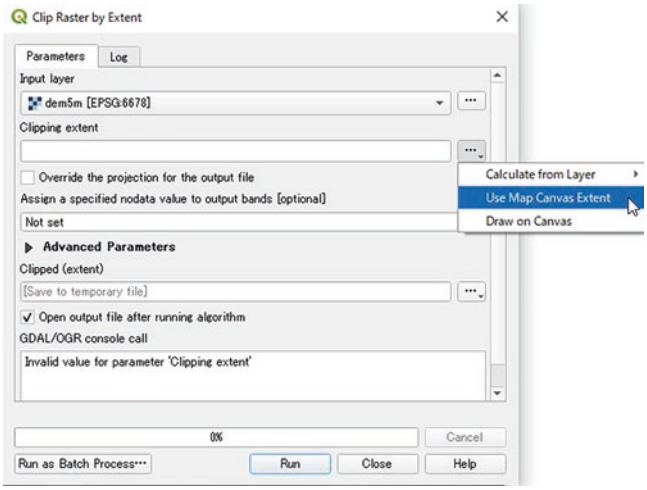

Fig. 33 Setting the crop command of the target area

Input layer and specify the Clipping extent. There are three ways to select a range. Here, select "Use Map Canvas Extent" to be cut out in the area displayed on the canvas, and click "Run" (Fig. 33). The cropped raster is added to the layer.

4. **Interpolation of rasters:**

In places where elevation values are missing, such as water bodies, interpolate from the elevation around the raster data. Click Fill no data value > "Analysis" in "Raster". Select the desired raster from "..." in the Input layer and enter the save location and name from "..." in the output raster. Click the "Run" button to start interpolation (Figs. 34 and 35).

8.4 Creation of 3D Microtopographic Map (MT3DM)

A three-dimensional microtopographic map (MT3DM) is a topographic map that can obtain a three-dimensional 3D effect by superimposing multiple layers created from DTM

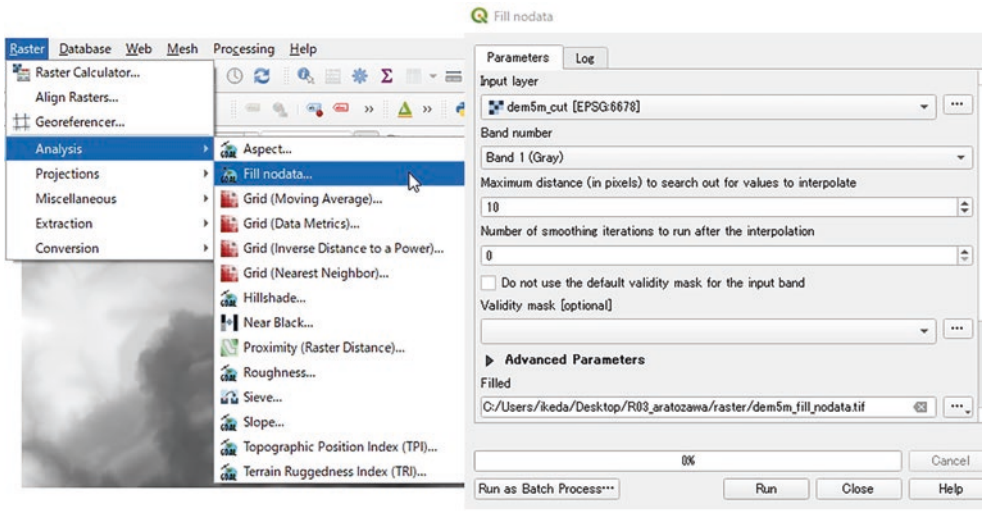

Fig. 34 Interpolation of raster data

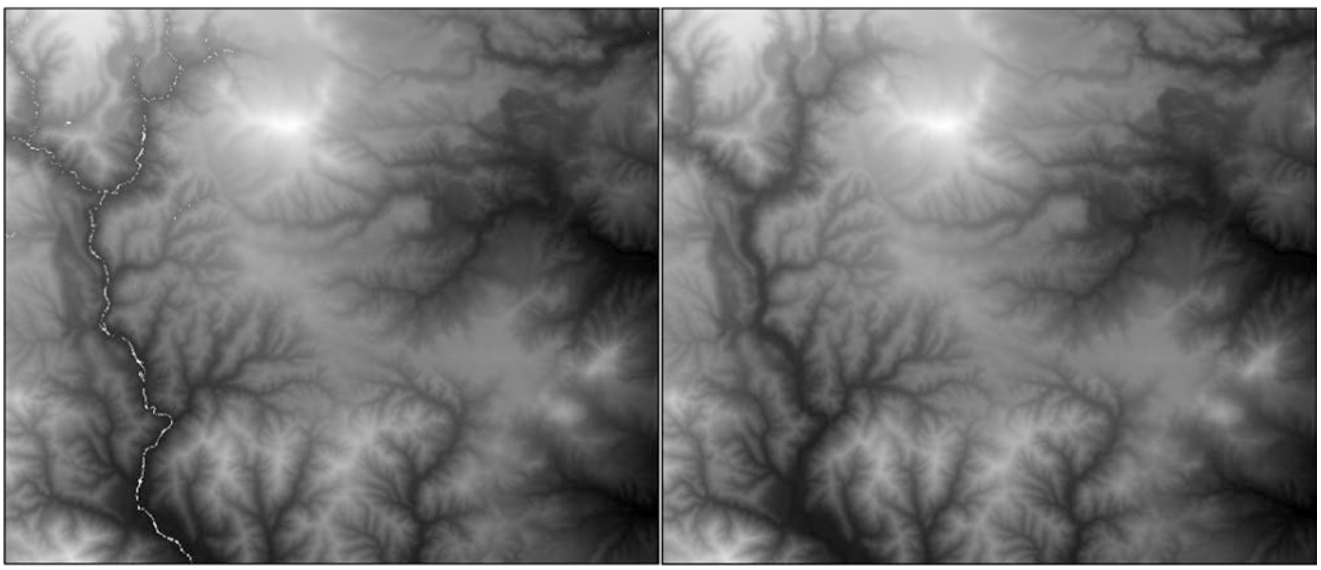

Fig. 35 The left figure is an example of a DTM raster with missing elevation values in the river channel, and is blank. When this is interpolated, the river part is interpolated as shown in the figure on the right

data. 3D microtopographic maps are created by combining four types of topographic maps. The four types of topographic maps are "Elevation maps, Slope maps and two types of Curvature maps". Ikeda created a three-dimensional microtopographic map from 5 m DTM, but this paper also introduces a method to create a higher-definition 1 m DTM (Fig. 36).

1. Elevation map creation

First, create an elevation map from a DTM raster. Right-click on the extracted DEM raster and click Properties. Symbology's "Render type" is "Single band pseudocolor" and is classified into five categories to become red-green-blue from the highest altitude. Adjust the number of color scales with "+" and "-", and click Value and color to set the elevation value and color. The elevation value is set appropriately while looking at the red-green-blue balance of the created altitude chart. To create an experiential experience, it is better to set the color setting to a dark color close to the primary color, as shown in Figs. 37 and 38.

2. Slope map creation

Next, create a slope map from the DTM raster. Click "Analysis" > "Raster" > "slope". Select the DTM raster as the Input layer, enter the save location after outputting the Parameter to slope and the name, and click "Run" (Fig. 39).

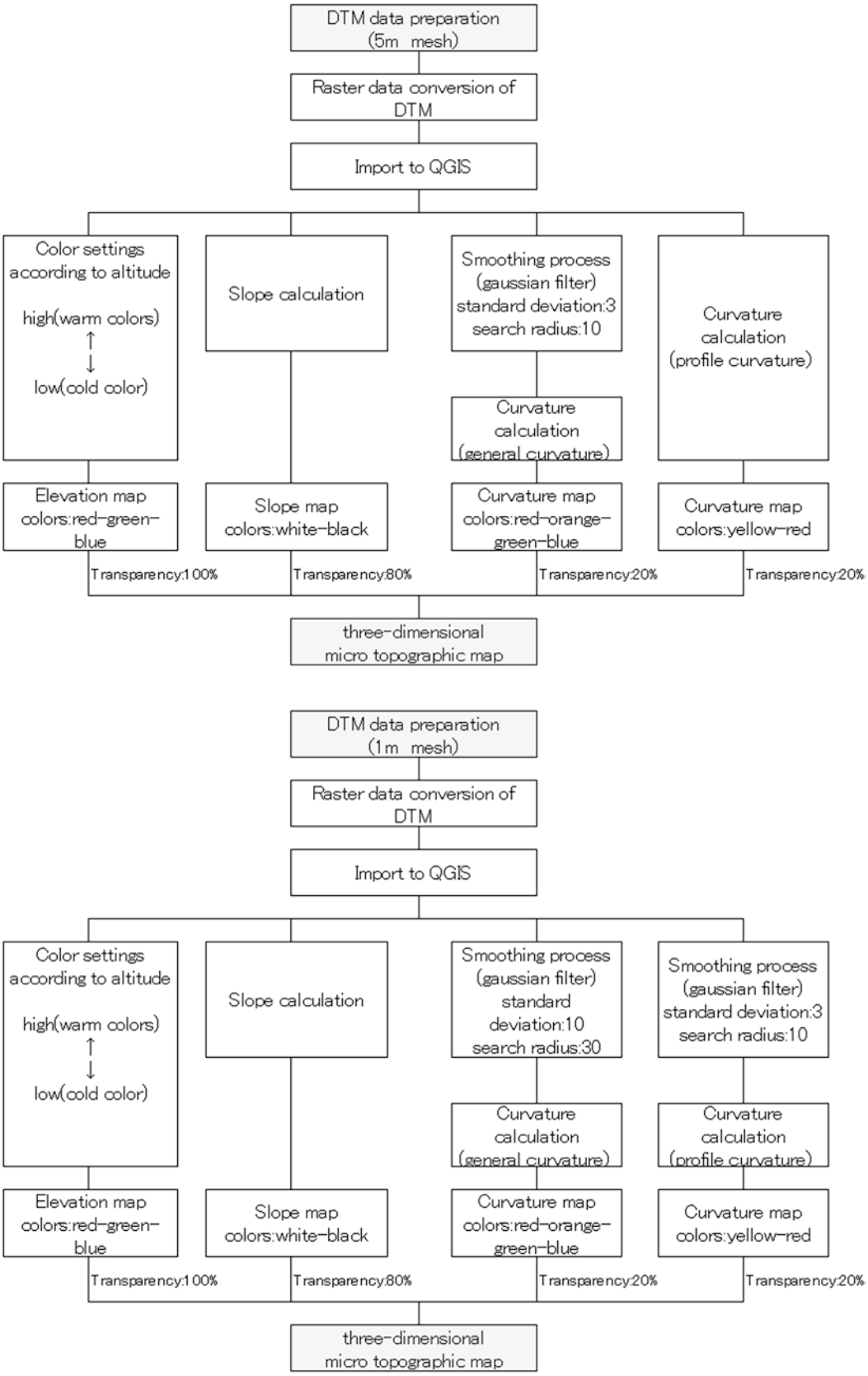

Fig. 36 Flow of creating a topographic map (top: 5 m DTM, bottom: 1 m DTM)

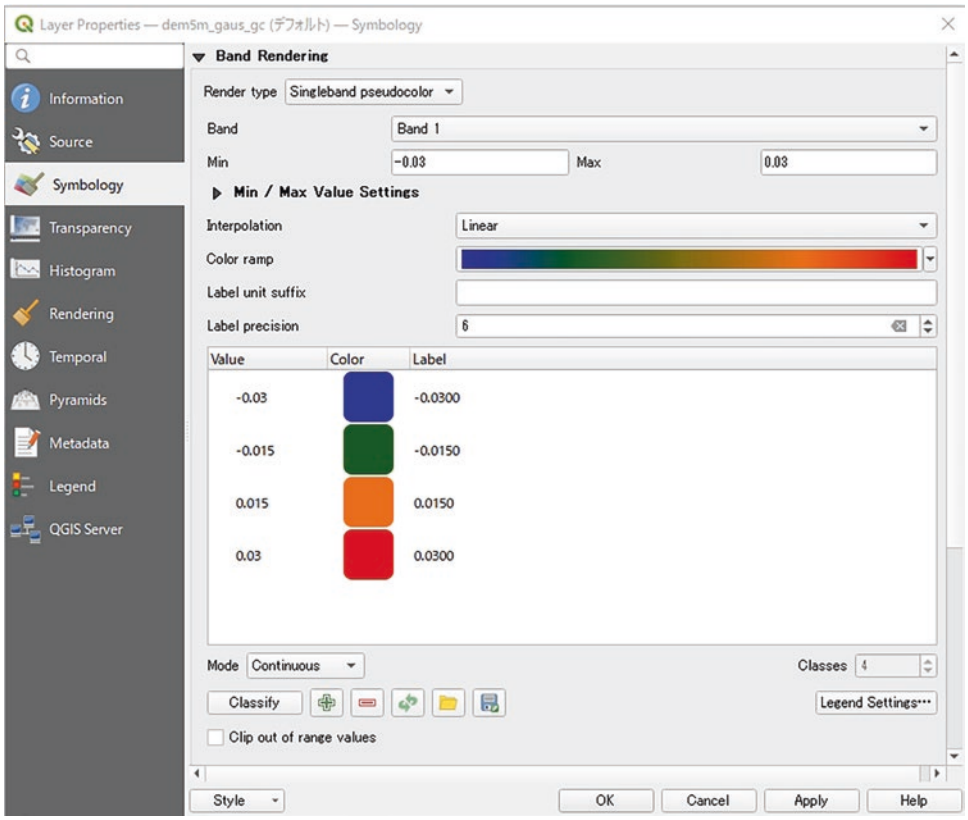

Fig. 37 Color setting of the high-stage color map

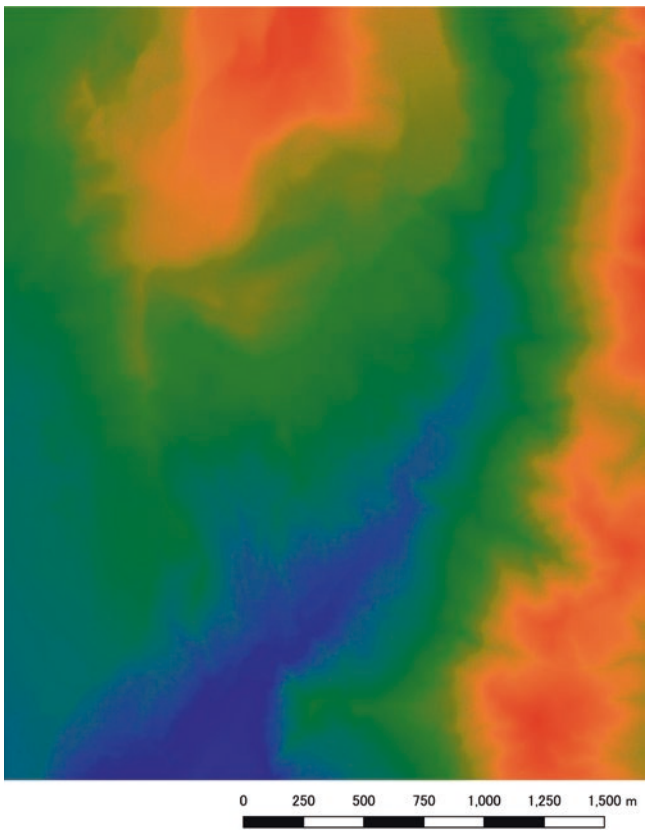

Fig. 38 Altitude-stage color drawing

Adjust the color of the slope map by right-clicking on Properties >Symbology>“ is Single band grey and “Color gradient“ is set to “White to Black” (Fig. 40). Next, adjust the scale (Min, Max) of the color gradient. The default maximum value (Max) is 90°, but, the Max is empirically set to 45°.

Finally, set the transparency of the slope map to 80% in Properties> “Transparency” (Figs. 41 and 42).

For any other formatting issue please refer to the.

3. Curvature map creation

Create two types of Curvature maps. One is the “Curvature map of small and medium topography”, and the other is the “Curvature map of micro topography”. We aimed to visualize unevenness suitable for each terrain scale. The procedure for creating these two types of curvature diagrams is different for 5mDTM and 1mDTM. The 5mDTM case and the 1 mDTM case are explained separately below.

< for 5mDTM>

- Curvature map of small and medium-scale topography

Smoothing DTM raster to create a Curvature map (Fig. 43) > Click “SAGA” > “Raster-filter” > “Gaussian filter”. Select the DEM raster in “Grid” and enter the name of the output file in “Standard Deviation” 3, “Search Mode” in [1] Circle, “Search Radius” in 10, and “Filter Grid”. Click Run to create a smoothed DTM raster.

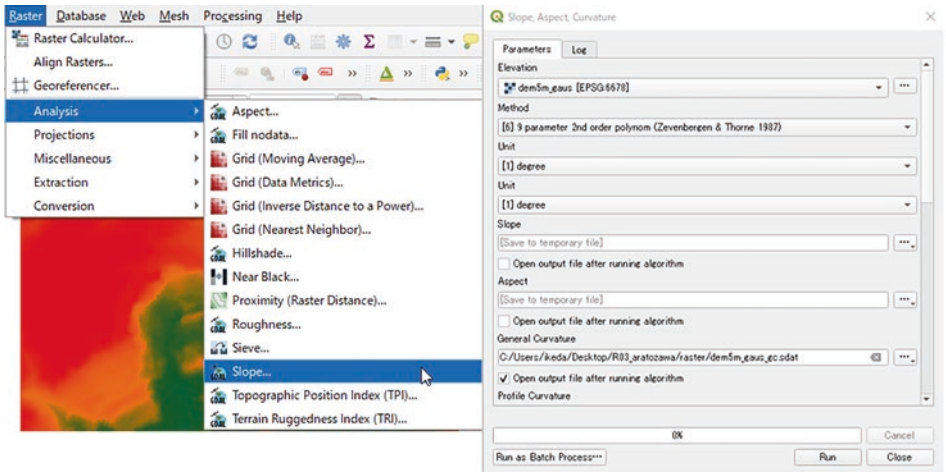

Fig. 39 Slope map creation command setting

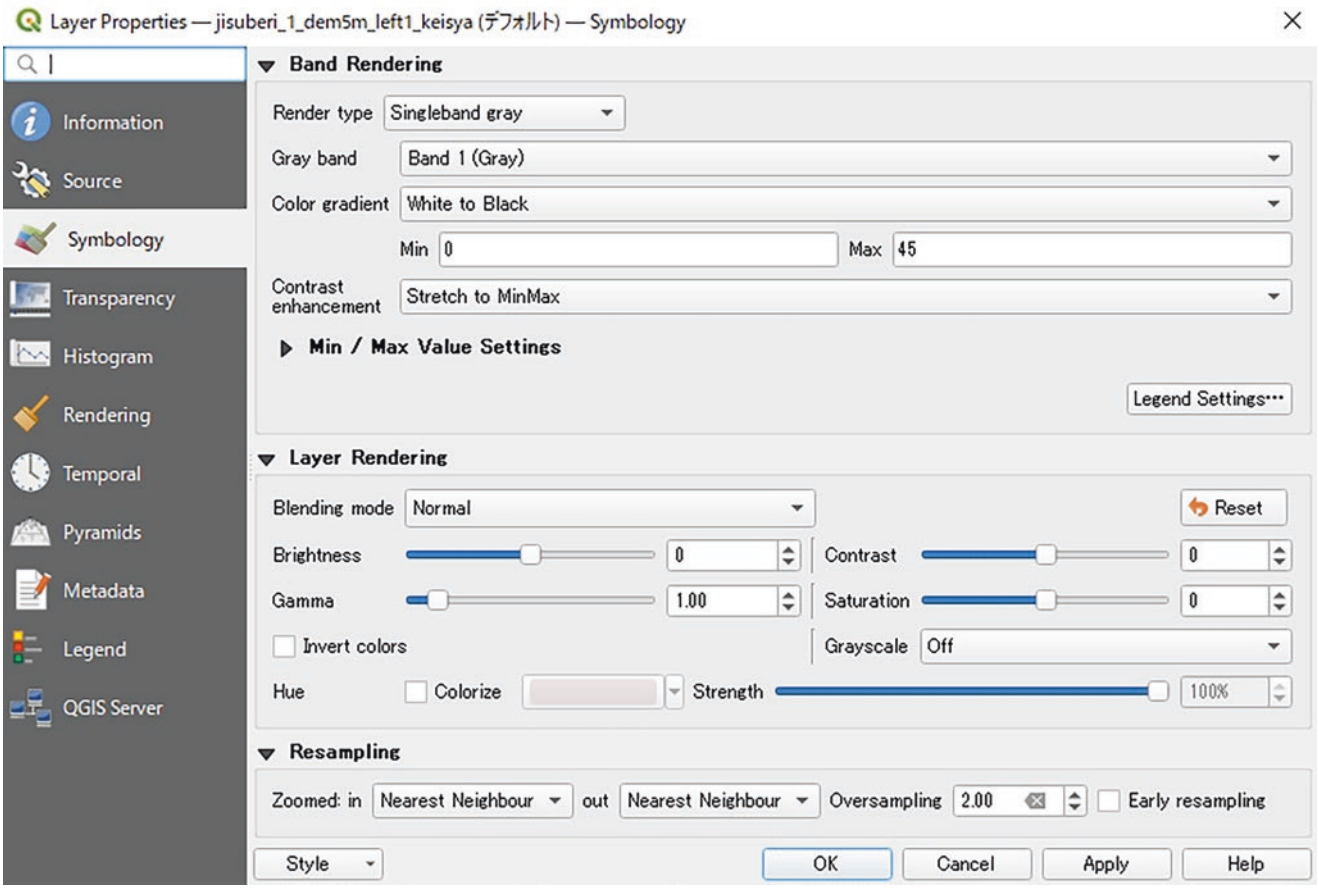

Fig. 40 Slope map color setting

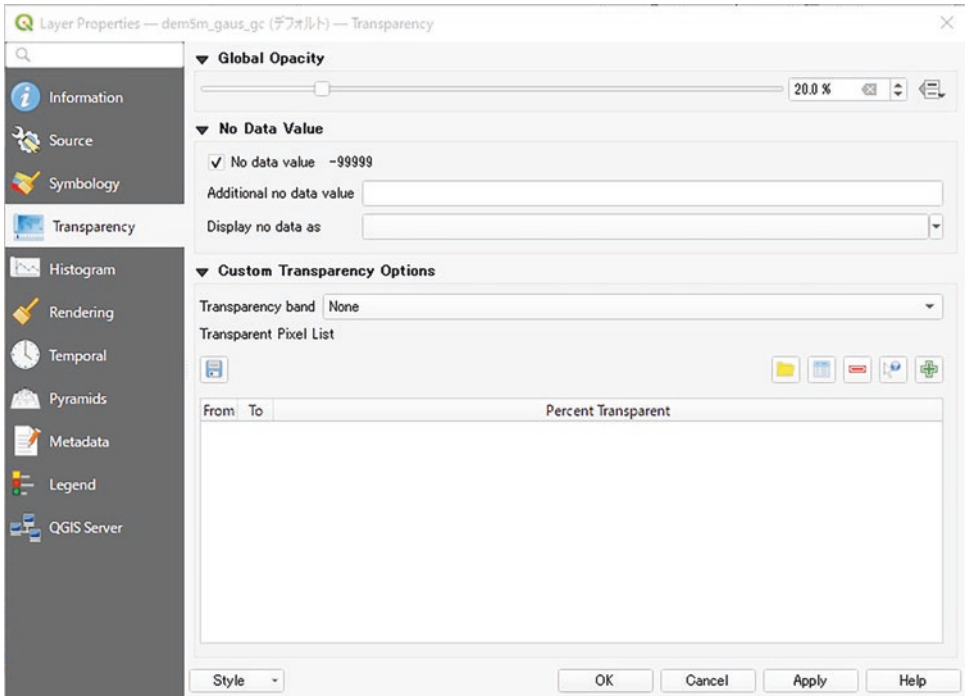

Fig. 41 Slope Map transparency setting

Fig. 42 Slope Map 80% transparency

Next, create a "Curvature map of small and medium topography" from the smoothed DTM raster. > Processing Toolbox> click SAGA Terrain Analysis-Morphometry> Slope, Aspect, Curvature. Select the DTM raster smoothed to Elevation, select the DTM raster smoothed to Elevation, Slope Unit and Aspect Unit" to [1], and enter the name of the output file in "General Curvature" (Fig. 44). Remove "Slope", "Plan Curvature", etc. because processing other than "General Curvature" ☑ is not performed. Click Run to create a Curvature map of small and medium topography.

Next, set the color of the created curvature diagram (Fig. 45). Right-click on the layer's curvature diagram to open Properties, under Symbology > Render type (Single band pseudocolor) and classify "Color ramp" into four so that + values (convex terrain) are red and -values (concave terrain) are blue. Min is set within −0.05 ~ −0.03, Max is set within 0.03 ~ 0.05. To emphasize ridges and valleys, Min is set to −0.03, and Max is set to 0.03. Finally, set "Properties" > "Transparency" to 20% (Figs. 46 and 47).

- Creation of the curvature map of microtopography

Create a Curvature map (microtopography) from a raster DTM. The procedure is similar to the Curvature map of small and medium topography. Processing Toolbox> SAGA> Terrain Analysis-Morphometry> click Slope, aspect, curvature. Select the DTM raster under Elevation, select the Slope

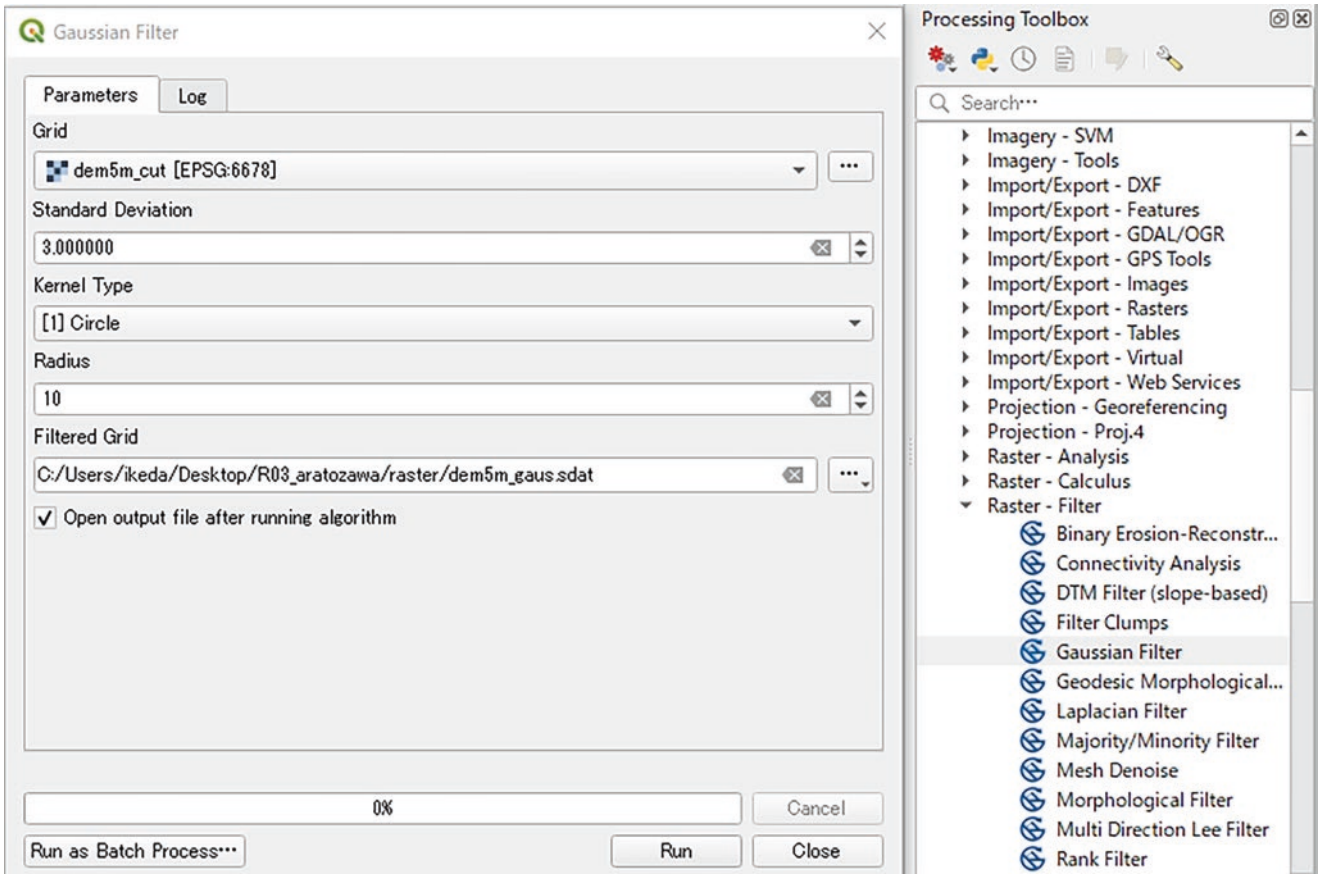

Fig. 43 Setting of smoothing command

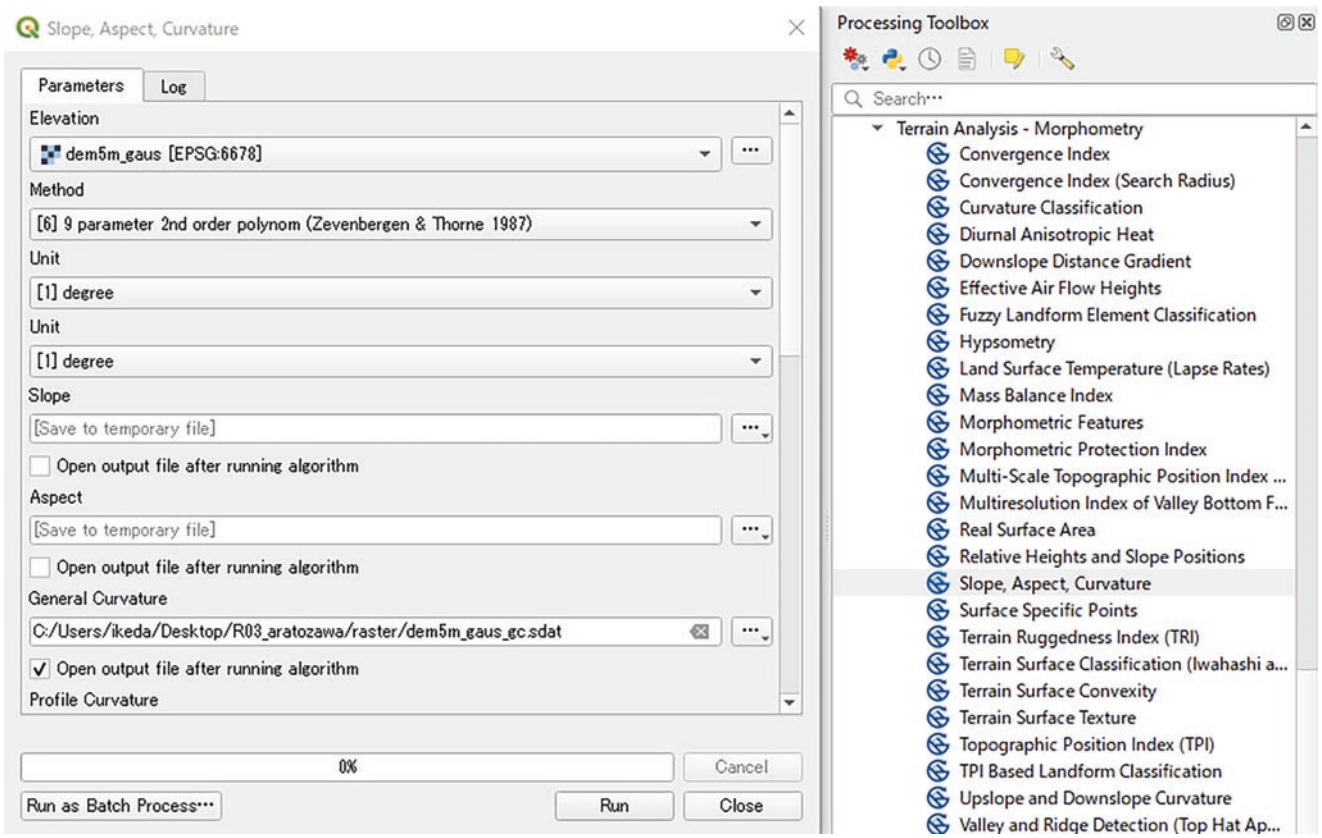

Fig. 44 Curvature drawing command

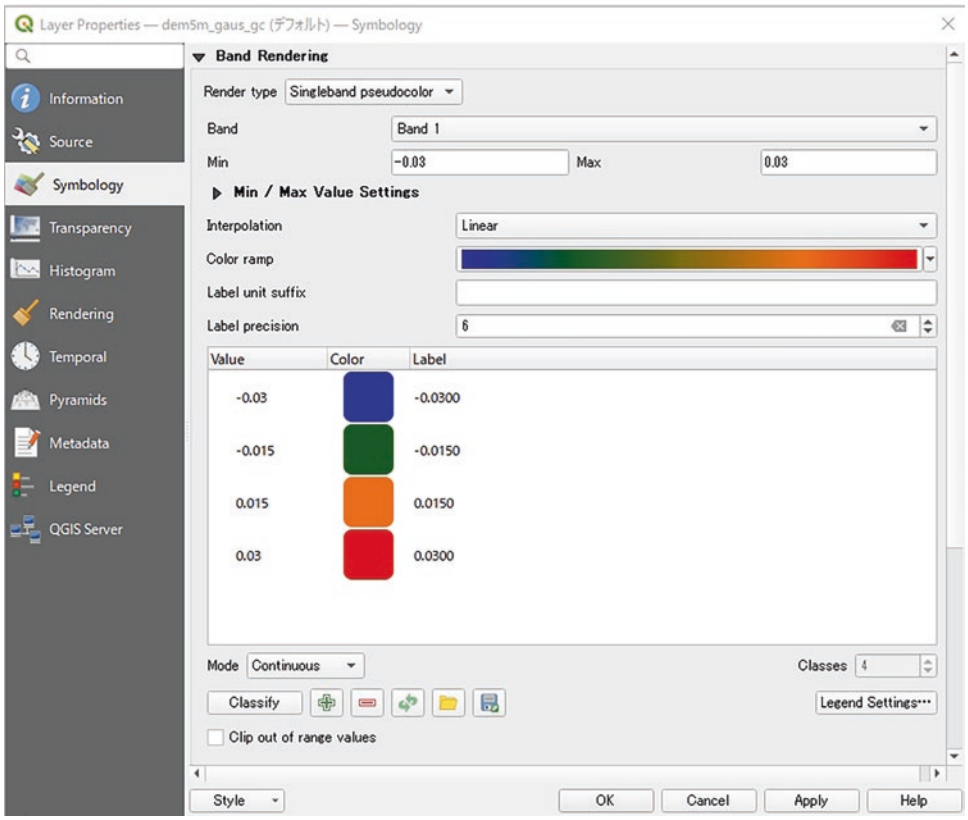

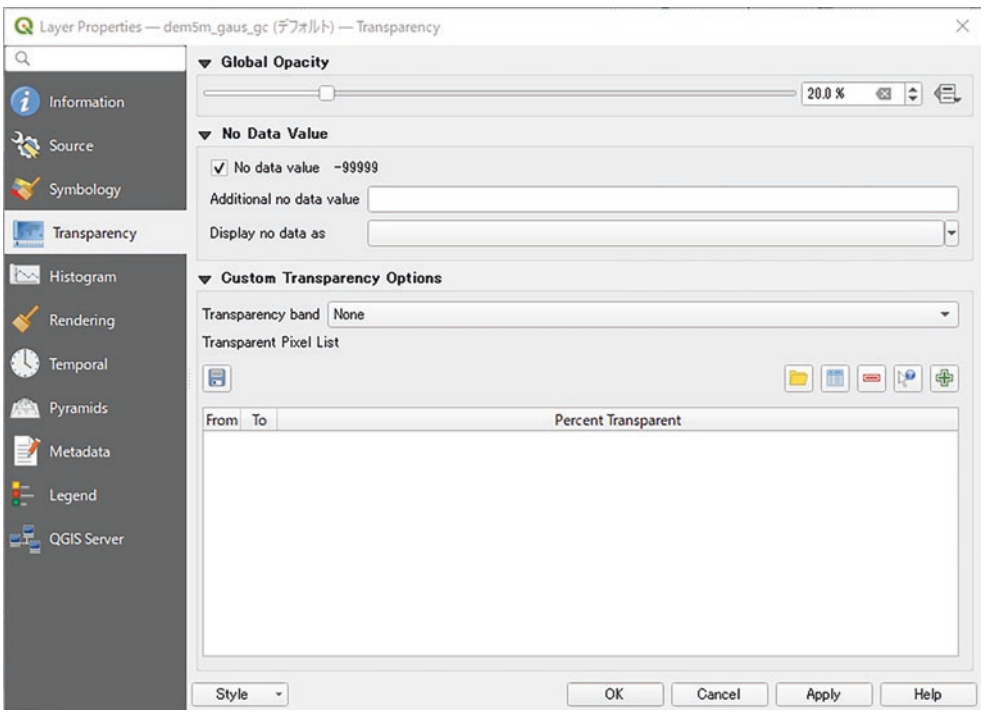

Fig. 45 Color setting of curvature diagram

Fig. 46 Permeability setting of curvature diagram

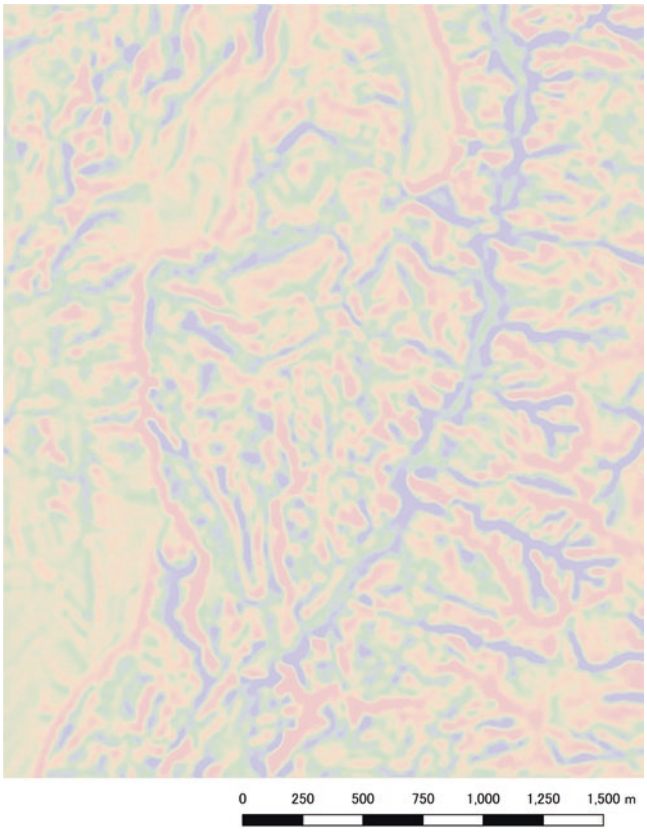

Fig. 47 Transparency of small and medium-sized terrain 20%

Unit and Aspect Unit [1], and input the output file into Profile Curvature. Remove ☑because processing other than Profile Curvature, such as Slope and Plan Curvature, is not performed. Click Run to create a curvature diagram.

Next, set the color of the created curvature diagram. Right-click on the layer's curvature diagram to open Properties. 「Symbology」 > 「Render type」to Single band pseudocolor，and Color ramp set「YlOrRd」. Set the scale within "-0.05 ~ −0.03" for Min and "0.03 ~ 0.05" for Max. Here, in order to emphasize the microtopography, Min is set to "-0.03", Max is set to "0.03", and finally "Properties" > "Transparency" is set to "20%" (Figs. 48, 49 and 50).

8.4.1 Completion of Three-Dimensional Microtopographic Map (MT3DM)

Slope map with transparent processing based on elevation and curvature maps (small and medium topography). A curvature map of microtopography is superimposed in layer order to create a "three-dimensional microtopography map (MT3DM)".

Figure 52 shows the "3D Microtopographic Map (MT3DM)" created by superimposing four types of topographic maps (Fig. 51). By superimposing contour lines on a three-dimensional microtopographic map, it is possible to express changes in the height of the terrain in an easy-to-understand manner (Figs. 52, 53, 54 and 55).

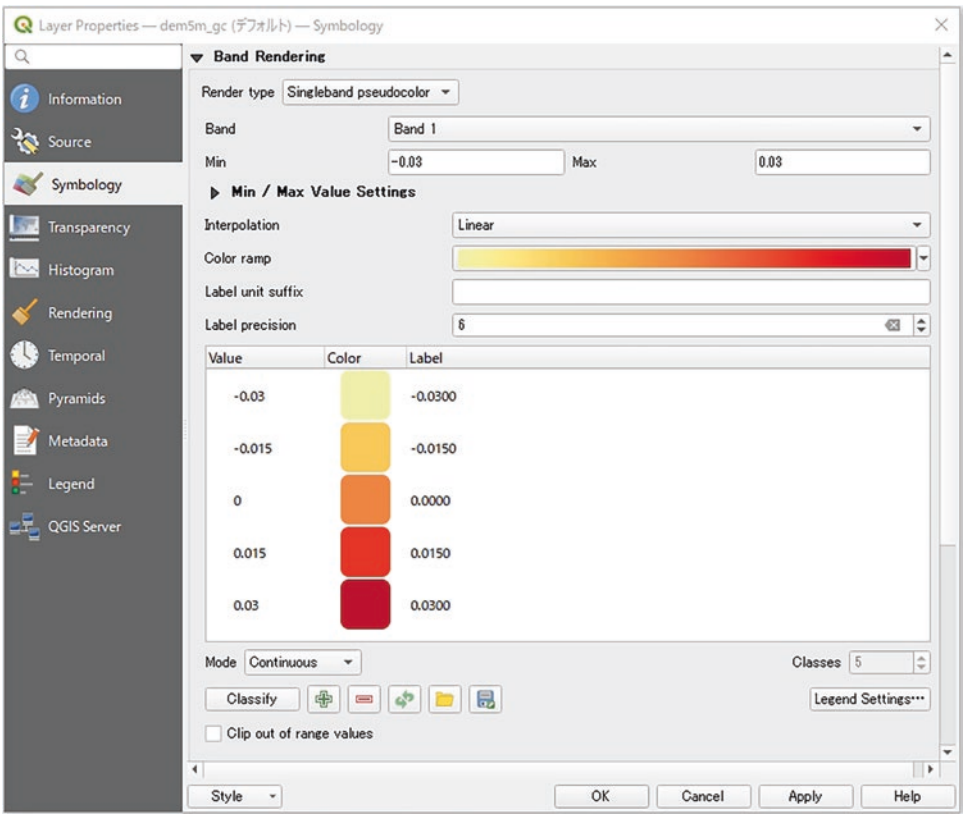

Fig. 48 Color setting of the curvature diagram of microtopography

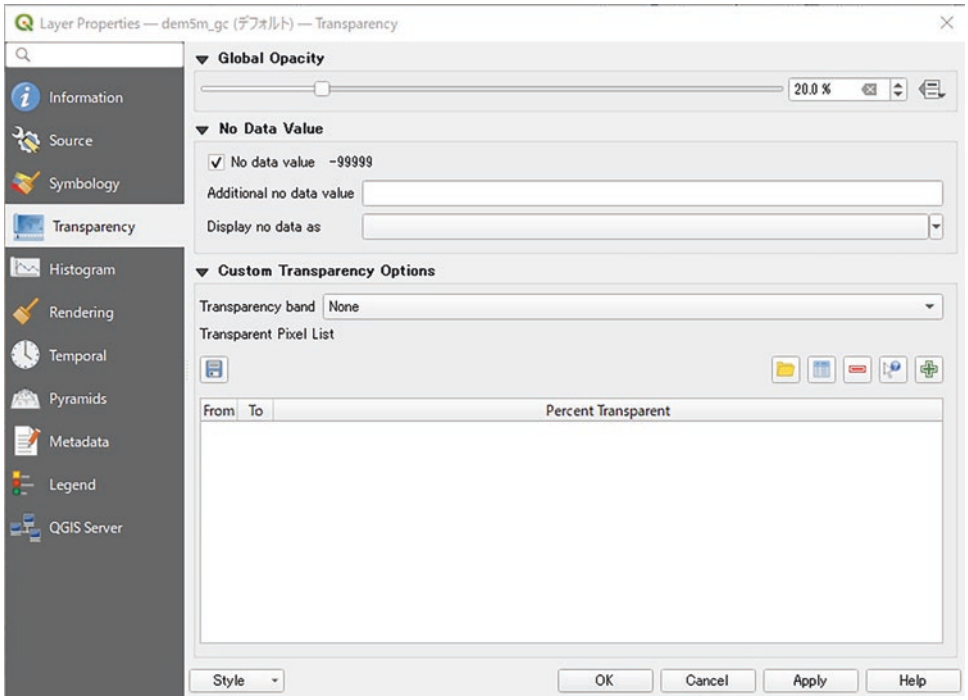

Fig. 49 Transparency setting of curvature diagram

Fig. 50 Curvature diagram of microtopography (permeability 20%)

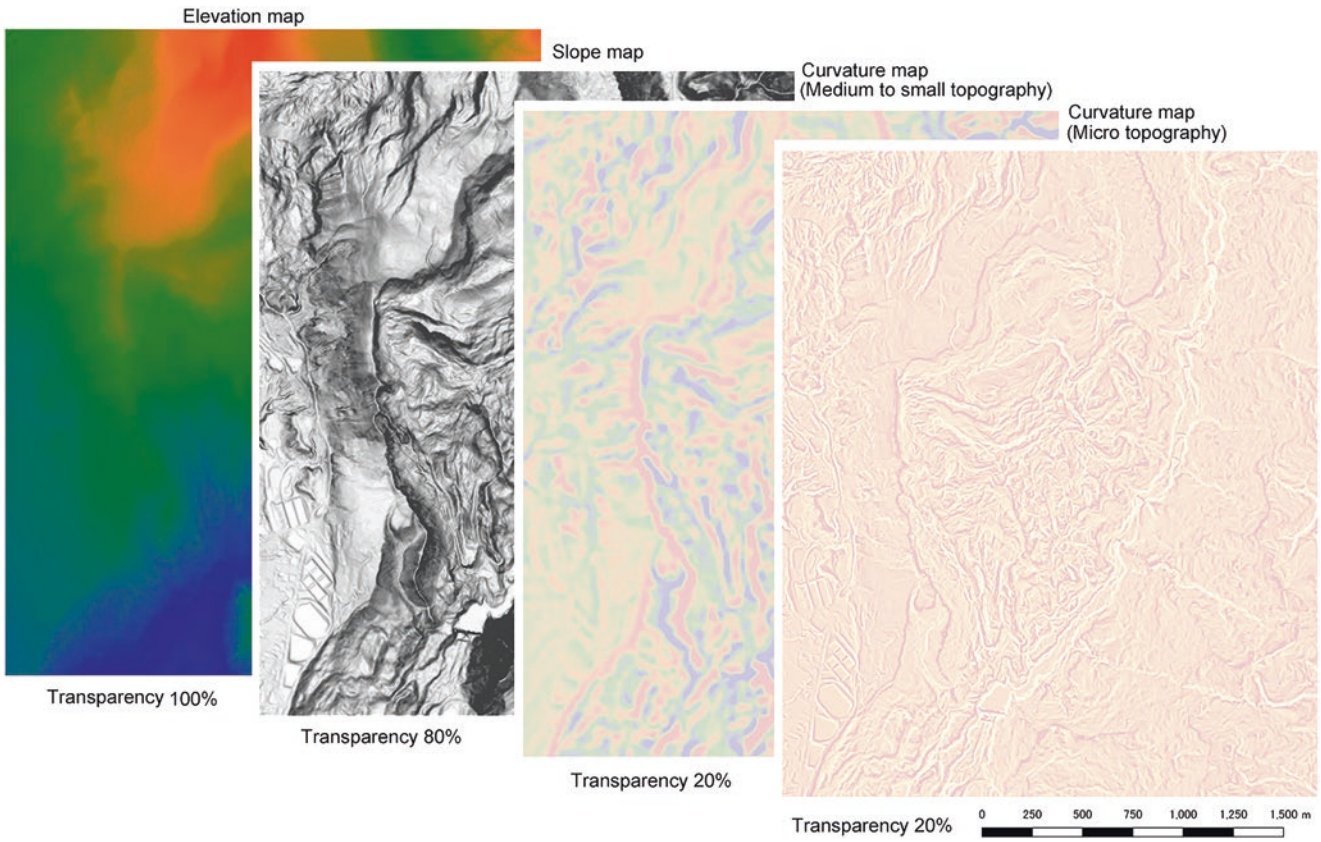

Fig. 51 Superposition of four types of topographic maps used for three-dimensional microtopography maps (MT3DM)

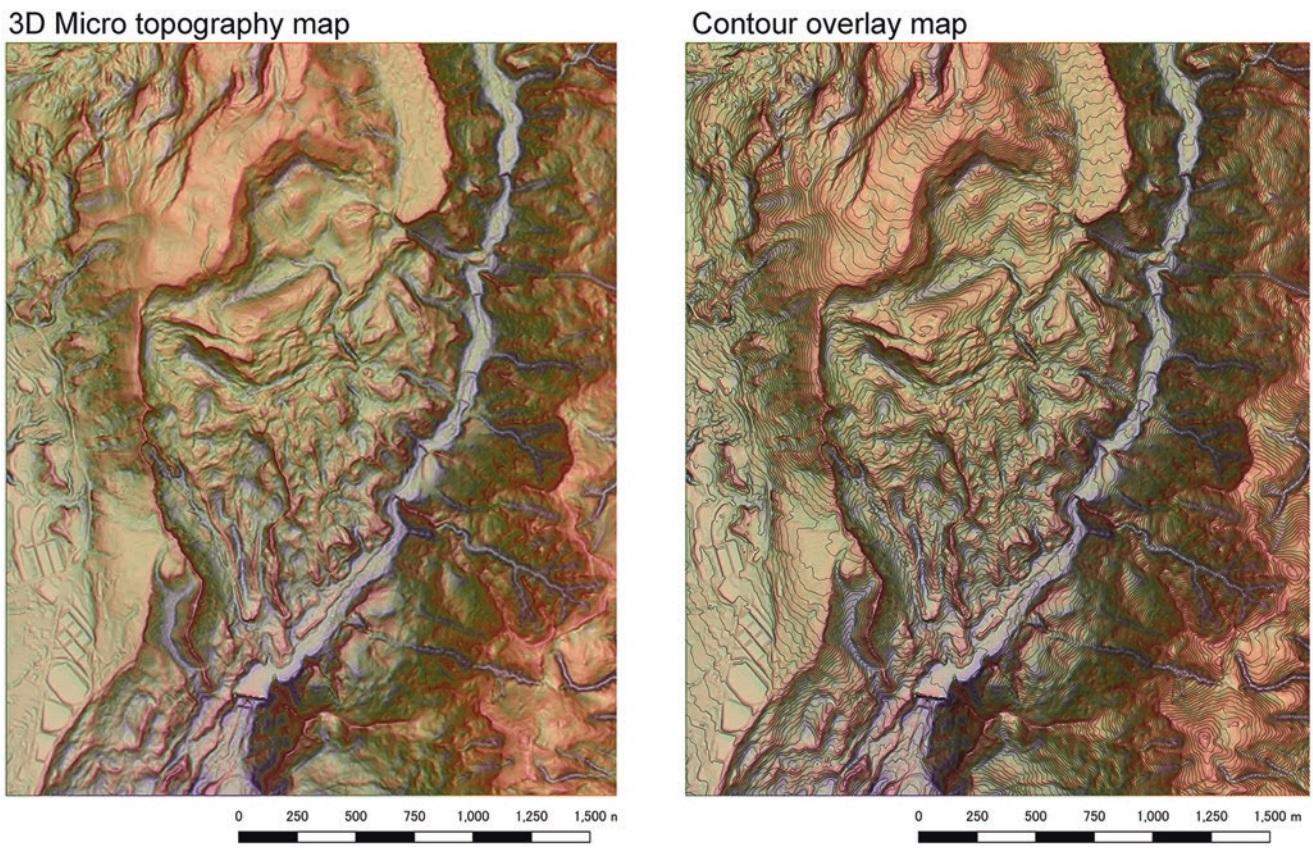

Fig. 52 3D Map left: 3Dmicrotopographic map, right: superimposed contour lines)

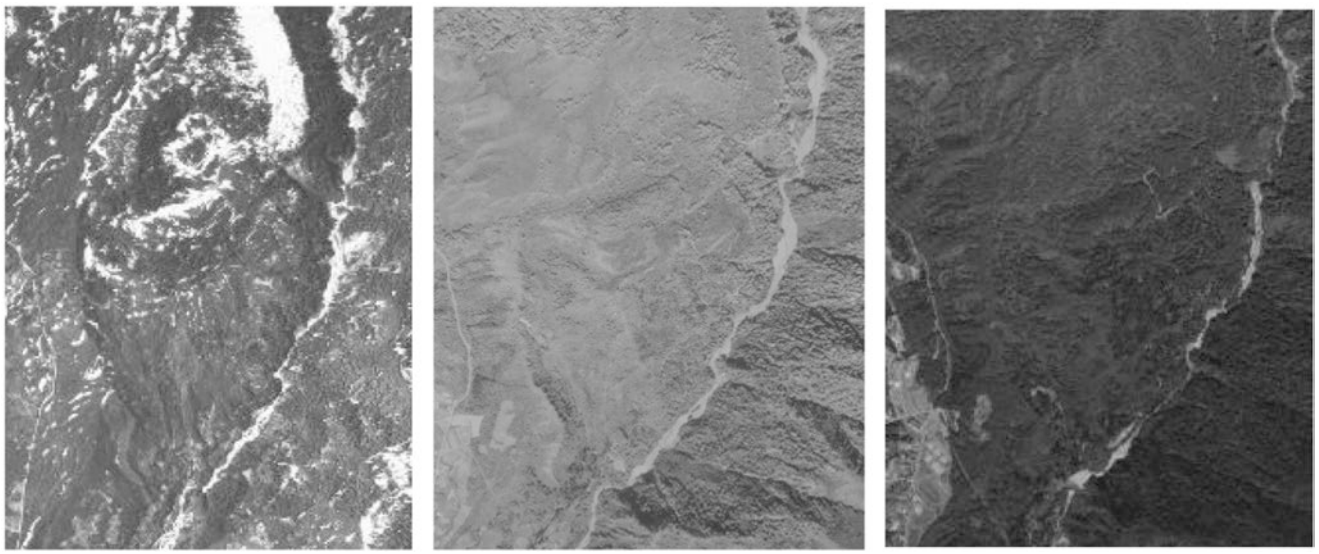

Fig. 53 Comparison of aerial photographs taken in different years (Geospatial Information Authority of Japan, USA-M1073-22, TO748Y-C1-15, TO20035X-C1-3)

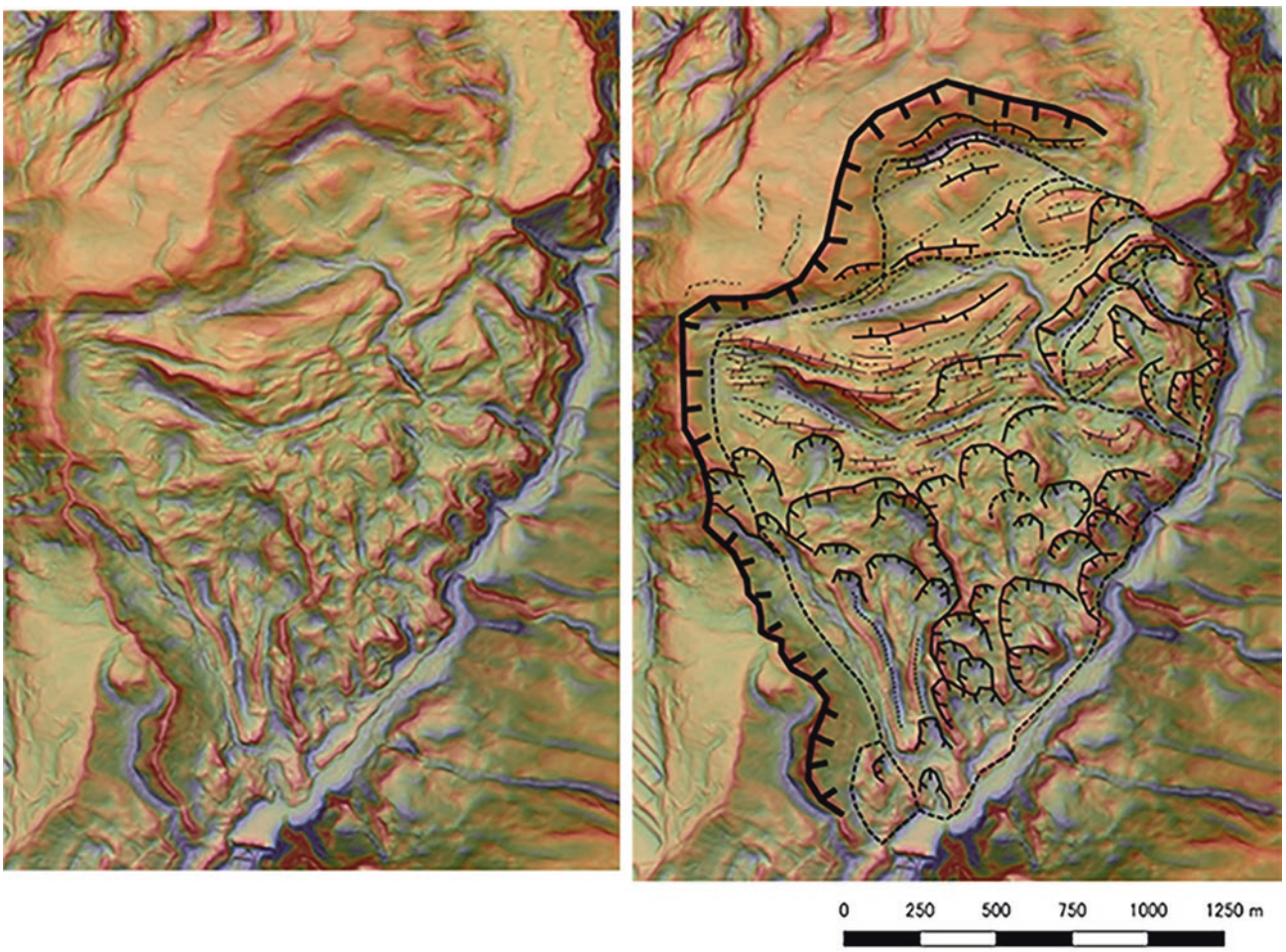

Fig. 54 Interpretation results of landslide topography based on a three-dimensional topographic map (prepared from the 5mDEM of the National Geospatial Science)

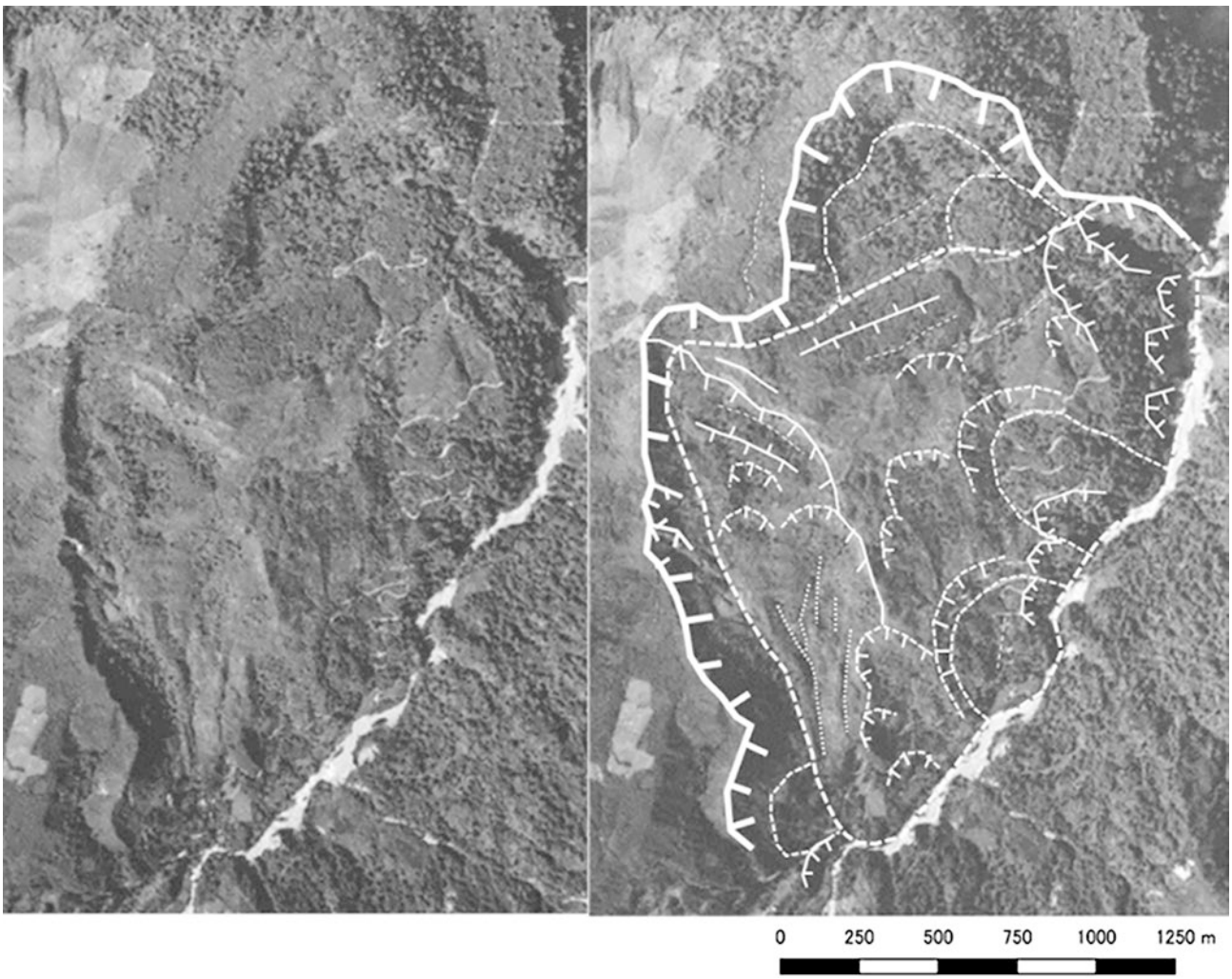

Fig. 55 Interpretation results of landslide topography by aerial photograph (TO 699Y-C4A-3-4)

8.5 Landslide Topography Decipherment Using 3D Microtopographic Map (MT3DM)

8.5.1 Topographic Decipherment Using 3D Microtopographic Maps (MT3DM)

Landslide topographic detection by aerial photo interpretation is a difficult technique that requires skilled reading skills, as it is a task to read the true shape of the terrain behind vegetation while considering the development process of landslides. In addition, when focusing on the resolution of the topography of aerial photographs, which has been conventionally used for deciphering landslide terrain, there are differences in photographic equipment, scale, shooting season, shooting time, etc., depending on the aerial photograph. Each aerial photograph has large variations in resolution, saturation, shading, vegetation conditions, etc. Therefore, which aerial photograph is used also greatly affects the accuracy of topographic decipherment.

Therefore, we focus on a three-dimensional topographic map created from DTM data. 3D topographic maps that eliminate the influence of vegetation and reproduce the topography itself help to simplify topographic decipherment, which requires skilled skills. The following is an example of landslide topographic decipherment using a three-dimensional microtopographic map.

8.5.2 Interpretation Example of Landslide Topography in the Active Phase

- Overview of landslide topography

The shape of the main sliding cliff is clear. However, due to the collapse occurring in the main sliding cliff, the general horseshoe shape is not shown, but the hoof-shaped shape

with both sides entering the mountainside is shown. In the middle ~ lower part of the moving body, many microtopographies such as cracks (steps) and flow marks are developed, and the microtopographic boundary is clear. In addition, where gully intrusion is observed along the flow scar, the collapse topography of the 0-shaped valley and the development of secondary slips are remarkable. Small and medium-sized landslides have also developed markedly at the ends of mobile bodies.

- Comparison of interpretation results of aerial photographs and three-dimensional microtopography maps

The outlines of landslide topography, such as main sliding cliffs and landslide moving objects, are almost the same interpretation. There was a large difference in the reading results regarding the microtopography inside the landslide topography. In particular, many areas are represented in three-dimensional microtopographic maps but cannot be read in aerial photographs due to vegetation. Furthermore, although similar microtopography could be extracted between the two, there were some differences in the shape of the microtopography (cracks, the extension of steep terrain, etc.). Since the microtopography is obscured by vegetation in aerial photographs, it is often necessary to grasp the shape of the microtopography, and there are many variations depending on the person.

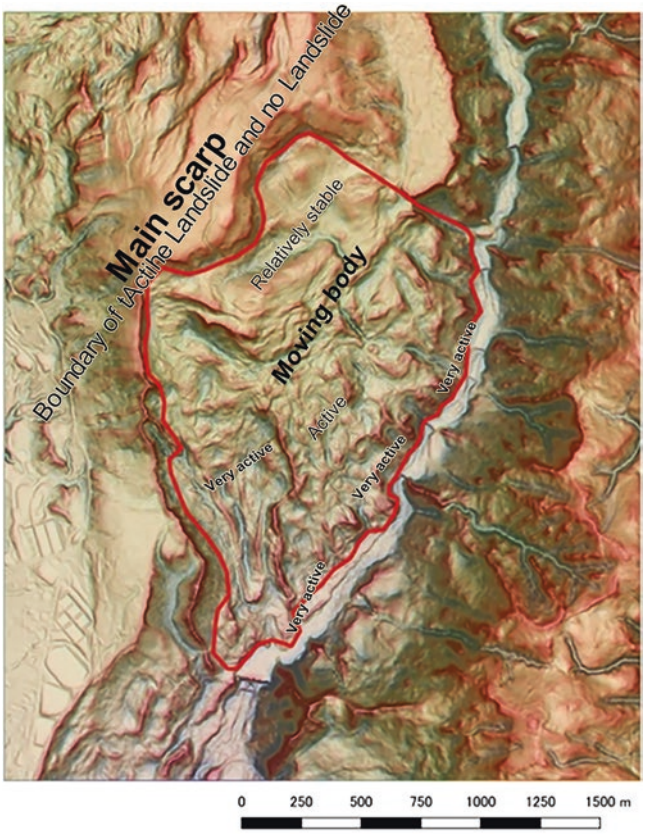

Fig. 56 Case 1 (Landslide landforms in the active phase)

8.6 Points to Note and Issues in the 3D Microtopographic Map (MT3DM)

8.6.1 Color Scale Thresholds and Terrain Representation

Regarding the threshold setting when setting the color of the slope and curvature diagrams, the numerical range is important for clearly expressing the landslide topography.

In the case of a slope map, depending on the setting of the maximum slope of the grayscale, there will be a difference in the shade of the color, which affects the topographic representation. When the maximum value of grayscale is increased, the microtopography in 5 m DTM shows a small angle (about 6° for micro terrain with a specific height difference of 1 m, about 11° for 2 m), resulting in pale colors and blurred microtopographic representation. In the 3D microtopographic map, the maximum grayscale value in the slope map is 45°. The maximum value of the color scale range is 0.05 ~ 0.03, and the minimum value is −0.05 ~ −0.03 for the curvature map. It is explained below.

8.6.2 Topographic Volume Analysis Results and Threshold Settings of Landslide Terrain

Figure 56 shows the results of the topographic volume analysis conducted to clarify the characteristic values of landslide landforms. The analysis analysed two cases of landslide landforms (landslide topography in the active phase and landslide landform in the demolition phase) with a large activity difference (Figs. 56 and 58).

The amount of terrain to be analyzed was calculated from 5 m DTM, and the types of topographic quantities were slope and curvature. There were two types of curvature: “curvature of small and medium-sized terrain” and “curvature of micro-terrain”.

The analysis range of the topographic volume characteristic value is the inside of the moving body where the kinetic characteristics of the landslide appear (Figs. 56 and 58), and the analysis results of the topographic volume characteristic values in each case are shown in Figs. 57 and 59. From the analysis results, even if there was a difference in the degree of landslide activity, no clear difference was observed in the frequency distribution of the topographic volume characteristic values, and it was generally within the same numerical range. In other

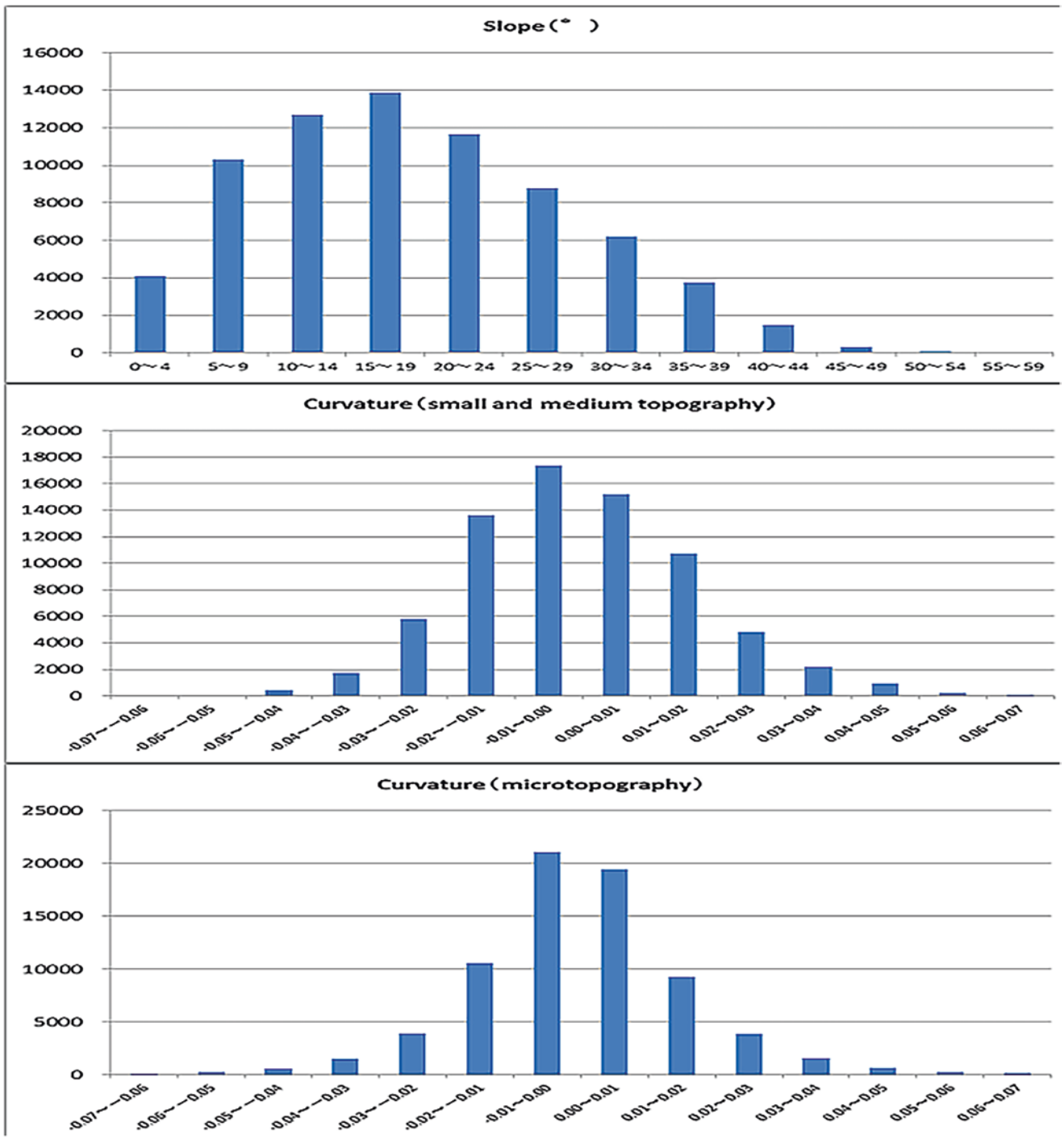

Fig. 57 Frequency distribution map of each (Case 1)

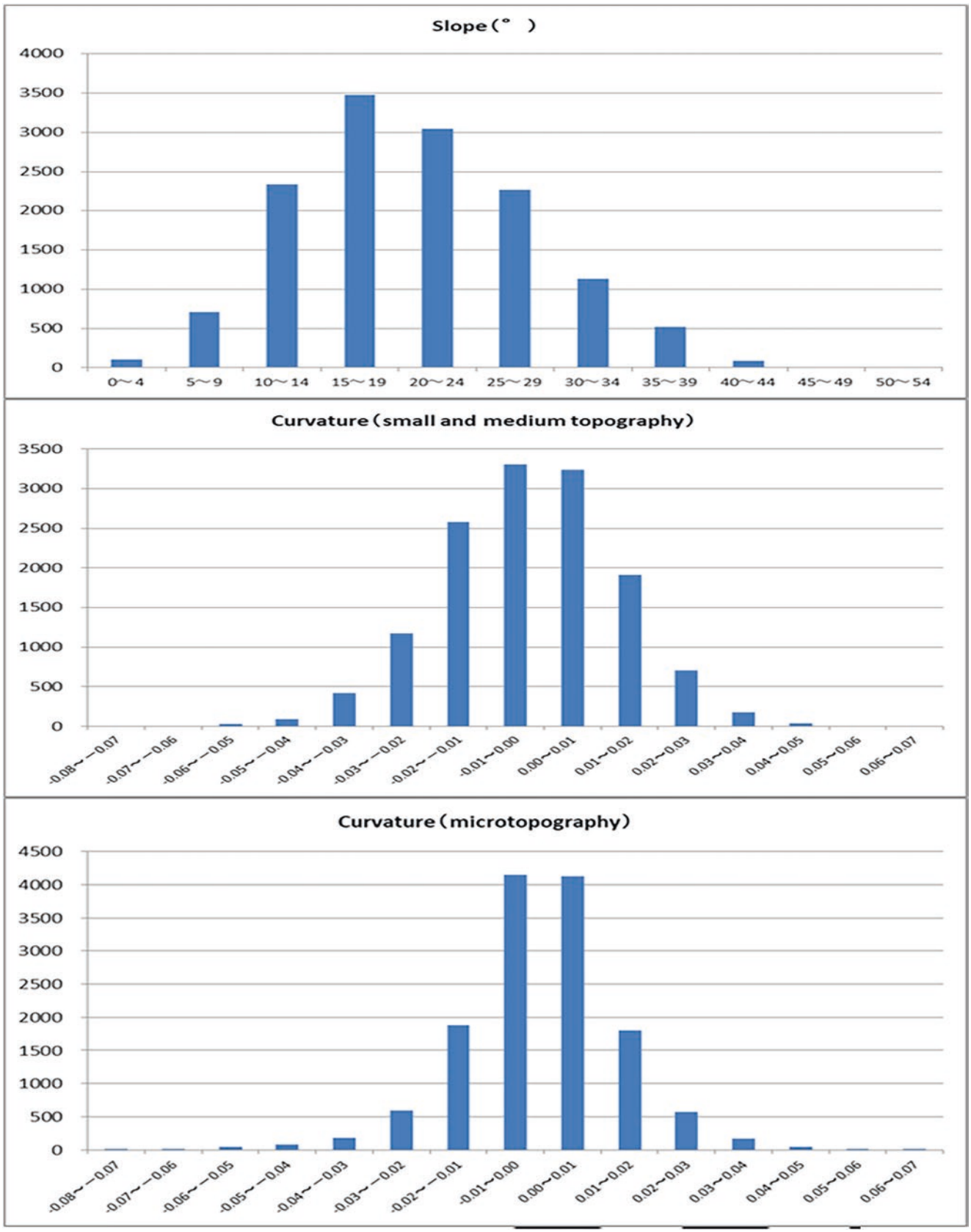

Fig. 58 Case 2 (Landslide topography in the demolition period)

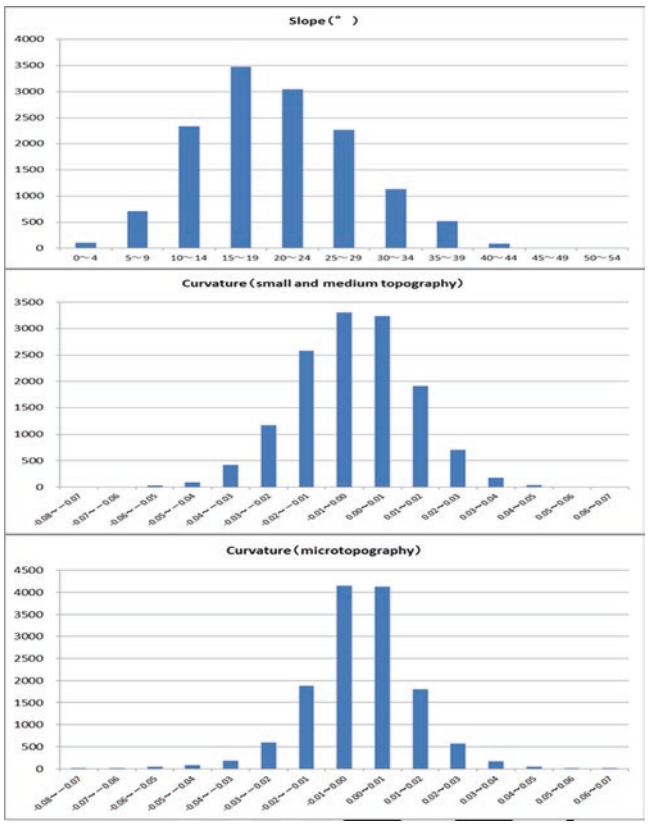

Fig. 59 Frequency distribution map of each topographic quantity (Case 2)

words, the slope was within the range of −0.05 ~ 0.05, and the range of −0.03 ~ 0.03 was concentrated in the range of −0.03 ~ 0.03. Therefore, this numerical range was taken into account when creating a three-dimensional microtopographic map, and the threshold value was used when setting the color.

8.6.3 Landslide Topography Representation and DTM Accuracy

The scale of landslide topography varies from several tens of meters to several hundred meters. The accuracy of the topographic representation of the 3D topographic map depends on the DTM accuracy, and it is considered that there is an appropriate DTM accuracy corresponding to the scale of the landslide. Niida pointed out the relationship between DEM accuracy and topographic decipherment, that there is a mesh size that is easy to read depending on the scale, such as the horizontal and specific height of the terrain. In other words, low-resolution DEMs are suitable for deciphering large terrains, and the higher the resolution, the more detailed valleys due to erosion and the linear topography with sudden changes in slope, such as tectonic lines and faults.

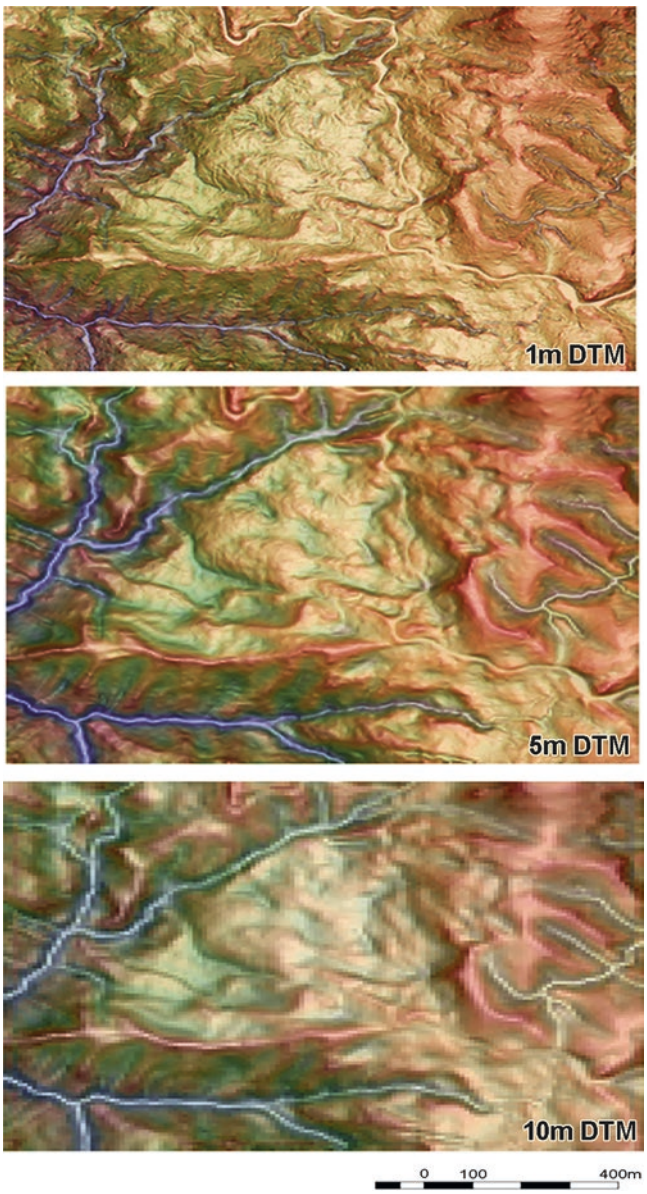

Fig. 60 3D landslide topography representation with different DTM size data. Left: 1 m DTM, Middle: 5 m DTM, Right:10mDTM

The 3D microtopographic maps are created from 5 m DTM. The accuracy of the terrain representation depends on the DTM accuracy, but it is necessary to understand the case in landslide terrain. We show a diagram comparing 3D microtopographic maps prepared from 1 m DTM, 5 m DTM, and 10 m DTM over a range of about 1 km *1 km (Fig. 60).

The figure created from 1 m DTM showed a lot of noise on the ground surface caused by falling rocks and fallen trees. Large-scale landslides can make it difficult to decipher the terrain. On the other hand, in the case of a small-scale landslide, it is considered that microtopography cannot be clearly expressed without the accuracy of 1 m DTM.

It can be judged that the 5 m DTM is suitable for deciphering landslide topography on a scale of several hundred meters or more. Therefore, 5 m DTM is not suitable for deciphering small-scale landslide terrain. The resolution of the 10 m DTM is too low. Although the outline of the landslide topography is legible, the internal microtopography is obscured even in a large landslide of several hundred meters or more. Therefore, although the main topography, such as sliding cliffs, can be read, it is extremely difficult to decipher the microtopography inside the moving body and is unsuitable for detailed landslide topography decipherment.

9 Conclusion

In this report, we summarize the contents of the exchange of opinions among the co-authors on the following points.

Observing objects in three dimensions is first necessary to grasp, classify, and map the tendency of topographic changes on slopes geomorphologically.

In the past, the main observation method was the real interpretation of aerial photographs, but sensing technology has made great progress in the last 10 years. This has led to major changes in topographic observation approaches. The biggest change is that it is now possible to visualize three-dimensional objects easily. There is a huge variety from aerial photography to the iPhone 14 pro.

Among them, the interpretation of aerial photographs was difficult to understand. Since the actual interpretation is a task of further handling images based on experience and knowledge, it is not easy to share information with others. This also lightens the significance of utilization. However, its usefulness has not been lost. It is effective as a means of observation that can easily observe the details of the current terrain.

On the other hand, digital 3D information can present visible data and maps corresponding to various requirements, even if it is only data processing technology. Even without experience in topographic surveys, disaster risk can be mapped semi-mechanically.

Needless to say, to predict the location of slope disasters, it is necessary to appropriately grasp and classify the topographic changes that take place on slopes, and basic knowledge of this is always necessary.

Aerial interpretation will be necessary to understand local disaster risk. At the same time, digital information will be revolutionary as a direct tool for visualizing and mapping disaster risk. It is necessary to master both.

This report summarizes the outline of the actual situation of slope change and its mapping. In the latter half of the report, we proposed a manual to overcome the difficulty of deciphering aerial photographs. At the same time, we summarized in an easy-to-understand manner a method for visualizing topography three-dimensionally using digital 3D data and grasping the fluctuation trend of landslides.

Acknowledgement In compiling this report, I would like to express my sincere gratitude to Prof. Kyoji Sassa (Professor Emeritus, Kyoto University, Secretary-General of ICL) and Prof. Kazuo Konagai (Professor Emeritus, The University of Tokyo, Leader of the Sri Lanka SATREPS Project) for their guidance. Thanks are due to JICA/JST SATREPS officials and collaborators from Japan, Vietnam, and Sri Lanka.

References

Daimaru H (2014) TXT-tool 1.081-2.2 interpreting topography from historical perspective—a case study of a tropical deeply weathered region. In: Sassa K, He B, McSaveney M, Nagai O (eds) ICL landslide teaching tools. Springer, Cham, pp 11–21

Dung ND, Miyagi T, Luong LH, Hamasaki H, Hayashi K, Tien DV, Daimaru H, Abe S (2016) Trial of landslide topography mapping using ALOS W3D data—case study along the National Road no. 7 in central Vienam. Trans Japanese Geomorphological Union 37:127–140

Hamasaki E, Miyagi T (2014a) TXT-tool 1.081-2.3 abstracting unstable slopes (landslide topography) using aerial photos and topographic maps: concept and frameworks. In: Sassa K, He B, McSaveney M, Nagai O (eds) ICL landslide teaching tools. Springer, Cham, pp 22–35

Hamasaki E, Miyagi T (2014b) TXT-tool 1.081-2.4 risk evaluation using the analytic hierarchy process (AHP)- introduction to the process concept. In: Sassa K, He B, McSaveney M, Nagai O (eds) ICL landslide teaching tools. Springer, Cham, pp 36–49

Highland LM, Bobrowsky P (2008) The landslide handbook—guide to understanding landslides. U.S. Geological Survey Circular 1325, Reston, Virginia, p 65

Ikeda K (2020) Three dimensional microtopography map for interpretation the detail structure of landslide area. In: Committee of evaluation study team, Japan Landslide Society (ed) Guidebook of the slope disaster risk evaluation. Asakura shoten, pp 74–92. In Japanese

Makabe S, Miyagi T, Daimaru H, Unome S (2015) Clarification of the reflectivity of extra high resolution laser data by SAKURA system in mangrove habitat, Amami Island, Japan. Restoration Studies 7:15–23. In Japanese

Miyagi T (2014) TXT-tool 1.081-2.1 landslide topography mapping through aerial photo interpretation. In: Sassa K, He B, McSaveney M, Nagai O (eds) ICL landslide teaching tools. Springer, Cham, pp 1–10

Miyagi T (2021) Landslide recognition and mapping for slope disaster risk reduction and management–keynote speech. WLF5 Books Understand Reducing Landslide Disaster Risk 2:9–31. https://doi.org/10.1007/978-3-030-60227-7

Miyagi T, Koiwa N, Takenaka J (1995) Hillslope development and environmental change since the last interglacial age in the Kawadoi Basin, Northeast Japan. The bulletin of Northeast Japan cultural institute. No. 27, pp 1–29. In Japanese

Miyagi T, Prasad GB, Tanavud T, Potichan A, Hamasaki E (2004) Landslide Risk Evaluation and Mapping-Manual of Aerial Photo Interpretation for Landslide Topography and Risk Management-Rep. National Research Institute for Earth Science and Disaster Prevention. No. 66, pp 75–137

Miyagi T, Yamashina S, Esaka F, Abe S (2011) Massive landslide triggered by 2008 Iwate-Miyagi inland earthquake in the Aratozawa dam area. Tohoku, Japan. Landslides 8:99–108

Nakayama T, Miyagi T (1984) Hillslope development and sediment yield under changing environment since 46,000 years B.P. In the Kawadoi basin, Northeast Japan. Ann Tohoku Geographical Assoc 36-1:25–38. In Japanese

Oyagi No (2007) “Interpretation of Landslide Topography by Aerial Photograph Interpretation”. Kin-miraisha. Ps. 316. In Japanese
Toda K (2014) Three-dimensional map and the interpretation by the combination of slope gradient and the curvature (CS3D map). Forest Habitat 56:75–79
UNDRR (2015) Sendai Framework Terminology and Disaster Risk Reduction. https://www.undrr.org/terminology/disaster. Last accessed 16 Oct 2023
Unome S (2020) Current status of airborne LiDAR system with a case study in Amami Oshima Island and the introduction of the latest LiDAR technology. Mangrove science 11:27–35. In Japanese
Vernes DJ (1978) Slope movement types and processes: landslide analysis and control. Highway Res Board Special Rep 176:11–33
Yem NT (2006) Assessment of landslides and debris flows at some prone mountainous area Vietnam and recommendation of remedial measures. Phase I: a study of the east side of the Hoang Lien Son Mountains area, Vietnam. Inst Geological Survey, Vietnam, p 121. In Vietnamese

Part II

Original Articles

Observation of Seismic Ground Motion and Pore Water Pressure in Lineated Valley Fill of Wakayama, Southwest Japan

Koji Matsunami, Kyoji Sassa, Loi Doan,
Ranjan Weerasinghe, and Tania Munasinghe

Abstract

We performed in-situ observations of seismic ground motion, pore-water pressure, and ground-water level at lineated valley fill (LVF) in Wakayama city, southwest Japan, from 2004 to 2008. In Wakayama city and its surrounding area, felt earthquakes often occur with epicenters in the northwestern part of the Kii Peninsula and the Nankai Trough off the coast of the Kii Peninsula. We obtained simultaneous observation records of surface ground motion and pore-water pressure from several small- to medium-sized earthquakes. The excess pore-water pressure was clearly observed during a medium-sized earthquake with magnitude Mj 4.5. From the detailed analysis of surface ground motion, we detected a long-period pulse, although it was usually hidden behind oscillating short-period components with large amplitudes. The strong shaking induced ground tilting motion, causing a step-like acceleration change in the seismometer pendulum. Although no ground deformation could be confirmed through visual observation during the earthquake, the in-situ instrumental observation revealed ground tilting motion. Theoretical long-period pulses were synthesized assuming models of ground tilting motion during an earthquake. From comparison of the theoretical model with the observed long-period pulse, the permanent tilt is of an order of 10^{-6} degree down nearly toward the direction of the valley line.

Keywords

Lineated valley fill · Strong ground motion · Pore-water pressure · Landslide

1 Introduction

In the process of expansion of large cities from alluvial plains to hilly areas, large-scale residential areas have been developed by filling valleys with soil. Such areas have often suffered damage from earthquake-induced landslides. To reduce damage, it is necessary to develop countermeasures based on damage prediction. To predict the damage by earthquake-induced landslide, it is necessary to understand the behavior of ground during moderate to strong earthquakes. For this purpose, in-situ continuous observation of seismic ground motion, pore-water pressure, etc. at landslide ground is necessary, but there are very few such observations (Ishihara et al. 1987, 1989; Iai and Kurata 1991; Kamai 2011).

We performed in-situ continuous observation of seismic ground motion, pore-water pressure, and ground water level at LVF in Wakayama city, southwest Japan. We obtained simultaneous observation records of surface ground motion and pore-water pressure during several small- to medium-sized earthquakes. In particular, excess pore-water pressure was clearly observed during the medium-sized earthquake with magnitude Mj 4.5.

In this paper, first we examine the relation between surface ground motion and pore-water pressure during earthquakes. Next, we detect minute signals caused by ground tilting motion from seismograms of surface ground motion when excess pore-water pressure occurs. We construct the model for ground tilting motion based on the detected sig-

K. Matsunami (✉) · K. Sassa
International Consortium on Landslides, Kyoto, Japan

L. Doan
International Consortium on Landslides, Kyoto, Japan

Institute of Transport Science and Technology, Hanoi, Vietnam

R. Weerasinghe
National Building Research Organization, Colombo, Sri Lanka

T. Munasinghe
ICL SATREPS Office, Colombo, Sri Lanka

University of Colombo, Colombo, Sri Lanka

B. Abolmasov et al. (eds.), *Progress in Landslide Research and Technology, Volume 3 Issue 1, 2024*, Progress in Landslide Research and Technology, https://doi.org/10.1007/978-3-031-55120-8_3

nal. Based on this model, the inclination of ground during an earthquake is estimated by fitting the theoretically calculated waveform for ground tilting motion to the observed one.

2 Observations

We performed in-situ simultaneous and continuous observations of seismic motion, pore-water pressure and groundwater level at a LVF in Wakayama city, from 2004 to 2008. In Wakayama city and its surrounding area, many felt earthquakes occur annually with epicenters in the northwestern part of the Kii Peninsula and the Nankai Trough off the coast of the Kii Peninsula (Figs. 1 and 2). A seismometer and a pore-water pressure transducer with a high dynamic range and wide frequency band were used for the observations. The observation site OIK is shown in Fig. 3. From this figure, we can see large changes of topography and ground structure of the observation site due to the urban planning. That is, the valley was converted into LVF, and many houses were built there. Furthermore, it should be noted that the residential area on the LVF is adjacent to a large pond. The topography and ground environment of the observation site satisfy the conditions for landslide occurrence. The observation site OIK is considered a suitable test site for the observation of earthquake-induced landslides.

We carried out surface wave exploration and boring survey at the site OIK. The results obtained are shown in Fig. 4. According to that, a sandy layer with an S-wave velocity (Vs) of 130–190 m/s and an *N*-value of 5 or less is deposited up to a depth of approximately 4 m. At a depth of 4 m or more, a gravel layer with Vs = 200 to ~260 m/s and *N*-value of 5 or more is deposited. This approximately 4 m-thick surface sandy layer corresponds to the artificially constructed soft ground. The groundwater level is approximately 2 m. It is thought to be saturated with water at depths of 2 m or deeper.

Figure 4 also shows the locations of seismometers, pore-water pressure transducer, ground-water level meter and GPS. The seismometers were installed on the ground surface. The pore-water pressure transducer was installed 2.9 m directly below the seismometer (GL-2.9 m). The groundwater level meter was installed at a depth of 2.9 m (GL-2.9 m) inside the well.

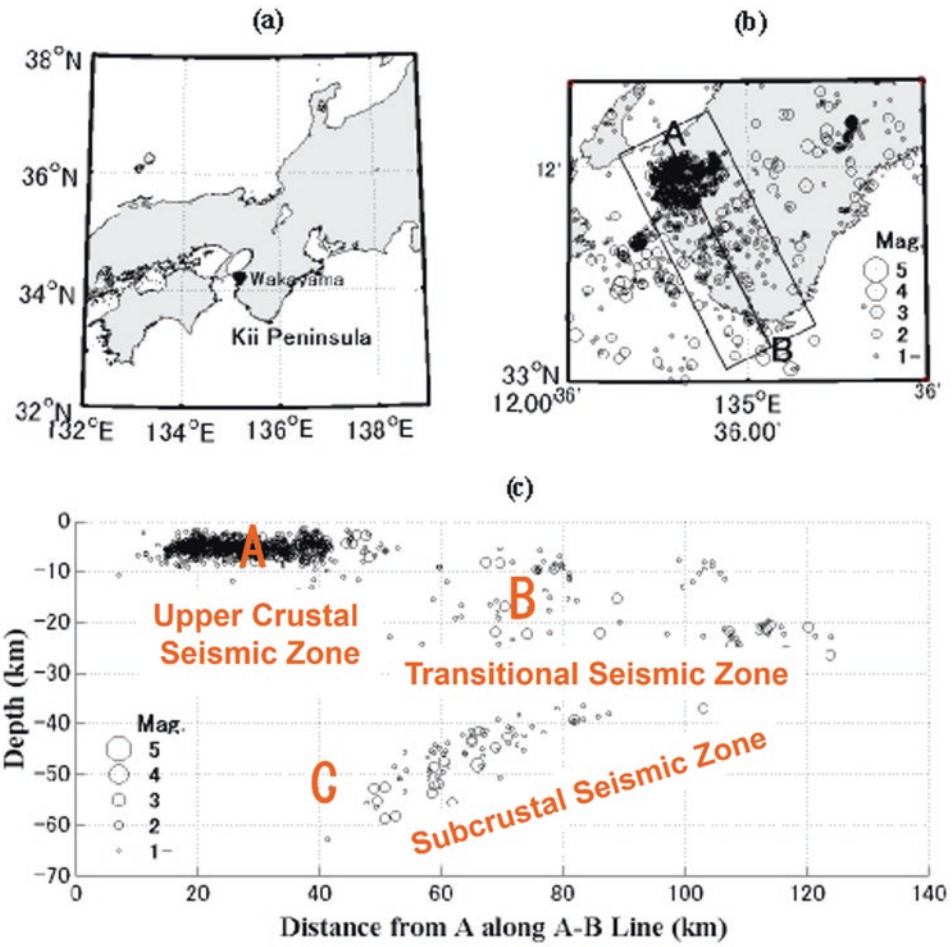

Fig. 1 (**a**) Wakayama area in the northwest of the Kii Peninsula, southwestern Japan. (**b**) Epicentral distribution of earthquakes observed for the period from 1 January 2000 to 31 December 2002 by the Wakayama Seismological Observatory of the Earthquake Research Institute, University of Tokyo, using the telemetered network for microearthquake observation. (**c**) Vertical distribution of earthquakes in and around the Kii Peninsula, obtained by projecting hypocenters of earthquakes located within the area indicated in Fig. 1b on a vertical plane along the A-B line in Fig. 1b. Most of the earthquakes in the upper crust are located in and around the Wakayama plain in the northwest of the Kii Peninsula, where intense swarm activity occurs. The earthquake swarm region is indicated by A in Fig. 1c

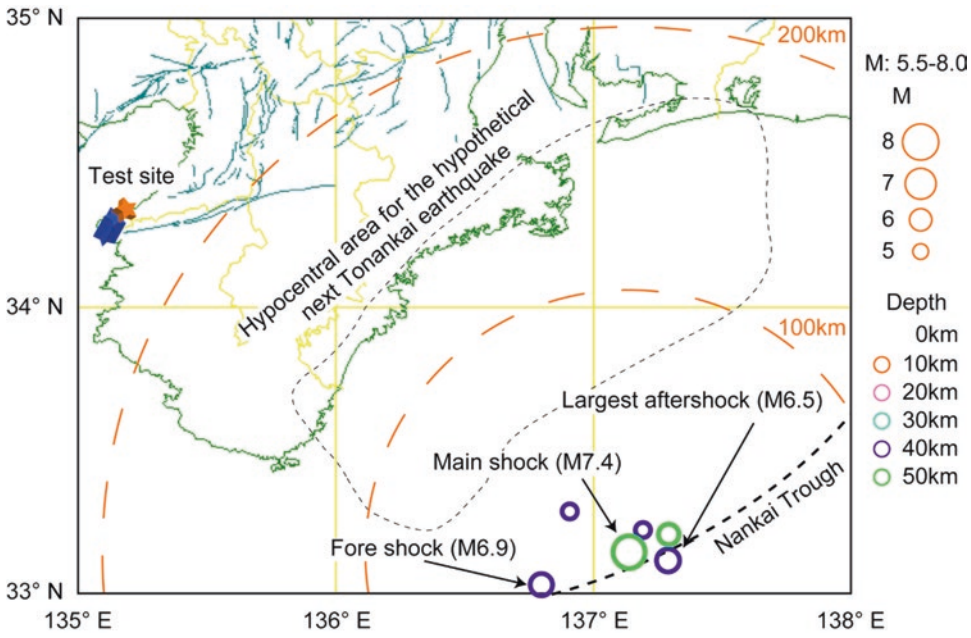

Fig. 2 A series of seismic activities off the coast of the Kii Peninsula in 2004. Pore-water pressure clearly responds to seismic motion during the six largest earthquakes in seismic activity

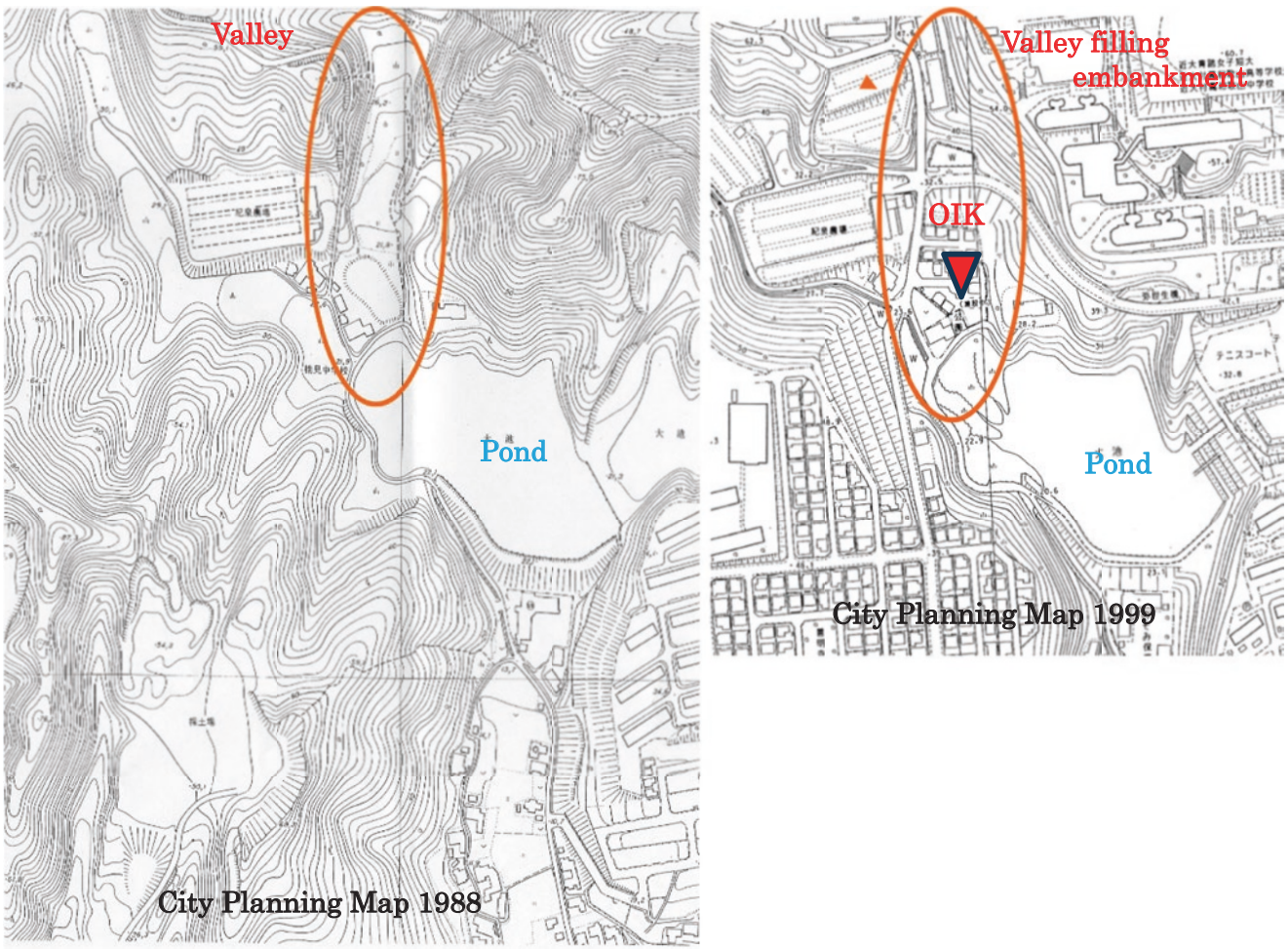

Fig. 3 Location of observation site OIK. As cities expanded from alluvial plains to hilly areas, large-scale housing ground, such as LVF, have been developed. The observation site is located on the ground adjacent to the pond

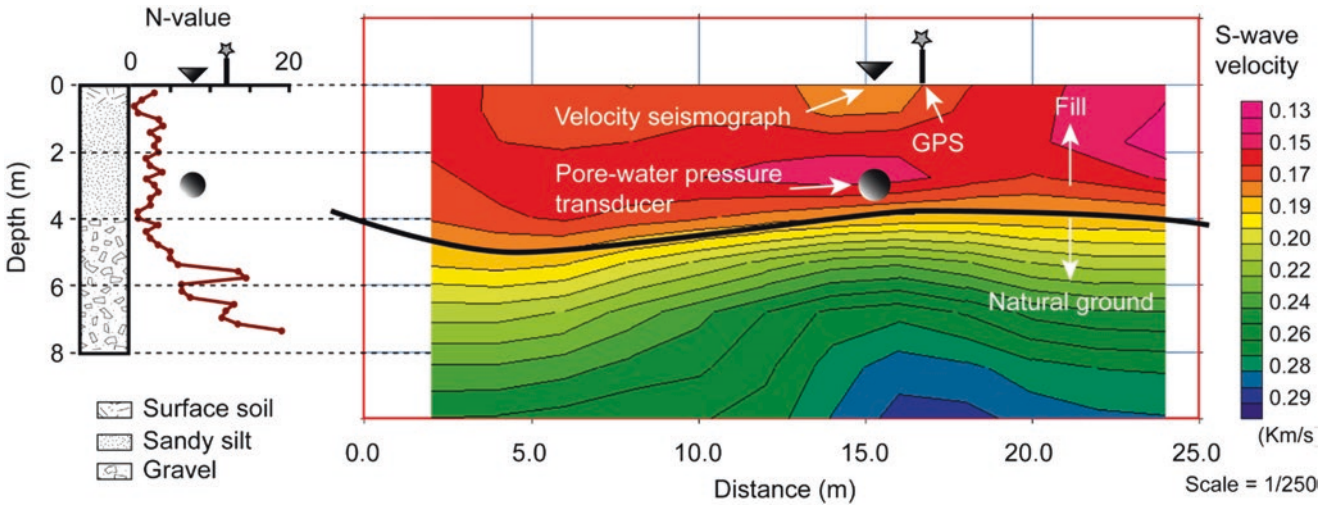

Fig. 4 Surface geological structure and S-wave velocity structure of OIK. This figure also shows the location of observation instruments

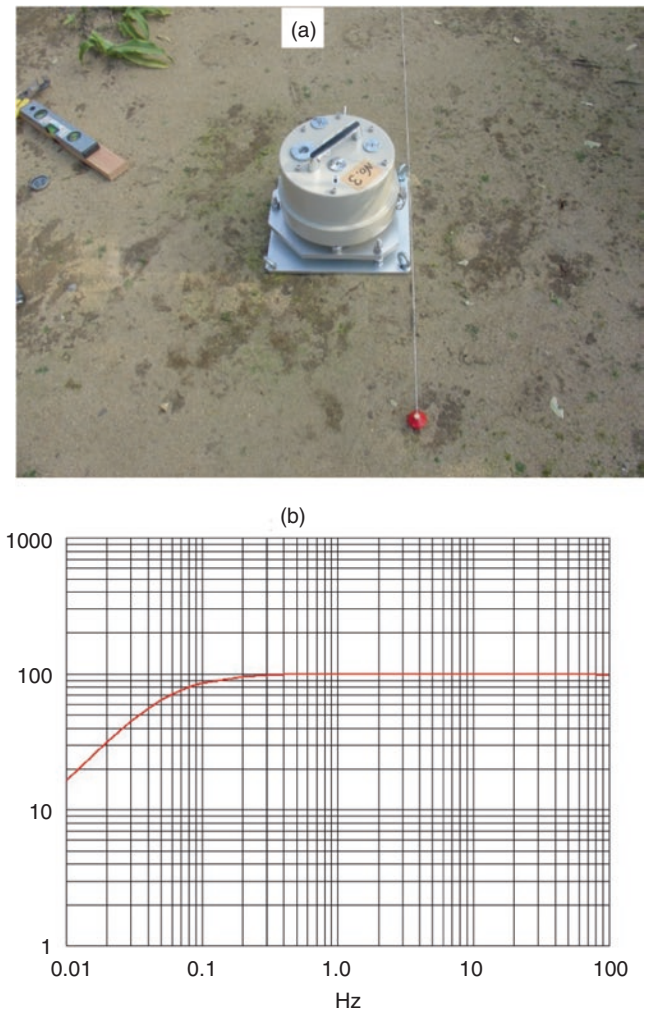

Fig. 5 (**a**) Servo-type velocity seismometer, (**b**) Frequency characteristics of servo-type velocity seismometer. Amplitude response is flat in the frequency range of 0.1–70 Hz

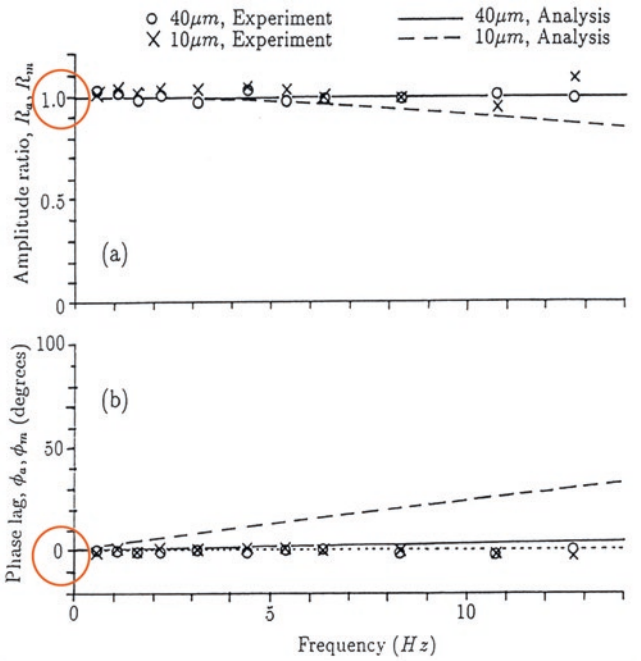

Fig. 6 Frequency characteristics of pore-water pressure transducer. Upper: amplitude. Lower: phase

Figure 5a shows a photograph of the velocity-type seismometer used. Figure 5b shows a frequency characteristics of the servo-type velocity seismometer used here. The amplitude response is flat in the frequency range of 0.1–70 Hz. The resolution is nearly 100μcm/s, and the maximum measurement range is ±20 cm/s. The observed seismograms were recorded into a data logger with 100 Hz sampling. Figure 6 shows a frequency characteristics of pore-water pressure transducer used here. The amplitude and phase

characteristics are flat to nearly 13 Hz. The observable range is from 0.024 kPa to 96 kPa. The observed pore-pressure is recorded into a data logger with 10 Hz sampling. Since the seismometer and pore-water pressure transducer have a flat characteristics in the wide frequency range, we can directly compare waveforms of pore-water pressure with those of surface velocity observed at the site OIK.

3 Data and Analysis

Figure 7 shows the records of pore-water pressure and water-level meter observed during the foreshock (M6.9) and the main shock (M7.4) shown in Fig. 2. We can see the rapid changes in pore-water pressure induced by seismic ground motion. The three-component waveforms (Rd, Vt, and Tr) of surface ground velocity observed at OIK during the main-shock are shown in Fig. 8. Rd is the radial component, Tr is the transverse component, and Vt is the vertical component. The radial direction is the direction from the epicenter to the observation point, and the transverse direction is the direction perpendicular to the radial direction. The maximum surface velocity is 1.171 cm/s in the transverse component (Tr) of seismograms. The vertical component (Vt) is smaller than the other two horizontal components. This is due to the soft surface ground. Figure 9 shows the waveform of pore-water pressure along with those of surface ground velocity.

According to Roeloffs (1996), the pore-water pressure Pw is proportional to the radial component (Rd) of surface ground velocity, that is, Pw ∝ Rd. This relationship holds true for both in case of P-wave arrivals and in case of S-wave arrivals. Figure 10 briefly summarizes the derivation process of Pw ∝ Rd. To confirm the relationship of Pw ∝ Rd., the pore-water pressure waveform (Pw) is superimposed on the three surface velocity waveforms (Rd, Vt, and Tr), in Fig. 11. From this figure, Pw appears to be similar to Rd. To examine this relationship in more detail, Pw and Rd. were passed through a bandpass filter with a center frequency (fc) and the two were compared. Figure 12 shows the case where fc is 1/2 Hz, and Fig. 13 shows the case where fc is 1/8 Hz. From these figures, it can be seen that the waveform of Pw matches that of Rd. very well in both P-wave and S-wave parts. Furthermore, the waveform of Pw matches that of Vt fairly well in both P-wave part and S-wave part. On the other hand, the waveform of Pw does not quite match the Tr component of the surface ground velocity. In this way, the relation of Pw ∝ Rd. was confirmed using observational data. We can also understand the relationship of Pw ∝ Rd. in that Pw depends not on shear strain, but on volumetric strain. Next, we investigate the case when excess pore-water pressure is generated during an earthquake.

On May 15, 2006, there was an earthquake with a maximum seismic intensity of 4, whose hypocenter was in the northern part of Wakayama city. The magnitude Mj of the earthquake was 4.5, and the depth of the hypocenter was approximately 3 km. Figure 14 shows surface velocity waveforms of Mj 4.5 earthquake observed at OIK. From this figure, it can be seen that Ts-p is smaller than 1.0 s, where Ts-p is the difference Ts-Tp between S-wave arrival time Ts and P-wave arrival time Tp. From this Ts-p, the hypocentral distance is estimated to be less than 10 km. Although the magnitude Mj was not so large, the intensity of the earthquake was high, probably because the depth of the hypocenter was shallow and the hypocentral distance was very short. As

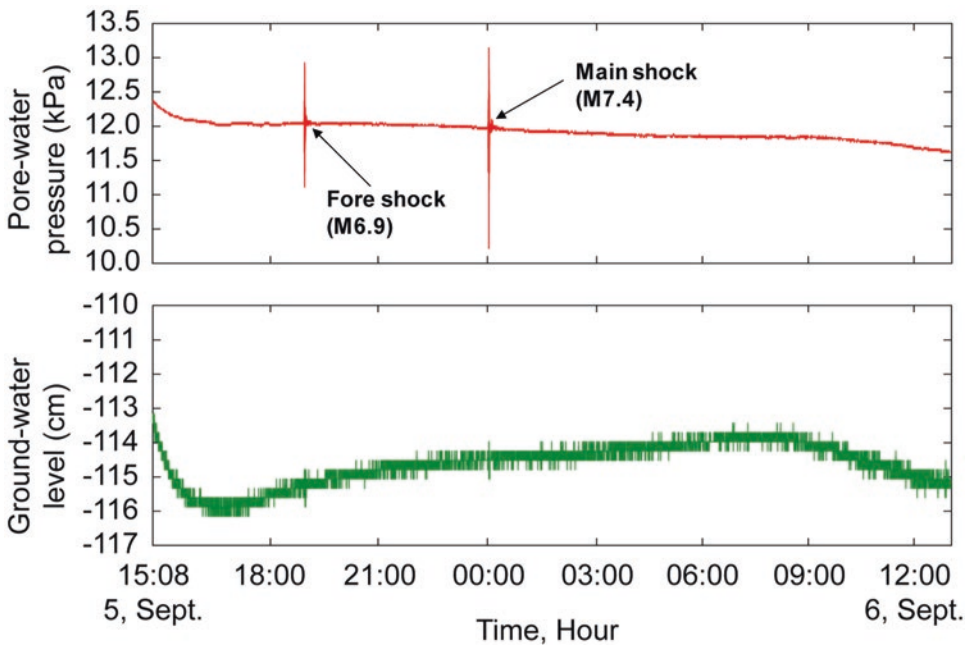

Fig. 7 Rapid changes of pore-water pressure induced by the foreshock and main shock

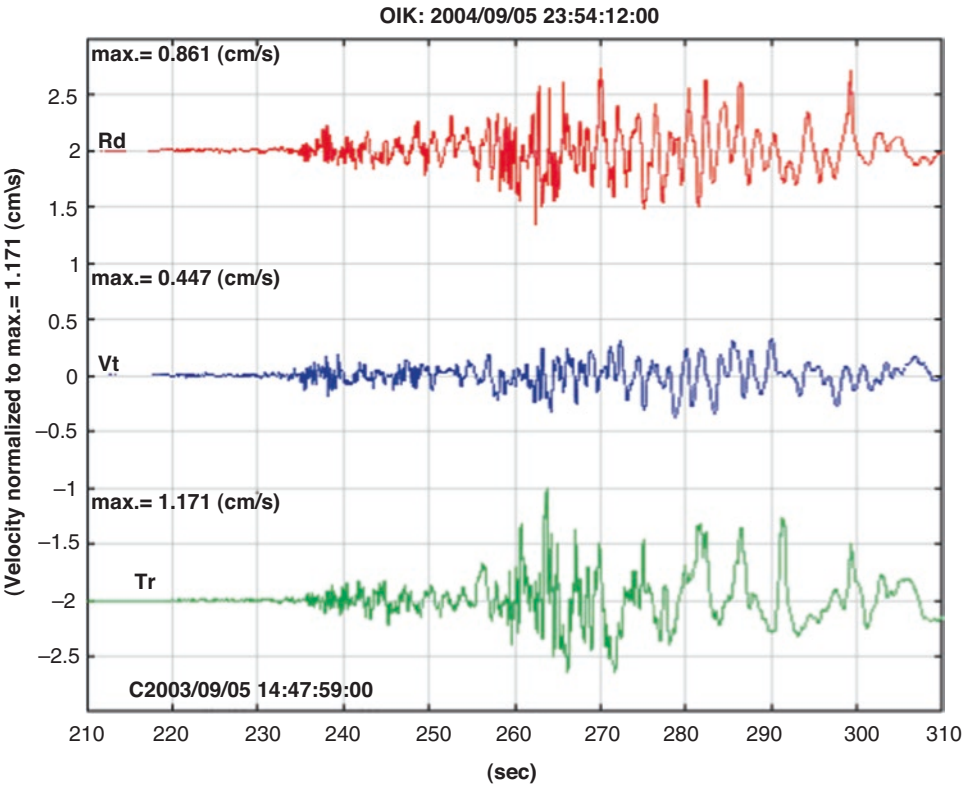

Fig. 8 Surface velocity seismograms observed at OIK during the main shock of M7.4

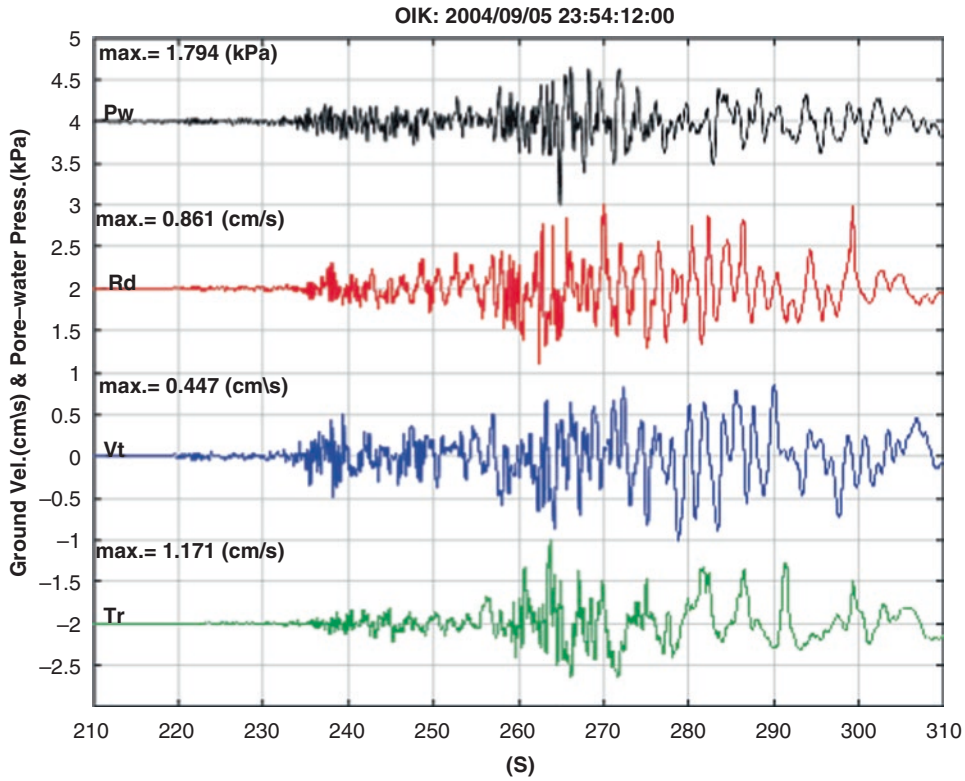

Fig. 9 Waveforms of pore-water pressure and surface velocity during the main shock of M7.4

From Roeloffs (1996)

$$P=-\frac{2GB}{3}\cdot\frac{1+\nu_u}{1-2\nu_u}\cdot e_{kk}=-BK_u e_{kk} \quad (1)$$

P: pore−water pressure, G: shear modulus, ν_u: Poisson's ratio
e_{kk}: volumetric strain, B: Skempton's coefficient, K_u: bulk modulus under undrained conditions.

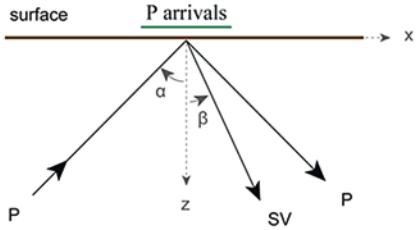

Derivation of the relationship between pore-water pressure and surface ground velocity

P arrivals $\quad \frac{z\omega}{V_P} \ll 1$ の時

$$e_{kk}(z,\omega)=-\frac{1+r_{PP}}{V_P(\sin\alpha+r_{PP}\sin\alpha+r_{PS}\cos\beta)}\cdot\left(1-i\frac{1-r_{PP}}{1+r_{PP}}\cdot\frac{\omega z\cos\alpha}{V_P}\right)\cdot\frac{\partial}{\partial t}U(z=0,\omega) \quad (2)$$

U: radial component of displacement, $\omega(=2\pi f)$: angular frequency
r_{PP} = P−wave reflection coefficient at the free surface, f: frequency
r_{PS}: P−to−SV reflection coefficient at the free surface

(1) と (2) より

$$P(z,\omega)=BK_u\cdot\frac{1+r_{PP}}{V_P(\sin\alpha+r_{PP}\sin\alpha+r_{PS}\cos\beta)}\cdot\left(1-i\frac{1-r_{PP}}{1+r_{PP}}\cdot\frac{\omega z\cos\alpha}{V_P}\right)\cdot\frac{\partial}{\partial t}U(z=0,\omega) \quad (3$$

V_P: near−surface P velocity, V_S: near−surface S velocity

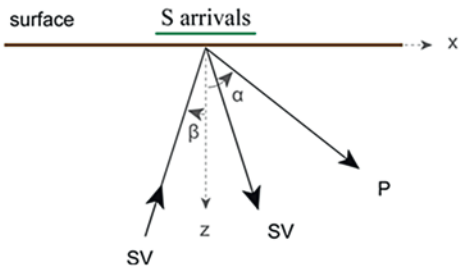

Derivation of the relationship between pore-water pressure and surface ground velocity

S arrivals $\quad \frac{z\omega}{V_P} \ll 1$ の時

$$e_{kk}(z,\omega)=-\frac{r_{PP}}{V_P(\cos\beta+r_{SS}\cos\beta+r_{SP}\sin\alpha)}\cdot\left(1+i\frac{\omega z\cos\alpha}{V_P}\right)\cdot\frac{\partial}{\partial t}U(z=0,\omega) \quad (4)$$

r_{SS}: S−wave reflection coefficient at the free surface
r_{SP}: SV−to−P reflection coefficient at the free surface

(1) と (4) より

$$P(z,\omega)=BK_u\cdot\frac{r_{SP}}{V_P(\cos\beta+r_{SS}\cos\beta+r_{SP}\sin\alpha)}\cdot\left(1+i\frac{\omega z\cos\alpha}{V_P}\right)\cdot\frac{\partial}{\partial t}U(z=0,\omega) \quad (5$$

$P(z,\omega)$ and $\frac{\partial}{\partial t}U(z=0,\omega)$: observable

Fig. 10 Derivation of the relationship between pore-water pressure and surface velocity. Upper: case of P-wave incidence. Lower: case of S-wave incidence

shown in Fig. 1, in the Wakayama Earthquake Swarm Region, most earthquakes occur at a depth of around 7 km. For this reason, felt earthquakes frequently occur in this area. Furthermore, what is characteristic of this observed waveform is that the vertical component Vt is significantly smaller than the two horizontal components Rd. and Tr. This is thought to be due to the soft surface ground of OIK.

Figure 15 shows pore-water pressure response (P) during the Mj 4.5 earthquake. As shown in Iai and Kurata (1991), it is also clear that P is composed of a step-like rising long-period component and a dominantly oscillating short-period component. In this paper, the former will be referred to as Pshear and the latter as Pcomp (P = Pshear + Pcomp). Pshear is obtained by filtering P. Pcomp is obtained by subtracting Pshear from P. The maximum value of Pshear is 0.128 kPa, and that of Pcomp is 0.992 kPa.

In order to compare the pore-water pressure waveform (P) and surface ground velocity waveforms (Rd, Vt, and Tr), they were displayed together. From Fig. 16, it can be seen that the rise time of Pshear matches that of S waves in Rd., Vt, and Tr. Figure 17 shows the separation process from total P to Pshear component. It can be seen that Pshear composed of a step-like rising long-period component is clearly different from Pcomp composed of oscillating short-period component with large amplitudes. This suggests that the cause for the generation of Pshear is different from that of Pcomp.

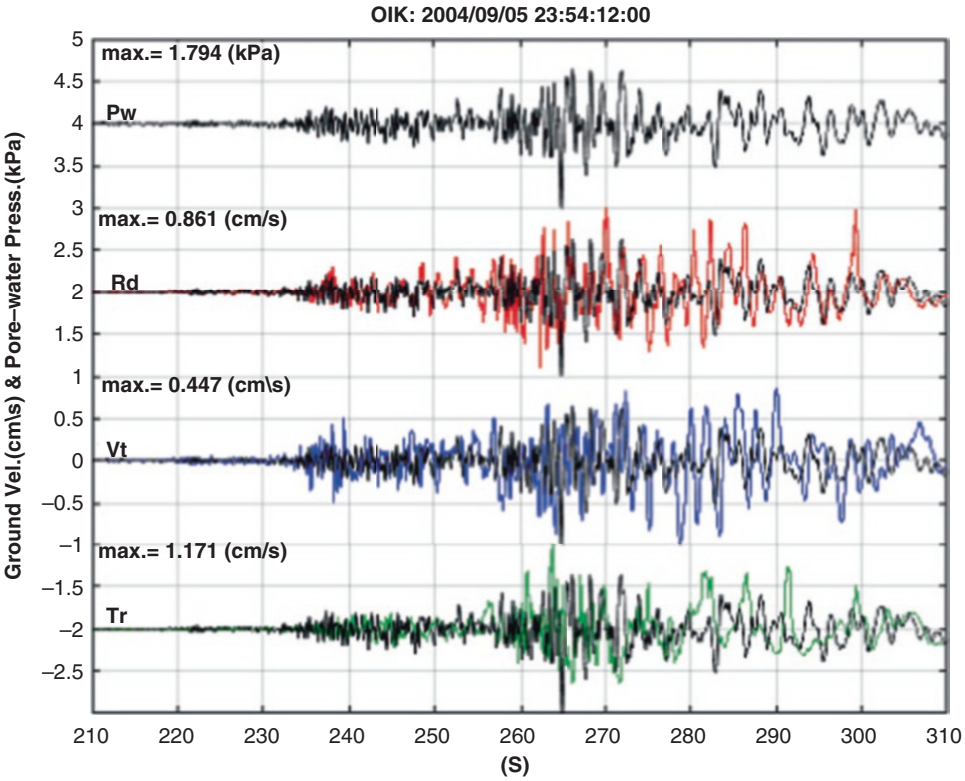

Fig. 11 Pore-water pressure waveform (Pw) superimposed on surface velocity waveform (Rd, Vt, and Tr)

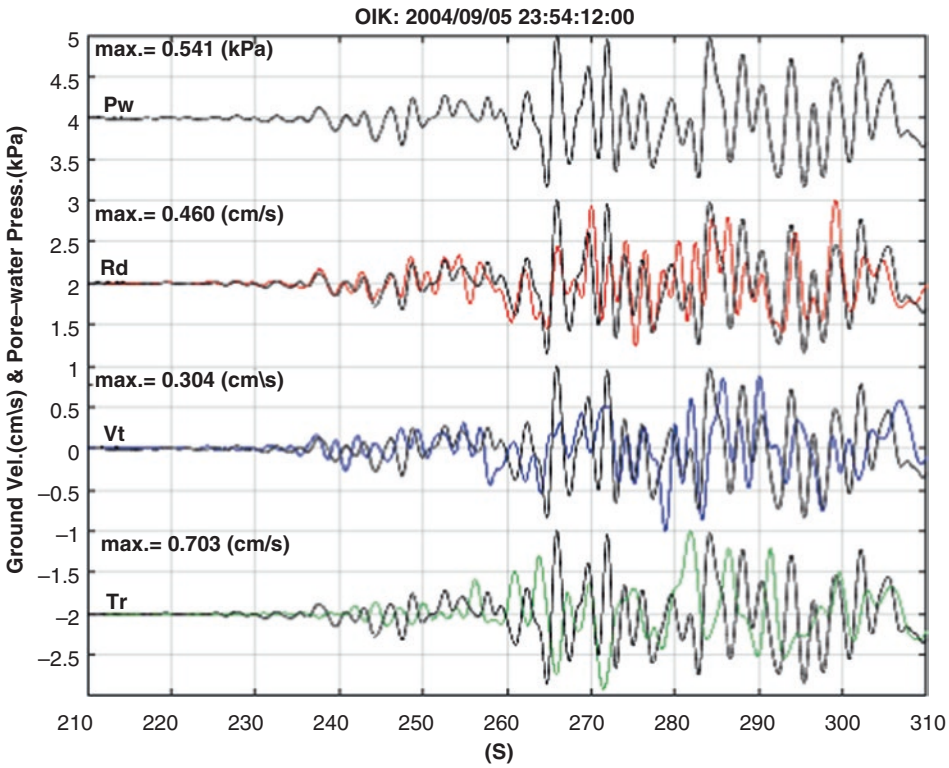

Fig. 12 Pore-water pressure waveform (Pw) superimposed on surface velocity waveform (Rd, Vt, and Tr). Case of bandpass filtered waveforms (fc = 1/2 Hz)

Pcomp is dynamic water pressure caused by vibration of pore-water pressure transducer exited by ground motion. Therefore, Pcomp depends on the installation direction of the pore-water pressure transducer.

In order to investigate the rising time of Pshear, its waveform is superimposed on those of surface ground motion. As seen in Fig. 18, the rising time of Pshear matches S-wave rising time in the three components,

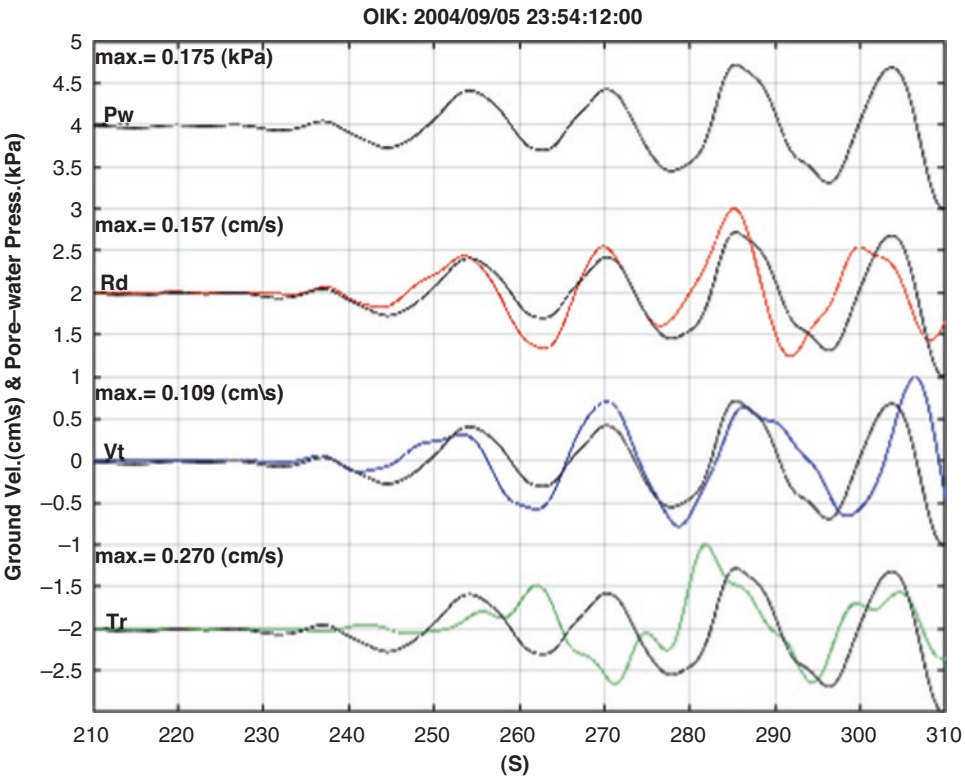

Fig. 13 Pore-water pressure waveform (Pw) superimposed on surface velocity waveform (Rd, Vt, and Tr). Case of bandpass filtered waveforms (fc = 1/2 Hz)

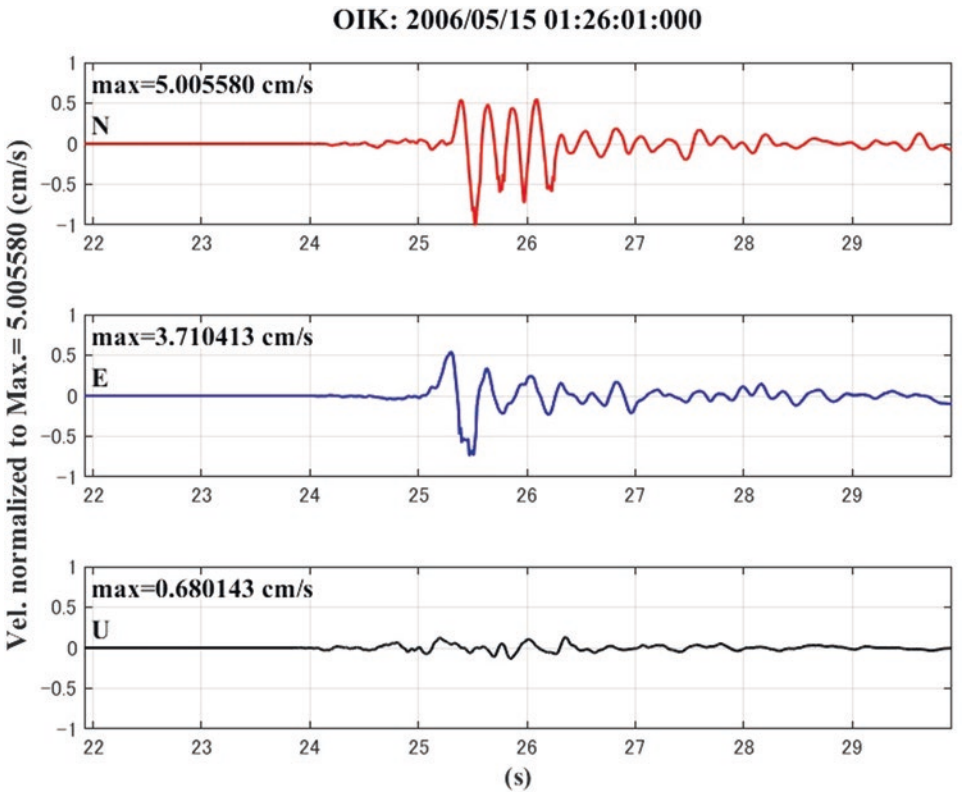

Fig. 14 Surface velocity waveforms during the Mj 4.5 earthquake that occurred on May 15, 2006. The hypocenter is in the northern part of Wakayama city, at a depth of 3 km

Rd., Vt, and Tr. The rising time of Pshear agrees well with that of Tr. Therefore, it is thought that shear S waves, that is, SH waves contribute to the generation of Pshear.

Next, to investigate the relationship between Pcomp and surface ground motion, Pcomp is superimposed on the three surface velocity waveforms (Rd, Vt, and Tr). To examine in more detail, Pcomp and the three velocity

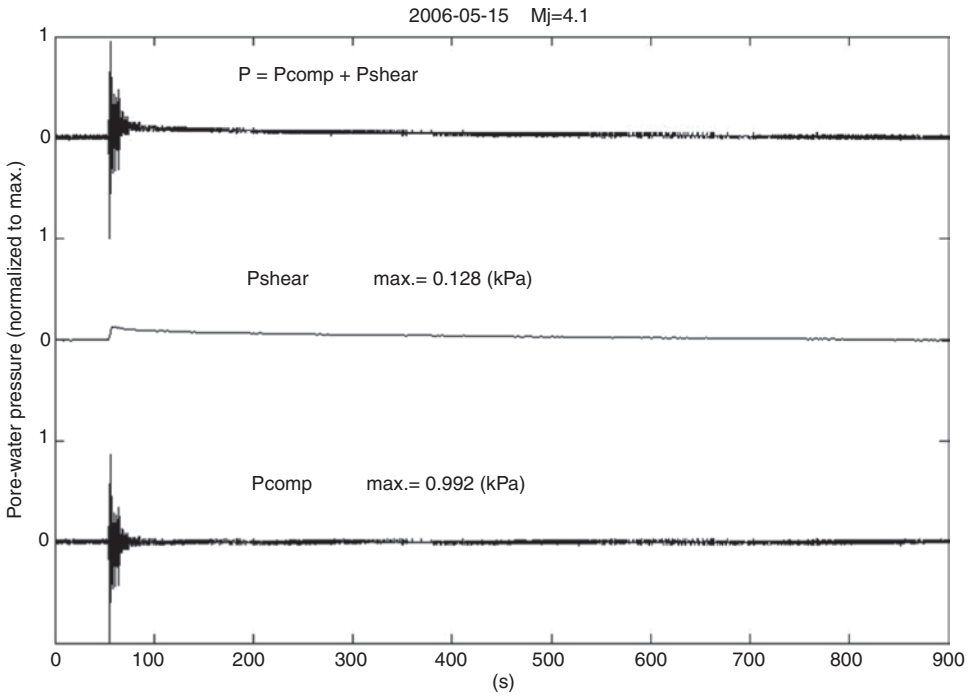

Fig. 15 Response of pore-water pressure (P) during the Mj 4.5 earthquake. P contains a step-like rising long-period component. P is decomposed as P = Pcomp + Pshear

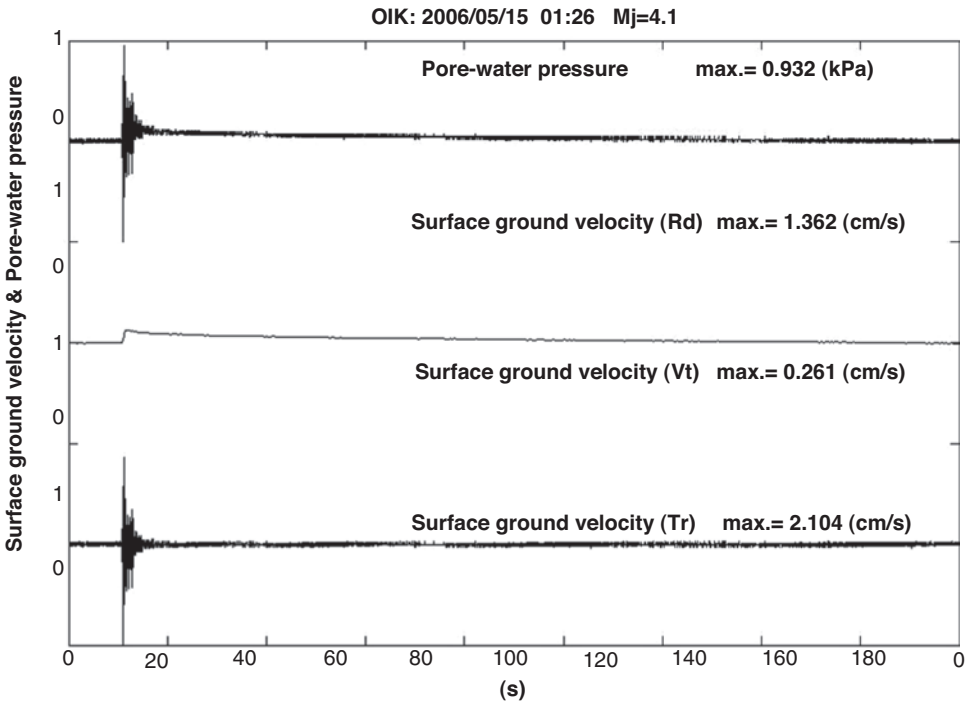

Fig. 16 Pore-water pressure along with surface velocity during the Mj4.5 earthquake

waveforms (Rd, Vt, and Tr) were passed through a band-pass filter with a center frequency (fc). Figure 19 shows the case where fc is 1/8 Hz. This figure shows that the waveform of Pcomp matches those of Rd. and Vt, and also its rise nearly matches those of Rd. and Vt. However, one phase at the time of rising of Pcomp is not consistent with that of Rd. This is because Pshear rose at that time and Pcomp was disturbed by Pshear. On the other hand, the waveform of Pcomp does not quite match that of the Tr component of the surface ground velocity. In this way, the relation of Pcomp $\propto$ Rd. was confirmed. Furthermore, it was found that Pcomp was generated by the incidence of P or SV waves on surface ground, and Pshear by the incidence of strong SH waves.

In Fig. 20, the observed waveform of ground motion is displayed at the normal display magnification of 1x. If a

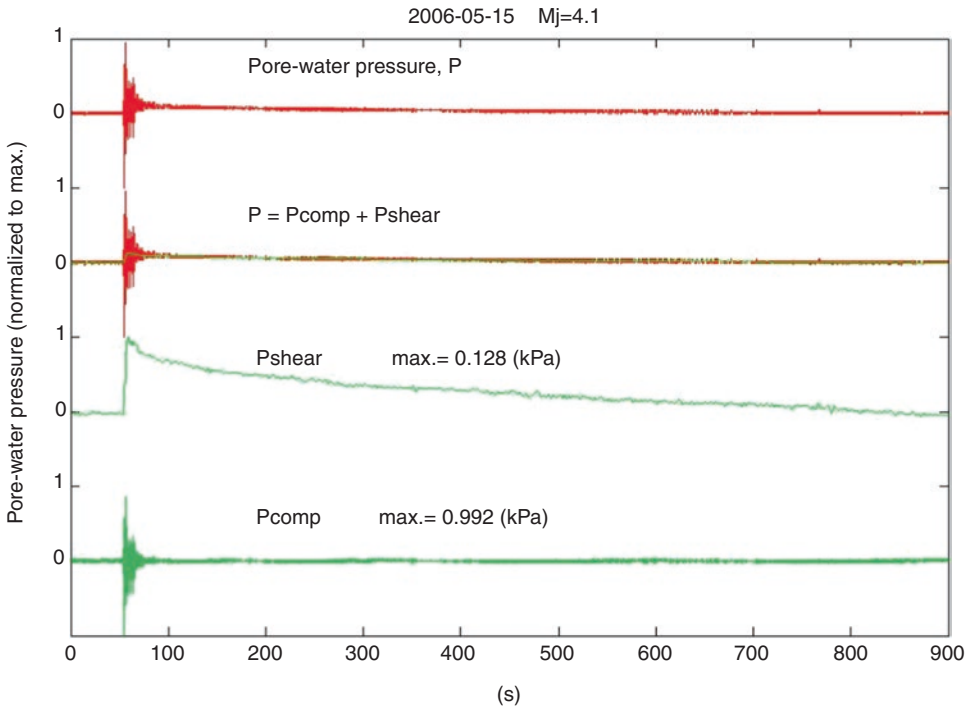

Fig. 17 Extraction of Pshear from P. Pshear is obtained by filtering P

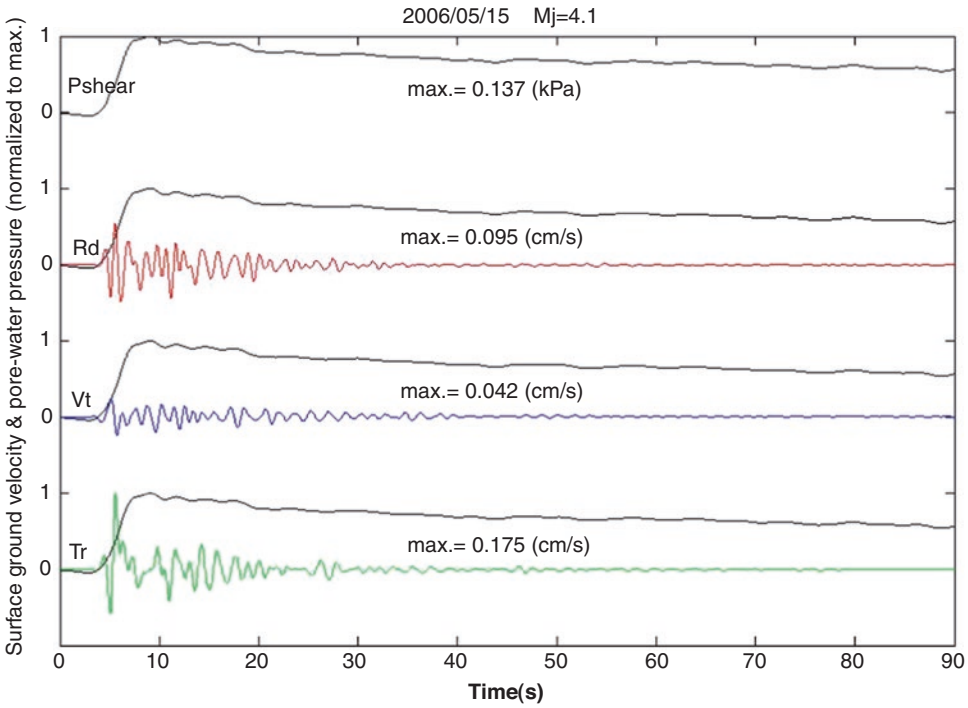

Fig. 18 Pshear superimposed on surface velocity waveform (Rd, Vt, and Tr). Case of bandpass filtered waveforms (fc = 1/2 Hz)

very small long-period component is hidden behind a dominantly oscillating short-period component with a large amplitude, the long-period component cannot be confirmed visually at the usual display magnification of 1×. The black line of Fig. 21 shows the waveform of the ground motion magnified 500 times and the red line shows waveforms smoothed by a time window with a width of 3 s. Fig. 22 shows a transient long-period waveform extracted in this way. Thus, ground motion observed at OIK during the Mj 4.5 earthquake contains long-period pulses, although they are hidden behind short-period components with large amplitudes. Since the period of the pulse are clearly exceeding the flat characteristic frequency range of the seismometer, the observed ground motion is not different from true ground motion at OIK. We need correct from the observed ground motion to true ground motion to examine the cause

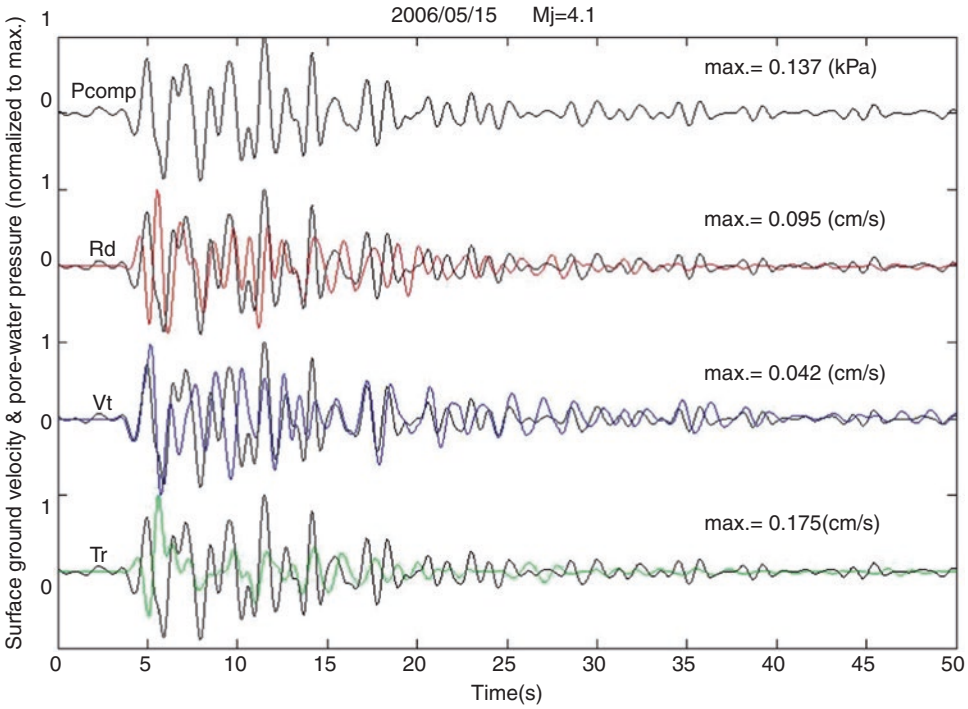

Fig. 19 Pcomp superimposed on surface velocity waveform (Rd, Vt, and Tr). Case of bandpass filtered waveforms (fc = 1/2 Hz)

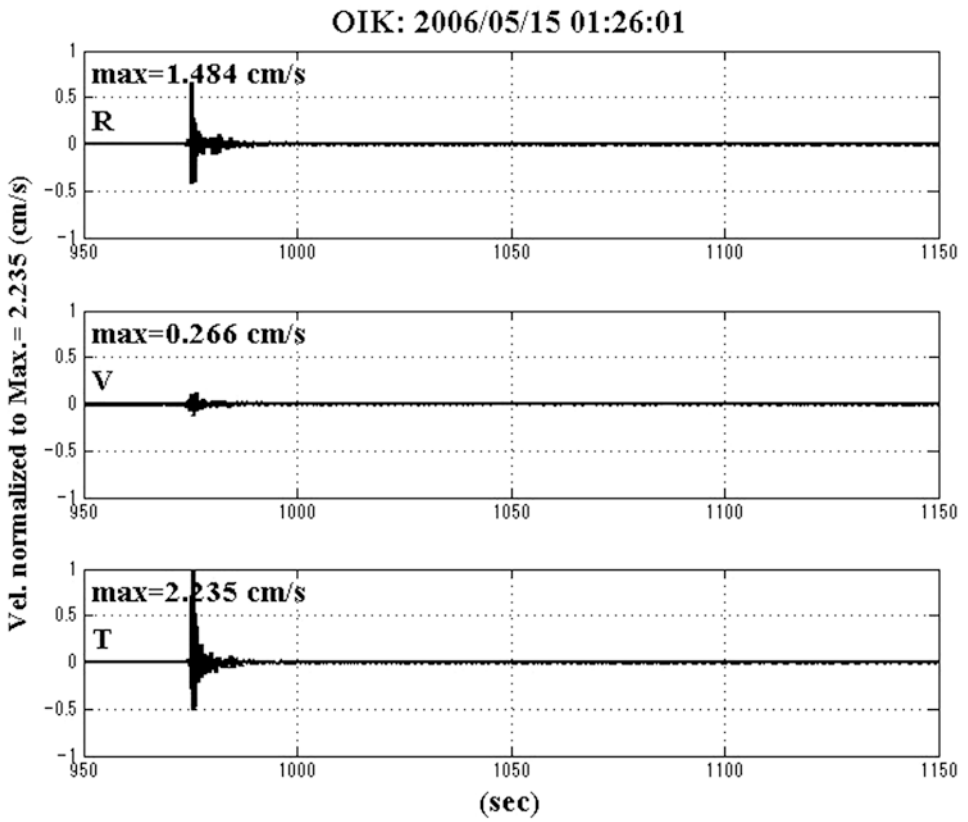

Fig. 20 Waveforms of surface velocity observed

of the long-period pulse generation. To do this, we need a transfer function of the seismometer.

Details of internal electronics of the seismometer were made public by the manufacturer for only the two horizontal components of the servo-type velocity seismometer. The seismometer has a flat amplitude response in the frequency range from 0.1 Hz to 70 Hz, as shown in the Fig. 5b. Using these data, the transfer function of the seismometer was

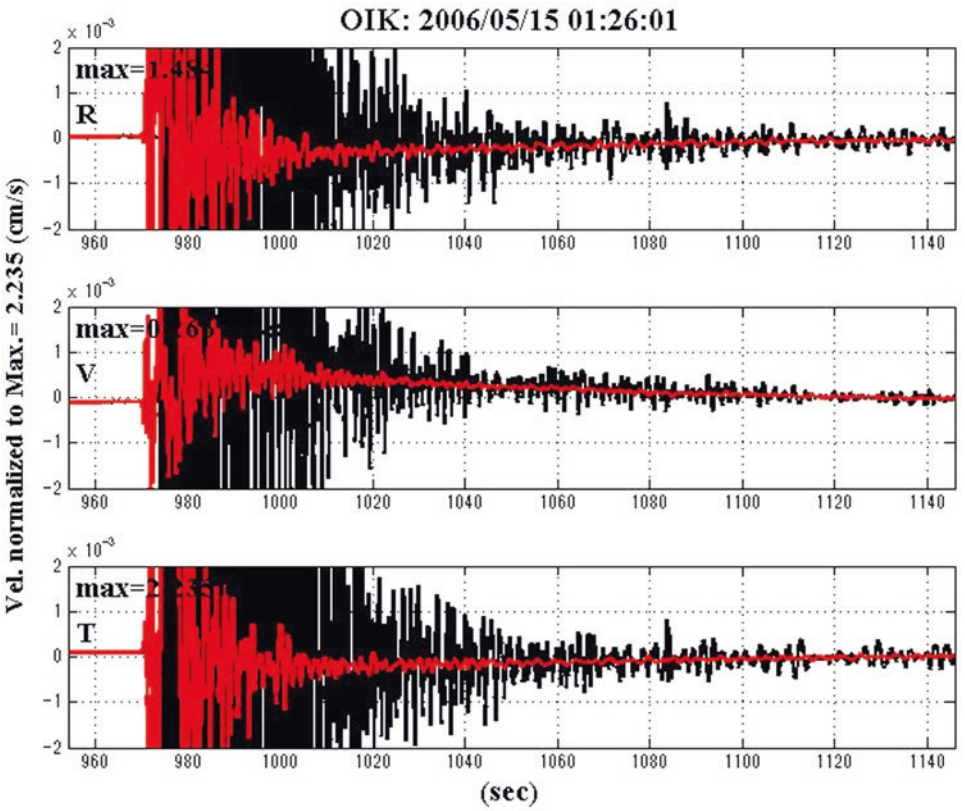

Fig. 21 Black line: waveforms magnified 50×. Red line: waveforms smoothed by time window with a width of 3 s

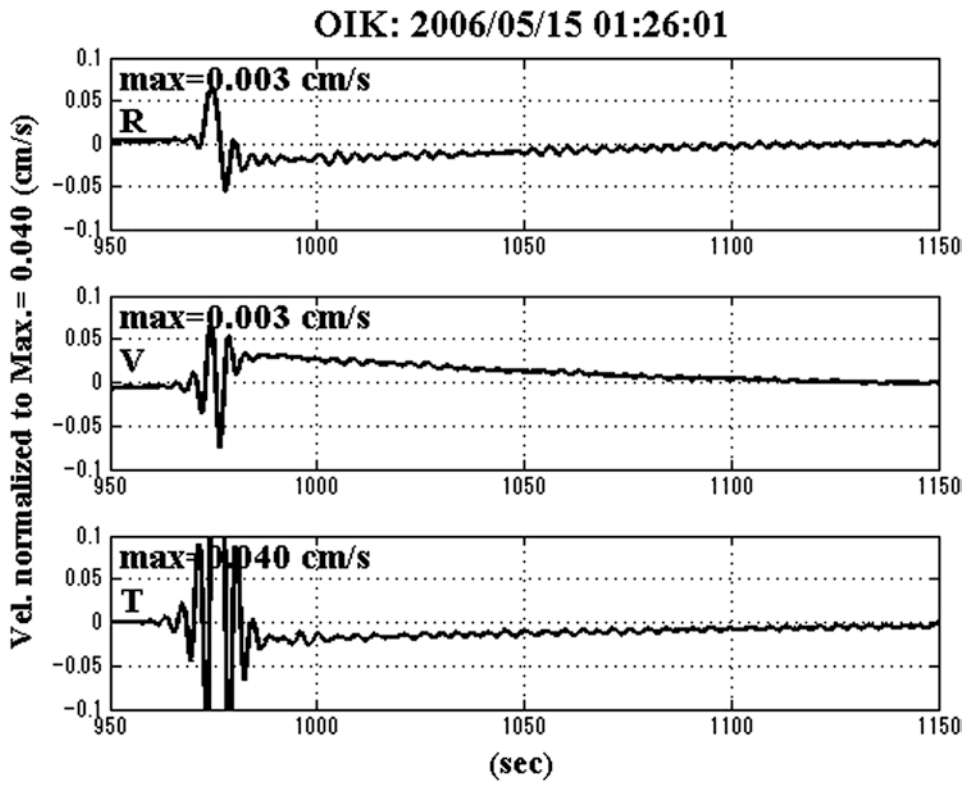

Fig. 22 Long-period component extracted by smoothing

calculated. When Xn is input to the seismometer, the output Yn from the seismometer is expressed as follows using the fifth-order recurrence formula.

$$Y_n = \sum B_i x\, X_{n-i} - \sum A_i x\, Y_{n-i} \mathrm{Y} \qquad (1)$$

Conversely, the input X_n can be calculated from the output Y_n using the following formula.

$$X_n = \left[Y_n + \sum A_i x\, Y_{n-i} - \sum B_i x\, X_{n-i} \right] \qquad (2)$$

A detailed explanation of the coefficients A and B is omitted in the present paper.

We corrected the observed ground motion (Fig. 23) to the true ground motion (black line of Fig. 24) using Eq. (2). As seen in Fig. 24, after oscillating short-period components, the corrected velocity waveform increases linearly in the negative direction for the NS component, and in the positive direction for the EW component. Such a monotonous increase (or decrease) of ground velocity is puzzling. However, since the seismometer is a velocity type, such a phenomenon occurs when a certain acceleration is applied to the seismometer. It is thought that a constant acceleration is applied to the seismometer.

We investigate the observed and corrected ground velocity when a certain acceleration is applied to the velocity-type seismometer. The most likely cause of the constant acceleration added to the seismometer is ground tilting motion. As shown in Fig. 25a, here, it is assumed that the tilting motion is represented by a step function with a rise time. The height of the step function is an acceleration applied to the seismometer by ground tilting motion. It is assumed that the ground tilting progresses gradually, and the progress velocity is taken into consideration by the rise time. From examination for cases where the rise time was 1, 2, 4, 8 and 16 s, it was found that the case of 1 s showed good agreement. Therefore, the rise time of 1 s was used in this study.

Figure 25a shows a step-like acceleration applied to the seismometer when the ground tilts. Figure 25b shows velocity waveform calculated from the acceleration applied to the seismometer. This velocity waveform is input into the seismometer. Figure 25c shows velocity waveform observed (output) by seismometer. As seen in this figure, the waveform is a smooth long-period pulse as in Fig. 22. This indicates that the narrowband frequency characteristic of the seismometer transforms a linearly increasing or decreasing

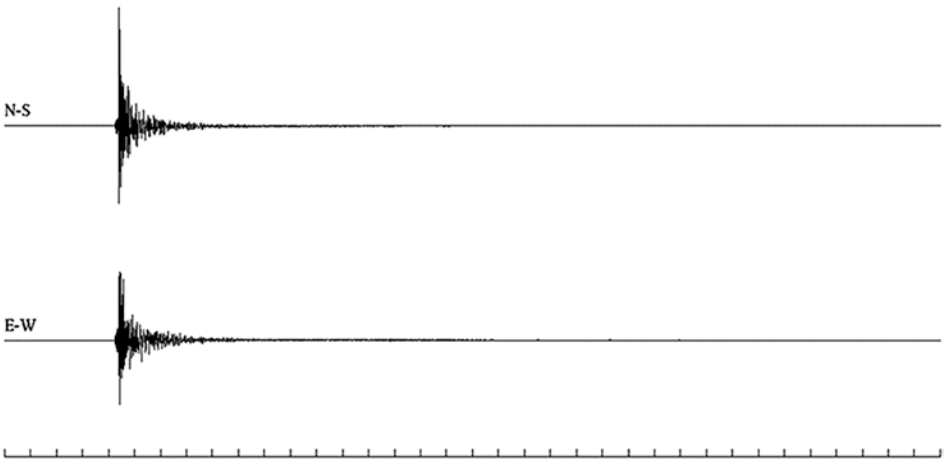

Fig. 23 Surface velocity waveform output from seismometer

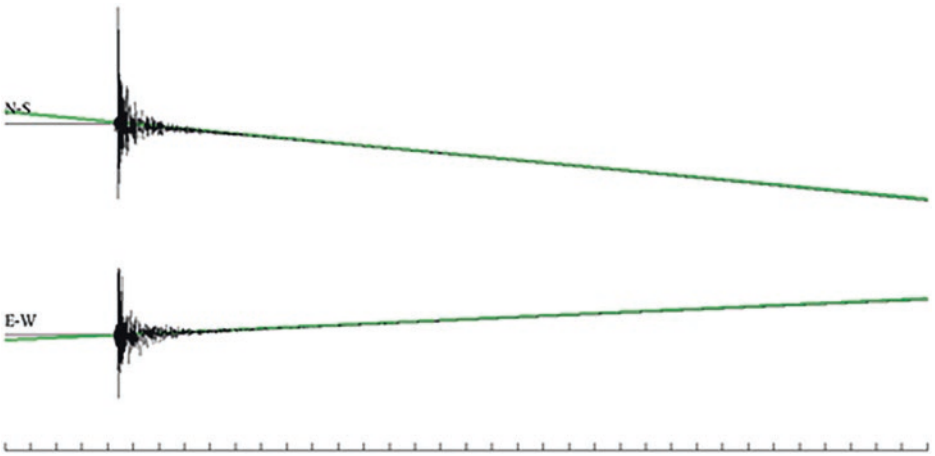

Fig. 24 Black line: waveform of actual surface velocity corrected by Eq. 2. Green line: straight line that best fits the black line (corrected waveform)

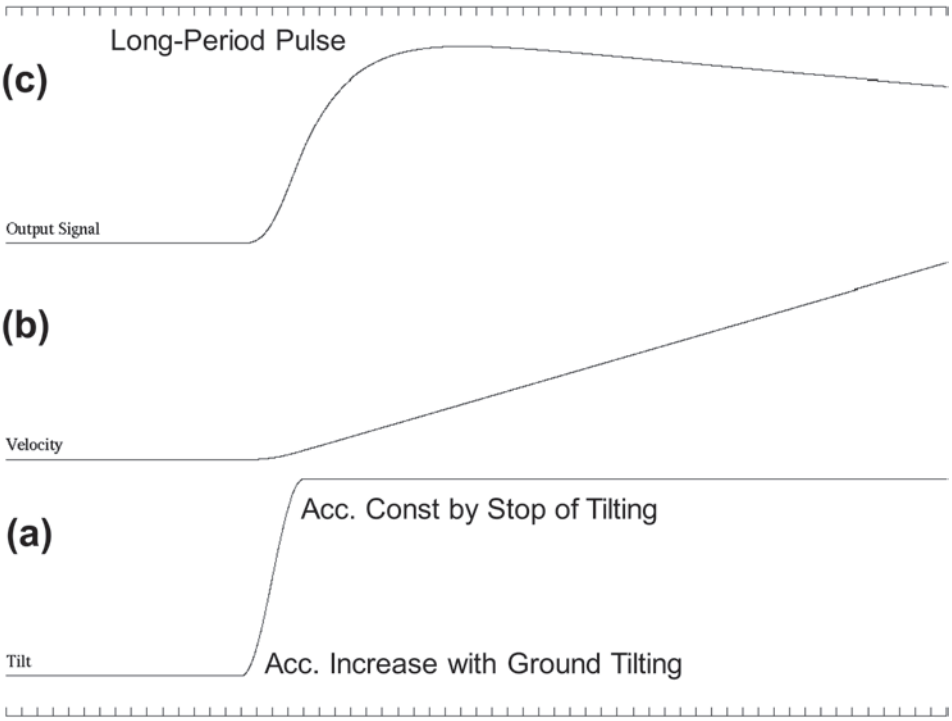

Fig. 25 Generation process of long-period pulse waves observed. (**a**) Step-like acceleration applied to seismometer. (**b**) Velocity obtained by integrating acceleration (**a**). (**c**) Output signal from seismometer. It is obtained by inputting (**b**) into Eq. (1)

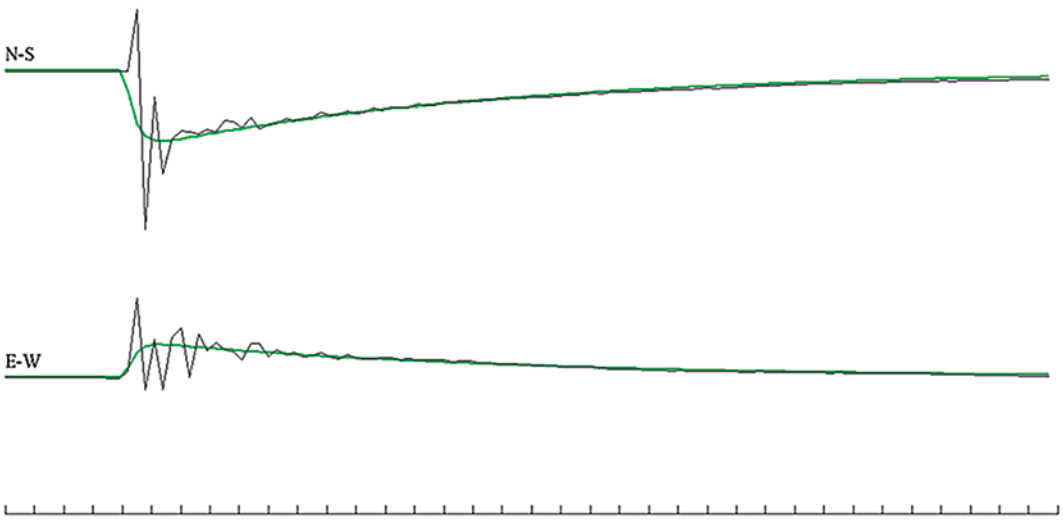

Fig. 26 Comparison of observed waves and theoretically calculated waves. Black line: by smoothing output wave from seismometer. Green line: by theoretical calculation based on ground tilting motion. The two are in good agreement

velocity wave into a pulse wave consisting of smooth long-period component.

Next, we estimated the acceleration applied to the seismometer using long-period pulse waves. Figure 26 shows the observed long-period pulse waves (black line) and the theoretically calculated waves (green line). The observed pulse wave is obtained by smoothing the originally observed wave using a time window with a width of 3 s. The theoretical wave is obtained as follows. As shown in Fig. 24, first, the acceleration (Acc) applied to the seismometer by ground tilting is determined from the slope of a green straight line fitted to a corrected velocity waveform monotonically increasing (or decreasing) with time (black line in Fig. 24). Next, a step function (height Acc, rise time 1 second) representing the acceleration applied to the seismometer is created. A theoretical velocity waveform input into the seismometer is obtained by integrating this acceleration step function. By inputting this theoretical waveform into Eq. (1), we obtain a

Table 1 Accelerations applied to seismometers, tilt of ground, and direction estimated

Eq.	E-W(m/s/s)	NS(m/s/s)	Direction(deg.)	Tilt(deg.)
2006/5/15 01:42 Mj4.5	1.4×10^{-7}	-1.0×10^{-6}	−8	5.9×10^{-6}

theoretical long-period pulse wave (green line in Fig. 26). The theoretical waves agree very well with the observed waves.

We calculated the amount of ground inclination from the inclination of the horizontal two components of seismometers. The ground tilting motion was assumed to be a step-like function with a rise time. We considered cases where the rise time was 1, 2, 4, 8, and 16 s. The case of 1 s showed a good agreement between the observed and theoretical long-period pulse waveforms. Table 1 lists accelerations applied to the two horizontal components of seismometer, the permanent tilt of tilting motion, and its direction.

4 Discussion

Iai and Kurata (1991) observed in-situ excess pore-water pressures and ground motions during the 1987 Chiba-Toho-Oki Earthquake of magnitude 6.7. The observed excess pore-water pressure record contained a smoothly rising long-period component with an amplitude of about 40 cm in water head and a dominantly oscillating short-period component. From a comparison of the short-period component waveform and the acceleration waveform observed in the ground, it was determined that this short-period component was dynamic water pressure caused by the vibration of the pore-water pressure transducer and the short-period component was separated by smoothing. Using these extracted long-period components, they conducted an earthquake response analysis that considered the rise in excess pore-water pressure and the nonlinearity of the ground.

Kamai (2011) conducted observations of seismic ground motion and pore-water pressure in valley fill in the southwestern Tokyo region from 2005 to 2011. The non-linear response of excess pore-water pressure in valley hill was observed during the 2005 Chibaken-Hokuseibu Earthquake of magnitude 6.0. After the arrival of the S-wave main motion, an asymmetrical rapid increase of about 0.75 kPa was observed. During the 2005 Miyagi Earthquake of magnitude 7.2, no nonlinear response of the pore-water pressure was observed. However, it has been reported that while the seismic ground motion ended in about 30 s, the pore-water pressure oscillations continued for 280 s, which is about 10 times longer. This kind of long-lasting pore-water pressure response has not been previously reported, even in the observations by Iai and Kurata (1991) and could not be confirmed in our observations, so this is an interesting report.

Although those observations succeeded in observing the nonlinear response of excess pore-water pressure, which is indicative of ground deformation during earthquakes, they did not precisely analyze ground acceleration records. Since seismic ground motion is also affected by ground deformation, it is necessary to perform a more precise analysis of observed ground motion. Our observation detected the very weak long-period pulse-like wave with an amplitude of 0.003 cm/s from surface ground motion record. Assuming that the long-period pulse was generated by ground tilting motion, the tilt of ground and its direction were estimated. An interesting result is that the direction of the estimated ground tilting motion closely corresponds to valley axis. However, ground deformation could not be confirmed through visual observation.

5 Conclusions

The principal conclusions of this study can be summarized as follows.

1. In-situ continuous observation of seismic ground motion, pore-water pressure, and ground-water level was performed at LVF in Wakayama city, southwest Japan. Simultaneous observation records during several small- to medium-sized earthquakes were obtained. Excess pore-water pressure was clearly observed during the medium-sized earthquake with magnitude Mj 4.5.
2. From comparison of Rd. (radial component of surface velocity) and pore-water pressure (Pw or Pcomp) during earthquakes, the waveform of Pw well agrees with that of Rd. (Pw $\propto$ Rd), indicating that Pw is generated by the incidence of P or SV waves on ground surface.
3. The observed excess pore-water pressure (P) can be decomposed into a step-like rising long-period component (Pshear) and a dominantly oscillating short-period component (Pcomp). Pcomp is the same as Pw in 1 mentioned above. The rising time of Pshear nearly agrees with that of Tr (transverse component of surface velocity), suggesting that shear S waves, that is, SH waves contribute to the generation of Pshear.
4. Seismograms of surface velocity observed at OIK during the Mj 4.5 earthquake contained long-period pulses, although they were hidden behind dominantly oscillating short-period components with large amplitudes.
5. The process of generating a long-period pulse-like signal is as follows. When the ground tilts with generation of

excess pore-water pressure, the acceleration change due to the ground tilting motion is added to the seismometer. The wave converted (integrated) from the added step-like acceleration to linear velocity with a constant slope is input to the seismometer. The seismometer outputs the wave filtered by its own transfer function. The long-period pulse-like wave is observed in this way.

6. Based on the generation model of a long-period pulse wave, accelerations applied to the two horizontal components of seismometer, the direction of ground tilting motion, the permanent tilt of ground tilting motion, and its direction are estimated as 1.4×10^{-7} (m/s/s), -1.0×10^{-6} (m/s/s), -8 (degree), 5.9×10^{-6} (degree), respectively
7. An interesting result is that the direction of the estimated ground tilting motion approximately corresponds to the line of the valley, although visual observation could not confirm ground deformation.

Acknowledgments The authors would like to express their sincerest gratitude to Takayuki Go for valuable discussion and helpful observations on strong ground motions and pore-water pressures in Wakayama.

References

Iai S, Kurata E (1991) Pore-water pressures and ground motions measured during the 1987 Chiba-Toho-Oki Earthquake. Technical Note of the Port and Harbour Research Institute, Ministry of Transport, Japan, No.718:1-19

Ishihara K, Anazawa Y, Kuwano J (1987) Pore-water pressures and ground motions monitored during the 1985 Chiba-Ibaragi earthquake. Soils Found 27(3):13–30

Ishihara K, Muroi T, Towhata I (1989) In-situ pore-water pressures and ground motions during the 1987 Chiba-Toho-Oki earthquake. Soils Found 29(4):75–90

Kamai T (2011) Seismic response of valley fills to strong earthquakes on residential region in Tokyo. J Jpn Landslide Soc 48(6):334–343

Roeloffs E (1996) Poroelastic techniques in the study of earthquake-related hydrologic phenomena. Adv Geophys 37:135–195

Global Warming May Accelerate Submarine Landslides in the Oceans -Possible Disaster Chain Reactions-

Hiroshi Kitazato

Abstract

Climate changes give affection to both atmosphere and hydrosphere. It is appeared in the form of rising both air and water temperatures on the Earth. The climate change introduces vigorous meteorological disasters in the world, such as super storms, heavy rain precipitations along linear rain belts, tornadoes and others on lands. Oceanic environments also should be affected from the climate changes. I try to figure out possible submarine hazards that may be increased in correlate to climate changes. The hazardous event may take place in the shape of disaster chain reactions as cascades.

Keywords

Global warming · Climate changes · Submarine landslides · Biogeochemical cycles · OMZ

1 Introduction

Climate changes take place in connection to air and water temperatures, carbon dioxide gas concentrations, humidity and other components on the Earth. IPCC report no. 5 (2013) made a couple of computer simulations. The simulated highest atmospheric temperature is going to increase 5.7 °C at the end of the twenty-first Century. Certainly, average temperature during 2011 to 2020 increased 1.09 °C in comparison to 1850~1900 according to IPCC no. 6 report (IPCC 2021). The climate change has certainly introduced vigorous meteorological disasters in the world, such as super storms, heavy rain precipitations along linear rain belt, tornadoes and others on lands. Oceanic environments should be affected from the climate changes.

Disastrous events have increased year by year in these decades. Interdisciplinary geo-scientists in ICSU (present ISC)-GeoUnions overviewed number of catastrophic events since 1980 up to 2015 (Cutter et al. 2015). They found that the number of disasters caused by natural events increased more than doubled since 1980 (Fig. 1). Among these, geophysical disasters, that are represented by earthquakes, tsunamis, and volcanic eruptions, were approximately doubled. In contrast, climatological, hydrological and meteorological disasters were tripled or more. This means that anthropogenic activities on Earth strongly change Earth's environmental conditions.

One of typical meteorological disasters is landslides at hilly areas. We should remember heavy rains- induced slope failures at Hiroshima Prefecture in 2018 and vigorous debris flows at Atami City, Shizuoka Prefecture 2021 and others.

H. Kitazato (✉)
Department of Earth Sciences, Faculty of Education and Integrated Arts and Sciences, Waseda University, Tokyo, Japan

Department of Marine Environmental Sciences, Tokyo University of Marine Science and Technology (TUMSAT), Tokyo, Japan

Danish Center for Hadal Research, Satellite office at TUMSAT, Odense, Denmark

B. Abolmasov et al. (eds.), *Progress in Landslide Research and Technology, Volume 3 Issue 1, 2024*, Progress in Landslide Research and Technology, https://doi.org/10.1007/978-3-031-55120-8_4

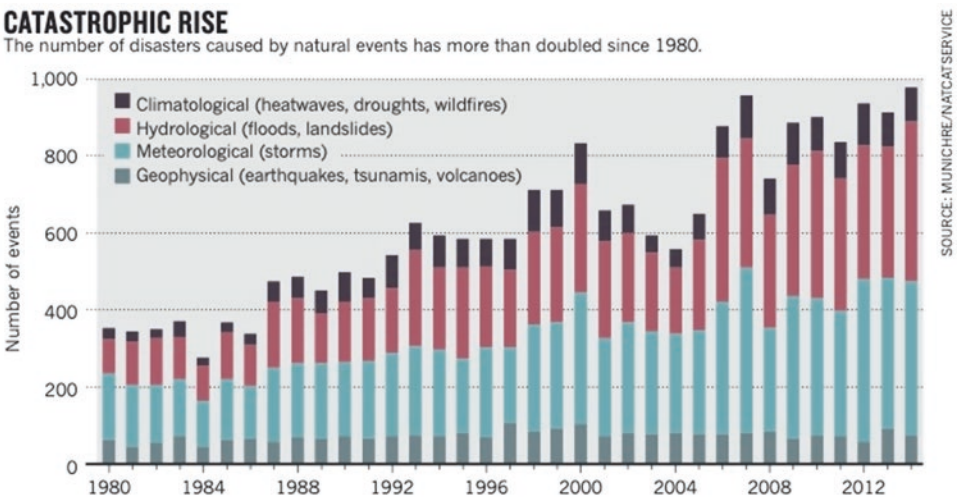

Fig. 1 The number of hazards caused by natural events. Natural disasters have taken place more than doubled since 1980 up to 2015. Climate Change events are three or four times more than geophysical disasters during 35 years interval (Cutter et al. 2015). © Springer-Nature CoLtd Source: Munichre/Natcatservice

2 Disaster Chain Reactions

Hazardous events have been increased rapidly, in these decades. Many of hazards are not occurred in a single factor but multiple factors, including anthropogenic activities either directly or indirectly in natural disaster. Artificial changes of lands sometimes cause of landslides and succeeding debris flows. Vigorous debris flow disasters at Aizome River, Atami City is a typical case of anthropogenic reasons where mass of artificial mounds were piled at the upstream area of the river. The artificial mound collapsed after heavy rains. We had been released a couple of policy briefs for reducing anthropogenic disaster risks (ISC_GU_SC_DRR, Policy Brief #05, 2021 and #06, 2022).

 Editor 1 et al. (eds), Progress in Landslide Research and Technology, Volume 1 Issue 1, 2022, Book Series of the International Consortium on Landslides. DOI 10.1007/978-94-007-2162-3_36.

3 Gas Hydrate May Introduce Submarine Landslide

As one of typical multiple hazards, we focus in gas hydrates. There are gas hydrates bearing strata at sea floor. Unstable gas hydrate should be produced submarine landslides.

Gas hydrate stability is decided with both hydraulic pressure and water temperature of the sea. Unstable conditions of strata may start around 1000 m in water depth. Stability of sedimentary bodies are developed slope basins, in particular deep in the sea.

Figure 2 shows physic-chemical model for gas hydrates bearing sea floors. Above 1000 m deep in seas, sediments that are bearing gas hydrates are unstable due to melting hydrates. When gas hydrates liquidize, sedimentary bodies may become unstable conditions. This liquefaction of hydrates from solid to gaseous conditions introduces unstable slope conditions and then slope destructions may take place.

Figure 3 shows global distribution map of the gas hydrate stability zone. Referring from Fig. 4, gas hydrate accumulates thickly in the permafrost areas both at Arctic and Antarctic regions. In contrast, gas hydrates are distributed along continental slope areas of both temperate to tropical area of the seas. Continental shelf to slope areas, slope failures may take place as gravity flows. Two triggers of slope failures may take place. The one is non-tectonic landslides, and the other is Earthquake-induced landslides. "Non-tectonic" means the cause that is not induced by the Earthquake shakes.

When water temperatures both in seas and lakes rise due to climate changes, it may introduce unstable sedimentary slopes where are bearing gas hydrates. Slope instabilities progress in connection to global climate changes even at sea floors. If heavy Earthquake takes place at unstable slope areas in the sea, it may also be induced tectonic landslides at sea floor and may generate Tsunami events.

Another possible cause of landslides is "artificial" changes of ground surfaces due to the anthropogenic activities. Recent years, artificial changes of the Earth's surface are frequently taken place at everywhere in the world. They should be the cause of unstable environment. They should introduce landslides and/or debris flows after heavy rain precipitations or Earthquake shakings.

As shown above, series of natural and anthropogenic hazards should cause big debris flows or landslides. Finally, it may generate anthropogenic disasters.

Disastrous events are not occurred by a single reason. Disaster chain reactions may be occurred by various causes

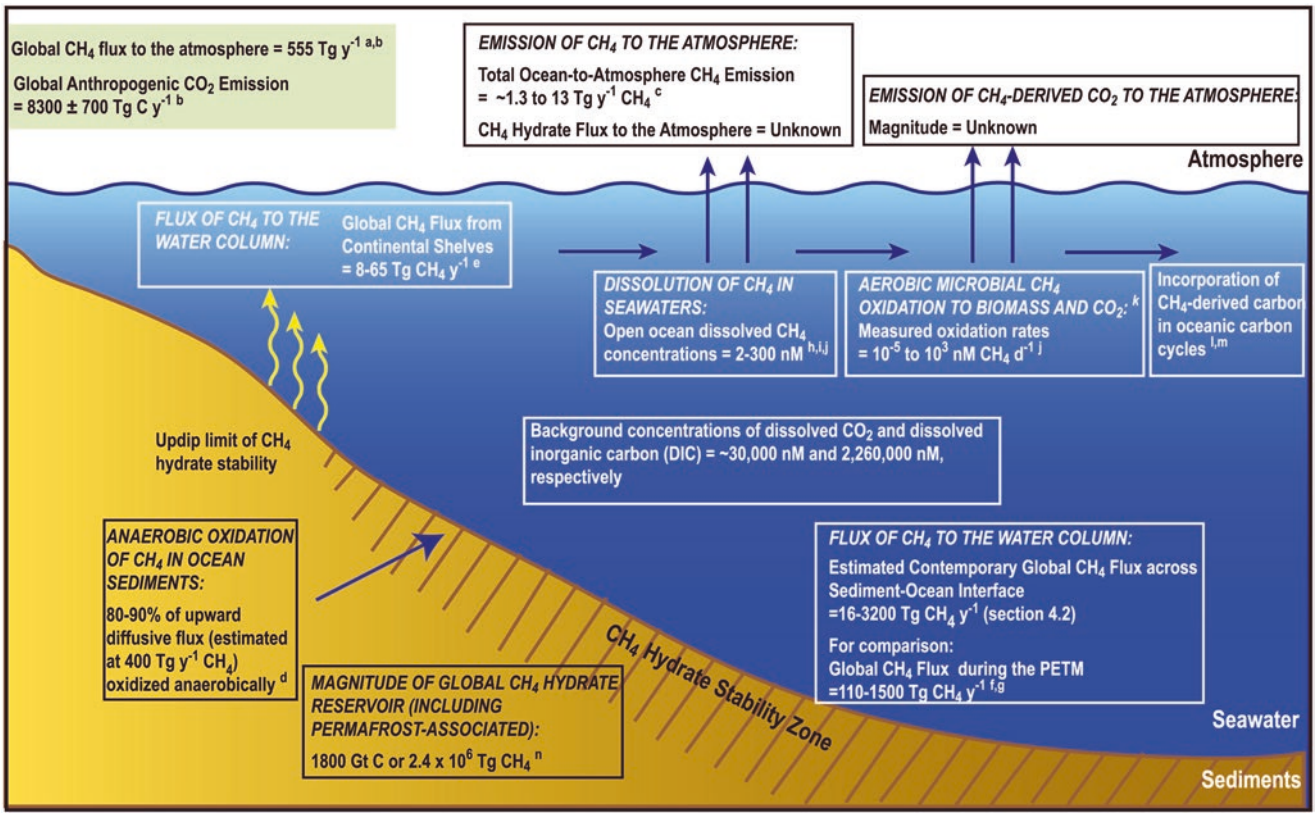

Fig. 2 Gas hydrate stability zone at continental margin areas (Ruppel and Kessler 2016)

as follows. It is well known that global warming raises up atmospheric temperatures. It introduces increase of atmospheric humidity's according to increase of evaporation amount from the Earth's surface, in particular to oceanic surface. These reactions take place around the world mostly at the same time. These phenomena should induce heavy rain precipitations and further introduces high water contents of soils and basement rocks. Series of natural responses should be triggers for landslides or debris flows at different shapes not only at terrestrial realms, but also at oceanic realms and or big lake regions.

4 Case Studies of Landslides in Connection to the Global Warnings

We can show a couple of case studies in connection to climate changes globally. Slope failures and succeeding big Tsunamis took place at the Storegga slope basins off.

Norway, 5000 years before. Tsunami deposits are widely distributed in the areas of both Norway and northern part of Great Britain Islands (Dawson et al. 2020). The Storegga region is well-known area where gas-hydrates bearing sediments distributed in slopes. It is probable to occur submarine landslide due to slope instabilities by the melting of gas hydrates. However, direct cause has not yet. Earthquakes? Iceberg scrapes slope sediments? or gravity flow took place in relation to the global warnings? We should continuously analyze what is the real reason of the Storegga landslides as discussed by Løvholt et al. 2017. Similar slope failures were known at Baiyun-Liwan submarine landslide off China on early Miocene (Zhu et al. 2019).

Fossil landslide layers are frequently found in the late Cenozoic marine sedimentary sequences. Kremer and others pointed out the landslide layers coincide well with interglacial times (Kremer et al. 2017). Similar submarine landslide deposits were described at the late Cenozoic marine sequences at Boso Peninsula (Mitsunashi et al. 1962).

Majima et al. (2019) and Nozaki et al. (2019) studied chemosynthetic clam communities from the Quaternary sedimentary sequences at the Boso and Miura Peninsulas, Central Japan. The clam fossil colony distributed horizons roughly coincide well with interglacial horizons. It can be explained that outgoing methene fluxes from sediments increase during interglacial time. Because methene should be provided due to the collapse of gas hydrate. These cases show that landslides should be caused in connection to global warnings.

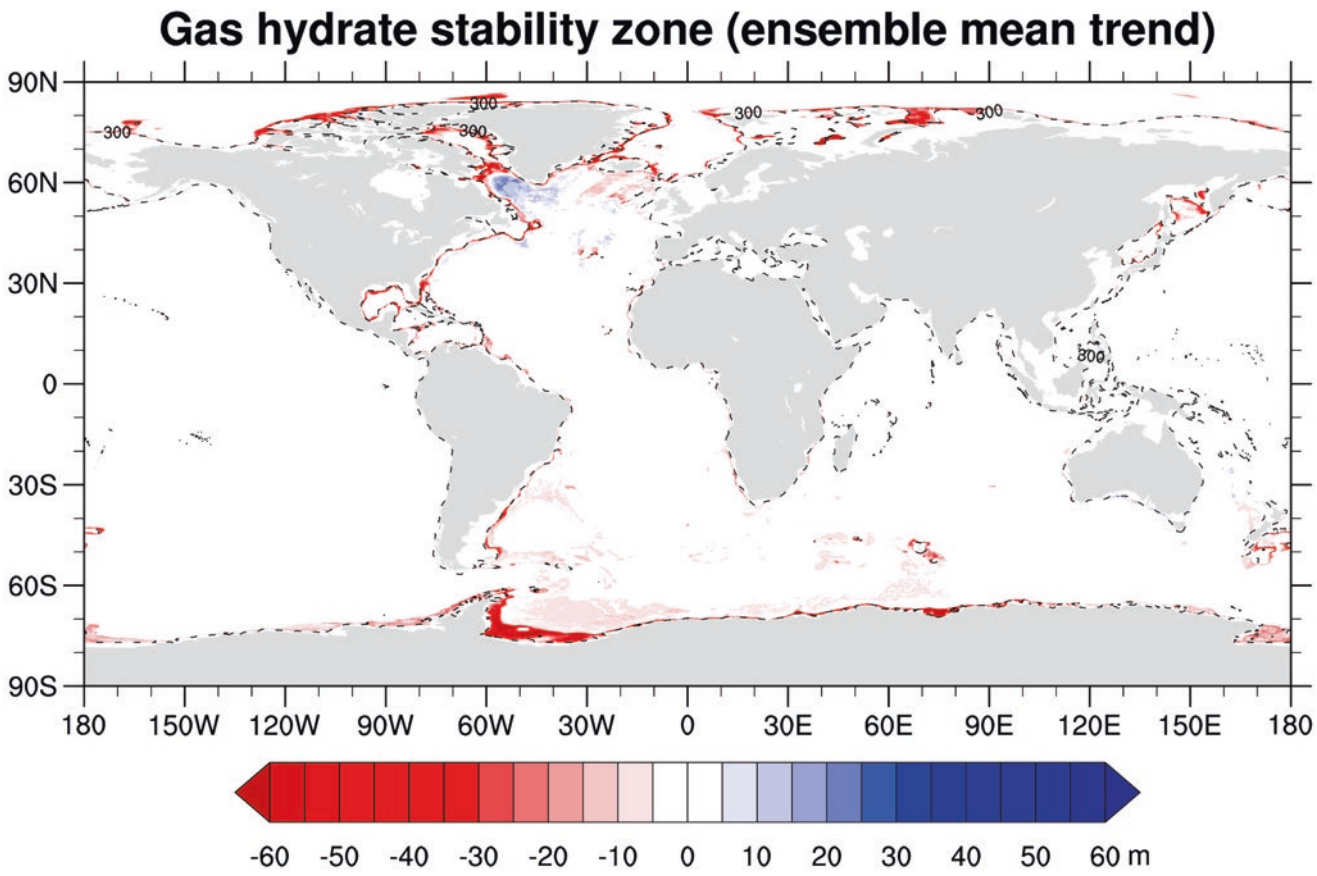

Fig. 3 Global distribution maps of the gas hydrate stability zone. Red color shows the reducing (both emission and accumulation balance) of gas hydrate regions. They are either permafrost or shallow polar seas. Blue shows the accumulating of gas hydrate. They are distributed in either middle to low latitude continental slopes of the Earth. (Ruppel and Kessler 2016)

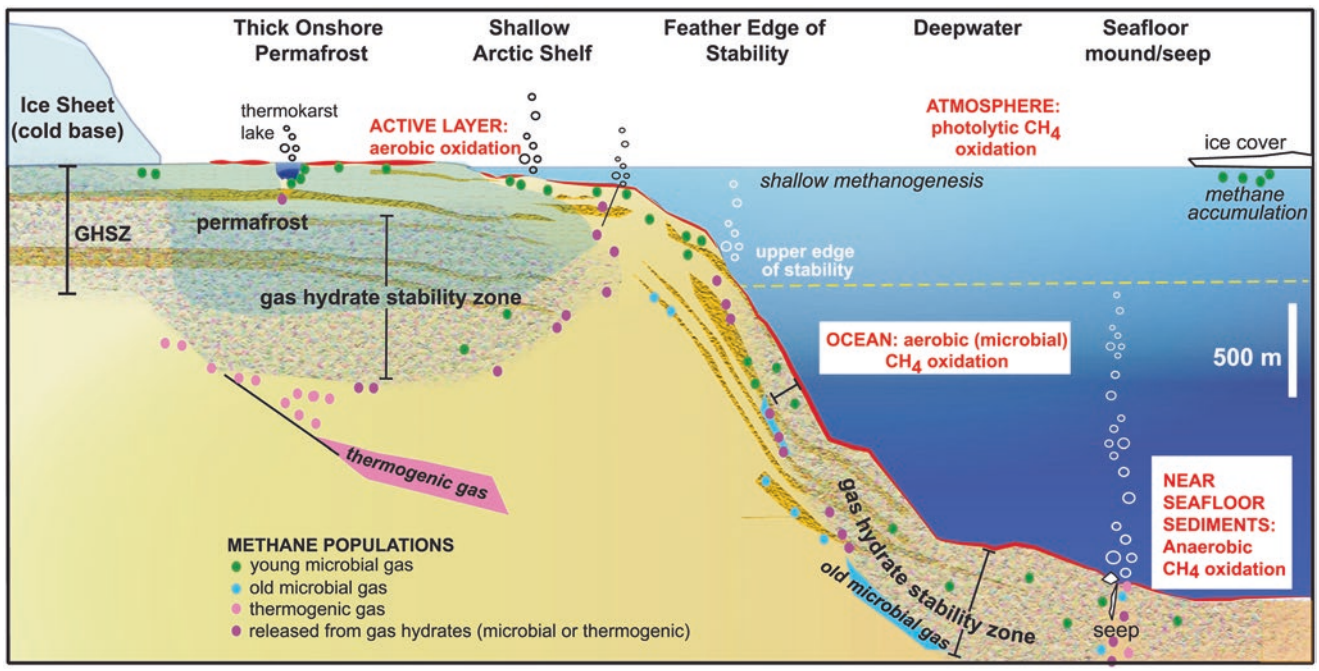

Fig. 4 Gas hydrate stability zone on the Earth, in particular to terrestrial zone to the ocean floor, and from subpolar permafrost and deep-sea where thick piles of gas hydrates develop. (Ruppel and Kessler 2016)

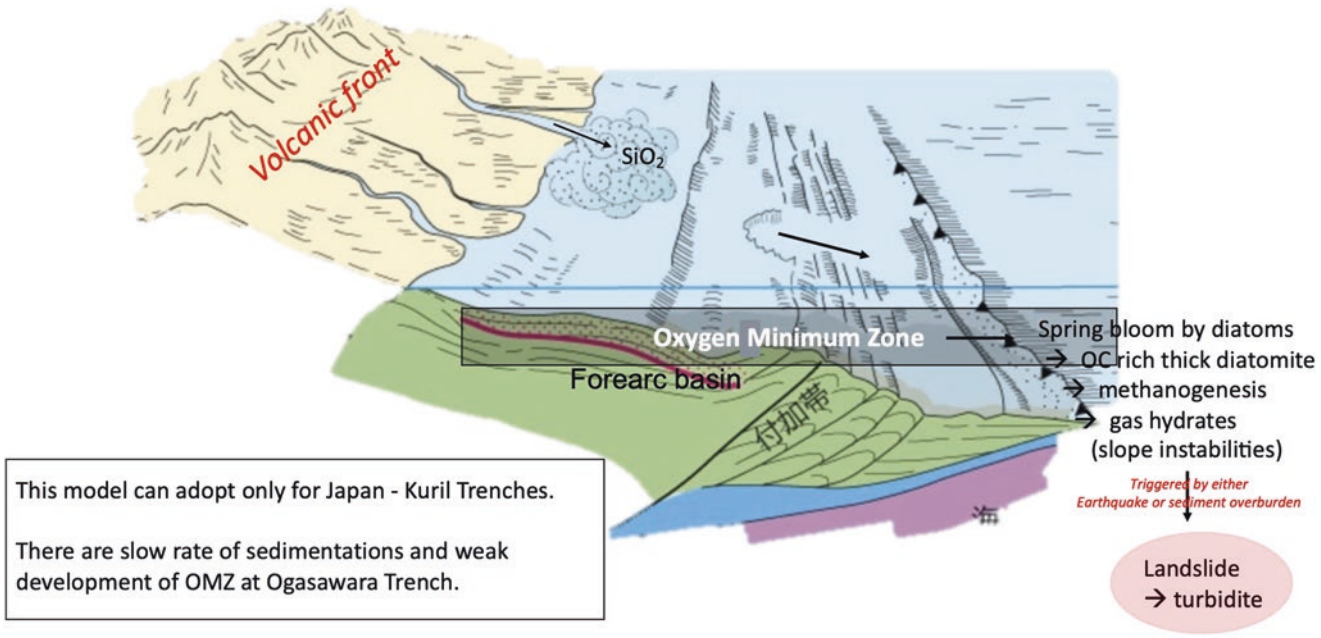

Fig. 5 Cartoon shows Oxygen Minimum Zone at forearc basin where diatomaceous muddy sediments are thickly deposited. Gas hydrate develops under OMZ. Red line in the cartoon shows Bottom Seismic Refraction (BSR) horizons, bottom limit of gas hydrate in sediments. The basic geologic features were drawn by Dr. Asahiko Taira

How can we construct sedimentary models for explaining submarine landslides at continental slopes. I propose the following environmental-tectonic model for submarine landslides in particular to active margin area such as Pacific rims (Fig. 5).

This model (Fig. 5) shows eutrophic continental slope to the trench environments such as the Kuril and Japanese Island Arcs where organic rich sediments are thickly deposited along the slope basins. High organic flux sustained by the high primary production such as diatom or other phytoplankton blooms. As a result, Oxygen Minimum Zone (OMZ) where low dissolved oxygen concentration layer develops at the upper to middle bathyal depths. OMZ mostly coincides with the depths of the upper limit of gas hydrate stable zone. When global warming progresses, unstable physic-chemical gas hydrate conditions, should start from shallower to deeper depths in the oceans. Slope failure and possible submarine landslides may highly probable to take place at upper bathyal depths in connection to sea water temperature rise.

On 2023, water temperature is high in the southern part of the Japanese Islands where western Pacific is distributed. Kuroshio Current flows further north in comparison to the normal year. These conditions may be introduced unstable bottom environments. Chain reaction in connection to global warmings are highly probable to take place along the middle to low latitude of the oceans. We should keenly watch climate changes on the Earth, not only on land but also in the sea further to the deep-sea.

5 Concluding Remarks

Submarine landslides are used to be explained by tectonic induced model in the sea. Continental slope basins shake strongly by vigorous Earthquakes and slope failures took place at continental slopes. Great East Japan Earthquake on 2011 should give nice case studies. Earthquakes and succeeding landslides observed at trench axial zone where oceanic plate subduct under the Japanese Islands. This is obviously a tectonic origin. However, slope basins off Tohoku in the Pacific Ocean are the area of active sedimentations. Tohoku area is an area for high in surface primary production. Eutrophic ocean produces a lot of organic carbon due to high rate of primary production and forms organic rich sediments. Forearc basin of the Northeast Japan is characterized by high concentration of organic carbon and should be gas-hydrate bearing sedimentary sequences potentially.

One probable scenario for forming frequent submarine landslides at Tohoku area can be figured out as follows. Primarily, slope sediments contain high organic carbon. It may introduce gas-hydrate bearing deposits. Gas-hydrate bearing strata is unstable and it is potential to produce gravity flows when big earthquakes are being occurred. Submarine landslides sometimes induce Tsunamis, so that disaster chain reactions may take place at the areas. We should keenly watch these disaster chain reactions at the active tectonic margin for decreasing disaster risk reduction.

Acknowledgments Acknowledgments are due to Prof. Kyoji Sassa and colleagues of the International Consortium of Landslides for valuable discussions and encouragements through preparing the manuscript. Dr. Loi Doan Huy helps to prepare and edit manuscript in excellent styles. Two figures in Appendixs 1 and 2 are reproduced from Talling and others, 2014 with permission from the Oceanography Society. Researches in terms of slope instabilities and their failures are funded by Danish National Research Foundation (DNRF145).

Storegga Slide and Landslide-Induced Tsunamis

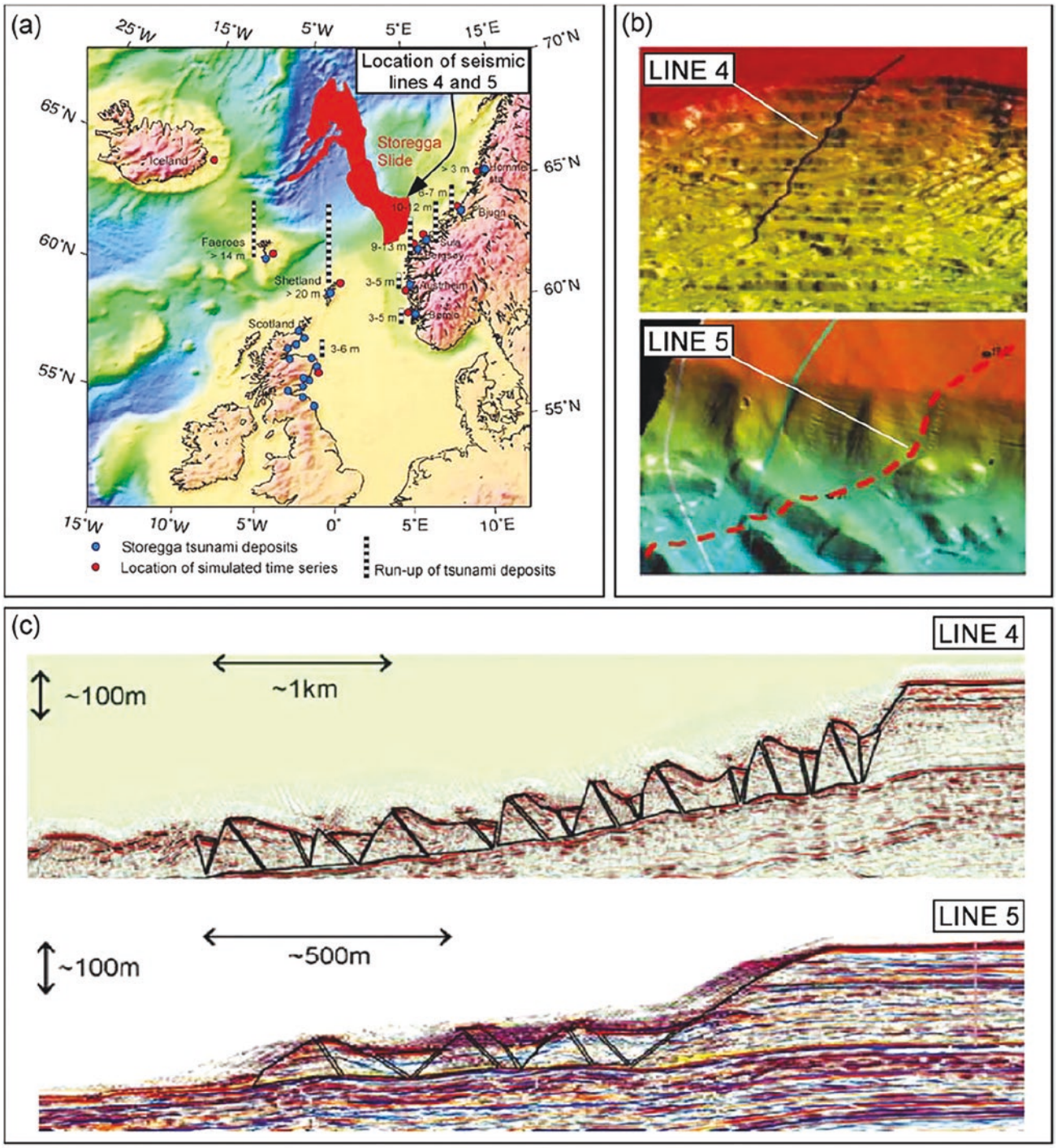

Stregga slide: from Locat J. and Lee H. (2008) Submarine Mass Movements and Their Consequences: An Overview. Landslides- Disaster Risk Reduction (eds: Sassa K, Canuti P.): 115–142.

3-D View of the Storegga landslide: from Talling, P.J.; Clare, M.; Urlaub, M.; Pope, E.; Hunt, J.E.; Watt, S. Large Submarine Landslides on Continental Slopes Geohazards, Methane Release, and Climate Change. *Oceanography* 2014, 27, 32–45.

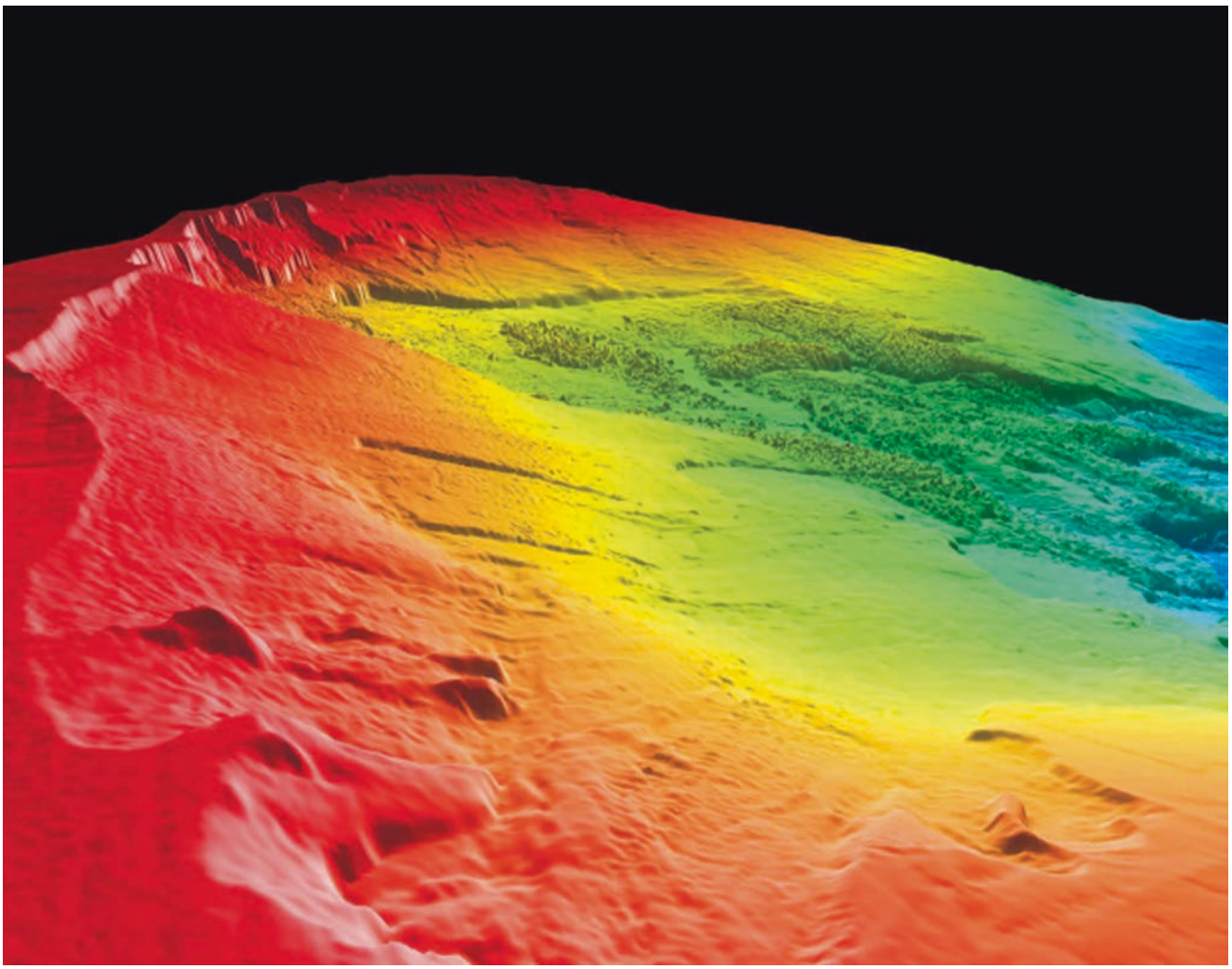

Gas Hydrate Melting Processes

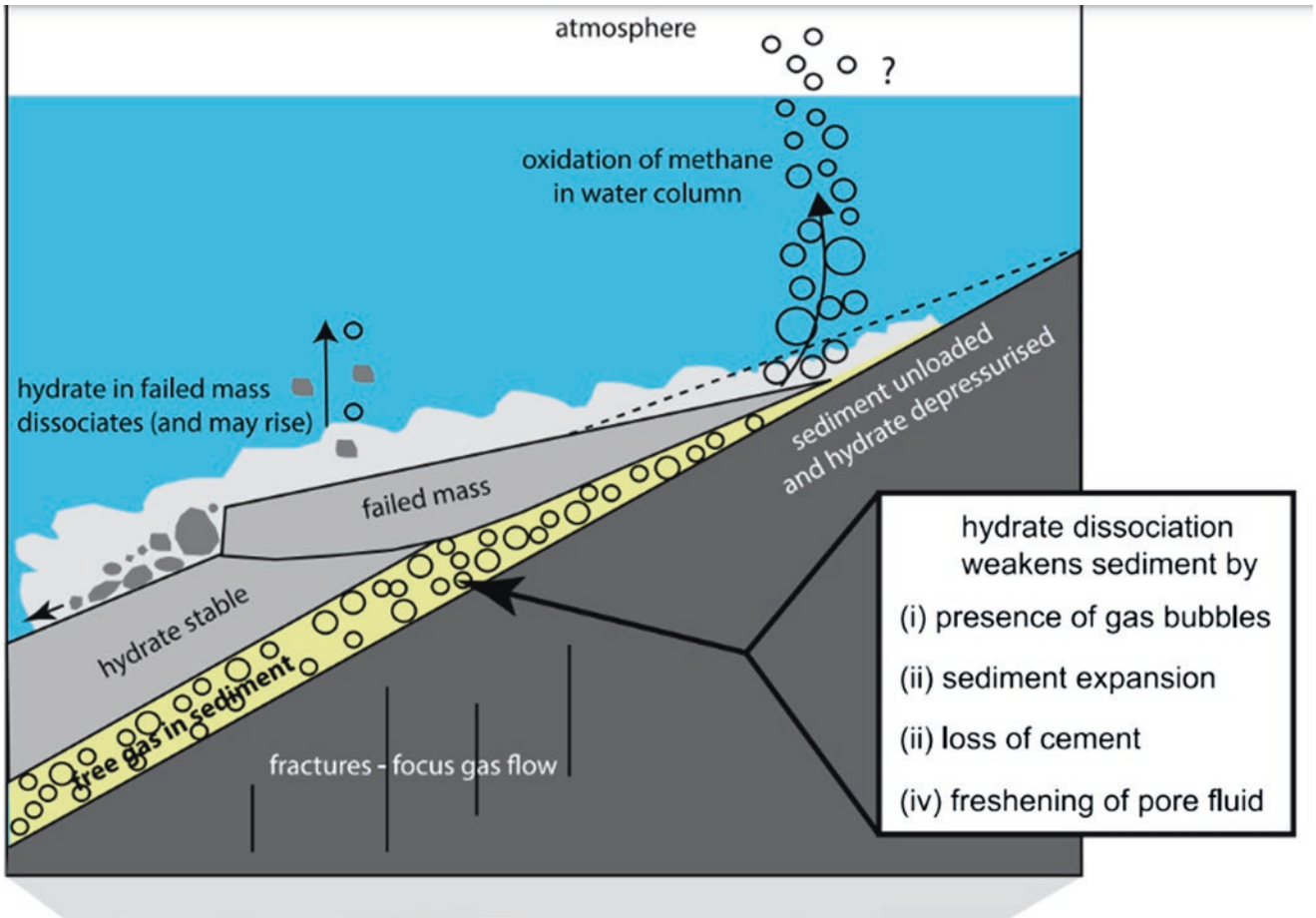

Gas hydrate melting processes that may cause submarine landslides or cause methane emissions: from Talling, P.J.; Clare, M.; Urlaub, M.; Pope, E.; Hunt, J.E.; Watt, S. Large Submarine Landslides on Continental Slopes Geohazards, Methane Release, and Climate Change. *Oceanography* 2014, 27, 32–45.

References

Cutter SL, Ismail-Zadeh A, Alcantara-Ayala I, Altan O, Baker DN, Briceno S, Gupta H, Holloway A, Johnston D, McBean GA, Ogawa Y, Paton D, Porio E, Silbereisen RK, Takeuchi K, Valsecchi GB, Vogel C, Wu G (2015) Pool knowledge to stem losses from disasters. Nature 522:277–279

Dawson AG, Dawson S, Bondevik S, Costa PJM, Hill J, Stewart I (2020) Reconsiling Storegga tsunami sedimentation patterns with modelled wave heights: a discussion from the Shetland isles field laboratory. Sedimentology 67:1344–1353

IPCC (2013) Climate change 2013: the physical science basis. In: Stocker TF, Qin D, Plattner G-K, Tignor M, Allen SK, Boschung J, Nauels A, Xia Y, Bex V, Midgley PM (eds) Contribution of working group I to the fifth assessment report of the intergovernmental panel on climate change. Cambridge University Press, Cambridge, 1535 pp

IPCC (2021) Climate Change 2021: the physical science basis. In: Masson-Dolmotle V, Zhai P, Pirani A, Conners SL, Péan C, Chen Y, Goldfarb L, Gomis MI, Robin Matthews JB, Berger S, Huang M, Yelekçi O, Zhou B, Lonney E, Maycock TK, Water field T, Leitzell K, Caud N, (eds), Contribution of working group I to the sixth assessment report of the intergovernmental panel on climate change. Cambridge University Press, Cambridge, 2409 pp

Kremer K, Usman MO, Satoguchi Y, Nagahashi Y, Vadakkepuliyambatta S, Panieri G, Strasser M (2017) Possible climate preconditioning on submarine landslides along a convergent margin, Nankai trough (NE Pacific). Prog Earth Planetary Sci 4. https://doi.org/10.1186/s40645-017-0134-9

Løvholt F, Bondevik S, Laberg JS, Kim J, Boylan N (2017) Some giant submarine landslides do not produce large tsunamis. Geophys Res Lett 44:8463–8472. https://doi.org/10.1002/2017GL074062

Majima R, Ochi M, Miura M, Hitomi M, Saito T, Namiki Y, Otsuka Y, Shimizu H, Nozaki A, Utsunomiya M, Kusunoki C, Sato K, Kawagata S, Wani R, Nakamura E, Sakai S, Wada H, Kitazato H (2019) Cold-seep-dependent fossil assemblages in the middle Pleistocene Kakinokidai formation at Kawayatsu, Kimitsu City, Japan: their temporal-spatial distribution and associated anuthigenic carbonates. J Geol Soc Japan 125:655–683

Mitsunashi T, Yazaki K, Kageyama K, Shinada T, Ono E, Yasukuni N, Makino T, Shinada Y, Fujiwara K, Kamata S (1962) "Futtsu-Otaki". Geological maps of the oil and gas field of Japan, no. 4. Geol Surv Japan

Nozaki A, Majima R, Kameo K, Sakai S, Kouda A, Kawagata S, Wada H, Kitazato H (2019) Geologu and age model of the lower Pleistocene Nojima, Ofuna, and Koshiba formations of the middle Kazusa Group, a forearc basin-fill sequence on the Miura peninsula, the Pacific side of Central Japan. Island Arc 23(2):157–179

Ruppel CD, Kessler JD (2016) The interaction of climate change and methene hydrates. Rev Geophys 55:126–168. https://doi.org/10.1002/2016RG000534

Zhu C, Cheng S, Li Q, Shan H, Lu J, Shen Z, Liu X, Jia Y (2019) Giant submarine landslide in the South China Sea: evidence, causes, and implications. J Marine Sci Eng 7. https://doi.org/10.3390/jmse7050152

Landslide Hazard Evaluation of a Large Waste Landfill in Bogotá City

Juan Lozano and Guillermo Ávila

Abstract

The Doña Juana waste landfill receives solid urban waste from about nine million people living in Bogotá and several nearby municipalities. This article describes the characteristics of this landfill which has suffered some important landslides with serious environmental effects, shows the main geotechnical studies carried out for the characterization of the materials, analyzes the operation and monitoring processes, especially the pore pressures generated by leachate and the results of the landslide hazard evaluation in terms of the probability of failure for static and pseudo-static conditions.

Keywords

Landslides · Landfill · Municipal solid waste · Hazards

1 Introduction

The waste amount produced by cities is directly proportional to the size of its population, and it is also related to economic development and social consumption patterns. The increasing waste production represents a significant problem for many cities in the world because it is very difficult to find suitable storage places since people are not willing to have sanitary landfills near their homes. For that reason, many of the existing waste landfills, also known as municipal solid waste (MSW), tend to prolong their useful life several years by increasing areas and heights of the fills. MSW are based on waste disposal in cells that are mechanically compacted and covered daily and whose leachate and gases are captured or recirculated by different procedures such as gravity drains, chimneys and forced pumping.

Doña Juana Landfill is the largest landfill in Colombia, occupying nearly 500 ha. It receives around 6300 tons (7250 m^3) of waste per day from Bogotá city and many nearby municipalities, serving around nine million people.

Doña Juana Landfill suffered a great landslide on September 27, 1997, in which more than 1,200,000 m^3 of garbage was mobilized, generating very serious environmental problems such as contamination of the Tunjuelo River, bad odours perceived from more than 10 km away, the proliferation of flies and, in general, damage to the surrounding communities. Since that moment, many studies have been carried out to understand the complex stability behaviour of this waste landfill. In 2015, a second landslide of 600,000 m^3 blocked the pipes of the evacuation leachate system, and in 2020, a third landslide of about 80,000 m^3 occurred with no significant impacts.

Doña Juana waste landfill started to operate in 1988, and it was designed to provide a useful life of nearly 25 years. However, it has not been possible to find a new place to dispose of this great amount of daily garbage, and the useful life of the landfill has had to be extended several times, creating new waste cells above the old ones. This represents a great challenge from the technical and environmental point of view and implies a detailed and continuous monitoring and landslide hazard evaluation under different operational scenarios. The monitoring results, the operational process and hazard analysis are discussed in this article, emphasizing mechanical parameters, pore pressures and stability calculations based on probabilistic analysis.

2 General Description of Doña Juana Waste Landfill and Previous Instability Problems

Doña Juana MSW covers an area of 500 ha, and its waste height varies from 30 to 120 m. Geologically, the area corresponds to a basin of sedimentary rocks, mainly claystone

J. Lozano (✉) · G. Ávila
Universidad Nacional de Colombia, Department of Civil and Agricultural Engineering, Bogotá, Colombia
e-mail: judlozanolo@unal.edu.co; geavilaa@unal.edu.co

B. Abolmasov et al. (eds.), *Progress in Landslide Research and Technology, Volume 3 Issue 1, 2024*, Progress in Landslide Research and Technology, https://doi.org/10.1007/978-3-031-55120-8_5

and limestone from the Bogotá Formation and Quaternary Deposits. It is in the Southwest of Bogotá city, near the Tunjuelo River, as shown in Fig. 1. The operational area has been divided into 14 internal sectors and each sector in turn divided into several sub-sectors or operational stages. Figure 2 presents a planned view of the study area with the historical landslides and all the Doña Juana Landfill areas.

There have been three important landslides in the more than 30 years of operation. The first, and the largest one, was a flow-type landslide that occurred on September 27, 1997, in which more than 1.2 million m^3 were removed and travelled about 1500 m in 20 min. The removed material clogged the Tunjuelo River (Caicedo et al. 2002). It caused severe environmental affectation, such as contamination of the river water and propagation of bad odours more than 10 km away. On October 2, 2015, a second landslide of approximately 600,000 m^3 occurred in the area called Terrace 1 (current area of operation). The slipped waste clogged a micro tunnel, which worked as an auxiliary leachate evacuation system because the main pipe had suffered frequent clogging. The third landslide occurred on April 28, 2020, removing about 80,000 tons of waste, but the situation was promptly controlled with no further affectations. One remarkable detail about the last event was the lack of an available disposal zone, the reason why the operator had to overfill the removed area.

From the first landside, many geotechnical studies have been carried out, including field and laboratory tests, stability analysis and modelling of the complex physical, chemical, and biological decomposition processes (Caicedo et al. 2002; González and Espinosa 2003a). The main conclusions from these studies are:

(a) Large changes in the material properties occur over time, due to the chemical and biological reactions that result in the conversion of solid materials into liquids or gases.
(b) One of the main causes of the first landslide was the recirculation of leachate in the waste cells, a method that is used in many industrialized countries to reduce the contaminant load of fluids.
(c) Pore pressure is severely affected by the gas pressure generated during the decomposition of the waste and for that reason, geotechnical analysis can be addressed by means of the unsaturated soil behaviour theories.
(d) Mechanical parameters were measured directly on the waste material using field shear tests, Mennard-type pressurometer and piezocone field tests (Caicedo et al. 2002).
(e) Field instrumentation and monitoring were recommended to avoid new instability problems in order to perform more precise stability models.

Fig. 1 General location of the study area

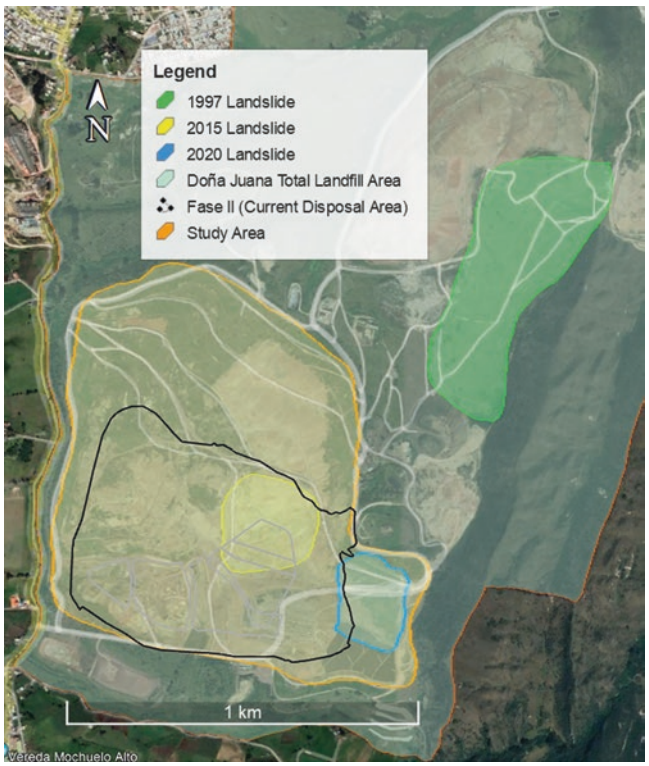

Fig. 2 General view of the Doña Juana MSW indicating the location of past landslides and the study area

3 Operational Problems Related to Leachate and Gas Evacuation

The initial design of the drainage system contemplated filters, pipes, ponding, and reinjection of leachate, as shown schematically in Fig. 3 (Collazos 1998). Leachate reinjection has been used in many MSW and according to Espinosa and González (2003a), some of the reported benefits are: reduction of wastewater treatment, temporary storage for leachate, with which its disposition differs in time, part of the leachate may evaporate during recirculation, settlements acceleration due to a more efficient biological degradation, etc. and some of the most important disadvantages are deformations of the internal facilities due to the high settlements, possible biological pipe obstruction and filter clogging, lack of experience related to the design and operation and a dangerous increase of pore pressures.

Leachate reinjection has been considered the main cause of the 1997 Doña Juana Landslide (Caicedo et al. 2002; González and Espinosa 2003a) because pore pressures increased significantly due to the inefficient leachate evacuation system. This problem increased with the second landslide (2015) because a micro-tunnel that served as a gravity-base leachate evacuation system was clogged so it was necessary to adopt contingent measurements for the leachate evacuation through the construction of smaller diameter pipes and pumping wells, as shown in Fig. 4 and in Fig. 5. However, the new system has not been efficient, because gas and leachate packets are frequently detected. Due to this condition, the National Environmental Licensing Agency (ANLA) imposed a preventive measure filed in which the temporary disposal of material in one of the terraces was prohibited, based on the increase in pressures of leachate and gases.

Another operation problem that has been reported is related to deficiencies in the compaction process and, for that reason, considerable settlements have occurred, affecting the gas and leachate extraction wells. According to a recent geophysical investigation, it is estimated that around seven million m^3 of non-extracted leachate are in the waste disposal zone (UAESP, UT INTER DJ,, and Saicon Ingenieria SAS 2023).

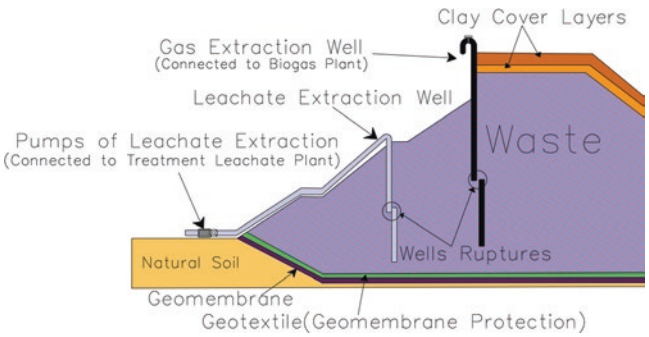

Fig. 4 Actual leachate management design

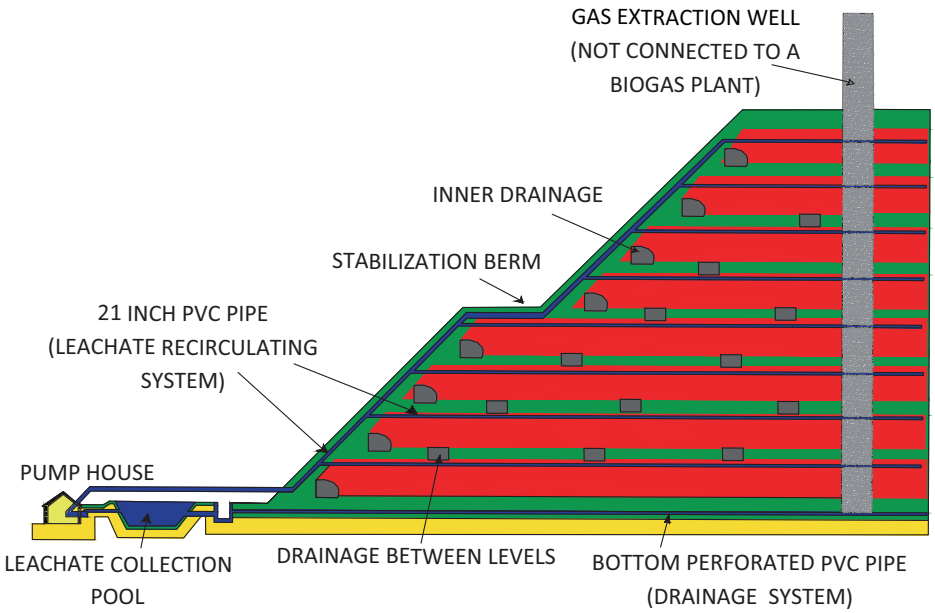

Fig. 3 Initial leachate management design, including gravity-based drainage and reinjection process. Adapted from (Collazos 1998)

Fig. 5 (**a**) Pressurized output of leachate through chimneys, (**b**) chimneys with extraction of leachate by pumping output of leachate through chimneys

4 Geotechnical Characterization and Monitoring

Doña Juana MSW has been the subject of several geotechnical studies. The first one with the objective of determining the causes and legal responsibilities of the 1997 landslide; In this case, a total of 14 piezocone tests with an average depth of 20 m. were performed. Also 4 in-situ pressure tests, waste sampling, large-size in-situ shear tests and many laboratory tests (Gonzalez and Espinosa 2003; Caicedo et al. 2002).

From 1998 to today, a system of vibrating wire piezometers was installed in old areas and sectors of the current operation, also 26 inclinometers were installed in the contacts between the waste cells. There are more than 300 piezometers in operation, but several of them are recent and have few records. Figure 6 shows the location of 195 piezometers in the current operating area, called the Optimization Fase II and its adjacent disposal areas. This figure also shows the sites where piezocone tests (CPTu) were carried out. In 16 of these test points, excess pore pressure dissipation tests were also carried out, stopping the advance of the cone and continuously recording the change in pressure until equilibrium was reached.

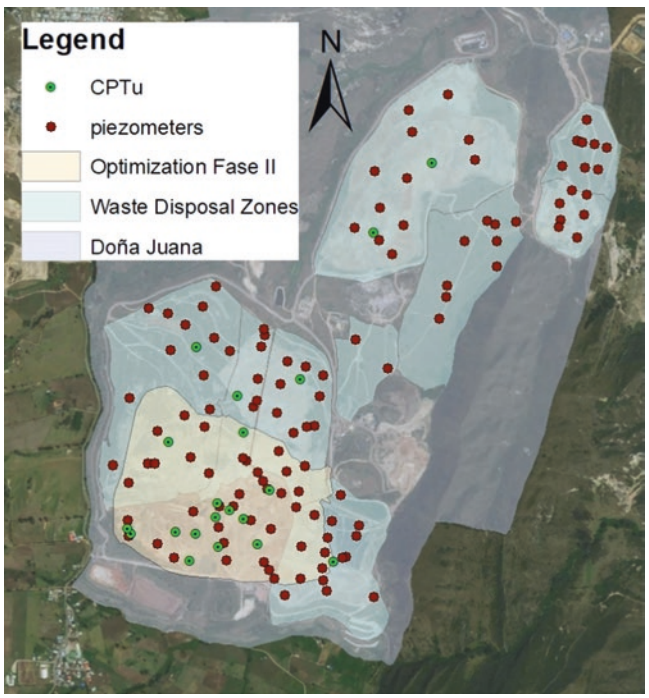

Fig. 6 Location of piezometer monitoring and points of CPTu tests

Another monitoring process consists of daily topographic controls. Initially, these controls were done using conventional topography, yet more recently, they have been done using drones. Geophysical monitoring, such as electrical resistivity tomography, is also carried out with the purpose of identifying the presence of leachate and gas pockets.

The classification of the materials from the CPTu tests was made based on the classification index (CI) methodology proposed by Robertson (2016).

$$CI = \left[\left(3.47 - \log\left(\frac{q_t}{P_a}\right)\right)^2 + \left(\log\left(Rf\right) + 1.22\right)^2\right]^{0.5}$$

Where, q_t is the tip resistance corrected for probe dimensions (kPa), P_a is the atmospheric pressure (100 kPa), and Rf is the friction ratio. The results of these tests are shown in Fig. 7. These results are consistent with those obtained in other sanitary landfills in Brazil, China, the United States, India and Portugal, presented by (Ramaiah et al. 2017), where the largest amount of reported data falls in zones 4 and 5, which are behaviours of silt mixtures and sand mixtures respectively.

The resistance parameters were calculated conventionally as:

$$\tau = \sigma_v^{'} \tan\left(\varphi'\right)$$

Where, $\sigma_v^{'}$ is the effective vertical stress, τ is the equivalent shear stress and $\varphi^{'}$ the friction angle. Internal effective, which was estimated using the correlation proposed by Kulhawy and Mayne (Kulhawy and Mayne 1990), given by

$$\varphi' = 17.6° + 11 * \log\left(q_{t1}\right)$$

Where, q_{t1} is the tip resistance normalized by stress, which is defined by:

$$q_{t1} = \frac{q_t - \sigma_{vo}}{\sigma_v^{'}}$$

Where, q_t is the tip resistance corrected for probe dimensions, σ_{vo} total vertical stress, and $\sigma_v^{'}$ effective vertical stress.

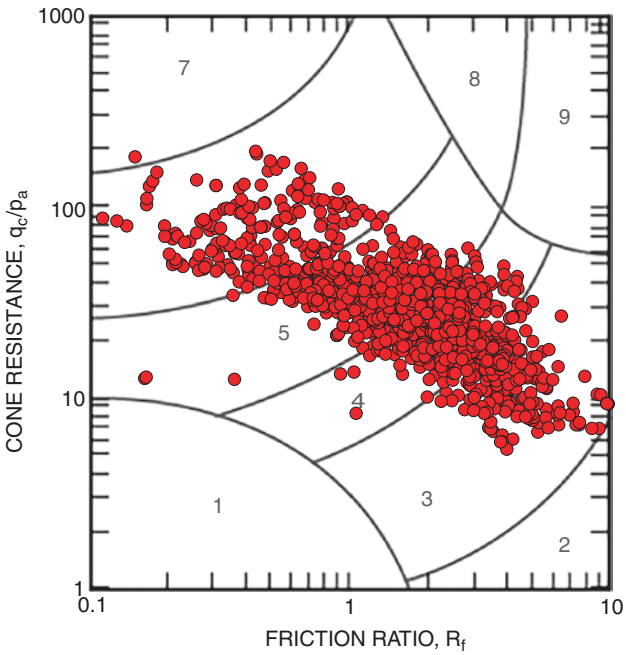

Fig. 7 Classification index of Doña Juana parameters in the Robertson (2016)

On the other hand, cohesion is not interpreted as the intercept of the line with the axis of the ordinates, in this case the criterion established by (González and Espinosa 2003b) is used, where the intercept is assumed as cohesion. of the envelope for an equivalent stress of 19 kPa (almost the pressure at 2 m deep).

Figure 8 shows the results of the cohesive resistance and friction angle parameters. It is observed that there is an inverse-proportional relationship between cohesion and friction. The greater the angle of friction, the less cohesion. Thus, a potential relationship between the resistance parameters is projected in which the cohesion value fluctuates between 11 kPa and 21 kPa for variable friction angles between 7° and 48°.

Figure 9 shows the results of the friction angle based on the relationship of Kulhawy and Mayne (1990) of all the CPTu tests with depth, highlighting the average in bold. This mean friction angle is used to calculate the cohesion behavior by the correlation of Fig. 8.

A decrease in the angle of internal friction with depth is observed as well as an increase in the cohesion with deep (Fig. 10), which is consistent with what was found by González and Espinosa 2003b) for the Doña Juana landfill, where a decrease in the friction angle with age is established, considering that the deeper the waste the older the material.

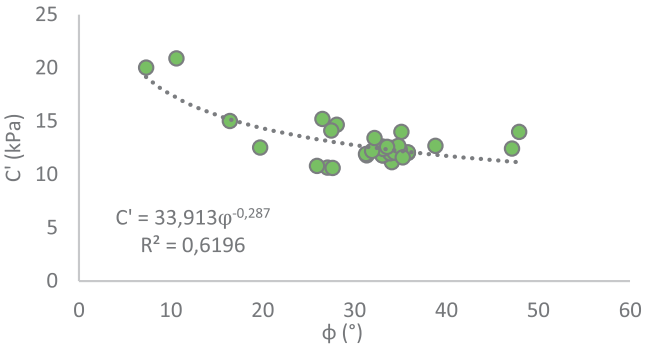

Fig. 8 Relationship between Cohesion and Friction Angle in Doña Juana MSW

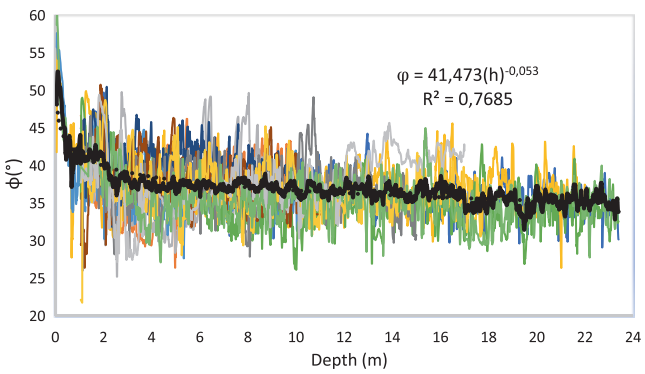

Fig. 9 Behavior of the friction angle with depth

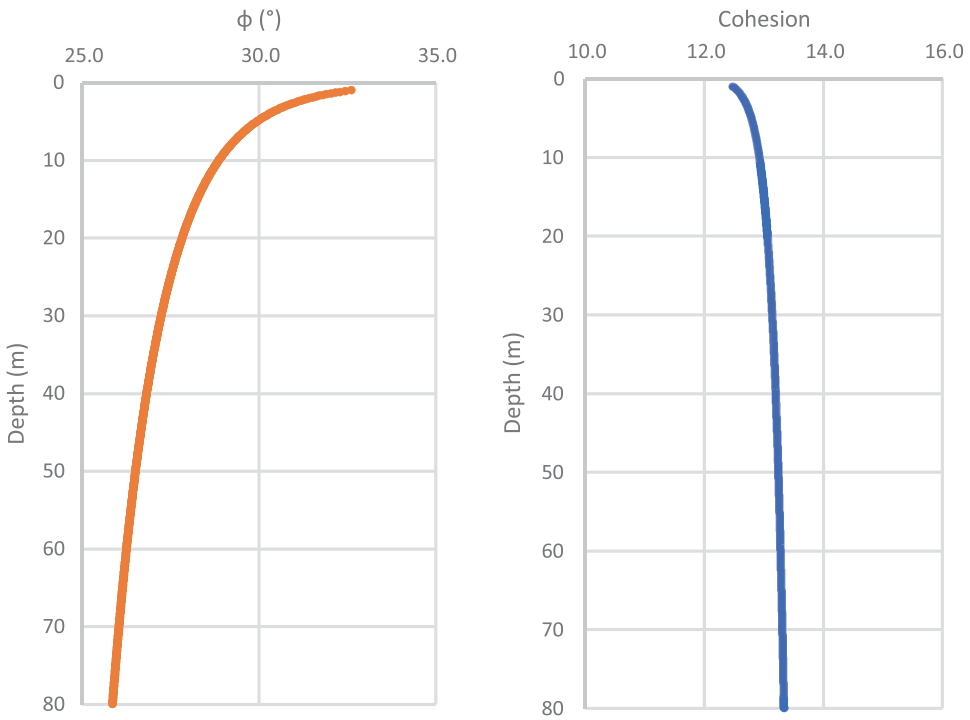

Fig. 10 Left, variation of friction angle with depth. Right, variation of cohesion with depth in Doña Juana MSW

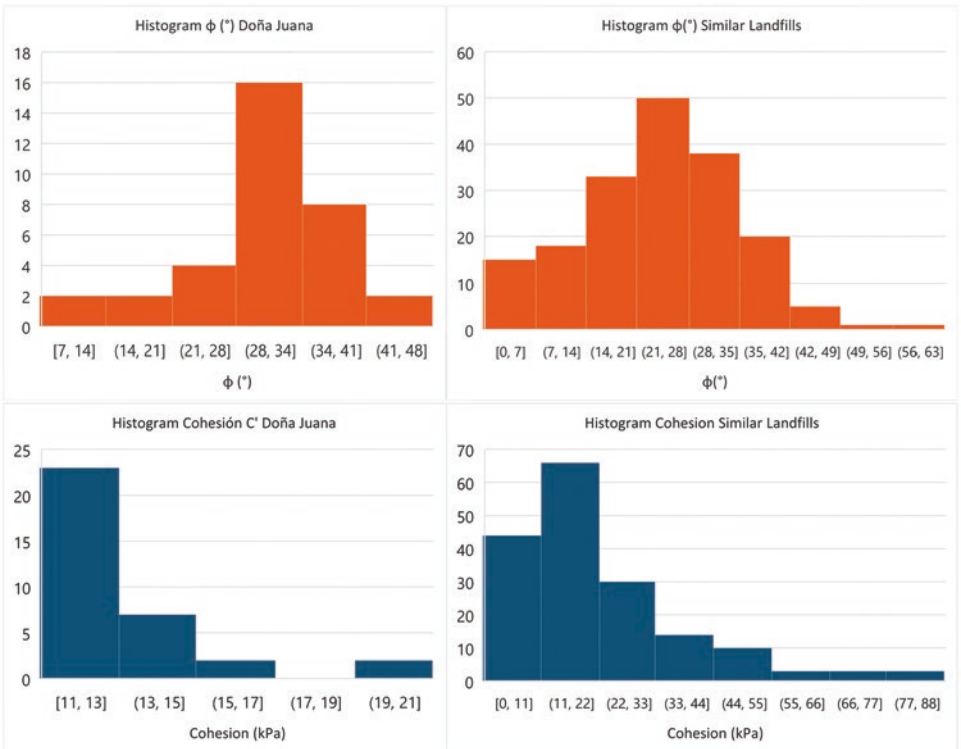

Fig. 11 Strength parameter histograms of Doña Juana MSW compared with strength parameters of similar MSW reported by (Daciolo 2020)

The statistical behaviour of the parameters obtained is consistent with the residue resistance parameter database created by (Daciolo 2020). It is observed in Fig. 11 that the distribution of the friction angle in Doña Juana material follows a normal distribution, and the value of cohesion follows a log-normal distribution. The following authors were revised to prepare a more complete database and the results (See Fig. 11).

5 Analysis of Pore Pressure and Efficiency of the Pumping Systems

Figure 12 shows pore pressure behaviour with depth within the current operating area, and Fig. 13 shows the results in areas outside the current operating polygon. As observed in the graphs, the pore pressure values in the adjacent external areas are lower than those in the current operating zone. This is explained because in the area of operation, the biodegradation of the garbage is in its early stages, and there is a higher leachate generation rate than in the adjacent areas.

For the stability analysis model, the Ru parameter is used, which is defined by:

$$Ru = U_f / \gamma H$$

Where, Uf is the pore pressure at a point in space, γ the unit weight of the material (in this case, the garbage), and H is the height or depth of the measurement point. In the case of garbage from the Doña Juana sanitary landfill, a unit weight value of 1.12 t/m³ is adopted, according to the mean value reported by the operator based on many waste density tests. The behavior indicated in Figs. 12 and 13, combined with the previous expression, is summarized in Table 1.

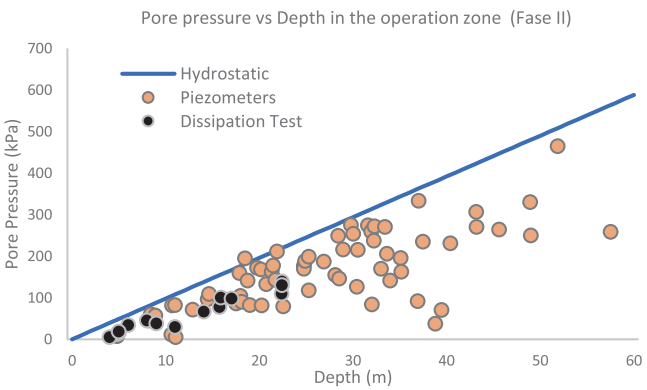

Fig. 12 Pore pressure variation in depth in the actual operation zone

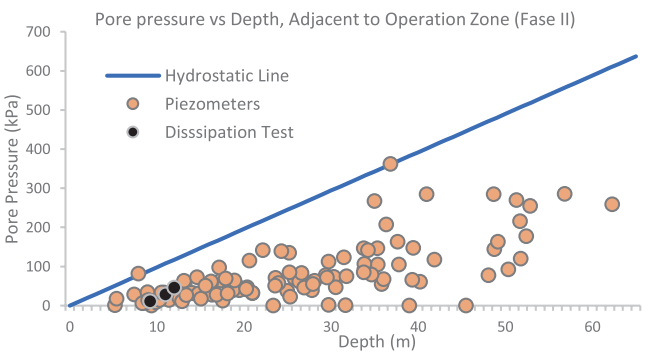

Fig. 13 Pore pressure variation in Depth in zones adjacent areas to the actual operation zone

Figure 14 shows the distribution of areas of equal pressure, according to the values recorded in April 2022. The red colours indicate high Ru values, above 0.7, and the orange colours, Ru values between 0, 5, to 0.7. According to the analysis made by the MSW operator, Ru values greater than 0.5 are considered to have a high potential to generate instability problems in the landfill.

Figure 15 compares the proportion of areas of high pore pressure (Ru > 0.5) with the precipitation values that occurred in different months between 2021 and 2022. As expected, areas of high-pressure level tend to increase as rainfall increases and decreases with rainfall reductions. Still, there is a delay in the response of 1 to 1.5 months.

Table 1 (a) Ru vs. depth in the actual operation area (Fase II area) and (b) in adjacent waste disposal zones (next to Fase II)

Depth (m)	Average	Standard deviation	Min	Max
FASE II				
0–10	0,35	0,21	0,11	0,51
10–20	0,42	0,29	0,00	0,89
20–30	0,56	0,19	0,00	0,82
30–40	0,49	0,21	0,08	0,79
40–50	0,54	0,06	0,49	0,61
50–70	0,55	0,17	0,39	0,78
Adjancent waste disposal zones to FASE II				
0–10	0,28	0,38	0,00	0,82
10–20	0,24	0,11	0,12	0,48
20–30	0,26	0,17	0,00	0,54
30–40	0,33	0,22	0,00	0,85
40–50	0,48	0,14	0,32	0,6
50–70	0,49	0,09	0,29	0,46

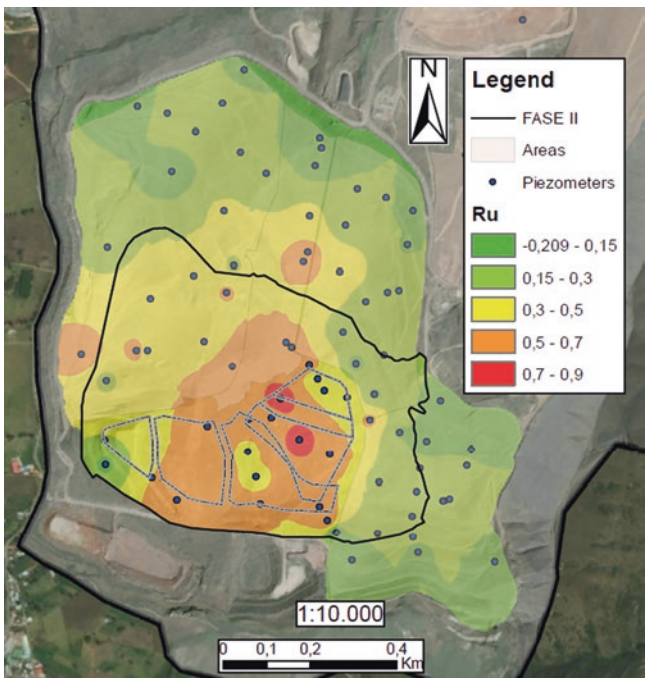

Fig. 14 Map of equal pore pressure according to the piezometric readings in April 2022

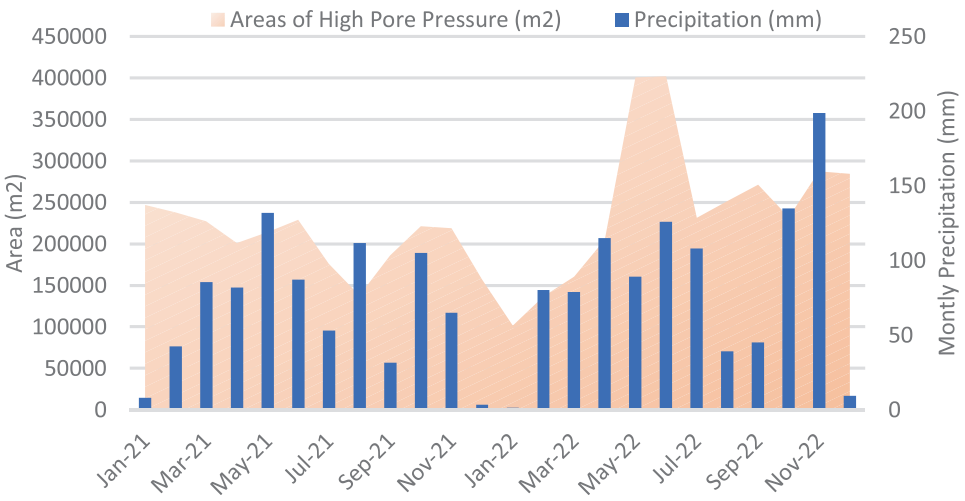

Fig. 15 Comparison between monthly precipitation and areas of high pore pressure (Ru > 0.5)

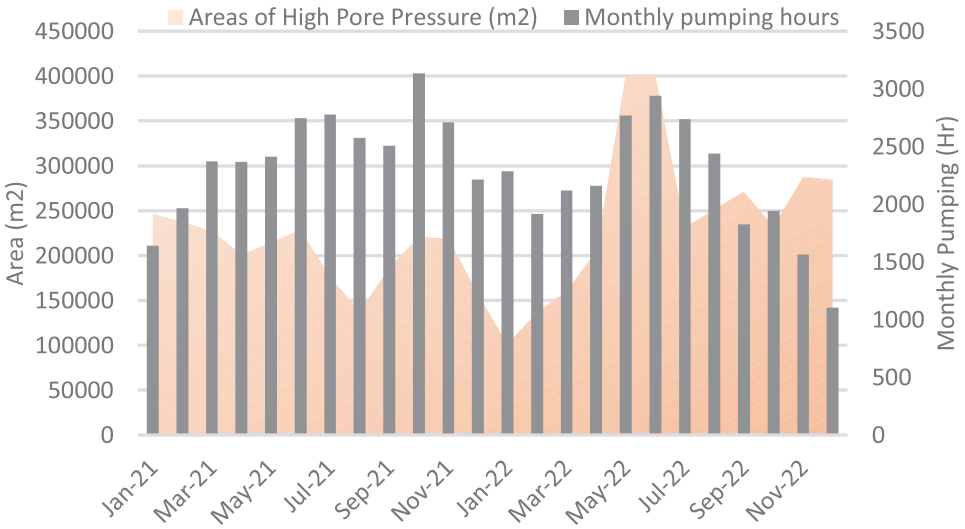

Fig. 16 Comparison between monthly forced pumping and areas of high pore pressure (Ru > 0.5)

To reduce pore pressure ratios, leachate extraction is made by forced pumping. In Fig. 16, the monthly pumping hours are compared with the areas of high pore pressure. It is observed that the operator tends to increase pumping hours when the rain increases. However, in many cases, pumping is not enough to reduce the areas of high pore pressure significantly and this is an important factor that may affect stability conditions.

6 Stability Models

For the construction of the geotechnical model, in the first place, a friction angle value was estimated at the surface level based on the interpreted data. Then an extrapolation of the friction values in depth was made using the relationship presented in Fig. 9. The analysis profiles are divided based on the relationship of the friction angle with the depth and cohesion (Fig. 8). Average friction and cohesion values were assigned as they correspond to the average depths of the stratum, and finally, the values were entered. Ru data is based on the mean values at depth according to what is reported in Table 1. It should be noted that, the methodology described was suggested by Saicon Engineering and Union Temporal INTER DJ companies which performed the CPTu essays.

In total, 6 profiles were made for stability analysis, as shown in Fig. 17. As part of the discretization, layers almost parallel to the surface are created and on which there are variations of the properties using the previously explained methodology. Figure 18 shows one of the analysis profiles. It is important to clarify that the different layers indicated there represent a differentiation of mechanical properties and do not represent a variation in the typology of materials, as is usually done in conventional geotechnical models, since it is a very heterogeneous material that makes up the waste.

For the threat analysis, stability modelling was carried out regarding the probability of failure, using the Monte Carlo method in the Slide software (Rocscience, 2005). For this modelling, the statistical values of the input parameters are needed, such as the mean, standard deviation, data distribution, and maximum and minimum values.

Table 2 shows the cohesion and friction values entered, which, together with Table 1, constitute the properties of the discretization of the model. Stability calculations were made by the simplified Bishop and Morgersten-Price methods for static and pseudo-static conditions. Table 3 summarizes the results of these analyses regarding the safety factor and the corresponding probability of failure.

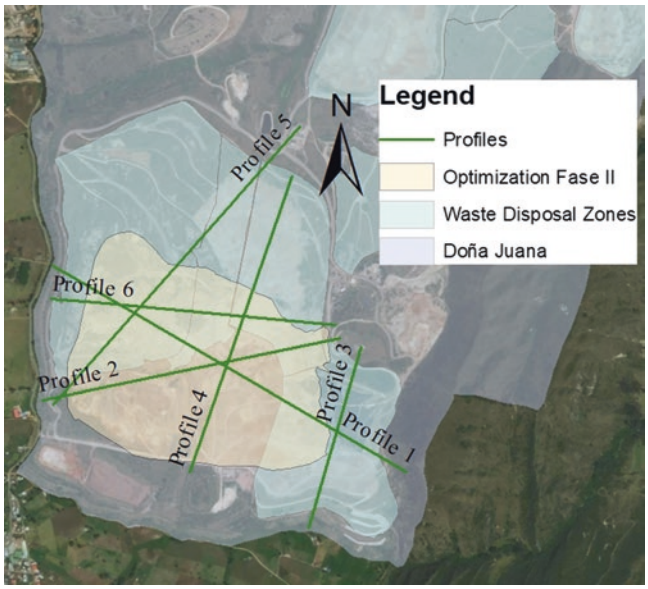

Fig. 17 Analysis profiles in the study area

Table 2 Parameters entered to each layer

Material Name	Property	Mean	Std. Dev.	Rel. Min	Rel. Max
Layer 1 0–10 m- Opt Fase II	Cohesion	12,8	2,2	2,4	7,9
	Phi	30,1	8,2	23,8	16,8
Layer 2 10–20 m - Opt Fase II	Cohesion	13	2,2	2,4	7,9
	Phi	28,3	8,2	23,8	16,8
Layer 3 20–30 m- opt Fase II	Phi	27,5	8,2	23,8	16,8
	Cohesion	13,1	2,2	2,4	7,9
Layer 4 30–40 m- Opt Fase II	Cohesion	13,2	2,2	2,4	7,9
	Phi	27	8,2	23,8	16,8
Layer 5 40–50 m- Opt Fase II	Cohesion	13,2	2,2	2,4	7,9
	Phi	26,6	8,2	23,8	16,8
Layer 1 0–10 m- Zona VII	Phi	33	8,2	23,8	16,8
	Cohesion	12,8	2,2	2,4	7,9
Layer 2 10–20 m- Zona VII	Cohesion	13	2,2	2,4	7,9
	Phi	30	8,2	23,8	16,8

Table 3 Results of the Fs calculation and the probability of failure of the profiles analyzed

	Static				Pseudostatic			
	Bishop		Mogersten-Price		Bishop		Mogersten-Price	
	Fs (Mean)	PF (%)	Fs (Mean)	PF (%)	Fs (Mean)	PF (%)	Fs (Mean)	PF (%)
Profile 1	2,16	0,0	2,17	0,0	1,21	19,9	1,24	16,4
Profile 2	1,93	1,14	1,94	1,04	1,03	51,7	1,04	50,4
Profile 3	2,40	0,0	2,41	0,0	1,44	4,7	1,46	3,5
Profile 4	1,71	0,34	1,72	0,26	0,97	59,2	0,99	55,2
Profile 5	1,69	1,0	1,70	0,84	1,05	45,5	1,06	46,3
Profile 6	2,24	0,00	2,25	0,0	1,17	25,2	1,19	22,3

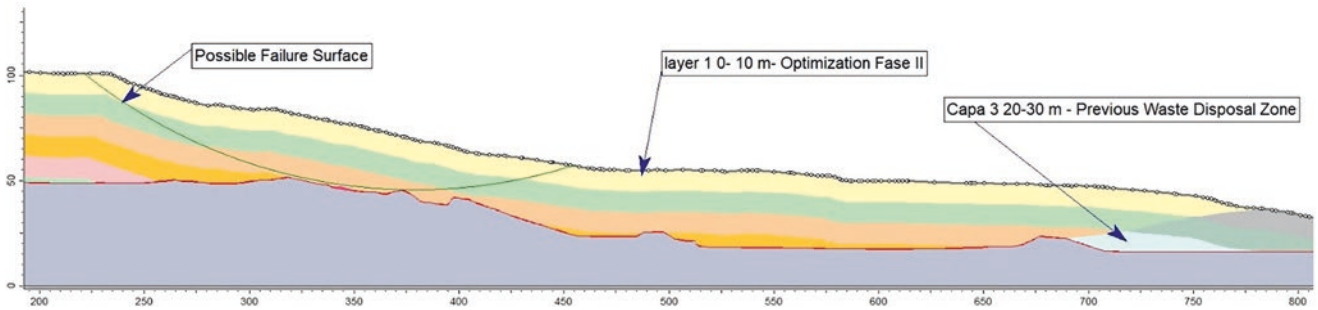

Fig. 18 Two-dimensional geotechnical model of profile 2

7 Hazard Analysis

Based on the stability analysis results, it is possible to make a hazard map in terms of the probability of failure (Pf). In this case, based on the methodological guide for studies of hazard, vulnerability, and risk of the Colombian Geological Service (Ávila et al. 2016), a high hazard level corresponds to an annual failure probability greater than 16%; a medium hazard level to a probability between 0.1% and 16%, and a low hazard level if the probability of failure is less than 0.1%. Figure 19 shows the hazard zoning map for static conditions. It can be seen on this map that there are two large areas in medium hazard level, and the rest is in low hazard level. One of the medium hazard level zones is near the Biogas treatment plant, which is one of the internal facilities of the sanitary landfill, located in a sector of high topographic slopes, and the other, in the sector of maximum pore pressure values, close to a neighbourhood called Mochuelo Alto. The stability models are very sensitive to slope and pressure, dictating these areas with the highest probability of failure.

Under pseudo-static conditions, the situation may be critical because, as shown in Table 3, predominates high-level hazard conditions with failure probabilities greater than 16%, showing the importance of a cautious operation in keeping the pore pressures as low as possible.

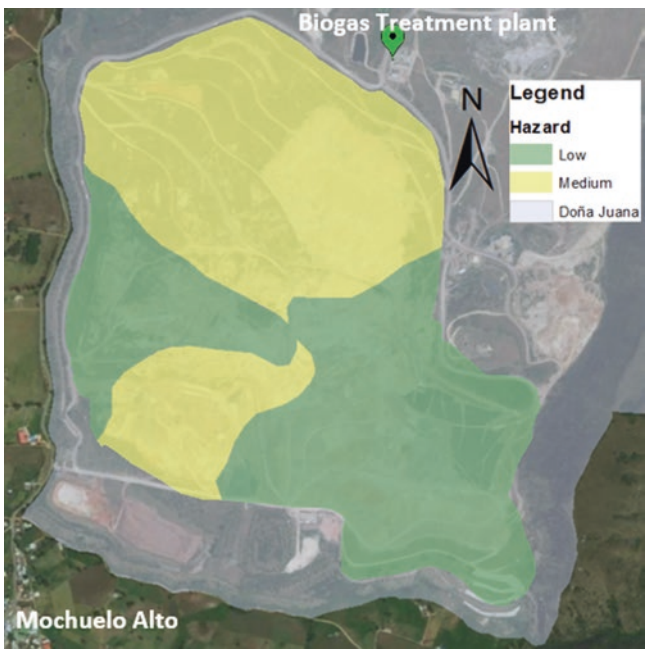

Fig. 19 Landslide Hazard map based on the probability of failure under static conditions

8 Conclusions

The Doña Juana Landfill has been forced to expand its useful life, forcing waste cells to be generated on top of older ones to optimize space. These changes have modified the original designs; therefore, continuous monitoring and opportune decision-making are required to guarantee stability.

Results of piezocone tests on the waste material showed that as depth increases, friction angle decreases and cohesion increases. This behaviour is consistent with the variation of the parameters in terms of the age of the waste material proposed by González and Espinosa (2003), who establish that the older a residue (more depth), the lower the friction angle and the greater cohesion.

The variable that most controls the stability of the waste landfill is the fluid pressure, for which an efficient extraction of leachate and gas is essential.

The leachate evacuation system by gravity suffered a general collapse and clogging, which made it necessary to adopt a forced extraction system by pumping. This system is not sufficient for an efficient leachate evacuation in a large sanitary landfill such as Doña Juana and although the hazard levels are in medium and low conditions, a failure or delay in the pumping could cause drastic increases in pressure and increase the hazard condition. It is also observed that with the current pressures, in the event of an earthquake, a high-hazard situation can be generated in a large proportion of the landfill.

The elements with the highest landslide exposure levels are Mochuelo Alto neighbourhood, where several low-income families live, and the internal biogas treatment plant.

Acknowledgements This paper has been based on the CPTu essays and the interpretation performed by Union Temporal INTER DJ and Saicon Engineering. The monitoring information was supplied by the UAESP (Special Administrative Unit of Public Services), managed by the District Administration of Bogotá. The authors wish to extend acknowledgement to these companies that shared the information.

References

Ávila G, Cubillos C, Granados A, Medina E, Rodríguez E, Rodríguez C, Ruiz G (2016) Guía metodológica para estudios de amenaza, vulnerabilidad y riesgo por movimientos en masa. Servicio Geológico Colombiano. 10.32685/9789589952856

Caicedo B, Giraldo E, Yamin L, Soler N (2002 January). *(PDF) the landslide of Dona Juana Landfill in Bogota. A Case Study*. Conference: Proceedings of the Fourth International Congress on Environmental Geotechnics (4th ICEG). https://www.researchgate.net/publication/274194377_the_landslide_of_Dona_Juana_Landfill_in_Bogota_A_Case_Study

Collazos H (1998) Deslizamiento de Basura en el Relleno Sanitario Doña Juana. CEPIS, Brussels

Daciolo V (2020) *Parâmetros de resistência de RSU: abordagem probabilística para análises de estabilidade de taludes de aterros de resíduos*. https://repositorio.ufscar.br/handle/ufscar/12886

González A, Espinosa A (2003a) *La falla Catastrófica del Relleno Sanitario Doña Juana en 1998—Bogotá—Colombia*

González A, Espinosa A (2003b). Presión de poros y Resistencia al Cortante en el Relleno Sanitario Doña Juana- Bogotá Colombia. *Boletín Colombiano de Geotecnia*

Kulhawy FH, Mayne PW (1990) Manual on estimating soil properties for foundation design. Electric Power Research Institute

Ramaiah BJ, Ramana GV, Datta M (2017) Mechanical characterization of municipal solid waste from two waste dumps at Delhi, India. Waste Manag 68:275–291. https://doi.org/10.1016/J.WASMAN.2017.05.055

Robertson PK (2016) Cone penetration test (CPT)-based soil behaviour type (SBT) classification system — an update. Can Geotech J 53(12):1910–1927. https://doi.org/10.1139/CGJ-2016-0044

UAESP, UT INTER DJ, & Saicon Ingenieria SAS (2023) *Report 3. Addition 9. Contract 130E - 2011*

Multiple Landslides in an Area Draped in Volcanic Matters: The Dual Impacts of Rains and Earthquakes

Alessandra M. Nakata, Kazuo Konagai, and Ryo Onishi

Abstract

The devastating 2018 Hokkaido Eastern Iburi Earthquake, with a moment magnitude (M_w) of 6.7, inflicted significant damage in the eastern part of Hokkaido, Japan, resulting in the tragic loss of 41 lives, with landslides accounting for 36 fatalities. The mountainous epicentral regions experienced a high number of landslides, primarily induced by the movement of tephra strati originating from eruptions associated with Shikotsu Caldera, Mt. Tarumae, and Mt. Eniwa. The combined intensity of the earthquake and the accumulation of rainfall played crucial roles in initiating these landslides. To gain comprehensive insights into the dynamics of this event, we utilized the Multi-Scale Simulator for the Geo-Environment (MSSG) to simulate the spatial and temporal patterns of rainfall from August 6 to September 5, 2018. Our simulation results were effectively validated against observed data from weather stations operated by the Japan Meteorological Agency (JMA) in the epicentral area. Impressively, the simulation accurately captured the intricate variations in rainfall, taking into account the influence of the region's mountainous terrain. Notably, our findings revealed a noteworthy relationship: as the peak ground acceleration (PGA) increases, the required threshold of rainfall for triggering landslides decreases. This study enhances our understanding of the complexities surrounding landslide dynamics in earthquake-prone areas and contributes to improved disaster preparedness and mitigation efforts.

A. M. Nakata (✉) · K. Konagai
International Consortium on Landslides, Kyoto, Japan

R. Onishi
Tokyo Institute of Technology, Tokyo, Japan
e-mail: onishi.ryo@gsic.titech.ac.jp

Keywords

Hokkaido Eastern Iburi earthquake · Landslides · Multi-Scale Simulator for the Geo-Environment · Peak ground acceleration

1 Introduction

Landslides are typically triggered by specific events such as heavy rainfall, intense earthquakes, or a combination of both. It is important to consider the combined effect of these factors, as even a seemingly minor event can ultimately lead to a devastating landslide if the mass is brought close to the tipping point. Recent research by Martino et al. (2022) has revealed a noticeable increase in landslide activity following low-magnitude earthquakes. Additionally, Sassa et al. (2010) conducted an enlightening study using real monitored earthquake records and an undrained dynamic-loading ring shear test. They demonstrated that a minor earthquake with a magnitude of 2.6, 22 km west of the source area, could have triggered the catastrophic 2006 Leyte landslide in the Philippines, claiming the lives of over 1000 people.

On September 6, 2018, at 3:08 a.m. JST, a powerful earthquake with a magnitude of M_w 6.7 struck the northern Japanese island of Hokkaido, leaving a lasting impact. The Japan Meteorological Agency (JMA) officially named it the "2018 Hokkaido Eastern Iburi Earthquake." This seismic event unleashed a series of devastating consequences, including the triggering of over 7,000 landslides within an approximately 20 km × 20 km area near Atsuma Town, as documented by Murakami et al. (2019a, b). These landslides ravaged homes that were sparsely scattered along the foothills of the mountains. The scale of the landslides caused by this intense tremor was unprecedented, encompassing an extensive area of 44 km^2, as the Japanese Ministry of Land, Infrastructure, Transport, and Tourism (MLIT) reported. This record-breaking extent surpassed any previous occurrence since the

B. Abolmasov et al. (eds.), *Progress in Landslide Research and Technology, Volume 3 Issue 1, 2024*, Progress in Landslide Research and Technology, https://doi.org/10.1007/978-3-031-55120-8_6

Meiji Era (1868-1910), highlighting the magnitude of the disaster. Tragically, around 80% of the 41 victims lost their lives due to suffocation, further emphasizing the severe consequences of this catastrophic event.

The intense seismic activity undeniably played a significant role in triggering the numerous landslides. Some news reports, such as The Asahi Shinbun (2018), raised the possibility that the landslides could have been influenced by the rainfall brought by Typhoon Jebi, which passed through Hokkaido one day before the earthquake, leaving a trail of destruction in its wake. However, the daily rainfall recorded at the Atsuma AMeDAS (Automated Meteorological Data Acquisition System) station, located near the area affected by multiple landslides, was only 12 mm. More importantly, the region had experienced rainfall that was 1.5 times higher than the average for August, adding further context to the weather conditions leading up to the event.

This unfortunate event has provided a unique and valuable opportunity to gain insights into its underlying causes, specifically the role of preceding rainfall and intense seismic activity. This event is particularly significant due to the considerable number of comparable landslides observed in the epicentral area, characterized by the presence of moist pumice-rich volcanic materials. In this article, we delve into the factors contributing to the landslides in the Atsuma region by employing the Multi-Scale Simulator for the Geo-Environment (MSSG) (Takahashi et al. 2006, 2013). This sophisticated model, designed to serve as a coupled non-hydrostatic atmosphere-ocean-land simulation tool, allows us to simulate the rainfall patterns in August and subsequent minor precipitation events, enabling a comprehensive analysis of their impact.

2 Multiple Landslides in the 2018 Hokkaido Eastern Iburi Earthquake

The epicentral area of the 2018 Earthquake in the eastern Iburi region of Hokkaido, located approximately 50 km southeast of Sapporo, was heavily affected by multiple landslides. These landslides were densely distributed throughout the mountainous terrain, with altitudes ranging from 200 to 400 m. The epicentral area is characterized by ridges and valleys, stretching from NNW to SSE. Smaller mountain streams have eroded the primary valley walls within this region, carving deep channels down to lower elevations. Figure 1 illustrates that multiple landslides appeared on these valley walls.

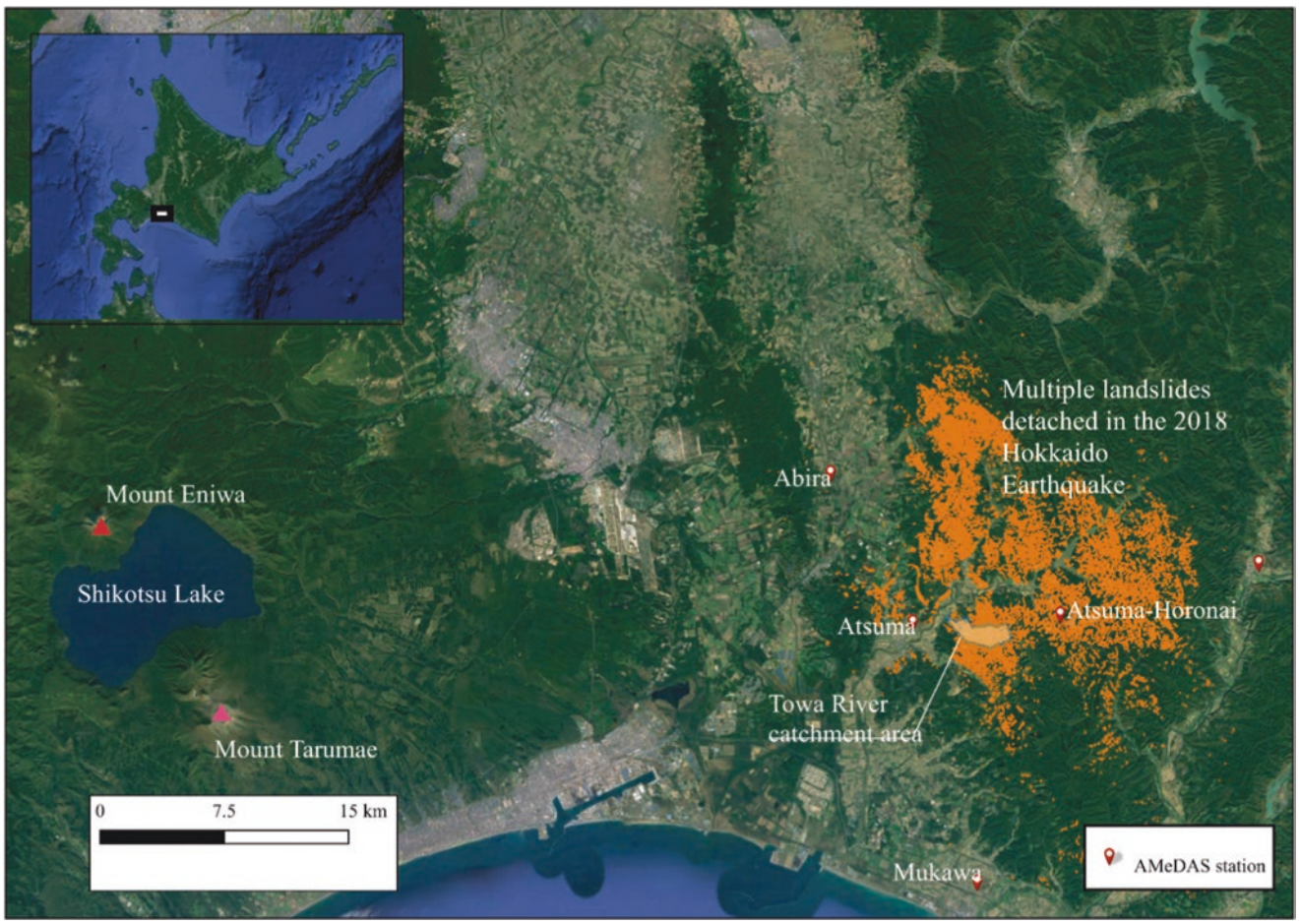

Fig. 1 Landslide inventory map prepared after the 2018 Hokkaido Eastern Iburi Earthquake (Coordinate Reference System: WGS 84 / UTM zone 54 N)

The basement complex of the area primarily consists of sedimentary rocks from the Neogene tertiary system, including layers of mudstone, siltstone, sandstone, and conglomerate (Ozaki and Komatsubara 2014). However, the entire region is significantly covered by three distinct pyroclastic fall deposits resulting from volcanic eruptions west of the area. One such notable feature is the Shikotsu Caldera, a magnificent volcanic caldera formed approximately 40,000 years ago through a massive eruption. Mount Tarumae, one of Hokkaido's most active volcanoes, has a long history of eruptions dating back around 20,000 years. Approximately 9000 years ago, Mount Eniwa volcano experienced a significant eruption that profoundly impacted the surrounding landscape. Consequently, the majority of the multiple landslides in the area were shallow and attributed to these layers of volcanic ash and debris, known as tephra strati (Kawamura et al. 2019).

Utilizing the LiDAR Point Cloud data obtained from the Geospatial Information Authority of Japan (GSI) and the multiple landslides polygons provided by Kita (2018) conducted an estimation revealing that the total area affected by the multiple landslides spans approximately 44 km^2. In another study, Murakami et al. (2019a) used a 5m-resolution Digital Elevation Model (DEM) provided by the GSI to examine the distribution of average gradients in the Towa River catchment, where shallow landslides accounted for 35.6% of the entire catchment area (refer to Fig. 2). Notably, the analysis indicated that most frequently occurring slope angle (mode value) was 27.5 °degrees, with over 70% of the slope angles measuring below 30 ° (Fig. 2 provides a visual representation of this distribution).

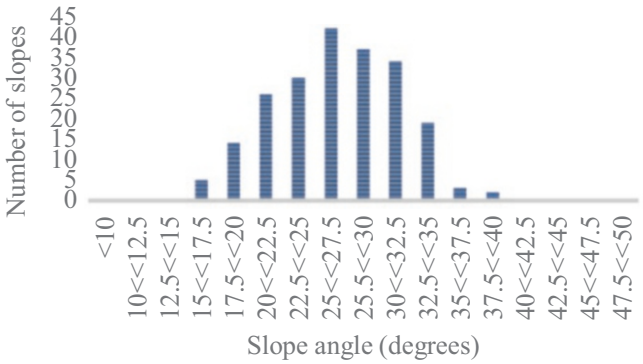

Fig. 2 Distribution of the average gradients of shallow landslides within the Towa River catchment (After Murakami et al. 2019a). The Zonal Statistics Plugin (QGIS) was used to calculate the average gradient for each landslide polygon

3 Preceding Rains

At the time of the earthquake, the epicentral area had four operational Automated Meteorological Data Acquisition System (AMeDAS) stations, which were part of the Japan Meteorological Agency (JMA) network. These stations were located in Abira (42.81333°N, 141.8283°E), Atsuma (42.73°N, 141.8883°E), Mukawa (42.59°N, 141.9333°E), and Hobetsu (42.76167°N, 142.14333°E), with distances between them ranging from 10 to 20 km (see Fig. 3). Figure 4 displays the cumulative rainfall data recorded by these four stations over a two-month period, from July 1 to September 6, 2018, the day of the earthquake. While the cumulative values differ among the stations, the overall patterns are similar. To emphasize this similarity, Fig. 5 normalizes the data, with the final normalized cumulative values converging to 1.0 on September 6. This normalization highlights that the epicentral area likely experienced a comparable rainfall pattern, albeit with varying amounts of rainfall recorded at each station. Specifically, the pattern consisted of heavy rain in early July lasting for two weeks, followed by three weeks of sunny weather, and then intermittent rainfall episodes from August 4 to September 5.

The influence of rainfall on landslides highly depends on the time-lapse between rainfall and the earthquake. This time-lapse plays a crucial role in determining the moisture conditions within the porous volcanic materials. During rain events, precipitation infiltrates the ground, leading to an increase in moisture content. However, subsequent drainage through seepage flows and evaporation from the ground surface can decrease moisture content. These fluctuations in moisture content directly impact slope stability and can have significant implications for the occurrence of landslides.

At this stage, our primary focus is directed toward the one-month period leading up to the earthquake on September 6. This particular time frame was chosen because the porous pumice, a prevalent material in the region, has a high-water retention capacity. Additionally, as depicted in Figs. 4 and 5, it is plausible that the entire epicentral area experienced a consistent pattern of rainfall. By specifically considering the one-month period of rain, our objective is to investigate the potential impact of this sustained precipitation on the subsequent occurrence of landslides triggered by the earthquake.

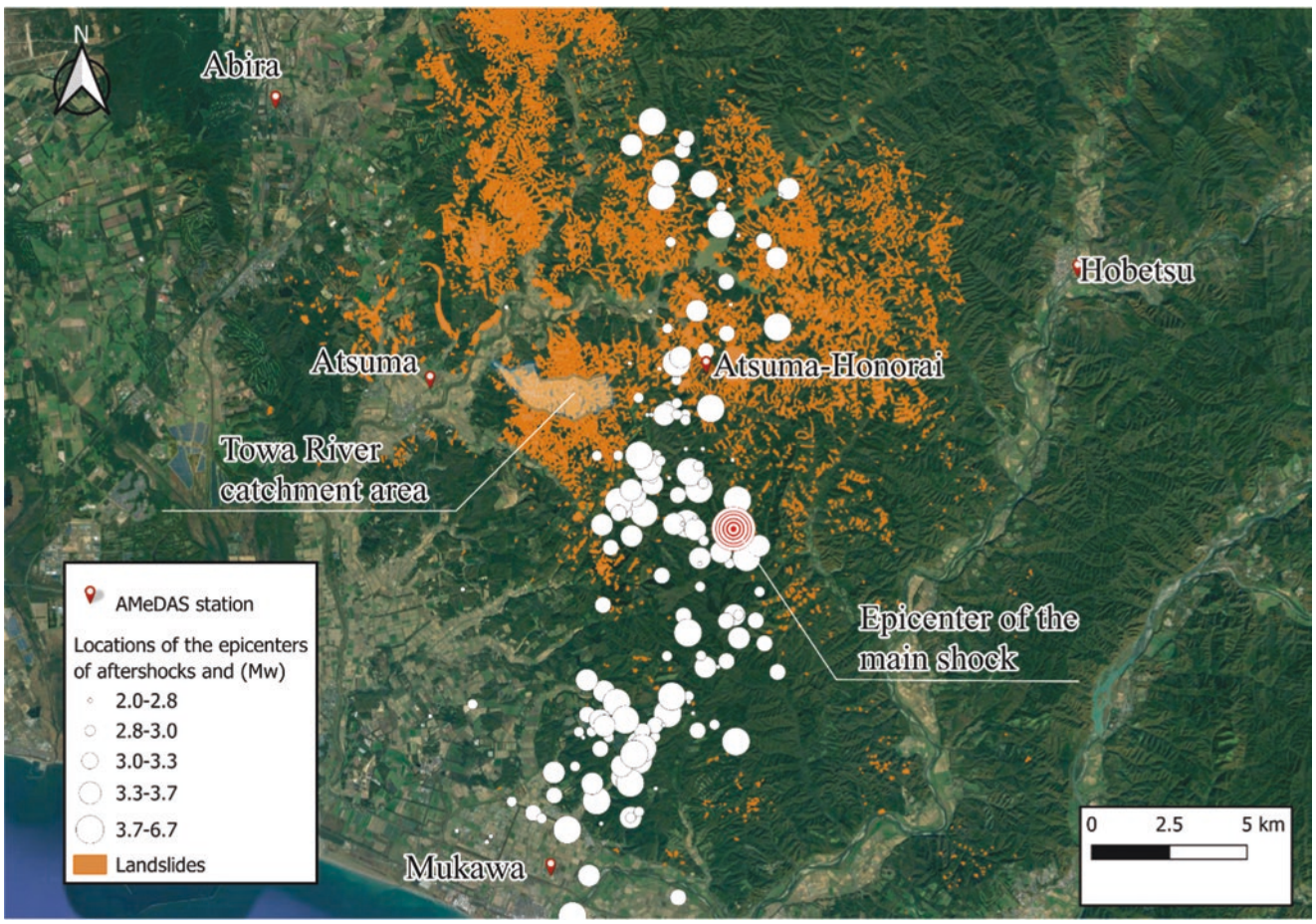

Fig. 3 AMeDAS Stations by JMA in the Epicentral Area: Atsuma-Horonai Station Commences Observation Three Weeks After Earthquake, Aiding Reconstruction Efforts (Coordinate Reference System: WGS 84 / UTM zone 54 N)

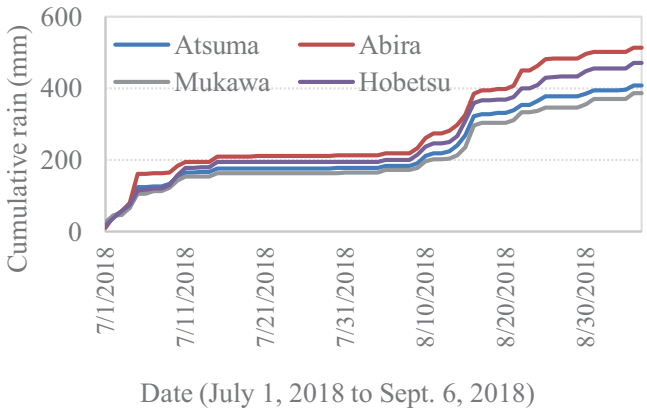

Fig. 4 Cumulative rains at four AMeDAS stations over about two-month from July 1 to September 6, 2018

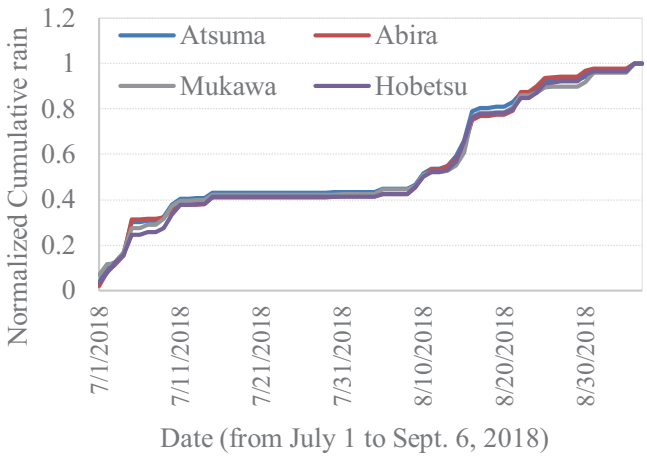

Fig. 5 Normalized Cumulative Rainfall: Two-Month Observation at Four AMeDAS Stations in the Epicentral Area (July 1 - September 6, 2018)

4 Method

The MSSG model(Takahashi et al. 2013, 2006), developed through a collaboration between JAMSTEC, Tokyo Institute of Technology, and Waseda University, offers a comprehensive and advanced tool for simulating and analyzing complex weather and climate phenomena. Its high-resolution capabilities, innovative grid systems, and consideration of turbulence-enhanced cloud dynamics make MSSG a valuable asset in understanding atmospheric processes at various scales and investigating rainfall patterns in mountainous regions susceptible to landslides.

For global-scale simulations, MSSG employs the innovative Yin-Yang grid system (Kageyama and Sato 2004), resembling the interconnected skins of a tennis ball. This grid system utilizes square patterns that minimize distortions, effectively overcoming challenges associated with the polar singularity. By accurately representing grid shapes and sizes, MSSG ensures a more precise depiction of global phenomena. Conversely, for regional-scale simulations, MSSG utilizes the conventional latitude-longitude system, offering a reliable framework to analyze localized weather phenomena and their regional impacts.

A notable feature captured by MSSG in its simulations is the turbulence-enhanced collision of cloud droplets. This phenomenon accounts for the rapid growth of cloud droplets, leading to the swift initiation of rainfall during the early stages of cloud development. MSSG explicitly incorporates this effect, which holds particular significance in mountainous regions facing prevailing winds. This characteristic makes MSSG particularly suitable for simulating rainfall in such environments prone to landslides, as it accurately captures the precipitation dynamics.

5 Rainfall Modeling

To conduct the numerical simulation, we employed a multi-domain approach, utilizing three nested domains with progressively finer grid spacings of 8 km, 2 km, and 300 m (refer to Fig. 6). The largest domain covered a significant portion of Hokkaido Island, while the smallest domain was specifically designed to encompass the target area of the epicenter. The geographical boundaries for this innermost domain were defined as 141.777°E to 142.0333°E in longitude and 42.5837°N to 42.83731°N in latitude. In order to ensure the accuracy and reliability of the simulation results, three AMeDAS stations, namely Abira, Atsuma, and Mukawa, were included within this domain for verification purposes.

Prominent meteorological agencies worldwide, such as the Japan Meteorological Agency (JMA), the United States National Centers for Environmental Prediction (NCEP), and the European Centre for Medium-Range Weather Forecasts (ECMWF), have developed advanced global numerical weather forecasting schemes. JMA, in particular, has been providing global weather forecasts since 1988, continuously enhancing its model by incorporating data from newly launched satellites and improving resolution in both the vertical and horizontal dimensions. To simulate the 2018 event, the boundary conditions for the outermost domain utilized the Global Spectral Model (GSM2003), featuring a horizontal grid spacing of 20 km and 128 layers extending up to the uppermost layer at 0.1 hPa.

Figure 7 presents the distribution of one-month simulated rainfall within the innermost nested domain, revealing a distinct concentration of orange polygons in the upper-right quarter. These polygons correspond to multiple landslides triggered by the M_w 6.7 earthquake that followed the August rain, with the largest open circle marking the earthquake's epicenter. Surrounding the epicenter, smaller open circles

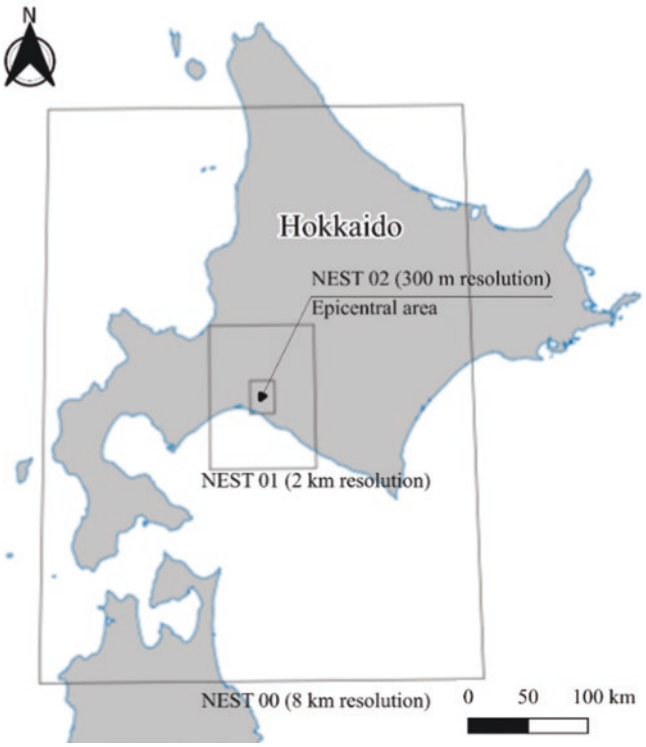

Fig. 6 Nested domains (Coordinate Reference System: WGS 84 / UTM zone 54 N)

indicate the locations of aftershock epicenters recorded on September 6 and 7. The swarm of landslides exhibits partial overlap with the cluster of aftershock epicenters. Interestingly, even the northwestern section of the landslides, situated several kilometers away from the outer periphery of the aftershock epicenter cluster, aligns with the area of intense rainfall accumulation. Hence, this figure underscores the contribution of both the earthquake's intense shaking and the accumulated rainfall to the occurrence of these numerous landslides.

(1) Centroids of landslide polygons within the innermost domain for rain simulation.
(2) One-month cumulative rains and hypocentral distances at centroids of landslide polygons.

In addition, the right side of Fig. 7 includes three sub-figures depicting the rainfall accumulations at the AMeDAS stations (Abira, Atsuma, and Mukawa). The observed rain accumulations are represented by thick orange lines, while the simulated accumulations for the three nested computational domains are also compared. As the grid spacing decreases, the estimated rainfall accumulation is closer aligned to the observed values at each station. This alignment highlights the improved capability of MSSG to capture detailed varia-

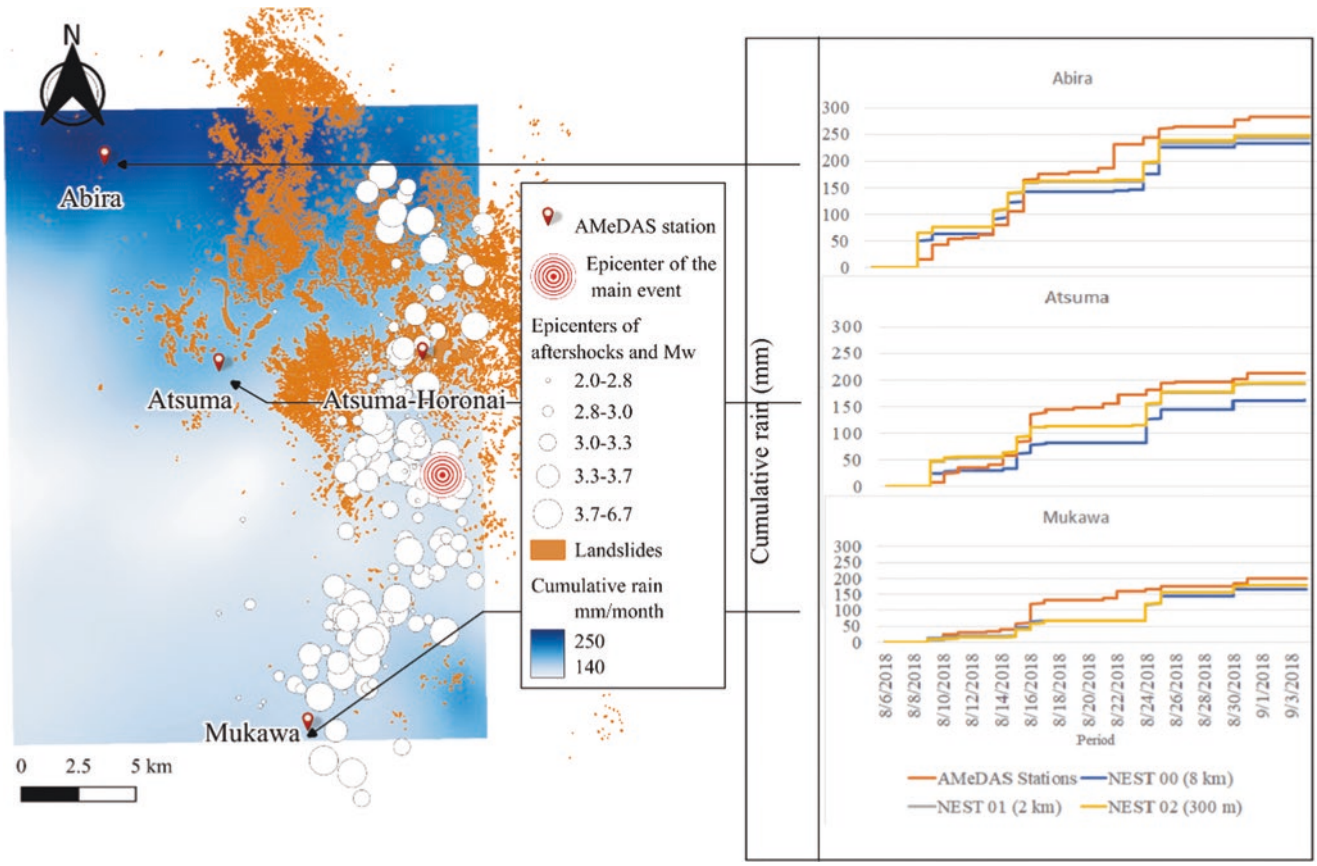

Fig. 7 Spatial distribution of simulated one-month rainfall within the finely-resolved nested domain and a comparative analysis of simulated and observed rainfall accumulations at AMeDAS Stations using MSSG

tions in rainfall patterns influenced by mountainous regions. Although the MSSG simulation did not perfectly replicate every event due to spatial and temporal fluctuations, the one-month simulated rainfall accumulations at the three AMeDAS stations (280 mm, 210 mm, and 200 mm) eventually concur with the observed values (250 mm, 190 mm, and 180 mm), thus validating the effectiveness of the current approach.

6 Impact of Rains and Earthquake

The peak ground acceleration (PGA) of the bedrock gradually diminishes as the hypocentral distance increases. Hence, in order to assess the influences of these contributing factors on the occurrence of multiple landslides in the region, the hypocentral distances and the values of one-month rainfall accumulation were estimated at the centroids of the landslide polygons. Firstly, the centroids of the 3551 landslide polygons within the innermost computational domain, NEST02, were extracted (see Fig. 8(1)). Subsequently, the hypocentral distances, representing the distances from all these 3551 points to the seismic focus of the main shock (42.6900°N, 142.0067°E, Depth = 37 km), were determined. The raster values of the rainfall accumulation were then sampled at these points, as depicted in Fig. 8(2). The upward-to-the-right inclination of the point cluster in this figure indicates that as the hypocentral distance increases, a higher amount of rainfall is required for a landslide to initiate sliding.

To estimate the PGA values at the centroids of the landslide polygons within the innermost domain NEST02, we utilized an empirical attenuation formula proposed by Si and Midorikawa (1999). This formula serves as a reliable method for predicting the PGA values based on specific parameters.

$$\log_{10} A = b - \log_{10} X_{eq} - kX_{eq}, \tag{1}$$

where

$$A = \text{peak ground acceleration}\left(\text{PGA}, \frac{\text{cm}}{\text{s}^2}\right) \text{or}$$

$$\text{peak ground velocity}\left(\text{PGA}, \text{cm/s}\right)$$

$$b = aM_w + hD + d + e, \tag{2}$$

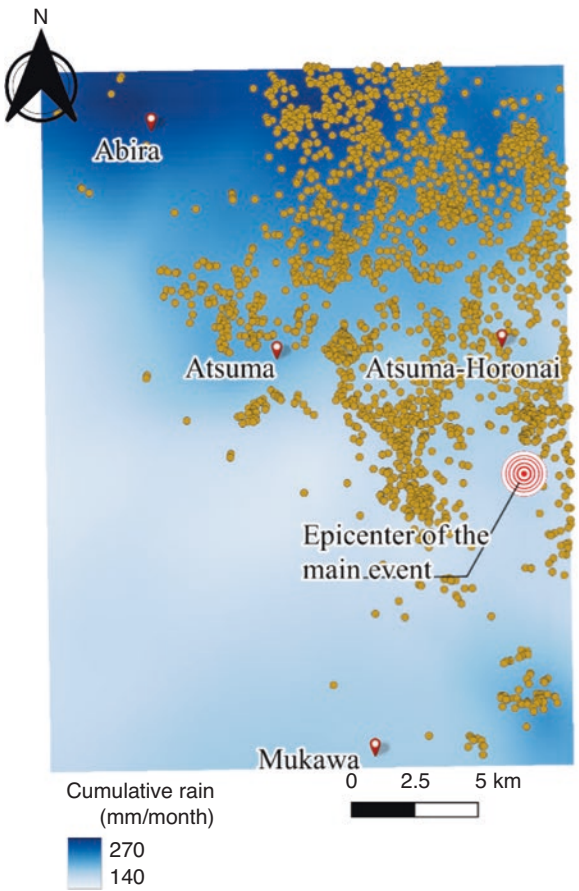

(1) Centroids of landslide polygons within the innermost domain for rain simulation.

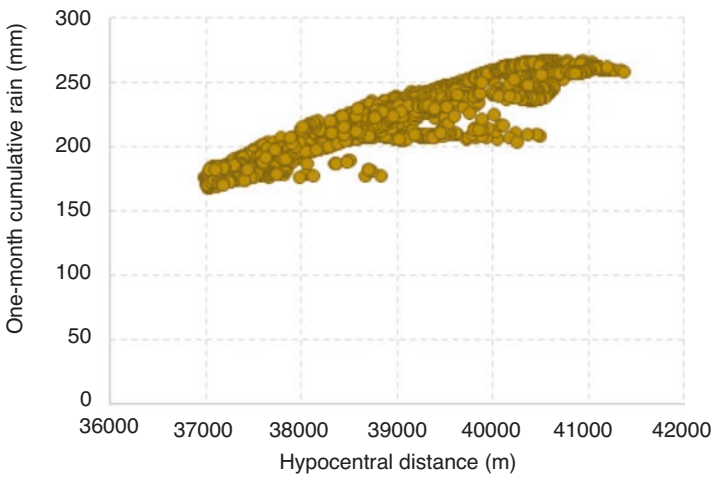

(2) One-month cumulative rains and hypocentral distances at centroids of landslide polygons.

Fig. 8 Simulation of One-month cumulative rains (mm) in the epicentral area. (Coordinate Reference System: JGD2011 / Japan Plane Rectangular CS XII)

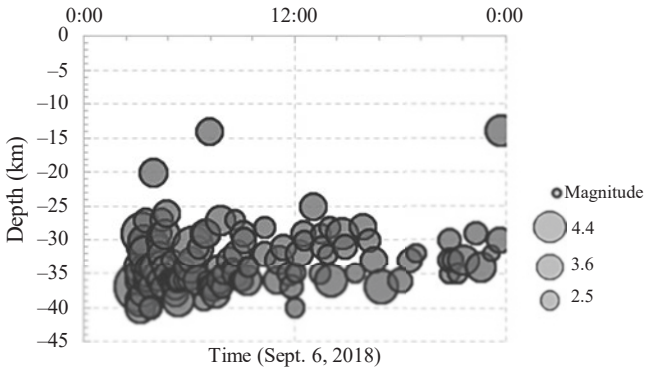

Fig. 9 Probing Depths of Aftershocks: Focal Depths Analysis on September 6, 2018 (The width of each circle represents the magnitude of the corresponding aftershock, which is also shown by the number inside).

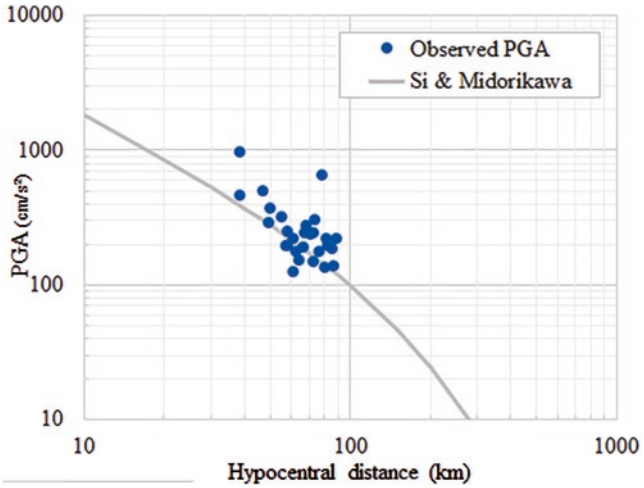

Fig. 10 Mapping Ground Shaking: Observation of Peak Ground Accelerations (PGAs) at 27 Hokkaido Observatories and Estimating PGA Attenuation Based on Epicentral Distance

with

$a = 0.5$, M_w= Moment magnitude, $h = 0.0036$, D = focal depth (km),

$$d = \begin{cases} 0.00 & \text{for crustal earthquakes} \\ 0.09 & \text{for interplate earthquakes} \\ 0.28 & \text{for } \textbf{intraplate earthquakes} \end{cases}, \quad e = 0.60,$$

and X_{eq} = Equivalent hypocentral distance (km),

$$k = \begin{cases} 0.003 & \textbf{for PGA} \\ 0.002 & \text{for PGV} \end{cases}$$

The equation shown above incorporates several variables, including the moment magnitude (M_w) of the earthquake, the fault distance or equivalent hypocentral distance (X), the focal depth (D), and constants representing the earthquake type (crustal, interplate, or intraplate). The equivalent hypocentral distance (X) is the energy-weighted arithmetic mean of the fault distances from each landslide to the sub-faults forming the complete fault rupture plane. In the case of this earthquake, since most of the aftershocks on September 6 had focal depths deeper than 30 km and close to the 37 km deep hypocenter of the main shock (as depicted in Fig. 9), it can be assumed that the equivalent hypocentral distance (X) is nearly equal to the hypocentral distance. Based on this assumption, Fig. 10 compares the estimated PGA values and the recorded values at 27 observatories in Hokkaido (Japan Meteorological Agency 2018). It is important to consider that not all observatories were situated on bedrock, which explains why the line of the attenuation formula aligns with the lower bound of the group of 27 points representing the observed PGA values. With this validation, Fig. 11 illustrates the estimated PGAs and the values of rainfall accumulation at the centroids of the 3551 landslide polygons within the innermost domain NEST02. The downward-to-the-right inclination of the point cluster in this figure signifies that as the PGA increases, less rainfall is required for a landslide to initiate sliding.

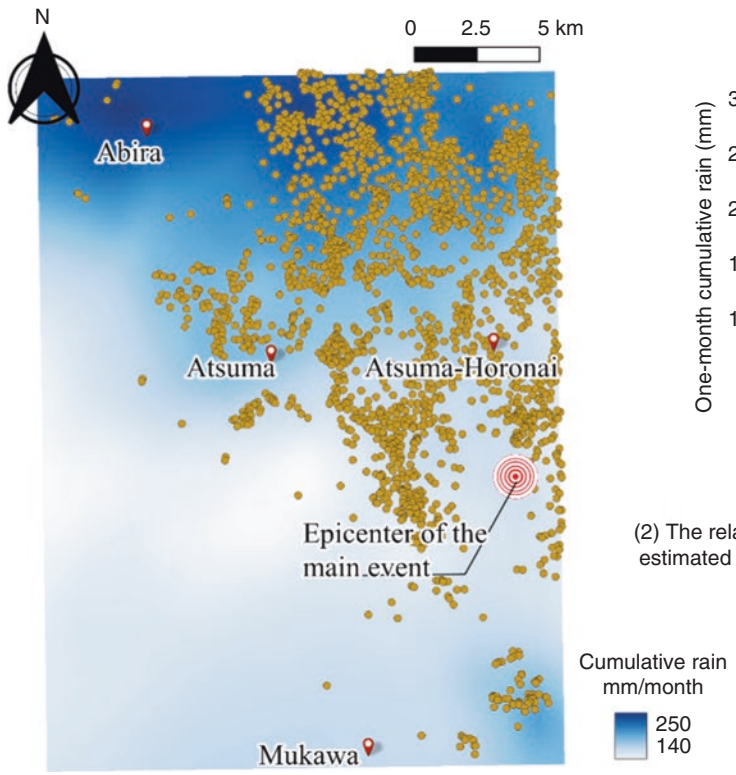

(1) Centroids of landslide polygons within the innermost domain for rain simulation.

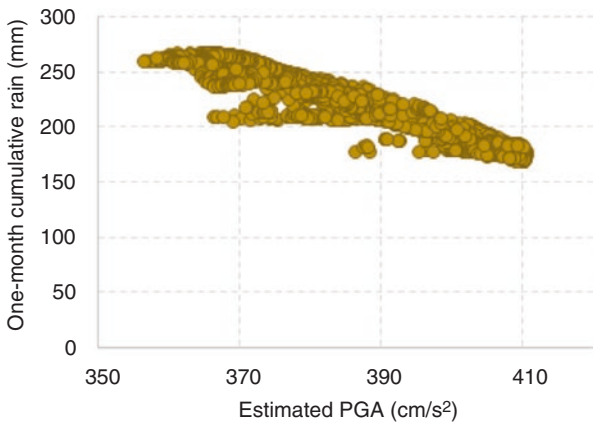

(2) The relation between the one-month cumulative rains and estimated PGAs at centroids of landslide polygons.

Fig. 11 Simulation of One-month cumulative rains (mm) in the epicentral area. (Coordinate Reference System: JGD2011 / Japan Plane Rectangular CS XII)

7 Conclusions and Future Works

The devastating 2018 Hokkaido Eastern Iburi Earthquake, with a moment magnitude (M_w) of 6.7, inflicted severe damage in the eastern part of Hokkaido, Japan, resulting in the tragic loss of 41 lives, with landslides responsible for 36 of those fatalities. The mountainous epicentral regions experienced numerous landslides, primarily triggered by the movement of tephra strati originating from eruptions associated with Shikotsu Caldera, Mt. Tarumae, and Mt. Eniwa. The combined intensity of the earthquake and the accumulation of rainfall played crucial roles in initiating these landslides.

To gain deeper insights into the dynamics of this event, we utilized the Multi-Scale Simulator for the Geo-Environment (MSSG) to simulate the spatial and temporal patterns of rainfall from August 4 to September 5. Our simulation results were validated against observed data from weather stations operated by JMA in the epicentral area. Impressively, the simulation successfully captured the intricate variations in rainfall influenced by the region's mountainous terrain. Notably, our findings indicated that less rainfall is required for a landslide to be triggered as the PGA increases.

To facilitate further rational discussions, we need to shift focus from one-month cumulative rainfall to soil water indices that quantify the moisture conditions of the soil. However, this process necessitates additional hydrogeological and geotechnical studies, particularly on the porous pumice—a prevalent material in the region known for its high-water retention capacity. Furthermore, slope angles must also be considered, and detailed findings in this regard will be presented in forthcoming publications.

Acknowledgments This study was undertaken as a component of the Japanese government program SATREPS (Science and Technology Research Partnership for Sustainable Development), specifically focusing on the "Development of Early Warning Technology for Rain-Induced Rapid and Long-Travelling Landslides" (Japan Science and Technology Agency 2020). Within this program, the accurate prediction of rainfall in mountainous regions constitutes a vital technological aspect.

Appendix: Timeline

The events in this article are presented in Japanese Standard Time (JST), which is 9 h ahead of he Coordinated Universal Time (UTC).

References

Japan Meteorological Agency (2018) Strong ground motion records – The Hokkaido Eastern Iburi Earthquake at 3:07 AM on Sept. 6, 2018, https://www.data.jma.go.jp/eqev/data/kyoshin/jishin/1809060307_hokkaido-iburi-tobu/index.html

Japan Science and Technology Agency (2020) Predict catastrophic landslides a day in advance: Development of Early Warning Technology of Rain-Induced Rapid and Long-Travelling Landslides, Science and Technology Research Partnership for Sustainable Development (SATREPS), https://www.jst.go.jp/global/english/kadai/r0110_sriLanka.html

Kageyama A, Sato T (2004) The Yin-Yang grid: an overset grid in spherical geometry. Geochem Geophys Geosyst 5:Q09005. https://doi.org/10.1029/2004GC000734

Kawamura S, Kawajiri S, Hirose W, Watanabe T (2019) Slope failures/landslides over a wide area in the 2018 Hokkaido Eastern Iburi earthquake. Soils Foundations 59(6):2376–2395., ISSN 0038-0806. https://doi.org/10.1016/j.sandf.2019.08.009

Kita K (2018) Shapefiles of landslides traced from the ortho aerial photographs of the epicentral area of the 2018 Hokkaido Eastern Iburi Earthquake provided by GSI, Japan. https://github.com/koukita/2018_09_06_atumatyou

Martino S, Fiorucci M, Marmoni GM et al (2022) Increase in landslide activity after a low-magnitude earthquake as inferred from DInSAR interferometry. Sci Rep 12:2686. https://doi.org/10.1038/s41598-022-06508-w

Murakami Y, Nishihara T, Mizugaki S (2019a) Terrain interpretation of multiple landslides caused by the 2018 Hokkaido Eastern Iburi Earthquake, Monthly Report of the Civil Engineering Research Institute for Cold Region, No. 801, 66-71, 2022. https://thesis.ceri.go.jp/db/documents/public_detail/64660/

Murakami Y, Mizugaki S, Nishihara T, Inami Y, Fujinami T (2019b) Characteristics of landslides triggered by Hokkaido Eastern Iburi Earthquake in 2018. Advances in River Engineering 25:645–650. https://doi.org/10.11532/river.25.0_645

Ozaki M, Komatsubara T (2014) 1:200,000 land geological map in the Ishikari depression and its surrounding area with explanatory note. https://www.gsj.jp/data/coastalgeology/GSJ_SGMCZ_S4_2014_03_b.pdf

Sassa K, Nagai O, Solidum R, Yamazaki Y, Ohta H (2010) An integrated model simulating the initiation and motion of earthquake and rain-induced rapid landslides and its application to the 2006 Leyte landslide. Landslides 7:219–236. https://doi.org/10.1007/s10346-010-0230-z

Si H, Midorikawa S (1999) New attenuation relationship for peak ground acceleration and velocity considering effects of fault type and site condition. J Struc Constr Eng AIJ 523(63–70):1999.6. https://doi.org/10.3130/aijs.64.63_2

Takahashi K, Peng X, Onishi R, Ohdaira M, Goto K, Fuchigami H, Sugimura T (2006) Multi-scale weather/Climate simulations with Multi-Scale Simulator for the Geoenvironment (MSSG) on the Earth Simulator, Annual Report of the Earth Simulator Center, April 2005–March 2006, pp. 31–39. https://www.jamstec.go.jp/es/jp/output/publication/annual/annual2005/pdf/P071_Takahashi.pdf

Takahashi K, Onishi R, Baba Y, Kida S, Matsuda K, Goto K, Fuchigami H (2013) Challenge toward the prediction of typhoon behaviour and down pour. J Phys Conference Series 454:012,072. https://iopscience.iop.org/article/10.1088/1742 6596/454/1/012072

The Asahi Shinbun (2018, Sept 6) Volcanic products and the Typhoon may have caused landslides, https://www.asahi.com/articles/ASL9651KHL96ULBJ00Y.html

Loess Landslides–Peculiarities of Deformation Mechanism

Oleg V. Zerkal and Olga S. Barykina

Abstract

Loess on the Earth occupies an area of more than 13 million km^2. The greatest spread of loess is in Europe and Asia (mainly south of 62°N), where vast areas are composed of loess from the surface, the thickness of which varies in Europe from a few meters to 20–30 m, and in the Caucasus, in intermountain hollows of Central Asia, China-from 50–60 m to 100 m and more. The peculiarity of loess is its predisposition to the development of subsidence-compaction during moistening under the action of both their own weight and external loads. As a result, in the areas of loess distribution, in addition to classical landslide forms, a special type of landslides is often observed, in the formation of which subsidence plays a significant role. The main factors in the formation of "subsidence landslides" are a decrease in the strength of loess as a result of increasing water cut. Underground water moistens the loess thickness from below to the state when its structure breaks under its own weight and subsidence begins with the formation of cracks on the day surface. Further moistening and destruction of the loess structure continues at the expense of both groundwater and atmospheric water absorbed through cracks. Such combination of conditions determines further development of subsidence phenomena and subsequent landslide deformations. The rate of displacement of such landslides depends on the extent and rate of subsidence development at the base of the slope. "Subsidence landslides" can be defined as a type of complex landslides.

Keywords

Loess · Subsidence · Loess landslides · Typology · Mechanisms

O. V. Zerkal (✉) · O. S. Barykina
Lomonosov Moscow State University, Geological Department, Moscow, Russia
e-mail: zerkalov@geol.msu.ru; barykina@geol.msu.ru

1 Introduction

Loess is a peculiar quaternary eolic deposit, mainly composed by silt and characterized by specific structure (macroporosity—up to 42–55% with predominance of open large pores) and properties (subsidence). It is widespread on a large territory of the Earth. The important question is to study the regularities of loess formation, properties and variability. The thickness of loess strata can vary from several meters to more than a 100 m. The development of landslides in loesses, which have significant variability of strength characteristics under watering, high sensitivity to dynamic impacts, often causes huge damage, and in some cases is catastrophic, especially in case of earthquakes (Zerkal 1994; Voznesensky and Zerkal 1997; Kalinin et al. 1998). Such peculiarities can cause landslides in regions were loess is widely spread.

The occurrence of landslides in the regions of loess spreading is characterized by certain peculiarities. These peculiarities are caused by the presence of some specific properties of loess:

- ability of loess in dry condition (at natural humidity less than 10%) to form vertical slopes;
- significant reduction of loess strength when moistened due to rapid destruction of structural connections formed by carbonates and water-soluble salts;
- predisposition of loess to subsidence—compaction under moistening under the action of both its own weight and external loads;
- ability of loess rocks to instantaneous loss of strength under dynamic impacts;
- cyclic structure of loess strata, which is an interlacing of loess and paleo-soil horizons.
- The paleo-soils present in the loess strata are more clayey and form relative waterfalls, contributing to uneven watering of massifs. As a consequence, the deformations of loess slopes are easily recognized in many parts of the

B. Abolmasov et al. (eds.), *Progress in Landslide Research and Technology, Volume 3 Issue 1, 2024*, Progress in Landslide Research and Technology, https://doi.org/10.1007/978-3-031-55120-8_7

earth and associated landslides are characterized by certain type of peculiarities, later on described in detail.

2 Loess and Its Prevalence

Loess is one of the most widespread type of continental Quaternary sediments. Loess on the Earth globe cover an area of more than 13 million km^2 (Trofimov et al. 2001, Ding, Editor 1 et al. (eds), Progress in Landslide Research and Technology, Volume 3 Issue 1, 2023, Book Series of the International Consortium on Landslides. DOI Ding et al. 2019). They cover more than 3% of the Earth's land area and are found on all continents except Antarctica. The loesses are most widely distributed in Europe and Asia.

In Europe, loess is not evenly widespread. Western and Central Europe are characterized by their "island" distribution (Trofimov et al. 2001; Haase et al. 2007; Jipa 2014). Scattered massifs of loess form a sublatitudinal belt up to 300 km wide, stretching from the north of France (Norman Upland) to Belgium and the Netherlands. To the south, loesses are widespread in the Danube River valley, in the middle and lower part of which they cover significant areas in Hungary, Bulgaria and Romania (Jipa 2014). In the southeastern part of the East European Plain, loess with a thickness of up to 30 m, sometimes even more, become widespread. They are widely common on the territory of Moldova, in the central and southern parts of Ukraine in the middle and lower parts of the valleys of large rivers (Dniester, Southern Bug, Dnieper), and also occupy watershed areas. Landslides in loess in Ukraine account for up to 37% of the total number of landslides in the region.

Within Russia, loess occupies more than 10% of the territory (Trofimov et al. 2001; Zerkal and Ershova 2014; Konishchev 2015; Galay et al. 2017). The main regions of their distribution are (Fig. 1):

– southern regions of European Russia—the coast of the Azov Sea, the valleys of the Don and Kuban rivers, their tributaries and adjacent watershed areas, the lower part of the Volga River valley, and the foothills of the Caucasus, where loess occupies up to 60% of the territory and its thickness reaches 50–60 m, more rarely up to 100 m;

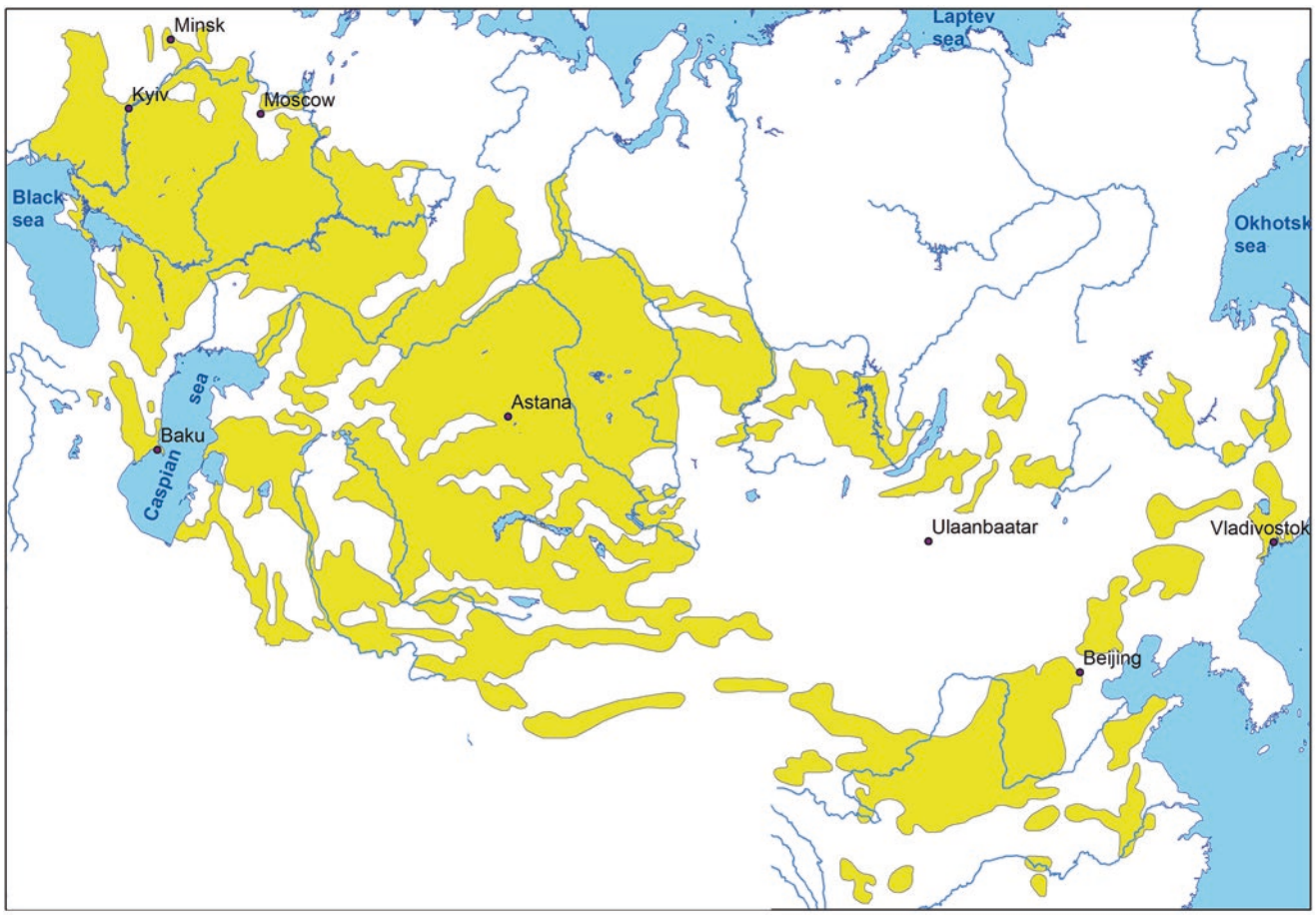

Fig. 1 Loess occurrence in Northern Eurasia

– the southern part of Western Siberia—the Priob plateau adjacent to the Ob River valley in its upper reaches, the foothills of the Salair and the Altai-Sayan mountain country;
– southern regions of Eastern Siberia—areas west of Lake Baikal, in the upper part of the Angara River valley.

In these regions, the largest landslides reach significant volumes. On the right bank of the Kuban River valley near the villages of Grigoropolisskaya and Temizhbekskaya in April 1987, landslide displacements involved a bank section up to 2.5 km long, up to 200 m wide and 55–60 m thick. The total volume of the landslide amounted to 30 million m^3 (Zaporodzenko and Derbinjan 1989).

In Central Asia, loess is widespread in Uzbekistan, Kyrgyzstan, and Tajikistan. In the Chirchik River valley in the Chatkal-Kuramin region of Uzbekistan, landslides in loess occupy 42% of the territory (Niyazov 1974).

One of the largest landslides in loess in Uzbekistan is the landslide "Sarybulak", formed on 27.11.1976 in the side of the same name gully (Niyazov 2015). The formation of the landslide occurred in 30 m thick loess underlain by Jurassic clays, on which a groundwater horizon was formed as a result of prolonged precipitation. The displacement of the landslide occurred in several phases. In the initial phase of slope deformations, apparently as a result of loess continuity disruption by subsidence phenomena, there was formation of a loamy avalanche with a volume of 800 thousand m^3, moving towards the Sarybulak gully channel with a velocity of more than 8 m/sec. The resulting air shock wave knocked down a shepherd on the opposite side of the shed. The second stage of deformations was a landslide-flow of strongly moistened loess (with humidity up to 30–32%) with the volume of more than two million m^3, displaced at a speed of 6–15 m/h during 4 days. Further, the development of landslide deformations continued for several years. In 1980, the total volume of the Sarybulak landslide reached 8.5 million m^3 (Niyazov 2015).

In Tajikistan, landslides in loess rocks, which is covering 16% of the territory and count for 27–28% of all landslides, and even up to 84–85% taking into account shallow landslides.

The highest intensity of landslide development in loess is characterized by medium-low-lying areas of arid regions of Tajikistan. In some areas (the valley of the Kharangon River, the left bank of the middle course of the Obi-Mazar River) landslides in loess occupy 35% of the total area (Skvaletsky 1988).

The largest landslides in loess in Tajikistan are the sesmogenic phenomena formed during Gissar earthquake 23.01.1989 in the northern part of Urtaboz plateau. Landslides were formed in the thickness of 73–90 m in the loess strata. The main factor of landslide formation was liquefaction of water-saturated loess under seismic impact (Zerkal 1994, 1996; Voznesensky and Zerkal 1997). The total cumulative volume of loess involved in displacements during the Gissar earthquake reached 65 million m^3. The largest of the seismogenic landslides is the Okuli landslide, 3.8 km long. Its velocity of flow was up to 3–3.1 m/sec (Zerkal 1994, 1996). The most catastrophic was the Sharora landslide with a total volume of up to six million m^3 (Zerkal 1994). This landslide partially destroyed the village of Sharora, located at the foot of the Urtaboz Plateau, killing more than 270 people.

In China, loess covers 6.6% of the land area, most of which forms the Loess Plateau with an area of about 430,000 km^2 (Bian et al. 2022; Zhuang et al. 2016). The thickness of loess strata ranges from a few meters to 300 m.

In North America, loess is distributed within the Great Plains in the Ohio, Missouri, and Mississippi River basins. In South America, loess covers vast areas in Argentina and in some parts of Uruguay.

In Africa and Australia, there are no large massifs of loess, being deposited locally. The loess is widespread in New Zealand, mainly in the South Island, where it covers 10% (Carey et al. 2017).

Loesses, widely developed in areas of intensive economic development, occur in a variety of conditions, composing surfaces of different morphology—from plains to slopes of considerable steepness. Specific properties of loesses associated with their genesis and subsequent diagenetic transformations cause the development of a whole complex of geological processes (subsidence, suffosion, pseudokarst, etc.), among which landslides are one of the most dangerous.

3 Specific Features of Landslide Occurrence in Loess Rocks

In general, among the slope deformations involving loess formation, several groups can be distinguished (in relation to their structure (by (Zerkal and Ershova 2014):

Type I - landslides, whose deformation zone is located in the loess strata;
Type II - landslides whose deformation zone is confined to the contact of loess and underlying rocks;
Type III - landslides where the loess plays a passive role in displacement, i.e. it is involved in displacements without deforming (e.g. in the upper part of the landslide block).

Type I landslides are formed in areas where loess rocks have significant thickness. Landslides of this type are most widely represented in the Pre-Caucasus. Type II landslides develop in areas where erosion uncovers loess underlying rocks, usu-

Fig. 2 Loess slide with cambering and bulging (Tadjikistan)

ally of clay composition. The thickness of loess rocks composing the slopes in this type of displacements can vary widely—from the first meters to 20–25 m and more. The development of landslides of this type in Russia is observed in the valleys of the Don, Kuban and Ob rivers, as well as in the southern regions of Siberia (Pribaikalia). Type III landslides are formed in areas with low thickness loess cover.

Almost all known types of landslides (by displacement mechanism) occur in loess (Varnes 1978; Cruden and Varnes 1996; Hungr et al. 2014):

1. Rotational slide:
   - Rotational loess slide, typical for type I and type III of the selected slope deformations.
   - Translational slide, typical for type II of the selected slope deformations.
   - Loess fall (local block collapses), which are characteristic of type I slope deformations in the areas of vertical scarps within the loess and are, as a rule, local in nature.
2. Flow slide:
   - Loess flow slide, typical of both type I and type II slope deformations.
   - Dry loam avalanche, arising (in the form of deformations, as a rule, of type II) at strong dynamic impacts on the strata of loess in the dry state during earthquakes.
   - Sudden liquefaction loess slide, formed by the effect of liquefaction of moistened loesses during earthquakes (in the form of type I or II deformations) or anthropogenic dynamic impact. Subsequently, the mass movement occurs as earth spreading (sudden spreading failures, by (Hutchinson 1988)).
3. Complex slide and transitional types of slope movements:
   - Rotational loess slide и loess flow slide, transforming into mudflow when reaching river valleys with subsequent turning and movement along river channels, accompanied by water saturation of shifting soil masses.
   - Rotational loess slide, transformed into liquefaction slide under dynamic impact at the moment of impact on the opposite slope of the valley.
   - Complex slope movements with cambering and bulging (by (Hutchinson 1988)), which are formed either in the conditions of uplift of the edge part of the landslide block or in the presence of a deeply buried horizon of strongly moistened loess in the massif (Fig. 2).

A special type of combined slope deformations occurring in loess should include suffosion slides (Fig. 3). The formation of suffosion loess slides (by (Zerkal and Barykina 2023) (in the form of type I or II deformations) is associated with suffosion soil removal by groundwater flow. Also, a special type of combined slope deformations of loess are landslides, the initial phase of displacements of which is caused by subsidence phenomena.

3.1 Rotational Loess Slides

Rotational loess slides (Fig. 4) in Russia are widely developed in the Pre-Caucasus, in the south of Western and Eastern Siberia, where their thickness can reach 40–100 m (Zerkal and Ershova 2014). The formation of sliding landslides occurs in loess rock massifs with low humidity ($W_e < W_p$). Landslide deformations occur in the form of displacement of one or several large blocks forming a typical terrace-like surface in the relief. The displacements occur along a small (3–5 cm, rarely more) zone, a sliding surface with a shape close to circular-cylindrical and uniform for each individual block.

Progressive motion of detached blocks down the slope is accompanied by rotational motion, which leads to overturning of blocks. Vertical amplitudes of one-time motions may be insignificant and therefore the probability of repeated deformations is high.

The thickness of rotational loess slides is from 6–7 m to 15–25 m, rarely more. N.N. Nilov (personal communication) believes that the depth of landslides in loess does not exceed the thickness of the subsidence zone. Volumes of sliding landslides in loess can be from the first hundreds and thou-

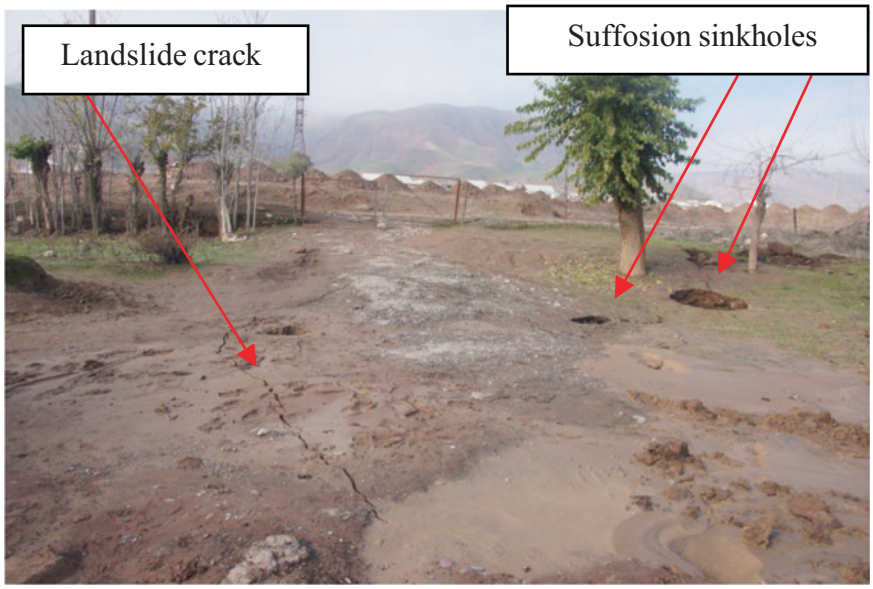

Fig. 3 Site of suffosion landslide formation in loess (Tajikistan)

Fig. 4 Rotational loess slide (valley Kuban river, Russia)

sands of m^3, reaching in some cases 1,5–two million m^3 and more. The development of rotational slides is activated by watering of loess massifs in spring and autumn periods, as a consequence of snowmelt and heavy precipitation. Displacement rates of landslides of the considered type in the periods of activation range from mm/day to first m/day, rarely more.

3.2 Translational Loess Slides

Translational loess slides in the territory of Russia are predominantly developed in the northern areas of loess distribution, where their thickness is up to 15–20 m, rarely more. In the southern parts of loess distribution on the territory of Russia translational loess slides are also quite widespread in foothill areas (North Caucasus, foothills of Salair and Altai-Sayan mountain country). The formation of translational loess slides occurs in loess rock massifs at sufficiently high moisture content (Wp < We < WL). Landslides of this type with volumes from the first hundreds and thousands of m^3, reaching in some cases several tens and first hundreds of thousands of m^3, prevail in the northern areas of loess rock distribution. The periods of development and activation of sliding landslides in loess rocks are close to the periods of development of sliding landslides. Displacement rates of

Fig. 5 Loess falls on the Azov Sea coast (Russia)

landslides of the considered type in the periods of their activation range from mm/day to the first m/day, rarely more.

3.3 Loess Falls

Loess falls (Fig. 5) are usually local deformations of subvertical scarps formed by dry loess ($W_e << W_p$). The volumes of loess falls are thousands, rarely tens of thousands m^3.

3.4 Loess Flow Slides

Loess flow slides (Fig. 6) are quite a common type of slope deformations formed in the areas of loess distribution. Within the composition of flow slides in loess rocks can be distinguished:

- shallow flow landslides—with thicknesses up to 3 m, more rarely up to 5 m, and volumes reaching thousands (shallow slide) and tens of thousands m^3;
- deep flow landslides with thicknesses of 5–10 m and more, with volumes reaching hundreds of thousands m^3, rarely several million m^3.

Shallow loess flow slides are formed due to infiltration and accumulation of atmospheric precipitation and are often confined to low slope areas—head parts of ravines, runoff troughs—which promote accumulation and infiltration of surface runoff. Shallow loess flow slides often develop in areas of anthropogenic humidifying of the upper part of loess massifs. Deep loess flow slides are formed in areas where their watering occurs both due to infiltration of atmospheric precipitation and groundwater. The formation of loess flow slides occurs in massifs with sufficiently high humidity ($W_e \geq W_L$).

In plan, loess flow slides have a glacial, pear-shaped, or, less often, circular-shaped form. The shape of loess flow slides depends both on the character of watering of the loess massif and on the morphology of the slope. Often loess flow slides due to the low viscosity of shifting masses, meeting obstacles on the way of their movement, flowing around them, sharply change the direction of displacement. Having reached the foot of slopes, loess flow slides can turn around and continue their displacement along the watercourse channel (along-channel displacements). This may result in additional watering of landslide masses and loess flow slides may be transformed into mudflow. The length of loess flow slides depends on the height and morphology of slopes and ranges from hundreds of meters to first kilometers with widths of tens and hundreds of meters, and in some cases up to a kilometer. Characteristic for landslides of this type is a significant (from 2–5 times) excess of the distance of spreading of landslide masses "length of the detachment surface".

The rate of displacement of landslides ranges from the first m/day-m/min to 4–5 m/s. The displacement velocity of landslides and the distance of their movement depend significantly on the day surface gradients and the viscosity of soils, which is determined by their initial moisture content. At the same time, the maximum flow velocities are characteristic of the central parts of the flows, which move, as a rule, for long distances. Having considerable kinetic energy, the flows, even on an almost horizontal surface (1°-1.5°), can

Fig. 6 Loess flow slides (Tadjikistan)

move for considerable distances. The displacement of loess flow slides is rather rapid and, as a rule, single-acting.

3.5 Dry Loam Avalanches and Sudden Liquefaction Loess Slides

Dry loam avalanches and sudden liquefaction loess slides on the territory of Russia are noted in areas of increased seismicity (North Caucasus, Altai-Sayan mountain country). At the same time, in recent decades, no strong earthquakes have occurred in the territory of Russia in regions with extensive loess development.

3.6 Suffosion Loess Slides

Suffosion loess slides are formed in loess rocks as a result of slope stability failure due to suffosion of material in the lower part of the slope by groundwater (often hydrostatic pressure). In this case, the hydraulic gradient reaches a certain critical value (Zerkal and Barykina 2023). Under the influence of filtration forces, material is carried out from the massif and a suffusion niche is formed. Landslide deformation begins with the collapse of the niche vaults, and the collapsed rocks together with the suffusion material form an unstructured landslide mass. Displacement of the landslide generally occurs as a flow landslide. Suffosion loess slides are drop-shaped, and their volumes reach tens of thousands of m^3. Landslides of this type are characterized by high—up to 5–7 m/min displacement velocities. The development of suffosion slides in loess rocks occurs in places where there is a temporary "barrier" on the way of water filtering in the massif, which leads to a sharp increase in head and creates conditions for a sharp activation of suffosion processes. Suffosion loess slides have been described on high slopes (20°-25° steepness) in the valleys of the Volga River, the Ob River and in the Northern Caucasus (Zerkal and Barykina 2023).

4 Stability of Slopes Composed of Loess Rocks and Factors Influencing Its Changes

The formation and development of landslides occurs under the influence of a variety of complex of factors. Among these, the stability of loess slopes can be influenced by:

- structure of loess rock massif;
- climatic (meteorological) conditions and surface water erosion activity depending on the first;
- character and degree of watering of loess strata, as well as manifestation of specific properties of loess rocks in conditions of moistening and under dynamic influences;
- morphology of slopes and their exposure;
- geomorphologic conditions and paleorelief features;
- tectonic disturbances;
- seismicity of the area;
- anthropogenic impact causing changes in hydrogeological conditions and properties of loess.
- In general, the factors affecting the stability of loess slopes, as in other cases, can be divided into slowly and rapidly changing ones. The first type of factors determin-

ing the general predisposition of the territory to the development of landslide processes includes the peculiarities of spatial distribution and structure of loess strata, the nature and type of tectonic disturbances of the area, seismicity, geomorphologic conditions, the history of recent geologic development reflected in the paleorelief features, and regional hydrogeologic conditions. The second type of factors includes watering of loess rocks both due to groundwater and under the influence of meteorological conditions and anthropogenic impact, as well as peculiarities of changes in the properties of loess in different conditions.

5 Conclusion

Loesses are widespread over vast areas in Europe and Asia, as well as in North America, where they form covers with thickness from several meters to the first tens of meters, and in the foothill areas and intermountain hollows of the Caucasus, Central Asia, and China—up to 100 m and more. The peculiarity of loess is, on the one hand, its ability to form high (up to tens of meters) subvertical ledges in dry condition, on the other hand, to be characterized by a significant decrease in strength characteristics when moistened, and in waterlogged condition it has the ability to liquefy. A specific feature of loess is the ability to subsidence

- self-compaction when moistened under the action of both its own weight and external loads.
- One of the consequences of sharp variability of strength properties of loess is high landslide activity in the regions of their distribution, where landslides can occupy up to 30–40% of the total area. The spread of landslides is also promoted by the unstability of loess to water erosion, which contributes to the rapid erosional dismemberment of the territory with the formation of high slopes.
- Almost all known types of landslides are formed in loess:
  - in dry loess—loess falls, rotational and translational loess slides, and dry loam avalanche can be formed during earthquakes;
  - in humidifying loess—loess flow slide and sudden liquefaction loess slide (sudden spreading failures, by (Hutchinson 1988));
  - at interlacing of relatively dry and moistened loess—complex slope movements with cambering and bulging (by (Hutchinson 1988)).
  - A special type of combined slope deformations—suffosion loess slides (by (Zerkal and Barykina 2023)) also occurs in the areas of loess distribution.
  - The high landslide activity is typical for the regions of loess widespread, the variety of landslide types formed in loess, require much more detailed study when assessing the landslide hazard in loess.

References

Bian S, Chen G, Zeng R, Meng X, Jin J, Lin L, Zhang Y, Shi W (2022) Post-failure evolution analysis of an irrigation induced loess landslide using multiple remote sensing approaches integrated with time-lapse ERT imaging: lessons from Heifangtai, China. Landslides 19(5):1179–1197. https://doi.org/10.1007/s10346-022-01859-x

Carey JM, McSaveney MJ, Petley DN (2017) Dynamic liquefaction of shear zones in intact loess during simulated earthquake loading. Landslides 14(3):789–804. https://doi.org/10.1007/s10346-016-0746-y

Cruden D, Varnes DJ (1996) Landslide types and processes. In: Turner AK, Schuster RLE (eds) Landslides: investigation and mitigation: Transportation Research Board. Special Report 247. National Academy Press, Washington, pp 36–75

Ding H, Li Y, Yang Y, Jia X (2019) Origin and evolution of modern loess science - 1824 to 1964. J Asian Earth Sci 170:45–55. https://doi.org/10.1016/j.jseaes.2018.10.024

Galay BF, Serbin VV, Plakhtyukova VS, Galay OB (2017) Loess ground Northern caucasus and crimea (comparative analysis). Nauka Innovatsii Tekhnologii 2:97–108. (in Russian)

Haase D, Fink J, Haase G, Ruske R, Pésci M, Richter H, Altermann M, Jäger K-D (2007) Loess in Europe—its spatial distribution based on a European loess map, scale 1:2,500,000. Q Sci Rev 26:1301–1312

Hungr O, Leroueil S, Picarelli L (2014) The Varnes classification of landslide types, an update. Landslides 11(2):167–194. https://doi.org/10.1007/s10346-013-0436-y

Hutchinson JN (1988) General report: morphological and geotechnical parameters of landslides in relation to geology and hydrogeology. In: Bonnard C (ed) Proceedings of the 5th international symposium on landslides. vol 1. Balkema, Rotterdam, pp 3–35

Jipa DC (2014) The loess-like deposits in the lower Danube Basin. Genetic significance. Geo-Eco-Marina 20:7–18

Kalinin EV, Panasyan LL, Zerkal OV (1998) The seismic wave effect on the slope stability. Environmental management. Sivakumar M, Chowdhury RN (eds.) Proc. of the 2nd intern. Conf. On environmental management (ICEM2). ElsevierAmsterdam 2, pp. 1065–1071

Konishchev VN (2015) Loess soil: new opportunities of its genesis study. Eng Geol World 5:22–36. (in Russian)

Niyazov RA (1974) Landslides in loess rocks of the southeastern part of Central Asia. Fan, Tashkent. 148 p. (in Russian)

Niyazov RA (2015) Landslides caused by Pamir-Hindu Kush earthquakes. Tashkent 224 p. (in Russian)

Skvaletsky EN (1988) Engineering-geological forecasting and protection of natural environment (on the example of development of loess territories of Tajikistan). Donish, Dushanbe. 254 p. (in Russian)

Trofimov VT, Balykova SD, Bolikhovskaya NS, Andreeva TV, Alexeev BA et al (2001) In: Trofimov VT (ed) The Earth's loess cover and its properties. MSU Press, Moscow. 464 p. (in Russian)

Varnes DJ (1978) Slope movement types and processes. In: Schuster RL, Krizek RJ (eds) Landslides, analysis and control: Transportation Research Board. Special Report 176. National Academy of Sciences, Washington, pp 11–33

Voznesensky EA, Zerkal OV (1997) Dynamic instability of saturated loesses. In: Marinos PG, Koukis GC, Tsiambaos GG, Stournaras GC (eds) Engineering geology and the environment. Proc. Intern. Symposium on Engineering Geology and the Environment. Balkema, Rotterdam, pp 1125–1130

Zaporodzenko EV, Derbinjan GA (1989) Stability of high loess terrace scarps in relation to anthropogenic activities. Eng Geol Loess Rocks Moscow 1:51–52. (in Russian)
Zerkal OV (1994) Seismic landslides caused by Gissar earthquake in 1989 (Tajikistan). Mosc Univ Geol Bull 49(2):57–63
Zerkal OV (1996) Mechanism of formation and development of deep seismogenous landslides due sudden liquefaction of loessal soils. In: Senneset K (ed) Landslides. Proc. of the 7th Internat. Symp. On landslides, vol 2. Balkema, Rotterdam, pp 1055–1060
Zerkal OV, Barykina OS (2023) Suffosion landslides as a specific type of slope deformations in the European part of Russia. I. Alcántara-Ayala et al. (eds.). Progress in landslide research and technology. Springer, 1(2): pp. 99–108
Zerkal OV, Ershova AV (2014) Landslides in loess rocks on the territory of Russia: peculiarities of development and factors of their formation. In: Kalinin EV, Zerkal OV (eds) Modern problems of engineering geodynamics. MSU Press, Moscow, pp 131–137. (in Russian)
Zhuang J, Peng J, Xu Y, Xu Q, Zhu X, Li W (2016) Assessment and mapping of slope stability based on slope units: a case study in Yan'an, China. J Earth Syst Sci 125(7):1439–1450. https://doi.org/10.1007/s12040-016-0741-7

Spatio-Temporal Distribution of Rainfall-Induced Landslides in Nicaragua (2000–2022): Preliminary Insights to Communicate Landslide Disaster Risk

Gema Velásquez-Espinoza and Irasema Alcántara-Ayala

Abstract

Nicaragua's location in the tropics makes it highly susceptible to tropical cyclones, with 22 such events causing significant damage between 1971 and 2020. The attendant risk of landslides and flooding from heavy rainfall associated with these phenomena is a grave concern. However, the absence of consistent policies to progress scientific development due to national socioeconomic and political constraints has impeded effective disaster risk management. This chapter presents an overview of landslide occurrences from 2000 to 2022 and offers preliminary insights for creating strategies to communicate landslide disaster risks.

Keywords

Landslides · Rainfall-induced · Hurricanes · Nicaragua · Disaster risk · Disaster risk communication · Landslide preparedness · Disaster risk awareness · Disaster risk reduction

1 Introduction

Multiple meteorological systems converge in Nicaragua, causing common atmospheric phenomena and heavy rainfall in the Caribbean. Consequently, the country is exposed to the annual impacts of tropical cyclones, which have caused substantial damage over the years. Between 1971 and 2020, 22 cyclones occurred, with 17 classified as hurricanes in categories 1–5, four as tropical storms, and one without an assigned class. The most destructive hurricanes were Mitch in 1998, Felix in 2007, and Joan in 1988, respectively (Velásquez-Espinoza and Alcántara-Ayala 2023).

Moreover, between 1994 and 2013, hydrometeorological events triggered disasters that resulted in yearly losses of US$301.75 million (CRED-UNISDR 2018). This amount is equivalent to an annual loss of 1.71% of the country's gross domestic product, highlighting the potential significance of major disaster events in the government's efforts to eradicate extreme poverty and confront the threat of setbacks in development, as emphasized by the World Bank (2021). Therefore, it is imperative to reduce vulnerability and exposure to improve disaster risk management strategies and reduce the economic and social impacts on the affected communities, particularly those associated with floods and landslides.

Recently, Central America experienced two devastating tropical cyclones, Eta and Iota, from November 1 to 18, 2020. The storms caused catastrophic damage to Honduras, Nicaragua, and Guatemala, with winds, flooding, and landslides affecting southern Mexico to northern Colombia. In Nicaragua, Hurricane Eta caused widespread flooding, damaging or destroying 43,000 homes, affecting three million people across 56 municipalities. The storm also caused power cuts, uprooted trees, road blockades, and two deaths in the Bonanza mining area due to a landslide (National Hurricane Centre 2021a; Borrowing Agency 2023).

Hurricane Iota caused damages of $564–741 million in Nicaragua, nearly half of the total damages for Central America. Despite being a Category 4 hurricane, it caused lower damage than anticipated due to landing where Hurricane Eta had already caused destruction. Approximately 900,000 people were affected, with 39 fatalities and 29 missing individuals. Likewise, 160,233 homes lost electricity, 10,000 homes were affected, 47,638 families lacked water services, and 35 communities had no telephone services due

G. Velásquez-Espinoza
Faculty of Sciences and Engineering, National Autonomous University of Nicaragua, Managua, Nicaragua

Postgraduate Programme in Geography, National Autonomous University of Mexico (UNAM), Mexico City, Mexico

I. Alcántara-Ayala (✉)
National Autonomous University of Mexico (UNAM), Institute of Geography, Mexico City, Mexico
e-mail: ialcantara@geografia.unam.mx

B. Abolmasov et al. (eds.), *Progress in Landslide Research and Technology, Volume 3 Issue 1, 2024*, Progress in Landslide Research and Technology, https://doi.org/10.1007/978-3-031-55120-8_8

to flooding and landslides (EM-DAT n.d.; National Hurricane Centre 2021b; Borrowing Agency 2023).

The historical impact of hurricanes in a country such as Nicaragua, where major development and support to scientific research on disaster risk is still lagging, requires strategies of diverse types, including the continuous development of landslide databases and sound inventories as essential ingredients for landslide hazard and risk assessments. This must be accompanied by initiatives to strengthen population knowledge and sensitivity about landslides' dynamics, disaster risk drivers and socio-economic and environmental impact.

At the global, national, and local levels, various strategies and initiatives have been implemented to mitigate the risk of landslide disasters. The Sendai Partnerships 2015–2025 (Sassa 2015) and Kyoto Landslide Commitment 2020 (KLC2020) (Sassa 2021) are examples of such efforts, which promote research and capacity building towards disaster risk reduction, with a particular focus on developing countries. Priority Action 5 of KLC2020 emphasizes fostering transparent communication between local governments and society through integrated research, capacity building, knowledge transfer, awareness-raising, training, and educational activities. This approach allows societies and local communities to develop effective policies and strategies for reducing landslide disaster risk, strengthen their capacities for preventing hazards from developing into major disasters, and enhance the effectiveness and efficiency of relief programs (Sassa et al. 2021).

Education and preparedness are widely considered to be among the most significant endeavours to reduce landslide disaster risk effectively. The past decade has seen a renewed importance of enhancing non-structural measures, which aim to reduce disaster risks and impacts through policies and laws, public awareness raising, training, and education, without physical construction (UNISDR 2015, 2017).

Regardless of this necessity, no one has established an integrated strategy for landslide disaster risk communication in Nicaragua to the best of our knowledge. With this in mind, this research proposed preliminary insights for communicating landslide disaster risk.

This chapter is divided into five additional sections to the introduction. Section 2 gives a brief overview of the importance of landslide databases. In the third section, general information about Nicaragua is provided. In the fourth section, the methodological approach is presented. Results and concluding remarks are presented in later sections.

2 Landslide Databases and Inventories

Creating a landslide inventory is paramount when evaluating landslide susceptibility, hazard, and risk. It serves as a vital source of information regarding the location, date, type, size, activity, and causal factors of landslides and the resulting damage. Moreover, they provide a means of storing and analysing spatial and temporal data, allowing for more efficient and effective management of this critical hazard. However, while some countries boast comprehensive inventories, others are developing national or regional databases, signifying varying abilities to conduct national-scale risk assessments (Van Den Eeckhaut and Hervás 2012).

Guzzetti et al. (2012) pointed out that having a record of landslides is important for understanding the impact and scale of landslides in different areas, whether a small area or an entire region. These records help determine the risk and hazard of landslides and analyse the distribution, types, and patterns in relation to the land features. They are also helpful in studying how landscapes change due to landslides. Landslide inventory maps are a valuable tool in evaluating the susceptibility, hazard, and risk of landslides, especially in the early stages of analysis.

The creation of landslide maps is a multifaceted process that involves the use of both traditional and innovative techniques. Traditional methods include field mapping and visual interpretation of aerial photos, whereas innovative methods utilize digital elevation models, satellite images, and new field mapping tools (Guzzetti et al. 2012). By leveraging these diverse methodologies, it is possible to create accurate and informative landslide inventories that aid in identifying and mitigating landslide risks.

In developing countries, national landslide databases often have notable deficiencies in providing essential hazard information, such as the classification, causes, magnitude, accessibility of data regarding the extent of damage, and continuity of information. These inadequacies hinder the ability to accurately assess the risks posed by landslides and take appropriate measures to mitigate their impact. They also hamper reporting progress, such as implementing the Sendai Framework for Disaster Risk Reduction (Bhuiyan et al. 2023).

Recent efforts have also focused on elaborating landslide inventory mapping by combining traditional field survey methods with innovative technology to provide precise and cost-effective information on landslide location, typology, extent, and damage. Participatory mapping involving local communities is particularly effective in areas with scarce data. The resulting data can be used to develop appropriate land-use planning to protect people and infrastructure from landslide hazards (Samodra et al. 2018).

One of the first attempts to understand the spatio-temporal occurrence of landslides in Nicaragua was carried out by Devoli et al. (2007a). This involved the identification of historical landslides before 1990 through research of historical sources at various institutions and the digitalization of landslide spatial locations. The study found that the landslides occurred mostly in combination with other natural phenomena. These were included in a geo-referenced inventory of

historical landslide events aimed to provide the basis for a more comprehensive landslide hazard assessment.

Afterwards, Devoli et al. (2007b) compiled a more robust digital database of landslides in Nicaragua in collaboration with the Instituto Nicaragüense de Estudios Territoriales (INETER), foreign development agencies, and other Nicaraguan institutions. The database contains spatial data in the form of geo-referenced points and polygons compiled from various sources, including newspapers, technical reports, and landslide inventory maps. This tool was created to support scientific research to assess landslide hazards and inform emergency management, land-use planning, policy development and early warning systems.

Despite that progress, Devoli et al. (2009) highlighted that the Nicaraguan database lacked reliable data. Therefore, they suggested that more quantitative and qualitative information should be collected during a landslide survey to improve future hazard zoning and risk mitigation. This includes estimates of volume, run-out distance, inundation area, height difference of the landslide deposit, and more sophisticated parameters like the geometrical shift of the centre of mass of the landslide. By gathering this additional information, a better assessment of potential hazards would allow for properly addressing the safety and well-being of at-risk communities.

A key problem with the existing landslide databases in Nicaragua is their lack of wide public direct and friendly accessibility to lay people. This creates legitimate worries about the sources of landslide risk understanding, prevention efforts and disaster response. Without easy access to comprehensive information about the distribution of past and contemporary landslides in space and time, it becomes challenging for non-experts to make informed decisions and take appropriate actions to prevent future disasters. This underscores the need for more transparent and easily accessible databases to help mitigate the impact of landslide disasters in the region, particularly in understanding how to avoid the construction of new landslide disaster risks and disasters.

3 Studied Area

Nicaragua is a Central American country located in the northern hemisphere, between 11°-15° north latitude and 83°-88° west longitude. It is situated in the middle of the isthmus, with coastal plains that rise to central interior mountains. Nicaragua shares land borders with Costa Rica and Honduras (Fig. 1).

It comprises 15 departments and two autonomous regions: the North and South Atlantic Autonomous Regions. The population comprises diverse ethnic groups, including mestizo (mixed Amerindian and White) 69%, White 17%, Black 9%, and Amerindian 5%. The surrounding oceans mainly influence Nicaragua's climate, and it receives little precipitation until the formation of TCs (Incer et al. 2000).

Nicaragua boasts a tropical climate that is characterized by two distinct seasons. The "wet" season spans the months of May through October, while the "dry" season occurs between November and April. In the latter half of July and early August, the "Canícula" arrives, marking a period of dryness that interrupts the wet season. Positioned in the path of Pacific cyclones and Atlantic hurricanes, Nicaragua is susceptible to heightened rainfall and strong winds from July to October. Furthermore, the El Niño Southern Oscillation (ENSO) fluctuations can bring varying weather conditions during June and August (CCKP-World Bank n.d.).

It is the largest country in Central America, with a land area of approximately 130,370 km^2 and a population of 6,948,392 as of 2022. Most of the population, 60%, resides in urban areas, with 67% of the urban population inhabiting slums in 2010. Furthermore, approximately 16,000 individuals have been internally displaced due to disasters. The forested area constitutes 28.3% of the land, while the economically active population is 3,017,985 in 2021 (World Bank 2021).

The Pacific coast has the most economic activity, while the Atlantic coast is less developed. Major export crops are coffee, sugar cane, cotton, bananas, sesame, and peanuts, with rice, beans, corn, and sorghum for domestic consumption (ALADI 2009).

Landslides usually happen on steep slopes of active or dormant volcanoes made of Quaternary volcanic rocks that have been altered by water. They can also occur on steep slopes of highly weathered soil and rocks, such as Paleozoic metamorphic rocks Tertiary volcanic and sedimentary rocks in mountain ranges. The main reason for landslides is heavy rain during the wet season, which tropical cyclones can cause. However, landslides can also be triggered by earthquakes and volcanic eruptions during the dry season (Devoli et al. 2009).

As per the recently published Inform Annual Report for 2021, with a rating between 0 and 10, Nicaragua has been assessed with a medium risk index of 4.6. The country's vulnerability and exposure have been rated at 5.3, while its vulnerability alone has been marked at 3.5. Additionally, the disasters related to natural hazards index for Nicaragua stands at 6.6, depicting the propensity and exposure of the region to such events. Although there is no exclusive risk index for landslides, floods have been categorized as medium with a score of 5.1 (Table 1) (Inter-Agency Standing Committee and the European Commission 2021). Unfortunately, the country's capacity to recuperate from disasters caused due to tropical cyclones, floods, and landslides has been severely hampered by past disasters like those associated with Hurricane Mitch in 1998 and, more recently, by Eta and Iota in 2020.

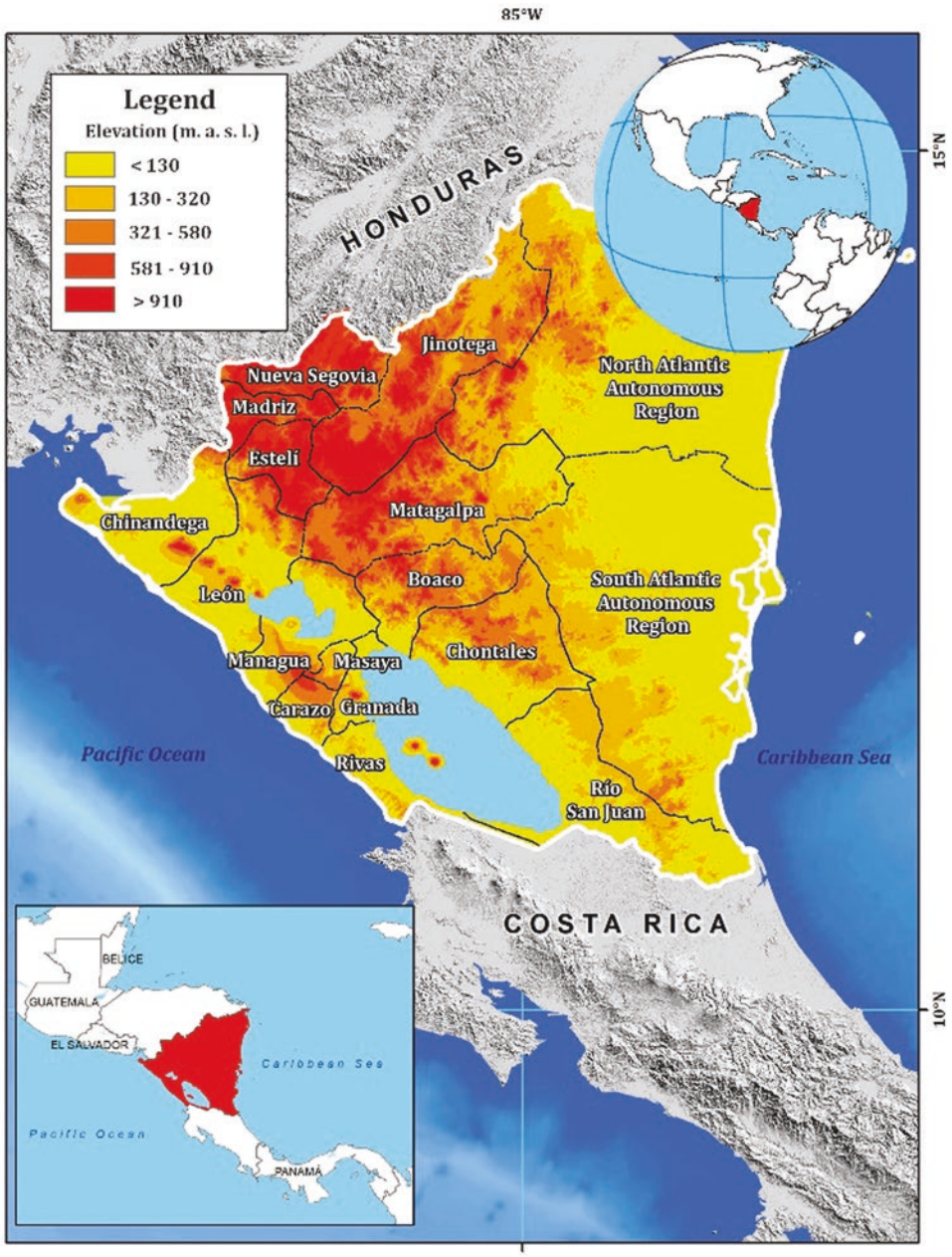

Fig. 1 Location of the studied area (own elaboration)

According to the most recent statistics available, which date back to 2016, almost a quarter of Nicaragua's population, specifically 24.9%, lived below the national poverty line (World Bank n.d.). This indicates that a significant portion of the country's residents could not meet their basic needs and lacked access to crucial resources and opportunities. Thus, they are highly vulnerable and exposed to the impact of landslides and other hazards (Fig. 2).

Economic, social and political instability is a significant obstacle to progressing disaster risk management in Nicaragua. This involves high levels of uncertainty in different aspects, especially concerning the absence of sustained policies. Financial and economic barriers, developing laws and regulation frameworks, lack of capacity building in education and research, professional and technical personnel, insufficiency of relevant land information concerning hazards, vulnerability and exposure, poor environmental data, lack of environmental justice, changings in governments and policies from one government to another, and an atmosphere of conflicts and societal unrest unfold the challenges faced by Nicaraguan people at risk and the diverse governments, at different territorial levels, to mainstreaming disaster risk into development practices.

Table 1 Nicaragua risk profile (Source: Inter-Agency Standing Committee and the European Commission 2021)

Inform Risk	**4.6**
3-year trend	Stable
Rank	60
Reliability Index[a]	3.6
Hazard & Exposure	**5.3**
Natural	6.6
Earthquake	9.5
Flood	5.1
Tsunami	8.1
Tropical cyclone	3.6
Drought	4.1
Epidemic	5.9
Human	3.6
Projected conflict risk	5.1
Current highly violent conflict intensity	0.0
Vulnerability	**3.5**
Socio-Economic Vulnerability	5.0
Development & Deprivation	6.0
Inequality	5.7
Economic dependency	2.4
Vulnerable groups	1.6
Uprooted people	0.9
Health conditions	1.0
Children U5	1.2
Recent shocks	1.9
Food security	4.5
Other vulnerable groups	2.3
Lack of Coping Capacity	**5.3**
Institutional	6.0
Disaster Risk Reduction	4.7
Governance	7.2
Infrastructure	4.5
Communication	4.1
Physical infrastructure	5.0
Access to healthcare	4.4

[a]Reliability Index: more reliable 0–10 less reliable

4 Methodology

In this empirical research study, a desk review was conducted. The search strategy concentrated on prior works that have been central in understanding the spatiotemporal occurrence of tropical storms and rainfall-induced landslides and their impact in Nicaragua. The information was obtained from primary and secondary sources. Original sources included the field recognisance of landslides published in the annual and monthly bulletins of the Nicaraguan Institute of Territorial Studies (INETER), which were used to produce the landslide inventory. Likewise, a desk review was conducted to collect relevant information regarding disaster risk and landslide risk communication from various secondary sources.

After analysing and gathering the information concerning the spatio-temporal occurrence of landslides in Nicaragua for the period 2000–2022, the recorded events were included in a database, which was overlayed on the national geologic map of Nicaragua (Instituto Geográfico Nacional, Servicio Geológico Nacional y Catastro y Recursos Naturales 1974) by using ArcGis 10.5.

5 Results

Rainfall was the main trigger for 51 registered landslides, while only five were associated with earthquakes. Landslide types included lahars, mudflows, debris flows, slides, flows, falls, rotational, shallow, and complex landslides (Table 2, Fig. 3).

The number of registered events per year ranged from 1 to 10, with the highest number of 10 events occurring in 2000.

Fig. 2 Affected people by the impact of Hurricane Felix in Puerto Cabezas, Nicaragua, in 2007 (Source: U.S. Navy photo by Mass Communication Specialist 2nd Class Todd Frantom, Wikimedia Commons)

Table 2 Spatio-temporal occurrence of rainfall-induced landslides in Nicaragua, 2000–2022

Date	Location	Triggering mechanism	Landslide type
13 May 2000	San Cristóbal volcano, Chinandega department	Intense and short-duration rainfall	Lahars
17 May 2000	San Cristóbal volcano, Chinandega department	Intense and short-duration rainfall	Lahars
19 May 2000	San Cristóbal volcano, Chinandega department	Intense and short-duration rainfall	Lahars
26 April - 6 May 2000	Matagalpa, San Simón de Palsila	Rainfall Tropical storm Katrina	Slide
23 May 2000	West-northwest slope of the Dipilto volcanic range, Nueva Segovia department	Rainfall Tropical storm Katrina	Shallow landslide
6 Jul 2000	Apoyo lagoon, department of Masaya. Quebrada Honda region, Pacaya, Diriomito, highway - Masaya, Valle La Laguna, Bajadero Norte, Bajadero Oeste, Mirador de Catarina, San Juan de Oriente (Zone 4), Diriá (El Boquete and Ardilla hill)	5.4 Richter magnitude earthquake, with an epicentre on the northern edge of the Apoyo caldera	Falls
Sep 20–30 & Oct 1, 2000	San Cristóbal volcano, Chinandega department	Rainfall hurricane Keith	Lahars
Oct 1, 2000	San Nicolás, department of Estelí	Rainfall hurricane Keith	Slide
Oct 1, 2000	El Crucero and Villa El Carmen, department of Managua	Rainfall hurricane Keith	Falls and shallow landslides
Oct 1–2, 2000	Apoyo lagoon, department of Masaya	Rainfall hurricane Keith	Falls
Jun 13, 2001	La Bujona hill, Quilalí, Nueva Segovia	4.9 magnitude earthquake, Richter scale	Falls
Jul 20, 2001	Loma de San Raúl, community of San Jeronimo, municipality of San Juan del Sur, Rivas	Rainfall	Slides and flows
Sep 16, 2001	El Congo Hill, El Congo River region, municipality of Boaco, Boaco	Rainfall: Tropical storm	Slide
Nov 2001	Lapan Tara and Lapan Sirpi Hills, community of Lapan, Puerto Cabezas	Rainfall Hurricane Michelle, category 4	Debris flows and mudflows
Jan 3, 2002	Casita volcano, Chinandega	Earthquake of magnitude 4.8 on the Richter scale, epicentre in the casita volcano	Slides and falls
Sep 21, 2002	Municipality of El Crucero	Rainfall hurricane Isidore, category 3	Slides, falls, and complex landslides
Oct 28 & 31, 2002	Concepcion volcano	Rainfall	Lahar
May 21, 2004	Concepcion volcano	Rainfall	Lahar
Jun 25, 2004	Musún Hill, municipality of Rio Blanco, department of Matagalpa	Rainfall	Slides
May 18, 2005	Concepción volcano, north slope	Rainfall: Hurricane Adrian, category 1	Lahars
Jun 29, 2005	Concepción volcano, north slope	Rainfall	
Oct 1–2, 2005	El Coyotepe hill, Masaya	Rainfall: Hurricane Beta, category 3	Mudflow and debris flow
Oct 15, 2005	Apoyo lagoon, El Chilamate sector, north slope	Rainfall: Hurricane Beta, category 3	Flow
Oct 29, 2005	Mateares, Northwest of San Andrés de Las Palancas	Rainfall: Hurricane Beta, category 3	Flow
Jun 16, 2006	San Cristobal volcano, Chinandega	Rainfall	Lahar
Jul 20, 2006	El Volcán hill, Dipilto Viejo, Ocotal	Rainfall	Slide
Oct 15 & 23, 2006	La Pita hill, Santa Teresa Carazo	Rainfall	
Sep 18, 2006	Ometepe Island, Rivas. Northeast slope of the Concepción volcano	Volcanic earthquake	Debris flow
Sep 16, 2009	Apoyo Lagoon, municipality of Masaya, Masaya	Rainfall	Debris flows and falls
Jun 1, 2014	San Cristobal volcano. West slope	Rainfall	Lahars
Oct 8 & 9, 2014	Concepcion volcano, Ometepe Island	Rainfall	Lahars
Oct 2014	Community of Aguas Agrias, finca el Cráter and Laguna de Apoyo, located in the municipality of Diriá, department of Granada	Rainfall: Tropical storm Hanna	Shallow landslide

Table 2 (continued)

Date	Location	Triggering mechanism	Landslide type
Oct 2014	Communities of las Carpas I and II, El Pital and Mancera, located in the rancho Grande municipality, department of Matagalpa	Rainfall: Tropical storm Hanna	Slide
May 2015	San Cristobal volcano and Chonco volcano	Rainfall	Lahar
August 4, 2015	El sauce, department of León	Seismic swarm	Fall and shallow landslide
Oct 18, 2016	Municipality of San Juan de Rio coco, Department of Madriz	Rainfall	Slides
May 5, 2017	Apoyo lagoon, department of Masaya	Rainfall	Falls and debris flows
Oct 7 & 8, 2017	El Llanito region, municipality of Santa Lucia, Boaco	Rainfall: Hurricane Nate, category 1	Falls
Oct 25 & 26, 2017	Municipality of Esquipulas, department of Matagalpa	Rainfall: Tropical storm Selma	Rotational slides and debris flows
Oct 15, 2017	Apoyo lagoon, department of Masaya	Rainfall	Shallow landslides
Oct 18, 2018	La Conquista community, Los Castros sector, Muy Muy municipality, Matagalpa department	Rainfall	Slides
Oct 23, 2018	Community of El Zompopo, municipality of Muy Muy, department of Matagalpa	Rainfall	
Sep 23, 2018	Colonia Rubén Darío, La Cruz community, municipality of Nueva Guinea, South Caribbean region	Rainfall	Slides
Oct 15–17, 2018	La Unión community, San Rafael del Norte municipality, Jinotega department	Rainfall	Slides
May 23, 2019	San Ramón community, Maderas volcano, Ometepe Island, Rivas department	Rainfall	Debris flows
May 28 & Jun 3, 2019	Caldera de Apoyo. NW slope, municipality of Catarina	Rainfall	Debris flow and falls
May 2019	Locality La Jungla, municipality of Jalapa, department of Nueva Segovia	Rainfall	Debris flow
May 2019	Los Castros community, Muy Muy, Matagalpa	Rainfall	Debris flow
Oct 18, 2019	San Ramón, Maderas volcano, Ometepe Island, Rivas department	Rainfall	Debris flow
Oct 31 - Nov 18, 2020	Telpaneca municipality, Madriz department	Rainfall: Hurricane eta and iota	Falls and debris flows
Oct 31 - Nov 18, 2020	Municipality of rancho Grande, Department of Matagalpa	Rainfall: Hurricane eta and iota. Tropical storm Bonnie	Slide
May 23, 2022	Pancasán community (El crater), municipality of Granada, Department of Granada	Rainfall	Debris flow Lahars
Sep 10, 2022	Rancho municipality, Matagalpa department	Rainfall	Slides and debris flows
Sep 10, 2022	Boaco municipality, Boaco department	Rainfall	Falls and rotational landslides
Oct 19, 2022	Ometepe Island, Rivas department	Rainfall: Tropical storm Bonnie and Hurricane Julia	Debris flow
Oct 7–10, 2022	Mombacho volcano, Department of Granada	Rainfall: Hurricane Julia	Debris flow

Source INETER n.d.

They were categorized according to lithological units, with extrusive volcanic rocks having the highest number of events, with 45. Likewise, 15 Departments, including Carazo, Estelí, León, Jinotega, Región Autónoma de la Costa Caribe Norte, Región Autónoma de la Costa Caribe Sur, Madriz, Boaco, Granada, Managua, Nueva Segovia, Chinandega, Masaya, Matagalpa, and Rivas were affected by landslides. The landslides had an adverse impact on forests, crops, pastures, orchards, water storage facilities, households, roads, highways, schools, churches, power lines, communication poles, and municipal parks.

Due to their dynamic nature and variation in size and location, landslides significantly threaten communities, livelihoods, infrastructure, and the environment. It is

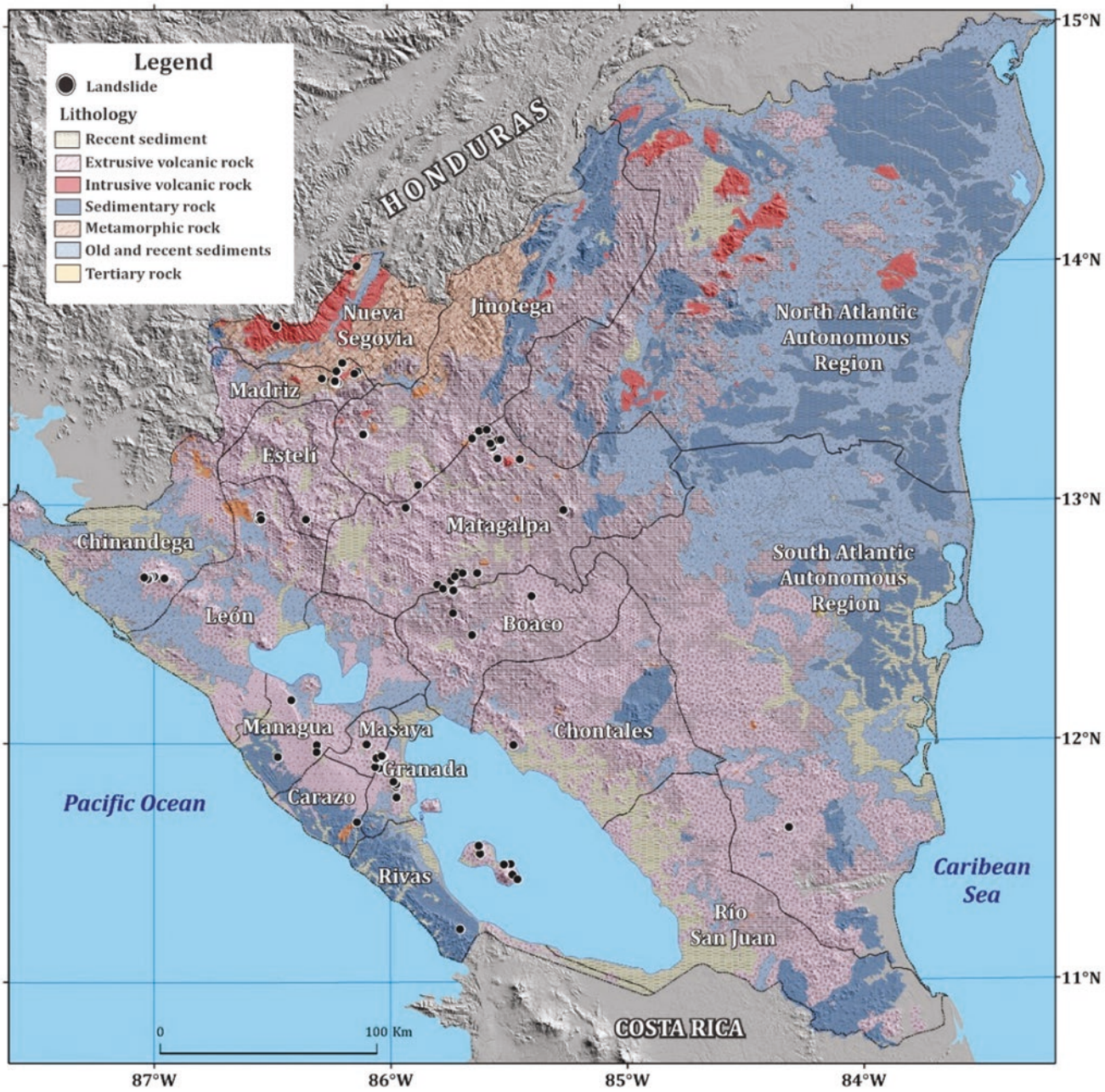

Fig. 3 Landslide inventory of Nicaragua 2000–2022 (Elaborated with information from INETER (n.d.) and Instituto Geográfico Nacional et al. 1974)

imperative to manage risks associated with these hazards from a comprehensive approach. The process entails producing knowledge on disaster risk, which encompasses the identification of hazards, vulnerabilities, exposure, and root causes. This knowledge serves as a foundation for preventing future risk by comprehending the social construction of risk and reducing existing risk through corrective and controlling measures. Additionally, the process encompasses preparing for response and recovering and rebuilding affected areas, including the population's social, economic, and physical recovery and livelihoods (Narváez et al. 2009) (see Fig. 5).

5.1 Landslide Disaster Risk Communication

Risk communication involves exchanging information and opinions concerning potential risks between individuals, groups, and institutions. This type of communication includes messages that convey the nature of risk and any concerns that may arise in relation to legal and institutional arrangements for risk management arrangements (National Research Council 1989). It is a crucial aspect of risk management that helps to ensure that all stakeholders have a clear understanding of potential risks and the measures that can be taken to mitigate them. Effective risk communication can help minimize the impact of risks and ensure that all parties are well-informed and prepared to deal with any potential issues.

In order to gain a comprehensive understanding of landslides, it is of utmost importance to possess a deep knowledge of both the natural preconditioning factors and the impact of human activities on the stability of the terrain. The destabilization of hillsides can occur due to many aspects, encompassing both naturally occurring and human-induced causes. Identifying the landslide disaster risk drivers is critical to developing effective disaster risk communication and mitigation strategies that can minimize the risks associated with these events.

The Sendai Framework for Disaster Risk Reduction emphasises the need for an integrated understanding of disaster risk. Informed disaster risk management policies and practices necessitate thoroughly comprehending vulnerability, capacity, exposure, hazard characteristics, and the environment. This knowledge can be leveraged for risk assessment prior to disasters, risk prevention and mitigation, and effective preparation and response to disasters. To achieve these objectives, real-time access to dependable data, the utilization of space and in situ information, such as geographic information systems (GIS), and the use of innovative information and communications technology are essential. Effective disaster risk communication is crucial in attaining the necessary understanding (UNISDR 2015).

At the national scale, some institutions and organisations have made considerable efforts to communicate diverse aspects associated with landslide disaster risk. For example, the British Geological Survey involves balancing scientific papers with the public interest. It provides free online resources for obtaining landslide data and an educational resource for all research levels. They also use social media for communication and data collection opportunities (Pennington et al. 2015).

Effective communication for landslide risk should provide all stakeholders with a comprehensive understanding of the potential hazards and factors contributing to vulnerability and exposure. Moreover, it should elucidate the underlying causes and drivers of risk to prevent its transmission to others. By conveying this information clearly and concisely, stakeholders, including laypersons, can make informed decisions and proactively mitigate landslide risks. (Alcántara-Ayala 2018).

One crucial aspect of mitigating the risks associated with landslide disasters is to engage the local community. This can involve several measures, such as building trust, adopting coordinated action strategies, implementing unsafe condition reduction programs, preventing risk exposure, establishing co-responsibility guidelines, and engaging in participatory processes that transcend political and religious affiliations. By implementing these measures, it is possible to manage landslide risk and ensure the safety of communities (Alcántara-Ayala 2018).

Various factors are predicted to increase rainfall-induced landslides, such as population growth, uncontrolled development, and climate change. In Nicaragua, the population experienced a substantial increase of 1.4 million people between 2000 and 2020. Furthermore, the population is expected to grow by 309,454 between 2020 and 2025 (INIDE 2007). Urbanisation in Nicaragua lacks proper territorial management and integrated disaster risk management (Fig. 4). Unfortunately, authorities often overlook the importance of disaster management due to competing priorities. In contrast, the community's risk perception is frequently shaped by their daily struggles and essential needs. It is vital to prioritize and implement measures to help mitigate the impact of rainfall-induced landslides in Nicaragua, especially through landslide disaster risk communication designed for non-experts. This requires community participation to identify the most appropriate mechanisms to communicate meaningful messages and the best way to implement them according to the living contexts of people at risk, along with previous experience, understanding, priorities and needs.

Fig. 4 Landslides occur frequently in Matagalpa, Nicaragua, due to housing construction on susceptible hillslopes (Source: cgonzalezsoza, Pixabay)

6 Concluding Remarks and Future Steps

It is of utmost importance to enhance the accuracy and precision of data collection about historical and contemporary landslides as it aids in evaluating disaster risks at a national scale. However, it is imperative to note that this data is a foundation for a more thorough and comprehensive assessment, which requires an integrated perspective.

Nicaragua, one of the poorest countries in the Americas, is still struggling with institutional weaknesses that hinder economic and scientific development as it works to recover from dictatorship, civil war, and disasters.

Economic, social, and political instability pose significant obstacles to disaster risk management in Nicaragua. These include policy uncertainty, financial and economic barriers, insufficient capacity building, lack of relevant land information regarding hazards, vulnerability and exposure, poor environmental data, and government changes.

To manage landslide risk, communities must have access to information and knowledge through training, workshops, and public campaigns. This raises awareness and encourages preparedness. Effective landslide disaster risk management includes hazard identification, analysis, strategy development, community participation, and mapping. This is a requisite to creating early warning systems, which are crucial in managing landslide disaster risk from an integrated approach by understanding, addressing, and responding to potential adverse effects, reducing the likelihood of a disaster.

Reviewing the information available regarding the spatio-temporal distribution of recent landslides in Nicaragua provided the possibility to elaborate a landslide inventory at a national scale. This will be used to further construct maps at the Department level that can be incorporated into specific materials for landslide risk communication for laypeople and as a base for organising participatory community workshops. However, it should be noted that the limitations of this work so far include not conducting fieldwork or using satellite images to validate the results. The guidelines of such strategies will consider the key processes of disaster risk management: 1. generating knowledge on disaster risk factors (hazards, vulnerabilities, and exposure); 2. preventing future disaster risk by identifying and addressing the social construction of disaster risk; 3. reducing risk involves implementing corrective and control measures when hazards are known, and effects can be mitigated before they occur; 4. preparing a response plan for disasters; 5. responding, rehabilitating; and 6. recovering and rebuilding affected areas and the population's ways of life. Furthermore, understanding the importance of the drivers of exposure and vulnerabil-

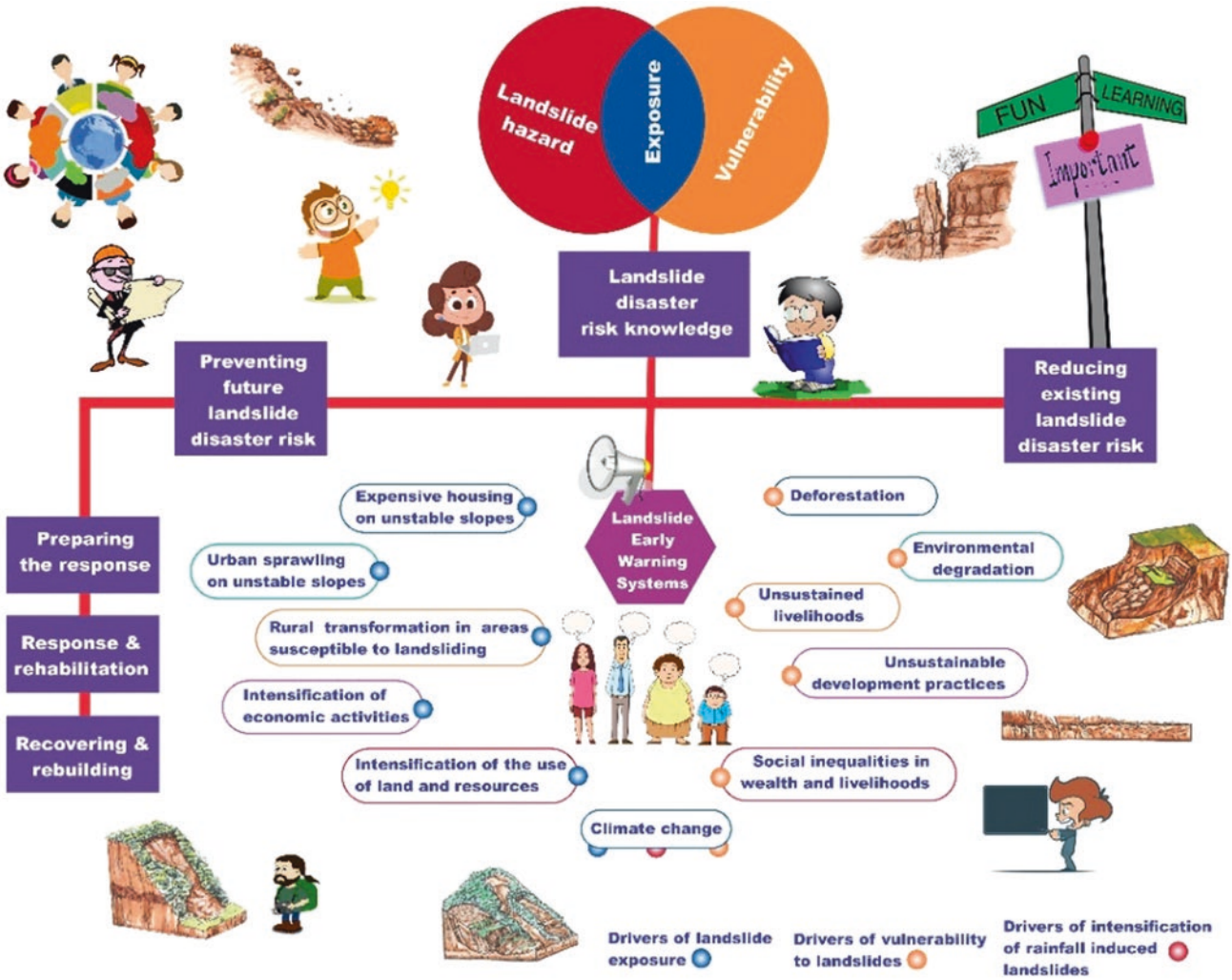

Fig. 5 General elements that must be integrated into landslide disaster risk communication strategies (own elaboration)

ity to landslides, along with the meaning of climate change in the intensification of rainfall-induced landslides in Nicaragua, will be at the core of landslide disaster risk communication (Fig. 5). These activities will be undertaken in 2024 at the municipalities most affected by landslides.

Acknowledgements Thanks to the National Council of Humanities, Sciences, and Technologies (CONAHCYT), who provided a student fellowship for Gema Velásquez-Espinoza and Ricardo J. Garnica-Peña for helping elaborate the maps.

References

Aladi (2009) Examen de las políticas comerciales: informe de la Secretaría de la Organización Mundial del Comercio: Nicaragua. In: OMC (ed) Library Catalog (Koha). ALADI. Secretaría General. In Spanish

Alcántara-Ayala I (2018) TXT-tool 4.052–1.1: landslide risk communication. Landslide Dynamics: ISDR-ICL Landslide Interactive Teaching Tools: Volume 2: Testing, Risk Management and Country Practices, 555–568

Bhuiyan TR, Muhamad N, Lim CS, Choy EA, Pereira JJ (2023) Assessing damage data availability in national landslide databases for SFDRR reporting: a case study of Kuala Lumpur as a local-level application. Landslides:1–20

Borrowing Agency (2023) Labor management procedures Nicaragua-hurricanes eta and iota emergency response project. D.C., World Bank Group, Washington

CCKP-World Bank (n.d.) Climate change knowledge portal for development practitioners and policy makers. World Bank, Washington, D.C.. https://climateknowledgeportal.worldbank.org/country/nicaragua

CRED-UNISDR (2018) Economic losses, poverty & disasters 1998–2017. Université Catholique de Louvain (UCL), Brussels, p 33

Devoli G, Morales A, Høeg K (2007a) Historical landslides in Nicaragua-collection and analysis of data. Landslides 4:5–18

Devoli G, Strauch W, Chávez G, Høeg K (2007b) A landslide database for Nicaragua: a tool for landslide-hazard management. Landslides 4:163–176

Devoli G, De Blasio FV, Elverhøi A, Høeg K (2009) Statistical analysis of landslide events in Central America and their run-out distance. Geotech Geol Eng 27:23–42

EM-DAT (n.d.). http://emdat.be/human_cost_natdis
Guzzetti F, Mondini AC, Chang KT (2012) Landslide inventory maps: new tools for an old problem. Earth Sci Rev 112(1–2):42–66
Incer J, Wheelock J, Cardenal L, Rodríguez AC (2000) *Natural disasters in Nicaragua. Guide to know and prevent them*, Nicaragua. Managua, 278 p In Spanish
INETER (n.d.) Nicaraguan Institute of Territorial Studies, https://webserver2.ineter.gob.ni/sis/bolsis/bolsis.html
INIDE (2007) National, departmental, and municipal population estimates and projections. In Spanish
Instituto Geográfico Nacional, Servicio Geológico Nacional y Catastro y Recursos Naturales (1974) Geological map of the Republic of Nicaragua., 1:1000,000, In Spanish
Inter-Agency Standing Committee and the European Commission (2021) INFORM REPORT 2021 shared evidence for managing crises and disasters, EUR 30754 EN. Publications Office of the European Union, Luxembourg
Narváez L, Lavell A, Ortega GP (2009) Disaster Risk Management: A Process-Based Approach, Secretaría General de la Comunidad Andina: Lima, Perú, In Spanish
National Hurricane Centre (2021a) Tropical cyclone report hurricane Eta (AL292020) https://www.nhc.noaa.gov/data/tcr/AL292020_Eta.pdf
National Hurricane Centre (2021b) Tropical Cyclone Report. Hurricane Iota (AL312020) https://www.nhc.noaa.gov/data/tcr/AL312020_Iota.pdf
National Research Council (1989) Improving risk communication. Committee on Risk Perception and Communication, Commission on Physical Sciences, Mathematics, and Resources, Commission on Behavioral and Social Sciences and Education. National Research Council, National Academy of Sciences, USA
Pennington C, Freeborough K, Dashwood C, Dijkstra T, Lawrie K (2015) The National Landslide Database of Great Britain: acquisition, communication and the role of social media. Geomorphology 249:44–51
Samodra G, Chen G, Sartohadi J, Kasama K (2018) Generating landslide inventory by participatory mapping: an example in Purwosari area, Yogyakarta, Java. Geomorphology 306:306–313
Sassa K (2015) ISDR-ICL Sendai partnerships 2015-2025 for global promotion of understanding and reducing landslide. Landslides 12(4):631–640
Sassa K (2021) The Kyoto landslide commitment 2020: launched. Landslides 18:5–20
Sassa K, Bobrowsky PT, Takara K, Rouhban B (2021) Kyoto 2020 Commitment for Global Promotion of Understanding and Reducing Landslide Disaster Risk. Volume 1 Sendai Landslide Partnerships and Kyoto Landslide Commitment 5th, 145–153
UNISDR (2015) Sendai framework for disaster risk reduction 2015–2030. UNISDR, Geneva
UNISDR (2017) Report of the open-ended intergovernmental expert working group on indicators and terminology relating to disaster risk reduction. UNISDR, Geneva
Van Den Eeckhaut M, Hervás J (2012) State of the art of national landslide databases in Europe and their potential for assessing landslide susceptibility, hazard and risk. Geomorphology 139:545–558
Velásquez-Espinoza G, Alcántara-Ayala I (2023) The chronological account of the impact of tropical cyclones in Nicaragua between 1971 and 2020. Acta Universitatis Carolinae Geographica 58(1)
World Bank (2021) Pooling Catastrophe Risk to Protect against Natural Hazards: Nicaragua's Experience in Disaster Risk Management and Finance, Results Briefs, November 1, 2021
World Bank (n.d.) Poverty and Inequality Platform, https://data.worldbank.org/indicator/SI.POV.NAHC?locations=NI

Emerging Seismicity Trends Linked to Catastrophic Landslides Behavior in Sri Lanka

A. A. Virajh Dias, A. A. Jagath Gunathilake, and Kyoji Sassa

Abstract

Sri Lanka was historically not known to be situated in a seismic hotspot. However, in 2022, the island nation experienced seven earthquakes, and in the past few months of 2023, nine seismic tremors have occurred. This marks a significant increase as typically 2–3 seismic events were reported annually. As the seismic activity in the region gains attention, it becomes imperative to understand how these seismic trends influence the stability of fragment rock slopes and nearby deposits. This paper investigates the emerging seismicity trends on the interpretation of major landslides and understanding catastrophic landslides settings in hill country. The outcomes of this study demonstrates that seismicity around Sri Lanka cannot be no longer ignored in slopes stability and should include seismic hazards assessment. Such approach will ultimately contributing to the development of effective mitigation strategies for enhancing public safety and safeguarding critical infrastructure in seismic-prone areas.

Keywords

Landslides · Rockslides · Seismicity · Earthquakes · Indian Ocean · Eurocode 8 · Reservoirs · SATREP

A. A. V. Dias (✉)
Post Graduate Institute of Science (PGIS), University of Peradeniya, Kandy, Sri Lanka

A. A. J. Gunathilake
Post Graduate Institute of Science, Engineering Geology Research Group (EGRG), Department of Geology, University of Peradeniya, Kandy, Sri Lanka

K. Sassa
International Consortium on Landslides (ICL), Kyoto, Japan

1 Introduction

Seismic activity is an inevitable factor affecting slope stability, particularly in the context of rockslides. Given the increasing frequency of seismic and micro-seismic events in the country (Abayakoon 1996), it has become imperative to comprehend the relationship between seismic activity and rockfall hazards, particularly in the geologically active regions of the mountainous slopes. This study will center on an in-depth evaluation of the most recent seismicity records in Sri Lanka, taking into account both historical data as shown in the Fig. 1 and contemporary trends in mountainous slopes.

Analyzing geological and geographical evidence related to landslides is a key aspect of understanding of any link between seismicity trends in the vicinity. The design of mountainous infrastructure and road development projects is a topic of extensive discussion, particularly when it comes to ensuring stability. This involves considering various factors responsible for detachment from the parent rock, due to extensive saturation potential in joints or foliations, interface friction between intact surfaces (Bhandari et al. 1993), human activities, transportation-induced vibrations, and seismicity-induced trends. However, incidents of this nature were not previously documented as seismic events but rather attributed to extensive periods of rainfall. Nevertheless, recent records have become more intriguing, featuring large boulders rolling downhill slopes, traversing various segments, and ultimately coming to rest on a road without inflicting significant damage to the pavement or the road's alignment during heavy rain, 2016. A similar failure was documented as plenty of boulders descended and rolled on densely forest reserved slope as a result of upland instabilities stemming from natural detachment processes and gravitational forces closer to the periphery of the Randenigala reservoir in 2007, as in Fig. 2. Nevertheless, there was no suitable mechanism in place to confirm whether this behavior was induced by seismic activity, primarily due to the absence of adequate monitoring systems Gunasekara (2000a, b).

B. Abolmasov et al. (eds.), *Progress in Landslide Research and Technology, Volume 3 Issue 1, 2024*, Progress in Landslide Research and Technology, https://doi.org/10.1007/978-3-031-55120-8_9

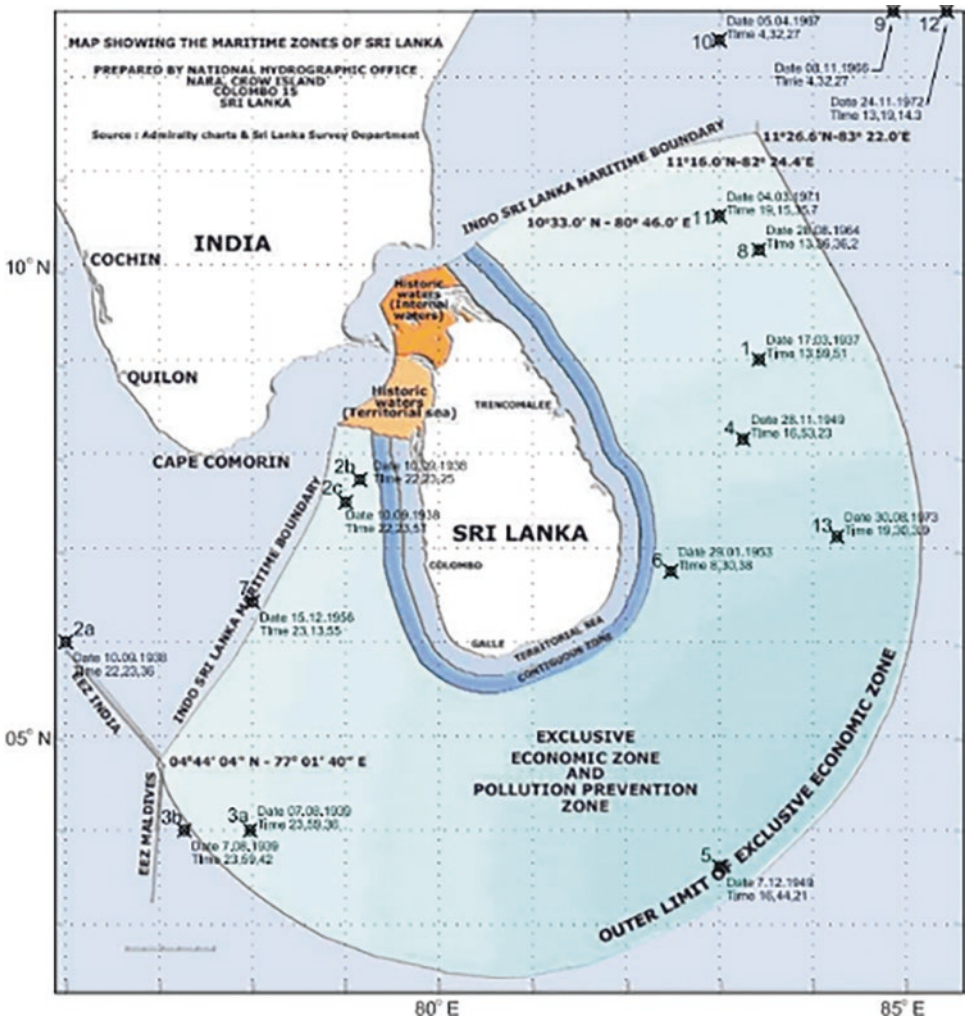

Fig. 1 History of most prominent earthquake epicenters in the Indian Ocean (Vitanage 1994 and updated)

Fig. 2 Roakslide was initiated from the upper mountain region of the reserved forest towards the reservoir second largest reservoir of the Randenigala Hydroelectric Power Project (*Photo by Gunathilake, A.A.J.K.*)

Interestingly, seismicity in the context of Sri Lanka has been somewhat overlooked, as noted by Vitanage (1994). In line with geological and geophysical analyses, study seeks to uncover potential links between seismic events and rockfall occurrences. By analyzing factors such as the spatial distribution, magnitude, and frequency of seismic events (Fernando and Kulasinghe 1986), this study aims to identify potential future seismic hazards. It emphasizes the importance of including the seismicity factor in the evaluation and design of rockfall incidents while taking into account the recorded seismic activity in Sri Lanka.

2 Landslides Initiation with Rockslides

The susceptibility to landslides and rockslides varies depending on geological and topographical factors (Sassa et al. 2010). Areas with steep slopes, loose soil, and a history of such events are more prone to them. Landslides and rockslides are natural geological processes that can occur when there is a sudden and rapid movement of rock, soil, and debris down a slope (Herath et al. 2014). One of the major factor of destabilization of fragment and massive rocks can be caused by factor of heavy rainfall, which saturates the soil and reduces its stability, which can lose interfaces strength of rocks and soil or withered surface that disturb the natural balance of slopes. This behavior reflects the sliding-surface liquefaction associated with grain crushing and the collapse of grain fabrics (Sassa et al. 2010). The one major incident was Aranayaka Landslide of large magnitude occurred in Aranayaka Divisional Secretariat on 17-05-2016. This completely buried parts of several villages and killed over 132 people and destroyed a large number of houses. The immediate triggering factor of this landslide was relentless rain for 4 days from 14th to 17th May, 2016. One of the key observation is sudden detachment which might suggest regolith sliding on a bedrock interface, foliation and jointed faces as in the Figs. 3, 4, 5 and 6.

Fig. 4 Close-up view of the crown of the Aranayaka landslide and rock and rock detachment along the foliation joint (*Photo by Dias, A.A.V., July 2017*)

Fig. 5 Highly fragmented rock at the crown of the slide (*Photo by Dias, A.A.V., July 2017*)

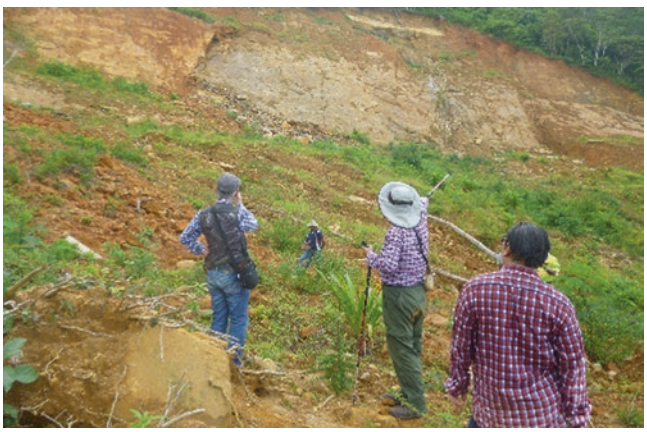

Fig. 3 Initial visit of the ICL-IPL landslide experts at Aranayaka Landslide, Sri Lanka (*Photo by Dias, A.A.V.; July 2017*)

Fig. 6 Failure along major rock-slope joint plane (*Photo by Dias, A.A.V., July 2017*)

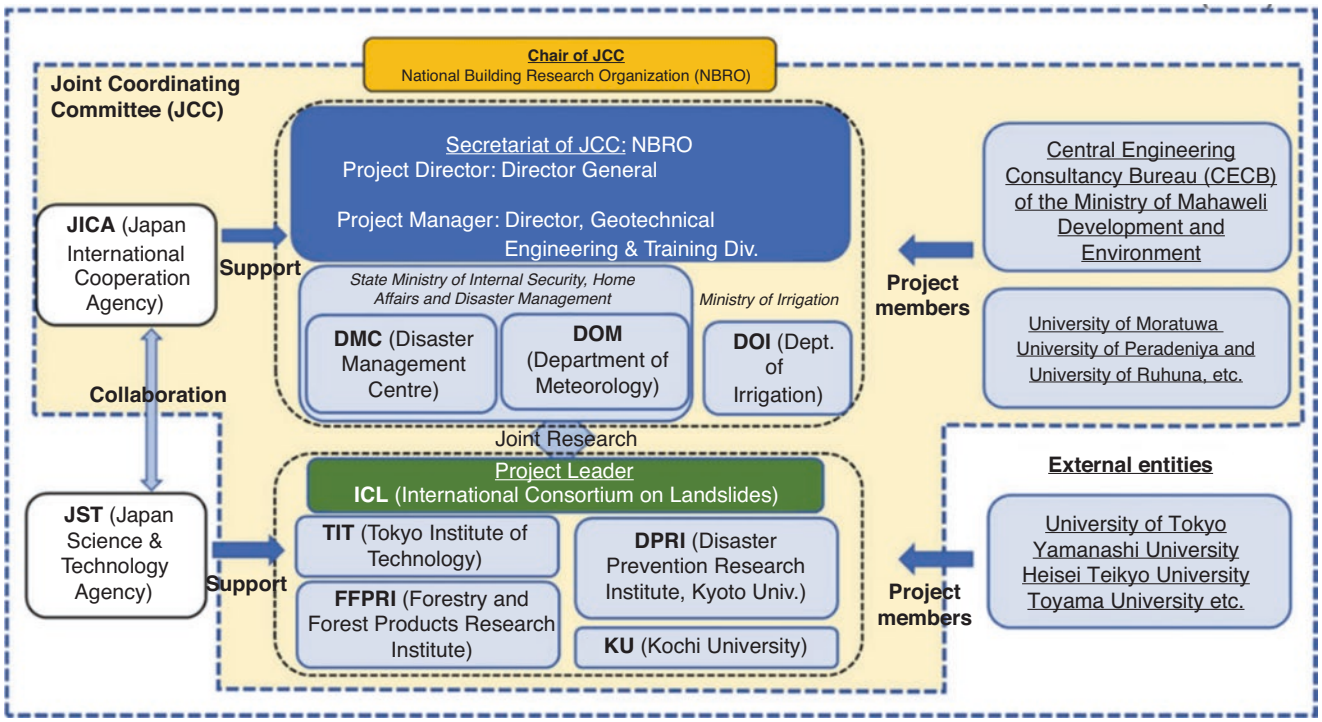

Fig. 7 Implementation structure for project RRLL of the SATREP project (2020–2025)

Table 1 Seismograph installation sites for landslide studies within the SATREP Project

Station	E	N	Sensor Number	Location Name	Installation location
1	80.42965	7.154178	1	Aranayake landslide	Bedrock outcrop (Mountain top)
2	80.43018	7.154362	3	Aranayake landslide	Potential unstable mass
3	80.43101	7.155041	2	Aranayake landslide	Debris (Landslide body)
4	80.41853	7.156085	5	Kalugala primary school	Bedrock outcrop
5	80.41865	7.155851	10	Kalugala primary school	Unstable soil (Cut slope)
6	80.65381	7.218914	6	Kandy	Bedrock outcrop
7	80.65978	7.22917	7	Kandy	Soil (Colluvium)
8	80.2813	6.538857	8	Athwelthota landslide	Bedrock outcrop
9	80.28446	6.541944	9	Athwelthota landslide	Unstable soil

The occurrence of interface failures at the crown of the Aranayaka landslide is a significant observation, as it appears to have triggered a much more substantial failure event as shown in the Figs. 5, 6 and 7. Interface failures in landslides typically refer to the separation or sliding of different geological layers or materials within the slope, often at a boundary where there is a change in the composition, structure, or frictional properties of the materials. These interface failures can have profound implications for the overall stability of the slope.

3 Facilitation from the SATREPS Project for Seismicity Monitoring in Landslides Proven Areas

The National Building Research Organisation (NBRO) of Sri Lanka, in collaboration with the Japan International Cooperation Agency (JICA), has initiated a project titled "Development of Early Warning Technology for Rain-Induced Rapid and Long-Travelling Landslides in Sri Lanka (RRLL)." This project has received funding from the Japanese government through the "Science and Technology Research Partnership for Sustainable Development (SATREPS)" initiative, spanning from 2020 to 2025. As a result of this project, additional capacity has been established for the continuous monitoring of micro-seismicity issues in Sri Lanka. This enhanced capacity includes the installation of nine sets of velocity-type seismometers dedicated to monitoring micro-earthquakes, as listed in Table 1, in addition to the existing acceleration-type seismometers. The SATERP project has garnered substantial technical backing from the Japanese government through JICA, and it has been crafted in partnership with a consortium of state organizations and universities, as depicted in Fig. 7. The project evaluation committee has acknowledged the critical importance of implementing a landslide early warning system, emphasizing the need to monitor the increasing trend in recent seismic activity.

4 History of Seismicity and Earthquake in Sri Lanka

Sri Lankan history further reveals a history of significant earthquakes originating in the Indian Ocean, providing a substantial body of scientific evidence to aid in advancing our understanding of potential risk scenarios.

4.1 First Recorded Earthquake in Sri Lanka

Throughout the recent past, Sri Lanka has seen numerous records of both confirmed and unverified earth tremors, dating back nearly 500 years to historical records like the one from 1615. It particularly devastating earthquake in Colombo, resulting in 2,000 deaths and the destruction of Colombo Fort, is well-documented in the National Archive Reports (Vitanage 1994). A section of the western side wall surrounding Colombo Fort collapsed and was braking in to more pieces and reduced to rubble. Additionally, a bastion crumbled, causing the tragic loss of four lives in a nearby house. The earthquake also wrought havoc on a stone bridge, leaving it in ruins. Moreover, deep fissures in the earth emerged as a consequence of the seismic event. According to a historical account reproduced in https://www.lankalibrary.com/geo/portu/earthquake.htm), these fissures reportedly emitted flames and sulfur a reasonable period after failure.

Knowledge of this earthquake is derived from a 4 page pamphlet published in Lisbon in 1616, the contents of which were brought to light by late Fr. S.G. Pereira, SJ a pioneer historian, proficient in several languages, Prof. in Missionology Georgian University Rome. Based on the damage reported in this article the earthquake is estimated to have a maximum moment magnitude of 6.5 (Seneviratne et al. 2020) corresponding to an intensity of eight on Modified Mercalli Scale. The Modified Mercalli Intensity (MMI) estimates the shaking intensity from an earthquake at a specific location by considering its effects on people, objects, and buildings. At high intensities (above MMI 6), earthquake shaking damage buildings.

4.2 Other Historical Records

There are no other verified historical records known to the period from 1615 to 1800 (Seneviratne et al. 2021). However many unverified Newspaper reports are available on earthquakes which occurred in or around Sri Lanka in 1882, 1924, 1938 and 1944. Many epicenter of earthquakes cannot be identified due to lack of data. However, it must have originated most likely in the Indian Ocean with close proximity to Sri Lanka. Table 2 display some unverified records, which, based on historical data, appear reasonable to consider.

Table 2 Reasonably informative but non verified data in seismicity events in Sri Lanka

Ref	Year	Description of the seismicity
1	1614	Major on-shore earthquake causing intensive damage (200 houses collapsed, 2000 dead, Colombo Fort, NA)
2	1814	Earthquake in Baticaloa area (National Achieves Report (NA)),
3	1823	Major offshore earthquake causing local damage (ODA review) 1979.
4	1882	Shock with intensity II on an arbitrary three part scale near Trincomallee (ODA Review 1979)
5	1938	Sept. seventh (Sept. 10th 1938, Magnitude 5.60 7.50 N; 79.00 E ODA Review 1979)
6	1939	Aug. 8th (Aug. seventh 1939, 5,60 magnitude 4; 00 N,77.50 E ODA Review 1979)
7	1967	Apr, 24th Record only 2033–2040 h(April 5th 1967, 12,30 N,83,00E, ODA Review,1979)
8	1968	June 22nd 2107 hrs, felt in hill country, MM scale 11 (no seismograph charts)
9	1973	Aug, 31st 0121 L.T., Epicenter 350 m approx., MM Scale III, Exact Epicenter 7 LM 84.3E (Aug.30th 1973, 7.15 N,84,33E, 5.80 M ODA Review, 1979)
10	1975	July seventh 1826 Local Time, Query by press seismograph record, Letter from Mr.,H,B.Senaratna of Golewela gives date as sixth July 1975.
11	1979	Oct. ninth 1617–1618 - felt in Spring Valley estate, Badulla Passara, recorded on seismograph intensity II-III
12	1993	Dec.8th 2.30 a.m. felt throughout the island. Epicenter 170 km west of Colombo (5.6 Richter scale)

Information pertaining to the submarine earthquake that occurred between Aceh, Indonesia, and Sri Lanka on December 26, 2004, stands as a devastating Tsunami event in Sri Lankan history. This seismic event resulted from the compression between the Indian and Burmese tectonic plates (Iyengar et al. 1999). Recent scientific findings suggest that the once-unified plate, stretching from India to Australia, has fractured into two distinct plates, thereby creating a new plate boundary (Weissel et al. 1980)—totaling 13 instead of the original 12. The initial seismic eruption, with a magnitude of 8.9, originated near the convergence point of the Australian, Indian, and Burmese plates Research indicates that this region is marked by compression, as the Australian plate undergoes counterclockwise rotation, impinging upon the Indian plate (Weissel et al. 1980). Consequently, this geological shift has activated a region of heightened seismic activity in the South Eastern Indian Ocean. The seismic conditions near Sri Lanka seem to be influenced by the geological events occurring in the western coastal region. Notably, the Mannar rift zone and Comorin ridge, both marked by significant tectonic activity, play a prominent role in shaping the seismic landscape (Seneviratne et al. 2020).

5 Reservoir Induced Seismicity Records

Seismicity issues related to reservoirs are a complex and multifaceted challenge. It is crucial to recognize the potential risks and implement proactive measures to mitigate these risks effectively. Sri Lanka's hydropower reservoirs are not only engineering successes but also vital components of the nation's renewable energy strategy. They not only generate electricity but also facilitate water management, agricultural development, and flood control. The large dams have been constructed under the accelerated Mahaweli development Programme (1980-1990), Kotmale (1982), Victoria (1984), Randenigala (1986), Rantembe (1988), Upper Kotmale reservoirs are situated in the central highland which encompasses major tributaries, agricultural and natural forest mountainous areas of the country. Due to the geological evidence, the presence of well-defined major lineaments (Vitanage 1994) in and around these projects is notable. The impoundment of water in large reservoirs can induce seismic activity in and around the reservoirs due to the incremental stress exerted by the standing water and the prominent lineaments. This can potentially trigger risks for infrastructure, communities, and the environment.

5.1 Micro-Seismicity Recording

The instrumentation and micro-seismic monitoring activity was initiated in 1982 in the Kotmale project area (Vitanage 1981) considering the above geological evidences and issues in and around the large reservoirs. The monitoring of micro-seismic were further extended to Victoria and Randenigala reservoirs by establishing seismicity measuring devices closer to the major reservoirs by the Department of Earthquake Engineering, University of Rookee, India and continuous monitoring was done by the Central engineering Consultancy Bureau (CECB). Observations explored the various aspects of seismicity issues associated with reservoir impounding stages as shown in the Fig. 8, (Vitanage 1994). The weight of water impounded in a reservoir exerts significant stress on the underlying rock and faults. Increased pore pressure in the subsurface due to reservoir filling can reduce the effective stress on existing geological faults, potentially triggering seismic events. No significant records were associated with the seismic induced landslide activity which were expected due to micro seismic nature around the reservoir. Nevertheless, numerous landslides were documented both before and after the impoundment of the

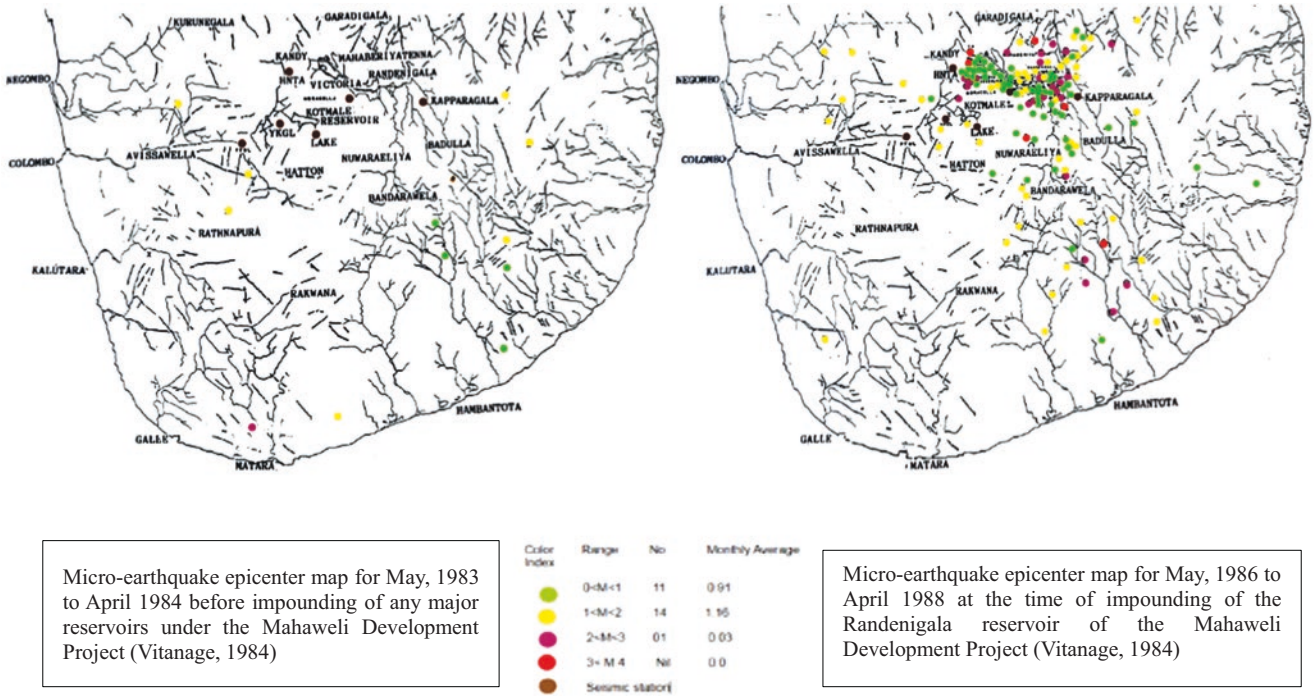

Fig. 8 Monitoring of micro-seismic activity at the Victoria and Randenigala hydropower reservoirs were conducted by the Central Engineering Consultancy Bureau (CECB) during 1983 to 2002

Kotmale reservoir. To ensure reservoir safety, it is crucial to implement thorough planning, continuous monitoring, and effective engineering solutions for the community safety. Additionally, raising awareness within the community about emergency preparedness can prove to be a valuable tool in many instances.

6 Emerging Trend of Earthquakes in the Indian Ocean

These historical observations, when combined with recent tremor records, emphasize the critical importance of gaining a scientific understanding of the depth of this issue. Some of the early seismic activity records could not be verified due to inadequate documentation or gaps in data. Consequently, the data presented in Table 1 cannot be effectively utilized for interpretations. Nonetheless, there are several Indian catalogues that comprehensively cover earthquake events in the South Indian region (Menon et al. 2010 and Senavirathna et al.). A study conducted using the Indian catalogue identified reliable data, including historical seismographic records, as depicted in Fig. 9 (source: Seneviratne et al. 2020; https://doi.org/10.4038/engineer.v53i2.7412). This data was used to investigate seismic activity in the region surrounding Sri Lanka, which is bounded by Latitude 0°N–20°N and Longitude 70°E–90°E. According to the recent literature measured earthquake data at Colombo should be available from 1909 to 1992 (Seneviratne et al. 2020). Based on historical newspaper records preserved in the national archives from 1938, it is evident that the seismic event left its mark on nearly every corner of the island (Kularathna, et al. 2015). Despite the undeniable sense of alarm and unease caused by the tremors, it is noteworthy that the region's preparedness

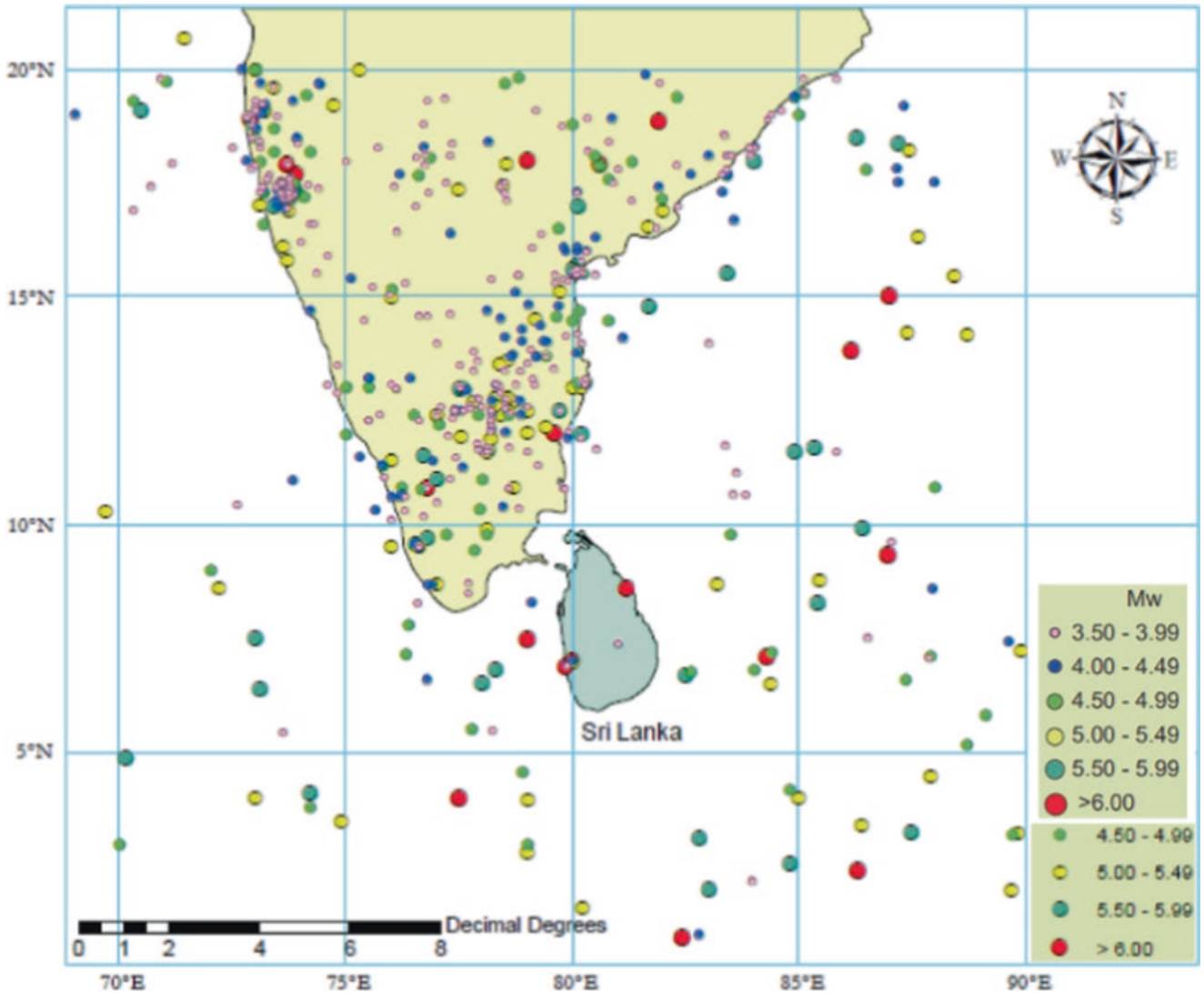

Fig. 9 Epicenters from recent earthquakes (*source*: Seneviratne et al. 2020) https://doi.org/10.4038/engineer.v53i2.7412)

and resilience were able to prevent any loss of life or significant harm to infrastructure and property. In the southwest, where the tremors were most strongly felt, communities came together to share their experiences and support one another during this unexpected event. The impact on the up-country areas, added a unique dimension to the narrative, as residents in these highland regions also felt the ground shake beneath their feet (Vitanage 1995).

7 Discussion on Regional Effects

The Indian Ocean region is highly seismically active due to the complex interactions of tectonic plates. The primary plate boundaries in this area are the Indo-Australian Plate to the south and the Eurasian Plate to the north, resulting in frequent seismic activity. As indicated early, Subduction zones are particularly significant in the Indian Ocean region. The Indo-Australian Plate is subducting beneath the Eurasian Plate to the north of Sri Lanka, creating a convergent boundary known as the Sunda Megathrust. This subduction zone is a major source of earthquakes and tsunamis in the region. The Indian Ocean has experienced several devastating earthquakes in its history. One of the most significant was the 2004 Indian Ocean earthquake and tsunami, which had its epicenter off the west coast of northern Sumatra, Indonesia (Parsons et al. 2021). This event caused widespread destruction across the Indian Ocean region, including Sri Lanka: While not located directly on a plate boundary, Sri Lanka is still vulnerable to earthquakes due to its proximity to the subduction zone. The increasingly oblique convergence moving northwest is accommodated by crustal seismicity along several transform and normal faults, including the Sumatra Fault. Deformation related to plate boundaries is not solely confined to the subduction zone (Dissanayake, 2005) and the overriding plate. In fact, the Indo-Australian plate is composed of two somewhat distinct plates, India and Australia, which are connected through a wide and actively deforming region. This region generates seismic activity extending several hundred kilometers to the west of the trench (Hayes et al. 2013). This deformation is exemplified by the recent earthquake sequence in April 2012, which included the strike-slip events of magnitude 8.6 and 8.2 on April 11, along with their subsequent aftershocks. Sri Lanka, as an island nation, has previously encountered moderate to strong earthquakes, and it remains susceptible to more significant seismic events in the future.

In summary, the historical records from 1938 provide us with valuable insights into the island's ability to withstand and recover from seismic events, while highlighting the shared experiences of those who lived through this significant event, particularly in the southwest and up-country areas. Various agencies and research institutions actively monitor seismic activity in the Indian Ocean, including the Indian National Centre for Ocean Information Services (INCOIS) and the United States Geological Survey (USGS). These organizations provide valuable data for earthquake prediction and risk assessment.

8 Recent Development of Seismicity Monitoring

The Geological Survey and Mines Bureau (GSMB) installed three seismometers at different places and also in year 2000 and 2010. The first was placed in Pallekele (PALK) in 2000 and connected to the Global Seismographic Network (GSN). The remaining two were set up in 2010, one in Mahakandarawa (MALK) and the other in Hakmana (HALK), both linked to the GEOFON Network. Access to waveform data and earthquake parameters recorded by these seismometers is available through the internet via the GSN and GEOFON networks, facilitated by GSMB. Therefore, Sri Lankan seismograph network currently has four permanent seismographs:

1. PALK (a 90 m deep borehole station with minimal ambient noise) in Pallekale,
2. Kandy; MALK in Mihintale,
3. Anuradhapura; HALK in Hakmana, Matara;
4. BULK in Buddangala, Batticaloa

Further the records obtained from stations in Sri Lanka indicate the seismic activities in closer to some of the major irrigation and water reservoirs as recorded in the Table 3 recorded as at 15.09.18, according to the GSMB.

These results shed light on the identification of 14 previously undocumented seismic events see the Table 4, that have occurred over the course of the past 7 months, the year 2023 in the Fig. 10. The recent observation regarding the tremor that occurred in April approximately 26 km off the

Table 3 Recently reported seismic events within Sri Lanka

Date	Reported area	N	E	M_L
08/28/2012	MaduruOya	7.48	81.15	2.9
09/14/2012	MaduruOya	7.46	81.08	2.3
09/28/2012	Siyambalaanduwa	7.04	81.44	2.6
10/06/2012	Weheragala Reservoir	6.55	81.21	2
12/01/2012	Wadinagala	7.28	81.67	2.2
12/14/2012	Wadinagala	7.14	81.33	2.1
01/25/2013	Wadinagala	7.17	81.44	2.7
25/01/2013	Ampara	7.17	81.49	3.2
07/10/2013	Bay of Bengal	6.11	85.32	4.5
16/10/2013	Dewalahinda Ampara	7.17	81.57	2.54
28/10/2013	Ampara	7.16	81.36	2.12
31/10/2013	Hambanthota	5.6	81.1	2.47
14/09/2018	Trincomalee	8.45	81.18	3.58

Source: (GSMB)

Table 4 Rigorously verified data obtained from the Geological Survey and Mines Bureau (GSMB) on seismicity records for the period from January 2023 to July 2023

No	Date	Location	UTC Time	Magnitude	Longitude	Latitude	Remarks
1	2023.02.10	Buttala, wellawaya area	6.41.26	3	81.18	6.73	Instrumental records, Bulletin issued, Felt reports
2	2023.02.10	Buttala	06.44.06	3.5	81.12 ± 12	6.80 ± 9	Instrumental records, Bulletin issued, Felt reports
3	2023.02.10	East of wellawaya town	22.18.06	2.3	81.12 ± 9	6.73 ± 2	Instrumental records, Bulletin issued, Felt reports
4	2023.02.22	Buttala Wellawaya area	6.14.51	3.3	81.07 ± 19	6.71 ± 3	Instrumental records, bulletin issued, felt reports
5	2023.03.18	Kirinda- Palatupana	13.16.40	2.6	81.39	6.21	Instrumental records, Bulletin issued, No felt reports
6	2023.03.18	Gomarankadawala - Thibirigaswewa	22.00.48	3	80.96 ± 3	8.70 ± 7	Instrumental records, Bulletin issued, No felt reports
7	2023.03.24	Sella Kataragama	13.24.13	2.4	81.31 ± 4	6.47 ± 3	Instrumental records, Bulletin issued, Felt reports
8	2023.03.30	24 km from Beruwala	07.32.08	3.7	79.79	6.38	Instrumental records, Bulletin issued, Felt reports
9	2023.04.12	Kotiyagala, Moneragala	12.32.42	2.3	81.48	6.74	Instrumental records, No felt reports
10	2023.04.23	25.8 km from Hambathota (Indian Ocean)	19.15.10	4.4	81.23	5.91	Instrumental records, Bulletin issued, Felt reports
11	2023.04.25	Buttala	05.38.10	2	81.21	6.71	Instrumental records, No felt reports
12	2023.05.15	Near Lunugamwehera	16.54.48	2.4	81.26 ± 4	6.38 ± 4	Instrumental records, Bulletin issued, Felt reports
13	2023.06.05	Close to Pupuresssa and Deltota (Nearest town:Gampola)	17.19.22	2	80.57 ± 4	7.16 ± 3	Instrumental records, Bulletin issued, Felt reports
14	2023.07.21	Monaragala	3.36.25	2.6	81.25 ± 3	6.83 ± 3	Instrumental records, Bulletin issued, Felt reports

Fig. 10 Red squire indicates the most recent occurrences of earthquake records within the period of January 2023 to July 2023)

coast of Hambantota at a 4.4(M_L) magnitude on the Richter scale was that it could have been an aftershock of the major earthquake that occurred in Indonesia. When a major earthquake takes place on an adjacent tectonic plate, it is possible for some of that stress to pass to the neighbouring plates. Notably, the events reached a magnitude of 4.4 (M_L) on the Richter scale, indicating a substantial seismic disturbance. Furthermore, the analysis reveals that three of these recorded events were of significant magnitude, each registering at or above Richter 3.5 (M_L). This underscores the importance of ongoing monitoring efforts (Thaldena et al. 2013) and the need for a robust early warning system to address seismic activity in the region effectively. These findings serve as a stark reminder of the dynamic and potentially hazardous geological conditions in the area, emphasizing the importance of continued research and preparedness to mitigate the impact of seismic events.

9 Micro-Seismicity Impact on Catastrophic Landslides

Micro-seismic events generate stress waves within the subsurface. These waves can redistribute stress along pre-existing geological interfaces, including the contact between soil and rock. In soil mechanics, effective stress is a critical concept. It's the stress that actually influences the behavior of

soil and rock. When micro-seismic events occur, they can momentarily increase or decrease effective stress along the soil-rock interface (Cooray 1994). This can lead to changes in the frictional resistance at the interface. Micro-seismic events can also affect pore pressure within the soil or rock mass. An increase in pore pressure can reduce effective stress, making the interface less stable and more prone to sliding. Repeated micro-seismic events can cause cumulative damage along the interface, weakening the cohesion and frictional resistance between the soil and rock. During the fifth International Symposium on Landslides (Sassa 1988), a special lecture titled "Geotechnical Modeling for Landslide Motion" aimed to replicate the Ontake landslide, which was initiated by the 1984 Naganoken–Seibu Earthquake (Sassa et al. 2010). This landslide involved a massive volume of 36 million cubic meters of material traveling over a distance exceeding 10 km through torrents. It is worth noting that micro-seismicity, referring to the occurrence of small-scale seismic events that are often imperceptible to humans, can indeed influence the reduction of friction at the interface between soil and rock. Recent finding noted that landslides may be triggered by earthquakes and both effects of earthquakes and pore water pressure. The border between rapid landslide and no movement was examined by earthquake loading in addition to pore pressure ratio. The preliminary test proved that the pore pressure ratio ru=0.4 does not cause landslide without earthquake loading though ru=0.5 will cause a rapid landslide (Sassa et al. 2010). Therefore, evaluation of potential catastrophic landslide behavior conditions to be reasonable to consider the micro-seismic impact and understand its sensitivity and missing parameters during prediction slope stability. The various guidelines are thoroughly discuss such matter in evaluation and prediction of the stability potential of rock slopes. The latest confirmed seismic activity data for Sri Lanka can be found in Table 3 and over-

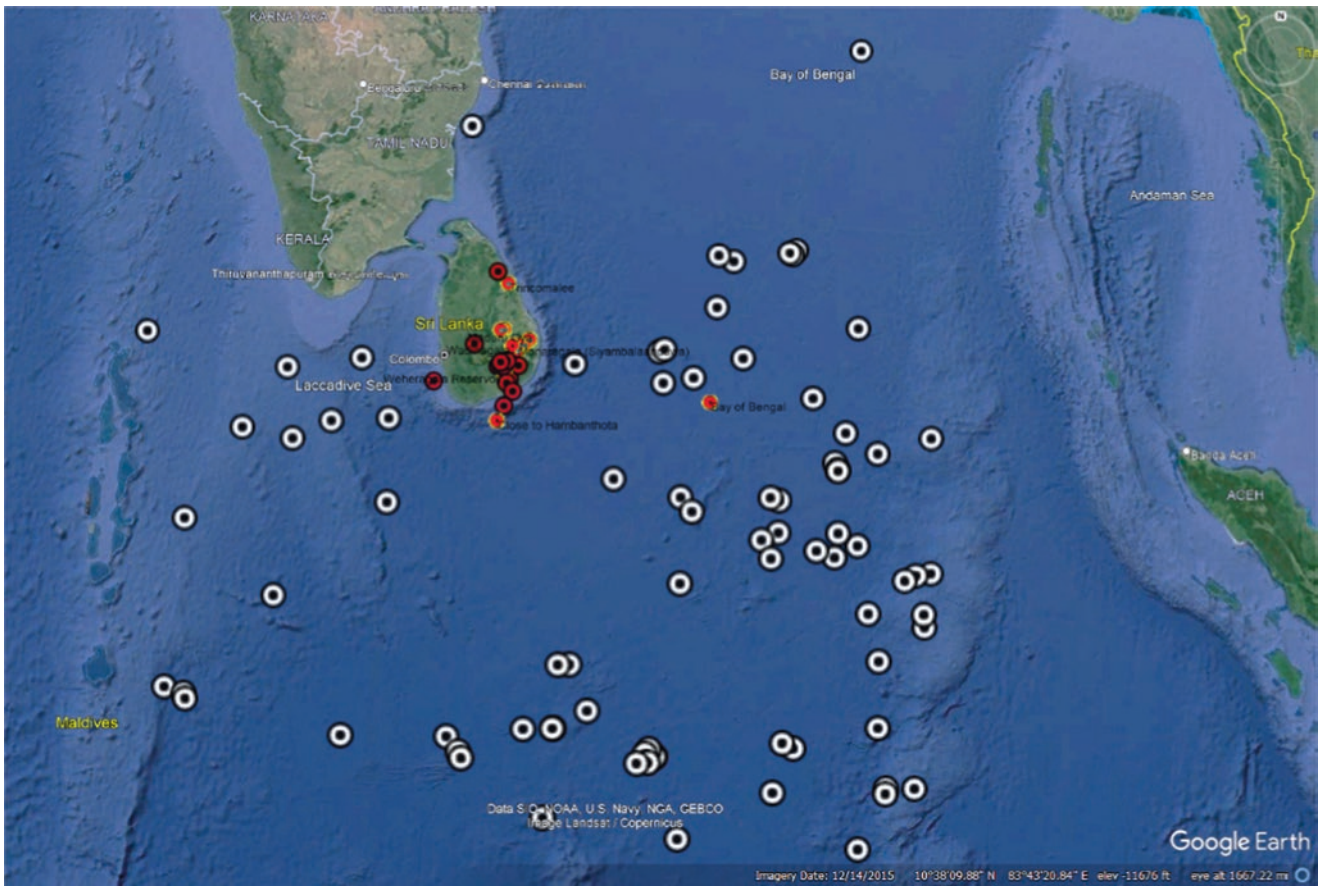

Fig. 11 Earthquakes epicenters of regional events reported around in Indian Ocean Sri Lanka, period of 1944.02.29 to 2023.07.01 in white color rounds (Data Source: United State Geological Survey); Orange and Red color indicates epicenters within and closer to Sri Lanka (Geological Survey and Mines Bureau)

all verified records within Indian ocean from 1944 to July 2023 as shown in the Fig. 11.

10 Stability Evaluations

The seismic ground acceleration coefficient plays a critical role in the evaluation of stability for various structures and geotechnical applications (Kodagoda et al. 2018). However, it also comes with certain limitations. Seismic ground acceleration coefficients are crucial in assessing the seismic hazard at a particular location. This information is used for urban planning and building code development to ensure structures are designed to withstand potential earthquakes.

As our awareness of micro-seismicity grows, it becomes increasingly vital to incorporate safe seismic coefficients into the evaluation and design of structures. Doing so ensures the safety of people, minimizes long-term risks, and protects against economic and environmental consequences. Moreover, adhering to updated building codes and regulations that consider safe seismic coefficients is not just a legal obligation but a moral imperative. In a world where seismic events can have far-reaching consequences, the consideration of safe seismic coefficients is a cornerstone of resilient and responsible infrastructure development. Many countries have seismic design codes that require engineers to consider these coefficients when designing structures. Compliance with these codes is essential for safety.

11 Seismic Coefficients According to Eurocode 8

This presents a summarized description of the seismic coefficients to be used in slope stability analyses, according to Eurocode 8 (EN 1998-1: 2004; EN 1998-5:2004). The horizontal seismic coefficient is given by the following equation (Eurocode (EC8)(2005):

$$k_h = 0.5\left(\frac{a_g}{g}\right)S\,S_T$$

Where:

- a_g represents the design value of (horizontal) seismic acceleration on a type A ground, which results from the product between maximum reference acceleration, a_gR, and an importance factor. Definition of the type of ground is recognized as
  - A - Rock.
  - B - Ground Very dense sand or gravel or very stiff clay.
  - C - Dense sand or gravel or stiff clay.
  - D - Loose to medium cohesionless soil or soft.

Table 5 Values of the topographic amplification factor, S_r (adapted from EN 1998-5:2004)

Conditions of the slope	
Slope angle less than 15°	1.0
Sites near the top edge of isolated cliffs and slopes	>12
Ridges with crest width significantly less than the base width, and average slope angle between 15° and 30°	>12
Ridges with crest width significantly less than the base width, and average slope angle greater than 30°	>14

- g is the acceleration due to gravity;
- S is the coefficient that takes into account the possible amplification of acceleration between the bedrock and the ground surface;
- S_T is the topographic amplification factor greater than 1.0 over or near cliffs, slopes longer than 30 m, and inclinations greater than 15°.

The calculation of a_g and S has been functioned with the topographic effects being particularly relevant in shallow landslides. The values of S_T are shown in Table 5 with the topographic effects being particularly relevant in shallow landslides. In deep landslides, in which the failure surface passes through the toe of the slope, the topographic effect can be ignored, as the seismic amplification factor decreases rapidly with depth. The vertical seismic coefficient is given by the following eqs. (NP EN 1998-5: 2004):

$$k_v = \pm 0.5 k_h \text{if} \frac{a_{vg}}{a_g} > 0.6$$

$$k_v = \pm 0.33 k_h \text{if} \frac{a_{vg}}{a_g} \le 0.6$$

It's important to note that Eurocode 8 is a complex standard, and its application to slope stability analyses requires a thorough understanding of geotechnical engineering principles and seismic design considerations (Open Source 2023). Engineers, geotechnical specialists and geologists should carefully study the specific sections of Eurocode 8 relevant to their project and seek guidance from experienced professionals when conducting slope stability analyses in seismic-prone areas.

Notes

- In the presence of a loose surface layer, the values of the three lines above should be increased by at least 20%.
- The value of S_T may be assumed to decrease as a linear function of the height above the cliff or ridge, and to be unity at the base.

12 Conclusions

In recent years, our understanding of increasing trends in seismic activity has significantly evolved, and we are more aware than ever of the presence and impact of micro-seismicity—small-scale seismic events that were previously unnoticed or underestimated. This new knowledge has highlighted the critical importance of considering safe seismic coefficients in the evaluation and design of slope stability, infrastructure, and buildings. In this article, we will explore why it is imperative to account for safe seismic coefficients, especially in the face of increasing trends in micro-seismicity.

Sri Lanka faces diverse terrain and evolving environmental factors. Continued research and tailored strategies are vital to safeguarding lives, infrastructure, and the natural environment from the potentially devastating impacts of catastrophic landslide behavior. The study on the impacts of emerging seismicity trends on mountainous slope stability interpretation in Sri Lanka underscores the critical importance of considering evolving seismic factors in geological assessments and hazard mitigation efforts.

As seismic events continue to evolve and pose new challenges, it is imperative to adapt our methodologies and strategies to ensure the safety and resilience of the region's landscapes and communities in the face of these dynamic geological phenomena. Monitoring of micro-seismic activity and earthquake occurrences has been enhanced, and we are now focusing on understanding the potential impacts of micro-seismic activity on rain-induced landslides and rockslides.

Acknowledgments This paper is an integral part of the research project titled "Digital Landscape Models for Interpreting Rock Slope Stability and Potential Rock Trajectory Adjacent to Roadways." It forms a segment of the author's PhD research, registered at the Post Graduate Institute of Science, University of Peradeniya, Sri Lanka. We extend our heartfelt gratitude to the Geological Survey and Mines Bureau (GSMB) for generously providing the most recent seismicity data, which has proven to be an invaluable resource for this study. We would like to offer special thanks to Ms. Nilmini Theldana, Senior Seismologist at GSMB, for her unwavering support in supplying and updating seismic information. Our appreciation also goes out to the dedicated staff of the Natural Resources Management and Laboratory Services at the Central Engineering Consultancy Bureau (CECB), as well as the Engineering Geology Research Group at the Department of Geology, University of Peradeniya, for their priceless assistance and support. It is important to emphasize that the opinions expressed in this paper solely represent those of the authors. We wish to convey our gratitude to Eng. B.A.S.S. Perera, Chairman, and Eng. S.A.U.D.C. Siriwardana, General Manager of the Central Engineering Consultancy Bureau, for their consistent encouragement and support throughout the course of this research endeavor.

References

Abayakoon SBS (1996) Seismic risk analysis of Sri Lanka. J Geol Soc Sri Lanka (GSSL) 6:65–72

Bhandari RK, Jeyatharan K, Raviskanthan A (1993) Dynamics of Rockfalls in Sri Lanka and Landslide Hazards. International Conference on Case Histories in Geotechnical Engineering, pp. 499–504

Cooray PG (1994) Geological factors affecting landslides in Sri Lanka; Proc. National Symposium of Landslides in Sri Lanka, Colombo 17-19th March, 1994, pp 15–22

Dissanayake CB (2005) A new plate boundary near Sri Lanka; implications for future geo hazards. J Natl Sci Found 33(1):5–8

Eurocode 8 (EC8) (2005) EN1998 1: "design provisions for earthquake resistance of structures, Part1: general rules, seismic actions and rules for buildings". European Committee for Standardization, Brussels

Fernando MJ, Kulasinghe ANS (1986) Seismicity of Sri Lanka. Phys Earth Planet Inter 44:99–106

Gunasekara KW (2000a) "First Earthquake in Sri Lanka", Sunday Observer, p. 34

Gunasekara KWM (4th June 2000b) "First Earthquake in Sri Lanka" - Sunday Observer

Hayes GP, Bernardino M, Dannemann F, Smoczyk G, Briggs R, Benz HM, Furlong KP, Villaseñor A (2013) Seismicity of the Earth 1900–2012 Sumatra and vicinity: U.S. Geological Survey Open-File Report 2010–1083-L, scale 1:6,000,000, https://pubs.usgs.gov/of/2010/1083/l/

Herath HM, Janaki MK, Kodagoda SSI, Dias AAV (2014) Shallow Modes of Slope Failure in Road Earth Cuttings in Sri Lanka; Proceeding of the World Landslide Forum3 (WLF3), Beijing, China, 2-6 June 2014; Volume 2, Landslide Science for a Safer Geoenvironment, PP 51- 58; ISBN 978-3-319-05049-2; Springer

Iyengar RN, Sharma D, Siddiqui JM (1999) Earthquake history of India in medieval times. Indian J Hist Sci 34(3):181–237

Kodagoda SSI, Herath HMJMK, Lakmali MADC, Dias AAV (2018) Design of Foundations and surrounding soil for reduction of liquefaction induced damages in Colombo and suburbs., Proceedings of the CECB Symposium, 2018, pp 235–242

Kularathna EKCW, Pitawala HMTGA, Senaratne A, Weerasinghe D (2015) "Gondwana Breakup and Development of Sedimentary Basins in Sri Lanka". Proc. 31st Annual Sessions of the Geol. Soc of Sri Lanka, pp 6

Menon A, Ornthammarath T, Corigliano M, Lai CG (2010) Probabilistic seismic Hazard macrozonation of Tamil Nadu in southern India. Bull Seismol Soc Am 1(3):1320–1341

Open Source (2023) Seismic coefficients to be used in slope stability analyses, according to Eurocode 8, https://ebrary.net/135783/engineering/annex_seismic_coefficients_used_slope_stability_analyses_eurocode#1391781. Last accessed on 26th September, 2023

Parsons AJ, Sigloch K, Hosseini K (2021) Australian plate subduction is responsible for northward motion of the India-Asia collision zone and 1000 km lateral migration of the Indian slab. Geophys Res Lett 48:e2021GL094904. https://doi.org/10.1029/2021GL094904

Sassa K (1988) Geotechnical model for the motion of landslides. In: Proc. 5th International Symposium on Landslides, "Landslides", Balkema, Rotterdam, vol. 1. pp. 37–56

Sassa K, Nagai O, Solidum R, Yamazaki Y, Ohta H (2010) An integrated model simulating the initiation and motion of earthquake and rain induced rapid landslides and its application to the 2006 Leyte landslide. Landslides 7(3):219–236

Seneviratne HN, Perera LRK, Wijesundara KK, Dananjaya RMS, de Jayawardana US (2020) Seismicity around Sri Lanka from historical records and its engineering implications. Engineer LIII(02):47–52.,

© The Institution of Engineers, Sri Lanka. https://doi.org/10.4038/engineer.v53i2.7412

Seneviratne HN, Perera LRK, Wijesundara KK (2021) Origin of Recent Microseismicity Around Digana, Sri Lankafrom Seismic Modelling, Proceedings of the 37th Technical Session of Geological Society of Sri Lanka, Published Online—25th February 2021

Thaldena S, Perera LRK, Prame W (2013) Present Status of Seismic Monitoring and Risk Assessment in and around Sri Lanka, Proceedings of the 4th International Conference on Structural Engineering and Construction Management. Kandy, Sri Lanka

Vitanage PW (1981) Geology and Strcture of the Kotmale Project; Sir Williom and Halcrow and Partners, Sri Lanka, 1 and 11, pp. 1–59

Vitanage PW (1994) Seismicity-Neglected aspects of Sri Lankan landslide studies; Proc. National Symposium of Landslides in Sri Lanka, Colombo 17-19th March, 1994, pp. 31–40

Vitanage PW (1995) Seismicity in Lineaments–Impact on Engineering Structures, In Handbook on Geology and Mineral Resources of Sri Lanka. Second South Asia Geological Congress, GEOSAS–II, pp. 59–62

Weissel J, Anderson R, Geller C (1980) Deformation of the Indo–Australian plate. Nature 287:284–291

Centrifuge Modeling of Slopes Subjected to Groundwater Flow and Rainfall Infiltration

S. H. S. Jayakody, Ryosuke Uzuoka, Kyohei Ueda, and Kenta Saito

Abstract

Due to the severe harm that they cause to society and the economy, landslides have become an infamous topic. Certainly, rainfall is one of the most important external factors that lower soil suction and shear strength, which in turn leads to shallow landslides. Indeed, landslide early warning mechanisms mostly rely on predicted or actual rainfall. However, the absence of a more thorough hydrological process involving groundwater flow means that temporal predictability still poses a challenge. Therefore, understanding the complex hydromechanical process using physical modeling techniques is of utmost importance. This paper aims to confirm the performance of the newly developed centrifuge soil container that facilitates the simultaneous functioning of groundwater flow and rainfall infiltration. Upon the validation of the functioning of the centrifuge chamber, landslide characteristics of unsaturated slopes were examined under the integrated effect of groundwater flow and rainfall. The results show that distinctive characteristics compared to slopes fail under rainfall infiltration.

Keywords

Slope stability · Unsaturated slopes · Groundwater flow · Rainfall infiltration · Centrifuge modeling

S. H. S. Jayakody (✉) · R. Uzuoka · K. Ueda
Disaster Prevention Research Institute, Kyoto University, Kyoto, Japan
e-mail: jayakody.sanchitha.8d@kyoto-u.ac.jp; uzuoka.ryosuke.6z@kyoto-u.ac.jp; ueda.kyohei.2v@kyoto-u.ac.jp

K. Saito
Kozo Keikaku Engineering, Tokyo, Japan
e-mail: kenta-saito@kke.co.jp

1 Introduction

Landslides are one of the pervasive natural hazards occurring on the planet. Each year these landslides cause not only billions of cash in economic losses but also a priceless socio-impact. In particular, Sri Lanka ranks the fourth place and the seventh place according to landslide events per 1000 km^2 and fatalities per million inhabitants (Gómez et al. 2023). In recent years, numerous measures, particularly the implementation of landslide early warning systems, have been taken to manage and minimize the damage brought on by relentless landslides. These developments are vital because early predictions are not only a viable option but also crucial for ensuring the safety of inhabitants, as it enables proactive evacuation plans and safeguard the lives at risk.

Certainly, rainfall is one of the most important external factors that lower soil suction and shear strength, which in turn leads to shallow landslides. However, the absence of a more thorough hydrological process involving groundwater flows means that temporal predictability still poses a challenge. Understanding the complex behavior of pre-existing groundwater flow and their recharge/surcharge during a rainfall event is essential for strengthening the landslide early warning mechanism. Hence, this study aims (1) to validate the functioning of the newly developed centrifuge chamber to reproduce both groundwater flow and rainfall infiltration and (2) to examine the initial condition of the soil-bedrock interface, influenced by the existing groundwater flow, on the slope's response to subsequent rainfall infiltration by centrifuge modeling.

2 Experimental Setup

2.1 Centrifuge Model Testing

Many centrifuge model studies have focused on slope behavior under rainfall infiltration, except a few recent studies

B. Abolmasov et al. (eds.), *Progress in Landslide Research and Technology, Volume 3 Issue 1, 2024*, Progress in Landslide Research and Technology, https://doi.org/10.1007/978-3-031-55120-8_10

incorporated groundwater flow effects in the simulation (Askarinejad et al. 2012; Lucas et al. 2020; Take et al. 2015). Therefore, there is an essential need to comprehensively discuss the hydromechanical behavior of slopes subject to pre-existing groundwater flow and rainfall infiltration.

A novel soil container was designed to conduct unsaturated slope stability analysis using centrifuge modeling. This container was capable of simulating both rainfall and groundwater flow conditions independently, allowing for parallel control of these two crucial occurrences. The schematic diagram of the centrifuge container, with dimensions of 800 × 150 × 600 (mm), is illustrated in Fig. 1. Scaling factors specific to this study can be found in Table 1 in which "N" represents the enhanced gravitational acceleration. It is important to note that all experimental results presented in this research are scaled models unless explicitly mentioned otherwise. The model testing was conducted at the geotechnical centrifuge facility at the Disaster Prevention Research Institute (DPRI), Kyoto University, under 50 g conditions. To simulate groundwater flow conditions, the water in the drainage tank was pumped up to the intermediate water tank via an overhead water storage tank using a container-mounted pump. To initiate the groundwater simulation, electrode sensors were activated, and water was subsequently released through the drainage slits located along the right-side boundary wall.

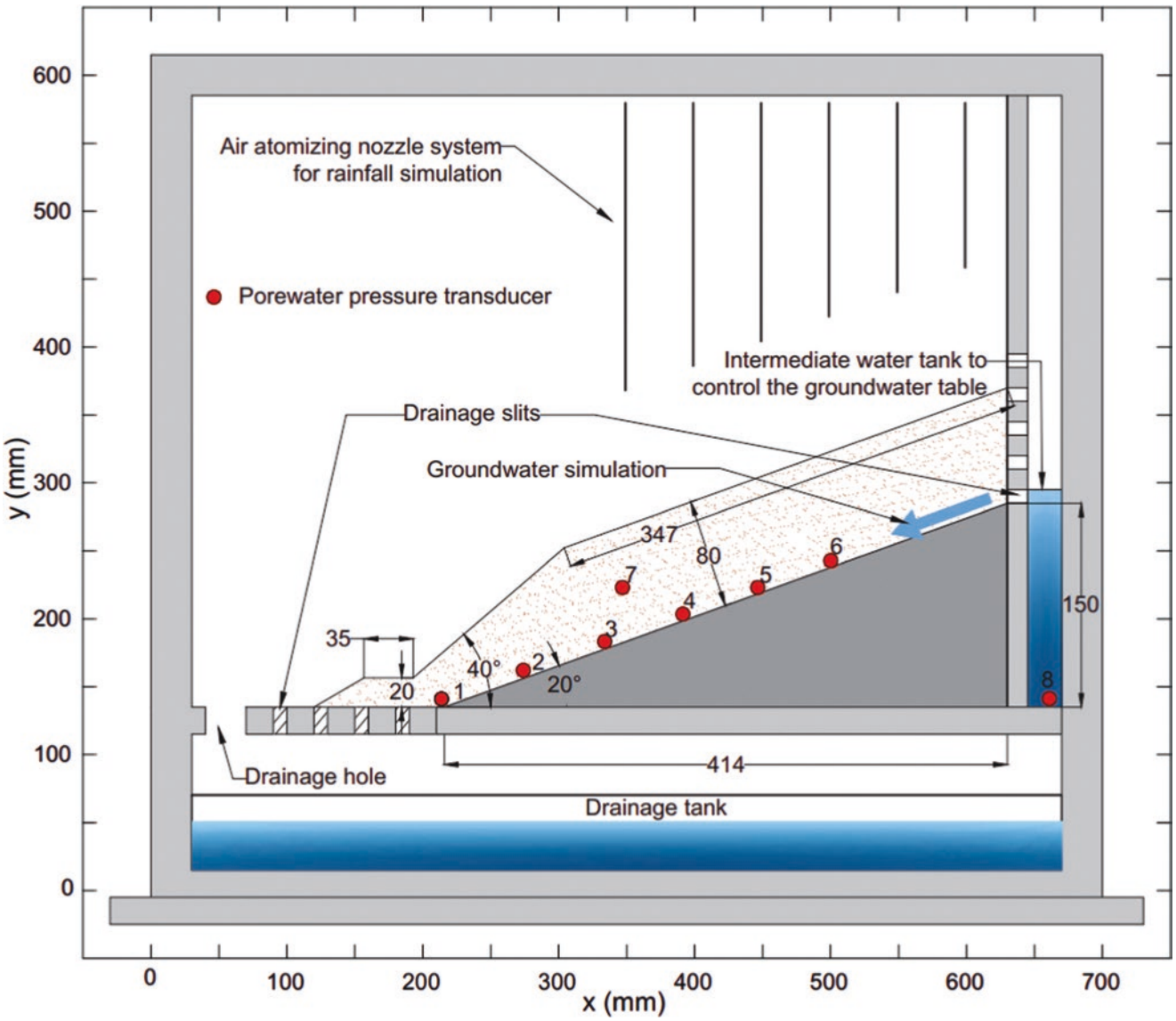

Fig. 1 Schematic diagram of the centrifuge container

Table 1 Centrifuge scaling laws applied in the experiments

Parameter and dimension	Model/Prototype
Stress [ML-1 T-2]	1
Length [L]	1/N
Time (diffusion) [T]	$1/N^2$
Rainfall intensity [LT-1]	N
Rainfall length [L]	1/N
Rainfall duration [T]	$1/N^2$
Rainfall frequency [1/T]	N^2
Hydraulic conductivity [LT-1]	N

Table 2 Material properties of Masado soil

Parameter and unit	Value
D60, D30, D10 (mm)	0.83, 0.32, 0.15
Particle density (Gs) (g/cm^3)	2.6
Max dry density (g/cm^3)	1.76
Optimum moisture content (%)	15.5
Sat. hydraulic conductivity (m/s)	4 × 10–5
SWCC parameters (wetting) (α,n,m)	0.41,2.2,0.55
Critical state friction angle	40°

2.2 Slope Construction

To analyze the development of transient porewater pressure and deformation before failure, the slope configuration was carefully established, as shown in Fig. 1. The soil slope's dry density was maintained at 1.5 g/cm^3. Air-dried soil with a gravimetric water content of 10% was mixed and homogenized for 24 hours before slope construction. The wet tamping method was employed to construct the slope layer by layer, with each layer being 20 mm thick.

During the construction process, porewater pressure transducers (PPTs) were strategically embedded at specific locations, as depicted in Fig. 1. However, it is important to note that the available PPTs were only capable of measuring changes in positive porewater pressure. Additionally, markers were positioned in such a way that facilitated the examination of the slope's deformation behavior throughout the progression of the landslide.

2.3 Slope Material

In this study, the experiments were conducted using a silty sand soil commonly known as "Masado soil" readily available in Japan. The index properties of the soil, along with the parameters of the soil water characteristic curve (SWCC), were determined. The SWCC parameters were established based on the van Genuchten model (van Genuchten 1980). The material properties of the soil are presented in Table 2.

2.4 Groundwater Flow Simulation

As mentioned earlier, one of the main objectives of this study is to validate the functionality of the newly developed centrifuge soil container. To achieve this, five identical unsaturated soil slopes were tested. Before inducing failure in the slopes through the combined effects of groundwater flow and rainfall, it is required to establish a steady-state groundwater flow condition. To accomplish this, the water level in the intermediate tank was controlled until porewater pressure transducers placed on the soil–bedrock interface produced steady values. The experimental procedure followed in this study to set up steady-state groundwater flow is illustrated in Fig. 2. Following similar steps, it was expected to achieve similar porewater pressure (PWP) values across corresponding PPTs in all five test cases.

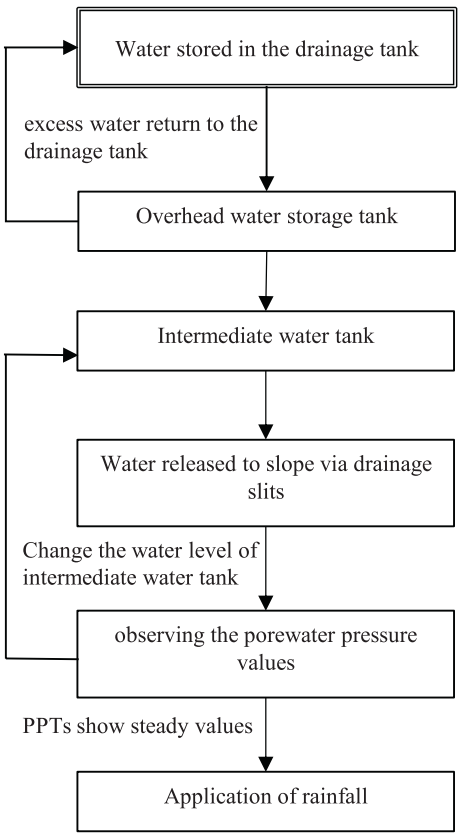

Fig. 2 Experimental steps followed in this study to set up steady-state groundwater flow

Firstly, the water stored in the bottom drainage tank was pumped to the overhead water tank using the pump mounted on the chamber. The overhead water tank has only a capacity

of 0.4 l. Therefore, an overflow line was connected back to the bottom drainage tank. The water stored in the overhead water tank can be discharged to the intermediate water tank by activating the electrode sensors and the water level can be maintained accordingly. Once the intermediate water tank is filled, water will be conveyed to the unsaturated soil slope through drainage slits. The water level in the intermediate tank is getting reduced during this process and once it reaches below the opening of the drainage slit, electrode sensors will be automatically activated to refill. This repetitive process facilitated obtaining steady values in PPTs and attaining steady–state groundwater conditions.

The water level was adjusted in the intermediate water tank as described above to generate a steady–state groundwater flow. However, it was understood that maintaining a constant water level (constant PWP) in the intermediate water tank was not a successful approach to establishing a steady-state groundwater flow. If the water level was maintained at a constant low level, it was hard to obtain steady–state conditions whereas, if the water level was maintained at a higher level, the pressure exerted on the right side of the slope was greater. Eventually, it resulted in undesirable movements in the slope. Therefore, as illustrated in Fig. 2, the water level in the intermediate water tank had to adjust to obtain steady and similar values in the PPTs placed along the soil-bedrock interface. It should be noted that this observation-based method, although utilized, cannot be considered a standard approach for achieving steady-state groundwater flow.

3 Validating the Functioning of the Centrifuge Chamber

3.1 Porewater Pressure Variation during Seepage

In Fig. 3, the PWP in the intermediate water tank varied mostly between 80 and 90 kPa during each test case. However, the time taken for the groundwater flow to reach a steady—state showed significant variations across the cases. This phenomenon can be attributed to two factors. Firstly, the system was not set up to change the water level spontaneously in the same manner for each case. Additionally, although the attempt was to prepare identical slopes using the wet tamping method, it is possible to have non-uniform conditions in each case. Consequently, the response of the PPTs could not be identical, and different test cases required varying time spans to exhibit

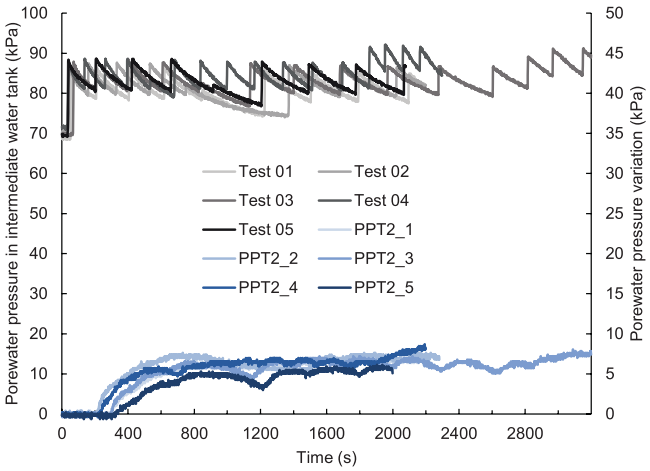

Fig. 3 Porewater pressure response while establishing a steady state groundwater flow

similar PWP responses. Figure 3 additionally illustrates the time histories of PWP response for PPT 2 in five test cases. It shows that the variation of time needed to reach steady–state conditions vary significantly. However, five cases show nearly identical PWP values obtained at the steady—state. Furthermore, it was understood that a more gentle variation of water level in the intermediate tank is preferred to generate a saturated soil layer on top of impermeable bedrock rather than changing the water level frequently. This procedure permits enough time for the slope to get saturated and thereby creates a more uniform groundwater flow.

3.2 Porewater Pressure Variation During Rainfall

After PPTs showed enduring values for approximately 100 s, rainfall was applied on the partially saturated slopes by maintaining the groundwater flow. Figure 4 depicts the PWP distribution of PPT 2, 3, and 4 during rainfall infiltration until the failure initiated in each case. -100 s to 0 s represents the time duration of steady–state groundwater flow before the rainfall. Notably, PPT 3 consistently showed higher values compared to PPT 2 and 4, which was observed across all cases. This discrepancy can be attributed to the boundary conditions adopted in these experiments. The coefficient of variation (standard deviation/ average) (CV) was utilized to examine the uniform response of the system of each PPTs as illustrated in Fig. 5. It shows that PPT 2 and 3 have CV val-

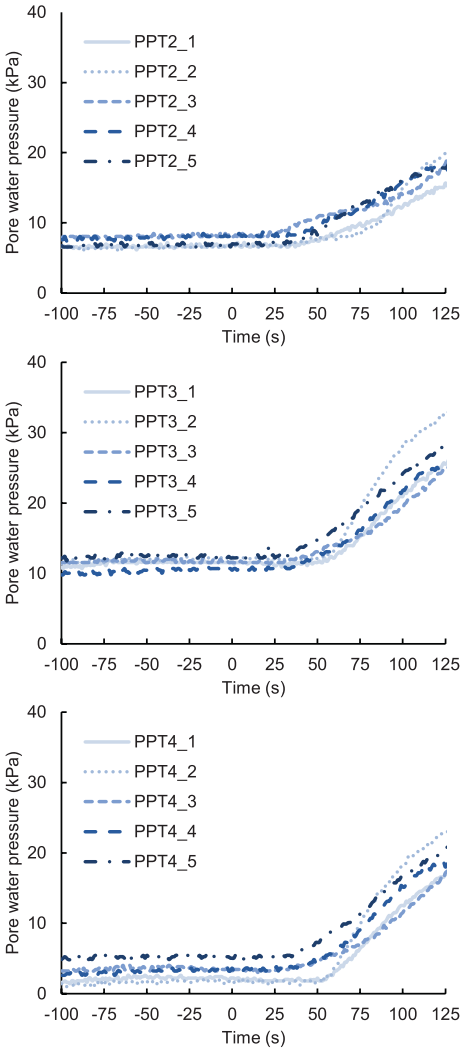

Fig. 4 PWP distribution of PPT 2, 3, and 4 during steady-state groundwater flow and rainfall infiltration until the failure

ues around 0.1 during both steady–state conditions and transient seepage conditions which suggest a high degree of uniformity that aligns with PWP variation. However, a thorough assessment of the PWP variation of PPT 4 in each test shows high variability and this observation was confirmed with relatively higher CV values with a moderate level of uniformity. Even though the variation lies inside the acceptable range, it is necessary to maintain cautious experimental steps to minimize inconsistency.

At 0 s, rainfall was applied on the slope. Following the introduction of rain, all the PPTs shown in Fig. 4 exhibited simultaneous responses at around 40 s. However, in the presence of pre-existing groundwater flow, the wetting front and

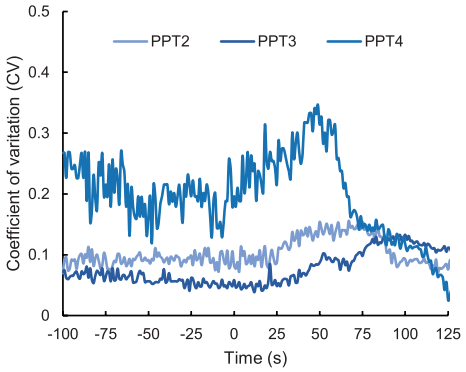

Fig. 5 Coefficient of variation of PWP distribution of PPT 2, 3, and 4

saturated flow quickly propagated throughout the slope, resulting in a rapid response to the rainfall. All the slopes started showing deformation while increasing PWP and eventually failed around 100 s.

3.3 Evolution of Failure

Figure 6 compares the horizontal displacement of marker no 06 (M6) in each test, and in general, the markers' displacement shows a similar deformation behavior. Therefore, it implied that five identical cases exhibited comparable landslide characteristics. The failure evolution of each case is presented in Fig. 7, which compares the slopes' initial condition at −100 s and the failure initiation around 100 s. At −100 s, there were some initial movements of about 4 mm in all cases which were initiated as a result of groundwater flow conditions. However, once the groundwater flow became steady, there were no signs of propagating the movements and the slopes were reinstated their stability. This observation can be further validated using the variation of CV value, which shows a constant value with high uniformity as presented in Fig. 8. With the increase of PWP, the failure surface developed during the tests showed that instability propagated from the steep slope to the mid-slope area. The uniformity during deformation is in acceptable range even during landslide progression as shown in Figs. 7 and 8.

The landslide progression observed can be characterized as a translational type of failure compared to a rotational type of failure, mostly occurring as a thick slice of failure in the steep slope as a result of rainfall infiltration. The unstable mass resulting from the tests was voluminous; therefore, the damage that happened under these conditions would be massive.

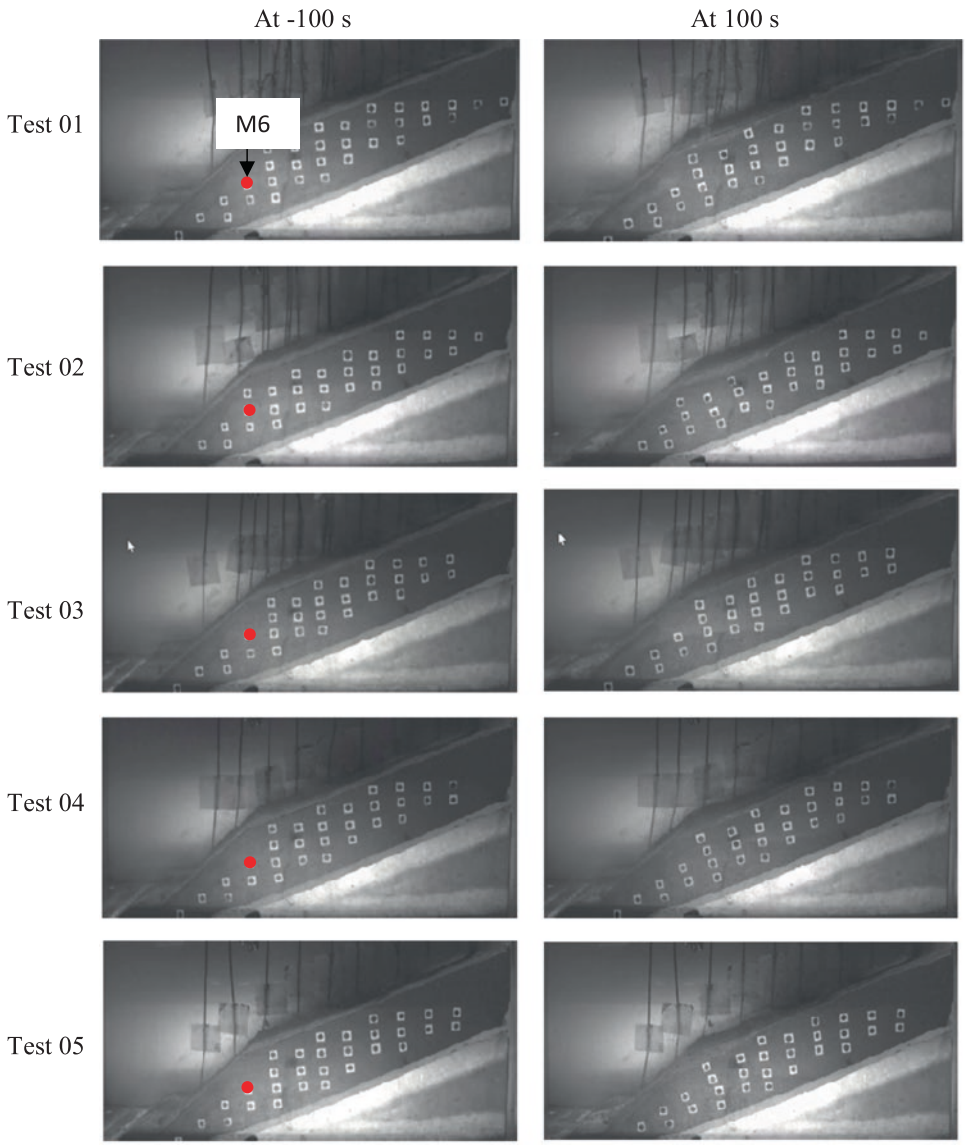

Fig. 6 Evolution of failure in each test case; location of marker no 06 (M6) is shown

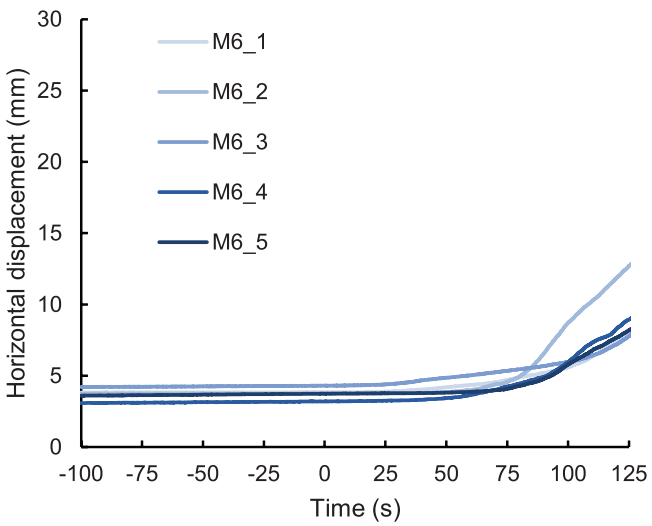

Fig. 7 Horizontal displacement of M6 in each test case

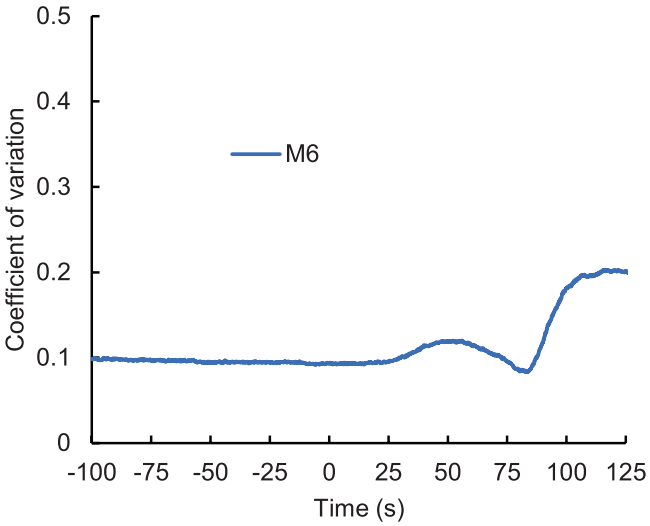

Fig. 8 Coefficient of variation of horizontal displacement of M6

4 Influence of the Initial Groundwater Flow on Landslide Initiation

Once the functions of the new device were confirmed another two tests were undertaken to assess the slopes' behavior with (Test 06) and without (Test 07) pre-existing groundwater flow. The objective is to examine the initial condition of the soil-bedrock interface, influenced by the existing groundwater flow, on the slope's response to subsequent rainfall infiltration by centrifuge modeling.

Test 06 was compared with Test 07 to critically discuss the impact of pre-existing groundwater flow on landslide initiation. The unsaturated soil slope in Test 06 was first subjected to pre-existing groundwater flow before being exposed to rainfall infiltration following the method discussed previously. Once the slope reached a steady–state groundwater flow, the PPTs along the soil–bedrock interface (PPT 02 to PPT 06) showed constant values. This has separated the initial unsaturated slope into a saturated layer and an unsaturated layer. In Test 07, the slope stayed completely unsaturated before applying rainfall. Therefore, these two tests allowed for assessing the significance of pre-existing groundwater flow on landslide initiation.

4.1 Porewater Pressure Variation

The variations in the PWP are depicted in Fig. 9. The dashed lines represent the PWP variation in Test 06 and the continuous lines represent the PWP variation in Test 07. Additionally, Fig. 9 shows the variation of PWP in PPT 08 which was placed inside the intermediate water tank of Test 6.

One of the major observations was that PPTs in Test 06 responded simultaneously to rainfall (red circle) whereas in Test 07 it clearly showed a sequential response (black circle) (Jayakody et al. 2023a). The possible reasons behind the simultaneous response to rainfall would be the presence of a capillary zone eased the advancement of the wetting front from top-to-bottom saturation over the saturated layer and thereby, the possibility of creating a preferential flow quickly. Further, this observation is a substantiation of uniform infiltration of rainfall to the unsaturated slope. The simultaneous porewater pressure response throughout the slope and quick reaction have made the slope fail much earlier in Test 06 compared to the slope in Test 07. However, in Test 06, the sequential response of PPTs was observed. This is the typical response to rainfall on initially unsaturated slopes, with the advancement of the wetting front, followed by saturated transmission of water flow, and the development of porewater pressure starting from the toe area of the slope. This comparison has highlighted how the change in initial conditions by introducing groundwater flow on soil—bedrock interface could change the response of PWP with rainfall infiltration.

As shown in Fig. 10, PPTs began to react with a rate ($\Delta PWP/\Delta t$) marginally above 0.2 when rainfall infiltration in Test 06 reached the groundwater surface, which was only after 10–20 s. However, later the rate further increased up to 0.35 around 60 s to 80 s which suggests a form of preferential flow paths from the slope surface to the groundwater

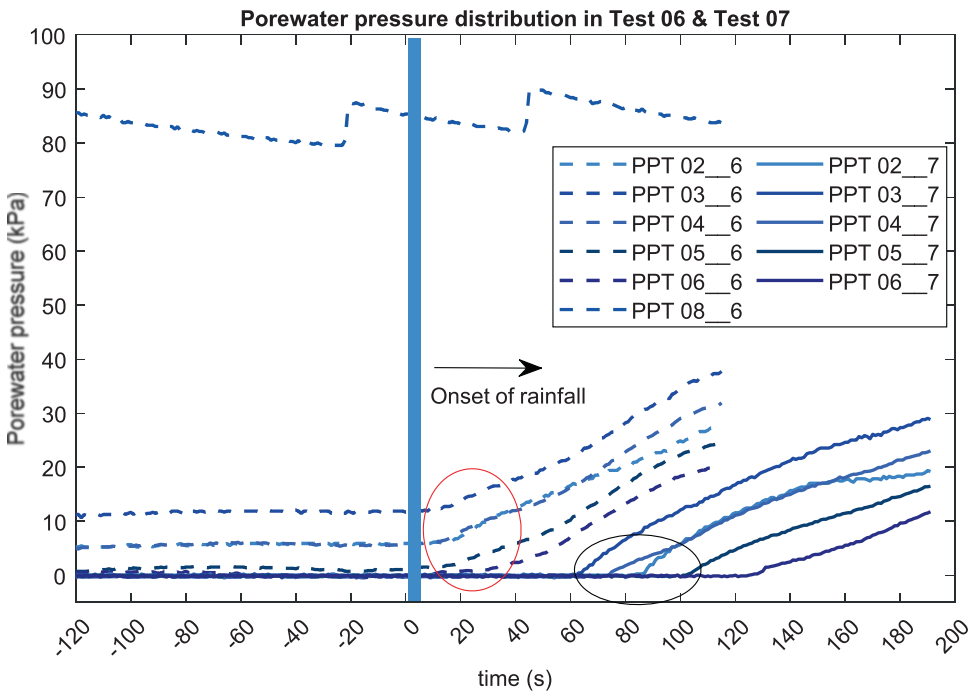

Fig. 9 Porewater pressure evolution in Test 06 and Test 07

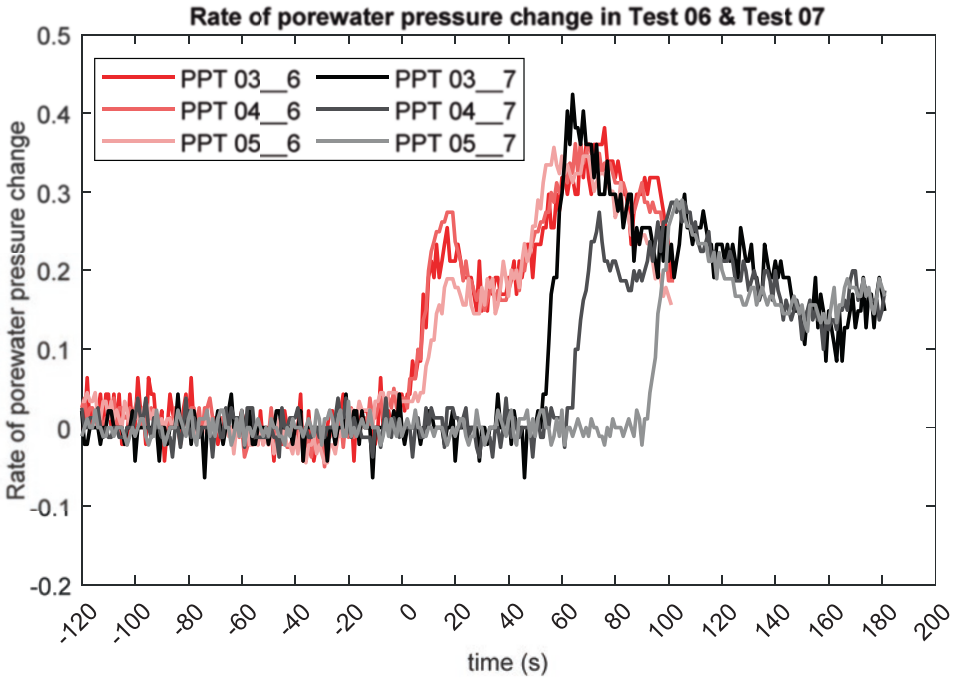

Fig. 10 Rate of porewater pressure change in Test 06 and Test 07

flow. Afterward, the rate mostly stayed around 0.3 until the slope reaches failure.

In contrast to Test 6, PPT 3 took around 50 s to respond to rainfall infiltration at first followed by PPT 4 and 5. At that instance, the rate showed a rate high as 0.4 but it did not continue to be stable with time and shows a rapid declining trend. Except at the time of generating a PWP on soil—bedrock interface, the rate was maintained in between 0.2 and 0.3. This observation was not only in PPT 3 but also in PPT 4 and 5 which eventually shows a less rate compared to the rate in Test 6. Therefore, if an unsaturated slope with a groundwater flow is exposed to rainfall infiltration, there is a high tendency for the rapid development of PWP, which could accelerate the initiation of a landslide. This conclusion can be drawn by looking at the PWP variation and rate of PWP change in Tests 06 and 07.

4.2 Evolution of Failure

The displacements of the markers recorded by the high-speed camera during centrifuge experiments were used to assess the evolution of failure and further quantitative measures. During the failure initiation and follow-up failures, two failure surfaces had very distinct features. In contrast to Test 07's initial failure surface, which resembles a rotational sliding failure, Test 06's initial failure surface is a more extensive translational type sliding failure surface, as shown in Fig. 11. A similar pattern was seen in the progressive failures that occurred after the initial failure, with Test 06 showing considerably greater progressive failures than Test 07. Further, vectors of total displacements at failure initiation in both test cases are also portrayed in Fig. 11 which shows the developed failure surfaces. In Test 06, a dense displacement field was formed not only in the steep slope area but also towards the mid-slope area around 110 s. However, Test 07, clearly shows that a thick localized failure surface has evolved in the top part of the steep slope around 180 s. This concentration of vector arrows is a contrasting behavior with the failure surface evolved in Test 06. With Test 06 revealing an initial failure surface of notably faster, greater dimensions and volume, the evolution of failure as described by physical modeling became fascinating. Even though debris flow and landslide runout were not covered in this article, Test 06 had a lot more failed volume than Test 07. Therefore, it is critical to have a comprehensive understanding of how groundwater flow and rainfall interact to analyze not just the onset of landslides but also their runout.

4.3 Landslide Mobility

As shown in Fig. 12, the displacement during landslide progression was compared in order to examine the mobility of landslides. The comparison of the horizontal displacement between Tests 06 and 07 demonstrates that the markers on both occasions had comparable displacements at a relatively low rate of up to 60 s. However, markers in Test 06 then started to move rapidly and exhibited longer travel distances with time. The simultaneous development in the saturation profile in Test 06 caused markers 5, 6, 11, and 12 to exhibit synchronous movements. However, in Test 07 in particular, markers

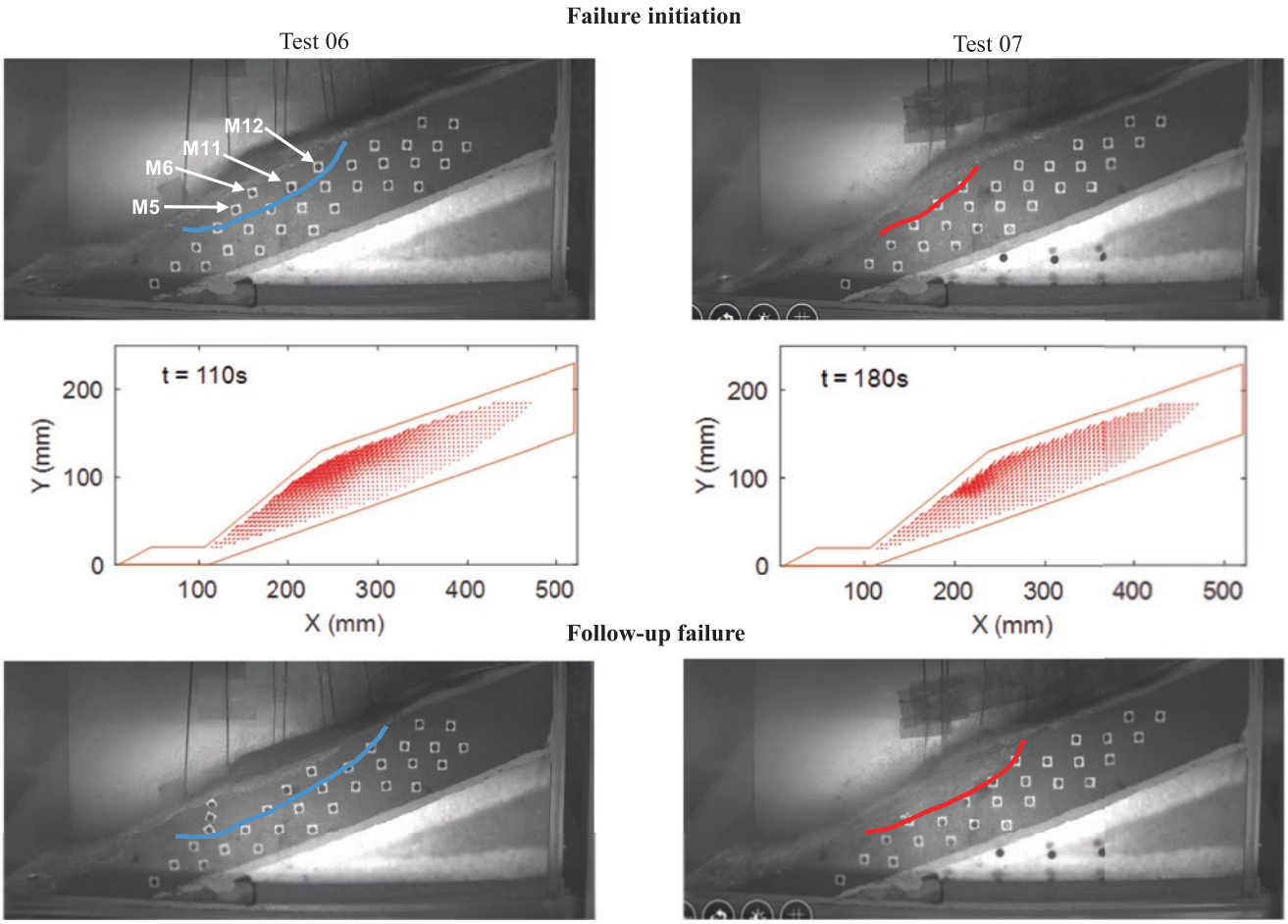

Fig. 11 Evolution of failure

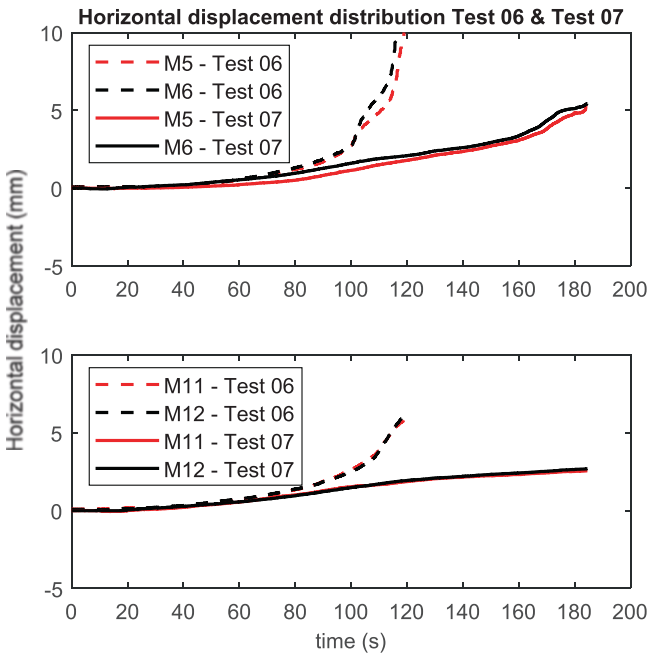

Fig. 12 Horizontal displacement of markers

05 and 06 demonstrated movement while markers 11 and 12 showed slight movement at the time of failure initiation.

Following the method described in Jayakody et al. 2023a, b, deviatoric strain analysis was carried out to further investigate the landslide mobility of Test 06 and Test 07. The deviatoric strain profiles were calculated employing horizontal and vertical displacements captured. Figure 13a depicts the deviatoric strain profile for Test 06 and it clearly presents that instability was spread over the steep slope as well as the mid-slope. Figure 13b illustrates the deviatoric strain profile for Test 07 and it is apparent that the initial failure surface is a thick slice localized towards the steep slope. The evolution of failure was assessed using not only physical observations but also quantitative measurements using displacement vectors, markers' displacement distribution, and deviatoric strain profiles. All this evidence guided a very conclusive decision that the impact of pre-existing groundwater flow could create a massive landslide compared to a landslide that occurred only by rainfall infiltration. Therefore, landslide mobility is much higher when the slope has an integrated effect of pre-existing groundwater flow and rainfall infiltration compared to when the slope is only exposed to rainfall infiltration.

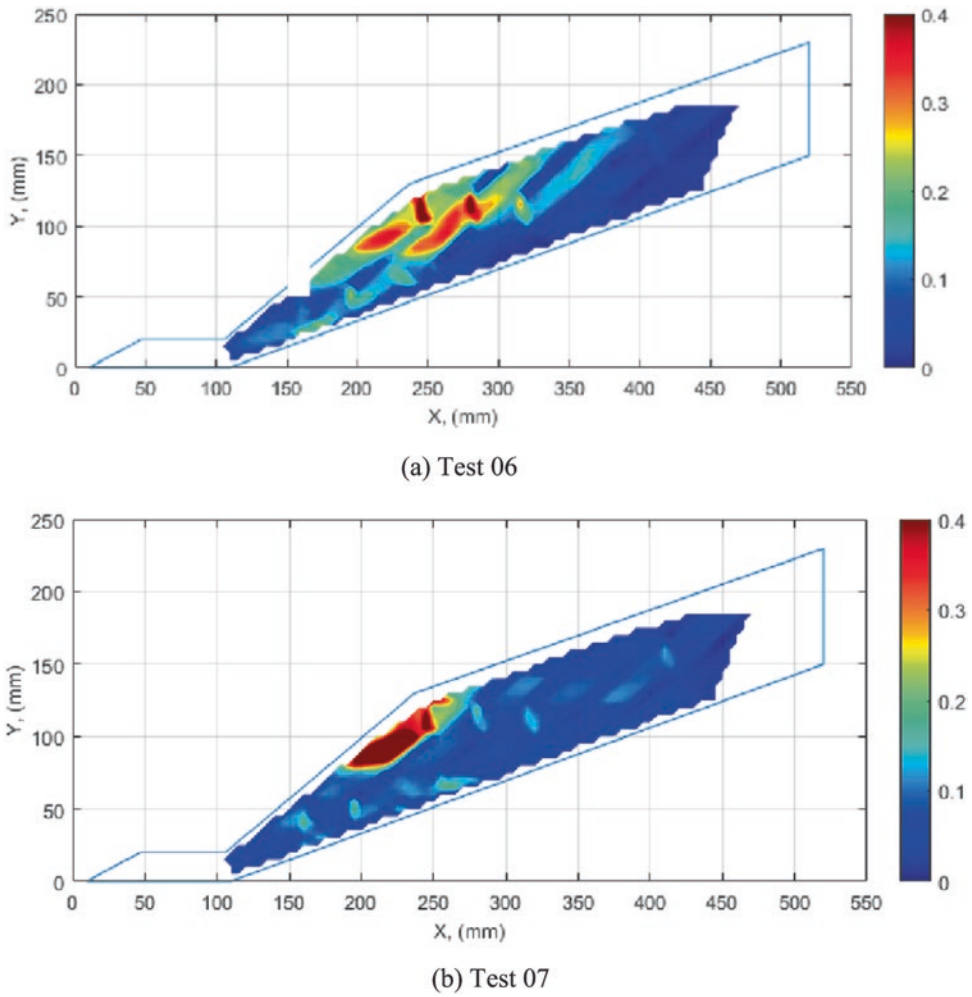

Fig. 13 Deviatoric strain graphs of (**a**) Test 06 and (**b**) Test 07

5 Conclusions

A newly developed centrifuge model container was used to investigate the importance of incorporating pre-existing groundwater flow in landslide initiation and its characteristics. The study aimed to validate the model container which can reproduce groundwater flow and rainfall as independent functions. Five tests were conducted under identical conditions to evaluate and analyze landslide behavior by monitoring PWP development and failure evolution. The model container demonstrated the capability to replicate comparable results under similar conditions consistently both in PWP generation and subsequent failure mechanism.

The influence of the integrated effect of groundwater flow and rainfall was emphasized by comparing Test 06 and Test 07. Analysis of PWP distribution graphs revealed that the simultaneous response of PPTs during rainfall infiltration resulted in voluminous landslides compared to those triggered solely by rainfall. Further, it was noticed that under the integrated conditions landslide initiation was accelerated. These findings highlighted the necessity of incorporating groundwater flow effects on landslide early warning systems especially to improve the temporal predictability.

Acknowledgments This research was supported by a project titled "Development of early warning technology of Rain-induced Rapid and Long-traveling Landslides" implemented by the Science and Technology Research Partnership for Sustainable Development (SATREPS) in collaboration between Japan Science and Technology Agency (JST, JPMJSA1910) and Japan International Cooperation Agency (JICA), and JSPS KAKENHI Grant Number 21H04575. The authors would like to acknowledge the International Consortium of Landslides (ICL) and the National Building Research Organisation (NBRO), Sri Lanka, for their extended support.

References

Askarinejad A, Laue J, Zweidler A, Iten M, Bleiker E, Buschor H, Springman SM (2012) Physical modelling of rainfall induced landslides under controlled climatic conditions. *Eurofuge* . http://www.cces.ethz.ch/projects/hazri/tramm/

Gómez D, García EF, Aristizábal E (2023) Spatial and temporal landslide distributions using global and open landslide databases. Nat Hazards. https://doi.org/10.1007/s11069-023-05848-8

Jayakody SHS, Uzuoka R, Ueda K (2023a) Centrifuge modelling of unsaturated slopes subjected to the integrated effect of groundwater and rainfall infiltration. In M. Bardanis (Ed.), *UNSAT 2023*. E3S Web of Conferences. https://doi.org/10.1051/e3sconf/202338210003

Jayakody SHS, Uzuoka R, Ueda K, Xu J (2023b) Unsaturated slopes behavior under antecedent intermittent rainfall patterns: centrifuge and numerical study. Acta Geotech. https://doi.org/10.1007/s11440-023-02017-w

Lucas D, Herzog R, Iten M, Buschor H, Kieper A, Askarinejad A, Springman SM (2020) Modelling of landslides in a scree slope induced by groundwater and rainfall. Int J Physical Modelling Geotechnics 20(4):177–197. https://doi.org/10.1680/jphmg.18.00106

Take WA, Beddoe RA, Davoodi-Bilesavar R, Phillips R (2015) Effect of antecedent groundwater conditions on the triggering of static liquefaction landslides. Landslides 12(3):469–479. https://doi.org/10.1007/s10346-014-0496-7

van Genuchten MT (1980) A closed-form equation for predicting the hydraulic conductivity of unsaturated soils. Soil Sci Soc Am J 44(5):892–898. https://doi.org/10.2136/sssaj1980.03615995004400050002x

Evaluation of Assessment Models for Landslide Susceptibility Mapping in Permafrost Areas

Yan Wang, Wei Shan, Ying Guo, Chengcheng Zhang, and Shuai Liu

Abstract

China's permafrost regions are affected by global warming and the thawing of permafrost, and the occurrence of landslide disasters has become more and more frequent, which makes the evaluation of the susceptibility to geologic hazards in China's permafrost regions is an urgent work to be carried out. Most of the existing geohazard susceptibility models have fewer test cases in the permafrost regions. Twelve evaluation factors, such as altitude, slope, slope direction, land use, and lithology, were selected to draw landslide hazard susceptibility maps by using three commonly used landslide susceptibility assessment models, including the information value model, the frequency ratio model and the random forest model, which can be implemented in GIS, taking the Lesser Khingan Mountains area located in the eastern part of permafrost region of northeast China as the study area. The applicability of the above commonly used landslide susceptibility assessment models in the permafrost regions is carried out by fieldwork and comparing the results of and model simulation. The Random Forest Model was also used to assess the importance of the factors that were adopted and to judge the degree of their influence on landslide development. The results show that the Information Value Model has a better applicability in the permafrost region. However, due to factors such as climate warming and permafrost degradation, the accuracy of the prediction results obtained by applying the existing commonly used landslide susceptibility assessment models in permafrost regions are still in need to be improved. Finally, thawing and degradation of permafrost will play a non-negligible role in influencing the occurrence of landslides in permafrost regions.

Keywords

Permafrost regions · Landslide susceptibility · Assessment models · Applicability

1 Introduction

As one of the prevalent types of natural hazards in the world's terrestrial environments with slopes (Froude and Petley 2018), landslides cause a large number of injuries, deaths and socio-economic losses every year (Corominas et al. 2014). The quantification of landslide susceptibility has also becoming increasingly important (van Westen et al. 2006; Gariano and Guzzetti 2016), evolving from the earliest qualitative comments to quantitative analysis (Ayalew and Yamagishi 2005), it has always been a hotspot for research by geologists and scholars from all over the world (Aleotti and Chowdhury 1999). The quality of its assessment is inextricably linked to the selected indexes and model. Adequate understanding of the factors of landslides is needed to evaluate the susceptibility of landslides. (Bozzano et al. 2010). Topography, geological formations (Xing et al. 2014) and climatic conditions (Gariano and Guzzetti 2016), are the main factors that influence the susceptibility of landslides. These will also serve as reference parameters for the identification of further indicators. Commonly used models for

Y. Wang · Y. Guo · C. Zhang · S. Liu
Institute of Cold Regions Science and Engineering, Northeast Forestry University, Harbin, China
e-mail: 2021126338@nefu.edu.cn; ying-guo@nefu.edu.cn; chengcheng@nefu.edu.cn; shuai_liu@nefu.edu.cn

W. Shan (✉)
Institute of Cold Regions Science and Engineering, Northeast Forestry University, Harbin, China

Ministry of Education Observation and Research Station of Permafrost Geo-Environment System in Northeast China (MEORS-PGSNEC), Harbin, China

Collaborative Innovation Centre for Permafrost Environment and Road Construction and Maintenance in Northeast China (CIC-PERCM), Harbin, China
e-mail: shanwei@nefu.edu.cn

B. Abolmasov et al. (eds.), *Progress in Landslide Research and Technology, Volume 3 Issue 1, 2024*, Progress in Landslide Research and Technology, https://doi.org/10.1007/978-3-031-55120-8_11

landslide susceptibility assessment include expert system models such as Analytic Hierarchical Progress (Kayastha et al. 2013), Expert Scoring method (Aleotti and Chowdhury 1999); Mathematical and Statistical models such as the Information Value Model (Che et al. 2012), Entropy Weighting scheme (Devkota et al. 2013), Right of Proof (Regmi et al. 2014), Logical Regression (Kavzoglu et al. 2014), and Machine- Learning models (Devkota et al. 2013), such as Decision Tree (Guo et al. 2021), Random Forest (Catani et al. 2013), Neural Network (Yang et al. 2019) and support vector machines (SVMs) (Pradhan 2013; Huang and Zhao 2018). Each of these models has its strengths, as well as certain weaknesses (Dou et al. 2019).

Compared with the expert system model, which is affected by human factors, and the machine learning model, which is difficult to debug the parameters, the Information Value Model (hereinafter referred to as IVM) as well as the Frequency Ratio model (hereinafter referred to as FR), both belonging to mathematical-statistical models, have the advantages of simple operation, wide application and good objectivity (Sharma et al. 2015; Wenyan and Xile 2020). In addition, it is possible to scientifically grade the intervals of each indicator. The emerging artificial intelligence algorithms are capable of high-speed processing of massive data and self-organized learning (Liu et al. 2020). Random forest algorithm (hereinafter referred to as RF) RF is an artificial intelligence algorithm known for its simplicity and efficiency, it integrates the decision tree as a unit for integrated learning tree classifier combination algorithm, integrates the Bagging algorithm and random selection of feature splitting characteristics, high accuracy, able to handle large data and evaluate the importance of each factor in classification (XinHai 2013). When there are many disasters and indicators to compute, the advantage of advanced computer technology is relevant (Genuer et al. 2010). Landslide susceptibility modeling using RF enables the importance of features to be measured using the impurity of the Gini index calculation node in the model (Archer and Kirnes 2008). It is applied to landslide sensitivity analysis without the need to set the factor weights in advance, and can be run on the visualization software SPSS Model, which is easy to use.

In recent years, the number of landslides has increased exponentially under global warming (Pei et al. 2023). The permafrost regions of northeastern China are also affected by climate impacts such as rising temperatures and frequent extreme precipitation (Haque et al. 2019). Continuing permafrost degradation (Shan et al. 2022) increased development of geologic hazards such as ground thawing, ground collapse, landslides, all of them caused by freeze-thaw processes. Landslides in mountainous regions such as the Great and Lesser Khingan Mountains and Taihang Mountains are widely scattered and the damage is very serious, causing great losses to the society and economy while destroying the ecological environment, which has severely constrained the construction and social development of the regions.

According to the China Environmental Science Data Center, there are more than 13,700 landslides in the permafrost regions of northeastern China (Fig. 1a). However, due to the high latitude and altitude of the Greater and Lesser Hingganling permafrost regions, as well as the ecological and climatic constraints, it is difficult to carry out comprehensive disaster statistics in the field, and the number of landslide hazards counted is much less than the actual. Therefore, it is of great significance to establish a scientific and reasonable landslide susceptibility assessment model and draw a high-precision landslide hazards map to provide support for accurate landslide prevention, control, and management. However, most of the landslide susceptibility assessment models commonly used in the existing research are targeted as fast landslides distributed in low-latitude areas with warm climates and high precipitation. Due to the difficulty of field surveys in the permafrost regions and the slow rate of landslide occurrence affected by permafrost thawing, It remains to verify the applicability and predictive accuracy of landslide susceptibility assessment models commonly used in current studies when used in permafrost areas.

Therefore, this study aims to use the frequency ratio model, the information value model, and the random forest model implemented by GIS to model landslide susceptibility in the study area, use the ROC curve to verify the simulation results of the model and to use the random forest method to judge the degree of influence of the assessment factors on the development of landslides. Such approach is to objectively verify the accuracy and applicability of the existing commonly used landslide evaluation models for susceptibility assessment and mapping in permafrost regions, and to provide intuitive and effective references for early warning of landslide disasters in permafrost regions.

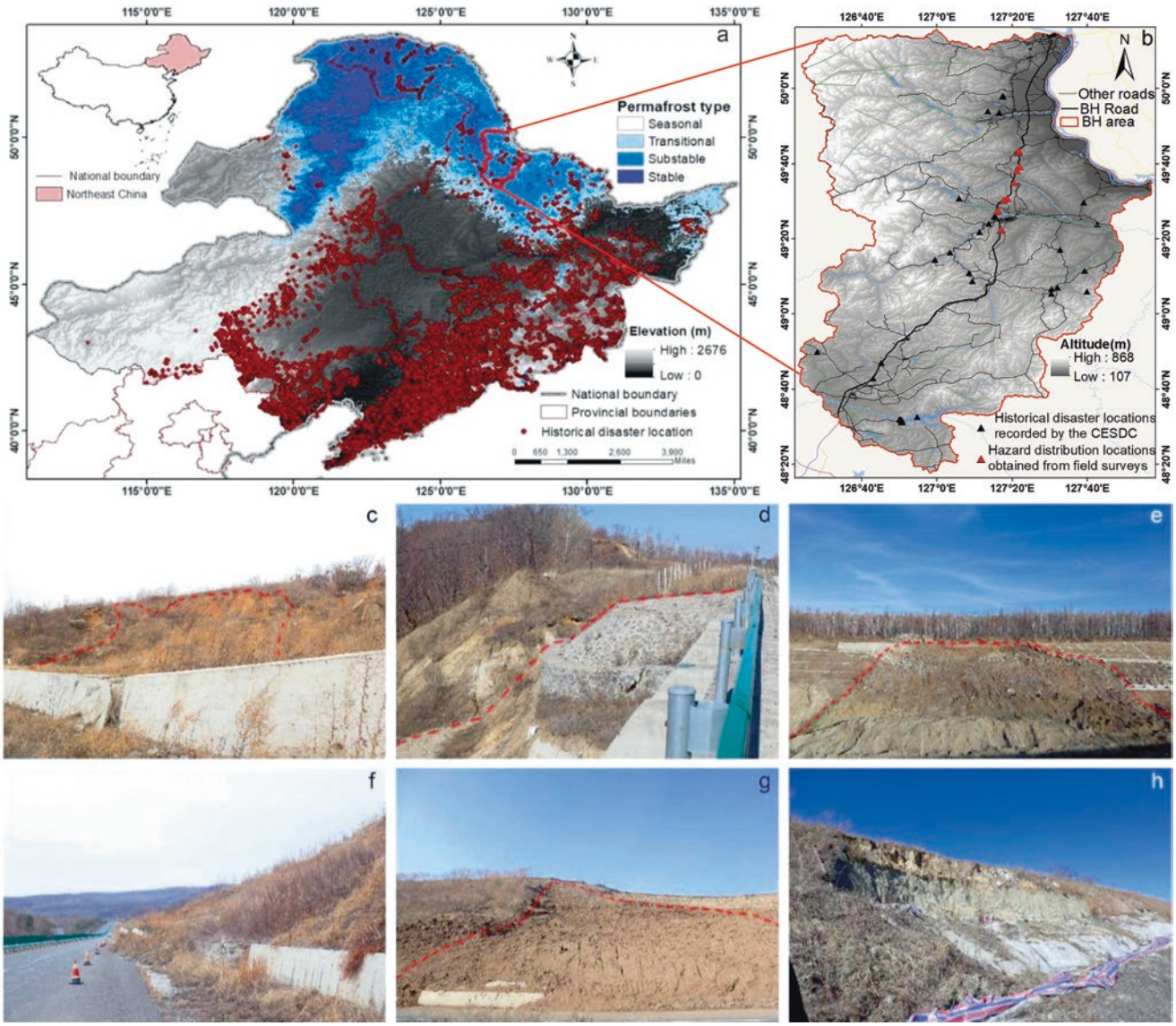

Fig. 1 (**a**) Geographic location of the study area; map of the distribution of different types of permafrost, elevation, and historical hazard sites in northeast China. (**b**) Showing landslides related to the BH highway roadside infrastructure, the distribution of major transportation roads, and the distribution and topography of the major bodies of water. (**c-h**) Uncounted landslides in parts of the study area obtained from the field reconnaissance, which are slow landslides caused by the thawing of permafrost, which has had a significant impact on the nation's roadway infrastructure, operational services, the environment, the progress of works in progress, and the economy are negatively affected

2 Study Area

The study area is the Beian to Heihe highway road area (hereafter referred to as BH) is located in the northwestern section of the Lesser Khingan Mountains in Northeast China, which ranges between longitude 127°17′31″~127°21′24″E and latitude 49°30′57″~49°41′50″N, and it is a region with the distribution of the island permafrost in China, which belongs to the low altitude, high-latitude permafrost area (Fig. 1b). The main mountain ranges within the study area are north-east and south-west trending, and the terrain is in the form of a narrow belt. The geological feature is a truncated middle or low mountain with granitic volcanic rocks as the main constituent lithology. The elevation is high in the east and low in the west, high in the south and low in the north. In the study area, terrestrial sedimentation is accompanied by marine sedimentation, and the rock types are mostly a combination of mudstone, granite, volcanic rocks, siltstone, and locally clay and loess. The slope of the area is mostly in the range of 0–50%. Land use and land cover in the area is mostly cropland, wasteland, mixed or dense forests. Many of the roads are flanked by unmanaged and muddy slopes, which increases the landslide susceptibility of the area. Landslides are frequent in the study area, but many of them are not registered by the Geological Hazard Census.

Through field investigation, there are dozens of slow-moving landslides caused by permafrost degradation along the BH alone. Which buried and destroyed retaining walls, blocked the highway (Fig. 1c, g), damaged transportation infrastructure such as embankments and retaining walls (Fig. 1d, h), and damaged unfinished construction works in process (Fig. 1e) which affected the progress of the project and resulted in economic losses. Considering the large amount of permafrost coverage in China, the economic importance of transportation in Northeast China, and the need for better landslide-related safety risk management and monitoring, the study of landslide susceptibility in permafrost regions is of great significance.

3 Materials

The factors affecting the development of landslides are complex, which are interconnected with each other (Nguyen et al. 2023). For example, the elevation data can reflect the topographic relief changes in the study area, and to some extent, it reflects the gullies, the vegetation changes, and the state of the accumulation. Slope orientation affects landslide development mainly by influencing the degree of weathering of hillside rocks and the growth of vegetation.

Slope gradient and profile curvature represent the degree of concavity and convexity of the terrain surface, which indirectly affects the extent of landslide development. (Yalcin 2008). River gullies also provide a source of hydraulic drive for permafrost thaw-affected landslides (van Westen et al. 2008). The selection of landslide assessment factors in this paper are mainly based on the distribution and development status of landslide hazards in the study area. After fully considering the difficulty of obtaining information in the study area as well as the scale, the distance from the water network (DW), the distance from the road (DR), the altitude, the direction of the slope, the slope gradient, the curvature of the profile, the degree of topographic relief, the land use, the Normalized Difference Vegetation Index (NDVI), the precipitation, the stratum lithology, and the distance from the fault (DF) have been selected as the assessment factors. The raster size, and data source of each factor are shown in Table 1.

In the mathematical and statistical model, the above factors are used as input data, and the detailed grading of each indicator is superimposed and analyzed with the landslide historical hazard location layer. In the IVM model, the information value is derived through the superposition analysis. Later on, rankings with zero value were preferentially merged with neighboring ones followed by the merging of rankings with similar value with neighboring scoring. Finally, calculate the consolidated grading values, to realize the optimal grading status of each evaluation index. The landslide susceptibility zoning map was drawn accordingly. Precipitation in the figure is annual precipitation. Stratigraphic lithology is classified according to the degree of susceptibility to landslides, with 1 being the area or lithology least susceptible to landslides, such as water bodies, beach wind deposits sands. 7 is the type of lithology most susceptible to landslides, such as collapsible loess with stratigraphic age Q3p, Qh. Since more than 300 types of soils and rock classifications are involved in the study area, they will not be enumerated when classifying them on the map.

4 Methods

Many countries and regions in the world, such as the United States, Australia, Western Europe, have successively carried out research on the risk mapping of geologic hazards, with

Table 1 Data sources for evaluation factors

NO.	Factor	Data sources	Raster size
1	DF	Geo-remote sensing ecological network platform； Open street map	30 m
2	DW		
3	Altitude	NASA (United States air and space agency) shuttle radar Topography Mission (SRTM)	
4	Slope direction	Arcgis DEM extraction	
5	Slope gradient		
6	Profile curvature		
7	Topographic relief		
8	Land use	Spatial distribution data of remote sensing monitoring of land use types in China, Institute of Geographic Sciences and Resources, Chinese Academy of Sciences	
9	NDVI	China Monthly Vegetation Index (NDVI) spatial distribution dataset, data Center of Resource and Environmental Science Data Center, Chinese Academy of Sciences, China	
10	Precipitation	Geographic data sharing infrastructure, global resources data cloud	1 km
11	Lithology	Geological cloud of the geological survey, China	1:1000000
12	DF		1:500000
13	Geohazard sites	Resource and environment science and data Center, China; Hazard distribution locations obtained from field surveys	Specific coordinates

landslide hazards as the main theme subject, while China's research work in this field is relatively weak. Whether in the theoretical study of landslide disaster risk assessment or the application of practice, the beginning is relatively late. (Huang 2007). With further work in disaster mitigation and prevention in China, the assessment of the risk of large-scale regional landslide disasters has been gradually carried out. Currently, the application of 3S technology is booming in the field of geosciences with GIS technology as the core, which provides a fruitful technical platform for landslide disaster risk assessment. (Guzzetti and Reichenbach 2000; Chae et al. 2017). GIS has a powerful spatial analysis function and spatial database management capability, which can analyze the statistical relationship between the occurrence of landslide disasters and environmental influencing factors from different spatial and temporal scales, and evaluate the probability of occurrence of landslide disasters and possible disaster consequences. (Yalcin 2008). In this study, several commonly used disaster susceptibility assessment models based on GIS were used to evaluate landslide susceptibility in the Lesser Khingan Mountains study area (North-Eastern China), to provide a reference for the risk prediction of landslide susceptibility in permafrost regions.

4.1 Information Value Model

IVM is a statistical analysis method developed based on information theory (Yin and Yan 1988; Westen 1993). It is an effective method for regional geohazard prediction, and the viewpoint of information prediction is that the generation of geohazards is related to the quantity and quality of information obtained in the prediction process, which can be expressed as the amount of information. The Geohazard phenomenon is affected by many factors. The size and nature of the role of various factors are not the same; in a variety of different environments, for the regional geohazard elements of a comprehensive study of the "optimal combination of factors", rather than staying in a single factor. Relying on the GIS platform to calculate the information content of individual indicators, and then weighted superposition of multiple indicators is the primary approach for comprehensive information content, to establish the assessment model of landslide susceptibility. Information content of the study area can be calculated by Eq. 1.

$$I = \sum_{j=1}^{n} \ln \frac{N_j / N}{S_j / S} \tag{1}$$

where I is the total information weighted by various assessment indicators, which can be used as a landslide susceptibility index; N_j is the number of landslides contained within a specific grading interval of a single evaluation indicator; N is the total number of landslides; S_j is the number of rasters within a specific grading interval of a single assessment indicator; and S is the total number of rasters.

The state-graded informativeness value of each evaluation indicator was assigned to the raster layer, and the spatial analysis tool was used to superimpose the informativeness raster layer of each evaluation indicator. This is to obtain the total informativeness value and, in the next step, to divide the total informativeness raster layer according to the watershed unit. The average of the total informativeness of the unit of the study area was finally used as the informativeness value of the sub-watershed and then reclassified (Fig. 2). The entire study area was categorized into four landslide susceptibility zoning classes: low susceptibility, medium susceptibility, high susceptibility, and very high susceptibility.

4.2 Random Forest Model

Random Forest Algorithm is an artificial intelligence algorithm known for its simplicity and efficiency. It uses decision trees as units for integrated learning of the treelike classifier combination algorithm and Integrates the features of the Bagging algorithm and the Random Choice Splitting method. The outcome is providing results with high accuracy and assessing the importance of each factor in classification, also as consequence of the capacity to handle large amount of data. The number of landslide hazard sites in the study area was categorized and 70% (35) of the hazard sites were used as a training set for random forest training calculations, and the remaining 30% (15) were used as a validation dataset to validate the results concerning the prediction rate.

Twelve assessment factors were selected through the characteristics of landslide development in the study area. Multiple sampling and training of decision tree models were performed. The individual decision trees generated were used to form a random forest, whose prediction results were averaged from the final decision tree, The sensitivity grading was performed based on the model prediction results, and a landslide sensitivity evaluation map of the study area was generated using GIS. The use of random forests for landslide sensitivity modeling also enables the use of the Gini index to calculate the impurity of nodes to measure the importance of features. The model is then compared with the FR and the IVM, which are widely used in probabilistic statistical methods and are simple and efficient, to objectively verify the RF. In such a way it is possible to objectively verify the effectiveness of the RF model, but also to provide an intuitive and effective reference for the early warning of landslides and other geologic hazards in northeast China.

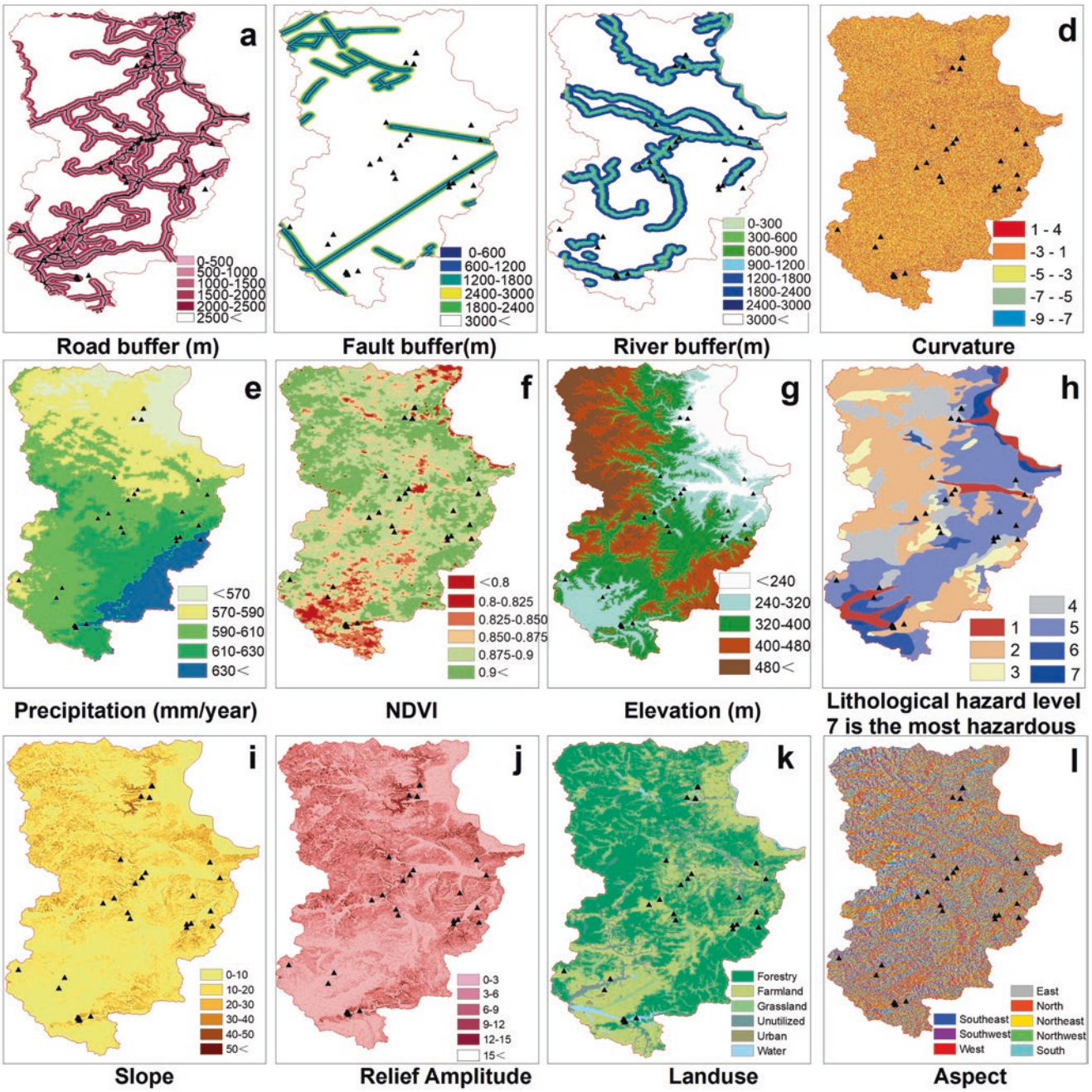

Fig. 2 Grading map for each assessment factor. a DR. b DF. c DW. d Profile curvature. e Precipitation. f NDVI. g Elevation. h Lithologic Hazard Level Classification. The danger level increases with increasing values, with 7 being the most hazardous. i Slope. j Topographic relief. k Land use. l Slope direction

4.3 Frequency Ratio Method

Utilizing the method of probabilistic statistics, the 12 evaluation factors were statistically calculated by the FR is statistically calculated for 12 evaluation factors, and then the assessment factors are superimposed to obtain the landslide sensitivity assessment map. Firstly 70% of the training set and 30% of the validation set divided by RF are utilized to classify the disaster sites. Secondly, the frequency ratio is calculated for each stream evaluation factor. Using ArcGIS, the landslide training set disaster sites are overlaid with each assessment factor map to extract the required data and calculate the frequency ratio for each category. This step was calculated for each evaluation factor (Table 2). Finally, a landslide sensitivity index was created and sensitivity mapping was performed by summing the frequency ratio values from the FR (Eq. 2)

Table 2 Frequency ratios of assessment factors that have the greatest impact on landslides

Factors	Class	No. of sites	Percentage of sites	No. of pixels	Percentage of domain	Information value
Slope degree (°)	0–10°	31	0.886	24,548,543	0.973	−0.094
	10–20°	3	0.086	633,957	0.025	1.227
	20–30°	1	0.029	35,340	0.001	3.015
	30–40°	0	0.000	2738	0.000	0.000
	40–50°	0	0.000	187	0.000	0.000
	50°<	0	0.000	11	0.000	0.000
NDVI	<0.8	2	0.057	70	0.004	2.549
	0.8–0.825	11	0.314	506	0.032	2.276
	0.825–0.85	5	0.143	1021	0.065	0.785
	0.85–0.875	8	0.229	2520	0.161	0.352
	0.875–0.9	9	0.257	6570	0.419	−0.489
	0.9<	5	0.143	4987	0.318	−0.801
The hazard level of lithology	1	1	0.029	1,266,375	0.047	−0.507
	2	12	0.343	9,442,928	0.354	−0.031
	3	7	0.200	1,794,932	0.067	1.090
	4	4	0.114	3,834,547	0.144	−0.229
	5	3	0.086	8,536,668	0.320	−1.317
	6	0	0.000	1,345,039	0.050	0.000
	7	0	0.000	477,431	0.018	0.000
Relief amplitude(m)	0–3	10	0.286	12,628,140	0.500	−0.560
	3–6	7	0.200	7,801,710	0.309	−0.435
	6–9	8	0.229	2,889,254	0.114	0.692
	9–12	4	0.114	1,037,120	0.041	1.023
	12<	6	0.171	894,449	0.035	1.577
DW (m)	0–300	10	0.286	11,414,173	0.427	2.324
	300–600	6	0.171	869,089	0.033	2.922
	600–900	2	0.057	739,936	0.028	2.670
	900–1200	2	0.057	739,936	0.028	0.030
	1200–1800	3	0.086	158,609	0.006	0.154
	1800–2400	1	0.029	740,818	0.028	0.725
	2400–3000	1	0.029	654,819	0.024	1.342
	3000<	10	0.286	11,414,173	0.427	−0.639

$$DSI = \sum_{j=1}^{n} \frac{M_{ij} / N_{ij}}{M_T / N_T} \quad (2)$$

where M is the number of factors, M_{ij} is the number of landslide hazard sites in the jth subclass of factor i; N_{ij} is the number of rasters occupied by the corresponding subclasses; M_T is the total number of landslide hazard sites; N_T is the total number of rasters occupied by the investigated area; DSI is the landslide susceptibility index, and the larger the susceptibility index is, the larger the probability of landslide occurrence.

4.4 ROC Curve Verification

In this paper, the ROC curve is used to test the evaluation results of the simulation of the models. The ROC curve, which is called the receiver operating characteristic curve (ROC), can take each disaster site and its evaluation factors composed of individuals as the test object, and then take the occurrence of landslides and the non-occurrence of landslides as a dichotomous classification (positive and negative categories) The ROC curve corresponding to each model and its area under the curve (ACU) have been analyzed. ACU is the criterion for judging the advantages and disadvantages of the model used. When:

- ACU = 0.5, it means that the model results does not have reference value, and
- ACU<0.5 means that the model does not conform to the real situation;
- ACU>0.5 and the value is closer to 1, it means that the model effect is more accurate.

5 Result and Discussion

The random forest algorithm model (RF) was constructed by SPSS software. This is to calculate the importance of the assessment factors according to the reduction of the average Gini value of each node of the decision tree, and to normalize

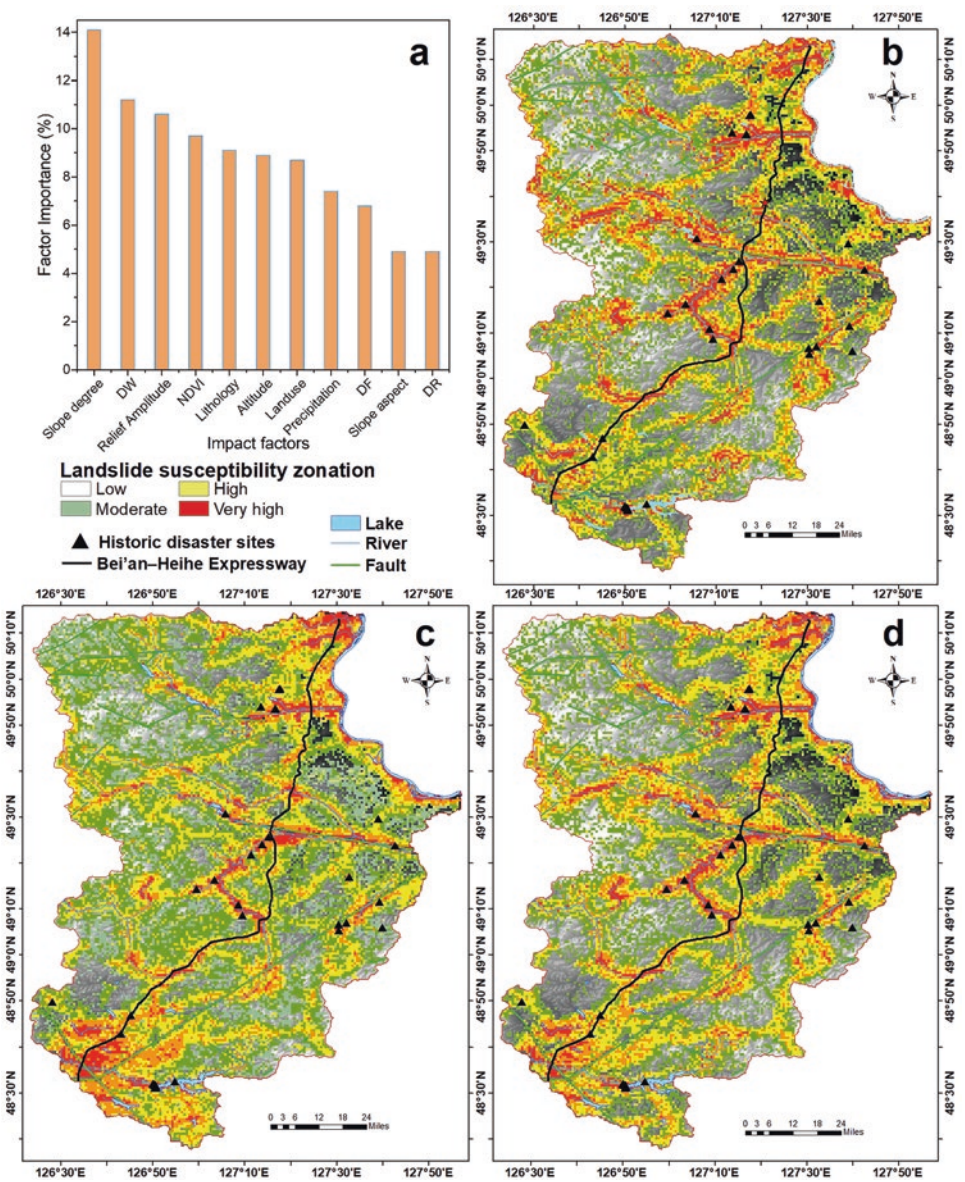

Fig. 3 (**a**) Importance of factors assessed by the RF method. (**b**) Assessment results for IVM, (**c**) Assessment results for FR, (**d**) Assessment results for RF

the calculated factor weights. The calculation results are shown in Fig. 3a.

Slope, DW, and topographic relief are three very important factors affecting landslide development in the study area, with an importance of more than 10%, accounting for 34.9% of all factors. NDVI, stratigraphic lithology, altitude, and land use, with an importance ratio of 36.4%, are more important in influencing landslide development. Other factors, with a cumulative importance of 28.7%, have a lesser influence on landslide development.

According to the results of the calculations, the five most influential factors are slope, DW, topographic relief, NDVI, and stratigraphic lithology. Based on the regional geological data and tectonic background analysis, the main reason for this result is, possibly, falling into the next two categories:

- small signaling for low altitude mountain slow landslides;
- landslides disaster intensive place, in the elevation rise of the semi-mountainside area, within the area of the slope changes in the larger range.

The slope gradient directly determines the force of the loose accumulation of the slope and controls the initiation conditions of the landslide disaster. Therefore, analyzed from an objective point of view, the slope and topographic relief have relatively large weights. Factors such as the density of the river network, the volume of runoff and the size of the within the watershed area reflect to some extent the landslide water source conditions and catchment capacity affected by permafrost freezing and thawing in the region, indirectly controlling the initiation conditions of landslide dynamics.

Table 3 Statistics of RF, IVM, FR model simulation and validation results

Items	RF	IVM	FR
Accuracy rate (%)	73.6	75.4	69.2
Prediction rate (%)	80.3	78.1	73.5
Very high-risk areas (%)	15.1	17.2	14.8
Proportion of landslide disasters (%)	56.6	58.0	49.6
High-risk areas (%)	23.1	19.2	16.5
Proportion of landslide disasters (%)	24.7	25.3	26.6
Moderate-risk areas (%)	25.1	24.0	39.2
Proportion of landslide disasters (%)	9.4	9.6	18.7
Low-risk areas (%)	36.7	39.6	29.5
Proportion of landslide disasters (%)	9.3	7.1	5.1

The Lesser Khingan and the Greater Khingan Mountains permafrost areas have natural forest stands, and high vegetation coverage, which is conducive to the protection of permafrost and water conservation, to prevent soil erosion and the role of land sand. When the surface vegetation cover is sparse or destroyed in a large area, it is easy to cause the weathering of the exposed rock on the surface, forming a large number of detritus accumulations, which is more likely to cause the occurrence of landslides. The factor with the least influence is the DR.

Through the evaluation index system established in Fig. 2, the IVM grades the status of each evaluation index based on the GIS platform, and then analyzes the spatial overlay with the landslide hazard points to get the distribution number of landslides in the graded interval of the status of each evaluation index. According to the formula of the IVM, the information quantity of each assessment indicator is calculated, and then the total information value is calculated through the raster superposition analysis. The information value is intermittently graded through the results of the fieldwork, to carry out the ranking of the landslide susceptibility in the study area. Finally, the landslide susceptibility map is drawn (Fig. 3b).

In the FR sensitivity assessment, the calculation results of several factors with the greatest impact on landslides derived from the RF were selected and displayed in Table 2 and then overlayed in ArcGIS according to Eq. (2), which resulted in the landslide FR sensitivity map as shown in Fig. 3c.

Since the sample disaster sites are divided into a training set and a validation set, a model accuracy ROC curve is obtained using the training set data, and the area under its curve is the accuracy of the model. The accuracy and prediction rate of each model are organized in Table 3.

By comparing the accuracy rate of each model, IVM has the highest accuracy rate of 75.4%, which indicates that the informativeness method is more accurate than the RF model training effect and FR simulation results. While the difference between the two prediction rates is large, the RF prediction rate reaches 80.3%, and its model predicts the results with high accuracy. The FR prediction rate is 73.5%, which has a certain gap compared with the RF, and the model prediction effect is average. The difference between the accuracy rate and the prediction rate can reflect the stability of the model. However, the difference between RF accuracy and prediction rate is 6.7%, and the difference between IVM is only 3.7%, and the simulation results of IVM in permafrost regions are more accurate and stable.

6 Conclusion

The permafrost regions in China are landslide-prone areas, and based on the topographic, geological, vegetation, and anthropogenic factors in the study area, 12 assessment factors and three models commonly used in existing studies were selected for landslide susceptibility evaluation, and the results of the models were verified with ROC curves. The following conclusions were obtained:

(1) The accuracy and prediction rate of IVM is higher than that of RF and FR methods, the difference between accuracy and prediction rate is smaller, and this means that the model is more stable, which is more suitable and effective for landslide sensitivity analysis in permafrost area.
(2) According to the importance analysis of assessment factors by the RF model, slope, distance from the water system and topographic relief, vegetation coverage (NDVI) and stratigraphic lithology are the factors that have the greatest influence on the development of landslides in the permafrost regions.
(3) Several factors that have the greatest influence on the development of permafrost directly or indirectly affect the permafrost condition, and also have a non-negligible influence on the freezing and thawing process of permafrost, so the state of permafrost should not be ignored on the influence of landslides. In addition to the traditional natural environment factors, the landslide susceptibility mapping in permafrost areas should also consider the influence of permafrost distribution and state.
(4) The number of landslide occurrences of all three models increases with the increase of susceptibility class, and the susceptibility grading is in line with the actual field investigation results, which proves that all three models have certain applicability in the permafrost region. Comparing the distribution ratios of landslide verification sites in each susceptibility class interval, the accuracy and zoning of the FR are greatly affected by the number of samples, while the IVM model is relatively more affected by the spatial distribution of the assessment factors, and the prediction results are relatively stable compared with those of the FR and RF models. However, the accuracy of several models is almost below 75%, and the disaster susceptibility assessment model

that is more applicable to the permafrost regions is waiting to be developed.

(5) Due to the large scale of the permafrost regions in northeast China, the natural environment is relatively complex. The permafrost is now severely degraded under global warming, which causes the historical statistical points and data of landslides to be much smaller than the actual number of landslides. Less statistical data will affect the simulation results of models such as RF and FR in the permafrost area, so the statistics and census of landslides in the permafrost regions and the study of the spatial distribution of permafrost are also urgently needed.

Acknowledgments We thank the National Natural Science Foundation of China (Grant No. 41641024), the Carbon Neutrality Fund of Northeast Forestry University (CNF-NEFU), and the Science and Technology Project of Heilongjiang Communications Investment Group (Grant No. JT-100000- ZC-FW-2021-0182) for providing financial support and the Field Scientific Observation and Research Station of the Ministry of Education—Geological Environment System of Permafrost Areas in Northeast China (MEORS-PGSNEC).

References

Aleotti P, Chowdhury R (1999) Landslide hazard assessment: summary review and new perspectives. Bull Eng Geol Env 58:21–44. https://doi.org/10.1007/s100640050066

Archer KJ, Kirnes RV (2008) Empirical characterization of random forest variable importance measures. Comput Stat Data Anal 52:2249–2260. https://doi.org/10.1016/j.csda.2007.08.015

Ayalew L, Yamagishi H (2005) The application of GIS-based logistic regression for landslide susceptibility mapping in the Kakuda-Yahiko Mountains, Central Japan. Geomorphology 65:15–31. https://doi.org/10.1016/j.geomorph.2004.06.010

Bozzano F, Mazzanti P, Prestininzi A, Scarascia Mugnozza G (2010) Research and development of advanced technologies for landslide hazard analysis in Italy. Landslides 7:381–385. https://doi.org/10.1007/s10346-010-0208-x

Catani F, Lagomarsino D, Segoni S, Tofani V (2013) Landslide susceptibility estimation by random forests technique: sensitivity and scaling issues. Nat Hazards Earth Syst Sci 13:2815–2831. https://doi.org/10.5194/nhess-13-2815-2013

Chae B-G, Park H-J, Catani F et al (2017) Landslide prediction, monitoring and early warning: a concise review of state-of-the-art. Geosci J 21:1033–1070. https://doi.org/10.1007/s12303-017-0034-4

Che VB, Kervyn M, Suh CE et al (2012) Landslide susceptibility assessment in Limbe (SW Cameroon): a field calibrated seed cell and information value method. Catena 92:83–98. https://doi.org/10.1016/j.catena.2011.11.014

Corominas J, van Westen C, Frattini P et al (2014) Recommendations for the quantitative analysis of landslide risk. Bull Eng Geol Environ 73:209–263. https://doi.org/10.1007/s10064-013-0538-8

Devkota KC, Regmi AD, Pourghasemi HR et al (2013) Landslide susceptibility mapping using certainty factor, index of entropy and logistic regression models in GIS and their comparison at Mugling-Narayanghat road section in Nepal Himalaya. Nat Hazards 65:135–165. https://doi.org/10.1007/s11069-012-0347-6

Dou Q, Qin S, Zhang Y et al (2019) A method for improving controlling factors based on information fusion for debris flow susceptibility mapping: a case study in Jilin Province, China. Entropy 21:695. https://doi.org/10.3390/e21070695

Froude MJ, Petley DN (2018) Global fatal landslide occurrence from 2004 to 2016. Nat Hazards Earth Syst Sci 18:2161–2181. https://doi.org/10.5194/nhess-18-2161-2018

Gariano SL, Guzzetti F (2016) Landslides in a changing climate. Earth-Sci Rev 162:227–252. https://doi.org/10.1016/j.earscirev.2016.08.011

Genuer R, Poggi J-M, Tuleau-Malot C (2010) Variable selection using random forests. Pattern Recogn Lett 31:2225–2236. https://doi.org/10.1016/j.patrec.2010.03.014

Guo Z, Shi Y, Huang F et al (2021) Landslide susceptibility zonation method based on C5.0 decision tree and K-means cluster algorithms to improve the efficiency of risk management. Geosci Front 12:101249. https://doi.org/10.1016/j.gsf.2021.101249

Guzzetti C, Reichenbach C (2000) Comparing landslide maps: a case study in the upper Tiber River basin, Central Italy. Environ Manag 25:247–263. https://doi.org/10.1007/s002679910020

Haque U, da Silva PF, Devoli G et al (2019) The human cost of global warming: deadly landslides and their triggers (1995-2014). Sci Total Environ 682:673–684. https://doi.org/10.1016/j.scitotenv.2019.03.415

Huang R (2007) Large-scale landslides and their sliding mechanisms in China since the 20th century. Yanshilixue Yu Gongcheng Xuebao/Chin J Rock Mechanics Eng 26:433–454

Huang Y, Zhao L (2018) Review on landslide susceptibility mapping using support vector machines. Catena 165:520–529. https://doi.org/10.1016/j.catena.2018.03.003

Kavzoglu T, Sahin EK, Colkesen I (2014) Landslide susceptibility mapping using GIS-based multi-criteria decision analysis, support vector machines, and logistic regression. Landslides 11:425–439. https://doi.org/10.1007/s10346-013-0391-7

Kayastha P, Dhital MR, De Smedt F (2013) Application of the analytical hierarchy process (AHP) for landslide susceptibility mapping: a case study from the Tinau watershed, West Nepal. Comput Geosci 52:398–408. https://doi.org/10.1016/j.cageo.2012.11.003

Liu Z, Guo D, Lacasse S et al (2020) Algorithms for intelligent prediction of landslide displacements. J Zhejiang Univ Sci A 21:412–429. https://doi.org/10.1631/jzus.A2000005

Nguyen CC, Vo P, Doan VL et al (2023) Assessment of the effects of rainfall frequency on landslide susceptibility mapping using AHP method: a case study for a mountainous region in Central Vietnam. In: Alcántara-Ayala I, Arbanas Ž, Huntley D et al (eds) Progress in landslide research and technology, volume 1 issue 2, 2022. Springer International Publishing, Cham, pp 87–98

Pei Y, Qiu H, Yang D et al (2023) Increasing landslide activity in the Taxkorgan River basin (eastern Pamirs plateau, China) driven by climate change. Catena 223:106911. https://doi.org/10.1016/j.catena.2023.106911

Pradhan B (2013) A comparative study on the predictive ability of the decision tree, support vector machine, and neuro-fuzzy models in landslide susceptibility mapping using GIS. Comput Geosci 51:350–365. https://doi.org/10.1016/j.cageo.2012.08.023

Regmi AD, Devkota KC, Yoshida K et al (2014) Application of frequency ratio, statistical index, and weights-of-evidence models and their comparison in landslide susceptibility mapping in Central Nepal Himalaya. Arab J Geosci 7:725–742. https://doi.org/10.1007/s12517-012-0807-z

Shan W, Zhang C, Guo Y et al (2022) Spatial distribution and variation characteristics of permafrost temperature in Northeast China. Sustain For 14:8178. https://doi.org/10.3390/su14138178

Sharma LP, Patel N, Ghose MK, Debnath P (2015) Development and application of Shannon's entropy integrated information value model for landslide susceptibility assessment and zonation in Sikkim Himalayas in India. Nat Hazards 75:1555–1576. https://doi.org/10.1007/s11069-014-1378-y

van Westen CJ, van Asch TWJ, Soeters R (2006) Landslide hazard and risk zonation - why is it still so difficult? Bull Eng Geol Environ 65:167–184. https://doi.org/10.1007/s10064-005-0023-0

van Westen CJ, Castellanos E, Kuriakose SL (2008) Spatial data for landslide susceptibility, hazard, and vulnerability assessment: an overview. Eng Geol 102:112–131. https://doi.org/10.1016/j.enggeo.2008.03.010

Wenyan L, Xile W (2020) Application and comparison of frequency ratio and information value model for evaluating landslide susceptibility of loess gully region. Ziranzaihai Xuebao 29:213–220

Westen CJV (1993) Application of geographic information systems to landslide hazard zonation. International Institute for Aerospace Survey and Earth Sciences, Enschede

Xing AG, Wang G, Yin YP et al (2014) Dynamic analysis and field investigation of a fluidized landslide in Guanling, Guizhou, China. Eng Geol 181:1–14. https://doi.org/10.1016/j.enggeo.2014.07.022

XinHai L (2013) Using "random forest" for classification and regression. Chin J Appl Entomol 50:1190–1197

Yalcin A (2008) GIS-based landslide susceptibility mapping using analytical hierarchy process and bivariate statistics in Ardesen (Turkey): comparisons of results and confirmations. Catena 72:1–12. https://doi.org/10.1016/j.catena.2007.01.003

Yang B, Yin K, Lacasse S, Liu Z (2019) Time series analysis and long short-term memory neural network to predict landslide displacement. Landslides 16:677–694. https://doi.org/10.1007/s10346-018-01127-x

Yin KL, Yan TZ (1988) Statistical prediction models for slope instability of metamorphosed rocks. Publ Rotterdam, A A Balkema, Lausanne, pp 1269–1272

The Slope Monitoring Using Embedded System with Optical-Thermal Image Fusion and Machine Learning

Chih-Chung Chung, Bo-Chi Chen, Te-Wei Tseng, and Yun-Tzu Lee

Abstract

Taiwan is at the junction of tectonic plates, with high mountainous terrain and abundant rainfall due to the rich moisture of the subtropical monsoon zone, which makes the already dangerous slopes even more unstable. By applying the digital camera measurement approach, with its moderate installation cost, high security, and mobility, it is possible to capture and monitor the hillside over an extended period, guaranteeing its stability. Photogrammetry is a recent technology that has gained popularity in many fields. Image analysis, achieved by capturing photographs, is a growing trend. It offers a cost-effective way of transmitting information in automated Internet of Things (IoT) systems, reducing human and financial resources. Therefore, this study aims to utilize close-range photogrammetry to analyze both 2D and 3D image data. Besides, this study encompasses thermal images, enabling researchers to evaluate observed objects' temperature differences quickly. Thus, this study aims to superimpose temperature information from thermal images onto optical images, in order to analyze slope information. It focuses on creating on-site cameras that use both optical and thermal imaging, building a three-dimensional point cloud using optical systems, investigating image displacements, and tracking unstable areas using thermal imaging. Additionally, the research explores the potential of AI interpretation to aid in this process. The laboratory and the preliminary field test support the feasibility of the proposed system and interpretation methods.

Keywords

Landslide · Photogrammetry · Thermal image · AI interpretation

1 Introduction

Due to geographical and environmental factors, Taiwan frequently experiences severe slope disasters during heavy rainfall and earthquakes. (Kaima et al. 2000; Wu et al. 2014). The types of slope failures can be classified based on modes of movement, including fall, topple, slide, slump, flow, and creep (Geoscience Australia). In particular, most slope failures can be categorized into deep-seated and shallow-seated slope failures. Shallow-seated slope failures typically occur in steep slopes with poorly cohesive geological materials, lacking vegetation cover, or on slopes with pre-existing landslide deposits. Nevertheless, rainfall often triggers shallow-seated sliding, which infiltrates the soil layer, altering the unsaturated soil's hydraulic characteristics. This includes changes in fluid movement and distribution, increasing soil moisture content while decreasing matric suction within the substrate. Consequently, the stability of the soil mass is reduced (Lu and Godt 2008; Bordoni et al. 2015; Cho 2016, 2017; Jeong et al. 2017).

Furthermore, deep-seated slope failures represent another significant area of concern (Varnes 1978). The mechanisms leading to large-scale collapses are complex, primarily influenced by geological structures and the rock layer distributions, including dip slopes, strike slopes, and oblique slopes. The causes of large-scale collapses can generally be attributed to seismic activity and rainfall. In the case of rainfall-induced collapses, the physical mechanisms are similar to those observed in shallow-seated failures. Rainwater infiltra-

C.-C. Chung (✉)
Department of Civil Engineering/Research Center for Hazard Mitigation and Prevention, National Central University, Taoyuan City, Taiwan
e-mail: ccchung@ncu.edu.tw

B.-C. Chen · T.-W. Tseng · Y.-T. Lee
Department of Civil Engineering, National Central University, Taoyuan City, Taiwan
e-mail: jessicalee9806@g.ncu.edu.tw

B. Abolmasov et al. (eds.), *Progress in Landslide Research and Technology, Volume 3 Issue 1, 2024*, Progress in Landslide Research and Technology, https://doi.org/10.1007/978-3-031-55120-8_12

tion into the subsurface raises pore water pressure within the soil and rock layers. It reduces effective stress of the surface soil layers and rock near the failure plane, which is the primary contributing factor.

In order to evaluate the slopes' stability, appropriate monitoring instruments are required (Segoni et al. 2018). Typical instruments used for slope monitoring currently are inclinometers, crack gauges, and piezometers. Although these monitoring instruments present high accuracy, reliability, and ease of measurement, they could be better for drilling and installation in rugged terrain.

According to the studies by Kromer et al. (2019), Kim and Gratchev (2021), and Núñez-Andrés et al. (2023), close-range photogrammetry proves extremely effective for rockfall monitoring in rock slopes, with precision measures reaching millimeter-level accuracy. For precise and stable observations of localized slopes over an extended period, close-range photogrammetry provides excellent monitoring quality and valuable benefits in reducing staffing and offering immediate monitoring and early warnings. Consequently, this study will create a long-term and stable slope monitoring system based on a close-range photogrammetry system.

Meanwhile, thermal imaging is increasingly being used for slope disaster prevention and mitigation alongside optical image analysis (Pappalardo et al. 2021; Yu et al. 2023). Unlike visible light imagery, it cannot provide detailed displacement information about objects. Fortunately, it can furnish temperature data, allowing monitors to track regional. Frodella et al. (2014) examined the possible usefulness of infrared thermal imaging technology for rock slope monitoring. Thermal images of diverse rock slope features (including structural discontinuities, cracks, steep slopes, and seepage) were attained at different intervals via aerial and ground-based photography. The investigation revealed that unstable regions on slopes, stemming from geographical influences, showed noteworthy differences in temperature in thermal image spectra at various time periods. Consequently, the combination of optical image analysis, which preserves the slopes' geometric information, and thermal image records to detect concealed unstable areas within these slopes can produce a more comprehensive monitoring dataset.

Based on the previous concerns, the main goal of this study is to utilize computer vision technology to merge thermal and optical imaging. The aim is to superimpose temperature data from thermal images onto optical images to analyze slope conditions (Chen 2022). Additionally, the study aims to develop equipment for practical on-site application of this method while exploring the incorporation of AI-assisted interpretation (Tseng 2023). Furthermore, in addition to maintaining the analysis of slope displacement, this research enables temperature difference analysis through thermal imaging. This facilitates the identification of potential hazard zones behind the slope, providing valuable assistance for future planning and tracking efforts.

After completing the development of on-site equipment in this study, the monitoring instruments will undergo evaluation via testing with a scaled-down model of a reverse slope. To serve as an example, a monitoring system will be installed on the rear slope of National Central University. Multiple sets of images will then undergo analysis to assess slope displacement. The research will monitor slope stability by post-processing three-dimensional information models. The experimental results show accuracy within 3 cm. Preliminary testing of AI-assisted interpretation demonstrated potential in detecting displacement. The subsequent outcomes will provide early warning, prevention, and post-disaster planning for slope disasters, resulting in practical decision-making data.

2 Instrument Design and Image Analysis Process

The instrumentation assembly plan for this study is based on establishing the target tasks and comprises four main components: hardware selection, instrument casing design, image change detection, and operational scripts. The hardware assembly design will be adjusted to ensure the monitoring operations run smoothly for photogrammetry. The design of the instrument casing will be revised based on practical assembly and imaging work to ensure safe and proper equipment operation.

Various training datasets will be compiled to enhance the accuracy of image change detection in diverse scenarios, such as changing scenes, lighting conditions, and viewing angles. Experiments will be performed regarding operational scripts to increase instrument automation and display outcomes clearly and straightforwardly.

The Raspberry Pi is a microcomputer developed by the Raspberry Pi Foundation (Halfacree and Upton 2012). It has grown in popularity as a miniature single-board controller in recent years due to its small size, convenience, and high development capabilities. Therefore, the basic hardware architecture of the surveillance system will initially encompass a microcontroller, the Raspberry Pi, an optical imaging camera module (Raspberry Pi Camera Module V2), and an infrared thermal imaging camera module (FLIR Lepton 2.5). The camera's low pixel count requires capturing numerous photos to enhance the quality of the model. A track-driven camera setup will be designed to capture more images. The camera will be mounted on a 3D-printed track, and GA12-N20 geared motors, as well as an L298N motor driver will be employed to move the camera along the track, enabling the capture of images from various locations. The protective casing for the electronic equipment in this study will be 3D-printed to ensure durability and reliability in natural environments (Fig. 1). The power supply will use lead-acid batteries and solar panels, allowing the monitoring equipment to operate for extended periods in

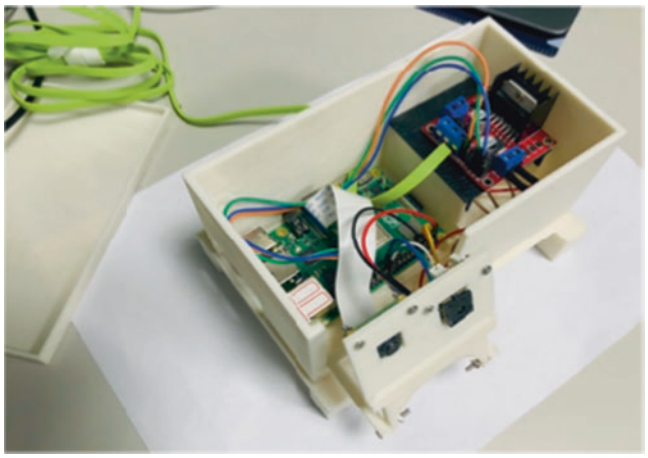

Fig. 1 Side view of electronic equipment and casing, as well as the optical and thermal cameras

the field using renewable energy sources (Chen 2022; Tseng 2023).

The process starts by capturing images from the Raspberry Pi hardware. Then, there is system preprocessing, which comprises camera lens calibration and forming a 3D point cloud model. After the model is built, Python Open3D will be used for point cloud displacement analysis, along with commercially available software like Pix4D Mapper and Cloud Compare. Using MATLAB point image analysis package, two-dimensional image analysis and comparison will also be executed.

Besides, thermal image analysis will be accomplished utilizing Python OpenCV. This process entails procedures such as image normalization and temperature difference analysis. The resulting analysis will be visualized using MeshLab to map the thermal image temperature differences onto the point cloud model.

This study further employs a machine learning model for optical image change detection proposed by Chen et al. (2021), as shown in Fig. 2, utilizing conventional neural network architectures like Convolutional Neural Networks, Transformer models, and Siamese Neural Networks. The self-trained change detection model extracts feature maps from pairs of optical images captured at the exact location but at different time intervals. The machine learning model then adjusts these feature maps utilizing a pre-trained neural network model. The difference in the feature maps of the two images predicts the change detection map for this pair of images. This study pre-processes self-captured optical images to generate a dataset for improved change detection models, promoting practical monitoring applications in various locations. The quantitative evaluation of these models employs binary confusion matrices for image classification and performs image segmentation. Common metrics, such as mean F1-score and mean Intersection over Union (IoU), are utilized to quantitatively evaluate the efficacy of the produced change detection models.

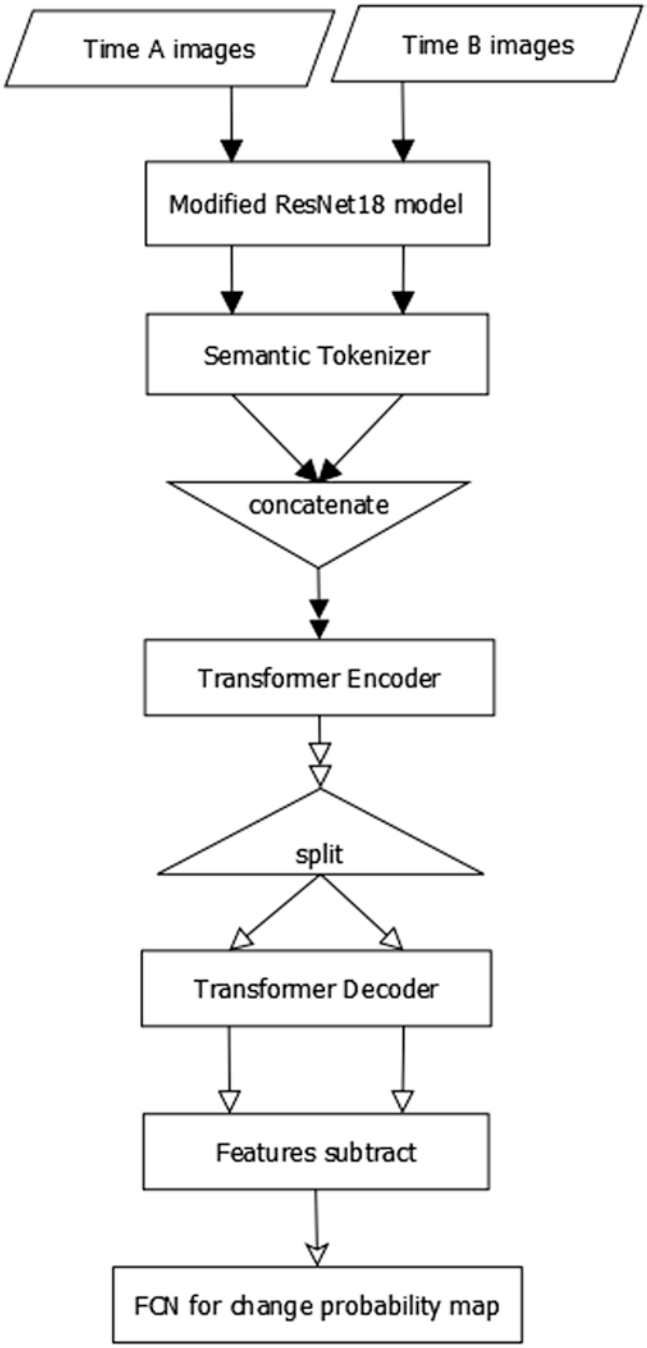

Fig. 2 Process of detecting inter-optical image changes (modified after Chen et al. 2021)

Additionally, this study utilizes a mathematical approach to analyze pairs of thermal infrared images captured at various time intervals for change detection in thermal infrared imaging. Linear interpolation is utilized to adjust the arrays in the two thermal infrared images captured at different intervals. The camera module's original grayscale values are subsequently converted to temperature values. The temperature values from the later time interval are subtracted from those of the earlier time interval to create a temperature change detection image for the pair of images. Then, this image is

overlaid onto the change detection image from the 2D optical imaging of the same pair of time-interval images. This presentation enables visualization of change detection outcomes from both the thermal and optical camera modules in one image, effectively displaying changes captured by both camera systems.

3 Laboratory Vibration Table Experiment

Before installing the instruments on the slope, an indoor testing is necessary to validate the feasibility of the optical camera in the displacement analysis system. The objective is to compare the displacement values analyzed from optical images with known object displacement values and evaluate the suitability of the optical image analysis process used in this research.

Vibration table experiments are typically used in geotechnical engineering to simulate and analyze slope failures. Studying the behavior of soil failure allows for a better understanding of related mechanisms. Chen (2020) conducted experiments simulating the mechanism and deformation of seismic-induced rockslide. The experiments utilized a scaled-down model of a reverse slope and vibration table, which was considered optimal for the optical image analysis system employed in this study. Therefore, this study utilizes Chen (2020) results to classify the slope failure type and conducts displacement analysis via optical images of slope failure.

The scaled-down model utilized in this study and its support structure were positioned on a unidirectional vibration table with a measurement of 90 x 90 cm. The top and front views of the experimental site are shown in Fig. 3.

The investigation began by adjusting the slope angle, along with the frequency and amplitude of vibrations. Before the onset of vibrations, 30 consecutive photographs were taken to record the experimental setup. After the camera returned to its initial position, the vibration started and images were captured continuously at one per second. The vibration ceased after taking 30 images, prompting the commencement of image analysis.

The Iterative Closest Point (ICP) method is widespread in 3D modeling to analyze distances. This method works by fitting all the point clouds around the feature points, extracting those feature points, and calculating the squared differences of the scale, direction, and rotation to obtain the best-fit three-dimensional model. Another commonly used 3D model calibration method is the Matching Bounding-Box Center (MBBC) method. This technique evaluates the location of the neutral point cloud in the model and establishes a box that envelops the point cloud model. The method then

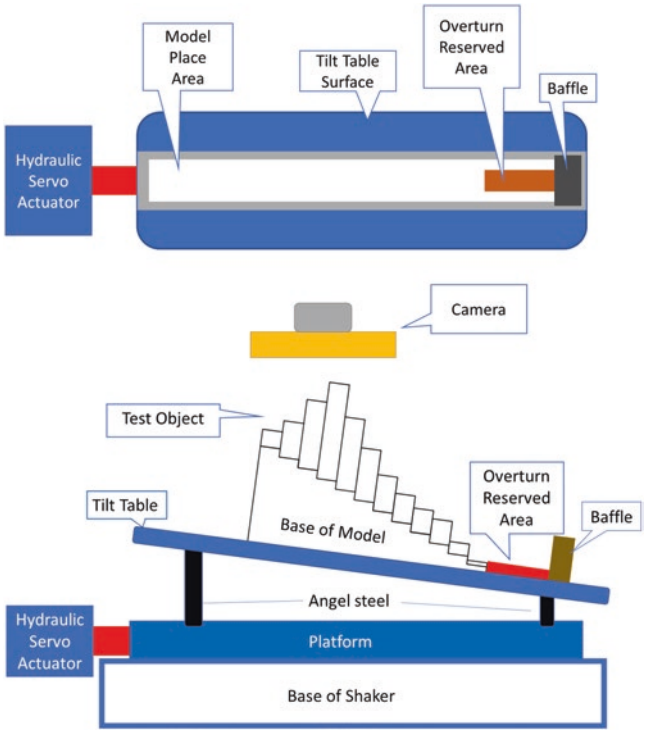

Fig. 3 Top view and front view of experiment

rotates and shifts the large square of two distinct point clouds to the center point, viewed as an overlap of the point cloud pattern. The point cloud is subsequently determined.

The image analysis for the indoor experiment will employ Pix4D Mapper software for image reconstruction. Pix4D Mapper, a 3D image processing software developed by Pix4D in Switzerland, utilizes the Structure from Motion (SfM) technique (Westoby et al. 2012) to compute the internal and external orientation parameters of the camera system. It extrapolates the coordinates of the image's characteristic points to construct a 3D image. After constructing a 3D image using Pix4D Mapper, the resulting model will be exported to Python for displacement analysis of the image, using the Open3D suite to calculate the displacement. The Euclidean Distance is calculated between the closest points in the two-point cloud diagrams based on the Cloud-to-Cloud Distance Computation (C2C) Method rather than the actual point cloud displacement distance.

Additionally, the slope's damage pattern is calculated using the PIV method both before and after the vibration process, and then compared to the average displacements within the landslide area through analysis. The PIV point image analysis tool suite provided by MATLAB will be used for 2D image analysis. Due to the back-and-forth shaking of the platform during vibration, the PIV mass point image analysis becomes disrupted. To counteract this, the summa-

Fig. 4 Comparison of experimental results before and after failure

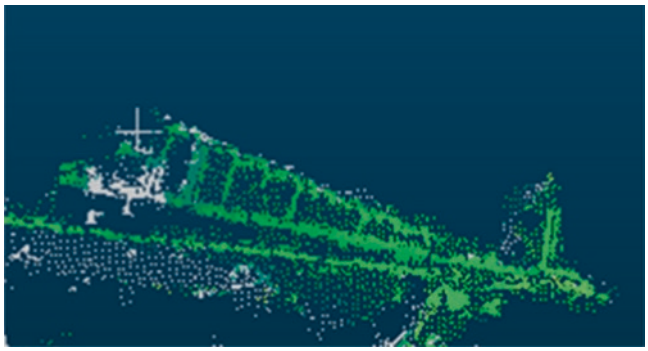

Fig. 5 Point cloud displacement map

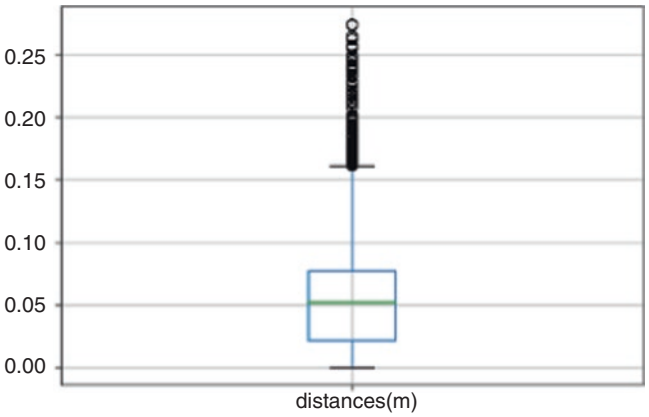

Fig. 6 Point cloud displacement statistics chart

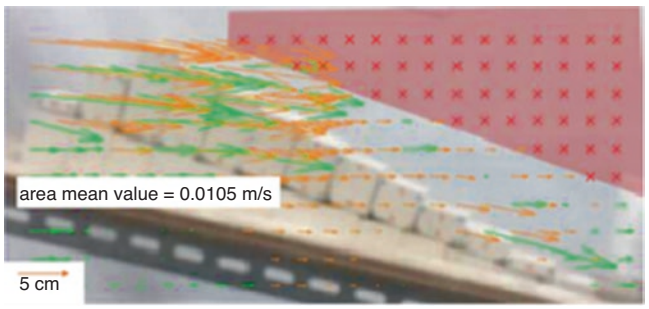

Fig. 7 Analysis results of PIV method

tion method is utilized in this study to superimpose the total displacement during shaking for analysis. The feasibility of the system is confirmed by combining and comparing the results of the two analyses.

Four experiments were conducted according to the experimental configuration. The A second set of experiments, which resulted in the most minor error, was analyzed as an example. (consisted of slope: 10°, amplitude: 2.48 mm, frequency: 6 Hz.) The specimen was destroyed after approximately 5 s, from the vibration table's shaking to the destruction of the specimen. According to the comparison before and after the experimental destruction (Fig. 4), except for the block at the top of the slope, which did not exhibit any noticeable movement, all other blocks demonstrated a significant inclination and displacement tendency. The average displacement distance of the blocks is 5 cm.

Figure 5 displays the results of the displacement analysis for the point cloud model. The white section indicates the inactive point between the two-point clouds, while the other colors illustrate the displacements at various scales. Figure 6 presents the displacement statistics for the point cloud system described in Fig. 5. The black points exclude values that deviate from the standard deviations, and hence are not included in the calculation. The green line indicates the mean value location, which measures 5.1 cm.

Figure 7 displays the results obtained from the PIV analysis. The calculation entails adding up the total displacement over the previous 5 s, followed by averaging the result. This

produces the average displacement magnitude present in the selected images. The total displacement can be determined to be 5.1 cm.

Due to the camera's positioning limitations, the shooting angle was not perfectly aligned with the motion direction of the target object. Initially designed for measuring particle velocities in two-dimensional flow fields, PIV remains a reliable method regardless of this constraint. When the motion direction of the target object is not perpendicular to the camera's optical axis, the accuracy of distance measurements may be impacted by the variable depth information of the target object in the images. Consequently, this research revealed a minor divergence between the results of PIV and point cloud displacement analysis in the other tests.

4 NCU Field Experiment

National Central University (NCU) is located in the Dianzih Lake Formation, mainly consisting of lower gravel and upper red soil layers. The gravel is primarily composed of white quartzite, dark gray siliceous sandstone, and light gray sandstone, among others. The soil properties have been determined through basic physical property tests, and according to relevant standards, the soil is classified as Clay Loam (CL). The nearby hillside next to the dormitories, with approximate distances of 55 m, 40 m, 40 m, and 20 m on its four sides, has a potential for shallow landslides, making it a suitable test site for installing the monitoring system in this research.

The experimental area, as shown in Fig. 8, primarily consists of rocky terrain. Although the upper parts of the rocky slope and the surrounding areas may have vegetation cover, the toe of the slope is often exposed to sand and gravel, making it highly suitable for thermal imaging identification.

The initial step involves experimenting with optical point cloud displacement analysis. The camera should be affixed at a fixed distance from the slope while control points are placed to monitor the absolute coordinates of image modeling. Additionally, checkpoints are established to validate the modeling quality, as shown in Fig. 9. Both control points and checkpoints contain known three-dimensional coordinates. The modeling results can be transformed into real-world coordinates by utilizing the control points, and the modeling quality is verified by employing the checkpoints.

After an accuracy analysis, we artificially displaced the rocks on the slope to test displacement recognition. Place feature points on the rocks, then move 15 cm, as Fig. 10 shows. Figs. 11 and 12 depict our results. As previously noted, we employed the C2C method to calculate the data. The C2C method calculates the elevation difference rather than the actual horizontal displacement when the rock is displaced 15 cm, which exceeds the rock's height difference. In

Fig. 9 Layout diagram of control points and checkpoints (red for control points, black for checkpoints)

Fig. 8 UAV Modeling near NCU Dormitories (Jian 2019)

Fig. 10 Illustration of artificially moved rocks

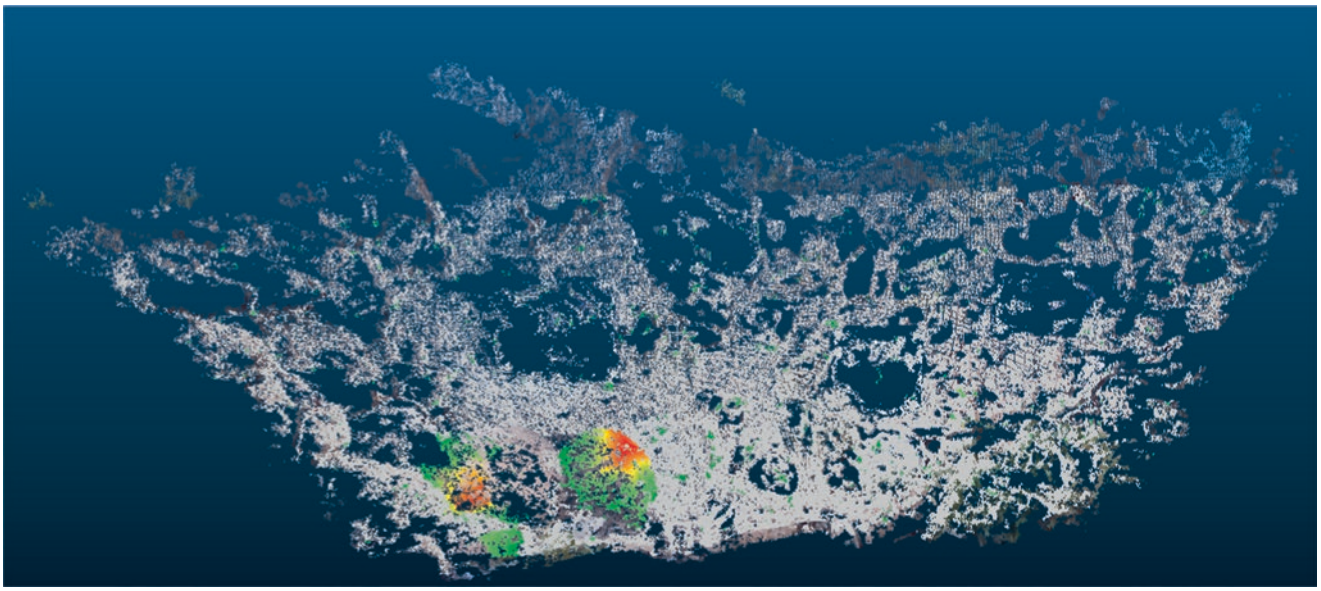

Fig. 11 Identification image of 15 cm rock displacement using C2C method

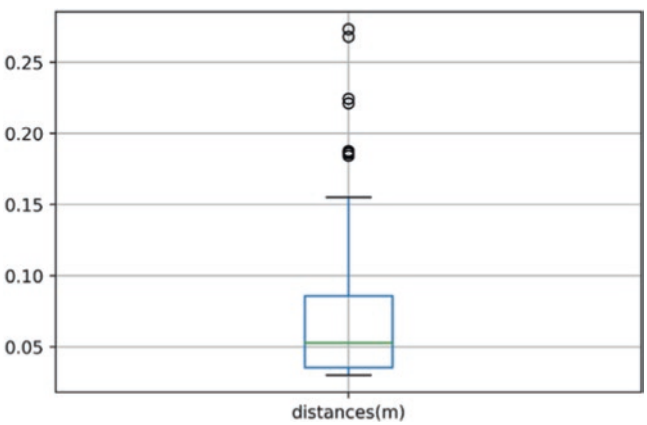

Fig. 12 Chart of mean 15 cm rock displacement using C2C method

order to validate the capability of the constructed point cloud model to compute the displacement distance, this study identified feature points on the point cloud models from two distinct periods, illustrated in Figs. 13 and 14. The feature points' coordinates were utilized to ascertain the displacement distance. Specifically, the computed displacement for a 15 cm movement was 16.2 cm, falling within a 2.59 cm margin of error.

A goal of this study was to observe the changes in the rock mass due to temperature variations. Therefore, temperature difference analyses were conducted at five selected time points, which were 5:00 PM, 12:00 AM, 7:00 AM on the next day, 1:00 PM on the next day, and 5:00 PM on the next day, in conjunction with optical image analysis. The temperature difference analysis results are shown in Fig. 15.

According to the analysis results in Fig. 15, it can be observed that from 7:00 AM to 1:00 PM, there is ample time for the slope to absorb sunlight as the sun rises to its zenith. This results in a higher temperature. From 1:00 PM to 5:00 PM, the temperature difference is more significant. This can be attributed to the fact that the sun has passed its zenith at 11:59 AM and is gradually moving westward. As a result,

Fig. 13 Illustration of feature points in rocks at three-dimensional and two-dimensional image positions (initial position)

Fig. 14 Schematic diagram of feature points in rock at three-dimensional and two-dimensional image positions (15 cm movement)

the slope cannot receive direct sunlight, and the abundant tree shade above the slope contributes to cooling. Therefore, for the slope in this experimental area, measuring the temperature variations between 7:00 AM and 1:00 PM, as well as between 1:00 PM and 5:00 PM, provides better examples for analysis.

Another preliminary investigation aimed to establish the correlation between thermal and visible images and generate a point cloud model utilizing thermal image data. The initial procedure involves texture mapping of the optical image onto the 3D point cloud generated from Pix4D Mapper. With the MeshLab, the point cloud containing the optical texture map (Mesh) is then exported. Next, the thermal image is imported into MeshLab, and its corresponding position is manually searched. The thermal image's texture is then mapped onto the point

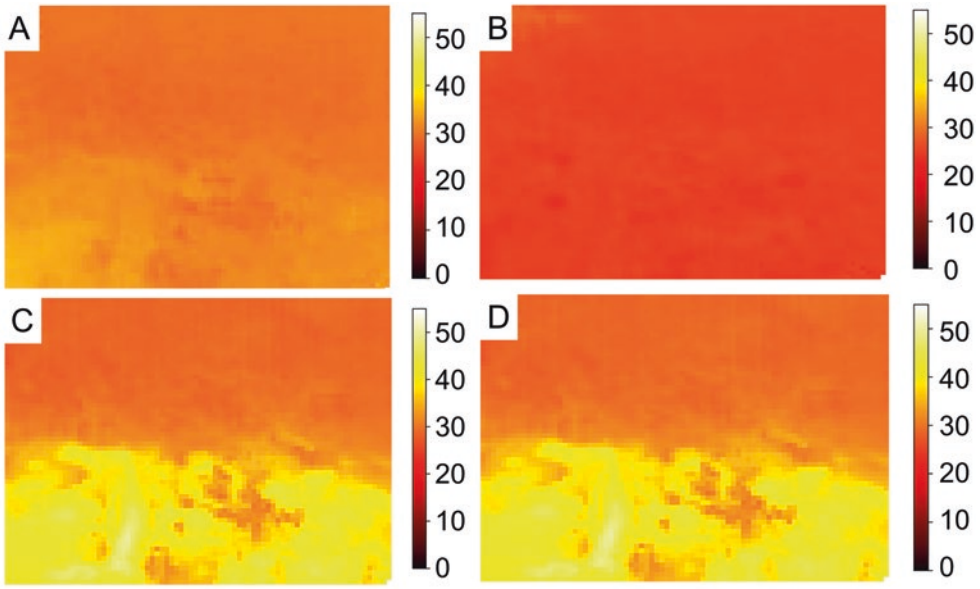

Fig. 15 Temperature Difference Analysis Chart. (**a**) Temperature Difference from 5 PM to 12 AM. (**b**) Temperature Difference from 12 AM to 7 AM. (**c**) Temperature Difference from 7 AM to 1 PM. (**d**) Temperature Difference from 1 PM to 5 PM

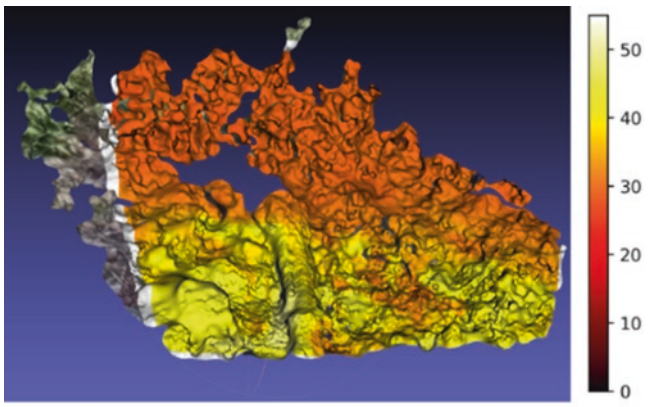

Fig. 16 3D Texture mapping of optical and thermal images

cloud with optical texture mapping. The result is shown in Fig. 16.

5 AI Image Analysis for Decision Support

With the development of artificial intelligence technologies like machine learning (ML) and deep learning (DL), which draw inspiration from the structure and function of the human brain, computer vision research has evolved significantly. Artificial neural networks (ANN), including various types such as convolutional neural networks (CNN) and recurrent neural networks (RNN), have become the primary focus in the field of computer vision (Bhatt et al. 2021). These AI technologies enable researchers to make predictions or decisions based on data using mathematical algorithms. Deep learning, in particular, has profoundly impacted on computer vision by allowing the automatic learning of patterns and features in labeled image datasets. This has significantly improved the ability to handle highly complex datasets and tasks related to image classification and detection Chen et al. (2021) adopted a novel approach to change detection in remotely sensed imagery by using machine learning techniques. Instead of relying on CNNs or complex architecture, such as U-Net, they aimed to improve efficiency by using a simpler network structure. They also incorporated Attention and Transformer mechanisms to process images in a sequence-like manner, enabling the model to capture comprehensive information. In this machine learning model, information from image segmentation is treated as tokens, analogous to natural language processing. Furthermore, this model utilizes encoder and decoder components inspired by Transformers to process these tokens. The output of the change detection is represented by the differences between two sampled images, which are compared with other methods of image change detection. The method resulting from the use of this approach is termed the Bitemporal Image Transformer (BIT) map, as presented in Fig. 17. The results

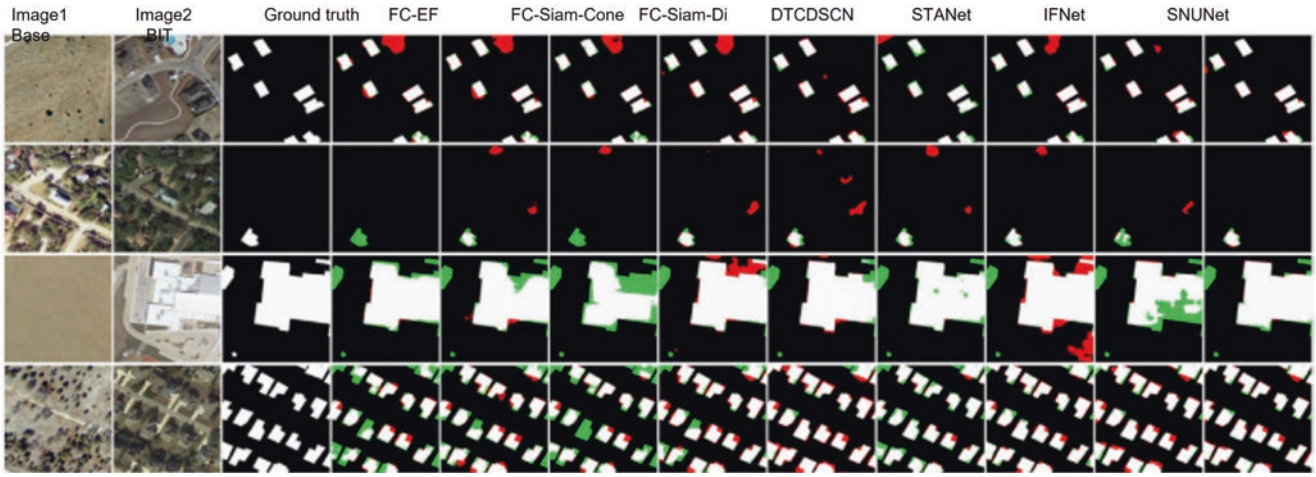

Fig. 17 Using BIT for change detection compared to other methods (modified after Chen et al. 2021)

indicate that this technique is effective at detecting changes with a high degree of accuracy.

While using data of the same type can directly compare changes, combining data from different data types can also yield excellent change detection results. These sensors may have different spatial, spectral, and temporal resolutions, but they provide additional possibilities for supplementing information and improving the accuracy of change detection. Therefore, developing techniques to compare or integrate data from different sensors and sources for change detection is meaningful. By integrating data from different types of sensors and sources, it becomes possible to gain a more comprehensive understanding of the types, extent, and scale of changes occurring in the imagery.

In summary, optical and infrared thermal imaging technologies have their roles and development potential in slope monitoring. Optical imaging technology is used for high-precision measurements of slopes, taking advantage of its unique imaging characteristics. In parallel, infrared thermal imaging technology can be employed to detect changes in the surface temperature of slopes. In this study, an integrated approach can enhance safety and stability assessment for on-site slopes through machine learning applied to optical images and computer vision techniques for change detection, coupled with infrared thermal imaging to monitor temperature changes on the slope surface.

The study conducted monitoring tasks to detect changes on the surface of a small slope located near the NCU (Fig. 8). The equipment and techniques specified above were utilized in this endeavor. The optical imaging-generated change detection model exhibited excellent performance during training, attaining an average F1-score of 0.9359 and an average Intersection over Union (IoU) of 0.8850 for the bitemporal image test collection. The model's application with thermal imaging for change detection resulted in productive real slope monitoring outcomes, as shown in Fig. 18.

Since the slope adjacent to the NCU parking lot remains generally stable and experiences few rapid natural environmental changes on its surface, this study established the effectiveness of machine learning for optical imaging change detection by deliberately altering the objects on the slope's surface. This was accomplished by manually relocating stones on the slope to initiate changes. Bitemporal images were taken before and after manually moving stones (Fig. 19). This study utilized a machine learning model in combination with thermal imaging for change detection, and the results obtained are shown in Fig. 20. While optical

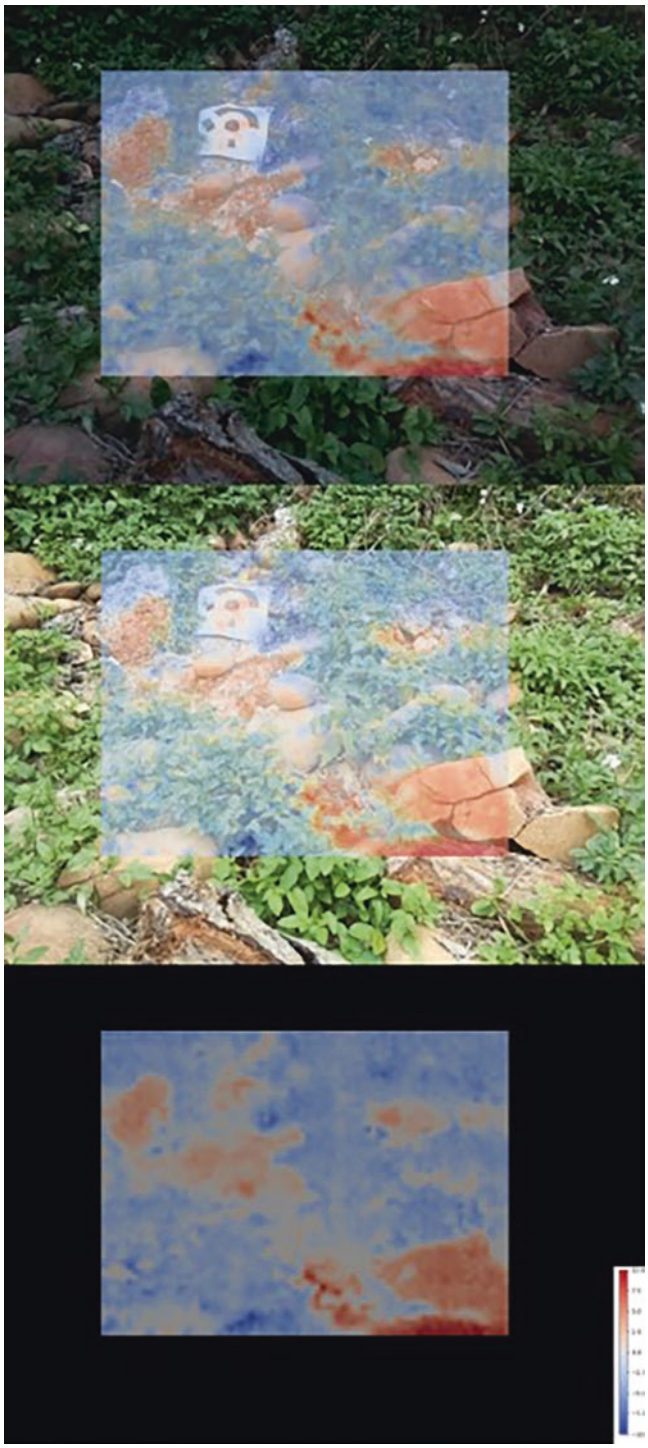

Fig. 18 NCU Parking lot slope change detection image (The first row is the image from the previous time period, taken on 2023/03/13 at 6 A.M., the second is the image from the later time period, taken on 2023/03/13 at 2 P.M., and the third is the machine learning change detection image. Black pixels represent no change; white pixels represent changes. The color bar on the lower right corresponds to temperature changes)

Fig. 19 Manual stone relocation diagram (red circles indicate stone movement)

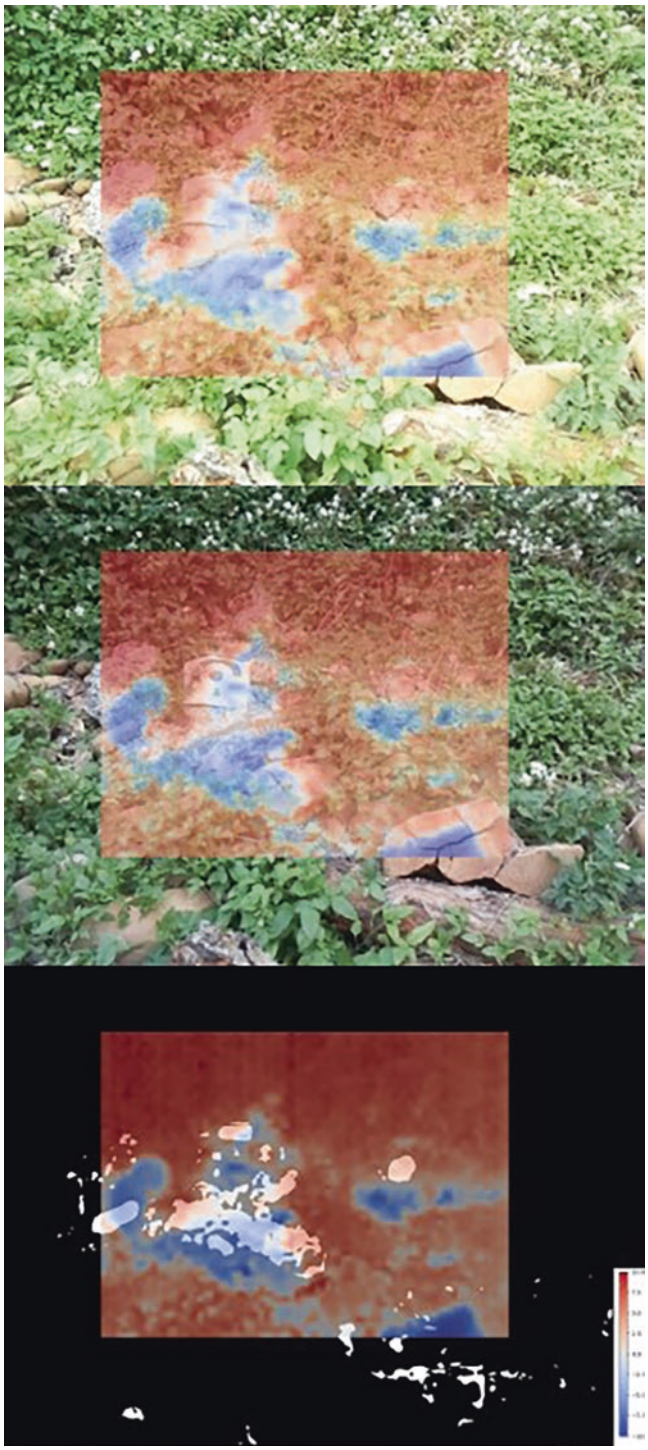

Fig. 20 NCU parking lot slope change detection image (The first row is the image from the previous time period, taken on 2023/03/17 at 2 P.M., the second row is the image from the later time period, taken on 2023/03/18 at 6 P.M., and the third row is the machine learning change detection image. Black pixels represent no change; white pixels represent changes. The color bar on the lower right corresponds to temperature changes)

imaging offers intuitive and visual results on the slope's surface, thermal imaging provides temperature difference information that is not available through optical imaging, making it a valuable asset for both research and user support.

6 Conclusion and Suggestions

This study described a new system and methodology to present an innovative approach to combine optical and thermal images for slope monitoring. The optical images can be used for photogrammetry as point clouds for displacement detection. Both the laboratory and field tests provided promising accuracy. The fusion of optical and thermal also revealed the apparent evidence to indicate the possible weak area of the slope.

The optical images were extended with a modified machine-learning method for automatic detection. Preliminary results at the NCU site guaranteed the feasibility of practice.

However, it highlights specific challenges that need to be resolved in the next step.

1. Implementing machine learning techniques for change detection in optical images is complicated due to two main stumbling blocks. The first is the diverse nature of the data that can impede analysis and the generation of established change detection results. The second is that supervised AI methods necessitate a vast amount of training data, which is time-consuming and demands intensive resources.
2. The durability and robustness of the instrument equipment at the field site near the slope is an area that requires further research on developing reliable monitoring data solutions in the face of interference from natural environmental factors.

References

Bhatt D, Patel C, Talsania H, Patel J, Vaghela R, Pandya S, Ghayvat H (2021) CNN variants for computer vision: history, architecture, application, challenges and future scope. Electronics 10(20):2470

Bordoni M, Meisina C, Valentino R, Lu N, Nittelli M, Chersich S (2015) Hydrological factors affecting rainfall-induced shallow landslides: from the field monitoring to a simplified slope stability analysis. Engin. Geol 193:19–37

Chen CC (2020) Seismic response study of anti-dip rock slope by shaking table test and discrete element method Ph.D. Dissertation, Chung Cheng Institute of Technology, National Defense University

Chen BC (2022) Fusion of optical and thermal imagery for a long-term stability application to slopes monitoring and evaluation. Master Thesis, National Central University

Chen H, Qi Z, Shi Z (2021) Remote sensing image change detection with transformers. IEEE Trans Geosci Remote Sens 60:1–14

Cho SE (2016) Stability analysis of unsaturated soil slopes considering water-air flow caused by rainfall infiltration. Eng Geol 211:184–197

Cho SE (2017) Prediction of shallow landslide by surficial stability analysis considering rainfall infiltration. Eng Geol 231:126–138

Frodella W, Morelli S, Gigli G, Casagli N (2014) Contribution of infrared thermography to the slope instability characterization. In Proceedings of world landslide forum. Vol. 3, pp. 144–147

Geoscience Australia, http://www.ga.gov.au/hazards/landslide/causes.jsp

Halfacree G, Upton E (2012) Raspberry pi user guide. John Wiley & Sons, New York

Jeong S, Lee K, Kim J, Kim Y (2017) Analysis of rainfall-induced landslide on unsaturated soil slopes. Sustain For 9:1280

Jian JH (2019) Development of the integrated monitoring system of IoT and TDR for shallow and deep-seated landslides. Master Thesis, National Central University

Kaima TW, Wang WN, Sguzui H (2000) The landslide disaster induced by the Taiwan chi-chi earthquake of 21 September 1999. Landslide News 13:8–12

Kim DH, Gratchev I (2021) Application of optical flow technique and photogrammetry for rockfall dynamics: a case study on a field test. Remote Sens 13(20):4124

Kromer R, Walton G, Gray B, Lato M, Group R (2019, 1890) Development and optimization of an automated fixed-location time lapse photogrammetric rock slope monitoring system. Remote Sens 11(16)

Lu N, Godt J (2008) Infinite slope stability under steady unsaturated seepage conditions. Water Resour Res 44(11):2008WR006976

Núñez-Andrés MA, Prades-Valls A, Matas G, Buill F, Lantada N (2023) New approach for photogrammetric rock slope premonitory movements monitoring. Remote Sens 15(2):293

Pappalardo G, Mineo S, Carbone S, Monaco C, Catalano D, Signorello G (2021) Preliminary recognition of geohazards at the natural reserve lachea islet and cyclop rocks (Southern Italy). Sustain For 13:1082

Segoni S, Piciullo L, Gariano SL (2018) Preface: landslide early warning systems: monitoring systems, rainfall thresholds, warning models, performance evaluation and risk perception. Nat Hazards Earth Syst Sci 18(12):3179–3186

Tseng TW (2023) The evaluation of slope monitoring using optical and thermal images fusion through machine learning. Master Thesis, National Central University

Varnes DJ (1978) Slope movement types and processes. Special report 176: 11–33

Westoby MJ, Brasington J, Glasser NF, Hambrey MJ, Reynolds JM (2012) Structure-from-Motion'photogrammetry: a low-cost, effective tool for geoscience applications. Geomorphology 179:300–314

Wu CH, Chen SC, Feng ZY (2014) Formation, failure, and consequences of the Xiaolin landslide dam, triggered by extreme rainfall from typhoon Morakot. Taiwan Landslides 11:357–367

Yu L, Jin C, Wang Q, Han T, Li G, Zhong X, Chen G (2023) Combining InSAR and infrared thermography with numerical simulation to identify the unstable slope of open-pit: Qidashan case study, China. Landslides. https://doi.org/10.1007/s10346-023-02076-w

Sendai Framework Voluntary Commitments: Monitoring Landslide Stakeholders' Contributions

Yuki Matsuoka

Abstract

Disasters caused by landslides have continued to occur in recent years resulting in loss of lives and livelihoods around the world. To prevent such disasters and reduce landslide risk, it is crucial to share good practices from around the world and promote all-of-society engagement. The Sendai Framework Voluntary Commitments (SFVC) online platform continues to take stock and monitor non-state actors' contributions to the implementation of the Sendai Framework for Disaster Risk Reduction 2015–2030. The platform not only keeps track of their contributions to the Sendai Framework's global targets, but it also details the hazards each commitment is aiming to address, including landslides. As of 31 March 2023, a total of 116 voluntary commitments have been published on the SFVC online platform. This article provides a statistical analysis of these voluntary commitments, looking into their deliverables, budgets, participating organizations, Sendai Framework targets and Sustainable Development Goals covered, among other variables. The quantitative analysis involves descriptive statistics that provide insights on commitments that are addressing landslides in their disaster risk reduction activities. Additionally, the article presents case studies from the voluntary commitments that demonstrate noteworthy efforts by stakeholders in reducing risks from landslides. As of 31 March 2023, 64 percent of the voluntary commitments published by stakeholders are implementing activities to build resilience against landslides. Initial findings indicate that among the 17 hazards documented on the SFVC online platform, landslides rank as the third most frequently addressed hazard. Although most voluntary commitments address landslides, it would be beneficial to encourage more action and improve current activities specific to landslide risk reduction especially for countries more vulnerable to landslides. The SFVC online platform endeavors to mobilize more stakeholders to address landslides, striving for a world where landslide risks no longer threaten communities.

Keywords

All-of-society engagement · Commitments · Disaster risk reduction · Sendai framework · Stakeholders

1 Introduction

The global community continues to be at risk of landslide hazards. Although the Emergency Events Database (EM-DAT) has shown a decline in annual landslides for the last two years, compared to the 20-year annual average (CRED 2022, 2023), other databases that record landslide events have indicated that the frequency and impact of landslides remains higher than what the EM-DAT database reports. Landslide events and subsequent losses incurred from these events are often underreported. This is likely because landslides are typically a secondary hazard that is triggered as a consequence of another hazard (Froude and Petley 2018). Between 1980 and 2018, there was an annual average of 400,000 rainfall-triggered landslides and 130,000 earthquake-triggered landslides (The World Bank 2021). According to the same report, there was an observed 1-2 percent increase in the average rainfall-triggered landslides each year, which could be indicative of a broader effect of climate change on a global scale. Additionally, according to several landslide databases, there is also an increasing percentage of landslides occurring from anthropogenic causes such as illegal mining and construction activities (Gómez et al. 2023). The EM-DAT database is also limited to landslide events that are considered disasters by their definition and it encompasses reports from only 82 countries. In contrast, other data-

Y. Matsuoka (✉)
UNDRR Kobe Office, Kobe-City, Hyogo, Japan
e-mail: matsuoka@un.org

B. Abolmasov et al. (eds.), *Progress in Landslide Research and Technology, Volume 3 Issue 1, 2024*, Progress in Landslide Research and Technology, https://doi.org/10.1007/978-3-031-55120-8_13

bases have a broader coverage and have recorded significantly more landslide events. While EM-DAT has recorded only 640 landslide disasters from 1903 to 2020 and 50,144 human losses, the global fatal landslide database has collected information on 5490 landslides from 2004 to 2017 corresponding to 64,218 human losses. The Global Landslide Catalog database has recorded 6784 landslides between 2007 and 2015 with a total of 25,386 human losses. Finally, the Desinventar database contains 25,195 unique records of landslides from 1906 to 2020 corresponding to 46,724 human losses. With these gaps in reporting and underestimations of occurrences and impacts, the global community must continue their efforts in addressing landslide risks through robust risk governance and management, and collaboration among various stakeholders.

To prevent disasters and reduce the risk of hazards, including landslides, the international community has committed to ambitious goals set out in the Sendai Framework for Disaster Risk Reduction 2015–2030. The Sendai Framework is a global agreement adopted by the United Nations (UN) General Assembly (GA) in 2015 at the Third UN World Conference on Disaster Risk Reduction (DRR) held in Sendai, Japan. The framework aims to reduce risks by advocating a comprehensive and all-of-society approach. It sets out seven targets and four priorities for action to guide countries and stakeholders in achieving substantial reductions in disasters and disaster losses. By emphasizing risk reduction rather than just response and recovery, the Sendai Framework seeks to create more resilient communities whilst promoting sustainable development in the face of increasing risks posed by natural and man-made hazards, such as that of landslides.

This year marks the midterm of the agreed duration of the framework and a review has been conducted by the United Nations Office for Disaster Risk Reduction (UNDRR) to share the progress made through global collective efforts. The Report of the Midterm Review (MTR) of the Implementation of the Sendai Framework for Disaster Risk Reduction 2015–2030 has concluded that although some progress has been made towards the expected outcomes and goals of the framework, it recognizes the increasing difficulties and challenges we face such as the COVID-19 pandemic, climate change and population growth which calls for course corrections to continue on a positive path towards disaster risk reduction by addressing these interconnected and systemic risks (UNDRR 2023). As UNDRR continues to advocate for an all-of-society approach, the MTR encourages increased participation and better coordination among all stakeholders for more impactful and effective interventions, including non-state actors. UNDRR recognizes that non-state actors, including non- governmental organizations, private sector, academic and research institutions, and media, have an important role in influencing the outcomes by 2030. The MTR has identified challenges and opportunities that can be addressed and supported by non-state actors including but not limited to: strengthening capacities for developing, collecting, analyzing and interpreting disaster risk data whilst improving the standard of official risk data and broadening the application of risk assessments; data sharing of risk information to and from non-state actors among government agencies and each other; and aligning digital innovations with local needs and robust engagement mechanisms for planning and delivery by national and local actors.

Since 2018, UNDRR has been monitoring and taking stock of non-state actors' contributions to the Sendai Framework through the Sendai Framework Voluntary Commitments (SFVC) online platform. The SFVC online platform was established in response to GA resolution A/69/283 (2015) calling for all stakeholders to share voluntary commitments (VCs) that are specific and time bound to address disaster risks at local, national, regional, and global levels. The SFVC online platform encourages and promotes voluntary actions by various stakeholders towards achieving the objectives of the Sendai Framework for Disaster Risk Reduction. It serves as a repository for commitments made by non-governmental organizations, businesses, civil society groups, networks, media as well as local governments and international organizations, showcasing their efforts to reduce disaster risks and enhance resilience. The platform allows stakeholders to share their commitments to the public, while also allowing them to monitor and report progress of their commitments. By facilitating transparency and accountability, the platform fosters collaboration, knowledge-sharing, and collective action in addressing disaster risks at local, national, regional, and global levels. The VCs submitted through this platform contribute to the implementation of the Sendai Framework, promoting a more resilient and sustainable future.

This article builds on a previous study conducted in 2020 on the SFVC online platform which showed preliminary results of 37 VCs covering landslides. UNDRR has continued to support stakeholders to submit their commitments so that their contribution to the Sendai Framework targets may be recognized. In so doing, the SFVC online platform has published a total of 116 VCs as of 31 March 2023, which has more than tripled since the previous study. This study aims to better understand VCs covering landslides through a comparative analysis of global trends and landslide VCs, landslide VCs and all published VCs, while determining gaps and opportunities that the SFVC online platform can address to support implementation of the Sendai Framework and reduce the risk of landslides.

2 Data and Methods

The source of the data used for this article is the Sendai Framework Voluntary Commitments (SFVC) online platform operated by UNDRR, specifically all published voluntary commitments (VCs) as of 31 March 2023. This dataset includes 116 published voluntary commitments involving a total of 670 organizations from around the world. Published VCs are stakeholders' submissions from around the world that are reviewed, validated, and collated by UNDRR to take stock of the non-state actors' contributions to the Sendai Framework. Each commitment reports various data points to verify the project's contribution to the Sendai Framework.

This article uses data from the SFVC online platform on variables including hazards, themes, Sendai priorities, targets, and indicators among others, which are further elaborated. *Hazards* are defined as "a process, phenomenon or human activity that may cause loss of life, injury or other health impacts, property damage, social and economic disruption or environmental degradation" (UNDRR, n.d.). Stakeholders may report that their commitments cover more than one hazard at a time. The SFVC online platform encompasses 17 hazards including landslides. Themes and issues (*themes*) are DRR-related topics that have been identified and standardized by the UNDRR aiming to be both wide and cross-cutting. The SFVC online platform covers 33 themes and issues and, similar to hazards, stakeholders may report the coverage of more than one theme at a time. The Sendai Framework outlines four *priorities* for action: Understanding disaster risk; Strengthening disaster risk governance to manage disaster risk; Investing in disaster risk reduction for resilience; and Enhancing disaster preparedness for effective response and to "Build Back Better" in recovery, rehabilitation, and reconstruction. In addition, seven *targets* and 38 *indicators* were identified to provide clear actionable goals for stakeholders and to measure the progress towards these goals. Priorities, targets, and indicators are also collected from each commitment,

allowing stakeholders to select multiple to better present their contribution to the implementation of the Sendai Framework. To promote coherence and alignment with the overarching sustainable development agenda, the platform also requests commitments to report the relevant Sustainable Development Goals (*SDGs*) that their project contributes to. Each commitment must be linked with an official entity that acts as the implementing organization (*implementers*). A commitment may have more than one implementer and may or may not have partner organizations (*other partners*) that also support the project, although partners are not necessarily directly involved in implementation. An organization can be involved as implementer or partner in more than one VC. Additionally, donor information is also collected (*donors*). The start of the commitment and the end of the commitment is also required for each commitment and are used to determine the *duration* of a commitment. Specific *deliverables* are also mandatory as a means of verification to showcase the outcomes of the commitment and stakeholders are requested to indicate *completed deliverables* within their commitments. Multiple deliverables are encouraged. Finally, *progress reports* are requested every 6 months from the last update of a commitment to ensure accountability.

Table 1 presents various variables and statistical measures for two datasets: VCs (all) and VCs (landslides). Insights were derived from this data and are found in the results section. Other variables were also used in the analysis such as geographical scope and country coverage.

Table 1 Summary statistics (selected variables)

	VCs (all)						VCs (landslides)					
Variable	Mean	SD	Min	Max	CV	n	Mean	SD	Min	Max	CV	n
Hazards	7.33	4.68	1	17	0.64	116	9.46	4.34	1	17	0.46	74
Themes	9.41	5.44	1	26	0.58	116	10.24	5.87	1	26	0.57	74
Priorities	2.73	1.00	1	4	0.37	116	2.82	1.01	1	4	0.36	74
Targets	3.30	1.54	1	7	0.47	116	3.64	1.57	1	7	0.43	74
Indicators	5.59	5.56	1	38	0.99	116	6.01	6.44	1	38	1.07	74
SDGs	4.72	3.10	1	17	0.66	116	4.91	3.03	1	17	0.62	74
Donors	1.17	2.97	0	27	2.53	116	1.08	1.86	0	8	1.72	74
Implementers	1.47	1.31	1	11	0.89	116	1.57	1.57	1	11	1.00	74
Other partners	5.53	13.75	0	115	2.49	116	6.93	16.71	0	115	2.41	74
Umbrella initiatives	1.03	1.28	0	6	1.24	116	1.14	1.26	0	6	1.11	74
Duration	8.79	6.26	0.3	18	0.71	116	9.93	6.17	0.3	18	0.62	74
Deliverables	5.12	6.66	1	51	1.30	116	5.20	5.82	1	47	1.12	74
Completed deliverables	4.34	6.85	0	51	1.58	116	4.34	6.02	0	47	1.39	74
Progress reports	0.87	1.39	0	6	1.60	116	0.93	1.40	0	6	1.50	74

Note: Variables indicate the selected data points from the data source. Mean represents the average value of the sample set. SD stands for standard deviation and CV for coefficient of variation as measures of dispersion. Min and Max indicate minimum and maximum values for each variable, respectively. Values under n present the number of VCs containing that observation.

The methodology for conducting analysis on these variables included a data cleaning process and a statistical descriptive analysis. As seen in Table 1, out of 116 VCs, 74 address landslides as a hazard being addressed by their commitment, which is 64 percent of the whole dataset. A review of relevant literature and databases was carried out on landslide disasters and events and this information was likened to the data from the SFVC online platform. A comparative analysis was conducted between the dataset for all published VCs and the dataset for VCs that cover landslides. Additionally, a qualitative review and quantitative text analysis of the description and deliverables of landslide VCs was undertaken.

3 Results

This section will further elaborate on the variables set out in the methodology to better understand VCs working on landslides. This includes understanding voluntary commitments overall through a comparative analysis of two datasets and looking deeper into landslide VCs.

4 Comparing Landslide-Related Initiatives with All Voluntary Commitments

The SFVC online platform presents information on VCs contributed by non-state actors. Out of 116 VCs, there are 74 VCs that address landslides as a hazard. Based on the basic characteristics of all VCs and VCs covering landslides, some differences and similarities can be derived (Fig. 1a, b).

Among the VCs covering landslides, the average number of hazards addressed in each commitment is higher (9.46) compared to the average for all VCs (7.33). This suggests that landslide VCs tend to encompass a broader range of hazards. The themes covered by landslide VCs have a slightly higher average (10.24) compared to all VCs (9.41), which may indicate that efforts targeting landslides often address more thematic areas. Landslide VCs have slightly higher averages for both targets (3.64) and indicators (6.01) compared to all VCs (3.30 and 5.59, respectively). This could imply a more detailed and comprehensive approach to setting targets and monitoring progress in landslide-related commitments. Landslide VCs also have a slightly higher average of partners involved (6.93) for each commitment compared to all VCs (5.53). This may suggest a relatively broader range of stakeholders involved in landslide-related initiatives. Finally, landslide VCs have a slightly longer average duration (9.93) compared to all VCs (8.79) and this may indicate that implementers are carrying out activities with the long-term outcomes in mind.

The average for other basic characteristics of landslide VCs is similar to that of all VCs including priorities for action, Sustainable Development Goals (SDGs), and implementers, among others (Fig. 1b). However, we did observe that donor involvement appears to be minimal in both types of commitments with an average of around 1 for both landslide VCs and all VCs. Additionally, the average number of submitted progress reports for both types of commitments is alarmingly low (less than 1), indicating that there is a need to

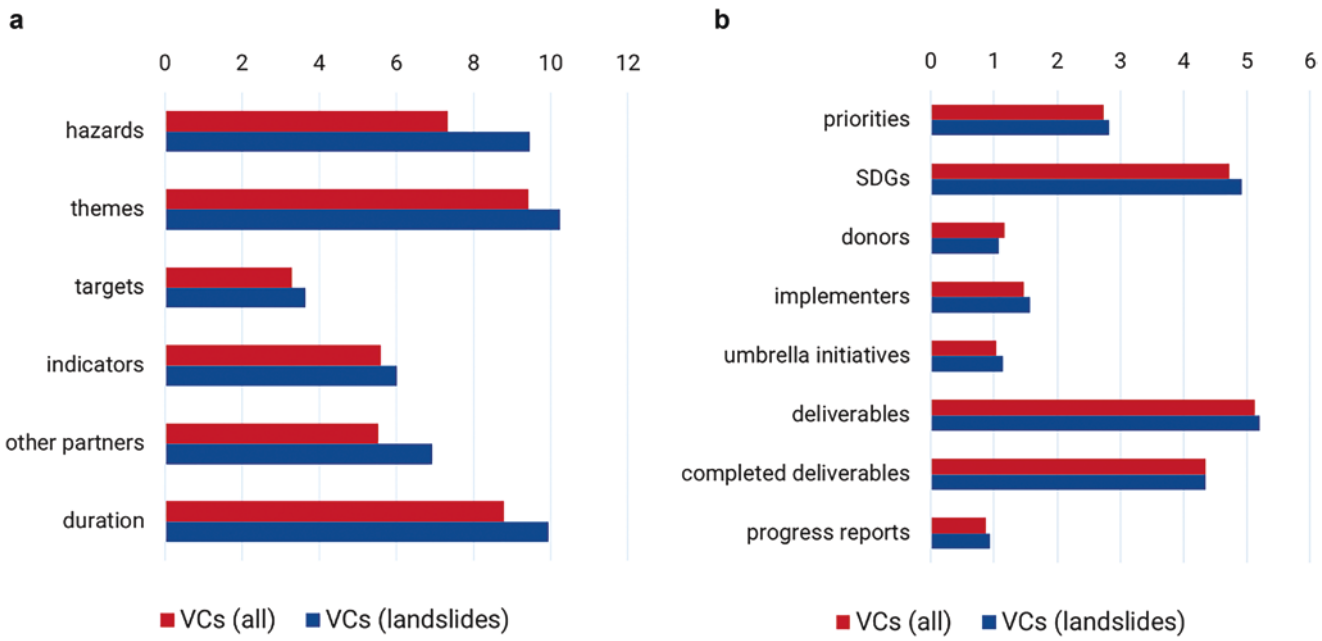

Fig. 1 (**a**) Basic characteristics with significant differences. (**b**) Basic characteristics with insignificant differences. *Source:* UNDRR Voluntary Commitments

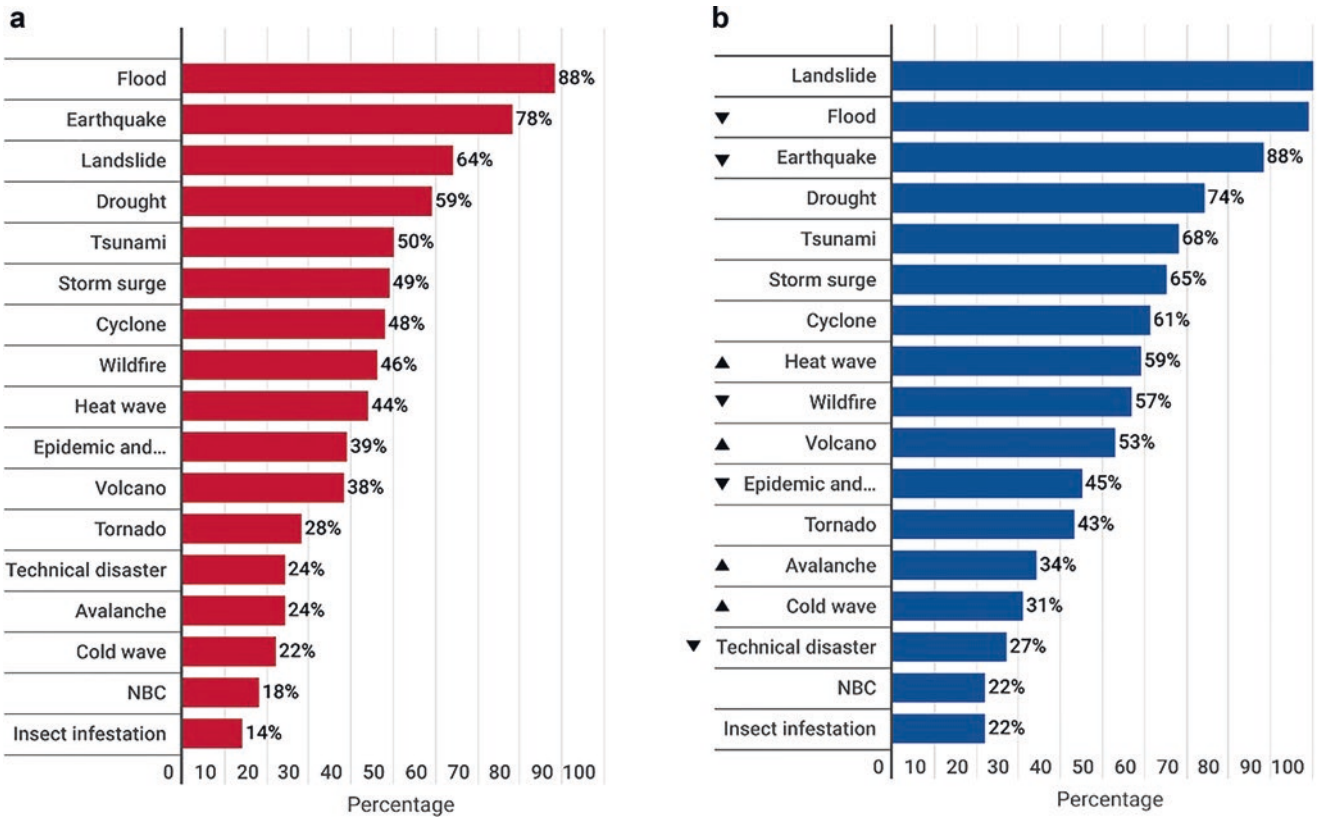

Fig. 2 (**a**) Hazards covered by VCs (all) (**b**) Hazards covered by VCs (landslides). *Source:* UNDRR Voluntary Commitments

encourage stakeholders to report on progress regarding their commitments.

Besides the basic characteristics above, we also investigated the secured budget and the status of completion for both datasets. While 59 percent of all VCs had fully secured their budget, there was a lower percentage of landslide VCs that had fully secured their budget at 54 percent. The same can be said about the status of completion where 32 percent of all VCs have already been completed, while only 30 percent of landslide VCs were completed. Both observations may be related to the longer duration of landslide VCs compared to all VCs.

Taking a closer look at the hazard coverage for both datasets, we can see that landslides are the third most covered hazard out of 116 VCs, while flood (88 percent) and earthquake (78 percent) are the first and second most covered type of hazard, respectively (Fig. 2a). Comparing the hazard coverage for landslide VCs, we see some changes in the ranking of the hazards, although the difference is not substantial (Fig. 2b). Landslides are often triggered by floods, earthquakes, cyclones, and volcanic eruption, among other hazards, which may likely be the reason for landslides being one of the most covered hazards.

Notes: Epidemic and… stands for Epidemic and pandemic. NBC stands for Nuclear, Biological and Chemical hazards.

The SFVC online platform also collects information on the geographical scope of the VCs, which can be global, regional, or national and local (Fig. 3). Comparing the two datasets, VCs covering all hazards have a more skewed distribution in terms of scope against VCs covering landslides. For landslide-related VCs, more than 50 percent of commitments have a global and regional scope, which suggests that VCs working on landslides may be taking a more comprehensive approach sharing knowledge and information across regions and among countries. The platform also requests information on regional and country coverage which informs Figure 4. There are no observed significant differences in the regional distribution, but it is worth noting that Asia is covered by more than half of the VCs for both datasets, excluding VCs with a global scope.

Examining the selected priorities for action for the two datasets, we can see that all priorities have increased coverage when only considering VCs (landslides) except for priority 4 on enhancing disaster preparedness for effective response and to "Build Back Better" in recovery, rehabilita-

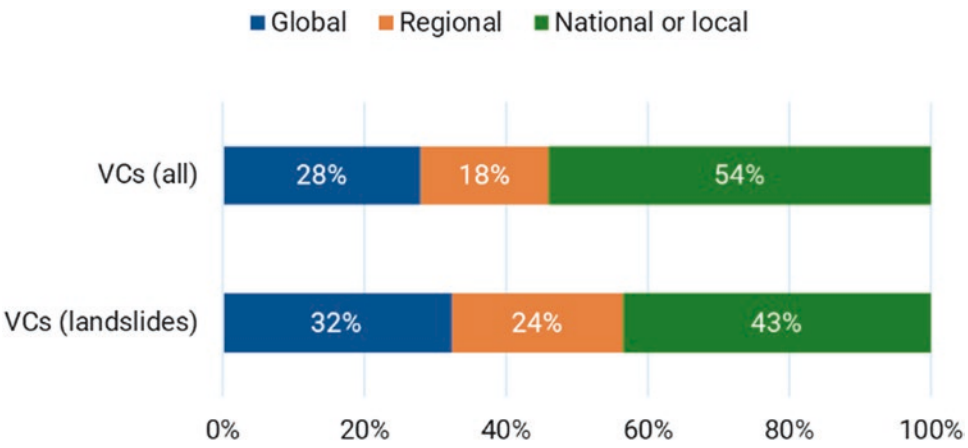

Fig. 3 Scope types for VCs (all) and VCs (landslides)

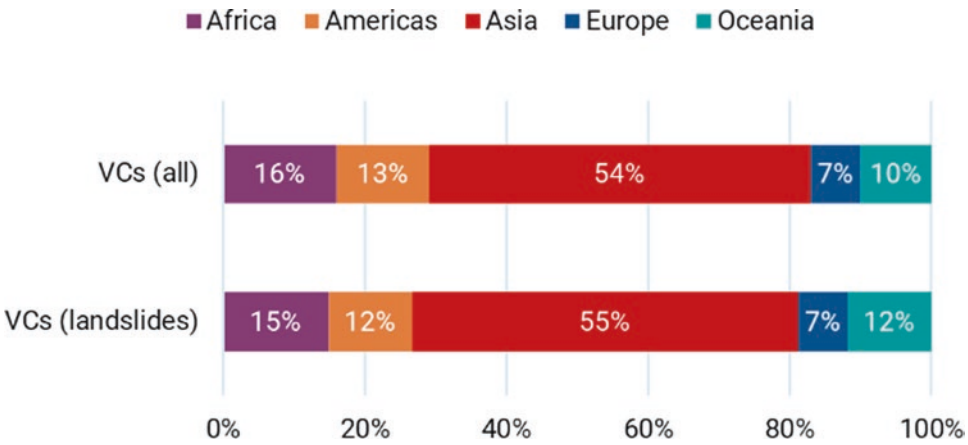

Fig. 4 Regions for VCs (all) and VCs (landslides). *Source:* UNDRR Voluntary Commitments

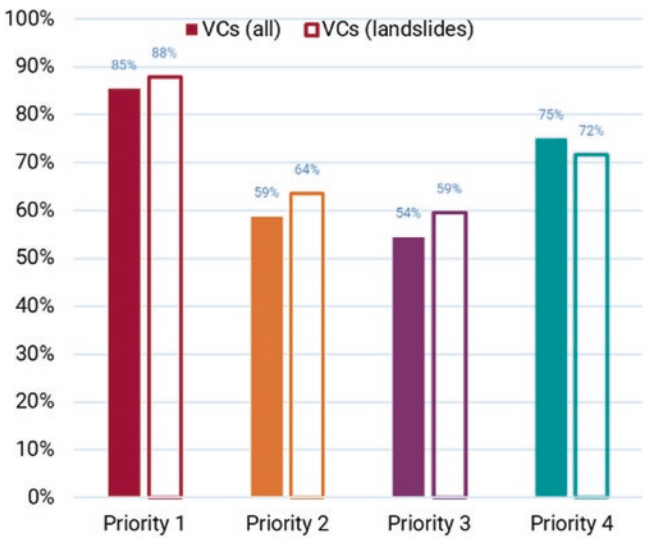

Fig. 5 Priorities for action for VCs (all) and VCs

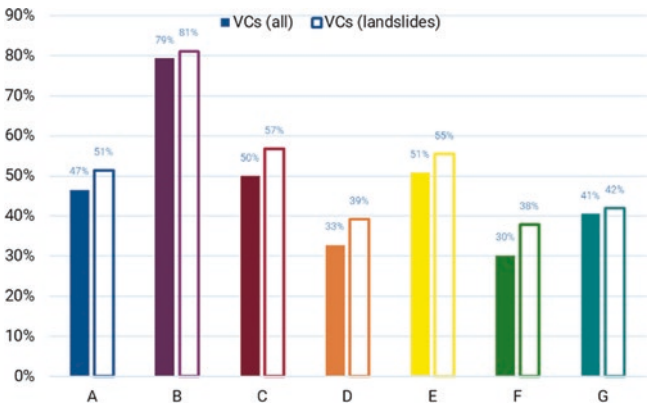

Fig. 6 Sendai Framework targets for VCs (all) and VCs (landslides) (landslides). *Source:* UNDRR Voluntary Commitments

tion, and reconstruction (Fig. 5). As for the targets, all targets have higher coverages for VCs covering landslides compared to all published VCs (Fig. 6). We observed particularly higher coverage for target C (7 percent difference), target D (6 percent difference) and target F (8 percent difference) among VCs covering landslides. These targets are relevant to reducing the risk of landslides, as landslides often cause significant damage to critical infrastructure, such as roads, bridges, and utilities, leading to disruptions in essential services. This may also result in cascading effects that disrupt livelihoods and hinder disaster response resulting in more significant economic losses. Finally, developing countries would benefit from international cooperation to enhance

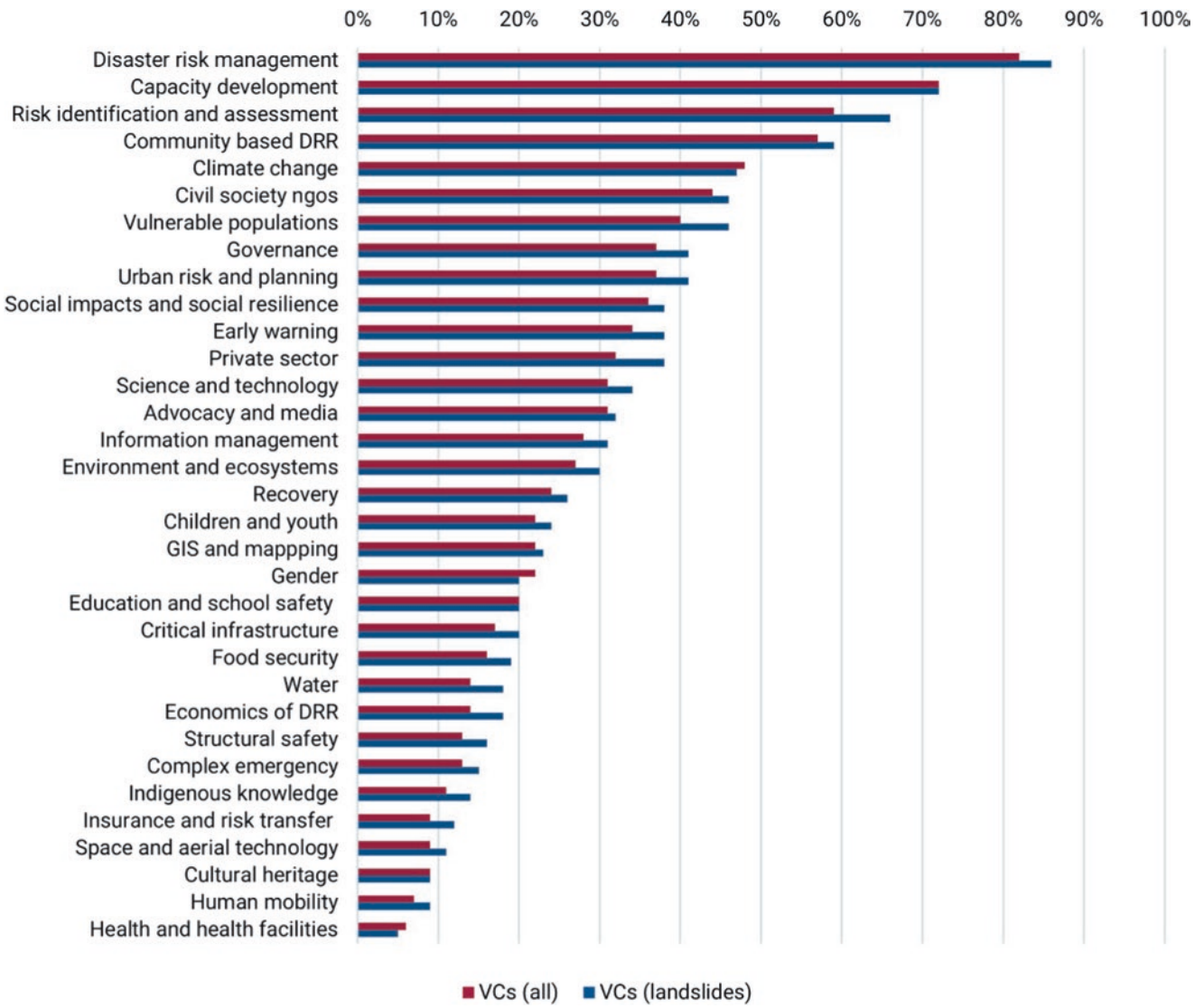

Fig. 7 Themes and issues for VCs (all) and VCs (landslides). *Source:* UNDRR Voluntary Commitments

landslide risk reduction efforts. Because developing countries must deal with bigger trade-offs between economic development and safety, their risk acceptance for landslides are often more lenient, thereby creating higher societal risk as they focus on activities that would boost economic growth such as job creation, infrastructure development and improved access (Sim et al. 2022). Developed countries can provide support through technical expertise and knowledge sharing, capacity building and training, and financial aid and resources to help developing countries mitigate landslide hazards.

The SFVC online platform requests focal points of VCs to select specific themes and issues related to DRR that are applicable to their respective commitments. Delving into these themes for all VCs and landslide VCs, we observed that the ranking of themes and issues based on percentage coverage of VCs remained the same between the two datasets with the top three being disaster risk management, capacity development, and risk identification assessment (Fig. 7). However, significant differences were found in the percentages of the following themes: disaster risk management, risk identification and assessment, vulnerable populations, governance, urban risk and planning, early warning, private sector, water, and economics of DRR. The highest discrepancies were found in risk identification and assessment, vulnerable populations, and private sector, where non-state actors seem to put more focus on such themes and issues in landslide VCs compared to all VCs.

Risk identification and assessment is particularly important for landslide mitigation to help determine areas prone to landslides, enabling targeted mitigation measures and early warning systems. There are many approaches or methods for landslide hazard assessments such as multivariate techniques, physically based models, and multi- criteria

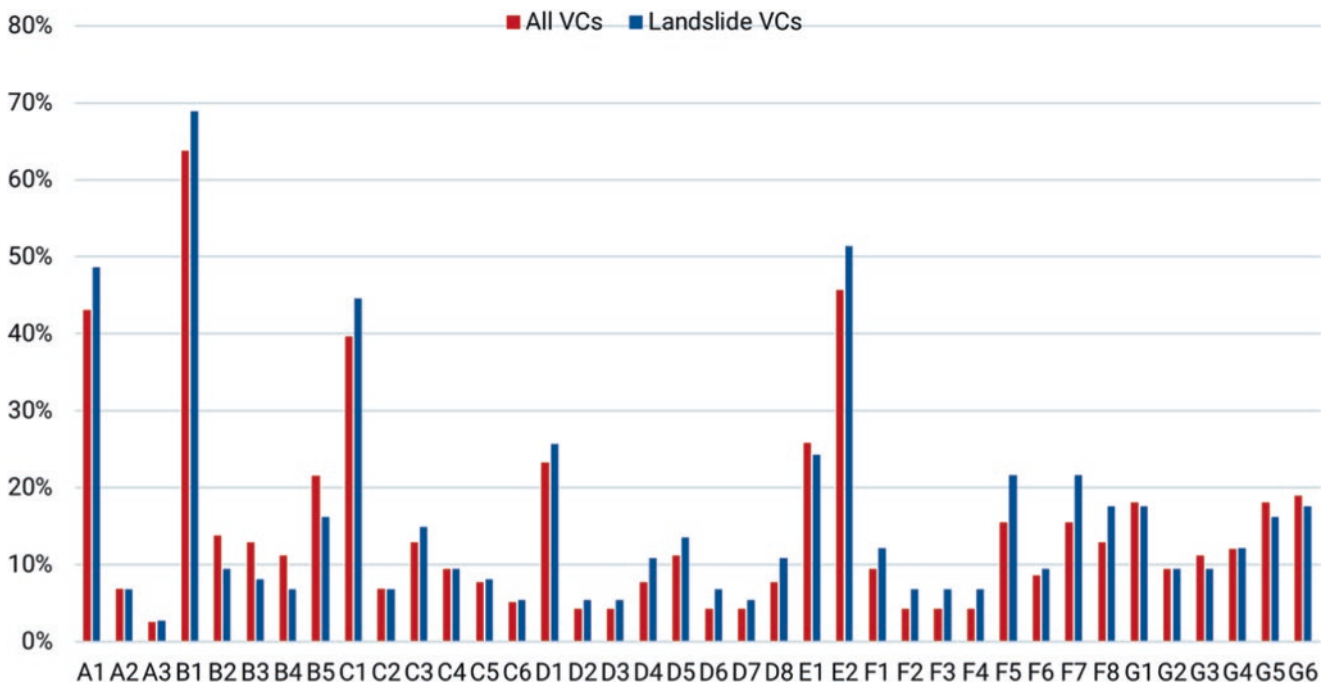

Fig. 8 Indicators selected for VCs (all) and VCs (landslide). *Source:* UNDRR Voluntary Commitments

decision-making approach (Pardeshi et al. 2013). Vulnerable populations, such as those living in informal settlements or areas with inadequate infrastructure, are at higher risk of landslides. Proper mitigation and response measures like early warning systems, evacuation plans, and slope stabilization can significantly reduce the risk of casualties and injuries and may also reduce the impact on their livelihoods. Finally, the private sector bears a significant stake in the mitigation of landslide risks, as such hazards can potentially lead to supply chain disruption, property damage, and business interruption due to suspension of electricity and water supply, resulting in significant economic losses. The participation of the private companies in landslide risk reduction would be beneficial for both the private sector and public sector and there is great potential for public-private partnerships to increase investments in landslide risk assessments and preventive measures to support vulnerable populations.

As mentioned previously, the average number of selected indicators by landslide VCs is higher than the average number of selected indicators for all VCs. Thus, the percentage of VCs covered by each indicator is mostly higher if note that same. However, there are 9 out of 38 exceptions, namely B2, B3, B4, B5, E1, G3, G5 and G6. However, it should be emphasized that target B and target G both have a compound indicator which is often selected by stakeholders instead of non-compound indicators (Fig. 8).

While other variables from the two datasets were also compared, no other significant variances were observed.

5 A Closer Look at Landslide-Related VCs

As mentioned in previous sections, VCs covering landslides make up 64 percent of all commitments in the SFVC online platform. They have a mix of geographical scope including 24 VCs with global scope, 18 VCs with a regional scope, and 32 VCs with a national or local scope. It is important to note that regional and national or local VCs may cover multiple regions and countries and UNDRR has distinguished five regions for their work. Landslide VCs have a wide coverage of regions and countries involving all five regions and 34 countries in total with a much larger concentration within the Asia region (Fig. 9).

In Asia, 38 landslide-related VCs cover a total of 15 countries involving 280 organizations. Data from various landslide databases show that Asia and the Americas are experiencing the highest risks and impacts from landslides (Gómez et al. 2023). The emphasis of VCs in Asia signifies a collective effort to address disaster risks and is a promising observation for landslide mitigation.

One such VC in the Asia region is *Underlining the risk and preventing disasters for Atakum Municipality* (ID 20230130_001). This is a local VC implemented by the Atakum Municipality local government in Türkiye. In line with the Provincial Disaster Risk Reduction Plan of the Samsun Province in the northern coast of Türkiye, Atakum Municipality is actively participating to fulfill its obligations and support the implementation of the local DRR plan. The

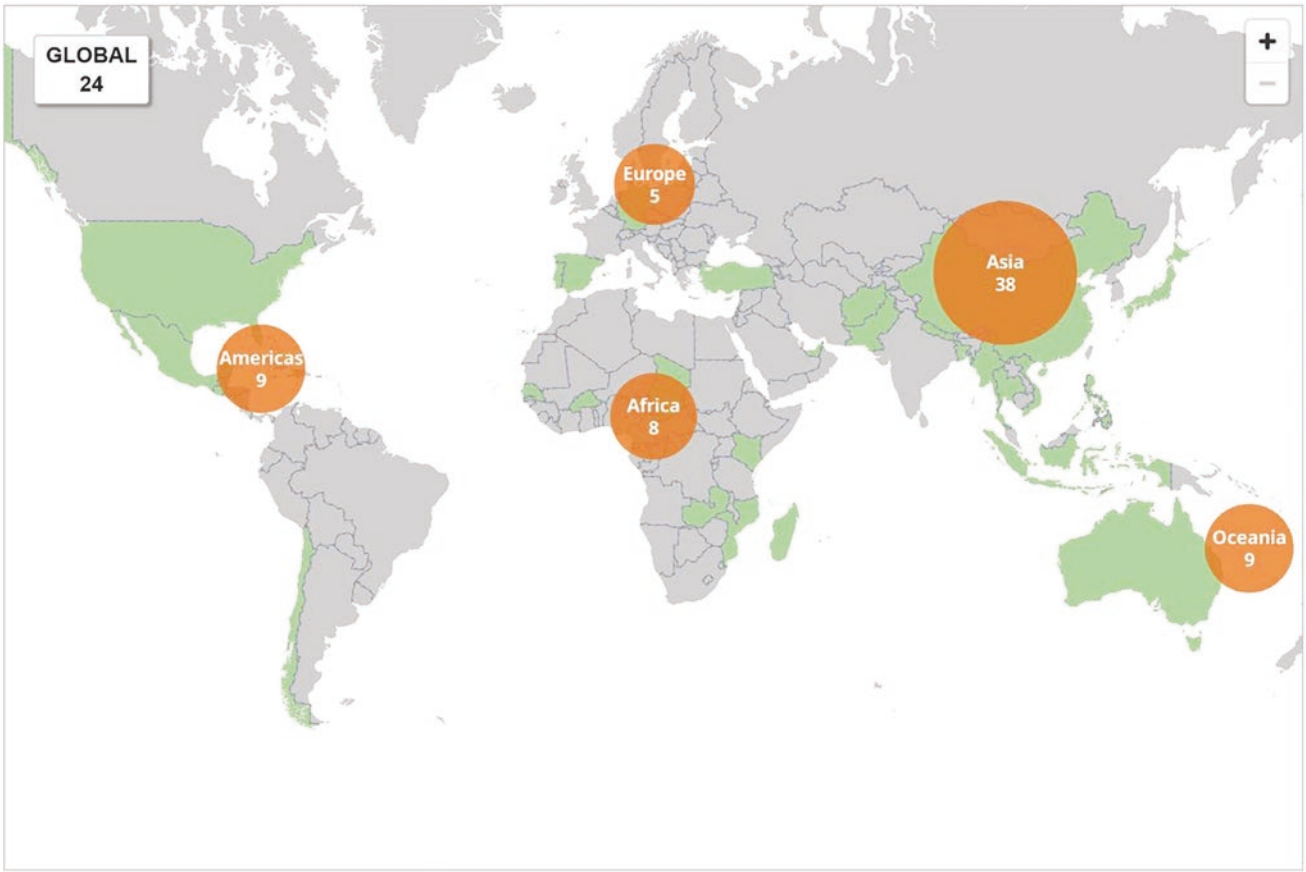

Fig. 9 Regions with countries and territories having VCs that cover landslide hazards around the world. *Source:* UNDRR Voluntary Commitments

municipality is dedicated to enhancing the community's disaster preparedness by implementing various measures, which include establishing a civil defense unit for disasters, creating designated disaster and emergency assembly areas, forming a search and rescue team, and utilizing a mobile earthquake simulation tool to increase the population's ability to respond effectively to disasters. This VC covers multiple hazards including earthquakes, floods, landslides, avalanches, and technical disasters. It focuses on supporting Priority 2 of the Sendai Framework, strengthening disaster risk governance to manage disaster risk, and Priority 4, enhancing disaster preparedness for disaster response. It also aims to contribute to target E of the Sendai Framework in the adoption and implementation of local DRR strategies in line with provincial and national strategies. Landslide risk mitigation and response is addressed here through the formation of a search and rescue team and the creation of disaster and emergency assembly areas.

An examination of several landslide databases show that China and Colombia are among the countries most significantly affected, along with India, Indonesia, the Philippines, Peru, Nepal, and Brazil (Gómez et al. 2023). In contrast, in the SFVC online platform, non-state actors from the Philippines and Nepal have submitted the most initiatives addressing landslides as presented in Figure 10. Although these countries were identified as among the most affected, there is still room for improvement and increasing landslide mitigation efforts by non-state actors in other high risk and high impact countries should be pursued.

In the Philippines, there are 11 landslide-related VCs, two of which are regional while nine are national or local in scope. This involves 44 organizations with a commitment of 76 deliverables. One notable VC that addresses landslide risk in the Philippines is the *Philippine Catastrophe Insurance Facility* (ID_20221102_001), a private sector-led commitment with a national scope. It is implemented by the National Reinsurance Corporation of the Philippines, Philippine Insurers and Reinsurers Association, and the Philippines Insurance Commission. The facility aims to create a risk-based system for determining insurance rates that can sustainably cover disasters. The goal is to increase the country's financial resilience by supporting more people to access and afford insurance protection against catastrophes. The VC covers 16 out of 17 hazards that the SFVC online platform accounts for. If successful, the commitment would directly contribute to reducing economic less attributed to disasters

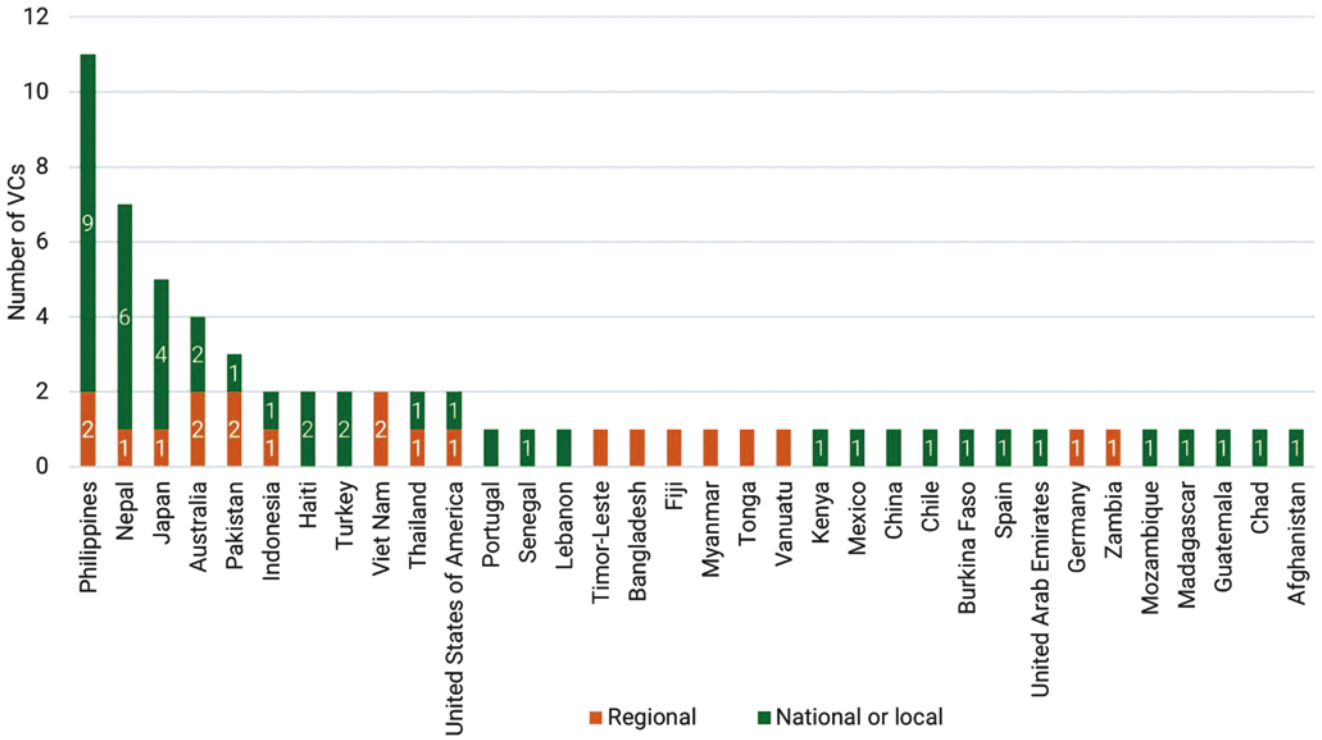

Fig. 10 Countries covered by VCs (landslides). *Source:* UNDRR Voluntary Commitments

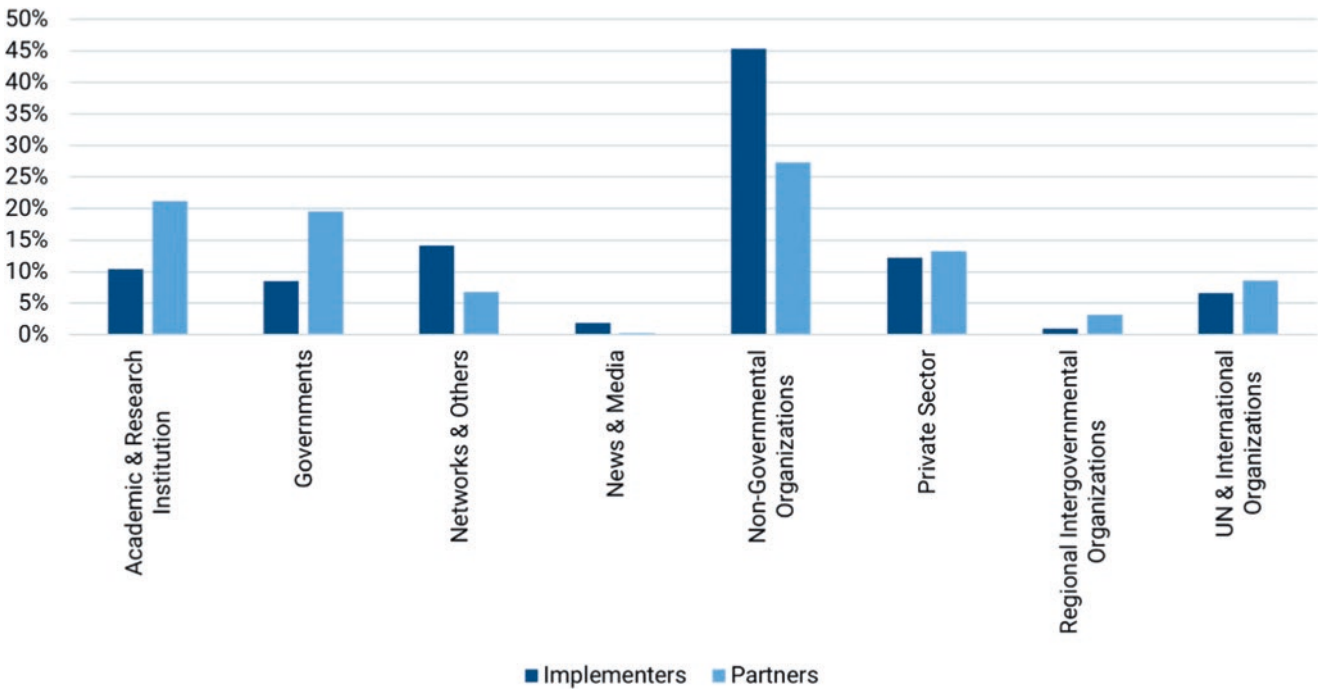

Fig. 11 Types of implementers and partners for VCs (landslides). *Source:* UNDRR Voluntary Commitments

(target C). The facility is also one of the few commitments on the platform that tackles insurance and risk transfer.

Organizations involved in landslide VCs are varied comprising 534 distinct organizations. There are 106 distinct implementers and 440 distinct partners. It is worth mentioning that organizations may participate in multiple commitments as either implementer or partner, thus the sum of the two does not amount to the total distinct organizations involved. Figure 11 shows the distribution of implementers and partners categorized into eight types with the lowest participation from news

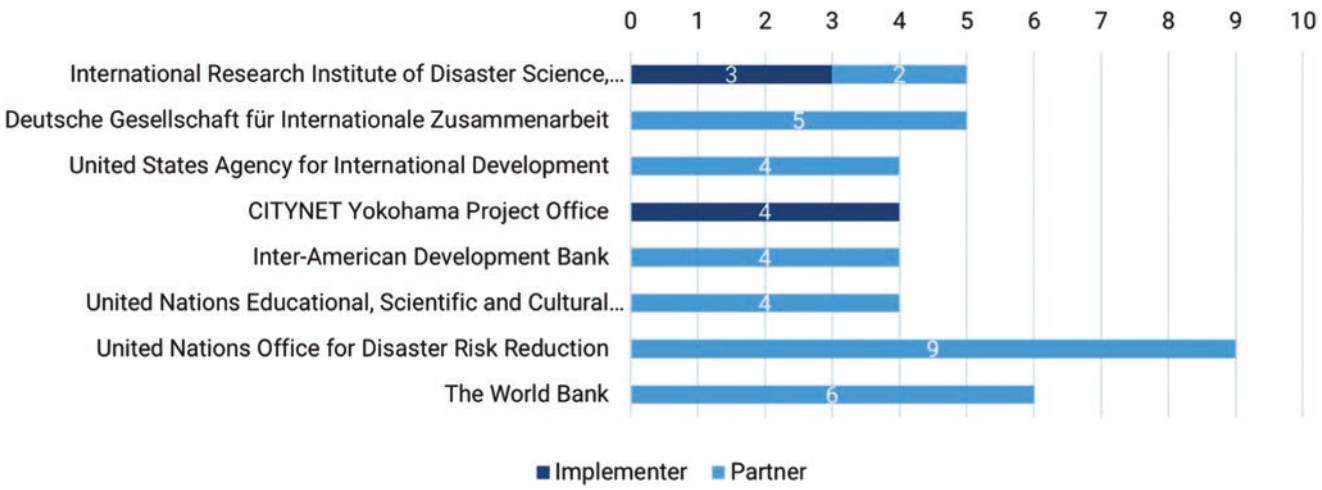

Fig. 12 Organisations participating in four or more landslide-related VCs. *Source:* UNDRR Voluntary Commitments

& media group and the regional organizations. Taking a closer look at the distribution of implementers and partners, we can observe that there is a much larger concentration of academic and research institutions as well as governments as partners in contrast with implementers. This could indicate that research institutions are inclined to be partners rather than direct implementers of commitments and this may be due to funding. It is crucial to point out that such institutions are a very important stakeholders for the implementation of the Sendai Framework as they can offer expertise, knowledge and capacity building especially in the themes of risk identification and assessment and science and technology.

The VC *MYRIAD-EU: Multi-hazard and Systemic Framework for Enhancing Risk-Informed Management and Decision-making* is a good example of a landslide VC that is implemented by a research institution, the Institute for Environmental Studies addressing the two themes for risk identification and assessment, and science and technology. The commitment involves a total of 16 partners from the private sector, other research institutions, networks, and non- governmental organizations. It covers 11 hazards including landslides and aims to develop a risk management framework that utilizes a comprehensive approach that considers multiple risks, sectors, and scales while also assessing trade-offs. Myriad-EU will be supporting five pilot areas to operationalize their framework through customized tools, products and services. This comprehensive framework is advantageous especially in the context of landslides, which are often triggered by floods and earthquakes, because it considers multi-hazard risk and impact assessments.

As previously mentioned, organisations can participate in more than one commitment as implementer or partner, and there are a number of organizations involved in multiple commitments (Fig. 12). In particular, eight organisations support four or more commitments. Remarkably, despite the low participation of UN & International organizations in the overall dataset, UN & International organizations make up half of the list, reflected in the figure as the last four organizations. The organization participating in the highest number of commitments is UNDRR as a partner to nine VCs.

Citynet Yokohama Project Office, which is considered under Network & Others, implements the largest number of VCs – two regional VCs encompassing Asia and two national VCs covering Nepal. This indicates that many initiatives are part of global partnerships and networks, emphasizing the importance of international cooperation in DRR. A further look into the participating organizations of each VC validates that many commitments involve multi-sectoral collaboration, including partnerships with local governments, private sector and NGOs

Finally, we also look deeper into the description section and deliverables section of landslide VCs through a quantitative and qualitative text analysis. The text analysis involved initial filtering to remove stop words, which are widely used words that provide little or no useful information. Sixty words were then identified for the description and the deliverables that accounted for the words with the highest frequency in each section. A second filtering was performed to remove "disaster", "risk", "resilience" and "DRR" as these are naturally terms that are often used to describe DRR initiatives. The end results show different ranking among the words with the highest occurrence and a few unique terms comparing the two sections. In landslide VC descriptions, the words with the highest frequency counts were community, local, climate, government and global. On the other hand, in the deliverables, the words with the highest frequency were city, business, government, local and community. The commonality between the two sections shows promising consistency in the focus on local, community, and government in landslide VCs. Additionally, it was also observed that more private sector related words were found

Fig. 13 Word cloud for the description of VCs (landslides). *Source:* UNDRR Voluntary Commitments

Fig. 14 Word cloud for the deliverables of VCs (landslides)

within the deliverables such as business and MSMEs. We also discovered unique words that could be found only in the top sixty words in the description and unique words in the deliverables. From the filtered words within the deliverables, unique terms were found which pertained to specific outputs such as report, event, project, participants, forum, and network (Figs. 13 and 14).

A qualitative review of both the description and deliverables section of landslide VCs show that common activities by non-state actors include capacity building and training, risk assessment and mapping of disaster-prone areas, development of emergency response and awareness campaigns. Some VCs show integration of technology such as artificial intelligence and unmanned aerial vehicles to conduct risk assessments and support early warning systems, while many initiatives emphasize research, innovation, and development of new tools and technologies for disaster risk reduction.

6 Conclusions

The analysis highlights that landslide VCs demonstrate a proactive and comprehensive approach to disaster risk reduction, encompassing a broader range of hazards, themes and issues, targets and indicators. Landslide VCs also involve a slightly higher number of partners. This indicates a collective effort to tackle landslide risks with long-term planning and a focus on engagement with various stakeholders. Landslide-related VCs have a more global and regional focus compared to all VCs. Geographically, a much larger concentration of commitments is focused on Asia, with the Philippines and Nepal implementing the most VCs addressing landslides.

Text analysis reveals a focus on local community, government involvement, climate change, global cooperation, private sector participation and urban cities. The commitments demonstrate a diverse range of activities and approaches to DRR, reflecting the need for multi- sectoral collaboration, technology integration, and community engagement in building resilience against disasters.

It should be emphasized that many initiatives by non-state actors have yet to be reflected in the platform. To conduct a more robust analysis, more stakeholders should be encouraged to submit their commitments to the platform for deeper insights into their contribution to disaster risk reduction with focus on different hazards such as landslides. Additionally, for future studies, it may be useful to conduct a survey among active stakeholders about interventions within their commitments specific to landslide risk reduction and response.

The prevalence of landslides globally underscores the need for continued efforts by non-state actors encouraging initiatives in particularly vulnerable countries. Strengthening partnerships with research institutions and the private sector could foster innovative and effective solutions for landslide risk reduction and address the need for broadening risk assessments and data sharing.

Acknowledgments The findings, interpretations, and conclusions expressed in this paper are entirely those of the authors. They do not necessarily represent the view of the United Nations Office for Disaster Risk Reduction (UNDRR). Maps, the designations employed, and the presentation of the data do not imply the expression of any opinion whatsoever on the part of the United Nations Secretariat concerning the legal status of any country, territory, city or area, or of its authorities, or concerning the delineation of its frontiers or boundaries.

Appendix

List of voluntary commitments covering landslides. For the latest information, please visit: https://sendaicommitments.undrr.org/commitments?selectedHazards=LAND_SLIDE

ID	Title	Implementing Organizations	Scope
20190110_001	Sendai Landslide Partnerships 2015- 2025	• International Consortium of Landslides	Global
20190121_002	Raise DRR awareness through faith- based organisations	• ACT Alliance—Geneva	Regional—Africa, Americas, Asia
20190128_001	Science Technology Commitment to support implementation of Sendai Framework	• Scientific and Technical Advisory Group	Global
20190203_001	Global Centre for Disaster Statistics (GCDS)	• Fujitsu • International Research Institute of Disaster Science, Tohoku University • United Nations Development Programme	Global
20190209_001	Building Resilience Through Capacity Development of DRR Young Scientist in Nepal	• Himalayan Risk Research Institute	National or local—Nepal
20190211_002	Support Urban Risk Reduction and Resilience Building	• Center for Urban Disaster Risk Reduction and Resilience	Global
20190213_002	Enhance Disaster Governance at National, Sub-national, Local level in Nepal	• Environment and Child Concern Organization	National or local
20190214_004	One Billion Coalition for Resilience	• Connecting Business initiative • International Federation of Red Cross and Red Crescent Societies • Interpeace • United Nations Children's Fund (Global Headquarters, New York) • World Food Programme	Global
20190219_001	Leadership of persons with disabilities in delivering the Sendai Framework	• Arbeiter-Samariter-Bund Indonesia and the Philippines • CBM International • Centre for Disability in Development • Humanity and Inclusion • Malteser International • Pacific Disability Forum • South Asian Disability Forum	Regional—Asia, Oceania
20190220_001	Seminars of the Sendai Framework for DRR for citizens in Sendai City	• International Research Institute of Disaster Science, Tohoku University • Sendai City	National or local—Japan
20190228_002	Building Community Resilience through Community-Based Disaster Risk Management	• Afghan Development Association • Agency for Humanitarian and Development Assistance for Afghanistan • Asociación de Servicios Comunitarios de Salud • Help in Need • Lutheran World Federation Chad • Society for Human & Natural Resource Development	National or local—Guatemala, Pakistan, Chad, Afghanistan
20190301_001	Localised Preparedness for More Effective Response with Affected Communities	• Citizens' Disaster Response Center • Comité Ecuménico para o Desenvolvimento Social • Sampan'Asa mombany Fampandrosoana/Church of Jesus Christ in Madagascar	National or local—Kenya, Haiti, Mozambique, Madagascar, Philippines
20190304_005	Building a preventive culture among school children from vulnerable communities in Mexico	• Mexican Red Cross Society—Delegation of Nuevo León	National or local—Mexico
20190305_003	Contributing via Business Strengths, DRR Innovation and Partnerships	• Kokusai Kogyo Co, Ltd.	Regional—Asia

ID	Title	Implementing Organizations	Scope
20190305_005	RegionsAdapt	• Network of Regional Governments for Sustainable Development	Global
20190305_006	"Decision-making and Taking Action"—Promotion of Women Leadership Program	• Sendai City • Sendai Gender Equal Opportunity Foundation	National or local—Japan
20190305_008	Resilience in the tourism sector: ARISE Japan Activity Plan 2019-2022	• ARISE Japan	National or local—Japan
20190307_002	Ecosystems protecting infrastructure and communities	• International Union for the Conservation of Nature	National or local—China, Chile, Burkina Faso, Senegal, Thailand
20190307_007	Promoting the Making Cities Resilient and Sustainable Campaign in Asia Pacific	• United Cities and Local Governments Asia-Pacific	Regional—Asia, Oceania
20190308_010	Intense Promotion of the Sendai Framework with the Haitian communities	• Centre de la Prédication Évangéliques d'Haiti • Global Network of Civil Society Organisations for Disaster Reduction	National or local—Haiti
20190517_001	Strengthen leadership, cooperation, and participation in disaster risk reduction in the Municipality of Amadora	• Câmara Municipal da Amadora	National or local—Portugal
20190830_001	Fostering Indonesian Youth and Young Professionals as the Generator of Innovation in Science, Engineering, and Technology for Disaster Resilience at National and Global Levels	• U-INSPIRE Indonesia	National or local—Indonesia
20191121_001	CITYNET Disaster Cluster	• CITYNET Yokohama Project Office	Regional—Asia
20191201_001	Africa Youth Advisory Board on Disaster Risk Reduction (AYAB DRR)	• Africa Alliance for Development Action • African Union Commission • Arab African Council for Sustainable Development • Association des Jeunes Congolais pour le Développement • Bukedi Action for Integrated Development Initiatives- International • Centre of Economic Study and Research for Development • Children and Youth Empowerment South Sudan • Consortium pays pour la Réduction des Risque de Catastrophe • GREEN Student • Green Africa Youth Organization • Partners Enhancing Resilience for People Exposed to Risk	Regional—Africa
20191206_001	CITYNET Disaster Cluster Annual Seminar	• CITYNET Yokohama Project Office • City Government of Makati • City of Yokohama	Regional—Asia
20200102_001	Capacity Building and Scientific Research for Sendai Framework by the Japan Society of Disaster Nursing	• Japan Society of Disaster Nursing	Global
20200611_002	International Flood Initiative (IFI)	• International Centre for Water Hazard and Risk Management	Global
20200828_001	Mitra Disaster Risk Reduction Learning Center	• CITYNET Yokohama Project Office	National or local—Nepal
20200916_001	Capacity building to reduce animal vulnerability for animal owners and governments	• World Animal Protection	Global
20201002_001	International Recovery Platform (IRP)	• International Recovery Platform	Global
20201225_001	Smart Community Infrastructures: Disaster Risk Reduction (ISO/TC268/SC1/WG6)	• International Research Institute of Disaster Science, Tohoku University	Global
20210209_001	Urban Planning Advisory Group (UPAG)	• Urban Planning Advisory Group	Global
20210224_001	The Global Innovation Lab for Climate Finance	• Climate Policy Initiative	Global

ID	Title	Implementing Organizations	Scope
20210302_001	Sustainable Environment and Ecological Development Society (SEEDS)	• Sustainable Environmental and Ecological Development Society	Regional—Asia
20210309_001	Cities Climate Finance Leadership Alliance	• Climate Policy Initiative	Global
20210318_001	Resilient Cities Network (R-Cities)	• Resilient Cities Network	Global
20210319_001	HelpAge Network in Asia Pacific	• HelpAge Asia	Regional—Asia
20210319_002	HelpAge International	• HelpAge International	Global
20210325_001	Sendai Symposium for Disaster Risk Reduction and the Future	• Sendai City	National or local—Japan
20210406_001	Grow Forests, Change Lives by the Lebanon Reforestation Initiative (LRI)	• Lebanon Reforestation Initiative	National or local—Japan
20210420_001	Asian Disaster Reduction and Response Network (ADRRN)	• Asian Disaster Reduction and Response Network	Regional—Asia
20210420_002	Honing Agents for National Disaster Awareness (HANDA) Program: Disaster Preparedness and Business Continuity Planning for MSMEs	• UP Institute for Small-Scale Industries	National or local—Philippines
20210426_001	Applied Risk Communications by Pacífico	• Pacífico Applied Risk Communications	Global
20210505_001	Bosai Culture and Disaster Education in Nepal	• CITYNET Yokohama Project Office	National or local—Nepal
20210506_001	ARISE UAE: First National ARISE in the Arab Region	• ARISE UAE	National or local—United Arab Emirates
20210512_001	Creating Systemic and Resilient Changes for Global Sustainability from the Global South	• Fundación Avina	Regional—Americas
20210525_001	Global Earthquake Model (GEM)	• Global Earthquake Model Foundation	Global
20210527_001	Promoting Multi-disciplinary DRR Through Research and Innovation in Higher Education in the Arab Region	• Arab Science and Technology Advisory Group for Disaster Risk Reduction	Regional—Africa, Asia
20210528_001	Disaster Risk Reduction Through High- quality, Original Stories from Africa	• Zulani TV	Regional—Africa
20210603_001	Making the World a Better, Safer Place	• Miyamoto International	Global
20210604_001	Disaster Recovery Institute International (DRI)	• Disaster Recovery Institute International	Global
20210617_001	Business Resiliency Program in Turkey (or "Saglam KOBI" in Turkish)	• International Development Management	National or local—Turkey
20210621_001	Sentinel Asia	• Asia-Pacific Regional Space Agency Forum	Regional—Asia, Oceania
20210624_001	Resilience policymaking in Nepal: giving voice to communities	• University of Sheffield	National or local—Nepal
20210628_001	MYRIAD-EU: Multi-hazard and Systemic Framework for Enhancing Risk-Informed Management and Decision-making	• Institute for Environmental Studies	Regional—Europe
20210707_001	Climate Change, Resilience and Informality in Cities by Cities Alliance	• Cities Alliance	Global
20210727_001	DARAJA: Developing Risk Awareness Through Joint Action	• Resurgence	Global
20210727_003	International DRM Research Colloquium on Disaster Risk Reduction in a Changing Climate towards Business Continuity	• Philippine School of Business Administration • Quezon City Local Government • University of the Philippines	Regional—Africa, Americas, Asia, Europe, Oceania
20210921_001	Survivor and community-led crisis response	• Local to Global Protection	Global
20211123_001	Avoidable Deaths Network (ADN)	• Avoidable Deaths Network	Global
20220211_001	EFDRR RoadMap 2021-2030	• United Nations Office for Disaster Risk Reduction - Regional Office for Europe & Central Asia	Regional—Europe
20220804_001	Promoting Multi-Hazard Early Warning Systems for All - From Timor-Leste and Beyond	• Similie	Regional—Asia, Oceania
20221006_002	Negros Occidental Impact 2025	• Habitat for Humanity Philippines	National or local—Philippines

ID	Title	Implementing Organizations	Scope
20221018_001	Ready-to-Fund Resilience Toolkit and Guide	• American Society of Adaptation Professionals • Climate Resilience Consulting	National or local—United States of America
20221031_001	Adopt-a-Municipality Project - Tiwi Albay	• Aboitiz Foundation • National Resilience Council	National or local—Philippines
20221102_001	Philippine Catastrophe Insurance Facility	• National Reinsurance Corporation of the Philippines • Philippine Insurers and Reinsurers Association • The Philippines Insurance Commission	National or local—Philippines
20221110_001	Development of MSME Disaster Resilience Tools for the Philippines	• Philippine Disaster Resilience Foundation	National or local—Philippines
20221114_002	Delivery of Get Ready Queensland 2022-2023 across Queensland	• Queensland Reconstruction Authority	National or local—Australia
20221114_004	Queensland Betterment Fund, investing to create stronger, more resilient Queensland communities	• Queensland Reconstruction Authority	National or local—Australia
20230109_001	Community-based Education on Family Disaster Preparedness—3S Kadets Program	• Kabuhayan sa Ganap na Kasarinlan Credit and Savings Cooperative • Kasagana-ka Development Center, Inc.	National or local—Philippines
20230130_001	Underlining the risk and preventing disasters for Atakum Municipality	• ATAKUM BELEDİYESİ	National or local—Turkey
20230202_001	Communities for Resilience (CORE): Partnerships Towards Climate-Smart Philippines Program	• Aboitiz Equity Ventures, Inc. • Climate Change Commission	National or local—Philippines
20230202_002	Building Business Resilience through Climate Strategy in the Philippines	• Aboitiz Equity Ventures, Inc.	National or local—Philippines
20230316_001	Ribadesella Community Resilience in Spain	• Protección Civil de Ribadesella	National or local—Spain

References

CRED (2022) 2021 Disasters in numbers. Brussels. Retrieved from https://cred.be/sites/default/files/2021_EMDAT_report.pdf

CRED (2023) 2022 Disasters in numbers. Brussels. Retrieved from https://cred.be/sites/default/files/2022_EMDAT_report.pdf

Froude MJ, Petley DN (2018) Global fatal landslide occurrence from 2004 to 2016. Natural Hazards and Earth System Sciences 18:2161–2181. https://doi.org/10.5194/nhess-18-2161-2018

Gómez D, García EF, Aristizábal E (2023) Spatial and temporal landslide distributions using global and open landslide databases. Nat Hazards 117:25–55. https://doi.org/10.1007/s11069-023-05848-8

Pardeshi SD, Autade SE, Pardeshi SS (2013) Landslide hazard assessment: recent trends and techniques. SpringerPlus 2:523. https://doi.org/10.1186/2193-1801-2-523

Sim KB, Lee ML, Wong SY (2022) A review of landslide acceptable risk and tolerable risk. Geoenvironmental. Disasters 9(3). https://doi.org/10.1186/s40677-022-00205-6

The World Bank (2021) The Global Landslide Hazard Map Final Project Report. Retrieved from https://datacatalogfiles.worldbank.org/ddh-published/0037584/DR0045411/global-landslide-hazard-map-report.pdf?versionId=2023-01-18T20:43:00.6156776Z

UNDRR (2023) The Report of the Midterm Review of the Implementation of the Sendai Framework for Disaster Risk Reduction 2015–2030. UNDRR, Geneva. Retrieved from https://www.undrr.org/publication/report-midterm-review-implementation-sendai-framework-disaster-risk-reduction-2015-2030

Influence of Intra-Particle Saturation Ratio on Strength Degradation of Pumice Soil

Dhanushka Jayathilake, Takashi Kiyota, Kazuo Konagai, Masataka Shiga, and Mohammad Nihaaj

Abstract

The 2018 Hokkaido Eastern Iburi Earthquake occurred on 6 September 2018 and caused more than 7000 landslides in and around Atsuma and Abira towns. The geology of this area is mainly formed by pyroclastic fall deposits. The rain gauges in the epicentral area showed little rain from typhoon Jebi (5 September 2018) and heavy rain in the middle of August 2018, about 3 weeks before the earthquake. A series of direct shear tests and single particle fragmentation tests were conducted to investigate the effect of soaking time on the strength reduction of Tarumae d (Ta-d) pumice. The median Single particle fragmentation strength of Ta-d particles decreases with the soaking time. The Intra-particle saturation ratio of Ta-d has increased with the logarithmic value of the soaking time. Samples were soaked in water for 1, 6, 24, 168 and 508 h before shearing. Peak shear strength was decreased with the soaking time. The residual strength is about 2 kPa for each soaking condition, which shows that there is no significant variation in residual strength with soaking time. The friction angle shows a sharp reduction from the peak value during the first 800 mm of shear strain and thereafter gradually stabilizes to the residual value. The peak shear stress of Ta-d pumice is reduced with the intra-particle saturation ratio. The mobilized frictional coefficient of Ta-d is not sensitive to the intra-particle saturation ratio.

D. Jayathilake (✉) · T. Kiyota · M. Nihaaj
Institute of Industrial Science, University of Tokyo, Tokyo, Japan
e-mail: kiyota@iis.u-tokyo.ac.jp

K. Konagai
University of Tokyo, Tokyo, Japan

M. Shiga
Nagaoka University of Technology, Tokyo, Japan
e-mail: shiga@vos.nagaokaut.ac.jp

Keywords

Volcanic Soil · Landslides · Intra-particle saturation ratio · Eastern Iburi Earthquake · Soaking time

1 Introduction

The 2018 Hokkaido Eastern Iburi Earthquake struck the eastern Iburi region of Hokkaido, the northern Japanese island, on 6 September 2018. The earthquake had a moment magnitude (Mw) of 6.6 corresponding to a JMA (Japan Meteorological Agency) magnitude (M_j) of 6.7 and a maximum seismic intensity of 7 on the JMA 7-stage seismic intensity scale. This earthquake exerted a severe socioeconomic impact on Hokkaido and all of Japan. (Osanai et al. 2019). This earthquake also caused a large number of shallow landslides and several large-scale deep-seated landslides.

The soil over the Atsuma area is mainly formed by the pyroclastic fall deposits caused by the three main volcanos. Specifically, the Tarumae volcano is abbreviated as "Ta" The eruption age of the typical deposits of Ta-d is 9000 years (Geology of the Chitose District 1980; Furukawa and Nakagawa 2010). Earthquake-induced slope failures in volcanic areas are of major concern due to the presence of problematic volcanic soils (Chiaro et al. 2018) and Rainfall and water content are the most influential factors for the ground stability when it is subjected to earthquakes (Kiyota et al. 2017).

During the investigation after the landslides (2018-09-18), Zhou et al. 2021 found that the volcanic deposits on the mountain slopes were close to saturation. Groundwater gushed from some landslide surfaces suggesting that heavy rainfall may have significantly contributed to the landslides during the earthquake. Typhoon Jebi hit the Hokkaido region on fifth September 2018, 1 day before the earthquake. However, rain gauges in the epicentral area showed little rain

B. Abolmasov et al. (eds.), *Progress in Landslide Research and Technology, Volume 3 Issue 1, 2024*, Progress in Landslide Research and Technology, https://doi.org/10.1007/978-3-031-55120-8_14

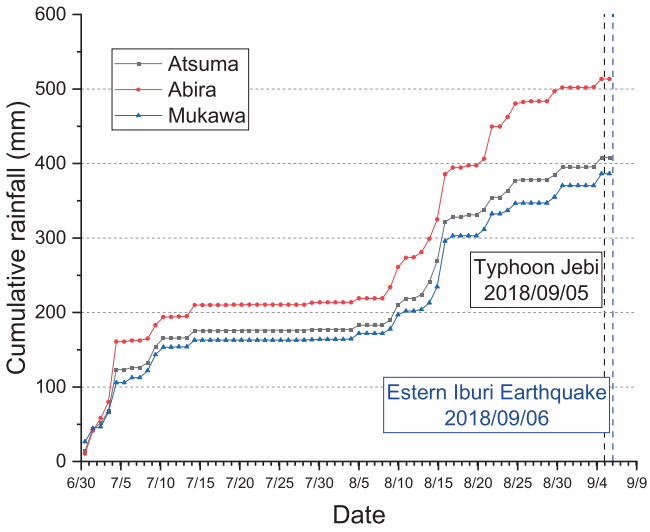

Fig. 1 Rainfall received by the Atsuma area in July, August, and September 2018—JMA Data stations of Atsuma, Abira and Mukawa

since the heavy rain in the middle of August 2018, about 3 weeks before the earthquake. Figure 1 shows the rainfall patterns recorded by the Automated Meteorological Data Acquisition System (AMeDAS).

Pumice particles are highly crushable, compressible, and lightweight due to their vesicular nature (Chaney et al. 2001; Kikkawa et al. 2013; Pender et al. 2006). They can retain water in their intra-particle voids for a while. Based on the on-site field reconnaissance from 2018-09-10 and the preliminary report (Hirose et al. 2018), the sliding zone of the majority of the Atsuma landslides is located in the Ta-d layer. Thus, the pumice layers are the most causative of the multiple landslides (Kawamura et al. 2019). In this study, a series of direct shear tests and single particle crushing tests on the pumice samples were conducted to clarify the strength reduction mechanism of Ta-d pumice soil with the soaking time. This paper discusses the effect of soaking time on the mechanical properties of the collapsed Ta-d pyroclastic fall deposits distributed over this area.

2 Material and Method

2.1 Material

Disturbed samples from Ta-d pumice soil were collected from Atsuma landslide sites. Basic soil parameters are listed in Table 1.

A series of physical tests were conducted: soil in-situ density tests, particle size distribution tests, Moisture content tests, and Specific gravity tests. Each test was implemented based on the JGS standards JGS 0191, JGS 0131, JGS 0121, and JGS 0111, respectively.

Table 1 Physical properties of Ta-d pumice soil

In-situ density (g/cm^3)	Natural water content (%)	Dry density (g/cm^3)	Specific gravity (g/cm^3)	Global void ratio (e)
1.05	208	0.34	2.75*	4.3

* Value of specific gravity on based on Watanabe et al. 2021

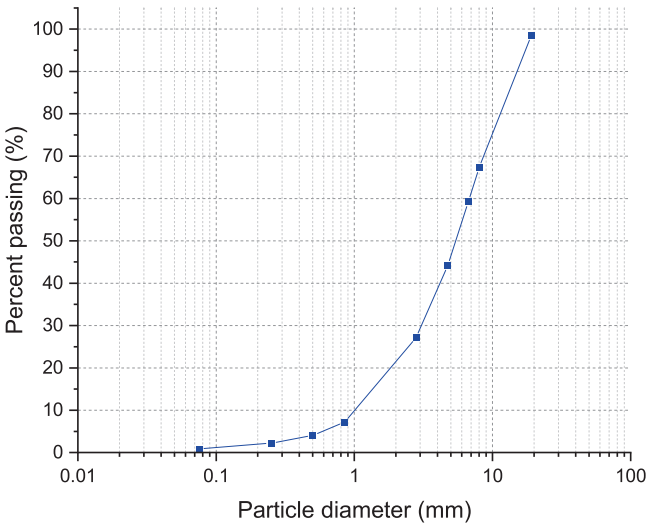

Fig. 2 Particle size distribution of sampled Ta-d soil

The results are summarized in Fig. 2 and Table 1. It is evident from the grain size distribution that the soil is mostly composed of coarse-grained soil particles and the mean particle diameter (D50) is 5.4 mm. In-situ density is 1.05 g/cm^3 with water content 208% at the sampling location and dry density was set to 0.34 g/cm^3 for direct shear test.

2.2 Test Method

2.2.1 Single Particle Fragmentation Test

Single particle fragmentation tests were performed by selected Ta-d particles whose particle diameter equals *D*50. The Samples were sieved from 6.7 mm and 4.75 mm sieves, and particles retained in 4.75 mm sieves were used for the test. Six batches of soil particles were prepared, and five were soaked in distilled water for 1, 6, 24, 168 and 508 h to make different soaking conditions. Distilled water is used to eliminate any undesirable impacts of chemical compounds. Another batch was used to evaluate single-particle strength in a dry state. Soil particles were placed between two smooth platens of the single-particle crushing apparatus with a maximum loading capacity of 5kN. The load was monotonically increased at a constant displacement rate of 0.1 mm/min until the particle was broken or crushed. More than 20 soil particles were tested in each batch to obtain statistically meaningful averages of the individual measurements on a

single particle to account for the size variability and other heterogeneity of individual soil particles. (e.g., shape or geometry, surface roughness) (Liu et al. 2021). Hence, more than 120 particles were tested in six batches. Particles were selected with higher angularity (>0.6) and sphericity (>0.6). because particles with lower sphericity and angularity showed irregular failures, which does not correlate with particle size, as observed by (Nakata et al. 2001) Particle fragmentation strength was calculated by using Eq. 1.

$$\sigma f = \frac{0.9Nf}{d2} \tag{1}$$

Where σf is the particle fragmentation strength, Nf is the load at failure, and d is the distance between the two points of contact between the particle and the platen. d should be the smallest dimension of the irregular particle. (Hiramatsu and Oka 1966; Jaeger 1967). Equation (1) includes a correction coefficient of 0.9 to account for the effects of imperfect particle geometry and surface roughness (Liu et al. 2021).

2.2.2 Determination of Intra-Particle Saturation Ratio

Pumice is characterized by the vesicular nature of its particles; each particle contains a dense network of fine pores, some of which may be interconnected and open to the surface, while others may be completely isolated within the particle. They are therefore easily absorbent, and a considerable amount of water could be trapped in the pores. The amount of saturation of pores inside the particles will be referred to as the Intra-particle saturation ratio hereafter. To identify the change in the intra-particle saturation ratio with soaking time, we conducted a series of grain soaking tests for different particle sizes as 6.7 mm, 4.75 mm and 2.8 mm.

Five batches of particles were prepared for each size, and one batch consisted of 10 oven-dried particles. Initially, selected particles were scanned using a 3D scanner, and the volume of the particles (V_T) was measured using the scanned 3D model. The weight of each batch was measured in dry condition and subsequently soaked in distilled water. The weight of the particle batches was measured at the defined soaking time as 1, 6, 24 and 168 h, as same as the single particle fragmentation strength test. These data calculated the intra-particle saturation ratio (S) for each particle size as follows.

$$S = Vw / Vv \tag{2}$$

where V_V is the volume of voids inside the particle (volume of intra-particle voids) and V_T &V_S are the total volume and volume of soils respectively. V_W is the volume of water absorbed by the particle.

$$V_V = V_T - V_S \tag{3}$$

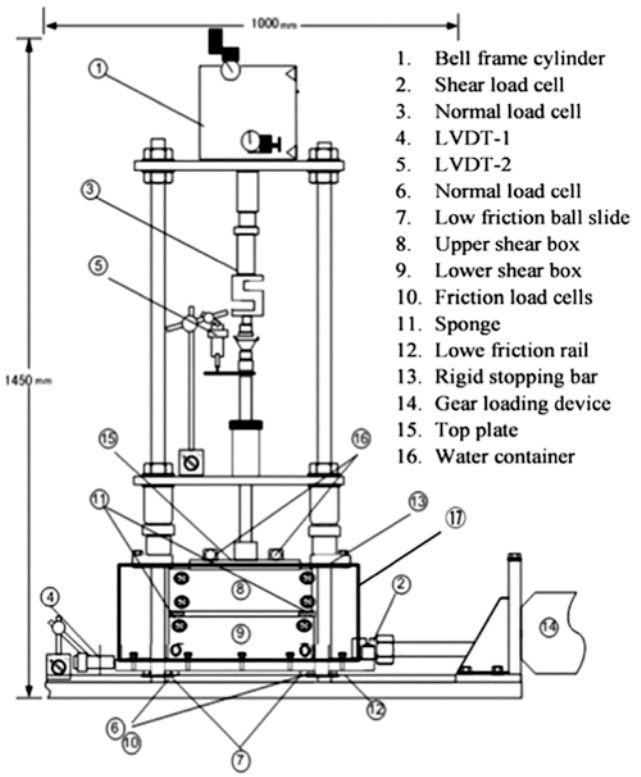

Fig. 3 Schematic diagram of modified direct-shear test apparatus (modified based on Kiyota et al. 2011)

V_V is the volume of intra-particle voids. V_S was calculated in terms of specific gravity. V_W was calculated by using the measured weight of the particle at each soaking time.

2.2.3 Direct Shear Tests

We conducted a series of cyclic direct box shear tests under constant-volume conditions for reconstitute samples to investigate the shear strength property of pumice fall deposits. Particles larger than 4.75 mm were removed, and the rest part of an in-situ particle size distribution curve was maintained in each test. A schematic view of the modified direct shear apparatus used in this study is shown in Fig. 3.

The initial dimension of the specimen was 200 mm in length, 200 mm in width, and 108 mm in height. The apparatus has the following essential features: (1) possible feedback control on both normal load and shear load to impose any prescribed stress path in the shear stress-normal stress space; (2) a lower shear box moving on a very low-friction rail, with two friction load cells to evaluate any friction at the bottom of the lower shear box; (3) Monotonic and cyclic loading test can conduct in constant volume and constant stress conditions. (Sharma et al. 2017; Kiyota et al. 2011).

The effect of the opening size between two halves of the direct shear apparatus was investigated. As per the results, it was decided that 10 mm is a suitable opening size for the Ta-d pumice soil. Flexible sponges were attached to the

lower shear boxes to fill 10-mm openings and prevent particle leakage during experiments. These sponges were flexible and negligibly affected the vertical and shear stresses (Sawatsubashi et al. 2021).

Disturbed samples were first sieved and separated into different particle sizes. In preparation, sieved samples were mixed propositionally as per the in-situ particle gradation curve. In each test, the same initial particle gradation curve was maintained so that it is possible to compare the particle crushability after each shearing. The direct shear test sample was divided into seven layers. Weight and height per layer were decided as per the measured in-situ density. The sample was prepared layer by layer in pre-determined density using the dry tamping method. This method was used to obtain equal density throughout the sample. The confining pressure for each soil type is decided per the depth of soil layers in Atsuma slopes. After initial preparation, samples were consolidated under the prescribed confining pressure. Consolidated samples were soaked in distilled water for 1, 6, 24 and 168 h within the direct shear apparatus. For this purpose, an additional water-sealed box was attached to direct the shear apparatus from outside the shear box. The initial density of the direct shear sample was controlled to obtain equal density at the start of shearing in each soaking condition. The samples were soaked for a predetermined time, and subsequently shearing was done.

We conducted constant volume cyclic loading direct shear tests to identify the effect of soaking time on peak shear stress and residual stress. In the monotonic loading condition, the maximum shear displacement is 20 mm, and Ta-d samples did not reach the residual stress conditions at 20 mm shear displacement. Hence, strain-controlled cyclic loading tests were conducted for 100 cycles until the sample achieved the residual stress condition. In the cyclic shear process, the initial vertical stress was 30 kPa, and horizontal displacement was automatically controlled from zero to 20 mm and − 20 mm. After each sharing test, sieve analysis was conducted to measure the particle breakage.

3 Results and Discussion

3.1 Single Particle Fragmentation Test

As per the results, the single particle fragmentation strength (σ_f) of Ta-d pumice reduces with soaking time, as shown in Fig. 4. Analysis based on simplified quartiles shows that, on average, the σf remains the same until 168 h. Still, the strength at 504 h decreased by 48% compared to dry conditions. In addition, when comparing the first and third quartiles, there is no decrease with soaking time up to 24 hours, but there is a decreasing trend after 168 h. The variation of crushing strength of particles gets smaller with the soaking time. As discussed by McDowell and Bolton, the crushing strength of crushable soil is more variable than that of non-crushable soil because the individual particles of crushable soil often consist of several minerals. Even if they consist of a single mineral, the degree of the weathering is different (McDowell and Bolton 1998) In addition, the asperities on a particle with an irregular shape can break more easily. Therefore, crushing phenomena for crushable soils are expected to occur at relatively low stress levels.

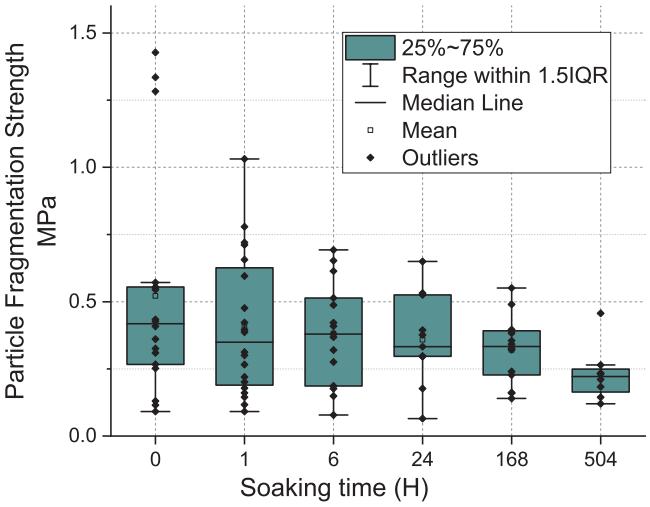

Fig. 4 Change of single particle fragmentation strength with soaking time

3.2 Intra-particle Saturation Ratio

The intra-particle saturation ratio (S) increases with the soaking time, as shown in Fig. 5. The figure shows the average value for the S for a particular particle size. Smaller particles show a higher saturation ratio than the bigger particles at a given time. This trend is because smaller particles have comparatively smaller volumes of voids and could be saturated within a shorter period. The average value of the S shows a good correlation with the logarithmic value of the soaking time, as shown in Fig. 5.

3.3 Direct Shear Test

Constant volume direct shear test results show that the peak undrained shear strength (τ_{peak}) of Ta-d pumice is reduced with the soaking time. Figure 6 shows a gradual decrease in τ_{peak} as the soaking time increases.

The τ_{peak} was reduced to 25 kPa at the 3 weeks (504 H) soaking from 40 kPa in dry condition. A similar trend was observed in the single particle fragmentation tests as well. In Fig. 6, the stress path shows a drastic reduction of shear

stress within the first few cycles of the cyclic loading, and the value stabilizes at around 2 kPa by the 15th cycle. The stable value could be considered as the residual strength of the Ta-d pumice soil under undrained conditions. There is no significant variation in residual strength with the soaking time, as shown in Fig. 7. Allowable vertical deformation in content volume direct shear test is 0.05% as per JGS 0560–2020 (Japanese Geotechnical Society Standard (JGS 0560-2020) 2015). During the experimental program, it could not maintain the vertical displacement within the allowable limit, which may affect the peak shear stress value. This will be addressed in future studies.

When the soaking time increases, the stress paths move away from the τ axis. In other words, the value of σ_v did not reach 0; the minimum value is increasing with soaking time increase. When the soaking time increases, the particle's

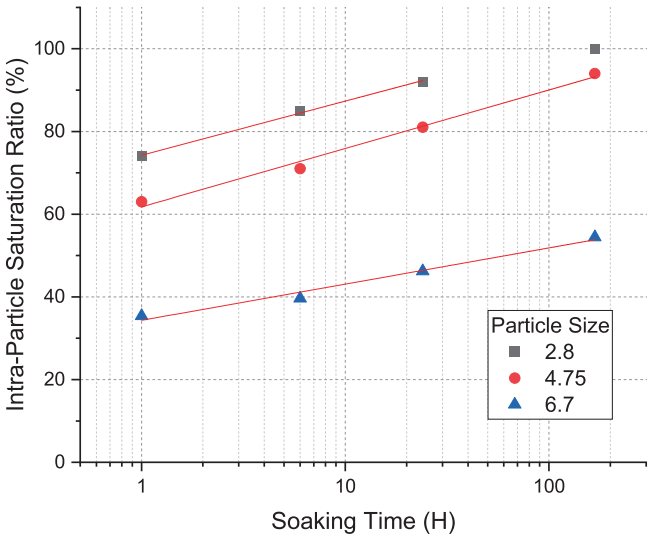

Fig. 5 Change of Intra-particle saturation ratio of different particles sizes with log value of time (H)

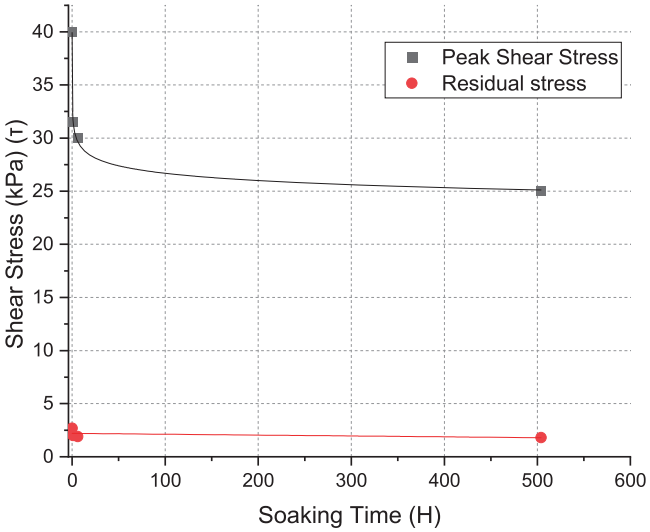

Fig. 7 Peak and residual stress variation with soaking time

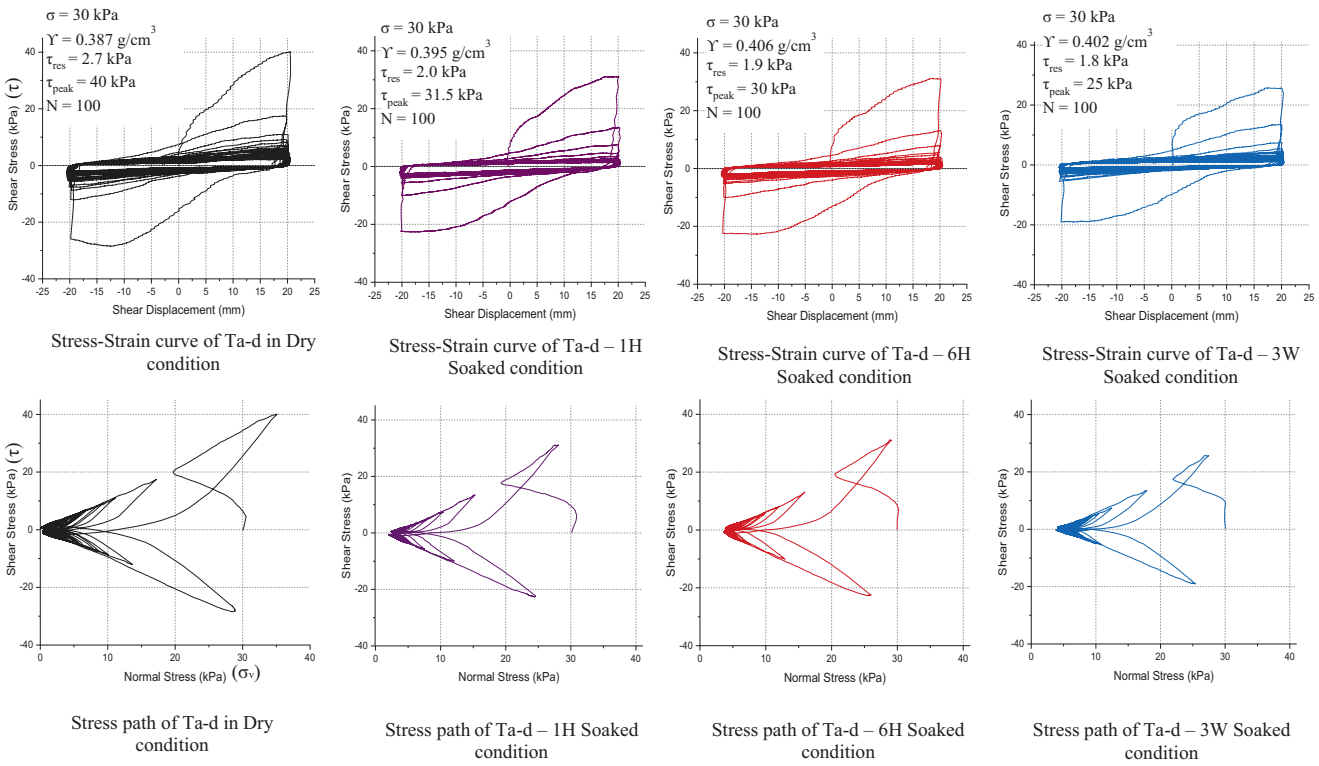

Fig. 6 Stress-strain curves and stress paths of Ta-d in different soaking conditions

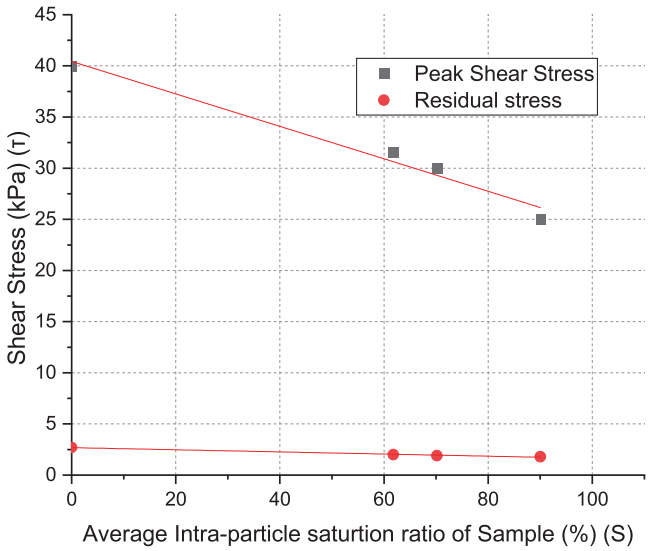

Fig. 8 Peak and residual stress variation with Intra-particle saturation ratio (S)

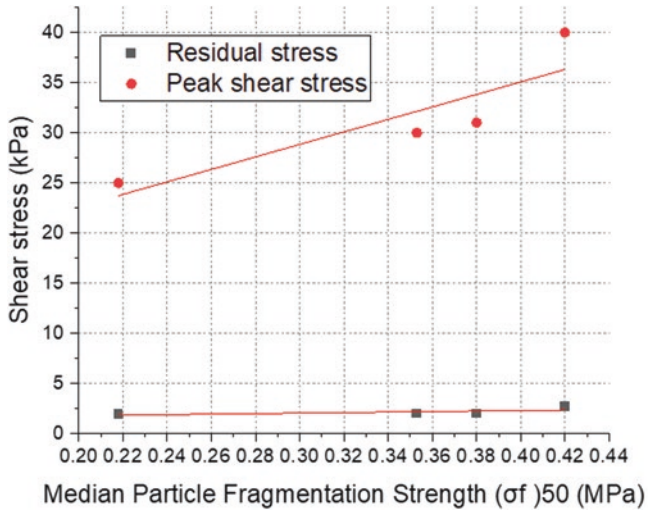

Fig. 9 Relationship of median particle fragmentation strength with peak and residual shear stress

crushability increases, and the volume change behavior decreases.

The τ_{peak} reduction in direct shear shows a good correlation with the S of Ta-d pumice. As shown in Fig. 8, peak strength reduces when the S increases. This strength reduction is observed in the single particle fragmentation strength test in the same manner, while S has no significant impact on residual strength.

The reduction of τ_{peak} may be caused by the particle strength reduction due to soaking. As shown in Fig. 6, σ_f reduced with the soaking time increased. The relationship between the peak shear stress and σ_f is shown in Fig. 9. Accordingly, there is very good evidence that the reduction of σ_f has caused the reduction in the τ_{peak} in the direct shear of the Ta-d pumice sample.

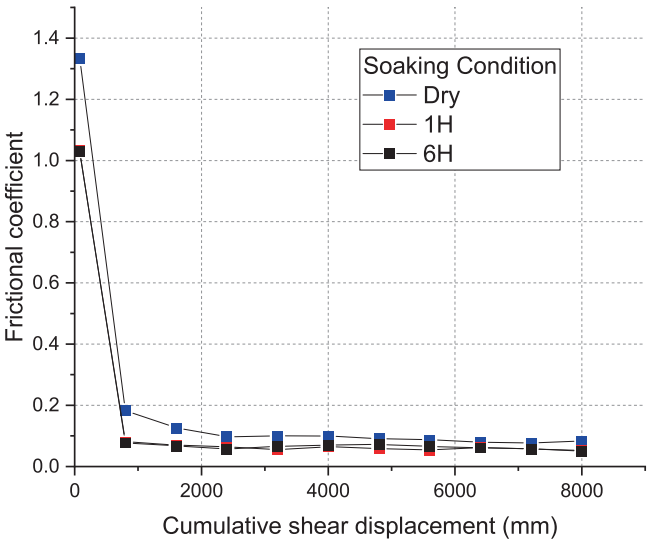

Fig. 10 Change of mobilized frictional coefficient with cumulative shear displacement

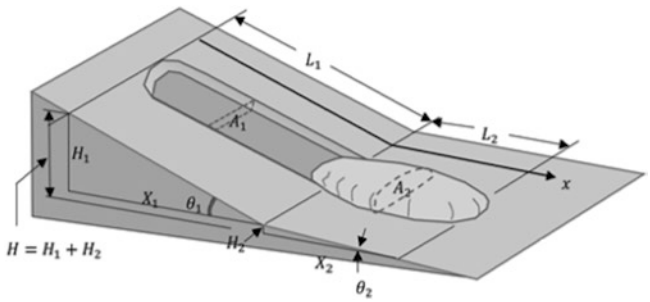

Fig. 11 —Measured dimensions of Landslides. (Konagai and Nakata 2019)

When the sample is subjected to cyclic loading, the friction angle (∅) is changed accordingly. Figure 10 shows the variation of the mobilized frictional coefficient (μ_m) with cumulative shear displacement (Assumed C = 0). As per the results, the peak frictional coefficient (μ_p) in dry conditions is 1.3 and μ_p for 1H and 6H soaking conditions is about 1. Thereafter, the μ_m shows a sharp reduction by the tenth cycle and subsequently, no significant reduction until the 100th cycle. The residual frictional coefficient (μ_r) is 4.7^0 for dry conditions and 3^0 for 1H and 6H soaking conditions.

Konagai and Nakata 2019 discuss the uniformity of the mobilized friction angles of about 30 studied landslides in the Atsuma area. They measured the dimensions of 30 landslide masses in Atsuma, Hokkaido, as shown in Fig. 11.

A landslide mass with its initial length L_1 and cross-sectional area A_1 is assumed to have decelerated as it travelled over flat land and stopped completely with its final length L_2 and cross-sectional area A_2 immediately when the whole mass left the slope L_1. The variations of A_1 and A_2 along the direction of the dip (x) are assumed to be substantially small and fluctuate little around their average values $\overline{A}$

$_1$ and $\bar{A}_2$. An equation incorporating mobilised frictional coefficients was developed by equating the initial potential energy of landslide mass with the work done by the landslide during the sliding process.

Multiple linear regression analysis for the relationship among the measured dimensions of 30 landslide masses has given the average values of mobilized frictional coefficients of 0.165 on the slip surfaces. However, Konagai & Nakata concluded that the value of the mobilized frictional coefficient for a smaller and gentler slope, which might have been wetter than the others, could have been even smaller than this average value and was obtained to be 0.05. (Konagai et al. 2018, 2021; Konagai and Nakata 2019). The mobilized fictional coefficient value obtained by the experimental program is 0.052 and 0.05 for the 1H and 6H soaking conditions. Two values obtained from statistical analysis and experimental program are comparable.

4 Conclusions

To investigate the effect of the intra-particle saturation ratio on the strength characteristics of Ta-d pumice soil, we conducted a series of single particle fragmentation tests and direct shear tests. Based on the study, the following conclusions are drawn,

Ta-d Pumice is characterized by a low specific gravity (1.7 g/cm^3) compared to non-volcanic soils. The Ta-d pumice samples had dry bulk densities of 0.34 g/cm^3, lower than typical non-volcanic soils.

The intra-particle saturation ratio of Ta-d pumice correlates well with the Logarithmic value of soaking time.

The Median particle fragmentation strength of Ta-d pumice reduces by 21% with the increase of the intra-particle saturation ratio.

Peak shear strength in the direct shear test is reduced with the increase of the soaking time or intra-particle saturation ratio, and the residual strength is not sensitive to the intra-particle saturation ratio.

The friction angles in the direct shear test change with the cyclic loading. The peak friction angle is 53^0 for dry conditions and 45^0 for 1H and 6H soaking conditions. The residual friction angle is 4.7^0 for dry conditions and 3^0 for 1H and 6H soaking conditions. The mobilized frictional coefficient is about 0.05 for the 1H & 6H soaking conditions.

Acknowledgement This study has been conducted together with estimating preceding rains in the mountainous epicentral area of the 2018 Hokkaido Earthquake in association with the SATREPS Project "Development of Early Warning Technology of Rain-Induced Rapid and Long-Travelling Landslides in Sri Lanka." The latter part regarding the estimation of preceding rains will be reported separately.

Fieldwork was conducted with the assistance of Dr. Yasuo Chimoto of Kiso-Jiban Consultants Hokkaido Branch.

References

Chaney R, Demars K, Wesley L (2001) Determination of specific gravity and void ratio of pumice materials. Geotech Test J 24(4):418. https://doi.org/10.1520/GTJ11139J

Chiaro G, Umar M, Kiyota T, Massey C (2018) *The Takanodai landslide, Kumamoto, Japan: Insights from post-earthquake field observations, laboratory tests, and numerical analyses*. 98–111. https://doi.org/10.1061/9780784481486.011

Furukawa R, Nakagawa M (2010) *Geological map of Tarumae volcano*. https://gbank.gsj.jp/volcano/Act_Vol/tarumae/index-e.html

Geology of the Chitose District (1980) Geological Survey of Japan

Hiramatsu Y, Oka Y (1966) Determination of the tensile strength of rock by a compression test of an irregular test piece. Int J Rock Mechanics Mining Sci Geomechanics Abstracts 3(2):89–90. https://doi.org/10.1016/0148-9062(66)90002-7

Hirose Y, Numamoto S, Matsumura N (2018) Information Acquisition of Forest Resources Using Photographing from UAV: case study in the Mie university Forest, Hirakura. J Forest Planning 22(2):33–37. https://doi.org/10.20659/jfp.22.2_33

Jaeger JC (1967) Failure of rocks under tensile conditions. Int J Rock Mechanics Mining Sci Geomechanics Abstracts 4(2):219–227. https://doi.org/10.1016/0148-9062(67)90046-0

Japanese Geotechnical Society Standard (JGS 0560-2020) (2015) *Method for consolidated constant volume direct box shear test on soils 1 Scope*

Kawamura S, Kawajiri S, Hirose W, Watanabe T (2019) Slope failures/landslides over a wide area in the 2018 Hokkaido eastern Iburi earthquake. Soils Found 59(6):2376–2395. https://doi.org/10.1016/j.sandf.2019.08.009

Kikkawa N, Orense RP, Pender MJ (2013) Observations on microstructure of pumice particles using computed tomography. Can Geotech J 50(11):1109–1117. https://doi.org/10.1139/cgj-2012-0365

Kiyota T, Sattar A, Konagai K, Kazmi ZA, Okuno D, Ikeda T (2011) Breaching failure of a huge landslide dam formed by the 2005 Kashmir earthquake. Soils Found 51(6):1179–1190. https://doi.org/10.3208/sandf.51.1179

Kiyota T, Konagai K, Shiga M (2017) Geotechnical damage caused by the 2016 Kumamoto earthquake, Japan. Int J Geoeng Case Histories 4:78. https://doi.org/10.4417/IJGCH-04-02-01

Konagai K, Nakata AM (2019) Runouts of landslide masses detached in the 2018 Hokkaido eastern Iburi earthquake. J Disaster FactSheets FS2018(E-0001):1–6. http://committees.jsce.or.jp/disaster/system/files/FS2019-E0001_0.pdf

Konagai K, Nishiyama S, Ohishi K, Kodama D, Nanno Y (2018) Large ground deformations caused by the 2018 Hokkaido eastern Iburi earthquake. J Disaster FactSheets FS2018(E-0003):1–8. http://committees.jsce.or.jp/disaster/system/files/FS2018-E0003.pdf

Konagai K, Tang AK, Eidinger JM (2021) *Recent Earthquakes that Hit Areas Covered and/or Underlain by Pyroclastic Matters and Their Impacts on Lifelines*. *1912*, 3–18. https://doi.org/10.1007/978-3-030-60713-5_1

Liu C, Liu F, Song J, Ma F, Wang D, Zhang G (2021) On the measurements of individual particle properties via compression and crushing. J Rock Mech Geotech Eng 13(2):377–389. https://doi.org/10.1016/j.jrmge.2020.06.009

McDowell GR, Bolton MD (1998) On the micromechanics of crushable aggregates. Géotechnique 48(5):667–679. https://doi.org/10.1680/geot.1998.48.5.667

Nakata Y, Kato Y, Hyodo M, Hyde AFL, Murata H (2001) One-dimensional compression behaviour of uniformly graded sand related to single particle crushing strength. Soils Found 41(2):39–51. https://doi.org/10.3208/sandf.41.2_39

Osanai, N., Yamada, T., Hayashi, S. ichiro, Kastura, S., Furuichi, T., Yanai, S., Murakami, Y., Miyazaki, T., Tanioka, Y., Takiguchi, S., & Miyazaki, M. (2019). Characteristics of landslides caused by the 2018 Hokkaido eastern Iburi earthquake. Landslides, 16(8), 1517–1528. doi:https://doi.org/10.1007/s10346-019-01206-7

Pender MJ, Wesley LD, Larkin TJ, Pranjoto S (2006) Geotechnical properties of a pumice sand. Soils Found 46(1):69–81. https://doi.org/10.3208/sandf.46.69

Sawatsubashi M, Kiyota T, Katagiri T (2021) Effect of initial water content and shear stress on immersion-induced creep deformation and strength characteristics of gravelly mudstone. Soils Found 61(5):1223–1234. https://doi.org/10.1016/j.sandf.2021.06.015

Sharma K, Kiyota T, Kyokawa H (2017) Effect of slaking on direct shear behaviour of crushed mudstones. Soils Found 57(2):288–300. https://doi.org/10.1016/j.sandf.2017.03.006

Watanabe K, Kyokawa H, Onodera T, Koseki J, & Aoyagi Y (2021). Evaluation of residual strength characteristics of reconstituted volcanic soil at Atsuma town, Hokkaido with stacked-ring shear tests. 20th International Conference on Soil Mechanics and Geotechnical Engineering

Zhou H, Che A, Wang L, Wang L (2021) Investigation and mechanism analysis of disasters under Hokkaido eastern Iburi earthquake. Geomat Nat Haz Risk 12(1):1–28. https://doi.org/10.1080/19475705.2020.1856201

Regional Debris Flow Hazard Assessment of the Grdelica Gorge (Serbia)

Miloš Marjanović, Biljana Abolmasov, Jelka Krušić, and Uroš Đurić

Abstract

Road infrastructure development is currently very intensive in Serbia. One such example is the Grdelica Gorge, where a new highway was aligned and put into service in 2019. The Gorge has provided a very challenging engineering environment imposing high levels of several hazard types: floods; slides; debris flows; and rockfalls. In this work, the debris flow hazard for the first 15 km of the road route was in focus. The assessment included an expert-driven analysis for identifying potential source areas, coupled with deterministic modelling of the flowing process originating from these source areas, resulting in detailed simulations of the final runout distance, height of deposit, and flow velocity, which are all reliable parameters for mitigating the hazard across the road alignment. A combination of geomorphological criteria, processed in a GIS environment was used to narrow down the search of source areas containing loose, erodible material which easily mobilizes under saturated conditions. The criteria were calibrated by the outlines of the available inventory, acquired by remote sensing techniques. The Digital Terrain Model with 12.5 m resolution was used for running RApid Mass Movement Simulation (RAMMS), using estimated bulk density and friction coefficients as input parameters. Since there was no recent debris flow in the area for the appropriate back-analysis of these parameters, experience-and lab-based estimations were used. Several simulations have reached the road alignment, wherein a few imposed significant threats with respect to deposit height and velocity that require additional attention.

Keywords

Hazard assessment · Debris flow · Runout · RAMMS · Regional scale

1 Introduction

Infrastructure development and investment strategies have put road construction in focus in Serbia in the past decade. Existing routes have been upgraded, but what is more challenging, entirely new routes have been designed through rugged terrains. One such example is the Grdelica Gorge along the South Morava River in the south of Serbia, which belongs to the international route E-75, connecting Central and South Europe. A new route with a full highway profile was designed through a relatively narrow gorge, while the previous E-75 route was recategorized as National Road No. 158. At present, the Gorge hosts the river, the previous road, a new full-profile highway, and a railway, as well as some local roads, in a corridor that is locally as narrow as 100 m, making the new highway construction a very difficult engineering task at the time. In addition, unrealistic deadlines, and legislative and political circumstances affected the usual design time frames and enforced design solutions before they were analysed from all aspects. For instance, the hazard assessment which is suitable for the feasibility and preliminary stage of the route design was undertaken at a later stage, leaving little or no possibilities for avoiding hostile sections of the route. Instead, these parts were resolved by a more complex and more costly solution, which faced constant problems during construction that had to be, and still are mitigated on the go. Hazard assessment and the downscaling investigation principle (investigating from wider to narrower area) is, therefore, imperative and must be undertaken at an early design stage to avoid at least some of the difficulties of road construction.

M. Marjanović (✉) · B. Abolmasov · J. Krušić
University of Belgrade, Faculty of Mining and Geology, Belgrade, Serbia
e-mail: milos.marjanovic@rgf.bg.ac.rs; biljana.abolmasov@rgf.bg.ac.rs; jelka.krusic@rgf.bg.ac.rs

U. Đurić
University of Belgrade, Faculty of Civil Engineering, Belgrade, Serbia
e-mail: udjuric@grf.bg.ac.rs

B. Abolmasov et al. (eds.), *Progress in Landslide Research and Technology, Volume 3 Issue 1, 2024*, Progress in Landslide Research and Technology, https://doi.org/10.1007/978-3-031-55120-8_15

1.1 Study Area

The Grdelica Gorge (Fig. 1) is located along the South Morava River, which is one of the largest river systems in the country. Stretching for more than 28 km, sloping up to 50°, and scaling significant relative altitudes from about 270 m to 900 m above sea level, the Gorge is a marble of nature, but at the same time, a very hostile terrain for any engineering endeavour. It connects the Neogene basins of Vranje (upstream) and Leskovac (downstream), which have more than 60 m of total elevation difference, indicating a strong neo-tectonic activity (relative subsidence of Leskovac and Vranje block in comparison to central Predejane block) and as a result, an intensive erosional incision into the weathered and jointed bedrock, represented mostly by low-grade crystal schists. In addition, the area was volcanically very active in early Tertiary, when numerous dacite-andesite dykes (a periphery of a large Surdulica volcanic complex to the south) penetrated the earlier gabbro intrusions and crystalline base throughout the valley (Fig. 2). The left valley slopes are capped by Cretaceous limestone, which provide a high-capacity water discharge at their contact with the impermeable schists laying below. The Gorge is echeloned along the major structural elements, i.e. NW-SE striking regional faults and anticlines, shifted by a younger set of NE-SW striking faults (Marković et al. 1995).

The abundance of water, lithologic diversity, tectonic conditions, and structural complexity are directly reflected in superficial processes (Marković et al. 1995). The high weathering rate and climatic conditions, especially in the schistose core of the valley, have produced a thick saprolitic topsoil, prone to erosional and landslide processes (Fig. 2). The entire watershed was systematically vegetated to suspend or moderate the erosion in 1970–1980, while short tributaries were featured with flood barriers to suppress torrents. Still, the slope processes are easily reactivated throughout the valley after any significant engineering activity (slope undercutting, embankment loading, tunnelling, etc.) which has been confirmed in the recent construction activities for the new highway. Seismically, the area is of no significant potential (Marković et al. 1995), whereas the climate, transiting from continental to alpine, shows common temperature and precipitation variance for such terrains, with no significant extremes. However, it is arguable whether any potential climate change could disturb such balance and introduce new aspects of the problem ahead.

The area of interest (AOI) does not encompass the entire Gorge (due to data coverage issues), but only the first 15 km

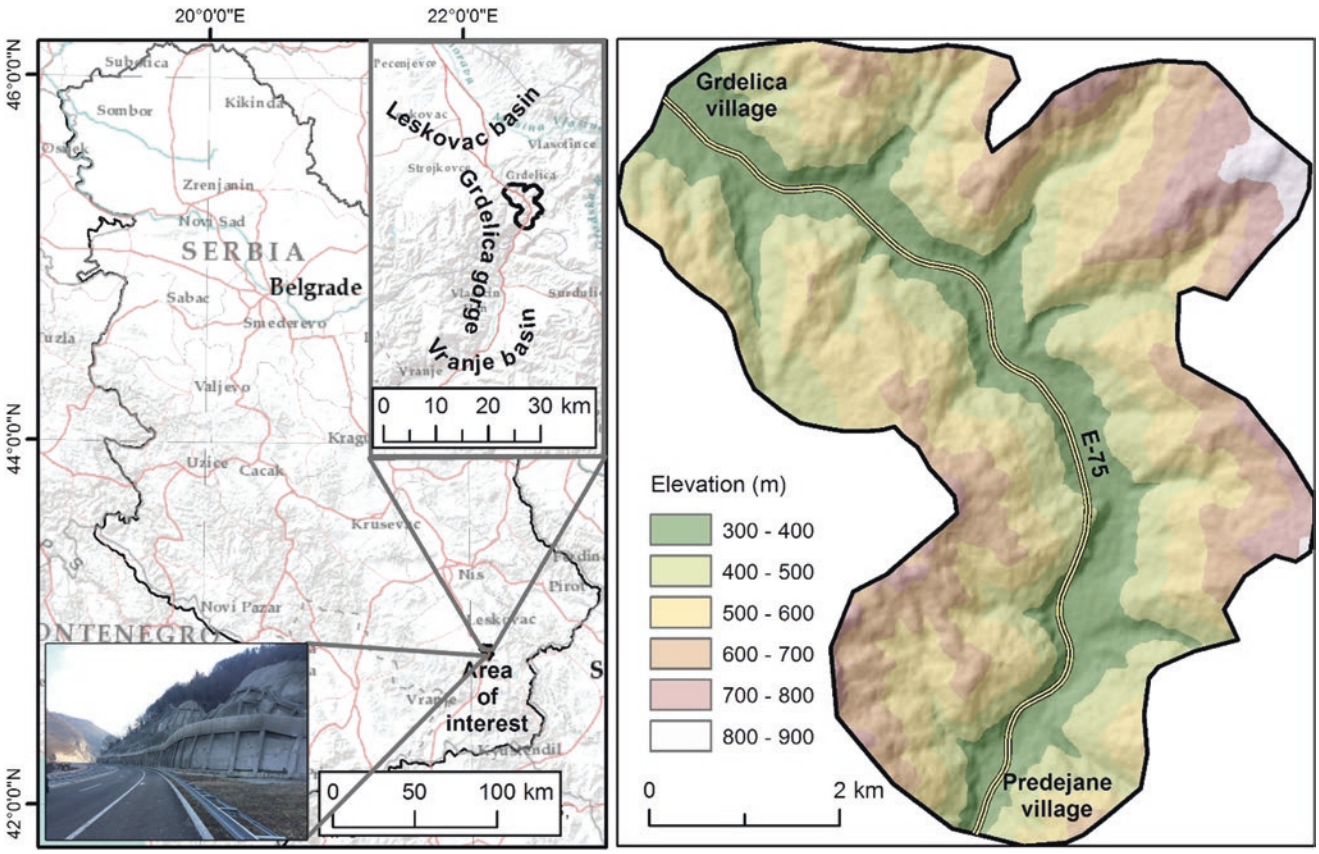

Fig. 1 Location of the AOI (left) and its Digital Elevation Model (right)

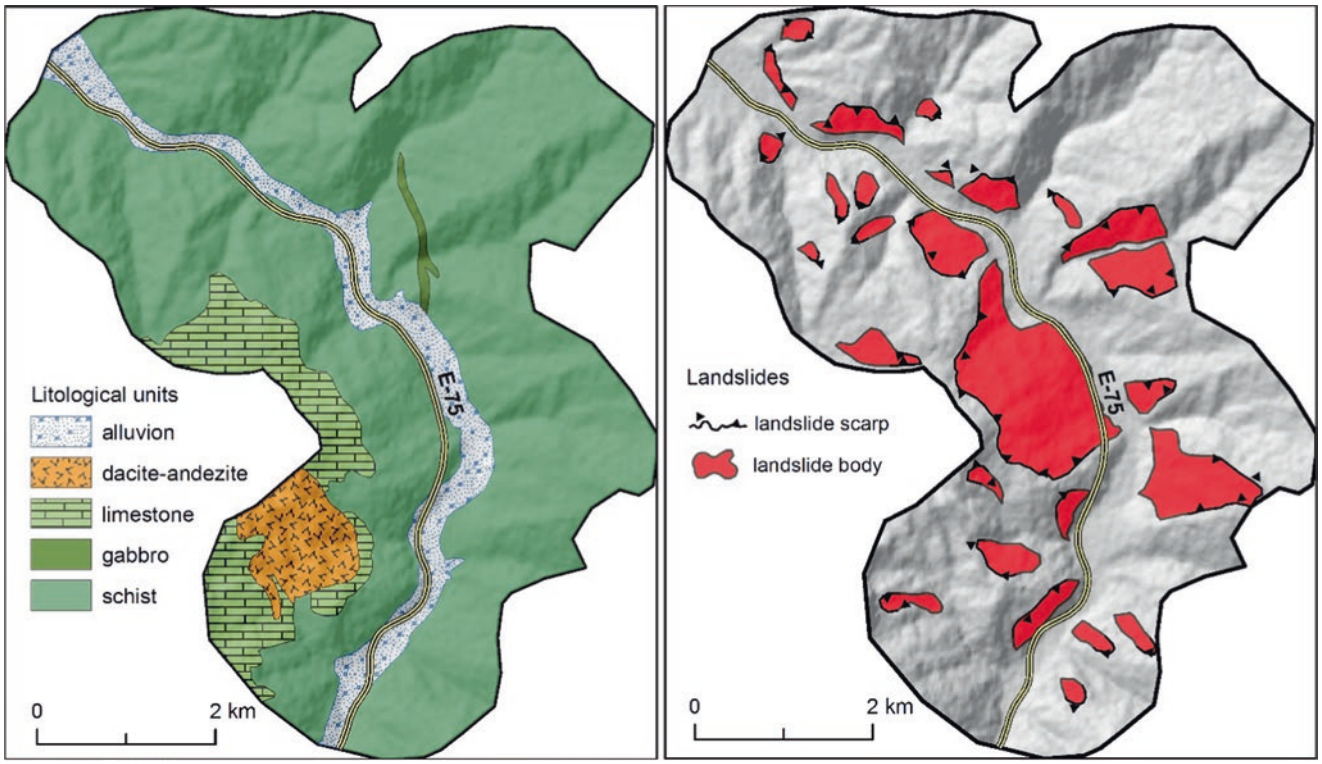

Fig. 2 Simplified geologial map (left) and Landslide inventory (right)

from its entrance, i.e., upstream of Grdelica village to Predejane village (Fig. 1), covering about 37 km2. Proliferating slope processes in this part have been investigated in the past (Marković et al. 1995), but the interest was renewed as the design of the new highway implied the use of the left valley side, which represents the inner area of interest (IAOI). The expected hazards were primarily characterized by shallow and dormant landslides, with seldom torrential floods, with associated gully erosion and alluvial fans, scree slopes, and rarely rockfalls. However, during the road construction and opening of wide and high cuts, many instabilities reoccurred (Abomasov et al. 2022). Therein, debris flows were singled out from the general landslide assessment to be separately analysed for the first time in domestic practice.

1.2 State-of-the-Art Regional Debris Flow Hazard Assessment

At regional scales (from several tens to several hundreds or thousands of km^2), debris flow models and simulations cope with uncertainty at each step of the way, beginning with accuracy of the source area inventory, input friction parameters' reliability, accuracy of the topographic surface models, level of approximation introduced in the flow models, etc. Thematic inventory focused solely on debris flows is uncommon (Guzzetti et al. 2012). They are a constitutive part of general inventories and are used in general landslide assessment practice, by implementing various approaches, from expert to deterministic (Krušić et al. 2017a), and mixed together with other landslide types, thereby inheriting a more general methodology of the assessment, which is more appropriate for short-ranged processes where source area and runout are not set far apart. This is not the case for debris flows, as they are rather long-ranged, even in regional scales, and require two-stepped analysis: (i) delineating the source areas and defining their material properties and water content, (ii) simulating the runout using appropriate flow model. Being that much different in their mechanism and that much outnumbered by slides within the general inventories, debris flows are commonly poorly represented in regional scale models. Their zone of influence is practically limited to the source areas, while their true hazard lies downslope and remains undetected.

This issue was recognized in the landslide assessment practice, and there have been numerous attempts to analyse the debris flows separately at regional scales. However, most of the authors have focused on (i), i.e., delineating and characterizing source areas using various techniques, ranging from expert-driven, statistics to deterministic, while complete (i) + (ii) procedures are rare. In fact, the debris-flow susceptibility is commonly related to (i) and includes upslope areas, while debris-flow hazard is related to both (i) + (ii) and includes the downslope areas, but primarily the runout zones

(commonly, there is some infrastructure sitting in the foot of the slope or bottom of the valley where flows are terminating).

For instance, Salvetti et al. (2008) are suggesting a probabilistic approach to replace deterministic in cases when input frictional parameters cannot be estimated. A credal network is applied on a set of coupled Geological, Hydrometeorological, and Topographic thematic layers fed into the model, which is based on Takahashi's debris flow theory, thereby delineating source areas. Blahut et al. (2010) used the Weight of Evidence statistical tool to filter viable source areas from inventories that included all kinds of landslides, wherein geological and topographic features were used as filtering criteria. According to their findings, the most important indicators of the source areas are altitude, land use, geology, slope, curvature, and flow accumulation. Similarly, Kang et al. (2017), suggested debris flow source area criterion based on the geomorphological characteristics, using an Artificial Neural Network model with a modified threshold for establishing the relationship between slope and upslope contributing area. Crowley et al. (2003) used hyperspectral imagery to detect freshly exposed source areas based on their higher oxide content than the surrounding ground. Liu et al. (2020) dealt with predicting debris flow triggering thresholds on large scales considering geological and topographical variations of effective rainfall. They have also underlined that zones with more complex terrain, thicker soil, and higher sand content would be more prone to initiation of debris flows. Our previous experience (Marjanović et al. 2016; Đurić et al. 2017) involved expert-driven delineation of source areas based on the shape of the fresh debris flow footprints, using multi-resolution and multi-temporal satellite imagery and field data. Full implementation is more common at local, site-specific scales, where the source area and runout distance are known, and back-analysis is performed to establish the triggering conditions (Krušić et al. 2017b; Krušić et al. 2018; Baggio et al. 2021). At regional scales, Zou et al. (2019) reported a method based on a hydrological response unit (a subsection of a regional watershed basin) to assess the debris flow risk on a river basin level. Another important aspect is the differentiation between debris flow and debris flood by their level of fluidization due to water contents, i.e., the amount of water accumulated from recharge (rainfall, snow thaw, etc.). Ilinca (2021) has discovered that a specific range of values of topographic parameters, such as Melton number, basin relief ratio, basin length, basin area, fan slope, and source area ratio control which of those two types will develop.

This work, inspired by some of the abovementioned research, tends to use a simple combination of GIS-based data-driven analysis and expert-driven calibration to outline the source area, and subsequently, simulate the debris flows initiated from those source areas, thereby imposing hazard to the exposed road, which is quantified by the outcoming velocity, and the debris hight.

2 Materials and Methods

Regional scale assessment is commonly operated using the worldwide available raster datasets, with resolutions ranging from 30 to 250 m, which are mainly open and free data. Implementation of the flow simulation can be done using several ways and tools, from commercial to open source, which means that the analyses are becoming more available with such policies (open data and software).

2.1 Data Inputs

Data needed for the two-fold flow analysis (i + ii) included various environmental features, primarily topographic and soil properties. For delineating the source areas, i.e., task (i), a Digital Elevation Model (DEM), DEM-derived slope and curvature, and topsoil thickness were used as inputs, as suggested in Blahut et al. (2010) and Liu et al. (2020). In addition, the expert-driven landslide inventory (Fig. 2) was used to supplement this task (i). For fulfilling the second task (ii) the same 12.5 m DEM was used, as well as the map of delineated source areas (Fig. 3), which is the outcome of (i). Table 1 summarizes the data sources and other basic information.

Laboratory data inter-alia included results from 45 soil direct shear tests (performed in the investigations for the road construction), wherein residual and peak shear strength were determined. They were sampled from boreholes spread around the IAOI. Source areas encompass the first several meters of material, so it is likely that most of these tests, involving mainly the topsoil and weathered schists, can directly apply to source areas. Cohesion and internal friction angle were in the range $c = 0–20$ kPa and $\varphi = 13–34°$, respectively, as well as the range of saturated unit weight $\gamma = 19–22$ kN/m^3 which was useful for estimating the range of input values for flow material mechanical properties (Table 2). Since there was no recent debris flow reported within the IAOI, even though the area is historically well known for debris flood events (witnessed by numerous anti-flood barriers in the local gullies), lab result extrapolation was the only option to calibrate the flow model.

2.2 Methodology

Task (i) firstly required standard GIS raster processing (cropping the rasters to the AOI domain, projection harmonization, etc.), followed by a raster calculator operation which

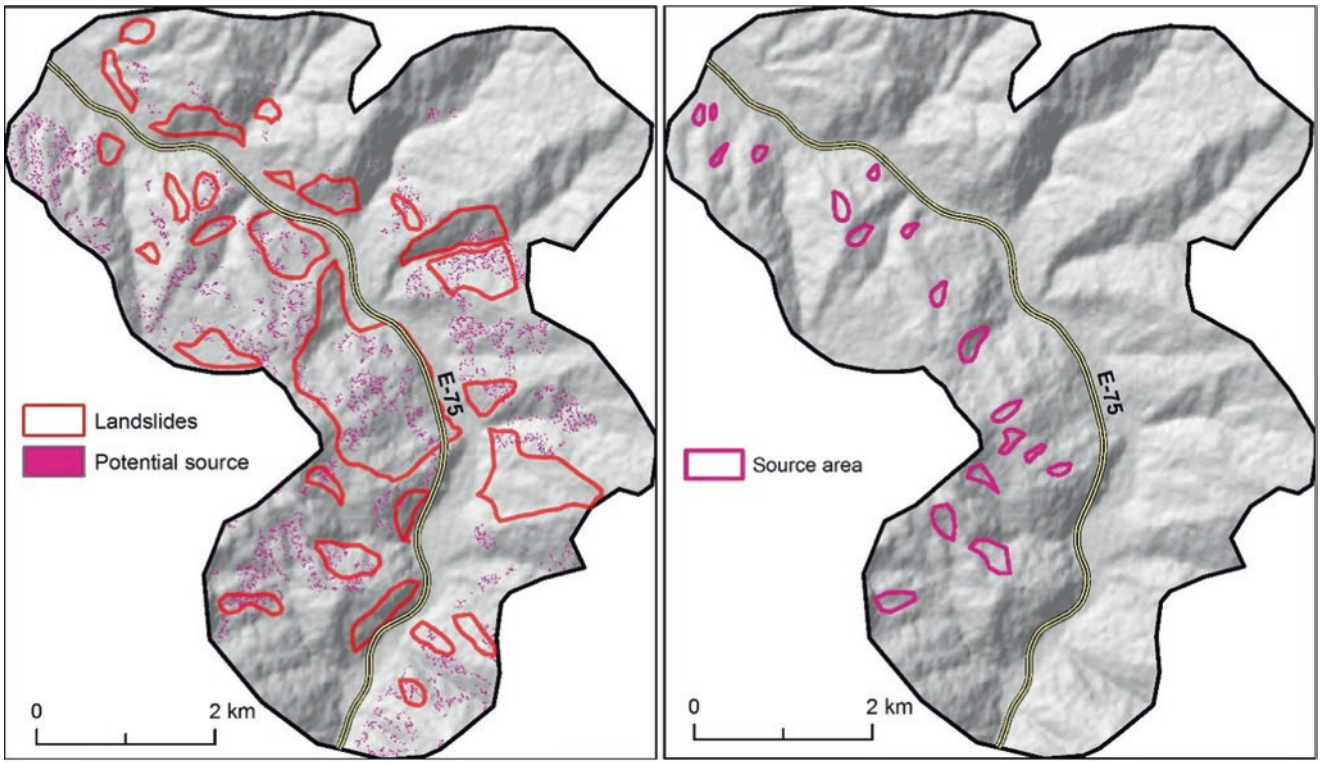

Fig. 3 Intermediate model of potential source areas with landslide inventory overlay (left) and final source area map (right)

Table 1 Input data types and sources

Input data	Data source	Resolution	Purpose
DEM	ALOS PALSAR mission	12.5 m	Task (i) source area delineation and task (ii) terrain surface for placing simulations
Slope	DEM-derived	12.5 m	Task (i) source area delineation
Curvature	DEM-derived	12.5 m	Task (i) source area delineation
Depth to bedrock	ISRIC world soil information	250 m	Task (i) source area delineation
Landslide inventory	Marković et al. (1995)	NA	Task (i) source area calibration
Source areas	From (i)	12.5 m	Task (ii) flow initiation points
Mechanical properties	From associated lab works	NA	Task (ii) input parameters for flowing material
Road section	Public Enterprise roads of Serbia	NA	Task (iii) exposure assessment

Table 2 Combinations of input parameters of the flow model

Combin. No.	μ	ξ (ms^{-2})	γ (kN/m^3)	Combin. No.	μ	ξ (ms^{-2})	γ (kN/m^3)
1	0.1	200	2200	12	0.35	200	1900
2	0.15	200	2200	13	0.1	500	2200
3	0.2	200	2200	14	0.15	500	2200
4	0.25	200	2200	15	0.2	500	2200
5	0.3	200	2200	16	0.25	500	2200
6	0.35	200	2200	17	0.3	500	2200
7	0.1	200	1900	18	0.35	500	2200
8	0.15	200	1900	19	0.1	500	1900
9	0.2	200	1900	20	0.15	500	1900
10	0.25	200	1900	21	0.2	500	1900
11	0.3	200	1900	22	0.25	500	1900
12	0.35	200	1900	23	0.3	500	1900

was used to narrow down the search for delineating optimal locations as source areas within IAOI (Fig. 3), using the following condition: (680 m > DEM > 400 m) & (23° > Slope > 13°) & (2.8 m > Depth to bedrock>2.4 m) & (−0.1 > Curvature> − 0.8). This condition implies that higher altitudes with moderately steep slopes and moderate topsoil thickness and concave relief are preferable. In the cases where these potential source areas coincided with the main scarp zone of the historical landslides, the local upstream micro basin (outlining the local ridge lines) is manually contoured as a source area (Fig. 3).

The second task was to simulate the flow over available terrain surface (DEM) using delineated source areas and estimated mechanical properties, friction coefficient $\mu = tg\varphi$, unit weight γ, and viscose-turbulence drag coefficient ξ. Table 2 summarizes all tested combinations of input parameters, which is in accordance with lab results and common practice (Sosio et al. 2008). The implemented frictional resistance bulk flow model was the Voellmy-fluid friction model, implemented through RAMMS: DEBRISFLOW software (Christen et al. 2012). There was no available local hydrographic data to model the saturation condition realistically. The same applies to the level of entrainment due to erosion of the flow itself. In effect, the modelling was performed solely by calibrating frictional properties under saturated conditions assuming that there was no entrainment erosion. This is on the safe side since such an approach is more conservative (volume is enlarged by entrainment, the mass is densified, while conditions do not need to be necessarily saturated). The output of the model includes the runout of the bulk flow (when the resistance forces in the flow overpower the kinetic), its velocity distribution along the way, as well as its debris deposit height in raster format, which are all convenient for quantifying the level of hazard and exposure to a road segment that sits below designated source areas.

The final task (iii) was to assess the hazard exposure along assigned road sections in vector format, obtained from the official road management service. The resulting distribution of relevant features (runout, velocity, heights) of the flows that have their runouts reaching beyond the road line is performed by segmenting the road vector into 50 m sections and performing statistical analysis of feature values (statistics of pixels of resulting rasters) that intersect the road in a GIS environment.

3 Results and Discussion

The outlining of the source areas resulted in 18 designated areas of various sizes (7–100 ha), hosted primarily in schists (12), but also in limestone (4) and dacite (2). For the convenience of the analysis, simulations were run according to these three groups, assuming that flows hosted in the same material will behave the same in the simulation. Vegetation and other land-use features were not considered. As indicated, local hydrograph information was not available, so the saturation threshold under extreme conditions was taken from the research on general landslide thresholds experienced in Serbia in 2014 (Marjanović et al. 2018).

Each source area was geometrically defined (length, width, depth to bedrock, natural slope angle). The natural slope angle was used as a control to define the range of friction values that are used for defining combinations in Table 2. The average natural slope angle equals 13 ± 3° which can be theoretically assumed as the upper friction angle value $\varphi = 13°$ ($\mu = 0.23$). This is justified given that in direct shear lab tests, the residual angle lower bounds were exactly 13°. Since there was no back-analysis example available, it was not possible to evaluate the best model, but the most hazardous one in terms of runout, velocity and deposited height. The worst-case scenario included the following input combination: $\mu = 0.1$, $\xi = 500$ ms^{-2}, $\gamma = 22$ kN/m^3. Higher values of solid friction coefficient increase the friction with the ground and within the material itself, while higher values of viscose friction do the opposite, and too high values, e.g., 1000 ms^{-2} or higher that are rarely used in practice (Mikoš and Bezak 2021), might lead to over-fluidization and switch to debris flood scenario, which is considered as a different phenomenon that does not correspond to the methodology used for designating source areas, adopted soil saturation principle, and the involved bulk fluid model (mixed phases, while in floods fluid phase is more dominant). The worst-case scenario (Fig. 4) included debris runout distances between 0.5 and 2.5 km, maximum velocities of 27.3 m/s, and deposit heights up to 21.8 m. Such events were not recorded within the wider area, but in climate-changing conditions, they might become realistic. As indicated before, it is difficult to define a realistic model without a back-analysis option, therefore, a trial and error using 200 and 500 ms^{-2} was used in various combinations with other parameters (Table 2).

Further analysis involved exposure assessment for the worst-case scenario. The level of fluidization in the worst case was such that debris flows of almost all source areas have reached the road line and beyond. However, not all of them introduced the same hazard level, as some would flow in too slowly to the road to leave any effect on the construction, while some did not create sufficient volume to reach significant height (road embankment height is 5–28 m). To identify the actual hotspots and sections of the road that are most exposed, a segmented road vector was introduced, and per each of its 313 sections (all 50 m long) the maximum value of the overlapping raster (both, velocity and height) was calculated (Fig. 5).

The hazard along the exposed road is divided into five classes, guided by the Natural Breaks Intervals of respective

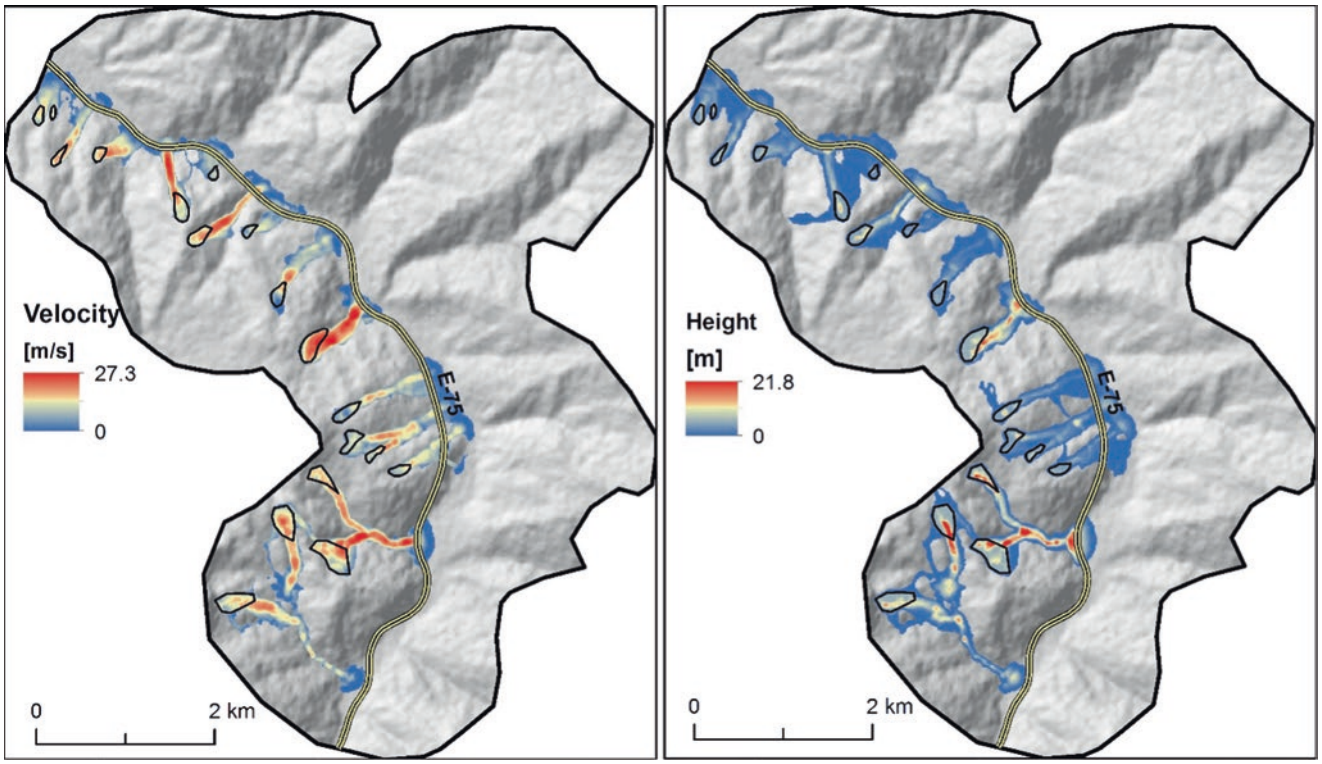

Fig. 4 The worst-case model simulation per velocity (left) and deposit height (right)

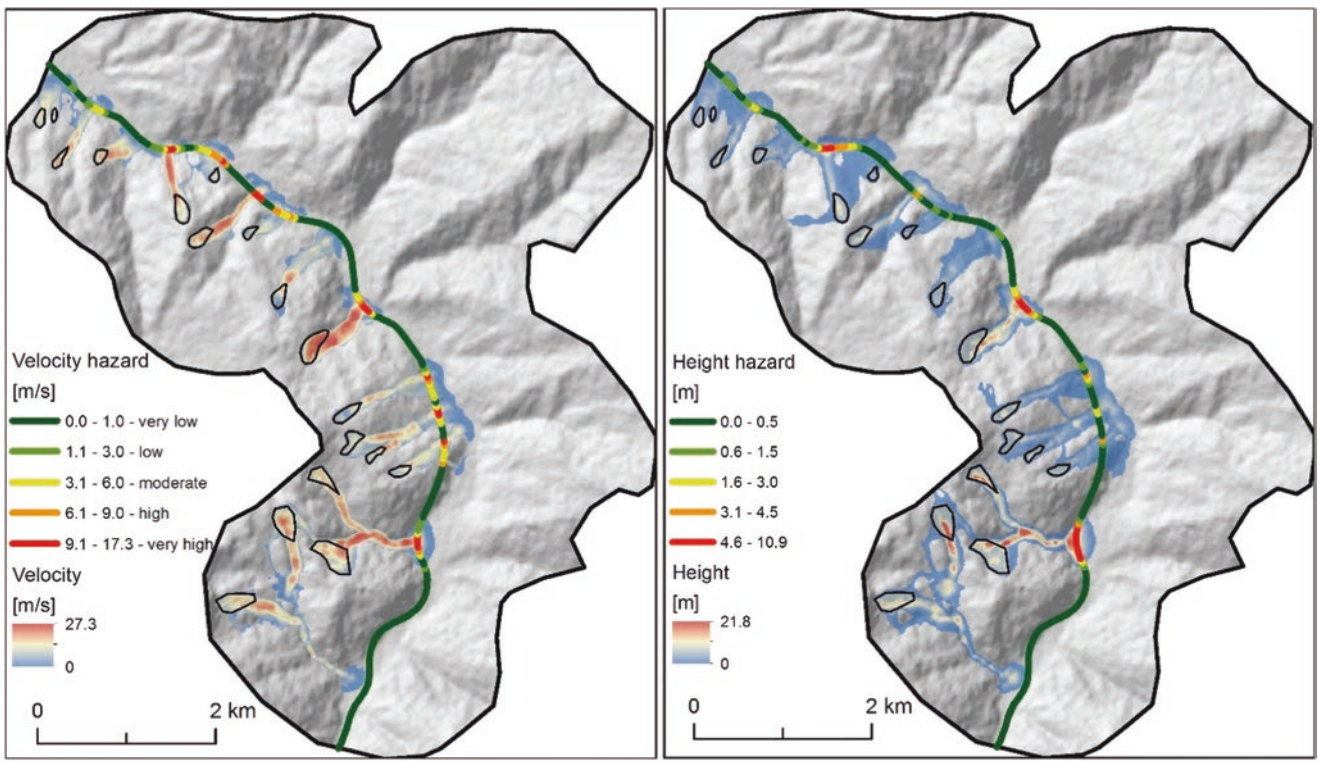

Fig. 5 Road exposure to hazard due to velocity (left) and deposit height (right)

values (maximum height and maximum velocity), ranging from very low hazard, low hazard, moderate, high, and very high class. The intervals are further adjusted according to the actual conditions. For instance, a simulated deposit height that is nearly reaching the minimal embankment height (5 m) must be considered as a very high hazard class, so all heights over 4.5 m were classified as such. Similarly, the flux capacities of road culverts were used for adjusting the velocity hazard interval. Assuming culvert diameter R = 2 m and length L = 30 m (double track full profile highway), a flux of 90 m^3/s is obtained. When back-calculated, the flow velocity that corresponds to such flux is 9 m/s (assuming that the flow channel and culvert cross-sections are equal), which was taken as the lower bond for the very high hazard class. If the culvert to channel cross-sectional area is for example 2, the required velocity (high hazard) is decreased to 6 m/s and so forth (for moderate, low and very low hazard).

The hazard exposure model outlines the areas that are highly affected as bright red stretches of the road versus dark green stretches which are hazard-free (Fig. 5). Along the road route which is 15.6 km long, very high hazard due to the flow deposit height occupies 4.5% (700 m), high hazard 3.2% (500 m), moderate hazard 3.8%, (600 m), low hazard 8.3% (1300 m), and very low hazard 80.2% (12,500 m) (Fig. 6). There are three very high hazard instances along the route. Among them, the longest continuous very high-hazard stretch of the road equals 400 m. Very high hazard due to flow velocity occupies 5.1% (800 m), high hazard 3.8% (600 m), moderate hazard 8.6% (1350 m), low hazard 4.8% (750 m), and very low 77.7% (12,100 m). Along the route, here are eight very high-hazard instances due to velocity. The longest stretch of the road affected by the very high hazard due to velocity is 150 m. The most adverse scenario is the spatial overlap of velocity- and height-related very high-hazard segments. Such overlap is found along 1.5% (400 m) of the road route.

4 Conclusion

In this work, a regional scale debris flow hazard assessment was demonstrated in a case study in Southern Serbia, covering about 37 km^2 of hilly-mountainous landscape, with a relatively simple geological setting, but intensively tectonized and weathered rock. The recently constructed high-road, that runs through the valley was in the focus, i.e., its 15.6 km long subsample. It was necessary to demonstrate at a specific design stage how the road is potentially affected by hazardous phenomena, the debris flows in this case. The approach involved three tasks (i) delineating theoretical source areas (ii) running simulations with calibrated parameters, and (iii) quantifying hazard exposure along the road route. In total, 18 source areas were used for running 24 simulations, based on 24 combinations of input flow friction parameters. It has been shown that there are several relatively large hot spots. The approach shows that it is possible to micro-locate and quantify the hazardous phenomenon, by simulating its impact velocity and deposit height at road level. In addition, it was possible to discern parts of the road route which are most affected by one of the two hazards, or both acting simultaneously. This implicates the possibility of planning the maintenance and other budgeting aspects, e.g., remediation, more precisely, by knowing the length or surface of the road affected and approximate remediation costs common in domestic practice per area or length (Radić et al. 2018). Further research can be directed toward fitting friction parameters per each source area separately, appending additional useful parameters, such as stress and pressure, and furthering the analysis from debris flow exposure to debris flow risk by using available traffic frequency data. It is important to demonstrate such tools, which can be used by road managing enterprises not only for planning budgets dedicated to existing roads but for hazard prevention prior to construction of the new corridors. The approach allows for avoiding or

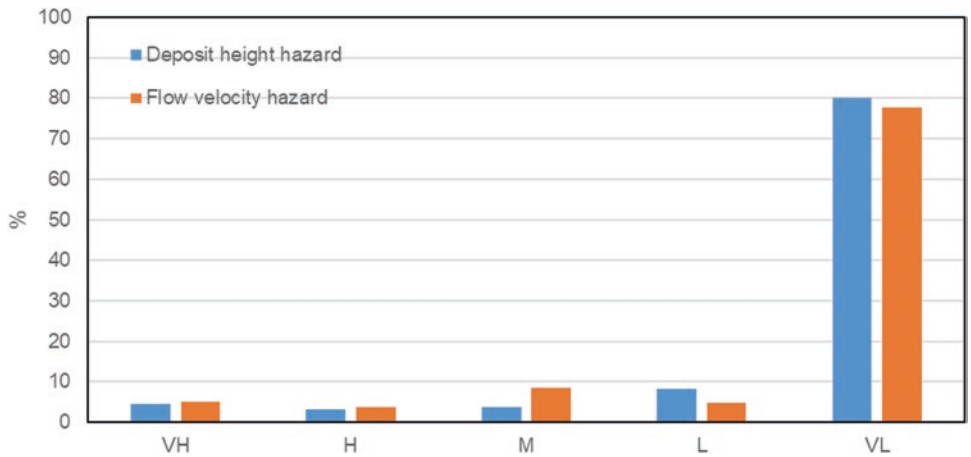

Fig. 6 Distribution of hazard classes (Very High—VH, High—H, Moderate—M, Low—L, Very Low—VL) along the exposed road

reducing the number of road intersections with high and very high hazard zones at regional scales, which is convenient for early road design stages, and should become a common practice, especially in developing societies.

References

Abomasov B, Skempas M, Milenković S, Radovanović J, Marjanović M (2022) Highway construction in fossil landslides zones—lessons learned from the Grdelica gorge, Serbia. In: Peranić J et al (eds) Landslide Modelling & Applications. Proceedings of the 5th ReSyLAB, Rieka, Croatia. Univ.of Rijeka, Faculty of Civil Engineering, Univ. of Zagreb, Faculty of Mining, Geology and Petroleum Engineering, Rijeka, pp 237–242

Baggio T, Mergili M, D'Agostino V (2021) Advances in the simulation of debris flow erosion: the case study of the Rio Gere (Italy) event of the 4th august 2017. Geomorphology 381:107664

Blahut J, van Westen CJ, Sterlacchini S (2010) Analysis of landslide inventories for accurate prediction of debris-flow source areas. Geomorphology 119:36–51

Christen M, Bühler Y, Bartelt P, Leine R, Glover J, Schweizer A, Graf C, McArdell BW, Gerber W, Deubelbeiss Y, Feistl T, Volkwein A (2012) Integral hazard management using a unified software environment: numerical simulation tool "RAMMS" for gravitational natural hazards. In: Koboltschnig G, Hübl J, Braun J (eds) 12th congress INTERPRAEVENT, 23–26 April 2012 Grenoble—France. Proceedings, vol 1. International Research Society Interpraevent, Klagenfurt, pp 77–86

Crowley JK, Hubbard BE, Mars JC (2003) Analysis of potential debris flow source areas on Mount Shasta, California, by using airborne and satellite remote sensing data. Remote Sens Environ 87:345–358

Đurić D, Mladenović A, Pešić-Georgiadis M, Marjanović M, Abolmasov B (2017) Using multiresolution and multitemporal satellite data for post disaster landslide inventory in the Republic of Serbia. Landslides 14(4):1467–1482. https://doi.org/10.1007/s10346-017-0847-2

Guzzetti F, Mondini AC, Cardinali M, Fiorucci F, Santangelo M, Chang KT (2012) Landslide inventory maps: new tools for an old problem. Earth Sci Rev 112:42–66

Ilinca V (2021) Using morphometrics to distinguish between debris flow, debris flood and flood (southern Carpathians, Romania). Catena 197:104982

Kang S, Lee SR, Vasu NN, Park JY, Lee DH (2017) Development of an initiation criterion for debris flows based on local topographic properties and applicability assessment at a regional scale. Eng Geol 230(29):64–76

Krušić J, Marjanović M, Samardžić-Petrović M, Abolmasov B, Andrejev K, Miladinović A (2017a) Comparison of expert, deterministic and machine learning approach for landslide susceptibility assessment in Ljubovija municipality, Serbia. Geofizika 34(2):251–273. https://doi.org/10.15233/gfz.2017.34.15

Krušić J, Andrejev K, Abolmasov B, Marjanović M (2017b) Preliminary results of the Selanac debris flow modelling in RAMMS - a case study. Proceeding of the 3rd ReSyLAB. Ljubljana, Slovenia, 11. - 13. Oct. 2017, Geological Survey of Slovenia, vol. 1, pp 95–100

Krušić J, Samardžić-Petrović M, Marjanović M, Abolmasov B, Miljković S (2018) Preliminary results of numerical modelling of debris flow - case study Leva reka, Serbia. Special Issue: XVI DECGE 2018: Proceedings of the 16th Danube-European Conference - Geotechnical hazards and risks: Experiences and practices, Skopje, Macedonia, June 6–9, 2018, Ernst & Sohn Verlag für Architektur und technische Wissenschaften, vol. 2, pp 707–712

Liu S, Wei L, Hu K (2020) Topographical and geological variation of effective rainfall for debris-flow occurrence from a large-scale perspective. Geomorphology 358:107134

Marjanović M, Vulović N, Đurić U, Božanić B (2016) Coupling field and satellite data for an event-based landslide inventory. Proceedings of the 12th International Symposium on Landslides, CRC Press/Associazione Geotecnica Italiana, Naples, Italy, June 12–19, 2016, pp 1361–1366

Marjanović M, Krautblatter M, Abolmasov B, Đurić U, Sandić C, Nikolić V (2018) The rainfall-induced landsliding in Western Serbia: a temporal prediction approach using decision tree technique. Eng Geol 232:147–159. https://doi.org/10.1016/j.enggeo.2017.11.021

Marković M, Pavlović R, Radovanović S, Glavatović B (1995) Nestabilnost padina, neotektonska i seizmička aktivnost Grdeličke klisure (In Serbian). Ann Géologiques De La Péninsule Balkanique 59(1):379–404

Mikoš M, Bezak N (2021) Debris flow modelling using RAMMS model in the alpine environment with focus on the model parameters and Main characteristics. Front Earth Sci 8:605061. https://doi.org/10.3389/feart.2020.605061

Radić Z, Đurić U, Radić Z (2018) Examples of landslide stabilization costs on the road infrastructure. Proceedings of the third Serbian road Congress, Belgrade, Serbia, June 14–15, 2018, pp 279–285

Salvetti A, Antonucci A, Zaffalon M (2008) Spatially Distributed Identification of Debris Flow Source Areas by Credal Networks. Proceedings of the International Congress on Environmental Modelling and Software iEMSs 2008, Barcelona, Spain, July 7–10, 2008, Vol. 1, pp 380–387

Sosio R, Crosta GB, Hungr O (2008) Complete dynamic modeling calibration for the Thurwieser rock avalanche (Italian Central Alps). Eng Geol 100:11–26

Zou Q, Cui P, He J, Lei Y, Li S (2019) Regional risk assessment of debris flows in China—an HRU-based approach. Geomorphology 340:84–102

Introducing Japanese Landslide Warning and Evacuation System to Sri Lanka: Field Survey of Social Aspect in the Arayanake Area

Kumiko Fujita

Abstract

The central highland in Sri Lanka has a landslide-prone geo-hydrological condition. In addition, Sri Lanka has extreme rainfalls in two monsoon seasons, and most of the landslides occur during two monsoon seasons. Landslides in the central highland had been isolated events. However, the area has been developed for agriculture and human settlements, a series of landslides occurred in the mid-1980s. Since the topography, such as mountains with steep slopes and weather, such as high precipitation, are similar in Japan and Sri Lanka, similar landslide phenomena have been seen. One of the common landslide phenomena is rain-induced rapid and long-travelling landslides (RRLL). Landslide disaster risk reduction technologies have recently been developed in Sri Lanka, and foreign technologies have been introduced. Early warning and evacuation using a hazard map is a major system for landslide disaster risk reduction both in Japan and Sri Lanka. Japan has already developed and used the early warning and evacuation system using hazard maps. Since the system has been developed based on Japan's socio-economic background, it is used successfully in Japan. Thus, when this Japanese technology is used in Sri Lanka, in addition to the engineers' availability to master technologies, local people's availability to accept the technology is also examined. In this research, the social background for introducing Japan's early warning system in Sri Lanka is analyzed based on the field survey at Arayanake. The questionnaire survey and interview were implemented in January 2023, and there were 50 respondents. The survey showed some essential conditions to be improved for the successful warning and evacuation.

Keywords

Sri Lanka · Landslide · Early warning · Evacuation · Hazard map · Information system

1 Introduction

Though similar landslide phenomena are seen in different countries, the landslide disaster risk reduction technology in one country may not be useful for other countries because of the differences in social background. Early warning and evacuation systems using hazard maps have been developed and used in Japan for landslide disaster risk reduction. It is reviewed since there are some essential conditions for effective use.

1.1 Similarity of the Natural Conditions Which Are the Causes of Landslides

The topography of the mountain area is similar in Japan and Sri Lanka. Japan has archipelagos and high steep mountains in the center of the main island. Most precipitation is brought during rainy seasons, and heavy rain-triggered landslides frequently occur in mountain areas. In Sri Lanka, the central part of the island's southern half is a mountainous area with steep slopes, and a large part of the landslide-prone area is covered with a metamorphosed layer of thick weathered gneiss (Konagai et al., 2023). Most of the landslides occur during extreme rainfalls in two monsoon seasons. The rainfall and geological conditions are the major triggers of landslides. Because of the similarity, similar landslide phenomena are seen in Japan and Sri Lanka.

K. Fujita (✉)
International Consortium on Landslides, Kyoto, Japan

B. Abolmasov et al. (eds.), *Progress in Landslide Research and Technology, Volume 3 Issue 1, 2024*, Progress in Landslide Research and Technology, https://doi.org/10.1007/978-3-031-55120-8_16

1.2 Different Social Backgrounds

For successful technology transfer, the social differences between both countries need to be recognized. For example, the mountain surrounding environment is different. The mountain in Sri Lanka is covered with farmland. However, the mountain in Japan is covered with forest. In addition, the population and age category in the mountain area is also different. Young people live in mountain areas in Sri Lanka, and the population is increasing. On the other hand, old people live in mountain areas in Japan, and the population is decreasing (Table 1; Fujita 2022). Since landslides in Japan have triggered frequent disasters, the old people in mountainous areas have experienced landslides and know the timing and safe route to evacuate, and the research for disaster risk reduction has been developed for a long time. The information system for evacuation is well developed, hazard maps are available, and disaster education is provided to the local people.

1.3 Necessary Social Background for Effective Early Warning and Evacuation in Japan

Based on accurate regional rainfall forecasting, early warning is effectively used under integrated management in landslide-prone areas in Japan. Following are essential conditions for local people to evacuate (Fujita and Shaw 2019).

1. Ability to interpret hazard maps by local people.
   Japan's map education starts from elementary school. Therefore, the hazard map is well understood. In addition, designated evacuation places are also on the map. However, map education in Sri Lanka is not compulsory since geography is an elective subject for senior secondary level from 14 to 15 years old (Kumara and Ananda 2006). Therefore, it is necessary to know whether the local people in the selected area can interpret the map.
2. Effective information system
   Since landslides occurred frequently in Japan, the information system in mountain areas has been developed. There are several information devices, wireless devices, fixed and mobile phones, etc. The network has also been developed between national and local governments, fire stations, firefighters, and local people.
3. External help for evacuation and after evacuation
   External help is also expected when they evacuate. In Japan, if evacuees can reach the designated evacuation places, they can receive necessities such as water, food, and blankets provided by various organizations and individuals such as central or local government, private companies, volunteers, etc.

Table 1 Socio-economic differences in mountain areas in Japan and Sri Lanka

	Japan	Sri Lanka
Land use	Already developed as a forest	Developing as farmland
Population	Decreasing	Increasing (newcomers)
Age category	Old	Young

2 Basic Information of Selected Area: Arayanake

Arayanake, Kegalle District (Fig. 1) was selected as the survey area. Rain-induced Rapid and Long-travelling Landslide (RRLL) occurred in Arayanake on 17 May 2016, due to the heavy rainfall from 15 May 2016. It caused 31 deaths and 96 missing persons (Handa et al. 2018). Small-scale family farming, especially tea farming, is common in this area.

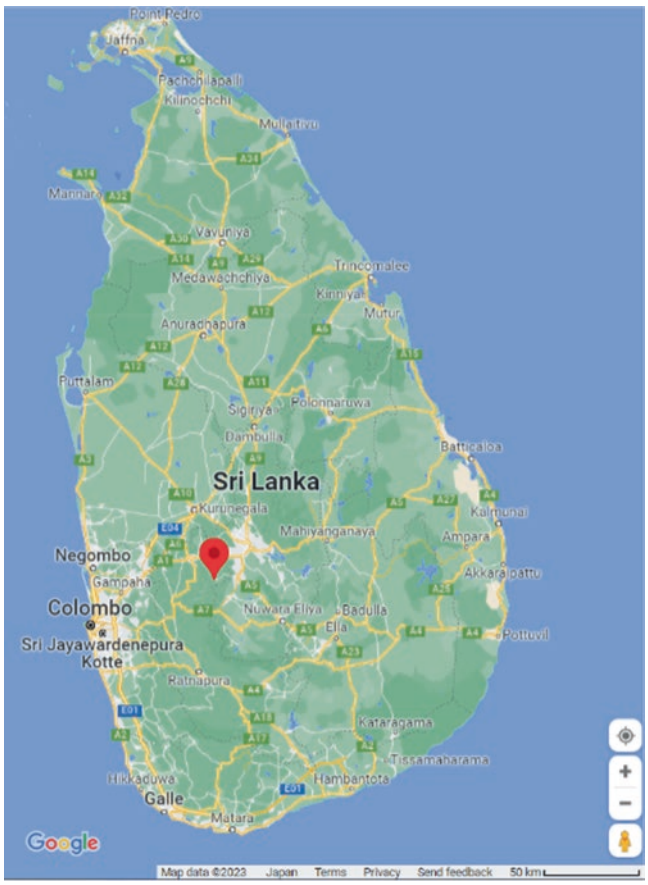

Fig. 1 Arayanake, Kegalle District

2.1 Questionnaire Survey

The social background for introducing Japan's early warning system in Sri Lanka is analyzed based on the literature review and field survey. The questionnaire survey was conducted near the Arayanake landslide area to know the local people's perception of landslide disaster risk reduction. The National Building Research Organisation (NBRO) provided the map of the river catchment in the Arayanake Landslide area (Fig. 2). The Red zone is the landslide area that occurred in 2016. Black spots are the buildings, and most of them are houses.

Based on the NBRO-provided map, two areas for the survey were selected, near the main road and mountain area. The questionnaire survey was conducted at 50 houses. All of them are Sinhalese. There are five categories of questions as follows:

1. Demographic information: Q1-11
2. Livelihood: Q12–14
3. Experience of landslide: Q15
4. Hazard map and early warning: Q16-29
5. External help: Q30-36

There were 50 respondents in the selected area, 16 males and 34 females (Fig. 3). The questionnaire survey and interview were conducted during the daytime at each respondent's house. The major age group is from 30 to 60. Most of them live in their own houses. 21 people out of 50 respondents work in their tea garden (Fig. 4) next to /near their houses. Since there was a landslide in May 2016, it was asked if they evacuated, and 49 respondents said yes.

2.2 Ability to Interpret Hazard Map By Local People

The 1:50,000 landslide hazard maps are available for the central highland (Bandara and Jayasingha 2018). Several maps are seen in the survey area (Fig. 5a and b). Figure 5a was put on the wall of a community center after the landslide in 2016. A few villagers at the community center said they realized they lived in a landslide hazard area after they saw the map.

Based on the literature review, it is said that map education is available. However, it cannot be said that they can interpret maps. As Fig. 6 shows, 21 respondents (42%) said they had never seen a hazard map in their living area. Figure 7

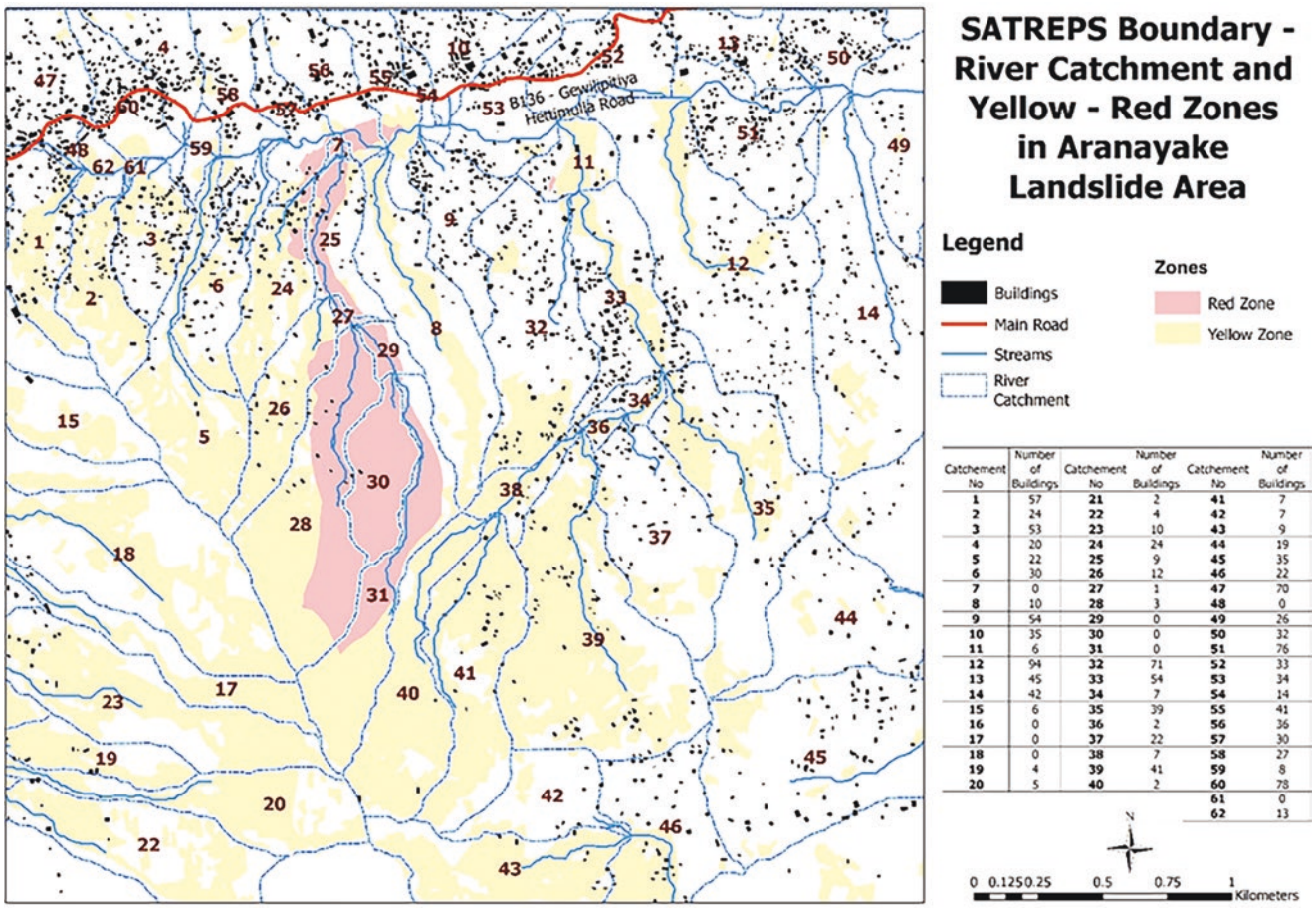

Catchement No	Number of Buildings	Catchement No	Number of Buildings	Catchement No	Number of Buildings
1	57	21	2	41	7
2	24	22	4	42	7
3	53	23	10	43	9
4	20	24	24	44	19
5	22	25	9	45	35
6	30	26	12	46	22
7	0	27	1	47	70
8	10	28	3	48	0
9	54	29	0	49	26
10	35	30	0	50	32
11	6	31	0	51	76
12	94	32	71	52	33
13	45	33	54	53	34
14	42	34	7	54	14
15	6	35	39	55	41
16	0	36	2	56	36
17	0	37	22	57	30
18	0	38	7	58	27
19	4	39	41	59	8
20	5	40	2	60	78
				61	0
				62	13

Fig. 2 Arayanake Landslide Area

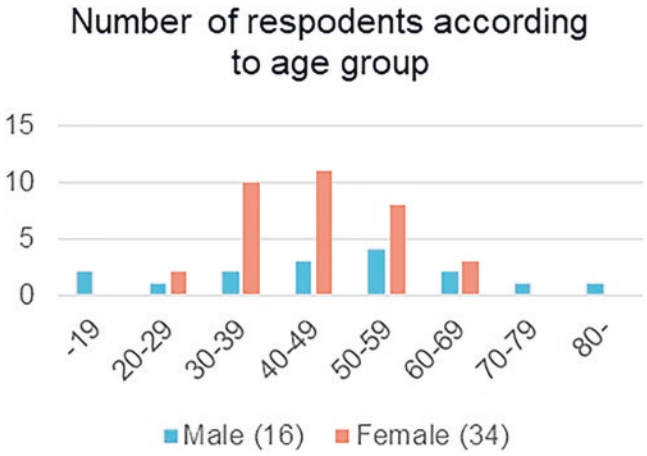

Fig. 3 Basic information of respondents

Fig. 4 Occupation of the respondents

shows where the questionnaire survey was conducted, colored blue if respondents have seen a hazard map and colored red if respondents have never seen a hazard map. There is no particular area which shows a high rate of map availability. Therefore, it is necessary to clarify whether there are hazard maps in each community.

2.3 Reliable/Available Information System for Warning and Evacuation

Fourty nine persons out of 50 respondents experienced a landslide in May 2016, six persons (12%) out of 49 respondents received a warning, and 43 persons (88%) did not receive the warning (Fig. 8). However, half of the respon-

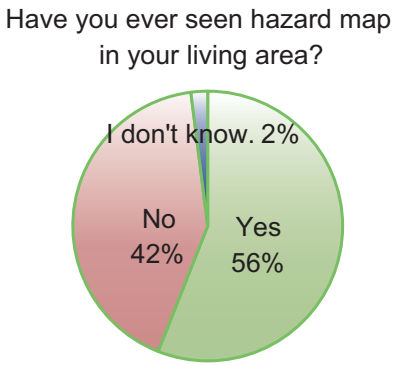

Fig. 6 Hazard map availability

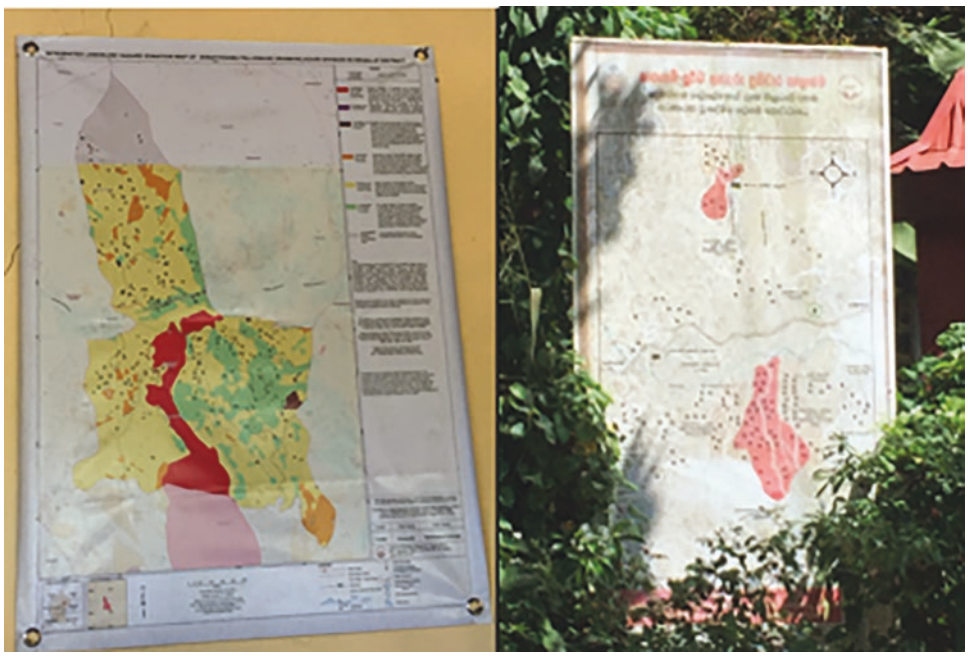

Fig. 5 (**a**) Left: Hazard map -Community center near Grama Niladhari Office (**b**) Right: Landslide early warning response plan -near Hathgampola Maha Vidyalaya (School)

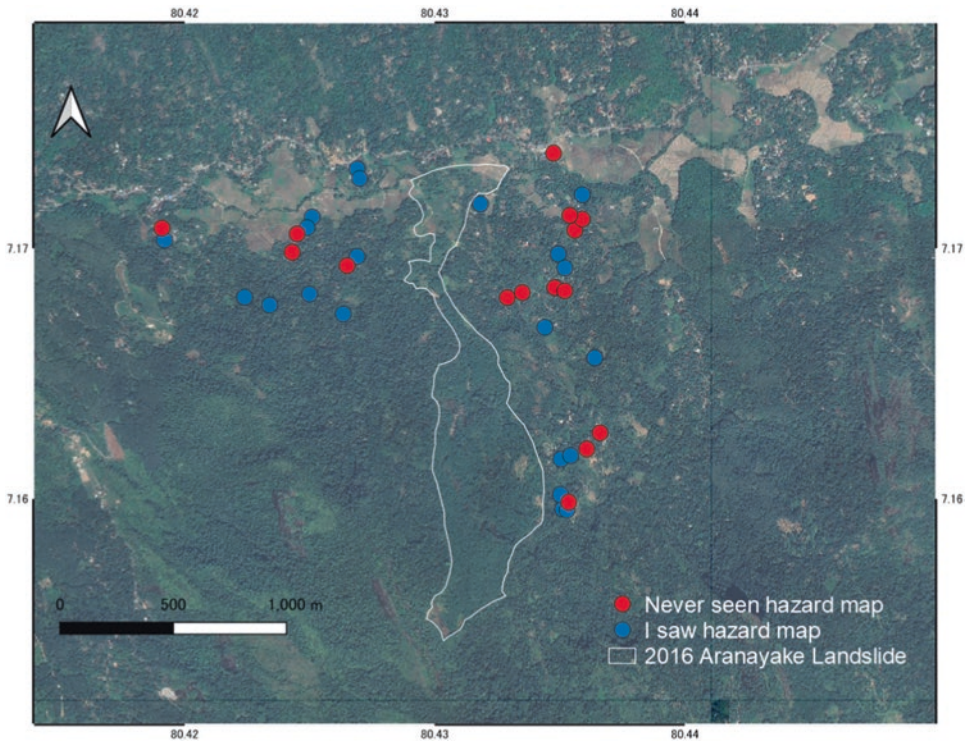

Fig. 7 Location of the respondents' houses: respondents who have seen the hazard map (blue points) or not (red points)

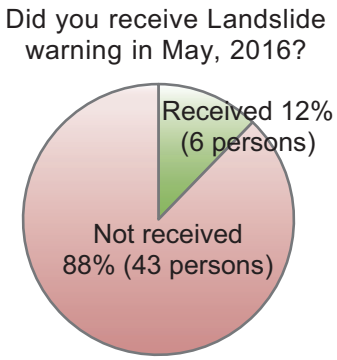

Fig. 8 Warning received / not received in case of landslide in May 2016

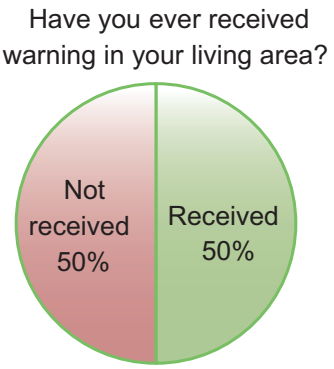

Fig. 9 Experience of receiving landslide warning

dents could receive early warning until now (Fig. 9). Figure 10 shows the locations which respondents have received a warning (blue points) or not (red points). There is no particular area which shows a high rate of warning reception. Even near the main road, some of them cannot receive a warning, and even in the hilly area, some of them can receive a warning. Since receiving early warning is important for evacuation, it is necessary to know more about the information system.

Getting information through many devices is preferred since one may not be enough in a disaster. For example, mobile phones may not be used during disasters, and other devices or communication systems may be effective. Therefore, available information devices are asked. As Fig. 11 shows, most respondents receive information through TV. Though the number who get daily information through mobile phones is 34, all of them have mobile phones. Mobile phones are useful not only for getting information but also for sharing information. Therefore, the use of a mobile phone is expected to be used during a disaster.

Since the use of mobile phones during a disaster is expected, the usable function of mobile phones is asked. As Fig. 12 shows, all of them use the phone function, and 41 use SMS, such as WhatsApp, Instagram, and Facebook. It seems sharing information during landslide disasters is possible through mobile phones. However, there is the issue of signal. Respondents, especially those who live on mountain slopes, said the signal is weak, and they cannot use mobile phones at home. They need to go out and find a place to use mobile

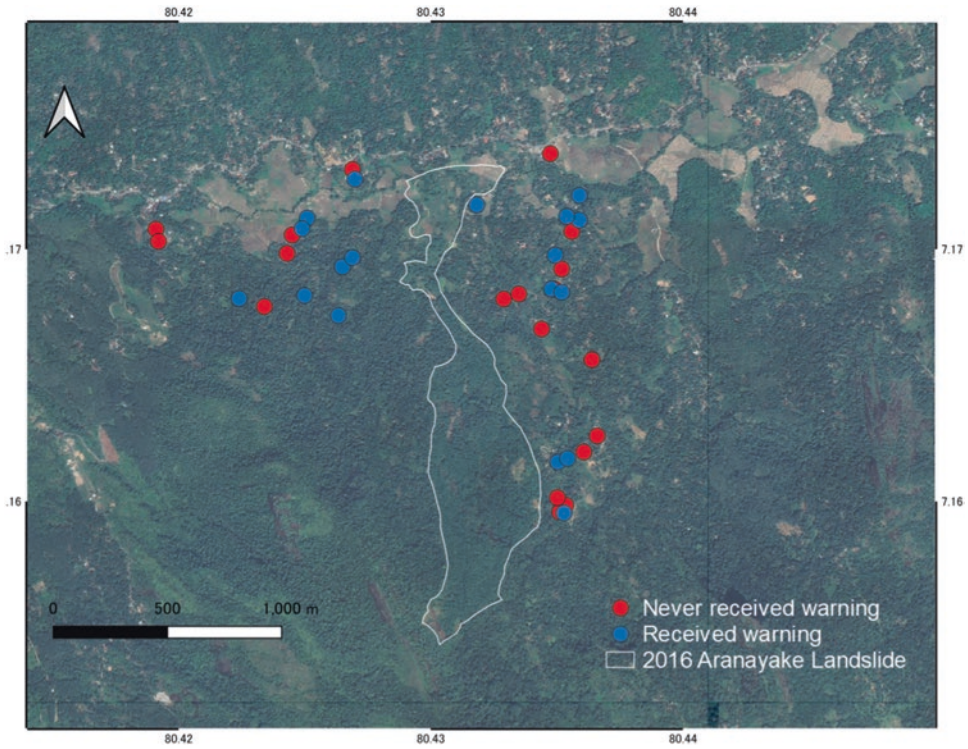

Fig. 10 Location of the respondents' houses: respondents who have received the warning (blue points) or not (red points)

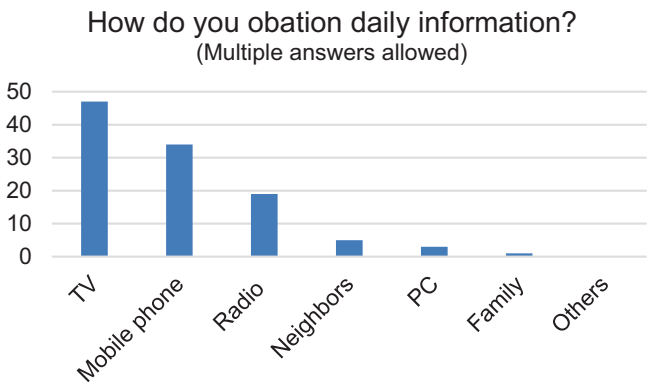

Fig. 11 Source of daily information

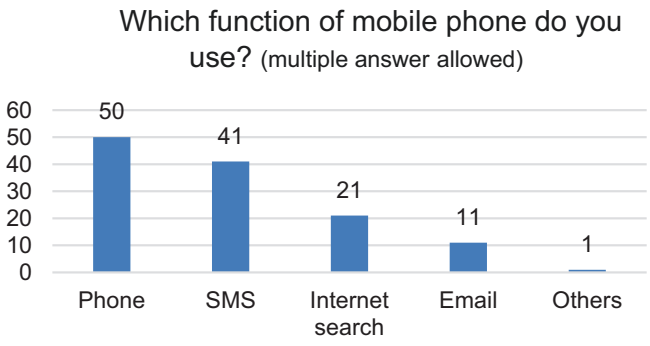

Fig. 12 Using the function of a mobile phone

phones. Though they cannot use mobile phones at home, there is a good community network, so if someone can receive emergency information in the community, they visit neighbors to convey information. In addition, the mobile phone is also expected to be used in the farm sector. However, poor internet literacy and accessibility are the issues (De Silva Lasanthi et al. 2012).

Then, the necessary information for evacuation is asked to know their needs for evacuation. 44 said they need information on where to evacuate (Fig. 13). Even if they can receive a warning, they don't know where to evacuate. However, they evacuated in case of a landslide in 2016. They were not sure whether their evacuated places were safe or not, so it can be said that they were luckily evacuated to safe areas.

2.4 External Help for Evacuation and after Evacuation

In the case of the landslide in May 2016, 49 respondents evacuated, and one person did not evacuate since she needed to take care of an old person in her family. Based on the interview, there were several reasons that they hesitated to evacuate and did not know the safe places for evacuation. One reason is because of their family members who are old and/or sick. Another reason is because of bad road conditions.

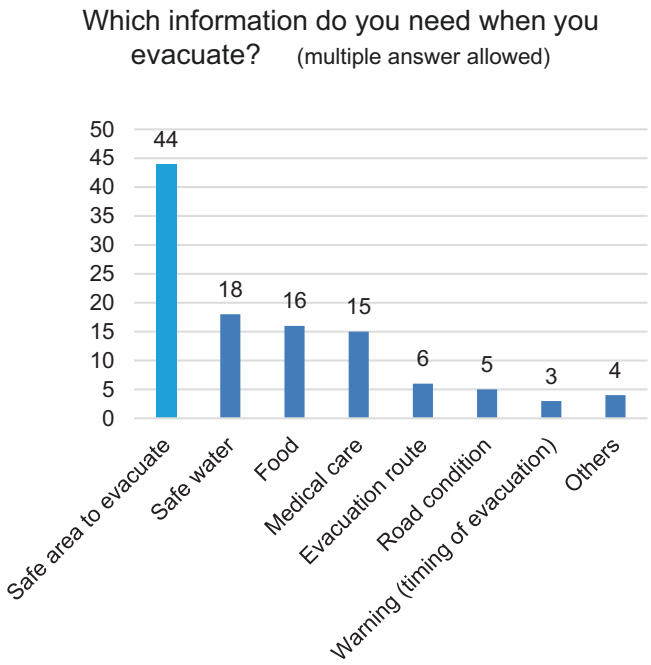

Fig. 13 Necessary information for evacuation

Figure 14 shows their evacuated places and the number of respondents who evacuated. Some of the respondents evacuated a few times in different places, therefore, the number of evacuated places is more than 50. Most of them evacuated temples or schools. Two respondents answered that they just evacuated to the main road since they did not know where to evacuate. Figure 15 shows where the questionnaire survey was conducted (50 red spotted houses), and the major places where they evacuated (yellow mark). Twenty-six respondents evacuated to the Rathnajoothia Ramaya temple, and 12 evacuated Hathgampala school. They are located along the main road. Dippitiya is also the area for them to evacuate, though it is about 2 km from Hathgampala. seven respondents evacuated to Dippitiya school.

When local people evacuate, external help is expected. Therefore, it was asked if there were external help during the evacuation. As Fig. 16 shows, safe water, food, etc. were provided by various organizations such as international NGOs, local government, etc. 21 respondents answered they didn't know.

Education for disaster risk reduction is also an external help, and the availability of disaster education was asked. The local government is the major organization that provides landslide disaster education (Fig. 17). Twelve respondents answered that they don't know.

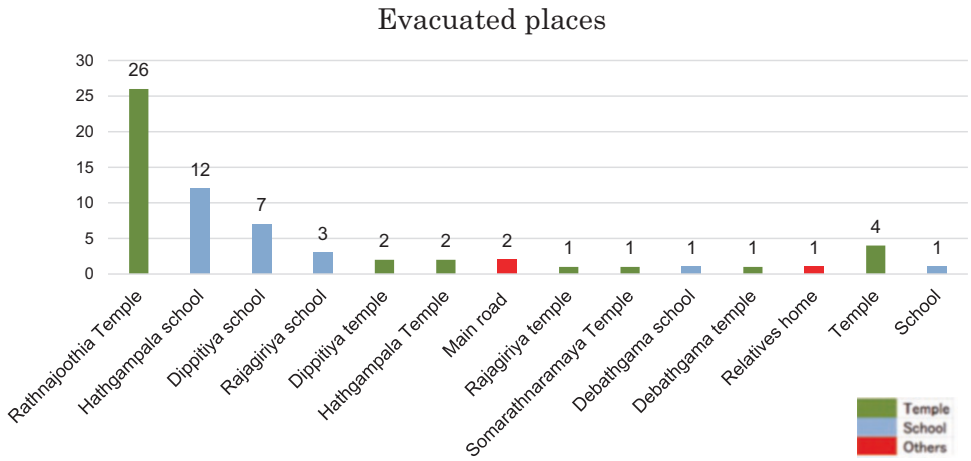

Fig. 14 Evacuated Places for Arayanake Landslide in May 2016

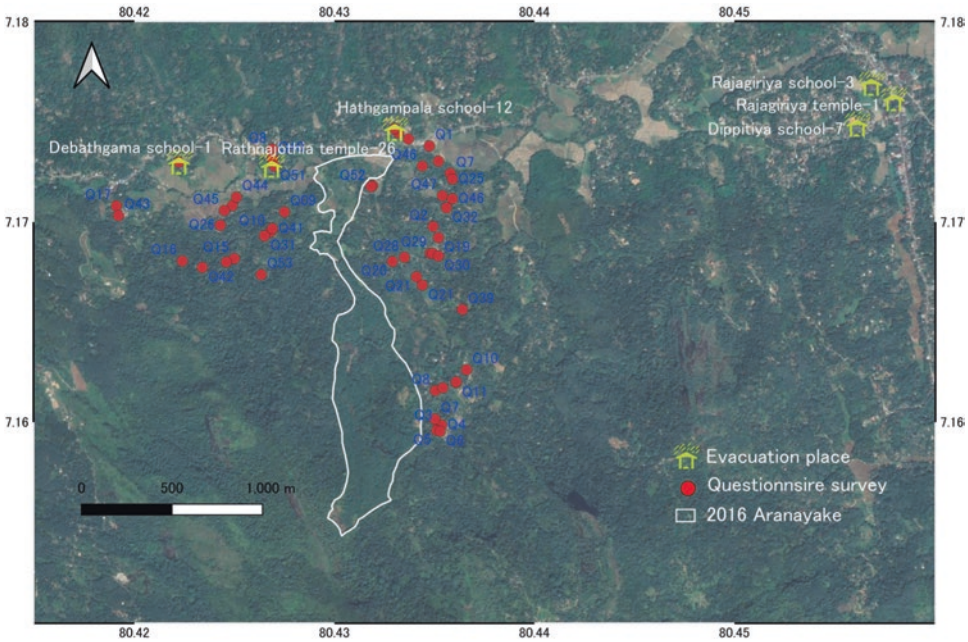

Fig. 15 Location of the houses of the respondents (red) and evacuated places (yellow)

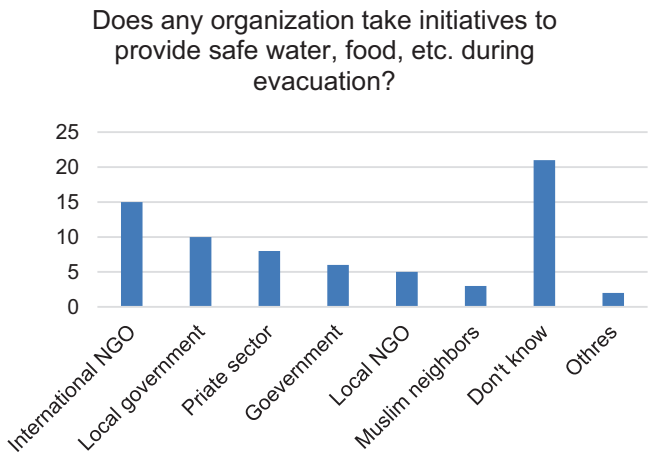

Fig. 16 External help of materials

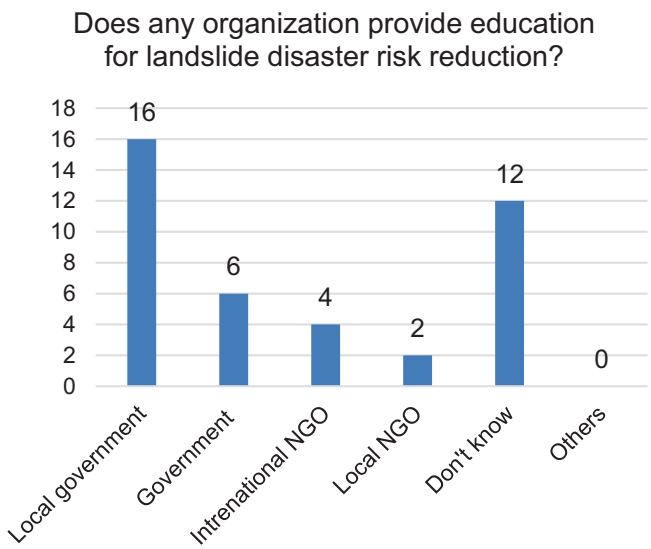

Fig. 17 Education of landslide disaster risk reduction

3 Interview at a Temple and Schools

Based on the result of the evacuation in the 2016 landslide, most people evacuated to temples, especially Rathnajoothia Ramaya (also called Rathnajothi /Rathnajothia /Viyaneliya temple) and schools, especially Hathgampala Maha Vidyalaya (also called Hathgampala school) (Fig. 12). Since they are not located inside the red and yellow zones of the map in Fig. 2, it is considered to be safe and suitable places to evacuate. Therefore, the interview was conducted with a monk at Rathnajoothia Ramaya temple and the principals at Hathgampala primary and secondary schools to know what external support is expected as expected evacuation places.

3.1 Rathnajoothis Ramaya Temple

Now, 5 monks live in the temple, and it was possible to interview one of them. When the landslide occurred in 2016, 600 people evacuated from the temple, and the longest period of evacuees was 3 months. There was no financial support from anybody. However, Muslim and local people provided food and water. Though he could not receive a warning from the government, warning information was shared by many villagers.

3.2 Hathgampala Schools

The interview was conducted with the principals of Hathgampala primary and secondary schools. The schools are located within walking distance. Disaster training is provided to students twice a year in Hathgampala Primary School, with about 200 students of 5–10 years old. The stu-

dents can study map education in environment class. Disaster education and geography class is provided at Hathbampala Secondary School, with about 800 students.

The schools were expected to be evacuation places when the landslide occurred in 2016. They could have temporary external help during and after the landslide, such as tents and sanitary toilets. The principals have been involved in a WhatsApp group called "Disaster Management Mawanell." They have received disaster information through the WhatsApp group, such as warnings, maps, and pictures from NBRO and other government organisations. In addition, they could share information through the WhatsApp group. WhatsApp is also used for communication among teachers and parents. However, some parents cannot receive information through WhatsApp because of the weak or no signal of mobile phones.

The training program in landslide disaster risk reduction is appreciated by both Hathgampala primary and secondary schools if materials are provided. The principal of the primary school said about 7 years have passed since the landslide occurred in 2016, and some students are still afraid of the landslides. For some students, it seems the landslide disaster is a past event, so it will be a good timing to have the disaster education with the help of others now.

4 Conclusion

As a result of the questionnaire survey and interview, three major essential conditions need improvement for successful early warning and evacuation. The following are the difficult conditions.

1. More than half of the respondents do not know if there is a hazard map or not.

   Since they live in a landslide-prone area, knowing the safe place to evacuate is important. If all of them can see the hazard map of their living area, they will know the available place to evacuate.
2. They have several information devices to receive a warning, however, six persons received a warning, and 43 persons did not receive a warning in case of the 2016 landslide disaster. In addition, half of them have never received a warning so far.

   Mobile phones are very useful not only for receiving information but for sharing information. However, because of no signal or weak signal, many respondents cannot receive information through mobile phones. Though mobile phones are not used by all, the community network is effective. The survey shows they already have a good communication network and know who cannot receive information through mobile phones. In this case, neighbors with good signals can knock on their doors and share information. However, it is appreciated that they can have a few ways to receive the information since only one way to receive the information is not working sometimes. A further survey for improving the information system is needed.
3. Even if they can receive a warning, 44 out of 50 respondents do not know the safe places to evacuate.

   The most important thing to be considered is that they do not know the safe area to evacuate. 49 respondents evacuated in the case of a landslide in 2016, however, 44 persons out of 50 respondents answered the questionnaire survey that "They need the information for a safe place to evacuate", so they were not sure whether their evacuated places were safe or not. They might evacuate based on their experience or intuition and lucky. Experience and intuition are important, however, if all of them in the selected area know the safe area to evacuate, the number of casualties will decrease. The temples and schools they evacuated are the right places to evacuate since they are out of the hazard area. If all local people recognize the safe area, it will be easier for them to evacuate. In addition, if some temples and schools are designated or recognized as evacuation places by both local people and external organizations such as official and private supporters, the local people will think they can receive any support, and supporters can provide necessary to the designated or recognized evacuation places. It will encourage the local people to evacuate.

Providing the training program is suggested to improve the above-mentioned difficult conditions for better early warning and evacuation. During the training program, it is necessary to clarify whether hazard maps exist in each community. If there is no hazard map, it can provide the hazard maps since NBRO already prepared the hazard maps. Map education is also possible be provided, then participants can know where they live, evacuation routes and the safe places to evacuate. In addition, during the training program, it is also possible to discuss the available information system and how to utilize it for warning and evacuation. Since the local government is the major organization to provide landslide disaster education, as the survey result shows, their collaboration is expected for providing the training program.

When the interview was conducted at both Hathgampala primary and secondary schools, a disaster training program is appreciated if materials are provided. Since the schools are well known, and many people evacuated there in case of the 2016 landslide, the Hathgampala schools are considered suitable organisations to start the training program. Then, providing training programs at some community centers may also be possible.

Acknowledgments The author wishes to thank the Japan International Cooperation Agency and Japan Science and Technology Agency for supporting the SATREPS Project "Development of Early Warning Technology of Rain-induced Rapid and Long-travelling Landslides in Sri Lanka." I also would like to thank all project members and colleagues of the International Consortium on Landslides (ICL), and appreciate the advice of Professor Kazuo Konagai and Professor Kyoji Sassa (ICL), Dr. Asiri Karunawardena and Dr. Gamini Jayathissa, National Building Research Organisation (NBRO), and Professor Jayalath Edrishinghe (University of Peradeniya). I would like to express special thanks to Mr. Dayan Munasinghe, (NBRO), and Ms. Tania Munasinghe at the ICL Sri Lanka Office for their meticulous support in conducting the field survey, and Professor Jagath Gunatilake and students at Peradeniya University for collecting and inputting data of field survey.

References

Bandara RMS, Jayasingha P (2018) Landslide disaster risk reduction strategies and present achievements in Sri Lanka. Geosci Res 3(3)., August 2018 http://www.isaacpub.org/images/PaperPDF/GR_100055_20180824153419008 57.pdf

De Silva Lasanthi NC, Goonetillake JS, Wikramanayake GN, Ginige A. (2012) Towards using ICT to enhance flow of information to aid farmer sustainability in Sri Lanka. 23rd Australasian Conference on Information Systems, 3–5 Dec 2012, Geelong

Fujita K (2022) Introducing Japanese landslide warning system to Sri Lanka: Analyzing the social differences for successful technology transfer. In: Sarkar R, Shaw R, Pradhan B (eds) Impact of climate change, land use and land cover, and socio-economic dynamics on landslides. Disaster risk reduction. Springer, Singapore. https://doi.org/10.1007/978-981-16-7314-6_17

Fujita K, Shaw R (2019) Preparing international joint project: use of Japanese flood hazard map in Bangladesh. Int J Disaster Risk Management 1(1):62–80. https://doi.org/10.18485/ijdrm.2019.1.1.4

Handa K et al (2018) Survey report of sediment disaster in Aranayake, Sri Lanka, on May, 2016. Int J Erosion Control Eng 11(1):2018

Konagai K et al (2023) Early warning system against rainfall-induced landslide in Sri Lanka. In: Sassa K, Konagai K, Tiwari B, Arbanas Ž, Sassa S (eds) Progress in landslide research and technology, volume 1 issue 1, 2022. Progress in landslide research and technology. Springer, Cham. https://doi.org/10.1007/978-3-031-16898-7_16

Kumara KK, Ananda U (2006) スリランカの教育制度の歴史と現状及びその問題点について (Past and present of the education system of Sri Lanka and corresponding problems). In: Suzuka International University journal: campana. No. 13, 2006

Towards an Optimization of Foundation Anchors of Landslide-Resisting Flexible Barriers: Dynamic Pullout Resistance of Anchors

Clarence Edward Choi, Jiaqi Zhang, and Dake Xiong

Abstract

Existing research on the design of flexible barriers to arrest the landslide mass mainly focuses on the optimization of the superstructure. Little attention has been given to the optimization of the foundation anchors used to transmit dynamic impact loading from the landslides to the ground. In fact, existing design guidelines for foundation anchors of landslide-resisting flexible barriers are based on quasi-static pullout theories even though field evidence suggests that the dynamic response of an anchor is fundamentally different. In this study, a new analytical model is proposed to predict the peak pullout resistance for anchors subjected to dynamic loading in saturated sand. A novel experimental apparatus was developed to evaluate the proposed analytical model. Dynamic effects are profound in saturated sand and less so in dry sand. Rate strengthening at the soil-anchor interface is governed by pore pressure change from dilation and soil damping. The proposed model is shown to give close predictions of the measured peak dynamic pullout resistance, which is up to three times those under quasi-static conditions. Findings imply that rate strengthening changes the critical failure mechanism of a foundation anchor from the soil-anchor interface for quasi-static loading to the potential rupturing of the steel tendon for dynamic loading. This study highlights the need for the dynamic analysis of foundation anchors of landslide-resisting flexible barriers.

Keywords

Landslide · Flexible barrier · Dynamic loading · Foundation anchor · Soil-anchor interaction

C. E. Choi (✉) · J. Zhang · D. Xiong
Department of Civil Engineering, The University of Hong Kong, Hong Kong, China
e-mail: cechoi@hku.hk; jiaqizjq@hku.hk; timxiong@connect.hku.hk

1 Introduction

Mountainous regions are susceptible to landslides, such as rock fall, avalanches, and debris flows (Froude and Petley 2018). To mitigate the effects of landslides, installing physical barriers on hillsides in densely populated mountainous areas, including Korea, Japan, Hong Kong, and Taiwan, will be increasingly important for protecting human life and infrastructure. For example, in Hong Kong, hundreds of barriers have been installed on hillsides in recent years. Under the current Landslip Prevention and Mitigation Program that was commissioned in 2010 by the Hong Kong Government, several new barriers are scheduled to be installed each year. Barriers not only require robust designs, but they also need to be sustainable. For instance, installing single large reinforced concrete barriers at the base of a slope is decreasingly viable in densely populated areas because of the challenges of land scarcity and the need to preserve the natural environment. Instead, the flexible barriers that blend in well with their natural surroundings are becoming the more sustainable and favorable option (Song et al. 2019a; Ng et al. 2017, 2020). Figure 1a shows the schematic of a typical flexible barrier with its superstructure and foundation. The superstructure, including the net, post and cables, directly arrests a dynamic landslide mass and transfers the load to the foundation. Figure 1b shows a flexible barrier installed in Kwun Yam Shan, Hong Kong.

Over recent years, extensive research efforts have been placed on the optimization of the superstructure of landslide-resisting flexible barriers (Song et al. 2019b; Choi and Goodwin 2020; Vicari et al. 2022; Wang et al. 2022; Ng et al. 2016; Song et al. 2018; Kong et al. 2021). However, the design and optimization of the foundation of a flexible barrier has received little to no attention despite field evidence of anchor failure under dynamic loading (Yu et al. 2019; Margreth and Roth 2008). Flexible barrier foundations are generally constructed as grouted anchors, which mobilize shear resistance against the pullout force from cables

B. Abolmasov et al. (eds.), *Progress in Landslide Research and Technology, Volume 3 Issue 1, 2024*, Progress in Landslide Research and Technology, https://doi.org/10.1007/978-3-031-55120-8_17

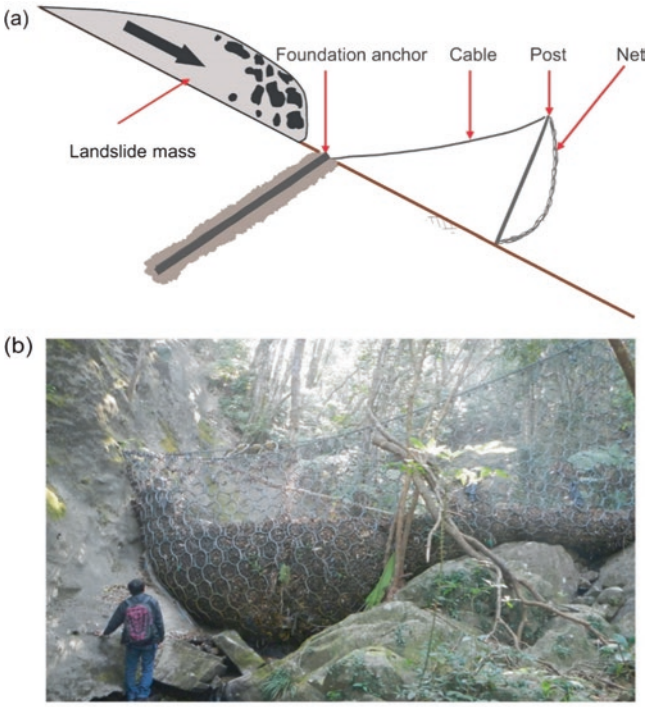

Fig. 1 Landslide-resisting flexible barriers. (**a**) Schematic of a typical flexible barrier, and (**b**) the flexible barrier installed in Kwun Yam Shan, Hong Kong (photo from HKIE 2020)

attached to the net (Cerro et al. 2016). Existing guidelines suggest that foundation anchors should be designed and tested based on quasi-static theories (Stelzer and Bichler 2013; Cerro et al. 2016). However, the dynamic impact load imposed on a foundation anchor abruptly increases to a peak load before diminishing in less than a second (Bertrand et al. 2012; Koo et al. 2017; Yu et al. 2019, 2021; Zhao et al. 2020; Song et al. 2019a). More importantly, field evidence shows that the load distribution along anchors subjected to dynamic loading differs drastically compared to that of quasi-static loading (Platzer et al. 2020). Evidently, there is a need to assess whether the existing design and test methods are adequate for dynamic loading conditions.

Researchers have attempted to extend the quasi-static pullout theories to consider the effects of loading rate on the dynamic penetration of piles and pullout of anchors in dry sand. The effects of loading rate have been reported to have minimal to significant influence on shaft resistance (Dayal and Allen 1975; Heerema 1979; Leprt et al. 1988; Tan et al. 2008; Huy et al. 2005; Aprialdi et al. 2014) depending on the surface roughness and pullout velocity. It is worthwhile to mention that due to practical reasons, these studies were commonly conducted in idealized lab conditions to obtain a controlled rate of loading. More importantly, in the above-mentioned studies, dry sand was used. Therefore, the effects of pore pressure change under dynamic loading were ignored.

The importance of pore pressure change can be shown by comparing dynamic element test results in dry and saturated sand. For dry sand, triaxial tests suggest only a 10% increase in strength from dynamic loading in timescales of less than a second (Casagrande and Shannon 1949; Whitman and Healy 1962; Lee et al. 1969; Schimming et al. 1966). Such a small increase may be considered negligible for engineering applications (Tan et al. 2008). In contrast, triaxial tests and direct shear tests conducted using saturated sand showed that the pore pressure change during tests can significantly influence soil strength, even in drained tests (Schimming et al. 1966; Seed and Lundgren 1954). More specifically, dynamic loading does not allow enough time for the generated excess pore pressure to fully dissipate, resulting in a partially drained condition (Shen et al. 2017). Evidently, the drainage condition and pore pressure change need to be carefully considered in the assessment of the dynamic pullout resistance as well.

Studies that investigate the effects of the loading rate on the pullout resistance in saturated sand are limited in the literature. Kyparissis (2016) pioneered pullout tests for a rough pipe buried in saturated sand subjected to different pullout velocities. In each experiment, the pore pressure at the soil-pipe interface and pullout force were measured. It was found that the peak negative pore pressure changed, and peak pullout force increased with pullout velocity. However, no displacement measurements at the pipe head were reported. Also, it is practically difficult to achieve a constant pullout velocity at such small displacements before the mobilization of the peak pullout force. Therefore, the pullout velocity, and thus, the loading rate could not be easily characterized. In addition, no quasi-static pullout resistances were reported, which limits the understanding of how dynamic effects contribute to the total pullout resistance. A rational analytical expression that can describe the dynamic pullout resistance in saturated sand does not yet exist in the literature.

This study aims to evaluate the dynamic pullout resistance of anchors in saturated sand to enhance the understanding of the effects of the loading rate on the pullout resistance of anchors and to improve existing design methods for the foundations of landslide-resisting flexible barriers. To achieve this, a new analytical model is proposed to estimate the peak dynamic pullout resistance by considering the effects of pore pressure change. Experimental investigations are performed by using a newly-developed experimental apparatus which can apply pullout force at designated velocities. A unique pullout test dataset is reported which explicitly includes quasi-static tests and tests in saturated sand. The proposed analytical model is evaluated by the produced dataset in this study and datasets in the literature.

2 New Dynamic Pullout Model

For quasi-static pullout, the effects of the loading rate are negligible so that the pullout resistance, F, is equal to the resistance induced by overburden, F_0. For dynamic pullout in saturated sand, the effects of pore pressure change should be included:

$$F = F_o + F_p \tag{1}$$

where $F_p$is the pore pressure change induced resistance. Details of quasi-static and dynamic pullout are discussed below.

2.1 Overburden

Since the burial depth, as a geometric length scale, is not directly related to the pullout velocity, overburden induced resistance is considered rate independent. A common assumption adopted in quasi-static pullout resistance theories is that the shear stress distribution is uniform along the length of a horizontal anchor. Although this assumption is an idealization compared to real shear stress distributions, pullout theories developed based on this assumption have been widely accepted by engineering practitioners and produced reasonable predictions (Powell and Watkins 1991; Lazarte et al. 2015; Ostermayer and Scheele 1978). One of the most commonly used theories was firstly proposed by Schlosser and Guilloux (1981) and then further developed by GEO (2008). If cohesion is ignored, the equation for quasi-static pullout resistance only considers the soil properties and anchor geometry as follows:

$$F_{o,peak} = 2DL\sigma_v^{'}\mu^* \tag{2}$$

where $F_{o,\,peak}$ is the peak overburden induced resistance, D is the outside diameter of the anchor, L is the length of the anchor, $\sigma_v^{'}$ is the vertical stress acting on the anchor, and μ^* is the apparent coefficient of friction. Normally, $\sigma_v^{'}$ is taken as $\gamma^{'}H$, where $\gamma^{'}$ is the effective unit weight of the soil and H is the burial depth of the anchor. Equation 2 is adopted in this study to characterize the resistance from overburden because of its practicality.

The apparent coefficient of friction, μ^*, is a key parameter that can be back-calculated from quasi-static pullout test results. In engineering design practice, $\mu^*$is taken as $\tan\phi^{'}$, where $\phi^{'}$ is the friction angle of soil (GEO 2008). However, the μ^* obtained from field measurements is usually four to 14 times larger than (Powell and Watkins 1991). This is because the soil at the rupture zone, which is a layer of soil that undergoes intensive shearing at the interface between the soil and anchor, dilates as the anchor is pulled. Dilation in turn increases the normal stress at the surface of an anchor (Luo et al. 2000).

2.2 Pore Pressure Change

The soil in the rupture zone dilates as an anchor is pulled. In saturated sand, the volume increase results in a negative pore pressure change. When the pullout is quasi-static, a drained condition applies, so that the pore pressure change may be ignored. However, when the pullout is dynamic, a partially drained condition applies so that pore pressure change should be considered. Based on the principle of effective stress, the normal effective stress acting on the surface of the anchor will increase by the same magnitude of negative pore pressure change (Terzaghi et al. 1996; Yin 2009). Assuming that the pore pressure change is uniform at the anchor surface and Coulomb's friction law applies, the change in pullout resistance induced by pore pressure change can be calculated as follows:

$$F_p = \pi DL\Delta\sigma_n^{'}\tan\delta = \pi DL(-p)\tan\delta \tag{3}$$

where $\Delta\sigma_n^{'}$ is the change in effective normal stress at the anchor surface, p is the pore pressure change, and δ is the friction angle of the soil-anchor interface. For a rough soil-anchor interface, δ can be taken as $\phi^{'}$ (Uesugi and Kishida 1986; Zhang et al. 2009). It is evident from Eq. 3 that to calculate F_p, the negative pore pressure change needs to be determined. However, the negative pore pressure change is rate dependent. For instance, when the pullout velocity increases, there is less time available for the excess pore pressure to dissipate. Therefore, the change in negative pore pressure increases. Consequently, the relationship between the pullout velocity and the pore pressure change needs to be determined to quantify the effect of loading rate on pullout resistance.

The generation of excess pore pressure is governed by volume change. Based on the definition of the dilation angle (Bolton 1986; Nemat-Nasser 1980), the rate of plastic volume change of the soil skeleton can be calculated as $\dot{V}^p = \dot{u}_y = \tan\psi\,\dot{u}_x = \tan\psi\, v$, where u_y is the thickness change of the rupture zone, $u_x$is the horizontal displacement of the anchor, ψ is the dilation angle of the soil, and v is the pullout velocity. Derived from elasticity theories by Taylor (1948), the elastic volume change rate of the soil skeleton can be calculated as $\dot{V}^e = 2(1+\mu)(1-2\mu)\Delta\dot{\sigma}_m^{'}h/E = 2(1+\mu)(1-2\mu)(-\dot{p})h/E$, where μ is the Poisson's ratio of the soil, E is the elastic modulus of the soil, $\Delta\sigma_m^{'}$ is the change in the mean effective stress, and h is the thickness of the rupture zone. The dissipation of excess pore pressure is governed by seepage. Based on Darcy's law (Harr 1991), the pore fluid inflow rate can be calculated as $q = ki$, where k is the hydraulic conductivity of the soil and i is the hydraulic gradient at the outer boundary of the rupture zone. i can be expressed as $\frac{1}{\gamma_w}\nabla p$, where γ_w is the unit weight of the

pore fluid. The volume of the soil particles can be assumed to be constant. More specifically, the voids created from volume change must be filled with inflowing pore fluid, which is expressed as follows:

$$V^p + V^e = q \tag{4}$$

When the negative pore pressure change is at its peak value, $-p_p$, the rate of change is zero, i.e., $-\dot{p} = 0$.

Although ψ is not constant during the pullout process, ψ can be assumed to be the peak angle of dilation, ψ_p, at the peak pullout resistance because the peak shear strength of soil is generally correlated with ψ_p (Luo et al. 2000). Therefore, Eq. 4 can be rewritten as:

$$\tan\psi_p v - k i_p = 0 \tag{5}$$

From Eq. 5, the peak hydraulic gradient can be determined. The hydraulic gradient at the rupture zone is assumed to be representative of the hydraulic gradient at a short distance from the rupture zone (i.e., less than 10% of the distance to the free surface). As such, the negative pore pressure change in the rupture zone can be estimated as follows:

$$-p = -p_m + is\gamma_w \tag{6}$$

where $-p_m$ is the measured negative pore pressure change and is the distance from the point of measurement to the rupture zone. However, it may not be feasible to obtain measurements of pore pressure changes in routine engineering practice. Therefore, the negative pore pressure change needs to be estimated without measurements.

It is difficult to explicitly capture the pore pressure distribution. This is because the generation and dissipation of excess pore pressure are highly transient since the time scale of a dynamic load may be less than a second (Bertrand et al. 2012; Koo et al. 2017; Yu et al. 2019, 2021; Zhao et al. 2020). Moreover, the pullout velocity and angle of dilation of the soil in the rupture zone, which drives the change in pore pressure, varies non-linearly from zero to a maximum value during the loading process (Hossain and Yin 2015). Therefore, analytically calculating the pore pressure change under such transient seepage condition may not be feasible. Instead, a conservative but semi-empirical method, which is modified from steady state seepage solutions (Fernández and Alvarez Jr. 1994) to account for transient seepage, is proposed to estimate negative pore pressure change:

$$-p = \eta i \frac{r^2}{4H} \frac{\left(1+\frac{4H_w^2}{r^2}\right)\ln\left(1+\frac{4H_w^2}{r^2}\right)}{\frac{2H}{r}}\gamma_w \tag{7}$$

where η is an empirical parameter accounting for the transient seepage, H_w is the distance from the anchor to the free surface of pore fluid, and r is the radius of the anchor. The value of η depends on the soil properties and the timescale of the problem. To develop the same hydraulic gradient, transient seepage requires lower pore pressure in the rupture zone compared to steady state seepage. Thus, the upper limit of η is unity, which represents a steady-state seepage condition. This value of η should provide an upper bound for the negative pore pressure change.

3 Physical Experiments

3.1 Dynamic Pullout Experimental Apparatus

A new experimental setup (Fig. 2) was developed to investigate the dynamic pullout resistance of a soil anchor and evaluate the proposed analytical model. This setup consists of two parts. The first part of the setup (Fig. 3a) is a box with dimensions of 1.2 m, 0.2 m, and 0.3 m in length, width, and height, respectively. Two plates, each with a thickness of 10 mm, were installed 0.7 m apart orthogonally to the pullout direction. The space in between the dividing plates forms a soil container with dimensions of 0.7 m, 0.2 m, and 0.3 m in length, width, and height, respectively.

The soil container is filled with sand before each test. At 10 mm beneath the centroid of each dividing plate, there is a circular opening with a diameter of 16 mm. An anchor, which is a steel bar with a length of 0.75 m and diameter of 16 mm was threaded through the circular openings. A layer of

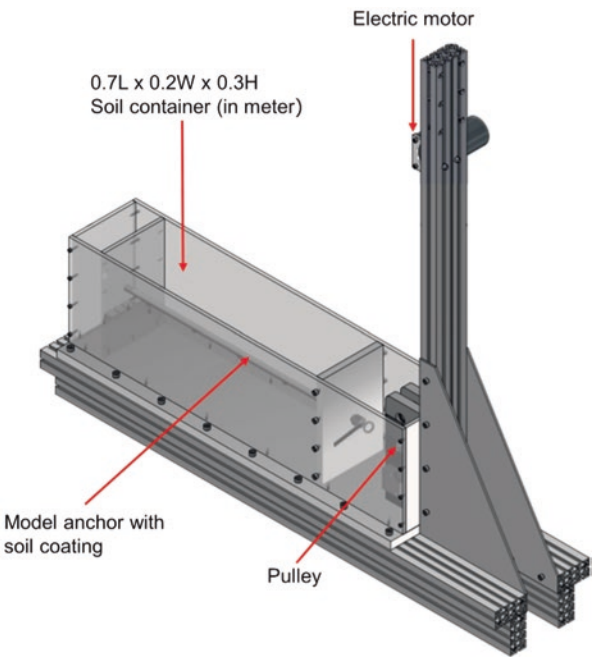

Fig. 2 Isometric view of the pullout experimental apparatus

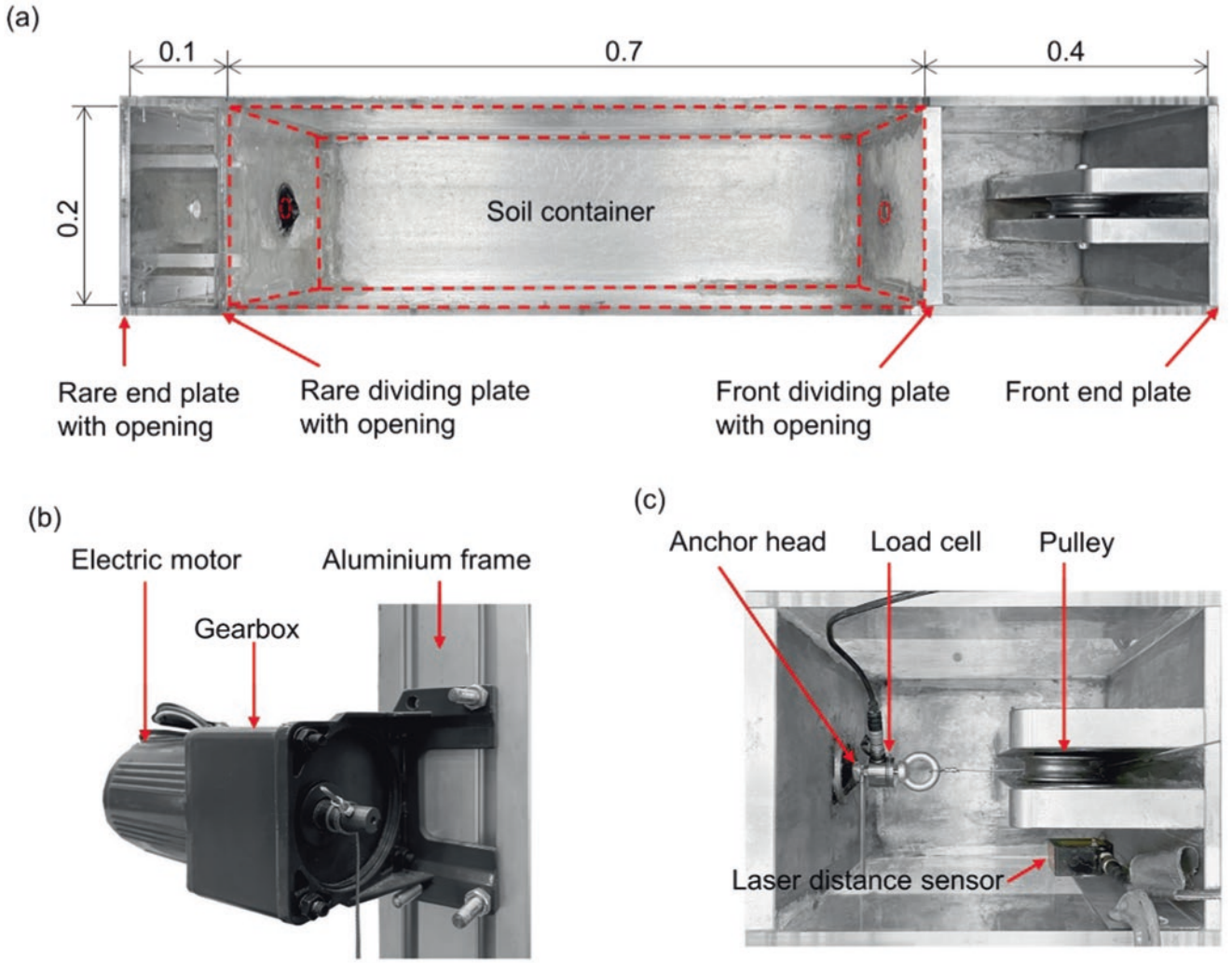

Fig. 3 Details of the pullout experimental apparatus (all dimensions in m): (**a**) soil container, (**b**) electric motor, and (**c**) connection and instrumentation at the inclusion head

Toyoura sand was glued to the anchor surface to achieve a rough interface condition (Nazir and Nasr 2013; Milligan and Tei 1998). An eyebolt was connected to the head of the anchor. The second part of the setup consists of a 40-watt power electric motor mounted to the vertical aluminum frame (Fig. 3b). A digital speed governor and gearboxes with different reduction ratios were used to control the rotational speed of the motor. A steel wire is connected to the electric motor and the eyebolt using a pulley. When the motor is powered on, the steel wire pulls the anchor at different preset velocities.

3.2 Instrumentation

Figure 3c shows a laser distance sensor mounted near the pulley to measure the distance from it to a target plate, which was attached to the anchor head. Therefore, the head displacement and pullout velocity can be measured. To measure the pullout resistance, a load cell with a capacity of 500N was attached to the anchor head. The mobilized resistance is considered equal to the pullout force because the inertial force was estimated to be less than 2% of the pullout force, which can be considered negligible. To obtain pore pressure measurements, two pore pressure transducers (PPTs) with a capacity of 100 kPa and a precision of 1 kPa were placed in the sand surrounding the anchor. One of the PPTs was placed on the top, and another PPT was on the side of the anchor. The PPTs were positioned at a radial distance of 12 mm from the anchor.

3.3 Modelling Procedures and Test Program

To obtain pore pressure measurements, two pore pressure transducers (PPTs) with a capacity of 101 kPa were placed in the sand surrounding the anchor. One of the PPTs was placed on the top, and another PPT was on the side of the anchor

Table 1 Test program

Saturation	Pullout velocity (mm/s)
Saturated	Quasi-static[a]
	4
	16
	26
	35
	50
Dry	Quasi-static[a]
	4
	25
	60

[a] The anchor is pulled out at a low velocity of less than 1 mm/s to mimic a quasi-static pullout test

(Fig. 3d). The PPTs were positioned at a radial distance of 12 mm from the anchor.

Toyoura sand with D_{50} = 0.18 mm and ϕ' = 34° was used in the experiments. In each test, the sand was prepared in three layers in the container. Dry (Schiavon et al. 2016; Hao et al. 2019) and wet pluviation (Levesque 2003; Kim and Kim 2019) methods were used for the dry and saturated tests, respectively, to achieve a target unit weight of γ = 14.65 kN/m^3. Under this state, the soil exhibits dilative behavior under shearing, and its peak dilation angle, is estimated to be 12° (Yang and Li 2004), and the hydraulic conductivity is estimated to be 0.06 cm/s (Yoshimi et al. 1975; Amer and Awad 1974). The anchor and PPTs were installed at the target depths. After the sand is prepared, the instrumentation and data logger is initiated. The speed governor is preset to a designated speed, and the motor is powered on. The anchor is then pulled by the steel wire.

In this study, pullout tests were conducted at velocities from 4 mm/s to 60 mm/s in both dry and saturated sand. The pullout velocities were back-calculated by considering the typical dynamic loading duration as reported in the literature (Yu et al. 2019; Platzer et al. 2020; Pradhan 2003; Lum 2007). A typical duration of 0.1 s and displacement of 2 mm gives an approximate pullout velocity of 20 mm/s. Table 1 gives a summary of the experimental program.

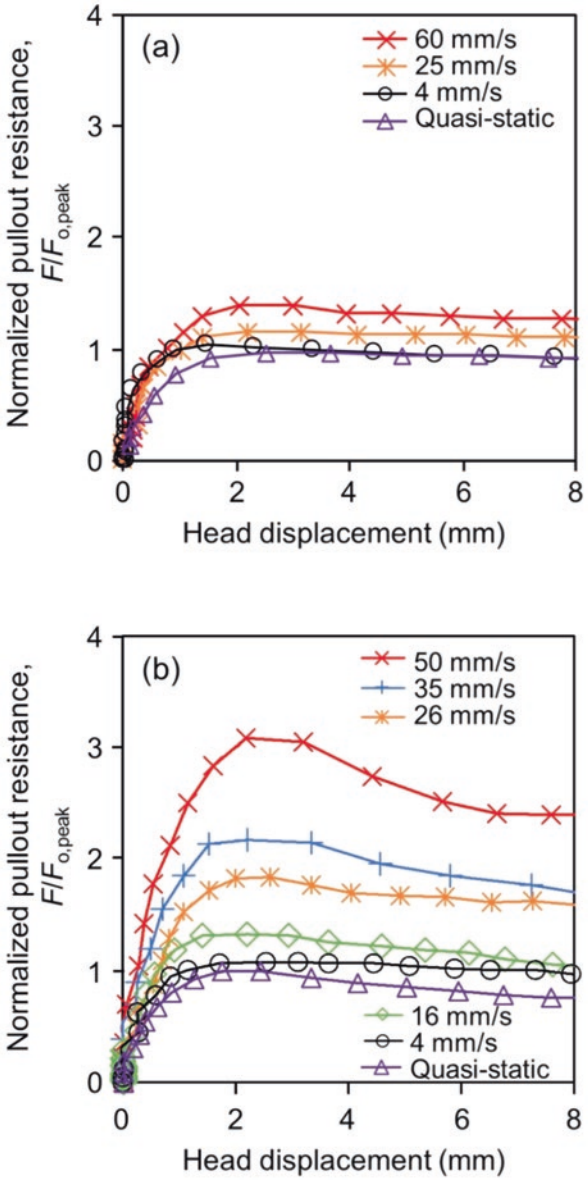

Fig. 4 The normalized pullout resistance against the head displacement for tests conducted at different velocities in: (**a**) dry sand, and (**b**) saturated sand

4 Result Interpretations and Discussions

4.1 Rate Effects from Dynamic Pullout

Figure 4(a, b) show comparisons of the normalized pullout resistance with head displacement at different pullout velocities in dry and saturated sand, respectively.

The normalized pullout resistance is defined as the measured pullout resistance divided by the peak quasi-static pullout resistance. It is noted that the magnitude of the pullout resistance of an anchor in saturated and dry sand cannot be directly compared with each other since they have different effective overburden stresses.

For each test, it can be observed that the pullout resistance increases to a peak value before decreasing. This is related to the initial increase and subsequent decrease of the mobilized friction and dilation angles of the soil in the rupture zone as the pullout displacement increases (Hossain and Yin 2010; Borana et al. 2016). The displacement required to mobilize the peak pullout resistance is referred to the critical shear displacement (Luo et al. 2000), which is governed by the shape and size of the granular material adopted (Billam 1972). Based on all tests, the critical shear displacement is from 2.0 to 2.5 mm. This range agrees with other studies that

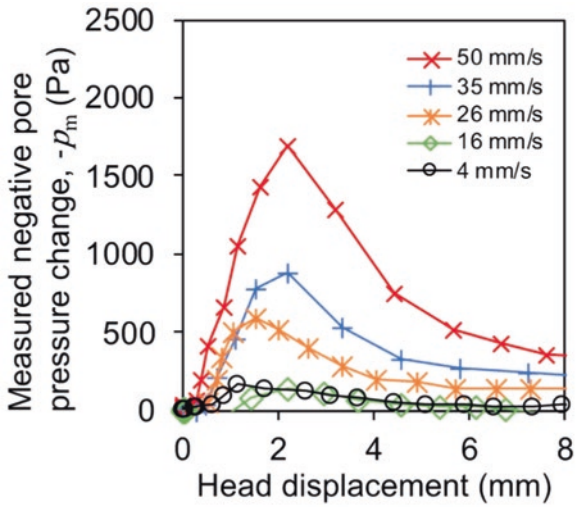

Fig. 5 Measured negative pore pressure change against the head displacement for tests conducted at different velocities in saturated sand

investigate the quasi-static pullout resistance of anchors (Chang et al. 1977; Luo et al. 2000). This finding, together with an obvious peak resistance, implies that the formation of the rupture zone is consistent for both dynamic and quasi-static loading in both dry and saturated sand. When comparing tests conducted at different pullout velocities, the pullout resistance increases with pullout velocity for both dry and saturated tests. This finding agrees with previous dynamic pullout tests (Kyparissis 2016; Tan et al. 2008; Aprialdi et al. 2014; Jenck et al. 2014), which attributed the increase in pull out resistance to rate effects. A comparison between Fig. 4(a, b) reveals that rate effects in saturated sand are more profound than those in dry sand. This phenomenon is because of the effect of negative pore pressure change from dilation. Evidently, the effects of pore pressure change must be considered when assessing dynamic pullout resistance.

Figure 5 shows the measured pore pressure changes with head displacement for the saturated sand tests. For each test, the negative pore pressure change increases abruptly before gradually decreasing with displacement. Additionally, the displacement that corresponds to the peak negative pore pressure change approximately coincides with the aforementioned critical shear displacement. This is because the change in pore pressure is driven by the initial increase and subsequent decrease of the dilation angle of the soil in the rupture zone. Before the critical shear displacement is reached, excess pore water pressures are generated because of the mobilization of the dilation angle. After the critical shear displacement is reached, the effect of soil dilatancy diminishes, and the effects of the dissipation of excess pore pressure becomes more apparent. When comparing tests conducted at different pullout velocities, the measured negative pore pressure change generally increases with pullout velocity. This is because a higher pullout velocity generates excess pore pressures at shorter timescales compared to that required for dissipation (i.e. towards undrained conditions), leading to more significant changes in pore pressure. The similarities of the above-mentioned trends observed between the pullout resistance and pore pressure changes show that the negative pore pressure change increases normal effective stress and thus pullout resistance, which is supported by Eq. 3. This implies that anchors installed in ground with high ground water tables will be more susceptible to rate effects.

4.2 Model Evaluation

Figure 6 shows a comparison of measured and calculated normalized peak pullout resistance ($F_{peak}/F_{o,\,peak}$) in saturated sand. Furthermore, the proposed model is evaluated against existing quasi-static ones. The peak overburden induced resistance, $F_{o,\,peak}$, is determined from the quasi-static tests conducted in this study. The peak overburden induced resistance is found to be 71N for experiments carried out in saturated sand. Therefore, the apparent friction coefficient, μ^*, can be back-calculated as 4 for saturated sand. This value agrees with the range reported from field quasi-static pullout experiments (Powell and Watkins 1991; Schlosser and Guilloux 1981). Experimental measurements from Kyparissis (2016), who conducted dynamic pullout tests in saturated sand, are shown for comparison. It is worthwhile to note that no quasi-static test data was reported in their study. Thus, $F_{o,\,peak}$ is estimated by linear extrapolation of the pullout resistance with the pullout velocity. At each burial depth, the intercept of the linear extrapolation is considered to be $F_{o,\,peak}$. The peak quasi-static pullout resistance based on overburden (i.e., Eq. 2) is the same regardless of the pullout velocity. In contrast, the measured data, at different pullout velocities, exhibits an increase in resistance with pullout velocity. At a pullout velocity of 70 mm/s, the effects of the loading rate increase the pullout resistance by 200% compared to the overburden resistance.

Existing quasi-static pullout theories (i.e., Eq. 2) underestimate the dynamic pullout resistance. For a soil anchor, such a significant underestimation may cause engineers to overlook the fact that the anchor can rupture before the failure of the interface between soil and anchor. For example, for a typical 13-m long anchor foundation of a debris flow resisting barrier, a soil-anchor interface strength was calculated to be about 313 kN (i.e., D= 125 mm, H = 8 m, $\tan\phi'$ = 34°, and γ' = 18 kN/m^3). To prevent tendon failure, engineers designed a tendon with a capacity of 519 kN. However, under dynamic loading, the soil-anchor interface strength can increase to 1000 kN, which largely exceeds the designed strength of the tendon. Thus, a larger diameter should be assigned to the tendon. Evidently, there is a pressing need to progress

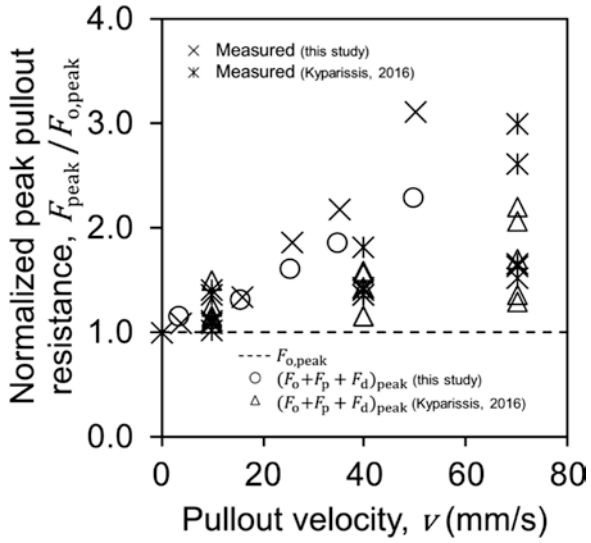

Fig. 6 Comparison of measured and calculated normalized peak pullout resistance for tests in saturated sand

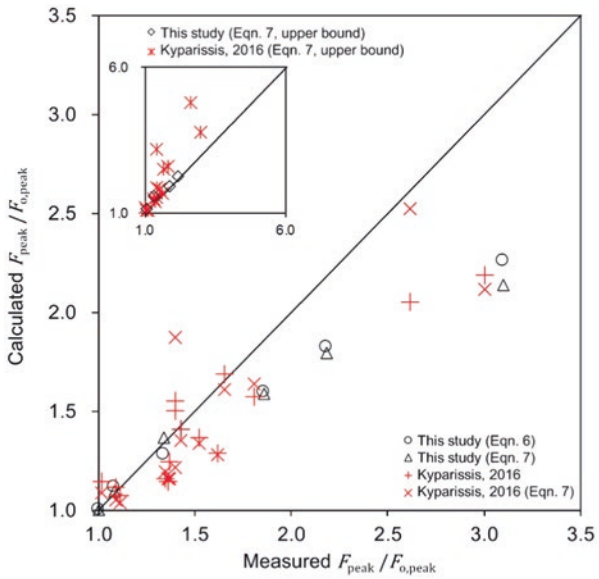

Fig. 7 Comparison of calculated normalized peak pullout resistance

towards a more rational estimation of the dynamic pullout resistance of anchors in saturated sand.

In saturated sand, the effects of pore pressure change should be considered in dynamic pullout. Equation 3 shows that the normal effective stress in the rupture zone is affected by changes in pore pressure. In this study, PPTs were not installed in the rupture zone to avoid disturbance to it. However, the pore pressure change measured by the PPT can be used to estimate the pore pressure change in the rupture zone by using Eq. 6. For the data reported by Kyparissis (2016), the PPT was placed at the anchor surface. Thus, the pore pressure change measured by the PPT can be regarded as that in the rupture zone. Correspondingly, the pore pressure induced resistance can be calculated by using Eq. 3. The normalized dynamic pullout resistance calculated by using Eq. 1 is shown in Fig. 6. The calculated values show the same trend and order of magnitude as the measured values. It is shown that Eq. 1 can be used to estimate the dynamic pullout resistance and Eq. 3 can be used to explain the effects of negative pore pressure change.

To evaluate Eq. 7, the calculated peak pullout resistance by the different proposed methods (i.e., with and without in-situ pore pressure measurement) and measured peak pullout resistances are compared in Fig. 7. The calculated normalized peak pullout resistance ($F_{peak}/F_{o,\,peak}$), with reference to pore pressure measurements, shows close agreement with the measured data.

As discussed, compared to the scatter of the data points in this study, a larger scatter for the external dataset (Kyparissis 2016) may be related to its lack of clear displacement measurements, and thus characterizable pullout velocities. If Eq. 7 is used without reference to pore pressure measurements, the empirical parameter, η, is determined by regression analysis to be 0.6 for this study and 0.4 for the external dataset. It is shown that the normalized calculated peak pullout resistance provided by Eq. 7 also produce close agreement with the measured values. Thus, Eq. 7 can be used to estimate pore pressure change reasonably without the need for additional measurements. If a value of unity is adopted for η, then Eq. 7 may be used as an upper bound for estimating the dynamic pullout resistance in all of the test cases in this study. Nevertheless, more experiment data can help to optimize the value of η.

5 Discussion

5.1 Radiation Damping

The measured and calculated normalized peak pullout resistance for dry sand is shown in Fig. 8.

As discussed, the peak overburden induced resistance, $F_{o,peak}$, is determined from the quasi-static tests conducted in this study. The peak overburden induced resistance is 157N for tests carried out in dry sand. Therefore, the apparent friction coefficient, μ^*, can be back calculated as 3 for dry sand. This value is in the range reported from quasi-static pullout experiments in the field (Powell and Watkins 1991; Schlosser and Guilloux 1981). In addition, dynamic pullout studies (Tan et al. 2008; Jenck et al. 2014; Aprialdi et al. 2014) in dry sand are also shown for comparison. Linear extrapolation of the pullout resistance was used to obtain $F_{o,peak}$ for data where quasi-static pullout data was not reported (Aprialdi et al. 2014; Jenck et al. 2014). In this study, at a pullout velocity of 40 mm/s, the pullout resistance increased 40% compared to

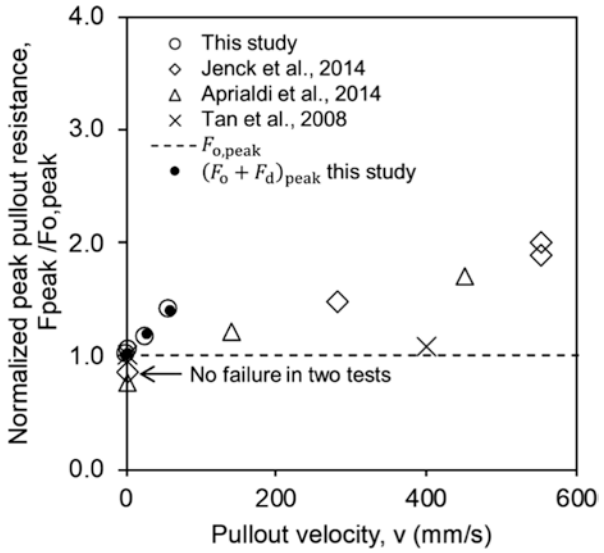

Fig. 8 Comparison of measured and calculated normalized peak pullout resistance for tests in dry sand

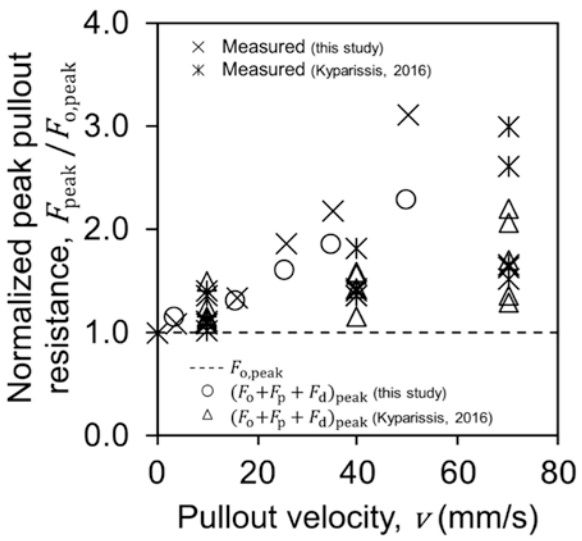

Fig. 9 Measured damping induced resistance for tests in dry sand and determination of actual damping coefficient

the quasi-static condition. In the study of Jenck et al. (2014), at a pullout velocity of 550 mm/s, the pullout resistance increased 100% compared to the quasi-static condition. Compared to tests in saturated sand (Fig. 6), the importance of pore pressure change is once again highlighted. Moreover, considering that the effects of pore pressure change are negligible in dry sand, there may also be other rate dependent resistance in dry sand.

It is proposed in the literature that radiation damping is a possible effect of dynamic loading on soil-anchor interaction (Tan et al. 2008). When a structure interacts with soil, elastic waves are generated. If a soil remains elastic, the energy carried by waves transmitted through an open boundary will dissipate. This energy dissipation phenomenon is called radiation damping and can be mathematically approximated by using dashpots (Dobry 2014; Novak 1974). Analytical solutions for a vibrating anchor in an infinite elastic soil medium have been reported (Nogami and Novak 1976; Novak et al. 1978; Gazetas and Makris 1991). During pullout, it is assumed that elastic shear waves are generated. However, the presence of a plastic rupture zone violates the assumption of an elastic soil. Therefore, the above-mentioned analytical solutions cannot be directly applied to a pullout problem. To address the above-mentioned shortcoming and quantify the damping effect on the pullout resistance of anchors, Tan et al. (2008) proposed an apparent damping coefficient:

$$F_d = Lc^* v \tag{8}$$

where F_d is damping induced resistance and c^* is the apparent damping coefficient.

To adopt the apparent damping coefficient into this study, Fig. 9 shows the measured damping induced resistance against the pullout velocity for dry sand. The damping induced resistance can be calculated by subtracting the overburden induced resistance from the dynamic pullout resistance. A linear fit, corresponding to c^* = 1500 Ns/m/m, can describe the relationship between F_d per unit length of anchor and v. The deduced damping value falls within the range reported by Tan et al. (2008). In addition, the peak frictional resistance calculated by $(F_o + F_d)_{peak}$ (i.e., c^* = 1500 Ns/m/m) is shown in Fig. 8. It can be found that damping induced resistance from dynamic loading can be well captured in dry sand.

Considering the physical origin of radiation damping (i.e., propagation of shear waves during pullout), the actual damping coefficient calculated from the dry sand tests is assumed for simplicity to be applicable to saturated tests since the pore fluid cannot transmit shear waves. It is worthwhile to point out that the reported data from Kyparissis (2016) does not include dry sand measurements, so their dataset cannot be directly used to separately evaluate the effects of pore pressure change from soil damping. Consequently, damping induced resistance needs to be back-calculated by using linear regression between the measured peak damping induced resistance and pullout velocity.

If the damping effect (i.e., c^* = 1500 Ns/m/m) is included, the calculated normalized peak pullout resistance is shown in Fig. 10 and the calculated peak pullout resistance by the different proposed methods is shown in Fig. 11. The close agreement between calculated and measured values suggests the theory proposed by Tan et al. (2008) may help to estimate the damping induced resistance in dynamic pullout. Nevertheless, there has been no direct measurement of elastic waves generated in dynamic pullout experiments. Therefore, more experimental data may be needed to support this theory and evaluate a rational range of the actual

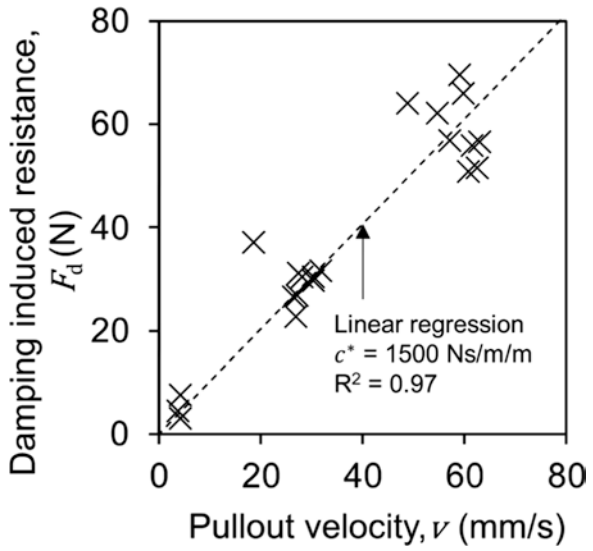

Fig. 10 Comparison of measured and calculated normalized peak pullout resistance, considering damping effect

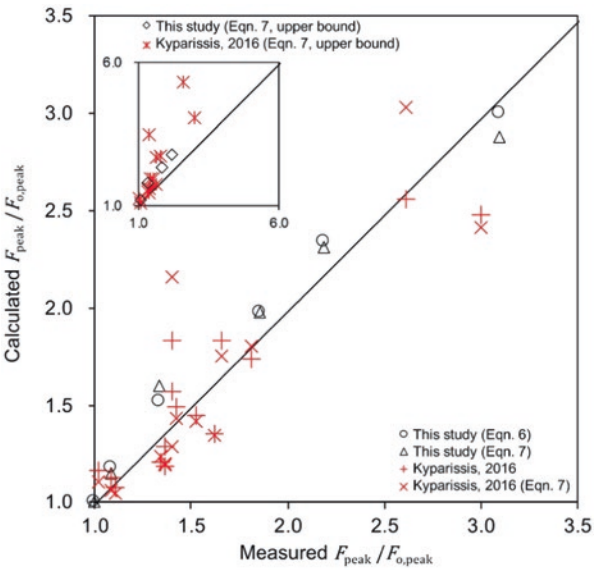

Fig. 11 Comparison of calculated normalized peak pullout resistance, considering damping effect

damping coefficient, which can hardly be calculated by closed-form equations due to the existence of the rupture zone.

6 Conclusions

The effects of dynamic loading on the pullout resistance of a foundation anchor in saturated sand were investigated by developing a new analytical model, which was then evaluated by data produced by a novel experimental setup and external datasets. Key findings may be concluded as follows:

1. The dynamic loading exerted on an anchor causes rate effects on the pullout resistance. The rate effects increase the pullout resistance to up to three times compared to quasi-static loading. However, existing design guidelines for foundation anchors of landslide-resisting flexible barriers adopt quasi-static pullout theories that overlooked rate effects. This can cause the unexpected tendon failure of the anchors because quasi-static design overlooks rate strengthening and assumes that the soil-grout interface is the weakest component of an anchor design. The need for the dynamic analysis of foundation anchors of landslide-resisting flexible barriers is highlighted in this study.
2. Dynamic loading effects are mainly attributed to the effects of pore pressure change. The pore pressure change effect is caused by a partial drainage condition, which is governed by the limited timescale for pore pressure dissipation. Because of the absence of pore pressure change, the rate effects in dry sand are less significant than those in saturated sand. Thus, for sites with anchors installed in the ground with high water tables, the rate effects are expected to be more significant and should be more carefully evaluated.
3. The proposed analytical model can well describe the effects of pore pressure change and provide estimations of the dynamic pullout resistance of anchors. Compared to existing quasi-static approaches, the proposed model can be used to provide a more rational estimation of the interface strength between the soil and anchor, which can contribute to scientifically designing the anchor foundation of landslide-resisting flexible barriers.
4. A new method is proposed to estimate the pore pressure change during dynamic pullout without the need for in-situ pore pressure measurements. This method serves as a quick and conservative guiding tool to assess the possible magnitude of pore pressure change caused by dynamic loading.

Acknowledgments The authors are grateful for the generous financial sponsorship from the Research Grants Council of Hong Kong (General Research Fund Grants 16209717; 16210219; AoE/E-603/18).

References

Amer AM, Awad AA (1974) Permeability of cohesionless soils. J Geotech Eng Div 100:1309–1316

Aprialdi D, Lambert S, Jenck O, Widyarti M (2014) An original testing apparatus for rapid pull-out test. Civil Eng Dimens 16:61–67

Bertrand D, Trad A, Limam A, Silvani C (2012) Full-scale dynamic analysis of an innovative rockfall fence under impact using the

discrete element method: from the local scale to the structure scale. Rock Mech Rock Eng 45:885–900
Billam J (1972) Some aspects of the behaviour of granular materials at high pressures. Proceedings of the Roscoe memorial symposium, Cambridge, pp 69–80
Bolton M (1986) The strength and dilatancy of sands. Géotechnique 36:65–78
Borana L, Yin J-H, Singh D, Shukla SK (2016) Interface behavior from suction-controlled direct shear test on completely decomposed granitic soil and steel surfaces. Int J Geomech 16:D4016008
Casagrande A, Shannon WL (1949) Strength of soils under dynamic loads. Trans Am Soc Civil Eng 114:755–772
Cerro M, Giacchetti G, Lelli M, Grimod A, Arul A (2016) ETAG certified rockfall barriers—new design approach according to UNI 11211: 4/2012. Proceedings of the first Asia pacific slope stability in mining conference, Australian Centre for Geomechanics, pp 443–456
Chang JC, Hannon JB, Forsyth RA (1977) Pull resistance and interaction of earthwork reinforcement and soil
Choi C, Goodwin G (2020) Interaction between granular flows and flexible obstacles: a grain-scale investigation. Comput Geotech 128:103800
Dayal U, Allen JH (1975) The effect of penetration rate on the strength of remolded clay and sand samples. Can Geotech J 12:336–348
Dobry R (2014) Simplified methods in soil dynamics. Soil Dyn Earthq Eng 61:246–268
Fernández G, Alvarez TA Jr (1994) Seepage-induced effective stresses and water pressures around pressure tunnels. J Geotech Eng 120:108–128
Froude MJ, Petley DN (2018) Global fatal landslide occurrence from 2004 to 2016. Nat Hazards Earth Syst Sci 18:2161–2181
Gazetas G, Makris N (1991) Dynamic pile-soil-pile interaction. Part I: analysis of axial vibration. Earthq Eng Struct Dyn 20:115–132
GEO (2008) Guide to soil nail design and construction (Geoguide 7). In: Geotechnical engineering office, HKSAR, China
Hao D, Wang D, O'loughlin CD, Gaudin C (2019) Tensile monotonic capacity of helical anchors in sand: interaction between helices. Can Geotech J 56:1534–1543
Harr ME (1991) Groundwater and seepage, Courier Corporation
Heerema E (1979) Relationships between wall friction, displacement velocity and horizontal stress in clay and in sand, for pile driveability analysis. Ground Eng 12
HKIE (2020) The landslip prevention and mitigation programme-new innovations and approaches ten years on. Hong Kong Inst Eng 48
Hossain MA, Yin J-H (2010) Behavior of a compacted completely decomposed granite soil from suction controlled direct shear tests. J Geotech Geoenviron Eng 136:189–198
Hossain MA, Yin J-H (2015) Dilatancy and strength of an unsaturated soil-cement interface in direct shear tests. International Journal of Geomechanics 15:04014081
Huy N, Dijkstra J, Van Tol A, Hölscher P (2005) Influence of loading rate on the bearing capacity of piles in sand. Proceedings of the 16th international conference on soil mechanics and geotechnical engineering, IOS Press, pp 2125–2128
Jenck O, Lambert S, Aprialdi D (2014) Soil-geotextile interaction when subjected to a dynamic load of impact type: development of a pull-out test apparatus. 10th international conference on geosynthetics, Berlin
Kim J-H, Kim D-S (2019) Soil displacement near a bucket foundation installed in sand by suction and jacking in a centrifuge. J Geotech Geoenviron Eng 145:06019015
Kong Y, Li X, Zhao J (2021) Quantifying the transition of impact mechanisms of geophysical flows against flexible barrier. Eng Geol 289:106188
Koo RC, Kwan JS, Lam C, Ng CW, Yiu J, Choi CE, Ng AK, Ho KK, Pun W (2017) Dynamic response of flexible rockfall barriers under different loading geometries. Landslides 14:905–916
Kyparissis A (2016) Shear strength of saturated sand-steel interfaces: geotechnical issues found at landfall operations. Master of Science
Lazarte CA, Robinson H, Gomez JE, Baxter A, Cadden A, Berg RR, Berg RR (2015) Geotechnical engineering circular no. 7 soil nail walls-reference manual. National Highway Institute
Lee KL, Seed HB, Dunlop P (1969) Effect of transient loading on the strength of sand. 7th international conference on soil mechanics and foundation engineering, Mexico, pp 239–247
Leprt P, Corte JF, Goulois A, Meunier J (1988) Shaft resistance during driving, for sand, from laboratory tests. 3rd international conference on the application of Stress Wave Analytical Model to Piles, Ottawa
Levesque CL (2003) Centrifuge modelling of helical anchors in sand, National Library of Canada=Bibliothèque nationale du Canada, Ottawa
Lum CW (2007) Static pullout behaviour of soil nails in residual soil. Doctor of Philosophy
Luo S, Tan S, Yong K (2000) Pull-out resistance mechanism of a soil nail reinforcement in dilative soils. Soils Found 40:47–56
Margreth S, Roth A (2008) Interaction of flexible rockfall barriers with avalanches and snow pressure. Cold Reg Sci Technol 51:168–177
Milligan G, Tei K (1998) The pull-out resistance of model soil nails. Soils Found 38:179–190
Nazir A, Nasr A (2013) Pullout capacity of batter pile in sand. J Adv Res 4:147–154
Nemat-Nasser S (1980) On behavior of granular materials in simple shear. Soils Found 20:59–73
Ng CWW, Song D, Choi C, Koo R, Kwan J (2016) A novel flexible barrier for landslide impact in centrifuge. Géotech Lett 6:221–225
Ng CWW, Song D, Choi CE, Liu L, Kwan JSH, Koo R, Pun WK (2017) Impact mechanisms of granular and viscous flows on rigid and flexible barriers. Can Geotech J 54:188–206
Ng CWW, Wang C, Choi CE, De Silva W, Poudyal S (2020) Effects of barrier deformability on load reduction and energy dissipation of granular flow impact. Comput Geotech 121:103445
Nogami T, Novak M (1976) Soil-pile interaction in vertical vibration. Earthquake Engineering & Structural Dynamics 4:277–293
Novak M (1974) Dynamic stiffness and damping of piles. Can Geotech J 11:574–598
Novak M, Aboul-Ella F, Nogami T (1978) Dynamic soil reactions for plane strain case. J Eng Mech Div 104:953–959
Ostermayer H, Scheele F (1978) Research on ground anchors in non-cohesive soils. Rev Fr Géotech:92–97
Platzer KM, Wendeler C, Brändle R, Stolz M (2020) Experimental investigation of forces along anchors subjected to dynamic loading under tension and compression in field tests. Can Geotech J 57:770–782
Powell G, Watkins A (1991) Improvement of marginally stable existing slopes by soil nailing in Hong Kong. Performance of reinforced soil structures. Thomas Telford Publishing
Pradhan B (2003) Study of pullout behaviour of soil nails in completely decomposed granite fill. Master of Philosophy
Schiavon J, Tsuha C, Neel A, Thorel L (2016) Physical modelling of a single-helix anchor in sand under cyclic loading. 3rd European conference on physical modelling in geotechnics (EUROFUGE 2016). IFSTTAR Nantes Centre, France, pp 1–3
Schimming BB, Haas HJ, Saxe HC (1966) Study of dynamic and static failure envelopes. J Soil Mech Found Div 92:105–124
Schlosser F, Guilloux A (1981) Le frottement dans le renforcement des sols. Rev Fr Géotech:65–77
Seed HB, Lundgren R (1954) Investigation of the effect of transient loading on the strength and deformation characteristics of saturated sands. Proc Am Soc Test Mater

Shen K, Wang L, Guo Z, Jeng D (2017) Numerical investigations on pore-pressure response of suction anchors under cyclic tensile loadings. Eng Geol 227:108–120
Song D, Choi CE, Ng CWW, Zhou G (2018) Geophysical flows impacting a flexible barrier: effects of solid-fluid interaction. Landslides 15:99–110
Song D, Zhou GG, Xu M, Choi CE, Li S, Zheng Y (2019a) Quantitative analysis of debris-flow flexible barrier capacity from momentum and energy perspectives. Eng Geol 251:81–92
Song D, Choi CE, Ng CWW, Zhou GG, Kwan JS, Sze H, Zheng Y (2019b) Load-attenuation mechanisms of flexible barrier subjected to bouldery debris flow impact. Landslides 16:2321–2334
Stelzer G, Bichler A (2013) ONR 24810—a comprehensive guideline for building better rockfall protection structures. 64th annual highway geology symposium, New Hampshire, USA
Tan S, Ooi P, Park T, Cheang W (2008) Rapid pullout test of soil nail. J Geotech Geoenviron Eng 134:1327–1338
Taylor DW (1948) Fundamentals of soil mechanics, LWW
Terzaghi K, Peck RB, Mesri G (1996) Soil mechanics in engineering practice. Wiley
Uesugi M, Kishida H (1986) Influential factors of friction between steel and dry sands. Soils Found 26:33–46
Vicari H, Ng CW, Nordal S, Thakur V, De Silva WRK, Liu H, Choi CE (2022) The effects of upstream flexible barrier on the debris flow entrainment and impact dynamics on a terminal barrier. Can Geotech J 99:1–13
Wang L, Song D, Zhou GG, Chen XQ, Xu M, Choi CE, Peng P (2022) Debris flow overflowing flexible barrier: physical process and drag load characteristics. Landslides:1–16
Whitman RV, Healy KA (1962) Shear strength of sands during rapid loadings. Journal of the Soil Mechanics and Foundations Division 88:99–132
Yang J, Li X (2004) State-dependent strength of sands from the perspective of unified modeling. J Geotech Geoenviron Eng 130:186–198
Yin J-H (2009) Influence of relative compaction on the hydraulic conductivity of completely decomposed granite in Hong Kong. Can Geotech J 46:1229–1235
Yoshimi Y, Kuwabara F, Tokimatsu K (1975) One-dimensional volume change characteristics of sands under very low confining stresses. Soils Found 15:51–60
Yu Z, Zhao L, Liu Y, Zhao S, Xu H, Chan S (2019) Studies on flexible rockfall barriers for failure modes, mechanisms and design strategies: a case study of Western China. Landslides 16:347–362
Yu Z, Luo L, Liu C, Guo L, Qi X, Zhao L (2021) Dynamic response of flexible rockfall barriers with different block shapes. Landslides 18:2621–2637
Zhang L, Zhang LM, Tang W (2009) Uncertainties of field pullout resistance of soil nails. J Geotech Geoenviron Eng 135:966–972
Zhao L, Yu Z-X, Liu Y-P, He J-W, Chan S-L, Zhao S-C (2020) Numerical simulation of responses of flexible rockfall barriers under impact loading at different positions. J Constr Steel Res 167:105953

Part III

Review Articles

Global Promotion of Understanding and Reducing Landslide Disaster Risk: Two Years on P-LRT

Shinji Sassa

Abstract

This article presents an overview and a concise review of a global promotion of understanding and reducing landslide disaster risk, based on 2 years of publication of Progress in Landslide Research and Technology (P-LRT). The Vol. 1 Issue 1, Vol. 1 Issue 2, Vol. 2 Issue1 and Vol. 2 Issue 2 of P-LRT were comprised of a total of ninety-seven articles from thirty-six countries/regions from Africa, Asia, Europe, North America, Oceania, and South America. The first four issues embody recent progress in landslide research and technology for practical applications and the benefit for the society contributing to the Kyoto Landslide Commitment 2020.

Keywords

Early warning and real-time prediction · Climate change · UNESCO · Experimental/numerical analysis · Standards and patents · Landslide-induced tsunami · Hazard mapping · Resilience and sustainability · Advanced monitoring technology · Earthquake-induced landslide · Rainfall-induced landslide · Giant landslides on volcanic islands and mountains · Rockslide · Reservoir landslide and landslide dam · Cultural heritage · Landslide-structure interaction · Risk communication · Education and network · Design and countermeasures · Socio-economic significance

1 Introduction

The Vols 1 and 2 of P-LRT: Progress in Landslide Research and Technology were composed of the contributions of ninety-seven relevant articles from thirty-six countries/regions worldwide, as shown in Fig. 1. The articles represented a total of forty-four original articles, ten review articles, four landslide lessons, a total of twenty-two articles on the projects of the International Programme on Landslides (IPL) and the World Centres of Excellence on Landslide Risk Reduction (WCoEs), and Kyoto Landslide Commitment, six teaching tools, six technical notes and case studies, and five world landslide reports from a total of four hundred and twenty-seven researchers/practitioners.

The themes were diverse and ranged from early warning and real-time prediction to climate change, UNESCO, experimental and numerical analysis, standards and patents, landslide-induced tsunami, hazard mapping, resilience and sustainability, advanced monitoring technology, earthquake-induced landslide, rainfall-induced landslide, giant landslides on volcanic islands and mountains, rockslide, reservoir

Fig. 1 Global promotion of understanding and reducing landslide disaster risk: Countries/regions with contributions to P-LRT highlighted in red

S. Sassa (✉)
Port and Airport Research Institute, National Institute of Maritime, Port and Aviation Technology, Yokosuka, Japan
e-mail: sassa@p.mpat.go.jp

B. Abolmasov et al. (eds.), *Progress in Landslide Research and Technology, Volume 3 Issue 1, 2024*, Progress in Landslide Research and Technology, https://doi.org/10.1007/978-3-031-55120-8_18

landslide and landslide dam, cultural heritage, landslide-structure interaction, risk communication, education and network, design and countermeasures, and socio-economic significance. An overview and a concise review of each theme above can be described as below.

2 Global Promotion of Understanding and Reducing Landslide Disaster Risk

2.1 Early Warning and Real-Time Prediction

The development and implementation of Landslide Early Warning Systems (LEWSs) in low-, lower-middle-, upper-middle-, and high-income countries (LICs, MICs, UMIs, and HICs) were reviewed by Alcántara-Ayala and Garnica-Peña (2023a, b, c) in light of the integrated disaster risk reduction (DRR) strategies perspective in line with the Sendai Framework for Disaster Risk Reduction (SFDRR) 2015–2030, addressing future challenges for the successful implementation and development of LEWSs. A recent development of real-time high-resolution predictions of orographic precipitation was presented by Onishi et al. (2023) and Bandara and Onishi (2023), based on the robust cloud microphysics for facilitating early warning of landsides due to orographic rainfall (Fig. 2). Gariano et al. (2023) presented an implementation of and challenges in defining frequentist rainfall thresholds using the statistics and an automatic tool for a landslide early warning system to forecast the occurrence of rainfall-induced landslides in two pilot areas in India. Konagai et al. (2023a) reported an outline of the joint research project between Japan and Sri Lanka, aiming at developing critical technologies for the early warning system against rainfall-induced landslides in Sri Lanka. Ha et al. (2023) proposed a landslide early warning system based on a landslide susceptibility map using a spatial multi-criteria evaluation (SMCE) method and an empirical rainfall threshold, showing the reliability of predicting the spatial and temporal occurrences of landslides in a case study in Vietnam. Fathani et al. (2023) presented an implementation of a new standard for community-based landslide early warning systems, the ISO (International Organization for Standardization) 22327:2018, to be used by communities vulnerable to landslides, and by government and non-governmental organizations at central, provincial, districts, sub-district, and village levels to reduce the possibility of injuries, loss of life, and damage to property and the environment. Ramesh et al. (2023a) proposed an Internet of Things (IoT) solution for building the real-time landslide monitoring and early warning system to provide community-scale disaster resilience, demonstrating the capability of the IoT system to gather spatiotemporal triggers for multiple types of landslides, detection and decision of specific scenarios, and the impact of real-time data on mitigating the landslide disaster (Figs. 3 and 4).

2.2 Climate Change

The prevalence of landslides in hilly and mountainous regions has increased due to climate change-induced extreme hydro-meteorological conditions. Wijaya et al. presented

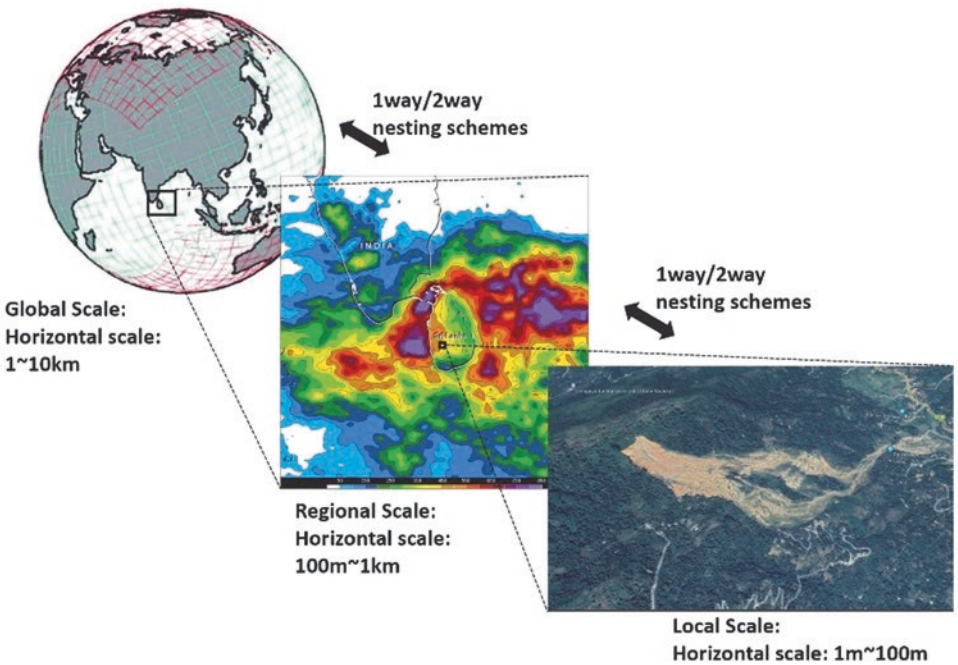

Fig. 2 Scales of atmospheric simulations. The nesting domain system is used in MSSG multiscale simulations. (**a**) Global simulations use Yin-Yang grid system, (**b**) regional simulations use the conventional longitude-latitude orthogonal grid system, (**c**) local (urban) simulations allow building and residential topography resolved. (Figure 1 in Bandara and Onishi 2023)

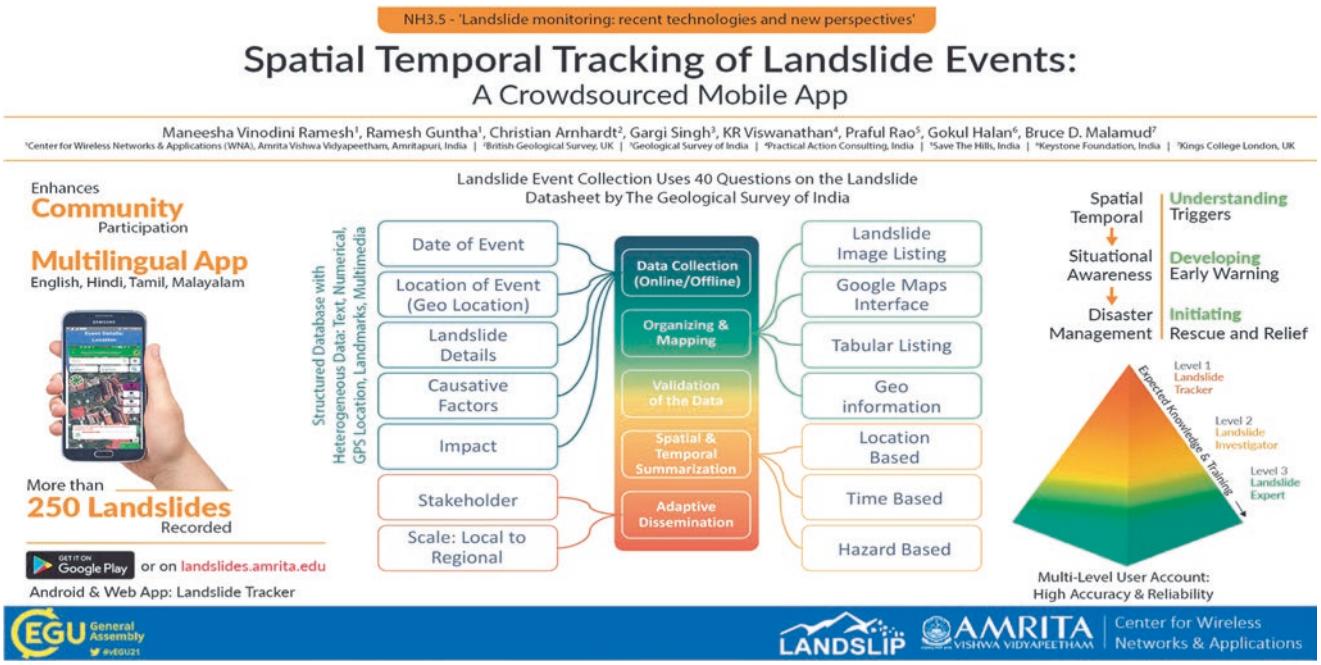

Fig. 3 Landslide Tracker: A Crowdsourced Mobile Application (Fig. 19 in Ramesh et al. 2023a)

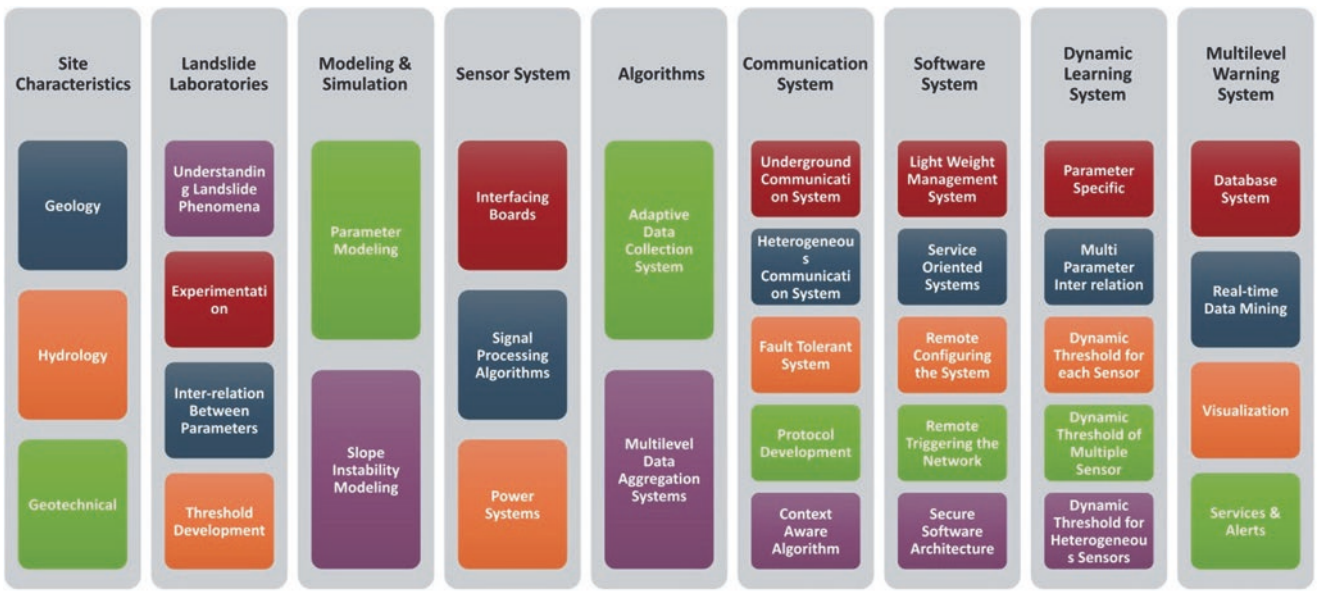

Fig. 4 Comprehensive Landslide Early Warning System (Fig. 20 in Ramesh et al. 2023a)

such climate change-induced regional landslide hazard and exposure assessment (Fig. 5) in mountainous regions under extreme rainfalls in Nepal, to aid climate resilient road infrastructure planning. Based on the extreme rainfall scenarios for the baseline period 1976–2005 and future horizons of 2030, 2050 and 2080, they developed high-resolution landslide hazard models adopting the Frequency Ratio (FR) and Analytical Hierarchical Process (AHP) methods, showing a significant increase of the landslide hazard under the future climate change scenarios. Beroya-Eitner et al. (2023) presented the projected decrease in rainfall and landslide susceptibility in a study area in the Philippines, whereas other hazards such as drought and water shortage might increase, which underscores the need for a multi-hazard assessment that takes into account the complex interrelationships between different hazards under changing climate. Abolmasov et al. (2023a) presented the framework of a project titled "Mainstreaming Climate Resilience in the Road Transportation Management in Serbia (CliRtheRoads)" comprising of a web portal for data entry and management

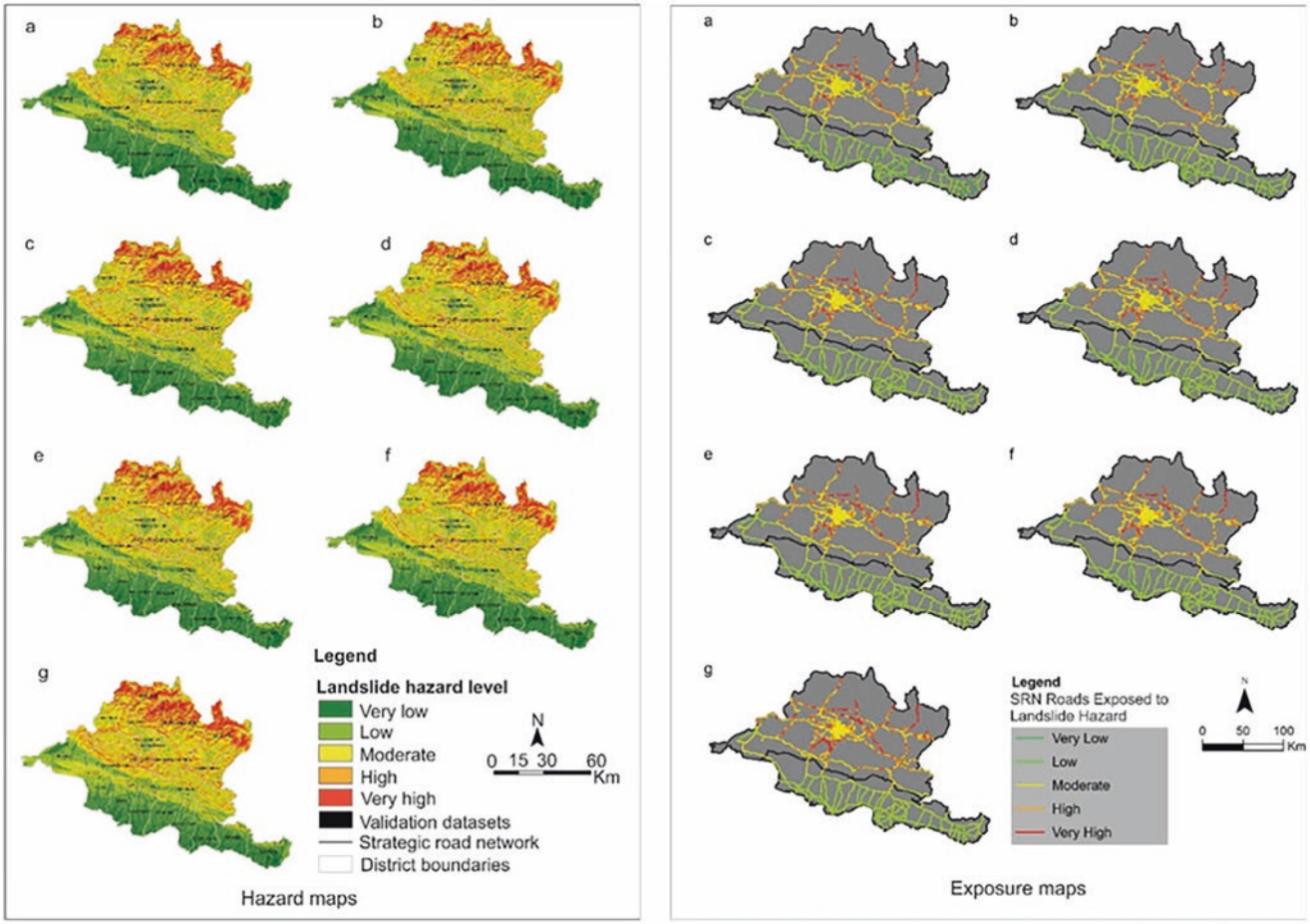

Fig. 5 Landslide hazard and exposure maps for (**a**) baseline period (1976–2005), (**b**) time horizon 2030s for RCP4.5, (**c**) time horizon 2030s with RCP8.5, (**d**) time horizon 2050s for RCP4.5, (**e**) time horizon 2050s for RCP8.5, (**f**) time horizon 2080s for RCP4.5 and (**g**) time horizon 2080s for RCP8.5. RCP denotes representative concentration pathways. (Figure 7 in Wijaya et al. 2023)

for authorised users, a publicly available web-GIS application, a mobile GIS application, and a back-end landslides database, to support decision- makers for better road management in climate changing conditions.

2.3 UNESCO

Delgado et al. (2023) reported the establishment of the Disaster Risk Reduction Unit in UNESCO and UNESCO's contribution to global resilience at all levels through multi-hazard, multi-discipline, and multi-stakeholder DRR mechanisms pertaining to landslide hazard under climate change, health, and sustainable development.

2.4 Experimental/Numerical Analysis

The application of spectral element method (SEM) in slope instability analysis was presented by Tiwari and Bhandary (2023), where the SEM procedure has three major benefits over the existing FEM procedures: (1) geometrical flexibility, (2) high computational efficiency, and (3) reliable spectral accuracy, which could be used in an effective design and implementation of various slope stability analysis. The use of experimental models to calibrate numerical models for slope stability and deformation analysis was presented by Tiwari and Tran (2023), showing how various soil and ground parameters influence the stability of slopes and how numerical models can be calibrated with the experimental modeling results to apply the calibrated numerical models for field slopes/landslides. Ajmera et al. (2023) presented the teaching tool and manual of LS-RAPID, an integrated simulation model capable of capturing the entire landslide process starting from a state of stability to landslide initiation and movement to the mass deposition, illustrating the applications to (1) a rainfall-induced failure, (2) an earthquake-induced failure, and (3) the case study of the Atami debris flow, as supplemented by the video tutorials.

Large-scale creeping landslides were experimentally simulated in Bhandary (2023), based on a modified ring shear machine, showing a comprehensive understanding on the residual-state creep deformation behavior of clayey materials for predicting landslide creep displacement and failure. Tan and Tang (2023) presented an in-situ triaxial creep test on gravelly slip zone soil of a giant landslide in the Three Gorges area of China, showing that the sliding zone soil behavior matches the observed landslide behavior. Loi et al. (2023) presented the teaching tool for the undrained dynamic-loading ring-shear testing with video to experimentally study landslide dynamics involving the entire process from the initial stage of stress before landslide occurrence and stress changes due to static, dynamic loading or pore pressure changes or other types of stress loading to the formation of a sliding surface and the steady-state shear resistance.

The sliding-surface liquefaction (SSL) concept (Fig. 6) and the undrained steady-state shear-strength to understand and reduce rapid landslide disaster risk were presented by Sassa et al. (2023a). SSL occurs even in dense sandy layers. SSL is caused by a series of phenomena, (1) grain-crushing due to shearing under overburden pressure in the shear zone, (2) volume reduction in the shear zone, (3) generation of high pore-water pressure in the shear zone, and (4) liquefaction of the shear zone material. After SSL, a mass of soil layer above the liquified sliding surface moves at high speed, and the generated pore pressure reaches a certain constant value which is the undrained steady-state shear-strength (USS).

The resultant feature of rapid and long- travelling landslides poses a high risk to people living in/near slopes.

Recent advancements in shear strength interpretation, testing, and use for landslide analysis were presented by Tiwari and Ajmera (2023), based on various soil testing involving direct shear tests, triaxial tests, ring shear tests, and cyclic simple shear tests. They summarized correlations developed in the literature to estimate various shear strengths, including the fully softened and residual shear strengths of soil (Fig. 7).

The behaviour of small-scale slope models supported by various remedial measures under artificial rain in 1 g conditions was presented and discussed in Arbanas et al. (2023), showing the impact of the appropriate mitigation measures on retaining the stability of the slopes, which otherwise collapsed, and hence reducing landslide disaster risk. Ariyarathna and Sasahara (2023) presented a procedure of data processing for the improvement of failure time prediction of a landslide using the velocity and acceleration of the displacement based on a small-scale slope model experiment and a field experiment on a natural slope.

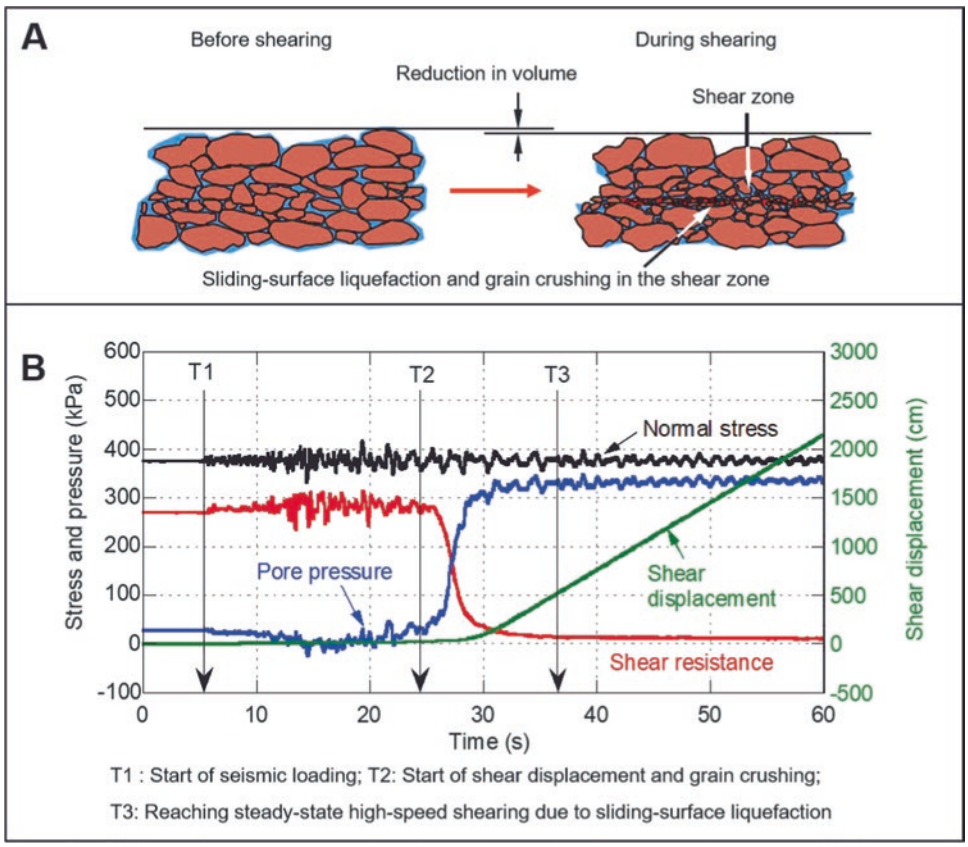

Fig. 6 Illustration and experimental data for the sliding-surface liquefaction (Fig. 3 in Sassa et al. 2023a)

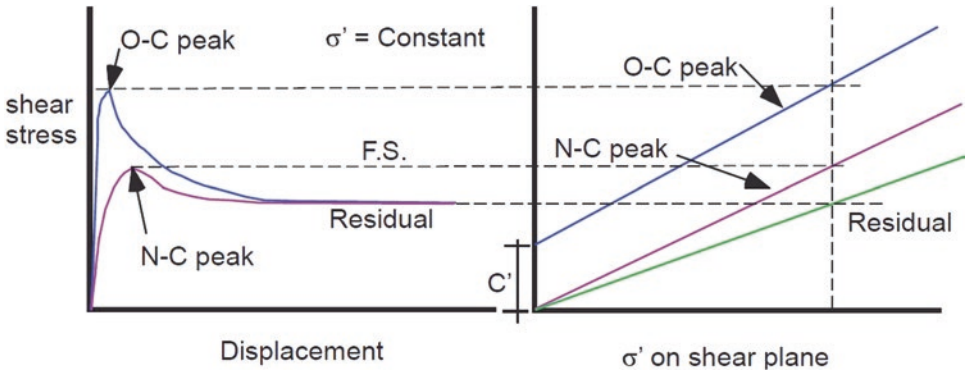

Fig. 7 Shear stress—shear displacement (left) and shear-stress-normal stress (right) relationship for over-consolidated and normally consolidated soils (Fig. 7 in Tiwari and Ajmera 2023)

2.5 Standards and Patents

Landslide-related patent documents were extracted from open-access databases in order to evaluate how well they relate to the field of landslide research and technology (Mikoš 2023a), showing potential of such intellectual property to find more application in real word solutions when planning and executing landslide disaster risk reduction.

A list of twenty-two international standards containing landslide-related terms (landslide, debris flow, rock fall) was presented by Mikoš (2023b), using the Online Browsing Platform by the International Organization for Standardization (ISO). A new standard published as ISO 22327:2018 empowers individuals and communities vulnerable to landslides to act in sufficient time, and in appropriate ways to reduce the possibility of injuries, loss of life, and damage to property and the environment, thereby strengthening the communities' resilience to landslide disasters (Fathani et al. 2023).

2.6 Landslide-Induced Tsunamis

Sassa (2023a, b) and Sassa et al. (2022, 2023b) presented some recent advances, the current state and challenges in understanding and reducing the disaster risk of landslide-induced tsunamis (e.g. Figs. 8 and 9), based on a global review and the outcome of a global panel discussion organized across America, Europe, and Asia and the review of the World Tsunami Awareness Day Special Event of the Fifth World Landslide Forum. Kawamura et al. (2023) reported ongoing persistent slope failures at the toe of a giant submarine slide in the Ryukyu trench that generated the AD 1771 Meiwa tsunami, based on the three dive surveys using a manned submersible in the trench. Dang et al. (2023) presented the development and application of the LS-Tsunami simulation code as a teaching tool, which utilizes landslide motion data from LS-RAPID to model landslide-induced tsunamis, illustrating several case studies (e.g. Fig. 10).

2.7 Hazard Mapping

Moncayo and Ávila (2023) presented the analysis of the database of 123 landslides from the Andean region of Colombia, where the empirical-statistical modeling incorporated landslide travel distances associated with landslide volume, slope angle, maximum landslide height, and geomorphological environment, resulting in a hazard map to identify possible zones affected by landslide processes in this area. Bornaetxea et al. (2023a) presented a landslide inventory mapping for the rocky mountains in British Columbia, Canada, based on the 1286 landslides in a 1200 km^2 area by classifying them into 11 categories and three levels of certainty. Nguyen et al. (2023a, b) presented the application of an Analytical Hierarchy Process (AHP) for landslide susceptibility mapping, showing significant effects of the rainfall frequency on landslide susceptibility in a mountainous region of central Vietnam. The AHP method was used to construct the landslide susceptibility maps in the Republic of Serbia (Abolmasov et al. 2023b) and in the tropical zone of Vietnam (Tien et al. 2023) based on the landslide identification using the unmanned aerial vehicles (UAV) and landslide mapping through the World Digital 3D and Google Earth maps. Mihalić Arbanas et al. (2023) presented the application of data and information from landslide inventory and landslide susceptibility maps (Fig. 11) based on LIDAR (Light Detection and Ranging) and DTM (Digital Terrain Model) for spatial and urban land-use planning in Croatia. The quality of a large-scale landslide susceptibility mapping was discussed by Krkač et al. (2023), based on a case study from Croatia, showing the impact of the spatial accuracy of the input data on the landslide susceptibility assessment. Bornaetxea et al. (2023b) and Bernat Gazibara et al. (2023b) presented a tool for the statistically-based landslide susceptibility zonation, LAND-SUITE, with its applications to the Gipuzkoa province in Spain and the Hrvatsko Zagorje area in Croatia. Paulín et al. (2023a, b) presented the landslide susceptibility assessment based on the digital terrain models (DTMs) derived from UAV and the multiple logistic regression (MLR) model with its application to areas affected by

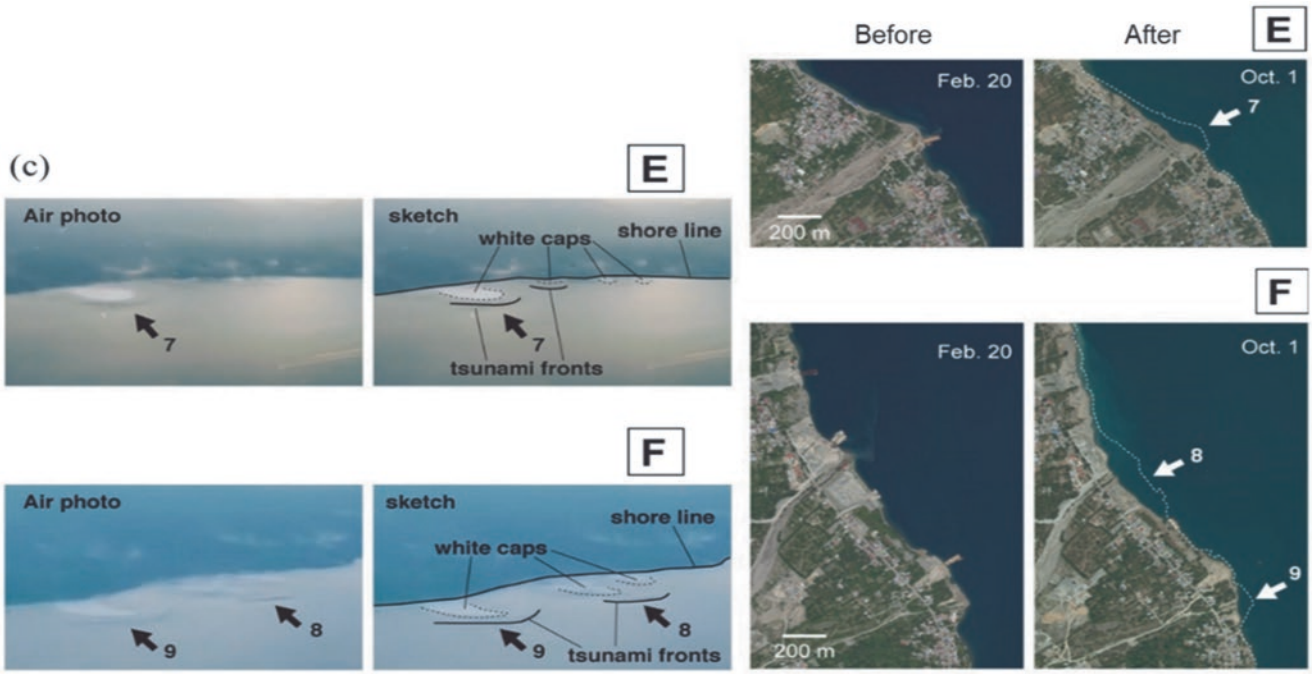

Fig. 8 Comparing the locations of multiple tsunami generations, alongshore distributions and directions with the locations, distributions and directions where the coastal lands collapsed and flowed due to the occurrence of liquefaction in the 2018 Indonesia Sulawesi earthquake (Fig. 4(c) in Sassa and Takagawa 2019) (Fig. 8 in Sassa et al. 2023b)

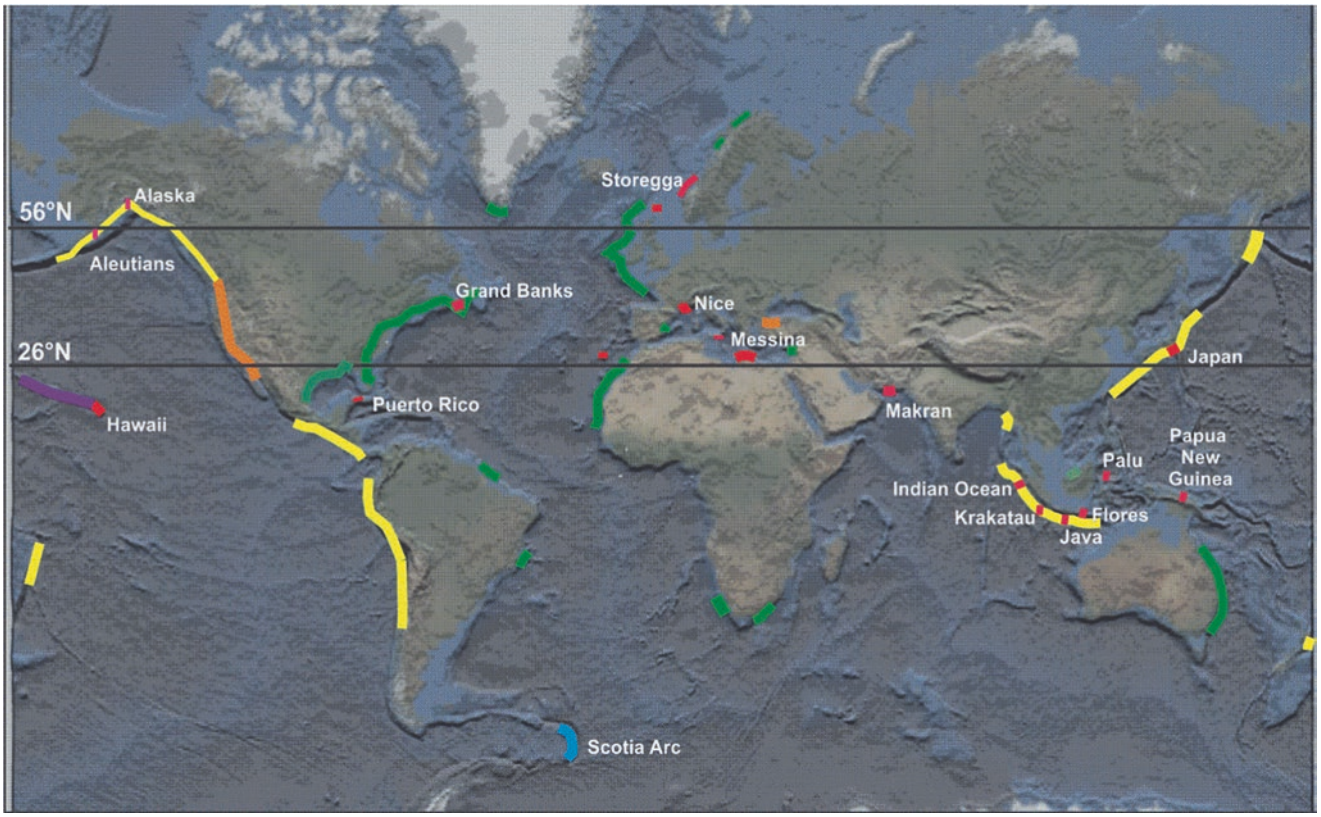

Fig. 9 Global distribution of mapped submarine landslides (SLs): Green, SLs on passive margins; Yellow, SLs located along convergent margins; Orange, SLs on strike slip margins; purple, volcanoes; Red, tsunamis associated with SLs (Tappin and Grilli 2020). Submarine landslide tsunamis (in red) are mainly located along convergent margins, but also along passive and strike slip margins and on flanks of volcanoes (Fig. 17 in Sassa et al. 2023b)

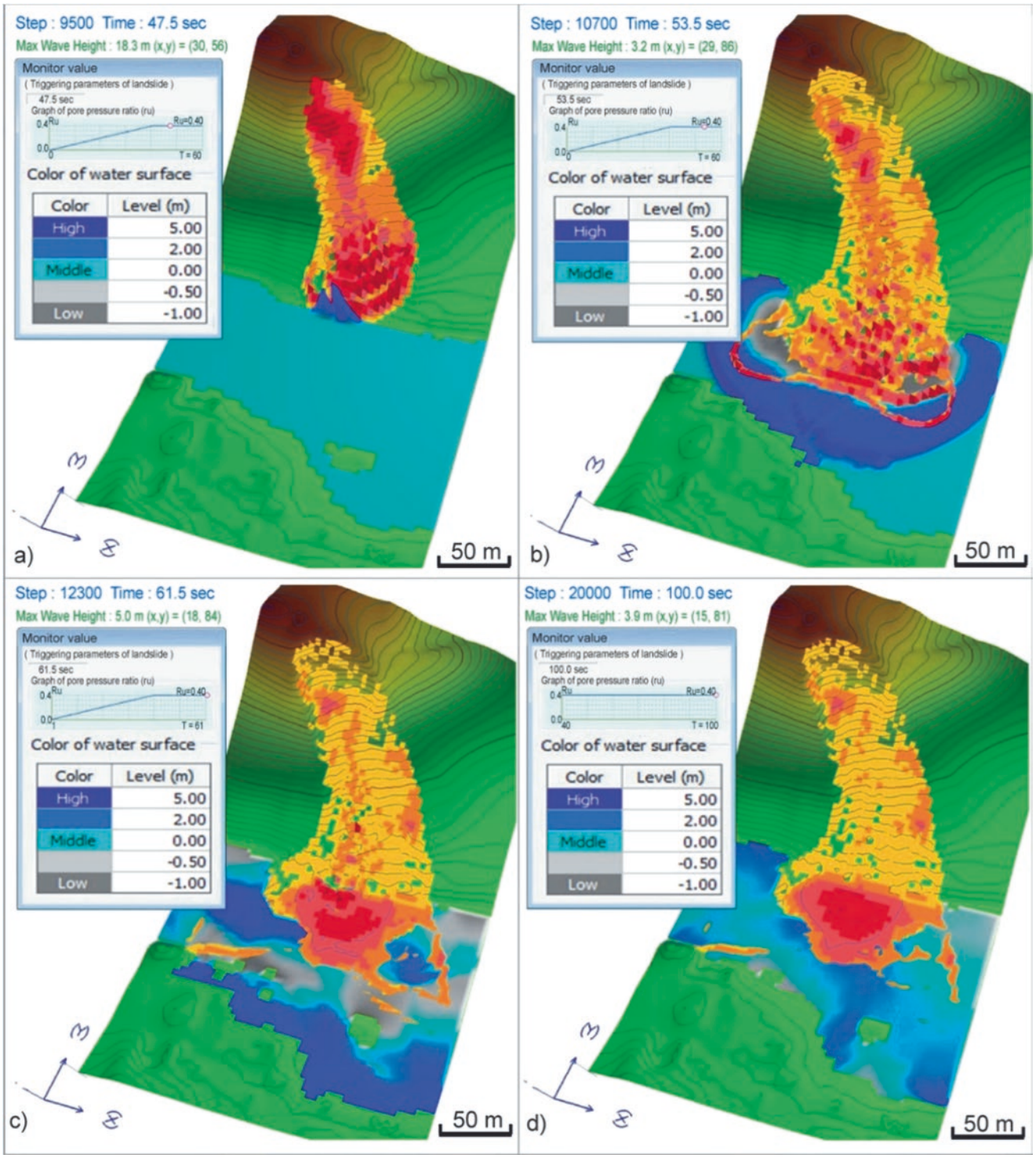

Fig. 10 Simulation of tsunami-like wave across the Truong River propagating from the landslide (from Duc et al. 2020) (Fig. 27 in Dang et al. 2023)

rockfalls and shallow landslides in State of Morelos and on the south flank of Pico de Orizaba volcano with more than six hundred landslides mapped into GIS and grouped into landform units, Mexico. Thirugnanam (2023) presented a review of the use of deep learning for landslide detection and landslide susceptibility mapping, emphasizing the need for further development.

Bernat Gazibara et al. (2023a) presented the landslide and soil erosion inventory mapping (Fig. 12) based on the visual interpretation of high-resolution remote sensing data in a

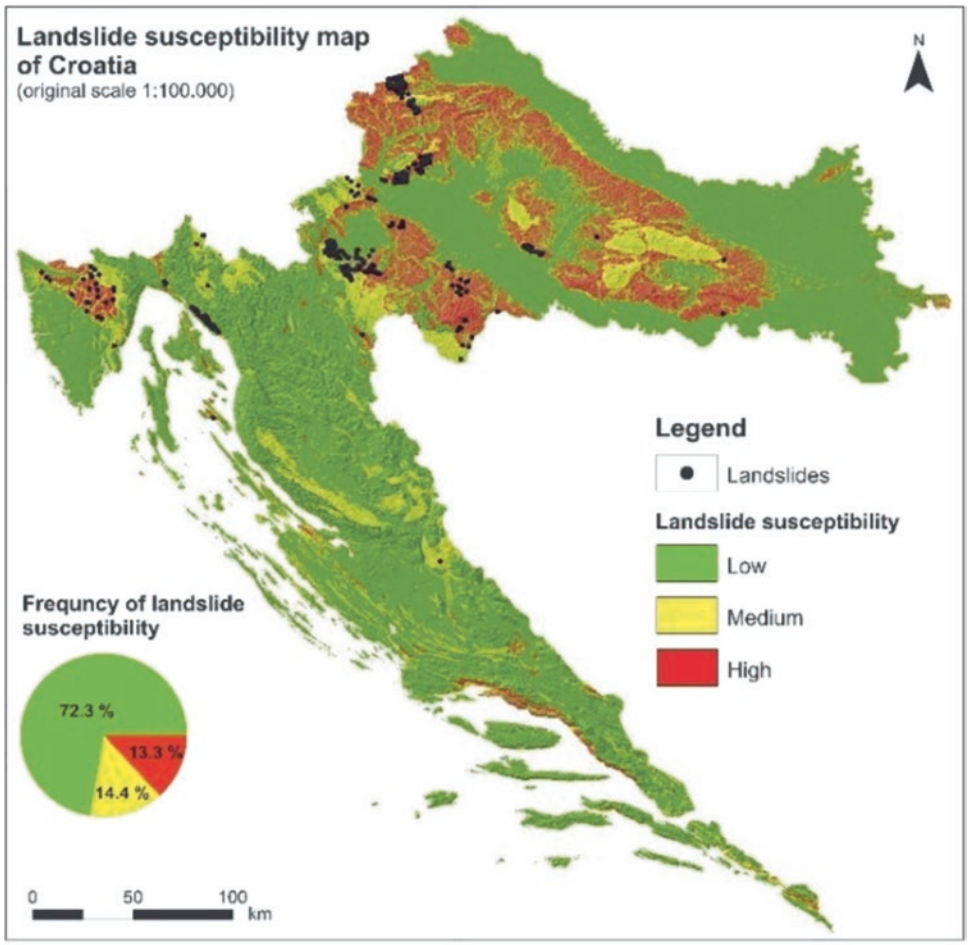

Fig. 11 Landslide susceptibility map of Croatia, original scale 1:100,000 (Bernat Gazibara et al. 2022) (Fig. 7 in Mihalić Arbanas et al. 2023)

case study from Istria, Croatia, showing the potential for the future landslide and erosion hazards management. Vacha et al. (2023) presented the post-wildfire monthly erosion rates at the catchment scale on GIS in the north-western Italian Alps, highlighting the marked increase (more than 20 times) in erosion rates in the post-fire scenario than the pre-fire one.

Erzagian et al. (2023) developed a landslide susceptibility map using the frequency ratio (FR) approach, where the controlling factors involving elevation, slope, aspect, lithology, lineament density, distance from streams, distance from roads, land use, and rainfall (Fig. 13), were combined with seven hundred and forty-four landslide data though GIS in the Kulon Progo Mountains Area, Indonesia. The frequency ratio (FR) approach combined with the fractal analysis considering the spatial relationship between past landslides and four landslide factors: distance to roads, distance to faults, distance to drainage, and distance to geological boundaries was presented by Duong et al. (2023a), to produce a landslide susceptibility map in Cao Bang province, Vietnam. Michel (2023) presented a consequence - frequency matrix approach as a tool to assess landslides risk and susceptibility with its application to Pont Bourquin Landslide in the Swiss Prealps, Switzerland. Beroya-Eitner et al. (2023) presented the rainfall-induced landslide susceptibility maps in Davao Oriental, Philippines in the historical period 1986–2005 and in the projected period 2046–2065, showing a decrease in the landslide susceptibility by the mid-twenty-first century (Fig. 14).

The rainfall-induced shallow landslide susceptibility map was produced for land-use planning in the High City of Antananarivo, Madagascar (Frodella et al. 2023a, Fig. 15).

2.8 Resilience and Sustainability

The use of natural-hazard-related-web-observatory as sustainable development took was discussed by Mikoš et al. (2023) to support the implementation of sustainable development at different scales, where the information gathered on the internet is structured, and shown using geolocators for different regions and/or countries susceptible to landslides. UNESCO's new disaster risk reduction unit aims to contribute to global resilience against multi-hazards involving landslides (Delgado et al. 2023).

The sustainability of geosynthetics-based solutions to mitigate landslide disaster risk was presented by Damians

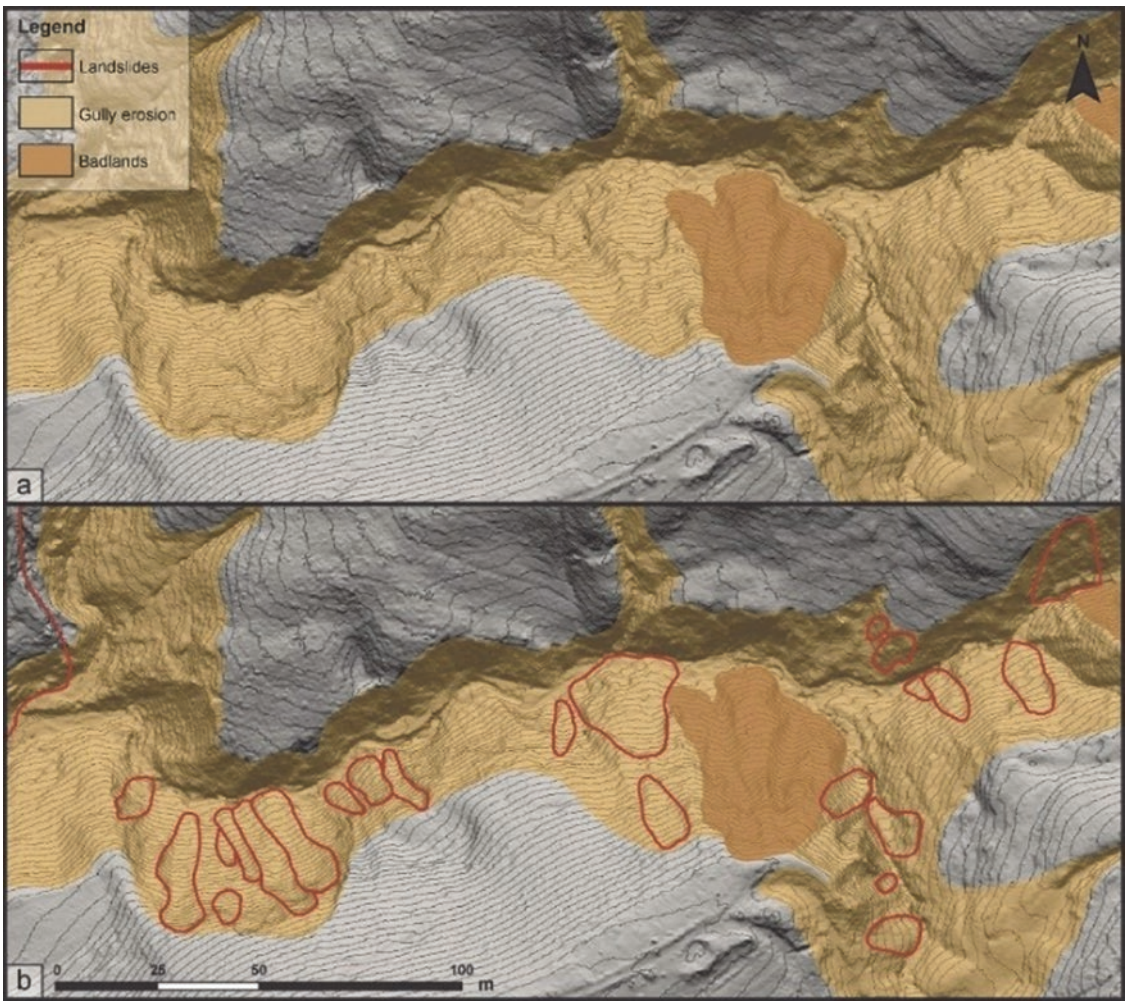

Fig. 12 Example of landslide mapping in areas affected by gully and combined erosion on LiDAR DTM derivatives (Fig. 9 in Bernat Gazibara et al. 2023a)

et al. (2023) by identifying the sustainability factors to consider when applying geosynthetics and showing how a value integrated model for sustainability evaluations (MIVES) methodology (Fig. 16) can be applied to evaluate and compare alternative methods for remediation of landslides.

Restoration works including the road cut slope protections, data gathering of constructed slopes, data evaluation, and design of remedial measures for mountainous regions/countries also contribute to the development of the landslide disaster resilience (Dias et al. 2023). Ramesh et al. (2023b) presented a framework to build and strengthen community-scale landslide resilience (Fig. 17) using a citizen-science approach involving a landslide tracker mobile app, social media data analysis, and community involvement, with its application to two case study areas Munnar and Chandmari in India, which can help policymakers, community leaders, change makers, administrative officials, and researchers in disaster management.

2.9 Advanced Monitoring Technology

Huntley et al. (2023a,b,c,d) reported an effective monitoring technology and practices involving the satellite Interferometric Synthetic Aperture Radar (InSAR) interferograms, UAV time-series photograms and the remotely piloted aircraft system (RPAS), and the ground-based real-time kinematic global navigation satellite system (RTK-GNSS) surveys to describe the form and function of a wide range of rapid and slow-moving landslides, combined with the field-based geological observations, terrain classification and boreholes, for the railway transportation corridors in south-western British Columbia, Canada (e.g. Figs. 18 and 19). Casagli et al. (2023) reported advanced monitoring techniques to estimate the temporospatial deformational evolution of landslide events by using the ground-based InSAR (GB-InSAR, Fig. 20), LIDAR, persistent scatterer InSAR (PS-InSAR), UAVs equipped with different sensors, GPS

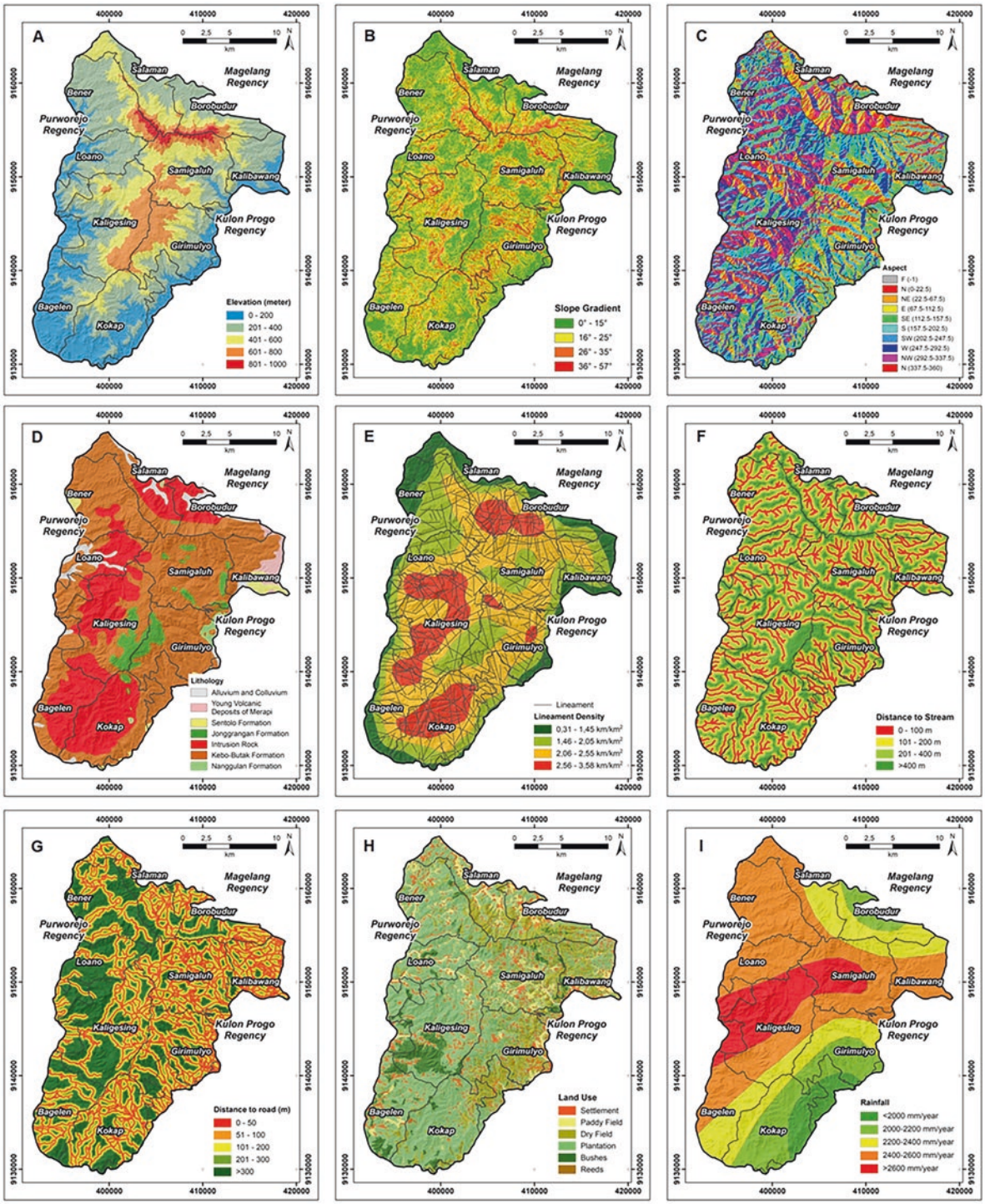

Fig. 13 Landslide-controlling factor maps: (**a**) elevation; (**b**) slope; (**c**) aspect; (**d**) lithology; (**e**) lineament density; (**f**) distance from streams; (**g**) distance from roads; (**h**) land use, and (**i**) rainfall (Fig. 3 in Erzagian et al. 2023)

antennas, infrared thermography and traditional instrumentation (e.g. strain gauges, inclinometers, piezometers), providing the satellite-based services at regional scale in Italy. Trofymchuk et al. (2023) reported the application of landslide monitoring comprised of the PS-InSAR, GIS database and DEM to the stability assessment of St. Andrew's Church in Ukraine. The application of an advanced PS-InSAR, SqueeSAR algorithm, to the Humarri slide in the Hunza-Nagar River valley in northern Pakistan was presented by Poggi et al. (2023). Hoang et al. (2023) applied an automatic

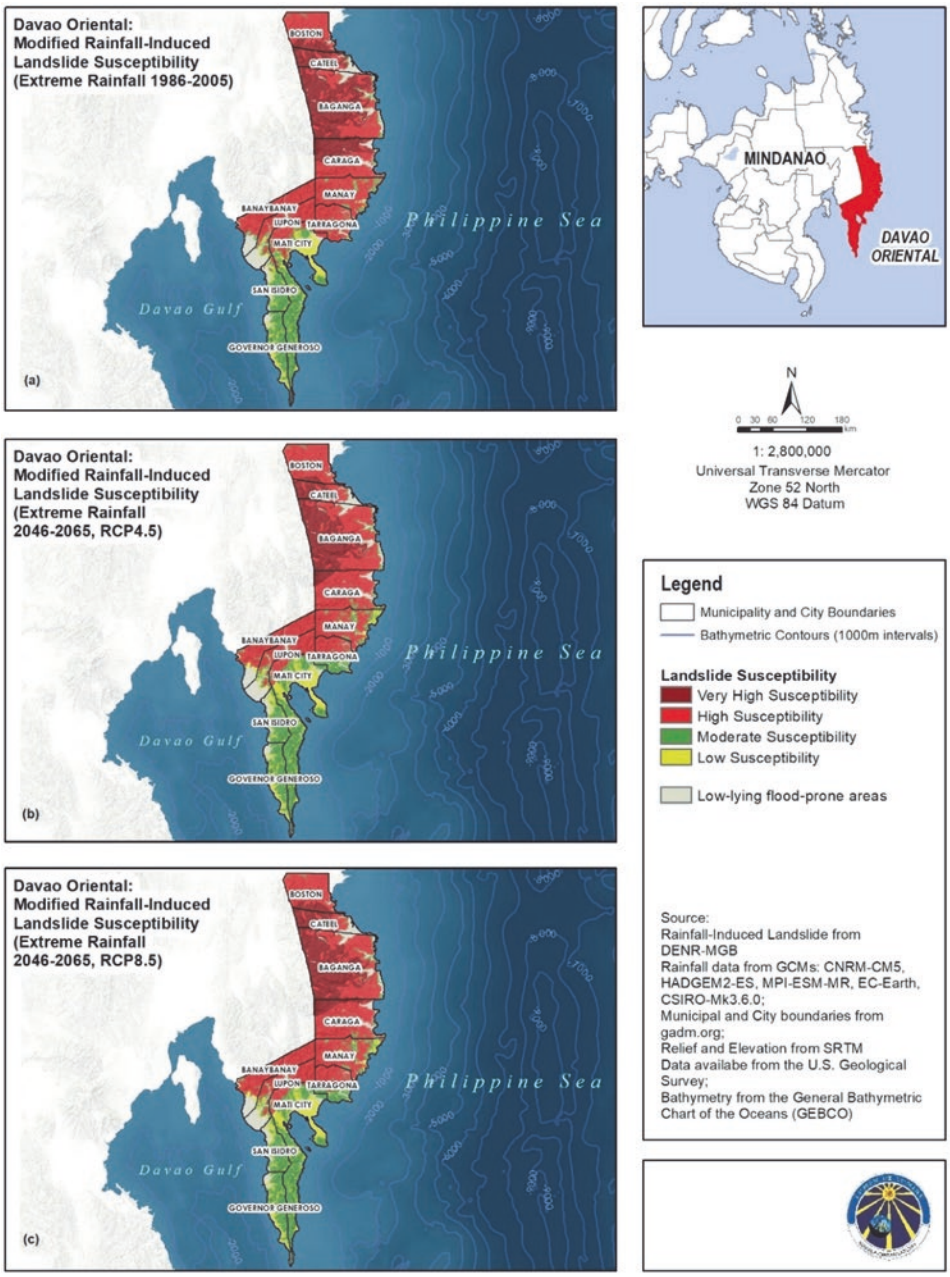

Fig. 14 Modified rainfall-induced landslide susceptibility maps of Davao Oriental (**a**) Historical (1986–2005), (**b**) Projected under RCP4.5 (2046–2065), and (**c**) Projected under RCP8.5 (2046–2065). A decrease in landslide susceptibility is expected by the mid-twenty-first century, mainly in Baganga, Cateel and Caraga, following a decrease in extreme rainfall in the area. (Figure 8 in Beroya-Eitner et al. 2023)

real-time landslide monitoring system with multiple GPS antennas to the Alishan highway traversing steep sloping land in Chiayi County, Taiwan. Fukuhara et al. (2023) presented the use of multi-point Micro Electro Mechanical Systems (MEMS) tilt sensors to detect the spatiotemporal variation of the behavior of vulnerable slopes. Thanh et al. (2023) showed a community-level monitoring network comprised of the UAVs, ALOS World 3 Digital (AW3D) Data, and Google earth images, with its application to mountainous areas in northern Vietnam. Bernat Gazibara et al. (2023a) presented the application of high-resolution remote sensing involving the LIDAR data and orthophoto images to small and shallow landslides and soil erosion processes in the Istrian flysch area in Croatia.

2.10 Earthquake-Induced Landslide

Wang and Nam (2023) reported the characteristics of the landslide disasters caused by the 2018 Eastern Iburi Earthquake in Hokkaido Japan, pertaining to the distinctive properties of the widely distributed, weathered Plinian Ta-d

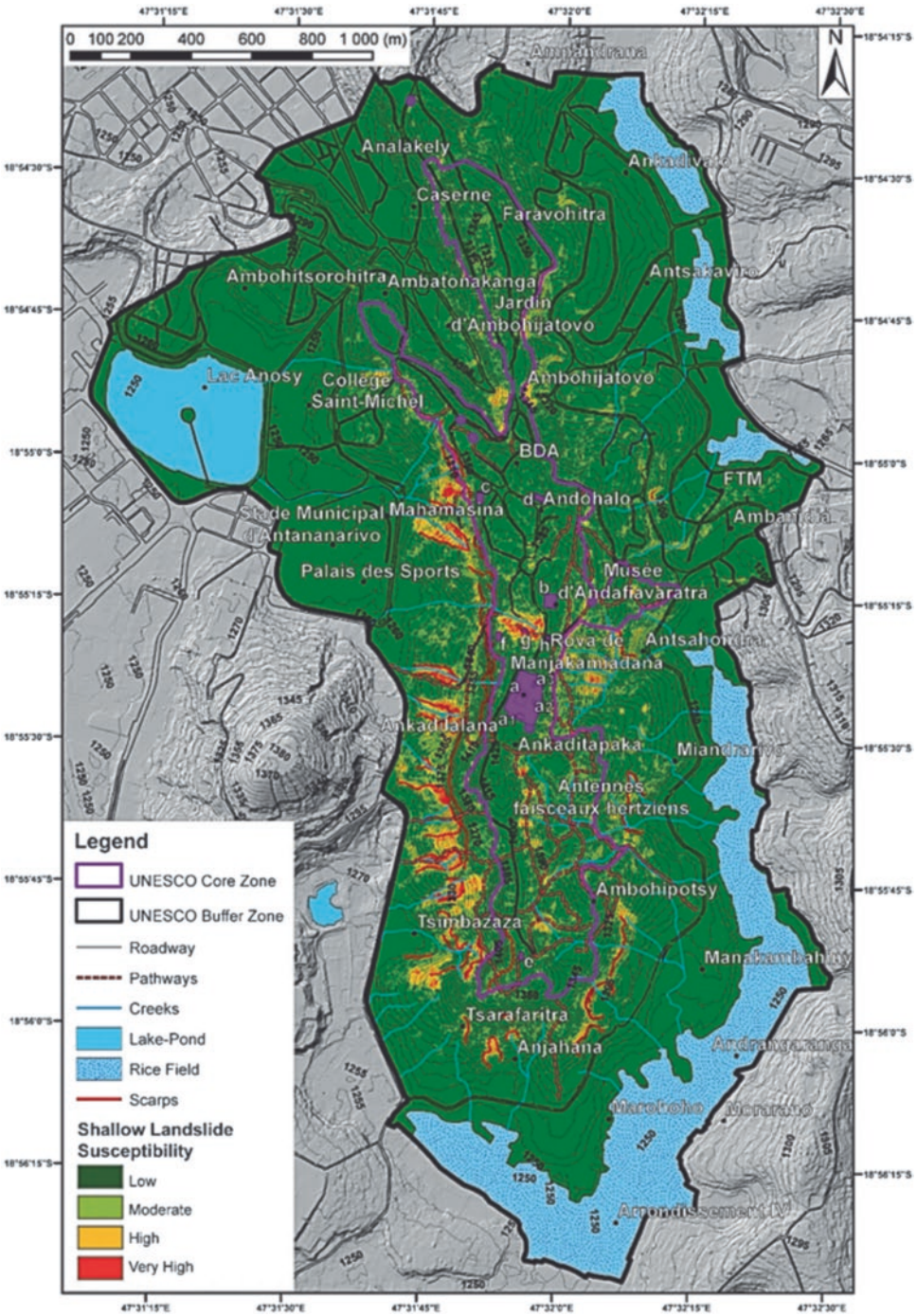

Fig. 15 Shallow landslide susceptibility map of the Analamanga Hill (modified after Frodella et al. 2022) (Fig. 3 in Frodella et al. 2023a)

tephra deposits from the Tarumae volcano and their impact on the spatial clustering of the Iburi landslides, together with the implementation of a countermeasure by removing the surficial volcanic ashes over the slopes (Fig. 21).

Konagai et al. (2023b) reported the post-earthquake deformations that can last for months in the grounds that have undergone liquefaction and spread laterally due to earthquakes (Fig. 22), by showing two case studies of the 2018 Sulawesi Earthquake, Indonesia and the 2015 Gorkha earthquake, Nepal. Konagai (2023) also reported the characteristics of the landslides in the 2004 Mid-Niigata Prefecture Earthquake, Japan, showing an estimate of the coseismic displacements and stress changes with their impact on the post-earthquake rehabilitations. Higaki et al. (2023) presented a

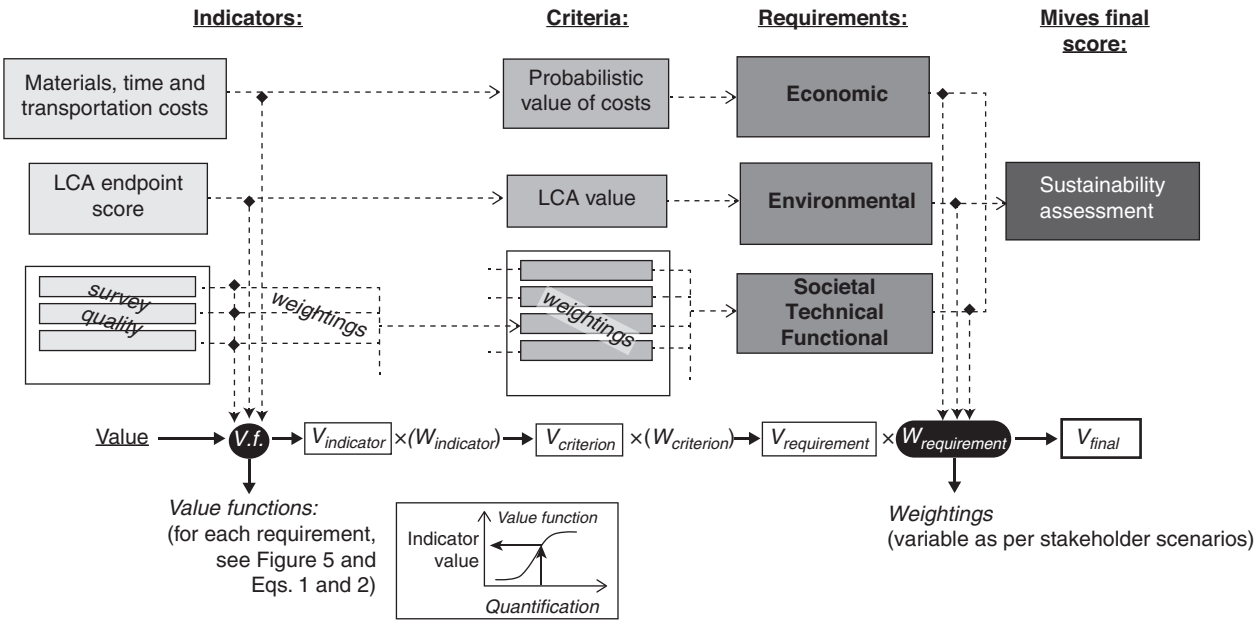

Fig. 16 Sustainability assessment flow chart or requirements tree proposal for landslide applications (modified from Damians et al. 2018) (Fig. 4 in Damians et al. 2023)

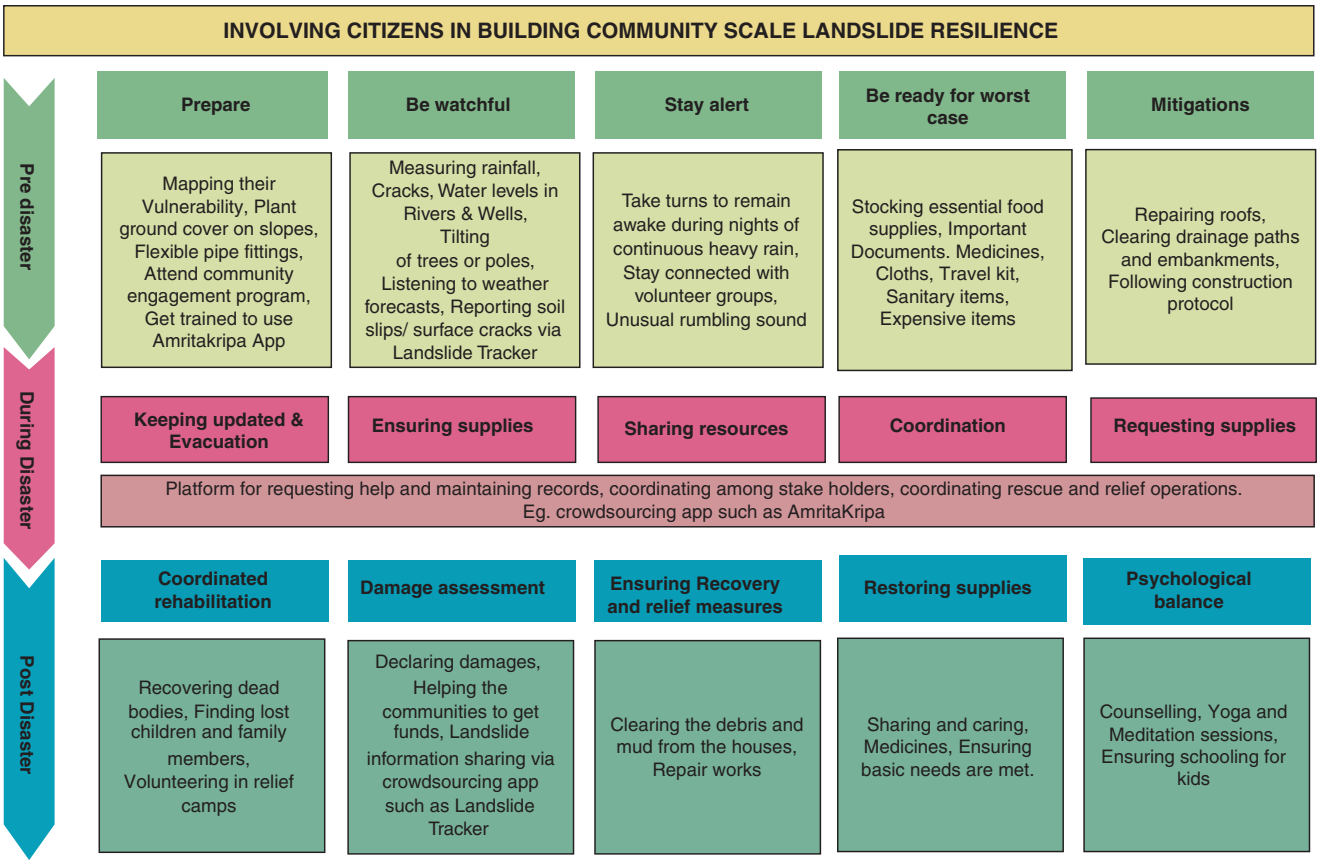

Fig. 17 Proposed framework for involving citizens in building community-scale landslide resilience (Fig. 1 in Ramesh et al. 2023b)

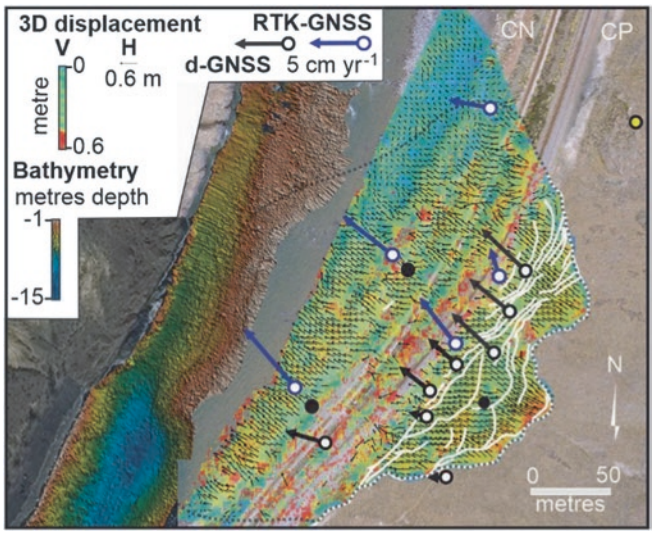

Fig. 18 Ripley Landslide surface displacement data derived from UAV overflights in 2016 and 2018 and multi-beam bathymetry data collected in 2018; plotted with RTK-GNSS (average annual rate for 2017, 2018 and 2019) and d-GNSS displacement data (November 2018 to June 2019, expressed as cm year^{-1}). Stable d-GNSS unit—yellow dot; active d-GNSS unit—black and white dot; inactive d-GNSS—black dot. Active GCP - blue dot (modified from Huntley et al. 2021) (Fig. 4 in Huntley et al. 2023b)

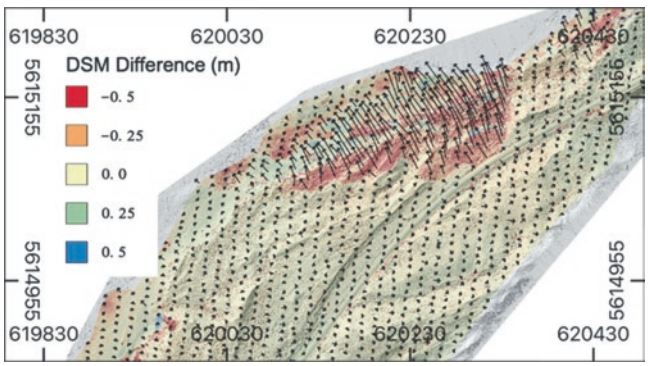

Fig. 19 3D RPAS deformation over North Slide between 2019-09-19 and 2021-09-28. Vectors indicate horizontal deformation from MicMac digital image correlation and colour scale represents difference in DSMs. Hill-shade transparency is applied for context (Fig. 5 in Huntley et al. 2023c)

review of the mega slide of Unzen-Mayuyama of Quaternary volcanic rock due to the 1792 earthquake, and the numerous shallow landslides that disrupted highway and rail traffic due to the 2016 Kumamoto earthquake, Japan (Fig. 23) as well as the subsequent unmanned slope stabilization works (Fig. 24) with earth retaining walls, embankments and re-vegetation.

2.11 Rainfall-Induced Landslide

Gratchev et al. (2023) presented the mechanisms of rainfall-induced shallow landslides in Australia, showing an important role of the formation of wetting (moisture) front, increases in water content, and the excess pore water pressure generation in jointed, bedded, and weathered sandstone deposits. Konagai et al. (2023a) reported a review of the rapid and long-travelling landslides that took place at Aranayake 2016 and Athwelthota 2017 in Sri Lanka and the joint research framework between Japan and Sri Lanka for developing essential technologies for an effective early warning system against such rainfall-induced landslides (Fig. 25). The effect of rainfall frequency on the susceptibility of rainfall-induced landslides was investigated by Nguyen et al. (2023a, b), using the Regional Frequency Analysis (RFA) in a case study for a mountainous region in Central Vietnam. The characteristics of suffusion landslides associated with the rise in groundwater level due to rainfall in the European part of Russia was presented by Zerkal and Barykina (2023). Yasufuku and Alowiasy (2023) and Higaki et al. (2023) presented the characteristics of heavy rainfall-induced landslides that took place in Kyusyu Island and Hiroshima, Japan, during the last decade, together with the mitigation and prevention measures adopted in those areas respectively. Duong et al. (2023b) presented the deterministic and probabilistic slope stability analysis using finite element (FEM) and limit equilibrium (LEM) methods in connection with the landslide events triggered by heavy rainfalls in the Sapa district, Vietnam, showing consistency with the actual landslides. Tofani et al. (2023) presented a high-resolution slope stability simulator (HIRESSS) model for analyzing the occurrence of shallow landslides during a rainfall event with its application to the Aosta Valley region in the northwest of the Alpine chain, showing a satisfactory validation against the 2009 event with a complete database of the landslides (Fig. 26). The historical and future rainfall-induced landslide susceptibility mapping of Davao Oriental, Philippines was presented by Beroya-Eitner et al. (2023) and described in the sections "Climate Change" and "Hazard Mapping" above. The rainfall-induced landslide hazard map based on the comparison between rainfall data and the recorded landslide events (Fig. 27) was generated for land-use planning in the High City of Antananarivo, Madagascar (Frodella et al. 2023a) and described in the section "Hazard Mapping" above.

2.12 Giant Landslides on Volcanic Islands and Mountains

Rowberry et al. (2023) presented a comprehensive online database of giant landslides on volcanic islands, describing a total of seventy-five landslide events from the Atlantic Ocean and Mediterranean Sea, sixty-seven landslide events from the Pacific Ocean, and forty landslide events from the Indian Ocean (Fig. 28). Ríos and Ávila (2023) presented the landslide risk assessment based on the two landslide events that took place in 2019 and 2020 in the city of Pereira in the

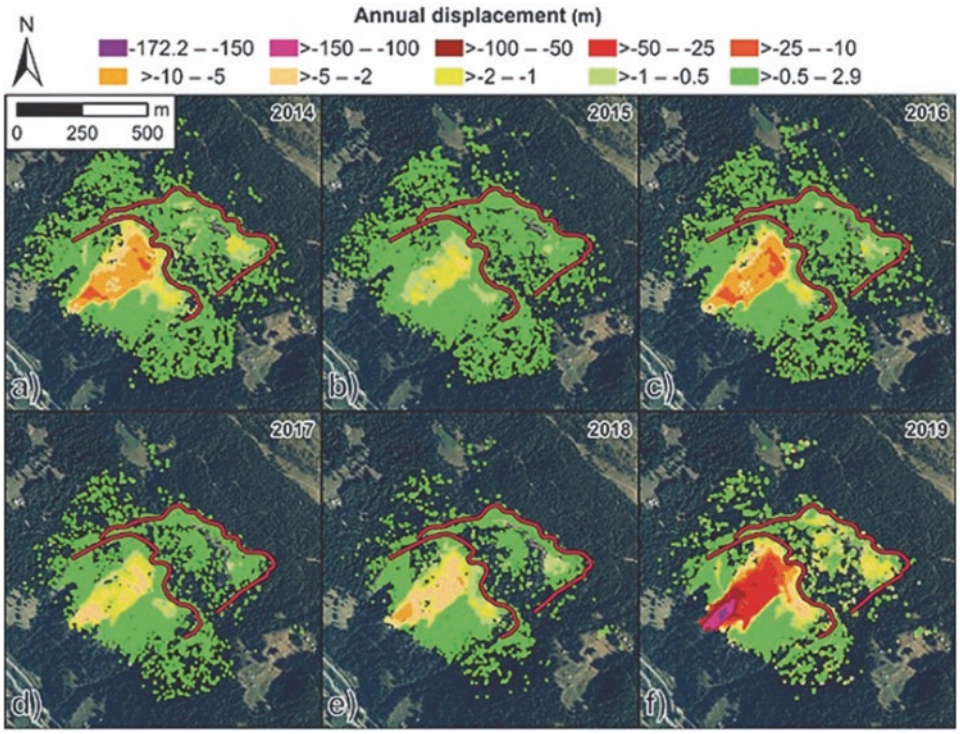

Fig. 20 Annual cumulative displacements of the Ruinon slide area measured by the GBInSAR system from 2014 to 2019 (**a**–**f**) (Fig. 1a–f in Casagli et al. 2023)

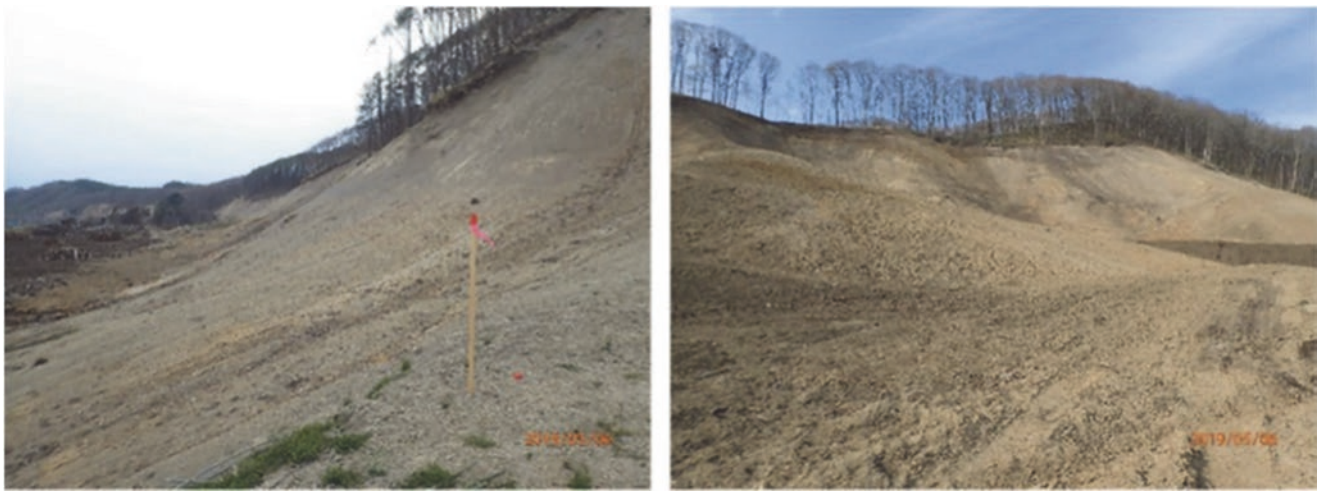

Fig. 21 The photos showing the slopes after removing the surficial volcanic ashes (Fig. 7 in Wang and Nam 2023)

Central Cordillera of the Colombian Andes mountainous region composed of volcanic soils.

2.13 Rockslide

Abe et al. (2023) presented the role of translational rockslides in the evolution of cuesta topography based on the field surveys in Japan, Taiwan, Switzerland, and Nepal, showing a common feature such that rockslides on cuesta's back slopes slide along the same laminar rock joints over a long term, thus maintaining the cuesta landscape. Strom (2023) presented large-scale rockslides, rock avalanches and manifestations of active tectonics leading to the compilation of a complete rockslide database of the entire Central Asia Region involving Afghanistan, China, Kazakhstan, Kyrgyzstan, Tajikistan, and Uzbekistan (e.g. Fig. 29). Dias et al. (2023) presented the characteristics of rock failures along mountainous road side slopes in Sri Lanka, comprised of wedge failure, translational slides and falling rocks (Fig. 30). The characteristics of a deep-seated weathered rockslide that occurred in 2020 on a natural slope near a highway to Sapa town in the northwestern Vietnam was presented by Nguyen et al. (2023a, b), together with the reme-

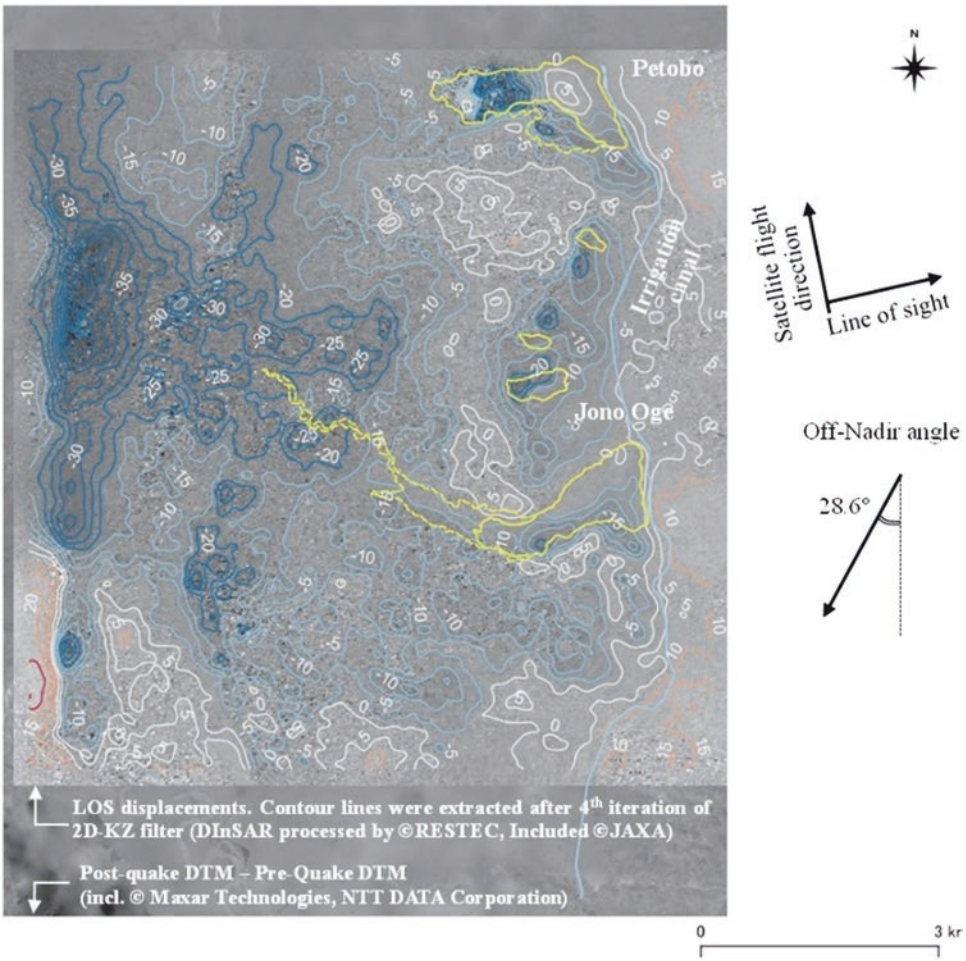

Fig. 22 Line-of-sight (LOS) deformations on two different days after the earthquake (October 12, 2018, and January 4, 2019): Yellow polygons show locations of extensive flow slides. (Konagai et al. 2022) (Fig. 5 in Konagai et al. 2023b)

Fig. 23 A slope failure induced by the mainshock near the Aso-Ohashi Bridge (Modified from the Kyushu Regional Development Bureau, MLIT 2021) (Fig. 10 in Higaki et al. 2023)

dial measures adopted with ground anchors, soil nails and drainage pipes to stabilize the slope. Wang et al. (2023) presented the spatial distribution, emplacement processes and mechanisms of the rock avalanches in the Tibetan Plateau of China (Fig. 31), involving the sedimentary structures of four typical rock avalanches with jigsaw structures, inner shear zones, diapiric structures, convoluted laminations, and faults, based on the remote sensing analysis, mapping using a fixed-wing UAV and detailed field investigations. Gallego et al. (2023) investigated potential rock slope instabilities that may affect the conservation of an archaeological site, which is described in "Cultural Heritage" below.

2.14 Reservoir Landslide and Landslide Dam

Tang et al. (2023) presented some key techniques of reservoir landslide prevention and control by considering seven evolution modes for rock slides and the optimal control measures suitable for each evolution mode and different evolution stages (e.g. Fig. 32) as established in the Three Gorges Reservoir area (TGRA), China. The characteristics and the

stability evaluation methods for the reservoir landslides (e.g. Fig. 33) in the TGRA were also summarized in Tang (2023). Based on a four year field observation and monitoring, Barjasteh (2023) presented the stability analysis of Ambal Salt Ridge in the Gotvand dam reservoir, Southern Iran, where the 2019 flooding event increased the landslide displacement and the situation is expected to be more critical under a moderate to high future earthquake in a tectonically active zone of the Zagros Fold Belt. Zerkal et al. (2023) reported the recent activity and analysis of the Buzulgan landslide (Fig. 34) that resulted in the formation of a landslide dam and its influence on the future debris flow hazard for the Tyrnyauz town in Northern Caucasus, Russia, showing the possible inundation zones. Sattar and Konagai (2023) reported the post-formation behaviour of the Hattain Bala landslide dam formed by the 2005 Kashmir earthquake and the post-breaching situation of the landslide dam in Kashmir, Pakistan.

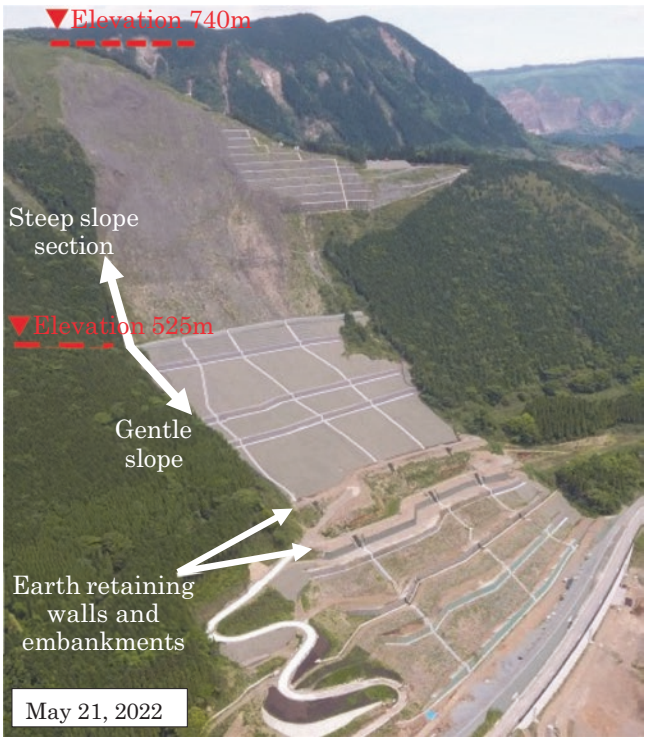

Fig. 24 Countermeasures adopted for the stabilization of each block (Embarkment and steel-reinforced soil at the lower slope and earth removal and soil shaping at the head slope) (Kyushu Regional Development Bureau, MLIT 2021) (Fig. 15 in Higaki et al. 2023)

2.15 Cultural Heritage

Elshayeb (2023) presented the development of landslide risk assessment during the last 30 years for the various Egyptian cultural heritage sites, leading to a better preservation of the temple of Queen Hatshepsut at Eldeir Elbahary, the Tomb of Ramses I at the Valley of the Kings and the Serapeum Tomb in Saqqara, Egypt. Frodella et al. (2023b) presented an overview of the last decade's activities for the conservation of Georgian rupestrian cultural heritage sites associated with the slope instability processes by integrating field surveys, close-range remote sensing involving the infrared thermography and UAV digital photogrammetry, and laboratory analyses for geotechnical-mineralogical and geological characterization, leading to the implementation of deep anchoring and retaining walls to protect the cultural heritage sites (Fig. 35). Based on the in-situ and laboratory tests on rock blocks and discontinuities, Gallego et al. (2023) reported the weathering and erosion-induced rock degradation processes and their impact on the potential slope instabilities affecting the AIUla archaeological sites in a rock cut landscape (Fig. 36) shaped for thousand years in the Kingdom of Saudi Arabia.

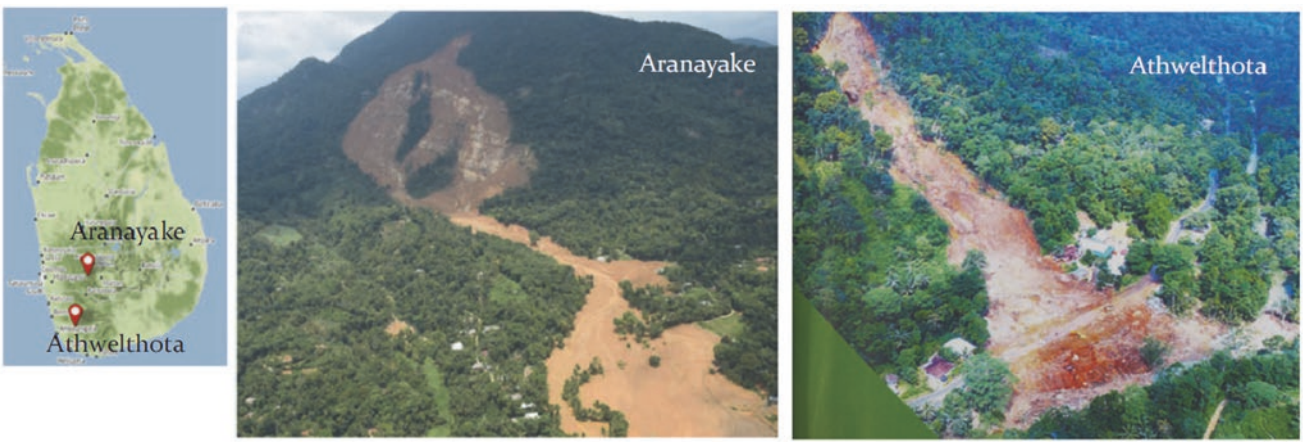

Fig. 25 Pilot study sites: (Left) Alanayake landslide in 2016, and (Right) Athwelthota landslide in 2017 (credit NBRO) (Fig. 10 in Konagai et al. 2023a)

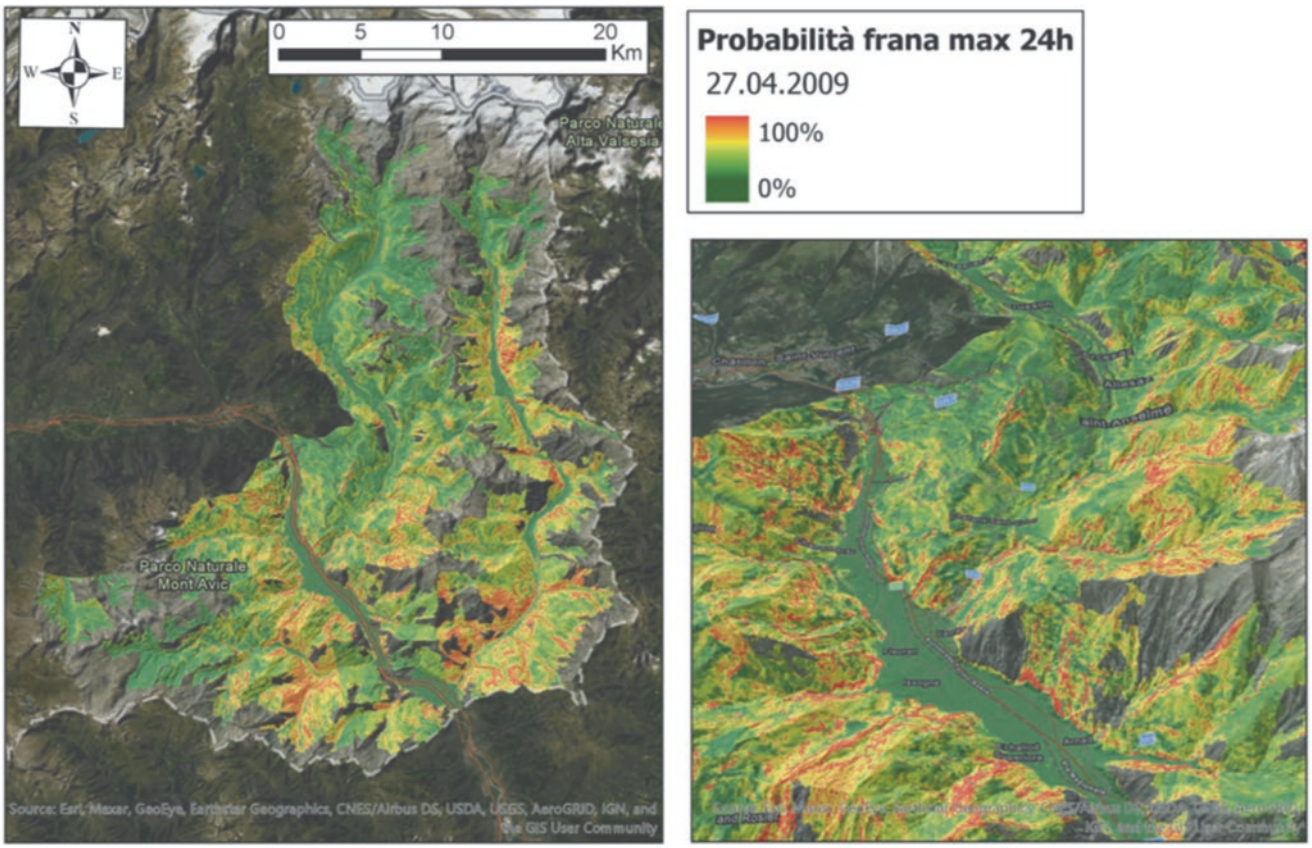

Fig. 26 HIRESSS 24-hr map of failure probabilities for the day of April 27 (Fig. 4 in Tofani et al. 2023)

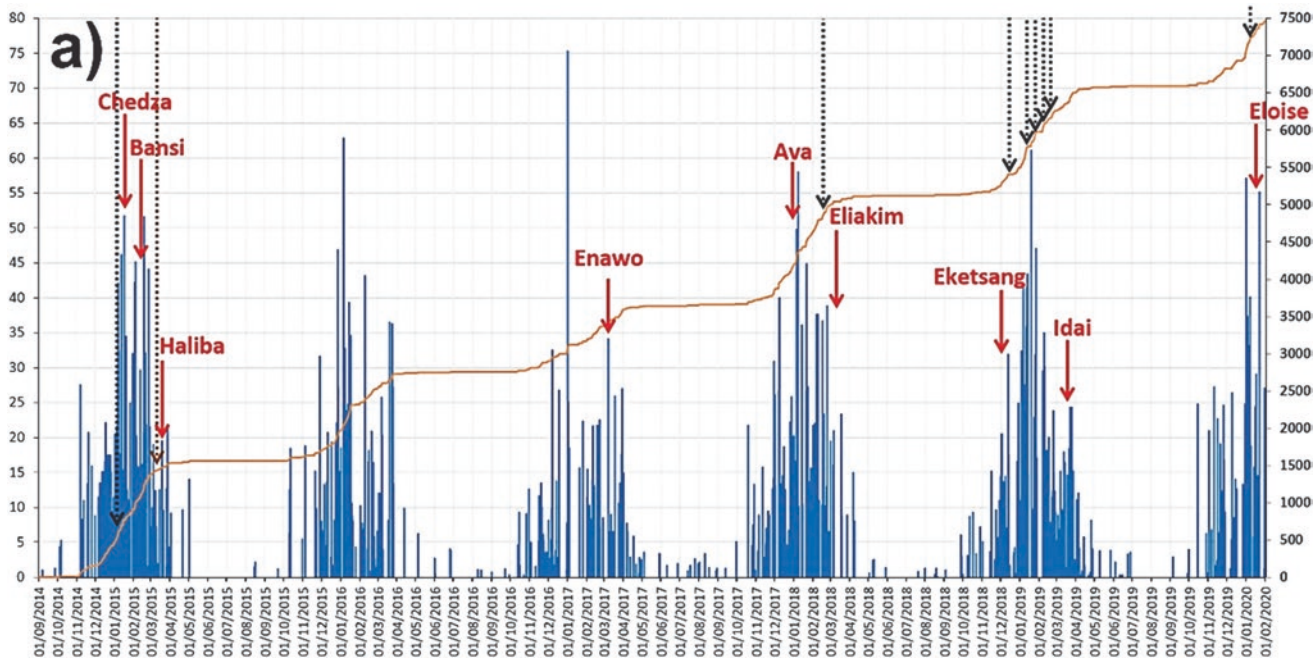

Fig. 27 Comparison between rainfall data from September 2014 to January 2020 (Daily and cumulated data from Climate Engine, 2015), the recorded landslide events (dashed black arrows), and the recorded Cyclones (red arrows), reported in Frodella et al. (2021) (a) (the Dashed brown arrow represents the Winter 2015 landslide event) (Fig. 5a in Frodella et al. 2023a)

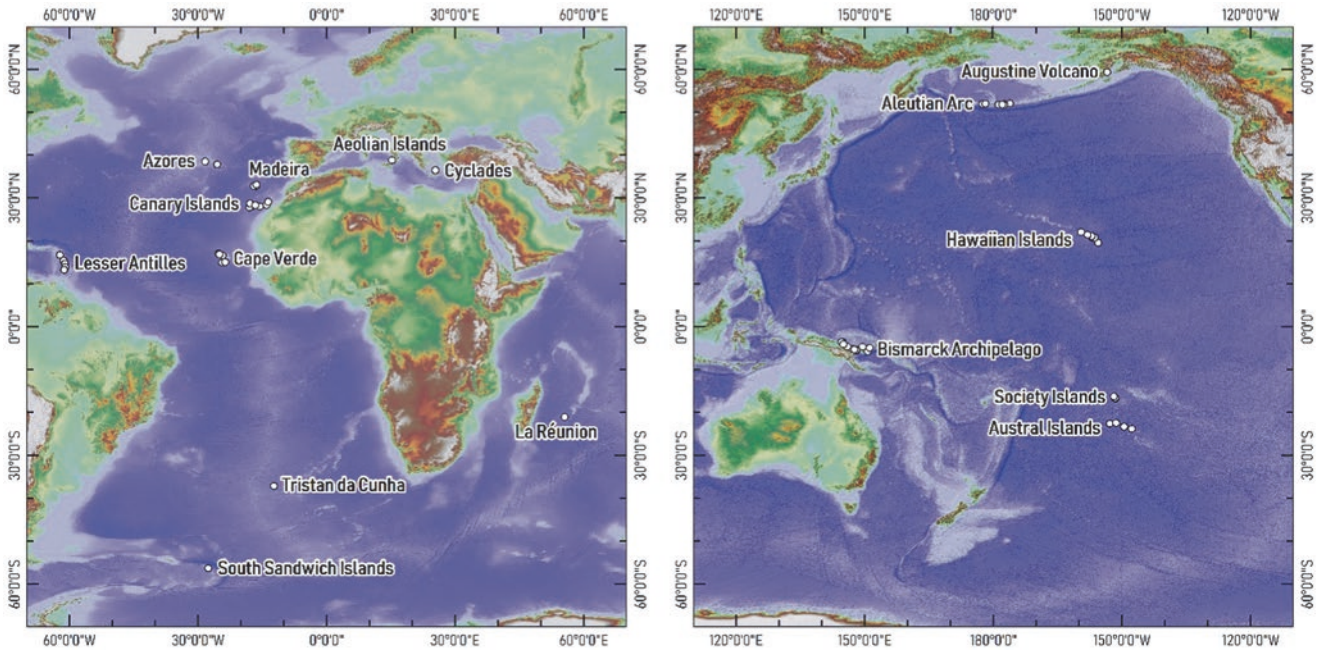

Fig. 28 Distribution of giant landslides on volcanic islands from the Atlantic and Indian Oceans (Left) and the Pacific Ocean (Right). Source: Global relief model derived from Global Bathymetry and Topography at 15 Arc Sec: SRTM15+ V2.1 (Tozer et al. 2019) (Figs. 4 and 5 in Rowberry et al. 2023)

Fig. 29 The 7.5 km long Chukurchak rock avalanche, Tien Shan, Kyrgyzstan. Headscarp is marked by elevation marks 2970 and 2250 m a.s.l., while other elevation marks are placed at the front of rock avalanche branches (Fig. 8 in Strom 2023)

Fig. 30 Example of rock formed failures along the road side slope. Wedge failure, translational slides and falling rocks are very much significant along the road sides. High hazard potential zone can be observed due to foliated and jointed rock formations (Fig. 13 in Dias et al. 2023)

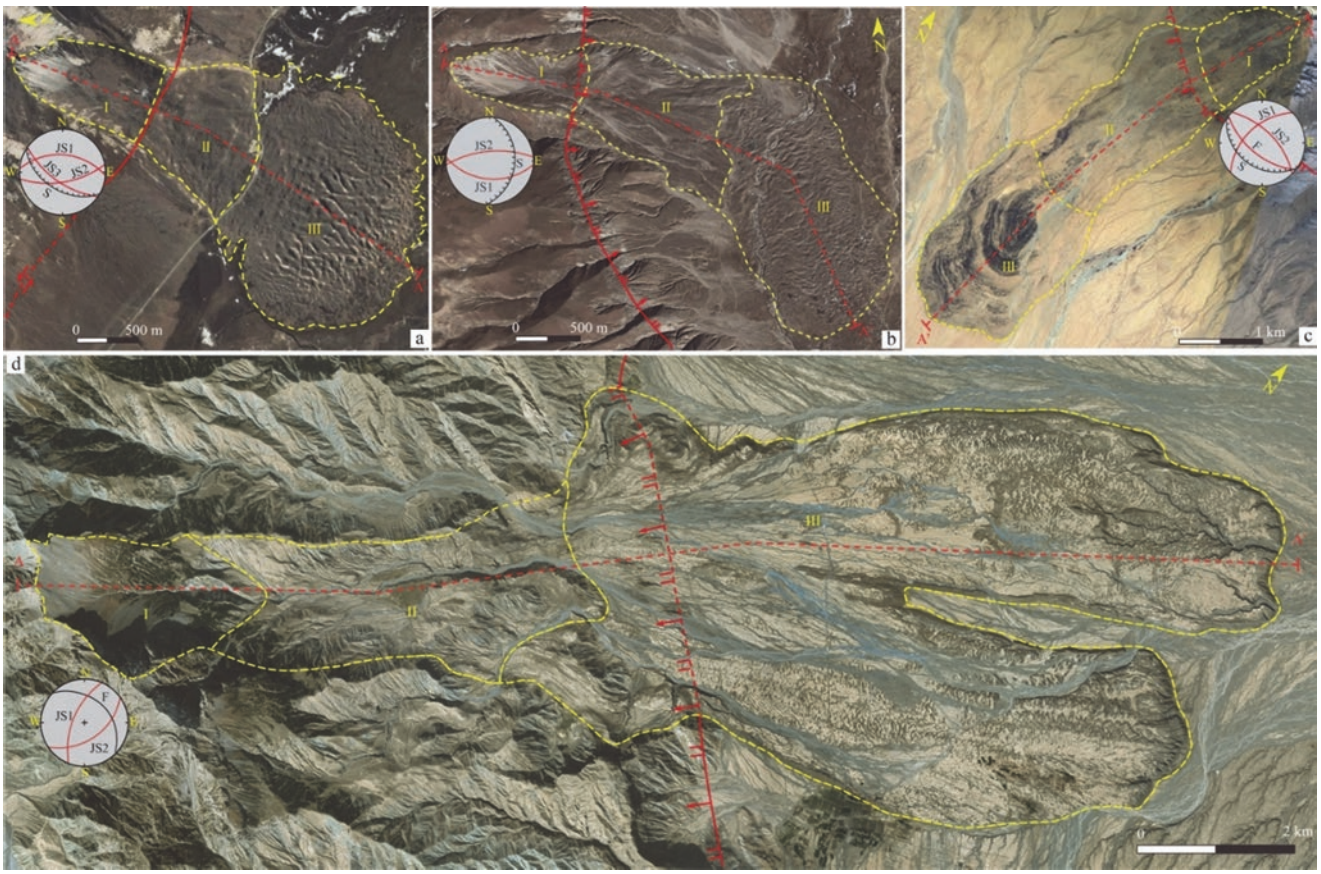

Fig. 31 Typical rock avalanches distributed in the Tibetan Plateau, China (**a**: Luanshibao rock avalanche; **b**: Nyixoi Chongco rock avalanche; **c**: Tagarma rock avalanche; **d**: Iymek rock avalanche) (Fig. 3 in Wang et al. 2023)

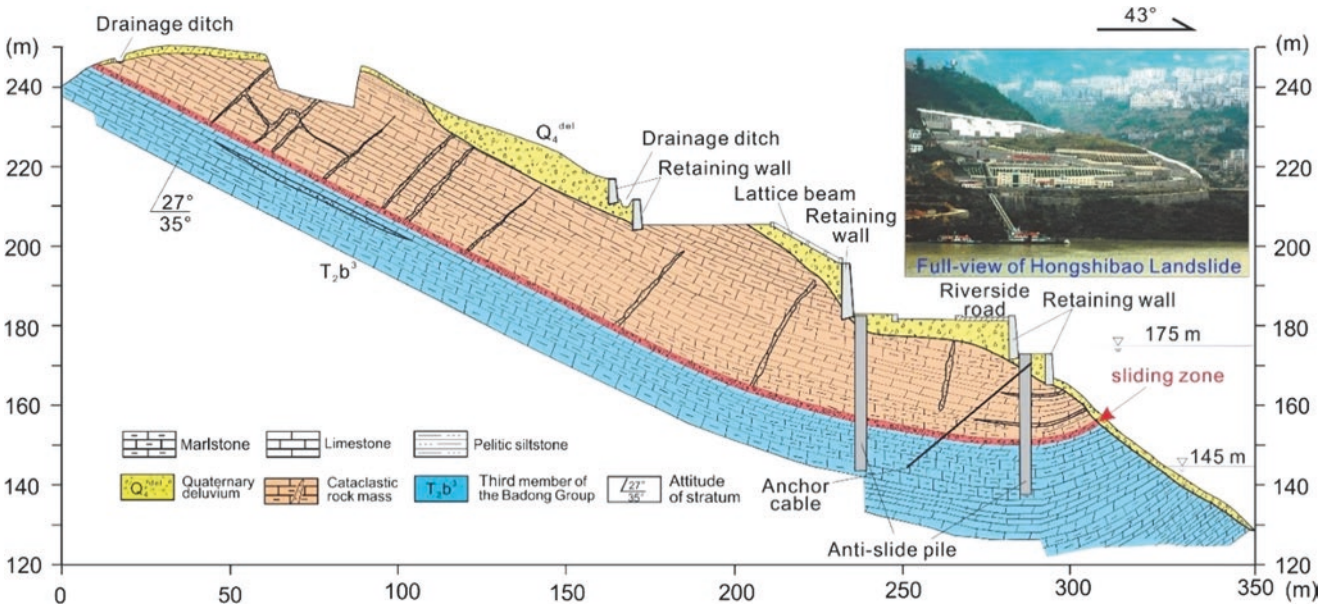

Fig. 32 Cross section of the Hongshibao landslide, whose toe is affected by fluctuations of the TGR level. Drainage ditches, retaining walls, lattice beams and stabilizing piles were constructed to stabilize this actively creeping landslide (Tang et al. 2019) (Fig. 2 in Tang et al. 2023)

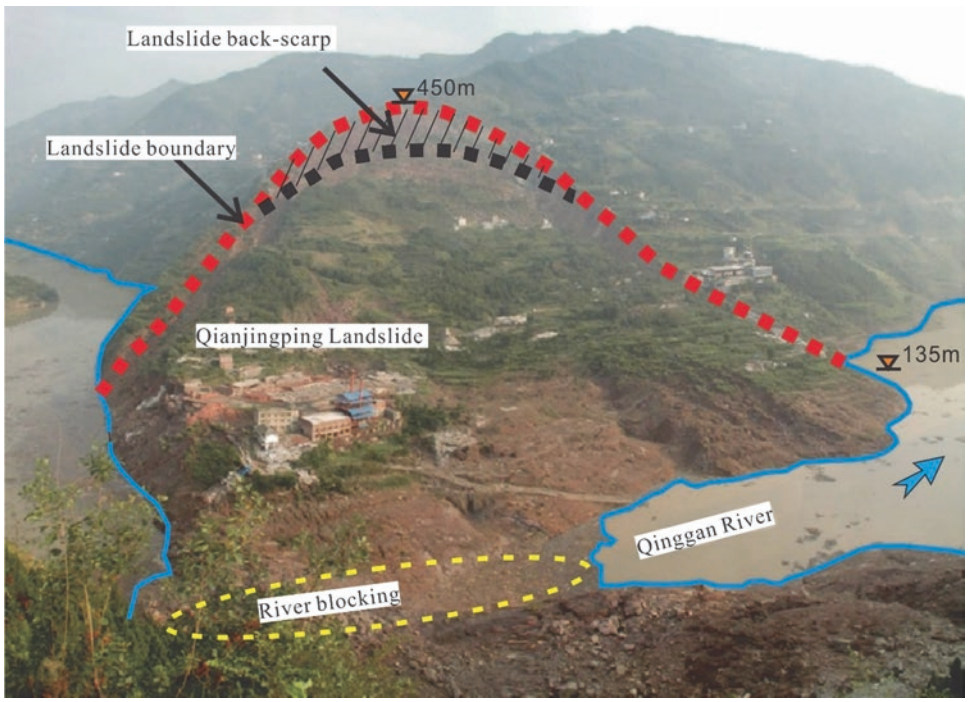

Fig. 33 Front view of the landslide, looking NW (after Tang et al. 2017) (Fig. 14 in Tang 2023)

2.16 Landslide-Structure Interaction

Cuomo et al. (2023) presented the analysis of landslide-structure interaction for flow-like landslides against protection barriers, based on a general conceptual scheme (Fig. 37), empirical, analytical and numerical approaches including the estimate of the amount of landslide volume overtopping the barrier. Perna et al. (2023) presented the Material Point Method (MPM) based modelling of landslide-structure interaction, showing that landslide pore water pressures undergo significant tempo-spatial evolution during a dynamic impact on the structure. Ng et al. (2023) presented the impact mechanisms of water, dry granular and two-phase debris flows on barriers of varying stiffness, openings and numbers based on physical and numerical results to mitigate debris flows, showing that debris flow composition governs the impact dynamics on barriers (Fig. 38).

Fig. 34 General view on the Buzulgan landslide (2020) (Photo of O.V. Zerkal) (Fig. 4 in Zerkal et al. 2023)

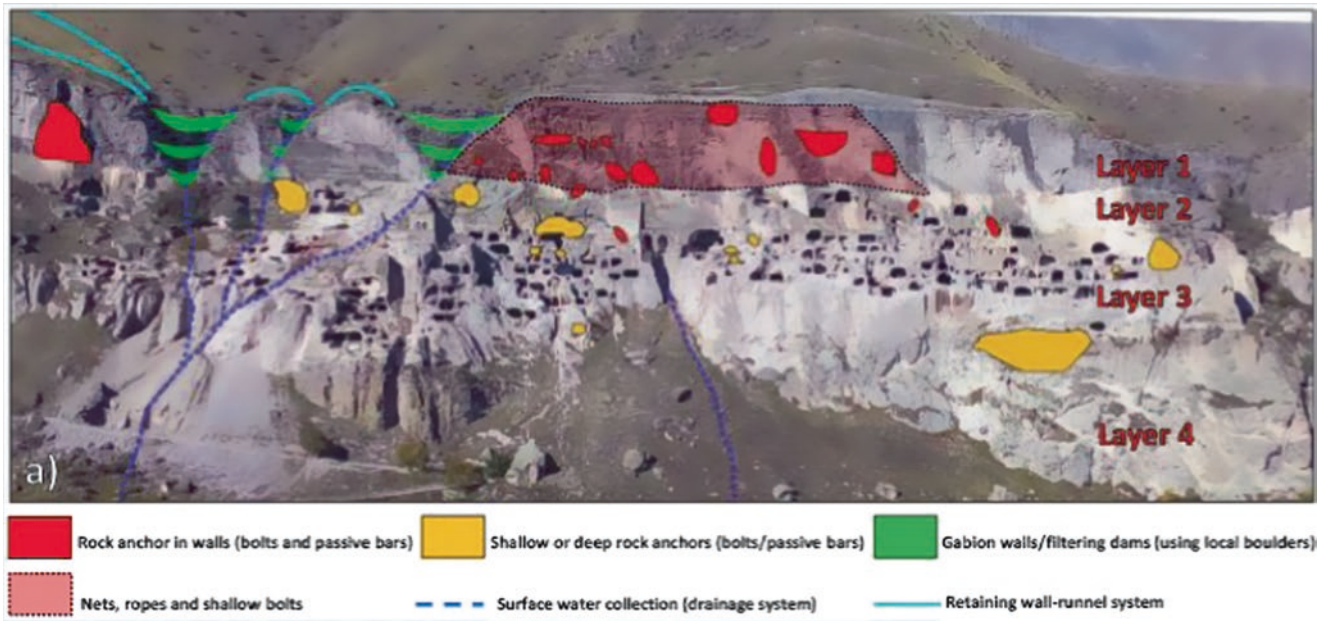

Fig. 35 General master plan for the proposed mitigation measures for the whole Vardzia Monastery (Fig. 11 in Frodella et al. 2023b)

2.17 Risk Communication, Education and Network

Arbanas and Mihalić Arbanas (2023) reported the 10th Anniversary of the Adriatic-Balkan Network (ABN) in the framework of International Consortium on Landslides (ICL) by showing the establishment, objectives and activities of ABN during the last ten years with the organization of biannual Regional Symposiums on Landslides in Croatia, Serbia, Slovenia, and Bosnia and Herzegovina. Nishikawa (2023) presented the need to effectively raise public awareness about landslides by showing the application of an Ichi-Nichi-Mae (The Day Before the Disaster) Project for landslide awareness and risk communication with the episodes by the survivors of landslides. Ahmed et al. (2023) reported the use of qualitative social science tools and techniques via key informant interviews to investigate the anthropogenic-induced landslide disasters in Chittagong hill districts, Bangladesh, showing that climate change-induced erratic rainfall is leading to more rainfall-induced landslides and presenting the

Fig. 36 General view of AlUla Old Town and the dangerous Western cliff (Fig. 21 in Gallego et al. 2023)

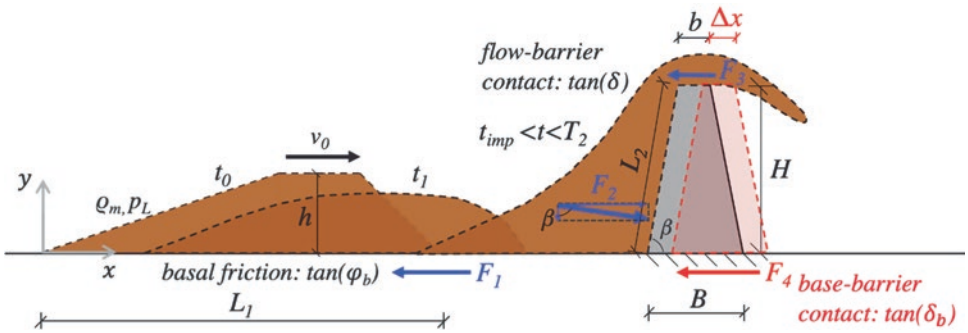

Fig. 37 General conceptual scheme for Landslide Structure Interaction (LSI) (Fig. 1 in Cuomo et al. 2023)

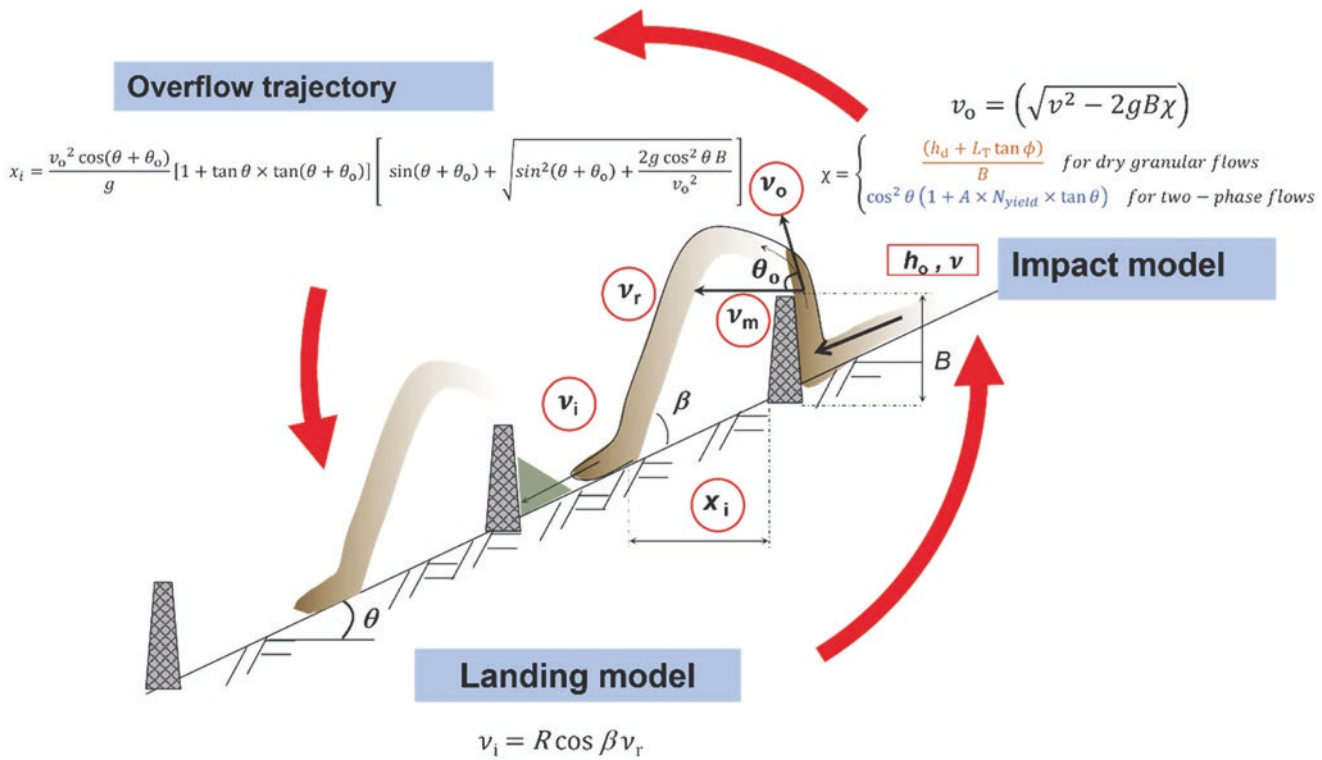

Fig. 38 A schematic diagram of the multiple barrier framework for both dry granular and two-phase flows. The framework includes (1) impact model, (2) overflow and landing kinematics, and (3) subsequent barrier impact (Fig. 7 in Ng et al. 2023)

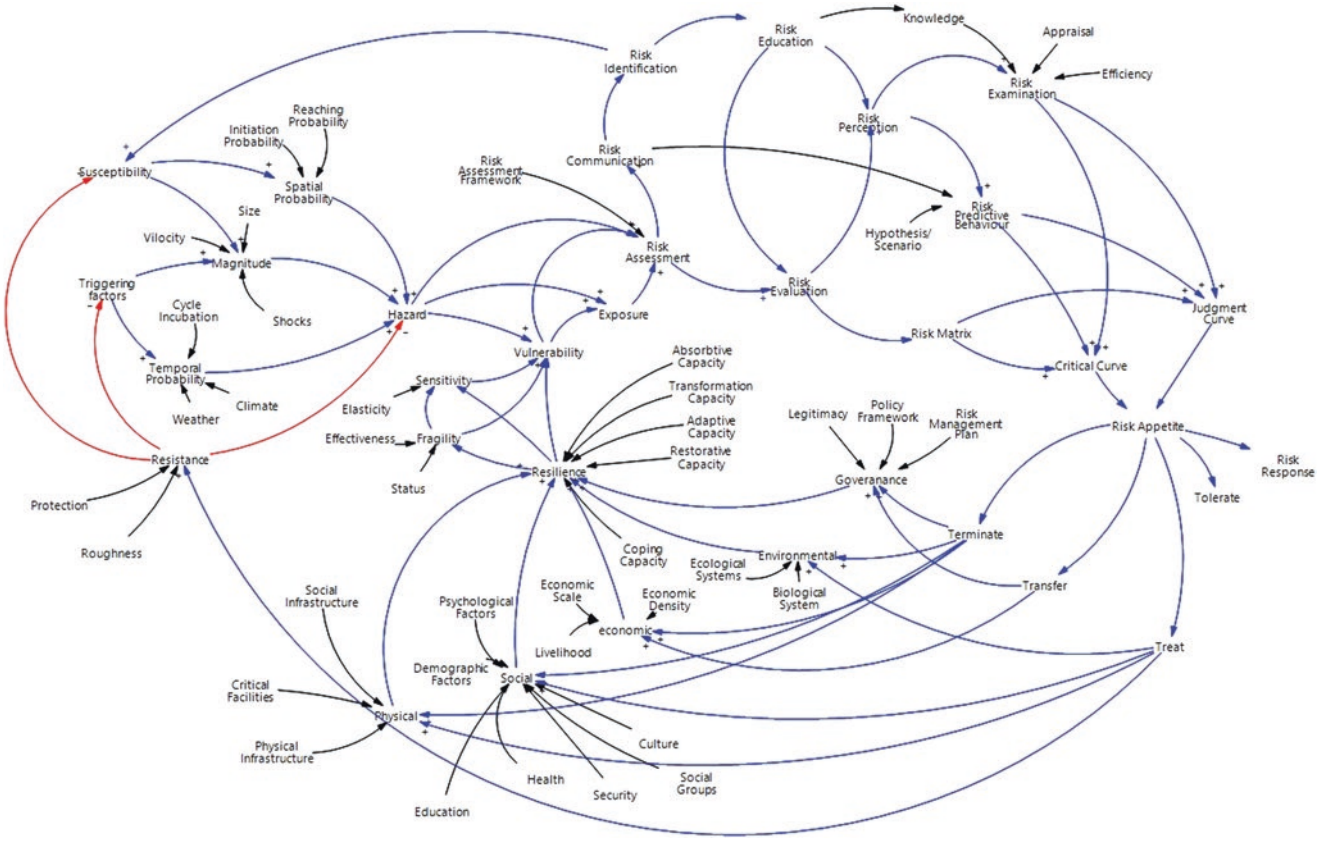

Fig. 39 Risk perspectives connections (a mind map) (Fig. 4 in Munasinghe et al. 2023)

recommendations to stop illegal hill cutting and deforestation and to raise risk awareness and coordination among the communities. Thanh et al. (2023) presented a community level landslide risk reduction program comprised of the creation of a communication- based evacuation mapping (CBEM) and the engagement of residents in slope disaster risk reduction in a mountainous area of northern Vietnam. Garnica-Peña and Alcántara-Ayala (2023) reported the expansion of the urban area of a community where in the last decade, landslides have not occurred in a mountainous zone highly susceptible to the hillslope instability in México by showing a key recommendation to implement a landslide disaster risk awareness program and include education programs at all levels. Based on diverse web tools and databases, Mikoš (2023c) presented an assessment of worldwide efforts in reduction at higher education levels and beyond, by focusing on the higher education study programmes offering courses on slope stability and landslide mitigation. Munasinghe et al. (2023) presented an outcome of a literature survey to consolidate a common set of risk assessment perspectives and approaches for measuring landslide disaster risk by using the PICO (Population, Intervention, Compression Intervention, and Outcome) method, identifying the future requirements of risk critical curve, judgment curve, and risk matrix (Fig. 39). Kamal et al. (2023) presented the refugees' perception of landslide disasters based on a structured questionnaire and survey of 400 people from the Rohingya camps in Cox's Bazar, Bangladesh, showing through a regression analysis (Proportional Odds Model) that exposure to previous landslides, mitigation measure quality, and emergency managers' roles were crucial in defining people's risk perception compared to the demographic characteristics of the Rohingya population.

2.18 Design and Countermeasures

Cuomo et al. (2023) presented different tools and options to design a protection barrier against flow-like landslides, where the different approaches adopted for analysis are summarized in "Landslide-Structure Interaction" above. Higaki et al. (2023) presented an overview of the emergent and permanent countermeasures adopted following the 2018 heavy rainfall-induced landslide disaster in Hiroshima, Japan, involving channel stabilization works using large sandbags to channel water downstream safely, installation of warning devices such as wire sensors to detect the occurrence of debris flows, and construction of 20 Sabo dams to trap sediments produced during heavy rains to protect the downstream area from the landslide and debris flow impacts (Fig. 40). Hirota et al. (2023) presented the application of vegetation works to protect unstable cutting slopes along highway where slope failures have repeatedly occurred in

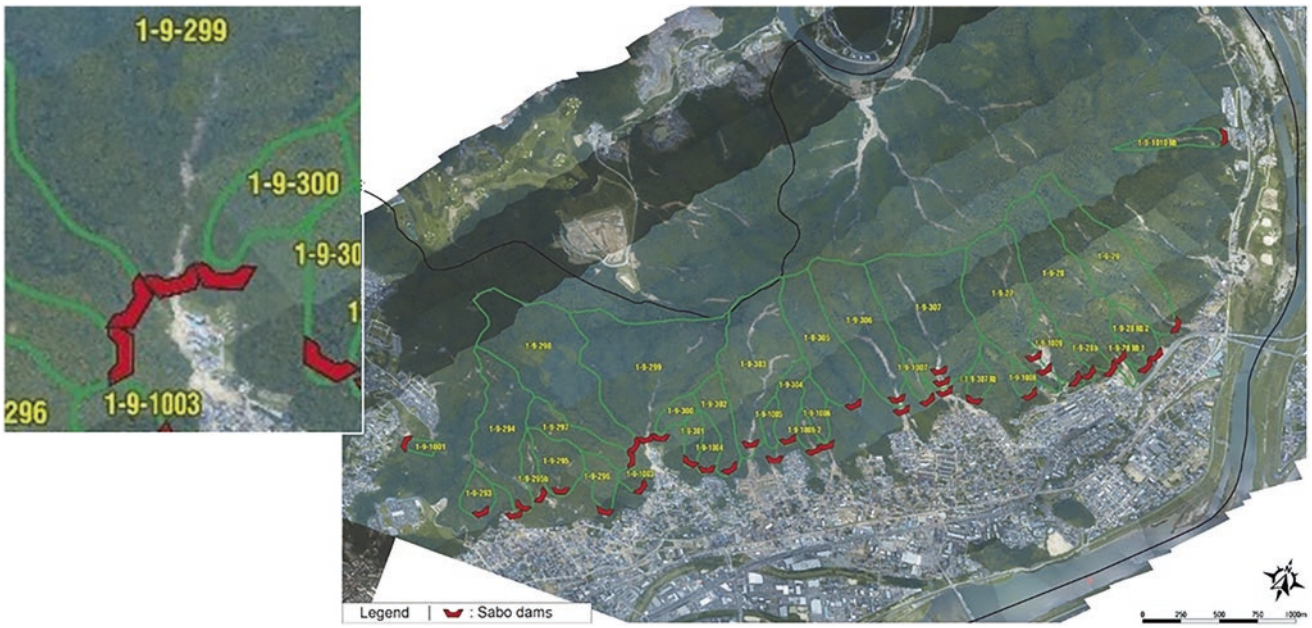

Fig. 40 Installation plan of sabo dams for disaster recovery in the catchment of debris-flow affected streams (Modified from the Chugoku Regional Development Bureau, MLIT 2019) (Fig. 25 in Higaki et al. 2023)

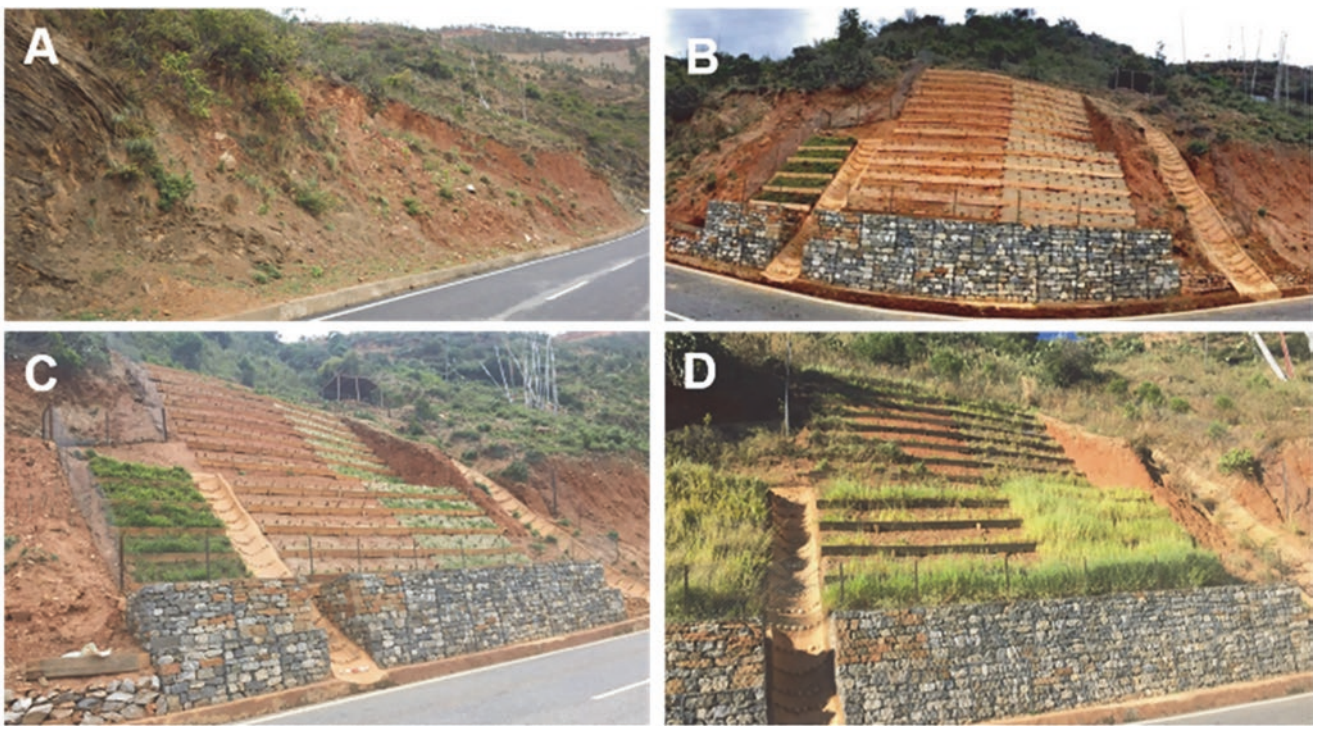

Fig. 41 Sequence of events at the site of vegetation works, Gangthangkha, Wangdue. (**a**) Slope before vegetation works, (**b**) Finished vegetation works, (**c**, **d**) Photos about a month after the vegetation works) (Fig. 22 in Hirota et al. 2023)

rainy seasons in Gangthangkha, Wangdue, Bhutan, by showing the site-specific optimal selection of seeds and methods suitable for the landslide stabilization due to vegetation (Fig. 41). Arbanas et al. (2023) presented a series of model slope experiments with various countermeasures where a gabion wall and buttressing embankment were installed in sandy and silty slopes and a pile wall with counterfort was constructed in a clayey slope (Fig. 42), showing that appropriate countermeasures realized the stability of the slope, which otherwise collapsed. Ng et al. (2023) presented the design of debris-resisting single and multiple barriers by proposing a new dimensionless overflow number with a

Fig. 42 Views at buttressing embankment behind the gabion wall in a silty slope and at pile wall, buttressing counterfort and excavated trenches in a clayey slope (Figs. 8g and 9e in Arbanas et al. 2023)

Table 1 Criteria for classifying socio-economically and environmentally significant landslides in India (Table 1 in Parkash 2023)

Low Socio-economic and Environmental Significance	Moderate Socio-economic and Environmental Significance	High Socio-economic and Environmental Significance
Number of human casualties: 1- 5 Number of injured people: 1- 10 Number of homeless people: 1- 15 Population affected: 1- 100 *Economic damage & loss: 1 - 5 Million (INR) [67,837.10 United States Dollar (USD)] (As per 20 Sep, 2021; 1 USD = 73.71 Indian Rupee) **Gross Domestic Product Loss: 0.5- 1% Impacts on Bio-diversity / Number of Trees affected or uprooted: 1-10	Number of human casualties: 6-10 Number of injured people: 11-20 Number of homeless people: 16- 25 Population affected: 101-199 *Economic damage & loss: 5-10 Million (INR) [67,837.10 United States Dollar (USD)] (As per 20 Sep, 2021; 1 USD = 73.71 Indian Rupee) **Gross Domestic Product Loss: 1%- 2% Impacts on Bio-diversity / Number of Trees affected or uprooted: 11-20	Number of human casualties: > 10 Number of injured people: > 20 Number of homeless people: >= 25 Population affected: >200 *Economic damage & loss: >10 Million (INR) [1,35,689.80 (USD)] (As per 20 Sep, 2021; 1 USD = 73.71 Indian Rupee) **Gross Domestic Product Loss :>2% Impacts on Bio-diversity / Number of Trees affected or uprooted: >20

*Includes any direct physical damage or a direct net loss. **The rate of the day needs to be considered i.e., the day when the disaster happened. *If the landslide event qualifies even any one of the criteria as given above in Table 1, then it can be categorized in either low, moderate, or high class of socio-economically and environmentally significant landslide event.*

threshold value of unity to design a rigid barrier for regulating discharge of debris material downstream while reducing the debris flow impact force. Tang et al. (2023) presented an optimal design and arrangement of stabilizing piles for the prevention and control of reservoir landslides with their applications to Hongshibao landslide (Fig. 32) and Majiagou landslide in the Three Gorges Reservoir area (TGRA), China.

2.19 Socio-Economic Significance

Parkash (2023) presented the archival records of socio-economically and environmentally significant landslides in India, by classifying a total of 412 landslides as low, moderate and high socio-economic significance to differentiate the degree of damages and losses, including both direct and indirect costs together with the key lessons learned from these events (Table 1).

3 Conclusion

This article has presented an overview and a concise review of two years of publication of Progress in Landslide Research and Technology (P-LRT). The themes for the Vols. 1 and 2 of P-LRT were indeed diverse as described above, with a total of four hundred and twenty-seven researchers/practitioners from thirty-six countries/regions from Africa, Asia, Europe, North America, Oceania, and South America, contributing to the Vols 1 and 2 of the ICL Open Access Book Series. It is hoped that P-LRT will continue to serve as a common platform for the publication of recent progress in landslide research and technology for practical applications and the benefit for the society contributing to the Kyoto Landslide Commitment 2020 for the global promotion of understanding and reducing landslide disaster risk.

References

Abe S, Higaki D, Hayashi K (2023) The role of translational landslides in the evolution of cuesta topography. Prog Landslide Res Technol 1(1):149–161

Abolmasov B, Stanković R, Marjanović M, Vulović N, Đurić U (2023a) CliRtheRoads—an integrated approach to landslide risk management on roads in Serbia. Prog Landslide Res Technol 2(2)

Abolmasov B, Marjanović M, Đurić U, Krušić J (2023b) An integrated approach to landslides risk management for local and national authorities. Prog Landslide Res Technol 2(2)

Ahmed B, Alam SMRA, Ahmed I, Sammonds P (2023) The anthropogenic aggravation of landslide disasters in Bangladesh: key informants' perspectives. Prog Landslide Res Technol 1(2):385–401

Ajmera B, Ahari HE, Loi DH, Setiawan H, Dang K, Sassa K (2023) LS-RAPID manual with video tutorials. Prog Landslide Res Technol 1(1):343–406

Alcántara-Ayala I, Garnica-Peña RJ (2023a) Landslide warning systems in low- and lower-middle-income countries: future challenges and societal impact. Prog Landslide Res Technol 1(1):137–147

Alcántara-Ayala I, Garnica-Peña RJ (2023b) Landslide warning systems in upper middle-income countries: current insights and new perspectives. Prog Landslide Res Technol 1(2):159–168

Alcántara-Ayala I, Garnica-Peña RJ (2023c) Landslide warning systems in high-income countries: past accomplishments and expected endeavours. Prog Landslide Res Technol 2(1)

Arbanas Ž, Mihalić Arbanas S (2023) 10th anniversary of ICL adriatic-Balkan network and 5th regional symposium on landslides. Prog Landslide Res Technol 1(2):223–234

Arbanas Ž, Peranić J, Jagodnik V, Prodan MV, Čeh N (2023) Remedial measures impact on slope stability and landslide occurrence in small-scale slope physical model in 1g conditions. Prog Landslide Res Technol 2(2)

Ariyarathna I, Sasahara K (2023) Procedure of data processing for the improvement of failure time prediction of a landslide based on the velocity and acceleration of the displacement. Prog Landslide Res Technol 2(2)

Bandara HAAIS, Onishi R (2023) High resolution numerical weather simulation for orographic precipitation as an accurate early warning tool for landslide vulnerable terrains. Prog Landslide Res Technol 2(2)

Barjasteh A (2023) March 2019 flood impact on the stability of Ambal salt ridge in the Gotvand Dam Reservoir, Southern Iran. Prog Landslide Res Technol 1(2):415–423

Bernat Gazibara S, Damjanović V, Krkač M, Sinčić M, Jagodnik P, Mihalić Arbanas S (2022) Landslide susceptibility map of Croatia based on limited data and fuzzy logic approach. In: Proceedings of the 5th regional symposium on landslides in the Adriatic-Balkan Region. Faculty of Civil Engineering, University of Rijeka and Faculty of Mining, Geology and Petroleum Engineering, University of Zagreb

Bernat Gazibara S, Jagodnik P, Lukačić H, Sinčić M, Krkač M, Šarić G, Arbanas Ž, Mihalić Arbanas S (2023a) Landslide and soil erosion inventory mapping based on high-resolution remote sensing data: a case study from Istria (Croatia). Prog Landslide Res Technol 2(1)

Bernat Gazibara S, Sinčić M, Rossi M, Reichenbach P, Krkač M, Lukačić H, Jagodnik P, Šarić G, Mihalić Arbanas S (2023b) Application of LAND-SUITE for landslide susceptibility modelling using difference mapping units. A case study in Croatia. Prog Landslide Res Technol 2(2)

Beroya-Eitner MAA, Vicente MCTM, Dado JMB, Dimain MRS, Maquiling JT, Cruz FAT (2023) Climate change as modifier of landslide susceptibility: case study in Davao Oriental, Philippines. Prog Landslide Res Technol 2(2)

Bhandary NP (2023) Experimental simulation of landslide creep in ring shear machine. Prog Landslide Res Technol 1(2):75–85

Bornaetxea T, Blais-Stevens A, Miller B (2023a) Landslide inventory map of the Valemount Area, British Columbia, Canada. A detailed methodological description. Prog Landslide Res Technol 1(2):373–381

Bornaetxea T, Rossi M, Reichenbach P (2023b) Zonation of landslide susceptibility in the Gipuzkoa province (Spain): an application of LAND-SUITE. Prog Landslide Res Technol 2(1)

Casagli N, Tofani V, Moretti S, Fanti R, Gigli G, Bianchini S, Segoni S, Frodella W, Carlà T (2023) Advanced technologies for landslides—ATLaS (WCoE 2020–2023). Prog Landslide Res Technol 1(1):267–275

Chugoku Regional Development Bureau, Ministry of Land, Infrastructure, Transport and Tourism (MLIT) (2019) The 2018 heavy

Cuomo S, Perna AD, Martinelli M (2023) Design protection barriers against flow-like landslides. Prog Landslide Res Technol 1(1):123–136

Damians IP, Bathurst RJ, Adroguer E, Josa A, Lloret A (2018) Sustainability assessment of earth retaining wall structures. ICE Environ Geotech 5(4):187–203

Damians IP, Miyata Y, Rimoldi P, Touze N, Kraus J (2023) Sustainability of geosynthetics-based landslide stabilization solutions. Prog Landslide Res Technol 1(1):197–205

Dang K, Sassa K, Loi DH (2023) Teaching tool for LS-Tsunami. Prog Landslide Res Technol 2(2)

Delgado LMB, Pavlova I, Yasukawa S, Esperancinha S (2023) Establishment of the disaster risk reduction unit in UNESCO and UNESCO's contribution to global resilience. Prog Landslide Res Technol 1(1):209–213

Dias AAV, Herath HMJMK, Kulathilake LKNS (2023) Landform geometry for restoration of mountain roads and landslide hazard resilience. Prog Landslide Res Technol 1(1):327–339

Duc DM, Khang DQK, Duc DM, Ngoc DM, Quynh DT, Thuy DT, Giang NKH, Tien PV, Ha NH (2020) Analysis and modeling of a landslide-induced tsunami-like wave across the Truong river in Quang Nam province, Vietnam. Landslides 17:2329–2341

Duong BV, Fomenko IK, Nguyen KT (2023a) Fractal-based evaluation of the spatial relationship between conditioning factors and the distribution of landslides (A case study in Tnih Tuc, Cao Bang province, Vietnam). Prog Landslide Res Technol 2(1)

Duong BV, Fomenko IK, Nguyen LC, Nguyen KT, Do TN, Gorobtsov DN, Zerkal OV, Dinh HT (2023b) Mathematical and numerical modeling of slope stability for the Mong Sen landslide event in the Trung Chai commune, Sapa, Vietnam. Prog Landslide Res Technol 2(1)

Elshayeb Y (2023) 30 Years of cultural heritage landslides and block movements risk assessment: case studies from Egypt. Prog Landslide Res Technol 1(2):169–175

Erzagian E, Wilopo W, Fathani TF (2023) Landslide susceptibility zonation using GIS-based frequency ratio approach in the Kulon Progo Mountains Area, Indonesia. Prog Landslide Res Technol 2(2)

Fathani TK, Karnawati D, Wilopo W, Setiawan H (2023) Strengthening the resilience by implementing a standard for landslide early warning system. Prog Landslide Res Technol 1(1):277–284

Frodella W, Spizzichino D, Ciampalini A, Margottini C, Casagli N (2021) Hydrography and geomorphology of Antananarivo High City (Madagascar). J Maps 17(4):215–226

Frodella W, Rosi A, Spizzichino D, Nocentini M, Lombardi L, Ciampalini A, Vannocci P, Ramboason N, Claudio Margottini C, Tofani V, Casagli N (2022) Integrated approach for landslide hazard assessment in the High City of Antananarivo, Madagascar (UNESCO tentative site). Landslides 19(11):2685–2709

Frodella W, Spizzichino D, Lazzeri G, Margottini C, Tofani V, Casagli N (2023a) Assessing landslide hazard in the High City of Antananarivo, Madagascar (UNESCO Tentative site). Prog Landslide Res Technol 2(2)

Frodella W, Gigli G, Spizzichino D, Margottini C, Elashvili M, Casagli N (2023b) Protection and conservation of Georgian rupestrian cultural heritage sites: a review. Prog Landslide Res Technol 2(1)

Fukuhara M, Wang L, Tao S, Tang Z, Tang W, Dong L, Fan Z (2023) A risk evaluation method of unstable slopes using multipoint tilting sensors. Prog Landslide Res Technol 2(1)

Gallego JI, Margottini C, Perisse I, Spizzichino D, Beni T, Boldini D, Bonometti F, Casagli N, Castellanza R, Crosta GB, Fratttini P, Gigli G, Lusini E, Rigamonti S, Rusconi G, Vitrano L (2023) Rock slope instabilities affecting the AIUla archaeological sites (KSA). Prog Landslide Res Technol 2(2)

Gariano SL, Melillo M, Brunetti MT, Kumar S, Mathiyalagan R, Peruccacci S (2023) Challenges in defining frequentist rainfall thresholds to be implemented in a landslide early warning system in India. Prog Landslide Res Technol 1(1):409–416

Garnica-Peña RJ, Alcántara-Ayala I (2023) Do not let your guard down: landslide exposure and local awareness in Mexico. Prog Landslide Res Technol 2(2)

Gratchev I, Ravindran S, Kim DH, Cui C, Tang O (2023) Mechanisms of shallow rainfall-induced landslides from Australia: insights into field and laboratory investigations. Prog Landslide Res Technol 1(1):113–122

Ha ND, Duong NH, Khanh NQ, Viet TT, Vung DV, Van NTH, Ninh NH (2023) Landslide early warning system based on the empirical approach-Case study in Ha Long City (Vietnam). Prog Landslide Res Technol 2(1)

Higaki D, Hirota K, Dang K, Nakai S, Kaibori M, Matsumoto S, Yamada M, Tsuchiya S, Sassa K (2023) Landslides and countermeasures in Western Japan: historical largest landslide in Unzen and earthquake-induced landslides in Aso, and rain-induced landslides in Hiroshima. Prog Landslide Res Technol 1(2):287–307

rain in July, 2018—sediment disasters, p 50 (in Japanese)

Hirota K, Suganuma Y, Iwasaki T, Kuwano T (2023) How to teach remotely the vegetation works to protect slope against mass wasting: a case of using video materials in Bhutan. Prog Landslide Res Technol 1(2):361–370

Hoang TV, Chou TY, Fang YM, Wang CT, Tsai MC, Nguyen QD, Nguyen QH, Bui QT, Nguyen QT (2023) Application of global satellite positioning and automatic monitoring in slopeland disaster prevention. Prog Landslide Res Technol 1(2):147–158

Huntley D, Bobrowsky P, MacLeod R, Cocking R, Joseph J, Rotheram-Clarke D (2021) Ensuring resilient socio-economic infrastructure: field testing innovative differential GNSS-InSAR-UAV monitoring technologies in mountainous terrain near Ashcroft, British Columbia, Canada. J Mountain Sci 18(1):1–20

Huntley D, Bobrowsky P, MacLeod R, Rotheram-Clarke D, Cocking R, Joseph J, Holmes J, Sattler K, Chambers J, Meldrum P, Wilkinson P, Donohue S, Elwood D (2023a) IPL project 202: landslide monitoring best practices for climate-resilient railway transportation corridors in southwestern British Columbia, Canada. Prog Landslide Res Technol 1(1):249–265

Huntley D, Rotheram-Clarke D, MacLeod R, Cocking R, LeSueur P, Lakeland B, Wilson A (2023b) Scalable platform for UAV flight operations, data capture, cloud processing and image rendering of landslide hazards and surface change detection for disaster-risk reduction. Prog Landslide Res Technol 1(2):49–61

Huntley D, Rotheram-Clarke D, MacLeod R, Cocking R, Joseph J, LeSueur P (2023c) Landslide monitoring with RADARSAT constellation mission InSAR, RPAS-derived point-clouds and RTK-GNSS time-series in the Thompson River Valley, British Columbia, Canada. Prog Landslide Res Technol 2(1)

Huntley D, Rotheram-Clarke D, Sattler K, Elwood D (2023d) Surficial geology and geomorphology of the North Slide, Thompson River valley, British Columbia, Canada: application of fundamental geoscience information to interpretations of geospatial monitoring results. Prog Landslide Res Technol 2(2)

Kamal ASMM, Samm AA, Ahmed B, Sammonds P (2023) Refugees' perception of landslide disasters: Insights from the Rohingya camps in Cox's Bazar, Bangladesh. Prog Landslide Res Technol 2(2)

Kawamura K, Oguri K, Inoue M, Hsiung KH, Kudaka T, Takai K (2023) Ongoing persistent slope failures at the Toe of a Giant submarine slide in the Ryukyu Trench that generated the AD 1771 Meiwa Tsunami. Prog Landslide Res Technol 1(2):63–74

Konagai K (2023) Coseismic stress changes, landslides in the 2004 mid-Niigata prefecture earthquake, and their impact on post-quake rehabilitations. Prog Landslide Res Technol 1(2):235–246

Konagai K, Furuta R, Kiyota T (2022) Widespread ground deformation over the Palu Basin caused by the 2018 Sulawesi, Indonesia Earthquake. JSCE J Disaster Factsheets FS2022-E-0001

Konagai K, Karunawardena A, Bandara KN, Sassa K, Onishi R, Uzuoka R, Asano R, Sasahara K, Jayakody S, Ariyarathna I (2023a) Early warning system against rainfall-induced landslide in Sri Lanka. Prog Landslide Res Technol 1(1):217–235

Konagai K, Kiyota T, Furuta R, Shiga M, Pokhrel RM, Ikeda T (2023b) Long-lasting post-quake deformation buildups in the grounds that spread laterally in recent earthquakes. Prog Landslide Res Technol 1(2):213–222

Krkač M, Gazibara SB, Sinčić M, Lukačić H, Šarić G, Mihalić Arbanas S (2023) Impact of input data on the quality of the landslide susceptibility large-scale maps: a case study from NW Croatia. Prog Landslide Res Technol 2(1)

Kyushu Regional Development Bureau, Ministry of Land, Infrastructure, Transport and Tourism, 2016–2020 (2021) Materials for technical study meetings on the restoration of slope failure in the Aso-Ohashi Bridge area (1st to 10th meetings). (ref. Aug 7 2021) (in Japanese)

Loi DH, Jayakody SHS, Sassa K (2023) Teaching tool "Undrained Dynamic Loading Ring Shear Testing with Video". Prog Landslide Res Technol 1(2):325–359

Michel J (2023) Consequence-frequency matrix as a tool to assess landslides risk. Prog Landslide Res Technol 2(2)

Mihalić Arbanas S, Gazibara SB, Krkač M, Sinčić M, Lukačić H, Jagodnik P, Željko A (2023) Landslide detection and spatial prediction: application of data and information from landslide maps. Prog Landslide Res Technol 1(2):195–212

Mikoš M (2023a) Landslide research and technology in patent documents. Prog Landslide Res Technol 1(2):29–48

Mikoš M (2023b) Landslide research and technology in international standards. Prog Landslide Res Technol 2(1)
Mikoš M (2023c) Landslide in higher education curricula and beyond. Prog Landslide Res Technol 2(2)
Mikoš M, Bezak N, Costa JP, Massri MB, Novalija I, Jermol M, Grobelnik M (2023) Natural-hazard-related web observatory as a sustainable development tool. Prog Landslide Res Technol 1(1):83–97
Moncayo S, Ávila G (2023) Landslide travel distances in Colombia from national landslide database analysis. Prog Landslide Res Technol 1(1):315–325
Munasinghe D, Fernando T, Keraminiyage K, Karunawardena A (2023) A review of the disaster risk assessment perspectives. Prog Landslide Res Technol 2(2)
Ng CWW, Poudyal S, Liu H, Bhatta A, De Silva WARK, Jia Z (2023) Investigation of debris flow impact mechanisms and designs. Prog Landslide Res Technol 2(2)
Nguyen CC, Vo P, Doan VL, Nguyen QB, Nguyen TC, Nguyen QD (2023a) Assessment of the effects of rainfall frequency on landslide susceptibility mapping using AHP method: a case study for a mountainous region in Central Vietnam. Prog Landslide Res Technol 1(2):87–98
Nguyen LC, Do TN, Nguyen QD (2023b) Characteristics and remedy solutions for a New Mong Sen Deep-Seated Landslide, Sapa Town, Vietnam. Prog Landslide Res Technol 1(2):403–413
Nishikawa S (2023) Application of Ichi-Nichi-Mae (the day before the disaster) project for landslide awareness and risk communication. Prog Landslide Res Technol 1(2):317–321
Onishi R, Hirai J, Kolomenskiy D, Yasuda Y (2023) Real-time high-resolution prediction of orographic rainfall for early warning of landslides. Prog Landslide Res Technol 1(1):237–248
Parkash S (2023) Lessons learned from landslides of socio-economic and environmental significance in India. Prog Landslide Res Technol 1(2):309–315
Paulín GL, Parrot JF, Castro-Miguel R, Miguel RC, Salinas LA, Quesada FA (2023a) Digital terrain models derived from unmanned aerial vehicles and landslide susceptibility. Prog Landslide Res Technol 2(1)
Paulín GL, Anaya RMA, Salinas LA, Parrot JF, Miguel RC (2023b) Use of GIS to assess susceptibility per landform unit to gravitational processes and their volume. Prog Landslide Res Technol 2(1)
Perna AD, Cuomo S, Martinelli M (2023) Modelling of landslide-structure interaction (LSI) through material point method (MPM). Prog Landslide Res Technol 2(1)
Poggi F, Montalti R, Intrieri E, Ferretti A, Catani F, Raspini F (2023) Spatial and temporal characterization of landslide deformation pattern with Sentinel-1. Prog Landslide Res Technol 2(1)
Ramesh MV, Thirugnanam H, Singh B, Kumar MN, Pullarkatt D (2023a) Landslide early warning systems: requirements and solutions for disaster risk reduction-India. Prog Landslide Res Technol 1(2):259–286
Ramesh MV, Thirugnanam H, Kumar MN, Singh B, Harichandana E, Guntha R (2023b) Community scale landslide resilience: a citizen-science. Prog Landslide Res Technol 2(2)
Ríos D, Ávila G (2023) Lessons from 2019–2020 landslide risk assessment in an urban area of volcanic soils in Pereira-Colombia. Prog Landslide Res Technol 2(1)
Rowberry M, Klimeš J, Blahůt J, Balek J, Kusák M (2023) A global database of giant landslides on volcanic islands. Prog Landslide Res Technol 1(1):295–304
Sassa S (2023a) Review of the Founding Issue of P-LRT: Progress in Landslide Research and Technology. Prog Landslide Res Technol 1(2):179–193
Sassa S (2023b) Landslides and Tsunamis: Multi-Geohazards. Landslides 20(7):1335–1341
Sassa S, Takagawa T (2019) Liquefied gravity flow-induced tsunami: first evidence and comparison from the 2018 Indonesia Sulawesi earthquake and tsunami disasters. Landslides 16(1):195–200
Sassa S, Grilli ST, Tappin DR, Sassa K, Karnawati D, Gusiakov VK, Løvholt F (2022) Understanding and reducing the disaster risk of landslide-induced tsunamis: a short summary of the panel discussion in the World Tsunami Awareness Day Special Event of the Fifth World Landslide Forum. Landslides 19(2):533–535
Sassa K, Loi DH, Dang K, Tien P (2023a) Sliding-surface liquefaction and undrained steady-state shear-strength. Prog Landslide Res Technol 2(1):L1
Sassa S, Grilli ST, Tappin DR, Sassa K, Karnawati D, Gusiakov VK, Løvholt F (2023b) Understanding and reducing the disaster risk of landslide-induced tsunamis: outcome of the panel discussion and the World Tsunami Awareness Day Special Event of the Fifth World Landslide Forum. Prog Landslide Res Technol 1(1):65–81
Sattar A, Konagai K (2023) Post-formation behaviour of Hattian landslide dam and post-breaching situation. Prog Landslide Res Technol 2(2)
Strom A (2023) Central Asia rockslides inventory: compilation, analysis and training—progress of the IPL WCoE. Prog Landslide Res Technol 1(1):285–294
Tan Q, Tang H (2023) In situ triaxial creep test on gravelly slip zone soil of a giant landslide: innovative attempts and findings. Prog Landslide Res Technol 1(2):109–121
Tang H (2023) Identification and mitigation of reservoir landslides: cases studied in the three gorges reservoir area of China. Prog Landslide Res Technol 2(1)
Tang HM, Yong R, Eldin MAME (2017) Stability analysis of stratified rock slopes with spatially variable strength parameters: the case of Qianjiangping landslide. Bull Eng Geol Environ 76:839–853
Tang H, Wasowski J, Juang CH (2019) Geohazards in the three Gorges Reservoir Area, China—lessons learned from decades of research. Eng Geol:105267
Tang H, Wang L, Li C, Zou Z (2023) Key techniques of prevention and control for reservoir landslides based on evolutionary process. Prog Landslide Res Technol 1(2):11–28
Tappin DR, Grilli ST (2020) The continuing underestimated tsunami hazard from submarine landslides. In: Sassa K, Mikoš M, Sassa S, Bobrowsky PT, Takara K, Dang K (eds) Understanding and reducing landslide disaster risk: volume 1 Sendai Landslide Partnerships and Kyoto Landslide Commitment. Part III Landslide-induced Tsunamis. Springer Nature, pp 343–350
Thanh NK, Miyagi T, Huy TC, Hamasaki E, Tien DV, Kasuya Y (2023) Community level slope disaster risk reduction program through multi-scale mapping by Mountain Ethnic Group in Northern Vietnam-Project Study by JICA/Lao Cai DARD/ITST. Prog Landslide Res Technol 2(1)
Thirugnanam H (2023) Deep learning in landslide studies: a review. Prog Landslide Res Technol 1(2):247–255
Tien DV, Thanh NK, Quang LH, Ngoc DHA, Sassa K, Miyagi T, Abe S (2023) Landslide risk assessment in the tropical zone of Vietnam as a contribution to the mitigation of natural disaster vulnerability. Prog Landslide Res Technol 2(1)
Tiwari B, Ajmera B (2023) Advancements in shear strength interpretation, testing, and use for landslide analysis. Prog Landslide Res Technol 2(2)
Tiwari RC, Bhandary NP (2023) Application of spectral element method (SEM) in slope instability analysis. Prog Landslide Res Technol 1(1):163–174
Tiwari B, Tran D (2023) Using experimental models to calibrate numerical models for slope stability and deformation analysis. Prog Landslide Res Technol 1(1):185–195
Tofani V, Masi EB, Rossi G (2023) Physically-based regional landslide forecasting modelling: model set-up and validation. Prog Landslide Res Technol 2(2)

Tozer B, Sandwell D, Smith W, Olson C, Beale J, Wessel P (2019) Global bathymetry and topography at 15 arc sec: SRTM15+. Earth Space Sci 6:1847–1864. https://doi.org/10.1029/2019EA000658

Trofymchuk O, Kaliukh I, Lebid O, Klymenko V, Vyshniakov V, Kreta D, Elshayeb Y (2023) Effect of landslide deformation on the stability of St. Andrew's Church (Kyiv, Ukraine): applications of remote sensing and mathematical modeling. Prog Landslide Res Technol 1(2):133–145

Vacha D, Mandrone G, Morresi D, Garbarino M (2023) Mapping post-fire monthly erosion rates at the catchment scale using empirical models implemented in GIS. A case study in Northern Italy. Prog Landslide Res Technol 1(1):99–112

Wang F, Nam K (2023) Landslide disasters caused by the 2018 Eastern Iburi Earthquake in Hokkaido Japan and the countermeasures to completely prevent the similar disasters in the future. Prog Landslide Res Technol 1(1):305–313

Wang Y, Cheng Q, Lin Q, Shi A, Ming J, Feng Z, Song Z (2023) Rock avalanches in the Tibetan Plateau of China. Prog Landslide Res Technol 2(2)

Wijaya IPK, Towashiraporn P, Joshi A, Jayasinghe S, Dewi A, Alam MN (2023) Climate change-induced regional landslide hazard and exposure assessment for aiding climate resilient road infrastructure planning: a case study in Bagmati and Madhesh Provinces, Nepal. Prog Landslide Res Technol 1(1):175–184

Yasufuku N, Alowiasy A (2023) Challenges and lessons learned from heavy rainfall-induced geo-disasters over the last decade in Kyushu Island, Japan. Prog Landslide Res Technol 1(2):123–132

Zerkal OV, Barykina OS (2023) Suffosion landslides as a specific type of slope deformations in the European Part of Russia. Prog Landslide Res Technol 1(2):99–108

Zerkal OV, Chernomorets SS, Iudina VA, Dokukin MD, Krylenko IN, Savernyuk EA, Vinogradova TA, Zaporozhchenko EV (2023) The modern activity of the Buzulgan landslide and its influence on the debris flow hazard for the Tyrnyauz town (Northern Caucasus, Russia). Prog Landslide Res Technol 2(1)

Landslide Prediction Model Based Upon Intelligent Processing of Multi-Point Monitoring Information: A Review

Changdong Li, Jingjing Long, Yong Liu, and Dewei Huang

Abstract

The construction of landslide displacement prediction model is crucial and effective in landslide prevention and mitigation. Intelligent processing methods are deeply required owing to the boost of monitoring datasets. Machine learning (ML) and deep learning (DL) methods are widely applied in landslide prediction. In this paper, aiming at the hydrodynamic pressure-driven landslides with step-like features in China Three Gorges Reservoir (CTGR) area, the improved ensemble learning models integrating the advantages of multifarious algorithms as well as considering the time series are proposed for prediction. Due to the limitations of monitoring sites and data missing, the multi-feature fusing transfer learning (MFTL) method is proposed for landslide prediction. It transfers the knowledge learned form a landslide with enough data to the other landslides with insufficient data. The successful applications in landslide prediction based on intelligent processing of monitoring information provide the efficient ways for further studies.

Keywords

Landslide prediction · Hydrodynamic pressure-driven landslides · Multi-point monitoring system · Ensemble learning · Transfer learning

C. Li (✉)
Badong National Observation and Research Station of Geohazards, China University of Geosciences, Wuhan, China

Faculty of Engineering, China University of Geosciences, Wuhan, Hubei, China
e-mail: lichangdong@cug.edu.cn

J. Long · D. Huang
Faculty of Engineering, China University of Geosciences, Wuhan, Hubei, China
e-mail: jingjinglong@cug.edu.cn; HDW@cug.edu.cn

Y. Liu
School of Mechanical Engineering and Electronic Information, China University of Geosciences, Wuhan, China
e-mail: yongliu@cug.edu.cn

1 Introduction

Landslides are the gravitational movement of mass down a slope, which have caused huge casualties and severe financial loss (Gong et al. 2021; Guo et al. 2021). In lately few decades, mountainous areas struggle with an increasing landslide risk as a consequence of industrialization, urbanization and population growth (Kang et al. 2009). In general, the frequent landslides with complicated mechanism are extremely hard to identify, and they seriously endanger the development of national economy and the safety of people's lives and property. To mitigate the global adverse effects of landslides geohazards, various strategies have been implemented (Cui et al. 2021; Juang 2021). Landslide displacement prediction based on monitoring data has been proven to be an effective way to predict and prevent landslide disasters (Wang et al. 2022). The visualization analysis of high-frequency terminology in title and abstract based on Web of Science and VOSviewer is used to better understand the research trends of "landslide displacement prediction" in recent years. The result (Fig. 1) shows that the most researches concentrated on China Three Gorges Reservoir (CTGR) area, were focused on selection of developed the most slide-prone strata (Criss et al. 2020). Many attempts have been made in landslide displacement prediction by applying Machine Learning (ML) and Deep Learning (DL) methods, such as artificial neural networks (ANNs); Support Vector Machine (SVM); Random Forest (RF) and Extreme Learning Machine (ELM) models, due to their inherently nonlinear advantage and excellent prediction ability (Yu and Ma 2021; Huang et al. 2020). Generally speaking, in the process of model construction, a regression or classification model have been trained through a complex nonlinear mapping with adjustable parameters based on external inducing factors and displacement datasets. More recently, to overcome the drawbacks of single method and make breakthroughs, multifarious ensemble models integrated two or three methods are put forward. Considering the time series

B. Abolmasov et al. (eds.), *Progress in Landslide Research and Technology, Volume 3 Issue 1, 2024*, Progress in Landslide Research and Technology, https://doi.org/10.1007/978-3-031-55120-8_19

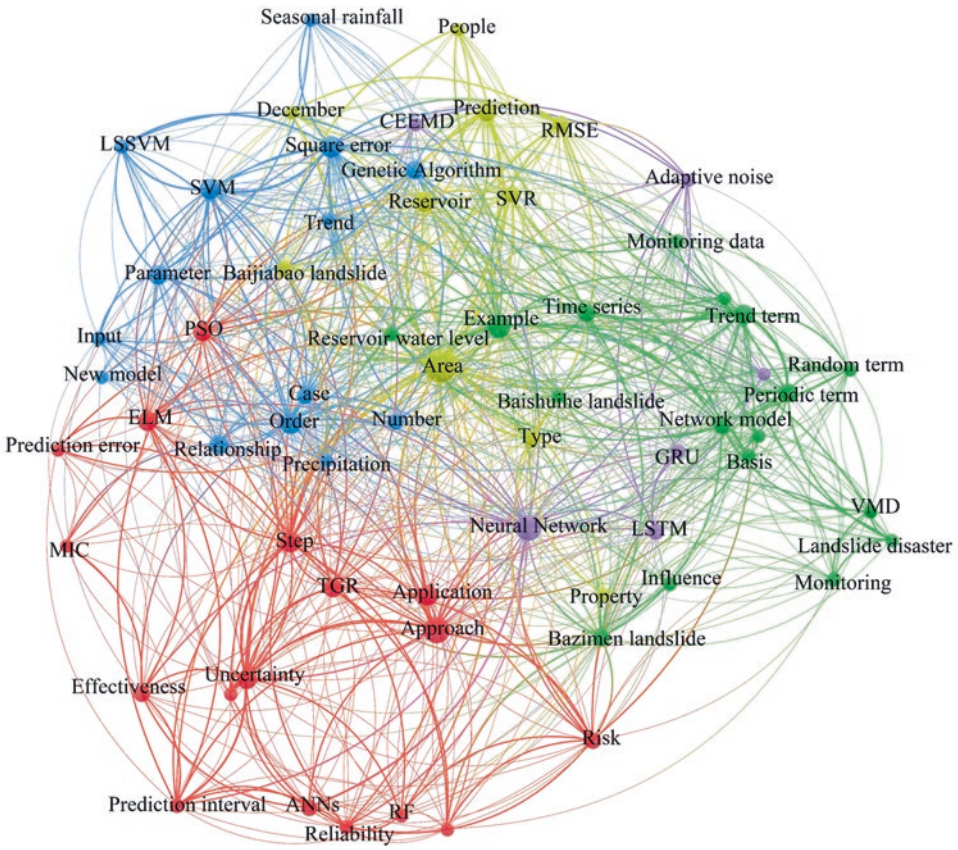

Fig. 1 The visualization analysis of high-frequency terminology in the title and abstract of "landslide displacement prediction" literatures

characteristics of displacement, the Recursive Neural Network (RNN) and Long Short-Term Memory (LSTM) are applied for prediction (Yang et al. 2019). Particularly, target for the typical landslides with step-like deformation characteristics, some researchers decomposed the accumulated displacement into trend item and periodic item through time filter algorithms, such as Complementary Ensemble Empirical Mode Decomposition (CEEMD) algorithm (Yeh et al. 2011).

$$A_t = T_t + P_t, t = 1, 2, 3, \ldots, N \tag{1}$$

where A_t is the landslide cumulative displacement at time t. T_t is the trend component that reflects the long-term trend over time, and it is determined by the geological conditions of the slope. P_t is a periodic component, which is affected by periodic events in natural environment. The prediction of landslide displacement is realized through adding the fitting trend component and the periodic composition predicted according to artificial intelligent (AI) model.

Traditionally, the mean square error (MSE), root mean square error (RMSE) and mean absolute error (MAE) are used to evaluate the overall prediction accuracy of a model. These indexes can be expressed as follows:

$$RMSE = \sqrt{\frac{1}{n}\sum_{t=0}^{n}\left(\widehat{Y}_t - Y_t\right)^2} \tag{2}$$

$$MSE = \frac{1}{n}\sum_{t=0}^{n}\left(\widehat{Y}_t - Y_t\right)^2 \tag{3}$$

$$MAE = \frac{1}{n}\sum_{t=0}^{n}\left|\widehat{Y}_t - Y_t\right| \tag{4}$$

where Y_t refers to the observed value and $\widehat{Y}_t$ refers to the predicted value. The MSE and RMSE are used to measure the deviation between observed and predicted values. The MAE is used to measure the average overall prediction error.

2 Case Study

The intensive and severe hydrodynamic pressure-driven landslides with obvious step-like deformation characteristics under the influence of precipitation and reservoir water level fluctuation, such as Baijiabao, Bazimen and Baishuihe landslides, are developed in Zigui basin, CTGR area (Tang et al. 2019). According to the field investigation (Figs. 2a, 3a, 4a), Baijiabao and Bazimen landslides are the anti-dip slopes located on the right bank of the Xiangxi River. Baishuihe landslide is a dip slope which located on the right bank of the Yangtze River.

The comparison of the geological information shows that the stratigraphic units of the three landslides all consist of sandstone interbedded with mudstone of the Early Jurassic

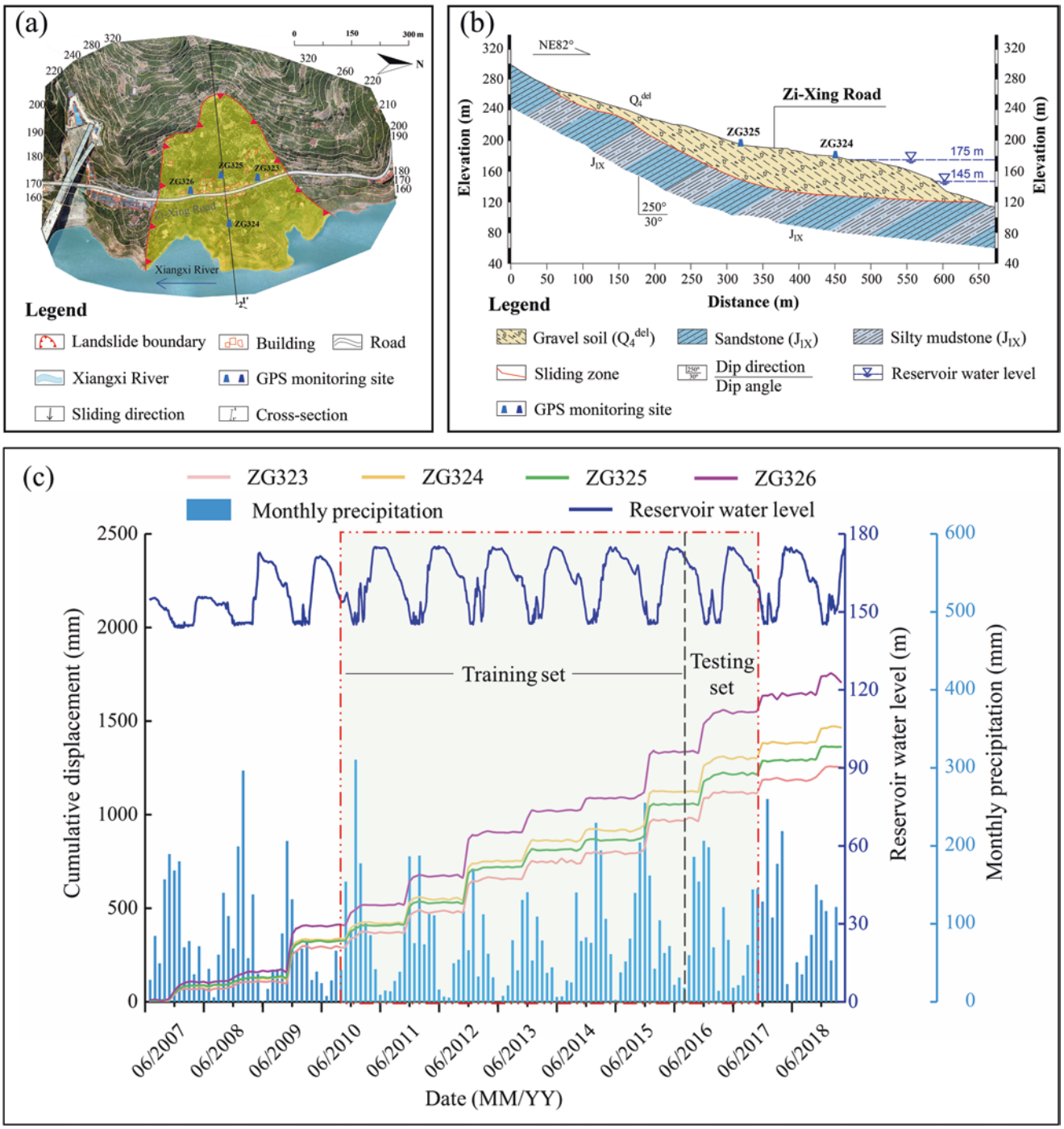

Fig. 2 (**a**) The plan map; (**b**) the profile map and (**c**) the monthly cumulative displacement, the monthly precipitation and reservoir water level of Baijiabao landslide (after Long et al. 2022)

Xiangxi Group (J_1x) (Figs. 2b, 3b, 4b). The sliding zones of the three landslides are Jurassic slide-prone strata composed of sedimentary rocks with poor weathering resistance and high permeability (Long et al. 2020). But the three landslides vary in volume. The Baijiabao landslide covers an area of 2.4×10^5 m^2, and has a volume of 1.0×10^7 m^3. The Bazimen landslide covers a total area of 1.18×10^5 m^2, and encompasses a volume of 2.35×10^6 m^3. The Baishuihe landslide covers an area of 2.15×10^5 m^3, with an estimated volume of 1.26×10^7 m^3.

Several GPS sites were set up in the three landslides to monitor the landslides deformation. However, due to various reasons such as reservoir water impoundment, some sensors have been damaged. Hence, the data of four GPS monitoring

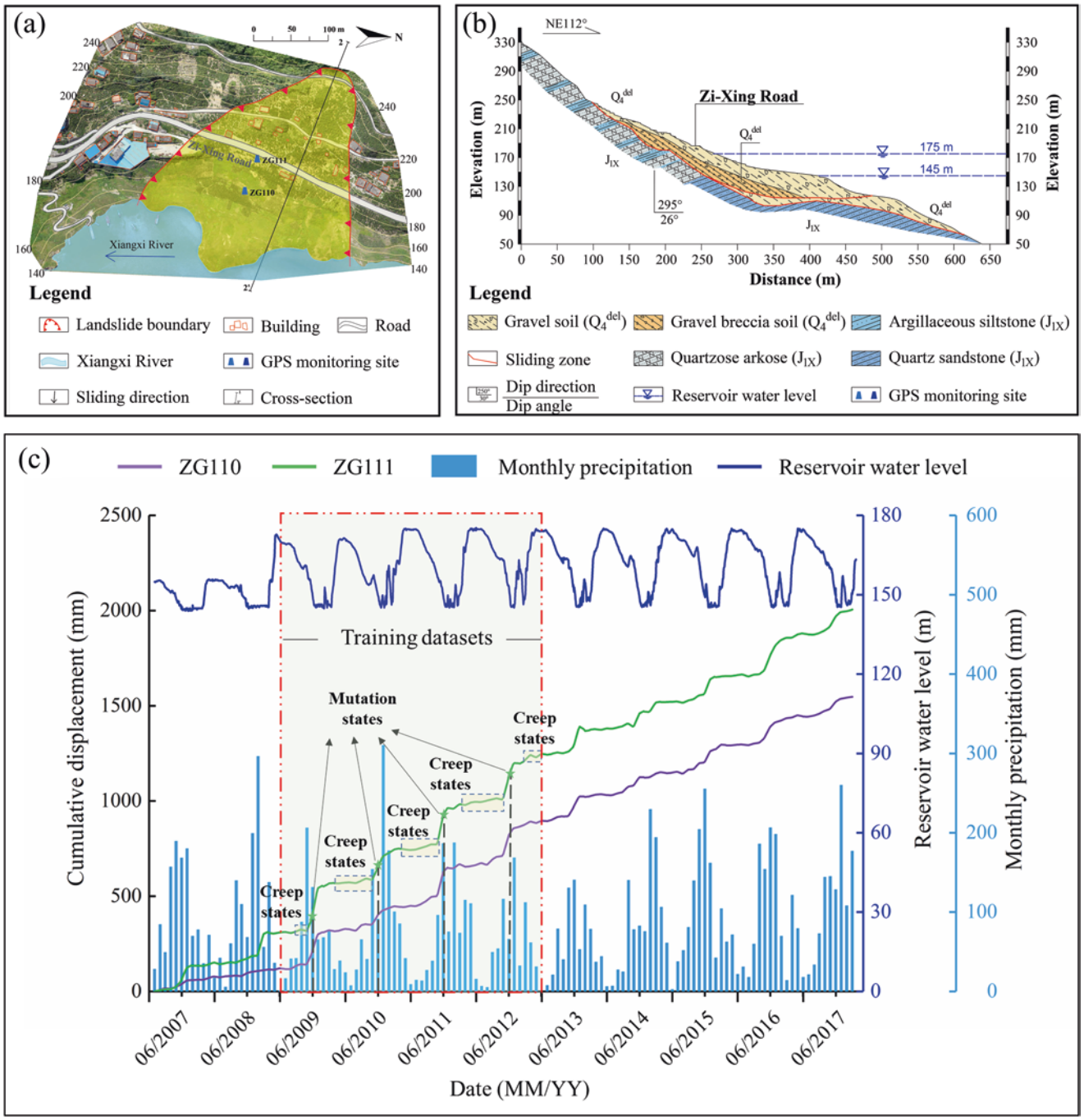

Fig. 3 (**a**) The plan map; (**b**) the profile map and (**c**) the landslide monthly cumulative displacement, the monthly precipitation and reservoir water level of Bazimen landside (after Long et al. 2022)

points (ZG323, ZG324, ZG325 and ZG326) in Baijiabao landslide (Fig. 2c), two GPS monitoring points in Bazimen landslide (ZG110 and ZG111) (Fig. 3c) and two GPS monitoring points in Baishuihe landslide (ZG93 and ZG118) (Fig. 4c); and the monthly precipitation, reservoir water level are collected for research.

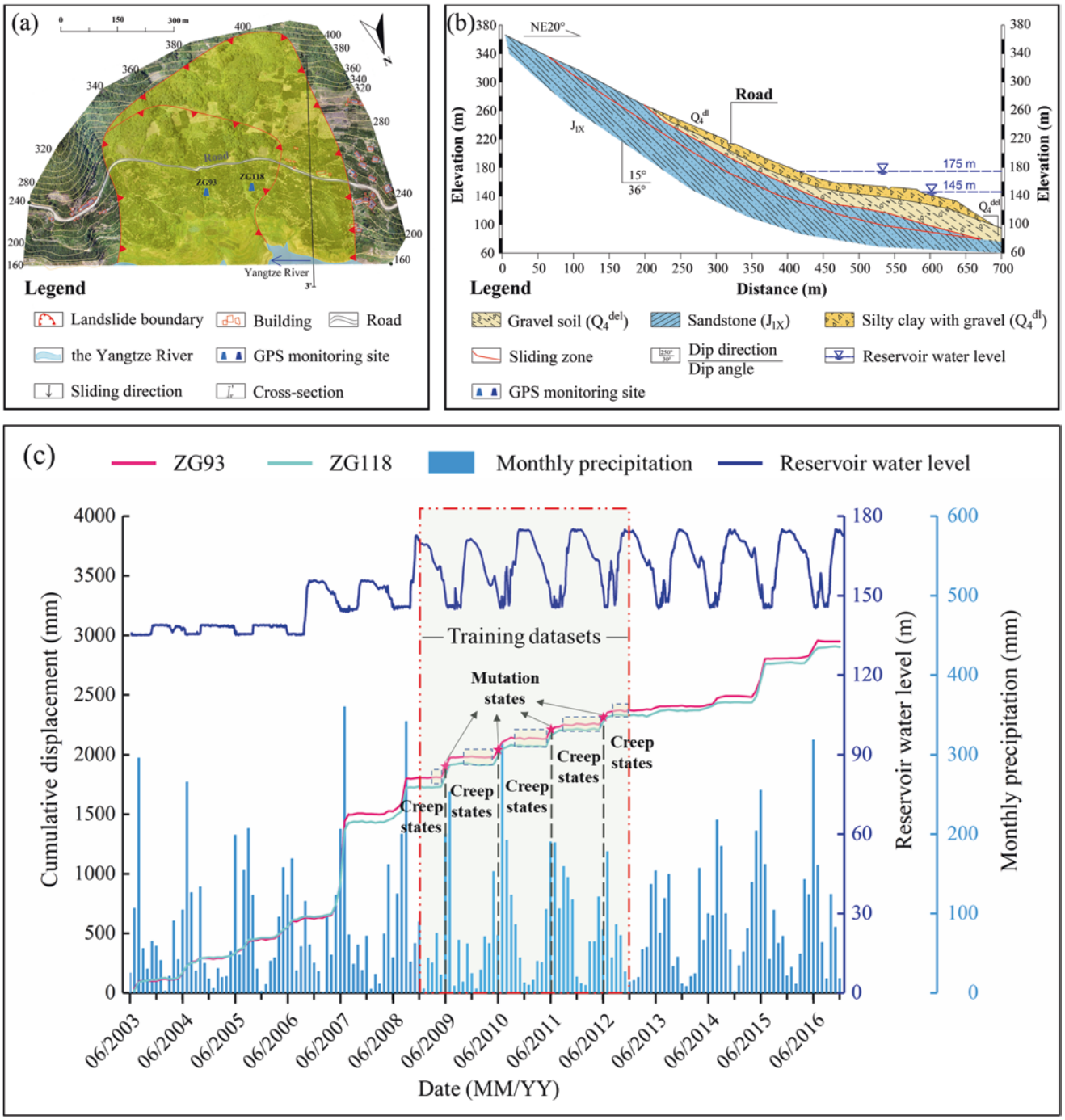

Fig. 4 (**a**) The plan map; (**b**) the profile map and (**c**) the landslide monthly cumulative displacement and the monthly precipitation, reservoir water level of Baishuihe landside (after Long et al. 2022)

3 Landslide Prediction Model Based on Ensemble Learning

3.1 Model Construction and Application

RF is an advanced ensemble algorithm based on Decision Trees (DT) with robust and accurate performance (Breiman 2001). And SVM algorithm (Ruping and Morik 2003) with high robustness and outstanding generalization capacity is regarded as one of the most famous ML methods for landslide displacement forecasting. In this paper, we construct the ensemble learning method called Greedy Algorithm (GA) -CEEMD-RF and GA-CEEMD-SVM algorithms for landslide displacement decomposition and prediction. It

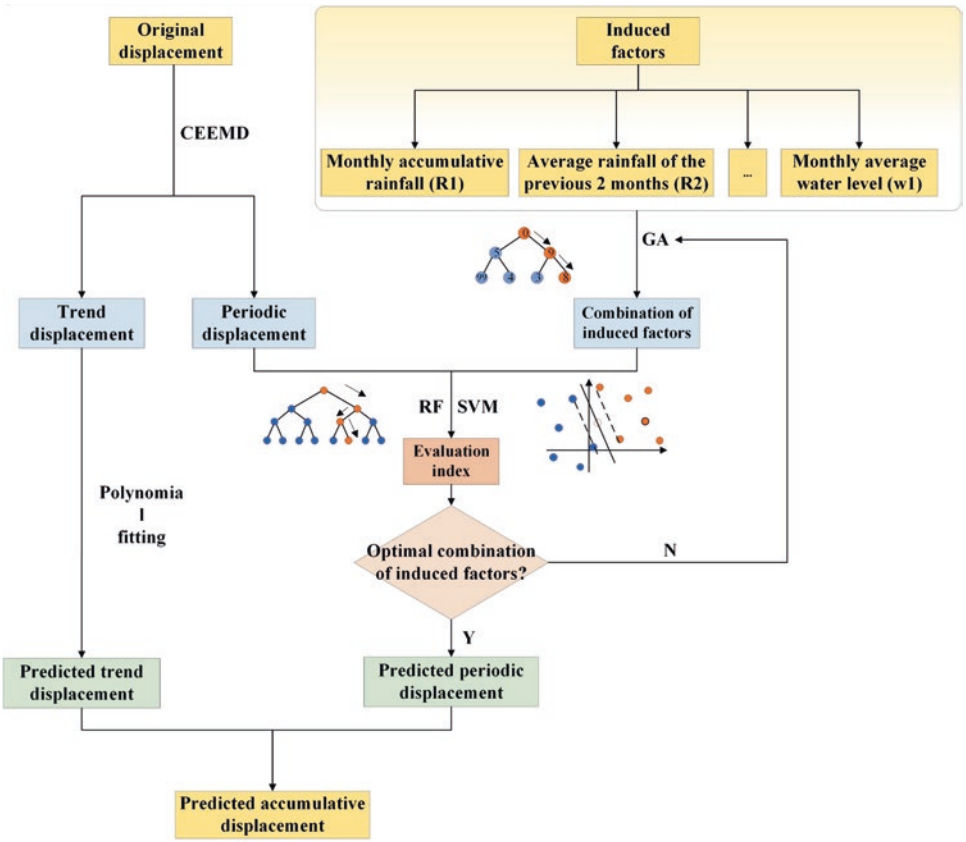

Fig. 5 The flowchart of GA-CEEMD-RF and GA-CEEMD-SVM model for landslide displacement prediction with step-like characteristics (after Li et al. 2021)

mainly includes four key steps and the flowchart is shown in Fig. 5.

Considering the data integrity, the monitoring displacement dataset (ZG323) from April 2010 to April 2017 of Baijiabao landslide is applied for model constuction as an example. At first, CEEMD algorithm is used to decompose the landslide accumulative displacement into trend component and periodical component.

Secondly, rainfall and variation of reservoir water level are regarded as the main landslide-related inducing factors in CTGR area. Hence, monthly accumulative rainfall (R1), accumulative rainfall of the previous 2 months (R2) and average rainfall of the previous 3 months (R3); monthly average water level (W1), monthly maximum variation of water level (W2), and maximum variation of water level of the previous 2 months (W3); and the high-frequency item of R4 and W4 obtained by the decomposition of R1 and W1 respectively based on CEEMD algorithm, are taken as direct inducing factors. Since the induction factors with similar information cannot be used simultaneously, the GA algorithm which makes the optimal decision at each step as it tries to find the overall optimal solution for the whole problem is applied to determine the optimal combination of inducers (Gribonval and Nielsen 2001). The eight direct induced factors are used to construct the different displacement prediction models, respectively. And goodness of fitting (R^2) of each model is calculated. The induced factors corresponding to the maximum R^2 are regressed one and 2 months considering the lag effect, and they are served as the inputs to construct models. The R^2 of the models are calculated and compared with values mentioned above. The induced factors corresponding to the maximum R^2 is regarded as the Optimal Combination of Induced Factors (OCIF) at the present stage. And next, the combination of the remaining seven direct induced factors with the OCIF is served as the inputs and the R^2 of these models can be obtained. The combination of induced factors corresponding to maximum R^2 of these models is regarded as the global OCIF at the present stage. Repeat the steps until the global OCIF is determined. The result indicates that the Gauss function shows good capacity for trend component prediction. The optimal inducers combination during this period including regression 2-month R2, R3, regression 1-month R4 and regression 2-month W2 is determined by GA method.

Finally, Gauss function is selected to fit the trend displacement. And the OCIF and the periodic composition are served as inputs and outputs of RF and SVM algorithms for constructing the displacement prediction model. In this study, 80% of data (from April 2010 to February 2016) are treated as training sets for periodical displacement prediction model construction, while the remaining 20% (from March 2016 to April 2017) are used as test data to check the effectiveness of the model. And the number of DT is set to 1000

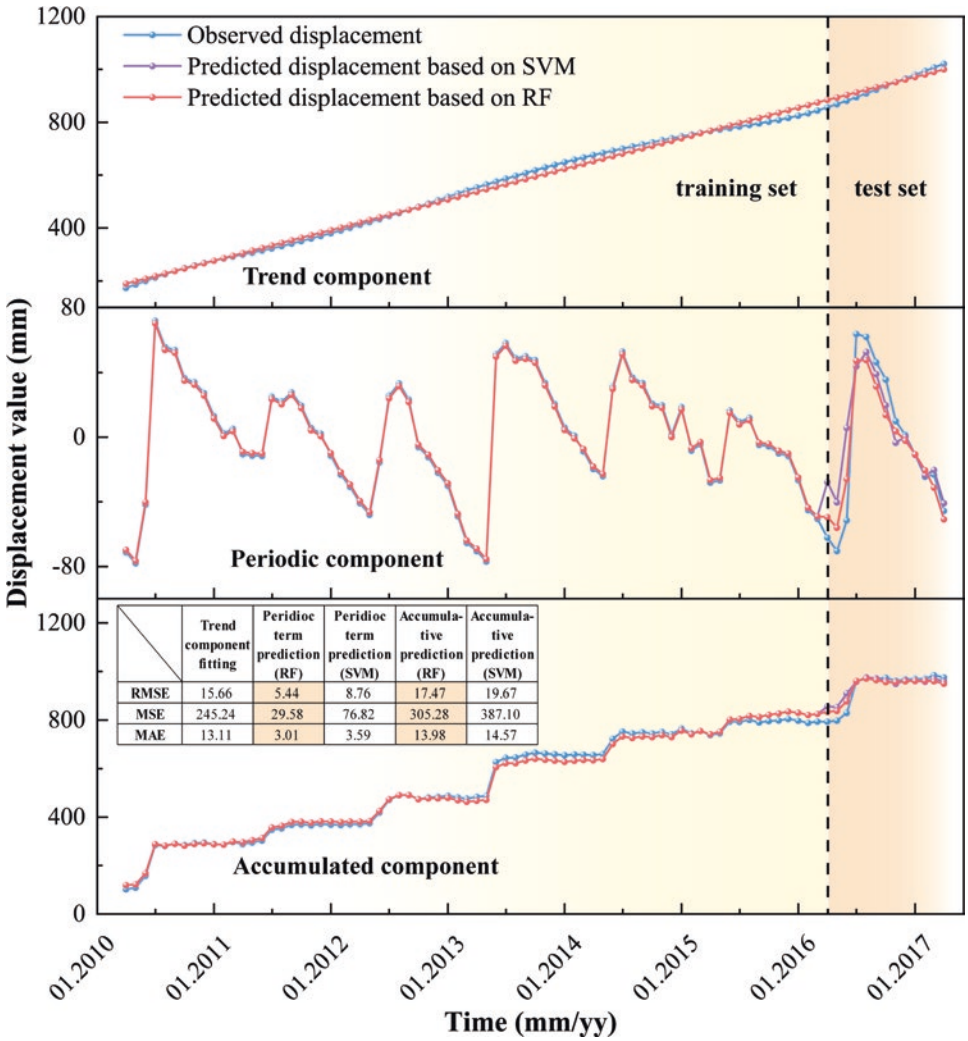

	Trend component fitting	Peridioc term prediction (RF)	Peridioc term prediction (SVM)	Accumulative prediction (RF)	Accumulative prediction (SVM)
RMSE	15.66	5.44	8.76	17.47	19.67
MSE	245.24	29.58	76.82	305.28	387.10
MAE	13.11	3.01	3.59	13.98	14.57

Fig. 6 The fitting result of the trend displacement with Gauss equation; the periodic component prediction result based on RF model and SVM model; the accumulative displacement prediction results of GA-CEEMD-RF model and GA-CEEMD-SVM model (after Li et al. 2021)

and the length of features set is set to 2 in RF algorithm. The optimal error penalty factor (C) and kernel function parameter (g) of SVM periodic component prediction model are calculated by grid cell method as 0.5 and 9.76×10^{-4}, respectively. The trend term and the periodic term are added together to get the cumulative displacement.

3.2 Result Evaluation and Verification

As shown in Fig. 6, the R^2 of fitting result of the trend displacement with Gauss equation is 0.9956. The RMSE is 15.66, MSE is 254.44, and MAE is 13.11. The RMSE, MSE and MAE of periodic displacement prediction based on RF algorithm are 5.44; 29.58 and 3.01, respectively. The RMSE, MSE and MAE of periodic displacement prediction based on SVM algorithm are 8.76; 76.82 and 3.59, respectively. And the RMSE, MSE and MAE of accumulative displacement prediction based on GA-CEEMD-RF method are 17.47; 305.28 and 13.98. And the RMSE, MSE and MAE of accumulative displacement prediction based on GA-CEEMD-SVM model are 19.67; 387.10 and 14.57.

As is known to all, the smaller the evaluation value, the better the model performance. Hence, the results comparison shows that both SVM model and RF model perform well on step-like landslide periodic component forecasting, but the GA-CEEMD-RF model possesses better prediction capacity than that of SVM model in general.

4 A Landslide Prediction Model Based on Transfer Learning

4.1 MFTL Model Construction

The monitoring system established in the Zigui basin can only cover the most destructive landslides due to manpower and equipment limitations. In addition, monitoring work interruption will cause data missing. Thus, a landslide of interest may lack training data, but data from other landslides located in

neighboring areas or with the same deformation characteristics can potentially be available. According to engineering geological analogy (EGA) method, landslides occurring under the same geological conditions generally have similar deformation characteristics, but vary in size. In such cases, the transfer learning (TL) approach inspired by the EGA method provides a solution, as the knowledge gained from a landslide case with sufficient monitoring data can be applied to other landslides that lack adequate training data (Pan and Yang 2010; Yi and Gianfranco 2010; Weiss et al. 2016). Multi-feature fusion transfer learning (MFTL) method is novelty proposed to transfer the knowledge learned from Baijiabao landslides to Bazimen landslide and Baishuihe landslide for further forecasting.

The evolution process of hydrodynamic pressure-driven landslides is affected by complex factors that cannot be simply expressed by a single variable (Liu et al. 2020). Hence, the landslide evolution state is proposed to represent the relationship between deformation and external factors. The process of multi-feature space projection and landslide evolution states construction is shown as follows: (Fig. 7) (Long et al. 2022):

1. The landslide evolution state (S_t) at time t is defined as a continuous response deviation:

$$S_t = \begin{bmatrix} R_t & R_{t-1} & R_{t-2} \\ K_t & K_{t-1} & K_{t-2} \\ \Delta W_t & \Delta W_{t-1} & \Delta W_{t-2} \end{bmatrix} \tag{5}$$

It is composed of consecutive incentive conditional space ($X = \begin{bmatrix} R_t & R_{t-1} & \cdots & R_0 \\ K_t & K_{t-1} & \cdots & K_0 \end{bmatrix}$) and sensitive states ($\Delta W_t = W_t^{'} - W_t$), where $\boldsymbol{R}$ refers to the monthly accumulative precipitation and $\boldsymbol{K}$ refers to the variation velocity of reservoir water level. The landslide incentive conditional space (X) and displacement (ω_t) are projected into Dynamic-Kernel Hilbert Space (DKHS) through different projection functions $f_1(x)$ and $f_2(w)$. W_t is the projection of displacement in the conditional space at time t. $W_t^{'}$ is the projection of displacement at time t. The difference in post-projection displacement is defined as the sensitivity state (ΔW_t) at time t under the current excitation conditions.

2. The distance $\left(RD_{S_{t_1}S_{t_2}}\right)$ is used to measure the similarity of landslide evolution states S_{t_1} and S_{t_2} at times t_1 and t_2, and it is defined as follows:

$$RD_{S_{t_1}S_{t_2}} = \sqrt{\sum_{k=0}^{2}\left(\left|R_{t_1-k} - R_{t_2-k}\right|^2 + \left|K_{t_1-k} - K_{t_2-k}\right|^2 + \left|\Delta W_{t_1-k} - \Delta W_{t_2-k}\right|^2\right)} \tag{6}$$

where R_{t_1-k}, R_{t_2-k}, K_{t_1-k}, and K_{t_2-k} denote incentive condition factors R_{t_1} and R_{t_2}, K_{t_1} and K_{t_2} at time $t-k$, respectively. ΔW_{t_1-k} and ΔW_{t_2-k} denote the sensitivity states $\varnothing W_{t_1}$ and $\varnothing W_{t_2}$ at time $t-k$, respectively.

3. The class centroids (CS) is defined as the average distance from every landslide evolution state. The class centroids are defined as follows:

$$CS_{N_i} = \frac{1}{M_i}\sum_{j=1}^{M_i}\left(S_{t_j}\right) \tag{7}$$

where N refers to the kinds of landslide deformation states. In this paper, the mutation state and creep state are taken into consideration. The default value of is equals to 2. One of the landslide deformation states N_i includes M_i landslide evolution states.

4. The total distance in the same class $\left(DC_{N_i}\right)$ is calculated as follows:

$$DC_{N_i} = \sum_{j=1}^{M_i} RD_{t_j,CS_{N_i}} \tag{8}$$

where $RD_{t_j,CS}$ refers to the distance between the landslide evolution state $\left(S_{t_j}\right)$ and a class centroid (CS).

5. Considering the characteristics of landslide displacement data, the expected mean distribution discrepancy (EMDD) method is defined to maintain consistency, and at the same time, obtain the minimum risk distribution for the structural features of landslide evolution states in the DKHS. The projection functions $f_1(x)$ and $f_2(w)$ can be adjusted with the EMDD method to separate the samples through classification hyperplane into different classes as much as possible:

$$EMDD = \min \mu\sum_{t=0}^{n} V\left(x_t,\omega_t,f_1,f_2\right) + \min\sum_{i=0}^{N} DC_{N_i} \tag{9}$$

where $\boldsymbol{\mu}$ is the penalty coefficient and $V(x_t,\omega_t,f_1,f_2)$ is the penalty function.

Considering the data integrity, the monthly cumulative displacement acquired from four GPS monitoring sites (ZG323, ZG324, ZG325, and ZG326) in Baijiabao landslide, monthly precipitation and variation velocity of reservoir water level from March 2009 to December 2012 are used to form the source domain. ZG111 located in Bazimen landslide and ZG93 located in Baishuihe landslide, and external incentive conditional space from December 2008 to

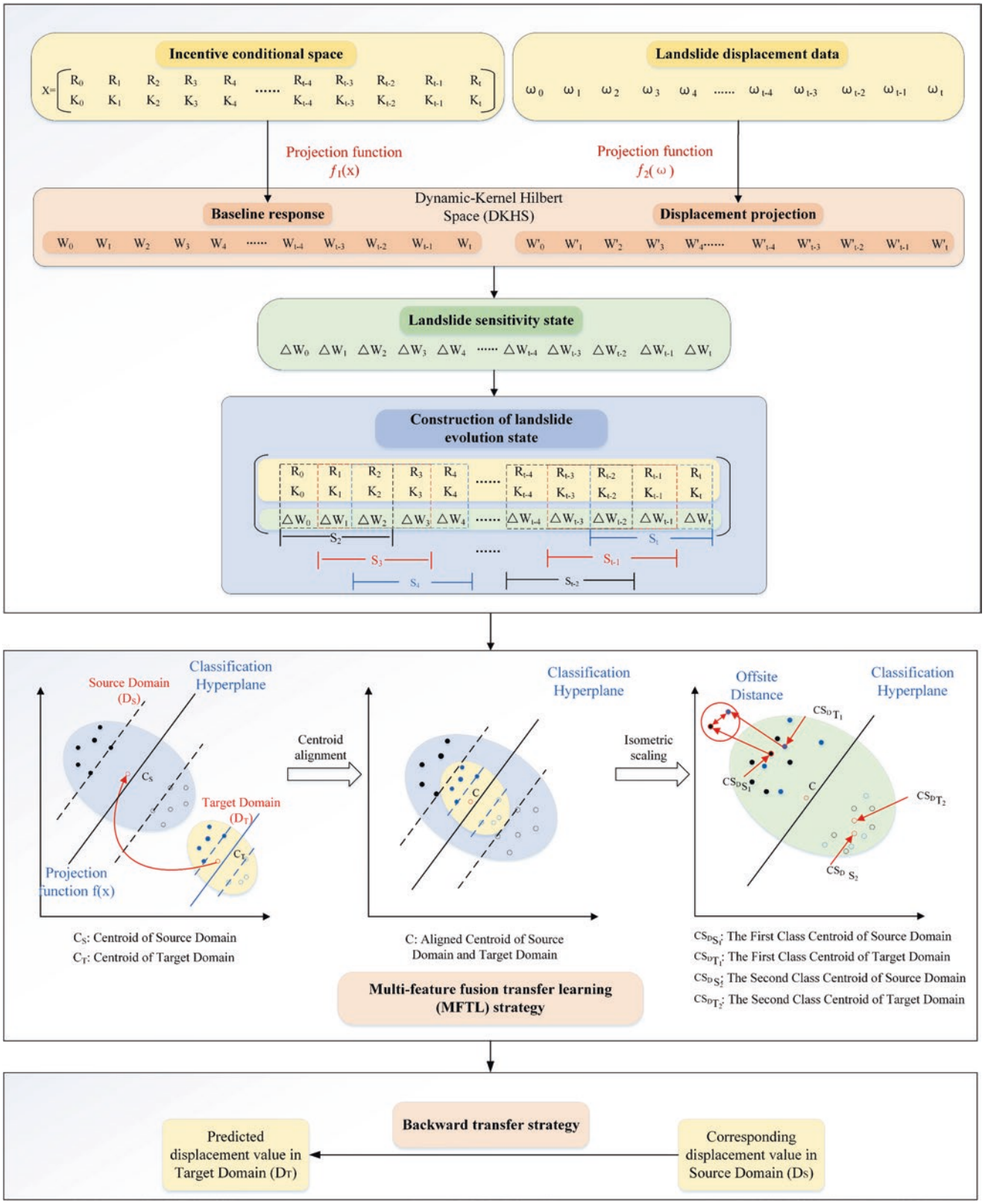

Fig. 7 The flowchart of MFTL model for landslide displacement prediction (after Long et al. 2022)

December 2012 are taken as the target domains. The steps mentioned above are repeated, and separate landslide evolution states are obtained to transfer landslide states.

To transfer knowledge from the source domain (D_S) to the target domain (D_T), the similarity of the landslide evolution state is determined through feature transformation. To avoid a negative transfer effect in landslide displacement prediction, a hybrid optimization method is proposed to measure the distribution similarity for datasets in source domain and target domain. The decision optimization function of the MFTL algorithm is shown as follows:

$$j = \min \eta \upsilon \parallel EMDD_S - EMDD_T \parallel^2 + \lambda d_f \left(D_S, D_T\right) \quad (10)$$

where regularization parameter η represents the degree of punishment for wrongly identifying samples. $\upsilon \parallel EMDD_S - EMDD_T\parallel^2$ is the structure risk function. $EMDD_S$ and $EMDD_T$ represent the data distributions in the source domain and target domain, respectively. By minimizing the EMDD according to the Structural Risk Minimization (SRM) criterion, the spatial distributions of data in source domain and target domain can be adjusted as similarly as possible. $d_f(D_S, D_T)$ is a measurement of the distance between the common features in source domain and target domain. The equilibrium parameter λ is related to the risk structure and the distribution distance between domains.

The MFTL strategy aims to align the centroids of two domains by moving the target domain samples towards the source domain; the movement direction is based on the centroid differences in the two domains, and centroid alignment and isometric scaling methods are applied (Zhu and Ma 2016). After moving the centroids, the data distributions will be similar, and the classifier trained in the source domain can be used to predict landslide displacement in the target landslide. Hence, through the centroid alignment and isometric scaling processes, the data scale of similar landslides with different sizes are transferred into a roughly same space, which heavily eliminate or weaken the scale effect. The objective function of MFTL method is shown as follows (Long et al. 2022):

$$g = \min_{D_S, D_T, \varepsilon_a^S, \varepsilon_b^T, \alpha, \delta} \frac{1}{2} \parallel w_S - w_T \parallel^2 + \mu_1 \sum_{a=1}^{M_1} \varepsilon_a + \mu_2 \sum_{b=1}^{M_2} \varepsilon_b + \sum_{t'=1}^{S'} RD_{\alpha(S_{t'}{}' - \delta), CS_{D_S}} \quad (11)$$

where $\frac{1}{2} w_S - w_T^{\,2}$ represents the feature difference between normal vectors in the source domain (w_S) and target domain (w_T) in DKHS. $\mu_1 \sum_{a=1}^{M_1} \varepsilon_a$ and $\mu_2 \sum_{b=1}^{M_2} \varepsilon_b$ are second-order soft interval classifiers. ε_a and ε_b are the slack variables for fault tolerance. μ_1 and μ_2 are the cost parameters. M_1 and M_2 are the numbers of landslide evolution states corresponding to mutation and creep, respectively. $\alpha(S_t' - \delta)$ refers to the samples transferred from the target domain (D_T) to the source domain (D_S). In this process, after the application of the centroid alignment method, the landslide evolution state in the target domain (S_t') is changed to $S_t' - \delta$, where δ denotes the alignment vector. After the application of the isometric scaling method, the state is changed to $\alpha(S_t' - \delta)$, where α denotes the scaling vector. CS_{D_S} is a class centroid in the source domain (D_S). $RD_{\alpha(S_{t'}{}' - \delta), CS_{D_S}}$ represents the distance between the transferred samples and class centroids in the source domain (CS_{D_S}).

Subsequently, the transferred landslide evolution states are substituted into the decision optimization function (Eq. 10), and $f(x)$ is further adjusted through the EMDD method (Eq. 9). After calculating the optimal function $f(x)$, the projection of the source domain and the projection of the target domain after transfers are complete should be recalculated, as should the function $d_f(D_S, D_T)$. In addition, $d_f(D_S, D_T)$ should be substituted into the Eq. 10 until obtaining the optimal function $f(x)$.

However, the spatial distance between the Baishuihe and Baijiabao landslide leads to some differences in characteristics. To reduce errors and enhance the transfer efficiency considering the dissimilarity between the two domains, landslide evolution state clustering is performed before applying transfer strategy.

After determining the classification of landslide deformation state for each sample in the target domain, the most similar landslide evolution state in source domain should be calculated by similarity measurement. Using the corresponding displacement under the most similar excitation condition, the displacement value in the target domain is obtained. The backward transfer strategy is shown as follows (Long et al. 2022):

1. For each landslide evolution state (S_t'), there is a closest corresponding landslide evolution state in the source domain (S_t). The distance is used to measure the similarity between landslide evolution states in target domain at current time t' and source domain at time t.

$$RD_{S_tS_{t'}} = \sqrt{\sum_{k=0}^{2}\left(\left|R_{t-k} - R_{t'-k}\right|^2 + \left|K_{t-k} - K_{t'-k}\right|^2 + \left|\Delta W_{t-k} - \Delta W_{t'-k}\right|^2\right)} \tag{12}$$

2. The distance between external incentive conditional space in source domain at time $(t + 1)$ and in target domain at time $(t' + 1)$ is used to measure the similarity:

$$D_{RK} = \sqrt{\left|R_{t+1} - R_{t'+1}\right|^2 + \left|K_{t+1} - K_{t'+1}\right|^2} \tag{13}$$

3. The displacement (ω_{t+1}) corresponding to the external incentive conditional space at time $(t + 1)$ in source domain can be obtained as follows:

$$D_{\min} = \min RD_{S_tS_{t'}} + \min D_{RK} \tag{14}$$

4. The backward strategy of isometric scaling and centroid alignment method aims is used to figure out the unknown displacement value $(\omega_{t'+1})$ in target domain at the next time $(t' + 1)$:

$$\omega_{t'+1} = \frac{\omega_{t+1}}{\alpha'} - \delta' \tag{15}$$

where α' refers to the backward scaling vector and δ' refers to the backward alignment vector.

4.2 Result Evaluation and Verification

To verify the accuracy and reliability of the MFTL model, the prediction results are compared with those of Back Propagation neural network (BPNN) and Least Square (LS) methods, which are generally used in landslide displacement forecasting. The monitoring data and conditional space of Baijiabao landslide are selected as the inputs, and the displacements of Bazimen and Baishuihe landslides are output through the training of the BPNN and LS method. Notably, Fig. 8 shows that the MFTL method provides the best prediction results and it is more accurate in both creep and mutation states than the other two methods. The error evaluation results for Bazimen and Baishuihe landslides are shown in Table 1. The MSE, RMSE and MAE values are lower in the MFTL method than in other methods, which indicates that the novel model can not only fill data gaps associated with disrupted monitoring, but also provide a real-time, whole-process and effective landslide displacement prediction based on accurate forecasts of rainfall data and periodic variations in reservoir water levels.

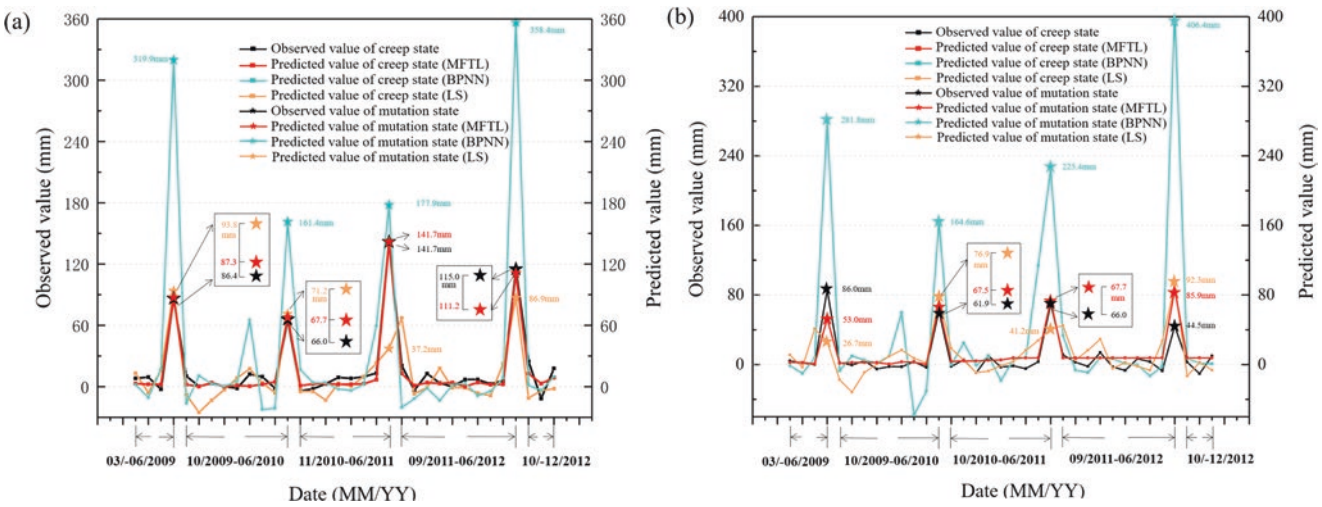

Fig. 8 The prediction results of (**a**) Bazimen landslide and (**b**) Baishuihe landslide based on MFTL, BPNN and LS methods. (after Long et al. 2022)

Table 1 The MSE; RMSE and MAE results of MFTL; BPNN and LS methods, respectively (after Long et al. 2022)

Landslide	Method / Index	MFTL	BPNN	LS
Bazimen landslide	MSE	30.653	4154.100	549.247
	RMSE	5.537	64.452	23.436
	MAE	3.598	31.408	14.480
Baishuihe landslide	MSE	91.899	6505.501	465.326
	RMSE	9.586	80.657	21.571
	MAE	0.831	37.827	16.631

5 Conclusions

In the digital era with explosive growth data, it is increasingly urgent to realize intelligent and automatic processing of landslide monitoring data. Literature review shows that ML model, DL model, and improved ensemble learning methods are widely applied in landslide displacement prediction, due to their outstanding data processing abilities. In this paper, the novel GA-CEEMD-RF and GA-CEEMD-SVM algorithms are proposed to decompose the landslide displacement and conduct displacement prediction of hydrodynamic pressure-driven landslide in CTGR area. It can solve the difficulties of determining the optimal combination of induced factors and weak stableness of prediction results using a single displacement prediction model.

Considering the limitations of monitoring equipment and data missing, the MFTL approach transfers the knowledge learned from the Baijiabao landslide to two other landslides with incomplete monitoring datasets. The successful transfer between Baijiabao landslide and Bazimen landslide, which share the nearly similar internal and external conditions, proves that the MFTL model is feasible in the landslides with the high similarity. And the model also works well for displacement prediction with the addition of clustering in different landslides, such as Baishuihe and Baijiabao landslides, which proves that the MFTL model exhibit positive generalization ability. The predicted results and traditional error evaluation indexes verify that the MFTL method performs better in landslide displacement prediction than traditional BPNN and LS methods.

However, the "black box" of data-based mathematical prediction models makes it impossible to obtain the internal variables and parameters and lacks interpretability. There are inherent disadvantages in generality if the data mining methods fail to consider the landslide physical mechanism. Hence, in the future, there is a growing tendency to construct multi-model coupled methods combining triggering and instability mechanisms to realize dynamic and reliable landslide deformation prediction.

Acknowledgement This work was supported by National Natural Science Foundation of China (Nos. 42090054, 41931295 and 41772376), National Natural Science Foundation of Hubei Province of China (2022CFA002) and the Technology Innovation Center of geohazards automatic monitoring, Ministry of Natural Resources (Chongqing Institute of Geology and Mineral Resources) (No. 2022058014).

References

Breiman L (2001) Random forests. Mach Learn 45(1):5–32

Cui P, Peng J, Shi P et al (2021) Scientific challenges of research on natural hazards and disaster risk. Geogr Sustain 2(3):216–223. https://doi.org/10.1016/j.geosus.2021.09.001

Criss RE, Yao W, Li C, Tang H (2020) A predictive, two-parameter model for the movement of reservoir landslides. J Earth Sci 31(6):1051–1057. https://doi.org/10.1007/s12583-020-1331-9

Gong W, Juang CH, Wasowski J (2021) Geohazards and human settlements: lessons learned from multiple relocation events in Badong, China—engineering geologist's perspective. Eng Geol 285. https://doi.org/10.1016/j.enggeo.2021.106051

Guo C, Xu Q, Dong X et al (2021) Geohazard recognition and inventory mapping using airborne LiDAR data in complex mountainous areas. J Earth Sci 32:1079–1091. https://doi.org/10.1007/s12583-021-1467-2

Gribonval R, Nielsen M (2001) Approximate weak greedy algorithms. Adv Comput Math 14(4):361–378. https://doi.org/10.1023/A:1012255021470

Huang F, Zhang J, Zhou C, Wang Y, Huang J, Zhu L (2020) A deep learning algorithm using a fully connected sparse autoencoder neural network for landslide susceptibility prediction[J]. Landslides 17(01):217–229. https://doi.org/10.1007/s10346-019-01274-9

Juang CH (2021) BFTS - engineering geologists' field station to study reservoir landslides. Eng Geol 284. https://doi.org/10.1016/j.enggeo.2021.106038

Kang G, Song Y, Kim T (2009) Behavior and stability of a large-scale cut slope considering reinforcement stages. Landslides 6(3):263–272. https://doi.org/10.1007/s10346-009-0164-5

Li C, Criss RE, Fu Z, Long J, Tan Q (2021) Evolution characteristics and displacement forecasting model of landslides with stair-step sliding surface along the Xiangxi River, three gorges reservoir region, China. Eng Geol 283. https://doi.org/10.1016/j.enggeo.2020.105961

Liu Y, Xu C, Huang B, Ren X, Liu C, Hu B, Chen Z (2020) Landslide displacement prediction based on multi-source data fusion and sensitivity states. Eng Geol 271:105608. https://doi.org/10.1016/j.enggeo.2020.105608

Long J, Li C, Liu Y, Feng P, Zuo Q (2022) A multi-feature fusion transfer learning method for displacement prediction of rainfall reservoir-induced landslide with step-like deformation characteristics. Eng Geol 297. https://doi.org/10.1016/j.enggeo.2021.106494

Long J, Liu Y, Li C, Fu Z, Zhang H (2020) A novel model for regional susceptibility mapping of rainfall-reservoir induced landslides in Jurassic slide-prone strata of western Hubei Province, three gorges reservoir area. Stoch Env Res Risk A 35(7):1403–1426. https://doi.org/10.1007/s00477-020-01892-z

Pan S, Yang Q (2010) A survey on transfer learning. IEEE T Knowl Data En 22(10):1345–1359. https://doi.org/10.1109/TKDE.2009.191

Ruping S, Morik K (2003) Support vector machines and learning about time. IEEE international conference on acoustics, speech, and signal processing. Proceedings. IEEE, IV-864-7 vol 4

Tang H, Wasowski J, Juang CH (2019) Geohazards in the three gorges reservoir area, China—lessons learned from decades of research. Eng Geol 261. https://doi.org/10.1016/j.enggeo.2019.105267

Wang G, Li C, He X et al (2022) Mechanism of interaction between anchored slide-resistant piles and landslides with weak-hard interbedded bedrock: model tests and theoretical interpretation. J Earth Sci. https://doi.org/10.1007/s12583-022-1663-8

Weiss K, Khoshgoftaar TM, Wang D (2016) A survey of transfer learning. J Big Data 3(1). https://doi.org/10.1186/s40537-016-0043-6

Yang B, Yin K, Lacasse S, Liu Z (2019) Time series analysis and long short-term memory neural network to predict landslide displacement. Landslides 16(4):677–694. https://doi.org/10.1007/s10346-018-01127-x

Yeh J, Shieh J, Huang N (2011) Complementary ensemble empirical mode decomposition: a novel noise enhanced data analysis method. Adv Adapt Data Anal 02(02):135–156. https://doi.org/10.1142/s1793536910000422

Yi, Y., Gianfranco, D. (2010). Boosting for transfer learning with multiple sources. 2010 IEEE computer society conference on computer vision and pattern recognition, pp 1855–1862. https://doi.org/10.1109/CVPR.2010.5539857

Yu S, Ma J (2021) Deep learning for geophysics: current and future trends. Rev Geophys 59(3). https://doi.org/10.1029/2021rg000742

Zhu L, Ma L (2016) Class centroid alignment-based domain adaptation for classification of remote sensing images. Pattern Recogn Lett 83:124–132. https://doi.org/10.1016/j.patrec.2015.12.015

Mud-Mark-Based Estimations of Mass-Wasting Processes Caused by the 2008 Iwate-Miyagi Nairiku Earthquake, Japan

Fumihiko Nomura, Kazuo Konagai, Md. Aftabur Rahman, and Yoshimitsu Tajima

Abstract

A 7.2 Magnitude (Moment Magnitude Mw: 6.8) earthquake occurred in the south inland of Iwate prefecture at 8:43 JST on June 14, 2008. Its epicenter was about 10 km northeast of Mt. Kurikoma, an active Nasu volcanic belt composite volcano whose lava flows from several eruption centers covering underlying crumbly secondary volcaniclastic deposits. Thus, the earthquake caused over 3000 mass-wasting events in its epicentral area, encompassing the Kurikoma Volcano's flank on the hanging side of the seismic fault. Though these mass-wasting events were blamed as the primary cause of deaths in this earthquake, they left tremendous marks of soil deformations and tsunami (seiche) runups along a dam reservoir. The earthquake thus provided unique opportunities to gain insights into the dynamics of the mass-wasting events. The traces of two highly significant mass-wasting events, namely a debris flow that buried the Komano-Yu hot spring inn and a landslide mass of about 70 million m^3 that induced a tsunami in the reservoir of Aratozawa dam, were highlighted in this paper. This paper reviews the findings from our observations in the referred papers. It also compares our findings with the other researchers' inferences from different approaches.

F. Nomura
Ministry of Land, Infrastructure, Transport and Tourism, Water and Disaster Management Bureau, Tokyo, Japan

K. Konagai (✉)
International Consortium on Landslides, Secretariat, Kyoto, Japan

M. Aftabur Rahman
Department of Civil Engineering, Chittagong University of Engineering & Technology (CUET), Chattogram, Bangladesh
e-mail: maftabur@cuet.ac.bd

Y. Tajima
Department of Civil Engineering, The University of Tokyo, Tokyo, Japan
e-mail: yoshitaji@coastal.t.u-tokyo.ac.jp

Keywords

Mud-mark-based estimation · Debris flow · 2008 Iwate-Miyagi Nairiku earthquake · Landslide-induced tsunami

1 Introduction

Mt. Kurikoma is located in the center of the Tohoku region, the northeastern portion of Honshu, the largest island of Japan, at an elevation of 1626 meters. It is a complex stratovolcano comprising some volcanic edifices with inferred eruption centers (Fujinawa et al. 2001). Lava flows from these eruption centers cover the secondary volcaniclastic deposits, the "reworked" products of the "direct" products of volcanic eruptions. Most of them are weakly cemented rhyolitic tuffs and, therefore, highly susceptible to mass wasting events once exposed.

A 7.2 Magnitude (Moment Magnitude Mw: 6.8) earthquake occurred about 10 km northeast of Mt. Kurikoma at 8:43 JST on June 14, 2008. The overwhelming majority of the reported failures are geotechnical. The earthquake caused over 3000 mass-wasting events within the aftershock area, which gives a reasonable estimate of the fault rupture area of the main quake, encompassing Kurikoma Volcano's flank on the hanging side of the earthquake fault (Miyagi et al. 2011). One of the most spectacular mass-wasting events was the Aratozawa Landslide at an upstream section of the Aratozawa Dam in Kurihara, Miyagi Prefecture. The volume of the sliding body near the dam is estimated to be about 68 million cubic meters. A foot of the landslide mass (4.22 million cubic meters) entered the water of the reservoir of Aratozawa Dam, causing a tsunami (seiche) in the reservoir. Though the quake hit the rural area, and thus, sparsely distributed dwellings suffered minor damage, 17 were confirmed dead, and six were still missing. Out of those with known causes, only

B. Abolmasov et al. (eds.), *Progress in Landslide Research and Technology, Volume 3 Issue 1, 2024*, Progress in Landslide Research and Technology, https://doi.org/10.1007/978-3-031-55120-8_20

two cases had no connection to sediment disasters. In other words, mass-wasting events were blamed as the primary cause of deaths in this earthquake, which included seven people believed to have been buried by a fluidized debris mass at the Komanoyu hot spring.

Though the area suffered severe damage, the earthquake left tremendous marks of soil deformations and tsunami run-ups along a dam reservoir, which provided unique opportunities to gain insights into the dynamics of the mass-wasting events. This paper summarizes the findings from our observations in the referred papers (Nomura et al. 2009; Rahman and Konagai 2016, 2017).

2 Geological and Geomorphological Setting of the Epicentral Area

Figure 1 shows a hill-shade map of the epicentral area encompassing Mt. Kurikoma and its widespread mountainside. Red circles and line segments on the southeastern flank of Mt. Kurikoma are the discontinuous fault ruptures identified through field surveys and LiDAR image interpretations by Maruyama et al. (2009). These red circles and line segments align with the southeastern bound of the group of the aftershocks' epicenters (white circles) observed from 8:43 JST on June 14 to 24:00 on June 15, 2008.

As said, Mt. Kurikoma is a complex stratovolcano comprising some volcanic edifices with inferred eruption centers

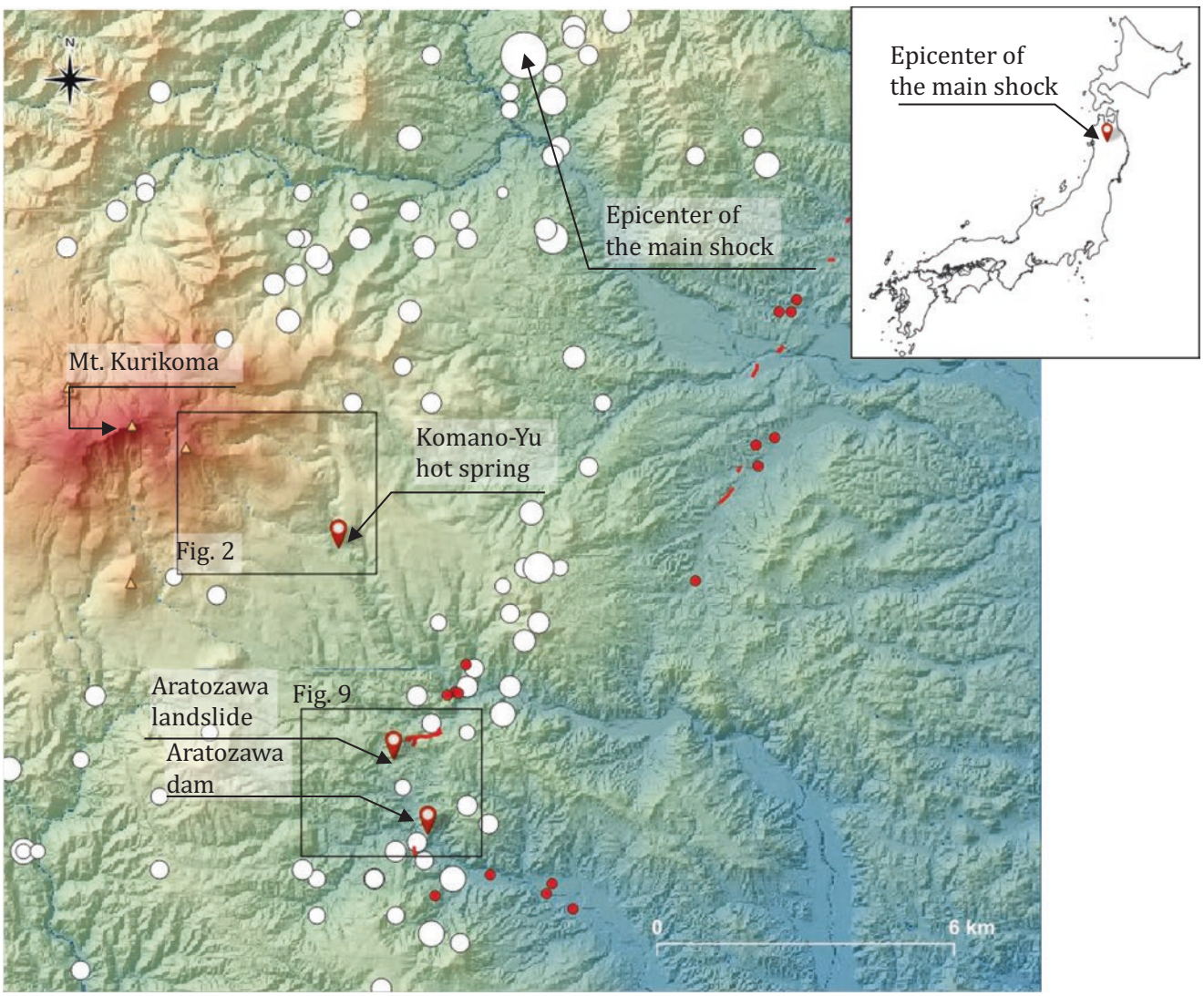

Fig. 1 Hill-shade illustration of the epicentral area encompassing Mt. Kurikoma and its widespread mountainside: Open circles indicate the locations of aftershock epicenters recorded on June 14 and 15, 2008. Redline segments and red circles are locations of surface fault ruptures that the reconnaissance team of the Research Institute of Earthquake and Volcano Geology, the National Institute of Advanced Industrial Science and Technology (AIST), identified and reported (Yoshimi et al. 2008a, b; Maruyama et al. 2009)

(Fujinawa et al. 2001). On the southeastern flank of Kuricoma Volcano, there are some eruption centers, such as pyroclastic cones and lava domes, with solidified lava flows spreading from them to lower elevations. These lava flows cover the secondary volcaniclastic deposits, the "reworked" products of the "direct" products of volcanic eruptions. This hill-shade relief shows that valley density above a specific elevation, ranging from 450 to 550 m a.s.l., is relatively low. In contrast, valleys below this elevation cut mountain slopes down to lower elevations. This feature suggests the presence of harder caprock (radiating lava flows and Ignimbrite) overlying relatively soft secondary volcaniclastic deposits (rhyolitic tuff), and the terrain below this elevation shows clear traces of not only soil mass movements triggered by this earthquake but also those of the past events, indicating that the area has been suffering from frequent geotechnical disasters.

3 Debris Flow that Hit the Komano-Yu Hot Spring Inn

Figure 2 shows a path that the 1.5 million m^3 debris mass flowed down from its source right beneath the snow remaining around the eastern peak of Mt. Higashi-Kurikoma (38.9584°N 140.8061°E), one of the volcanic edifices making up the Kurikoma volcano. The fluidized debris mass ran down along the Dozozawa River Channel. A part of the mud flow of about a 0.5 million m^3 volume, whose path was clogged with another landslide mass (38.9389°N 140.8406°E), surged up to "Komano-Yu" hot spring inn (38.9377°N 140.8378°E), where seven people were killed in soil and rubble.

Some eyewitness accounts vaguely tell us the fluidized debris mass reached the "Komano-Yu hot spring inn" 6 to 9 min after they felt the intense quake (Ikeya et al. 2009).

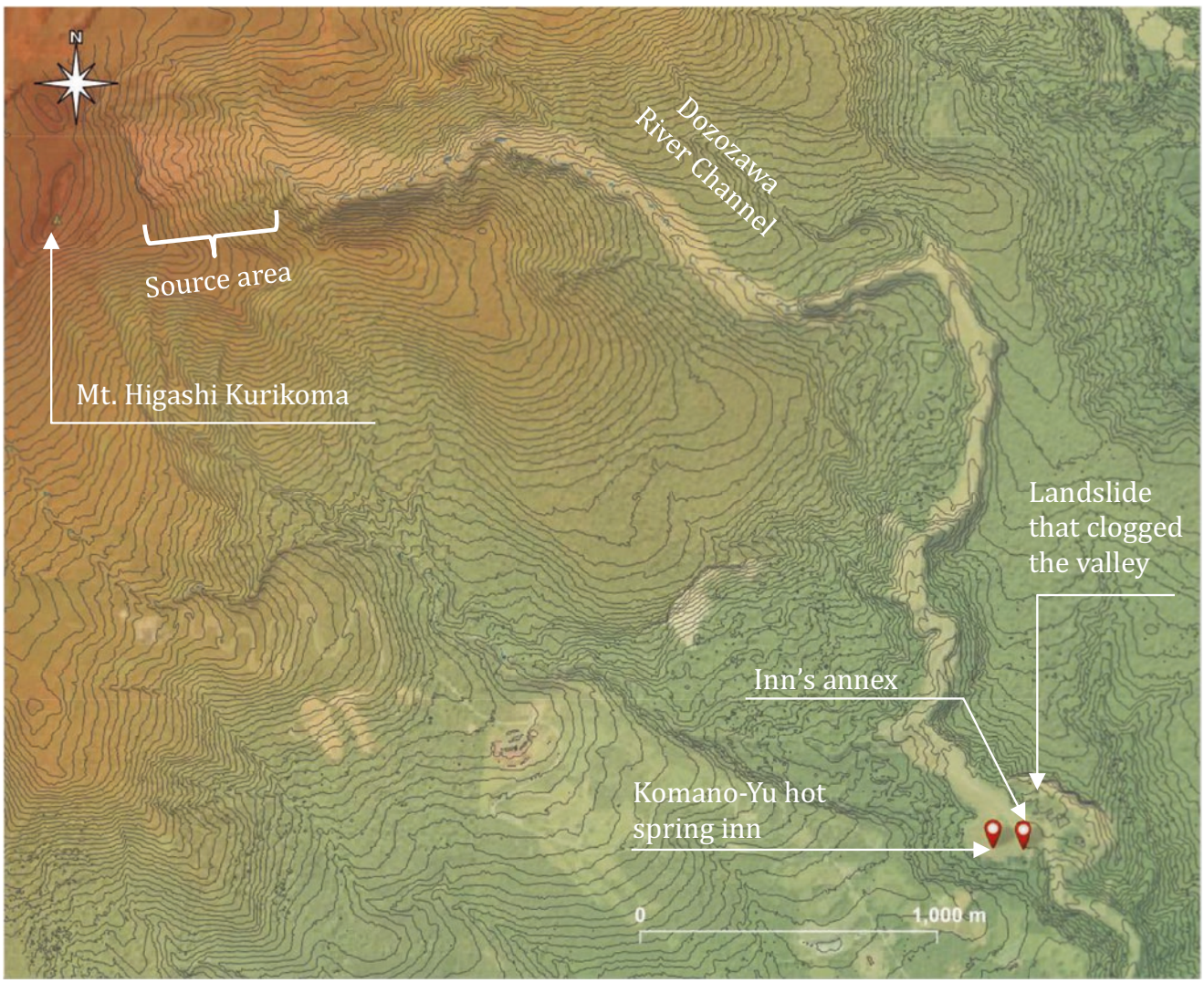

Fig. 2 Dozozawa River Channel and Komano-Yu Hot Spa inn (38.93779°N, 140.83756°E)

Though these testimonies tell little about the exact times of the succeeding post-quake events till the debris mass hit the hot spring inn, it was a vital testimony of Mr. Sugawara, one of the inn owners, that a guest, who was staying in the inn's annex, ran up to him and reported that a landslide took place across the valley, whose mass seemed to have clogged up the valley before the debris flow reached the inn. Given these testimonies and mud marks remaining on the valley walls, Ikeya et al. (2009) first estimated the peak discharges of the debris mass at several curved channels with remaining mud marks of super-elevations. Then they used a numerical method by Miyamoto and Ito (2002) to simulate the non-steady debris flow associated with erosional and depositional processes. The simulation showed that the fluidized debris reached the landslide mass blocking the river channel at the "Komano-Yu hot spring inn" and started stagnating about 9 min after the quake. Then the slurry started flowing upstream along the southern valley wall, hitting the inn's buildings (9 min. 40 s after the quake). They also ran a simulation assuming that the landslide mass didn't block the river channel and concluded that the inn would not have been hit by the debris mass. So, it was a sequence of unfortunate events that eventually claimed seven lives there.

Nomura et al. (2009) used the Depth-Averaged Material Point Method (DAMPM) developed by Abe and Konagai (2017), Abe et al. (2007) to simulate the flowing process of the fluidized debris mass. DAMPM is based on the concept of describing a debris mass as a cluster of upright material columns that move through cells of computational fixed Eulerian mesh (Konagai and Numada 2002), and a simple semi-empirical model for describing equivalent fluid (Hungr 1995) has been implemented for the material columns. The idea to describe material columns through a fixed computational grid is based on the scheme for the Material Point Method proposed by Sulsky et al. (1994). The advantage of this scheme is that it can represent large deformation and provide a Lagrangian description that is not subject to mesh tangling. In the DAMPM, governing equations are integrated along the z direction to ignore the motions of particles within each column. Eventually, this procedure leads to shallow water and consolidated elastoplastic assumptions for liquefied and coherent debris mass flows, respectively.

Figure 3 shows a material column in the DAMPM. The net driving force acting on a boundary block between the columns consists of the tangential component of weight, the basal resisting force, T, and the tangential internal pressure resultant, P. The resultant pressure term, P, is described by the pseudo-three-dimensional Drucker-Prager model whose yield surface is assumed to circumscribe the Mohr-Coulomb yield surface expressed in terms of the material cohesion, c, and the angle of internal friction, φ.

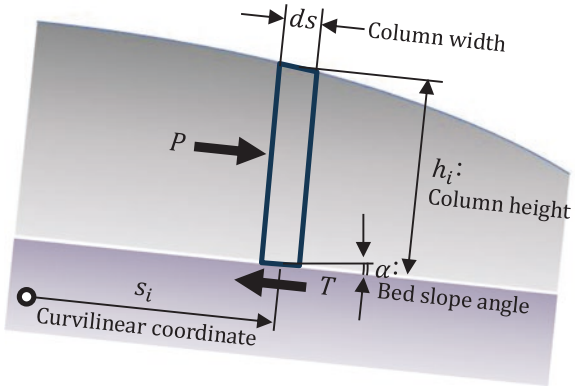

Fig. 3 Forces acting on an upright column other than weight: P=tangential internal pressure resultant, T=basal resisting force (Hungr 1995)

In the DAMPM, the Voellmy bi-parametric model (Eq. (1)) defines the basal resisting force, T, because it gives the most consistent results with field-measured data.

$$T = A\left\{\rho g h\left(\cos\alpha + \frac{a_c}{g}\right)\left(1 - r_u\right)\mu + \rho g\frac{\bar{v}^2}{\xi}\right\} \tag{1}$$

where, A = basal area, ρ = bulk unit density of the column, g = gravitational acceleration, h = height of the column, α = bed slope angle, a_c = centrifugal acceleration, dependent on the vertical curvature radius of the flume, r_u = pore-pressure coefficient (ratio of pore pressure to the total normal stress at the base of the column), μ = the basal frictional coefficient, $\bar{v}$ = local depth-averaged velocity, and ξ = turbulence coefficient that describes the thickness of the basal layer, dilatant flow, viscosity, and turbulence.

The number of necessary Lagrangian parameters for the DAMPM simulation is seven, as listed in Table 1. These seven parameters were then calibrated to adjust the simulated debris flow velocities to the velocities estimated from super-elevations of the debris flow. Figure 4 shows a simulated debris flow at t = 0.6, 15, 30, 60, 120, 180, 300, 420, and 600 s (10 min) after the debris mass started flowing, consistent with witness accounts.

A super-elevation, which is the difference in flow surfaces at the outer and inner boundaries of the channel, characterizes the open channel flow in a bend with radius R_c. Assuming that the velocity $\bar{v}$ of an open channel flow is uniform across the channel width B and the radius R_c is substantially larger than the channel width B, we can relate the super-elevation Δh to the flow velocity by equating fluid pressure to centrifugal force:

$$\bar{v} = \sqrt{R_c g' \frac{\Delta h}{B}} \tag{2}$$

Table 1 Parameters used for the Dozozawa debris flow

No.	Input parameter	Symbol	Unit	Value
1	Density	ρ	kg/m^3	1600
2	Young's modulus	E	Pa	2.0×10^6
3	Poisson's ratio	ν	–	0.3
4	Internal friction angle	ϕ	Degree	30
5	Basal friction	μ	–	0,075
6	Dilatancy angle	ψ	Degree	0
7	Turbulence coefficient	ξ	m/s^2	285

where $g' = g \cos \alpha$ with g being acceleration due to gravity and α being the channel inclination.

However, the debris flow velocity is not uniform across the channel. Moreover, the energy can dissipate through the flowing process of the viscous slurry. This equation was modified and applied to debris flows by introducing a correction factor k to estimate debris-flow velocities v_{mud} (e.g.,

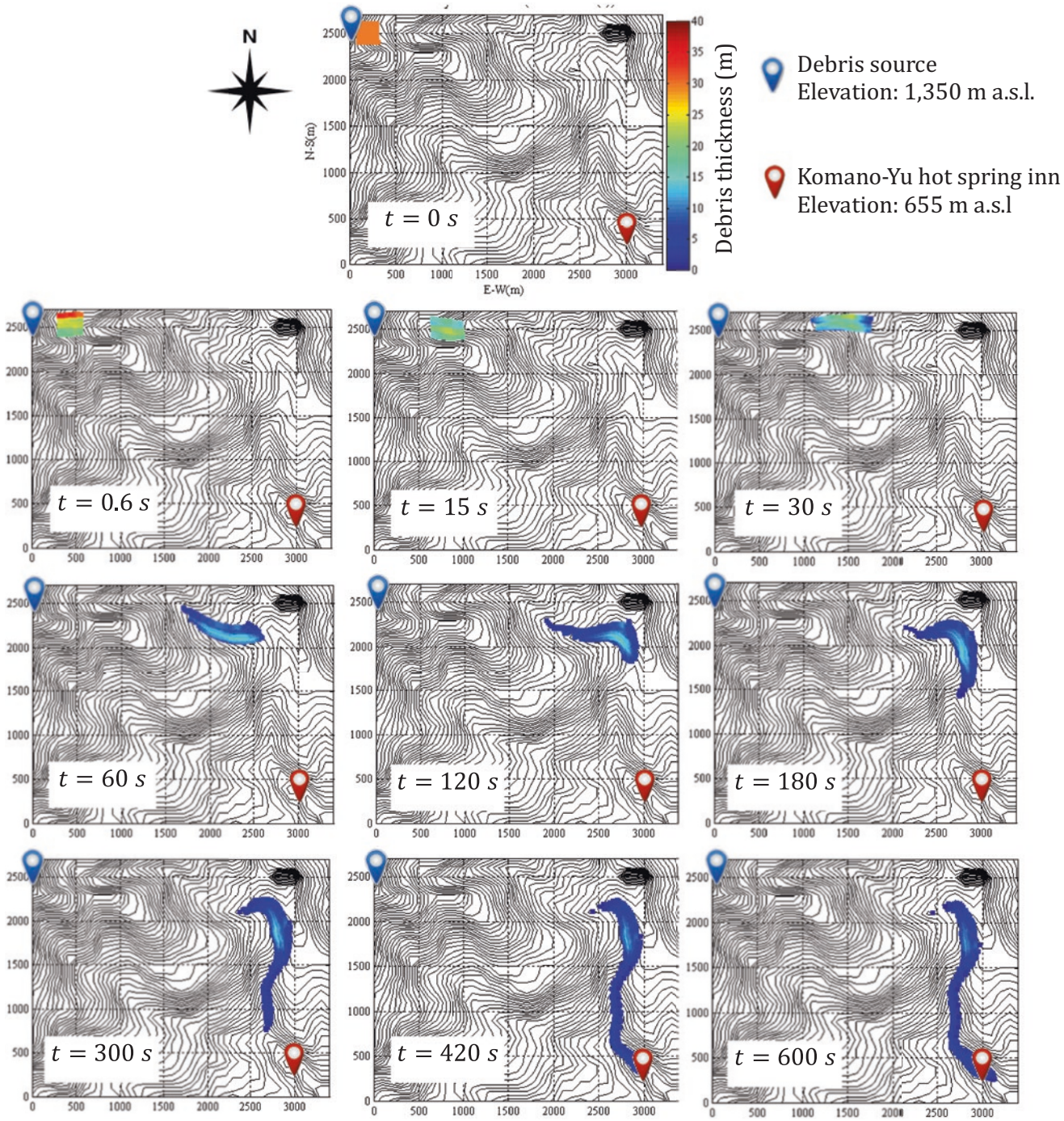

Fig. 4 Simulated debris flow (Nomura et al. 2009)

Hungr et al. 1984; Chen et al. 2014; Bulmer 2002; Prochaska et al. 2008):

$$v_{mud} = \sqrt{\frac{R_c g'}{k}\frac{\Delta h}{B}} \tag{3}$$

This k, which is 1 for a pure water flow with uniform velocity across the channel, is often empirically set at a value larger than 1, considering the viscous features of debris flows. Ikeya et al. (2009) set k at 10 in their simulations of the debris flow that hit the "Komano-Yu hot spring inn." Nomura et al. (2009) also adjusted the geotechnical parameters (Table 1) to make the simulated debris velocities to become close to the super-elevation-based flow velocities for $k = 10$ in Eq. (3).

Even though practicing engineers have widely used super-elevations and channel geometries in post-event field surveys to estimate flow velocities, extracting these parameters from the field is challenging. The determination of bend radius and super-elevation is especially affected by the unsteady flow traces and terrain morphology. The selection of the radius of curvature depends on the curve of the natural channel with abrupt changes. Another significant anomaly is that only the highest flow marks of an unsteady debris flow are seen on site; these marks often estimate the super-elevation, which is lower than the actual maximum super-elevation that the particular cross-section experiences during the flow. Figure 5 illustrates the scenario that happens *in situ*. Measurement of super-elevation from the mud marks inaccurately predicts the speed of flowing slurry, as was proven by the previous research work (Iverson et al. 1994). Extensive study is thus required to develop or modify the strategy for plausible estimation of velocities.

To seek better ways to fix this anomaly, Rahman and Konagai (2016, 2017) carried out a series of three-dimensional numerical curved flume tests using smoothed particle hydrodynamics (SPH). The first procedure of this

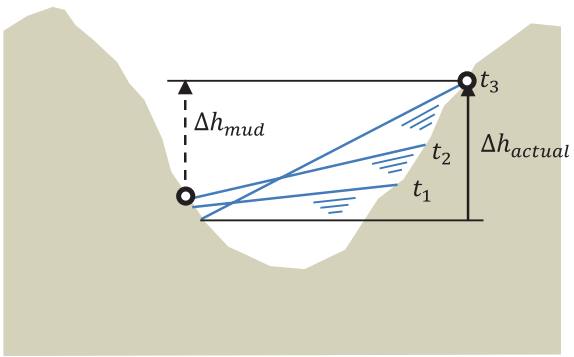

Fig. 5 Problems encountered in reality when determining super-elevation from mud marks: We are dealing with an unsteady flow whose surfaces differ at different times, t_1, t_2, and t_3. Therefore, the actual maximum super-elevation Δh_{actual} differs from the observable post-event super-elevation Δh_{mud} (Rahman and Konagai 2016, 2017)

method is to determine the radii of curvature along an irregularly curved natural flume. This procedure is based on a simplified assumption that the time T for a flowing slurry to reach its maximum super-elevation is associated with the sloshing period T_s of the slurry confined within a representative transverse cross-section of this curved flume. The SPH simulations showed that the time T nearly equals 1/3 of the sloshing period, T_s.

The second procedure estimates the maximum flowing slurry velocities from the observable super-elevations remaining at particular locations of the flume, where super-elevations are not identical to the maximum super-elevations reached during the event. Velocities v_{real} are often underestimated, particularly near the debris source where the unsteady nature of the flowing debris slurry is more predominant. A number of SPH simulations for a variety of flume configurations showed that the mud-mark-based estimates of the velocities v_{mud}, obtained from Eq. (3) with the k value set at 1.0, can be related to v_{real} by the following equation:

$$\frac{v_{mud}}{v_{real}} = 1 - e^{-\beta X} \quad for\ X > 1 \ \text{with}\ \beta = 0.4880 \tag{4}$$

where, β is an adjustment factor and X is the normalized distance given by:

$$X = \frac{x}{L} = \frac{\text{Distance from source front}}{\text{Initial source length}} \tag{5}$$

Rahman and Konagai (2017) chose the Newtonian fluid model to describe the debris slurry's flowing nature, and the above Eq. (4) is found to be almost identical to that derived in their previous study for Bingham-type debris flows (Rahman and Konagai 2016), except that the adjustment factor β in Eq. (4) is slightly larger for the Bingham-type flows and is about 0.5721. Equation (4) is thus used to adjust the super-elevation-based estimates of velocities.

Rahman and Konagai (2017) used the iterative approach (the first procedure mentioned above) to determine bend radii along the Dozozawa River Channel objectively. They chose locations of the point of highest super-elevations. Then at each point of the highest super-elevation, an arbitrarily chosen stretch along the curved ravine was approximated by an arc in the least square sense. Several transverse cross-sections were taken strip-wise along this stretch to obtain the average cross-sectional shape. The length of the selected stretch was then updated from the sloshing period of the slurry confined within the obtained average cross-section, and the procedure was repeated until sufficient convergence was reached.

Substituting the obtained bend radii along the river channel in Eq. (3) ($k = 1$) yielded the mud-marks-derived velocities v_{mud} and then Eq. (4) estimated the actual slurry velocities v_{real} at these bends (Fig. 6). The slurry velocity for each section between two adjacent bends is assumed as the average of the slurry

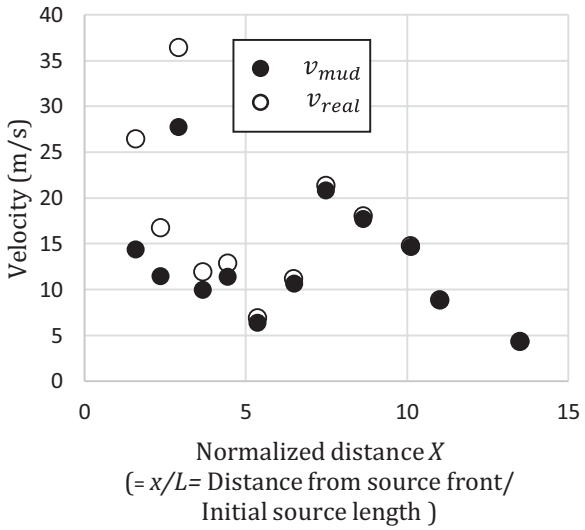

Fig. 6 Mud mark-based estimation of velocities and adjusted velocities for the debris flow that hit the Komano-Yu hot spring inn (Rahman and Konagai 2017)

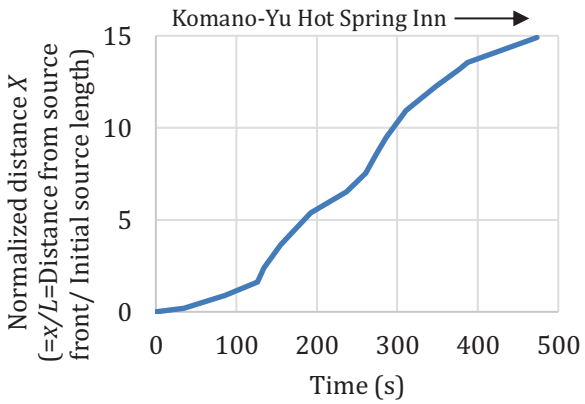

Fig. 7 Travel-time curve of the debris flow that hit the Komano-Yu hot spring inn (Rahman and Konagai 2017)

velocities at these two bends. The travel-time curve was obtained by summing up the sectional times, as shown in Fig. 7. Figure 7 shows that it took around 8 min for the debris mass to reach Komano-Yu hot spring inn. This travel time, obtained by adjusting the mud-marks-derived velocities using Eq. (4), is slightly shorter than 9 min and 40 s, and 10 min estimated by Ikeya et al. (2009) and Nomura et al. (2009), respectively.

4 Aratozawa Landslide

The earthquake caused a massive landslide, about 1300 m long, 900 m wide, and thicker than 100 m, to be detached from the gentle mountain flank of Kurikoma, the secondary volcaniclastic deposits (weakly cemented rhyolitic tuffs), leaving a vast depression akin to a hole punched in the mountainside (Fig. 8). The total volume of the detached soil mass, estimated to be 67 million m^3, broke into some blocks and moved over an underlying gentle slip surface dipping at about 2.6 degrees south-southwest and developed through a layer of alternating sandstones and siltstones beneath the rhyolitic tuff (Kazama et al. 2012).

Figure 9 compares the pre- and post-earthquake topographies of the Aratozawa Landslide area. The mountain flanks on the west and east sides of the landslide exhibited a tiered profile, suggesting similar mountain blocks fell one on the other in past similar landslide events. Fig. 9(b) also shows one of the fault ruptures traces that the reconnaissance team of the Research Institute of Earthquake and Volcano Geology, the National Institute of Advanced Industrial Science and Technology (AIST), identified and reported (Yoshimi et al. 2008a, b; Maruyama et al. 2009). Though the causal relationship is unclear, scars of the significant landslides, including those that occurred in the past (recognized from the mountain flank's tiered surface profile), line up on the extension of this fault rupture (See Cross-section AA' in Fig. 9(b)).

Most blocks of the landslide mass moved over 200 to 300 m toward open areas along a small tributary of the Nihasama River flowing from north to south and the reservoir of Aratozawa Dam. The frontal blocks hit the eastern valley wall of the small tributary, and a fraction of the landslide mass of about 1.5 million m^3 entered the reservoir, causing a sunami (seiche).

This fraction of soil mass, about 2% of the total volume of the landslide mass, was calculated from both the changes in bathymetries before and after the earthquake and the 2.4 m increase in the reservoir's water level from 268.5 m to 270.9 m. Due to this unusual tsunami surge, mud marks remained along the shores of the reservoir, indicating the tsunami inundation heights shown in Fig. 10 (Johansson et al. 2008). Based on the measured tsunami inundation heights, Nomura et al. (2009) attempted to estimate the velocity of the landslide mass that entered the reservoir.

Numerical simulations of the tsunami surge were conducted based on the nonlinear long-wave theory. The governing equations for the tsunami surge with the effect of the reservoir bed uplifts are given on the Cartesian coordinates (x, y) as:

$$\frac{\partial \eta}{\partial t}+\frac{\partial M}{\partial x}+\frac{\partial N}{\partial y}-\frac{\partial \xi}{\partial t}=0 \tag{6}$$

$$\frac{\partial M}{\partial t}+\frac{\partial}{\partial x}\left(\frac{M^2}{D}\right)+\frac{\partial}{\partial y}\left(\frac{MN}{D}\right)+gD\frac{\partial \eta}{\partial x}+f_B\frac{M\sqrt{M^2+N^2}}{D^2}=0 \tag{7}$$

$$\frac{\partial N}{\partial t}+\frac{\partial}{\partial x}\left(\frac{MN}{D}\right)+\frac{\partial}{\partial y}\left(\frac{N^2}{D}\right)+gD\frac{\partial \eta}{\partial y}+f_B\frac{N\sqrt{M^2+N^2}}{D^2}=0 \tag{8}$$

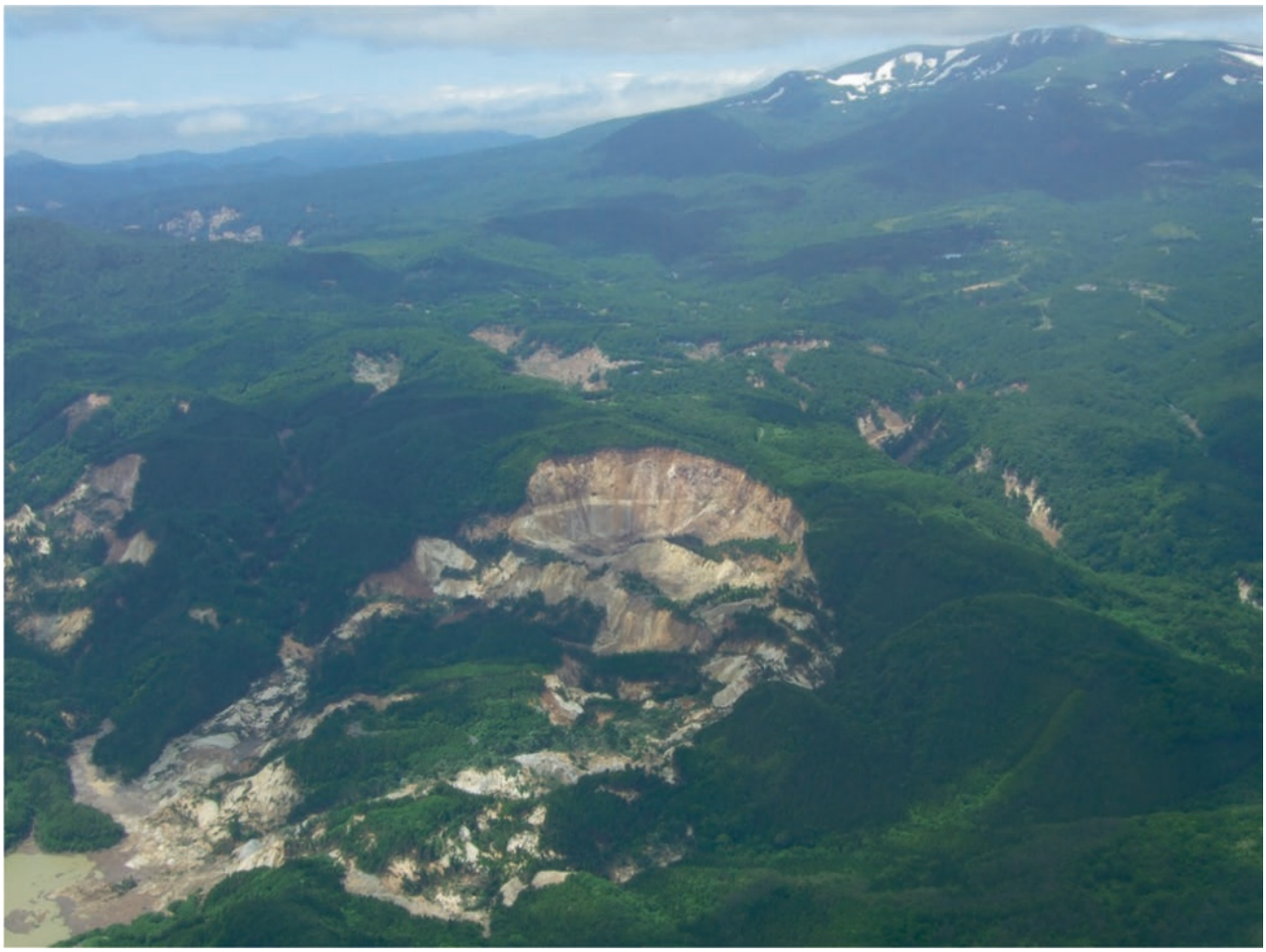

Fig. 8 Aratozawa Landslide and Mt. Kurikoma (Photo by K. Konagai, June 15, 2008)

where, $M = uD$ = flux in x direction with u= velocity in x direction, $N = vD$ = flux in y direction with v = velocity in y direction, h = initial depth of water, η = change in water level, $D = h + \eta$ = total depth of water, ξ = reservoir bed's uplift, and $f_B = gn^2/D^{1/3}$ = frictional coefficient of reservoir bed with n = Manning's coefficient.

Equation (6) shows the mass conservation law, including the effect of dam bed uplifts. Equations (7) and (8) describe motions in the x and y directions. They have advection terms, hydrostatic pressure terms, and frictional terms based on Manning's formula for free surface flows.

Figure 11(a) shows the change in the depths of the reservoir bed, which was obtained by subtracting bathymetry data in 1998 from that immediately after the earthquake (from June to July 2008). The simulation reproduced the effect of debris mass entering the reservoir by lifting reservoir-bottom elements one by one from where the debris mass first entered the reservoir to the point where the frontal end of the mass finally stopped (see Fig. 11(b)). The mass's inflow velocity, V, was obtained by dividing the entire stretch of the debris mass immersed in water by the time for the whole reservoir-bed uplift process.

Bars and lines in Fig. 12 are, respectively, the measured and simulated tsunami inundation heights at the points along the reservoir shoreline where the heights of the tsunami marks were measured (Fig. 10). The simulated inundation heights are affected mainly by the velocity V of the debris mass that entered the reservoir and the reservoir's bed frictional coefficient f_B in Eqs. (6) to (8). Gradually changing these key parameters, the numerical simulation result was accommodated to the optimum solution in the least square sense.

The left side of Fig. 12 shows the effect of the inflow velocity on the simulated tsunami heights, while the right side shows the effects of reservoir bed friction. Simulated tsunami heights are highly susceptible to the landslide mass velocity, while they are less sensitive to the reservoir bed friction. This tendency is particularly true near the source of the tsunami wave (open circles in Fig. 12). Through the least square optimization of the tsunami heights, the inflow velocity V was estimated to be around 4.4 m/s (see Fig. 13).

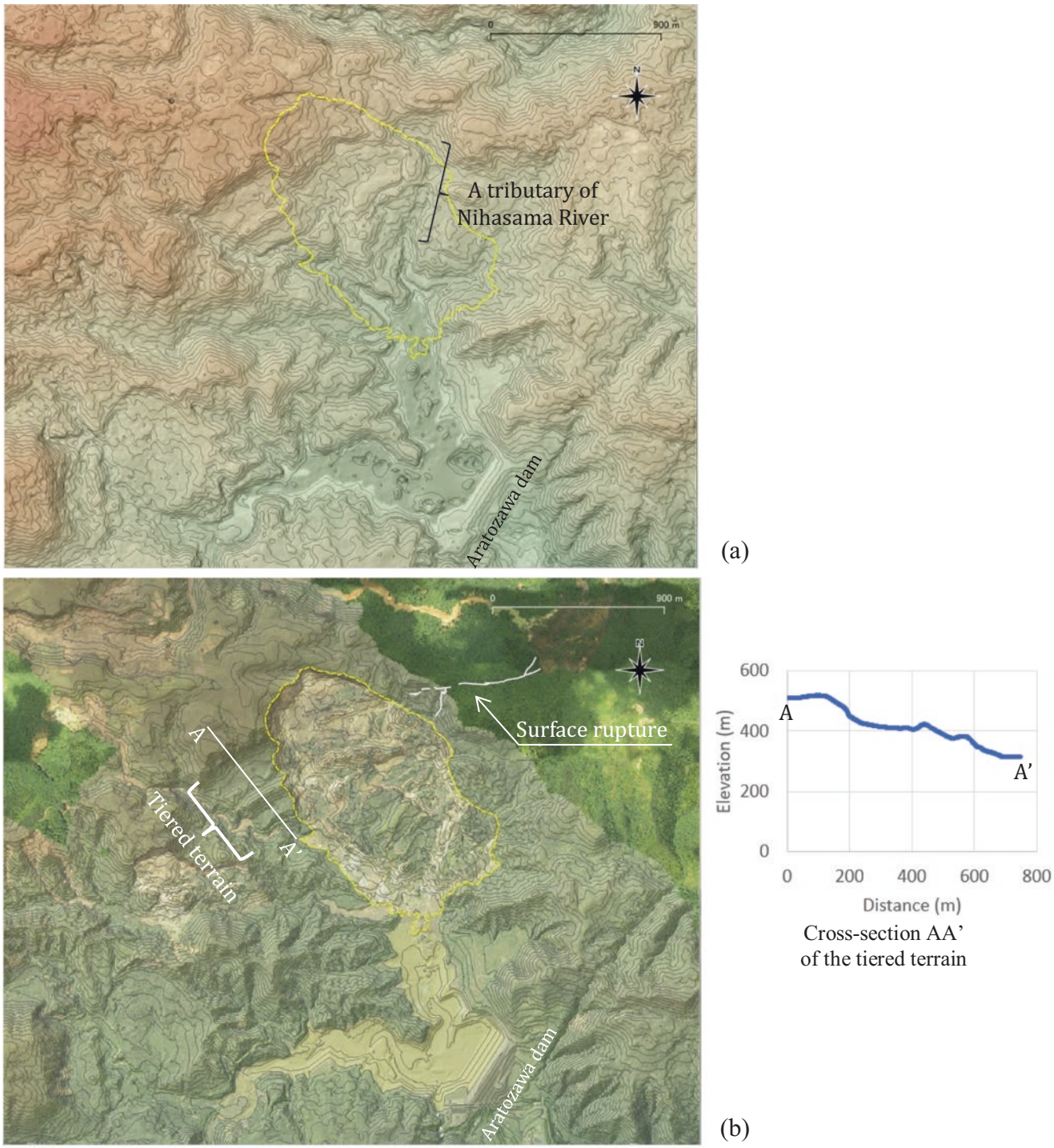

Fig. 9 Hill-shade maps of the (**a**) Pre-quake terrain of Aratozawa: The photogrammetric image was obtained by using aerial photos of Sept. 23, 2006, Geospatial Information Authority of Japan), and the (**b**) post-quake terrain of Aratozawa: Orthophoto of the area immediately after the quake was laid over the hill-shade illustration as a semi-transparent layer. Surface rupture trace was reported by Yoshimi et al. (2008a, b). Yellow broken lines show the landslide extent

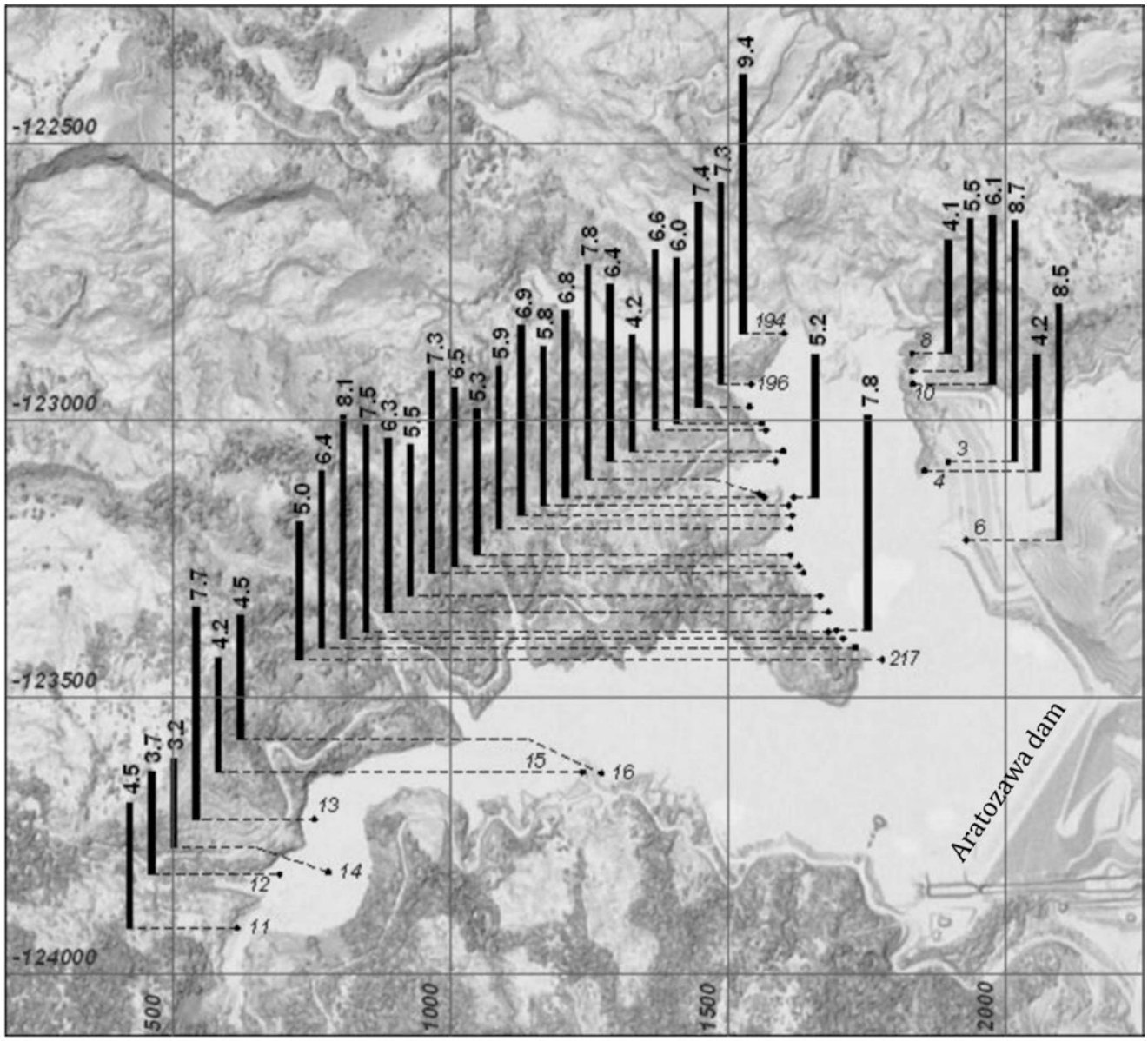

Fig. 10 Seiche heights (unit: m), with respect to lake elevation before the earthquake (268.5 m), as measured in the field on July 13 and July 25, 2008. (Johansson et al. 2008)

It is probably premature to deduce that the entire landslide mass had this velocity of 4.4 m/s only from the above-mentioned simulations for the tsunami caused by the 2% volume of the whole landslide mass. As for the frontal blocks of the landslide mass that hit the eastern valley wall of the small tributary of the Nihasama River, Kazama et al. (2012) considered that these blocks that hit the valley wall might have caused a ground motion, which may have been recorded by seismographs at Aratozawa dam, and nearby seismometer stations. Examining seismic records at these stations and assuming that the propagating velocity of the impact-induced ground motion was about 3 km/s, they deduced that the blocks hit the valley wall 60 s after the landslide initiation. During the 60 s, the frontal blocks moved over about 320 m distance. Thus, they estimated that the velocity of the blocks was about 5.3 m/s, which was slightly faster than the tsunami-mark-based velocity of the debris mass that entered the reservoir.

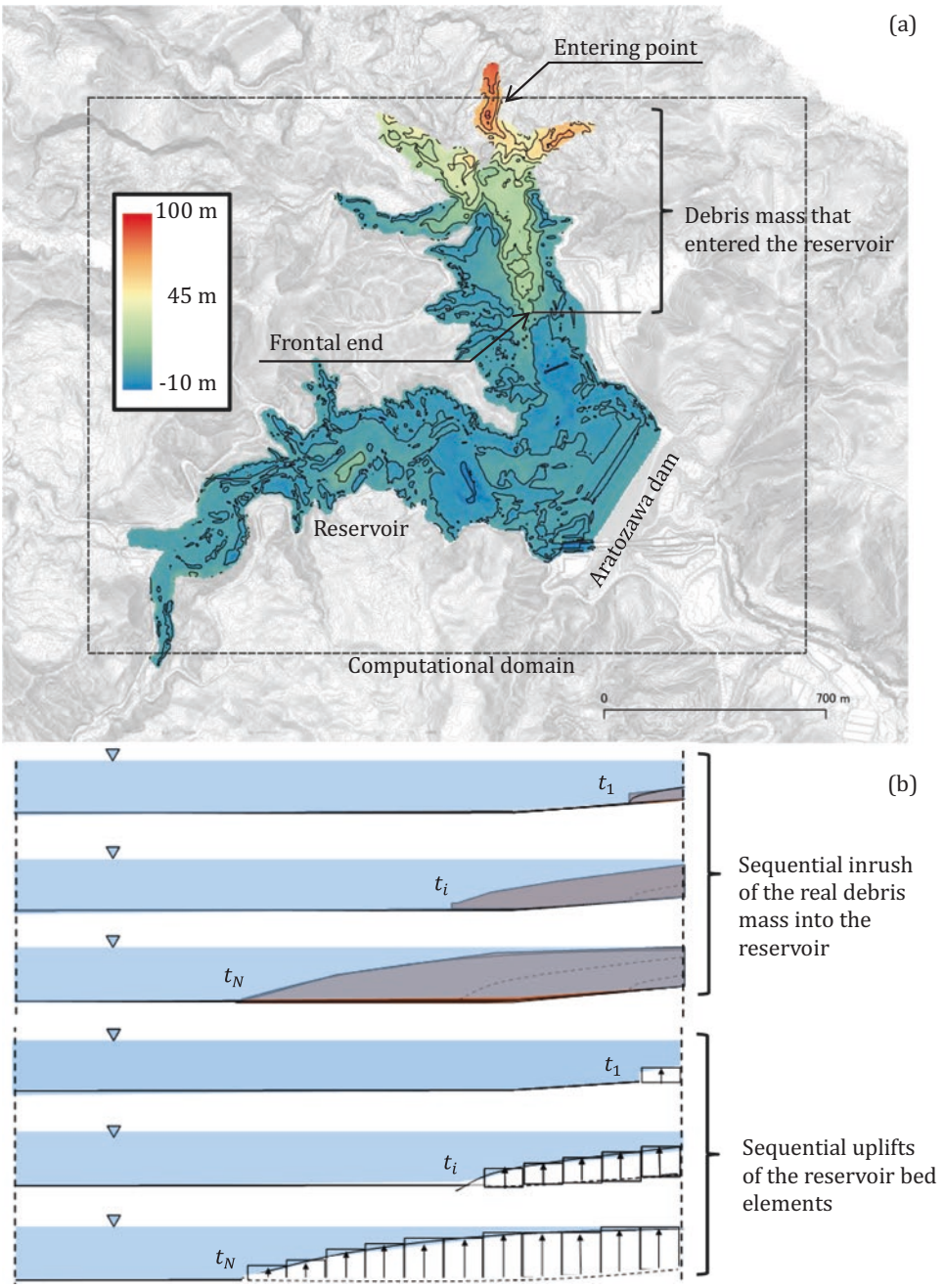

Fig. 11 (**a**) Change in the depths of the reservoir bed and (**b**) schematic presentation of the way to reproduce the effect of debris mass entering the reservoir by lifting reservoir-bottom elements one by one (after Nomura et al. 2009)

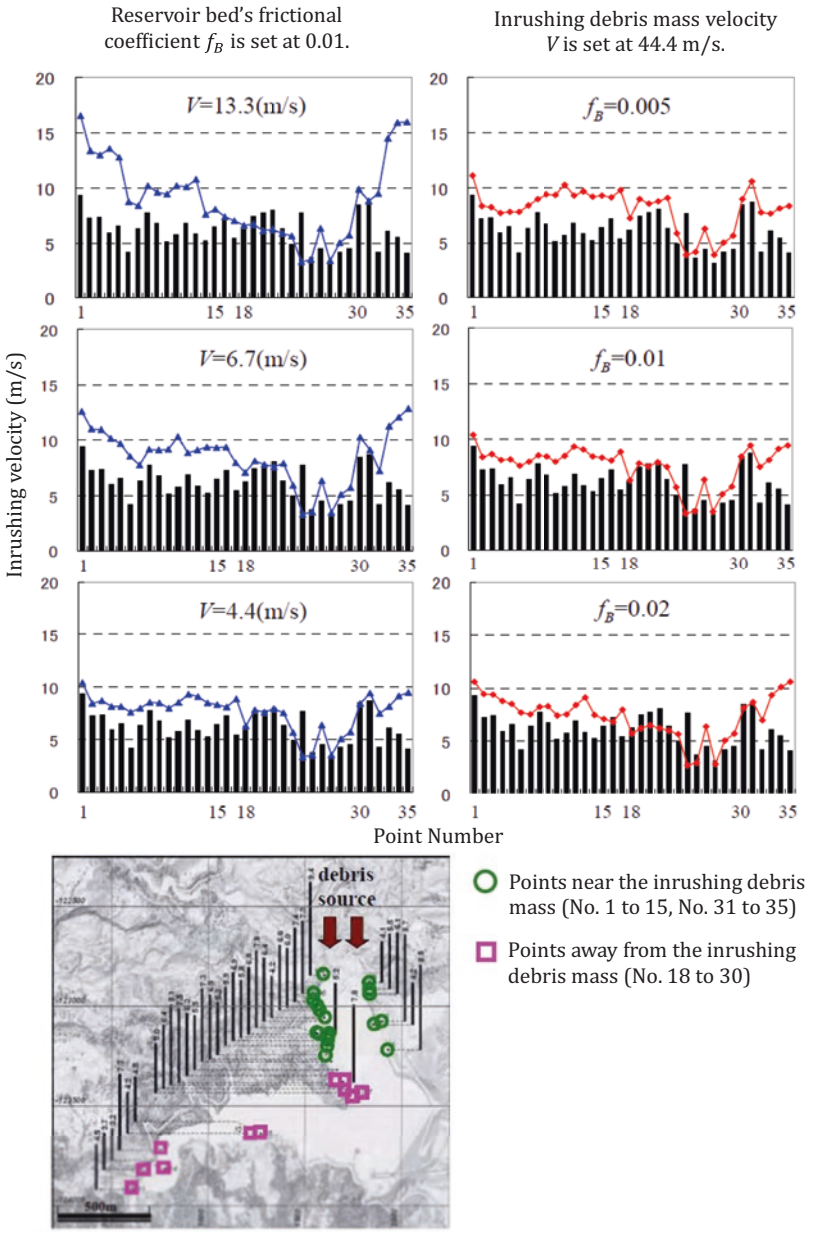

Fig. 12 Observed and simulated tsunami run-up heights along the reservoir shore line (Nomura et al. 2009)

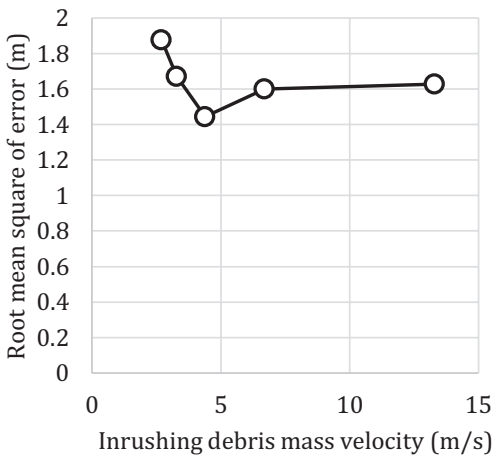

Fig. 13 Root mean square error between estimated and measured tsunami inundation heights (Nomura et al. 2009)

5 Conclusions

A 7.2 Magnitude earthquake occurred about 10 km northeast of Mt. Kurikoma, a complex stratovolcano comprising some volcanic edifices, at 8:43 JST on June 14, 2008. Though the quake hit the rural area, and thus sparsely distributed dwellings suffered minor damage, 17 were confirmed dead, and six are still missing. Though the quake-induced mass-wasting events were blamed as the primary cause of deaths in this earthquake, they left tremendous marks of soil deformations and tsunami runups along a dam reservoir, which provided unique opportunities to gain insights into the dynamics of the mass-wasting events. This paper summarized the findings from our observations in the referred papers (Nomura et al. 2009; Rahman and Konagai 2016, 2017) and compared these

findings with the other researchers' inferences from different approaches.

Ikeya et al. (2009) and Nomura et al. (2009) estimated the time for the fluidized debris mass from the eastern flank of Mt. Higashi-Kurikoma to reach the "Komano-Yu" hot spring inn (38.9377°N 140.8378°E), where seven people were killed in wet soil and rubble. They both used maximum flowing slurry velocities calculated from the observable super-elevations remaining at particular locations of the Dozozawa River Channel to adjust the parameters for the numerical tools that they used (A numerical simulation tool introducing the erosion rate equation (Miyamoto and Ito 2002) and the Depth-Averaged Material Point Method (DAMPM) by Abe and Konagai (2017), Abe et al. (2007), respectively. The estimated times were 9 min and 40 s (Ikeya et al. 2009) and 10 min (Nomura et al. 2009). As a matter of course, they are very close to each other.

We must be aware that the mud-mark-based super-elevations are not identical to the maximum super-elevations reached during the unsteady debris flow event. The actual peak velocities of v_{real} are often underestimated, particularly near the debris source where the unsteady nature of the flowing debris slurry is more predominant. Rahman and Konagai (2016, 2017) conducted a number of SPH simulations for a variety of flume configurations. Their result showed that the mud-mark-based estimates of the velocities v_{mud} can be related to v_{real} by the following equation (same as Eq. (4)):

$$\frac{v_{mud}}{v_{real}} = 1 - e^{-\beta X} \quad for\ X > 1 \text{ with } \beta = 0.4880$$

where, X is the normalized distance given by:

$$X = \frac{x}{L} = \frac{\text{Distance from source front}}{\text{Initial source length}}$$

Rahman and Konagai (2016, 2017) also developed an iterative approach to determine objectively bend radii along a natural flume with abrupt changes. Adjusting the slurry velocities using the above equations, Rahman and Konagai (2017) estimated that the debris mass reached Komano-Yu hot spring inn about 8 min after the debris flow initiation.

The earthquake caused a massive landslide, about 1300 m long, 900 m wide, and thicker than 100 m, to be detached from the gentle mountain flank of Mt. Kurikoma (Aratozawa Landslide). The total volume of the detached soil mass, estimated to be 67 million m^3, broke into some coherent blocks. These blocks moved over 200 to 300 m toward open areas along a small tributary of the Nihasama River flowing from north to south and the reservoir of Aratozawa Dam. The frontal blocks hit the eastern valley wall of the small tributary, and a fraction of the landslide mass of about 1.5 million m^3 entered the reservoir, causing a tsunami. Nomura et al. (2009) attempted to estimate the velocity of the landslide mass from the remaining tsunami inundation marks. Through the least square optimization of the tsunami heights by changing two critical parameters for the simulation, namely the velocity of the landslide mass entering the reservoir and the friction of the reservoir's bed, they estimated the velocity to be around 4.4 m/s. This velocity is slightly smaller than that (5.3 m/s) of the frontal blocks to move over a 320 m distance until it hit the valley wall of the small tributary of the Nihasama River; Kazama et al. (2012) deduced this velocity by examining seismic records from Aratozawa Dam and nearby seismometer stations.

As stated above, mud-marks-based estimation of velocities of mass-wasting processes from different approaches showed similar results. In every approach, it was unavoidable that we had unknown parameters because we were dealing with a mass-wasting process whose interior can hardly be seen and inferred. We must keep comparing and reviewing different approaches because we will always need clarification about the unknown parameters in each approach and refine the estimated results, which will help us be prepared for the next significant events in similar areas.

Acknowledgments This study is financially supported by the Foundation for the Promotion of Science (Project No. 20254003; leader: Kazuo Konagai, and Project No. 26249069; leader: Kazuo Konagai). The first author, Nomura F., conducted a significant part of the analyses. The second and corresponding author, Konagai K., provided his expertise as the project leader for mud-mark-based estimations of mass-wasting processes. The third author, Md Aftabur Rahman, developed a unique formula through his SPH analyses to adjust mud-mark-based estimation of debris flow velocities. The fourth author, Tajima Y., provided expertise in analyzing landslide-induced tsunamis. The authors are indebted to Dr. Keita Abe, Associate Professor at the Department of Civil Engineering, Nihon University, who has provided his numerical program, Depth-Averaged Material Point Method (DAMPM), for analyzing the debris mass flow that hit Komano-Yu hot spring Inn. The authors are also thankful to Dr. Johansson, J. at the Norwegian Geotechnical Institute and Mr. Date, M., who have devoted much of their energies, especially to frequent surveys of tsunami inundation heights.

References

Abe K, Konagai K (2017) Numerical simulation for runout process of debris flow using depth-averaged material point method. Soils Found 56(5):869–888. https://doi.org/10.1016/j.sandf.2016.08.011

Abe K, Johansson J, Konagai K (2007) A new method for run-out analysis and motion prediction of rapid and long-traveling landslides with MPM. J Jpn Soc Civil Eng C 63(1):93–109. https://doi.org/10.2208/jscejc.63.93

Bulmer MH (2002) An empirical approach to studying debris flows: implications for planetary modeling studies. J Geophys Res 107:5033. https://doi.org/10.1029/2001JE001531/

Chen HX, Zhang LM, Zhang S (2014) Evolution of debris flow properties and physical interactions in debris-flow mixtures in the Wenchuan earthquake zone. Eng Geol 182(Part B):136–147. https://doi.org/10.1016/j.enggeo.2014.08.004

Fujinawa A, Fujita K, Takahashi M, Umeda K, Hayashi S (2001) Development history of Kurikoma Volcano, Northeast Japan. Bull Volc Soc Japan 46(5):264–284. https://www.jstage.jst.go.jp/article/kazan/46/5/46_KJ00001052964/_article/-char/en

Hungr O (1995) A model for the runout analysis of rapid flow slides, debris flows, and avalanches. Can Geotech J 32:610–623. https://doi.org/10.1139/t95-063

Hungr O, Morgan GC, Kellerhals R (1984) Quantitative analysis of debris torrent hazards for design of remedial measures. Can Geotech J 21(4):663–677. https://doi.org/10.1139/t84-07

Ikeya H, Matsui M, Michihata R, Suzuki T (2009) A consideration of the debris flow that hit the "Komano-Yu hot spring inn". The 58th JSECE annual conference. The Japan Society of Erosion Control Engineering, C3-11. http://www.jsece.or.jp/event/conf/abstract/2009/pdf/01_oral/O3-11.pdf

Iverson RM, LaHusen RG, Major JJ, Zimmerman CL (1994) Debris flow against obstacles and bends: dynamics and deposits. EOS Trans Am Geophys Union 75:274. https://api.semanticscholar.org/CorpusID:132931592

Johansson J, Konagai K, Fujita T (2008) Aratosawa dam and landslide induced seiche. in the "Geoengineering and Seismological Aspects of the Iwate Miyagi-Nairiku, Japan Earthquake of June 14, 2008," Robert Kayen, Brady Cox, Jorgen Johansson, Clint Steele, Paul Somerville, Kazuo Konagai, Yu Zhao, Hajime Tanaka, GEER Web Report 2008 v.1, Geotechnical Extreme Events Reconnaissance (GEER) Association https://geerassociation.org/index.php/component/geer_reports/?view=geerreports&layout=build&id=52

Kazama M, Kataoka S, Uzuoka R (2012) Volcanic mountain area disaster caused by the Iwate–Miyagi Nairiku Earthquake of 2008, Japan. Soils Found 52(1):168–184. https://doi.org/10.1016/j.sandf.2012.01.003/

Konagai K, Numada M (2002) Pseudo-three-dimensional Lagrangian particle finite difference method for modeling long-traveling soil flows. J Jpn Soc Dam Eng 12(2):123–128. https://doi.org/10.11315/jsde1991.12.123

Maruyama T, Toda S, Yoshimi M, Omata M (2009) Application of airborne LiDAR to mapping surface ruptures and active faults: an example from the 2008 Iwate-Miyagi Nairiku, Japan, earthquake (Mw 6.9). Active Fault Res 30:1–12

Miyagi T, Yamashina S, Esaka F, Abe S (2011) Massive landslide triggered by 2008 Iwate–Miyagi inland earthquake in the Aratozawa Dam area, Tohoku, Japan. Landslides 8:99–108. https://doi.org/10.1007/s10346-010-0226-8

Miyamoto K, Ito T (2002) Numerical simulation method of debris flow introducing the erosion rate equation. J Jpn Soc Erosion Control Eng 55(2):24–35. https://doi.org/10.11475/sabo1973.55.2_24

Nomura F, Konagai K, Tajima Y (2009) Extraction of geotechnical parameters from traces left in the June 14th, 2008, Iwate-Miyagi Inland earthquake. Bulletin of Engineering for Resilient Society Research Group (ERS) (formerly, Research Center for Earthquake Resistant Structure), Institute of Industrial Science, University of Tokyo, vol 43, pp 13–24. http://www.ers.iis.u-tokyo.ac.jp/ers-no43.html

Prochaska AB, Santi PM, Higgins JD, Cannon SH (2008) A study of methods to estimate debris flow velocity. Landslides 5:431–444. https://doi.org/10.1007/s10346-008-0137-0

Rahman MA, Konagai K (2016) Substantiation of debris flow velocity from super-elevation: a numerical approach. Landslides 14:633–647. https://doi.org/10.1007/s10346-016-0725-3

Rahman MA, Konagai K (2017) A hands-on approach to estimate debris flow velocity for rational mitigation of debris hazard. Can Geotech J 55(7):941–955. https://doi.org/10.1139/cgj-2017-0211

Sulsky D, Chen Z, Schreyer HL (1994) A particle method for history-dependent materials. Comput Methods Appl Mech Eng 118(1–2):179–196. https://doi.org/10.1016/0045-7825(94)90112-0

Yoshimi M, Toda S, Maruyama T (2008a) Fault rupture traces with the 4 to 7 m right lateral offsets north of Aratozawa dam associated with the 2008 Iwate-Miyagi Nairiku, Japan, earthquake (Mw 6.9). Active Fault Research 29:1

Yoshimi M, Maruyama T, Toda S (2008b) Surface Rupture Connecting Deep-Seated Landslides of the Mw6.9 14 June 2008 Iwate- Miyagi Nairiku, NE Japan, Earthquake. American Geophysical Union, Fall Meeting 2008. abstract id. T53D-2001, Bibcode: 2008AGUFM.T53D2001Y

Assessment of the Structural Geological, Hydrogeological, and Geomorphological Relationships of the Athwelthota Landslide, Sri Lanka

D. M. D. S. Dissanayaka, A. R. P. Weerasinghe, S. H. S. Jayakody, Shino Asano, and K. N. Bandara

Abstract

Landslides pose a significant threat to Sri Lanka, causing loss of life and property damages. The Athwelthota landslide in Kalutara District, occurred on May 26, 2017, resulting in casualties and severe property destruction. This study focuses on understanding the relationship between structural geology, hydrogeology, and geomorphology in the Athwelthota landslide area to comprehend the causes of landslides. We conducted field surveys, geotechnical investigations, and seismic surveys to gather data on geological features, soil properties, and rainfall patterns. The findings reveal that slope instability is influenced by the shear strength of soil overburden, jointed bedrock, deformation, and highly weathered garnet biotite gneiss. Groundwater flow through geological discontinuities and intense rainfall during the Southwest Monsoon contribute to increased pore water pressure and reduced shear strength, triggering landslides.

The study emphasizes the importance of assessing these factors for hazard assessment, early warning systems, and sustainable development in landslide-prone regions. By understanding the geological and hydrological characteristics of the area, it is possible to identify vulnerable areas and implement appropriate mitigation measures. This research is part of a larger project aimed at developing an early warning technology for rain-induced rapid and long-traveling landslides. The insights gained from this study can help land-use planning, infrastructure development, and disaster management strategies in landslide-prone areas, ultimately contributing to the protection of lives, reduction of property damage, and the sustainable development of the region.

Keywords

Athwelthota landslide · Structural geology · Hydrogeology · Geomorphology

1 Introduction

Landslides could be utterly devasting natural hazards and they have a significant impact on the economy of Sri Lanka and create several severe problems, such as loss of human life, damage to property, and damage to the natural environment. One such catastrophic rain-induced landslide happened in the Athwelthota area in Kalutara District, Sri Lanka around 05.00 a.m. on 26 May 2017 causing nine deaths and destroying four houses completely. The landslide is situated on the right-hand side (RHS) upper slope of the 49-kilometer post of Thiruwanaketiya-Agalawatta road (B421), in Palindanuwara Divisional Secretariat, Kalutara District. The geographical position of the site is 6.543586°N, 80.283905°E. The Athwelthota area is known for its hilly terrain and is prone to landslides, especially during the rainy season.

2 Objectives

Studying rain-induced rapid and long-traveling landslides is significantly important for Sri Lanka in many contexts such as hazard assessment in climatic change, development of early warning systems, and infrastructure planning. Centering the primary objective of development of early

D. M. D. S. Dissanayaka (✉) · A. R. P. Weerasinghe · K. N. Bandara
National Building Research Organisation, Colombo, Sri Lanka

S. H. S. Jayakody
Disaster Prevention Research Institute, Kyoto University, Kyoto, Japan
e-mail: jayakody.sanchitha.8d@kyoto-u.ac.jp

S. Asano
National Research and Development Agency, Forest Research and Management Organization, Tsukuba, Japan
e-mail: shiho03@ffpri.affrc.go.jp

B. Abolmasov et al. (eds.), *Progress in Landslide Research and Technology, Volume 3 Issue 1, 2024*, Progress in Landslide Research and Technology, https://doi.org/10.1007/978-3-031-55120-8_21

warning technology to manage recurring landslide events, the National Building Research Organization (NBRO) and the International Consortium on Landslides (ICL) have initiated a 5-year research project called "Development of Early Warning Technology for Rain-induced Rapid and Long-travelling Landslides" (Project RRLL) in collaboration with the framework of SATREPS (Konagai et al. 2021).

The Athwelthota landslide has been selected as one of the pilot sites for field studies under Project RRLL. This study attempts to understand the relationship between structural geological features and geomorphological features in and around the Athwelthota landslide area to comprehend the causes of landslides. This study focuses on determining the contribution of in-situ features to the occurrence of landslides. However, equal attention shall be paid to external features such as rainfall infiltration and slopes' in-situ conditions for landslide initiation (Figs. 1 and 2).

Fig. 1 Athwelthota landslide before failure (*Source: Google Earth, Feb.2017*)

Fig. 2 Athwelthota landslide after the failure (Source: *Google Earth, Dec.2017*)

3 Methodology

3.1 Field Survey

An extensive field survey was undertaken covering the landslide area to investigate the crown area, main escarpment, landslide boundaries, variation of slope angle, bedrock exposures, and their properties. In this assessment, more attention has been paid not only to hydrogeological conditions but also to the general geology of the area and soil condition.

3.2 Seismic Survey

Seismic surveys were undertaken along two traverses, as shown in Fig. 3. These two traverses were determined based on the possibility of future landslides that could happen with torrential rainfall conditions. Further to this, the results of the seismic survey can be used as primary information to determine the borehole locations.

The collected subsurface data through borehole drilling were used to validate and refine the seismic survey data. This calibration ensures that the seismic traverse profile accurately represents the subsurface conditions and assists in interpreting seismic data for further analysis or exploration.

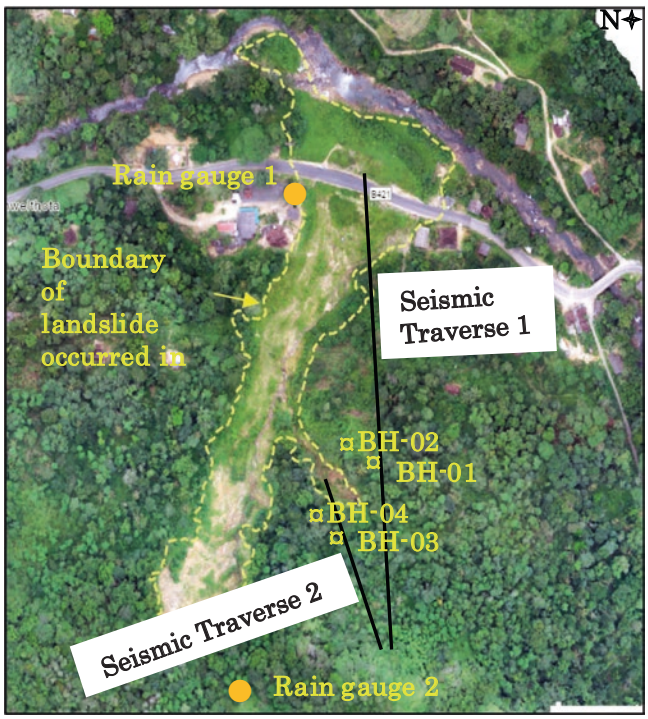

Fig. 3 Borehole locations and seismic traverse at Athwelthota landslide area

Table 1 Summary of boreholes and instruments

Location name	GPS coordinates		Elevation (m)	Depth (m)	Monitoring instrument
	E	N			
BH-1	80.284485	6.541930	1494.02	24.0	Water level meter
BH-2	80.284454	6.541945	1468.81	24.0	Inclinometer
BH-3	80.283980	6.541494	1453.52	30.0	Inclinometer
BH-4	80.283982	6.541491	1453.04	24.0	Water level meter

3.3 Geotechnical Investigation

Geotechnical investigations including borehole drilling were commenced on 01st December 2022 and completed by 20th March 2023. Borehole investigations were carried out at BH-01, BH-02, BH-03, and BH-04 locations (Table 1). Rock coring was done using a double tube core barrel having a 54 mm core diameter. Soil strata changing depths were recorded by carefully analyzing soil and rock samples. Both disturbed and undisturbed soil samples were collected and sealed as soon as possible at the same time/day to preserve their natural moisture content. Upon the completion of the boreholes, the borehole inclinometers, borehole extensometers, and water level meters were installed to monitor the movements and fluctuation of the groundwater table (Table 1).

4 Results and Analysis

4.1 Evaluation of the Geological Condition

The structural geology of a landslide refers to the geological features and structural characteristics that influence the occurrence and behavior of the landslide. These features can include the types and orientations of rock layers, fractures, faults, and folds in the area. The site itself is composed of Charnockitic biotite gneiss and Biotite gneissic rock. The site is located close to a shear zone trending 133 degrees (Fig. 4). The studied slope exists on the Northern escarp slope of the ridge. Hence, the unstable soil and rocks that exist on the slope move in the northeast direction. Moderate to highly weathered Garnetiferrous hornblende biotite gneiss with spheroidal weathering could be observed. According to field observations, the mafic content (Mica and Hornblende) of the rock is high, and it gradually increases.

Bedrock is dipping towards the southwest direction with an angle of 80 degrees. The bedrock of the region could be identified as highly jointed and highly fractured. Three major joint sets can be identified at the site as shown in Fig. 4. Table 2 summarises the discontinuities observed in the area.

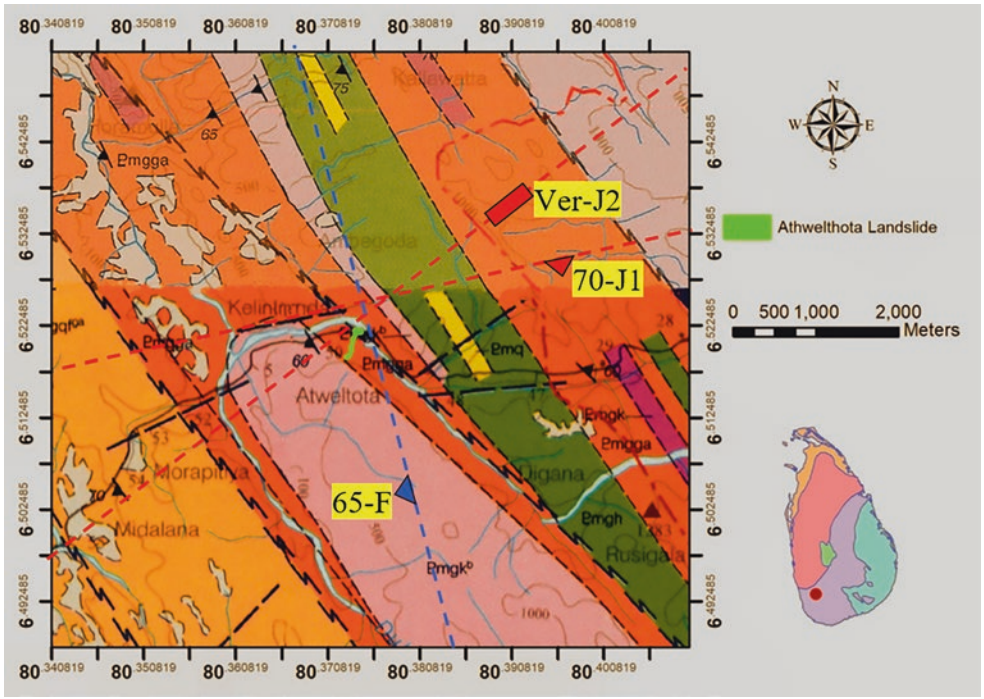

Fig. 4 Geology map of the project area

Table 2 Summary of structural geological data

Discontinuity	Dip direction	Dip angle	Density	Condition
Foliation	242°	65 °	3 m^{-1}	Tight joint
Joint 1	160 °	70 °	5 m^{-1}	Tight joint
Joint 2	135 °	Vertical	3 m^{-1}	Tight joint
Joint 3	058 °	Vertical	2 m^{-1}	Tight joint

The bedrock of the crown region is highly deformed where the micro folds can be observed, and the slickensides of the rock suggest a shearing event. Pegmatitic intrusions, consisting of 1–10 cm thick quartzite bands were also observed in the upper region. Interbanded clay and gravely sand soil layers could be found in the completely weathered bedrock with slippery conditions. The landslide has been initiated as two separate branches. The main landslide and the branch originated from the left side of the landside. They followed the existing main and minor valleys, where those valleys had been formed due to two separate springs coming through the geological discontinuities. The water flowing through these discontinuities recharges the landslide body directly. Hence this will increase the groundwater table and accelerate the failure.

The orientation of the foliation is not facilitating the failure as it is oriented into the slope. Hence, an escarpment slope is created. In this case, the foliation is dipping at 60 to 65 degrees and oriented at 242 degrees. Hence, breaking along the foliation planes is not possible. Joint set 1 is dipping at 70 degrees and oriented in a 160-degree direction, which also doesn't support the slope failure. Joint Set 2 and 3 are vertically oriented joints and their intersections could lead to direct toppling (33%) and oblique toppling (33%) as shown in the kinematic analysis results (Fig. 5). For this analysis friction angle was assumed to be 34 degrees.

4.2 Comparison of Daily Precipitation

The study area receives heavy rainfall during the Southwest Monsoon, which occurs from May to September 2017. This period is associated with inter-monsoonal rains and is characterized by intense showers and thunderstorms. The daily rainfall recorded from the Baduruliya weather station during 2016 and 2017 are shown in Figs. 6 and 7 respectively. The compared rainfall data indicates that the area has received much more intense rain in year 2017 than year 2016.

Attributed to the geological discontinuities, the landslide mass could have saturated not only from the top-down wetting front but also from the bottom-up wetting front. These integrated conditions could have created favorable conditions for landslide initiation in May 2017 with 245 mm daily precipitation as highlighted by the red circle in Fig. 7. This idea can be further verified by referring to the continuous stream flow that appeared after the landslide. Therefore, it is important to analyze the adjacent soil slopes which are highly susceptible to future landslides.

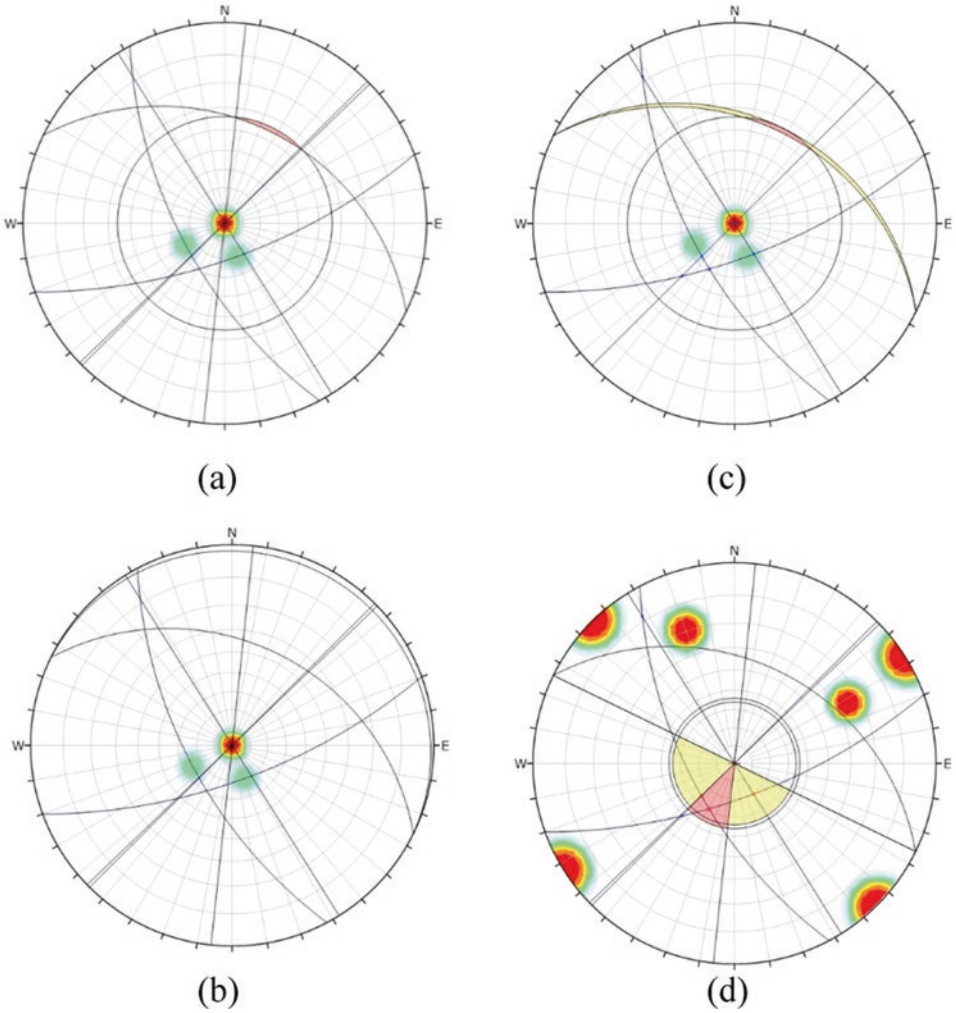

Fig. 5 (**a**) Planar sliding (**b**) Flexural toppling (**c**) Wedge sliding (**d**) Direct toppling

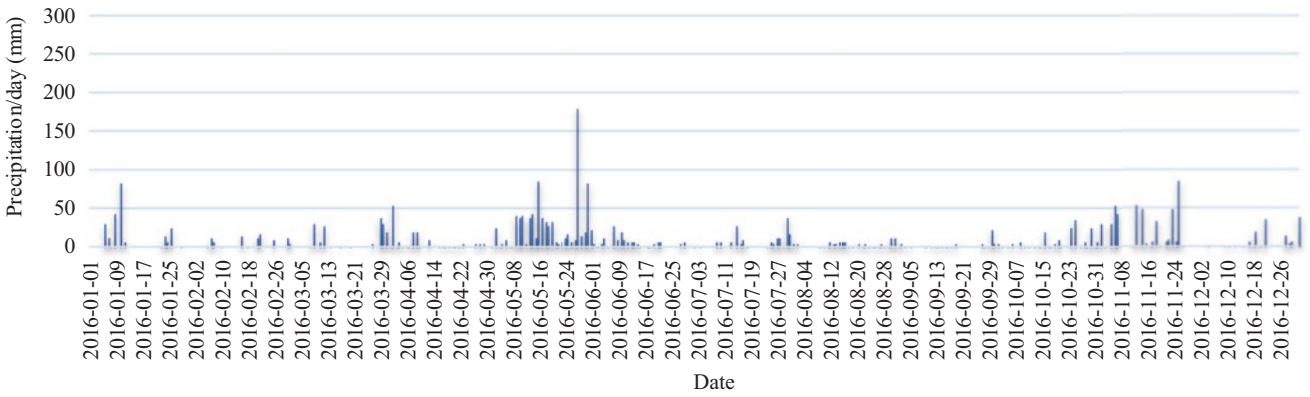

Fig. 6 Daily rainfall during the year 2016

4.3 Subsurface Stratification of the Soil Remained at the Right-Hand Side of the Slope

As described in Sect. 3.2, two seismic surveys were conducted to obtain more information required to portray the subsurface conditions of potential landslide masses. Traverse 1, extends around 300 m whereas traverse 2 covers about 100 m. Based on traverse 1 and by combining the BH-01 data the following description can be made.

The topmost part of the soil profile consists of loose colluvium soil, which is dark brown to yellowish brown, grav-

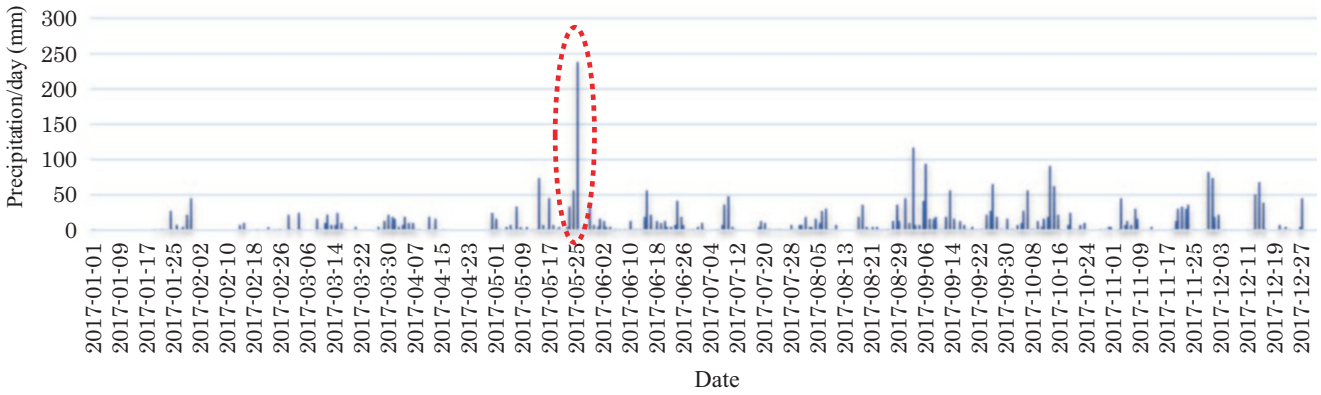

Fig. 7 Daily rainfall during the year 2017

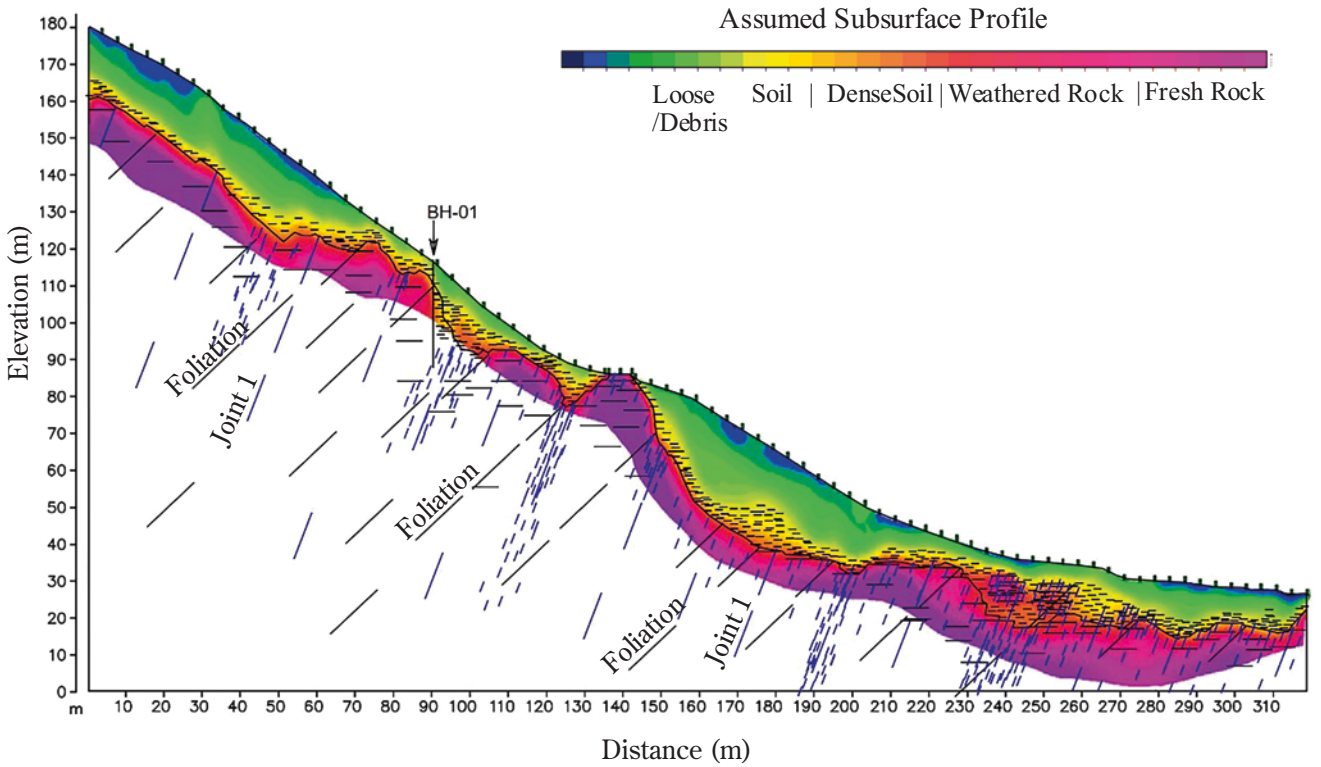

Fig. 8 Subsurface profile along the Seismic traverse 1

elly silty fine to medium sand with weathered rock fragments (Colluvium). Underlying the topsoil is a very dense, yellowish brown, sandy silty gravel. Sand is angular fine to coarse-grained, and the gravel is fine to medium-grained. Even though the soil thickness at the borehole location is 1.45 m, extending about 20 m in both the upper slope and down slope area as visualized in Fig. 8. The soil overburden thickness of BH-03 is 9 meters. Beyond that, it transitions into highly fractured boulders and bedrock (Fig. 9).

The bedrock is garnet biotite gneiss, moderately weak, light grey, metasedimentary, moderately to highly weathered, and highly fractured.

The geotechnical investigation at borehole location 3 revealed the following soil and rock conditions;

0.00 m to 0.9 m

This layer consists of loose, light brown, slightly gravelly silty sand. The sand particles range from fine to coarse in size, and gravel is also present. The presence of organic matter suggests that this layer is of residual origin.

0.90 m to 2.85 m

In this layer, the soil is described as medium dense to dense, with a black color mottled with reddish brown and light

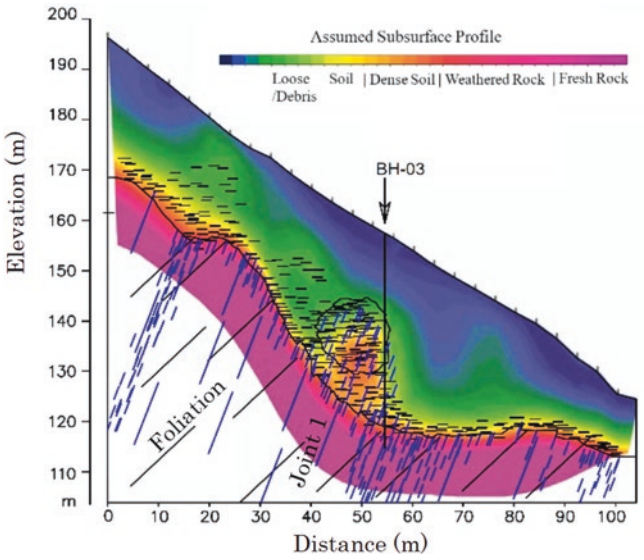

Fig. 9 Subsurface profile along the Seismic traverse 2 (BH-03)

brown. It consists of silty fine to medium sand and is also of residual origin.

2.85 m to 4.80 m
This layer is similar to the previous layer, with medium-dense soil that is black-mottled with reddish brown and yellowish brown. The soil composition is silty fine to medium sand and is also of residual origin.

4.80 m to 6.00 m
This layer is described as very dense and consists of yellowish brown and light grey silty fine to medium sand.

6.00 m to 10.50 m
This interval corresponds to a highly fractured in-situ boulder. This fact indicates the presence of a large rock mass that has undergone significant fracturing. 10.50 m to 12.00 m: The final layer consists of dense, completely weathered rock. This indicates that the rock has undergone significant weathering processes, which can alter its strength, stability, and other engineering properties. The specific characteristics of the completely weathered rock would need to be evaluated to assess its suitability for other geotechnical considerations.

Bedrock Description The identified bedrock at this location is described as light grey, highly to moderately weathered, and highly fractured biotite gneiss rock. Biotite gneiss is a type of metamorphic rock composed primarily of biotite minerals and characterized by a banded or foliated structure. The rock's high degree of weathering and fracturing can significantly impact its engineering properties, such as strength and stability, and reduce the shear resistance.

4.4 Hydrogeological Condition

The highly jointed and moderately to highly weathered bedrock beneath the soil overburden in the landslide area plays a significant dual role in hydrogeology and slope instability due to the influence of joints and fractures on water flow and the mechanical stability of the rock mass.

The fractured rock at the site, characterized by three sets of joints and weak foliation planes, forms an intricate network of interconnected hydrogeological pathways. These pathways act as conduits for the movement of water, leading to crucial implications for groundwater flow dynamics.

The specific catchment area of the landslide spans 5 ha, featuring a gentle slope covered by a dense forest and a loose, organically rich topsoil. This topography facilitates the infiltration of surface water into the subsurface, effectively recharging the groundwater system. The fractures within the rock significantly enhance the permeability and porosity of the rock mass in contrast to unfractured rock formations. This enhanced permeability allows water to flow more freely through the rock, leading to increased potential for groundwater storage and movement. Water can find its avenue through these fractures more rapidly compared to its movement through intact rock or even soil overburden.

The highly jointed rock acts as a natural aquifer, holding water close to the unstable soil slope. This stored water is gradually released through natural springs into the existing valleys on the site. Throughout the year, both the mainstream and its branch stream, following the existing valleys, consistently discharges water. During the dry season, the discharge rate is approximately 10 liters per minute, while in the wet season, it rises more than 100 liters per minute.

Fractures serve as conduits for increased water infiltration into the rock mass. However, this process can also contribute to the weakening of the rock structure as water erodes surfaces along the fractures and raises the pore water pressure within these fractures. The groundwater monitoring records at location BH-01 reveal a notably swift reaction to the rainfall experienced in the region (Fig. 10).

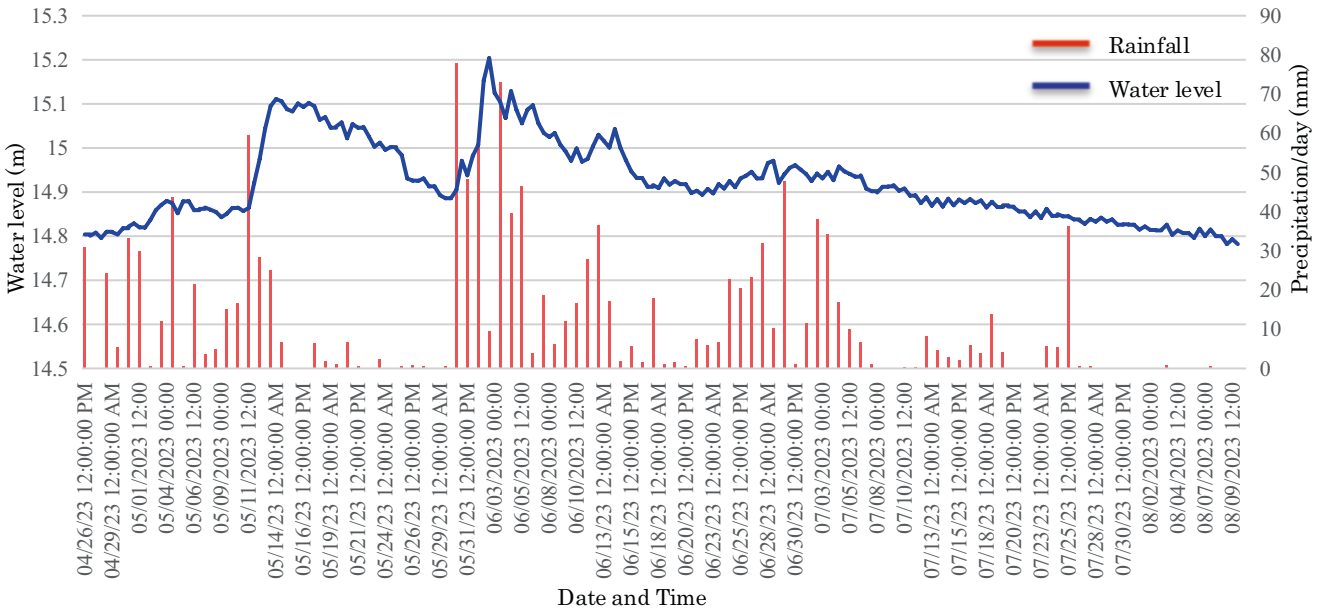

Fig. 10 Groundwater monitoring records at BH01 location and rainfall records at Rain gauge 1

5 Conclusions

The intense rainfall recorded on May 25th, 2017, likely played a critical role in triggering the Athwelthota landslide. However, complex unique hydrogeological conditions associated with the local arena may also be vital to clearly understand landslide initiation. Therefore, a detailed examination was conducted to understand the relationship among hydrogeology, structural geology, and geomorphology of the Athwelthota landslide. The following conclusions can be drawn based on the study:

The Athwelthota landslide area is composed of Charnockitic biotite gneiss and Biotite gneissic rock. The site is between two shear zones trending towards 255 degrees and dipping about 60 degrees to the southwest direction. The bedrock is highly jointed and exhibits signs of deformation, including micro folds and slickensides. Pegmatitic intrusions and inter-banded clay and gravely sand soil layers are also present.

These geological features contribute to the instability of the slope.

The landslide area is influenced by groundwater flow through geological discontinuities. Two separate springs in the region recharge the landslide body directly, increasing the groundwater table and potentially accelerating the failure. During the Southwest Monsoon, heavy rain saturates the soil and geological discontinuities, further contributing to instability. It can be said that the Athwelthota landslide was influenced by not only rainfall infiltration but also excessive subsurface drainage. Understanding these relationships is crucial for landslide hazard assessment, early warning systems, and infrastructure planning in landslide-prone regions.

Acknowledgments The authors gratefully acknowledge funding from a Japan-Sri Lanka bilateral SATREPS (Science and Technology Research Partnership for Sustainable Development) project titled "Development of Early Warning Technology for Rain-induced Rapid and Long-traveling Landslides," a joint program running from 2019 to 2025. The International Consortium on Landslides (ICL) and the National Building Research Organization of Sri Lanka (NBRO) are implementing this project.

Reference

Konagai et al. (2021) Development of Early Warning Technology for Rain-induced Rapid and Long-travelling Landslides

Part IV

IPL Projects, World Centres of Excellence on Landslide Risk Reduction, and Kyoto Landslide Commitment 2020

Increasing the Local Road Network Resilience from Natural Hazards in Municipalities in Serbia

Biljana Abolmasov, Miloš Marjanović, Ranka Stanković, Uroš Đurić, and Nikola Vulović

Abstract

This work is exampling a strategy for increasing climate resilience on local roads infrastructure in the Republic of Serbia, under the World Bank project framework. Methodological approach is briefly described as well as related mobile and web applications, labelled MaPLoRDs, which offers sustainable solution for resolving common issues encountered in road management at local, municipality level. It utilizes field and spatial data modelling as separate procedures which can be coupled or produce outputs independently, with minimal interaction with the operating staff. Collected data are translated into scores of exposure to main types of hazard (landslides, rockfalls, floods and flash floods) followed by vulnerability and criticality scores allocated per each road link. Final risk calculation allows ranking of highly impacted links that can be prioritized during subsequent road investment planning, enabling more rational budgeting. The concept is tested on two neighbouring pilot areas, the City of Kraljevo and the Aleksandrovac Municipality in Serbia, which are very different in terms of capacity, equipment and experience in dealing with natural hazards. Initial investment simulations for both pilots imply that MaPLoRds is a powerful tool for undertaking the first steps toward climate resilient roads.

Keywords

Local roads · Natural hazards · Climate resilience · MaPLoRds · Municipalities · Local road network · Natural hazards

B. Abolmasov (✉) · M. Marjanović · R. Stanković · U. Đurić
Faculty of Mining and Geology, University of Belgrade, Belgrade, Serbia
e-mail: biljana.abolmasov@rgf.bg.ac.rs; milos.marjanovic@rgf.bg.ac.rs; ranka.stankovic@rgf.bg.ac.rs; udjuric@grf.bg.ac.rs

N. Vulović
ENVI Software Solutions, Belgrade, Serbia

1 Introduction

The Republic of Serbia has experienced extreme climate conditions in the last two decades, especially floods, flash floods and mass movements (Prohaska et al. 2014; Marjanović et al. 2018a; Abolmasov et al. 2021). The frequency and intensity of floods and droughts have increased over the last 50 years, causing great socio-economic and environmental damage such as increased forest fires, desertification, decreased agricultural outputs and other negative consequences. According to the national climate changing projection, it is expected that average temperatures will increase between 1.7 and 2.3 °C in the next 50 years and that overall precipitation will drop, but the frequency of intensive precipitation is expected to be five times higher than in reference period 1981–2010 (Kržić et al. 2011; Rajković et al. 2013; Đurđević et al. 2018).

Roads in Serbia are the backbone of its transportation system and an important part of the European road network (TEN-T). The total length of roads in the country is 44,794 km. They are categorized as national-state roads (total length 13,505 km) and local (municipal) roads (total length approximately 31,289 km). All state roads in Serbia are maintained by the public, nation-wide, road construction company, The Public Enterprise Roads of Serbia (PERS), while local roads are maintained by municipal administration/public companies. Municipal local road networks vary in length and depend on municipality area, population, and number of settlements, as well as local morphological conditions. Only two-thirds of all municipal roads are paved.

More than 150 municipalities (out of 194) have suffered from flash floods, mass movements and riverine flooding in Serbia in the last decade. National road network, local roads, even urban streets, and assets including other roads structures such as bridges and culverts, are constantly threatened by flash floods, riverine floods and landslides. For instance, Serbia was heavily affected in May 2014, by extraordinary rains, which have caused severe flooding/flash flooding/land-

B. Abolmasov et al. (eds.), *Progress in Landslide Research and Technology, Volume 3 Issue 1, 2024*, Progress in Landslide Research and Technology, https://doi.org/10.1007/978-3-031-55120-8_22

sliding, unprecedented in the past 120 years. Recovery need assessment analysis done for 24 out of 38 affected municipalities in 2014, suggests that total effect on transport infrastructure was approximately EUR 166.5 million, out of which 96 million was estimated damage and 70.5 million was estimated loss. Rough assessment by PERS suggested that more than 2000 landslides were activated on the state roads and more than 3000 on the local roads (Jotić et al. 2015).

Review of the international practices related to climate resilience in the road sector shows considerable effort given to the national roads level. The methodologies for the inclusion of climate resilience considerations into the national roads transport management have been developed and tested successfully worldwide (Bíl et al. 2015, 2016). However, there is a limited number of methodologies related to the increasing local (municipality) road network resilience from natural hazards. Majority of projects in the World relate to the rehabilitation and construction of the road assets, but a small number of projects analyze the impact of climate change and natural hazards on the local road network (Andrejev et al. 2017; Marjanović et al. 2019).

Previous experience on national road network exposure and vulnerability assessment (Marjanović et al. 2022; Abolmasov et al. 2023b) recognized an urgent need to tackle local road network resilience and management in Serbia. This has been confirmed in practice, since 70 percent (in terms of the road length) of damages on the road transport network from natural hazards occurred at the local level (Jotić et al. 2015; Marjanović et al. 2018b; Marjanović et al. 2019).

Within the scope of the Japan-World Bank Program for Mainstreaming Disaster Risk Management in Developing Countries the World Bank received a grant from the Global Facility for Disaster Reduction and Recovery (GFDRR) for the Project "Improving Resilience and Safety of the Local Road Transport Network in the Republic of Serbia" in 2022. The University of Belgrade, Faculty of Mining and Geology (UBFMG) together with ARUP d.o.o. Belgrade directly contributed to realization of the Project Tasks, which included capacity building for local road network climate change adaptation planning and management within the beneficiary Local Self Governments (LSGs).

The Project activities directly contributed to the obligation of LSGs to prepare their local Disaster Risk Assessments, Protection and Rescue Plans and Disaster Risk Reduction Plans as per stipulations of the Law on Disaster Risk Reduction and Emergency Management adopted at the end of 2018 (Abolmasov et al. 2023a). UBFMG has been supporting activities of the national authorities as well as local authorities in the field of landslides disaster risk reduction and strongly contributes to the Sendai Framework for Disaster Risk Reduction 2015–2030. In this paper, the activities of WCoE on the Project realization on landslide risk reduction on the local road network will be presented.

2 Project Objectives

Due to fundamental differences between local and national road networks' characteristics, it is not possible to simply transfer national level resilience measures to local transport networks. For one, local transport networks are usually much denser than the national, whereas, the quality of the road transportation links on a local level are much lower than that on the national level. Furthermore, local communities have little, if any, capacity to deal with this issue. Consequently, road state monitoring, and availability of related data, are by far poorer for local roads. While basic concepts of resilience from natural hazards are universal for all road networks, the approaches for diagnostics, prioritization, and asset management of the local network are therefore specific, and additionally dependent on country context and local capacities. The methodological solution should cover all basic elements of the local road network resilience but should be simple enough for usage by the local level authorities and local technical staff and adaptive to poorer or limited data input.

The Project comprises of four main sets of tasks: (i) Developing methodology for LSGs to assess local road transport network exposure, vulnerability, risk, and criticality to the specified hazards; (ii) Local Road Transport Network Resilience Diagnostic Tool; (iii) Local Transport Network Resilience and Investment needs Assessment in Pilot LSG and (iv) Capacity building through several practical/field workshops with selected LSGs and local/national authorities.

3 Methodology

The goal of the methodology is focused on the outputs, which will enable LSGs to sustainably prioritize parts of the local road network they plan to invest in, such as: maintenance (routine, periodic and urgent), rehabilitation, or reconstruction. These outputs include:

- manually developed spreadsheet reports (based on manual field data collection and spreadsheet prioritization process), and
- automated map products and spreadsheet reports (based on field and spatial data collection, and as part of automated prioritization process),

both with a purpose to aid and supplement decision making process on the municipality level during the process of planning the investment in local road network. It allows for more

efficient, systematic, and economically justified solutions for available budgets and more responsible management in limited budgeting circumstances, and sets course towards higher social benefits.

The Methodology tends to compensate for all possible shortcomings originating from these shortages, while still providing a certain level of support for LSGs decision-makers. As portrayed in Fig. 1, it supports decision-making through two modelling streams:

(i) Part 1 - automated modelling based on field data (collected by LSGs staff)
(ii) Part 2 - background modelling based on available spatial data in raster format (by external experts).

According to the methodology, the LSG staff only needs to collect the data, without knowing the modelling process, as it is automated. It results in a preliminary priority and preliminary report for the needed investments. It can be further combined, with the expert-based model which is generated under (ii). It is an optional, but strongly encouraged part. Their subsequent combination into a final model is thereby enriching expert-based model with realistic field data, and vice-versa, gives the field data theoretical background, which is useful for supporting decisions before the field data is fully acquired (which might be lengthy process).

The LSGs should ideally do both: (i) assign trained staff to collect specific field data (about natural hazards that affect the roads, road conditions, consequences to traffic demand and infrastructure, etc.); (ii) hire specialists in the field of natural hazards, roads, and traffic (geological, civil, and traffic engineers, etc.) to conduct spatial analysis. Naturally, the support will be more reliable if both (i) and (ii) are undertaken. The methodology allows that either (i) or (ii) is missing or being incomplete, while still providing support to a decision-making process. Apart from basic level of knowledge on the hazard processes, road asset elements and protection/remediation measures that could be undertaken to resolve the problem at hand, some basic knowledge of handling mobile devices, may be required from the LSG staff while using such tool.

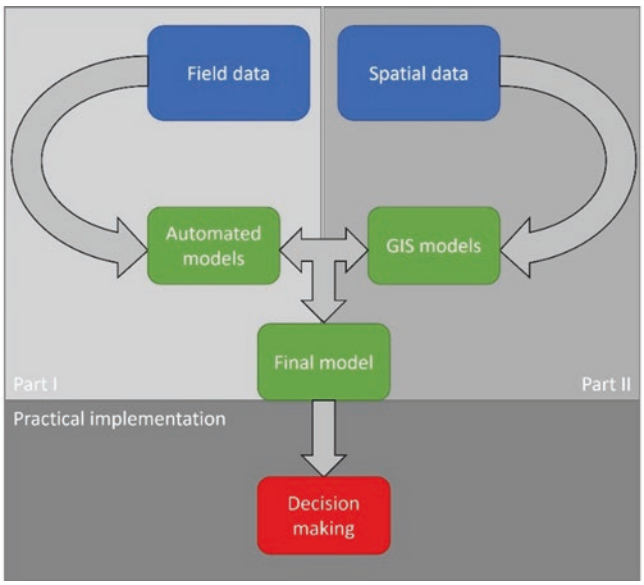

Fig. 1 General modelling scheme; Note: Light grey field implies involvement of LSG staff, medium grey is for involvement of external experts, while the darkest shade of grey involves decision-makers

The methodology is based on step-by-step procedure for assessment of the road network vulnerability, risk, criticality, and prioritization, which has been already developed in previous projects for national level network, now simplified/automated for LSGs local road networks. The Project Methodology is principally separated into five interdependent domains (Fig. 2) which are subject to overlapping and/or combining:

Input data pre-processing (red box Fig. 2)

1. Input data 1 - data from field acquisition needed for Automated models)
2. Input data 2 - acquisition and pre-processing of various raster datasets, such as terrain model, geological, soil, environmental and other thematic maps needed for background spatial modelling
3. Input data 3 - climate and climate change parameters in raster format, for baseline (reference period), medium (2050y), and long-term (2100y) projections needed for Background modelling

Preliminary prioritization (light blue box Fig. 2)

1. Automatization 1 - field-based *Dot map*
2. Automatization 2 - translating *Dot map* over road links into *Preliminary Priority map*

Background spatial modelling (orange box Fig. 2)

1. Background 1 - Exposure (per road links/sub-links)
2. Background 2 - Criticality (per road links/sub-links)
3. Background 3 - Vulnerability (per road links/sub-links)
4. Background 4 - *Control map* (per road links/sub-links)

Data fusion (blue box Fig. 2)

1. Final priority map (combining *Control map* and *Preliminary Priority map*)
2. Final spreadsheet report (per link)

Investment planning (violet box Fig. 2)

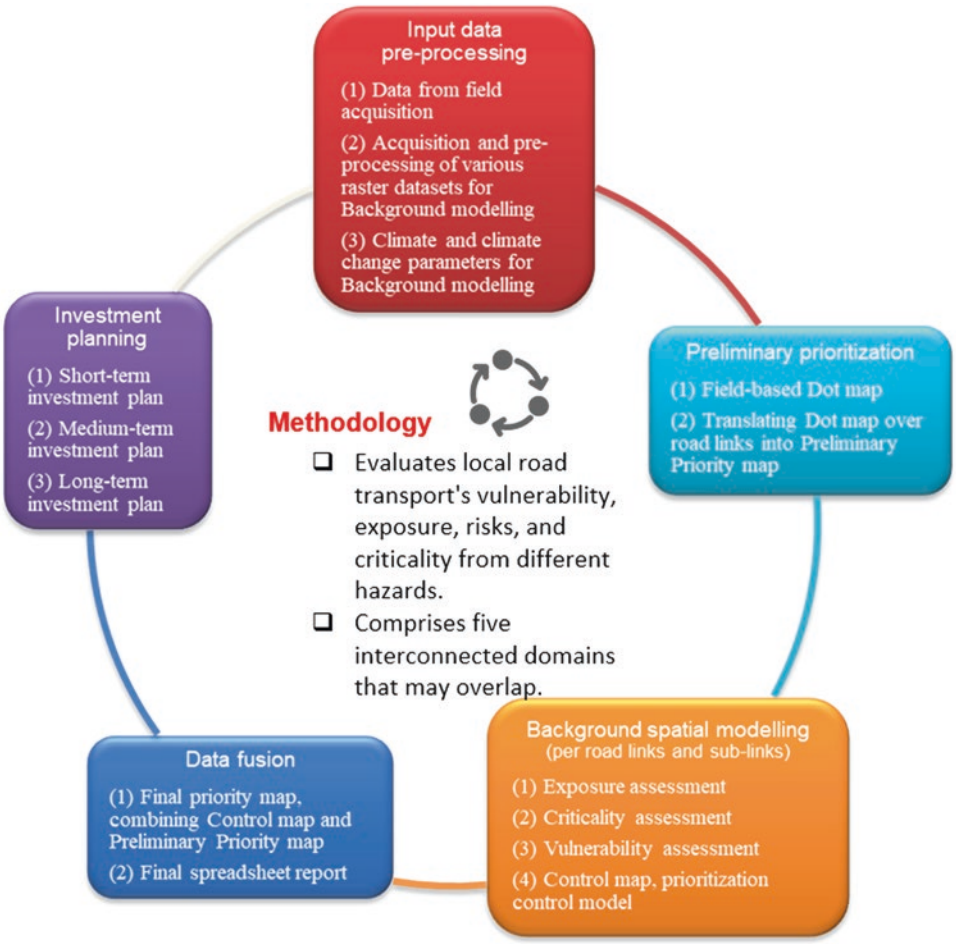

Fig. 2 The methodology flow chart

1. Short-term investment plan
2. Medium-term investment plan
3. Long-term investment plan

4 Local Road Resilience Diagnostic Tool

The Methodology, especially Part 1 (Fig. 1), seems very suitable for mobile implementation. Since fixed scoring criteria are utilized to translate what observer reports on the field into a numerical value (score), a simple, user-friendly mobile application that would support this process seems very reasonable. Mobile application would use the location services of hosting mobile device to enable all foreseen aspects of the Methodology.

Such tool for mobile devices is developed to facilitate the data collection in the field, while web application is developed for further local road network data analysis, resilience and priority assessment based on the methodology (MaPLoRds mobile and web app). The tools are simple to use, intuitive and with user friendly interface for utilization by engineers or technicians in the LSGs' administration.

Collected data are stored first on a mobile device memory and then uploaded to the back-end, central database to be easily accessible to different users. A set of different reports are available for onscreen preview and for export to Excel. This enables authorities to prioritize the activities, review the types of hazards, network, and links vulnerabilities, etc. in the familiar, spreadsheet, environment.

In general, development of information systems includes design of components for data collection, system analysis, requirements gathering, asset data definition and data management processes, levels of GIS service and implementation of basic API-s (Application Programming Interface).

Development of the MaPLoRds mobile application (for Android and iOS) and web GIS application enables users to perform continuous data collection related to occurred road hazards events, upon which priority assessment will be made based on the developed methodology. The workflow overview of the developed system is presented in Fig. 3. The implemented decision support system relies on both up-to-date field data and data obtained through the Background modelling (spatial modelling of specific hazard types, road vulnerability and criticality).

The language of the mobile and web application is Serbian, Latin alphabet by default. Application interface and

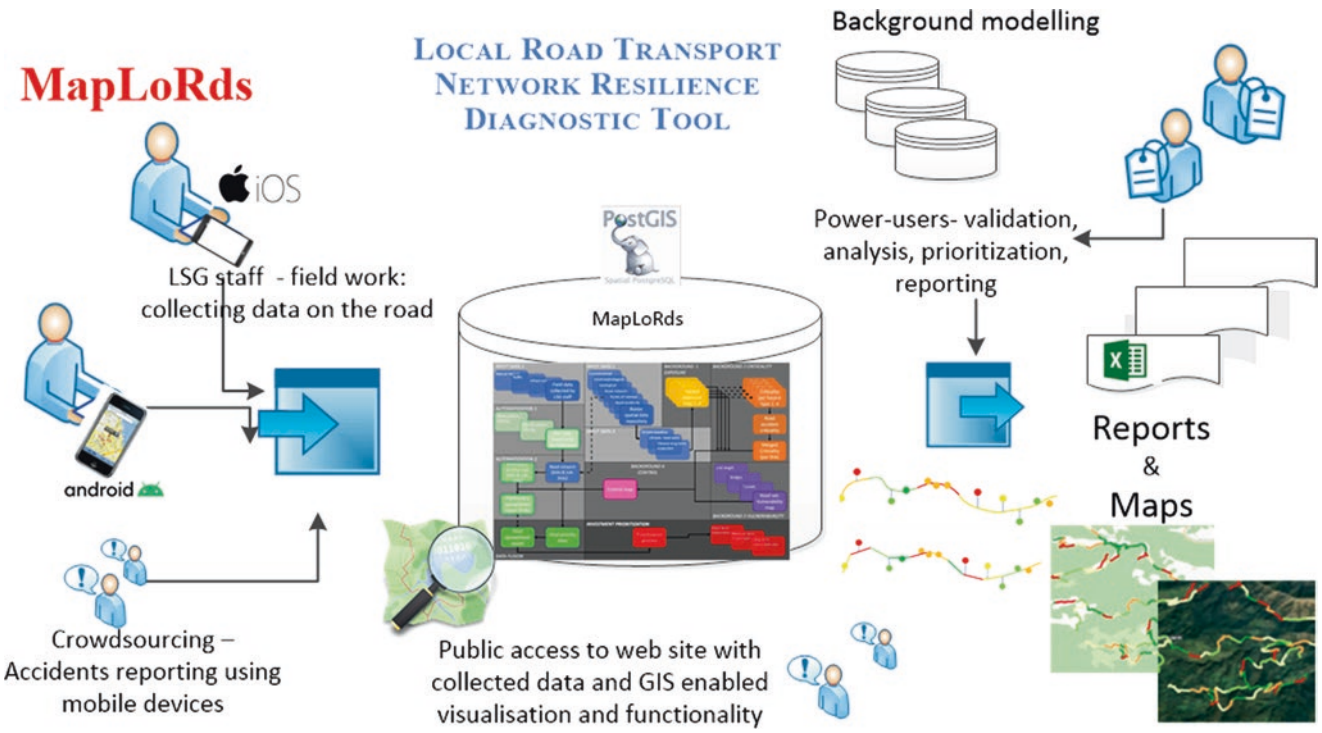

Fig. 3 MaPLoRds system data collection and analysis workflow

data classification labels includes English as well. The bilingual glossary, in Serbian and English, is produced for developed version of the application, introducing key terms and phrases that are required for the MaPLoRds interface, both for mobile and web application. Mobile application is enabled to work in online and offline mode. Since internet connectivity may not be accessible at remote locations, offline mode is needed to enable the collection of necessary field data and its storage on a mobile device. Once an internet connection is re-established, the status or datasets will be updated, transferred, and synchronized with the back-end database (Figs. 4 and 5).

Two pilot areas have been chosen to test the methodology, the Aleksandrovac Municipality and the City of Kraljevo (Fig. 6). The former, less developed pilot was expected to cope more with the execution of the task in comparison to the latter, well developed pilot, experienced in hazard assessment (with developed capacities, equipment, procedures, etc.). Conveniently, pilot areas are adjacent so direct comparisons, and other favoring effects (such as cooperation in bordering zones) are enabled. The selected neighboring LSGs represent communities exhibiting significant differences in population, geography, and economic development aspects. The local road networks within these LSGs serve as vital transportation links for both urban and rural areas. These road networks are vulnerable to a range of hazards, including flooding, landslides, rockfalls, erosion, and extreme weather events. It is imperative to understand and address these hazards to ensure the resilience of the local road infrastructure. A brief comparative overview of the main characteristics of the pilot LSGs is presented in Table 1.

Following the initial visit and the appointment of focal point persons, the project team established a close collaboration with pilot LSGs. This collaboration encompassed ongoing communication and correspondence with the LSGs' representatives. Assigned LSGs' teams diligently collected data and actively worked in close cooperation with the project team to support efficient information exchange.

In addition to the communication channels, workshops and joint fieldwork were conducted to facilitate the project objectives. The workshops and training sessions were specifically designed to provide valuable training to the representatives of the selected LSGs, enabling them to actively participate in diagnostic tool development (debugging), testing and methodology implementation. The primary aim of these workshops was to foster collaboration and ensure that all participants possess the necessary skills and knowledge to contribute meaningfully to the success of the project.

The workshop consisted of two parts. The first part focused on presenting the project and its objectives, as well as the MaPLoRds application. During this session, participants were provided with detailed information about the project goals, target outcomes, and the functionalities of the developed application.

The second part of the workshop enforced participants to focus on implementing the MaPLoRds mobile application in real-world settings. Participants had the opportunity to put

Fig. 4 Overview of the main MaPLoRds mobile app panels with illustrated dataflow

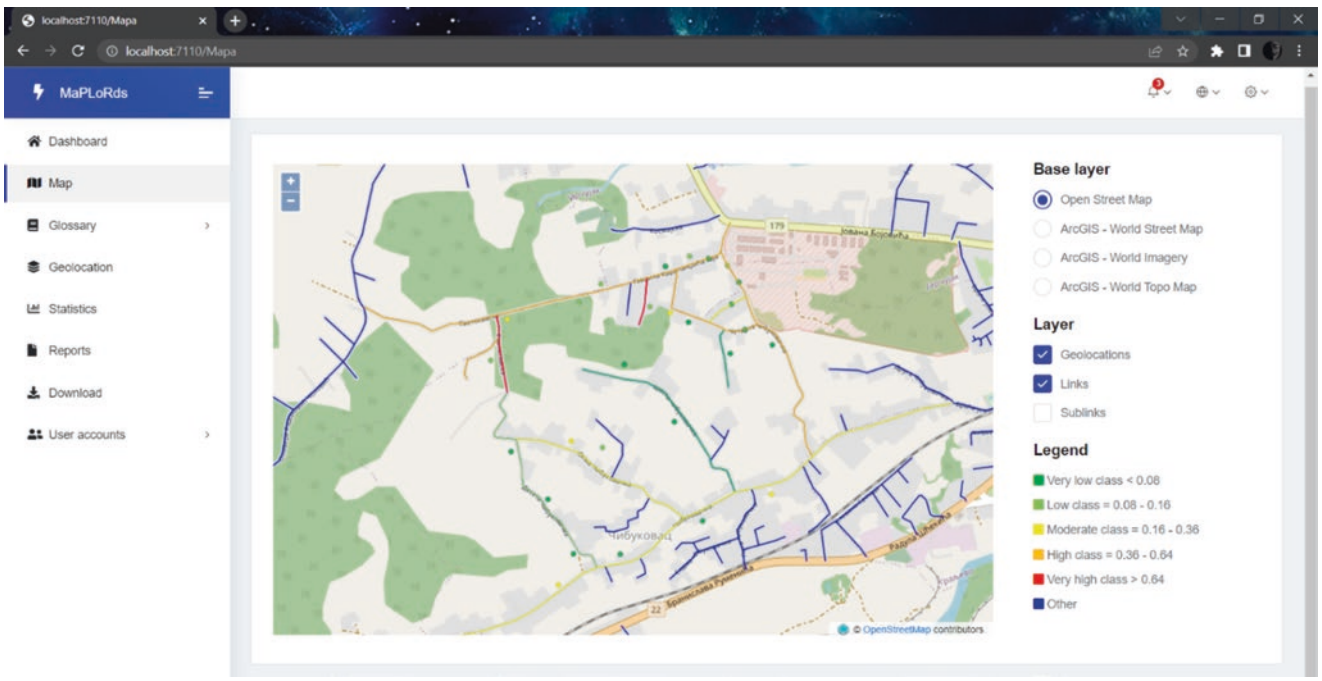

Fig. 5 Web GIS app with illustrated interactive map, hosting point and link view with Open Street base map

their theoretical knowledge into practice by using the application during the fieldwork activities. This hands-on experience allowed them to understand how the application functions in real-world scenarios and provided valuable insights for further improvements or adjustments (versioning of the app). These the two parts of the workshop complemented one another, providing participants with both theoretical knowledge and practical skills to effectively utilize the project application during their fieldwork.

The field visit was targeted to familiarize the users with functionalities of the application and provide guidance on technical aspects. It also served as an opportunity to address

Fig. 6 Position of selected LSGs within Central Serbia; Kraljevo City (red dot, red map) and Aleksandrovac Municipality (violet dot, yellow map)

Table 1 Comparative overview of the main characteristics of the pilot LSGs

Aspect	Kraljevo	Aleksandrovac
Geography	Valley, formed by two main rivers, separates two mountain regions in the north and south	Flanked by Goč, Kopaonik, and Jastrebac mountain ranges
Area	1529 km^2	387 km^2
Population	111,491	22,339
Population density	72.92 people/ km^2	57.72 people/ km^2
Economic activities	Diverse across 11 sectors, with emphasis on trade and manufacturing industries	Specialization in viticulture and fruit-growing industry
Local road network	326.2 km among which 200.2 km (61%) paved	407.4 km among which 218.1 km (53%) paved
Sensitivity to climate change	Vulnerable to floods, flash floods, landslides and rockfalls	Vulnerable to landslides in hilly areas and occasional urban flash floods

Fig. 7 Photos from workshop organized for recruited LSGs staff—Kraljevo and Aleksandrovac

any ongoing technical issues and report any bugs encountered in the mobile application. Establishing direct contact between the field working LSG staff and the project experts responsible for implementing the methodology and developing the MaPLoRds application was of the utmost importance (Fig. 7).

5 Conclusion

The local road transport network is the weakest link in natural disaster emergency situations, especially in climate changing conditions. Improving the national road network resilience is important but without complementary activities on the local level, natural disasters may still impact considerable number of people and services. Particularly vulnerable are people living in remote settlements, which might be completely cut-off during a severe hazard event, which might prevent their timely evacuation, or halt their supply chain and essential services. In such a case, resilient national road nearby is not as useful as it would be if the entire system was to endure the hazard impact. The need to follow resilience standards applied to national road infrastructure therefore must be recognized and implemented at local roads level, as well. The primary obstacle to achieving full (national and local road) climate resilience is understaffed and underequipped authorities that oversee road management. One approach would be to resolve these issues systematically but slowly, by hiring, training and equipping authorities in charge. Alternatively, the problem could be reduced by developing methodologies that offer automated, ready-to-use outputs, requiring minimal interaction with the operative staff. MaPLoRds has shown such capabilities and confirmed them on practical examples for the City of Kraljevo and the Aleksandrovac Municipality. The generated maps and reports were directly used in investment planning simulation, enabling decision makers to identify which road links are of the highest priority, and what type of investment is suitable and cost-effective. It is important to comment that full implementation, coupling both Part 1 and Part 2 procedures, i.e., outputs based on real field data, and outputs based on spatial modelling, respectively, offer much more reliable outputs, although both parts might be used independently. In addition, accounting for climate change impacts is not possible without including spatial modelling procedure.

Acknowledgments This research is conducted in the framework of the World Bank project: "Improving Resilience and Safety of the Local Road Transport Network in the Republic of Serbia".

References

Abolmasov B, Samardžić PM, Stanković R, Marjanović M, Krušić J, Đurić U (2021) Extreme rainfall event and its aftermath analysis—IPL 210 project progress report. In: Sassa K, Mikoš M, Sassa S, Bobrowsky PT, Takara K, Dang K (eds) Understanding and reducing landslide disaster risk. WLF 2020. ICL contribution to landslide disaster risk reduction. Springer, Cham, pp 267–273. https://doi.org/10.1007/978-3-030-60196-6_19

Abolmasov B, Marjanović M, Đurić U, Krušić J (2023a) An integrated approach to landslides risk management for local and national authorities. P-LRT 2(2) In press

Abolmasov B, Stanković R, Marjanović M, Vulović N, Đurić U (2023b) CliRtheRoads—an integrated approach to landslide risk management on roads in Serbia. P-LRT 2(2) In press

Andrejev K, Krušić J, Đurić U, Marjanović M, Abolmasov B (2017) Relative landslide risk assessment for the City of Valjevo. In: Mikoš M et al (eds) Advancing culture of living with landslides, proceedings of 4th world landslide forum, Ljubljana 29 May-02 June 2017, vol 3. Springer, pp 525–523. https://doi.org/10.1007/978-3-319-53483-1_62

Bíl M, Vodák R, Kubeček J, Bílová M, Sedoník J (2015) Evaluating road network damage caused by natural disasters in The Czech Republic between 1997 and 2010. Transp Res A 80:90–103

Bíl M, Kubeček J, Andrášik E, Bílová M, Sedoník J, (2016) RUPOK—a web-map application for assessment of impacts of natural hazards on the transportation infrastructure. Geophysical Research Abstracts, vol 18, EGU General Assembly 2016-4310, Vienna, Austria

Đurđević V, Vuković A, Vukadinović Mandić M (2018) Osmotrene promene klime u Srbiji i projekcije buduće klime na osnovu različitih budućih emisija. UNDP Srbija, ISBN-978-86-7728-302-5 (in Serbian) https://www.klimatskepromene.rs/wp-content/uploads/2021/08/Osmotrene-promene-klime-i-projekcije-buduce-klime.pdf. 11 Aug 2023

Jotić M, Vujanić V, Jelisavac B, Zlatković M, Milenković S (2015) Klizišta i štete na saobraćajnoj infrastrukturi u Srbiji. IZGRADNJA 69(5–6):215–224. in Serbian

Kržić A, Tošić I, Djurdjević V, Veljović K, Rajković B (2011) Changes in climate indices for Serbia according to the SRES-A1B and SRES-A2 scenarios. Climate Res 49:73–86. https://doi.org/10.3354/cr01008

Marjanović M, Krautblatter M, Abolmasov B, Đurić U, Sandić C, Nikolić V (2018a) The rainfall-induced landsliding in Western Serbia: a temporal prediction approach using decision tree technique. Eng Geol 232:147–159. https://doi.org/10.1016/j.enggeo.2017.11.021

Marjanović M, Abolmasov B, Đurić U, Krušić J (2018b) Assessment of landslide-related hazard and risk on the road network of the Valjevo city, Serbia. Proceedings of the 16th Danube-European Conference—Geotechnical hazards and risks: experiences and practices, vol 1, Skopje, Macedonia. Willey and Sons. pp 365–370

Marjanović M, Abolmasov B, Milenković S, Đurić U, Krušić J, Samardžić Petrović M (2019) Multihazard exposure assessment on the Valjevo City road network. In: Pourghasemi HR, Gokceoglu C (eds) Spatial modeling in GIS and R for earth and environmental sciences, Elsevier Inc., pp 671–688. ISBN 978-0-12-815226-3

Marjanović M, Abolmasov B, Đurić U, Krušić J, Bogdanović S (2022) Regional rockfall exposure assessment, experience from Serbia. In: Peranić J, Vivoda Prodan M, Bernat Gazibara S, Krkač M, Mihalić Arbanas S, Arbanas Ž (eds) Landslide modelling & applications. Proceedings of the 5th regional symposium on landslides in the Adriatic-Balkan Region. Croatian Landslide Group University of Rijeka, Faculty of Civil Engineering University of Zagreb, Faculty of Mining, Geology and Petroleum Engineering, pp 145–

150. https://5resylab.uniri.hr/wp-content/uploads/2022/04/2_Proceedings-of-the-5th-ReSyLAB.pdf
Prohaska S, Đukić D, Bartoš Divac V, Božović N (2014) Statistical significance of the rainfall intensity that caused the May 2014 flood in Serbia. Water Res Manag 4(3):3–10
Rajković B, Vujadinović M, Vuković A (2013) Report on revisited climate change scenarios including review on applied statistical method for removing of systematic model errors, with maps of temperature, precipitation and required climate indices changes; second national communication of the Republic of Serbia under the United Nations framework convention on climate change. MERZ, Belgrade, Serbia (on-line) available at http://haos.ff.bg.ac.rs/climatedb-srb/. 5 Aug 2023

Recent UL FGG Contributions to the 2020 Kyoto Commitment

Matjaž Mikoš, Nejc Bezak, Timotej Jurček, Tamara Kuzmanić, Matej Maček, Simon Rusjan, and Jošt Sodnik

Abstract

University of Ljubljana, Faculty of Civil and Geodetic Engineering (UL FGG) is a Full Member of the International Consortium on Landslides, and an Official Promoter of the 2020 Kyoto Commitment for Landslide Risk Reduction. In this article, the activities in the period 2020–2023 that have contributed to the 2020 Kyoto Commitment are shortly reviewed. The main research and capacity-building activities were conducted within the framework of the World Centre of Excellence (2020–2023) on Landslides in Weathered Heterogenous Sedimentary Rock Masses such as Flysch, and a few International Programme on Landslides (IPL) projects: IPL-225, IPL-261, and IPL-262. UL FGG also supported the activities of the UNESCO Chair on Water-related Disaster Risk Reduction (WRDRR) at the University of Ljubljana which was active in research of rainfall-induced landslides, their triggering and mitigation. The reviewed activities also contributed to the UNESCO Intergovernmental Hydrological Program and its IXth phase (2022–2029), the Sendai Framework on Disaster Risk Reduction (2015–2030), and the United Nations Sustainable Development Goals.

Keywords

Disaster risk reduction · Field studies · Laboratory studies · Landslide research · Sendai framework · Sustainable development goals

M. Mikoš (✉)
University of Ljubljana, UNESCO Chair on Water-related Disaster Risk Reduction, Ljubljana, Slovenia
e-mail: matjaz.mikos@fgg.uni-lj.si

N. Bezak · T. Jurček · T. Kuzmanić · M. Maček · S. Rusjan
Faculty of Civil and Geodetic Engineering, University of Ljubljana, Ljubljana, Slovenia
e-mail: nejc.bezak@fgg.uni-lj.si; timotej.jurcek@fgg.uni-lj.si; tamara.kuzmanic@fgg.uni-lj.si; matej.macek@fgg.uni-lj.si; simon.rusjan@fgg.uni-lj.si

J. Sodnik
Faculty of Civil and Geodetic Engineering, University of Ljubljana, Ljubljana, Slovenia

TEMPOS d.o.o, Ljubljana, Slovenia
e-mail: jost.sodnik@fgg.uni-lj.si

1 Introduction

1.1 About the Faculty

The Faculty of Civil and Geodetic Engineering of the University of Ljubljana (UL FGG), covering engineering disciplines, including water science and technology, has been involved in landslide risk reduction activities at the national level in Slovenia (former Yugoslavia, until 1991) for decades (eg., Mikoš 2020, 2021). In 2008, UL FGG became an ICL Full Member and has gradually developed its ICL engagement (ICL 2023a). UL FGG has been awarded the title of the World Centre of Excellence (WCoE) in Landslide Risk Reduction for 5 consecutive periods (2008–2011, 2011–2014, 2014–2017, 2017–2020, 2020–2023)—it is now applying as a WCoE for a new period (2023–2026). Together with the Geological Survey of Slovenia, in 2017 UL FGG hosted the 4th World Landslide Forum in Ljubljana, Slovenia.

UL FGG strongly supports diverse activities of the International Consortium on Landslides, Kyoto, Japan, and thus contributes to the 2030 Agenda for Sustainable Development as well as the Sendai Framework for Disaster Risk Reduction 2015–2030 (UNDRR PreventionWeb 2015). UL FGG was a signatory of the Sendai Landslide Partnerships 2015–2030 (Sassa 2015) and is a dedicated Official Promoter of the Kyoto Landslide Commitment 2020 (ICL 2023b), a SF DRR voluntary commitment by ICL. This commitment supports the implementation, follow-up, and review of the Sendai Framework 2015–2030, the UN 2030 Agenda for Sustainable Development, the New Urban Agenda, and the

B. Abolmasov et al. (eds.), *Progress in Landslide Research and Technology, Volume 3 Issue 1, 2024*, Progress in Landslide Research and Technology, https://doi.org/10.1007/978-3-031-55120-8_23

Paris Climate Agreement as it addresses the adverse effects of climate change related to landslides (Sassa 2021a).

In 2016, UL FGG started to host the University of Ljubljana UNESCO Chair on Water-related Disaster Risk Reduction (WRDRR), being still the only UNESCO Chair at this university, and one of a few in Slovenia. Among its activities, in 2022 the WRDRR Chair supported the launching of the regional platform called ResiliEnhance for enhancing the resilience to disasters for sustainable development. UL FGG also supports the activities of the Slovenian National Committee for UNESCO Intergovernmental Hydrological Programme (IHP), now working on the IHP-IX programme (2022–2029).

UL FGG is actively involved in many international (bilateral) and national research projects in the field of hydrology and hydraulic engineering, including topics such as landslide research, landslide risk mitigation, natural risk dialogue, and capacity building for society resilience.

In terms of capacity building, UL FGG offers several courses for graduate and postgraduate students in landslide mechanics and dynamics, landslide stabilization and landslide risk mitigation.

1.2 The Focus of This Article

UL FGG has been a full ICL member since 2008, and it is fully dedicated to the ideals and activities of the ICL, which was recently re-confirmed by being one of the first 2020 KLC signatories (Sassa 2021a).

The article presents a review of research and other activities of UL FGG from early 2020 to mid-2023, which contributed to 2020 Kyoto Commitment for Landslide Risk Reduction—in various ways, including and primarily as a full ICL member and the World Centre of Excellence in Landslide Risk Reduction 2020–2023.

2 WCoE (2020–2023) Landslides in Weathered Heterogeneous Sedimentary Rock Masses Such as Flysch

The World Centre of Excellence in Landslide Risk Reduction at the University of Ljubljana, Slovenia, was confirmed during the 5th World Landslide Forum in Kyoto, Japan, as a prolongation of the WCoE 2017-2020 entitled "Landslides in Weathered Flysch: From Activation to Deposition" (Mikoš et al. 2021a), and had the following two objectives:

(i) The main scientific aim will be to study weathering processes of heterogeneous sedimentary rock masses such as flysch bedrock both in laboratory (using standard tests) and on-site (using remote sensing techniques on different landslides in flysch).
(ii) Enhancement of landslide science in the Adriatic-Balkan Region through capacity development at the regional level as an outcome of regional scientific and high-education projects and cooperation.

2.1 Laboratory Research

Laboratory research is also needed to collect relevant input data for different kinds of models and to investigate landslide dynamics. In recent years, we have investigated rheology characteristics of natural debris material from different landslides (Fig. 1) (Bezak et al. 2021a; Jurček 2020; Jurček et al. 2022). As an example, in the scope of the study conducted by Jurček et al. (2022), the rheological parameters were measured at different sediment concentrations using two shear-rate controlled coaxial cylinder rheometers (Brookfield DV3T HB and ConTec Viscometer 5) and standard tests for determining the workability and flowability of construction materials (e.g., funnels, V-funnel, flow channel, flow table,

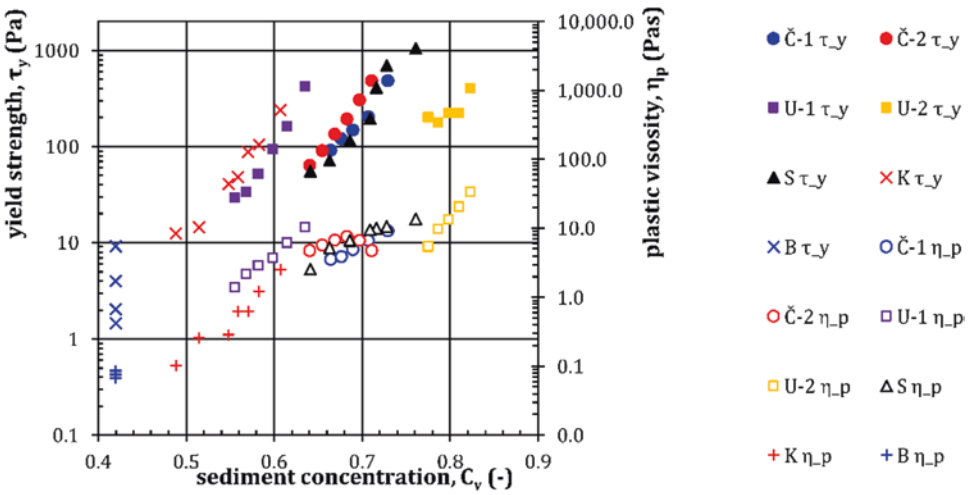

Fig. 1 Bingham model parameters of samples from the Urbas (U), Čikla (Č), and Stože (S) landslides. The results are compared from the literature data (K—Kaitna et al. (2007) & B—Bisantino et al. (2010)) (Source: Fig. 6 from Bezak et al. (2021a))

L-box). The measured data were evaluated by using the Bingham rheological model. The study conducted by Jurček et al. (2022) showed that the rheological parameters measured with the coaxial cylinder rheometers give reasonably good predictions of standard test results, while vice versa, i.e., from these standard tests estimation of rheological parameters is not possible. Additionally, the results of laboratory small-scale experiments were also used to evaluate the performance of multiple hydrological rainfall loss methods (Bezak et al. 2022a). The results of the previously mentioned study showed that the initial parameters of the rainfall loss model can satisfactorily reproduce the experimental results in some cases (Bezak et al. 2022a). Despite the fact that the slope material characteristics used in the laboratory experiments were relatively homogenous, some well-known methods yielded inaccurate results (Bezak et al. 2022a). Hence, this indicated the importance of model calibration.

Coarse (and fine) rock or debris particles are subjected to abrasion (wearing away) during their routing in sedimentary environments, leading to mass loss and changes in the particles' morphology (Mikoš and Jaeggi 1995). The particles become more spherical, rounded, and smooth, as determined using dynamic image analysis of particles (Kuzmanić and Mikoš 2022a, b). Such processes cover fluvial processes, as well as gravitational processes, including mass movements. Different-energy-level abrasion in Los Angeles and micro-Deval apparatuses was compared using mass loss and rounding of sediment particles as a proxy for natural processes in the field (Kuzmanić et al. 2023). Los Angeles (high-energy) abrasion resulted in higher mass loss values than micro-Deval (low-energy) abrasion. The mass loss results can be brought to comparable values by a newly introduced mass- and power-dependent coefficient. Low-energy abrasion resulted in faster rounding than high-energy abrasion, whereas the form stayed nearly the same. In contrast, the form changed rapidly during high-energy abrasion.

The ongoing extensive testing of gravel-sized granular material aims to recognize and evaluate the effect of naturally occurring freezing and thawing cycles on the abrasion characteristics of such natural materials in different granulometric and energetic conditions. Laboratory investigation on flysch material was conducted within the scope of a national project J1-2477 "Erosional processes on coastal flysch cliffs and their risk assessment". Flysch samples from different locations on the Slovenian coastal cliffs were subjected to cyclical wetting and drying in a slake-durability apparatus to compare the durability properties of flysch material. The testing was conducted using a standardized procedure, with additional slaking cycles (up to five cycles—I_{d5}). Flysch samples were also tested using the Leeb hardness tester, to compare the material hardness between sampling locations and identify the weaker cliff locations. For these laboratory tests, only preliminary results have been obtained so far.

2.2 Field Research

In order to detect mechanisms of landslides and their dynamics detailed geological, geotechnical, geodetic, and remote sensing investigations and field research is needed (Mikoš 2020). A case study in the Koroška Bela area, NW Slovenia, was conducted, where the Urbas landslide has been investigated for years (e.g., Bezak et al. 2021a; Peternel et al. 2022a, b, c). Recently it was found that the Urbas landslide dynamics (Figs. 2 and 3) differs along the landslide area and depends on local geological and hydrogeological conditions (Peternel et al. 2022a, b, c).

In recent years, field research also focused on in-depth investigation related to the triggering of rockfalls in eastern Slovenia (Jemec Auflič et al. 2022)—as a result of the project entitled "Deciphering the sensitivity of rock faces to climatic changes and freeze-thaw cycles in permafrost-free regions" (IPL-262 project, Geological Survey of Slovenia, with UL FGG collaboration, 2022–2024).

Another detailed field study was undertaken in the torrential area upstream of the Krvavec ski resort, NW Slovenia, where a short but extreme debris flood occurred in 2018 (Bezak et al. 2020). In order to protect the ski lift cabin car, several mitigation measures were planned, some of which have already been implemented. The mitigation includes the restoration of local streams, the construction of a large slit check dam for sediment retention, the construction of several smaller check dams and the construction of multiple flexible net barriers for controlling in-channel erosion in steep torrential streams.

Moreover, to observe and monitor potential future extreme events, an extensive monitoring system has been established in the investigated area, including measurements of flexible nets' corrosion, estimation of concrete abrasion at check dams, periodical geodetic surveys using small drones (UAV), hydro-meteorological measurements using rainfall gauges and water level sensors. A video recording system will be established for closer observation of future disaster events (Sodnik and Mikoš 2022a, b). The project is still in its starting phase.

2.3 Numerical Modelling Studies

Several modelling studies have also been conducted in recent years, where RAMMS model has been used for modelling debris floods and debris flows (Fig. 4) (Bezak et al. 2020, 2021a).

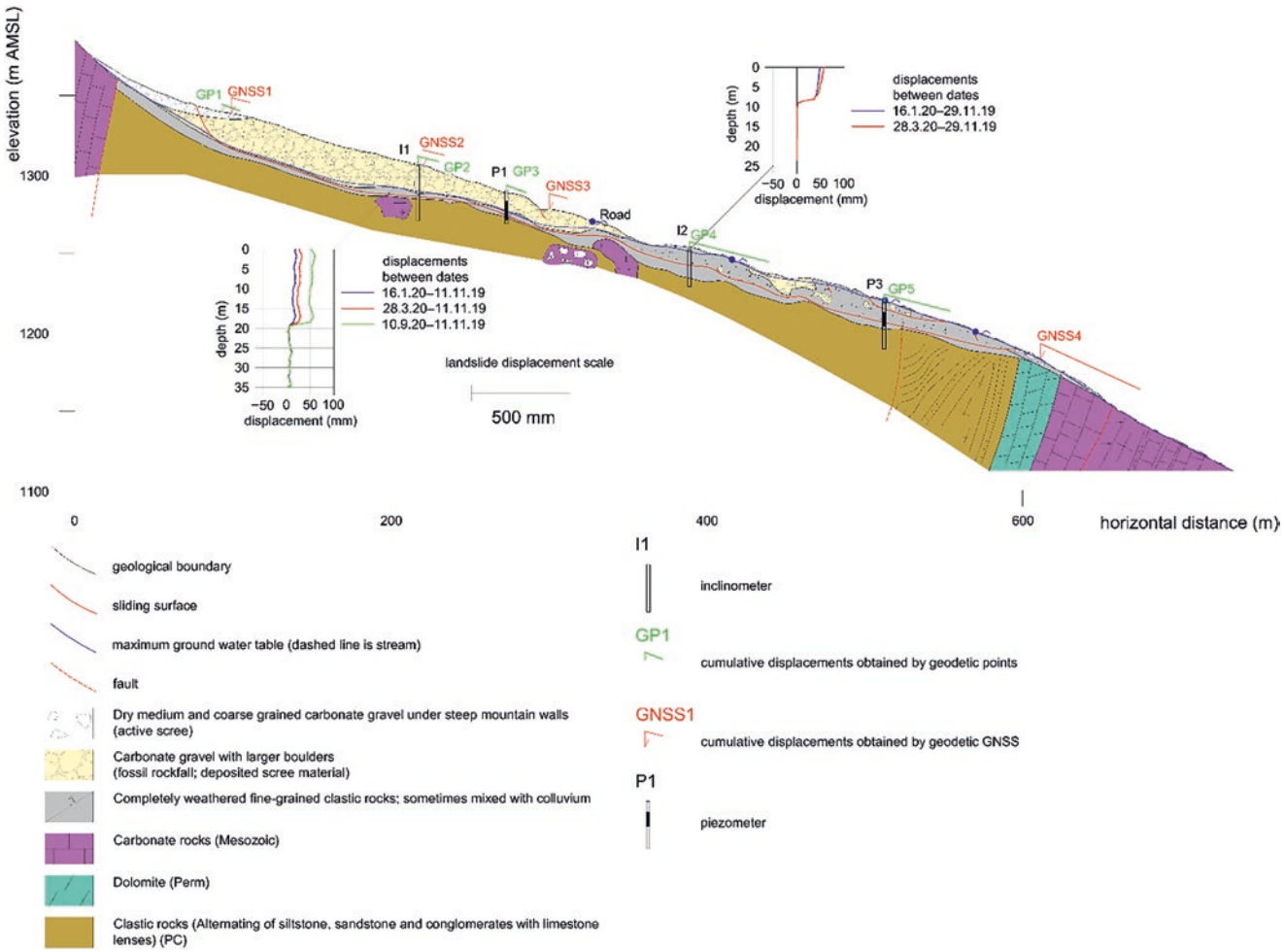

Fig. 2 A cross-section along the Urbas landslide with data overview showing geological and hydrogeological settings, cumulative surface displacements obtained from GNSS, in situ object-point geodetic measurements, and deep displacements obtained by the inclinometer (Source: Fig. 5 from Peternel et al. (2022b), CC BY 4.0)

Bezak and Mikoš (2021) also conducted a review of different RAMMS model applications in the Alpine environment. Based on the review conducted, it is clear that RAMMS parameter ranges were relatively wide, and model calibration using debris-flow post-event survey field data is the essential step that should be done before applying the RAMMS model. However, an overview of the parameters can help to limit the parameter ranges. Particularly when considering the similarity between relevant case studies conducted in similar environments.

Additionally, modelling and classification of alluvial fans with DEMs were done using different machine learning algorithms (Babič et al. 2021)—as a result of the project entitled "Recognition of potentially hazardous torrential fans using geomorphometric methods and simulating fan formation" (IPL-225 project, UL FGG 2017–2020).

2.4 Large-Scale Studies

Additionally, in recent years several large-scale studies have also been conducted ranging from an analysis of freeze-thaw cycles in Slovenia (Mikoš et al. 2022) to an investigation of rainfall events above empirical rainfall thresholds in Europe (Bezak and Mikoš 2021). While Bezak et al. (2022b) prepared a review of recent research in this field, Mikoš et al. (2022) investigated the rock frost weathering and rockfall activity in Slovenia and tested several different rockfall susceptibility models. It was found that slope and lithology are the two factors that significantly affect the model performance. On the other hand, some other input data such as the seismic-hazard map had a smaller impact on the model performance (Mikoš et al. 2022).

Bezak et al. (2021b) investigated the performance of reanalysis of soil moisture data for the prediction of landslides in Italy. It was found that at such large-scales precipitation is a better predictor of landslide activity (Bezak et al. 2021b).

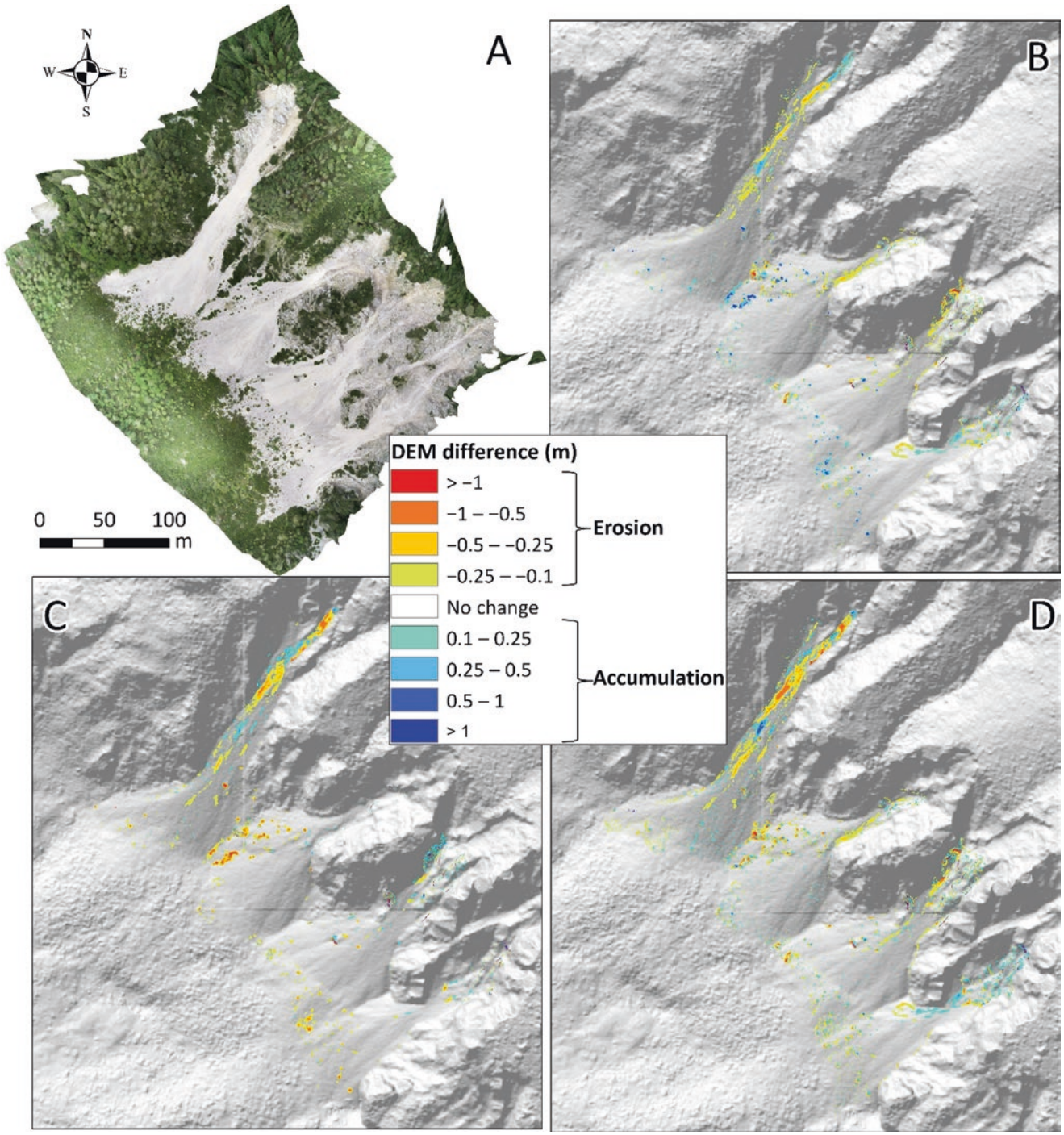

Fig. 3 (**a**) Orthophoto of a steep slope above the Urbas landslide obtained by unmanned aerial vehicle (UAV) photogrammetry in May 2020; (**b**) DEM difference (DoD) between August 2019 and May 2020; (**c**) DEM difference (DoD) between May 2020 and August 2020; (**d**) DEM difference (DoD) between August 2019 and August 2020 (Source: Fig. 9 from Peternel et al. (2022b), BB CY 4.0)

Bezak and Mikoš (2021) found that around 15% more rainfall events were detected above the selected empirical rainfall thresholds, as recently compared to the past period of around 1961, meaning that the frequency of landslides in Europe could increase.

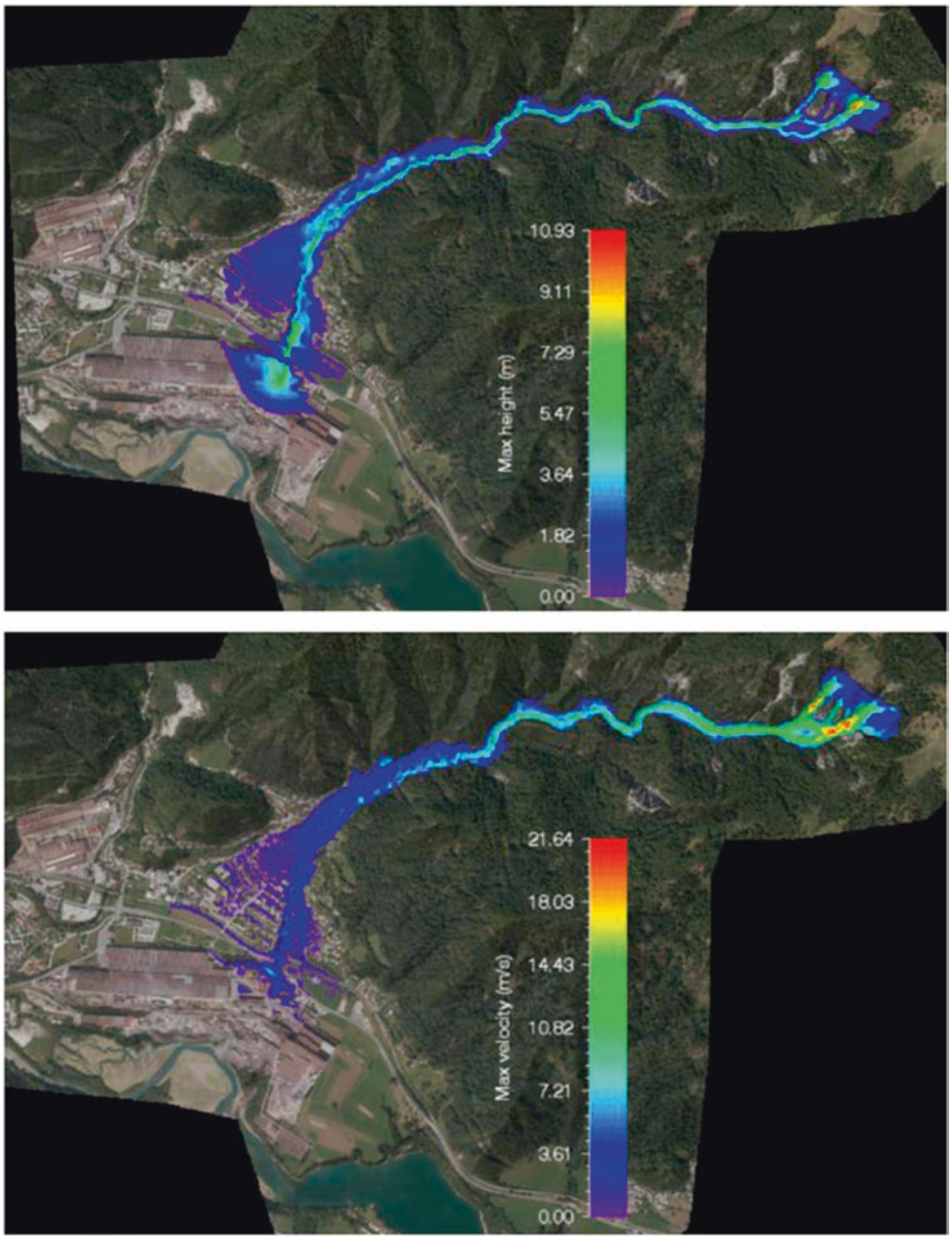

Fig. 4 A typical RAMMS modelling result for the Urbas landslide (Koroška Bela Municipality, Slovenia) in a case of potential debris flow triggering. Maximum debris flow height and velocity are shown. Results using $\mu = 0.075$ and $\xi = 200$ m/s^2 and a hydrograph volume of 200,000 m^3 and a peak discharge of 2680 m^3/s are presented (Source: Fig. 2 from Mikoš and Bezak (2021), CC BY 4.0)

Several studies have investigated rockfall activity in flysch formations in Slovenian Istria (Verbovšek et al. 2021, 2022). In 2023, a regional rockfall hazard map for the coastal area of Slovenia is under preparation, which will take into account field geological data, meteorological data (air temperature, wind velocity and direction, precipitation), sea wave characteristics, etc. The map will be prepared using different methodological steps and validation will be performed using field surveys.

3 IPL-261 World-Wide-Web-Based Landslide Observatory (W3bLO) (2022–2024)

This is a joint project of the University of Ljubljana (UL FGG and UNESCO Chair on Water-related Disaster Risk Reduction) and the International Research Centre on Artificial Intelligence at the Jožef Stefan Institute under the auspices of UNESCO, all in Ljubljana, Slovenia. The main project field of development is in technical development.

A web-based Landslide Observatory will be developed, capable of collecting/presenting nearly now-cast information on the present status of selected indicators relevant for land-

slide risk reduction at the global scale, based on the EU project NAIADES (2022). For its development, Artificial Intelligence (AI) techniques (e. g. Deep Learning, and other algorithms) and selected large databases with data from the public domain will be applied (NAIADES Water Observatory 2023). The observatory is a first step towards building a Digital Twin of Landslide Risk Assessment. The study area is the global scale using different on-line satellite data (i.e., Sentinel) and large web databases. In 2022, the methodology was tested on selected natural hazards (floods & heat waves) that offered enough social media and news information to be analyzed using available text-mining tools (Mikoš et al. 2023a, b).

The planned project activities were submitted to the Open-Ended Working Group for operationalization of the IXth programme of the Intergovernmental Hydrological Programme of UNESCO (2022). The next steps will be: i) the Development of AI tools and techniques to be used for Landslide Observatory, ii) Building up the observatory using available and curated open datasets and filtered news feeds.

The methodology will be tested in Slovenia and elsewhere, where publicly available databases in different languages can provide sufficient data for validation. Thus, other ICL members will be invited to support the development in its second phase to provide data, and test the observatory in their country and language. After the final inauguration of the observatory, the general public and experts worldwide will be able to use it to plan prevention measures to mitigate and reduce landslide risk at regional and local scales.

4 Other ICL/IPL Activities at UL FGG

UL FGG served the ICL by taking different leading roles in the Consortium, for example, a UL FGG member served as Chair of IPL Evaluation Committee, twice as ICL Vice President, and was elected to Co-Chair and in 2021 to Chair of the Global Promotion Committee of IPL-KLC (https://www.landslides.org/ipl-info/ipl-klc-global promotion-committee/).

UL FGG has been strongly supporting the journal *Landslides*: Journal of the International Consortium on Landslides, published by Springer Nature (https://link.springer.com/journal/10346) since its launch in 2004 (Mikoš et al. 2021b). UL FGG works for the journal in the roles of reviewers and an associate editor, and regularly publishes its top research results in the journal (e.g., Bezak et al. 2020, 2021a, b; Bezak and Mikoš 2021) as well as disseminates information important for capacity building in landslide risk reduction—such as results of bibliometric studies on the journal *Landslides* and ICL books.

Since 2022, UL FGG has contributed several articles to the newly introduced open-access book series "Progress in Landslide Research and Technology" (Sassa 2021b):

- an introductory article on the new book series (Sassa and Mikoš 2023),
- a review article on the history of the International Programme on Landslides (IPL) (Mikoš et al. 2023a),
- an original article on the natural-hazard-related web observatory as a sustainable development tool (Mikoš et al. 2023b),
- an original article on landslide research and technology in patent documents (Mikoš 2023a),
- an original article on landslide research and technology in international standards (Mikoš 2023b),
- an original article on landslides in higher education curricula and beyond (Mikoš 2023c),
- a review article on UL FGG contributions to the 2020 KLC Commitment (this volume)

5 University of Ljubljana UNESCO Chair on Water-related Disaster Risk Reduction (2016–2020 and 2020–2024)

Much landslide-related research and capacity building for sustainable development and society resilience is underpinned by the UNESCO Chair on Water-Related Disaster Risk Reduction at University of Ljubljana.

5.1 About the Chair

Experiences and knowledge accumulated in the past decades at the Chair on Hydrology and Hydraulic Engineering at UL FGG in the field of (applied) hydrology in experimental basins, hydraulic engineering, landslide research, landslide risk reduction, and flood risk management culminated in 2016 in the establishment of the UNESCO Chair on Water-related Disaster Risk Reduction (WRDRR Chair 2023) at the University of Ljubljana. The UNESCO WRDRR Chair was positively evaluated by UNESCO in 2020 and prolonged for another 4 years (2020–2024). The Chair is associated with the university twinning and networking UNITWIN UNESCO—Kyoto University—ICL on "Landslide and Water-Related Disaster Risk Management".

The UNESCO WRDRR Chair is involved in many international (bilateral) and national research projects (for a list see: https://www.unesco-floods.eu/). Their results are timely

reported in the scientific literature (https://www.unesco-floods.eu/category/publications/).

5.2 ULTRA Project: University of Ljubljana Sustainable Development Pilot Projects (2022–2025)

In 2022, the UNESCO Chair started to head one of the University of Ljubljana pilot projects on Sustainable Development (2022–2025; www.unesco-floods.eu/ultra-pilot-projects/) to modernize university professional study programmes, especially in civil engineering, and to increase students' competences for sustainable development, including disaster risk reduction and capacity and resilience building.

5.3 ResiliEnhance Program and Platform

In 2022, the UNESCO WRDRR Chair supported the launching the ResiliEnhance Platform to enhance resilience to disasters for sustainable development (CEI 2022). The platform is part of the ResiliEnhance Program that is at the moment geographically focused on Central and Eastern Europe (SPRINT 2022), and supported by the Central European Initiative (CEI)—a regional intergovernmental forum of 17 Member States in Central, Eastern and South-Eastern Europe—it fosters European integration and sustainable development through regional cooperation and its work is focused on achieving two main goals: Green Growth & Just Societies.

The ResiliEnhance program is currently launching an expert platform to explore effective ways and means for strengthening territorial resilience to adverse events and critical situations in the context of complexity and systemic risk. The model for this new platform is the one of the Global Alliance for Disaster Risk Reduction & Resilience in the Education Sector (GADRRRES 2023). GADRRRES is a multi-stakeholder platform comprised of UN agencies, international non-governmental agencies, leading humanitarian and development organizations, private sector organizations, and similar regional alliances.

UNESCO WRDRR Chair is supporting these activities another UNESCO Chair on Intersectoral Safety for Disaster Risk Reduction and Resilience, University of Udine, Italy. The ResiliEnhance platform will also be included in the newly launched (first meeting was in July 2023) interactive platform for regional cooperation of the UNESCO Science-related Chairs and Centres in South East Europe—an initiative supported by the UNESCO Regional Bureau for Science and Culture in Europe, Venice, Italy, and agreed during their first meeting on October 26–28, 2022 (UNESCO Venice 2022). UNESCO WRDRR Chair was one of the 28 UNESCO Science-related Chairs and Centres from 8 countries that adopted the Palazzo Zorzi Declaration.

All this networking in the region will help increase the UNESCO WRDRR Chair's visibility, while its activities in the field of disaster risk reduction for sustainable development, including landslide risk reduction, will get more international attention, also for the International Consortium on Landslides.

5.4 IHP-IX Program (2022–2029)

UL FGG has supported the activities of the Slovenian National Committee for UNESCO Intergovernmental Hydrological Programme (NC IHP 2023) for many years, hosting it at the Faculty of Civil and Geodetic Engineering, University of Ljubljana. The focus of the activities is the development of the IHP-IX Programme (2022–2029).

The Intergovernmental Hydrological Program and its ninth phase (IHP-IX) have defined 5 priority areas (or streams of action) (UNESCO 2022):

1. Scientific Research and Innovation
2. Water Education for the Fourth Industrial Revolution including Sustainability
3. Bridging the data and knowledge gaps
4. Integrated and Inclusive Water Resources Management under conditions of global change
5. Water Governance based on science for mitigation, adaptation and resilience

The UNESCO WRDRR Chair as a member of the ICL will contribute to the following proposed activities, being defined by the Operational Implementation Plan for IHP-IX (UNESCO 2023):

- *Priority 1.5—Undertaking and sharing assessments on the interaction between humans and water, in line with socio-hydrology by the scientific community supported to develop adaptive pathways, scenarios and strategies for water management.*
- Activity: Contribution to research, knowledge generation and dissemination on socio-hydrology, including socio-hydrogeology, as a follow-up of the Panta Rhei decade and previous IHP initiatives in partnership with IAHS.
- WRDRR contribution: Course on Socio-hydrologic assessment of flood protection (5 ECTS) - coursebook
- *Priority 1.6—Scientific knowledge, methodologies and tools in addressing water-related disasters, such as flood and drought elaborated and/or enhanced towards timely forecasting.*
- Activity: Research and knowledge generation on the scientific advances in addressing and timely forecasting of

water-related disasters, such as (flash) floods, (flash) droughts and rainfall-induced landslides; and on additional impact of synchronous and/or cascading water-related hazards, in partnership with EGU, AGU, IAHS, ISEH and ICL—International Consortium on Landslides and IPL—International Programme on Landslides, including good practices and lessons learned.
- ICL/IPL contributions: journal *Landslides*, P-LRP book series, World Landslide Forums
- *Priority 2.3—Teaching and learning materials on water-related matters for formal, non-formal and informal education at all levels elaborated towards a better understanding of the importance of water in lives and communities.*
- Activity: Development of a series of modules, using the available new technologies and innovative learning processes, based on the existing material and developing new learning material and tools catering to the priorities and needs of the Member States and partners, including the development of a multilingual glossary on water, Case Studies in Socio-Hydrology; Compendium of Case Studies; and custom-made module together with, and for use by, Pan African Virtual and E-University (PAVEU).
- WRDRR contribution: Leading the development of a multilingual glossary on water.

The Implementation Plan for IHP-IX is continuously developing and is monitored by the IHP Secretariat in UNESCO Headquarters, Paris.

6 Conclusions

UL FGG, as one of the World Centres of Excellence in Landslide Risk Reduction, hosts the UNESCO Chair on Water-Related Disaster Risk Reduction. It strongly supports ISDR-ICL Sendai Partnerships 2015–2025 for global promotion of understanding and reducing landslide disaster risk, and its extension to 2030 and beyond: the Kyoto 2020 Commitment for Global Promotion of Understanding and Reducing Landslide Disaster Risk, which was signed in November 2020. UL FGG is proud to be its Official Promoter and will specifically work for Actions 2, 5, 6, 9, and 10.

The worldwide landslide community is invited to support the efforts for society's resilience against landslides by intensifying their efforts for capacity building in parallel to their research activities. For the International Consortium on Landslides, the KLC 2020 Commitment for Global Promotion of Understanding and Reducing Landslide Disaster Risk (Sassa 2021a) is a standing support and reminder to be active (also) in the field of capacity building, not only through research but also education.

The ICL activities are supporting the implementation of the ninth phase of the UNESCO Intergovernmental Hydrological Programme (IHP-IX) 2022–2029 (UNESCO 2023).

Acknowledgments This article resulted from the research and capacity-building activities of the UNESCO Chair on Water-related Disaster Risk Reduction at the University of Ljubljana (2020–2024), and of the World Centre of Excellence on Landslide Risk Reduction (2020–2023) at the Faculty of Civil and Geodetic Engineering, University of Ljubljana, Slovenia.

The authors would like to acknowledge the financial support of the Slovenian Research and Innovation Agency (ARIS) by core funding P2–0180, and of the University of Ljubljana from the Development Fund for the activities of the UNESCO Chair on Water-related Disaster Risk Reduction (WRDRR). This contribution is also part of projects J1-2477 and J1-3024, which are financed by the Slovenian Research and Innovation Agency.

The authors would like to acknowledge suggestions and edits of an anonymous reviewer, which improve the article.

References

Babič M, Petrovič D, Sodnik J, Soldo B, Komac M, Chernieva O, Kovačič M, Mikoš M, Calì M (2021) Modeling and classification of alluvial fans with DEMs and machine learning methods: a case study of Slovenian torrential fans. Remote Sens (Basel) 13(9):1711. https://doi.org/10.3390/rs13091711

Bezak N, Jež J, Sodnik J, Jemec Auflič M, Mikoš M (2020) An extreme May 2018 debris flood case study in northern Slovenia: analysis, modelling, and mitigation. Landslides 17(10):2373–2383. https://doi.org/10.1007/s10346-019-01325-1

Bezak N, Mikoš M (2021) Changes in the rainfall event characteristics above the empirical global rainfall thresholds for landslide initiation at the pan-European level. Landslides 18(5):1859–1873. https://doi.org/10.1007/s10346-020-01579-0

Bezak N, Sodnik J, Maček M, Jurček T, Jež J, Peternel T, Mikoš M (2021a) Investigation of potential debris flows above the Koroška Bela settlement, NW Slovenia, from hydro-technical and conceptual design perspectives. Landslides 18(12):3891–3906. https://doi.org/10.1007/s10346-021-01774-7

Bezak N, Jemec Auflič M, Mikoš M (2021b) Reanalysis of soil moisture used for rainfall thresholds for rainfall-induced landslides: the Italian case study. Water 13(14):1977. https://doi.org/10.3390/w13141977

Bezak N, Peranić J, Mikoš M, Arbanas Ž (2022a) Evaluation of hydrological rainfall loss methods using small-scale physical landslide model. Water 14(17):2726. https://doi.org/10.3390/w14172726

Bezak N, Mikoš M, Jemec Auflič M (2022b) Rainfall-induced landslides and debris flows under the influence of climate change: review of recent Slovenian studies. In: Peranić J et al (eds) Landslide modelling & applications: proceedings of the 5th ReSyLAB, pp 7–12. https://repozitorij.rgn.unizg.hr/islandora/object/rgn:2214/datastream/FILE0/download. Accessed 20 July 2023

Bisantino T, Fischer P, Gentile F (2010) Rheological characteristics of debris-flow material in south-Gargano watersheds. Nat Hazards 54:209–223. https://doi.org/10.1007/s11069-009-9462-4

CEI (2022) Building resilience in a changing environment - launch of ResiliENHANCE platform. Central European Initiative, Trieste, Italy. https://www.cei.int/news/9470/building-resilience-in-a-changing-environment-launch-of-resilienhance-platform. Accessed 21 July 2023

GADRRRES (2023) Global Alliance for Disaster Risk Reduction & Resilience in the Education Sector. https://gadrrres.net/. Accessed 21 July 2023

ICL (2023a) International Consortium on Landslides. https://www.landslides.org/. Accessed 28 Jan 2023

ICL (2023b) International Consortium on Landslides. Kyoto 2020 Commitment. https://www.landslides.org/ipl-info/2020-landslide-kyoto-commitment/. Accessed 26 Jan 2023

Jemec Auflič M, Šegina E, Peternel T, Zupan M, Jež J, Žebre M, Kralj P, Zajc M, Mikoš M, Bezak N, Kobal M (2022) Monitoring of rockfall prone areas in eastern Slovenia. In: Peranić J et al (eds) Landslide modelling & applications: proceedings of the 5th ReSyLAB, pp 75–79. https://repozitorij.rgn.unizg.hr/islandora/object/rgn:2214/datastream/FILE0/download. Accessed 20 July 2023

Jurček T (2020) Laboratorijske meritve reologije naravnega drobirskega materiala = Laboratory analysis of natural debris material rheology. MSc Thesis, University of Ljubljana, Faculty of Civil and Geodetic Engineering, 76 p, https://repozitorij.uni-lj.si/IzpisGradiva.php?id=119485. Accessed 20 July 2023

Jurček T, Mikoš M, Maček M (2022) Laboratory rheology measurements of natural debris material. In: Peranić J et al (eds) Landslide modelling & applications: proceedings of the 5th ReSyLAB, pp 207–212. https://repozitorij.rgn.unizg.hr/islandora/object/rgn:2214/datastream/FILE0/download. Accessed 20 July 2023

Kaitna R, Rickenmann D, Schatzmann M (2007) Experimental study on rheologic behaviour of debris flow material. Acta Geotech 2:71–85. https://doi.org/10.1007/s11440-007-0026-z

Kuzmanić T, Mikoš M (2022a) Effect of coarse gravel and cobble size particles' shape on their dynamic image analysis results. EGU General Assembly 2022, Vienna, Austria, 23–27 May 2022, EGU22-4865. https://doi.org/10.5194/egusphere-egu22-4865

Kuzmanić T, Mikoš M (2022b) Dynamic image analysis of clasts' morphological changes due to fluvial abrasion. Proceedings of the 39th IAHR World Congress (Online), pp 582–587. https://doi.org/10.3850/IAHR-39WC252171192022937

Kuzmanić T, Lebar K, Mikoš M (2023) Comparison of different-energy-level abrasion in Los Angeles and micro-Deval apparatuses using mass loss and rounding of sediment particles. Appl Sci 13(10):6102. https://doi.org/10.3390/app13106102

Mikoš M (2020) After 2000 Stože landslide—part I - development in landslide research in Slovenia. Acta Hydrotech 33(59):129–153. https://doi.org/10.15292/acta.hydro.2020.09

Mikoš M (2021) After 2000 Stože landslide: part II - development of landslide disaster risk reduction policy in Slovenia. Acta Hydrotechnica 34(60):39–59. https://doi.org/10.15292/acta.hydro.2021.04

Mikoš M (2023a) Landslide research and technology in patent documents. In: Alcántara-Ayala I et al (eds) Progress in landslide research and technology. Volume 1 Issue 2, 2022, pp 29–48. https://doi.org/10.1007/978-3-031-18471-0_3

Mikoš M (2023b) Landslide research and technology in international standards. In: Alcántara-Ayala I et al (eds) Progress in landslide research and technology. Volume 2 Issue 1, 2023. in print

Mikoš M (2023c) Landslides in higher education curricula and beyond. In: Abolmasov B et al (eds) Progress in landslide research and technology. Volume 2 Issue 1, 2023. in print

Mikoš M, Jaeggi MNR (1995) Experiments on motion of sediment mixtures in a tumbling mill to study fluvial abrasion. J Hydraul Res 33:751–772. https://doi.org/10.1080/00221689509498550

Mikoš M, Bezak N (2021) Debris flow modelling using RAMMS model in the alpine environment with focus on the model parameters and main characteristics. Front Earth Sci 8:605061. https://doi.org/10.3389/feart.2020.605061

Mikoš M, Bezak N, Logar J, Maček M, Petkovšek A, Petrovič D, Sodnik J (2021a) Landslides in weathered flysch: from activation to deposition (WCoE 2017–2020). In: Sassa K, Mikoš M, Sassa S, Bobrowsky PT Takara K, Dang K (eds) Understanding and reducing landslide disaster risk. WLF 2020. ICL contribution to landslide disaster risk reduction. Springer, Cham. 235–240. https://doi.org/10.1007/978-3-030-60196-6_15

Mikoš M, Sassa K, Arbanas Ž (2021b) The ICL journal landslides—16 years of capacity development for landslide risk reduction. In: Sassa K, Mikoš M, Sassa S, Bobrowsky PT, Takara K, Dang K (eds) Understanding and reducing landslide disaster risk. WLF 2020. ICL contribution to landslide disaster risk reduction. Springer, Cham. https://doi.org/10.1007/978-3-030-60196-6_9

Mikoš M, Jemec Auflič M, Jež J, Bezak N (2022) Rock frost weathering and rockfall activity assessment in Slovenia. In: Peranić J et al (eds) Landslide modelling & applications: proceedings of the 5th regional symposium on landslides in the Adriatic-Balkan Region, pp 137–144. https://repozitorij.rgn.unizg.hr/islandora/object/rgn:2214/datastream/FILE0/download. Accessed 20 July 2023

Mikoš M, Sassa K, Han Q (2023a) International Programme on landslides—a short overview of its historical development. In: Sassa K, Konagai K, Tiwari B, Arbanas Ž, Sassa S (eds) Progress in landslide research and technology, volume 1 issue 1, 2022, Progress in landslide research and technology. Springer, Cham, pp 45–62. https://doi.org/10.1007/978-3-031-16898-7_3

Mikoš M, Bezak N, Pita Costa J, Besher M, Novalija I, Jermol M, Grobelnik M (2023b) Natural-Hazard-related web observatory as a sustainable development tool. In: Sassa K, Konagai K, Tiwari B, Arbanas Ž, Sassa S (eds) Progress in landslide research and technology, volume 1 issue 1, 2022, Progress in landslide research and technology. Springer, Cham, pp 83–97. https://doi.org/10.1007/978-3-031-16898-7_5

NC IHP (2023) Slovenski Nacionalni odbor za Medvladni hidrološki program IHP UNESCO—Slovenian National Committee for IHP UNESCO. https://www.ncihp.si/. Accessed 20 July 2023

Peternel T, Jež J, Janža M, Šegina E, Zupan M, Markelj A, Novak A, Jemec Auflič M, Logar J, Maček M, Bezak N, Sodnik J, Mikoš M (2022a) Mountain slopes above Koroška Bela (NW Slovenia)—a landslide prone area. In: Peranić J et al (eds) Landslide modelling & applications: proceedings of the 5th regional symposium on landslides in the Adriatic-Balkan region, pp 13–18. https://repozitorij.rgn.unizg.hr/islandora/object/rgn:2214/datastream/FILE0/download. Accessed 20 July 2023

Peternel T, Janža M, Šegina E, Bezak N, Maček M (2022b) Recognition of landslide triggering mechanisms and dynamics using GNSS, UAV photogrammetry and in situ monitoring data. Remote Sens (Basel) 14(14):3277. https://doi.org/10.3390/rs14143277

Peternel T, Šegina E, Jež J, Jemec Auflič M, Janža M, Logar J, Mikoš M, Bavec M (2022c) Review of the research and evolution of landslides in the hinterland of Koroška Bela settlement (NW Slovenia). Geologija 65(2):129–147. https://doi.org/10.5474/geologija.2022.008

NAIADES (2022). https://naiades-project.eu/. Accessed 20 July 2023

NAIADES Water Observatory (2023) Monitoring water related events to explore relevant water issues. http://naiades.ijs.si/. Accessed 20 July 2023

Sassa K (2015) ISDR-ICL Sendai partnerships 2015–2025 for global promotion of understanding and reducing landslide disaster risk. Landslides 12(4):631–640. https://doi.org/10.1007/s10346-015-0586-1

Sassa K (2021a) The Kyoto landslide commitment 2020: launched. Landslides 18(1):5–20. https://doi.org/10.1007/s10346-020-01575-4

Sassa K (2021b) New open access book series "Progress in Landslide Research and Technology". Landslides 18(11):5–20. https://doi.org/10.1007/s10346-021-01759-6

Sassa K, Mikoš M (2023) Introduction: aim and outline of the book series "Progress in Landslide Research and Technology". In: Sassa K, Konagai K, Tiwari B, Arbanas Ž, Sassa S (eds) Progress in landslide research and technology, volume 1 issue 1, 2022, Progress in landslide research and technology. Springer, Cham, pp 1–8. https://doi.org/10.1007/978-3-031-16898-7_1

Sodnik J, Mikoš M (2022a) Celovito reševanje problematike masnih tokov na hudournikih pod Krvavcem. In: 33. *Mišičev vodarski dan - zbornik : 5. oktober 2022, Maribor*. pp 95–107, https://www.mvd20.com/mvd33/MVD33-pdf.pdf

Sodnik J, Mikoš M (2022b) The Krvavec bottom cabin lift station protection against torrential hazards by a new slit check dam and a series of flexible net barriers. In: Peranić J et al (eds) Landslide modelling & applications: proceedings of the 5th ReSyLAB, pp 219–224. https://repozitorij.rgn.unizg.hr/islandora/object/rgn:2214/datastream/FILE0/download. Accessed 20 July 2023

SPRINT (2022) RESILIENHANCE program. UNESCO Chair on Intersectoral safety for disaster risk reduction and resilience, SPRINT-Lab, University of Udine, Italy. https://unescochair-sprint.uniud.it/en/resilienhance-program/. Accessed 21 July 2023

UNDRR PreventionWeb (2015) Sendai framework for disaster risk reduction 2015–2030. United Nations Office for Disaster Risk Reduction, Geneva. Available at: https://www.preventionweb.net/files/43291_sendaiframeworkfordrren.pdf. Accessed 28 Jan 2023

UNESCO (2022) IHP-IX: strategic plan of the intergovernmental hydrological programme: science for a water secure world in a changing environment, ninth phase 2022–2029. UNESCO, Paris. 51 p. https://unesdoc.unesco.org/ark:/48223/pf0000381318. Accessed 9 Feb 2023

UNESCO (2023) IHP-IX: operational implementation plan: key activities and output-level performance indicators; science for a water secure world in a changing environment, ninth phase 2022–2029. UNESCO, Paris. 35 p. https://unesdoc.unesco.org/ark:/48223/pf0000384615. Accessed 21 July 2023

UNESCO Venice (2022) First regional meeting of science-related UNESCO Centres and chairs for south-East Europe and the Mediterranean. UNESCO Regional Bureau for Science and Culture in Europe, Venice, Italy. https://www.unesco.org/en/articles/first-regional-meeting-science-related-unesco-centres-and-chairs-south-east-europe-and-mediterranean?hub=66976. Accessed 21 July 2023

Verbovšek T, Rožič B, Žvab Rožič P, Vrabec M, Jordanova G, Dolenec M, Fifer Bizjak K, Bezak N, Mikoš M, Kuzmanić T, Kregar K, Kozmus Trajkovski K, Žagar D (2021) Ocena relativne erodibilnosti klifov na Slovenski obali. In: Rožič B (ed) Razprave, poročila = Treatises, reports: 25. posvetovanje slovenskih geologov = 25th Meeting of Slovenian Geologists, pp 146–147

Verbovšek T, Rožič B, Žvab Rožič P, Vrabec M, Jordanova G, Dolenec M, Fifer Bizjak K, Bezak N, Mikoš M, Kuzmanić T, Kregar K, Kozmus Trajkovski K, Žagar D (2022) An upgrade to the erosion risk assessment method of active flysch cliffs along the Slovenian coast. In: Peranić J et al (eds) Landslide modelling & applications: proceedings of the 5th ReSyLAB, p 34. https://repozitorij.rgn.unizg.hr/islandora/object/rgn:2214/datastream/FILE0/download. Accessed 20 July 2023

WRDRR Chair (2023) UNESCO Chair on water-related disaster risk reduction. University of Ljubljana, Slovenia. https://www.unesco--floods.eu/. Accessed 21 July 2023

The Integrated Landslides Monitoring System of Gimigliano Municipality, Southern Italy

Giovanna Capparelli, Serena Artese, Andrea Carri, Margherita Lombardo, Andrea Segalini, Alessandro Valletta, and Francesco Muto

Abstract

Monitoring the stability of a slope is one of the non-structural measures aimed at reducing the risk of landslides. Displacement detection is now possible through numerous monitoring techniques, including remote sensing and ground-based solutions. In particular, in-situ monitoring allows some advantages related to using low-cost instruments whose communication can be facilitated by IoT technologies. In this chapter, we illustrate an example of an intelligent system for the integrated monitoring of the main landslide bodies of Gimigliano (CZ), southern Italy.

The station includes clusters for monitoring deep movements and piezometric levels, as well as for urban structures through specific sensors and a network of sensors for topographic surface monitoring. The system was designed to be almost fully automatic and oriented to support near real-time warning activities. The data recorded by the deep and surface monitoring instruments confirm that the study area is affected by complex phenomena requiring long-term on-site monitoring.

Specifically, analysis of the deep movements revealed some critical events during spring 2022 and summer 2023 that resulted in positive and negative millimetric deformations, measured by the tilt meters installed in correspondence with the monitored sites. Surface topographic analysis indicates displacement rates of 2.5–5 cm/year.

Keywords

Landslide monitoring · On-site monitoring systems · Early warning · IoT technologies

G. Capparelli (✉)
C.A.M.I. Lab, Department of Computer, Modeling, Electronic, and System Engineering, University of Calabria, Rende, Italy
e-mail: giovanna.capparelli@unical.it

S. Artese
Spring Research S.r.l., University of Calabria, Rende, Italy
e-mail: serena.artese@unical.it

A. Carri
ASE – Advanced Slope Engineering S.r.l., Via R. Koch 53/A, 43123 Fraz. Pilastrello, Parma, Italy
e-mail: andrea.carri@aseltd.eu

M. Lombardo
Department of Civil, Environmental, Land, Building Engineering, and Chemistry, Polytechnic University of Bari, Bari, Italy
e-mail: margherita.lombardo@poliba.it

A. Segalini · A. Valletta
Department of Engineering and Architecture, University of Parma, Parma, Italy
e-mail: alessandro.valletta@unipr.it

F. Muto
Spring Research S.r.l., University of Calabria, Rende, Italy

Department of Biology, Ecology and Earth Sciences,, University of Calabria, Rende, Italy
e-mail: francesco.muto@unical.it

1 Introduction

Landslides are caused by disturbances in the natural stability of a slope. They can be activated by heavy rains or follow other natural disasters such as earthquakes or volcanic eruptions.

Landslides are generally classified (Cruden 1991) by type of movement (slides, flows, spreads, topples, or falls) and type of material (rock, debris, or earth).

Sometimes, more than one type of movement occurs within a single landslide, and since the temporal and spatial relationships of these movements are often complex, their analysis often requires a detailed interpretation of both landforms and geological sections or cores (Meng 2023).

Landslides pose a recurrent hazard to human life and livelihood in most parts of the world, especially in some regions that have experienced rapid population and economic growth.

B. Abolmasov et al. (eds.), *Progress in Landslide Research and Technology, Volume 3 Issue 1, 2024*, Progress in Landslide Research and Technology, https://doi.org/10.1007/978-3-031-55120-8_24

Roughly 4500 people are killed worldwide yearly by landslides (Froude and Petley 2018), and related risk is expected to increase due to climate change and urbanization (Ozturk et al. 2022).

Italy is one of the countries most affected by mass movement, often involving urban areas (Salvati et al. 2010; Haque et al. 2016). According to the most recent mosaics, more than 8% of the Italian peninsula lies at high landslide hazard, with more than one million people and more than five hundred thousand buildings at significant risk (Trigila et al. 2021).

Hazards are mitigated mainly by non-structural measures, by restricting or even removing populations from areas with landslides, by restricting certain types of land use, and by installing early warning systems based on the monitoring of ground conditions such as strain in rocks and soils, slope displacement, and groundwater levels.

Risk mitigation strategies also include structural measures, acting directly on the hazard (Dai et al. 2002), such as internal slope reinforcement, anchors, barriers, slope reshaping, plumbing, and drainage (see, e.g., Genevois et al. 2022), but the implementation of such structural solutions is not always feasible mainly due to cost, environmental impact, and long-term maintenance needs (Anderson et al. 2022).

Moreover, as came out from the Kyoto 2020 Commitment for Global Promotion of Understanding and Reducing Landslide Disaster Risk (KLC2020), a comprehensive approach to landslide risk mitigation should prioritize actions aiming at improving the technologies for monitoring slope stability and supporting early warning. Thus, landslide monitoring became an important prerequisite for proactive landslide risk management, contributing to increased safety and resilience in landslide-prone areas (Huntley et al. 2023).

In order to mitigate landslide-related risk, several landslide-monitoring systems have been developed. Such significant growth was possible due to the development of landslide monitoring technologies (Eberhardt 2012; Klimeš et al. 2017) over the last decades, including both remote sensing (Kimura and Yamaguchi 2000; Casagli et al. 2023) and ground-based solutions (Tarchia et al. 2003; Maheshwari and Bhowmik 2021).

They involve different technologies and processing methods according to landslide type and spatial and temporal scale of analysis. In general, nanotechnology has led to the development of smaller, cheaper, more reliable, and more functional borehole sensors that, together with wireless data acquisition and transmission, have significantly increased the temporal resolution of soil deformation.

Due to their complex kinematics and extension over large and low-accessible areas, landslides often call for the integration of different methods and techniques in order to measure surface and deep modification (Nikolakopoulos et al. 2017). Instruments can include total stations (Artese and Perrelli 2018; Stiros et al. 2004; Tsaia et al. 2012), photogrammetry (Scaioni et al. 2015), laser scanners (Kasperski et al. 2010; Mallet and Bretar 2009), Global Navigation Satellite System (GNSS) (Josep et al. 2000).

However, despite significant progress in Earth observation, satellite-based techniques are mainly used during pre-investigation phases, providing an overview of slope stability issues in the area of interest. On the contrary, ground-based and on-site systems usually provide details for local investigations (Pecoraro et al. 2019).

In particular, on-site monitoring systems involve using sensors and instruments directly within or near the area prone to landslides (see, e.g. Wang et al. 2022) to provide an understanding of slope behavior over time and typical responses to external factors, such as rainfall.

Some common components of on-site monitoring systems include geotechnical and hydrogeological devices such as tiltmeters, inclinometers, piezometers, rainfall gauges, and seismic sensors, together with GPS receivers (Auflič et al. 2023).

Key requirements for a well-designed monitoring system are cost effectiveness, robustness, flexibility, scalability, and suitability for long-term and real-time monitoring (Lau et al. 2023). Recent advances in landslide monitoring include emerging technologies such as the Internet of Things (IoT), allowing interoperability and intelligent communication with services and applications in the cloud using Internet standards (Thirugnanam et al. 2022).

By analyzing collected data from these instruments, often involving low-cost sensors (Glabsch et al. 2009; Artese et al. 2015), on-site monitoring can provide real-time information about changing conditions, allowing effective landslide early warning (Xu et al. 2020).

This information is essential for implementing an evacuation plan and making informed decisions to reduce the potential impact of the hazardous event (Strouth and McDougall 2022).

Within the above framework, this paper describes the almost fully automatic monitoring system in the municipality of Gimigliano, in the Calabria region, South of Italy, as an example of a multi-parametric structure for early warning and risk management purposes.

For monitoring and enforcing the understanding of the mechanism of large-scale landslides, we designed a system that can operate autonomously and in near real-time mode, an essential requirement for risk mitigation procedures. The monitoring system is composed of clusters including sensors for controlling deep movements and pore water pressure, as well as specific strain gauge sensors for the control of urban structures—buildings, walls—and a network of local sensors for topographic surface monitoring using a global positioning system.

After a detailed description of the involved area, the sections provide the analysis of the main components of the monitoring system and the devices adopted for early-communication, then some results of the recent activity focusing on movements recorded in 2022 and 2023.

2 Study Area: Geographical and Geological Setting

The Municipality of Gimigliano covers an area of 33 square kilometers and is located in Calabria, Southern Italy. The site is located within the structural geological framework of northern Calabria and, more precisely, of Sila Piccola. This sector is made up of the metamorphic units of the Alpine chain, which overlay the Apennine carbonates. The alpine and Apennine thrust sheets structures of the Sila Piccola result offset by regional high-angle faults starting from the Neogene-Quaternary time. The occurrence of tectonic deformation phases affecting the study area contributed to the alteration of rocks and the geological predisposition to landslide. The entire territory of the town of Gimigliano consists of a complex and articulated geological setting, both stratigraphically and structurally. The entire structure of the Gimigliano area is made up of overlain Paleozoic crystalline rocks overthrust on Mesozoic metamorphic ophiolithiferous rocks (Chidichimo et al. 2023). From bottom to top, the lithologies out-cropping in the Gimigliano area are composed of metamorphic rocks such as phyllites, schists, and quartzites belonging to the deepest tectonic unit. These rocks are overthrusted by a succession composed of serpentinites and greenschists with a cover of metalimestones, marbles, metarenites, and metapelites belonging to the upper Mesozoic ophiolitic nappe. The uppermost thrust sheet is made up of schists, porphyroids, ortho, and paragneiss of the Paleozoic-derived nappes.

The complex geological framework is affected by brittle deformation with the development of open antiformal folding, extensional low-angle faults (Muto and Perri 2002; Mattei et al. 2002; Rossetti et al. 2001), high-angle tectonic structures such as regional and local strike-slip fault systems cross-cutting, and displaying the metamorphic rocks (Tansi et al. 2007; Brutto et al. 2016; Tripodi et al. 2018). The main landslide is 1.100 m in length and about 600 m wide. Along the contact between the lower and the upper ophiolitic rocks, at a depth of 46–60 m, has been recognized the sliding surfaces of gravitational origin of the main active landslide (Ausilio and Zimmaro 2017; Chidichimo et al. 2023) named GIM 2 in this study (Fig. 1). The Gimigliano area is also affected by several landslide phenomena, characterized by medium (GIM 1 in Fig. 1) to shallow depth with different state of activity, areal distributions, and magnitude (Fig. 1).

Mass movements are mainly triggered by intense precipitation, usually in single daily rainfall events, which strongly impacts the weathering and degradation of the rocks. The presence of large and medium-sized landslides, as well as movements considered superficial, is evidenced by the continuous deformation of all the infrastructures and buildings studied and surveyed.

Among all the instability phenomena that affect the territory of Gimigliano, the landslides that affect the most recently urbanized area deserve the most attention. They can be divided into two main bodies (GIM1 and GIM2 in Fig. 1) and a series of minor bodies characterized by predominantly sliding kinematics and different activity states.

Previous studies and investigations indicate the Gimigliano landslide as a deep-seated landslide phenomenon with a well-identified sliding surface around the depth of 60 m in the central zone of the landslide body.

The movement appears active, with velocities ranging from slow to very slow (1 cm/year to 5 cm/year). Other landslides in the area of the main scarp cover the main body. These are composite and complex landslide types with depths not exceeding 15 m. Frequent superficial and fast phenomena are triggered as debris flows and avalanches from the crowning-scarp zone.

Previous studies described the highly complex and articulated geological-structural framework of the Gimigliano area (see, e.g., Van Dijk et al. 2000; Tansi et al. 2007; Bianchini et al. 2013; Brutto et al. 2016; Gullà et al. 2021).

The area of the main landslide (GIM 2 in Fig. 1) is also characterized by a complex hydrogeological pattern, which has been the subject of studies and numerical modelling (Chidichimo et al. 2023). Groundwater circulation is strongly influenced by the permeability of the different lithological units, phyllites, serpentinites, greenschists, marbles, and their different degrees of alteration and fracturing. Piezometric measurements and the presence of numerous water springs have provided useful information on the interstitial pressure regime (Chidichimo et al. 2023). The combination of deep and shallow phenomena, whose effects add up in time and space, exposes the entire Gimigliano slope to a very high landslide risk.

In selecting the areas to be monitored, priority was given to areas with high population density, presence of strategic buildings, and communication routes, while areas affected by structural measures to reduce the risk and areas with manual monitoring stations (fixed inclinometers and piezometers) were excluded.

However, in order to monitor and understand the ongoing phenomena, we planned a system capable of operating

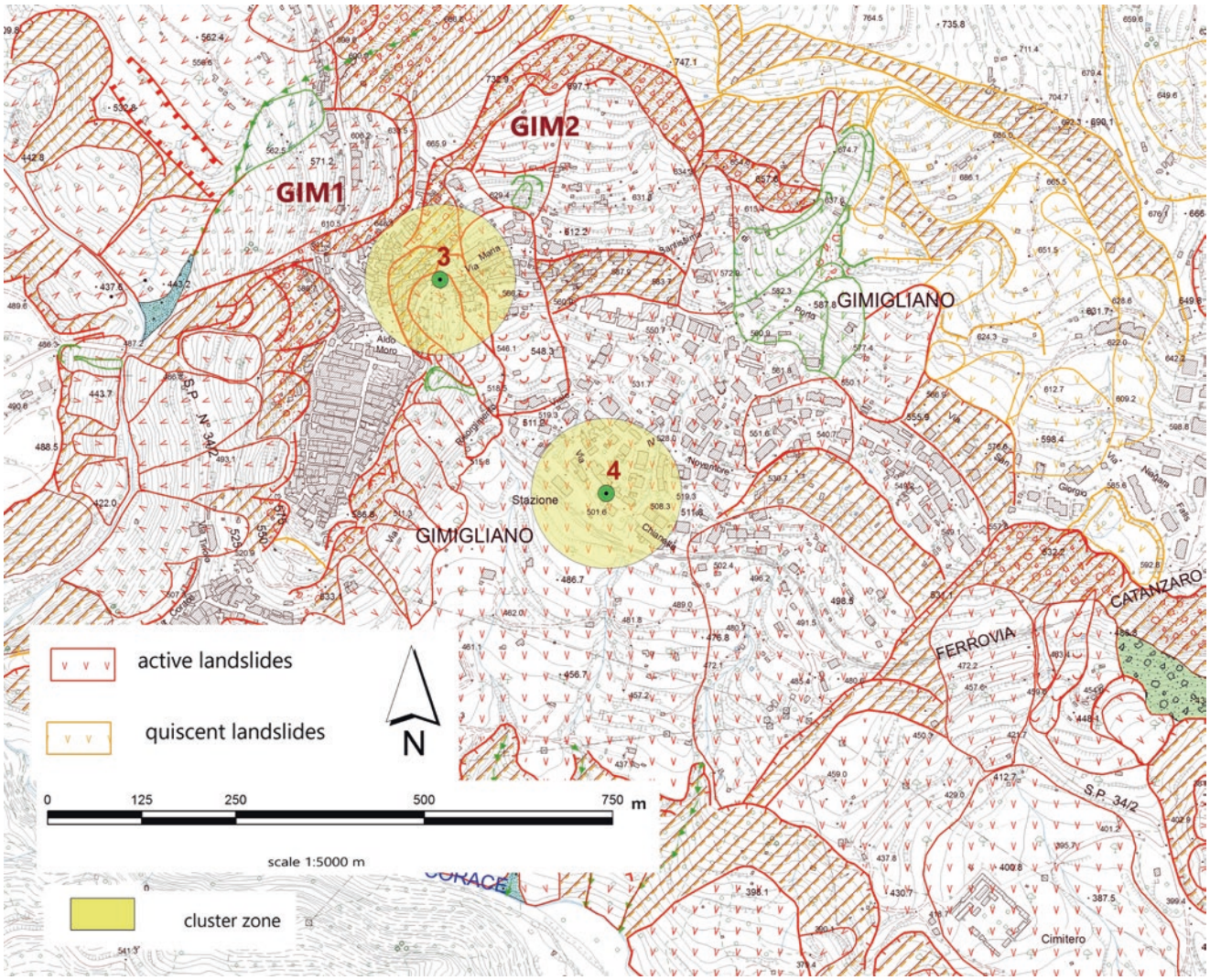

Fig. 1 Location and landslide distribution of the study area

autonomously and in near real-time mode, a prerequisite for risk mitigation.

The proposed monitoring network is composed of the following elements: cluster stations for the monitoring of deep movements and piezometric levels, as well as for the control of urban structures through specific sensors, and a network of sensors for topographic surface monitoring. They will be discussed in detail in the following sections.

3 Description of the Monitoring Systems

3.1 Deep Movements and Piezometric Levels Monitoring

The monitoring activity of the municipality of Gimigliano was planned to assess the effect of slope movements on different parts of the area of interest, focusing on the definition of underground displacements and consequences for buildings and infrastructure.

These requirements made it necessary to design a system that integrates sensors based on different technologies to provide a comprehensive description of the observed phenomenon.

Following this approach, an automatic monitoring system based on MUMS (Modular Underground Monitoring System) technology was designed and installed on-site.

MUMS is an innovative monitoring system developed and patented by ASE S.r.l. (IT), composed of a series of synthetic resin nodes, named Links, connected by an aramid fibre cable and a single quadrupole electrical cable to form an arbitrarily long array of sensors (Segalini et al. 2014).

MUMS devices are customizable for the sensor's number, distance, and typology, thus obtaining a multi-parametric

structure able to measure different physical quantities depending on the specific case study requirements.

The monitoring process is completely automated, using Internet of Things (IoT) technologies to enhance communication and interaction among system components.

Through this approach, it becomes feasible to achieve high sampling frequencies and gather a significant amount of information about the monitored element.

Moreover, integrating algorithms to identify potentially critical events allows for implementing this system for early warning and risk management. The result is a synergic procedure incorporating data acquisition, processing, storage, and representation (Carri et al. 2021).

For the case study discussed here, the monitoring system was designed to include both traditional instrumentation and innovative MUMS-based devices. Specifically, several crack meters and tilt meters were installed on selected structures of the area (i.e., buildings and retaining walls) in order to detect their interaction with potential slope movements. Moreover, two In Place Array were installed on site, with Links placed at specific depths defined according to previously available data.

Array DT0174 is 70 m long, while the instrumented part of the device is located between 45 and 65 m in depth with a node distance of 2 m. These devices will allow the detection of local and cumulative displacements with a near-real-time approach thanks to the automated process for data acquisition and transmission. Additionally, the Array integrates four piezometers installed at 10, 25, 42, and 67 m of depth in order to measure the water level variation over time.

Array DT0176 is 30 m long and presents a variable distance between Links depending on their position: one every 2 m from 2 to 12 m of depth and one every 3.50 m from 12 to 26 m. It also includes two piezometers located 11 and 28 m in depth.

A comprehensive overview of the position of each device installed in the area of interest is given in Fig. 2.

Due to the system complexity and extension of the area, the site of interest was divided into two main Clusters and five zones to provide a clearer identification of the position of each device, allowing more efficient planning for the installation of data loggers.

Cluster 1 contained the western area of interest, including the current and the Old Town Hall, a private building, the local Police station, and two retaining walls, and it is divided into three zones.

Cluster 2 is located on the eastern side of the municipality and encompasses two schools and three retaining walls, and it is divided into two more zones. Tables 1 and 2 provide additional details regarding the instrumentation features, referring to Cluster 1 and 2, respectively.

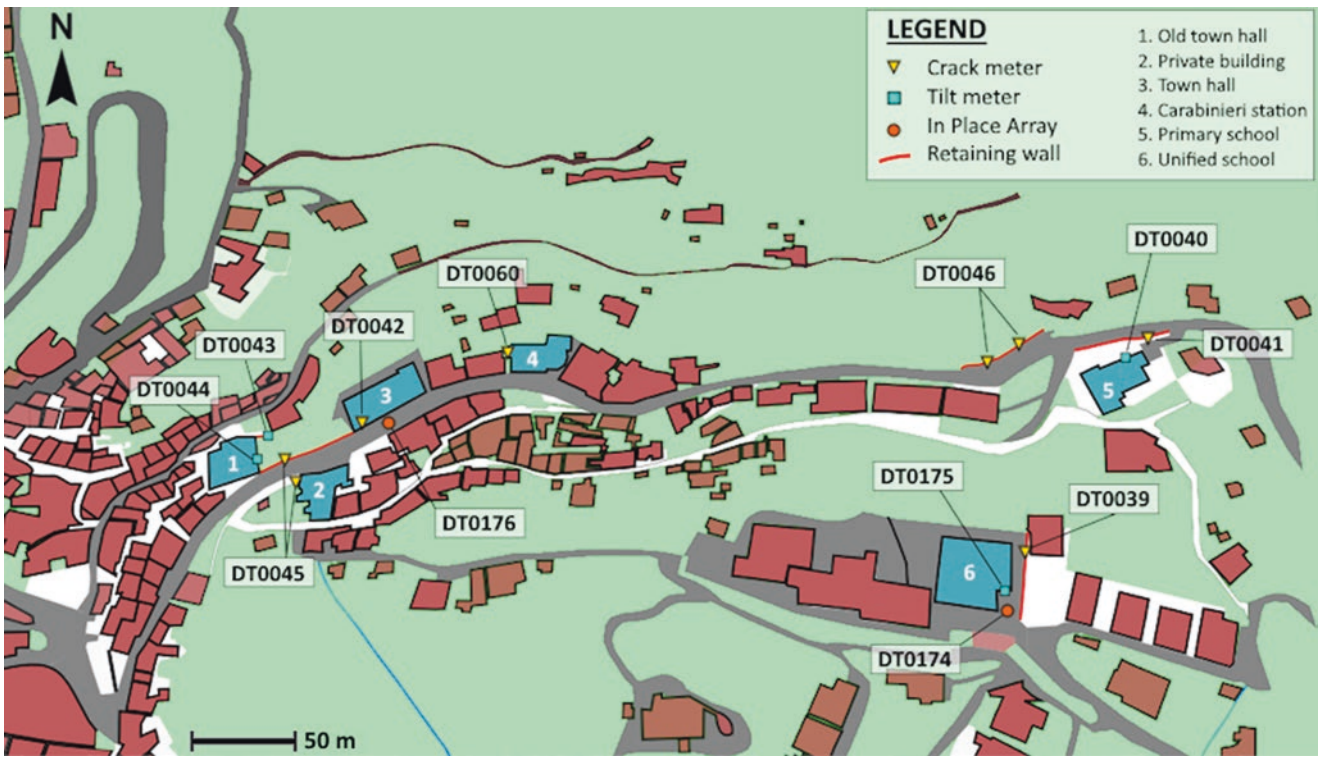

Fig. 2 Monitoring system installed in the study area

Table 1 Monitoring instrumentation installed in Cluster 1

Zone	Datalogger ID	Array ID	Array type	Sensors	Reference reading date [dd/mm/yyyy]
4	ID0143	DT0039	Analog	1x crack meter	02/12/2021
4	ID0143	DT0174	In place	1x barometer 4x piezometer 11x in place link HD	13/01/2022
4	ID0143	DT0175	Klino	2x tilt meter	01/12/2021
5	ID0144	DT0040	Klino D2W	1x tilt meter	12/01/2022
5	ID0145	DT0041	Analog	1x crack meter	02/12/2021

Table 2 Monitoring instrumentation installed in Cluster 2

Zone	Datalogger ID	Array ID	Array type	Sensors	Reference reading date [dd/mm/yyyy]
1	ID0146	DT0042	Analog	1x crack meter	02/12/2021
1	ID0146	DT0176	In place	2x piezometer 10x in place link HD	11/02/2022
2	ID0147	DT0043	Klino D2W	1x tilt meter	12/01/2022
2	ID0148	DT0044	Klino D2W	1x tilt meter	12/01/2022
2	ID0149	DT0045	Analog	2x crack meter	02/12/2021
3	ID0150	DT0046	Analog	2x crack meter	03/12/2021
4	ID0172	DT0060	Analog	1x crack meter	23/02/2022

3.2 Geodetic Monitoring

The geodetic monitoring of the surface is based on the analysis of the variations over time of the angular and distance measurements of points (inside and/or near the landslide) with respect to reference points.

As a result, the graphical and numerical restitution of the geometric characteristics and the morphological variations are obtained, thus contributing to studying the evolutionary trend of the deep gravitational phenomenon. Since the Gimigliano area is already involved in geodetic monitoring, steps were taken to verify the existing network's functioning and then define its integration. Specifically, a Leica 1201+ precision robotic station was used for the survey activities. Targets were placed throughout the survey area, almost all anchored to buildings in the city center.

The lack of a stable point within the measuring range of the instrumentation and the visibility problems due to the topography of the area did not allow the installation of a single permanent robotic station that would allow the measurement of the entire area affected by the phenomenon under study.

Two stations were then installed, and periodic monitoring was carried out. The station points were selected to guarantee their stability and to maximize the visibility of the area affected by the landslide and the number of points visible by both stations. Station 1 is situated on the terrace of the rectory church, located in the historic center of the town.

The monumentation of the station was achieved by fixing a tripod for surveying instruments directly on the terrace floor. Station 2 is situated on a terrain in front of the historical centre and opposite to station 1, characterized by rocky outcrops. On this last point, an iron pillar was built with the connection base of the total station at the top.

Three stable orientations were chosen for referencing the monitoring network, visible from the two station points. Each orientation was materialized using two long-range corner reflectors close to each other and oriented to the two station points.

The first corresponds to a rock protruding under a metal cross about 8 m high on Mount Gimigliano, which dominates the historic center. The second orientation points are placed on the north wall of an abandoned building in the valley below the town.

The last orientation points are positioned on the north wall of an isolated house in front of Gimigliano, about 200 m from the Soluri hamlet, on the border between Gimigliano and the near Tiriolo town. These points were used for orientation operations and setting the instrument's reference system (Fig. 3).

Fig. 3 Location of Station (red dots) and Orientation Points (yellow dots)

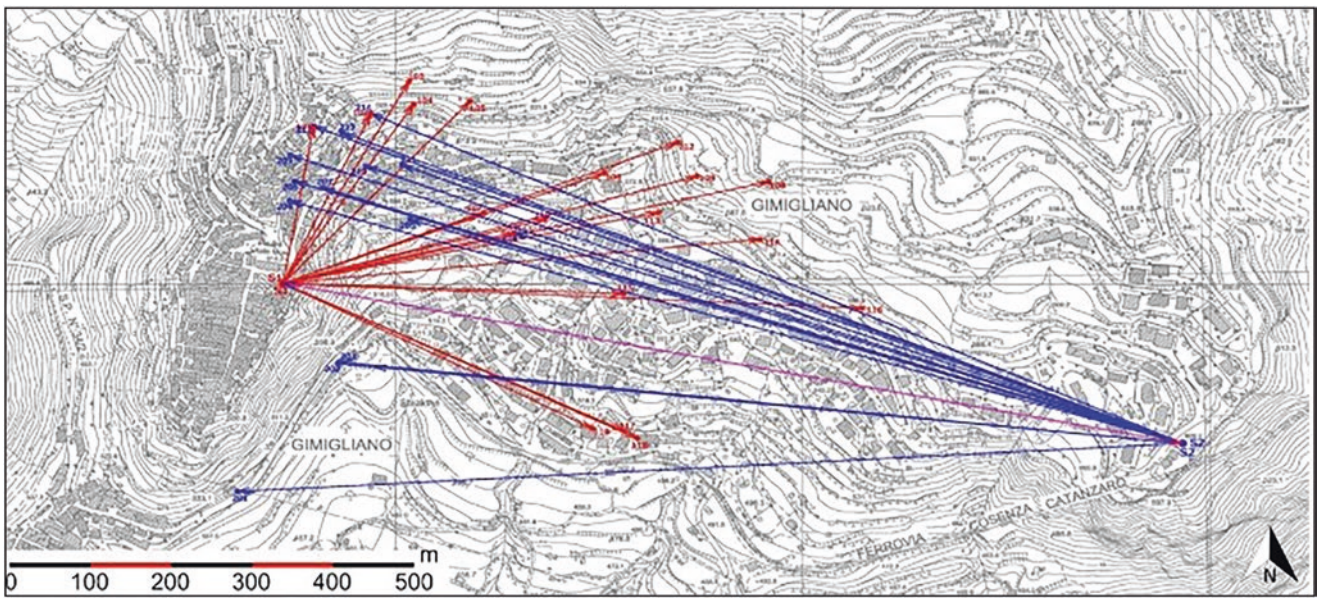

Fig. 4 Monitored points. Red arrows are the vectors measured from S1; blue arrows are the vectors measured from S2

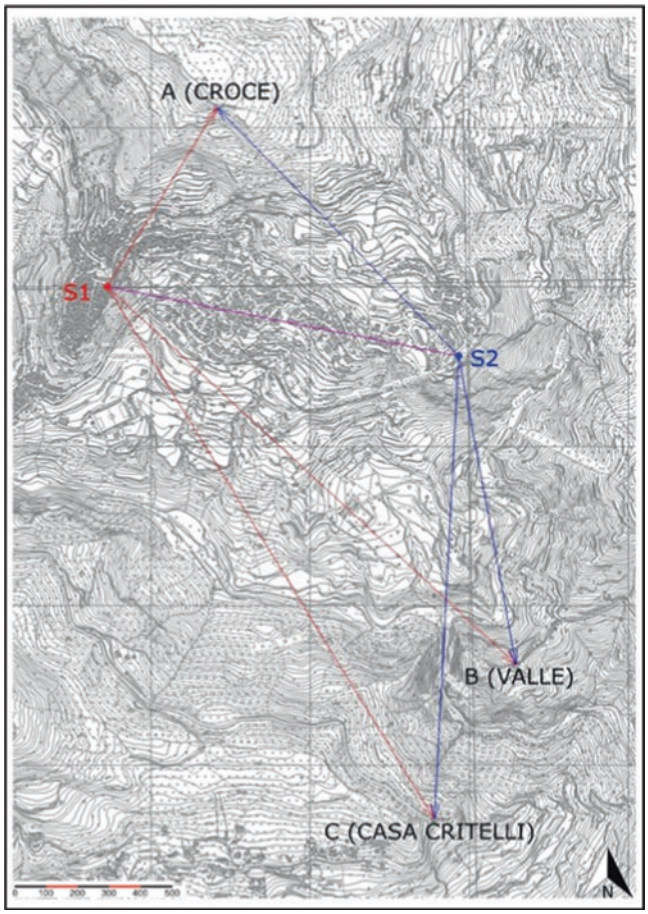

Fig. 5 Location of Station and Orientation Points. Red arrows are the vectors measured from S1; blue arrows are the vectors measured from S2

Figure 4 shows the layout of monitored points. Red vectors are acquired from station 1, while blue vectors are obtained from station 2.

A few double points are measured from both stations: this allows us to perform some verifying and to link further the surveyings carried out. Figure 5 shows the orientation points. Since the total station is periodically placed and the stations are placed near the landslide, these points are used to recalculate the station position and to compensate for possible displacements. Furthermore, the possibility to measure the three points from both stations, along with the reciprocal monitoring of the station points and the GNSS surveying of their position, allows to link the independent measurements and to have a common referencing of the observations.

4 Results and Discussion

4.1 Deep Movements

The availability of multiple devices in the same area makes it possible to detect the occurrence of anomalous events and to verify whether they affect different areas of the monitored site.

In the example discussed here, it is possible to observe the data sampled by tilt meters DT0043 and DT0044, installed respectively on a small wall connected to the old town hall and the building itself. Note that due to their relative position, the X-axis of the first sensor is aligned with the Y-axis of the second, and vice versa (Fig. 6a, b). The dataset of interest reports the tilt variation measured along both instrumental axes for the two sensors. It refers to an event that occurred on May 16, 2022. As shown in Fig. 6c, both instruments recorded a simultaneous variation of 0.18° along the X-axis for DT0043 and the Y-axis for DT0044. The similarity in the magnitude of the tilt variation recorded along two aligned axes is a good indication of the event's actual occurrence. It allows a reliable evaluation of the tilt direction. In addition, it can be noted that only DT0043 measured a tilt variation along the perpendicular axis, indicating that the retaining wall was more affected compared to the monitored building.

It should also be noted that the displacement data collected by In Place Array DT0174, the closest to the Old Town Hall included in Cluster 1, did not show any significant movement during this time period. This observation, together with the relatively small amount of tilt variation, allowed this event to be categorized as a non-critical event, and no consequences were noted at the monitored site.

DT0046 Analog Array reads two crack meters installed on the retaining wall in Cluster 2 along the main road that crosses the community. Specifically, the first sensor is installed on the right side of the wall, while the second sensor is installed on the left side at a distance of approximately 12 m (Fig. 7a, b). By comparing the measurements collected by the crack meters during the same time, it is possible to prove whether a movement affects the entire structure or a specific section of the wall.

The data set considered for this example was collected over 2 months of monitoring activity, June and July 2023, and is shown in Fig. 7c.

From this graph, it is possible to see some events where the sensor behavior diverged, showing a difference in deformation values. One of these events began on June 13 and involved only Node 1, which measured a positive deformation of 0.8 mm, corresponding to a crack opening, while Node 2 showed no trend deviation. After about 10 days, the

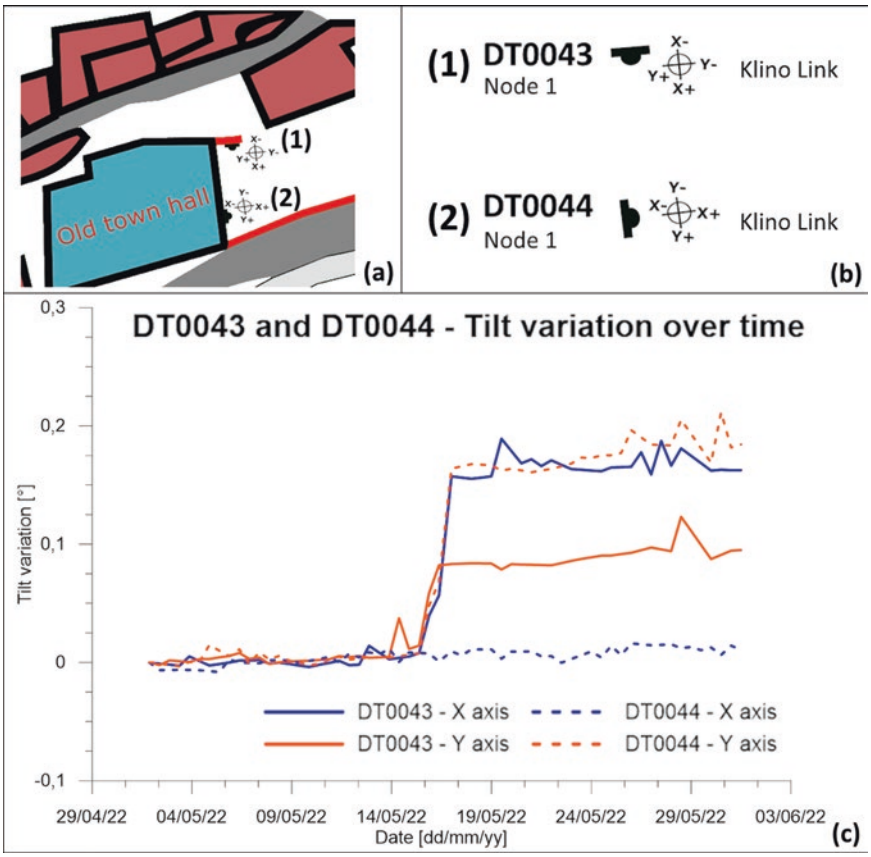

Fig. 6 (**a**) position of DT0043 and DT0044 (**b**) Frame of reference and sensor typology (**c**) tilt variation over time measured by the two tilt meters in May 2022

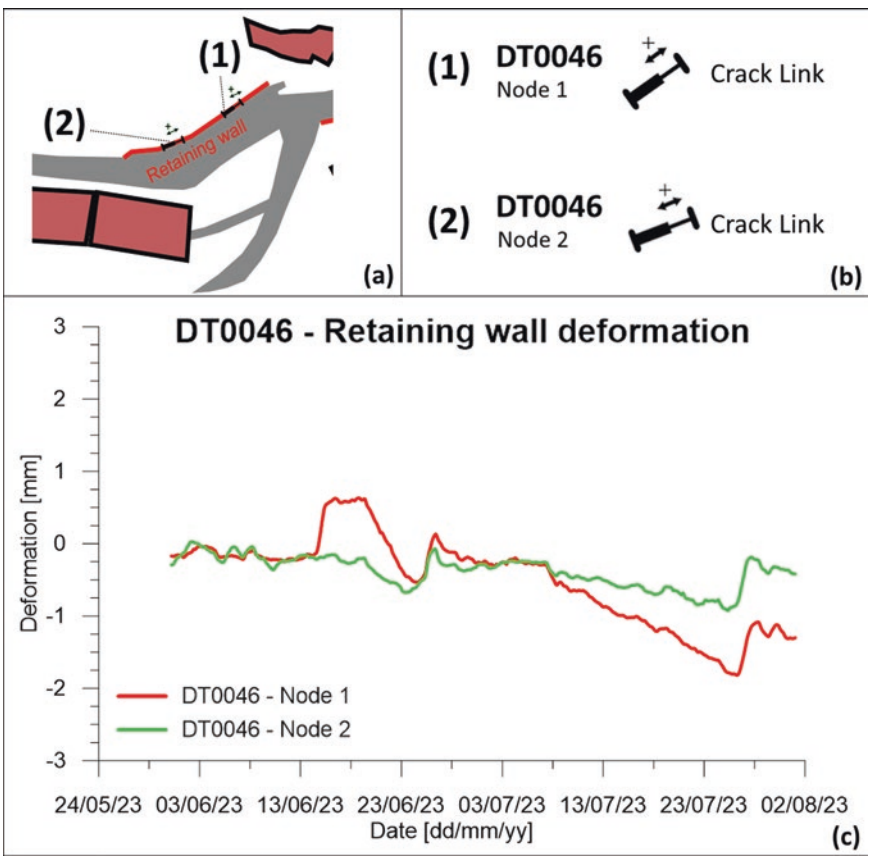

Fig. 7 (**a**) position of the crack meters integrated in DT0046 (**b**) Frame of reference and sensor typology (**c**) deformation variation over time measured by the two crack meters in June and July 2023

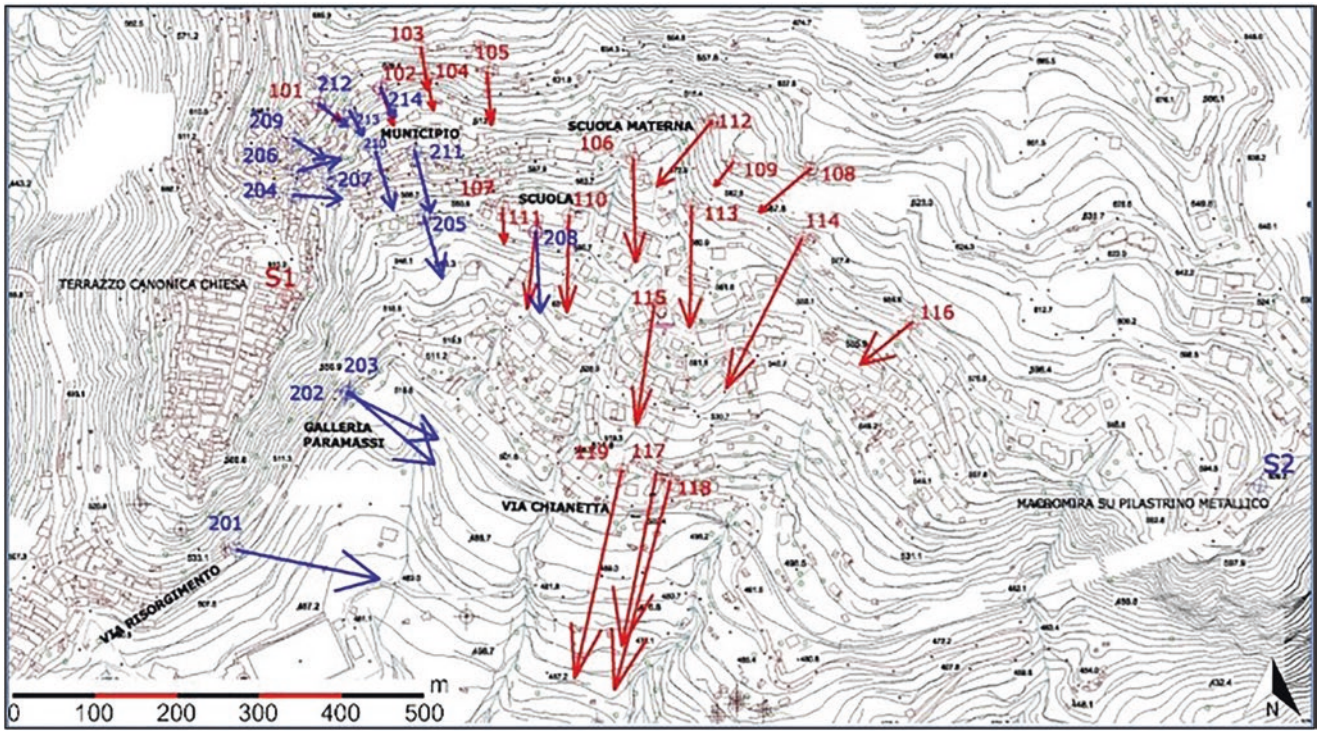

Fig. 8 The horizontal movements of the monitored points. Red arrows are the movements obtained from S1; blue arrows are the movements obtained from S2

deformation regressed, and the crack meter returned to its original position.

Another event can be observed in early July, where the deformation measured by Node 1 began to follow a downward trend, eventually reaching a value of −1.8 mm, while Node 2 showed a relatively similar pattern, although much less obvious. On the other hand, the last part of the dataset shows an example of more similar behavior for both sensors, with a slight positive increase in deformation on July 27 before reaching a stable state.

4.2 Surface Movements

A map of the detected horizontal movements of the monitored points is shown in Fig. 8. The speed of surface displacements, based on the surveys carried out, is in the range of 2.5–5 cm/year. For the same site, Fortunato and Ferrucci (2012) estimated movement speeds of up to 24 mm/year from 1993 to 2000 and up to 14 mm/year from 2002 to 2010 from the analysis of Synthetic Aperture Radar (SAR) data.

5 Conclusions

Landslides represent a significant threat to human life, properties, infrastructure, and natural environments for which in-depth analysis and increasingly reliable systems for risk control and mitigation are required. Extensive and in-depth research projects were started mainly on developing different technologies for detecting, predicting, and monitoring landslides.

Many advanced tools provide the opportunity to apply new techniques for the different stages of landslides and susceptibility, hazard, and risk assessment.

This work describes an integrated monitoring system set up for monitoring Gimigliano village, where the risk of landslide is too high and no longer justifiable for the responsible communities.

It integrates a permanent system, including devices for deep movement and piezometric levels, with periodic surface topographic monitoring. In particular, the system includes both traditional and innovative sensors as the MUMS-based devices supported by modern Internet of Things technologies for communication and interaction procedures.

The periodic monitoring over time revealed considerable deformation cycles corresponding to crack openings and regressions. Tilt meters have measured both positive and negative deformations, and surface monitoring activity has

provided the estimation of a wide field of speeds of surface displacement.

The presented system offers the advantages of a low-cost, precise, and accurate measurement system for landslide displacements, low power consumption, continuous measurements, and wireless data communication between the measurement grid and a central server. Aggregated data collected from the system makes possible an important interpretation both for defining the structural measures for risk mitigation plan but also for assessing possible highly critical situations outstanding to issue evacuation orders or orders banning traffic on the main access routes into the municipalities.

The ongoing activity of the network contributes to the collection of accurate and punctual information for future research on landslide behavior. The next goals are concerned with improving the system with an impact on the timely alerts of the surrounding communities. In particular, future activities require an enhancement of the existing system with an extension for the areas not currently monitored and a monitoring activity with highly specialized technicians trained not only for managing the monitoring network but also for direct survey control to support the decision-making phases.

Acknowledgments The authors gratefully acknowledge the financial support provided by the framework project Civil Protection Department n.473/2017 and to the Municipality for all support provided in the realization of the activities.

References

Anderson CC, Renaud FG, Hanscomb S, Gonzalez-Ollauri A (2022) Green, hybrid, or grey disaster risk reduction measures: what shapes public preferences for nature-based solutions? J Environ Manage 310:114727

Artese S, Perrelli M (2018) Monitoring a landslide with high accuracy by total station: a DTM-based model to correct for the atmospheric effects. Geosciences 8(2):46

Artese G, Perrelli M, Artese S, Meduri S, Brogno N (2015) POIS, a low cost tilt and position sensor: design and first tests. Sensors 15(5):10806–10824

Auflič MJ, Herrera G, Mateos RM et al (2023) Landslide monitoring techniques in the geological surveys of Europe. Landslides 20(5):951–965

Ausilio E, Zimmaro P (2017) Landslide characterization using a multidisciplinary approach. Measurement 104:294–301

Bianchini S, Cigna F, Del Ventisette C, Moretti S, Casagli N (2013) Monitoring landslide-induced displacements with TerraSAR-X persistent scatterer interferometry (PSI): Gimigliano case study in Calabria region (Italy). Int J Geosci 4:1467–1482

Brutto F, Muto F, Loreto MF, De Paola N, Tripodi V, Critelli S, Facchin L (2016) The neogene-quaternary geodynamic evolution of the central Calabrian Arc: a case study from the western Catanzaro Trough basin. J Geodyn 102:95–114

Carri A, Valletta A, Cavalca E, Savi R, Segalini A (2021) Advantages of IoT-based geotechnical monitoring systems integrating automatic procedures for data acquisition and elaboration. Sensors 21:2249

Casagli N, Intrieri E, Tofani V, Gigli G, Raspini F (2023) Landslide detection, monitoring and prediction with remote-sensing techniques. Nat Rev Earth Environ 4(1):51–64

Chidichimo F, De Biase M, Muto F, Straface S (2023) Modeling a metamorphic aquifer through a hydro-geophysical approach: the gap between field data and system complexity. Hydrology 10(4):80

Cruden D (1991) A simple definition of a landslide. Bull Eng Geol Environ 43(1)

Dai FC, Lee CF, Ngai YY (2002) Landslide risk assessment and management: an overview. Eng Geol 64:65–87

Eberhardt E (2012) Landslide monitoring: the role of investigative monitoring to improve understanding and early warning of failure. In: Clague J, Stead D (eds) Landslides: types, mechanisms and modeling. Cambridge University Press, Cambridge, pp 222–234

Fortunato G, Ferrucci F (2012) Interferometria satellitare, DEM ed analisi della dinamica altimetrica 1993–2010 –Rapporto Tecnico

Froude MJ, Petley DN (2018) Global fatal landslide occurrence from 2004 to 2016. Nat Hazards Earth Syst Sci 18(8):2161–2181

Genevois R, Tecca PR, Genevois C (2022) Mitigation measures of debris flow and landslide risk carried out in two mountain areas of north-eastern Italy. J Mt Sci 19(6):1808–1822

Glabsch J, Heunecke O, Schuhbäck S (2009) Monitoring the Hornbergl landslide using a recently developed low cost GNSS sensor network. J Appl Geod 3(3):179–192

Gullà G, Nicodemo G, Ferlisi S et al (2021) Small-scale analysis to rank municipalities requiring slow-moving landslide risk mitigation measures: the case study of the Calabria region (southern Italy). Geoenviron Disasters 8:1–25

Haque U, Blum P, Da Silva PF, Andersen P, Pilz J, Chalov SR et al (2016) Fatal landslides in Europe. Landslides 13:1545–1554

Huntley D, Rotheram-Clarke D, MacLeod R, Cocking R, LeSueur P, Lakeland B, Wilson A (2023) Scalable platform for UAV flight operations, data capture, cloud processing and image rendering of landslide hazards and surface change detection for disaster-risk reduction. Progress in landslide research and technology, Volume 1 Issue 2. Springer, pp 49–61

Josep A, Gilia JA, Corominasa J, Riusa J (2000) Using global positioning system techniques in landslide monitoring. Eng Geol 55(3):167–192

Kasperski J, Delacourt C, Allemand P, Potherat P, Jaud M, Varrel E (2010) Application of a terrestrial laser scanner (TLS) to the study of the Séchilienne landslide (Isère, France). Remote Sens (Basel) 2(12):2785–2802

Kimura H, Yamaguchi Y (2000) Detection of landslide areas using satellite radar interferometry. Photogramm Eng Remote Sens 66:337–344

Klimeš J, Stemberk J, Blahut J et al (2017) Challenges for landslide hazard and risk management in 'low-risk' regions, Czech Republic—landslide occurrences and related costs (IPL project no. 197). Landslides 14:771–780

Lau YM, Wang KL, Wang YH, Yiu WH, Ooi GH, Tan PS et al (2023) Monitoring of rainfall-induced landslides at Songmao and Lushan, Taiwan, using IoT and big data-based monitoring system. Landslides 20(2):271–296

Maheshwari S, Bhowmik R (2021) Detection, monitoring, and early warning of landslides using in-situ ground-based monitoring techniques: a review. Indian geotechnical conference, Springer Nature, Singapore, pp 169–176

Mallet C, Bretar F (2009) Full-waveform topographic Lidar: state-of-the-art. ISPRS J Photogramm Remote Sens 64(1):1–16

Mattei M, Cipollari P, Cosentino D, Argentieri A, Rossetti F, Speranza F, Di Bella L (2002) The Miocene tectono-sedimentary evolution of the southern Tyrrhenian Sea: stratigraphy, structural and palaeomagnetic data from the on-shore Amantea basin (Calabrian Arc, Italy). Basin Research 14(2):147–168

Meng X (2023) Landslide. Encyclopedia Britannica https://www.britannica.com/contributor/Xingmin-Meng/6226
Muto F, Perri E (2002) Evoluzione tettono-sedimentaria del bacino di Amantea, Calabria occidentale (tectonic-sedimentary evolution of the Amantea basin, western Calabria). Boll Soc Geol Ital 121:1–19
Nikolakopoulos K, Kavoura K, Depountis N, Kyriou A, Argyropoulos N, Koukouvelas I, Sabatakakis N (2017) Preliminary results from active landslide monitoring using multidisciplinary surveys. Eur J Remote Sens 50(1):280–299
Ozturk U, Bozzolan E, Holcombe EA, Shukla R, Pianosi F, Wagener T (2022) How climate change and unplanned urban sprawl bring more landslides. Nature 608(7922):262–265
Pecoraro G, Calvello M, Piciullo L (2019) Monitoring strategies for local landslide early warning systems. Landslides 16:213–231
Rossetti F, Faccenna C, Goff'e P, Moni'e P, Argentieri A, Funiciello R, Mattei M (2001) Alpine structural and metamorphic segnature of the Sila Piccola Massif nappe stack (Calabria, Italy): insights for a tectonic evolution of the Calabrian Arc. Tectonics 20(1):112–133
Salvati P, Bianchi C, Rossi M, Guzzetti F (2010) Societal landslide and flood risk in Italy. Nat Hazards Earth Syst Sci 10(3):465–483
Scaioni M, Feng T, Barazzetti L et al (2015) Some applications of 2-D and 3-D photogrammetry during laboratory experiments for hydrogeological risk assessment. Geomat Nat Haz Risk 6(5–7):473–496
Segalini A, Chiapponi L, Pastarini B, Carini C (2014) Automated inclinometer monitoring based on micro electromechanical system technology: applications and verification. In: Sassa K, Canuti P, Yin Y (eds) Landslide science for safer geoenvironment. Springer, Cham, pp 595–600. ISBN 978-3-319-05050-8
Stiros SC, Vichas C, Skourtis C (2004) Landslide monitoring based on geodetically derived distance changes. J Surv Eng 130(4):156–162
Strouth A, McDougall S (2022) Individual risk evaluation for landslides: key details. Landslides 19(4):977–991
Tansi C, Muto F, Critelli S, Iovine G (2007) Neogene-quaternary strike-slip tectonics in the central Calabrian Arc (southern Italy). J Geodyn 43(393):414
Tarchia D, Casagli N, Fanti R, Leva D, Luzic G, Pasuto A, Pieraccini M, Silvano S (2003) Landslide monitoring by using ground-based SAR interferometry: an example of application to the Tessina landslide in Italy. Eng Geol 68:15–30
Thirugnanam H, Uhlemann S, Reghunadh R, Ramesh MV, Rangan VP (2022) Review of landslide monitoring techniques with IoT integration opportunities. IEEE J Sel Top Appl Earth Obs Remote Sens 15:5317–5338
Trigila A, Iadanza C, Lastoria B, Bussettini M, Barbano A (2021) Dissesto idrogeologico in Italia: pericolosità e indicatori di rischio - Edizione 2021. ISPRA, Rapporti 356/2021
Tripodi V, Muto F, Brutto F et al (2018) Neogene quaternary evolution of the forearc and backarc regions between the Serre and Aspromonte Massifs, Calabria (southern Italy). Mar Pet Geol 95:328–343
Tsaia Z, Youa GJY, Leea HY, Chiub YJ (2012) Use of a total station to monitor post-failure sediment yields in landslide sites of the Shihmen reservoir watershed. Geomorphology 139:438–451
Van Dijk JP, Bello M, Brancaleoni GP, Cantarella G, Costa V, Frixa A, Golfetto F, Merlini S, Riva M, Torricelli S, Toscano C, Zerilli A (2000) A regional structural model fort the northern sector of the Calabrian Arc (southern Italy). Tectonophysics 324(4):267–320
Wang H, Zhong P, Xiu D, Zhong Y, Peng D, Xu Q (2022) Monitoring tilting angle of the slope surface to predict loess fall landslide: an on-site evidence from Heifangtai loess fall landslide in Gansu Province, China. Landslides 19:719–729
Xu Q, Peng D, Zhang S, Zhu X, He C, Qi X et al (2020) Successful implementations of a real-time and intelligent early warning system for loess landslides on the Heifangtai terrace, China. Eng Geol 278:105817

Part V

Technical Notes and Case Studies

Assessing Landslide Distribution for Landform Hazard Zoning Purposes: A Case Study on the Western Flank of Iztaccíhuatl Volcano, Puebla, México

Gabriel Legorreta-Paulín, Marcus Bursik, Lilia Arana-Salinas, and Miguel Medina-Jaen

Abstract

In volcanic terrains, landslides are major natural hazard, posing risks to human settlements and economic activity. The characterization and analysis of landslide distribution is important in understanding their behavior in the landscape. The aim of this paper is to present results of the ongoing research project in the Institute of Geography at the National Autonomous University of Mexico (UNAM), to analyze the distribution of landslides, and characterize landforms that are prone to slope instability. For the Río Xopanac watershed on the western flank of Iztaccíhuatl volcano, landforms and landslide distribution were ascertained through a landslide inventory map created from multi-temporal aerial photographs, field investigations and adaptation of the Landslide Hazard Zonation Protocol of the Washington State Department of Natural Resources, Forest Practices Division, in a GIS-based technology. This analysis divided the watershed into 13 mass-wasting landforms that were assigned slope-stability hazard ratings from low to very high. The overall hazard rating for this watershed was very high. The implementation of the technique yields information essential for policy makers here and in other areas of Mexico.

G. Legorreta-Paulín (✉)
Instituto de Geografía, Universidad Nacional Autónoma de México, Circuito Exterior, Ciudad Universitaria, Ciudad de México, Mexico

M. Bursik
Department of Geology, University at Buffalo, Buffalo, NY, USA
e-mail: mib@buffalo.edu

L. Arana-Salinas
Universidad Autónoma de la Ciudad de México, Colegio de Ciencias y Humanidades, Academia de la Licenciatura Protección Civil y Gestión de Riesgos, Ciudad de México, Mexico

M. Medina-Jaen
Dirección de Salvamento Arqueológico del Instituto Nacional de Antropología e Historia, Ciudad de México, Mexico

Keywords

GIS · Geomorphometric mapping · Landslide inventory map · Landslide hazard map · Iztaccíhuatl volcano

1 Introduction

Worldwide, landslide hazard scientists and mitigation workers seek to determine landslide type and distribution at multiple scales to build susceptibility zonation maps. To that end, they may compile landslide inventories and model landslide susceptibility by using a GIS (Washington State Department of Natural Resources (WSDNR), Forest Practices Division 2006; Hervás and Bobrowsky 2009; Slaughter et al. 2017; Shao et al. 2022). To estimate landslide hazard, the frequency, density, and geometry of landslides are recorded using historical or multi-temporal landslide inventory maps and their related geodatabases (Hervás and Bobrowsky 2009; Guzzetti et al. 2012; Slaughter et al. 2017; Du et al. 2020; Shao et al. 2022). This landslide mapping is the foundation for modeling landslide susceptibility and hazard.

In Mexico, local landslide mapping has been carried out by using GIS and remote sensing (Capra and Lugo-Hubp 2006; Legorreta-Paulín et al. 2013; Gaidzik et al. 2017; Murillo-García and Alcántara-Ayala 2017; Oliva-González and Gallardo-Amaya 2018; Montgomery et al. 2020). Despite these efforts, there are few landslide inventory maps—landslide hazard maps that systematically record the type, distribution, abundance, and hazard within any region of Mexico. In addition, one main issue in modeling landslide hazard is the lack of systematic comparison of methods to outline the advantages and limitations of mapping the spatial distribution of landslides and the landslide hazard. There is no standardized procedure to prepare inventory or hazard maps.

This is the case for Iztaccíhuatl volcano, the third highest mountain in Mexico (5215.128 m a.s.l.), which has great potential to produce landslides because of its large area of

B. Abolmasov et al. (eds.), *Progress in Landslide Research and Technology, Volume 3 Issue 1, 2024*, Progress in Landslide Research and Technology, https://doi.org/10.1007/978-3-031-55120-8_25

weakened deposits affected by steep slopes, high seasonal rainfall, and tectonic activity. The Río Xopanac on the western flank of Iztaccíhuatl volcano has been selected as a case study area. Landslides form major natural hazards in hilly terrain in the area and cause extensive damage to roads, human settlements, and agricultural land. Therefore, it is important to prepare a landslide inventory map and a hazard map of the region.

The main goal of this work is to develop a multi-temporal landslide inventory map and a landslide hazard zonation map per landform to provide a standard methodology for mapping that supports governmental authorities in planning and mitigation in Mexico. During this study, 345 landslides covering 0.203 km^2 were mapped from Google Earth imagery, aerial photographs, and GIS thematic layers (such as elevation, slope, hill shade, aspect, and geology), and verified in the field. A map of landslide hazard per landform unit was prepared by using the Landslide Hazard Zonation (LHZ) Protocol of the WSDNR, Forest Practices Division (WSDNR, Forest Practices Division 2006), supported by GIS. Derivation of landform units used classification of morphometric parameters, expert knowledge, and field verification. This analysis divided the watershed into 13 mass wasting landforms that were assigned slope stability hazard ratings from low to very high. For each landform the landslide area rate (LAR) and the landslide frequency rate (LFR) were calculated, as well as the overall hazard rating for the watershed. The overall hazard rating for the study area was found to be very high.

2 Study Area

The Río Xopanac is at 19°08′05″-19°09′06″ N latitude and 98°32′02″-98°26′03″ W longitude, on the western flank of Iztaccíhuatl volcano, within Puebla state, Mexico (Fig. 1). The volcano is in the eastern part of the Trans-Mexican Volcanic Belt (TMVB) physiographic province. The TMVB is an active volcanic chain that extends 1000 km in an approximately west-east direction, from the Pacific Ocean to the Gulf of Mexico. The dormant Iztaccíhuatl volcano is the third highest peak (5215.128 m a.s.l.) in Mexico. The volcano presents a great potential threat for the formation of landslides triggered by rain, earthquakes, and anthropic activity. The study area covers 6.6 km^2 with an elevation range from 2304 to 2880 m a.s.l. and hillslopes between <5° (inner valleys of relatively flat plains) and 66° (mountainous terrain). Climate is classified as Subtropical semi-cold (C(E)(w2)) at 2300–2750 m a.s.l., and Subtropical temperate, subhumid (C(w2)) at >2750 m a.s.l. (INEGI 2008). The Río Xopanac erodes through Tertiary and Quaternary volcanic avalanche deposits, pyroclastic flows, lahars, and fall deposits (García Tenorio 2008). The study area is prone to landslides due to its large area of weathered and/or disaggregated material, under high seasonal rainfall and earthquakes. Also, the area is prone to landslides due to deforestation and agricultural activity. In the study area, episodic evacuation of debris by shallow mass movement takes place along the watershed. The steep hills capped with ash and pyroclastic deposits are affected by active and dormant deep-seated landslides, and where the stream erodes compact pyroclastic deposits, rock falls have occurred.

3 Method

Landslide data were collected from background information, Google Earth imagery, two sets of aerial photographs, and fieldwork, to create a multi-temporal landslide inventory map. Background information included roads, topographic, and geologic hardcopy maps at a scale of 1:50,000, and hardcopy maps of land use, climate, and hydrology at a scale of 1:250,000. All hardcopy maps were converted to a 10 m raster format, georeferenced, and incorporated as GIS layers into ArcMap. Google Earth images were from 2001, and two sets of aerial photographs and orthophotos were from 1993 and 1995 at a scale of 1:20, 000. A 3-m LiDAR digital elevation model (DEM), and its derived slope angle, slope curvature, and vertical erosion maps were used.

Information was collected from these sources to establish a generalized characterization of landslide processes and to aid analysis, interpretation, and mapping of mass wasting potential per landform.

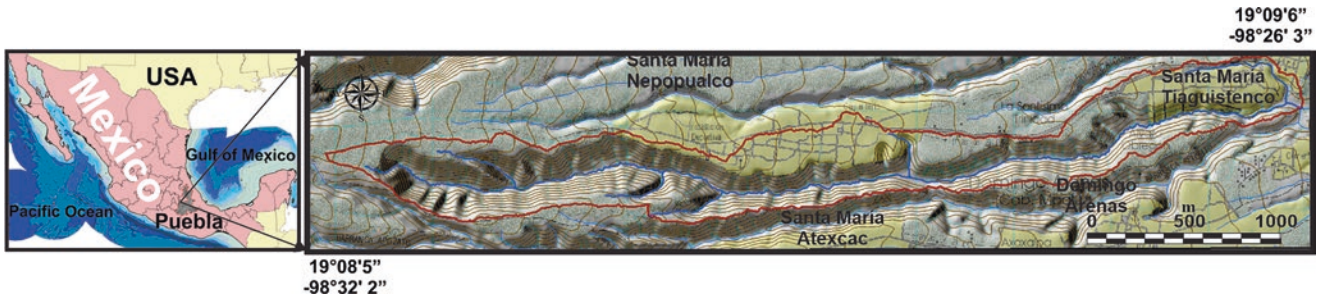

Fig. 1 Study area, Rio Xopanac, State of Puebla, Mexico

Fieldwork was conducted twice in 2002 along the main river and in some tributaries. Field verification supported the existence of 15% of all mapped landslides, which enhances confidence in the assessment from images. Landslides were mapped and classified into shallow undifferentiated landslides, debris flows, debris slides, deep-seated landslides, earthflows and rock falls, according to the landslide hazard zonation protocol (2006) of WSDNR, Forest Practices Division 2006. Shallow undifferentiated landslides are characterized by very shallow failures composed mostly of soil. They are called undifferentiated because satellite imagery and/or aerial photograph interpretation alone may not be able to differentiate between various types (debris slide, debris flow) and processes, including slump, translational, or flow (Sarikhan et al. 2008).

All landslides were mapped onto photo transparencies and digitized directly onto the screen into GIS at the same scale as the photographs. In parallel with the digitizing, a spatial geo-database of landslides was constructed. Pertinent attributes of mapped landslides were recorded in the GIS geo-database, including: 1) a slide-specific identification tag, 2) type of mass wasting process, 3) degree of certainty of the observation (definite: the (human) originator of the landslide information is certain that this is a landslide; probable: the originator of the landslide information is almost certain that this is a landslide; questionable: the originator of the landslide information is not certain that this is a landslide, but is including it for completeness of the inventory), 4) landslide size (length, width, and depth), 5) landslide area, 6) landslide activity (active, inactive or relict), 7) slope shape (divergent, convergent, or planar), 8) field slope gradient, 9) map gradient measured from the 3 m DEM, 10) land use, 11) elevation at point of origin of the landslide, 12) landform, 13) date of landslide identification in the field or on aerial photograph, 14) field or aerial photograph identification number, and 15) researcher's comments (WSDNR, Forest Practices Division 2006).

In parallel with the landslide mapping, areas of similar landslide potential were grouped into distinct landforms. Specific landforms that exist across the study area were defined by rules adopted by Washington Forest Practices Protocol to address landslide hazards (WSDNR, Forest Practices Division 2006). These landforms are called rule-identified landforms (inner gorges, bedrock hollows, convergent headwalls, outer edges of meanders, and active scarps of deep-seated landslides). Their differentiation is based on slope gradient and shape, lithology, landslide density, and sensitivity to forest practices.

GIS layers and fieldwork were also used to identify other areas that do not meet the DNR's rule-identified slope landform definitions. These areas are called non-rule-identified landforms (such as non-rule-identified inner gorges, non-rule-identified bedrock hollow, and convergent headwalls). For instance, both rule- and non-rule-identified bedrock hollow landforms are colluvial, bedrock or simple hollows with concave spoon-shaped topography. Mapping them as one or as another landform depends only on the slope. Rule-identified bedrock hollows have slopes steeper than 70%, whereas non-rule-identified bedrock hollows involve slopes of 30–70% (WSDNR, Forest Practices Division 2006; Sarikhan et al. 2008). Both rule- and non-rule-identified landforms were entered into GIS as part of a landform polygon feature.

A landform hazard map per landform, as well as the overall hazard ratings for the entire study area were produced based on a semiquantitative approach (WSDNR, Forest Practices Division 2006). By default, all rule-identified landforms received a high hazard rating. They may later be "upgraded" to be flagged as having "very high" hazard on the basis of a semi-quantitative assessment. For both rule- and non-rule-identified landforms, the semi-quantitative overall hazard rating is derived from values that correspond to the landslide area rate (LAR) and landslide frequency rate (LFR) (Fig. 2a). The LAR is the area of landslides within each landform, normalized by the period of time spanned by the aerial photographs used, and by the area of each landform. These values are then heuristically multiplied by one million and rounded for easier interpretation (Powell 2007). The LFR is calculated similarly, however, the number of landslides is used instead of the area of landslides. This procedure is restricted to those landslides that deliver sediment to public resources. After the LAR and the LFR were determined, each landform was assigned a Low, Moderate, High, or Very High hazard rating (Fig. 2b). The DNR established the hazard rating class boundaries for LAR and LFR through limited applications in some watersheds of Washington State (WSDNR, Forest Practices Division 2006; Powell 2007; Sarikhan et al. 2008). The LAR and LFR values were then entered into a matrix (Fig. 2c) to determine the Overall Hazard Rating to be assigned to the landforms and the watershed. For instance, the rule-identified bedrock hollows landform has a LFR value of 32,649.8 (32 landslides/32.67 acres/30 years × 1000000) and a LAR value of 3805.7 (3.73 acres/32.67 acres/30 years × 1000000). Each of these values is classified as very high (Fig. 2b). Based on the plotting of these two qualitative values from Fig. 2b into Fig. 2c, this landform has a Very high landslide susceptibility.

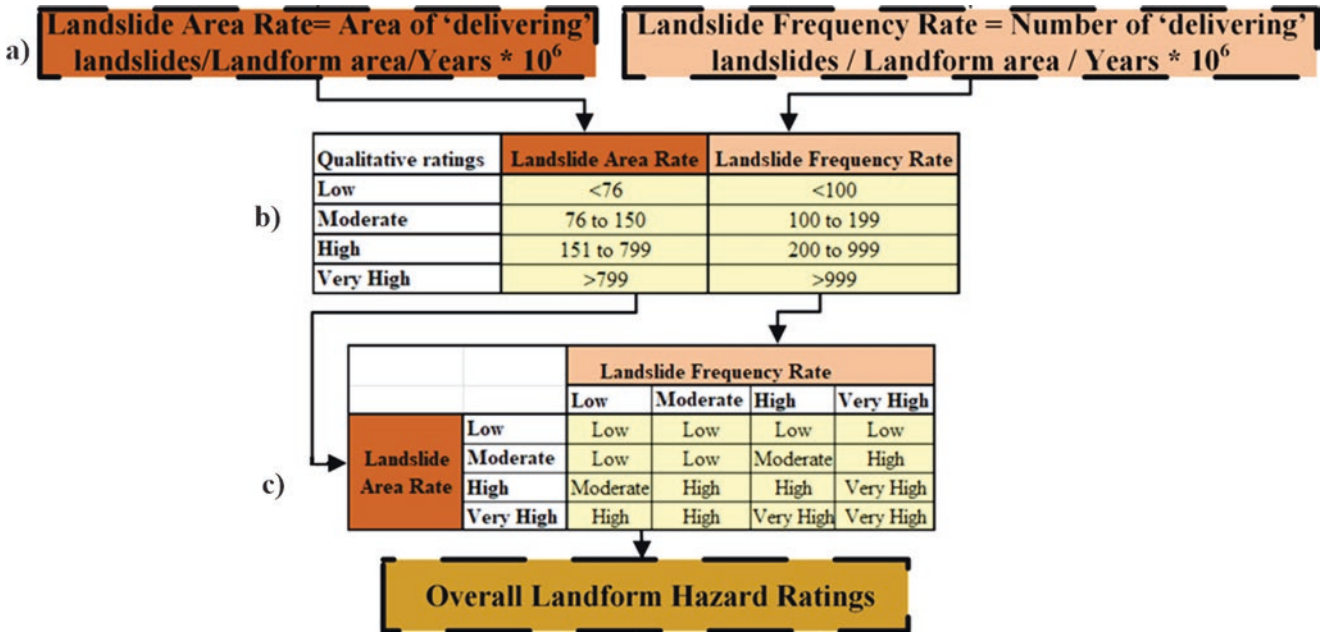

Fig. 2 General procedure for producing landslide inventory and landform hazard map: (**a**) obtain LAR and LFR. (**b**) qualitative ratings matrix for numerical LAR and LFR. (**c**) assign overall hazard rating for each landform and for the watershed

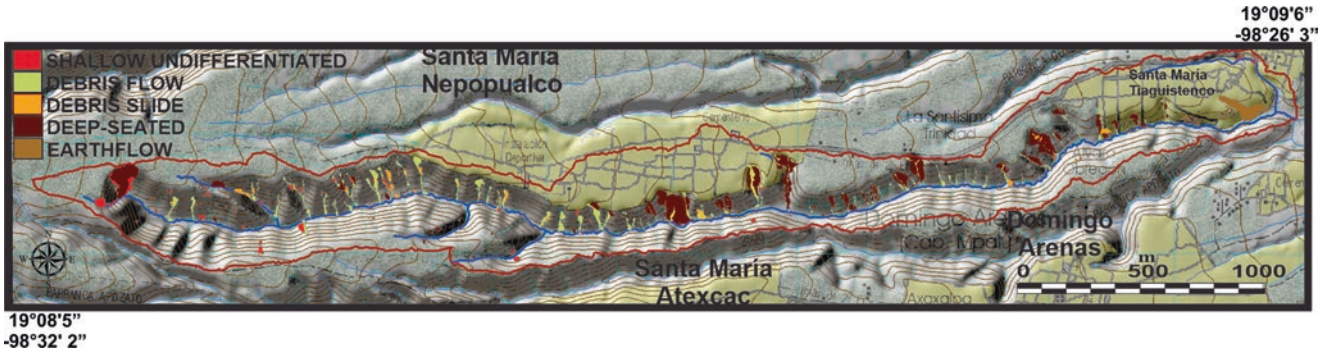

Fig. 3 Landslide inventory map

Table 1 Landslide features mapped in the Río Xopanac watershed

Mass wasting type	Number of mass wasting features mapped	Area (km^2) of mass wasting features	Number of mass wasting features mapped as definitive	Number of mass wasting features mapped as probable
Shallow undifferentiated landslide	123	0.03	111	12
Debris flow	166	0.03	165	1
Debris slide/avalanche	25	0.01	25	0
Deep-seated landslide	47	0.09	40	7
Earthflow	1	0.03	1	0
Total	362	0.19	342	20

4 Results

During assessment of the Río Xopanac, a representative sample of 362 mass-wasting features was inventoried (Fig. 3). Five types of mass wasting processes were identified: 34.1% were shallow undifferentiated failures, 45.9% were debris flows, 6.9% were debris slides, 13% were deep-seated landslides, and 0.3% were earthflows. Of the 362 inventoried landslide features, 94.5% were classified as definite, and 5.5% as probable (Table 1).

Thirteen landforms were recognized from physical attributes of the landscape (Fig. 4 and Table 2). They may be

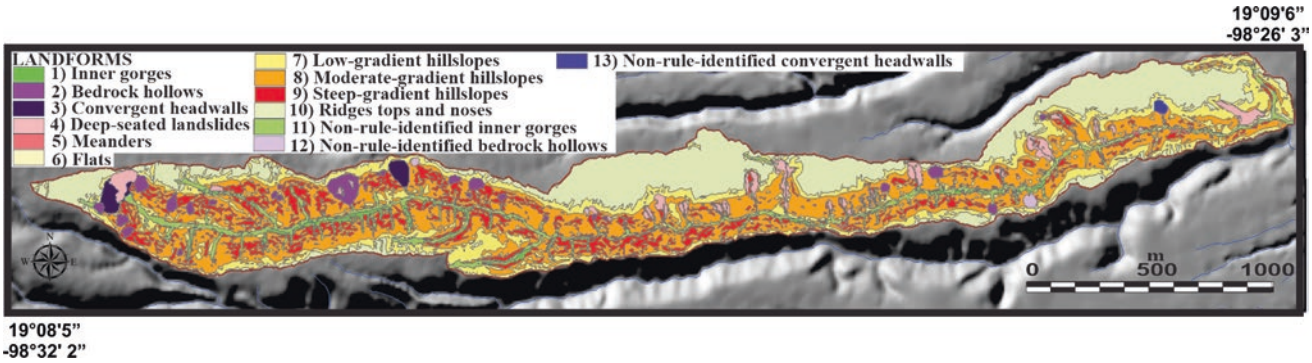

Fig. 4 Landform distribution in the Rio Xopanac watershed

Table 2 Landslide hazard rating of landforms

Name of landform	Slope instability hazard	Slope of landform	Area (km^2)	No. landslides in landform
Inner gorges	Very high	>70%	0.126	12
Bedrock hollows	Very high	>70%	0.132	33
Convergent headwall	Very high	>70%	0.054	13
Active scarps of deep-seated landslides	Very high	>70%	0.194	38
Meander bends/ overbank deposit/ surge plain	Very high	40–70%	0.009	17
Flats	Low	<10%	0.016	0
Low-gradient hillslopes	High	11–40%	1.239	18
Moderate-gradient hillslopes	Very high	41–70%	2.071	118
Steep-gradient hillslopes	Very high	>70%	0.760	83
Ridges tops and noses	Low	<10%	1.658	1
Non-rule identified inner gorges	Very high	30–70%	0.354	20
Non-rule-identified bedrock hollow	Very high	<70%	0.015	3
Non-rule-identified convergent headwall	Very high	<70%	0.009	6
Total			6.634	362

used to predict areas within the watershed that pose hazards for mass wasting, and are as follows:

1. Inner gorges cover 1.89% of the watershed area and represent 3.3% of the mapped landslides. Their potential for mass wasting and delivery is very high. The inner gorges can be either asymmetrical or symmetrical and may be intermittent lateral extent. Slopes are generally >70%, although the failure area of these gorge landforms may include convergent to planar slopes of <65%.
2. Bedrock hollows cover 1.99% of the area and represent 9.1% of the mapped landslides. Their potential for mass wasting and delivery is very high. Bedrock hollows are also called colluvium-filled bedrock hollows, swales, bedrock depressions, or simply hollows. They are long, pointed ellipses or round in planform, and on a hillslope occur as inverted spoon-shaped features. These features are found primarily on convergent slopes but can also occur on planar slopes. They are often found upslope from inner gorges and on steep slopes (>70%). Bedrock hollow failures can also occur on less steep terrain.
3. Convergent headwalls cover 0.81% of the area and represent 3.6% of the mapped landslides. Their potential for mass wasting and delivery is very high. Convergent headwalls are funnel-shaped landforms, broad at the ridge top and terminating where headwaters converge into a single channel. A series of convergent bedrock hollows may form the upper part of a convergent headwall. They are often found upslope from inner gorges and on steep slopes (>70%). This landform unit is generally uniformly scattered in the hilly terrain throughout the basin. The region mapped into this landform unit likely contains unmapped inner gorges and bedrock hollows.
4. Active scarps of deep-seated landslides cover 2.92% of the area and represent 10.5% of the mapped landslides. Their potential for mass wasting and delivery is very high. This landform encompasses active head and lateral scarps of deep-seated landslides. There is a high potential for additional secondary landsliding within the entire area (headscarp, body and toe) of active deep-seated landslides due to post-landslide steepening by streams that cut through the features.
5. Meander Bends/Overbank deposits/Surge Plains cover 0.13% of the area and represent 4.7% of the mapped landslides. Their potential for mass wasting and delivery is very high. In the watershed, slope failures occur through stream undercutting of the outer banks of meanders along valley walls or high terraces of an unconfined meandering stream.

6. Flats cover 0.24% of the area, but no landslides have been mapped in this landform. Their potential for mass wasting and delivery is low. They include slope forms that are mostly gentler than 10%. Although the landform includes gentle slopes, there are occasional cuts with slopes >62%. This category consists predominantly of valley bottoms, floodplains, and flat terrace surfaces.
7. Low-gradient hillslopes cover 18.67% of the area, represent 5% of the mapped slope failures, and include all slope forms (convergent, divergent, and planar) and gradients between 11% and 40%. Their potential for mass wasting and delivery is high.
8. Moderate-gradient hillslopes cover 31.21% of the area, represent 32.6% of the mapped slope failures, and include all slope forms (convergent, divergent, and planar) with gradients that range between 41% and 70%. Their potential for mass wasting and delivery is very high.
9. Steep-gradient hillslopes cover 11.45% of the area, represent 22.9% of the mapped slope failures, and include all slope forms (convergent, divergent, and planar) with gradients of >70%. This category contains other very-high-hazard landforms (e.g. inner gorges and bedrock hollows) that are the initiation points for many debris slides and debris flows. The potential for mass wasting and delivery is very high.
10. Ridges tops and noses cover 24.99% of the area, represent 0.3% of the mapped slope failures, and include all ridge tops and ridge noses with gradients between 0% and 10%. Landslides have occurred below and adjacent to some of these low-gradient ridge tops. Their potential for mass wasting and delivery is low.
11. Non-rule-identified inner gorges cover 5.34% of the area and represent 5.5% of all slope failures. Their potential for mass wasting and delivery is very high. This category has characteristics similar to those of rule-identified inner gorges but involves convergent slopes of 30–70% gradient. They appear as gentle-slope-walled canyons or gullies on DEM slope maps, and seem to have been eroded by stream action, but with evidence of mass wasting along their sidewalls. They may be either symmetrical or asymmetrical in profile and are commonly intermittent in lateral extent.
12. Non-rule-identified bedrock hollows cover 0.23% of the area and represent 0.8% of the mapped landslides. Their potential for mass wasting and delivery is very high. This category has characteristics similar to those of rule-identified bedrock hollows, but involves convergent slopes of <70% gradient. This landform is the initiation point for many debris slides and debris flows.
13. Non-rule-identified convergent headwalls cover 0.13% of the area and represent 1.7% of the mapped landslides. The potential for mass wasting and delivery is very high. This category (slope <70%) includes bedrock hollows and inner gorges that are usually separated one from another by steep ridges. The slope geometry within this landform concentrates both surface water and groundwater, which produces areas of positive pore pressures during intense or extended precipitation events.

5 Discussion and Conclusions

The implementation and development of a GIS-based landslide inventory map and its related geo-database, in conjunction with a landslide hazard zonation methodology is fundamental in prognostic studies of slope instability. In this paper we briefly introduce the implementation of a method for mapping and modeling landslide hazard by adapting the WSDNR, Forest Practices Protocol. The landslide inventory shows that, in the study area, shallow landslides (including debris slides and debris flows) are the predominant type (86.7%), followed by deep-seated landslides (including earthflows) (13.3%). Along this stretch of the Rio Xoponac on the western flank of Iztaccíhuatl, we recognized 13 landform units. Two landforms (Moderate- and Steep-gradient hillslopes) encompassed more than a half of the landslides (55.5%), followed by active scarps of deep-seated landslides (10.5%), bedrock hollow (9.1%), and inner gorge (8.8%; including Rule- and Non-rule-identified) landforms.

Field observations and satellite and aerial imagery suggest that a predisposition to trigger landslides may stem from the combined effect of land-use changes, geological conditions, and the occurrence of very highly susceptible landform units. For example, the Moderate-gradient and Steep-gradient hillslopes units had very high landslide susceptibility. These landforms, originally covered by forest, are on fertile weathered and unconsolidated soils that have favored a conversion of large areas to agriculture; however, unsuitable treatment of the remaining forest has triggered the high incidence of gravitational processes and erosion. The landforms are more prone to landslides in the middle and upper portions of the watershed, where there are steep slopes, loose volcanic ash, pyroclastic deposits and a buffer width of only 50–100 m of forest along the hillsides.

This finding is important in understanding the long-term evolution of the stream system on the western flank of Iztaccíhuatl volcano, and may prove useful in the quantification, assessment, and modeling of landslides that occur continually in volcanic terrains. The coalescence up-stream of landslides in the watershed has increased the destructive power of mass wasting processes that threatens towns such as Santa Maria Nepopualco, Santa Maria Tianguistenco, and Cholula, with a total population of >141,000 people.

We acknowledge that there is a more quantitative geomorphological method to define and characterize landform units.

However, the production of morphometric maps is time consuming, and requires expert knowledge in geomorphology. The Landslide Hazard Zonation Protocol of the WSDNR, Forest Practices Division used here was preferable; it focuses on a more generic and rapid approach to allow the definition and classification of volcanic landform units of the study area. Nevertheless, the resulting landslide hazard classes allow comparison between landforms because their semi-quantitative value is normalized by the landform size. The landform units and the hazard classification could also be correlated to the volume delivered, and may therefore be useful in the quantification, assessment, and modeling of debris flows in neighboring areas.

Future research should involve the assessment and modeling of landslide volume per individual landform, and the calibration of the WSDNR, Forest Practices Division, method to other Mexican watersheds. Knowledge of the landslide inventory and hazard mapping issues is essential in informing policies determined by local authorities in Mexico.

Acknowledgments The authors thank authorities from the International Consortium on Landslides (ICL) and the International Programme on Landslides (IPL) for their approval and help.

This research was supported by the Programa de Apoyo a Proyectos de Investigación e Innovación Tecnológica (PAPIIT), UNAM. # IN100223.

Declarations of Interest The authors declare no competing interests.

References

Capra L, Lugo-Hubp J (2006) Fenómenos de remoción en masa en el poblado de Zapotitlán de Méndez, Puebla: Relación entre litología y tipo de movimiento. Revistamexicana de cienciasgeológicas 20(2):95–106

Du J, Glade T, Woldai T, Chai B, Zeng B (2020) Landslide susceptibility assessment based on an incomplete landslide inventory in the Jilong Valley, Tibet, Chinese Himalayas. Engineering Geology 270:105572

Gaidzik K, Ramírez-Herrera MT, Bunn M, Leshchinsky BA, Olsen M, Regmi NR (2017) Landslide manual and automated inventories, and susceptibility mapping using LIDAR in the forested mountains of Guerrero, Mexico. Geomat Nat Haz Risk 8(2):1054–1079

García Tenorio F (2008) Avalancha de escombros del pleistoceno tardío del cono Los Pies, complejo volcánico Iztaccíhuatl (Masterthesis). Escuela Superior de Ingeniería, Sección de Estudios de Posgrado e Investigación, Unidad Ticomán, Instituto Politécnico Nacional, México). 147 p

Guzzetti F, Mondini AC, Cardinali M, Fiorucci F, Santangelo M, Chang KT (2012) Landslide inventory maps:newtools for an old problem. Earth Science Review 112:42–66

Hervás J, Bobrowsky P (2009) Mapping: inventories, susceptibility, hazard and risk. In: Sassa K, Canuti P (eds) Landslides—disaster risk reduction. Springer, Berlin., ISBN 978-3-540-69966-8, pp 321–349

INEGI (2008) Conjunto de datos geográficos de la carta de clima, 1:1000000. On line: https://www.inegi.org.mx/app/biblioteca/ficha.html?upc=702825267568. Accessed 15 Aug 2023

Legorreta-Paulín G, Bursik M, Ramírez-Herrera MT, Contreras T, Polenz M, Lugo-Hubp J, Paredes-Mejía LM, Arana-Salinas L (2013) Landslide inventory mapping and landslide susceptibility modeling assessment on the SW flank of Pico de Orizaba volcano, Puebla-Veracruz, Mexico. Zeitschrift für Geomorphologie 57(3):371–385

Montgomery J, Candia G, Lemnitzer A, Martinez A (2020) The September 19, 2017 Mw 7.1 Puebla-Mexico City earthquake: observed rockfall and landslide activity. Soil Dyn Earthq Eng 130:105972

Murillo-García FG, Alcántara-Ayala I (2017) Landslide inventory, Teziutlán municipality, Puebla, México (1942–2015). J Maps 13(2):767–776

Oliva-González AO, Gallardo-Amaya RJ (2018) Evaluación del riesgo por deslizamiento de una ladera en la ciudad de Tijuana, México. Tecnura 22(55):34–50

Powell L (2007) Mass wasting assessment: landslide hazard zonation project Major Creek Bingin watershed, Klickitat County, Washington, 43 p. with plates

Sarikhan IY, Stanton KD, Contreras TA, Polenz M, Powell J, Walsh TJ, Logan RL (2008) Landslide reconnaissance following the storm event of December 1 to 3, 2007, in western Washington. Washington Division of Geology and Earth Resources Open File Report, 5

Shao X, Xu C, Wang P, Li L, He X, Chen Z, Huang Y, Xu X (2022) Two public inventories of landslides induced by the 10 June 2022 Maerkang earthquake swarm, China and ancient landslides in the affected area. Natural Hazards Research 2(4):269–272

Slaughter SL, Burns WJ, Mickelson KA, Jacobacci KE, Alyssa B, Contreras TA (2017) Protocol for landslide inventory mapping from lidar data in Washington State: Washington Geological Survey Bulletin 82, 27 p. text, with 2 accompanying ESRI _le geodatabases and 1 Microsoft Excel _le. http://www.dnr.wa.gov/Publications/ger_b82_landslide_inventory_mapping_protocol.zip

Washington State Department of Natural Resources, Forest Practices Division (2006) Landslide Hazard Zonation (LHZ) Mapping Protocol, version 2.1, accessed at: http://www.dnr.wa.gov/Publications/fp_lhz_protocol_v2_1_final.pdf

Identification of Potential Natural Slope Failure Zones by Geomorphological Analyses Using Raster Slope Shading of LiDAR; Case Study from Kegalle, Sri Lanka

Sandaruwan Karunarathna, Priyantha Bandara, Satoshi Goto, and Sajith Bandaranayake

Abstract

There are three approaches to defining the potential instability zonation of natural slopes. The first approach is to understand the failure mechanism through soil properties in a slope, and the mechanisms of failure and movement. The second approach aims to understand the tendency of slopes to fail, with terrain factors that form the essential characteristics of slopes. Understanding the spatial distribution of slope failures and their patterns on a particular slope is the third approach and the focus of this research. All approaches require field verification with expert knowledge.

Slope failure zones contain unique topographic patterns that can be used to identify the failure shape and its dimensions. Slope failures are one of many natural denudation processes. Most slope failure landform units, considered as past slope failures tend to expand naturally. If there is no human involvement, zones of past natural slope failure can be also categorized as potential zones of future slope failure. The large-scale geomorphological analysis is the best approach for clearly identifying landform units associated with potential zones of slope failures. The best scale is 1:10,000. Two-dimensional or three-dimensional raster interpretation of slopes can be used to visualize more clearly the actual shape of slope failures. For the study, raster geomorphological mapping uses LiDAR survey data to characterize the landform units of slope failures and to prepare a landslide susceptibility evaluation.

Keywords

Geomorphological mapping · Slope failures · LiDAR · Digital elevation model · Slope shading

1 Introduction

Sri Lanka is an island near the equator in the Indian Ocean, with central highland terrains frequently subjected to slope failures due to highly intense rainfalls, especially during two monsoon periods. The failure-prone area has reportedly increased from 20% (13,000 km^2) to 30% (19,500 km^2) of the country's total land area over the last two decades (LHMP Annual Report 2017). Every year, human losses and economic damage are recorded due to the expansion of human settlement and other activities into landslide-prone areas without land-use management practices (e.g., plantation, improper soil excavation). Some failures are reported as reactivations of past failures within the same terrain in the database of the National Building Research Organization.

All of these failures start with the reduction of the shear strength of an unstable soil mass. Shear failure along a slip surface occurs as shear strength values (resisting force) of slope materials become smaller than the shear stresses (driving force) acting on soil mass (Igwe 2014). Potential susceptibility and damage zones are defined based on understanding the failure mechanism of soil overburden and the downslope spreading mechanism (propagation). This process is one of the most widely used approaches to identify zones susceptible to failure initiation and for use in numerical downslope movement simulations.

S. Karunarathna (✉) · S. Bandaranayake
Integrated Graduate School of Medicine, Engineering, and Agricultural Sciences, University of Yamanashi, Yamanashi, Japan

P. Bandara
Landslide Hazard Mapping Project, Landslide Research and Risk Management Division, National Building Research Organization, Colombo, Sri Lanka

S. Goto
Faculty of Engineering, Graduate Faculty of Interdisciplinary Research, University of Yamanashi, Yamanashi, Japan
e-mail: goto@yamanashi.ac.jp

B. Abolmasov et al. (eds.), *Progress in Landslide Research and Technology, Volume 3 Issue 1, 2024*, Progress in Landslide Research and Technology, https://doi.org/10.1007/978-3-031-55120-8_26

Landslides are triggered by terrain factors that affect the shear strength of the soil and shear stress acting on the soil. Expressed as a function of failure initiation, these essential characteristics of slopes are geological, geomorphological, and associated with human activities (NBRO User Manual 1995). Another approach studies the process of failure initiation with terrain factors and is used for landslide susceptibility evaluation. Triggering events are various external factors (external stimuli) that change within short periods, such as rainfall and earthquakes.

Past failures in a landscape create unique topographic patterns and shapes that can be used to identify potentially unstable terrain. Geomorphological analysis of areas where particular landforms are identified leads to mapping past failures and failure zones. Most landform units derived from past slope failures tend to expand naturally. Consequently, areas of slope failures and colluviums identified by geomorphological analysis can be mapped as zones of potential slope failure. Through this approach, an understanding can be gained of the spatial distribution of failures and their patterns on a particular slope: used for evaluating future potential landslide susceptibility.

To best characterize and understand the typical landslide units, geomorphological analyses require high-resolution terrain data. Light Detection and Ranging (LiDAR) data with at least 2 m resolution is recommended for analysis of surface morphology (Trevisani et al. 2012; McKean and Roering 2004).

2 Study Area

Our study focuses on a 336,500 m^2 area with debris flow propagation starting as a slope failure recorded in Ganthuna Udagama, Kegalle in Sri Lanka. The study area coordinates are N7.130°, E80.430° to N7.136°, E80.435° WGS84 coordinate system with slope failure initiation location at N7.135°, E80.434° WGS84 coordinate system, at an elevation of 780 m above mean sea level.

Properties in the local community which sprawls downstream on gentle slope zones and a minor road were damaged by the failure (Fig. 1).

Granitic gneiss and biotite gneiss with interlayered quartzite are the predominant metamorphic lithologies of the area. In the failure initiation area, the general foliation and lithological layers of granitic gneiss dip 40° with a dip direction of 245° (40°/245°). Two joint sets at 90°/050°/3 m^{-1} and 60°/355°/2 m^{-1} (dip/dip direction/intensity) can be observed (Source: LHMP, NBRO). Since the slope failure starts in the azimuth of 245°, the failure is geo-structurally controlled. Also, the debris propagation follows the general valley pattern pre-conditioned by geological structures shaped by natural denudation and erosion. With valley patterns and denudation processes mainly controlled by geological structures and weathering conditions of lithologies in this metamorphic terrain, geomorphological mapping of typical landform units and spreading patterns is considered the best approach to evaluate slopes for susceptibility to failure.

Compared to the general density of town areas in Sri Lanka the community density in the study area is low. However, settlements are confined to the valley bottoms and spread along the main highways and secondary roads (Fig. 2). Road patterns follow the surface morphology due to hilly terrain (Fig. 1). The study area mainly comprises tea-cultivated lands, pine-cultivated lands, degraded forest lands, bedrock outcrops, and human ettlements.

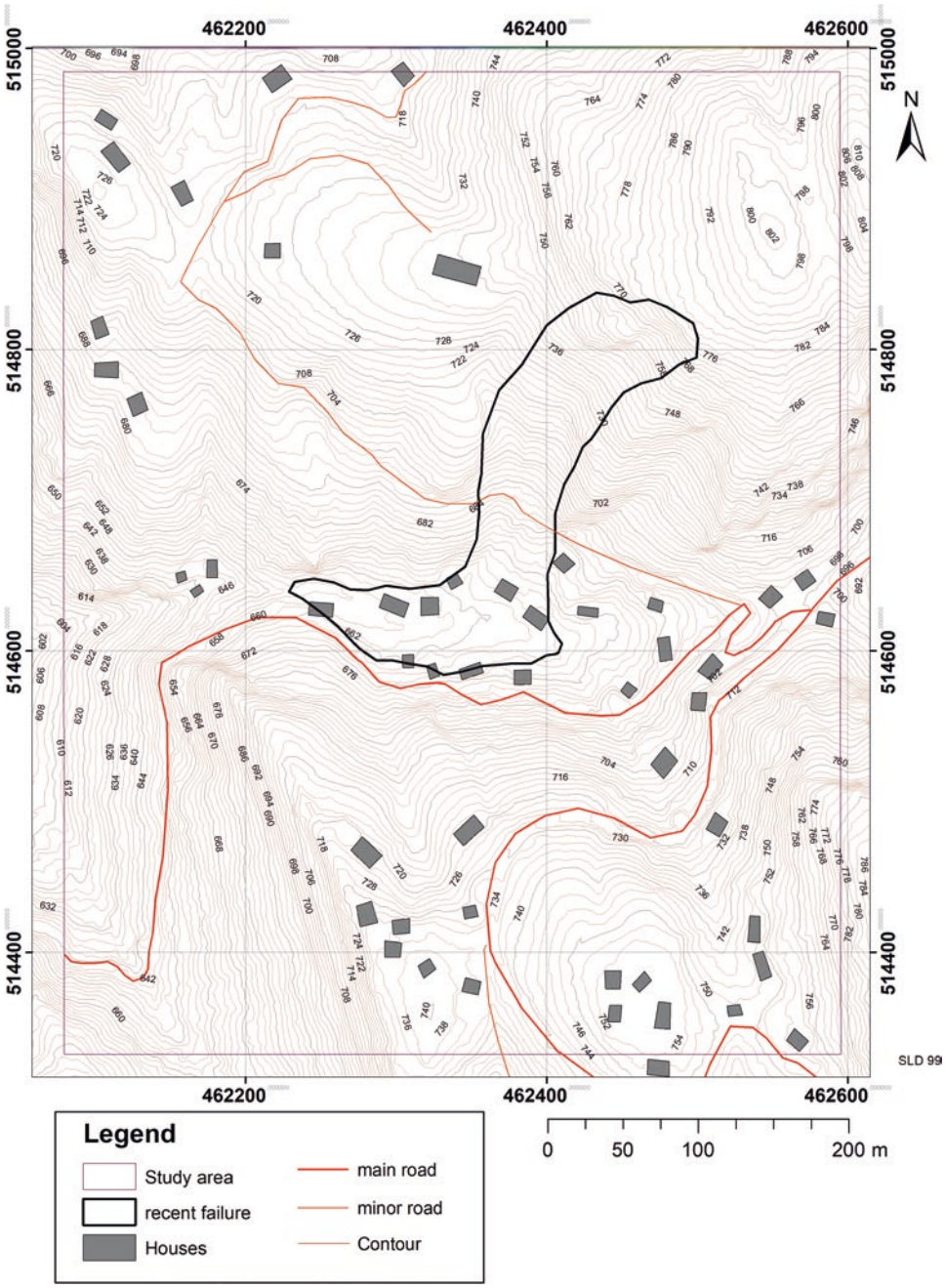

Fig. 1 Study area and the recent failure

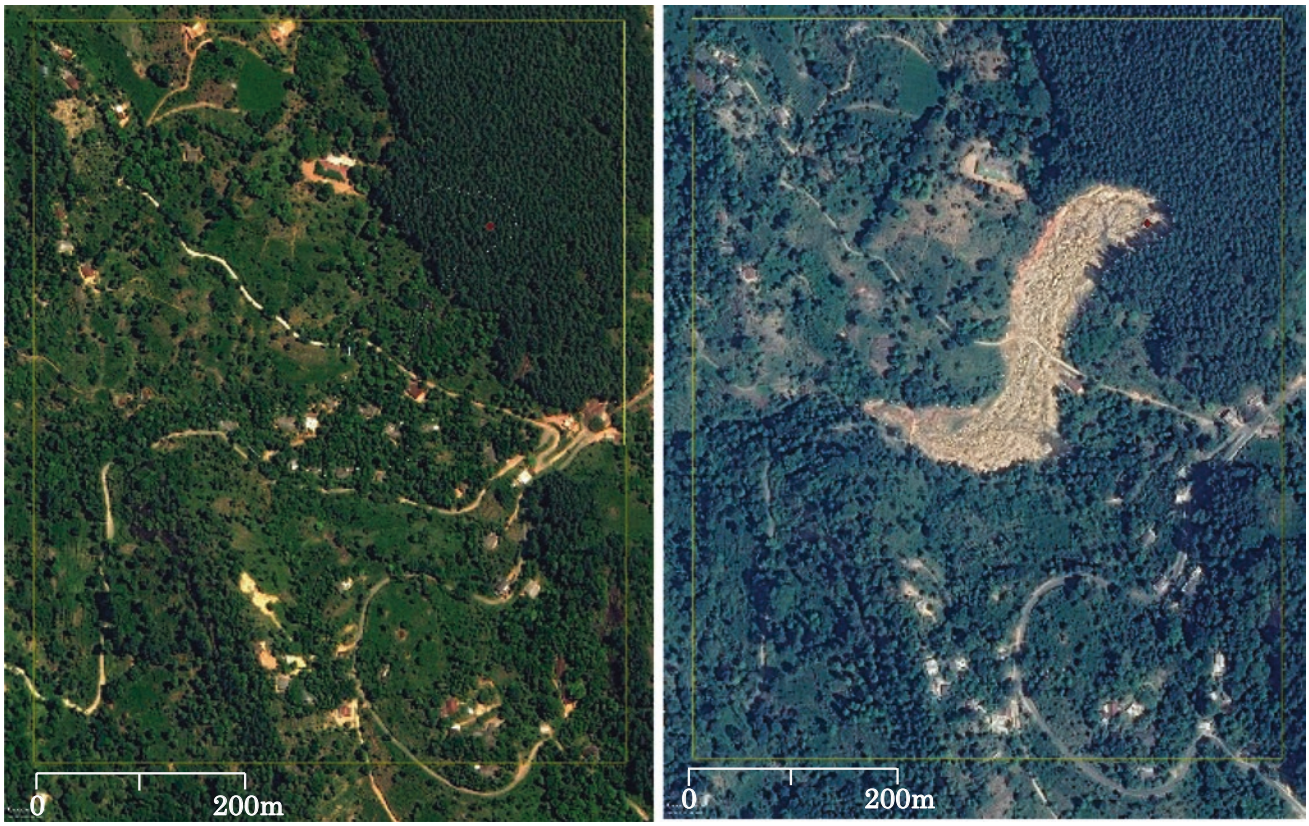

Fig. 2 Focused study area for the research (Google image): (**a**) before the failure 3/2016; (**b**) after the failure 2/2017

3 Methodologies

Traditional geomorphological mapping is a two-dimensional record of three-dimensional landform units recorded in the field. However, two-dimensional or three-dimensional raster interpretation of slopes can be used to geospatially visualize the actual morphological conditions more accurately without going to the field to survey.

In this study, high-resolution LiDAR point cloud data, processed with vegetation filtering facilitated the accurate identification of the morphological state of the landscape. The airborne laser scanned the ground surface at 100,000 to 200,000 samples per second (laser pulses were reflected from objects on the ground and travel time was converted to elevation) to obtain a geospatial dataset of all laser pulse returns from the ground (i.e., point clouds). Aircraft position was precisely measured so that the position and orientation of the laser were always known (JICA 2016). GPS base stations broadcast corrections to airborne GPS units (JICA 2016). The point clouds were generated from a Digital Elevation Model (DEM) of the bare terrain (surface morphology) after filtering the laser pulses reflected from vegetation, buildings, and infrastructure. A prepared DEM was then used to analyze the distribution of geomorphological features on the ground.

For this study, the slope-shading method in ArcGIS was used. Hill-shade analysis could also be used for this purpose, but this approach generated an azimuthal-biased morphological visualization and so was not used for this research. Preparation of the slope map from the DEM and shading was completed using the raster stretch and raster resample method. This analysis removed the azimuthal bias of hill shades from the slope map with artificial sunlight directly overhead with no azimuth. The change in slope gradient was depicted continuously from white to black by flat surfaces in white; low gradients in light grey; moderate gradients in dark grey; and very steep surfaces in black. A color-ramped, partly transparent DEM was overlayed on the slope shading map in ArcGIS to better visualize landform units with elevation differences. The slope map is generally the most important tool for interpreting landform units with slope failure initiations and deposits.

To capture the landform units of slope failures, both the manual method (with field and geomorphological identification experience), and an analysis of raster plan curvatures by slope map method can employed. However, the raster curva-

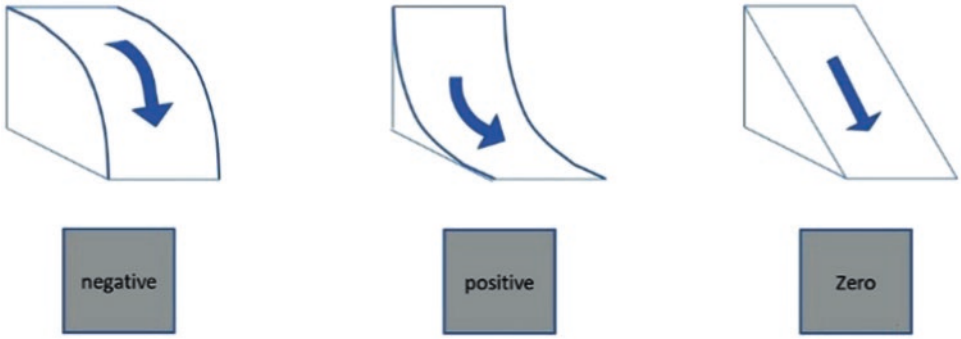

Fig. 3 Profile curvature landform representation

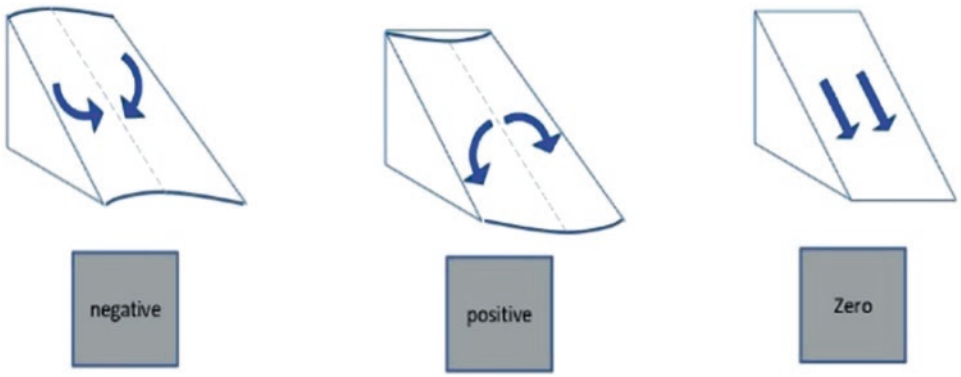

Fig. 4 Plan curvature landform representation

ture analysis required expert knowledge to filter unnecessary zones not susceptible to failure (through field verification and filtering). For this study, the analysis of raster plan curvatures by slope map was used.

Raster modeling of slope morphology was represented as profile curvatures and plan curvatures (Peckham 2011; Pennock et al. 1987). The profile curvature represented the direction of the maximum slope. A negative value of profile curvature represented an upwardly convex slope; a positive value of profile curvature represented an upwardly concave slope, and the zero value represented a planar slope (Fig. 3). The plan curvatures represented a measurement perpendicular to the maximum slope (Rana 2006).

The negative values represented the sideward concave at the pixel; while the positive values represented the sideward convex at the pixel, and the zero value represented the straight slope (Fig. 4).

Landform units that were susceptible to failure could be detected based on both spatial plan curvature value distributions and the minimum slope gradient that was vulnerable to failure initiations. Zones susceptible to failures were determined using Eq. (1).

$$\begin{aligned}&(\text{Plan curvature} < 0)\times\\&\quad(\text{slope} >= \text{minimum slope angle for failure initiation})\end{aligned} \tag{1}$$

Landslide initiation required negative plan curvature values with the slope angle greater than the minimum slope gradient for the failure of the terrain.

4 Results

The 2 m × 2 m pixel resolution DEM (Fig. 5) of the study area is prepared from the LiDAR data (survey period: 12/2015-4/2016) collected by the Survey Department of Sri Lanka (JICA 2016) prior to the recent failure. The slope map of the study area is prepared from the DEM using the ArcGIS tools with slope shading and visualization stretched using a standard deviation of n = 3. A resample during display is undertaken using the bilinear interpolation for continuous data. The resulting visualization appears as continuous shading of slopes, that enables interpretation of landform units (Fig. 6).

A partly transparent DEM with a rainbow colour ramp is overlayed on the slope shading map to better visualize elevation differences of the terrain in the study area (Fig. 7). Past slope failures are depicted on the slope shading map overlain by the colour ramped DEM (Fig. 8). Six past failures can be identified using this method (Fig. 8). The recent failure is mapped as a reactivation of past slope failures (Fig. 9).

The plan curvature distribution of the study area prepared from the ArcGIS tools represents the propagation potential for convergence and divergence through the surface of the landform. The negative values of plan curvature (plan curvature <0) represent the sideward concave landforms and are expressed as topographic units of failure propagation. In the Ganthuna Udagama zone within the Kegalle District, a slope of 27° is the minimum vulnerable angle for slope failure initiations (Annual Report of LHMP 2017). The intersects of

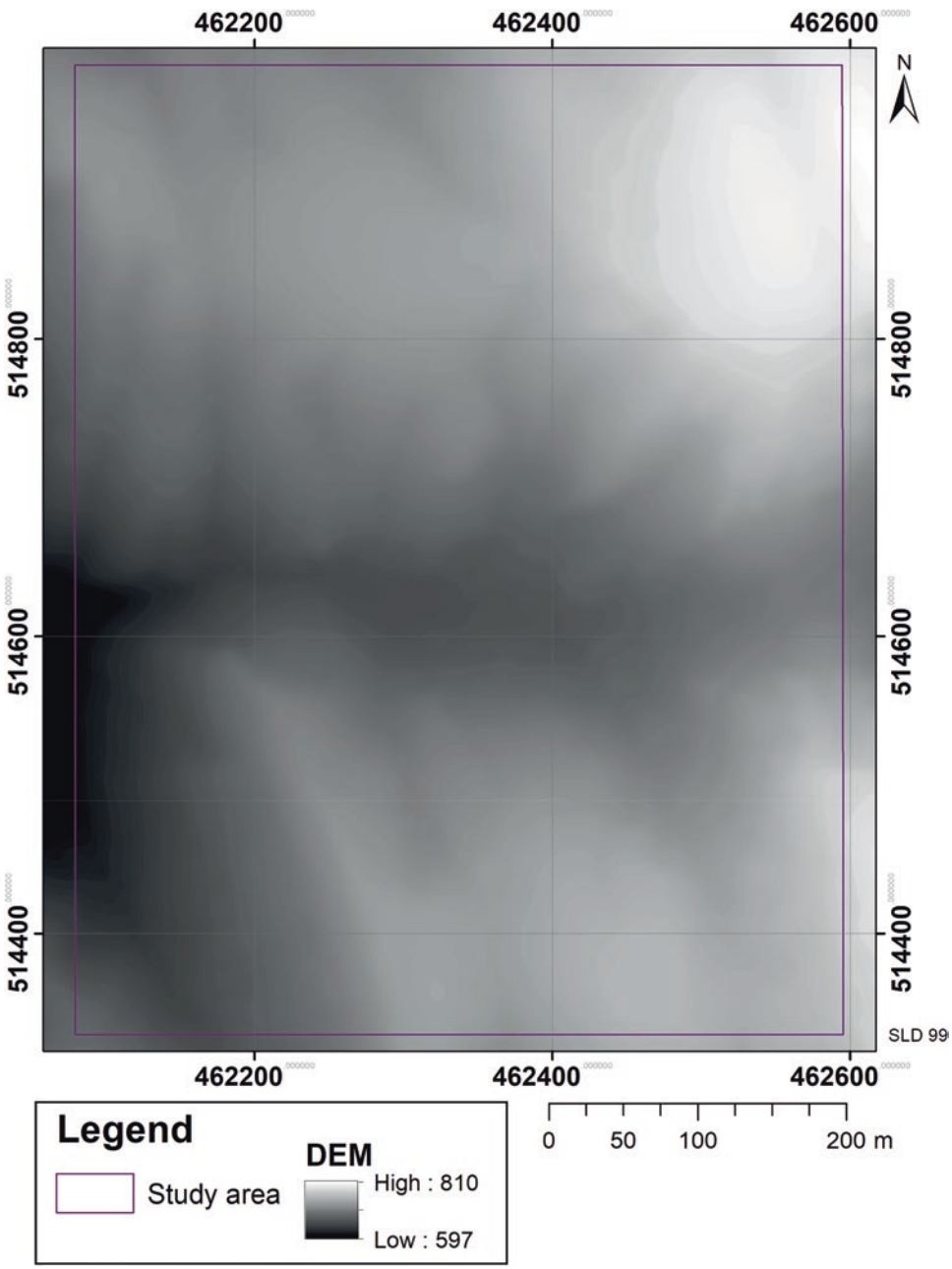

Fig. 5 Digital elevation model of the study area (resolution of 2 m), prepared in ArcGIS

both "negative values of plan curvature" and "slopes greater than 27°" are represented as the susceptible zones for failure initiations (Fig. 10). For terrain in the study area, plan curvatures with highly negative values indicate greater sideward concave representation leading to the recognition of more morphological units vulnerable to failure propagation. Terrain with plan curvatures of less than −1 (Plan curvature < −1) intersecting with the minimum angle for the failure initiation (27°), represent the highest susceptibility for failure initiations. With this interpretation, two susceptibility zones for future failures are identified (Fig. 10). Using the raster calculator in ArcGIS, the zones with the highest susceptibility for failure initiation are derived by (Plan curvature < −1) × (slope > = 27°). The medium susceptibility zone for failure initiation is defined by (Plan curvature <0) × (slope > =27°) using the raster calculator in ArcGIS.

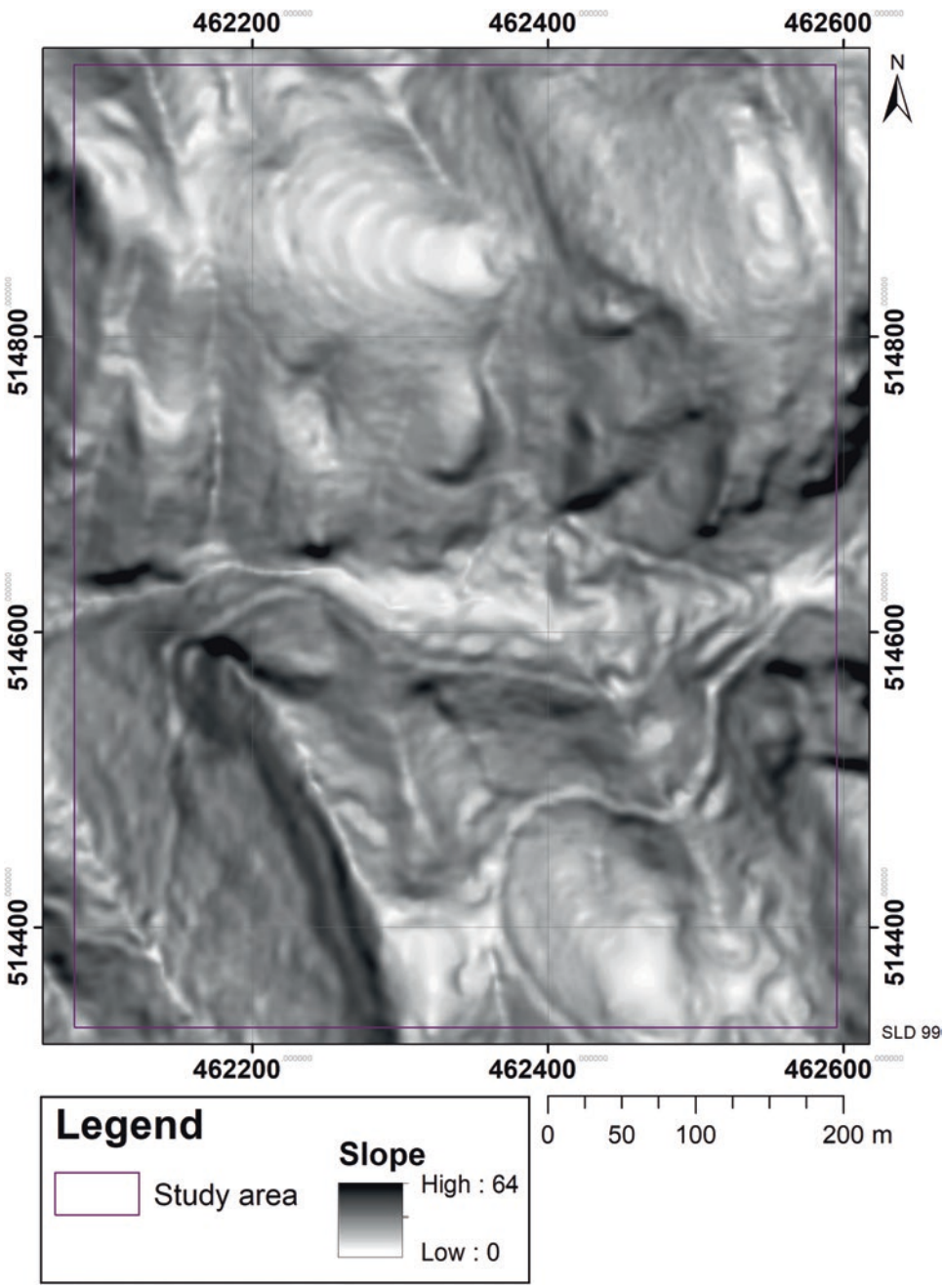

Fig. 6 Slope shading map of the study area (resolution of 2 m), prepared in ArcGIS (Invert color ramp)

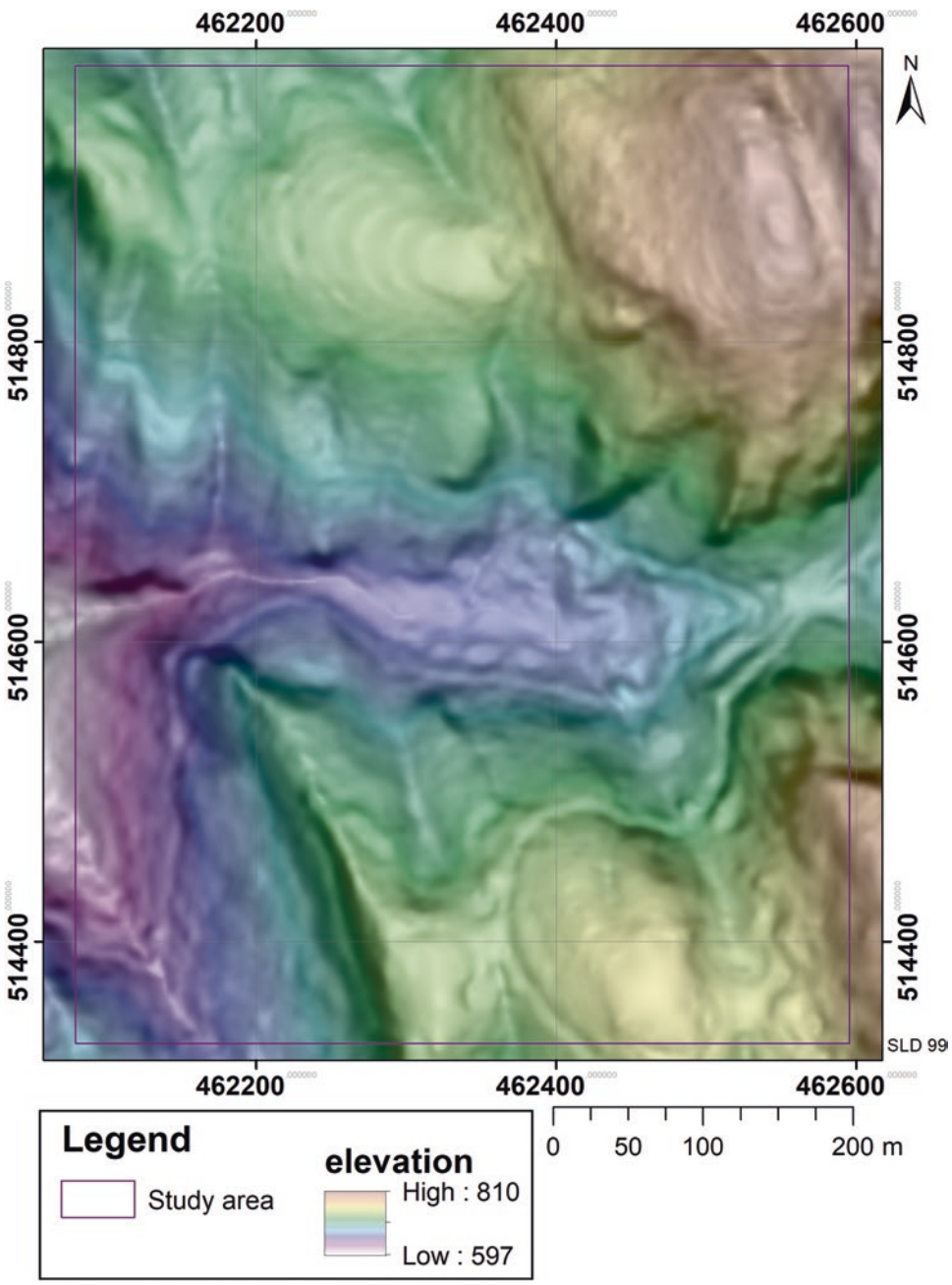

Fig. 7 Slope shading map overlayed by DEM (resolution of 2 m), prepared in ArcGIS

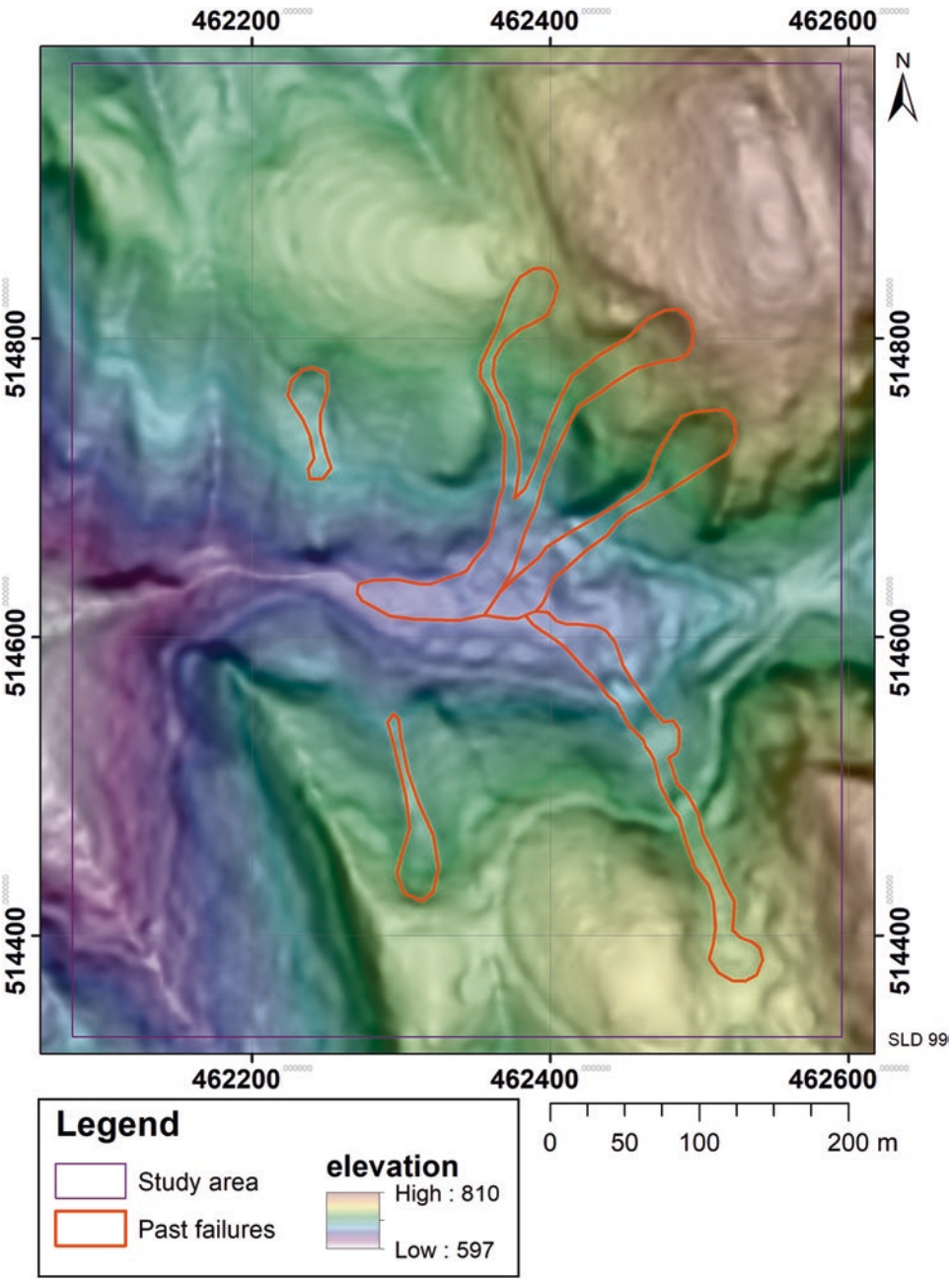

Fig. 8 Past failures captured from the slope shading map overlayed by DEM, prepared in ArcGIS

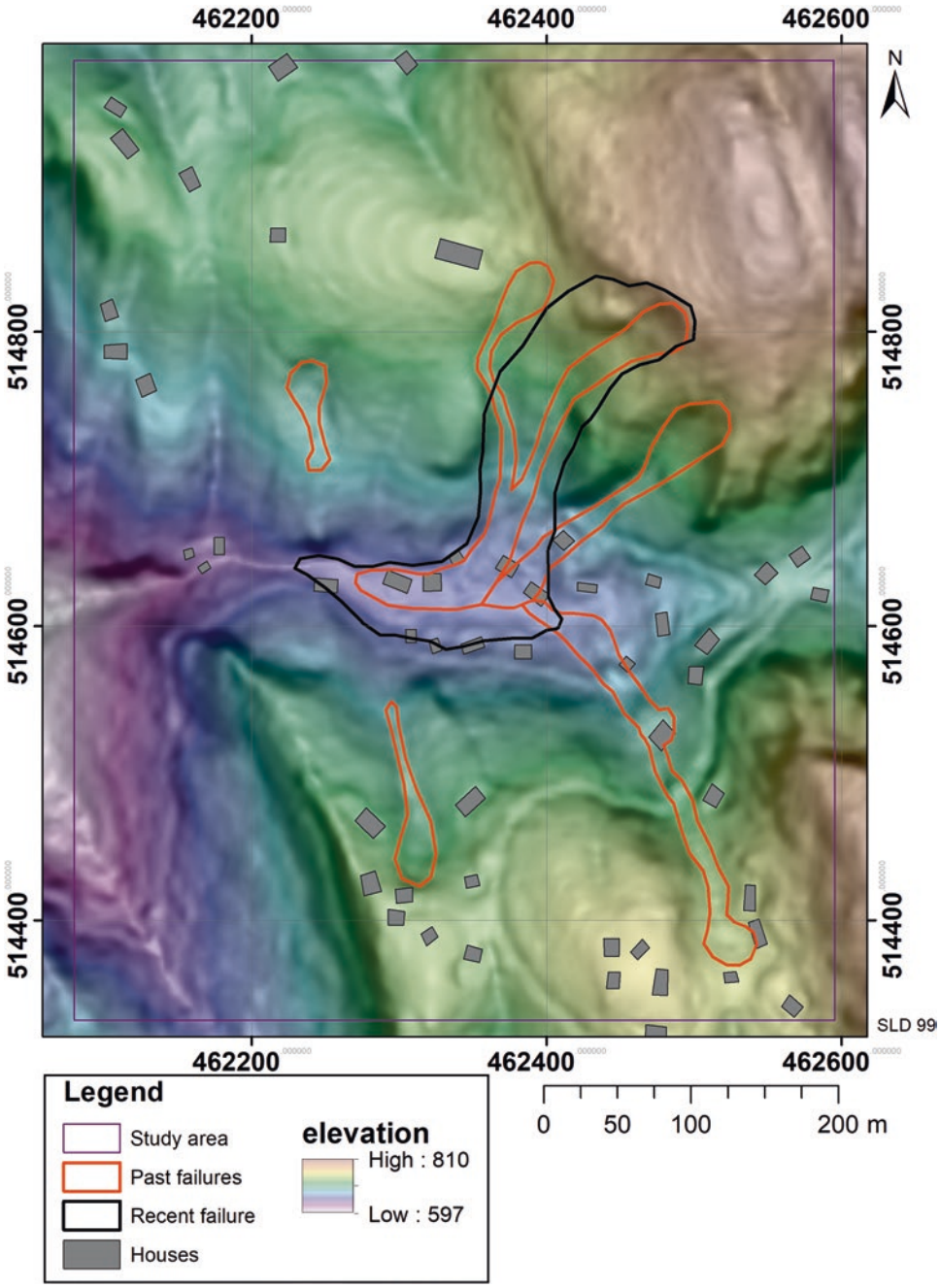

Fig. 9 Failure in May 2016 can be identified as a reactivation of the past failure

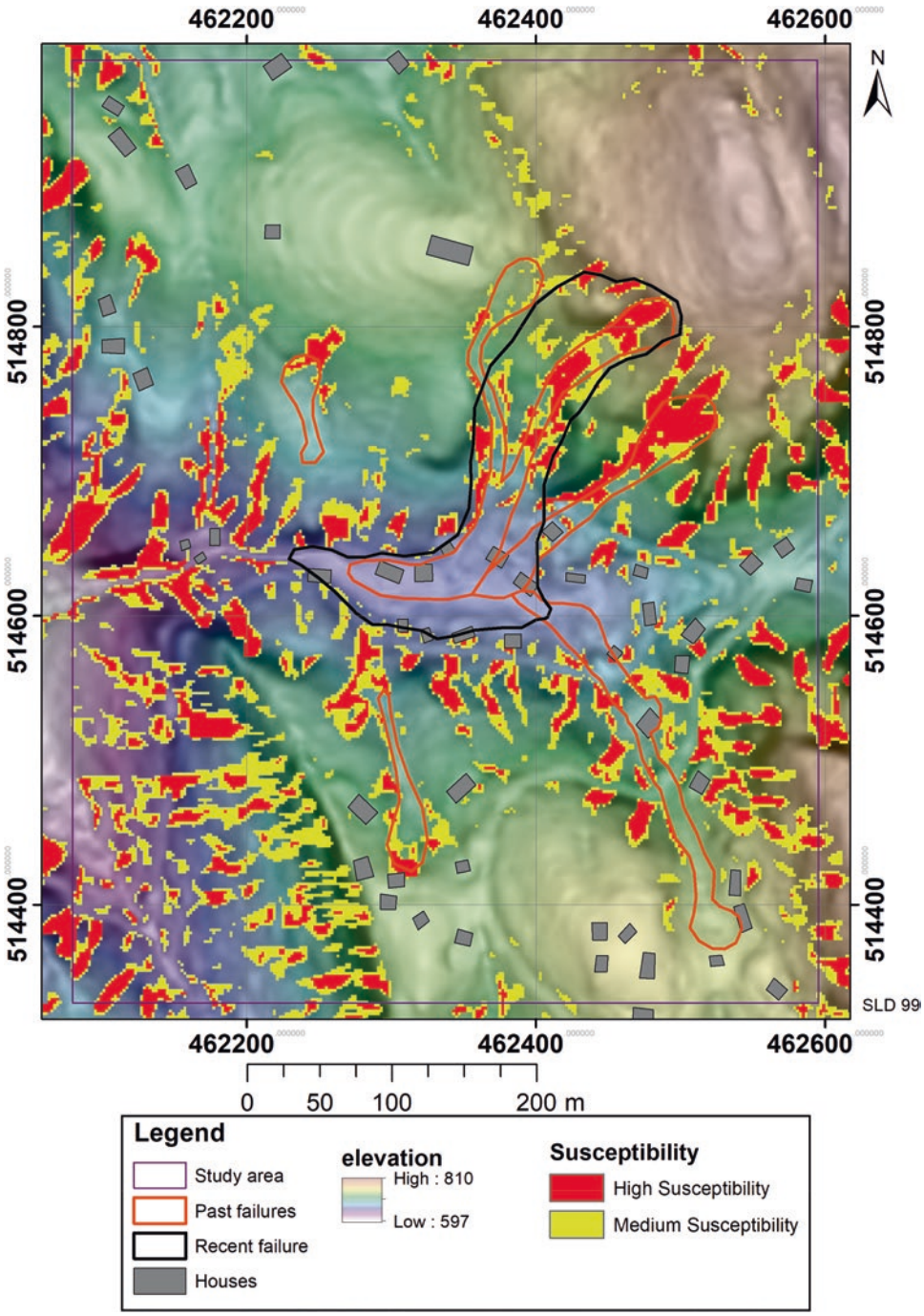

Fig. 10 Susceptibility map for failure initiation prepared through the geomorphological analysis by slope shading and plan curvature analyses

5 Discussion

The LiDAR data used for this study was obtained prior to the recent Ganthuna Udaganma failure incident date: 17th of May 2016. The LiDAR survey was carried out during the period from December 2015 to April 2016 by JICA (JICA 2016). The susceptibility map prepared using geomorphological analysis (raster plan curvature analysis method) represented zones susceptible to future failures (Fig. 10). As this map was completed before the recent Ganthuna Udagama landslide, the successful prediction of failure initiation (Fig. 10) warranted further inspection of the method's precision and accuracy. To this end, the boundary of the recent failure is used to determine the best values for the susceptibility evaluation Eq. (1).

Negative values of plan curvature (<0) represent the sideward concave at the pixel, with higher negative values representing greater concavity, and are indicators of the propagation paths. This phenomenon can be observed with plan curvatures < −0.5, plan curvatures < −1, plan curvatures < −1.5, plan curvatures < −2, and more. If the minimum angle for failure initiation of the particular terrain (determined using the geomorphology approach) intersects with these values, then susceptibility zones be confidently mapped. For the terrain under investigation, the minimum slope angle for failure initiation is a fixed value. Thus, to identify terrain susceptible to failure initiation only requires increasing negative values of plan curvatures. The best agreement for the recent failure is (plan curvature <0) × (slope > =27°). Greater precision on the size of zones and locations for failure initiation can be gained by increasing the negative values (e.g., plan curvature < −0.5, plan curvature < −1, plan curvature < −1.5, plan curvature < −2) in Eq. (1). For example, a reduction of the area of susceptible zones obtained from (Plan curvature <0) × (slope > = 27°) is achieved by increasing the negative values (plan curvature < −0.5, plan curvature < −1, plan curvature < −1.5, plan curvature < −2) (Fig. 11).

Field verification confirms the exact locations (1 and 2) of the Ganthuna Udagama failure zones (Fig. 12). The flow path contains transported soil (colluvial deposits) with boulders that may further settle in future (Fig. 12). The map identifies susceptibility zone number 3 as highly vulnerable to failure in future (Fig. 11). This zone is also just upstream of a past landslide indicating susceptibility to reactivation of the past failure. Field observations of large boulders confirm the possibility of failures (Fig. 13).

Zones 4 and 5 are also highly susceptible to reactivation-type failures in the future (Fig. 11).

Other high-susceptibility zones (6 to 8) are categorized as highly susceptible to failure as first initiations (Fig. 11).

Predicted susceptibility zones of future failures cover an area of 64,610 m^2 (Fig. 11) or 19.2% of the total study area. In the center of the study area, the main valley drains from east to west.

Here, most zones identified as susceptible to failure initiation led to the failure of valley walls. Past landslides identified by geomorphological analyses fail into this valley. Recent failure also failed into this valley.

In contrast, the morphology of the south-west part of the study area consists of susceptible zones for failure initiation in valleys trending south-east to north-west.

Villages are the lowest administrative level in Sri Lanka. The study area consists of two villages called "Ganthuna Udagama", and part of "Narangala" in the south-east. Most of the failure susceptibilities intersect with "Ganthuna Udagama" compared to "Narangala" village.

Identifying the susceptibilities for failure initiation within the lower administrative level is more important to disaster management activities in the future, considering the public safety and socio-economic consequences of catastrophic landslide events.

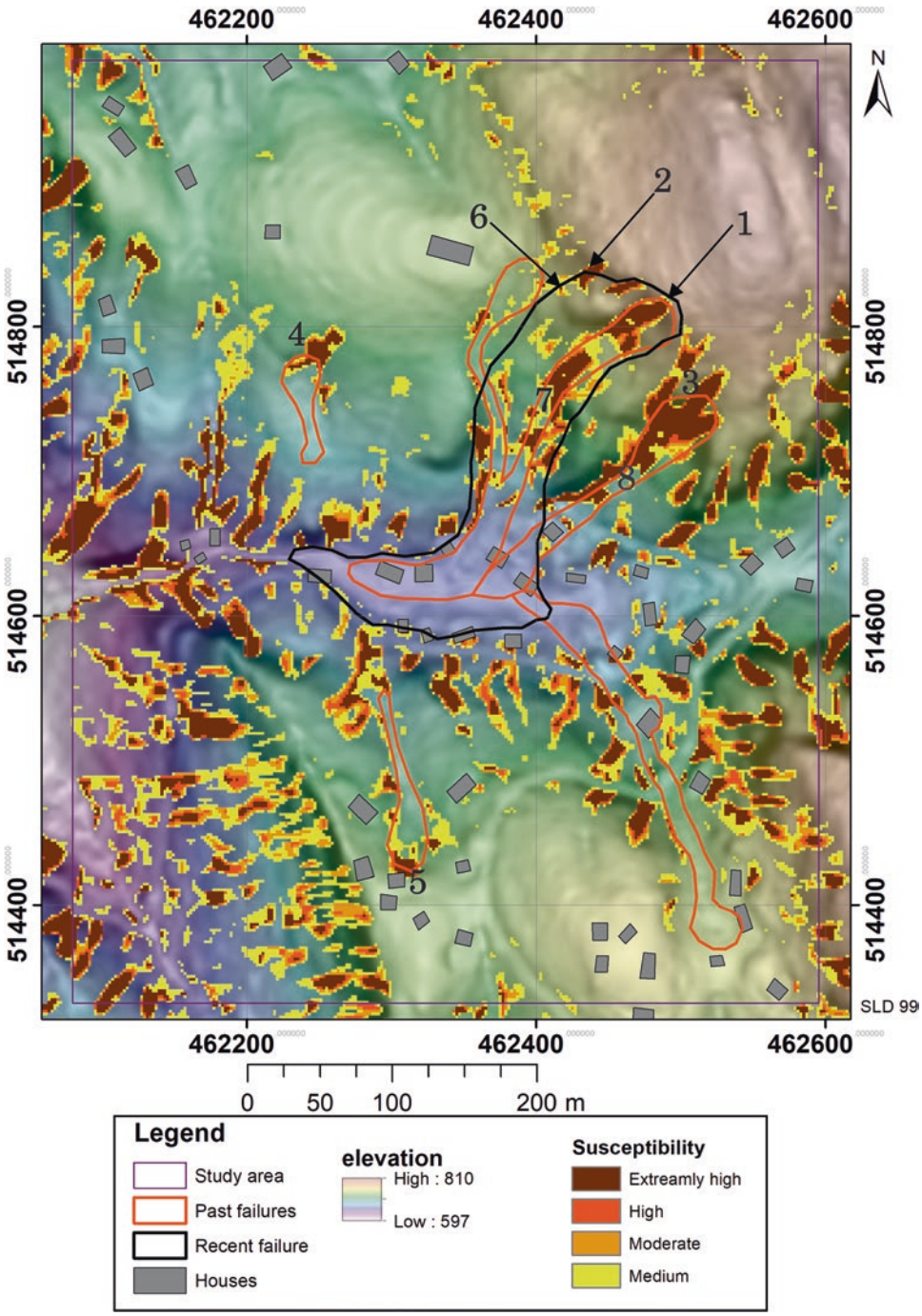

Fig. 11 Susceptibility evaluation for failure initiation by geomorphological analysis

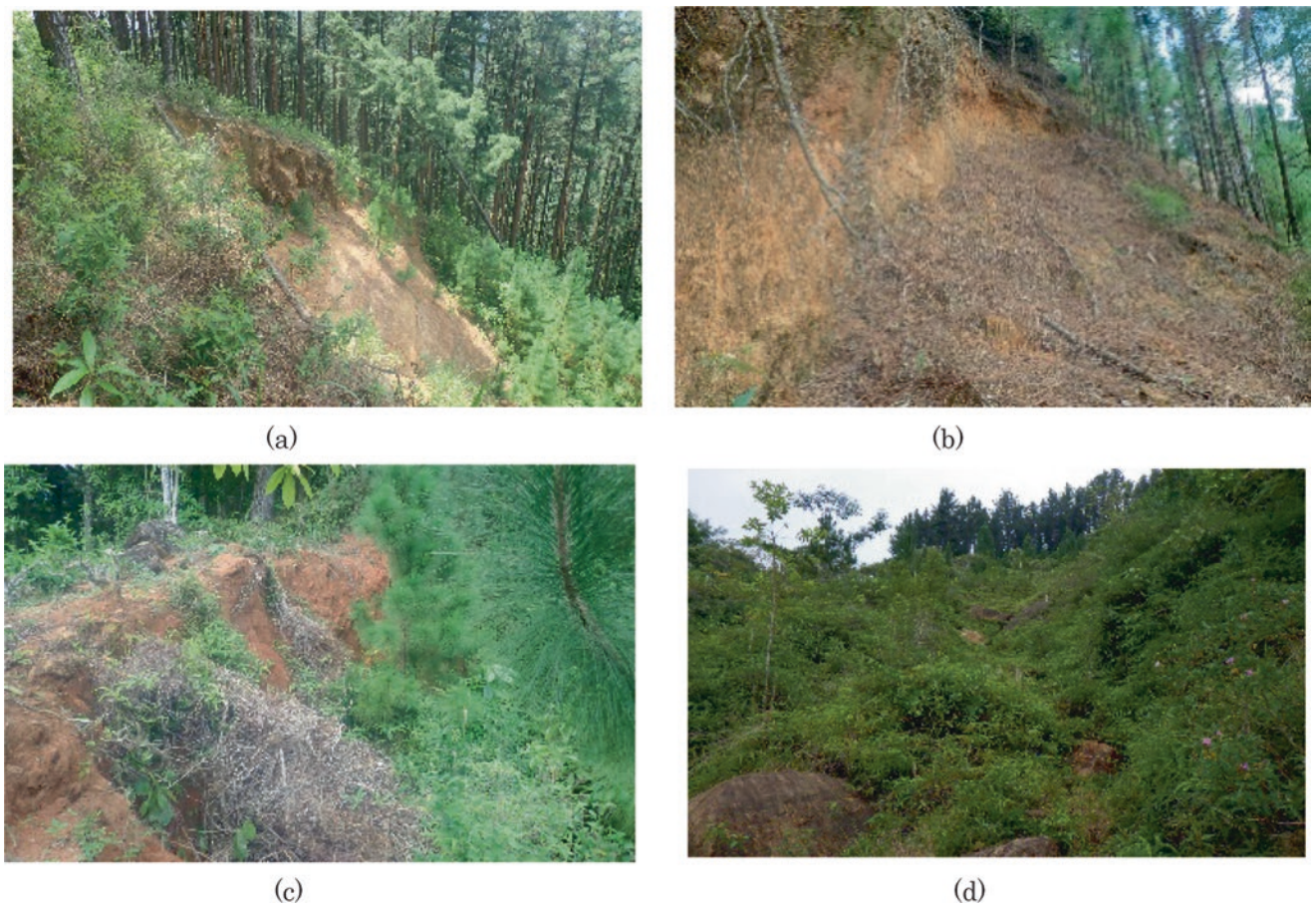

Fig. 12 Photos taken from field verification process in recent failure (Fig. 11). (**a**) Location 1, (**b**) Location 2, (**c**) Location 6, (**d**) unstable colluvial deposits in location 7

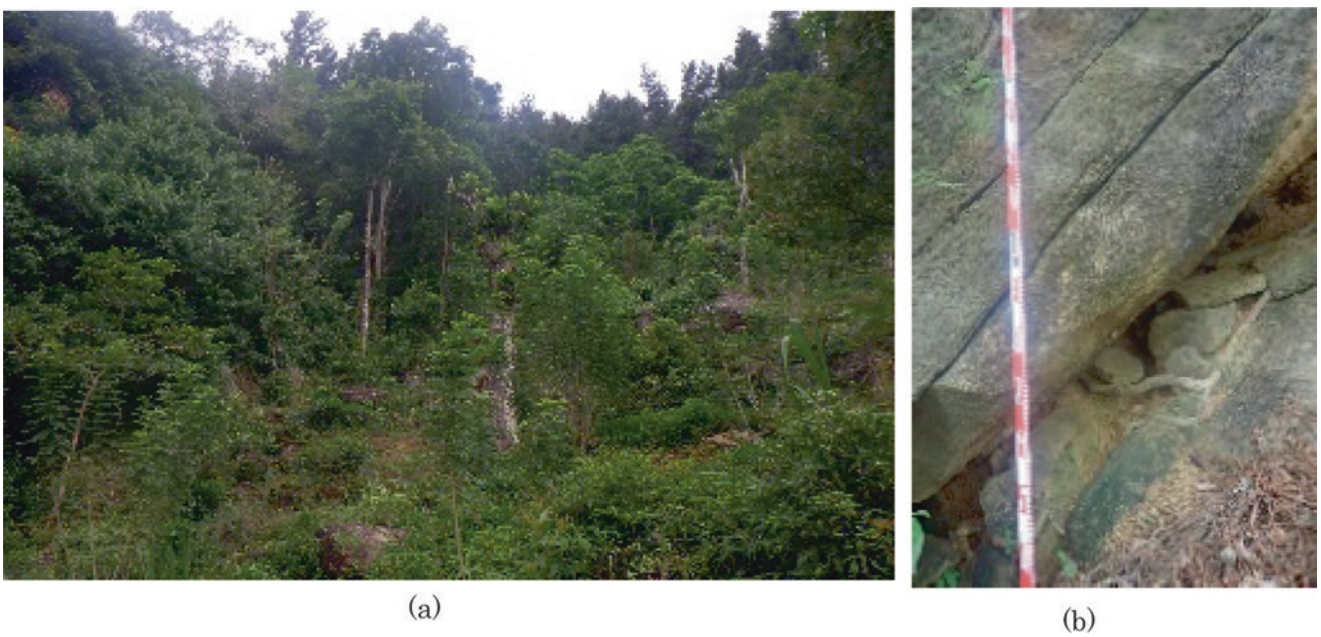

Fig. 13 Photos taken from unstable zone that taken from field verification process (Fig. 11). (**a**) Location 8, (**b**) Location 3

6 Conclusions

Geomorphological analyses identifying past failures and the potential susceptibility zones for failure initiations were successfully applied to metamorphic terrains in Sri Lanka. Results vary depending on the resolution of the DEM used in ArcGIS. This study demonstrates that LiDAR data with at least 2 m resolution is recommended to accurately define and assess susceptibility zones of future failures. Those zones identified with the highest susceptibility to landslide initiation can be flagged for future disaster management activities.

Zones with the predicted highest susceptibility for failure initiation were field-verified with observations of the recent and past failure boundaries in Ganthuna Udagama.

However, the highest susceptibility zones of the map are not fully field verified or filtered with expert knowledge. Moreover, the susceptibility evaluation is based on current morphological landform units (i.e., the small surface feature) that can be easily changed by natural and anthropogenic activities. Anthropogenic involvement in landform changes must be better understood.

Damage zone assessment and risk mapping can be undertaken by incorporating the results of an evaluation of susceptibility to failure initiation. Susceptibility zones identified are only for failure initiations and do not show all damage zones of initiation, flow paths, and deposition areas. The results presented in Fig. 10 can be used to delimit initiation zones (with maximum potential depths from overburden maps produced by NBRO) to simulate the downslope movement, and to identify the total potential damage zones in the study area. The potential damage zones can then be used to identify all the "elements at risk" and "exposure" (i.e., spatial overlay of geological hazards and elements at risk) to calculate the spatial distribution of landslide risks. Both damage zone assessment maps and risk maps should be used for future landslide disaster management in Sri Lanka.

Lastly, our results can be compared and combined with Landslide Susceptibility Maps produced by the National Building Research Organization obtained by a terrain factor-based model and directly used for community-based future disaster management activities in Sri Lanka.

Acknowledgments We thank the Landslide Hazard Mapping Project (LHMP), Landslide Research and Risk Management Division (LRRMD) of the National Building Research Organization (NBRO) for providing the LiDAR data and the information about the Ganthuna Udagama failure. The first author is indebted to the Engineering Department, Integrated Graduate School of Medicine, Engineering, and Agricultural Sciences, University of Yamanashi, Japan for providing the working facilities and laboratories for the research work. We also thank the International Consortium of Landslides (ICL), Japan for the technical and funding support for the field survey in Sri Lanka as a part of the SATREPS activities. We also thank Prof. Kyoji Sassa, Secretariat in the International Consortium of Landslides (ICL), and Prof. Kazuo Konagai, professor emeritus, at the University of Tokyo for their kind guidance in this research.

References

Igwe (2014) The analysis of rainfall-induced slope failures at Iva Valley area of Enugu state, Nigeria. Environ Earth Sci 71:2465–2480

JICA (2016) Capacity development project for creating digital elevation model enabling disaster resilience in the Democratic Socialist Republic of Sri Lanka, pp 1–64

LHMP Annual Report (2017) Landslide Hazard Mapping in Sri Lanka, Landslide Hazard Mapping Project, pp 10–35

McKean J, Roering J (2004) Objective landslide detection and surface morphology mapping using high-resolution airborne laser altimetry. Geomorphology 57(3–4):331–351

NBRO User Manual (1995) Landslide hazard mapping in Sri Lanka, Landslide Hazard Mapping Project SRL89/001, pp 44–85

Peckham SD (2011) Profile, plan and streamline curvature: a simple derivation and applications. Proc Geomorphometry 4:27–30

Pennock DJ, Zebarth BJ, De Jong E (1987) Landform classification and soil distribution in hummocky terrain, Saskatchewan, Canada. Geoderma 40(3–4):297–315

Rana S (2006) Use of plan curvature variation for the identification of ridges and channels on DEM. Progress in spatial data handling. Springer, Berlin. https://doi.org/10.1007/3-540-35589-8_49

Trevisani S, Cavalli M, Marchi L (2012) Surface texture analysis of a high-resolution DTM: interpreting an alpine basin. Geomorphology 161:26–39

Assessing the Potential Rapid and Long Travelling Landslides in Sri Lanka: A Case Study of Athwelthota Landslide

A. R. P. Weerasinghe, S. H. S. Jayakody, N. P. G. Amali, H. R. Maduranga, and Doan Huy Loi

Abstract

Landslides are a significant natural hazard in Sri Lanka, causing colossal damage to infrastructure, property, and loss of life. The country is highly susceptible to landslides due to its mountainous terrain, frequent heavy rainfall, and poor land-use practices. This study focuses on the dynamics of the Athwelthota landslide that occurred in 2017 and on the potential instabilities of the surrounding slopes that were evaluated using LS-RAPID numerical simulation software. The physical properties of the soil were examined by testing samples from the study area using an undrained ring-shear apparatus. Firstly, the geomorphological features in the study area and geotechnical parameters of soil were used to calibrate the LS-RAPID model by simulating the past landslide. The calibrated model then simulates two nearby potential failure slopes to assess the hazard. Additionally, the study discusses the triggering mechanism and causes of the past landslide and the two nearby slopes, considering factors such as heavy rainfall and groundwater. In conclusion, the Athwelthota landslide was found to be a complex phenomenon involving multiple factors, such as rainfall and groundwater table fluctuations.

Keywords

Athwelthota landslide · LS-RAPID · Numerical modelling

A. R. P. Weerasinghe (✉) · N. P. G. Amali · H. R. Maduranga
National Building Research Organization, Colombo, Sri Lanka

S. H. S. Jayakody
Disaster Prevention Research Institute, Kyoto University, Kyoto, Japan
e-mail: jayakody.sanchitha.8d@kyoto-u.ac.jp

D. H. Loi
International Consortium on Landslides, Kyoto, Japan

Institute of Transport Science and Technology, Hanoi, Vietnam

1 Introduction

Sri Lanka's landslides susceptibility is primarily attributed to its geological, topographical, and climatic conditions. The island's mountainous terrain, composed of steep slopes and unstable geological formations in the central highlands, increases landslide vulnerability (Ratnayake and Herath 2005; Jayasinghe et al. 2018). These geological factors and a tropical climate can cause weathering and erosion. Additionally, Sri Lanka's monsoon climate and high precipitation levels, especially in the central and southern regions, lead to soil saturation and increased pore water pressure, triggering landslides (Ratnayake and Herath 2005). Changes in rainfall patterns in recent years have exacerbated the situation (Jayasinghe et al. 2018). Poor land-use practices, such as deforestation, mining, and agriculture on steep slopes, further weaken the soil structure, making landslides more frequent and damaging, affecting infrastructure, property, and lives (Nissanka et al. 2015).

The Athwelthota landslide is one of the recent examples of a devasting rain-induced rapid and long-travelling landslide (RRLL) in Sri Lanka. It occurred on May 26th, 2017, in the Palindanuwara Divisional Secretariat of the Kalutara District (Fig. 1). This landslide, triggered by unprecedented daily rainfall of more than 241 mm, resulted in nine deaths and severe damage to infrastructure, including the destruction of seven houses. The Kalawana-Baduraliya Road and Palan Ganga (River) were also blocked with debris, and the Athwelthota Gangaramaya temple was partially destroyed.

Similar to the above event, the island nation experiences recurring landslide events. Hence, it became a contemporary need to minimize the catastrophic loss due to landslides. In this regard, a joint research program was initiated between the International Consortium on Landslide (ICL) and the National Building Research Organisation (NBRO). The title of the project is "Development of Early Warning Technology of Rain-Induced Rapid and Long-Travelling Landslides in Sri Lanka (Project RRLL)" (Konagai et al. 2021). One of the

B. Abolmasov et al. (eds.), *Progress in Landslide Research and Technology, Volume 3 Issue 1, 2024*, Progress in Landslide Research and Technology, https://doi.org/10.1007/978-3-031-55120-8_27

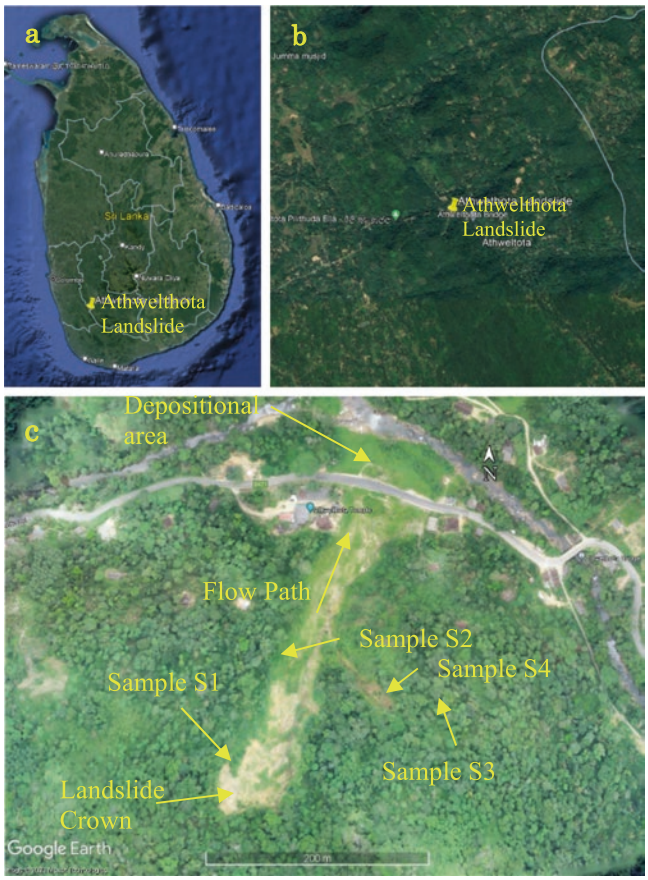

Fig. 1 Satellite (**a** and **b**) and drone image (**c**) of Athwelthota landslide location including its main features and sample locations. (Source base map: Google satellite imagery)

vital objectives of the project RRLL is to identify the causes and contributing factors of the landslide that happened in Athwelthota, one of the pilot sites of this research study.

This study aims to reproduce the 2017 Athwelthota landslide and discuss future hazards of nearby potential landslides. For this aim, the study will use a combination of historical records, geomorphological field surveys, geospatial data, soil parameters, rainfall data, geospatial information, landslide geometry, and other relevant data.

2 Methodology

This study employs a multi-pronged approach to investigate the Athwelthota landslide hazard. The methodology consists of four key components:

1. **Desk study:** The first step was reviewing the available literature and geospatial data, including satellite imagery. This review helped identify potential landslide areas and gather information on past landslides in the region.
2. **Fieldwork:** The fieldwork was conducted to identify past and potential landslides in the study area. This work involved geomorphological mapping and the collection of soil samples for laboratory testing. A few locations were selected for soil sampling (Fig. 1c) by considering the soil type variation of the past landslide and potential landslide area.
3. **Geotechnical laboratory testing:** Soil samples were tested at the Geotechnical Laboratory of NBRO. The primary objective of this testing was to obtain the geotechnical parameters required for numerical simulation. The undrained dynamic ring shear loading apparatus (ICL-2) was used to determine the shear strength properties of the soil (Sassa et al. 2004a).
4. **Numerical analysis using LS-RAPID:** The LS-RAPID (Landslide Simulator for Risk Assessment and Prediction of Inundation Disasters) model, developed by Sassa et al. (2010), has emerged as an essential tool in the field of landslide research and risk assessment. The foundation of the LS-RAPID model can be traced back to Sassa's work in 1988 when he initially formulated a geotechnical model for landslide motion. The laboratory test results, field observations, and geospatial data were inputs to the LS-RAPID numerical model to simulate the past landslide in 2017. The LS-RAPID model has been successfully used to simulate landslides in various geological and environmental conditions, providing valuable insights into landslide mechanics and failure factors. For example, the model was used to simulate the Aranayake landslide in Sri Lanka (Tan et al., 2020), the Oso landslide in the United States (Brien et al. 2016), and the Izu-Oshima landslide in Japan (Tsuyoshi et al. 2017).

3 Results and Discussion

Satellite imagery shows that the study area comprises several undulations, which could be possible past landslides. However, field observations revealed two past landslides that had failed earlier. One of these landslides occurred in 2017, and the other occurred at an unknown period (Fig. 2). Both landslides shared the same flow path and depositional area but had separate initiation areas. Both these initiation areas are located near the valley's axis, which trends north.

Two potential landslides were identified during the field survey on the slope to the right of the valley, next to the previously identified past landslides (Fig. 2). These landslides exhibited tensional cracks and depressions as potential landslide features. These tensional cracks occurred during the same period as the failure of the past landslide in 2017.

Fig. 2 Identified Past and Potential Landslides and their features in Athwelthota

Table 1 Summary of undrained ring shear test results

Sample	$Ø_m$	τ_{up} (kPa)	τ_{ur} (kPa)	DL (mm)	DU (mm)
S1	41	220	61	8	200
S2	44	215	118	6	80
S3	40	178	73	4	250
S4	41	215	52	9	300

Note: $Ø_m$ = mobilized friction angle at failure, τ_{up} = undrained peak shear strength, τ_{ur} = undrained shear strength at steady state, DL = shear displacement at the start of the strength reduction, DU = shear displacement at the start of steady state

After the sample collection phase, laboratory tests were performed, and the results of these tests and their corresponding parameter values from the ring-shear apparatus are presented in Table 1.

Rain infiltration leads to an increase in the groundwater level, thus generating significant pore pressure to trigger an RRLL. The pore pressure ratio R_u, a dimensionless parameter defined as the ratio of the pore water pressure to the vertical effective stress (Bishop and Morgenstern 1960), rationally provides the RRLL's threshold. The SLIDE model (Liao et al. 2010) was used in this study to calculate the R_u value.

The chronological record of the rain in May 2017 (Fig. 3(b)), together with the landslide morphology, soil properties, and infiltration rates, was given as input to the SLIDE model to obtain the buildup of the R_u value (Fig. 3(a)). The laboratory testing results and estimated geotechnical parameters in Table 2 were used to simulate the Athwelthota landslide. The generated results for the Athwelthota landslide mass are depicted in Fig. 4.

At 67 h 01 min in the simulation, when the pore pressure ratio (R_u) reached 0.43, the central part of the soil mass parching atop the slope started to detach (Fig. 4(a)). Subsequently, at approximately 68 h and 36 min ($R_u = 0.43$), the entire landslide mass started sliding (stage 2 in Fig. 4). Finally, the fluidized soil mass came to a halt at 68 h and 38 min after the simulation started (stage 3 in Fig. 4), which corresponds to 4:38 a.m. on May 26th, 2017 (Table 3). The actual landslide was considered to have occurred at around 5:15 a.m. on that day (NBRO n.d.), which was eventually close to 4:38 a.m., the time estimated by using LS-Rapid. Although a relatively small landslide occurred as a branch of the main landslide a few hours later, only the main landslide of the Athwelthota Landslide was considered for the numerical modelling due to its complexity.

Since the LS-RAPID model with the given parameters could reproduce the real 2017 RRLL adequately, as described above, it was then used to simulate the behavior of the identified two potential failures, L1 and L2 (Figs. 5 and 6), and assess their potential impacts. The morphology of the potential landslides was inferred from the local geomorphology and geological observations, with particular attention to the features of previous landslides.

A usual simulation approach, which incorporates porewater pressure as a critical parameter within the model, was

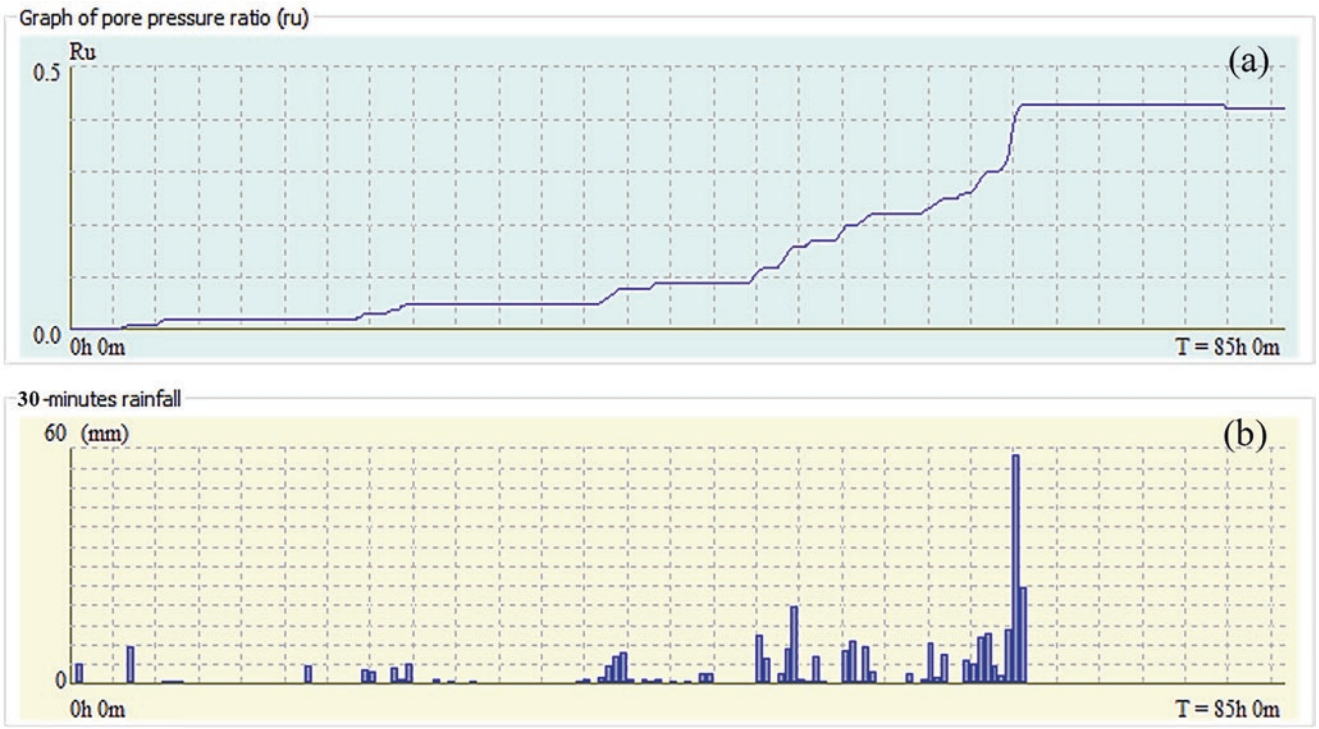

Fig. 3 (**a**) Calculated R_u values, (**b**) rainfall histogram in 24th–26th May, 2017

Table 2 Geotechnical parameters utilized in the LS-RAPID software for Athwelthota Landslide

Parameter	Value	Source
Lateral pressure ratio ($k = \sigma_h/\sigma_v$)	0.4	Estimation
Friction coefficient inside landslide mass ($tan\varphi i$)	0.5	Estimation
Friction coefficient during motion ($tan\varphi m$)	0.96	Test data (ring shear)
Steady-state shear resistance (τ_{ss})	52 kPa	Test data (ring shear)
Pore pressure generation rate (B_{ss})	0.5	Estimation
Peak friction coefficient ($tan\varphi p$)	0.96	Test data (ring shear)
Peak cohesion at sliding surface (c_p)	50 kPa	Estimation
Shear displacement at the start of strength reduction (DL)	8	Test data (ring shear)
Shear displacement at the start of steady state (DU)	100	Test data and estimation (ring shear)
Total unit weight of the mass (γ_t)	17.9 kN/m^3	Test data

employed to simulate these potential failures. It is important to mention that these potential landslides were not exposed to a triggering rainfall event. Therefore, the simulation was conducted, increasing values of the R_u parameter until the landslide mass reached the critical point of equilibrium and started sliding. The two hypothetical landslides, L1 and L2, have R_u thresholds of 0.67 and 0.64, respectively. The notable aspect here is that these R_u values surpass the corresponding R_u value of the past landslide. This disparity in R_u values illuminates why the prospective landslides had not yet been set into motion. The higher R_u values indicate that the slopes have been more stable than those that failed in the past, which included the 2017 landslide. Though the potential landslides appear to be relatively more minor than the past landslides, they still pose a significant risk of debris flow and long traveling, damaging the surrounding environment and infrastructure while potentially endangering lives and properties.

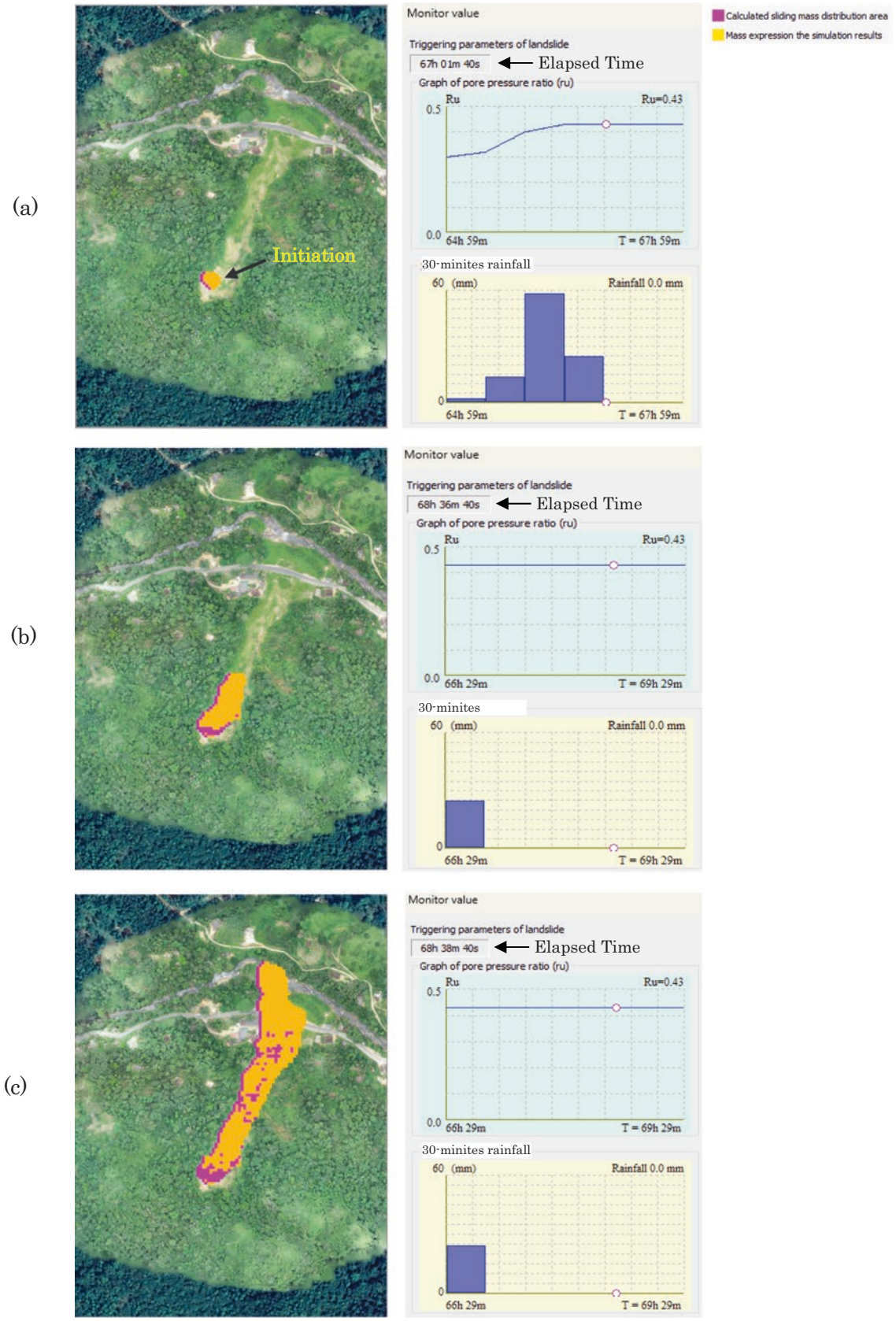

Fig. 4 Simulated landslide failure process for the Athwelthota landslide at each stage using the LS-RAPID with R_u and rainfall data: (**a**) initiation, (**b**) start of sliding, and (**c**) end of sliding

Table 3 Model and real time of Athwelthota landslide

Event	LS-RAPID model time	Real-time represent by model in 2017
Start of simulation	0 h 0 min	09:00 AM – 24th May
Initiation of landslide	67 h 01 min	03:01 AM – 26th May
Movement of landslide	68 h 36 min	04:36 AM – 26th May
End of simulation	68 h 38 min	04:38 AM – 26th May

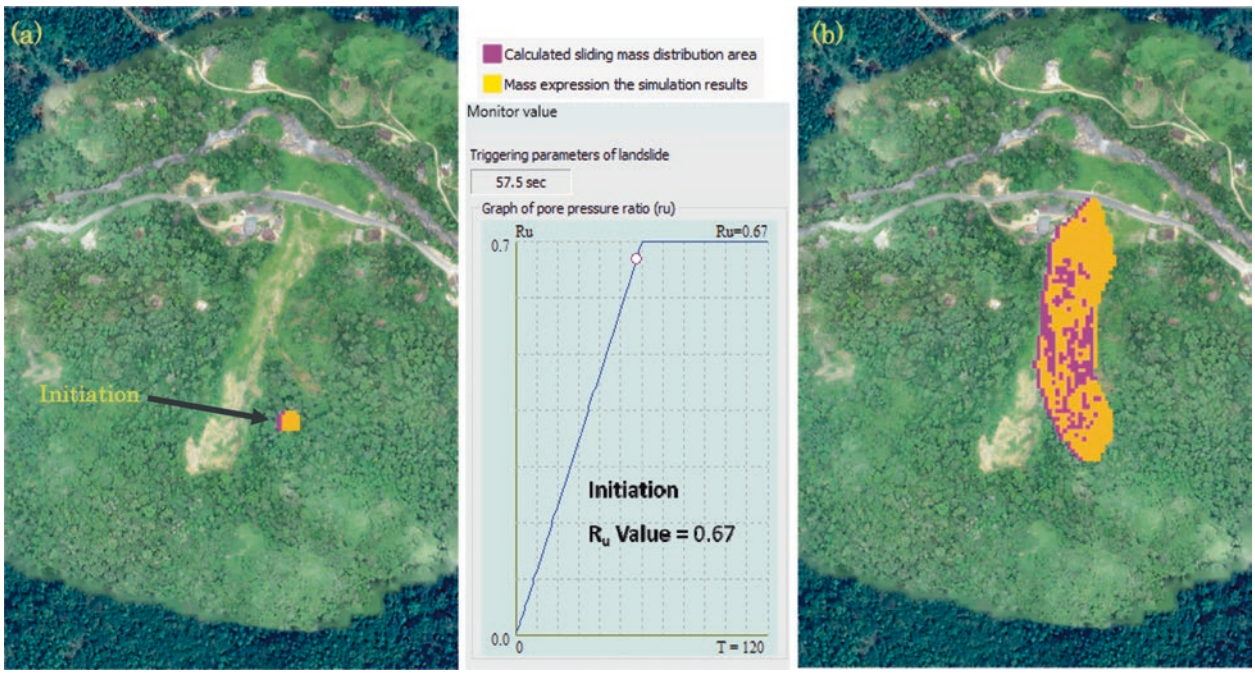

Fig. 5 Simulated landslide failure process for potential landslide L1 using the LS-RAPID with R_u data (**a**) initiation and (**b**) failure

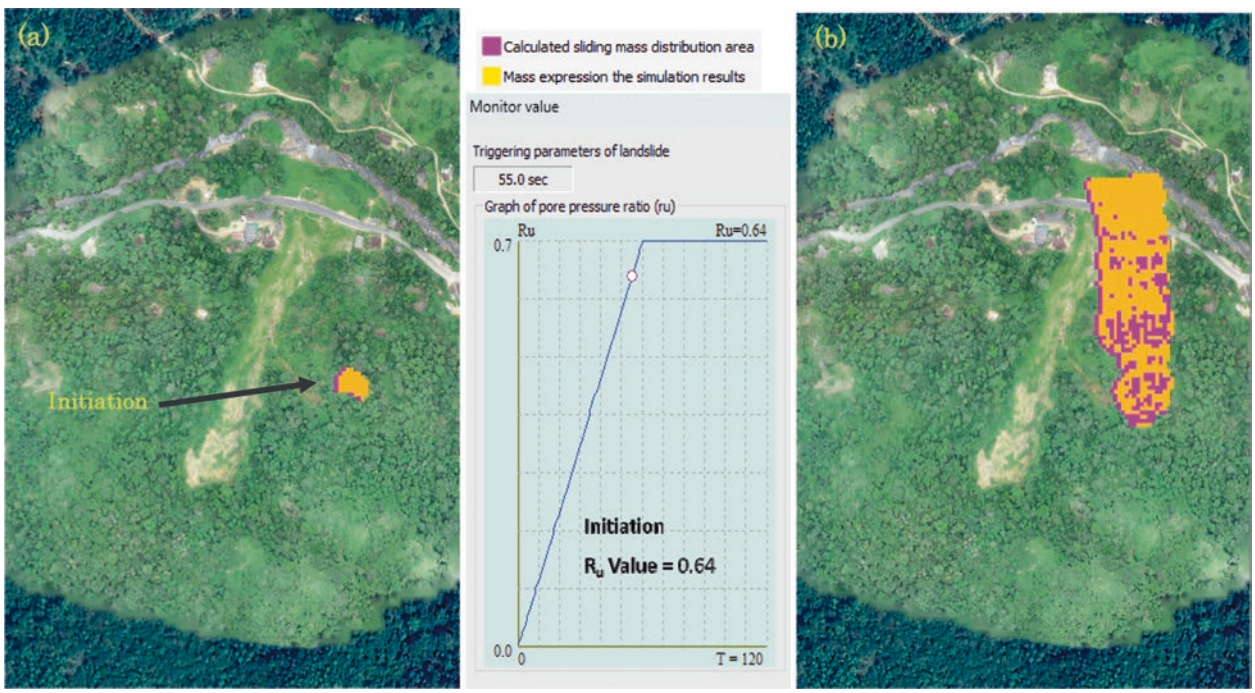

Fig. 6 Simulated landslide failure process for potential landslide L2 using the LS-RAPID with R_u data (**a**) initiation and (**b**) failure

4 Conclusions

This study focused on applying LS-RAPID numerical simulation software to understand the future landslide potential around the Athwelthota past landslide. Firstly, the numerical model was validated by reproducing the landslide in May 2017 by incorporating geospatial data and geotechnical parameters determined using the ICL-2 ring shear apparatus. It was found that the time of landslide initiation and the landslide boundary reached comparable outcomes with field data recorded. Upon validation, the simulation was extended to assess the probability of two future landslides adjacent to the past landslide. The simulation results found that the R_u value needed to trigger future landslides was higher than the previous landslide. This evidence provides a rationale for not initiating the landslide during the May 2017 rain spell.

However, it is crucial to acknowledge the limitations of this study, including data availability, data quality, uncertainties related to model parameters, and variations in soil properties.

Future research endeavors should explore site-specific factors contributing to landslide susceptibility, encompassing land-use practices, vegetation cover, and groundwater conditions.

In summary, this study provides valuable insights into Athwelthota specific landslide dynamics and contributes to the broader knowledge of landslide risk management. By addressing the unique challenges of this region and highlighting the potential for early warning systems and site-specific mitigation strategies, our research underscores the critical role that comprehensive analysis and modeling play in minimizing the catastrophic impact of landslides. This study stands as a testament to the ongoing efforts to safeguard lives, infrastructure, and ecosystems in landslide-prone areas.

Acknowledgments The authors gratefully acknowledge funding from a Japan-Sri Lanka bilateral SATREPS (Science and Technology Research Partnership for Sustainable Development) project titled "Development of Early Warning Technology of Rain-Induced Rapid and Long-Traveling Landslides joint program from 2019 to 2025 (Project RRLL)". Equipment and software used in the study were obtained with financial support from the SATREPS program. The International Consortium on Landslides (ICL) and the National Building Research Organization of Sri Lanka (NBRO) are implementing this project.

References

Bishop AW, Morgenstern NR (1960) The stability of earth slopes. Geotechnique 10(4):153–175

Brien DL, Baum RL, Reid ME, Coe JA, Allstadt KE (2016) Integrating field mapping, LiDAR, and numerical modeling to estimate the extent, volume, and potential mobility of rock avalanches in the Glacier Peak area, northern Cascade Range, USA. Eng Geol 209:28–48

Jayasinghe PM, Vithanage M, Tobschall HJ (2018) Recent trends in landslides in Sri Lanka: analysis using the open-source geographical information system. Environ Earth Sci 77(5):177

Konagai K, Sassa K, Karunawardena AS, Nishida K (2021) Development of early warning technology of rain-induced rapid and long-travelling landslides in Sri Lanka (project RRLL). In: Proceedings of the 11th international symposium on landslides. Springer Nature Switzerland, Cham, pp 2137–2144

Liao SH, Chen YH, Lin CY (2010) SLIDE: a geotechnical model for dynamic factor of safety analysis due to rainfall infiltration. Comput Geotech 37(1):118–131

National Building Research Organization (NBRO) (n.d.) Landslide Damage & Loss Assessment Report. Retrieved from https://www.nbro.gov.lk/images/2016_pdf/publications/DAR_Compiled-Report_V1_low-quality.pdf

Nissanka SP, Siriwardana CHER, Dissanayake DMSK (2015) Landslide disaster risk management in Sri Lanka: a critical review. J Natl Sci Found 43(1):1–11

Ratnayake U, Herath S (2005) Changing rainfall and its impact on landslides in Sri Lanka. J Mt Sci 2:218–224

Sassa K (1988) Geotechnical model for the motion of landslides. In: Proceedings of 5th international symposium on landslides, "Landslides", vol 1, Balkema, Rotterdam, pp 37–56

Sassa K, Fukuoka H, Wang G, Ishikawa N (2004a) Undrained dynamic-loading ring-shear apparatus and its application to landslide dynamics. Landslides 1(1):7–19

Sassa K, Nagai O, Solidum R, Yamazaki Y, Ohta H (2010) An integrated model simulating the initiation and motion of earthquake and rain induced rapid landslides and its application to the 2006 Leyte landslide. Landslides 7(3):219–236

Tan Q, Sassa K, Dang K, Konagai K, Karunawardena A, Bandara RMS, Sato G (2020) Estimation of the past and future landslide hazards in the neighboring slopes of the 2016 Aranayake landslide, Sri Lanka. Landslides 17:1727–1738

Tsuyoshi H, Ayumu O, Kengo M, Hideaki M (2017) Numerical simulation of the 2013 Oshima landslide using the LS-RAPID model. Landslides 14(5):1745–1756. https://doi.org/10.1007/s10346-017-0839-7

Experimental Study on Residual Shear Strength of Soil Using Undrained Ring Shear Apparatus

N. P. G. Amali, H. R. Maduranga, and A. R. P. Weerasinghe

Abstract

In general, studies of residual shear strength are minimal for soils on landslide-prone slopes in Sri Lanka. This study focuses on determining the residual shear strength of the soil samples taken from the Athwelthota landslide area, by conducting a series of undrained monotonic shear-stress control ring shear tests. The shear behavior of soil under different effective normal stress conditions was observed and further, the shearing behavior of soil samples with different contents of silt and clay was analyzed. The results showed that a small cohesion was exhibited at low effective normal stress conditions and the mobilized friction angle became constant at higher normal stresses. It was also found that peak and steady-state shear strengths decreased when the fine content increased, resulting a higher brittleness index. And the brittleness index decreases with the increase of effective normal stress. Monitoring the pore water pressure during the shearing shows that it increased with shear displacement. A significant reduction in the shear strength could result from the shear failure due to the buildup of excess pore-water pressure within the shear zone. The specimen confined under identical stress conditions generated higher excess pore water pressure within the shear zone when the fine content was higher.

Keywords

Ring shear apparatus · Shear strength · Fine content

1 Introduction

Understanding the shear strength behavior of landslide soil is important to study the rapid and long-traveling landslides in Sri Lanka. Peak and steady-state shear strength parameters of the landslide soil are usually required for stability analysis, flow path prediction, and mitigation designs. To obtain the shear strength behavior of soil numerous laboratory and field experiments have been used such as direct shear test, triaxial test, ring shear test etc.

During the past decade, limited studies have been done to observe the peak and ultimate relations between the shear stress, s′ and the effective mean normal stress t′ of landslide soil in Sri Lanka using triaxial tests (Dias et al. 2014). Some experimental studies have been conducted using ring shear apparatus for the soil samples from the Aranayake landslide area in Sri Lanka to obtain peak and residual strength parameters required for LS-RAPID to simulate the initiation and downward movement of landslide mass (K. Konagai et al. 2022).

Ring shear test is a very common method used to determine the residual shear strength of landslide soil materials. The significant advantage of the ring shear apparatus is that it can develop large shear deformations in the specimen, and there is no change in the shear plane area during shearing. Therefore, a ring shear apparatus is a major tool used in the analysis of the residual shear strength of the soil.

As stated by D. H. Loi et al. (2022), ring shear test was introduced by Bishop et al. (1971), and it was improved by Bromhead (1979), Savage and Sayed (1984), Sassa (1984), Hunger and Morgenstern (1984), Tika (1989), and Garga and Infante Sedano (2002). Sassa et al. (1997) developed and improved a series of ring shear apparatus that can used to study landslide dynamics by simulating the entire process of the landslide.

In this study, we assess the shear behaviors of landslide soil material by performing undrained ring shear tests under different effective normal stress conditions. Landslide soil samples with different fine contents have been used to study the effect of fine content on the shearing behavior using the undrained ring shear apparatus, ICL-2.

N. P. G. Amali (✉) · H. R. Maduranga · A. R. P. Weerasinghe
National Building Research Organisation, Colombo, Sri Lanka

B. Abolmasov et al. (eds.), *Progress in Landslide Research and Technology, Volume 3 Issue 1, 2024*, Progress in Landslide Research and Technology, https://doi.org/10.1007/978-3-031-55120-8_28

2 Testing Program

2.1 Materials

The test series consists of several samples collected from the Athwelthota landslide area. This landslide occurred in the Athwelthota area in Baduraliya DS division, Kalutara District, on May 26, 2017, at around 0500 h due to heavy precipitation. The field investigations indicate that the landslide was initiated at two locations on the mountain crest of Paru Pana Mukulana Kanda. For this study, we collected undisturbed box samples from landslide crest and middle areas as shown in Fig. 2.

Sieve and hydrometer analysis, Atterberg limits and specific gravity tests were conducted on these soil samples to determine the index soil properties. Figure 1 shows the grain size distribution curves. The soil samples' fine content was 26, 42, 47, and 55 percent by weight (termed F26, F42, F47, and F55, respectively) (Fig. 2). According to the BS soil classification, the soil can be categorized as Silty Sand or Sandy SILT. Table 1 summarizes the liquid limit, plastic limit, plasticity indices, and particle densities of the soil samples.

2.2 Ring Shear Apparatus

This paper's ring shear test results are obtained using ICL-2 undrained ring shear apparatus, donated to the National Building Research Organization, Sri Lanka, under the Science and Technology Research Partnership for Sustainable Development (SATREPS) project in 2022.

According to D. H. Loi et al. (2022), Sassa and his colleagues in the Disaster Prevention Research Institute (DPRI), Kyoto University, and International Consortium on Landslide (ICL) have developed nine designs dynamic loading ring shear apparatus since 1984 (DPRI-1, DPRI-2, DPRI-3, DPRI-4, DPRI-5, DPRI-6, DPRI-7, ICL-1, and ICL-2). The details of the ICL-2 ring shear apparatus and basic ring shear experiments have been discussed comprehensively in his study. ICL-2 undrained ring shear apparatus is having a maximum loading capacity of 1000 kPa.

In this study the residual shearing behavior of landslide soil was examined by performing a series of undrained ring shear tests. For the soil sample with a fine content of 26% (F26), monotonic shear-stress control, undrained ring shear tests were conducted in saturated condition, with shear stress increment rate of 0.25 kPa/sec under effective normal stress of 100 kPa, 200 kPa, 300 kPa, 400 kPa and 500 kPa.

For the soil samples with different fine contents (F26, F42, F47, and F55) undrained ring shear tests been conducted to study the influence of fine particles on the shear behavior. Table 2 summarizes the test conditions used for each test.

Due to the size of the shear box, dry soil passing a 2 mm sieve is used, as shown in Fig. 3. About 0.8 kg of dry soil is placed in a plastic container, and de-aired water is poured into it up to 3 mm above the soil surface. It is placed in the vacuum tank to remove entrapped air in the soil to saturate the soil sample until the air bubbles cease escaping, as shown in Fig. 4.

The shear box is set up in the ring shear apparatus, and the first empty shear box is filled with CO_2 and then de-aired water to remove entrapped air in the shear box. Then the de-aired soil sample is slowly built in the shear box and the sample surface is leveled, as shown in Fig. 5.

After setting up the sample in the ring shear apparatus, de-aired water circulates through the shear box to remove trapped air. Bd valve is checked to measure the degree of saturation; if it is greater than 0.95, the sample is in the saturated state.

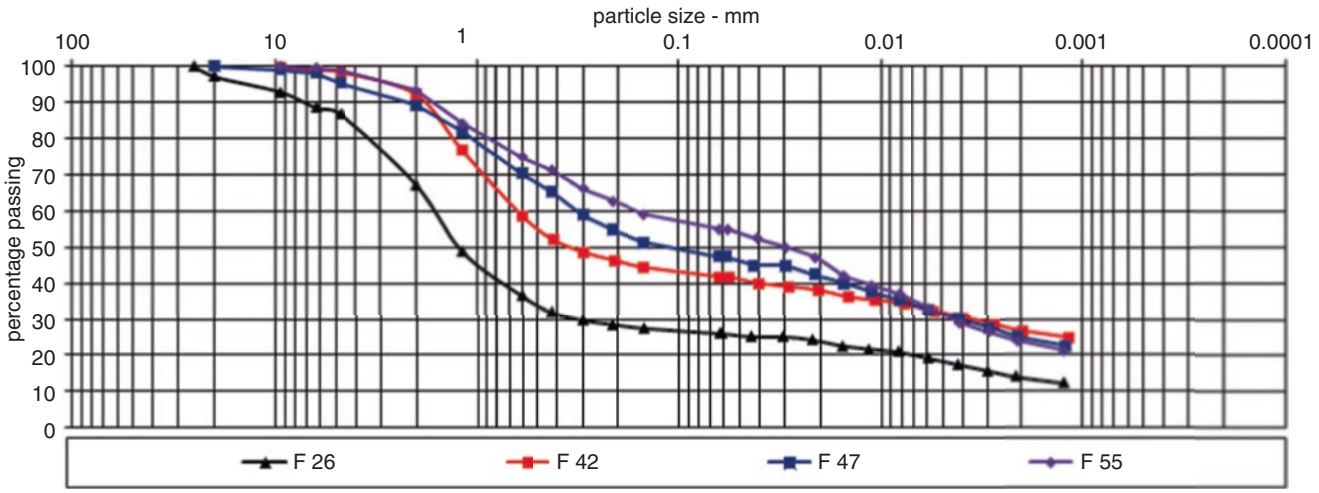

Fig. 1 Grain size distribution of soil samples

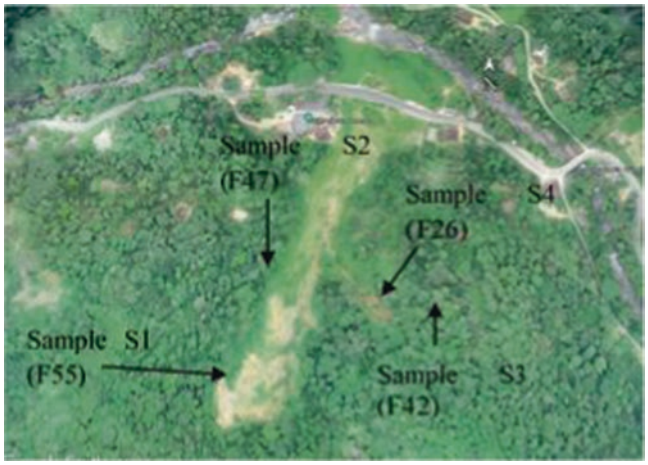

Fig. 2 Athwelthota landslide area with sampling locations

Table 1 Physical properties of the soil

Sample	Gravel (%)	Sand (%)	Silt & Clay (%)	Clay (%)	LL (%)	PL (%)	PI (%)	Soil type	Specific gravity
F26	33	41	26	14	53	37	16	SM	2.59
F42	8	50	42	27	57	40	17	MS	2.60
F47	11	42	47	25	51	35	16	MS	2.57
F55	7	38	55	24	62	45	17	MS	2.58

Fig. 4 De-airing the soil sample

Table 2 Ring shear test conditions

Sample	Dry density (g/cm^3)	Initial void ratio	B_D	Normal stress (kPa)	Shear speed (kPa/s)	Shear displacement (m)	Drainage
F26	1.29	1.01	0.90	100	0.25	10	Undrained
F26	1.23	1.10	0.90	200	0.25	10	Undrained
F26	1.15	1.25	0.90	300	0.25	10	Undrained
F26	1.28	1.02	0.90	400	0.25	10	Undrained
F26	1.22	1.12	0.95	500	0.25	10	Undrained
F42	1.14	1.29	0.96	500	0.25	10	Undrained
F47	1.11	1.32	0.93	500	0.25	10	Undrained
F55	0.96	1.70	0.94	500	0.25	10	Undrained

Fig. 3 Sample preparation

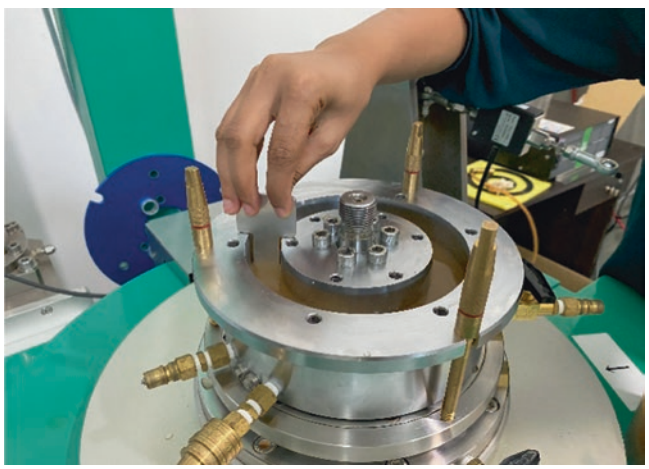

Fig. 5 Leveling the sample surface

After the saturation, soil specimen is consolidated to simulate the initial stress conditions of the sample and the shearing is carried out under the undrained condition through a servo-controlled motor at a 0.25 kPa/sec stress-controlled condition. Pore-water pressure, shear displacement, shear stress, normal stress, and vertical displacement of the specimen are monitored during the ring shear test to study the soil's shear behavior.

3 Test Results

For the soil sample with 26% fines, undrained ring shear test results under normal stresses of 100 kPa, 200 kPa, 300 kPa, 400 kPa and 500 kPa are shown in Fig. 6. For different normal stress conditions, the effective stress path was plotted and the residual failure line was obtained.

Undrained ring shear tests results for the soil samples with different fine contents F26, F42, F47, and F55 are presented in Figs. 7, 8, 9, and 10.

From Fig. 7(a), we obtained mobilized friction angle at failure (Øm =440), steady state shear resistance (τss =118 kPa) for the sample with 26% fines. The shear stress and shear displacement relationship, Fig. 7(c) shows shear displacement at the start of the strength reduction (DL=6 mm) and shear displacement at the start of steady state (DU=80 mm).

From Fig. 8(a), we obtained mobilized friction angle at failure (Øm =410), steady state shear resistance (τss=61 kPa) for the sample with 42% fines. The shear stress and shear displacement relationship, Fig. 8(c) shows shear displace-

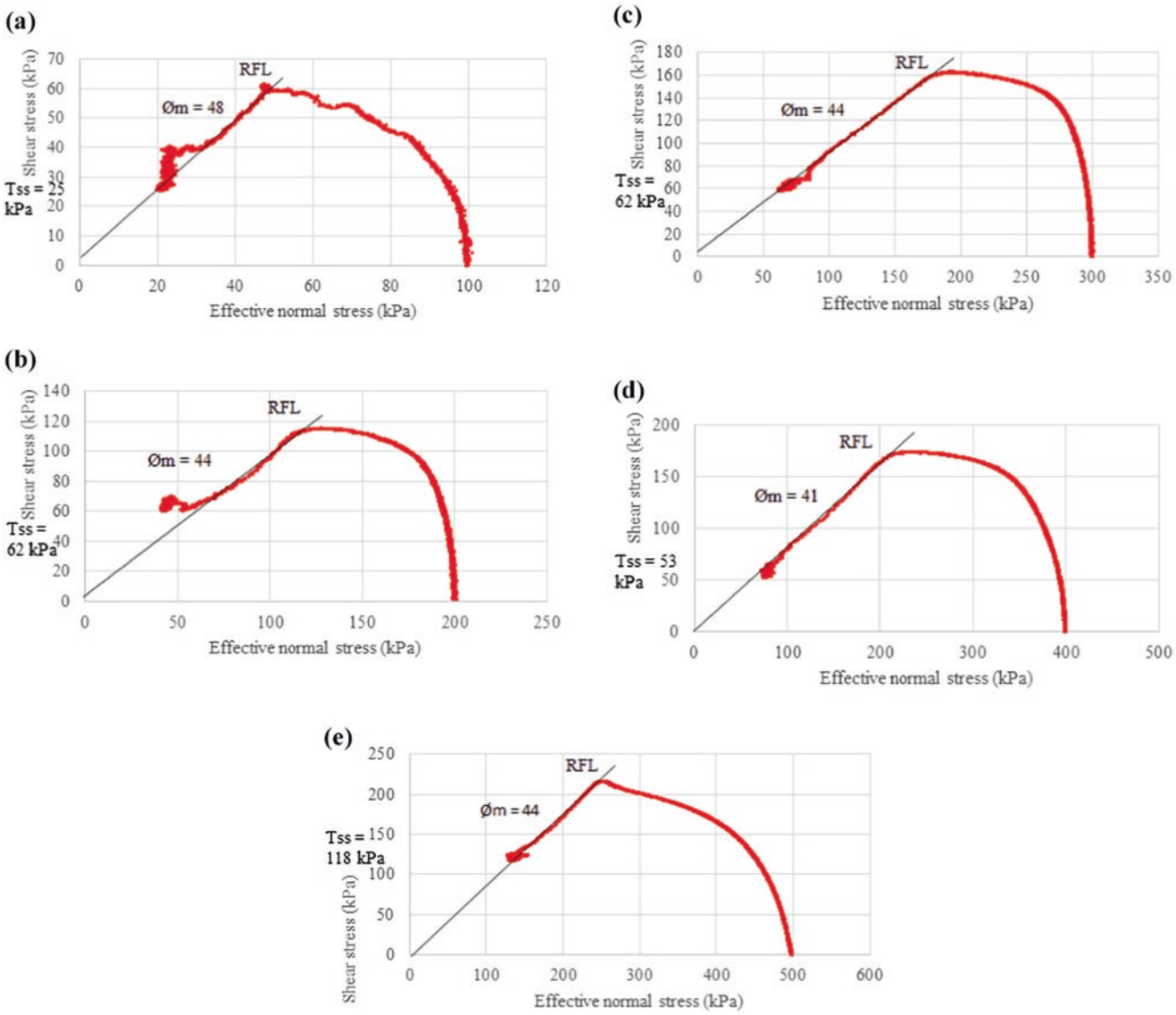

Fig. 6 Results of stress path from undrained ring shear test under different normal stresses on silty sand with 26% fines, RFL-residual failure line

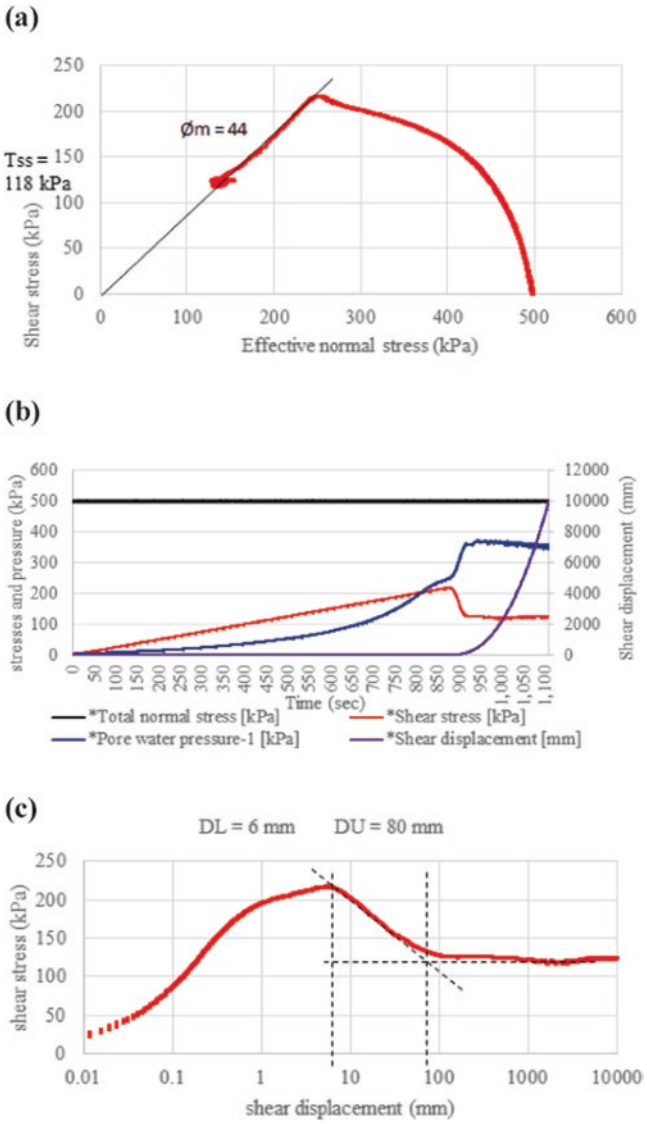

Fig. 7 Results of undrained ring shear test. (**a**) Stress path, (**b**) Time series of data, (**c**) Shear stress and shear displacement relationships. Test conditions: sample: silty sand with 26% fine content, BD = 0.94, normal stress = 500 kPa, shear stress increment rate: 0.25 kPa/s

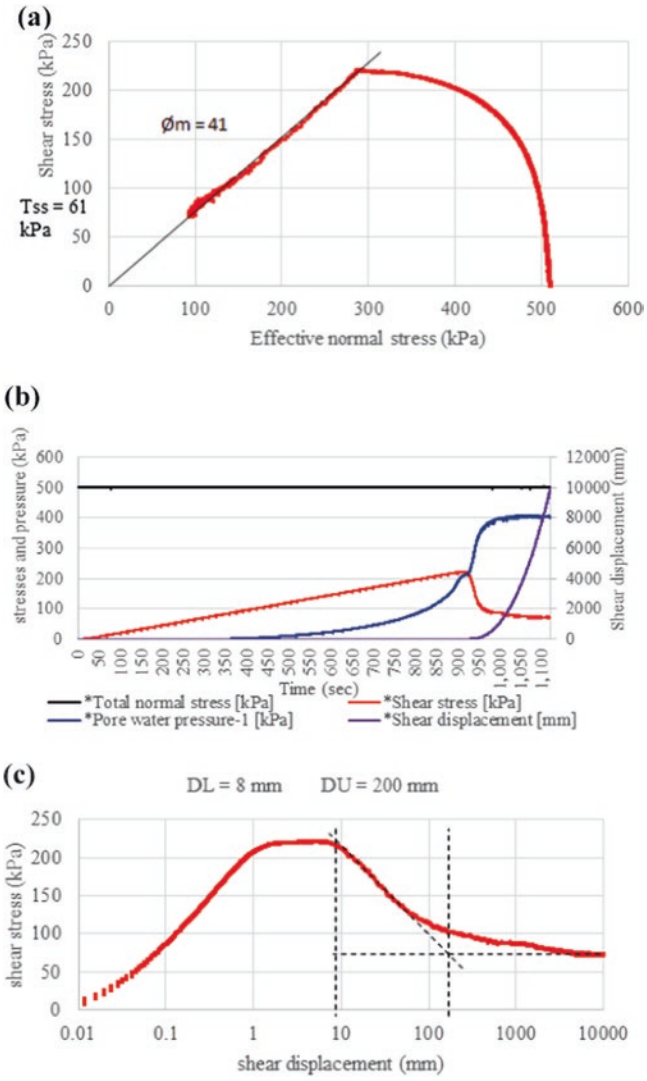

Fig. 8 Results of undrained ring shear test. (**a**) Stress path, (**b**) Time series of data, (**c**) shear stress and shear displacement relationships. Test conditions: sample: sandy silt with 42% fine content, BD = 0.93, normal stress = 500 kPa, shear stress increment rate: 0.25 kPa/s

ment at the start of the strength reduction (DL=8 mm) and shear displacement at the start of steady state (DU=200 mm).

From Fig. 9(a), we obtained mobilized friction angle at failure (Øm =410), steady state shear resistance (τss =52 kPa) for the sample with 47% fines. The shear stress and shear displacement relationship, Fig. 9(c) shows shear displacement at the start of the strength reduction (DL = 9 mm) and shear displacement at the start of steady state (DU =300 mm).

From Fig. 10(a), we obtained mobilized friction angle at failure (Øm =400), steady state shear resistance (τss=73 kPa) for the sample with 55% fines. The shear stress and shear displacement relationship, Fig. 10(c) shows shear displacement at the start of the strength reduction (DL = 4 mm) and shear displacement at the start of steady state (DU=250 mm).

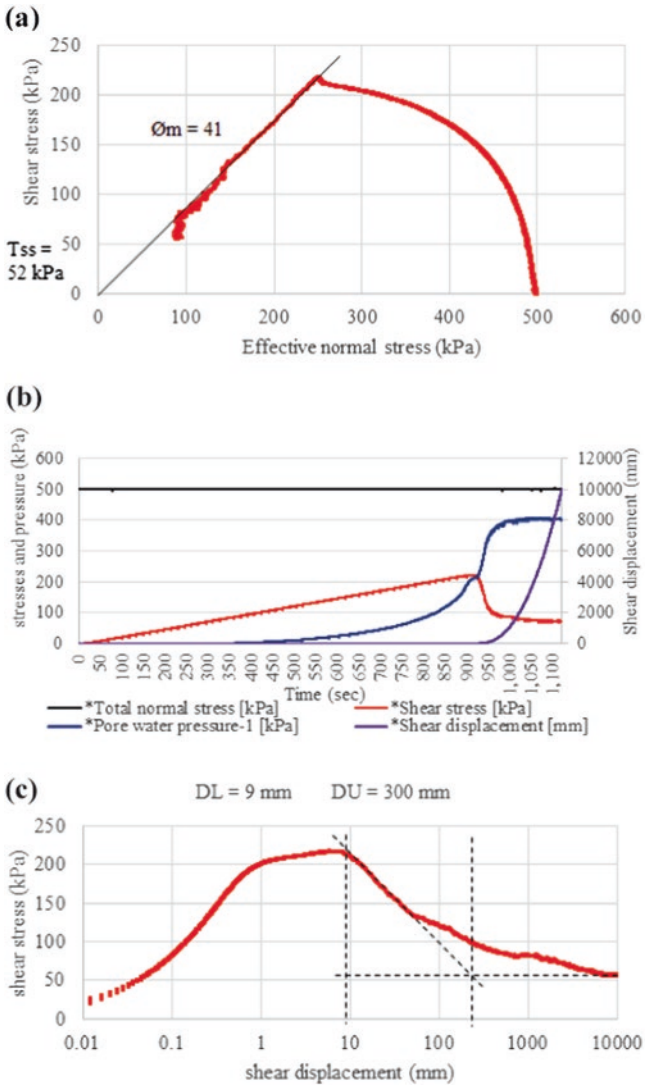

Fig. 9 Results of undrained ring shear test. (**a**) Stress path, (**b**)Time series of data, (**c**) Shear stress and shear displacement relationships. Test conditions: sample: sandy silt with 47% fine content, BD = 0.95, normal stress = 500 kPa, shear stress increment rate: 0.25 kPa/s

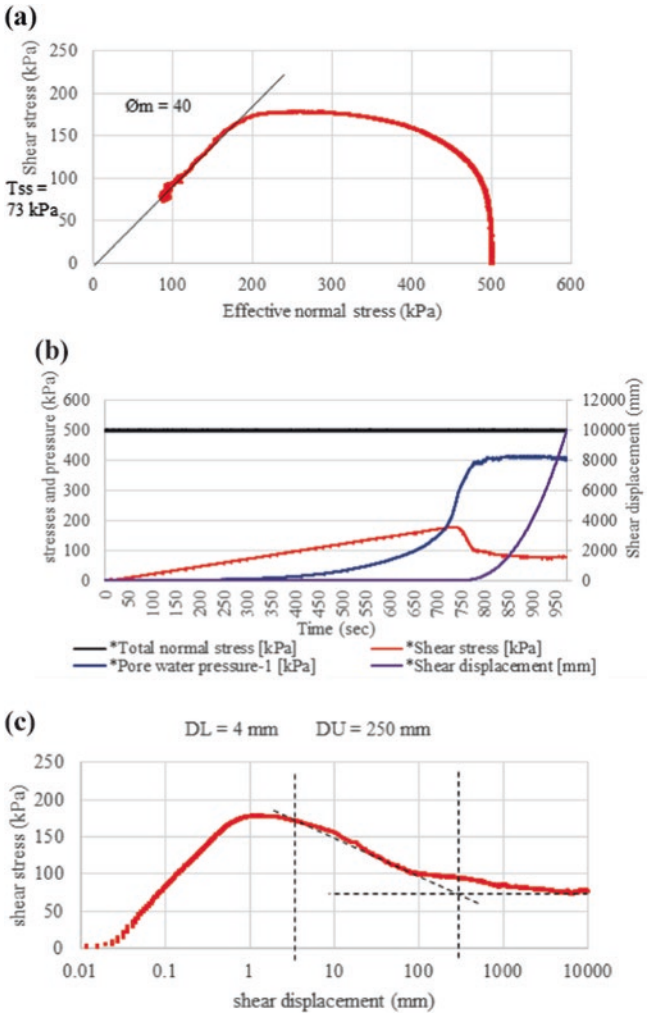

Fig. 10 Results of undrained ring shear test. (**a**) Stress path, (**b**) Time series of data, (**c**) shear stress and shear displacement relationships. Test conditions: sample: sandy silt with 55% fine content, BD = 0.96, normal stress = 500 kPa, shear stress increment rate: 0.25 kPa/s

Table 3 Summery of undrained ring shear test results

Sample	C′ (kPa)	$Ø_m$	τ_{up} (kPa)	τ_{ur} (kPa)	DL (mm)	DU (mm)
F26 (100 kPa)	2	48	61	26	9	200
F26 (200 kPa)	2	44	115	62	7	90
F26 (300 kPa)	4	44	162	58	6	90
F26 (400 kPa)	0	41	173	61	6	90
F26 (500 kPa)	0	44	215	118	6	80
F42 (500 kPa)	0	41	220	61	8	200
F47 (500 kPa)	0	41	215	52	9	300
F55 (500 kPa)	0	40	178	73	4	250

Table 3 contains the corresponding residual shear strength parameters for all test specimens in tabular form.

4 Discussion

Many factors influence the residual shear behavior of the soil. In this study, the effect of normal stress was observed by conducting several sets of undrained ring shear tests. Most residual failure envelopes were reasonably linear for the range of normal stresses used in this study. Based on the test results, the residual failure envelopes often show cohesion values equal to zero or small values of cohesion as presented in Fig. 11. In the lower normal stress conditions, residual strength envelopes give small values of cohesion, with a maximum value of c equal to 4 kPa. A constant value of residual friction angle with zero cohesion was achieved at high normal stresses.

The effect of fine content on the residual shear behavior was also studied and when comparing the stress path of the four different soil specimens, it shows that fine content have some effect on the shear behavior as shown in Fig. 12(a). The effective stress paths obtained from the undrained ring shear tests shows the mobilized friction angle at failure decreases with the increase of the fine content. Figure 12(b) shows the shear strength tends to decreases as the fine content increases. The soil specimen with less fines, tend to show greater peak strengths than the specimens with more fines. When subjected to large shear displacements the excess pore water pressure developed within the shear zone increases with the increase of fine content as shown in Fig. 12(c).

As shown in Fig. 12(a), each sample in this undrained ring shear test series undergoes some amount of reduction in the shear strength after the failure, and this reduction differs for different samples. Therefore, the brittleness index (Bishop 1967) is used to analyze the consequences of shear failure.

$$IB = \frac{\tau p - \ddot{A}s}{\tau s} \quad (1)$$

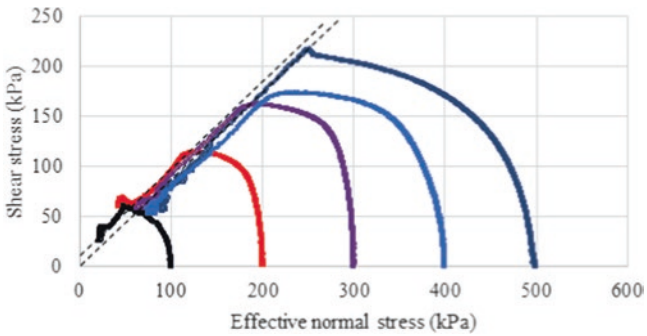

Fig. 11 Results of stress path from undrained ring shear test under different normal stresses on silty sand with 26% fines

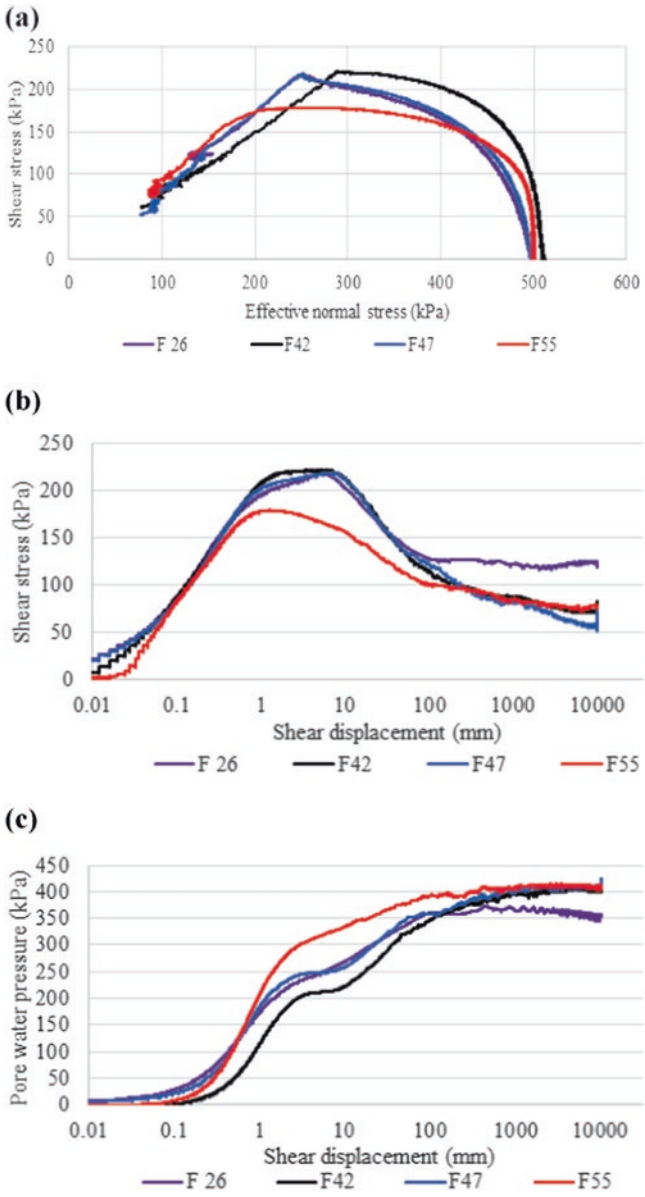

Fig. 12 Results of undrained ring shear tests on soil samples of different fine contents (26%, 42%, 47% and 55%) (**a**) Effective stress paths; (**b**) Shear resistance versus shear displacement; and (**c**) pore-water pressure versus shear displacement

Where τ_p is peak shear strength (kPa) and τ_s is shear strength at steady state (kPa)

The brittleness index is commonly used to evaluate the strain-softening behavior of soil. Brittle material often

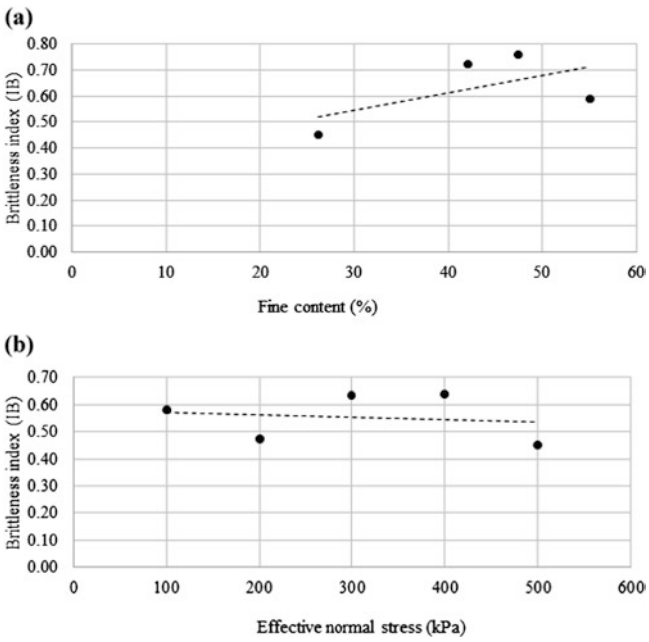

Fig. 13 Brittleness index relationships (**a**) Brittleness index versus fine content; (**b**) Brittleness index versus effective normal stress

observed the highest strength loss in first time failure. The test results showed that the brittleness index increases with the increase of fine content and decreases with the increase of effective normal stress (Fig. 13).

5 Conclusion

A Series of ring shear tests were conducted for the soil samples collected from the Athwelthota landslide area to study the shear behavior of landslide soil. The effects of the effective normal stress and fine content on the shear behavior in undrained monotonic loading conditions were examined based on the test results. The following conclusions were obtained.

1. Many of the landslide soil exhibited a small cohesion at low values of effective normal stress, but the mobilized friction angle at failure achieved a constant value at higher normal stresses.
2. With the increase of the fine content, the mobilized friction angle at failure decreases.
3. When the fine content increased high excess pore water pressures were developed within the shear zone when subjected to large shear displacement.
4. With the increase of fine content, the brittleness index is increased and it decreases with the increase of effective normal stress.

Acknowledgments The authors gratefully acknowledge the International Consortium on Landslides (ICL) and the National Building Research Organization (NBRO) of Sri Lanka for implementing the "Development of Early Warning Technology of Rain-induced Rapid and Long-traveling Landslides" project which provides the funding and support for this study. This is a five-year joint research project within the framework of the SATREPS project (Science and Technology Research Partnership for Sustainable Development).

References

Dias AV, Abayakoon SBS, Bhandari RK (2014) Discrete boundary shear strength of a landslide at high rainfall precipitation zone in Sri Lanka. In Landslide Science for a Safer Geoenvironment: Vol. 1: The International Programme on Landslides (IPL) (pp. 101–106). https://doi.org/10.1007/978-3-319-04999-1_9

Bishop AW (1967) Progressive failure-with special reference to the mechanism causing it. PYOC. Geotech. Conf.., Oslo 2, 142–150

Bishop AW, Green GE, Garga VK, Andresen A, Brown JD (1971) A new ring shear apparatus and its application to the measurement of residual strength. Geotechnique 21(4):273–328. https://doi.org/10.1680/geot.1971.21.4.273

Bromhead EN (1979) A simple ring shear apparatus. Ground Eng 12(5)

Garga VK, Sedano JI (2002) Steady state strength of sands in a constant volume ring shear apparatus. Geotech Test J 25(4):414–421

Hunger O, Morgenstern NR (1984) Experiments on the flow behaviour of granular materials at high velocity in an open channel. Géotechnique 34(3):405–413. https://doi.org/10.1680/geot.1984.34.3.405

Konagai K, Karunawardena A, Bandara KN, Sassa K, Onishi R, Uzuoka R, Asano S, Sasahara K, Jayakody S, Ariyarathna I (2022) Early warning system against rainfall-induced landslide in Sri Lanka. Prog Landslide Res Technol 1(1):217–235. https://doi.org/10.1007/978-3-031-16898-7_16

Loi DH, Jayakody SH, Sassa K (2022) Teaching tool "Undrained Dynamic Loading Ring Shear Testing with Video". Prog Landslide Res Technol 1(2):325–359. https://doi.org/10.1007/978-3-031-18471-0_25

Ma J, Zhao X, Li S, Duan Z (2021) Effects of high shearing rates on the shear behavior of saturated loess using ring shear tests. Geofluids 2021., Article ID 6527788, 12 p. https://doi.org/10.1155/2021/6527788

Sassa K (1984) The mechanism starting liquefied landslides and debris flows. Proceedings of 4th international symposium on landslides, Toronto, June, pp 349–354

Sassa K (1997) A new intelligent-type dynamic-loading ring-shear apparatus. Landslide News 10:33

Savage SB, Sayed M (1984) Stresses developed by dry cohesionless granular materials sheared in an annular shear cell. J Fluid Mech 142(1):391. https://doi.org/10.1017/s0022112084001166

Tika TM (1989) The effect of rate of shear on the residual strength of soil. PhD Thesis, University of London (Imperial College of Science and Technology), 494p

Part VI

World Landslide Reports

Physical Mechanism and Numerical Simulation of Landslide Dam Formation

Pham Van Tien, Tran Thanh Nhan, Le Hong Luong, and Tran Quoc Cuong

Abstract

Landslide dam formation creates one of the most hazardous geomorphic phenomena, which often threaten the safety of upstream and downstream communities by causing various secondary hazards, such as backwater inundation, dam breaches, debris flows, and outburst floods. Understanding the conditions and processes of the landslide dam formation is useful for hazard assessment and its disaster countermeasures. This research presents the physical mechanism of landslide dams and their entire formation process through three typical cases, namely the large-scale Kuridaira and Akatani landslide dams in Nara prefecture, Japan and the massive Jure landslide dam in Sindhupalchok district, Nepal, by using ring shear tests and integrated simulation with LS-RAPID model. The results from ring shear tests show that the samples of the sliding surfaces underwent substantial grain crushing and sliding-surface liquefaction due to a rapid generation of pore water pressure and significant loss of shear strength. In the computer model, the formation processes of the three landslide dams consisted of four main stages from stable slopes to local failures through progressive failures to massive slope movement at high speeds and river damming at the end of the motion. The analysis indicates the high mobility behavior that governs the rapid motion of the landslides is a primary contributing factor to the dam formation.

Keywords

Landslide dam · Rainfall · Formation process · Mobility · Modelling · LS-RAPID

1 Introduction

Landslide dams are one of the typical geomorphic processes whereby the downslope movement blocks a river channel, forming a reservoir in the valley floor. Most landslide dams are formed by rock/debris avalanches, rock/soil slumps and slides, mud/debris/earth flows triggered by excessive rainfall and snow melt, and earthquakes (Schuster and Costa 1987). Landslide dams can be classified into six types based on geomorphological features (Schuster and Costa 1987) or three classes based on their evolution, including unformed dams, formed-unstable dams and formed-stable dams (Stefanelli et al. 2015). The formed-stable dams form a lake basin due to a complete stream blockage. In comparison, the formed-unstable type indicates the complete river damming to create a lake basin. It remains for a variable period (from hours to centuries) until external contributing factors can trigger the failures. Although the complete damming can persist for varying durations from few minutes to many thousands of years, many dam reservoirs tend to fail within 1 year from their initial formation (Korup and Wang 2015). The landslide dam evolution often poses sequential hazards to the public in upstream and downstream regions. The potential hazards resulting from the dam formation are upstream inundation, overflow and overtopping, dam breach, outburst discharge, downstream flooding, debris flows, and river bank erosion (Schuster and Costa 1987; Korup 2005). There are numerous recorded events of

P. Van Tien (✉)
Institute of Geological Sciences, Vietnam Academy of Science and Technology, Hanoi, Vietnam

Research group on Natural Resources and Environmental Management (NREM-HUMG), Hanoi, Vietnam
e-mail: pvtien@igsvn.vast.vn

T. T. Nhan
University of Sciences, Hue University, Hue City, Vietnam
e-mail: ttnhan@hueuni.edu.vn

L. H. Luong
Institute of Transport Science and Technology, Hanoi, Vietnam

T. Q. Cuong
Institute of Geological Sciences, Vietnam Academy of Science and Technology, Hanoi, Vietnam
e-mail: tqcuong@igsvn.vast.vn

B. Abolmasov et al. (eds.), *Progress in Landslide Research and Technology, Volume 3 Issue 1, 2024*, Progress in Landslide Research and Technology, https://doi.org/10.1007/978-3-031-55120-8_29

landslide dams that have caused disastrous effects on communities; for example, the 2009 Shiaolin landslide dam caused over 400 fatalities in Taiwan (Tsou et al. 2011), and the 2014 Jure landslide dam claimed 156 lives in Nepal (Tien et al. 2021). Notably, the 2013 catastrophic Kedarnath flood disaster resulting from the breach of the Chorabari Tal Glacial landslide dam killed more than 5000 fatalities in Uttarakhand, India (Ray et al. 2016). It is, thus, essential to assess the possibility of landslide dam formation and associated secondary hazards for disaster risk reduction and prevention.

Many researchers have investigated the mechanisms and conditions governing landslide dam formation. Among them, the geomorphic approach is widely used based on global and regional datasets of landslide dams (Costa and Schuster 1987; Korup 2002, 2005; Ermini and Casagli 2003; Fan et al. 2012). The topography of narrow valleys surrounded by steep slopes and high mountains is the preliminary setting for the evolution of landslide dams. This feature is commonly in regions with active geological processes, where slope materials are characterized by fractured and sheared or hydrothermally altered bedrock. These topographical and geological features make slopes very susceptible to landslides. Narrow valleys are crucial factors that increase the possibility of complete channel blockage. It facilitates the potential of river-damming completion by relatively small volumes of sliding. The high and steep terrain is often prone to rapid-moving landslides that can quickly block rivers before their deposit can be swept away by water flows (Schuster and Costa 1987). Notably, several geomorphological indexes that combine various morphological parameters related to the landslides (such as: the volume, depth, and travelling speed) and the river valley (e.g., slope parameters, catchment area, valley width) have been extensively suggested to evaluate the landslide dam evolution for its risk assessment (Costa and Schuster 1987; Korup 2004; Evans 2006; Ermini et al. 2006; Stefanelli et al. 2017).

Landslide dams have complex geomorphic characteristics and cascading processes (Dal Sasso et al. 2014). Although the conditions for the dam formation are strongly governed by the initiation and motion of the landslides, the physical mechanisms of their formation have not been fully understood so far (Tien 2018). Literature reviews show that research topics on landslide dams are primarily descriptive and mainly focused on susceptibility assessment of dam failures associated with secondary hazards, e.g. dam-break floods and backwater inundation. Landslide dam formations were separately addressed as a single process consisting of the occurrence of landslide itself, the creation of dams and its natural lakes, or the potential of secondary hazards (Korup 2002). Since the hydrodynamic interaction between landslides and rivers, and the involved processes for dam formation have yet to be established in an approved theory, modelling the entire process of dam evolution is still developing (Dal Sasso et al. 2014). The simulation of landslide dam formation with input parameters has only based on the trial-and-error analysis, calibration-based analysis or back-analysis instead of using soil physical properties. These previous 2D models could only investigate the kinematic effects of the landslides and its interaction with the terrain of slopes. However, they could not reproduce the effects of groundwater changes and pore water pressure build-up due to rainfall, Tien et al. 2021). Therefore, this study aims to physically investigate the formation mechanisms and simulate the landslide dam formation through an integrated landslide simulation model of the ring shear apparatus (ICL-2) and the computer model (LS-RAPID).

2 Case Studies

Three typical case studies of rainfall-triggered deep-seated landslides forming natural dams were addressed in this research, namely the large Kuridaira and Akatani landslide dams in Nara prefecture, Japan and a huge landslide dam in Jure village, Sindhupalchok district, Nepal. The large-scale Kuridaira and Akatani landslides created the two largest natural dams among 17 obstruction locations triggered by extreme rainfall during the severe tropical storm Talas in September 2011 (Hayashi et al. 2013). The Jure landslide dam induced by a very high accumulative rainfall in August 2014 is considered the worst rainfall-induced landslide creating the biggest natu-

Table 1 Description of Kuridaira, Akatani and Jure landslide dams

Description/areas	Kuridaira	Akatani	Jure
Large-scale landslides			
Location	Wakayama, Japan	Wakayama, Japan	Sindhupalchok, Nepal
Occurrence time	23:06:13 September 3, 2011	7:22:15 September 4, 2011	2:30:00 August 2, 2014
Landslide area (m^2)	548,500	423,700	588,600
Volume of collapsed sediment (million m^3)	23.0	10.2	13.0
Slope angle (degree)	31.0	34.0	31.5
Slope height (m)	410	610	733
Width (m)	600	300–500	800
Length (m)	800	1000	1300
Maximum depth (m)	100	67	43
Landslide dams			
Basin	Second-order streams of Kumano River		Mainstream of Sunkoshi River
Dam height (m)	> 100 (Stable)	85 (Stable)	47 (Breached)
Storage capacity (million m^3)	7.5	5.5	11.5
Impoundment catchment (km^2)	8.7	13.2	–

(Data sources: Tien 2018; Tien et al. 2021)

ral dam reservoir in Nepal (Tien 2018). Due to high risks from sequential hazards (like overflows, debris flows, river erosion, dam breach,…), these three landslide dams and their reservoirs were forced under urgent countermeasures by countries' governments. The details of the three case studies are presented in Table 1.

The Kuridaira and Akatani dams were formed by massive movements triggered by heavy rainfall, with a record-breaking cumulative precipitation of about 1800 mm in the period from August 31 to September 4 (Fig. 1). The Kuridaira landslide was approximately 100 meters in depth, 800 meters in length, and 600 meters in width, with a material volume of 23.0 million m^3. The Akatani block, which had a landslide volume of 10.2 million m^3, was 67 m deep, 1000 m long and 300–500 m wide at its head and toe. The Kuridaira and Akatani sliding blockages created natural reservoirs with

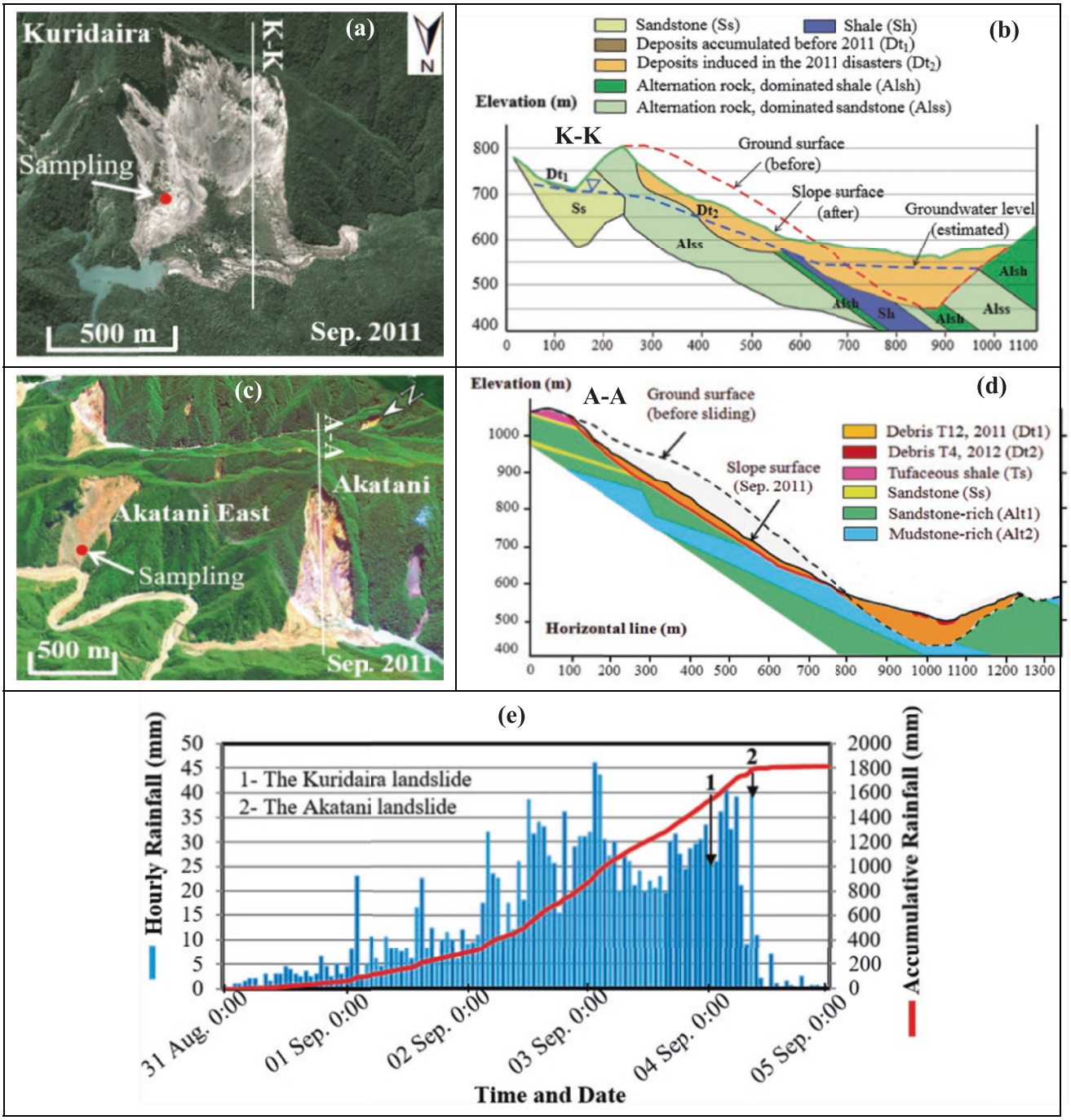

Fig. 1 (**a**, **c**) Google Earth images and (**b**, **d**) slope profiles of Kuridaira and Akatani landslide dams (Sassa et al. 2023), and (**e**) rainfall data during Typhoon Talas in September 2011 (Tien et al. 2018)

heights of 100 m and 85 m and storage capacities of 7.5 and 5.5 million m^3, respectively (Tien 2018; Tien et al. 2018). The Kuridaira landslide was characterized by alternating layers of sandstone and shale rocks, as well as clastic deposits. The landslide slid along the northwest dip-slip faults within the shale and sandstone layers or their interbedded layers. While the Akatani slope strata exposed interbedded rock layers of sandstone, sandstone- or mudstone-rich materials formed along the sandstone-rich layers (Fig. 1b, d). The Kuridaira landslide took place at 23:06:13 on September 3 in 100 s. In comparison, the Akatani block failed at 7:22:15 on September 4, lasting for 70 s, with a maximum estimated velocity ranging between 80 km/h and 100 km/h (Yamada et al. 2012; Chigira et al. 2013). The cumulative rainfall amounts triggered Kuridaira and Akatani mass movements were 1516.5 mm and 1746 mm, respectively (Fig. 1e).

The Jure catastrophic landslide was induced by prolonged rainfall at 2:30 AM local time on August 2, 2014, in Jure Village, Nepal (Fig. 2). The topographical map and slope profile of the Jure landslide are shown in Fig. 2b, c. The sliding is characterized by a rockslide-debris avalanche, moving along bedding-plane faults of weathered metamorphic rocks of phyllite and schist on the slope of an ancient landslide topography (Tien et al. 2021). The landslide disaster claimed 156 people in Ramche, Mankha Tekanpur, and Ghuskun villages. The rapid-moving landslide travelled at a maximum velocity of about 60–70 m/s, swept away and buried communities comprising 60 households in the villages of Iteni and Kagu. Then, the dis-

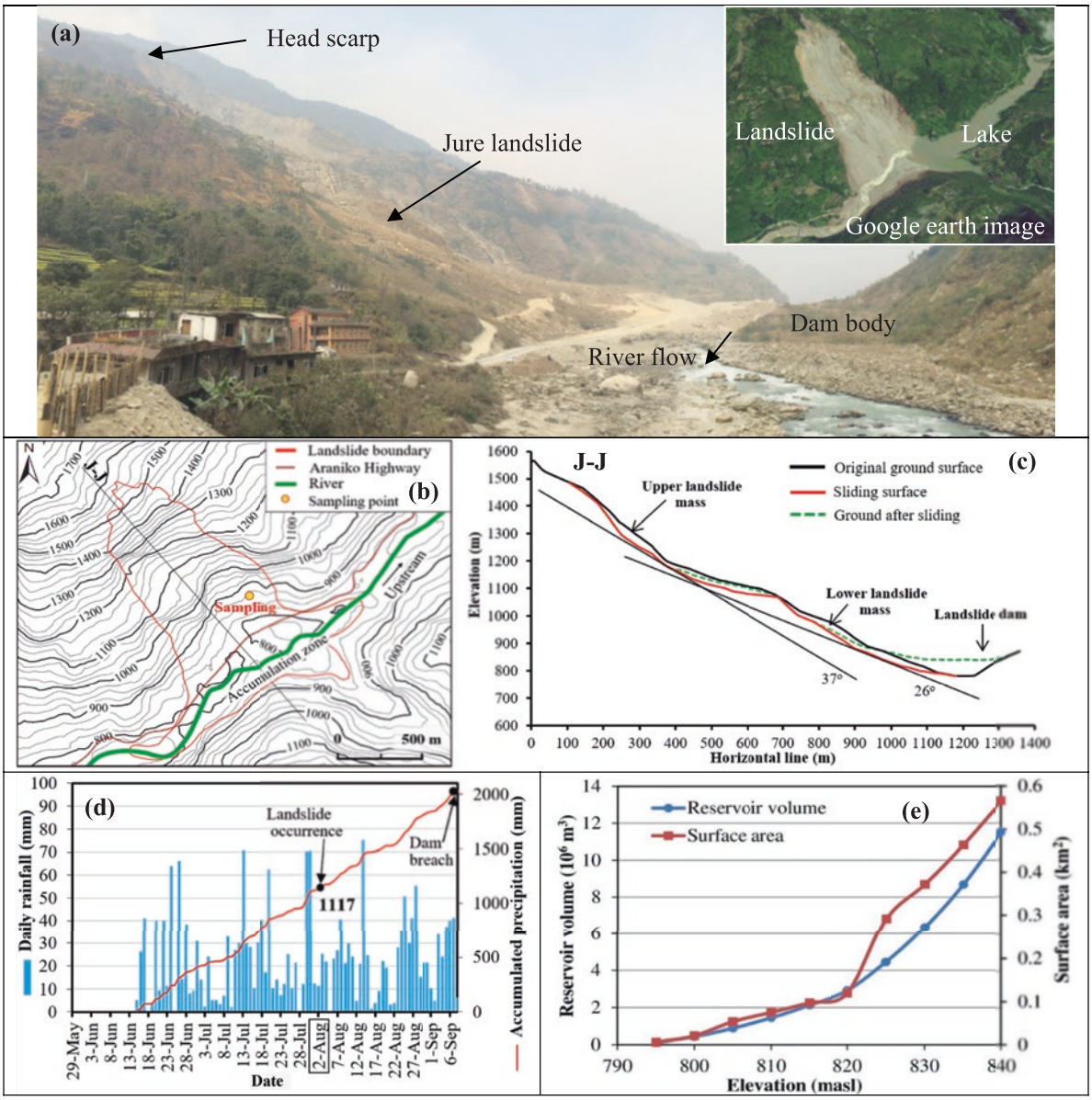

Fig. 2 (**a**) Photograph of the Jure landslide dam taken in December 2016 and a google image of the natural lake after damming in August 2014, (**b**, **c**) topographic map and longitudinal profile (J-J) of the landslide, (**d**) rainfall data at the Barhabise station and (**e**) elevation-volume and elevation-surface area curves of the dam reservoir (Tien et al. 2021)

placed mass rushed downward to Jure village and destroyed 1.0 km of the Araniko National Highway, causing significant disruptions to vital trade activities between Nepal and Tibet, China. The landslide, measuring 1300 m in length and with a volume of 13 million m^3, completely blocked the narrow river valley within 2–3 min. The massive sliding created a natural dam that was 700 meters long and 370 meters wide on Sunkoshi River in Jure village. The impounded lake had a maximum depth of 47 m, a length of 3.1 km and a maximum storage capacity of 11.5 million m^3 (Fig. 2a).

The impounded water flooded a section of the highway and approximately 100 houses situated along the banks of the Sunkoshi River. Although the Nepal Army took emergency countermeasures against the dam failures and overtopping by excavating the dam body and opening the drainage channels, the reservoir was breached due to the continuous heavy rainfall. The resulting outburst flood not only destroyed the Araniko Highway and Sunkoshi Hydropower Plant but also caused damage to the areas within about 6 km downstream along the river basin (Tien et al. 2021). The landslide was triggered by a prolonged period of heavy rainfall, which accumulated to a high total of 1117 mm from May 29 to August 2 (as shown in Fig. 2d). The relationships between elevation-volume and elevation-area of the Jure dam reservoir are denoted in Fig. 2e.

3 Materials and Method

Ring shear tests were carried out on landslide samples to examine the physical mechanisms responsible for the formation of landslide dams in river valleys. Soil samples were collected from the sliding surface layers of the landslides. These samples were passed through a 2-mm sized sieve and tested using the undrained high-stress, dynamic-loading ring shear apparatus (ICL-2), which has a capacity of 3.0 MPa in normal stress. A graph showing the grain-size distribution of shale sample (K2), sandstone-rich material (A1) and weathering material of schist (J2) of three Kuridaira, Akatani and Jure landslides, respectively, is presented in Fig. 3. For ring shear simulation, the initial stress state of landslide samples due to gravity was calculated from the sliding depth (H), slope angle (θ), and soil unit weight (g), namely normal stress $\delta_0 = g.H.\cos^2\theta$ and shear stress $\tau_0 = g.H.\cos\theta.\sin\theta$. The initial normal stresses of 1000 kPa, corresponding to 70 m depth of the sliding surface, were employed for the Kuridaira and Akatani landslides. A normal stress of 600 kPa estimated based on the maximum sliding surface depth of 43 m was applied to study the Jure landslide. In this research, pore pressure control tests were performed to indirectly simulate the rainfall-triggered landslides due to the rise of the groundwater table to investigate the physical mechanisms governing the landslide dam formation.

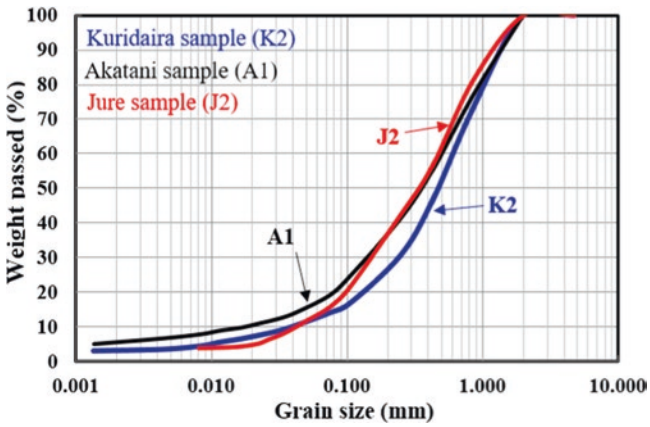

Fig. 3 (**a**) Grain-size distributions of landslide samples: Kuridaira sample (K2), Akatani sample (A1) and Jure sample (J2)

The LS-RAPID landslide simulation model was employed to simulate the entire process of the formation of three landslide dams, starting from stable slopes, through sliding initiation and motion, and ending with river blockage to create natural lakes behind the dams. The LS-RAPID model integrates the sliding initiation and motion progress from the stable state to failure and eventually reaching a steady state in the post-failure condition (Sassa et al. 2010). This computer model incorporates geotechnical soil parameters measured in the ring shear experiments. Topographical input of this 3D model employed DEM data of three landslides before and after the sliding. In the LS-RAPID model, pore water pressure increment indirectly simulating the rise of groundwater level under rainfall was employed as the landslide triggering factor.

4 Formation Mechanism of Rainfall-Induced Landslide Dams by Ring Shear Tests

4.1 Test Results on Kuridaira and Akatani Landslide Samples

In pore water pressure control tests, the saturated samples of K2 and A1 were first consolidated to normal stress of 1000 kPa and shear stress of 600 kPa and 620 kPa for Kuridaira and Akatani landslides in drained condition. These values correspond to the initial stress states (black line) of the Kuridaira and Akatani landslide samples with an inclination of 31° and 34°, respectively. Then, the simulation of rainfall-induced landslides was reproduced by the pore water pressure increment that indirectly simulated the increasing of groundwater level due to rainfall. The increment rates of pore pressure values were maintained at a constant rate of 1.0 and 0.5 kPa/s for samples K2 and A1, respectively. The results of pore water pressure control tests on samples K2 and A1 are present in Fig. 4.

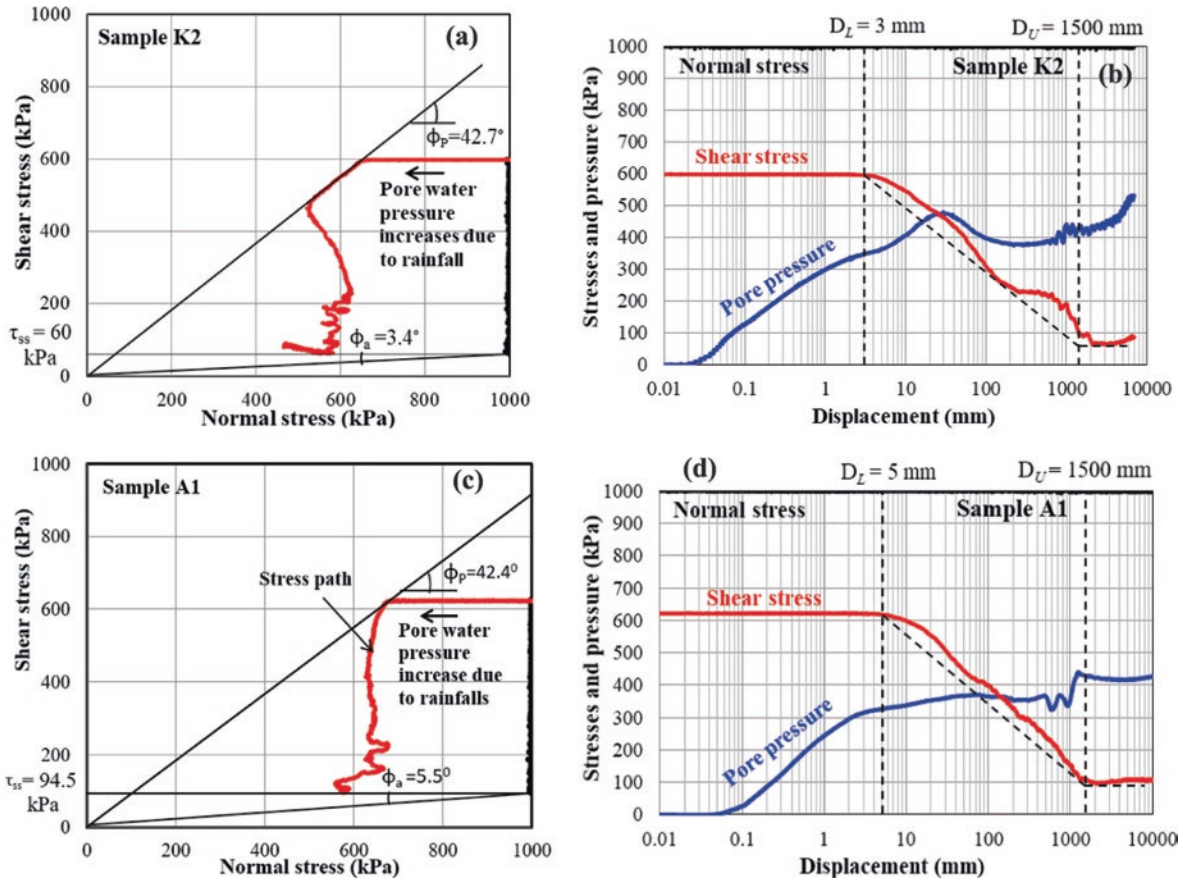

Fig. 4 Pore-water pressure control tests on samples K2 and A1: (**a**, **c**) stress path and (**b**, **d**) stresses and pore water pressure in the progress of shear displacement

Test results present that the Kuridaira and Akatani samples failed at the pore pressure increment of about 340 and 370 kPa. These values indicate that the critical pore water pressure ratios (r_u) due to rainfall initiated the Kuridaira and Akatani landslides were 0.34 and 0.37, respectively. The parameter r_u is defined as the ratio between the pore water pressure value at the point of failure and the normal stress. The values of friction angle at the peak are 42.7° for the Kuridaira sample and 42.4° for the Akatani sample, while the corresponding apparent friction angles mobilized at 3.4° and 5.5°. The residual shear strengths are 60 and 94.5 kPa for samples K2 and A1. Both the Kuridaira sample (K2) and Akatani sample (A1) show the high mobility behavior due to the excess generation of pore water pressure, which leads to a significant reduction in shear resistance. As a result, the high-speed landslides were observed during the ring shear simulation. The shear displacement values at the starting and end points of shear strength reduction (D_L and D_U values, respectively) are 3.0 and 1500 mm for sample K2. The D_U and D_L values are 5.0 and 1500 mm for sample A1. The failure of the landslide samples experienced four main periods from stable (pre-failure, $D < D_L$) to failure ($D = D_L$), through transient stage ($D_L < D < D_U$) to steady-state ($D > D_U$).

4.2 Test Results on Jure Landslide Sample

For the rainfall-triggered landslide simulation, normal stress of 600 kPa and shear stress of 360 kPa representing the initial stress condition of the Jure slope were applied to sample J2 in the drained condition. Next, pore water pressure rose at a rate of 1 kPa/s until the failure of the sample. The failure occurred when the path of the effective stress reached the failure line at the peak friction angle of about 35°. The landslide was triggered by a pore water pressure of 158 kPa which corresponds to a critical pore pressure ratio of $r_u = 0.26$. It indicates that a high value of pore water pressure resulting from rainfall can cause slope failure (Fig. 5a, b). In the simulation, a rapid-moving landslide was monitored during shearing, which suggests a very high mobility of the sample J2. Since steady-state shear behavior and the value of excess pore pressure were not precisely monitored in this drained condition test. The saturated sample J2 was investigated in an undrained shear displacement control test (Fig. 5c, d). In this test, the sample failure occurred as the path of effective stress reached the failure line at a friction angle at a peak of 34.5°. The shear strength value significantly reduced in the progress of shear displacement due to the excess generation of pore water pressure. A very high pore pressure value was measured at a shear

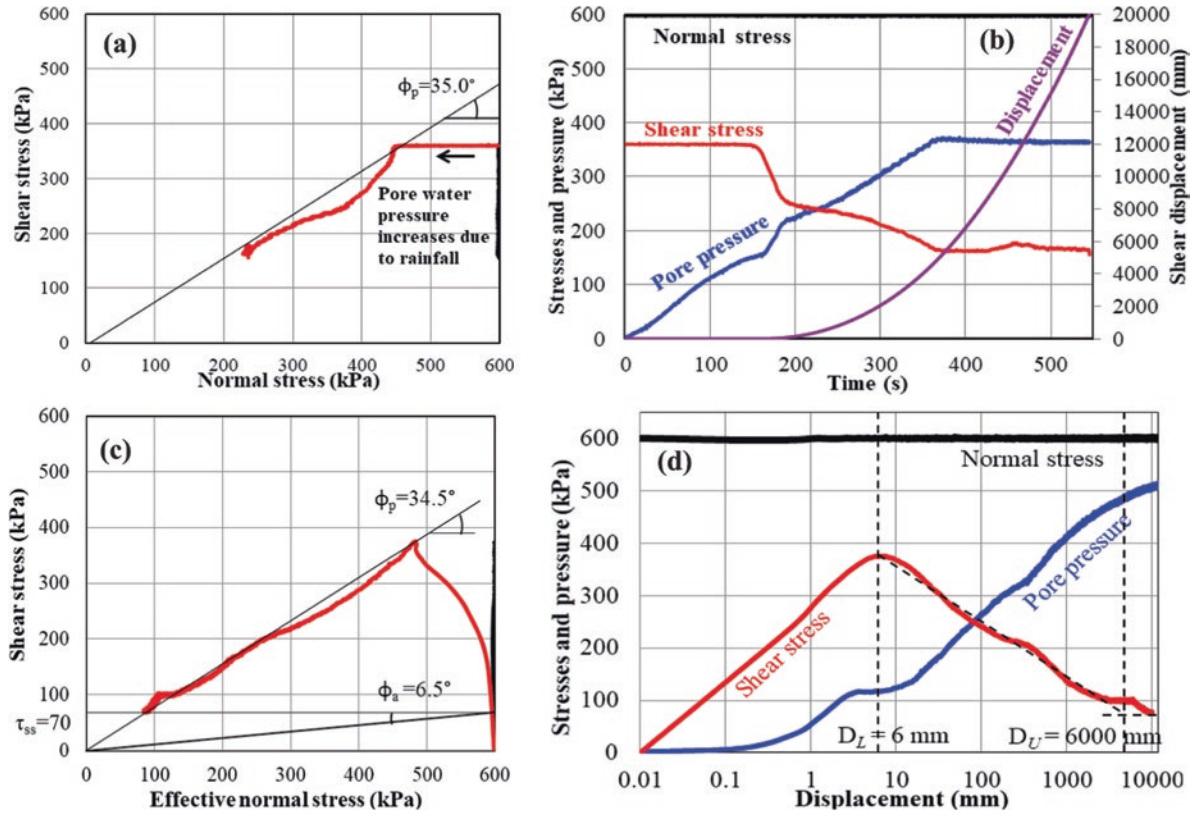

Fig. 5 Test results on Jure sample J2: Pore-water pressure control test with stress path (**a**) and time series data (**b**); and undrained shear displacement control test with stress path (**c**), and stresses and pore water pressure in the progress of shear displacement (**d**)

displacement of 20 m. The sample stayed at a low residual strength of 70 kPa and a small value of apparent friction angle of 6.5°. The acceleration of rapid motion at the steady state also indicates the high mobility behavior of the sample. The test result indicates that the values of D_U and D_L are 6 and 6000 mm for sample J2.

5 Simulating the Entire Evolution Process of the Three Landslide Dams

The entire evolution process of the three landslide dams is investigated in the LS-RAPID model. The input of soil parameters measured in the ring shear experiments is shown in Table 2. Remarkably, the model employed pore water pressure ratios as a triggering factor of the rainfall-triggered landslide dams. The ratios of 0.34, 0.37 and 0.26 for pore water pressure are set up for the computer simulation of the Kuridaira, Akatani and Jure landslide dams, respectively. The pore water pressure ratios were increased to designed values within 10 s and set constant for the duration of 150 s for all the simulations. The modeling results of the landslide dams induced by rainfall are present in Fig. 6. The result analysis indicates that the critical pore water pressure ratios

Table 2 Soil parameters in the LS-RAPID model

Soil parameters	Value for the landslides			Source
	Kuridaira sample K2	Akatani sample A1	Jure sample J2	
Total unit weight of the soil mass (γ_t, kN/m^3)	19.5	20.2	18.7	Test data
Unit weight of water (γ_w, kN/m^3)	9.81	9.81	9.81	Assumed
Lateral pressure ratio ($k = \sigma_h/\sigma_v$)	0.35–0.35	0.35–0.42	0.35–0.42	Estimated
Pore pressure generation rate (B_{ss})	0.25–0.85	0.25–0.9	0.5–0.98	Estimated
Friction angle during motion (Φ_m, °)	41.5	39.5	31.0	Test data
Peak friction angle (Φ_p, °)	44.1	42.1	34.5	Test data
Steady state shear resistance (τ_{ss}, kPa)	25–95	94.5–150	70	Test data
Shear displacement at the start of strength reduction (D_L, mm)	3	5	6	Test data
Shear displacement at the end of strength reduction (D_U, mm)	1500	1500	6000	Test data
Triggering factor of pore pressure ratio (r_u)	0.33	0.36	0.26	Test data

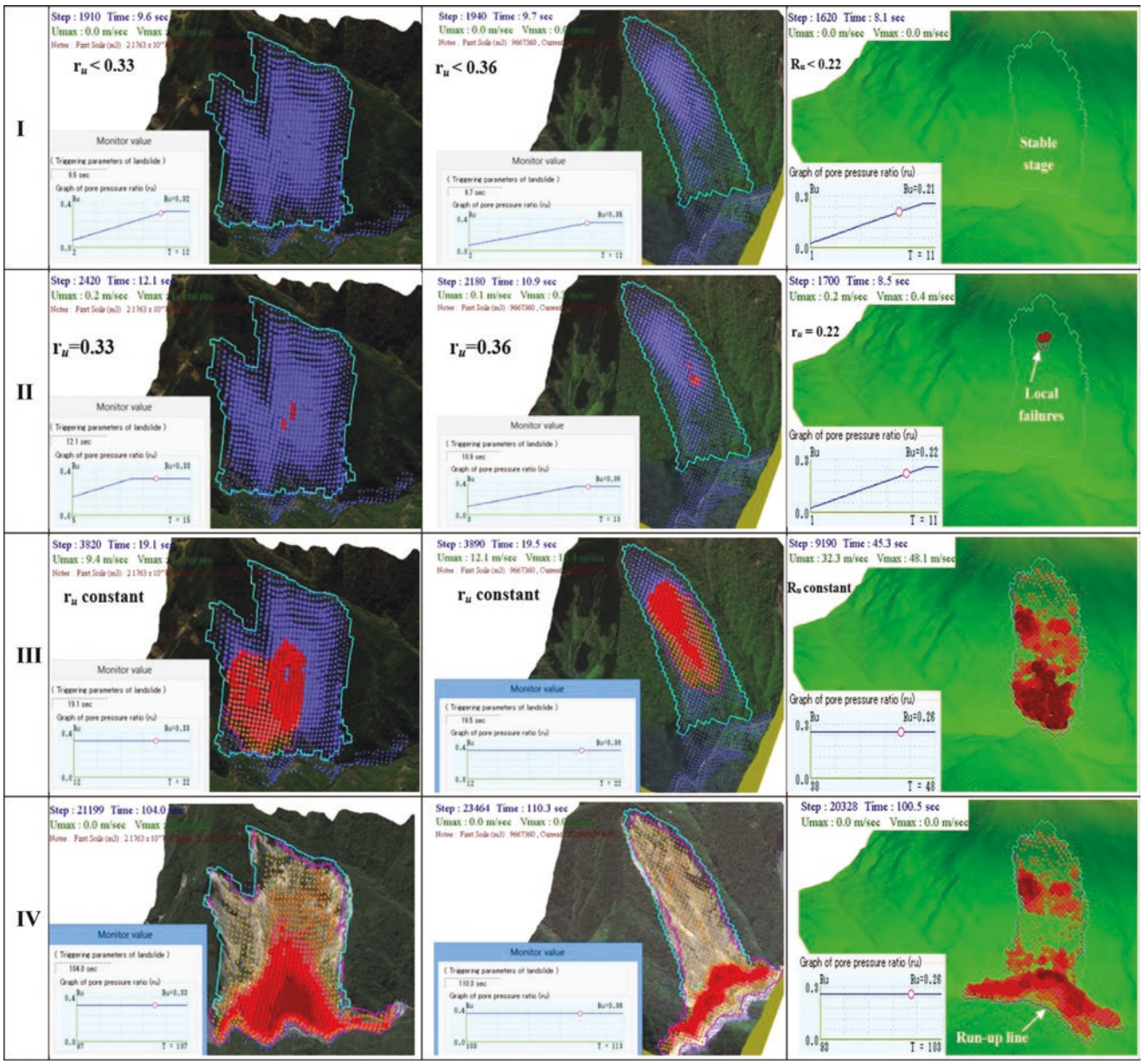

Fig. 6 Results of computer simulation model of three landslide dams (Tien et al. 2018, 2021)

triggering the Kuridaira, Akatani and Jure sliding were 0.33, 0.36 and 0.22, respectively.

The entire landslide dam formation process consists of four main periods: stable slope (I), local failures (II), progressive failures at transient period (III), and massive slope movement and river damming (IV). All slopes were stable at the first state if the pore water pressure ratios were lower than critical values. When the ratios of pore water pressure due to groundwater/rainfall reached critical values, local failures occurred in the middle parts of Kuridaira and Akatani slopes and the upper part of the Jure slope. The failures of the Kuridaira, Akatani and Jure slopes extended to neighboring areas, and then gradually expanded to a large area of the slopes. The progressive slope failures were characterized by the downward movement of the upper parts, resulting from the loss of support at the base and the dynamic loading impacts from the upper zones. The landslide accelerated its movement with increasing velocities during the transient stage. After that, the mass movements rushed down the river valleys and collided with the opposite walls. The landslide debris started accumulating on the river floor and then widely spread out in downstream and upstream areas due to the high mobility behavior of the sliding materials. In the final stage, the sliding motions decelerated and soon ceased when the

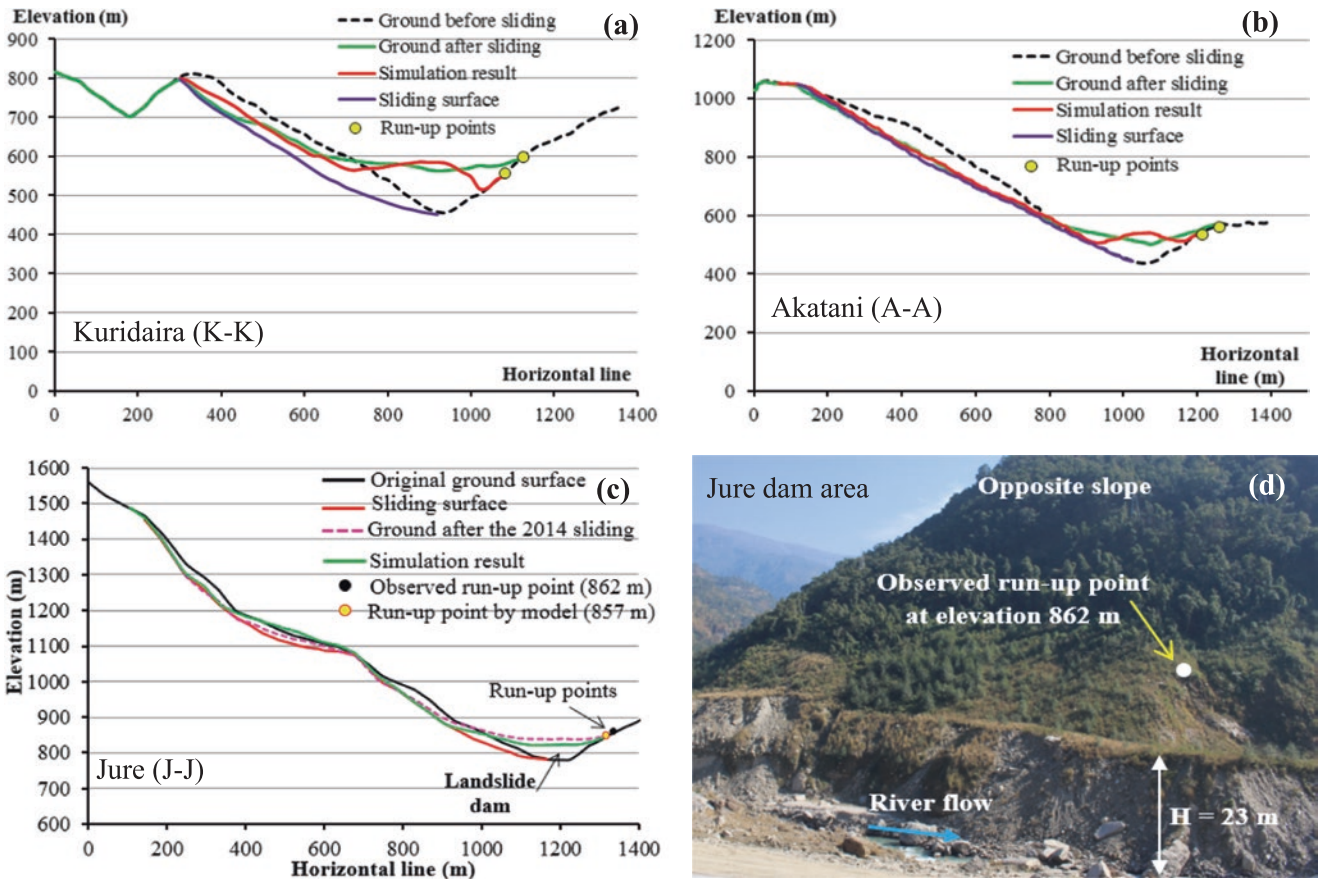

Fig. 7 (**a**–**c**) Topographic data of three landslides in comparison with model results and (**d**) an observed run-up point on the opposite slope in the Jure area (Tien et al. 2018, 2021)

whole mass movement slid down to the valley. The completion of river damming was observed in the narrow V-shaped valleys of the Kuridaira, Akatani and Jure areas. Specifically, the sufficient volume of the massive landslides completely dammed the river to form natural reservoirs in a short period. The results of the computer simulation for the K-K, A-A, and J-J cross-section and run-up point of the three landslides are presented in Fig. 7. The topographic data obtained from the LS-RAPID model that were well compared with the original terrain before the sliding. The run-up points of the three landslides were nearly the same as those drawn from the original DEM data before sliding.

6 Conclusions

This paper presents the investigation of the physical mechanism and entire landslide dam formation process through three typical case studies of Kuridaira, Akatani and Jure slopes. The laboratory tests indicate that the landslides were triggered by an increase in pore water pressure under rainfall conditions. The values for pore water pressure triggering the Kuridaira, Akatani and Jure landslides are 0.34, 0.37 and 0.26, respectively. In the tests, all samples of K2, A1 and J2 show a high mobility behavior because of a significant loss of shear strength from an excess generation of pore water pressure. The mobility behavior was expressed by low mobilized friction angles and residual strength of the landslide samples at the steady state. As a result, the rapid motions were monitored in the rainfall-induced landslide simulation by ring shear apparatus. Notably, the evolution of the three landslide dams was simulated in the LS-RAPID computer model that incorporated geotechnical soil parameters measured from the ring shear tests. The entire evolution of the landslide dam comprises four main stages: stable slope, local failure, progressive failures, massive slope movement and river damming. In the model, three landslides travelled downward to their river valleys at high speeds and created natural lakes. The high mobility behavior of the soil samples characterized by rapid-moving landslides and the sufficient volume of sliding materials played essential factors in the dam formation. The mobile landslides with wide-spreading and rapid motions allow the displaced material blocks to completely block the river channels quickly before their extensive erosion by upstream water flows. The result analysis suggests that landslide

mobility is a significant parameter for hazard assessment of landslide dams. In addition to geomorphic features, the high mobility behavior of the Kuridaira, Akatani and Jure landslides was one of the significant contributing factors for the dam formation in the study areas.

Acknowledgments This research is funded by Vietnam National Foundation for Science and Technology Development (NAFOSTED) under grant number 105.08-2019.14.

References

Chigira M, Tsou C-Y, Matsushi Y, Hiraishi N, Matsuzawa M (2013) Topographic precursors and geological structures of deep-seated catastrophic landslides caused by Typhoon Talas. Geomorphology 201:479–493

Costa JE, Schuster RL (1987) The formation and failure of natural dams, US Geological Survey, Open-File Report, pp 87–392

Dal Sasso SF, Sole A, Pascale S, Sdao F, Bateman Pinzón A, Medina V (2014) Assessment methodology for the prediction of landslide dam hazard. Nat Hazards Earth Syst Sci 14:557–567

Ermini L, Casagli N (2003) Prediction of the behaviour of landslide dams using a geomorphological dimensionless index. Earth Surf Process Landf 28:31–47

Ermini L, Casagli N, Farina P (2006) Landslide dams: analysis of case histories and new perspectives from the application of remote sensing monitoring techniques to hazard and risk assessment. Ital J Eng Geol Environ 1(2006):45–52

Evans SG (2006) The formation and failure of landslide dams: an approach to risk assessment. Ital J Eng Geol Environ 1

Fan X, van Westen CJ, Xu Q, Gorum T, Dai F (2012) Analysis of landslide dams induced by the 2008 Wenchuan earthquake. J Asian Earth Sci 57:25–37

Hayashi S, Uchida T, Okamoto A, Ishizuka T, Yamakoshi T, Morita K (2013) Countermeasures against landslide dams caused by Typhoon Talas 2011. Asia-Pacific Tech Monitor 30(1):20–26

Korup O (2002) Recent research on landslide dams—a literature review with special attention to New Zealand. Prog Phys Geogr 26(2):206–235

Korup O (2004) Geomorphometric characteristics of New Zealand landslide dams. Eng Geol 73(1):13–35

Korup O (2005) Geomorphic hazard assessment of landslide dams in South Westland, New Zealand: Fundamental problems and approaches. Geomorphology 66:167–188

Korup O, Wang G (2015) Multiple landslide-damming episodes. In: Davies T (ed) Landslide hazards, risks, and disasters. Elsevier, Amsterdam, pp 241–261

Ray PKC, Chattoraj SL, Bisht MPS, Kannaujiya S, Pandey K, Goswami A (2016) Kedarnath disaster 2013: causes and consequences using remote sensing inputs. Nat Hazards 81:227–243

Sassa K, Nagai O, Solidum R, Yamazaki Y, Ohta H (2010) An integrated model simulating the initiation and motion of earthquake and rain induced rapid landslides and its application to the 2006 Leyte landslide. Landslides 7(3):219–236

Sassa K, Doan L, Dang K, Tien P (2023) Sliding-surface liquefaction and undrained steady-state shear-strength. Prog Landslide Res Technol 1(1):2022

Stefanelli CT, Catani F, Casagli N (2015) Geomorphological investigations on landslide dams. Geoenviron Disasters 2:21

Stefanelli CT, Segoni S, Casagli N, Catani F (2017) Assessing landslide dams evolution: a methodology review. Advancing culture of living with landslides, pp 253–258

Tien PV (2018) Mechanisms and hazard assessment of rainfall-induced landslide dams. PhD thesis, Kyoto University

Tien PV, Sassa K, Takara K, Fukuoka H, Khang D, Shibasaki T, Setiawan H, Ha ND, Loi DH (2018) Formation process of two massive dams following rainfall-induced deep-seated rapid landslide failures in the Kii Peninsula of Japan. Landslides 15(9):1761–1778

Tien PV, Luong LH, Sassa K, Takara K, Sumit M, Nhan TT, Dang K, Duc DM (2021) Mechanisms and modeling of the catastrophic landslide dam at Jure Village, Nepal. J Geotech Geoenviron Eng 147(11):05021010

Tsou C-Y, Feng Z-Y, Chigira M (2011) Catastrophic landslide induced by Typhoon Morakot, Shiaolin, Taiwan. Geomorphology 127:166–178

Yamada M, Matsushi Y, Chigira M, Mori J (2012) Seismic recordings of landslides caused by Typhoon Talas (2011), Japan. Geophys Res Lett 39:L13301

An Integration of the Fractal Method and the Statistical Index Method for Mapping Landslide Susceptibility

Binh Van Duong, Igor K. Fomenko, Denis N. Gorobtsov, Kien Trung Nguyen, Dang Hong Vu, Daria D. Shubina, and Ha Ngoc Thi Pham

Abstract

Appropriate land use planning and the sustainable development of residential communities play a crucial role in the development of mountainous provinces in Vietnam. Because these regions are especially prone to natural disasters, including landslides, landslide studies can provide valuable data for determining the evolution of the landslide process and assessing landslide risk. This study was conducted to assess landslide susceptibility in Muong Khoa commune, Son La province, Vietnam, using the Statistical Index method (SI) and the integration of the Fractal method and Statistical Index method (FSI). To produce landslide susceptibility zonation (LSZ) maps, eight causative factors, including elevation, slope aspect, slope, distance to roads, distance to drainage, distance to faults, distance to geological boundaries, and land use, were considered. Using SI and FSI models, two landslide susceptibility zonation maps (LSZ) were produced in ArcGIS, and the study territory was categorized into five susceptibility zones: very low, low, moderate, high, and very high. The area percentage of susceptibility zones predicted by the SI model is 10.11, 18.49, 29.71, 28.59, and 13.10%, respectively. Meanwhile, the susceptibility map generated by the FSI model divided the study area into zones with corresponding area proportions of 18.92, 18.71, 20.01, 22.94, and 19.42%. Using the ROC method, the prediction performance of the two models was determined to be AUC = 71.18% (SI model) and AUC = 75.18% (FSI model). The AUC > 70% indicated that the models established a good relationship between the spatial distribution of past landslides and causative factors. In addition, the two models accurately predicted the occurrence of landslides in the study area. The FSI model has improved prediction performance by identifying the role of each factor in the landslide occurrences in the study area and, therefore, may be effectively utilized in other regions and contribute to Vietnam's landslide prevention strategy.

Keywords

Landslide susceptibility · Fractal method · Statistical index method · ROC method · Muong Khoa · Son La · Vietnam

1 Introduction

As a result of the rapid urbanization occurring in the northern mountainous regions of Vietnam, long-term territorial planning and sustainable development of residential areas are essential tasks. The expansion of urban areas and agricultural land coincides with the decrease in natural forest areas, resulting in an increase in the probability of natural disasters (Nguyen et al. 2019). Sediment-related disasters, such as landslides, have attracted a great deal of attention from researchers in Vietnam and worldwide due to their diversity in magnitude, morphological characteristics, and severity of damage (Biswas et al. 2022; Sim et al. 2022).

Numerous qualitative (Dahl et al. 2010; Wang et al. 2013), quantitative (Ma et al. 2020; Ou et al. 2021), and

B. Van Duong (✉) · H. N. T. Pham
Department of Engineering Geology, Hanoi University of Mining and Geology, Hanoi, Vietnam
e-mail: duongvanbinh@humg.edu.vn

I. K. Fomenko · D. N. Gorobtsov · D. D. Shubina
Department of Engineering Geology, Ordzhonikidze Russian State Geological Prospecting University, Moscow, Russia

K. T. Nguyen
Department of Hydrogeology and Engineering Geology, Institute of Geological Sciences, Vietnam Academy of Science and Technology, Hanoi, Vietnam

D. H. Vu
Vietnam Institute of Geosciences and Mineral Resources, Hanoi, Vietnam

B. Abolmasov et al. (eds.), *Progress in Landslide Research and Technology, Volume 3 Issue 1, 2024*, Progress in Landslide Research and Technology, https://doi.org/10.1007/978-3-031-55120-8_30

semi-quantitative (Guillen et al. 2022) landslide susceptibility assessments have been conducted at various spatial scales. The main goal of landslide susceptibility assessments is to identify areas with the highest landslide potential based on an inventory of past landslide events and associated factors. When identifying landslide susceptibility zones, statistical models have demonstrated their simplicity and prediction efficiency, and consequently, they have been extensively utilized worldwide (Juliev et al. 2019; Ram et al. 2020).

Using the Statistical Index (SI) and Fractal-Statistical Index (FSI) models, landslide susceptibility assessments were conducted in Muong Khoa commune, Bac Yen district, Son La province, Vietnam. The analysis results demonstrated that the FSI model provided greater prediction efficacy, and this model is prospective for use in landslide studies in other regions of Vietnam.

2 Study Area

Similar to other "hot spots" for landslides in the Northwest area of Vietnam (Thanh Thi Pham et al. 2020), the mountainous terrain, tropical climate, geological conditions, and human activity in Son La province have all contributed to the significant number of landslides (1689 events) (Bui et al. 2022). Bac Yen district, located in the eastern portion of Son La province, is distinguished by highly complicated topographical characteristics. In the Bac Yen district, a high frequency of landslide and debris flow occurrences has been documented, accompanied by severe consequences. The results of a field survey and statistical analysis in the Bac Yen district have identified seven areas with a high density of landslides, including Muong Khoa commune (VIGMR 2014). Muong Khoa (84.16 km^2) is a mountainous commune in the western portion of the Bac Yen district with elevations between 115 and 1563 m (Fig. 1). The landslide process that was documented in this area mostly developed in the weathering crust formed from the rocks of the Ban Cai Formation (D_3bc), the Da Nieng Formation (C_1đn), and the Vien Nam Formation (T_1vn). Rainfall is the main trigger of landslide events, while human activity, weathering crust, vegetation cover, etc. are considered conditioning factors.

The landslide event (Fig. 2) occurred on Highway 37 near the Muong Khoa market in the Muong Khoa commune of the Bac Yen district. There were no fatalities caused by the landslide, but three houses were completely devastated. The sliding mass has an estimated size of 80 by 160 m and occurred in a 10- to 15-meter-thick weathering crust. The landslide was first triggered in early 2020 and reactivated in September 2022 due to a prolonged rain event. The field survey results determined that the landslide was triggered by heavy accumulated rainfall and formed in a thick weathering crust on terrain with a high slope gradient caused by human construction activities.

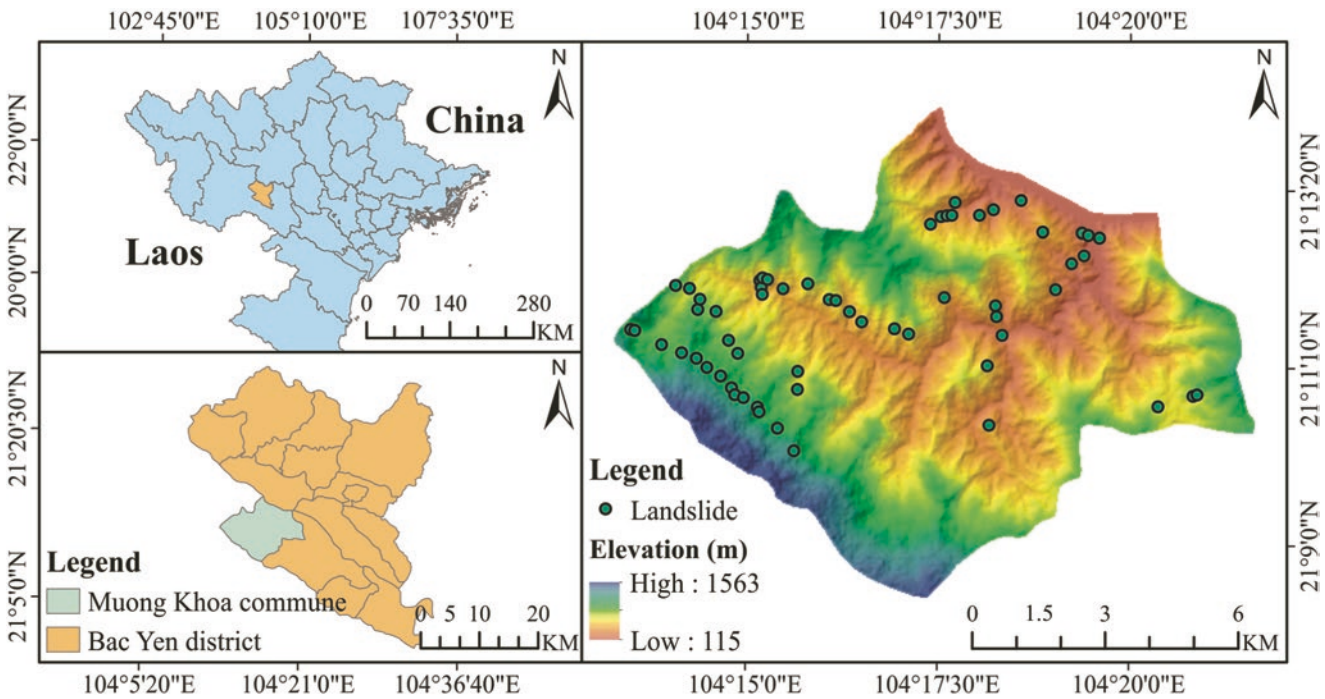

Fig. 1 Location of study area

Fig. 2 Photos of landslide event in the study area. Photo by T. K. Nguyen

3 Landslide Susceptibility Assessment Using the Statistical Index and Fractal-Statistical Index Methods

3.1 Methods

Developed by Van Westen (1997), the statistical index model has proven effective for quantitatively assessing the potential for landslides in various regions around the globe (Rai et al. 2022; Wang et al. 2016). The class weight (W_{SI}) values of causative factors are determined using the following formula based on the distribution of landslides within the factor classes:

$$W_{SI} = Ln\left(D_{LSi} \Big/ D_{LS}\right) \tag{1}$$

where: D_{LSi} is the landslide density in the i_{th} factor class and D_{LS} is the landslide density in the study area. Positive W_{SI} values represent areas with significant landslide potential, while negative W_{SI} values represent areas with low landslide density. The value $W_{SI} = -1$ is assigned to the factor class due to the lack of landslide distribution (Zhang et al. 2016).

Because the statistical index method only provides information on the class weight values of the causative factors, fractal analysis was utilized to quantify the contribution of each causative factor in the development of the landslide process in the study area. Since being introduced by Mandelbrot (1967), the fractal theory has been successfully used in studies to determine the geometrical features of landslides (Pourghasemi et al. 2014) and predict the spatial distribution of landslides (Liu et al. 2019; Zhao et al. 2021). The fractal theory expresses the variation in fractal dimension D as a function of the linear scale (r) (Liu et al. 2019):

$$D = f(r) \tag{2}$$

Rouai and Jaaidi (2003), based on their analysis, concluded that the distribution of landslides is characterized by a heterogeneous fractal structure. Therefore, the variable dimension fractal method (VDFM) was utilized to determine the D value for the causative factors based on the relative density of landslides (Hu et al. 2020). The factor weight (W_i) value of each causative factor is calculated using the following formula:

$$W_i = D_i \Big/ \sum_{i=1}^{n} D_i \tag{3}$$

Finally, the formula [4] is used to determine the landslide susceptibility index (LSI) value:

$$LSI = \sum W_{SI} \times W_i \tag{4}$$

3.2 Spatial Relationship Between Conditioning Factors and Landslide Distribution

The landslide inventory map in this study was established using aerial photography and field survey data. A total of sixty landslide sites were identified, with estimated volumes ranging from 8.75 m^3 to 21,000 m^3 (Fig. 3). According to statistical analysis results, 34 landslides have a mass volume of less than 200 m^3, 22 sliding masses have a mass volume between 200 and 1000 m^3, and the remaining four landslides range in mass volume from 1000 to 21,000 m^3. The volume of small sliding masses accounts for only 7.74% of the total landslide volume in the study area, while the remaining 22 and four landslides account for 20.74 and 71.52%, respectively. All sixty landslides were used to build landslide susceptibility models for the study area.

For mapping landslide susceptibility in the study area, eight causative factors, including elevation, distance to roads, slope, distance to geological boundaries, distance to faults,

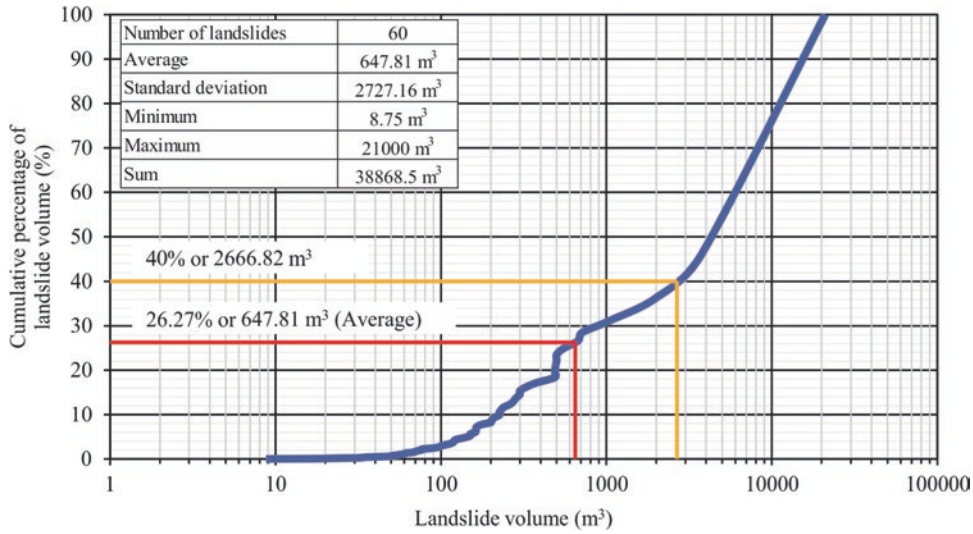

Fig. 3 Landslide volume statistics in the study area

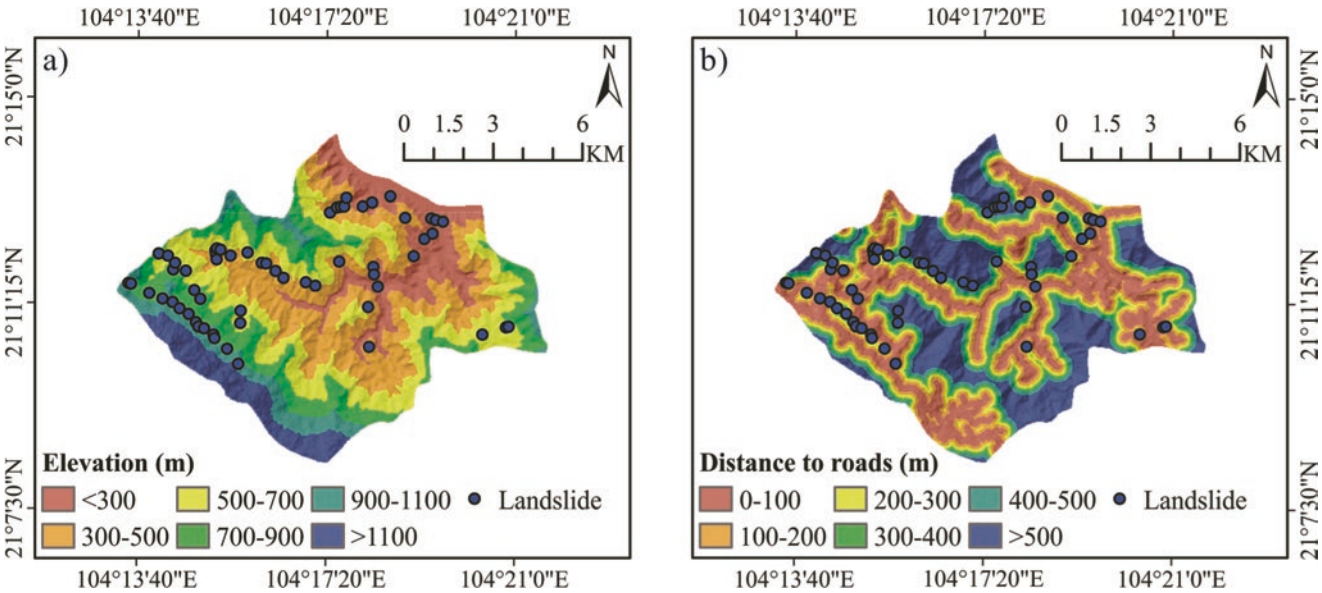

Fig. 4 (**a**) Elevation map and (**b**) map of distance to roads

land use, slope aspect, and distance to drainage, were selected in this study. The EarthData database (https://www.earthdata.nasa.gov) was first accessed to download the open-access global ASTER DEM (30-meter resolution). Afterward, DEM-derived factor maps, including elevation (Fig. 4a), slope (Fig. 5a), slope aspect (Fig. 7a), and distance to drainage (Fig. 7b), were prepared in ArcGIS 10.5. The relationship between these factor maps and past landslides was then analyzed by subdividing them into subclasses. The map of distance to roads (Fig. 4b) was produced in ArcGIS using OpenStreetMap data downloaded from the Geofabrik database (https://download.geofabrik.de) and then divided into six subclasses. The Vietnam Institute of Geosciences and Mineral Resources (VIGMR) provided the data employed to prepare maps displaying the distance to geological boundaries (Fig. 5b) and faults (Fig. 6a). In this study, land use classification was performed in ERDAS 2015 using Landsat 8 Operational Land Imager (OLI) (Date Acquired: 10/15/2022, Path 128, Row 45), and the study territory was divided into water, urban area, forest, shrubland, agricultural land, bare land, and river bed (Fig. 6b). The results of the analysis of the relationship between landslide distribution and causative factors using the SI method are shown in Table 1.

3.3 Results of Landslide Susceptibility Assessment Using Statistical Index and Fractal-Statistical Index Methods

The analysis of the relationship between past landslides and causal factors (Table 1) revealed that 47% of landslides occurred in areas below 500 m in elevation. Less

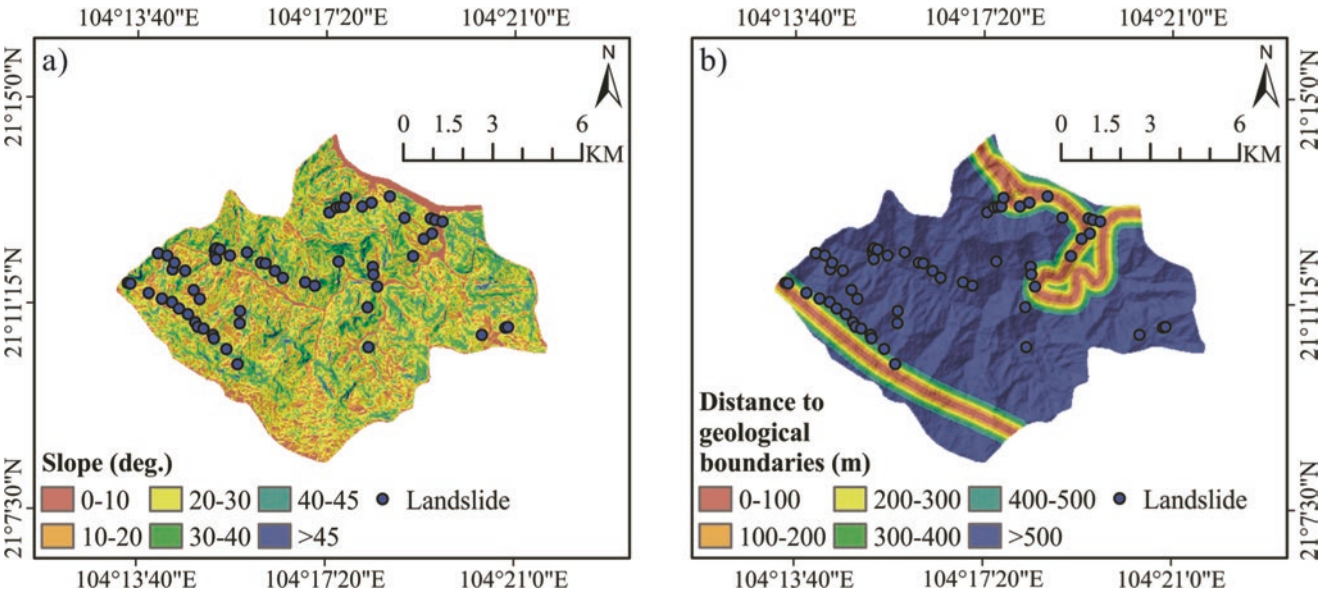

Fig. 5 (**a**) Slope map and (**b**) map of distance to geological boundaries

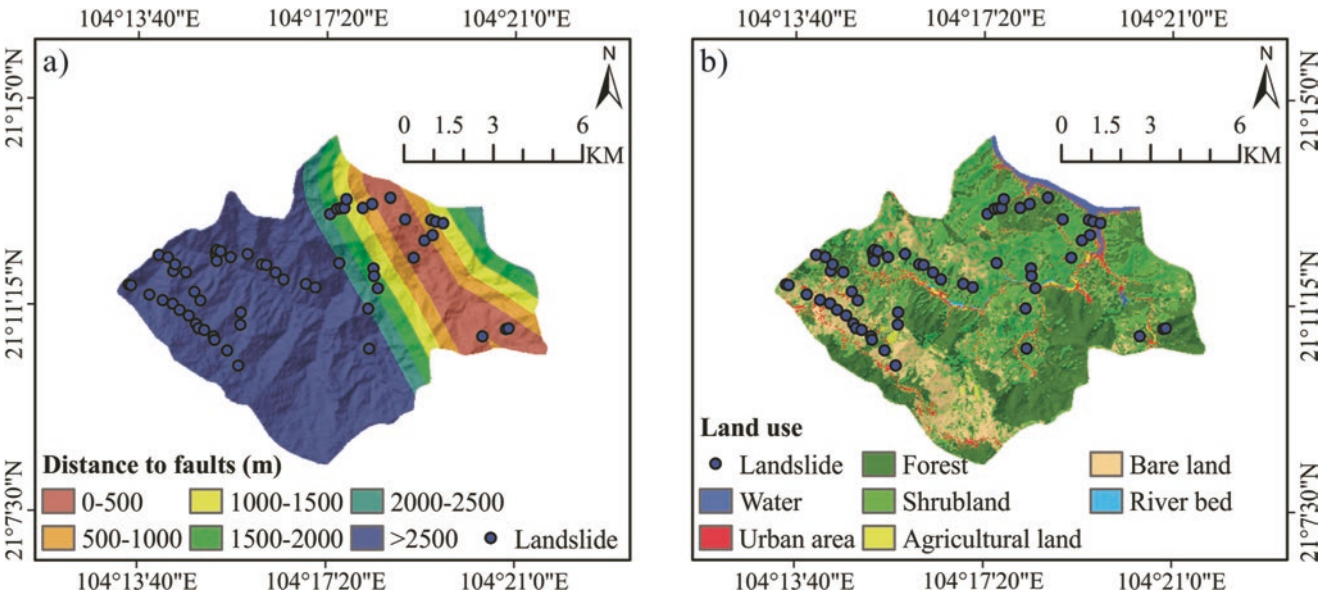

Fig. 6 (**a**) Map of distance to faults and (**b**) land use map

than 100 m from roads is associated with a significant frequency of landslides. This result indicates that construction activities in the study area have increased the likelihood of landslides. Therefore, landslides occurred frequently in areas with slopes between 10 and 30°. The highest W_{SI} values were determined for urban areas, agricultural land, and bare land. This distribution highlights the significance of vegetation cover and the influence of human activities on the development of landslides in the study area. The highest frequency of landslides was recorded on the east, south, and southwest slope aspects. Due to the correlation between the drainage system and the degree of saturation of the slope material, landslides occurred frequently within 300 m of the drainage system. The landslide process in the study area is also related to the geological boundaries and fault system. According to Table 2, fractal analysis results showed that the distance to drainage is the most significant factor in the landslide process in the study area (Fig. 7).

Figures 8 and 9 show the LSZ maps and the distribution of susceptibility zones in the Muong Khoa commune. As depicted in Fig. 9a, 18.92% of the study area was predicted

Table 1 Analysis of the relationship between landslide distribution and causative factor using SI method

Factor	Class	Class pixel	% Class pixel	Landslide	% Landslide	W_{SI}
Elevation (m)	<300	14,085	15.064	10	16.667	0.101
	300–500	25,032	26.772	18	30	0.114
	500–700	23,144	24.753	14	23.333	−0.059
	700–900	16,693	17.854	7	11.667	−0.425
	900–1100	7477	7.997	11	18.333	0.830
	>1100	7068	7.559	0	0	−1
Distance to road (m)	0–100	25,279	27.037	20	33.333	0.209
	100–200	14,995	16.038	8	13.333	−0.185
	200–300	12,648	13.527	7	11.667	−0.148
	300–400	8973	9.597	6	10	0.041
	400–500	8054	8.614	4	6.667	−0.256
	>500	23,550	25.187	15	25	−0.007
Slope (deg.)	0–10	7000	7.487	2	3.333	−0.809
	10–20	22,125	23.663	21	35	0.391
	20–30	38,050	40.696	23	38.333	−0.060
	30–40	22,992	24.591	12	20	−0.207
	40–45	2671	2.857	1	1.667	−0.539
	>45	661	0.707	1	1.667	0.858
Distance to geological boundaries (m)	0–100	6471	6.921	6	10	0.368
	100–200	5351	5.723	5	8.333	0.376
	200–300	5520	5.904	1	1.667	−1.265
	300–400	4072	4.355	5	8.333	0.649
	400–500	4126	4.413	3	5	0.125
	>500	67,959	72.684	40	66.667	−0.086
Distance to faults (m)	0–500	10,622	11.361	7	11.667	0.027
	500–1000	7499	8.02	5	8.333	0.038
	1000–1500	6848	7.324	3	5	−0.382
	1500–2000	7195	7.695	6	10	0.262
	2000–2500	5584	5.972	1	1.667	−1.276
	>2500	55,751	59.627	38	63.333	0.060
Land use	Water	1609	1.722	0	0	–
	Urban area	3378	3.615	5	8.333	0.835
	Forest	33,193	35.522	13	21.667	−0.494
	Shrubland	39,711	42.497	25	41.667	−0.020
	Agri. land	751	0.804	1	1.667	0.729
	Bare land	14,596	15.62	16	26.667	0.535
	River bed	206	0.22	0	0	−1
Slope aspect	Flat	924	0.988	0	0	−1
	North	16,531	17.68	7	11.667	−0.416
	Northeast	19,443	20.795	12	20	−0.039
	East	13,970	14.941	12	20	0.292
	Southeast	8284	8.86	6	10	0.121
	South	6509	6.962	8	13.333	0.65
	Southwest	8588	9.185	7	11.667	0.239
	West	8995	9.62	3	5	−0.654
	Northwest	10,255	10.968	5	8.333	−0.275
Distance to drainage (m)	0–100	27,232	29.125	21	35	0.184
	100–200	21,430	22.92	18	30	0.269
	200–300	18,356	19.632	15	25	0.242
	300–400	11,976	12.809	5	8.333	−0.43
	400–500	8667	9.27	1	1.667	−1.716
	>500	5838	6.244	0	0	−1

Table 2 Calculated factor weights based on fractal analysis

Factor	Linear regression formulation	Correlation coefficient (R^2)	D_i	W_i
Elevation	y = 1.4008x + 0.8049	0.9991	1.4008	0.122
Distance to road	y = 0.86x + 0.2206	0.9995	0.86	0.075
Slope	y = 1.4093x + 0.8526	1	1.4093	0.123
Distance to geological boundaries	y = 1.5477x + 0.6255	0.9996	1.5477	0.135
Distance to fault	y = 1.5897x + 0.2328	0.9994	1.5897	0.138
Land use	y = 1.5472x + 0.8353	0.9999	1.5472	0.135
Slope aspect	y = 1.5399x + 0.61	0.9995	1.5399	0.134
Distance to drainage	y = 1.5949x + 0.2683	0.9997	1.5949	0.139

to be a very low (VL) susceptibility zone using the FSI model. Compared to the outcome predicted by the SI model (10.11%), this result is highly significant for land use planning and residential area development. The SI model predicted a higher percentage of low (L), moderate (M) and high (H) susceptibility zones, whereas the FSI model indicated that 19.42% of the study area was classified as a very high (VH) susceptibility zone, which is 6.32% larger than the SI model. The model efficiency is evaluated based on the number (area) of predicted landslides, especially in the VH zone. Figure 9b reveals that 58.33% of landslides were predicted in the VH zone, compared to 48.33% predicted by the SI model. This outcome proved the effectiveness of the FSI model in this study when compared to the SI model.

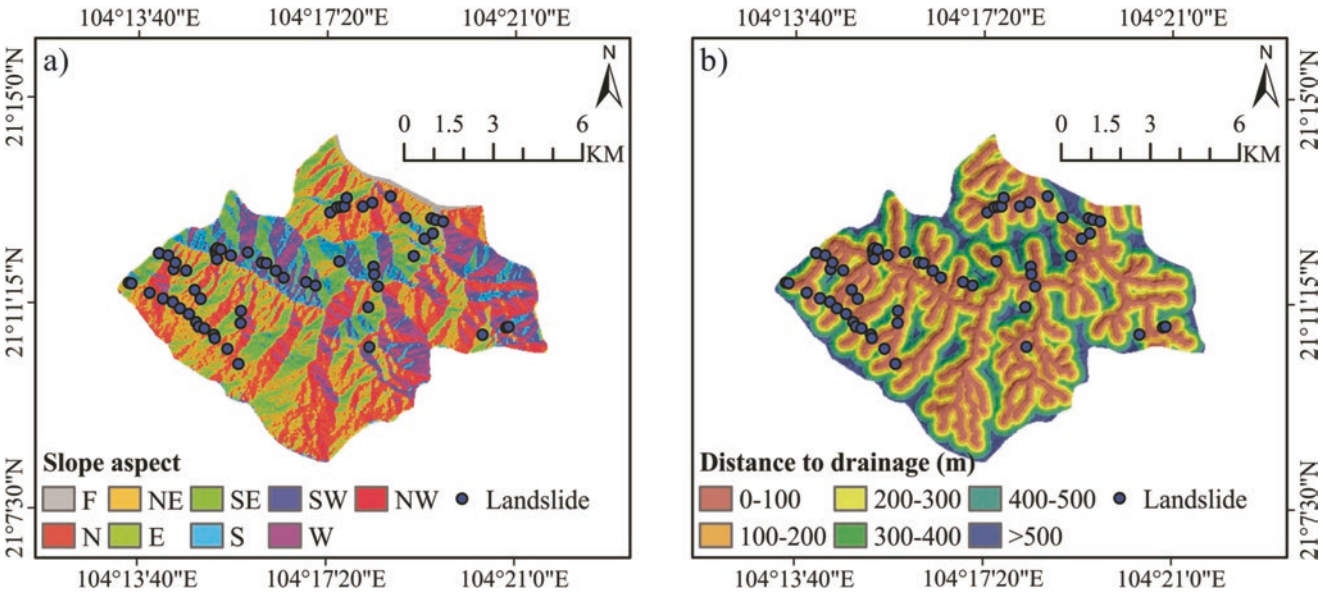

Fig. 7 (**a**) Slope aspect map and (**b**) map of distance to drainage

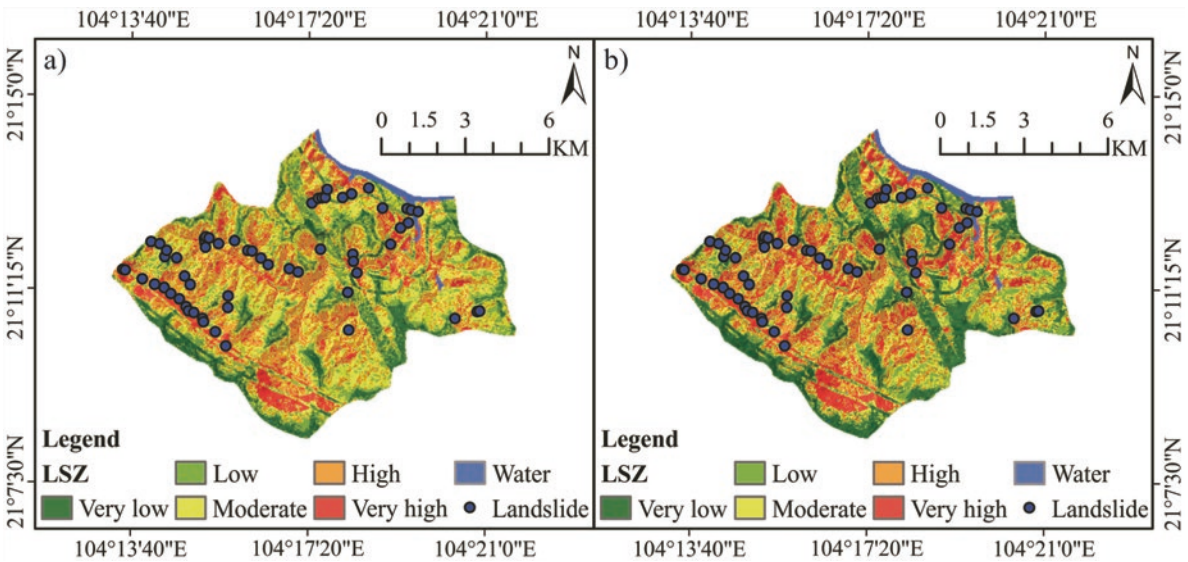

Fig. 8 LSZ map using (**a**) SI and (**b**) FSI models

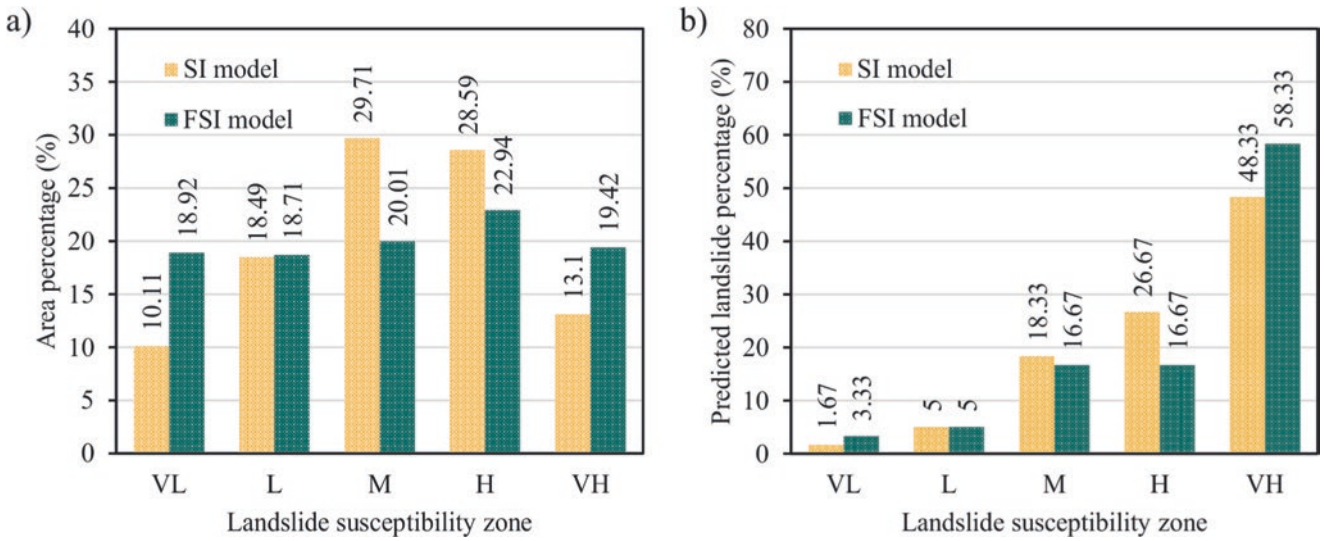

Fig. 9 (**a**) Area percentage of landslide susceptibility zones and (**b**) predicted landslide percentage using SI and FSI models

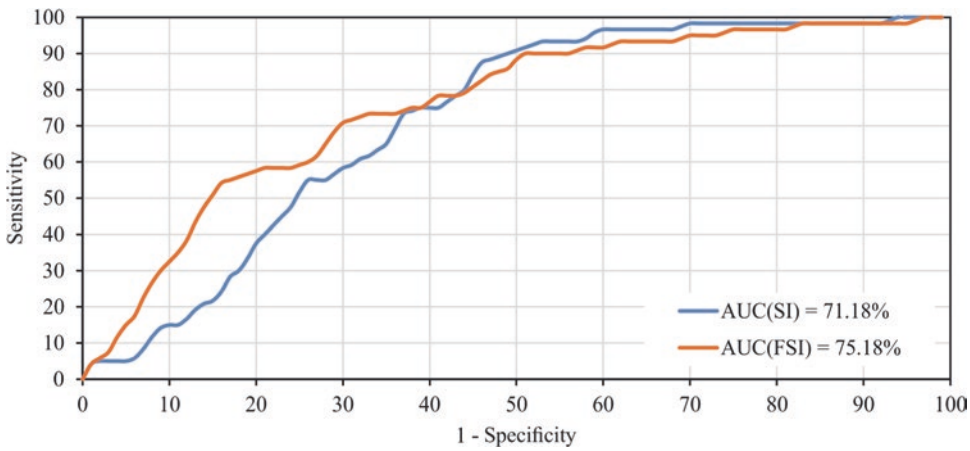

Fig. 10 ROC curves of landslide susceptibility models

The prediction model's performance was evaluated using the ROC method (Swets 1986), and the ROC curves are displayed in Fig. 10. All the AUC values for the models are greater than 70%, indicating that the models have good performance and are suitable for assessing the spatial distribution of landslides in the study area. Because fractal analysis evaluated the role of each factor in the landslide process, the FSI model provided better performance. Future studies can improve the performance of the FSI model with improved input data quality and an up-to-date landslide inventory map.

4 Conclusions

Bivariate statistical methods have been extensively utilized in landslide studies because of their efficiency and simplicity. This study employed an integration (FSI) of the Fractal method and the Statistical Index method to enhance the efficacy of assessing the potential for landslide development in Muong Khoa commune, Bac Yen district, Son La province. Statistical analyses were conducted to determine the class weight of each causal factor, whereas the factor weight values were calculated using the fractal method. A higher AUC value indicates that the FSI model improved the accuracy of the landslide susceptibility zonation maps, as demonstrated by the conducted analyses. Simultaneously, the FSI model predicted a larger area with very low landslide susceptibility, providing a significant base for territorial planning and land use management. Consequently, the fractal method can be combined with other statistical methods to produce highly accurate prediction models. In addition, the methodologies and results of this study can be employed in landslide studies in other areas of Vietnam.

Acknowledgments The authors would like to express our gratitude to the Vietnam Institute of Geosciences and Mineral Resources (VIGMR), Institute of Geological Sciences, Vietnam Academy of Science and Technology, and the national science and technology project under grant number ĐTĐL.CN-81/21 for providing the data utilized to conduct this study.

References

Biswas NK, Stanley TA, Kirschbaum DB, Amatya PM, Meechaiya C, Poortinga A, Towashiraporn P (2022) A dynamic landslide hazard monitoring framework for the Lower Mekong Region 10. https://doi.org/10.3389/feart.2022.1057796

Bui QD, Ha H, Khuc DT, Nguyen DQ, von Meding J, Nguyen LP, Luu C (2022) Landslide susceptibility prediction mapping with advanced ensemble models: Son La province, Vietnam. Nat Hazards. https://doi.org/10.1007/s11069-022-05764-3

Dahl MPJ, Mortensen LE, Veihe A, Jensen NH (2010) A simple qualitative approach for mapping regional landslide susceptibility in The Faroe Islands. Nat Hazards Earth Syst Sci 10(2):159–170. https://doi.org/10.5194/nhess-10-159-2010

Guillen KADLP, Mendoza ME, Macías JL, Solis-Castillo B (2022) Landslide susceptibility analysis based on a semiquantitative method in the sierra-costa region, michoacán, Mexico. Phys Geogr 43(4):463–486. https://doi.org/10.1080/02723646.2021.1899476

Hu Q, Zhou Y, Wang SX, Wang FT, Wang HJ (2020) Fractal-based spatial distribution analysis of geological hazards and measurement of spatial association with hazard-related predisposing factors. Int Arch Photogramm Remote Sens Spatial Inf Sci:XLII-3/W10125-131. https://doi.org/10.5194/isprs-archives-XLII-3-W10-125-2020

Juliev M, Mergili M, Mondal I, Nurtaev B, Pulatov A, Hübl J (2019) Comparative analysis of statistical methods for landslide susceptibility mapping in the Bostanlik District, Uzbekistan. Sci Total Environ:653801-814. https://doi.org/10.1016/j.scitotenv.2018.10.431

Liu L, Li S, Li X, Jiang Y, Wei W, Wang Z, Bai Y (2019) An integrated approach for landslide susceptibility mapping by considering spatial correlation and fractal distribution of clustered landslide data. Landslides 16(4):715–728. https://doi.org/10.1007/s10346-018-01122-2

Ma S, Qiu H, Hu S, Pei Y, Yang W, Yang D, Cao M (2020) Quantitative assessment of landslide susceptibility on the Loess Plateau in China. Phys Geogr 41(6):489–516. https://doi.org/10.1080/02723646.2019.1674559

Mandelbrot B (1967) How long is the coast of Britain? Statistical self-similarity and fractional dimension. Science 156(3775):636–638

Nguyen V-T, Tran TH, Ha NA, Ngo VL, Nadhir A-A, Tran VP, Duy Nguyen H, Malek MA, Amini A, Prakash I, Ho LS, Pham BT (2019) GIS based novel hybrid computational intelligence models for mapping landslide susceptibility: a case study at Da Lat City, Vietnam. Sustainability 11(24). https://doi.org/10.3390/su11247118

Ou P, Wu W, Qin Y, Zhou X, Huangfu W, Zhang Y, Xie L, Huang X, Fu X, Li J, Jiang J, Zhang M, Liu Y, Peng S, Shao C, Bai Y, Zhang X, Liu X, Liu W (2021) Assessment of landslide hazard in Jiangxi using geo-information technology 9. https://doi.org/10.3389/feart.2021.648342

Pourghasemi HR, Moradi HR, Fatemi Aghda SM, Sezer EA, Goli Jirandeh A, Pradhan B (2014) Assessment of fractal dimension and geometrical characteristics of the landslides identified in north of Tehran, Iran. Environ Earth Sci 71(8):3617–3626. https://doi.org/10.1007/s12665-013-2753-9

Rai DK, Xiong D, Zhao W, Zhao D, Zhang B, Dahal NM, Wu Y, Baig MA (2022) An investigation of landslide susceptibility using logistic regression and statistical index methods in Dailekh District, Nepal. Chin Geogr Sci 32(5):834–851. https://doi.org/10.1007/s11769-022-1304-2

Ram P, Gupta V, Devi M, Vishwakarma N (2020) Landslide susceptibility mapping using bivariate statistical method for the hilly township of Mussoorie and its surrounding areas, Uttarakhand Himalaya. J Earth Syst Sci 129(1). https://doi.org/10.1007/s12040-020-01428-7

Rouai M, Jaaidi EB (2003) Scaling properties of landslides in the Rif mountains of Morocco. Eng Geol 68(3):353–359. https://doi.org/10.1016/S0013-7952(02)00237-5

Sim KB, Lee ML, Wong SY (2022) A review of landslide acceptable risk and tolerable risk. Geoenvironmen Disasters 9(1). https://doi.org/10.1186/s40677-022-00205-6

Swets JA (1986) Indices of discrimination or diagnostic accuracy: their ROCs and implied models. Psychol Bull 99(1):100–117. https://doi.org/10.1037/0033-2909.99.1.100

Thanh Thi Pham N, Nong D, Raghavan Sathyan A, Garschagen M (2020) Vulnerability assessment of households to flash floods and landslides in the poor upland regions of Vietnam. Clim Risk Manag 28. https://doi.org/10.1016/j.crm.2020.100215

Van Westen CJ (1997) Statistical landslide susceptibility analysis. Van Westen CJ, López AS, Cornejo PU, Ardanza GC (eds) ILWIS 2.1 for Windows application guide. ITC Publication, Enschede. ISBN: 73-84

VIGMR (2014) Report on landslide situation in Son La province (in Vie). Ministry of Natural Resources and Environment, Hanoi

Wang HB, Wu SR, Shi JS, Li B (2013) Qualitative hazard and risk assessment of landslides: a practical framework for a case study in China. Nat Hazards 69(3):1281–1294. https://doi.org/10.1007/s11069-011-0008-1

Wang Q, Li W, Wu Y, Pei Y, Xie P (2016) Application of statistical index and index of entropy methods to landslide susceptibility assessment in Gongliu (Xinjiang, China). Environ Earth Sci 75(7). https://doi.org/10.1007/s12665-016-5400-4

Zhang G, Cai Y, Zheng Z, Zhen J, Liu Y, Huang K (2016) Integration of the statistical index method and the analytic hierarchy process technique for the assessment of landslide susceptibility in Huizhou, China CATENA 142233-244. https://doi.org/10.1016/j.catena.2016.03.028

Zhao B, Ge Y, Chen H (2021) Landslide susceptibility assessment for a transmission line in Gansu Province, China by using a hybrid approach of fractal theory, information value, and random forest models. Environ Earth Sci 80(12). https://doi.org/10.1007/s12665-021-09737-w

KLC2020 Official Promoters

The Kyoto Landslide Commitment 2020 (KLC2020)

Kyoto 2020 Commitment for Global Promotion of Understanding and Reducing Landslide Disaster Risk

A Commitment to the Sendai Landslide Partnerships 2015–2025, the Sendai Framework for Disaster Risk Reduction 2015–2030, the 2030 Agenda Sustainable Development Goals, the New Urban Agenda and the Paris Climate Agreement

KLC2020 Official promoters are public and private organizations who promote the Kyoto Landslide Commitment 2020 and provide financial support for the implementation of the KLC2020 activities including the Open Access Book Series "Progress in Landslide Research and Technology."

Host organization

International Consortium on Landslides (ICL)/Željko Arbanas.

Public sectors: KLC2020 Official Promoters-public

International Unions/Associations, Governmental organizations, Universities and Research institutes

- The International Union of Geological Sciences (IUGS)/John Ludden
- The International Union of Geodesy and Geophysics (IUGG)/Chris Rizos
- The International Association for the Engineering Geology and the Environment/Vassilis Marinos
- International Geosynthetics Society (IGS)/John Kraus
- Geological Survey of Canada, Natural Resources Canada, Canada/Daniel Lebel
- Faculty of Civil and Geodetic Engineering, University of Ljubljana, Slovenia/Matjaž Mikoš
- China University of Geosciences, Wuhan, China/Huiming Tang
- Department of Civil Engineering, National Taiwan University, Chinese Taipei/Louis Ge
- Institute of Rock Structure and Mechanics, the Czech Academy of Sciences/Josef Stemberk
- Institute of Cold Regions Science and Engineering, Northeast Forestry University/Wei shan.

Private sectors: KLC2020 Official Promoters-private

Companies and corporation.

- Marui & Co. Ltd, Japan
- Nippon Koei Co., Ltd, Japan
- Ellegi srl, Italy
- Chuo Kaihatsu Corporation, Japan
- Godai Kaihatsu Corporation, Japan
- Kiso-Jiban Consultants Co., Ltd, Japan
- Kokusai Kogyo Co., Ltd., Japan
- OSASI Technos, Inc., Japan.

B. Abolmasov et al. (eds.), *Progress in Landslide Research and Technology, Volume 3 Issue 1, 2024*, Progress in Landslide Research and Technology, https://doi.org/10.1007/978-3-031-55120-8

Geological Survey of Canada, Natural Resources Canada

GSC-Pacific Division

Geological Survey of Canada: Who We Are

The Geological Survey of Canada (GSC) is part of the Earth Sciences Sector of Natural Resources Canada. The GSC is Canada's oldest scientific agency and one of its first government organizations. It was founded in 1842 to help develop a viable Canadian mineral industry by establishing the general geological base on which the industry could plan detailed investigations. Throughout its long and colourful history, the GSC has played a leading role in exploring the nation.

Today, the GSC is Canada's national organization for geoscientific information and research. Its world-class expertise focuses on the sustainable development of Canada's mineral, energy and water resources; stewardship of Canada's environment; management of natural geological and related hazards; and technology innovation (Fig. A.1).

The GSC celebrated its 175th anniversary in 2017 which coincided with Canada's 150th anniversary of Confederation. The GSC co-leads the Canada-Nunavut Geoscience Office and works with dozens of universities and research institutes, industry organizations, other federal departments, provinces, territories and municipalities in Canada and across the world. In particular, we work closely with other geological survey organizations in Canada through the unique Intergovernmental Geoscience Accord.

Every year, we publish hundreds of maps, Open Files, peer-reviewed papers and other reports. Our scientists are recognized worldwide and sought after for their expert advice on locating mineral, energy and groundwater resources, reducing risk from natural hazards and reviewing environmental assessments.

Fig. A.1 Paleotsunami investigations in order to understand regional earthquake cycles and submarine landslide hazards

Strategic Priorities

The GSC has attempted to plot a course through this changing, uncertain world.

First, we identify three core areas of persistent scientific endeavour, which reflect stable, long-term needs of society:

- **Geological knowledge for Canada's onshore and offshore lands**
- **Geoscience for sustainable development**
- **Geoscience for keeping Canada safe.**

Next, we outline a new, fourth area of endeavour, Geoscience for society, which is the need to address the uncertainties of the changing world by expanding the reach and impact of geoscience knowledge in land-use decision making and in efforts to reduce the risk of disasters.

Finally, we recognize that our strength lies in a fifth area of endeavour, Our people, Our science, which we need to nurture to maintain a high-performing workforce capable of world leading innovative geoscience for the benefit of Canada.

GSC-Pacific Division
GSC-Pacific Division, Vancouver, BC, Canada
e-mail: David.Huntley@nrcan-rncan.gc.ca

B. Abolmasov et al. (eds.), *Progress in Landslide Research and Technology, Volume 3 Issue 1, 2024*, Progress in Landslide Research and Technology, https://doi.org/10.1007/978-3-031-55120-8

(a) **Geological knowledge for Canada's onshore and offshore lands**

Geoscientific knowledge is fundamental to managing our onshore and offshore lands and their abundant resources. With its 10 million km^2 of onshore land and an additional 7 million km^2 of ocean estate, Canada is a vast country and a core mission of the GSC is to map and understand the land and its resources. Our Geo-mapping for Energy and Minerals (GEM) program continues to advance our knowledge of the North and by 2020 will complete a first mapping of surface geology at a coarse scale.

In the offshore lands, our geoscience knowledge also serves to confirm the farthest extents of the Canadian territory. Our joint program with Global Affairs Canada and Fisheries and Oceans Canada to delineate the outer limits of the continental shelf in the Atlantic and Arctic Oceans will reach a critical milestone in 2019. The program will file its Arctic submission under the United Nations Convention on the Law of the Sea (UNCLOS) (Fig. A.2).

(b) **Geoscience for sustainable development**

Finding new resources remains a major challenge. Many near-surface deposits have been discovered in Canada, but significant mineral resources remain to be found in less accessible regions and at depths below the surface. Finding new resources requires systematic, intensive and innovative methods to assess the mineral potential in remote locations.

It requires searching beneath overburden cover, imaging the 3-D structure of the earth and understanding the geological processes that lead to concentration of minerals in certain locations (Fig. A.3).

For the Energy sector, the greatest challenge is in the transition to a low-carbon economy. Although global fossil fuel use is likely to continue to grow over the foreseeable future, the trend will likely be at a decreasing rate. Canada has an abundant supply of conventional and unconventional (oil sands and shale) oil and gas, so development in frontier areas is likely to be slow. In addition, the government has placed a moratorium on exploration activity in the Arctic offshore lands.

(c) **Geoscience for keeping Canada safe**

The GSC will continue to work on understanding how landscapes will change, how infrastructure will be affected and how resilience to climate change can be built into new infrastructure. Climate change will likely have a significant impact on the water cycle. GSC research will shed light on the risk to potable water supplies, hydroelectric power generation, and hazards from floods and drought (Fig. A.4).

(d) **Geoscience for society**

The scientific knowledge required to assess cumulative effects is broad. The complex interactions between land use, water management and waste management require an integrated approach at a landscape scale. The GSC is a national provider of information on both land (surficial and solid geology) and water, including the integration of surface water and groundwater into the complete water cycle (Fig. A.5).

The GSC recognizes that this area of endeavour involves inherent complexities and that our goals in this area will be to some degree aspirational. However, we will investigate new ways of planning our programs, undertaking our fieldwork, interacting with key stakeholders, and communicating our expert knowledge in ways that contribute positively to decision making about resource development.

(e) **Our people, Our science**

As a science organization within the federal government, the GSC's mandate is to conduct world-class science to inform public decision making. The Canadian government has articulated and adopted the principle of evidence-based decision making and reaffirmed the need for government science to be objective and non-partisan.

To remain at the leading edge, our scientists need to work with a variety of partners. We need to reinforce the central role that the GSC plays in the Canadian geoscience community by building networks of collaboration, fully participating in national geoscience initiatives, and advocating for Canadian geoscience at the international level (Fig. A.6).

Fig. A.2 The GSC studies the sea floor of the Arctic to understand its geology and geohazards. Here a small craft surveys the bottom of Southwind Fjord (Baffin Island, N Nunavut)

Fig. A.3 GSC geologists near the Heiberg Formation in northern Ellesmere Island (NU) as part of the geo-mapping for energy and minerals program. This formation is the primary host of major gas accumulations in the Canadian High Arctic

Fig. A.4 The GSC conducts climate change studies, here documenting the effects of fast melting permafrost leading to extreme coastal erosion on Pelly Island, NT

Fig. A.5 The GSC conducts geohazard studies to reduce risks to people and infrastructure, here installing equipment to monitor landslide activity above a critical railway corridor in central BC

Fig. A.6 Among many celebratory activities for the GSC's 175th anniversary in 2017, the GSC held a Rock and Fossil Exhibit, at its site at the Bedford Institute of Oceanography (Dartmouth, NS), as part of a two-day open-house event, where more than 20,000 visitors participated

Moving Forward

Some of the objectives and goals that the GSC has set represent familiar territory for a national geoscience organization, but many others will pull us out of our comfort zone. We will take the time to better understand the challenges of delivering objective, nonpartisan science to support evidence-based decision making in Canada at a time of great technological and social change.

We will not be able to do this alone, so we look forward to strengthening our ties to other federal departments, provinces and territories, universities, Indigenous organizations, the private sector and civil society as a whole.

We ask all our stakeholders to contact us, to challenge us and, most importantly, to join with us to assure the future of Canada through thoughtful, respectful dialogue about the land we live on, its resources and its future (Fig. A.7).

Exploring Canada

Through its history, the GSC has been responsible for mapping the land mass of Canada, which supported the integration of the western provinces and northern territories into the country that we have today. The limit of Canada's offshore territory is still being extended today though surveys conducted by the GSC and the Canadian Hydrographic Service.

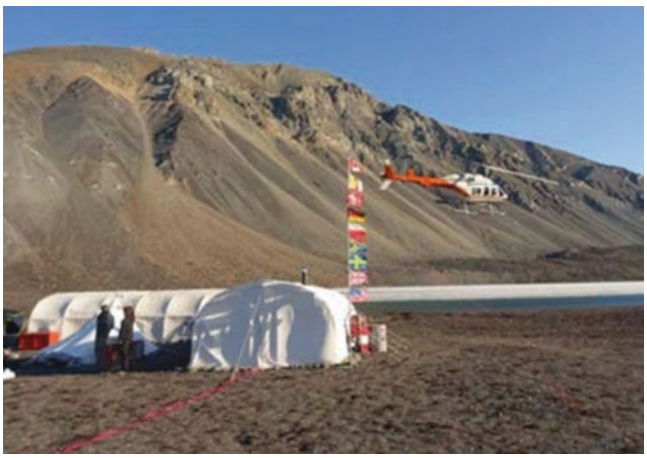

Fig. A.7 Joint Canadian/German (GSC/BGR) field mapping camp on northern Ellesmere Island, looking west as the fog covered sea ice of Yelverton Inlet, 2017

In more recent years, the GSC helped find the first economic diamond deposit in the Northwest Territories, leading to the expansion of diamond mining in Canada. These are only a few of the key GSC achievements that have built our knowledge of Canada's lands and provided the building blocks of its natural resource economy.

Today, exploration of this vast land is still reaping its natural resource rewards. The search for natural resources is difficult, akin to looking for a needle in a haystack.

The GSC's GEM program is exploring vast tracts of Canada's North, a land mass roughly equivalent to the combined areas of Quebec, Ontario and Manitoba, to find the "haystacks" with resource potential. This information is shared with the provinces and territories, as well as the private sector, so that the search for the "needles" can continue. The information is also critical to inform land-use planning.

In November 2016, the Royal Canadian Geographical Society (RCGS) awarded its prestigious Gold Medal to the GSC in recognition of the Survey's outstanding contribution to the development of Canada on the occasion of it's 175th anniversary.

Faculty of Civil and Geodetic Engineering, University of Ljubljana

Matjaž Mikoš

Summary

The Faculty of Civil and Geodetic Engineering of the University of Ljubljana (UL FGG) covering engineering disciplines, including water science and technology, has been involved in landslide risk reduction activities at the national level in Slovenia (former Yugoslavia, until 1991) for decades. In 2008, UL FGG became an ICL Full Member and has gradually developed its ICL engagement. UL FGG has been awarded the title of the World Centre of Excellence (WCoE) in Landslide Risk Reduction for 5 consecutive periods (2008–2011, 2011–2014, 2014–2017, 2017–2020, 2020–2023). Together with the Geological Survey of Slovenia, UL FGG hosted in 2017 the 4th World Landslide Forum in Ljubljana, Slovenia.

UL FGG strongly supports diverse activities of the International Consortium on Landslides, Kyoto, Japan, and thus contributes to the 2030 Agenda for Sustainable Development, as well as to the Sendai Framework for Disaster Risk Reduction 2015–2030 (SF DDR). UL FGG was a signatory of the Sendai Landslide Partnerships 2015–2030, and is a dedicated official promoter of the Kyoto Landslide Commitment 2020, a SF DRR voluntary commitment by ICL.

In 2016, UL FGG started to host the University of Ljubljana UNESCO Chair on Water-related Disaster Risk Reduction (WRDRR), being still the only UNESCO Chair at this university, and one of a few in Slovenia. Among different activities, in 2022 the WRDRR Chair supported the launching of the regional platform called Resili- Enhance for enhancing the resilience to disasters for sustainable development. UL FGG also supports activities of the Slovenian National Committee for UNESCO Intergovernmental Hydrological Programme (IHP), now working on the IHP-IX programme (2022-2029).

UL FGG is actively involved in numerous international (bilateral) and national research projects in the field of hydrology and hydraulic engineering, including topics such as landslide research, landslide risk mitigation, natural risk dialogue, and capacity building for society resilience.

In the field of capacity building, UL FGG offers several courses for graduate and postgraduate students in landslide mechanics and dynamics, landslide stabilization and landslide risk mitigation. In this article, a short overview of the past and current activities of UL FGG as ICL Full Member and KLC2020 Official Promoter is shown.

World Centre of Excellence on Landslide

Risk Reduction and IPL projects

WCoE activities

The title of World Centre of Excellence (WCoE) on Landslide Risk Reduction is given to a governmental or non-governmental entity, which contributes to the landslide disaster risk reduction at a regional and/or global level in a specific unique field of expertise, as well as helps promoting International Programme on Landslides (IPL) and landslide research intellectually, practically and financially (https://www.landslides.org/ipl-info/world-centre-of-excellence/). UL FGG was granted the title of WCoE five consecutive times:

- WCoE 2008–2011 & 2011–2014: Mechanisms of landslides in over -consolidated clays and flysch.
- WCoE 2014–2017: Mechanisms of landslides and creep in over-consolidated clays and flysch.
- WCoE 2017–2020: Landslides in Weathered Flysch: from activation to deposition.
- WCoE 2020–2023: Landslides in Weathered Heterogenous Sedimentary Rock Masses such as Flysch.

M. Mikoš
Faculty of Civil and Geodetic Engineering, University of Ljubljana, Ljubljana, Slovenia
e-mail: matjaz.mikos@fgg.uni-lj.si

B. Abolmasov et al. (eds.), *Progress in Landslide Research and Technology, Volume 3 Issue 1, 2024*, Progress in Landslide Research and Technology, https://doi.org/10.1007/978-3-031-55120-8

The research efforts at UL FGG were focused on:

- Mechanisms of triggering such landslides (mud flows), estimation of debris-flow magnitudes triggered as shallow or deep-seated landslides (debris slides), and triggering of shallow rainfall-induced landslides using advanced statistical methods.
- Field and laboratory investigations of suction in over-consolidated clays and flysch, such as to improve the understanding of softening in stiff over–consolidated clays and marls, using soil matrix suction as an indicator for mudflow occurrence, and executing suction long-term monitoring of the Slano Blato landslide.
- Laboratory investigations of coarse debris-flow rheological parameters and soil–water characteristic curve of residual soil from a flysch rock mass.
- Mathematical modelling of debris flows (hazard assessment in deposition areas), using different numerical models and different digital terrain models.

The WCoE activities were financially supported by the Slovenian Research Agency through the Research Programme P2-0180 "Water Science and Technology, and Geotechnical Engineering: Tools and Methods for Process Analyses and Simulations, and Development of Technologies," as well as by several national (Fig. A.8) and international (bilateral) research projects.

UL FGG and the Geological Survey of Slovenia jointly organized 4th World Landslide Forum (WLF4), in Ljubljana between May 29 and June 2, 2017. With over 600 participants from 49 countries and 5 international organizations, WLF4 was promoting the culture of living with natural hazards.

IPL projects

An important ICL activity is IPL projects (https://www.landslides.org/projects/ipl-projects/). The IPL Evaluation Committee examines the submitted proposals of ICL members by carefully reading the written proposals and by listening to their presentations at annual ICL conferences. The initially accepted proposals by the IPL Evaluation Committee are discussed and then approved at the annual Board of Representatives meeting of ICL members (Annual Assembly). Finally, the IPL projects are approved annually by the Global Promotion Committee IPL-KLC. UL FGG has successfully submitted several proposals for IPL projects and has been so far actively involved in the following ones:

- IPL-151 Soil matrix suction in active landslides in flysch - the Slano Blato landslide case (2010–2012).
- IPL-225 Recognition of potentially hazardous torrential fans using geomorphometric methods and simulating fan formation (2017–2020).
- IPL-226 Studying landslide movements from source areas to the zone of deposition using a deterministic approach (2017–2020) - coordinated by the Geological Survey of Slovenia.
- IPL-261 World-wide-web-based Landslide Observatory (W3bLO) (2022-2024)

ICL Thematic and Regional Networks

Following the ICL Strategic Plan 2012–2021, several thematic networks and regional networks have been established (for an overview, see https://www.landslides.org/projects/icl-networks/).

Landslide Monitoring and Warning Thematic Network – LaMaWaTheN

In 2012, UL FGG proposed the ICL landslide monitoring and warning thematic network - almost 10 ICL members joined the initiative. The general objective of the proposed network was to compare experiences in the field of landslide monitoring and installed early warning systems for active landslides in various regions of the world. Lately, we contributed to the network activities by preparing practice guidelines on monitoring and warning technology for debris flows.

The idea of the network was partially taken over by the web database ICL World Report on Landslides (https://www.landslides.org/projects/world-report-on-landslides/), created to be a platform to share landslide case studies among the global landslide community, with monitoring and warning systems being a part of the platform.

ICL Adriatic-Balkan Network – ICL ABN

Jointly with other ICL members from Croatia and Serbia, in 2013, UL FGG proposed to establish an ICL Adriatic-Balkan Regional Network. Various network activities were proposed, the most active being the organization of biennial regional symposia on landslide risk reduction in the Adriatic-Balkan Region (called ReSyLAB). UL FGG supported the 1st Symposium in Zagreb (Croatia 2013), 2nd in Belgrade (Serbia 2015), 3rd in Ljubljana (Slovenia 2017), 4th (Sarajevo 2019), and 5th in Rijeka (Croatia 2022).

In the last decade, UL FGG has signed bilateral research projects with the ICL members in the region: "Adriatic-Balkan Regional Network: Landslide Risk Mitigation for Society and Environment" (2012–13 with University of Belgrade, Serbia), "Study of landslides in flysch deposits: sliding mechanisms and geotechnical properties for landslide modelling and landslide mitigation SoLiFlyD" (2014–15 with University of Rijeka, Croatia), and "Laboratory investigations and numerical modelling of landslides in flysch deposits in Croatia and Slovenia" (2016–17 with the University of Rijeka, Croatia). This joint research has helped strengthen regional cooperation within the ICL ABN regional network.

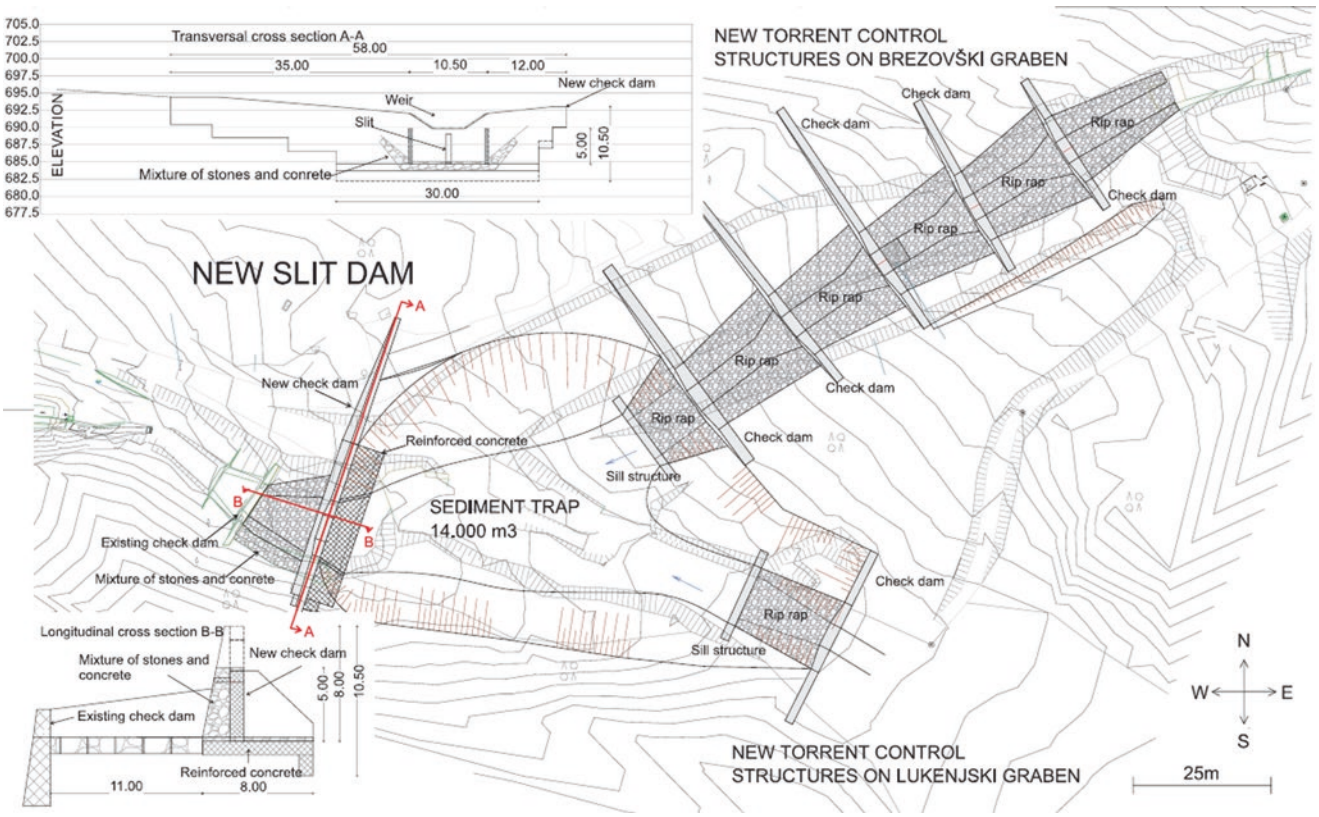

Fig. A.8 Technical countermeasures for future debris floods threatening the cabin station of the Krvavec ski area in N Slovenia. An extreme May 2018 debris flood case study in northern Slovenia: analysis, modelling, and mitigation. Landslides 17: 2373-2383, DOI https://doi.org/10.1007/s10346-019-01325-1).

Other ICL-Related International Activities

UL FGG served the ICL by taking different leading roles in the Consortium, i. e. UL FGG member served as Chair of IPL Evaluation Committee, twice as ICL Vice President, and was elected to Co-Chair and in 2021 to Chair of the IPL-KLC (https://www.landslides.org/ipl-info/ipl-klc-globalpromotion-committee/).

UL FGG has been strongly supporting the journal Landslides: Journal of the International Consortium on Landslides, published by Springer Nature (https://www.link.springer.com/journal/10346) since its launch in 2004. UL FGG works for the journal in the roles of reviewers and an associate editor, and regularly publishes its top research results in the journal, as well as disseminates information important for capacity building in landslide risk reduction – such as results of bibliometric studies on the journal Landslides and ICL books.

UL FGG also contributed to the two-volume set of Landslide Dynamics: ISDR-ICL Landslide Interactive Teaching Tools (LITT), namely to Vol. 1: Fundamentals, Mapping and Monitoring by practice guidelines on monitoring and warning technology for debris flows (https://www.springer.com/gp/book/9783319577739), and to Vol. 2: Testing, Risk Management and Country Practices (https://www.springer.com/gp/book/9783319577760) by a state-of-the-art overview on landslide disaster risk reduction in Slovenia, a study on two-dimensional debris-flow modelling and topographic data, and by study on intensity duration frequency curves for rainfall-induced shallow landslides and debris flows using copula functions.

UL FGG also contributed to the open-access book series "Progress in Landslide Research and Technology" Vol. 1 by a review article on the history of the International Programme on Landslides (IPL) (https://doi.org/10.1007/978-3-031-16898-7_3), an original article on the natural-hazard-related web observatory as a sustainable development tool (https://doi.org/10.1007/978-3-031-16898-7_5), and an original article on landslide research and technology in patent documents (https://doi.org/10.1007/978-3-031-18471-0_3).

University of Ljubljana UNESCO Chair on Water-related Disaster Risk Reduction (2016–2020 and 2020–2024)

Experiences and knowledge accumulated in the past decades at the Chair on Hydrology and Hydraulic Engineering at UL FGG in the field of (applied) hydrology in experimental basins, hydraulic engineering, landslide research, landslide risk reduction, and flood risk management, culminated in 2016 in the establishment of the UNESCO Chair on Water-related Disaster Risk Reduction (WRDRR Chair; www.unesco-floods.eu) at the University of Ljubljana. The UNESCO WRDRR Chair was positively evaluated by UNESCO in 2020 and prolonged for another 4 years (2020–2024). The Chair is associated to the university twinning and networking UNITWIN UNESCO – Kyoto University – ICL on "Landslide and Water-Related Disaster Risk Management".

The UNESCO WRDRR Chair is involved into numerous international (bilateral) and national research projects. Their results are timely reported in scientific literature (https://www.unesco-floods.eu/category/publications/).

In 2022, the UNESCO Chair supported launching of the ResiliEnhance Program for enhancing the resilience to disasters for sustainable development (https://www.unescochair-sprint.uniud.it/en/resilienhance-program/). The program is at the moment focused to Central and Eastern Europe, and supported by the Central Europe Initiative (CEI).

In 2022, the UNESCO Chair started to lead the University of Ljubljana project on Sustainable Development (2022-2025; https://www.unesco-floods.eu/ultra-pilot-projects/)to modernize university professional study programmes, especially in civil engineering, to increase students' competences for sustainable development, including disaster risk reduction and resilience building.

UL FGG supports activities of the Slovenian National Committee for UNESCO Intergovernmental Hydrological Programme (https://www.ncihp.si) – focus of the activities is the development of the IHP-IX Programme (2022–2029).

Conclusions

UL FGG as one of World Centres of Excellence in Landslide Risk Reduction, hosts the UNESCO Chair on Water-related Disaster Risk Reduction. UL FGG strongly supports ISDR-ICL Sendai Partnerships 2015–2025 for global promotion of understanding and reducing landslide disaster risk, and its extension to 2030 and beyond: the Kyoto 2020 Commitment for Global Promotion of Understanding and Reducing Landslide Disaster Risk that that was signed in November 2020. UL FGG is proud to be its Official Promoter, and will specifically work for its Actions 2, 5, 6, 9 and 10.

This review article is intentionally written without a list of references to described activities. For this purpose, listed websites and links may be used.

The author wants to thank colleagues from UL FGG and University of Ljubljana, and from the ICL community for the past and long-lasting excellent cooperation with a joint vision to reduce landslide disaster risk.

China University of Geosciences, Wuhan

Huiming Tang, Changdong Li, and Qinwen Tan

Introduction

China University of Geosciences, Wuhan (CUG), founded in 1952, is a key national university affiliated with the Ministry of Education. It is also listed in the National "211 Project", the "985 Innovation Platform for Advantageous Disciplines," and the "Double First-class Plan". CUG, featuring geosciences, is a comprehensive university that also offers a variety of degree programs in science, engineering, literature, management, economics, law, education, and arts. Its Geology and Geological Resources & Engineering have both been ranked as the national number one disciplines.

CUG has two campuses in Wuhan. The main campus is the Nanwang Mountain Campus, located in the heart of the Wuhan East Lake National Innovation Demonstration Zone, which is popularly known as China Optics Valley. The Future City Campus is located in the east of Wuhan and is 27 km from the main campus. These two picturesque campuses cover a combined area of 1,474,353 m2. They are ideal places to study, work, and enjoy life. CUG owns a 4A-Level tourist attraction— the Yifu Museum. CUG also boasts four field training centers: Zhoukoudian in Beijing, Beidaihe in Hebei Province, Zigui in Hubei Province, and Badong in Hubei Province.

CUG has established a complete education system. As of December 2020, 30,239 full-time students, including 18,080 undergraduate students, 9302 master's students, 1916 doctoral students, and 941 international students, have enrolled in its subsidiary 23 schools and 86 research institutes. CUG currently has a faculty of 1858 full-time teachers, among which there are 539 professors (11 of which are members of the Chinese Academy of Sciences) and 984 associate professors.

CUG is focused on fostering high-quality talent. Among its over 300,000 graduates, many have gone on to become scientific and technological elites, statesmen, business leaders and athletes. And they have made great contributions to the nation and society, represented by former Premier WEN Jiabao and 39 members of the Chinese Academy of Sciences and Chinese Academy of Engineering.

CUG has strengthened exchanges and cooperation with international universities. It has signed friendly cooperation agreements with more than 100 universities from the United States, France, Australia, Russia, and other countries. CUG has actively carried out academic, scientific, and cultural exchanges with universities around the world. There are about 1,000 international students from more than 100 countries studying at CUG. It also sponsors more than 900 teachers and students to study abroad or conduct international exchanges and invites more than 400 international experts to visit, lecture, and teach at CUG every year. In 2012, CUG initiated and co-established the International University Consortium in Earth Science (IUCES) with 11 other world-renowned universities. IUCES is committed to promoting the common development of geosciences education and scientific research through resource sharing, exchange, and cooperation among its member institutions. In addition, CUG has partnered with Bryant University from the USA, Alfred University from the USA, and Veliko Turnovo University from Bulgaria in establishing three Confucius institutes on their campuses (Fig. A.9).

Strategic Plan of Building a World-Renowned Research University in Earth Sciences: A Beautiful China and a Habitable Earth: Towards 2030

CUG reviewed and approved Strategic Plan of Building a World-Renowned Research University in Earth Sciences on December 25 of 2019.

H. Tang · C. Li · Q. Tan
China University of Geosciences, Wuhan, P.R. China
e-mail: tanghm@cug.edu.cn

B. Abolmasov et al. (eds.), *Progress in Landslide Research and Technology, Volume 3 Issue 1, 2024*, Progress in Landslide Research and Technology, https://doi.org/10.1007/978-3-031-55120-8

Fig. A.9 Strategic plan of building a world-renowned research university in earth science

Themed "A Beautiful China & A Habitable Earth", the Plan depicts the blueprint of the second goal of the "three-step strategic goals", which is to build a world-renowned research university in Earth Sciences by 2030 based on the attained goal of developing CUG into a "high-level university with first-class Earth Sciences and coordinated development of multi-disciplines".

According to the Plan, our education missions are: Remaining true to CUG's core value of "seeking harmonious development between man and nature" we are committed to cultivating innovative talents who have lofty morality, solid foundation, and profound expertise and who pursue the unity of knowing and doing. We should provide personnel support and endeavor to innovate, apply and spread knowledge in order to provide theories, technologies, and approaches for the construction of a Beautiful China and a Habitable Earth. We should strive to optimize governance, reform culture, and fully invigorate the vitality of running a university. We should provide our service to the construction of an innovative country and to the promotion of a harmonious co-existence between man and nature. We should provide our service to the people and the governance of China. We should provide our service to the consolidation and development of the system of socialism with Chinese characteristics. We should provide our service to the reform and opening up and to the construction of socialist modernization.

According to the Plan, our endeavoring goals are: By 2030, we will have built a world-renowned research university in Earth Sciences, whose main indexes will have reached or nearly reached the level of other world-class universities. To upgrade CUG into a world-class university, we will endeavor to make the discipline of Earth Sciences rank top in the world and forge boldly ahead in competition to improve the quality of other disciplines of CUG. We will assemble a contingent of teachers and researchers with international competitiveness and influences to build a university with Chinese characteristics and superiority. We will build a world-class university that will be fully engaged in international exchange and cooperation and that will achieve educational, academic, cultural, and administrative excellence.

Outstanding Recent Achievements

In recent years, CUG has achieved significant progress in the research fields of geohazards, water resource, geochemistry, paleontology, geodetic surveying and lunar exploration program, etc. To keep to the theme of KLC2020, recent achievements on geohazards researches of CUG are focused and introduced.

(a) **Approval of National Observation and Research Station for Geohazards in the Three Gorges Reservoir Area, Hubei**

CUG was newly approved **National Observation and Research Station for Geohazards in the Three Gorges Reservoir Area, Hubei**. This station, founded and administrated by Prof. Huiming Tang, is responsible to carry out field observations and scientific research on geohazards in condition of reservoir operation.

The central site of the station is located in Badong County of the Three Gorges Reservoir area (hereinafter abbreviated as the TGR area), and a larger monitoring network of multiple sites has been established, including the geohazard field test site for the Majiagou landslide, Zigui County, and systematic geophysical monitoring station for the whole TGR area, etc.

The Badong field site (also named Badong in-situ large-scale experimental station) is located in the Huangtupo landslide area, which has been recognized the largest reservoir landslide by volume in the TGR area. The field site consists of a tunnel complex and a series of monitoring systems (Fig. A.10). The tunnel complex, built in the Huangtupo riverside sliding mass #1, consists of a main tunnel with a length of 908 m and a width of 5 m, five branch tunnels (5 m to 145 m long, 3.5 m wide), two test tunnels, and 35 observation windows. The test tunnels exposed the sliding zones of the landslide, facilitating their direct observation and the execution of scientific experiments, such as large-scale in-situ mechanical tests and deep deformation monitoring. The monitoring systems measure deformation as well as hydrologic, meteorological and hydro-chemical variables. The deformation system is composed of a slope surface displacement measurement unit and an underground displacement measurement unit. The slope surface displacement unit includes a number of GPS (Global Positioning System) and BDS (BeiDou Navigation Satellite System) measurement points, as well as an IBIS-FL (Interferometric Radar) monitoring system (Fig. A.12). The underground displacement unit includes nine deep inclinometer boreholes, a number of crack meters installed on the ground and the walls of tunnels, and many hydrostatic level gauges that measure the settlement of the tunnels in the sliding mass. The hydrologic system includes a number of devices that allow for observation of the water level of the Yangtze River, the ground water level and water discharge of the tunnels (Fig. A.12). A small meteorological station is located on the landslide and provides rainfall data. So far, multiple and massive data have been collected for the landslide area since the year 2012, when the field site was constructed; over 10,000 people with a variety of geology-related backgrounds from > 20 countries have visited this experimental station.

(b) **Approval of the Basic research on the prediction and forecasting of major landslides program supported by the Major Program of NSFC**

CUG was approved the **Basic research on the prediction and forecasting of major landslides program** (2021–2025), supported by the Major Program of the National Natural Science Foundation of China. The program was designed for the prediction and forecasting of major landslides, with the concentration on the core scientific problems of landslide evolution process and physical-mechanical mechanism. Three key scientific problems, including correlation mechanism for landslide initiation, physical-mechanical mechanism for landslide initiation, and prediction and forecasting theory based on landslide evolution were proposed.

Five topics were set up to achieving those objectives. Topic 1 was proposing the initiation classification of major landslides based on large field test platform, with the adoption of field prototype test and other technical means. Topics 2-4 aimed to reveal the physical and mechanical mechanism of locked-segment dominated landslide, static liquefaction loess landslide and hydrodynamic pressure-driven landslide, and to establish the corresponding landslide initiation criteria, respectively. Topic 5 was responsible to established the prediction mode and real-time forecasting system. Ultimately, the landslide prediction and forecasting theory based on the evolution process and physical-mechanical mechanism would be put forward. The scientific thought for the implement of research is exhibited in Fig. A.11.

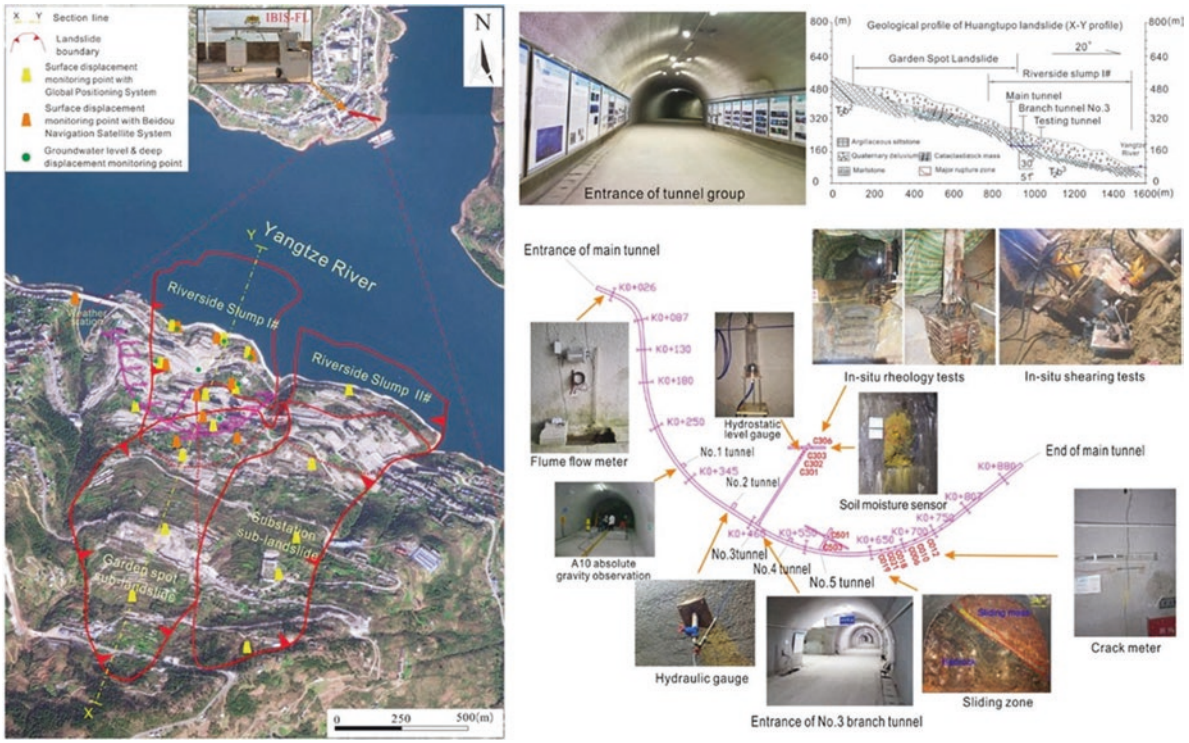

Fig. A.10 Badong in-situ large-scale experimental station of the National Observation and Research Station for Geohazards in the Three Gorges Reservoir Area, Hubei

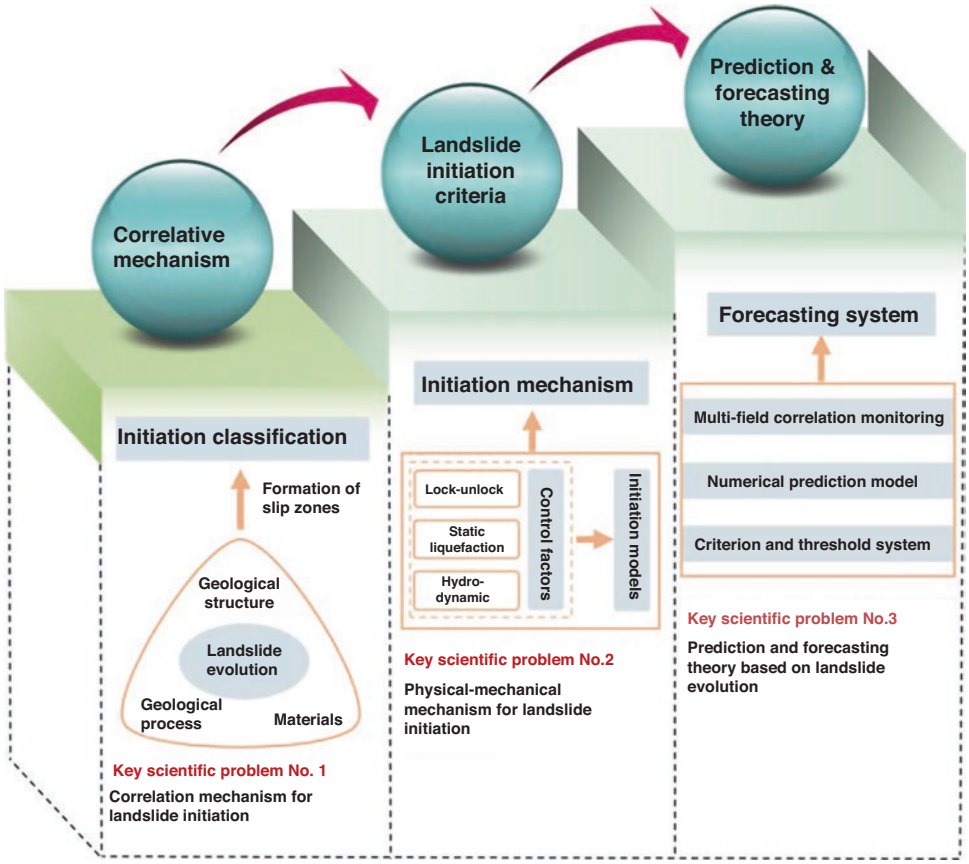

Fig. A.11 Scientific thought for the implement of research

Fig. A.12 Photo of old Badong County, showing the populated area built on the Huangtupo landslide (Tang et al. 2015a)

The implementation of the research is respected to lay the geological, mechanical and physical foundation for the above three types of landslide prediction, and to substantially promote the research on landslide prediction.

Figure A.12 shows the old Badong county, situated in the Huangtupo landslide area, and the exposures of the main rupture zones are now more than 50m below the water surface of the Three Gorges Reservoir (Tang et al. 2015a). During the second relocation from 1982 to 2003, the county moved from Xinling town to the Huangtupo landslide area (Gong et al. 2021). A series of investigations were conducted during that period, and the new county area was further confirmed to be on the site of an ancient landslide then (Gong et al. 2021). Huangtupo landslide is developed in the Middle Triassic Badong Formation strata, within which interbedded strata structures are often observed, and many geohazards developed. The material composition of the Huangtupo landslide includes mudstone, pelitic siltstone, and argillaceous limestone (Tang et al. 2015b). Multiple slumps formed the complex mass at least 4000 years ago (Tang et al. 2015b). The elevation of the crown of the landslide is about 600 m asl., while its toe varies from 50 to 90 m, submerged in the Yangtze River. The composite landslide covers an area of 1.35 km2, and its volume of nearly 70 million m3 makes it the largest reservoir landslide in China (Tang et al. 2015b). Considering the risk of landslide reactivation by long-term reservoir operation and human activities, the drainage system and the anchored defense structures along its leading edge were constructed to control the landslide. Huangtupo demonstration base was designed and constructed in 2012, during the third relocation period from 2007 to 2017 (Gong et al. 2021). At that time, some Badong county residents still lived in the Huangtupo area, facing the unsure threat. The old giant landslide is in need of further research to ensure its safety as well as provide access for landslide hazard study. The demonstration base was in great request. With the building and development of the demonstration base, Over 10,000 people with various geology-related backgrounds from more than 20 countries have visited. A national observation station was also settled rely on the base in 2020.

References

Tang H, Li C, Hu X, Wang L, Criss, R, Su A, Wu Y, Xiong, C (2015a) Deformation response of the Huangtupo landslide to rainfall and the changing levels of the Three Gorges Reservoir. Bull Eng Geol Environ. 74(3):933–942.

Tang H, Li C, Hu X, Su A, Wang L, Wu Y, Criss R, Xiong C, Li Y (2015b) Evolution characteristics of the Huangtupo landslide based on in situ tunneling and monitoring. Landslides 12(3):511–521.

Gong W, Juang CH, Wasowski J (2021) Geohazards and human settlements: Lessons learned from multiple relocation events in Badong, China—Engineering geologist's perspective. J Eng Geol 285:106051.

Department of Civil Engineering, National Taiwan University

Department of Civil Engineering, National Taiwan University

Introduction

National Taiwan University (NTU) was originally established in 1928, when Taiwan was under Japanese rule, as Taihoku Imperial University. The current name dates back to 1945. As Taiwan's oldest and most prestigious university, we are also the largest comprehensive higher education institution (HEI) in the country. The academic freedom that we cherish and our excellent faculties attract both domestic and international students. Throughout our 90-year history, we have nurtured many talents, including leading academics and leaders in the public and private sectors. Our campus is vast, and spans across multiple locations, including Taipei, Yilan, Hsinchu, Yunlin, and mountainous areas in central Taiwan—accounting for nearly 1% of Taiwan's total land area. This provides teachers and students with an environment rich in biological and ecological diversity.

As the leading university in Taiwan, we are strongly committed to social responsibility as we strive to drive sustainable development and influence positive change in society. This was also reflected in the first University Impact Rankings launched in 2019 by Times Higher Education (THE), which measure the contributions of HEIs to the United Nations' Sustainable Development Goals (SDGs). We were ranked 70th in the world overall, and 1st in the world for SDG16: Peace, Justice, and Strong Institutions. Starting from creating a sustainable culture on campus, we aim awareness about sustainability throughout the university, through innovative teaching and research, environmental protection and recycling efforts, and a school administration that supports equality and wellbeing. Our sustainability efforts extend beyond our campus through industry-academia collaborations and service teams deployed to remote areas. In the near future, we will continue to reinforce the spirit of innovation and sustainability thinking among all faculty members and students. We will also continue our efforts to address economic, environmental, and social challenges through interdisciplinary collaboration, as we create connections between the local and the international community. The Department of Civil Engineering (Fig. A.13) can be regarded as the root of The College of Engineering. The early civil engineering education covers a wide range of professions. With the development and differentiation of various social industries, some fields have gradually separated and established specialized departments. We have also moved on, combining different fields and top-notch technology to remain as the leader of the tide.

Civil engineering is inseparable from the development of human civilization. From the beginning of civilization, all man-made structures have enchased and highlighted the value of civil engineering. NTU Civil Engineering is no exception. From the Department of Civil Engineering of the Imperial College of Taipei to the National Taiwan University Department of Civil Engineering today, the majority of Taiwan's significant constructions is and will always be our finest gallery.

In National Taiwan University, you will obtain high-quality guidance in and out of the classroom. Academic resources in the classroom and sports culture clubs, various student activities throughout the year, will bind you together with peers of the same dream. These friends may also be partners that can help you in future careers. If you are willing to take civil engineering as a career and take on the challenges and step forward as a team, then listen to your inner call, join us, and let us stride ahead hand in hand (Fig. A.14).

Department of Civil Engineering, National Taiwan University
Department of Civil Engineering, National Taiwan University, Taipei, Taiwan
e-mail: louisge@ntu.edu.tw

B. Abolmasov et al. (eds.), *Progress in Landslide Research and Technology, Volume 3 Issue 1, 2024*, Progress in Landslide Research and Technology, https://doi.org/10.1007/978-3-031-55120-8

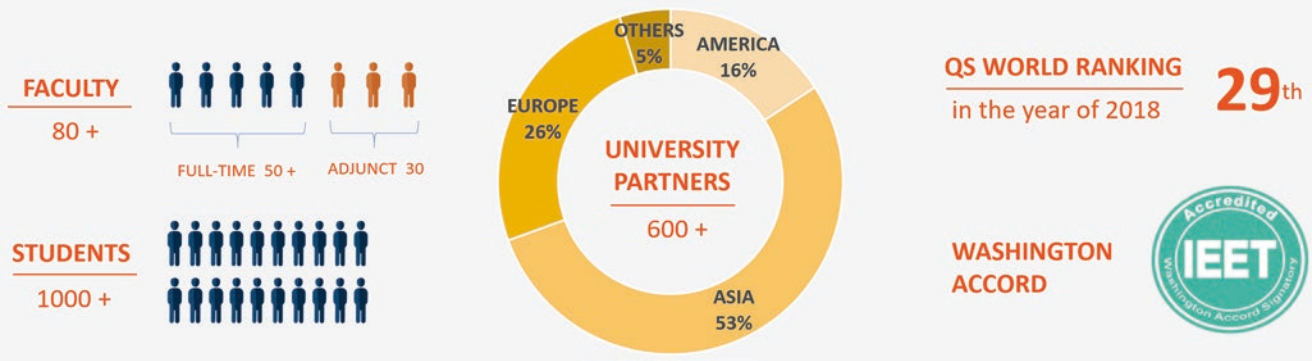

Fig. A.13 Quick facts of the Department of Civil Engineering

Fig. A.14 Life beyond Classroom

Outstanding Recent Achievements

Mitigating the Impacts of Natural Disasters via Cutting Edge Technology

Taiwan is located in the Circum-Pacific seismic belt, with many active faults and frequent typhoons. Due to the effects of climate change, extreme rainfall events that used to occur once in a century are now becoming more frequent, exacerbating the threat of landslides and debris flows. The prevention and mitigation of natural disasters such as earthquakes and flooding have therefore become a priority for the twenty-first century.

(a) **Earthquake Early Warning Systems: gain valuable response time**

For most natural disasters, potential losses to life and property can be mitigated through early warning and prevention. After the earthquake disaster of September 21st, 1999, building safety inspections needed to be conducted all across Taiwan. Our faculty and students with expertise in civil engineering and geology were quick to respond to this urgency, working closely with the National Center for Research on Earthquake Engineering to help the government improve the earthquake resistance standards and test specifications. Moreover, they proposed a more elaborate system for earthquake damage and liquefaction assessment, and conducted a complete review and classification of the earthquake risk tolerance for all areas in Taiwan. The team also developed new disaster prevention technologies. One of the most significant contributions was to assist the public high (vocational) schools around Taiwan with assessments of the earthquake resistance and reinforcement needs of old buildings. In the numerous earthquakes that have since occurred, the effect of these reinforcements has become apparent. The stronger earthquake resistance of these buildings has improved safety for 2.65 million teachers and students around Taiwan (Fig. A.15).

Our school has also developed technology to monitor the status of bridges with high traffic volumes. This optical fiber monitoring system will emit a warning whenever poor conditions are recorded, prompting an early response from management that can prevent a disaster from happening. When bridges in remote areas are damaged, a lightweight bridge developed by NTU out of composite materials can be assembled by residents in short time. In this way, access to affected areas can be quickly restored, and disaster relief provided more efficiently. In the event of an earthquake, Taiwan's citizens will immediately receive an emergency alert by text message. This warning system, which was developed by Professor Wu, Yih-Min at our Department of Geosciences, analyzes the properties of a P-wave within three seconds after detecting the wave so that it can issue an alert to citizens more than 10 seconds before the S-wave, which is most likely to cause damage arrives. This early warning system is accurate and fast, giving people valuable seconds to escape to safety. Because it is also much cheaper to manufacture network of multiple sites has been established, including the geohazard field test site for the Majiagou landslide, Zigui County, and systematic geophysical monitoring station for

the whole TGR area, etc. than previous seismographs, it could be rapidly rolled out to several hundred elementary and junior high schools, ensuring better protection of our country's younger generation. Moreover, this system has been successfully introduced in other earthquake-threatened countries, such as Indonesia, India, Vietnam, Nepal, and Mexico.

(b) **After the Flood: Rapid Mobilization and Improved Ability to Provide Relief**

Another critical area is flood disaster prevention. Also here, our faculty and students are actively involved in key activities ranging from early warning and response during the disaster, to raising the awareness of, and capability for, disaster prevention among citizens more generally. Our Center for Weather Climate and Disaster Research comprises experts in meteorology, hydrology, bioenvironmental engineering, and geology etc. This center helped New Taipei City and Keelung City establish an extreme weather and flood monitoring & warning system. Other projects include combining advanced deep learning with the analysis of radar data, which allows for closer monitoring of rainfall data in hydrologically sensitive areas. The improvement of flood models increases the accuracy of flood warnings and provides disaster prevention units with valuable information for them to rapidly formulate response strategies. From past experiences outside of Taiwan, we know that self-help and mutual support account for the largest share of the relief effort (90%) in the event of a disaster. In other words, even if flood warnings are effective, people in the affected area still need to be able to take own measures to protect themselves. At NTU, we actively participate in the community-level disaster relief preparations around the country, as well as in the training of disaster relief officers. Our experts provide citizens with the most up-to-date knowledge in disaster prevention, operate independent disaster relief systems, and evaluate the safety of shelters. These efforts contribute to the resilience and ability of local communities to mitigate impact, helping them recover more quickly. A plan for how to improve the disaster relief ability in the country proposed by our experts is another example of how we help make sure that the best disaster response capacity is in place. After improving the ability to respond to disasters, NTU's team also contributed to disaster prevention infrastructure around Taiwan, such as seismic isolation technology for buildings and equipment, or detention ponds in communities at risk. Our work and efforts in these areas help protect lives and property. As climate change continues to impact the world, we hope to leverage our technologies and expertise in these domains even further, and help strengthen the capacity to prevent and withstand natural disasters throughout the world.

Fig. A.15 Taiwan Earthquake Loss Estimation System (TELES)

Institute of Cold Regions Science and Engineering, Northeast Forestry University

Wei Shan and Ying Guo

Introduction

Institute of Cold Regions Science and Engineering of Northeast Forestry University (ICRSE-NEFU) is committed to the environmental geology and engineering geology of high latitude permafrost region and deep seasonal frozen area under the background of climate change, and attaches importance to the combination of basic research and applied research. With undergraduate, master, doctor, postdoctoral professional training system and standards, ICRSE-NEFU initiated "Geological environment risk research plan for permafrost degraded areas in Northeast China (GERRP)". With the support of the Chinese government, "Field scientific observation and research station of the Ministry of Education—Geological environment system of permafrost area in Northeast China (FSSE-PFNEC)" was established. Its observation stations cover all kinds of permafrost areas in Northeast China. At the same time, in order to develop and transfer technologies related to environmental governance and infrastructure construction in permafrost regions, "Provincial Collaborative Innovation Centre, Environment and road construction & maintenance in permafrost area of Northeast China (PCIC-PFER)" was established. Over the years, ICRSE-NEFU have continuously established cooperation with academic institutions and organizations at home and abroad, held various academic exchanges and regularly held "Academic Seminar on Engineering Geology and Environmental Geology in the Permafrost Along the Sino-Russian-Mongolian Economic Corridor", edited and published research cases of geoenvironmental disasters in permafrost regions in Northeast China, and shared the research results of GERRP. At present, the research results of GERRP are gradually enriched, some of them have highly academic value, and have been put into engineering practice. ICRSE-NEFU has gradually shown its unique research charm since it became an ICL member in 2003 2002. In 2012, ICRSE-NEFU established a landslide research network in cold regions (ICL-CRLN), and then Research

Center of Cold Regions Landslide was built.

Permafrost as one of the elements of the cryosphere, the change of thermodynamic stability of permafrost will directly affect the changes of hydrosphere, biosphere and lithosphere. Under the trend of global warming, the frequency and intensity of environmental and engineering geological disasters caused by permafrost degradation are getting higher and higher (Figs. A.16 and A.17). Taking the cold area in the southern boundary of the permafrost zone in Northeast China as study area, disasters such as ground subsidence, slope icing, landslides and other disasters caused by permafrost melting were studied. At the same time, we found melting permafrost also leads to seasonally high concentrations of greenhouse gases, triggering wildfires that may further accelerate permafrost degradation and environ- mental changes of terrestrial ecosystems and roads.

W. Shan · Y. Guo
Institute of Cold Regions Science and Engineering Northeast Forestry University, Harbin, China
e-mail: shanwei456@163.com

B. Abolmasov et al. (eds.), *Progress in Landslide Research and Technology, Volume 3 Issue 1, 2024*, Progress in Landslide Research and Technology, https://doi.org/10.1007/978-3-031-55120-8

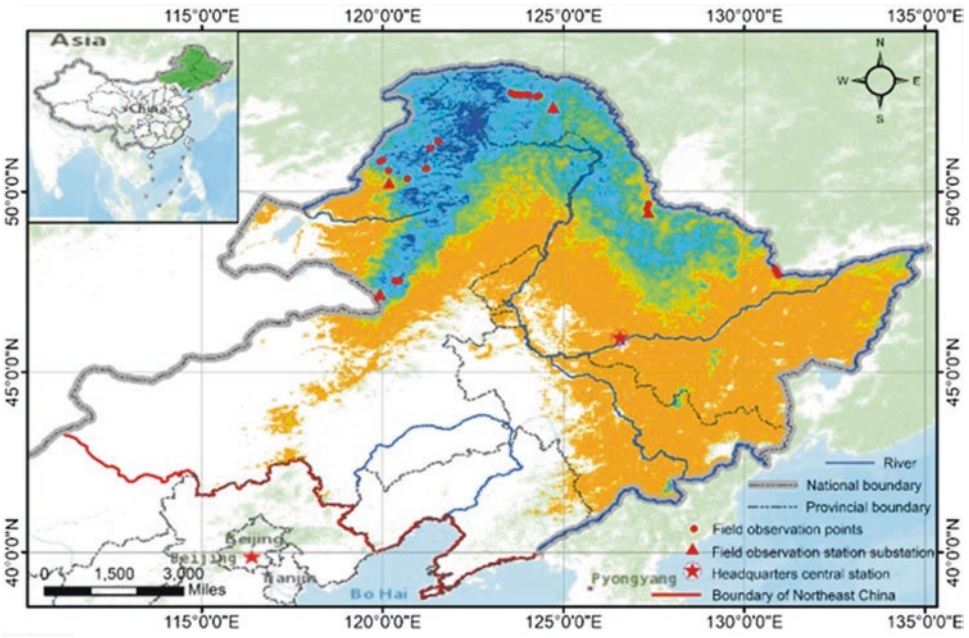

Fig. A.16 Permafrost distribution in NE of China (2014–2019)

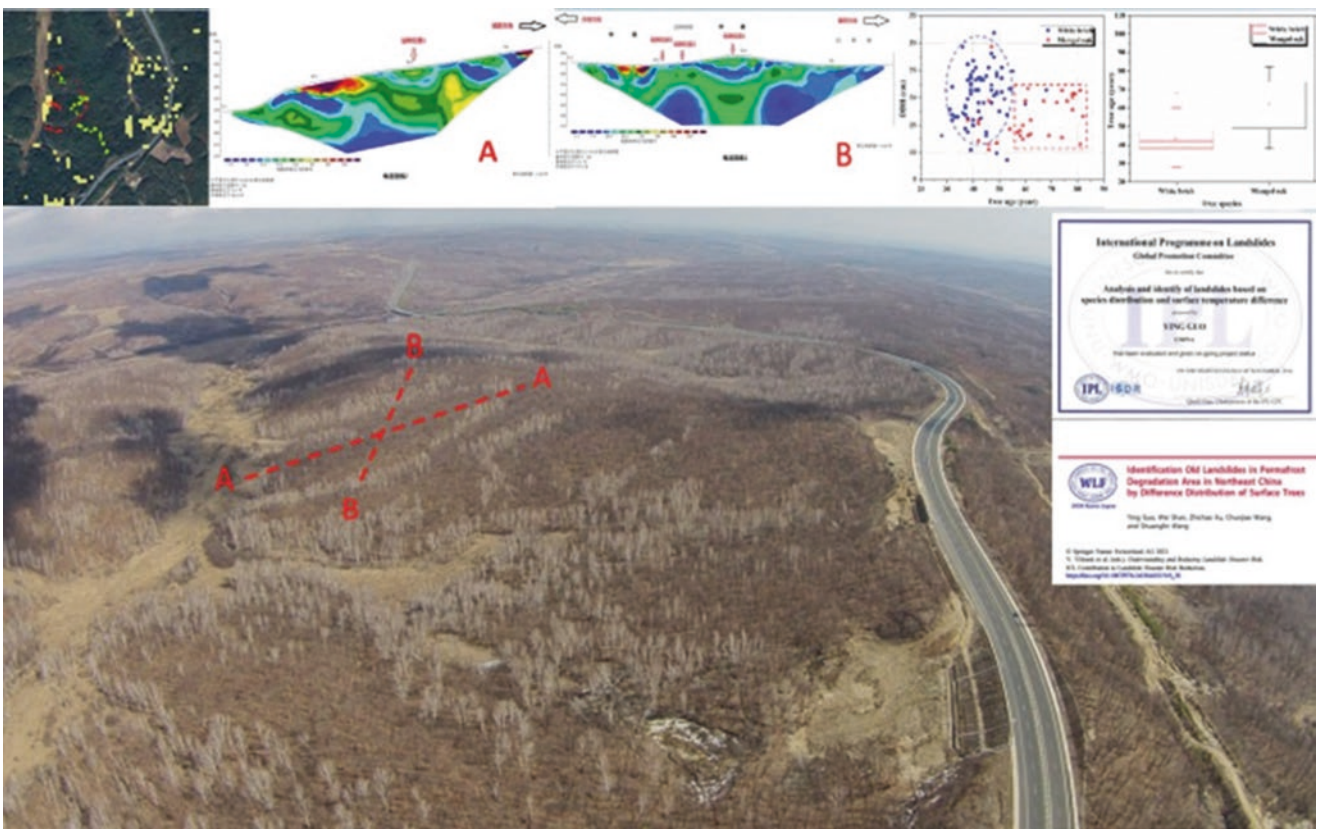

Fig. A.17 Different tree species and ages in the landslide area caused by permafrost degradation

Marui & Co. Ltd.

Taketoshi Marui and Yuji Ikari

Introduction

Marui & Co. Ltd. celebrated its 100th anniversary in 2020. Marui, as one of the leading manufacturers of testing apparatuses in Japan, has constantly been striving further to improve its service since its foundation in 1920, thus contributing to the sustainable development of our nation and society. Our main products cover various destructive and non-destructive testing apparatuses in geotechnical engineering, concrete engineering (mortar, aggregates, etc.), and ceramic engineering (Fig. A.18). Of particular note is that Marui has been helping manufacture ring-shear apparatuses (Fig. A.19) for the past half-century based on the leading-edge idea of Dr. Kyoji Sassa, Professor Emeritus at Kyoto University. Marui has delivered seven ring-shear apparatuses to the Disaster Prevention Research Institute, Kyoto University, and two to the International Consortium on Landslides. Also, the apparatuses were exported to the United States of America, China, Croatia, and Vietnam.

Since 2002, Marui has been a supporter of the International Consortium on Landslides (ICL) and has gradually been intensifying its contribution to the ICL's worldwide efforts for landslide risk reduction and international promotion of landslide research. According to NASA, more frequent and intense rainfall events due to climate change have been causing frequent landslides, particularly in mountains of Asian regions, including Japan, where waters can be stored in various ways. Summer monsoon rains, snow and glacier melt waters can destabilize steep mountainsides, triggering landslides, which are down-slope movements of rocks, soils, water, trees, etc. Marui, as an engineering supporter, commits deeply to various activities of research, particularly on triggering mechanisms of landslides.

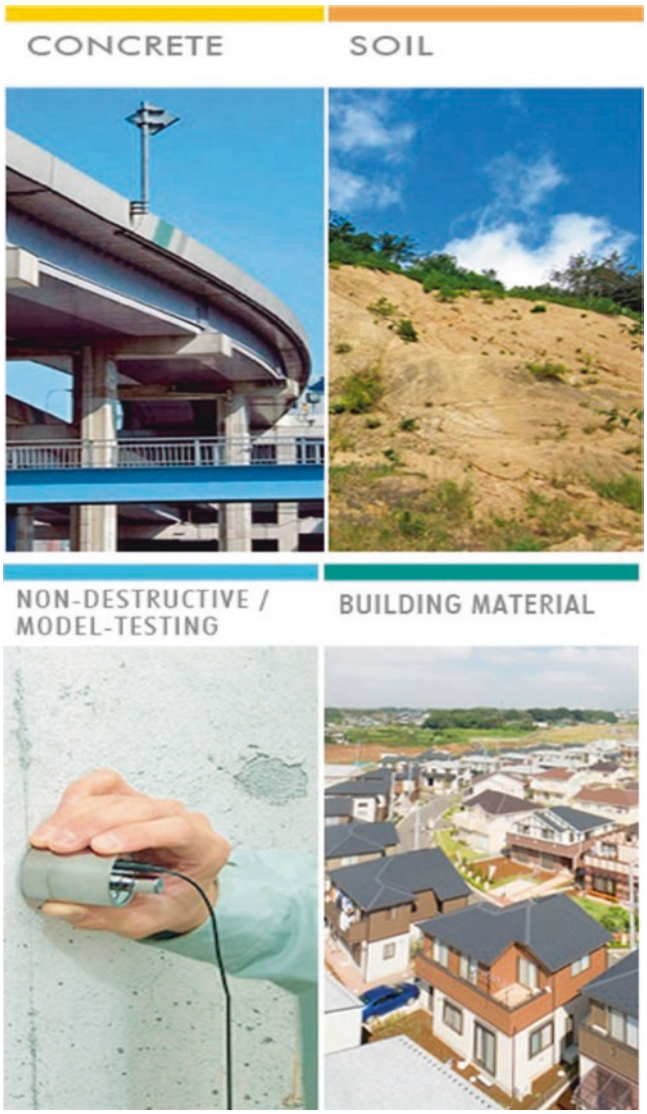

Fig. A.18 Products of testing apparatus such as non-destructive/model-testing for measuring intensity, physical property, durability, etc. for concrete, soil, building material, etc.

T. Marui · Y. Ikari
Marui & Co. Ltd., Osaka, Japan
e-mail: hp-mail@marui-group.co.jp;
http://marui-group.co.jp/en/index.html

B. Abolmasov et al. (eds.), *Progress in Landslide Research and Technology, Volume 3 Issue 1, 2024*, Progress in Landslide Research and Technology, https://doi.org/10.1007/978-3-031-55120-8

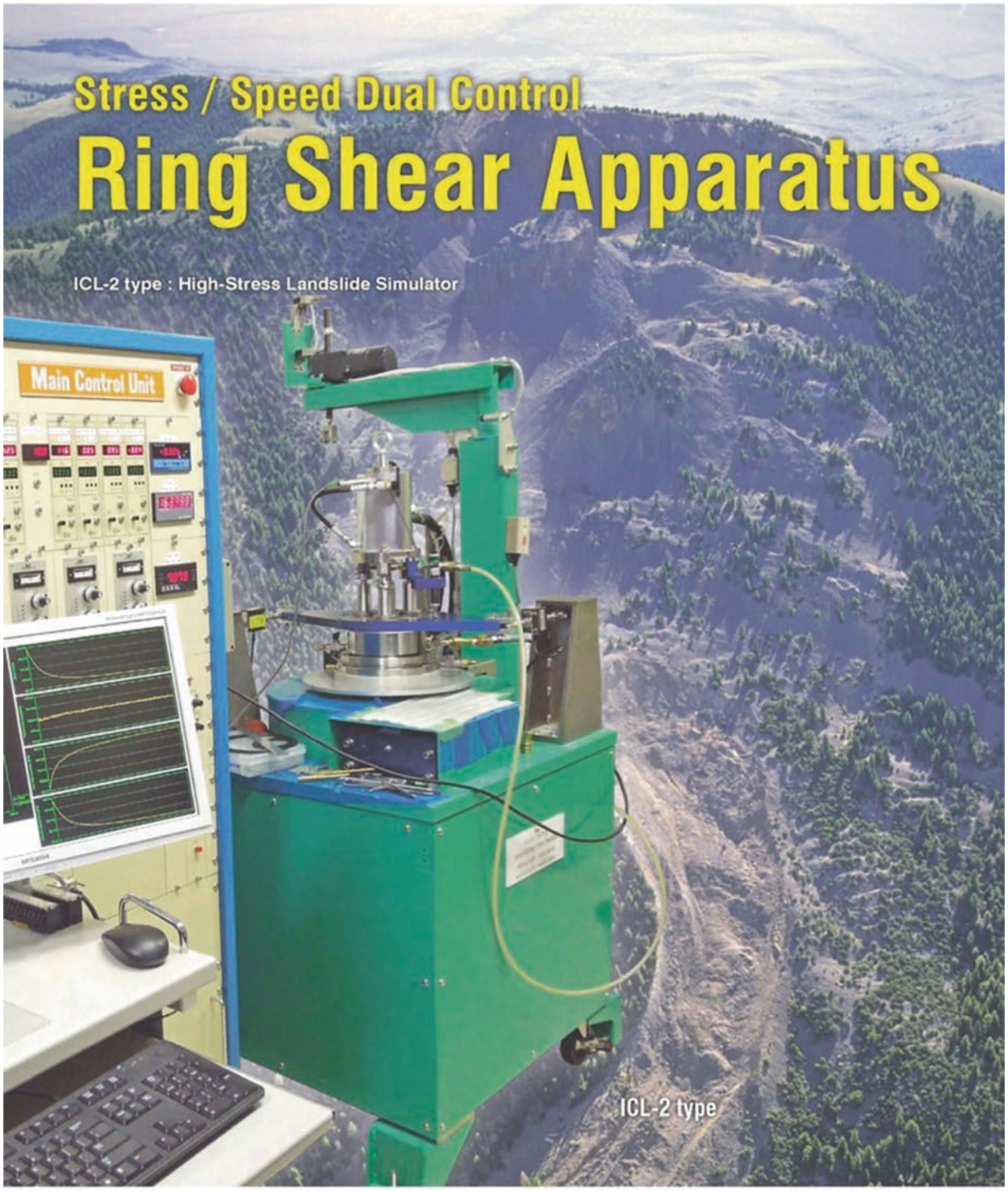

Fig. A.19 High-stress landslide simulator

Compliant standards	JGS 0541 / JGS 0542
Dynamic vertical load	Pneumatic servo system: 1 kN
Static vertical load	Servo motor method: 5 kN
Side pressure load	Air regulator method: 1 MPa
Back pressure load	Air regulator method: 0.5 MPa
Dynamic control method	Load/displacement control: 0.05 to 1.0 Hz
Static control method	Displacement control: 0.005 to 5.0 mm/min
Three-axis room	• Three-pillar fixed system • Specimen size: φ50 × H 100 mm
Measurement	• Axial pressure (external): 5 kN • Axial pressure (internal): 1 kN • External displacement: 25 mm • Internal displacement: ± 2 mm x 2 • Side pressure: 1 MPa • Pore pressure: 1 MPa • Volume change: 50 cc

Fig. A.20 Cyclic triaxial testing machine

In addition to the ring-shear apparatuses mentioned above, our company develops and sells soil and ground testing equipment. For example, our standard cyclic triaxial testing machine (Fig. A.20) is used by geological consultants, research laboratories, and educational institutions such as universities and technical colleges. Ground destruction phenomena, which often occur concurrently with earthquakes, significantly affect the seismic resistance of superstructures. Cyclic triaxial tests are used to determine the constants required to judge the liquefaction potential and to determine the cyclic deformation characteristics of the ground required for seismic response analysis.

This equipment can perform not only liquefaction and deformation tests, but also static triaxial tests, isotropic consolidation tests, and anisotropic consolidation tests.

In addition, control and data recording can be processed entirely on a personal computer.

Marui & Co. Ltd. takes great pleasure in developing, manufacturing, and providing new products of high value, sharing the sense of s achievement with our customers and thus contributing to social development. The entire staff of Marui is determined to devote ceaseless effort to keep its organization optimized for its speedy and high-quality services, by the motto “Creativity and Revolution,” and strive hard to take a step further as a leading manufacturer of testing apparatuses, to answer our customer's expectations for the 22nd century to come.

Marui continuously contributes to the 2030 Agenda for Sustainable Development and the Sendai Framework for Disaster Risk Reduction 2015-2030. In line with this, Marui signed KLC2020 in 2019 and will strongly support its actions, especially KCL2020 Actions 3,4,5, and 9.

Nippon Koei Co., Ltd., Geohazard Management Division

Hiroaki Tauchi

Introduction

The Nippon Koei Group (NK) has been a leading international consultant providing engineering consulting services to over 5500 multi-disciplinary infrastructure and development projects in 160 countries worldwide. The landslide prevention specialist team (now called Geohazard Management Division) was established in 1966 to provide countermeasures against sediment disasters. Over the last 50 years, we have significantly improved the capacity of countries to respond and reduce risk from debris flows, slope instabilities, landslides, avalanches, and rock falls due to torrential rains, large-scale earthquakes, and volcanic eruptions that threaten a country's vital economic infrastructure lifelines, especially the road networks. At present, approximately 160 engineers provide a variety of technical consulting services to protect communities from disasters, as shown in Fig. A.21.

During disasters, we utilize remote sensing technologies such as 3D point clouds and interferometric SAR to create 3D models and gather surface and damage information to conduct a broad area survey, as shown in Fig. A.22. Based on this information, we provide experienced professional engineers to assess risk quickly and promptly respond with engineering design analyses and emergency and permanent measures based on our extensive experience and know-how. In order to efficiently plan and design disaster countermeasure works, we have implemented the automated design using visual programming. This automated design enables us to perform the 3D design of countermeasures quickly and calculate project costs, streamlining the overall process. Organizing design and construction information in 3D facilitates the construction process and allows for permanent maintenance by passing it on to the maintenance management phase as BIM (Building Information Modeling). As a result, the information necessary for effective maintenance is readily available and can be utilized throughout the project's lifespan.

To maximize the effectiveness of infrastructures, we address efficient countermeasure plans, design, and research regarding cost reduction and cost-effectiveness using various numerical analyses such as the finite element method (FEM) and discrete element method (DEM), etc.

With climate change, the scale of disasters is enlarged and the frequency of disasters is increasing. This has resulted in more severe damage in more widespread and more urbanized areas, and more diverse and higher risks of disasters. In addition, in response to the SDG concept of "leaving no one behind," developing countries are lagging behind in hazard zoning and other efforts, which must be resolved. For this reason, NKG believes that it is important to assume that multiple types of disasters, such as floods, landslides and tsunamis, occur at the same time and in the same place. NKG provides risk mapping services using multi-hazard analysis as shown in Fig. A. 23.

In Japan, we have worked hard to restore and recover from sediment-related disasters caused by earthquakes and heavy rainfalls that have frequently occurred in recent years (the 2011 Great East Japan Earthquake, the Northern Kyushu Flood in 2017, etc.). We have received letters of appreciation from national and local governments for our efforts.

Our major international projects include "The Project for Countermeasure Construction Against the Landslides on Sindhuli Road Section II, Nepal," "The project for the rehabilitation of Sindhuli road affected by the 2015 Gorkha Earthquake, Nepal," and "The project for landslide prevention for National Road 6 in Honduras"; all funded by the Japan International Cooperation Agency (JICA) grantsin-aid. Through these projects, we are contributing to the socio-economic development of each country by improving vulnerable locations in road networks against sediment disasters, promoting traffic safety, and providing logistics assistance for road users. In particular, the 1st of the three NK's projects mentioned above won the "3rd JAPAN Construction International Award" from the Ministry of Land, Infrastructure, Transport and Tourism as the project

H. Tauchi
Geohazard Management Division, Nippon Koei Co., Ltd.,
Tokyo, Japan

B. Abolmasov et al. (eds.), *Progress in Landslide Research and Technology, Volume 3 Issue 1, 2024*, Progress in Landslide Research and Technology, https://doi.org/10.1007/978-3-031-55120-8

that has realized "high-quality infrastructures" through its excellent know-how, technical capabilities, and project management capabilities.

NK is an ICL member using its technology to reduce geohazard risk. Through various projects, NK continuously contributes to the 2030 Agenda for Sustainable Development and the Sendai Framework for Disaster Reduction 2015–2030. Using our full capability with abundant experiences in Japan and Asia prone to natural disasters, we hope to contribute much more to reducing global sediment disasters, including landslides (Fig. A.24). In line with this, NK has signed the KLC 2020 and will strongly support its actions.

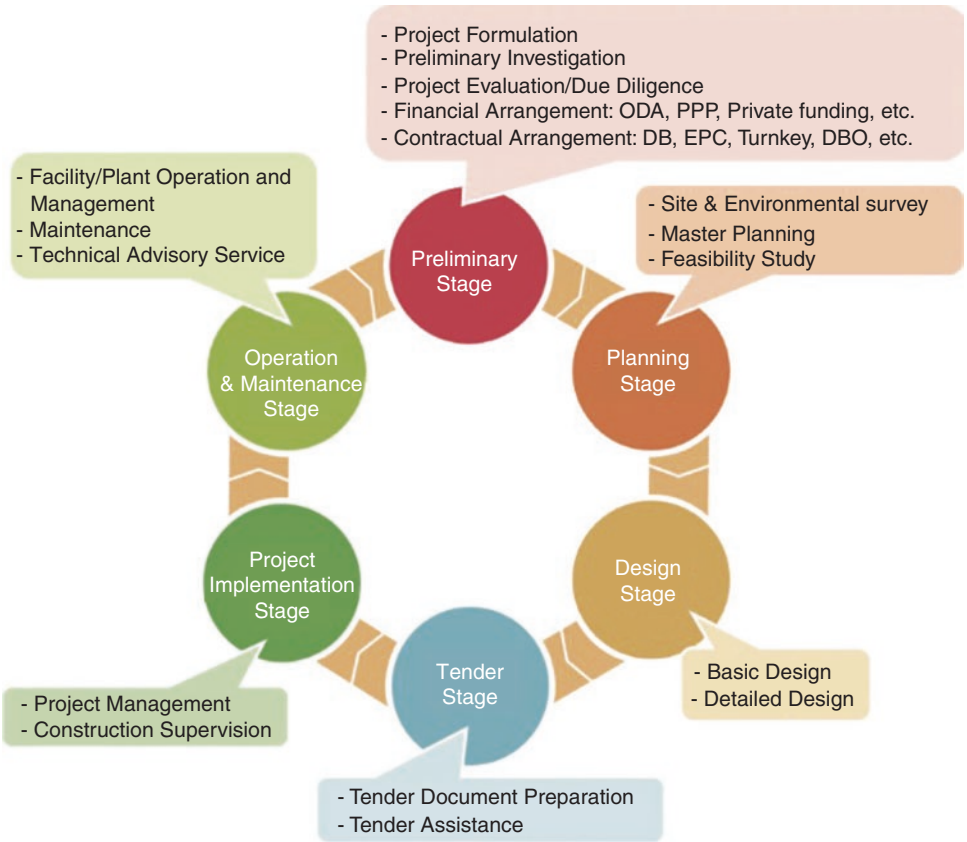

Fig. A.21 Our service for geohazard management

Fig. A.22 (left)a Landslide site, (right)3D Point Clouds

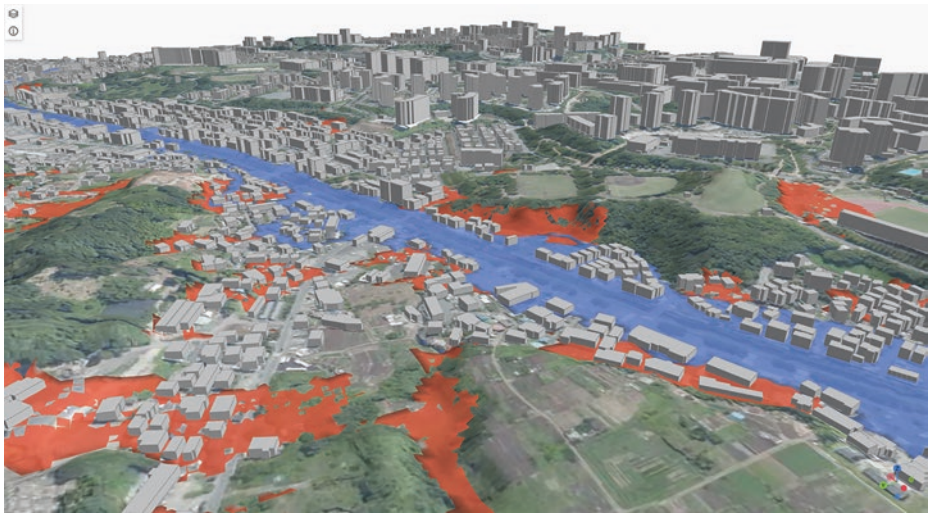

Fig. A.23 Visual programming and Automated design

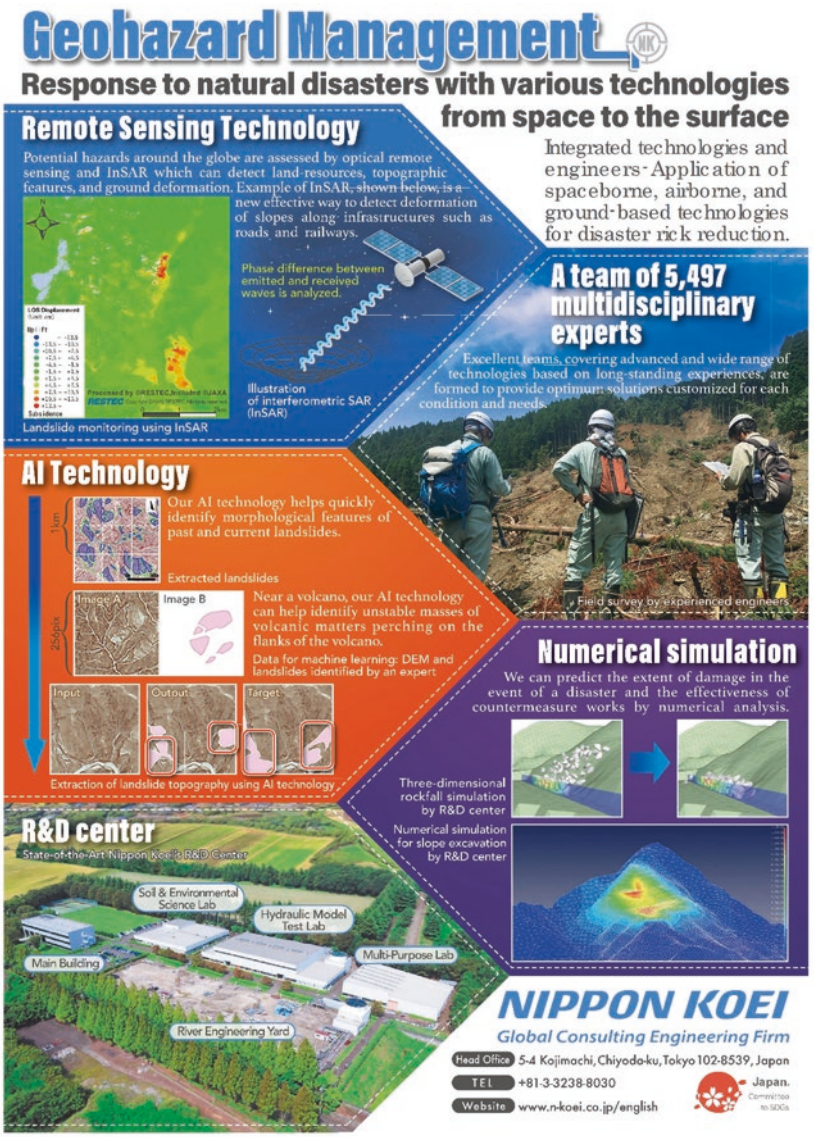

Fig. A.24 Introduction of our survey analysis technology for geohazard

Ellegi Srl

Ellegi Srl

Introduction

Ellegi srl provides worldwide monitoring services and produces Ground Based synthetic aperture radar (GBInsAR) for remote measurement of displacements and deformations on natural hazards and manmade buildings using its own designed and patented LiSALab system.

Its activities started in 2003 as a spin off project to exploit commercially the Ground Based Linear Synthetic Aperture Radars technology developed by European Commission's Ispra Joint Research Centre and based on the results of more than 10 years of research. Since then, Ellegi has industrialized and developed the core technology of the LiSALab system and latest LiSAmobile system represents the 5th generation of development.

In 2003 it was the first commercial company in the world to provide GBInSAR measurements of natural hazards and structure (Figs. A.25 and A.26).

Ellegi srl offers:

- Displacement fields measurement, control and monitoring of the deformation caused by natural hazards, like landslides, rockslides, sinkhole, volcanic deformation in every operative condition, including emergencies,
- Structural strain fields measurement, control, monitoring and diagnosis of the deformation affecting buildings, bridges, viaducts, dams.
- GBInSAR monitoring systems, installation, management and maintenance in order to provide information about natural hazards or anthropic activity, that can generate or cause slopes failures or buildings instabilities.

In all the above-mentioned activities Ellegi srl uses the GBInSAR LiSALab technology that represents a real "break-through".

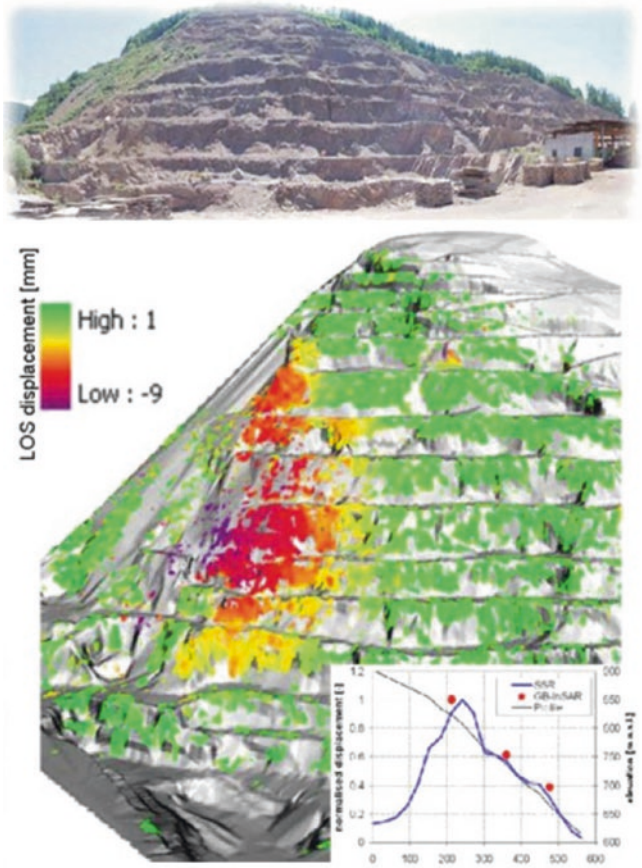

Fig. A.25 GBInSAR LiSALab technology quarry monitoring example and displacements' field comparison between the GBInSAR measurement and FEM model results

E. Srl
Como, Italy

B. Abolmasov et al. (eds.), *Progress in Landslide Research and Technology, Volume 3 Issue 1, 2024*, Progress in Landslide Research and Technology, https://doi.org/10.1007/978-3-031-55120-8

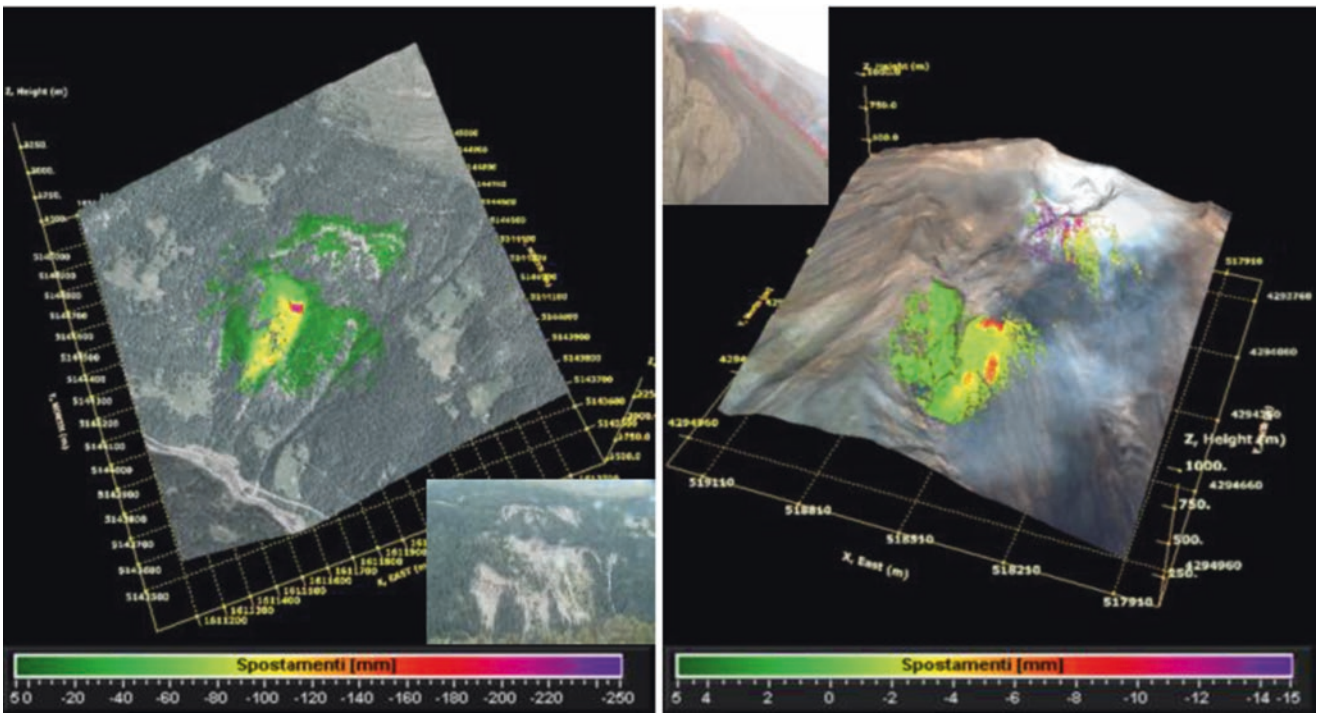

Fig. A.26 GBInSAR LiSALab technology result in monitoring a slope affected by a landslide (left) and a volcanic slope affected by deformation (right). Landslide or moving area mapping and boundaries identification is made easy by GBInSAR LiSALab technology

Chuo Kaihatsu Corporation

Lin Wang

Introduction

Chuo Kaihatsu Corporation (CKC) was founded in 1946, and has been aiming to become the "Only One" consultant for our customers. We engage in the hands-on work that will "Remain with the earth, Remain in people's hearts, and Lead to a prosperous future". We focus on road, river and dam engineering to flesh out industrial infrastructures specifically by means of geophysical/geotechnical/geological investigations, civil engineering surveys and project implementations. In recent years, we make significant efforts on earthquake disaster mitigation, sediment disaster prevention/mitigation and ICT information services. Many achievements of ours have already contributed to the mitigation of natural disasters such as landslides, earthquakes and slope failures in Japan, Asia and the Pacific Region. We aim to provide technological contributions so that a sustainable society will continue to develop in the future (Figs. A.27, A.28, A.29, and A.30).

Fig. A.27 Design for various structures

L. Wang
Chuo Kaihatsu Corporation, Tokyo, Japan
e-mail: wang@ckcnet.co.jp; https://www.ckcnet.co.jp/global;
https://www.ckcnet.co.jp/contactus/

B. Abolmasov et al. (eds.), *Progress in Landslide Research and Technology, Volume 3 Issue 1, 2024*, Progress in Landslide Research and Technology, https://doi.org/10.1007/978-3-031-55120-8

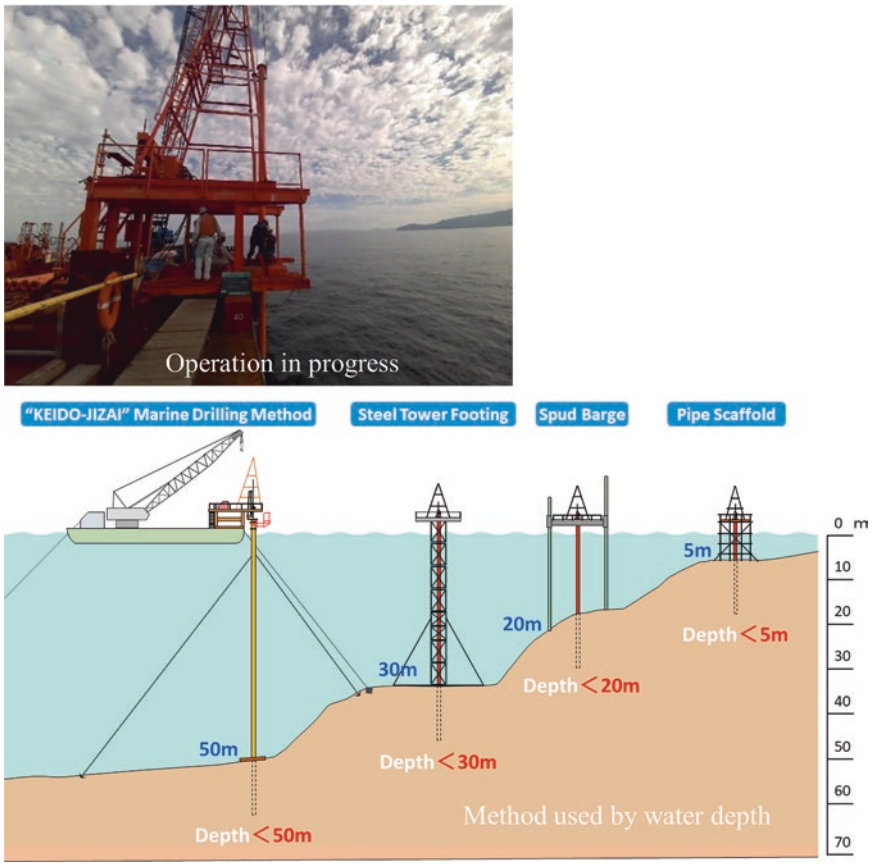

Fig. A.28 Deepwater drilling surveys

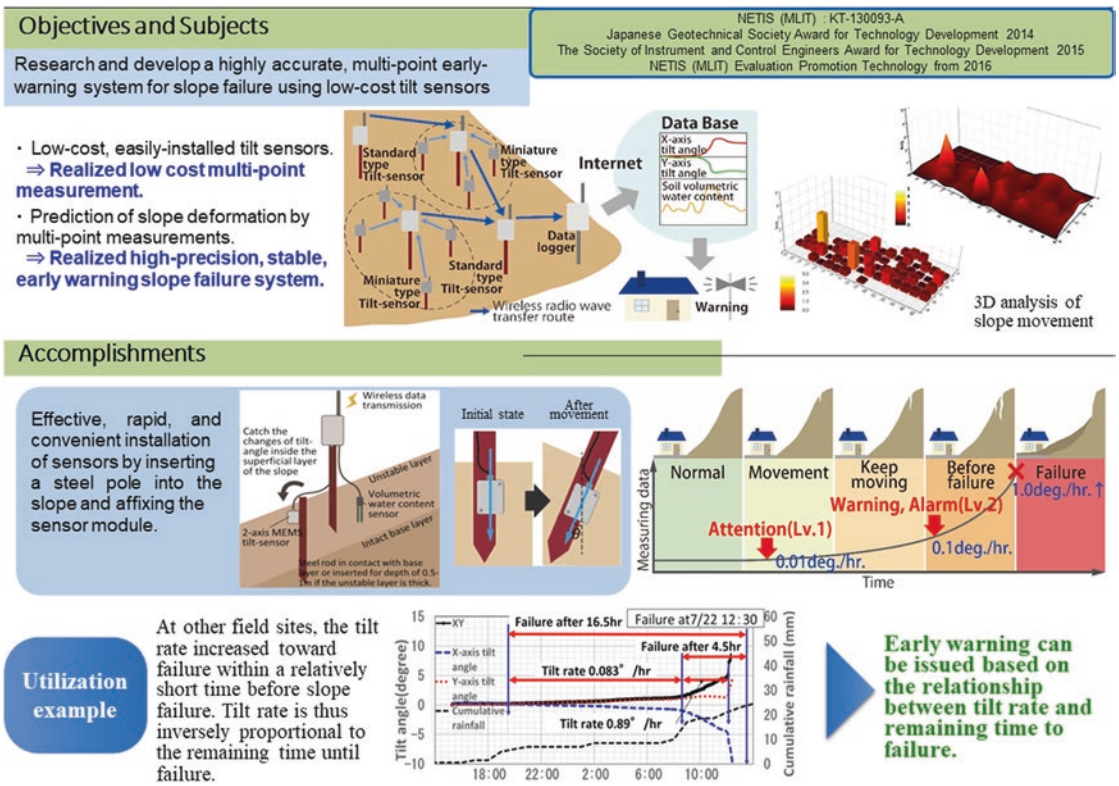

Fig. A.29 The early warning monitoring system of slope failure using multi-point tilt change and volumetric water content

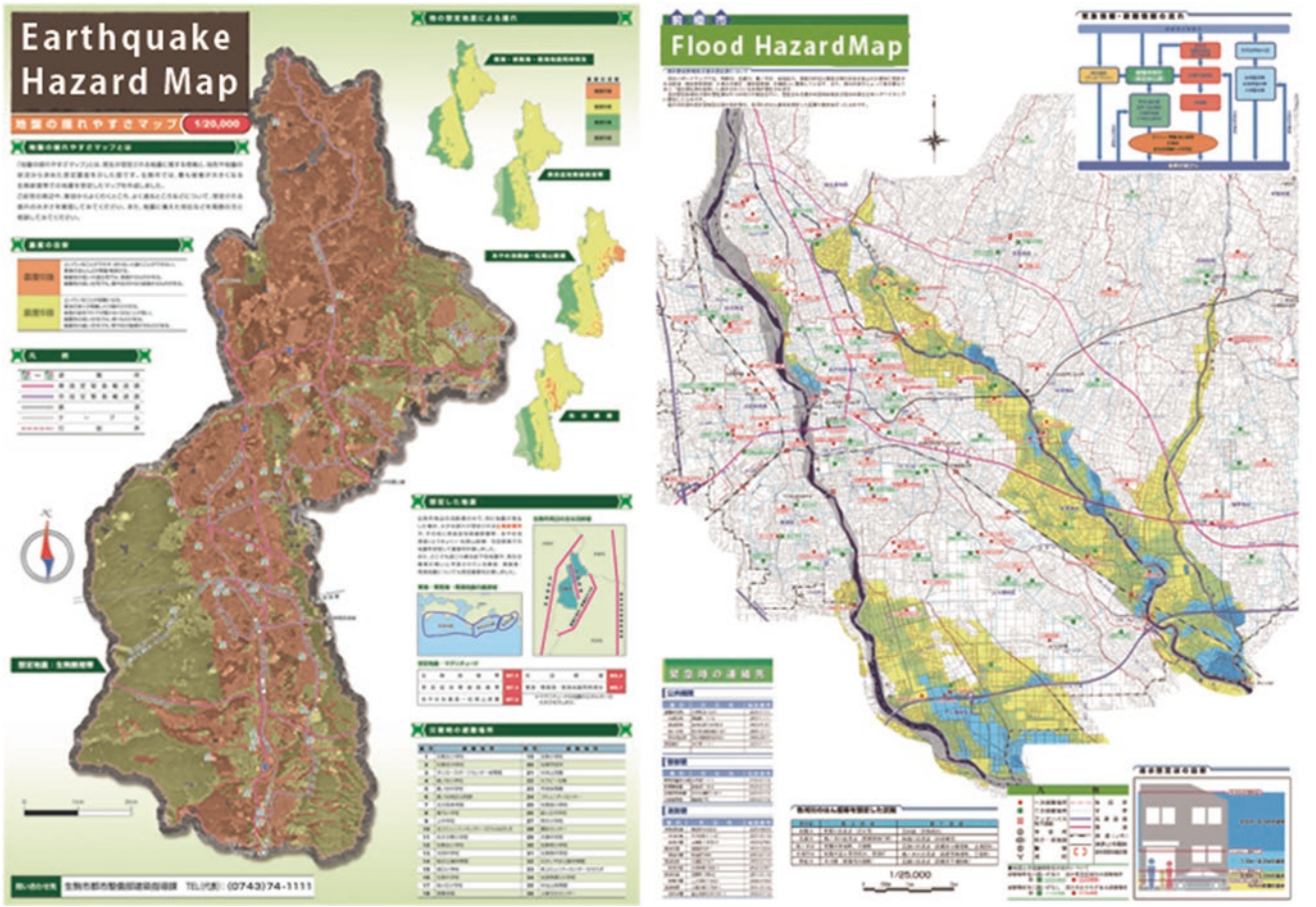

Fig. A.30 Making hazard map for sediment disaster, tsunami, flood, earthquake, liquefaction, etc.

Godai Kaihatsu Corporation

Godai Kaihatsu Corporation

Introduction

Ever since its foundation in 1965, Godai Kaihatsu Co. Ltd. a civil engineering consulting firm, has long been providing a variety of software and measures particularly for natural disaster mitigation. With its rich expertise in both civil engineering and information technology (IT), the company has its primary goal to address real-world needs of disaster mitigation. All the staff of Godai Kaihatsu Co. Ltd. feels it more than happy that their cutting-edge technologies help mitigate natural disasters (Figs. A.31, A.32, A.33, and A.34).

Godai Kaihatsu Corporation
Godai Kaihatsu Corporation, Kanazawa, Ishikawa, Japan
e-mail: pp-sales@godai.co.jp; https://www.soft.godai.co.jp/soft/

B. Abolmasov et al. (eds.), *Progress in Landslide Research and Technology, Volume 3 Issue 1, 2024*, Progress in Landslide Research and Technology, https://doi.org/10.1007/978-3-031-55120-8

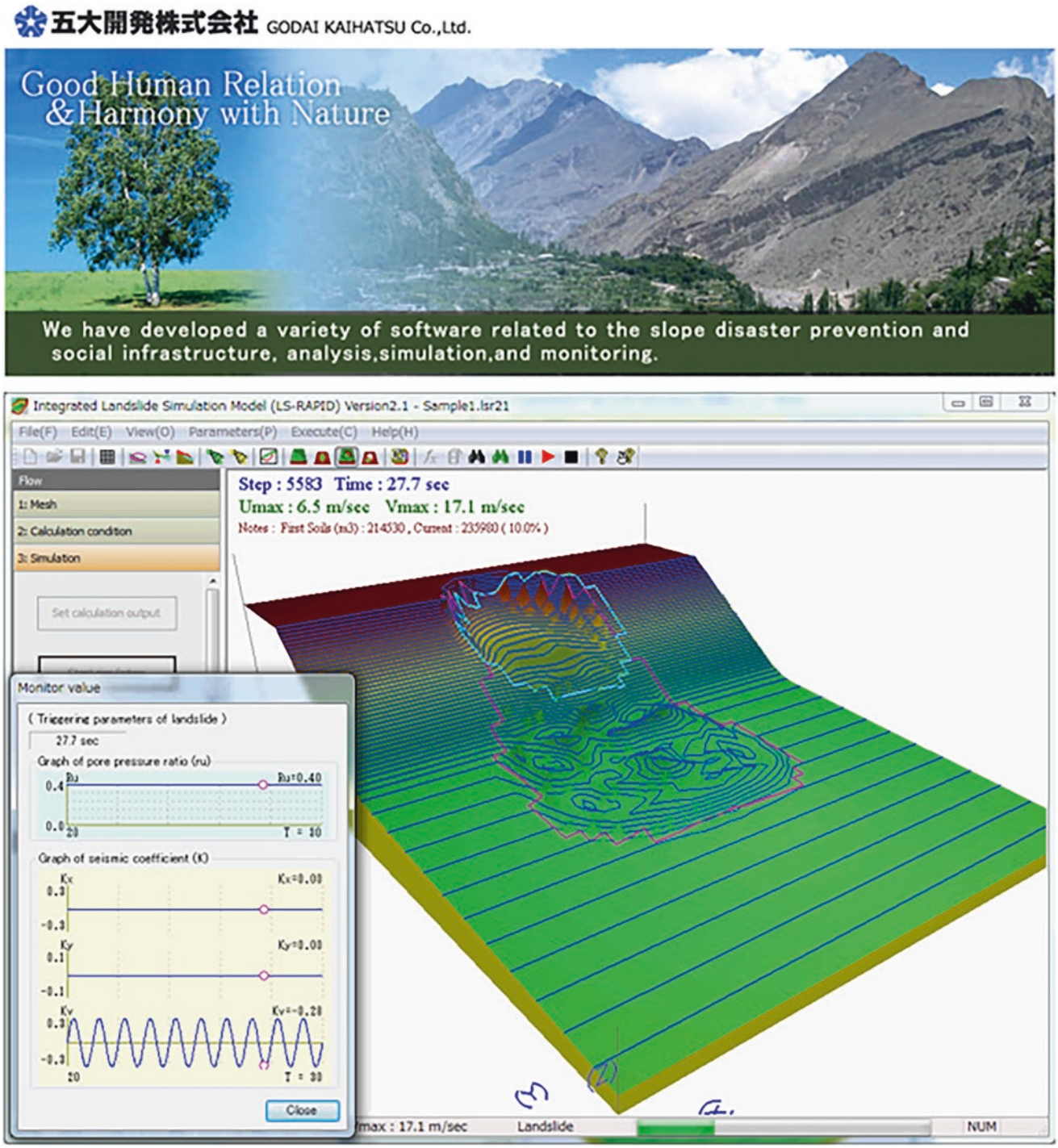

Fig. A.31 Integrated model simulating of earthquake & rain induced rapid landslides (LS-RAPID)

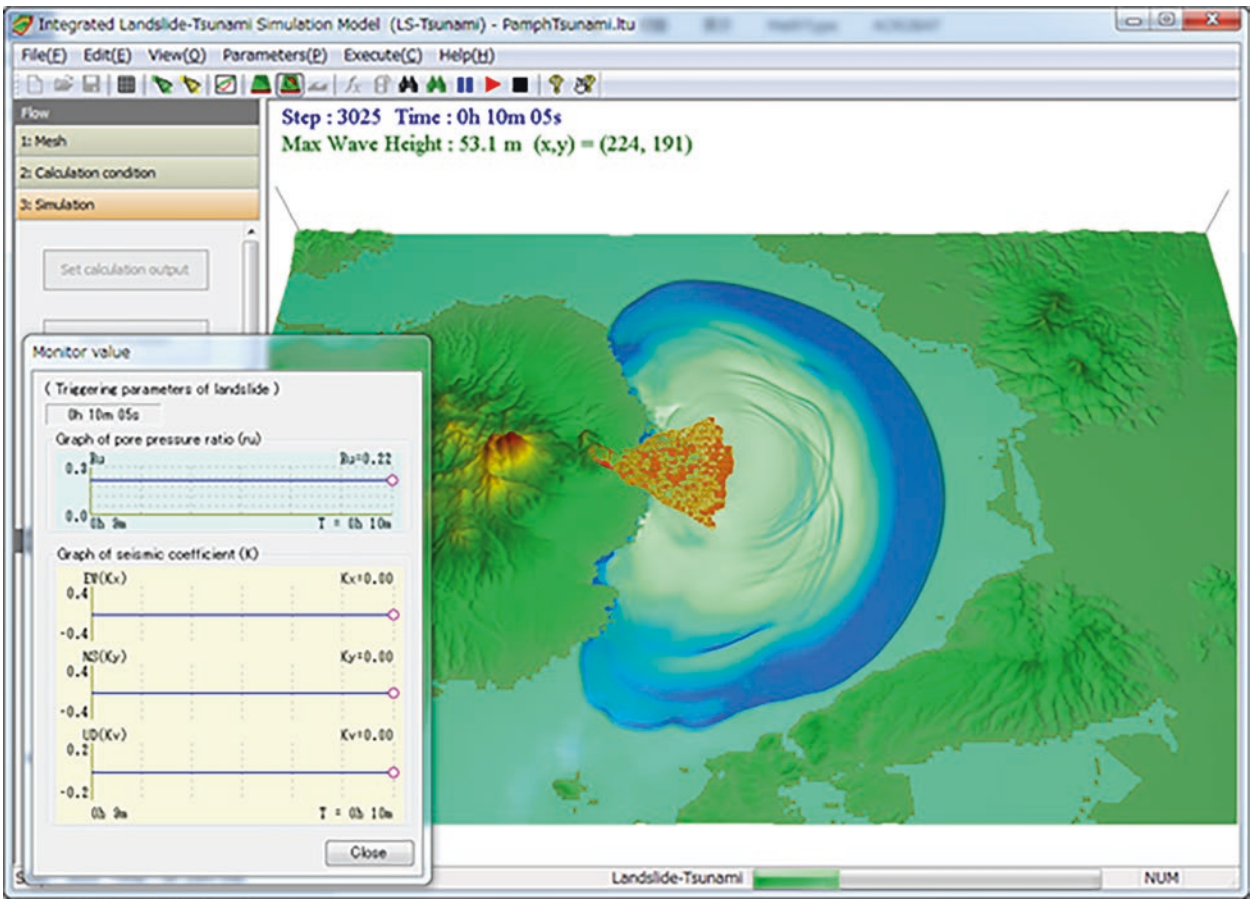

Fig. A.32 Tsunami model (LS-Tsunami)

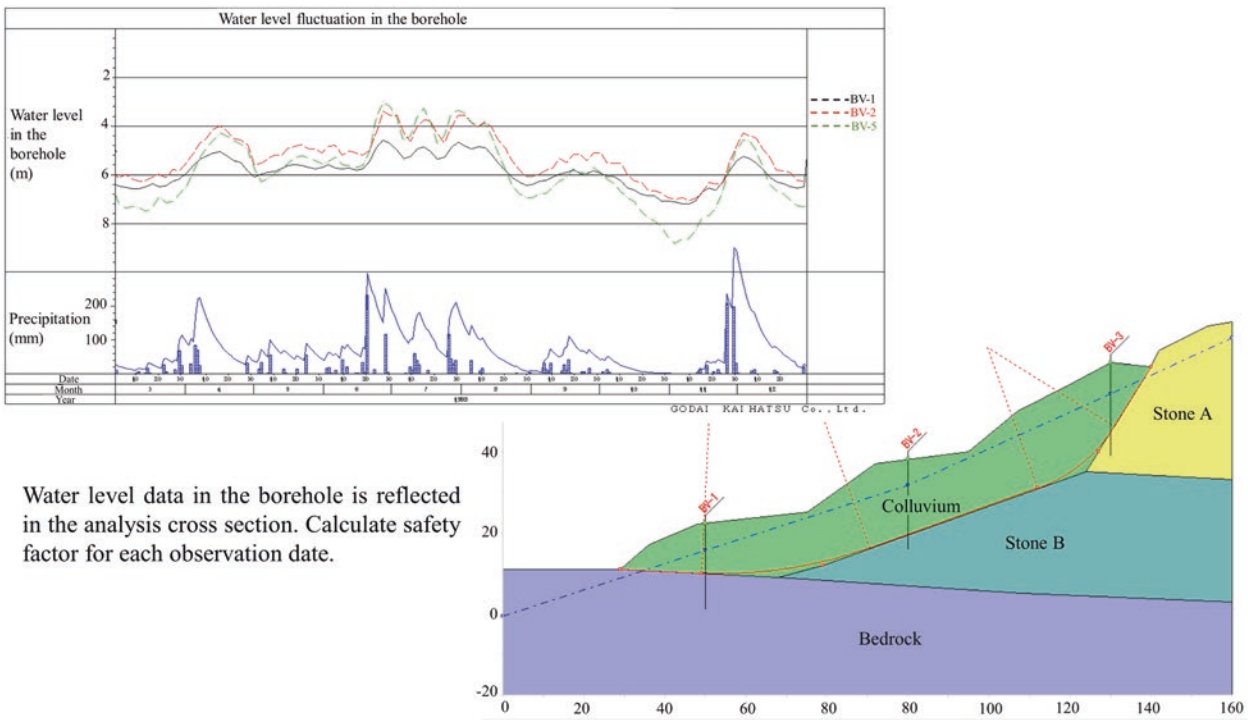

Fig. A.33 Power SSA PRO-Two-dimensional slope stability calculation of earthquake and rain induced landslide

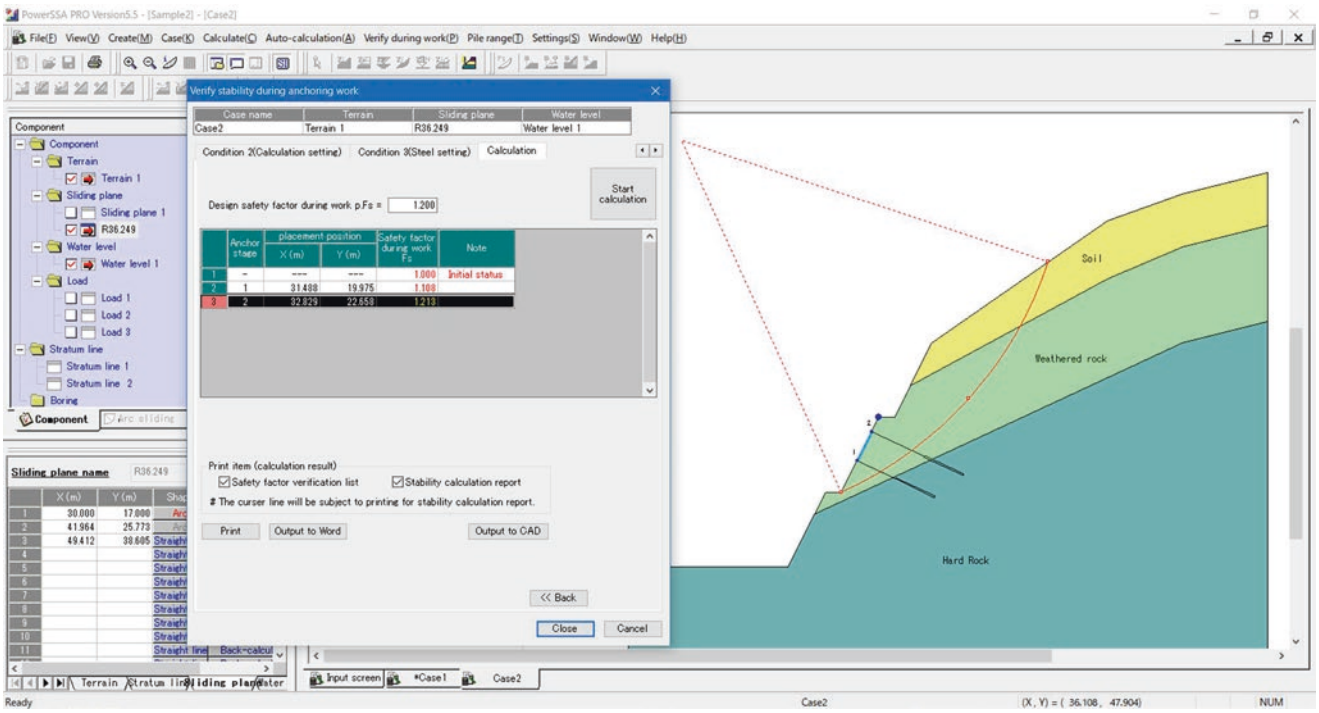

Fig. A.34 Anchor software-slope stability analysis for ground ancho

Kiso-Jiban Consultants Co. Ltd

Kaoru Hanai and Junichiro Odaka

Introduction

Since its establishment in 1953, Kiso-Jiban has been contributing on the development of social infrastructure as a "comprehensive construction consultant with strong geotechnical capabilities" in various situations, such as ground investigation, laboratory testing, analysis, civil structure design, etc. Kiso-Jiban has been working on the technological development for disaster prevention and mitigation against the recent exacerbation of natural disasters.

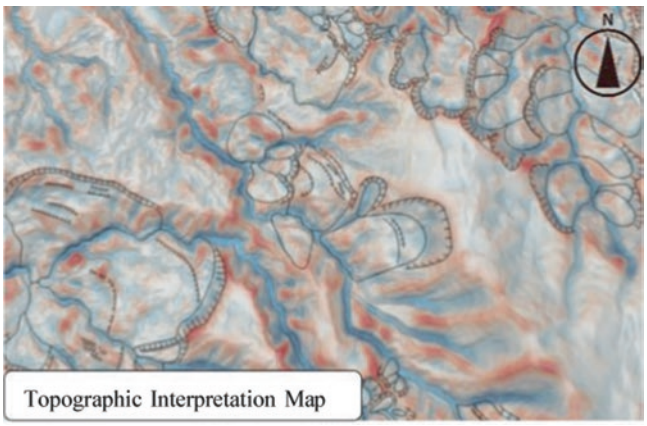

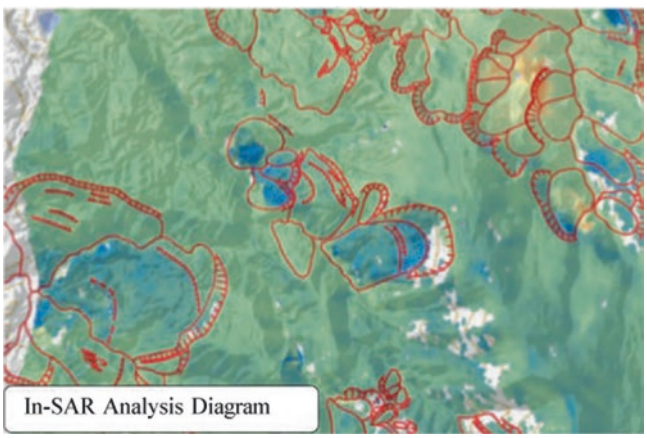

InSAR (Interferometric Synthetic Aperture Radar)

SAR is a technique that utilizes interference of radio waves for precise determination of distance. Kiso-Jiban has succeeded in estimation of both extent and rate of landslide movements by combining the topography interpretation and InSAR analysis.

GP (Gel-Push) Sampling

GP Sampling can collect gravelly soil, etc., which is difficult to be collected by conventional samplers, by using a highly-concentrated water-soluble polymeric gel. GP Sampling was introduced in ISO 22475-1: 2021 revised in October 2021 as Category A, which provides the highest quality soil samples.

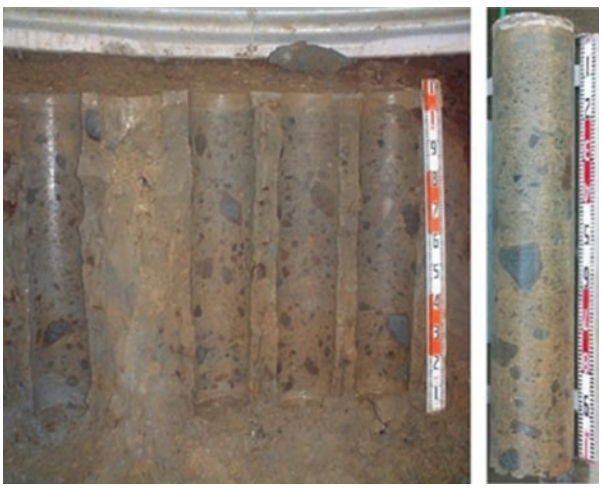

GP Sampling was performed in the disturbed soil mass right above the landslide surface (left) and the soil sample collected (right)

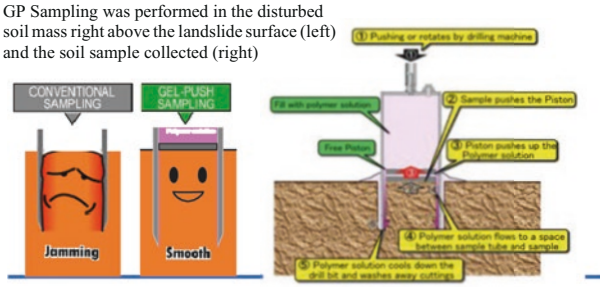

K. Hanai · J. Odaka
Kiso-Jiban Consultants Co. Ltd., Tokyo, Japan
e-mail: kisojiban-contactus@kiso.co.jp;
https://www.kisojiban.com/

B. Abolmasov et al. (eds.), *Progress in Landslide Research and Technology, Volume 3 Issue 1, 2024*, Progress in Landslide Research and Technology, https://doi.org/10.1007/978-3-031-55120-8

Inspection Technique for Disaster Danger Spots Using Mixed Reality (MR) Technology

MR (Mixed reality) is a technology that blends physical and digital worlds by superimposing 3D data and digital information on the real world as computer graphics.

Dangerous slopes with rockfall sources are spots where many unstable bedrocks and floating rocks exist. In many cases, approaching the inspection point on an outcrop is a difficult and dangerous task for investigators. Using MR technology makes it possible to realistically reproduce the outcrop situation at the site as a hologram. The outcrop situation can be safely inspected and confirmed without going to the site.

Slope Stability Analysis and Evaluation

Kiso-Jiban provides a wide range of numerical analyses related to slope stability evaluation. We have a wide range of analysis methods, from general two-dimensional limit equilibrium analysis to finite element analysis and analysis of rock masses with discontinuities, and we are challenging on the analysis that considers variability of ground and modelling uncertainty.

3D Rockfall Simulation

3D Finite Element Analysis

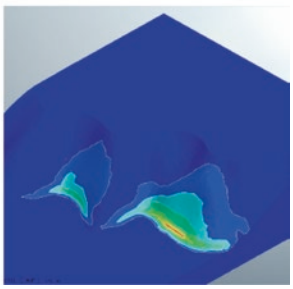

Kokusai Kogyo Co. Ltd

Kokusai Kogyo Co. Ltd.

Introduction

Kokusai Kogyo Co. Ltd. as a leading company of geospatial information technologies has long been providing public services with its comprehensive expertise to address real-world needs and cutting-edge measurement technologies. Kokusai Kogyo Co. Ltd. helps rebuild "Green Communities," which has been of our great concern in terms of "environment and energy," "disaster risk reduction" and "asset management". Kokusai Kogyo Co. Ltd. offers advanced and comprehensive analyses of geospatial information for developing new government policies, maintaining and operating social infrastructures safe and secure, and implementing low-carbon measures in cities. Influenced by the recent global climate change, extreme rainfall events have become more frequent worldwide and resultant hydro-meteorological hazards are creating more deaths and devastations particularly in many developing countries where effective advanced countermeasures are not readily available. Kokusai Kogyo Co. Ltd. is proud of its achievements in establishing resilient infrastructure systems and implementing effective monitoring/early warning systems in developing countries, which have long been helping reduce the risks from natural hazards (Figs. A.35, A.36, A.37, and A.38).

Fig. A.35 Our realtime hazard map reflects up-to-date information of soil natures and precipitations at landslide hazard sites, etc. that can constantly be changing, and evaluates area-wide hazard risk in real-time

B. Abolmasov et al. (eds.), *Progress in Landslide Research and Technology, Volume 3 Issue 1, 2024*, Progress in Landslide Research and Technology, https://doi.org/10.1007/978-3-031-55120-8

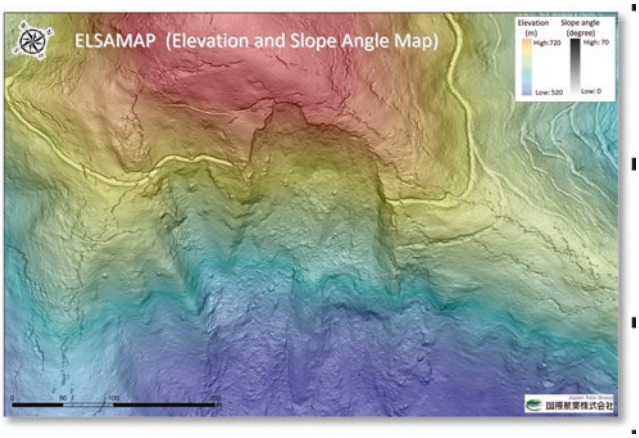

Fig. A.36 ELSAMAP is our cutting-edge 3D terrain visualization method allowing great geomorphological details to be visualized in one glance with gray-scaled slope inclinations and colored altitudes. ELSAMAP has been used to interpret micro-topographies, landslides and some other things

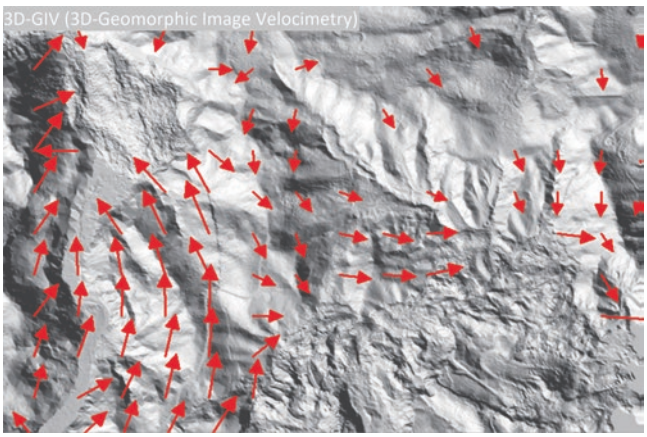

Fig. A.37 3D-GIV can help grasp the ground surface displacement caused by natural phenomena such as landslide by analyzing differences between digital geomorphic images obtained through ad hoc Airborne Laser Surveys

Fig. A.38 "Shamen-net" is a total monitoring system integrating GNSS and other monitoring device (Measurement precision: ± mm, on a real time basis)

OSASI Technos, Inc.

OSASI Technos, Inc.

Introduction

OSASI Technos, Inc. has been making its best efforts to develop its cutting-edge technologies for landslide early warning. Its unique compact and lightweight sensors making up the Landslide Early Warning System enable long-term monitoring of unstable landslide mass movements, precipitations, porewater pressure buildups, etc. in a remote mountainous area where commercial power is often unavailable. OSASI Technos, Inc. is also proud of its advanced technology to transfer observed data even in areas with poor telecom environments as proven in the successful implementations in South Asia. All staff members of OSASI Technos work together for mitigation of landslide disasters worldwide (Figs. A.39, A.40, A.41, and A.42).

OSASI Technos, Inc.
OSASI Technos, Inc., Kochi-shi, Kochi, Japan

B. Abolmasov et al. (eds.), *Progress in Landslide Research and Technology, Volume 3 Issue 1, 2024*, Progress in Landslide Research and Technology, https://doi.org/10.1007/978-3-031-55120-8

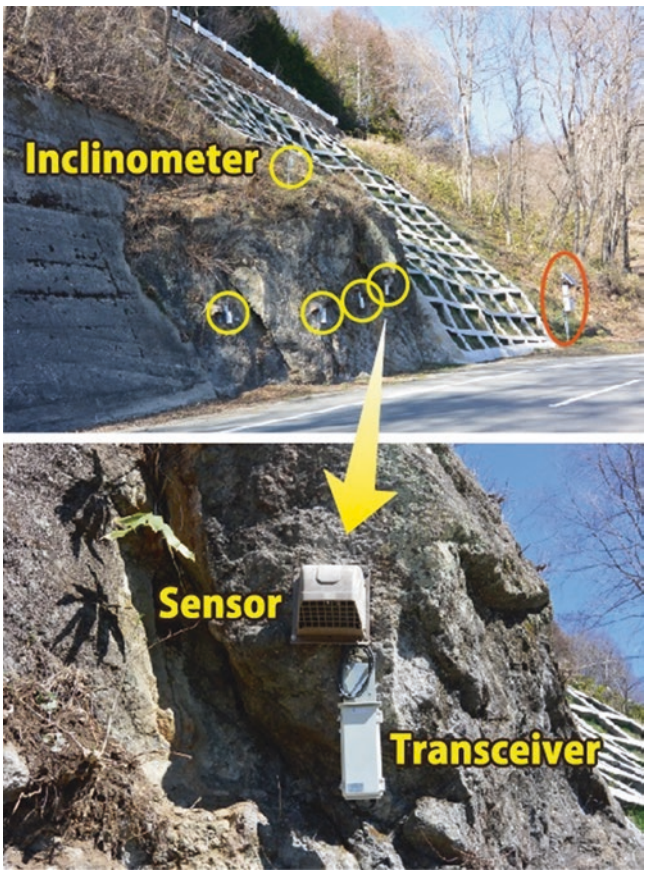

Fig. A.39 Bedrock slope monitoring (maintenance control)

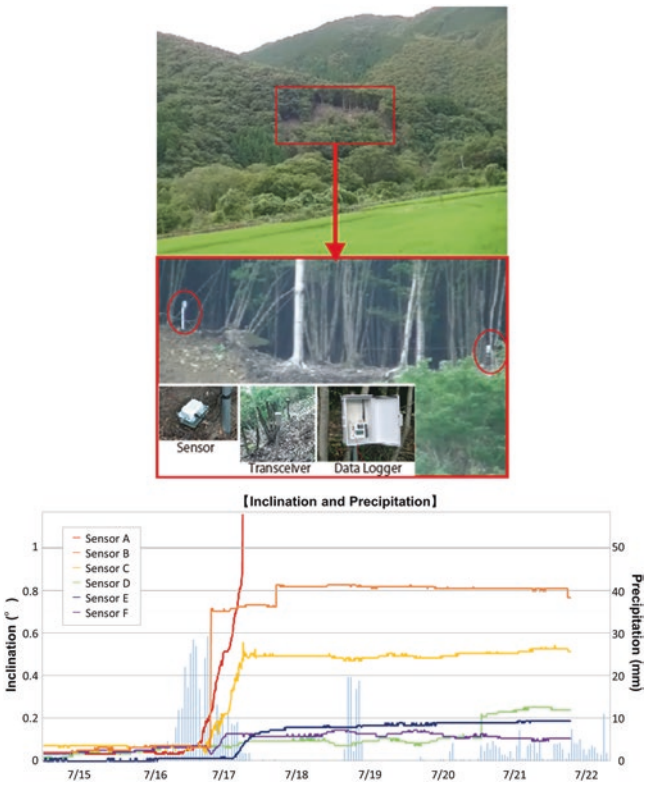

Fig. A.40 Measurement of the dynamic state of landslide using inclinometers with a wireless function

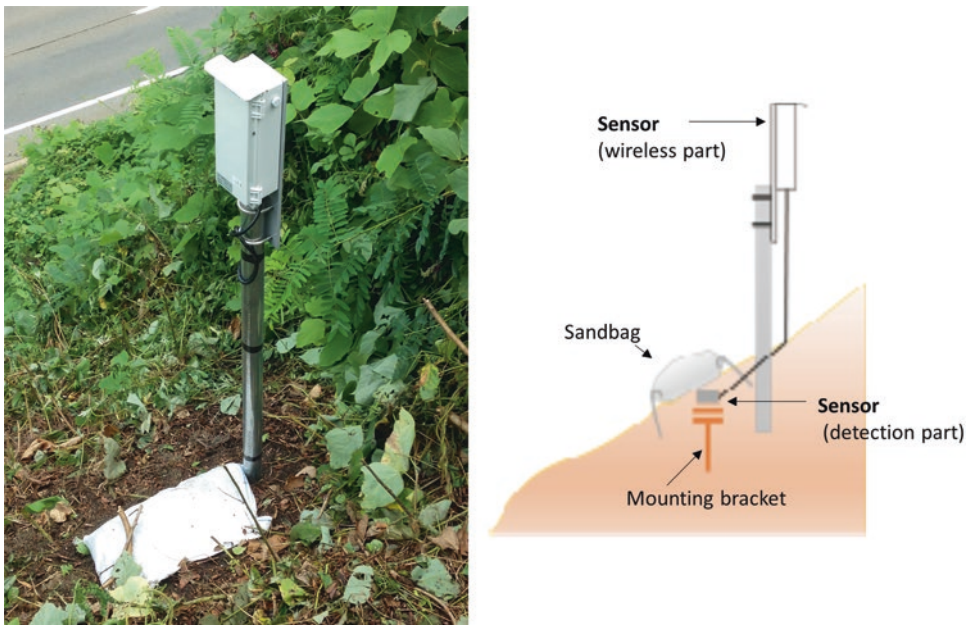

Fig. A.41 Example of sensor installation

Fig. A.42 Compact alarm device to alert local people to landslide risk

List of ICL Members

International Consortium on Landslides
An international non-government and non-profit scientific organization promoting landslide research and capacity building for the benefit of society and the environment
President: Željko Arbanas (University of Rijeka, Croatia)
Vice Presidents: Nicola Casagi (University of Florence, Italy), Faisal Fathani (Gadjah Mada University, Indonesia), David Huntley (Geological Survey of Canada, Canada), Biljana Abolmasov (University of Belgrade, Serbia), Giovanna Capparelli (University of Calabria, Italy), Chih-Chung Chung (National Central University, Chinese Taipei) Executive Director: Kaoru Takara (National Research Institute for Earth Science and Disaster Resilience, Japan), Treasurer: Kyoji Sassa (Prof. Emeritus, Kyoto University, Japan)

Country/Region	ICL Full member
Bosnia and Herzegovina	The Geotechnical Society of Bosnia and Herzegovina
Brazil	Center for Scientific Support in Disasters – Federal University of Parana
Canada	Geological Survey of Canada
	University of Alberta
China	Northeast Forestry University, Institute of Cold Regions Science and Engineering
	China University of Geosciences
	Chinese Academy of Sciences, Institute of Mountain Hazards and Environment
	Tongji University
	Shanghai Jiao Tong University
	Geotechnical Engineering Office, Civil Engineering and Development Department, Government of the Hong Kong Special Administrative Region
	Tsinghua University
	The State Key Laboratory of Geohazard Prevention and Geoenvironment Protection (SKLGP), Chengdu University of Technology
	Civil Engineering and Development Department, Geotechnical Engineering Office, Hong Kong
	The Hong Kong University of Science and Technology
	The University of Hong Kong
Colombia	Universidad Nacional de Colombia
Croatia	Croatian Landslide Group from Faculty of Civil Engineering University of Rijeka and Faculty of Mining, Geology and Petroleum University of Zagreb
Czech Republic	Charles University, Faculty of Science
Egypt	The American University in Cairo
Germany	Technische Universitat Darmstadt, Institute and Laboratory of Geotechnics
Georgia	Department of Geology of National Environmental Agency of Georgia
India	Amrita Vishwa Vidyapeetham, Amrita University
	National Institute of Disaster Management, New Delhi
Indonesia	Gadjah Mada University, Center for Disaster Mitigation and Technological Innovation (GAMA-InaTEK)
	Parahyangan Catholic University
	Agency for Meteorology, Climatology, and Geophysics of the Republic of Indonesia (BMKG Indonesia)
Italy	UNESCO Chair for the prevention and the sustainable management of geo-hydrological hazards - University of Florence
	ISPRA-Italian Institute form Environmental Protection and Research
	University of Calabria, DIMES, CAMILAB
	Istituto di Ricerca per la Protezione Idrogeologica (IRPI), of the Italian National Research Council (CNR)
	Centro di Ricerca CERI - Sapienza Università di Roma
	National Institute of Oceanography and Applied Geophysics - OGS, Italy
Japan	Kyoto University, Disaster Prevention Research Institute
	Japan Landslide Society
	International Consortium on Geo-disaster Reduction
	National Research Institute for Earth Science and Disaster Resilience

B. Abolmasov et al. (eds.), *Progress in Landslide Research and Technology, Volume 3 Issue 1, 2024*, Progress in Landslide Research and Technology, https://doi.org/10.1007/978-3-031-55120-8

Korea	Korean Society of Forest Engineering	
	National Institute of Forest Science	
	Korea Authority of Land & Infrastructure Safety	
	Korea Institute of Civil Engineering and Building Technology	
Mexico	Institute of Geography, National Autonomous University of Mexico (UNAM)	
Russia	Moscow State University, Department of Engineering and Ecological Geology	
	JSC "Hydroproject Institute"	
Serbia	University of Belgrade, Faculty of Mining and Geology	
Slovakia	Comenius University, Faculty of Natural Sciences, Department of Engineering Geology	
Slovenia	University of Ljubljana, Faculty of Civil and Geodetic Engineering (ULFGG)	
	Geological Survey of Slovenia	
Sri Lanka	Central Engineering Consultancy Bureau (CECB)	
	National Building Research Organization	
	Engineering Geology Research Group (EGRG), Department of Geology, University of Peradeniya	
Chinese Taipei	Landslide group in National Central University from Graduate Institute of Applied Geology, Department of Civil Engineering, Center for Environmental Studies	
	National Taiwan University, Department of Civil Engineering	
Thailand	Ministry of Agriculture and Cooperatives, Land Development Department	
	Asian Disaster Preparedness Center (ADPC)	
Ukraine	Institute of Telecommunication and Global Information Space	
United Kingdom	British Geological Survey	
USA & Nepal	California State University, Fullerton & Tribhuvan University, Institute of Engineering	
Viet Nam	Institute of Transport Science and Technology	
	Vietnam Institute of Geosciences and Mineral Resources (VIGMR)	
Country/Region	**ICL Associate member**	
Belgium	Liege University, Georisk and Environment (G&E) group	
China	State Key Laboratory of Geohazard Prevention and Geoenvironment Protection (Chengdu University of Technology)	
	State Key Laboratory of Plateau Ecology and Agriculture (Qinghai University)	
Czech Republic	Czech Geological Survey	
	Institute of Rock Structure and Mechanics, Department of Engineering Geology	
Italy	Department of Earth and Environmental Sciences, University Aldo Moro, Bari	
	University of Sannio, Department of Sciences and Technologies	
	Geotechnical Engineering Group (GEG), University of Salerno	
	Department of Earth and Environmental Sciences – University of Pavia	
	University of Chieti-Pescara, Department of Engineering and Geology	
	Federico II University of Naples, Department of Earth, Environmental and Resource Sciences	
	DIA – Università degli Studi di Parma	
	University of Urbino "Carlo Bo", Department of Pure and Applied Sciences	
	University of Turin	
Japan	Ehime University, Center for Disaster Management Informatics Research	
	Kochi University	
	National Institute of Maritime, Port and Aviation Technology	
North Macedonia	Macedonian Association for Geotechnics	
Russia	Russian State Geological Prospecting University n.a. Sergo Ordzhonikidze (MGRI-RSGPU)	
Slovenia	University of Ljubljana, Faculty of Natural Sciences and Engineering (UL NTF)	
Switzerland	Institute of Earth Sciences, Faculty of Geoscience and Environment/University of Lausanne	
USA	Iowa State University	
Country/Region	**ICL Supporter**	
Italy	IDS GeoRadar s.r.l.	
Japan	Marui & Co., Ltd., Osaka	Okuyama Boring Co., Ltd., Yokote
	Ohta Geo-Research Co., Ltd., Nishinomiya	Japan Conservation Engineers Co., Ltd., Tokyo
	Sabo Technical Center, Tokyo	GODAI Kaihatsu Corp., Kanazawa
	OYO Corporation, Tokyo	Kokusai Kogyo Co., Ltd., Tokyo
	OSASI Technos Inc., Kochi	NIPPON KOEI CO., LTD.
Chinese Taipei	Sinotech Engineering Consultants, Inc	

ICL Secretariat
Secretary General: Kyoji Sassa
International Consortium on Landslides, 138-1 Tanaka Asukai-cho, Sakyo-ku, Kyoto, 606-8226, Japan
Web: https://www.landslides.org/, E-mail: secretariat@landslides.org
Tel: +81 (75) 723 0640, Fax: +81(75) 950 0910

Index

B. Abolmasov et al. (eds.), *Progress in Landslide Research and Technology, Volume 3 Issue 1, 2024*, Progress in Landslide Research and Technology, https://doi.org/10.1007/978-3-031-55120-8